NANOSTRUCTURES: PHYSICS AND TECHNOLOGY

13th International Symposium

St Petersburg, Russia, June 20–25, 2005

Co-Chairs
Zh. Alferov
L. Esaki

PROCEEDINGS

Ioffe Institute
St Petersburg, 2005

Published by
Ioffe Physico-Technical Institute
26 Politekhnicheskaya, St Petersburg 194021, Russia
http://www.ioffe.ru/

Publishing license ΛP No 040971 of June 16, 1999.

ISBN 5-93634-017-1

The International Symposium "Nanostructures: Physics and Technology" is held annually since 1993. The first Symposium was initiated by Prof. Zh. Alferov and Prof. L. Esaki who are its permanent co-chairs. More detailed information on the Symposium is presented on the World Wide Web **http://www.ioffe.ru/NANO2005/**

The Proceedings include extended abstracts of invited talks and contributed papers to be presented at the Symposium. By tradition this book is published before the beginning of the meeting.

The volume was composed at the Information Services and Publishing Department of St Petersburg Physico-Technical Centre of RAS for Research and Education from electronic files submitted by the authors. When necessary these files were converted into the Symposium style without any text revisions. Only minor technical corrections were made by the composers.

Design and layout: N. Vsesvetskii
Desk editor: L. Solovyova

Information Services and Publishing Department
St Petersburg Physico-Technical Centre of RAS for Research and Education
8, bld. 3 Khlopina, St Petersburg 195220, Russia
Phones: (812) 534-58-58
Fax: (812) 534-58-50
E-mail: nano@mail.ioffe.ru

Printed in Russian Federation

This book is dedicated to the cherished memory
of Dr. **Boris Egorov**
who made an invaluable contribution
to organization and success of the Symposium

The Symposium is held under the auspices of
the Russian Academy of Sciences

Organizers

Scientific Engineering Center for Microelectronics at the Ioffe Institute

Ioffe Physico-Technical Institute

St Petersburg Physico-Technical Centre of RAS for Research and Education

in association with

the institutions of the Russian Academy of Sciences

Division of Physical Sciences

St Petersburg Scientific Center

Acknowledgments

The Organizers gratefully acknowledge the following
for their contribution to the success of the Symposium:

Russian Academy of Sciences

Russian Foundation for Basic Research

AIXTRON AG, Germany

Defense Advanced Research Projects Agency (DARPA)

European Office of Aerospace Research and Development of the United States Air Force

Air Force Office of Scientific Research

United States Air Force Research Laboratory

Location and Date

Symposium is held in St Petersburg, June 20–25, 2005.

Advisory Committee

G. Abstreiter (*Germany*)
Zh. Alferov (*Russia*)
Y. Arakawa (*Japan*)
A. Aseev (*Russia*)
G. Bastard (*France*)
D. Bimberg (*Germany*)
L. Eaves (*United Kingdom*)
L. Esaki (*Japan*)
S. Gaponov (*Russia*)
E. Gornik (*Austria*)
Yu. Gulyaev (*Russia*)
N. Holonyak Jr. (*USA*)
L. Keldysh (*Russia*)
G. Landwehr (*Germany*)
J. Merz (*USA*)
M. Shur (*USA*)
M. Skolnick (*United Kingdom*)
R. Suris (*Russia*)
B. Zakharchenya (*Russia*)

Programme Committee

R. Suris, Chair (*St Petersburg, Russia*)
V. Evtikhiev, Secretary (*St Petersburg, Russia*)

A. Andronov (*Nizhny Novgorod, Russia*)
N. Bert (*St Petersburg, Russia*)
C. Chang-Hasnain (*Berkeley, USA*)
A. Chaplik (*Novosibirsk, Russia*)
V. Dneprovskii (*Moscow, Russia*)
V. Dubrovskii (*St Petersburg, Russia*)
Yu. Dubrovskii (*Chernogolovka, Russia*)
B. Egorov (*St Petersburg, Russia*)
A. Gippius (*Moscow, Russia*)
S. Gurevich (*St Petersburg, Russia*)
S. Ivanov (*St Petersburg, Russia*)
Yu. Kopaev (*Moscow, Russia*)
P. Kop'ev (*St Petersburg, Russia*)
Z. Krasil'nik (*Nizhny Novgorod, Russia*)
V. Kulakovskii (*Chernogolovka, Russia*)
M. Kupriyanov (*Moscow, Russia*)
X. Marie (*Toulouse, France*)
I. Merkulov (*St Petersburg, Russia*)
V. Panov (*Moscow, Russia*)
O. Pchelyakov (*Novosibirsk, Russia*)
E. Poltoratskii (*Moscow, Russia*)
H. Sakaki (*Tokyo, Japan*)
N. Sibel'din (*Moscow, Russia*)
M. Stutzmann (*Garching, Germany*)
V. Timofeev (*Chernogolovka, Russia*)
V. Volkov (*Moscow, Russia*)
L. Vorobjev (*St Petersburg, Russia*)

Organizing Committee

M. Mizerov, Chair (*Center for Microelectronics*)
B. Egorov, Secretary (*Ioffe Institute*)
O. Lashkul (*St Petersburg Scientific Center*)
D. Donskoy (*St Petersburg Scientific Center*)
G. Mikhailov (*St Petersburg*)
N. Sibel'din (*Lebedev Physical Institute*)
E. Solov'eva (*Ioffe Institute*)
V. Zayats (*Division of Physical Sciences*)

Award Committee

Zh. Alferov, Chair (*Russia*)
Y. Arakawa (*Japan*)
D. Botez (*USA*)
G. Eisenstein (*Israel*)
L. Esaki (*Japan*)
J. Harris (*USA*)
M. Heuken (*Germany*)
L. Keldysh (*Russia*)
R. Suris (*Russia*)
V. Timofeev (*Russia*)

Contents

Quantum Wires and Quantum Dots

Spin Related Phenomena in Nanostructures

Lasers and Optoelectronic Devices

Microcavity and Photonic Crystals

Metal Nanostructures

Tunnelling Phenomena

Transport in Nanostructures

Nanostructure Devices

Infrared and Microwave Phenomena in Nanostructures

Si-Ge Based Nanostructures

Wide Band Gap Nanostructures

Nanostructure Technology

Excitons in Nanostructures

Nanostructure Characterization and Novel Atomic-scale Probing Techniques

2D Electron Gas

Nanostructures and Life Sciences

Closing Plenary Session

Unprinted Papers

The papers listed below are included in the Symposium Programme, but not printed in the Proceedings, as the authors had not submitted electronic files in due time.

OPS.01pl *Zh. Alferov*
From molecular generators to quantum dot lasers

OPS.02pl *E. Gornik*
Generation of a plasma instability in semiconductor quantum structures

OPS.03pl *Y. Arakawa*
Advances in nanophotonic devices with quantum dots and photonic crystal

OPS.04pl *E. Kapon*
Site-controlled quantum wires and dots grown on nonplanar substrates: physics and applications

QWR/QD.16p *K. S. Zhuravlev*, D. D. Ree, V. G. Mansurov, A. Yu. Nikitin, A. K. Gutakovskiy and Ph. Vennegues
Growth and photoluminescence of wurtzite gan quantum dots in AlN matrix

SRPN.05i *R. Fereira*
Energy and spin relaxation in semiconductor quantum dots

LOED.06o *D. L. Huffaker*, G. Balakrishnan, S. H. Huang, A. Kosakhlagh, P. Rotella, A. Amtout, S. Krishna, L. R. Dawson and C. P. Hains
2 μm laser on Si(100) using AlSb quantum dot nucleation

LOED.19p *O. Smolski*, E. Johnson, L. Vaissie and J. O. Daniel
Semiconductor lasers with monolithically integrated diffractive optical elements

MPC.08p *A. V. Baryshev*, K. Nishimura, H. Uchida, and M. Inoue
Light propagation in the conjugate opal photonic crystal

TP.04p *P. I. Arseev* and N. S. Maslova
Effects of electron-phonon interaction in tunneling processes in heterostructures

IRMP.01i *K. Hirakawa*
Dispersive terahertz gain of non-classical oscillator: Bloch oscillation in semiconductor superlattices

IRMP.09p O. P. Pchelyakov, V. V. Preobrazhenskii, M. A. Putyato, *A. A. Kovalyov*, N. N. Rubtsova, E. Sorokin, and I. T. Sorokina
GaSb/InGaAsSb/GaSb single and multiple quantum wells: optical properties engineering and application

WBGN.20p Hsiang-Chen Wang, Yen-Cheng Lu, Cheng-Yen Chen, Fang-Yi Jen and *C. C. Yang*
Ultrafast carrier dynamics in InGaN with nano-clustered structures

NT.01i *J. Harris*
(GaIn)(NasSb) MBE growth and heterostructures devices

NT.10p *A. W. Hassel*, B. B. Rodriguez, S. Milenkovic and A. Schneider
Directionally solidified eutectics as a route for the formation of self organised nanostructures

AIXTRON Young Scientist Award

In 1999, the Symposium Programme Committee and the Board of AIXTRON AG (Germany) established a special award to honour a young scientist who will present at the Symposium the best paper in the field of solid state nanostructures. The award comprises a diploma and since 2004 a $1000 reward sponsored by AIXTRON.

The AIXTRON Young Scientist Award recipients are:

1999 **Alexey R. Kovsh**, Ioffe Institute, St Petersburg, Russia
2000 **Thomas Gruber**, Physikalisches Institut, Universität Würzburg, Würzburg, Germany
2001 **Ivan Shorubalko**, Department of Solid State Physics, Lund University, Lund, Sweden
2002 **Scott Kennedy**, Department of Electrical and Computer Engineering, University of Alberta, Edmonton, Canada
2003 **Sergey A. Tarasenko**, Ioffe Institute, St Petersburg, Russia
2004 **Ivan A. Dmitriev**, Ioffe Institute, St Petersburg, Russia[1]

Dr. Ivan Dmitriev
became the recipient of AIXTRON Award for the presentation of the paper:

Quantum cascade laser based on quantum dot superlattice

Co-author: *R. A. Suris*.

Ivan Dmitriev was born February 6, 1975, in St Petersburg. **1989–1991** Lyceum "Physical-Technical School". **1997** MS degree in Solid State Physics from Physics and Technology Department of St Petersburg State Polytechnical University. **2003** PhD in Semiconductor Physics from Ioffe Institute; PhD thesis: *Electrical properties of quantum dot superlattices*. **2000–present** Research fellow at the Department of Theoretical Bases of Microelectronics at the Ioffe Institute, St Petersburg, Russia.

Current research interests:

Quantum transport in low-dimensional nanostructures out of equilibrium. Transport properties of regular arrays of quantum dots in a strong electric field: electronic spectrum/Stark localization; Bloch oscillations; resonance intersubband tunneling; possibility of cascade lasing; electronic relaxation mechanisms in quantum dots, including polaronic effects, multi-phonon processes and anharmonic decay; combined influence of disorder and interaction on transport properties of quantum dot superlattices.

Quantum/quasiclassical magnetotransport in a 2D electron gas irradiated by microwaves: magnetooscillations in photo/dynamical conductivity and compressibility; transport in 'zero-resistance states' emerging under certain conditions at higher microwave power; relativistic effects near the cyclotron resonance.

Awards:

2002 Prize for the Best Research on the International Workshop Frontiers in Electronics, USA, 6–11 January 2002
2001 Ioffe Institute Prize for Junior Scientists for the Best Research of a Year
1999 Prize for the Best Research on the Russian National Conference on Physics of Semiconductors and Semiconductor Opto- and Nanoelectronics for Junior Scientists, St Petersburg, 1999

[1] Current affiliation: Institut für Nanotechnologie, Forschungszentrum Karlsruhe, Germany

13th Int. Symp. "Nanostructures: Physics and Technology"
St Petersburg, Russia, June 20–25, 2005

Optical spectroscopy of 2D nanoislands in quantum wells: lateral island profile and nature of emitting states

A. Reznitsky[1], A. Klochikhin[1,2], S. Permogorov[1] and C. Klingshirn[3]

[1] Ioffe Physico-Technical Institute, St Petersburg, Russia
[2] Nuclear Physics Institute, 188350, St Petersburg, Russia,
[3] Institut für Angewandte Physik, Universität Karlsruhe (TH), 76128 Karlsruhe, Germany

Abstract. Results of experimental study of photoluminescence (PL) and PL excitation (PLE) spectra of MBE grown single quantum wells (QWs) formed by insertion of few CdSe monolayers in ZnSe matrix are reviewed. PL spectra of such quantum objects originate from the luminescence of CdSe-rich nano-islands. Two types of island emitting states, namely, ground and metastable ones contribute to the low- and high-energy parts of the PL band, respectively. An interplay between these contributions is responsible for the anomalous temperature dependence of the PL band maximum position. PLE spectra of ground and metastable states have strongly differing character at excitation below some characteristic energy E_{ME}. This energy is identified as the exciton percolation threshold. The optical orientation and optical alignment experiments at resonant excitations allow to elucidate the nature of the two types of the emitting states. Theoretical model of the absorption spectra of emitting island states is presented and practical application of the model for the characterization of the island lateral concentration profiles is reported.

1. Introduction

At present it is well known that at epitaxial growth of QWs formed by the solid solutions a strong mismatch of the lattice constants of solution components acts as a driving force leading to inhomogeneous distribution of solvent atoms over the QW plane. As a result, the regions of nanometer size appear in QW, in which the content of the narrow-gap solution component essentially exceeds the average QW value. Depending on the growth conditions and/or post–growth treatment these regions can have a form of planar islands (called also 2D discs) [1–4], or 3D dot-like structures (see, for example, [5]) or include both kinds. Nowadays, the most reliable and comprehensive structure characterization of these objects can be obtained with a high-resolution transmission electron microscopy (HRTEM). In this talk we review the recent applications of optical spectroscopy for the characterization of the electronic states of islands forming the emission spectra of these quantum objects. As we shall see, the optical spectroscopy of island states in QWs gives an important information on the nature of electronic states and its relaxation properties and opens a way for simple and non-destructive characterization of the ensemble of islands in such quantum objects.

In what follows we summarize the results obtained for QWs with planar nanoislands. We shall illustrate the model description of exciton localization in such objects by experimental results obtained for ZnSe/ZnCdSe/ZnSe heterostructures, since these systems are most developed technologically and most studied experimentally. The main experimental results for these systems obtained by different research groups are in fairly good agreement [1–5].

Since all epitaxial growth techniques are essentially non-equilibrium, the structural characteristics of QWs in particular cases strongly depend on the growth conditions. We studied the epitaxial samples grown by (i) MBE technique with CdS-compound as a Cd source and elemental Se source [1], (ii) conventional MBE [2], and (iii) by multi-cycle migration enhanced epitaxy deposition of CdSe (below 0.5 ML per cycle) in ZnSe matrices with the different growth interruption times after each Cd and Se pulses [3,6]. The structure of most samples used in experiments or samples grown in similar conditions were characterized by HRTEM and the corresponding data can be found in Refs. [1,2,6].

2. PLE spectra of QWs with islands: two types of the emitting states

In Fig. 1 the PLE spectra for different detection energies within the PL band are presented. Being normalized at excitation energies slightly below the barrier exciton, they are diverging below the energy E_{ME} identified as exciton mobility edge in the QW with nano-islands [7]. Similar behavior of the PLE spectra was also detected for other samples with Cd-enriched islands in QWs. The depth of potential well of a quantum island, which is the difference between the emission energy and threshold energy E_{ME}, has an order of 0.1–0.3 eV in the samples under study. Obtained potential well depths and the island sizes estimated from HRTEM allow to calculate the exciton wave-functions. The extension of wave functions outside the islands is much smaller than the mean inter-island distance, thus it can be concluded that the most part of islands is spatially isolated.

The behavior of the PLE spectra shown in Fig. 1 allows to conclude that two different types of emitting states with essentially different relaxation rates contribute the PL band. The characteristic feature of PLE spectra of the states on the high-energy side of PL band is the strong dependence on the detection energy. The oscillating structure with the period close to the optical phonon energy is detected for these states (Fig. 1). Such behavior indicates that the corresponding part of PL band is due to the emission of excited states of the islands which are subjected to further energy relaxation to ground states. Relaxation rates of these states strongly depend on the temperature, and at low temperatures they are metastable [9]. On the other hand, the PLE spectra of the states forming the low energy part of the PL band do not depend on the detection energy, which indicates that these states have no ways for further relaxation and, therefore, are the ground states of islands. Lifetimes of

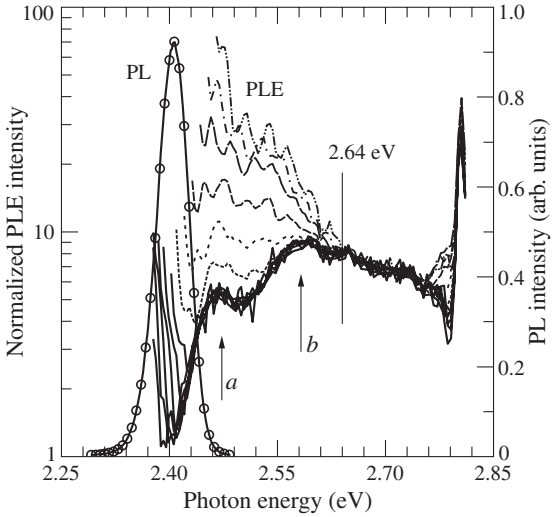

Fig. 1. PL spectrum at above ZnSe barrier excitation (solid line with symbols) and normalized PLE spectra for different detection positions inside the PL band separated by 10 meV: six spectra for detection in spectral range 2.34–2.39 eV (solid lines) and six spectra for the range 2.40–2.45 eV (dashed-dotted lines). All spectra are obtained at $T = 5$ K. Exciton mobility threshold E_{ME} at 2.64 eV is indicated by vertical solid line.

these states are governed by the inter band recombination processes. The fast increase of relaxation rate of the metastable states with temperature leads to depopulation of these states and to the low-energy shift of PL band (see insert to Fig. 2). With further increase of temperature the establishment of the equilibrium between metastable and ground states of the islands occurs, which results in high-energy shift of the PL band maximum. This explains the anomalous ("S-shape") behavior of the PL band maximum.

The low-temperature PL spectrum (curve 1 in Fig. 2) is a superposition of emission of ground and metastable states averaged over the island ensemble. Taking into account that the processes responsible for the red-shift of the band maximum

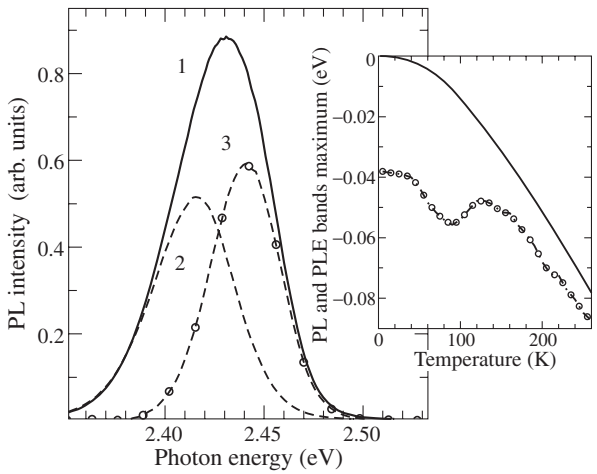

Fig. 2. PL spectra at above ZnSe barrier excitation at $T = 2$ K and 100 K (solid line 1 and dashed line 2, respectively). Line 3 with symbols is the difference between bands 1 and 2. Insert: temperature dependence of the PL band maximum (solid line with symbols) and that of PLE maximum (solid line) for the same sample. Spectral position of low energy PLE band maximum at $T = 2$ K is used as a point of reference.

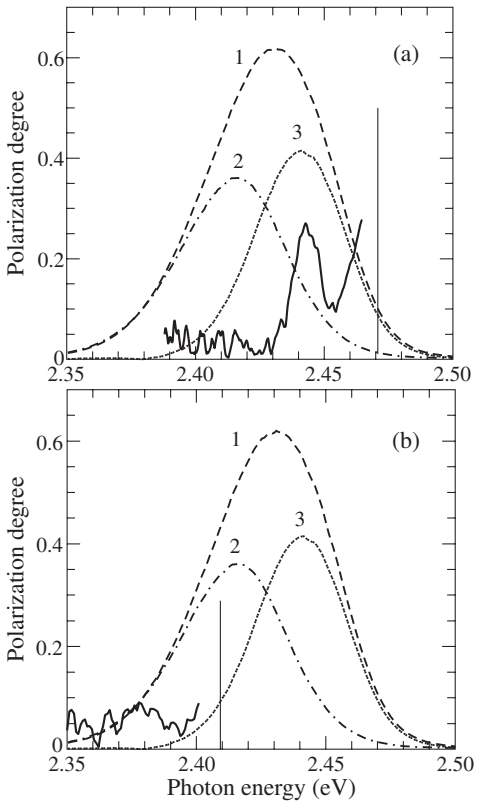

Fig. 3. Solid lines: Spectra of optical alignment rat resonant excitations for differentenergies (shown by solid vertical lines): 2.471 eV (a) and 2.409 eV (b). Dashed lines: PL band at above ZnSe band gap excitation (curve 1). Subbands due to recombination through ground (curve 2) and metastable (curve 3) states are shown for convenience.

occur in the temperature range where the equilibrium population of the excited states is negligible, the PL spectrum corresponding to the minimum of the S-shape dependence (curve 2 in Fig. 2) can be considered as the spectrum of the ground island states and the difference between these two spectra (curve 3 in Fig. 2) as the spectrum of the metastable states.

3. Polarization of resonantly excited PL spectra as a clue to the nature of emitting states

In order to elucidate the nature of metastable and ground states of the islands, the optical orientation and optical alignment experiments at resonant excitation at low temperature were performed. It was found that at resonant excitation of the island states by linear polarized light the resulting emission of the metastable states shows a considerable degree of corresponding polarization (optical alignment, see Fig. 3a). This indicates that the metastable states have an exciton nature and are populated as a result of cascade energy relaxation of localized excitons originally excited within the island. In distinction, at resonant linearly polarized excitation of the ground states the linear polarization of the emission is not observed (Fig. 3b). At the same time, the circular polarization at circularly polarized excitation (optical orientation) was observed in both cases (not shown here).

The obtained polarization characteristics of the emission can be explained if we assume that a considerable part of CdSe islands in ZnSe matrix contains extra electrons (both compounds are unintentionally weakly n-doped) and that the

deepest island states represent mostly the ground states of trions. This assumption is in agree with the results of magneto-optical study of single narrow lines detected in μ-PL measurements [8]. In turn, the metastable states in the charged island correspond to the exciton states in local potential island minima spatially separated from the absolute minimum occupied by excess electron.

4. Lateral concentration shape and exciton absorption spectra of islands

The PLE spectra of the states forming the low energy part of the PL band do not depend on the detector position. This fact indicates that the PLE spectra of these states can be considered as the absorption spectrum of the ensemble of island states participating in the emission spectrum. Two maxima a and b clearly seen in Fig. 1 are a common feature of the spectra of all samples under study. However, its relative intensity depends on the growth conditions and post-growth treatment (Fig. 4). For these reasons they cannot be attributed to the heavy and light hole excitons. An island arises as a result of in QW plane deviation of the Cd distribution from the average value $C(\vec{\rho}) = \overline{C}+\delta C(\vec{\rho})$. Taking now the value $E(\overline{C})$ as the point of reference for the energy, we introduce the deviation $\delta E(\vec{\rho}) = E(C(\vec{\rho}))-E(\overline{C})$, which describes the lateral potential configuration of the island.

In order to simulate the experimental absorption spectra of the island states we have considered [9] the model island potential $\delta E(\rho = |\vec{\rho}|)$ corresponding to the following deviations of the Cd concentration $\delta C(\rho)$ in (x,y) plane of QW

$$\delta C_{\rm bas}(\rho) = \delta C_{\rm max}\left\{\Theta(R_1-\rho) + \frac{\Theta(\rho-R_1)}{\cosh^2[(\rho-R_1)/R_2]}\right\} \quad (1)$$

where $\Theta(X)$ is the theta-function. In Eq. (1) the ratio between R_2 and R_1 defines the "basin"-like form of potential. Insert in Fig. 4 presents the radial shapes of the island potentials given by Eq. (1).

The characteristic two maxima of spectral DOS corresponding to both deepest and shallowest states appear for the basin-like potential if the values of R_1 and R_2 parameters are of the same order. Two others limiting cases ($R_2/R_1 \ll$ or $\gg 1$) produce only one maximum corresponding to the deepest or the shallowest states, respectively. Lateral potential shapes obtained by the best fit of their absorption spectra for islands in different samples are in qualitative agreement with the lateral island profiles obtained by HRTEM technique.

5. Summary

We have shown that the coexistence of ground and metastable states within particular island is a characteristic property of MBE grown QWs with islands and reflects nonequlibrium character of epitaxial growth. The existence of metastable features of the emitting states in islands can be proved by the very fact of anomalous ("S-shape") temperature behavior of PL band maximum, which was observed in different QWs based not only on II–VI, but also on III–V compounds. It seems very probable that even for nominally undoped barriers, QWs and quantum dots an appreciable part of islands contains an extra charge due to background doping of the heterostructure constituents. As a result, the deepest states of the islands represents mostly the ground state of trions, while the metastable states in

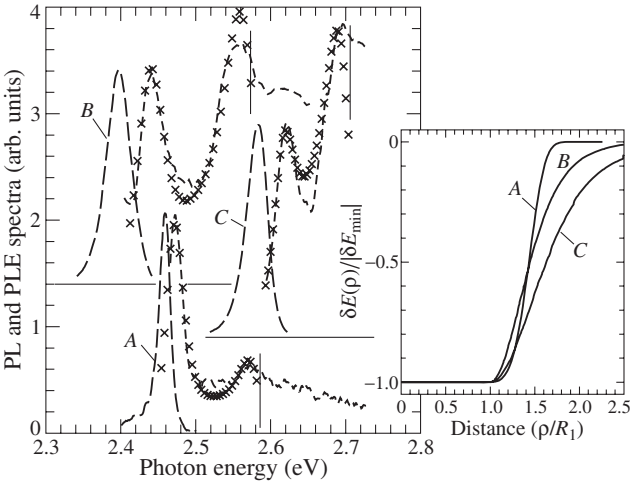

Fig. 4. PL (dashed lines) and absorption spectra (dotted lines) of the three samples A, B, and C with different CdSe content, grown by the different MBE techniques. Absorption spectra of the island emitting states were obtained by PLE technique (see text). Short vertical lines indicate the $E_{\rm ME}$ positions. Spectra are shifted in vertical direction for clarity. Crosses show the fit of the absorption spectra calculated with the model basin-like potential with the following values of the ratio R_2/R_1: 0.04 (sample A), 0.18 (B), and 0.25 (C). Insert: normalized shapes of the model in-plane potentials $\delta E(\rho)/\delta E_{\rm min}$ for typical islands in samples A, B, and C.

such charged islands correspond to the exciton states spatially isolated from an extra localized charges. We have shown that the absorption spectra of excitons localized in islands strongly depend on the very general characteristics of the island potential well such as its size, its depth, and its profile and can be used for the nondestructive characterization of such quantum objects.

Acknowledgements

Part of the experimental data presented here was obtained as a result of multinational cooperation of several research groups in different countries. We thank with pleasure H. Kalt, D. Litvinov and D. Gerthsen (Karlsruhe, Germany) for encouragement and valuable discussions. We thank also E. Kurtz, H. Preis, S. Sorokin, I. V. Sedova and S. Ivanov for the samples used in the experiments. This work was partly supported by Deutsche Forschungsgemeinschaft, by RFBR (projects No.03-02-17562 and No.03-02-17565), and by the Programs of RAS ("Physics of Solid State Nanostructures" and "Low-dimensional quantum structures").

References

[1] E. Kurtz *et al.*, *Appl. Phys. Lett.* **79**, 1118 (2001).
[2] D. Litvinov *et al.*, *phys. stat. sol. (b)* **224**, 147 (2001)
[3] S. Sorokin *et al.*, *J. Cryst. Growth* **201/202**, 461 (1999).
[4] K. Leonardi *et al.*, *J. Cryst. Growth* **201/202**, 1222 (1999).
[5] M. Rabe *et al.*, *J. Cryst. Growth* **184/185**, 248 (1998).
[6] N. Peranio *et al.*, *Phys. Rev.* **B 61**, 16015 (2000).
[7] A. Reznitsky *et al.*, *phys. stat. sol.(b)* **229**, 509 (2002)
[8] I. A. Akimov *et al.*, *Appl. Phys. Lett.* **81**, 4730 (2002).
[9] A. Klochikhin *et al.*, *Phys. Rev. B* **69**, 085308 (2004).

13th Int. Symp. "Nanostructures: Physics and Technology"
St Petersburg, Russia, June 20–25, 2005

Inhomogeneous broadening in quantum dot layers: expanding towards broadband sources

S. Raymond[1], C. Nì. Allen[1,2], C. Dion[3], P. J. Poole[1], P. Barrios[1], A. Bezinger[1], G. Ortner[1], G. Pakulski[1], W. Render[1], M. Chicoine[5], F. Schiettekatte[5], P. Desjardins[3] and S. Fafard[4]

[1] Institute for Microstructural Sciences, National Research Council of Canada, Ontario, Canada, K1A 0R6
[2] Physics Department, University of Ottawa, Ottawa, Ontario, Canada, K1N 6N5
[3] Département de Génie Physique, École Polytechnique de Montréal, P.O. Box 6079, Station Centre-Ville, Montréal, Québec, Canada, H3C 3A7
[4] Cyrium Technologies Inc., Ottawa, Ontario, Canada
[5] Département de physique, Université de Montréal, P.O. Box 6128, Station Centre-Ville, Montréal, Québec, Canada, H3C 3J7

Abstract. Inhomogeneous broadening inherent to self-assembled Quantum Dot layers is often viewed as an adverse effect preventing the building of a device in which all the elements contribute to, for example, the same lasing mode. On the other hand, this natural 'tunability' of the atomic-like properties of Quantum Dots can be seen as an asset one can use. To demonstrate this, an external cavity laser is built using an InAs/InGaAsP/InP QD laser diode as the active element. The typical linewidth of the electroluminescence of the QD layers is of the order of 80 nm around 1.59 μm, giving a lasing tuning range of 110 nm in the external cavity Littrow configuration. To broaden the scope of potential applications, one also needs to find methods to control the inhomogeneous broadening in a layer of QDs. Here we show the initial steps towards a spatially selective intermixing method which provides the possibility to tune the inhomogeneous broadening of a QD layer. Two methods are exemplified, one using ion implantation and one using grown-in defects, providing peak emission tunability in excess of 375 nm in both cases.

Introduction

Tunable and broadband light sources are continuously finding new applications in various scientific fields, especially in biology and medical treatment [1]. These sources are continuously improving and Quantum Dot (QD) tunable lasers are another step in the quest to get more efficient light emitters with a larger bandwidth. The zero-dimensionality of QDs, which leads to rapid filling of the energy levels with injected current can be viewed as a benefit in this regard, for at least two reasons. First, the excited state (higher energy) emission contributes to enlarging the gain bandwidth and second, once the QDs are filled, their absorption is quenched [2]. Thus, an inhomogeneous ensemble of QDs used as the active region of a tunable laser can provide efficient, tunable single wavelength emission even at low injection currents. Moreover, the bandwidth can be extended if one learns to modify the gain spectrum in a spatially selective way.

In this paper, we investigate the tuning properties of an external cavity laser driven by an InAs/InGaAsP/InP QD laser diode to obtain tunable stimulated emission at telecom wavelengths. Moreover, we investigate methods to increase the device bandwidth even further by means of spatially selective bandgap shifting. To this effect, two material intermixing test methods are investigated: ion implantation QD intermixing (IIQDI) and grown-in defects QD intermixing (GIDQDI) [3, 4].

1. Experimental

The laser diode structure was grown by chemical beam epitaxy on exactly oriented (100) InP n-type substrates. The undoped active region of the lasers consisted of five stacked layers of self-assembled InAs quantum dots embedded in $In_{0.816}Ga_{0.392}As_{0.392}P_{0.608}$. The sample was microfabricated into standard ridge lasers of various lengths and widths. A 300 g/mm grating with 90% reflection in the first order was used as the tunable feedback element of the external cavity. More details about the growth, packaging and spectroscopy of these structures can be found elsewhere [5].

The sample used for IIQDI and GIDQDI were grown by MOCVD and CBE respectively, and each consisted of a single InAs QD layer embedded in InP with respective cap thickness of 200 and 1000 nm. The InP cap of the GIDQDI sample was grown in non-optimal condition to obtain a concentration of point defects, and terminated with a 33 nm InGaAs cap. Following growth, different pieces of the sample were annealed in successive 60 s time increments for temperatures ranging from 400 to 750 °C. For IIQDI, sample pieces were irradiated with P^+ ions at an energy of 30 keV with doses ranging from 1×10^{11} to 1×10^{14} ions/cm^2, followed by successive 60 s rapid thermal anneals at temperatures ranging from 400 to 700 °C. Further details of the growth, implantation, anneal and spectroscopy procedures can be found elsewhere [6, 7].

2. Results

Fig. 1 (a) shows the evolution of the external cavity laser emission spectrum as a function of grating angle for a $\sim$ 1-mm long and $\sim$ 2.5-μm wide ridge laser placed inside a Littrow external cavity. The diode was mounted on a Pelletier cooler, regulating the temperature to 18 °C, and the injection current was pulsed with a 1% duty cycle at a frequency of 1 kHz. At extreme grating angles, the product of gain and external feedback (reflectivity) of the grating is smaller than the product of peak gain and facet feedback, and the natural mode of the laser diode dominates. For intermediate angles, the former dominates and the emission tunes with the grating angle. For each angle of the grating, one can obtain an L-I-V characteristic and Fig. 1 (b) shows the current tresholds thus obtained as a function of the emission wavelength of the laser. This treshold is fairly

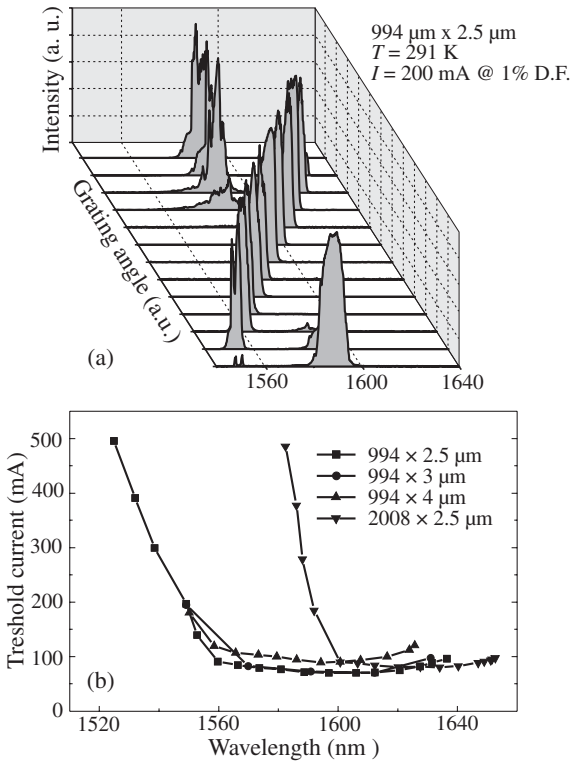

Fig. 1. (a) Emission spectra of the QD laser as a function of grating angle. (b) Treshold currents obtained for various emission wavelenghts.

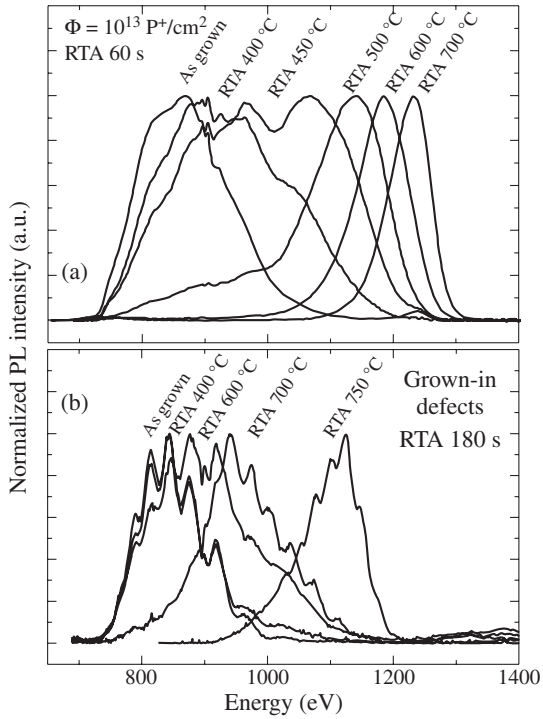

Fig. 2. Low Temperature (77 K) Photoluminescence spectra obtained from IIQDI (a) and GIDQDI (b) samples processed at various annealing temperatures.

flat over a range of 80 nm, and allowing larger injection currents the tuning range can be extended up to 110 nm. For the longer 2 mm cavity, the tuning range becomes narrower and is shifted towards longer wavelengths. The extension towards longer wavelengths comes from increased gain per roundtrip as compared to facet losses. The higher losses at shorter wavelengths remains unexplained, but one could expect that it does not originate from re-apsorption in excited states since the latter should be filled at higher injection currents. However, it is possible that Auger re-emission processes play a role in preventing perfect state-filling, and thus one might prefer to operate the diodes at lower injection currents.

One possibility to enlarge the gain at low injection currents is to shift the gain bandwidth in a spatially selective way. Fig. 2 shows the emission spectrum obtained from single layer QD samples processed with IIQDI (a) and GIDQDI (b). For clarity, the annealing temperature is the only processing parameter varied in the results presented. In both cases large blueshifts can be measured, increasing with annealing temperature up to 375 nm. The nature of the defect or mechanism promoting intermixing in either case may be different, as suggested by the difference in temperature treshold between both methods. However, from an applied perspective it is interesting to note that in the case of IIQDI and GIDQDI, the magnitude of the shift obtained for given annealing conditions is proportional to implant dose and thickness of the GID layer respectively.

3. Conclusion

A QD laser tunable trough 1.55 microns was demonstrated, thus reiterating the potential use of quantum dot inhomogeneous broadening for broadband applications. Techniques to widen the spatial inhomogeneity of QD layers have been investigated and both IIQDI and GIDQDI show promising properties towards the production of QD devices with very large bandwidth.

References

[1] D. Huang *et al*, *Science*, **254**, 1178 (1991).
[2] R. Heitz, T. Warming, F. Guffarth, C. Kapteyn, P. Brunkov, V. M. Ustinov and D. Bimberg, *Physica E*, **21**, 215 (2004).
[3] J. E. Haysom, G. C. Aers, S. Raymond and P. J. Poole, *J. Appl. Phys.*, **88**, 3090 (2000).
[4] J. E. Haysom, P. J. Poole, R. L. Williams, S. Raymond and G. C. Aers, *Solid State Communications*, **116(4)**, 187 (2000).
[5] C. Nì. Allen, P. J. Poole, P. Marshall, J. Fraser, S. Raymond, S. Fafard, *Appl. Phys. Lett.*, **80**, 3629 (2002).
[6] C. Dion, P. Desjardins, S. Raymond, F. Schiettekatte and M. Chicoine, *to be published*.
[7] J. F. Girard, C. Dion, P. Desjardins, C. Nì. Allen, P. J. Poole and S. Raymond, *Appl. Phys. Lett.*, **84**, 3382 (2004).

13th Int. Symp. "Nanostructures: Physics and Technology"
St Petersburg, Russia, June 20–25, 2005

Carrier transfer and radiative recombination in self-organized InAs/GaAs QD array: DC current injection pump-probe experiment and solvable models

A. V. Savelyev[1], A. S. Shkolnik[1], S. Pellegrini[2], L. Ya. Karachinsky[1], A. I. Tartakovskii[3] and R. P. Seisyan[1]

[1] Ioffe Physico-Technical Institute, St Petersburg, Russia
[2] School of Engineering and Physical Sciences, Heriot-Watt University, Edinburgh, UK
[3] Department of Physics and Astronomy, Sheffiled University, Sheffield, UK

Abstract. Carrier transfer between quantum dots with following recombination has been studied experimentally and theoretically. New experimental method based on pump-probe spectroscopy of electrically pumped samples was used and qualitative description in terms of the coherent-medium approximation has been presented. Photoluminescence decay kinetic equations and its exact solution were obtained in assumption of the microscopically homogeneous media and compared with earlier experiments.

Introduction

Self-assembled quantum dots (QDs) are currently of much interest due to predicted advantages of an atomic-like energy state density. Number of applications have been proposed in last decade such as high-efficiency opto-electronic devices [1,2] and single-electron devices [3,4]. Optimization of parameters of those devices requires understanding of physical processes of charge carrier localization and carrier transfer between QDs. As it was shown in previous papers [5–7] processes including carrier transfer between QDs with following radiative recombination (CTR) play important role in the carrier dynamics. A nature of the transfer can be of two types: thermally activated escape from the QD with following capture or direct tunnelling between adjoining QDs that dominates at low temperature. In the previous works [5–7] CTR was studied in time-resolved photoluminescence (TRPL) experiments. In the present paper we introduce measurements of a carrier density in the InAs/InGaAs/GaAs QD array under dc electrical pumping. These measurements were made using well-developed technique of polarization-resolved pump-probe spectroscopy at helium temperature [8,9]. Under low injection most of the QDs are empty and injected electrons and holes are likely captured into the empty QDs and dominating recombination process is CTR. Dependence of an average QD filling with carriers versus injection current was measured and explained in terms of CTR processes. Theoretical discussion is also presented. Mass-rate equations are obtained for dynamics of low-density relaxation what leads to qualitative description of the DC injection experiment presented here. Under assumption of equal transfer rate for all QD exact kinetic equations have been solved analytically and applied to describing previous TRPL experiments.

1. Experiment

Array of self-organized InAs/InGaAs/GaAs QDs grown by strain-driven decomposition of the InGaAs alloy embedded in a conventional *p-i-n* laser diode structure was studied. Structure contains 5 layers of InAs QD covered by InGaAs QW with surface density $N_S = 5-6\times10^{10}\,\mathrm{cm}^{-2}$ and energy of ground state optical transition $E_0 = 1.03\,\mathrm{eV}$. A temperature of the experiment $T = 6\,\mathrm{K}$ eliminates carrier escape from QDs. The method used allows measuring fraction η of QD filled with carriers [9] that are injected as a dc current applied to *p-i-n* junction. While there is no current $\eta = 0$, but at a high injection a significant part of QDs are filled with carriers (Fig. 1) because of stochastic nature of carrier captures into QDs. As it was shown earlier [10] crossover from high to low injection regime with corresponding decreasing of QD filling is ruled by recombination mechanism different from direct radiative recombination. We suggest here that the CTR plays major role when injection becomes as low as 10^5 carriers per dot per second what corresponds to transfer-and-recombination time $\tau \sim 10^3\,\mathrm{ns}$.

2. Solvable models

Tunnelling transfer of electrons can be treated as a random walk in a stochastically disordered two-dimensional media and described by effective diffusion coefficient D within coherent-medium approximation [11]. In the InAs/GaAs QD system electron transfer rate is much higher than hole one [7] hence holes are assumed fixed. Lets denote electron (hole) surface density as $n(p)$. Number of sites visited by one electron in time t is $s(t) \sim DN_S t$ and probability of meeting a hole is $s(t)p/N_S$. Finally following equation for the recombination

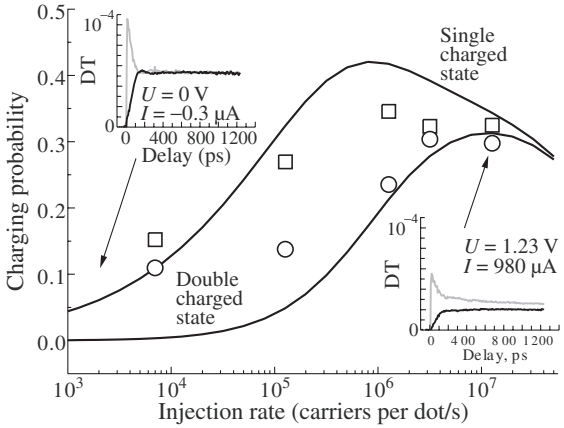

Fig. 1. QD single (squares) and double (circles) charged state probabilities at different injection current. Inset: Differential transmission time curves for $\sigma^+\sigma^+$ (gray line) and $\sigma^+\sigma^-$ (black line) polarizations of pump and probe pulses.

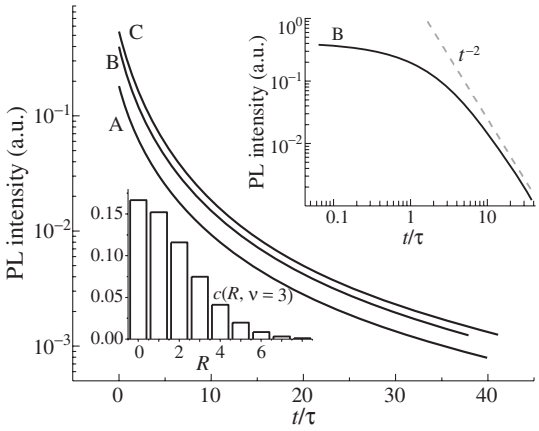

Fig. 2. Theoretical PL decay curves for $\nu = 1$ (A), $\nu = 3$ (B) and $\nu = 5$ (C). Left inset: $c(R, \nu)$ for $\nu = 3$ (see text). Right inset: asymptotical behavior of the PL decay for large t.

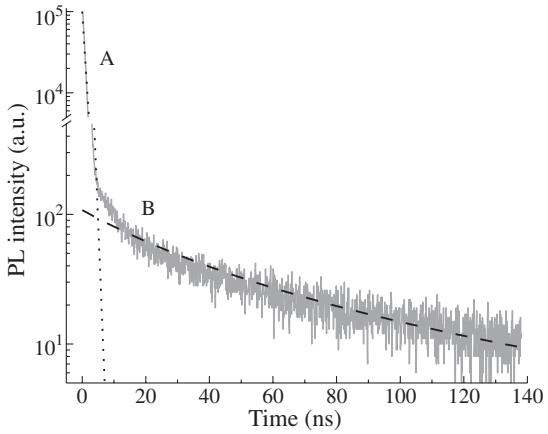

Fig. 3. Experimental PL decay (solid line) and calculated one (curve B). $\tau = 25$ ns and $\nu = 3$ is chosen for best fit with the experiment. Curve A corresponds to fast radiative recombination.

rate can be obtained: $dn/dt = -ADnp$, where dimensionless parameter A is of the order of 1. One can calculate probability of QD to be occupied by a charge carrier using this equation and method suggested earlier [11]. Result of calculation shown in Fig. 1 by solid line demonstrates qualitative agreement with the experimental points.

Next we discuss PL decay experiments [5–7] in that evidence of the CTR was reported. Case of sufficiently high temperature when carrier escape is more probable than tunnelling transfer is under investigation. An origin of the CTR in the PL decay is the stochastic nature of carrier captures into the QDs. That leads to the fluctuations of number of electrons and holes captured into QD. Let us assume the average number of the electrons and holes captured per one QD is ν and that carriers are captured independently from each other. A probability that number of electrons in QD is higher than number of holes by R equals to $c(R, \nu) = e^{-2\nu} I_R(2\nu)$ (see left inset in Fig. 2). Just after injection pulse direct radiative recombination is the major process with characteristic time $\tau_r \sim 1$ ns [5] though only some part of the injected carriers can recombine by that way. Remaining carriers recombine after some transfers between QDs.

In the low-density regime total escape rate and probability of being captured by a QD containing hole in it are both proportional to carrier concentration $n = p$, so the recombination rate is $dn/dt = - < \tau^{-1} > n^2/N_S$, where $< \tau^{-1} >$ is an averaged reciprocal escape time. Solution for large t is $n(t) \sim t^{-1}$, and $PL(t) \sim dn/dt \sim t^{-2}$. PL decay in all density range can be described after assumption of the same transfer time τ for all electrons in all QDs. Kinetic equations can be written as:

$$\tau \frac{dn_r}{dt} = -rn_r + n_{r-1} n/N_S \text{ for } r = 1 \ldots \infty ,$$
$$\tau \frac{dp_r}{dt} = -n \left(p_{r+1} - p_r \right) / N_S \text{ and } p_r(t = 0) = c(r, \nu) ,$$

where n_r (p_r) is surface density of the QDs containing r electrons (holes). It is assumed here that transfer time is much greater than radiative lifetime so electron and hole in one QD recombine immediately. Analytical solution of that infinite system of non-linear differential equations still can be obtained with respect to $n(t)$ and $PL(t)$ in the following form:

$$n(\Theta) = \sum_{q=1}^{\infty} \sum_{r=q}^{\infty} \frac{c(r, \nu) q \Theta^{r-q}}{(r-q)!} e^{-\Theta} ,$$

$$PL(\Theta) = \frac{n}{\tau N_S} \frac{dn}{d\Theta} \text{ and } t(\Theta) = \int_0^{\Theta} \frac{\tau N_S dx}{n(x)} .$$

PL decay is close to exponential in the beginning (Fig. 2). For $t \sim 10\tau$ density of carriers $n \ll N_S$ and low-density regime with corresponding power decay is realized (see right inset on Fig. 2). Theoretical result can be compared with PL decay time dependence presented earlier [7] (Fig. 3). Measurements were made with InAs self-organized QD array at $T = 200$ K. Fast decay ($\tau_r \sim 1$ ns) is also shown in Fig. 3 as line A. Theoretical curve (curve B in Fig. 3) well fits the experimental data for delay times greater than 15 ns. There is noticeable non-exponential behavior of the experimental and theoretical curves. For smaller delays $t = 5 \ldots 15$ ns PL decay demonstrates behavior different from expected by our model. The possible reason is a wide transfer times distribution in the inhomogeneous QD ensemble that should be included in further theoretical consideration of the PL decay.

References

[1] Y. Arakawa and H. Sakaki, *Appl. Phys. Lett.*, **40**, 939 (1982).
[2] S. S. Mihrin *et al*, *Semiconuctors*, **36**, 1315 (2002).
[3] E. Biolatti *et al*, *Phys. Rev. Lett.*, **85**, 5647 (2000).
[4] T. Lundstrom *et al*, *Science*, **286**, 2312 (1999).
[5] L. Ya. Karachinsky *et al*, *Appl. Phys. Lett.*, **84**, 7 (2004).
[6] A. S. Shkonick *et al*, *Proc. of 12th Int. Symp. "Nanostructures: physics and technology" (SPb, Russia, 2004)*, Ioffe Institute, p. 244 (2004).
[7] S. Pellegrini *et al*, *Proc. of SPIE Int. Symp. "Photonic West", (San Jose, USA, 2005)*, [5725–45].
[8] A. I. Tartakovskii *et al*, *Phys. Rev. Lett.*, **97**, 057401 (2004).
[9] A. I. Tartakovskii *et al*, *Appl. Phys. Lett.*, **85**, 2226 (2004).
[10] R. P. Seisyan *et al*, *Proc. of 3rd Int. Symp. "Woman in Fundamental Science", (SPb, Russia,2004)*, BBM, SPb, p. 54 (2004).
[11] T. Odagaki and M. Lax, *Phys. Rev. B*, **24**, 5284 (1981).

13th Int. Symp. "Nanostructures: Physics and Technology"
St Petersburg, Russia, June 20–25, 2005

Steering of electron wave in three-terminal small quantum dot

O. A. Tkachenko[1,2], V. A. Tkachenko[1], Z. D. Kvon[1], D. G. Baksheev[1,3], J.-C. Portal[2] and A. L. Aseev[1]

[1] Institute of Semiconductor Physics, 630090 Novosibirsk, Russia
[2] Grenoble High Magnetic Field Laboratory, F-38042 Grenoble, France
[3] Now at ZAO "Intel A/O", 630090 Novosibirsk, Russia

Abstract. We report new interference effect in ballistic transport through a three-terminal small quantum dot — switching of electron current between two outlet ports with increasing Fermi energy.

Introduction

A variety of nanostructures (T-, Y-junctions, ring interferometers) include places of connection of quantum channels. In the systems based on two-dimensional electron gas (2DEG) a many-level quantum dot of triangular shape is formed at the region of junction of three channels. This dot causes strong intermode mixing and resonances of reflection of electron waves [1-3]. In Y-junctions, steering of electron current has been predicted [4] and observed when a tilt voltage had been applied to side gates [5] or outlet ports [6]. We have found another effect in ballistic transport through a three-terminal quantum dot, switching of electron current between the outlet ports with increasing Fermi energy. This effect results from asymmetry that is always present in real device.

1. Experiment

Three-terminal quantum dots were fabricated on the basis of a high-mobility 2DEG in an AlGaAs/GaAs heterojunction [3,7]. Antidots located at the vertices of equilateral triangle with 400 nm side and insulating cuts were created by electron lithography followed by plasma-chemical etching. The device was covered by a metal gate. Figure 1 shows a microphotograph and calculated electrostatic potential in the plane of 2DEG of the studied device. The antidots shape the quantum dot into a small triangular electron lake connected to 2DEG reservoirs via three constrictions, numbered 1 to 3. The dot is asymmetric.

Figure 2 shows experimental conductance coefficients G_{ij}, between reservoirs i and j, as a function of gate voltage. The dot is more open for transmission between reservoirs 2 and 3, than for directions 1–2 and 1–3. It means that the first constriction is the narrowest one. Alternating crossing of curves G_{12} and G_{13} demonstrates the effect of switching in the probability current between left and right outlet ports. At zero gate voltage there are minimum of G_{12} and large maximum of G_{13}, so almost all electrons are scattered to the third reservoir. On the contrary, at $V_g = -25$ mV the second reservoir receives two times as much electrons as the third reservoir. In other words, this change in the gate voltage modifies parameter of polarization $\gamma = (G_{12} - G_{13})/(G_{12} + G_{13})$ from -0.7 to $+0.4$. There are several places with such a switching.

Additional measurements prove interference origin of oscillations [3]. The presence of even a weak magnetic field suppresses the oscillations. The structure of the oscillations is more complex than that of single-electron oscillations. Fine structure and doublet splitting of the peaks are observed. Calculation of the gate capacitance shows that dip spacing $\delta V_g = 20-25$ mV on the total conductance curve $G_{12} + G_{13}$ corresponds to addition of 6–8 electrons to the dot [3]. Thus the small quantum dot operates as an interference transistor switched between scattering states by addition of a few electrons to the dot.

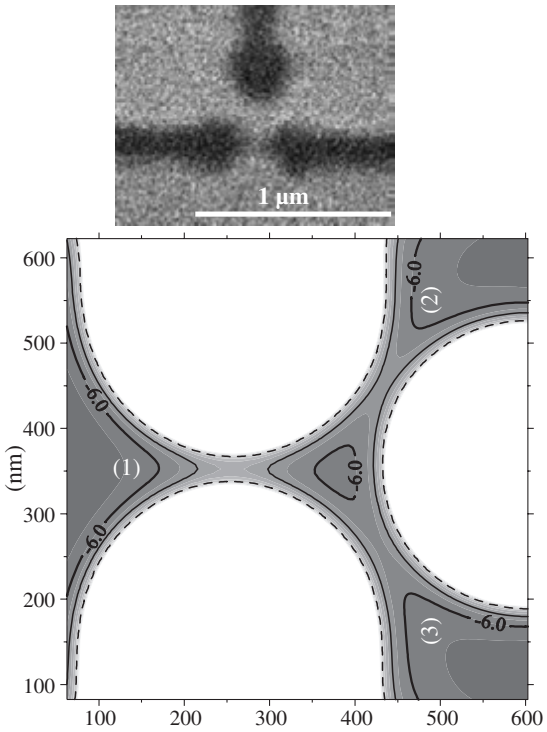

Fig. 1. A micrograph of device and calculated electrostatic potential $U(x, y)$ [meV] in 2DEG (only regions $U \leq 0$ are shown).

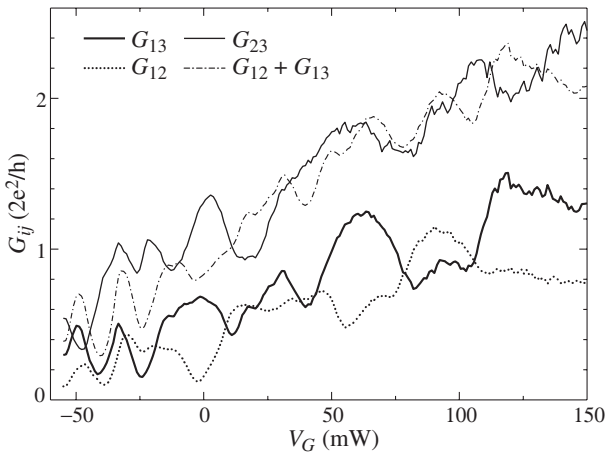

Fig. 2. Gate voltage dependences of conductance coefficients G_{ij} from i-th reservoir to j-th reservoir.

2. Theory

We have modelled the electrostatics and coherent magneto-transport of the three-terminal quantum dot. To simulate a weak asymmetry of the device, variations within 10 nm have been introduced to the distance between the antidots and the depth of etching. Three-dimentional Poisson equation was solved numerically to obtain effective potential in the plane of 2DEG. Then one-particle problem of transmission through the dot with the determined shape was solved by S-matrix or recursive Green function techniques.

We calculated energy dependence of transmission coefficients from reservoir 1 to reservoirs 2 or 3, T_{12} and T_{13} respectively, for two slightly different realizations of electrostatic potential U_1 (Fig. 1) and U_2. In the case of potential U_2 the dot is less open. Total conductance of the dot, $T_{12} + T_{13}$, shows deep dips (Fig. 3). Energy separation between the dips corresponds to addition of about 10 electrons to the dot and agrees with experiment. Curves $T_{12}(E_F)$ and $T_{13}(E_F)$ intermittently intersect with each other so that coefficient of polarization $\gamma = (T_{12} - T_{13})/(T_{12} + T_{13})$ alternates within almost full range from -1 to 1. In the region of this "alternating antiphase," the electrons incident at port 1 are mainly scattered into ports 2 or 3. The described effect is associated with a weak asymmetry of the ports.

Figure 4 shows wave functions calculated for the states marked by a–d on the transmission curves in case U_2 (Fig. 3). Electrons are incident from the left in the first transverse mode of the inlet channel. With increasing Fermi energy the electrons are emitted from the dot mainly from bottom port 3 at $E_F = 0.1$ meV, totally reflected back to inlet port 1 at $E_F = 1.7$ meV, steered to upper port 2 at $E_F = 2.5$ meV, reflected back at $E_F = 3.9$ meV, guided to lower port 3 again at $E_F = 5$ meV, and so on. At the dips of transmission, $T_{12} + T_{13} \approx 0$, the wave function becomes a standing wave between the barrier of inlet constriction and the opposite antidot. When transmission through one of the outlet ports is blocked ($T_{1j} \ll T_{12} + T_{13}$, $j = 2, 3$) there is a sort of standing wave between the closed consriction and opposite antidot as well. This Fermi-energy dependent dominance of one of the outlet ports in the transmission through the three-terminal quantum dot is associated with a weak asymmetry of the ports. It means that quantum dot acts as quantum steering wheel.

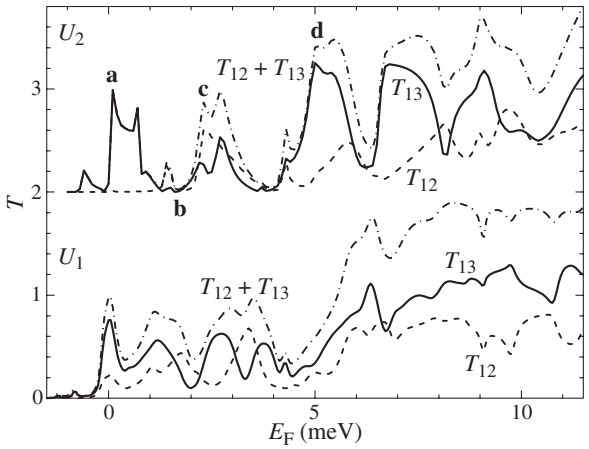

Fig. 3. Energy dependence of transmission coefficients T_{12}, T_{13}, and $T_{12} + T_{13}$ for U_2 and U_1 (curves for U_2 are offset).

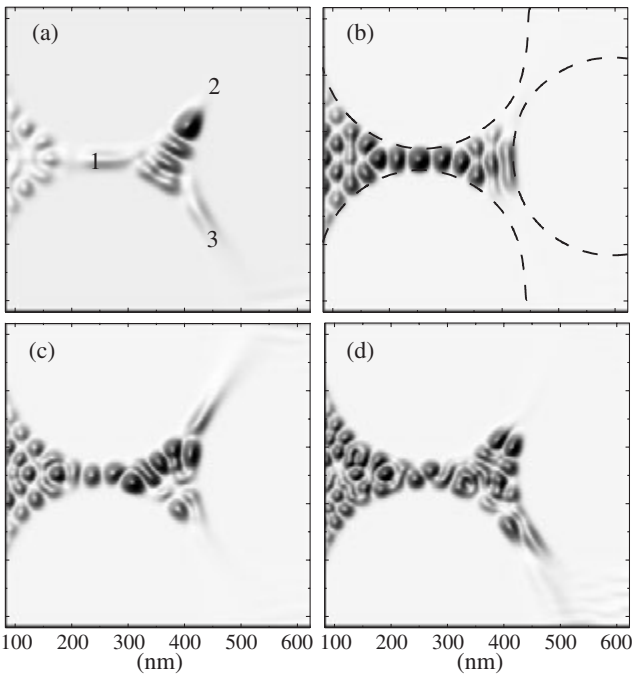

Fig. 4. Distribution of the probability density for states a–d marked in Fig. 3. The dashed lines show the boundaries of classically allowed region $E_F = U_2$.

3. Conclusion

We have theoretically and experimentally studied switching of electron current through three-terminal quantum dot by controlled change of Fermi energy. Similar interference behavior is expected to occur in propagation of waves of any origin (e.g. acoustic or electromagnetic waves) through splitters of wavelength size.

Acknowledgements

We thank A. I. Toropov, A. E. Plotnikov, A. S. Medvedev and L. A. Nenasheva for fabrication of the structures. This work was supported by RFBR (project 05-02-16591-a), INTAS (grant 01-0014) and RAS (program "Low-Dimensional Quantum Structures"). The work at Grenoble was funded by CNRS. O. A. T. acknowledges IDRIS Supercomputing Center, Orsay, France (project 41778) for the possibility of performing the calculations.

References

[1] O. A. Tkachenko *et al*, *JETP Lett.* **71**, 255 (2000).
[2] O. A. Tkachenko *et al*, *JETP Lett.* **79**, 293 (2004).
[3] V. A. Tkachenko *et al*, *JETP Lett.* **80**, 588 (2004).
[4] T. Palm and L. Thylén *Appl. Phys. Lett.* **60**, 237 (1992).
[5] G. M. Jones *et al*, cond-mat/0408644 (2004).
[6] I. Shorubalko *et al*, *Appl. Phys. Lett.* **79**,1384 (2001); S. Reitzenstein *et al*, *Phys. Rev. Lett.* **89**, 226804-1 (2002).
[7] V. A. Tkachenko *et al*, *JETP Lett.* **76**, 720 (2002).

13th Int. Symp. "Nanostructures: Physics and Technology"
St Petersburg, Russia, June 20–25, 2005

Dynamical control of decoherence in double quantum dot

V. A. Burdov[1] and D. Solenov[2]

[1] University of Nizhni Novgorod, 603950 Nizhni Novgorod, Russia
[2] Clarkson University, Potsdam, NY 13699-5822, USA

Abstract. The role of decoherence in controllable electron dynamics in a double quantum dot, influenced by external ac and dc electric fields, has been analyzed. It was shown that the dissipation caused by phonon environment disappears under certain relations between electric field parameters. In this case one may perform the dynamic localization and form stable electron states localized within one of the dots.

Introduction

Recent progress in nanotechnology creates the base for the development of single-electron technique. Suitable objects for investigation in this field include structures consisting of several tunnel-coupled quantum dots or wells. In particular, the possibility to create coherent electron states localized in some "site" and then transfer it to the neighbouring "site" has been discussed for double quantum dots [1] and wells [2] as well as lattices of quantum wells and dots [3]. Such the dynamical control of electron states is based on dynamic localization phenomenon [4]. In this case, strong oscillating electric field "locks" electron density within one of the dots, while switching ac-field off, one would observe coherent electron wave packet oscillations between the dots with the frequency defined by the splitting energy of bonding and anti-bonding states.

Dissipation can lead to decoherence processes in double quantum dots [5, 6]. Moreover, some authors have shown that decoherence is able to destroy the regime of dynamical control [7]. In particular, relocation of electron density in double quantum dot under the action of adiabatically changing external electric field is turned out to be incomplete even at zero temperature. As a result, the final electron state after the transfer is not at all a pure state but a mixture. Does the electron-phonon interaction destroy the dynamic localization? If so, then how much we can influence this destructive action choosing the system parameters, such as the magnitude and the frequency of electric field? In our investigation we will try to obtain the answers to these questions.

1. Theoretical model

We consider a symmetric double quantum dot interacting with phonon environment in the presence of constant, E, and alternative harmonic, $F\cos\omega_0 t$, electric fields directed along the structure. The total Hamiltonian operator of the problem has the form

$$H=\sum_{\mathbf{k}}\omega(\mathbf{k})a^{\dagger}_{\mathbf{k}}a_{\mathbf{k}}-(\Delta/2)\sigma_X-e\ell(E+F\cos\omega_0 t)\sigma_Z + \sum_{\mathbf{k}}\left(g_{\mathbf{k}}a^{\dagger}_{\mathbf{k}}+g^{*}_{\mathbf{k}}a_{\mathbf{k}}\right)\sigma_Z\,, \qquad (1)$$

where the first sum represents the energy of the phonon environment, $a^{\dagger}_{\mathbf{k}}$ and $a_{\mathbf{k}}$ are the creation and annihilation operators of the phonon with the wave vector $\mathbf{k}$, $\omega(\mathbf{k})$ is a phonon frequency. Here and throughout the paper $\hbar=1$. The next two terms stand for the Hamiltonian operator of the single-electron system described with two-level pseudo-spin approximation. Splitting energy Δ of symmetric, $|0\rangle$, and anti-symmetric, $|1\rangle$, states of double quantum dot is considered to be significantly less than the size-quantization energy and the electron potential energy due to electric fields in double-dot structure of length 2ℓ. σ_X and σ_Z are Pauli matrices. Electron part of the total Hamiltonian operator is written here in the basis of orthonormal states $|L\rangle=(|0\rangle+|1\rangle)/\sqrt{2}$ and $|R\rangle=(|0\rangle-|1\rangle)/\sqrt{2}$, which are almost completely localized in the left and right quantum dots. The last term in Eq. (1) corresponds to the electron-phonon interaction, and $g_{\mathbf{k}}$ is the interaction constant between $\mathbf{k}$-th phonon mode and electron subsystem. For the estimations we may accept the following values of the characteristic energies: ~ 1 meV for Δ; ~ 10 meV for $eE\ell$, $eF\ell$ and ω_0; and ~ 100 meV for the size-quantization energy. These values and the relationships are quite feasible in dc and ac fields with magnitudes of 10^3-10^4 V/cm for silicon quantum dots with the sizes of ~ 10 nm or less, embedded into a SiO_2-matrix.

It is well known that the irreversibility in such the description arises from the infinite number of phonon modes. In this case, it is convenient to analyze time evolution of electron system by a reduced density matrix, ρ_e, which is defined as a trace of the total density matrix over all phonon modes $\rho_e(t)=Tr_{\rm ph}\rho(t)$. Time-dependence of the density matrix is given by Liouville equation

$$i\dot{\rho}(t)=L\rho(t)\,, \qquad (2)$$

where L is Liouville super-operator. Its action may be formulated by means of the relation $LO\equiv[H,O]$, where O is any operator.

2. Results and discussion

Let us examine the choice of initial distribution that is often discussed for the phenomena of dynamic localization and dynamical control. In particular, electron density distribution in the double dot will be considered fully polarized, i.e. the whole electron charge is initially placed in one of the dots. Such the state is natural, from the energy point of view, for an electron situated in a double-dot structure in electric dc-field. For the sake of definiteness, the left dot may be chosen occupied, i.e. $\rho_{LL}(0)=1$. In this case, we obtain explicit expressions for the density matrix in the "left-right" representation

$$\rho_{LL}(t)=\frac{1+\exp\{-t/\tau\}}{2}=1-\rho_{RR}\,, \qquad (3)$$

where the decrement τ^{-1} is:

$$\tau^{-1}=4\gamma\frac{\Delta^2 J^2_{-1}(\lambda)}{\Delta^2 J^2_{-1}(\lambda)+(2eE\ell-\omega_0)^2}\,. \qquad (4)$$

Here $J_{-1}(\lambda)$ stands for the Bessel function of argument $\lambda = 2eF\ell/\omega_0$. It is not difficult to show that the off-diagonal elements $\rho_{RL}(t) = \rho^*_{LR}(t)$ are nonzero, but always remain small. They are directly proportional to the constant of electron-phonon interaction γ. Diagonal elements $\rho_{LL}(t)$ and $\rho_{RR}(t)$ change from the values of 1 and 0 to 1/2 at $t \to \infty$, respectively. This means that extremely polarized at $t = 0$ double quantum dot will be almost equally populated and lose its polarization, when $t \gg \tau$.

As we see, even weak connection between the double quantum dot and the phonon environment leads to the relaxation processes, which set equal population of both quantum dots. In a certain sense such the behavior of the electron density under the action of strong dc and ac electric fields is similar to the one that takes place for static and symmetric double-dot without any external fields. Nevertheless, there is an essential difference between these two cases. This difference is caused by the characteristic decay-time τ, which appears in solution (3).

While the decay-time in a static two-level system depends only on the constant of electron-phonon interaction, the time of decay in two-level system with strong dc and ac electric fields has a nontrivial dependence on the harmonic field amplitude F and the magnitude of the constant field E, as it clearly follows from the definition of τ (4). Decrement τ^{-1} as a function of dimensionless parameters $\eta = 2eE\ell/\omega_0$ and $\lambda = 2eF\ell/\omega_0$ is plotted in Fig. 1. Any cross-section of the represented surface with the plane $\lambda = const$ is a Lorentz-like curve. On η-axis, the decrement has maximum at $\eta = 1$, which corresponds to the resonant condition between frequencies of the ac-field and the ground quantum transition of the electron system in the dc-field.

Remarkable feature, however, is that τ^{-1} vanishes at infinite number of points on λ-axis, independently on η. These points are the roots λ_j of Bessel function $J_{-1}(\lambda)$. This yields the following values for ac-field amplitude: $F_j = \omega_0\lambda_j/2e\ell$. Thus, choosing the amplitude of the ac-field close or equal to any value of F_j, we can significantly reduce decrement τ^{-1} or even make it zero to the first order in γ. In this case, as it follows from Eq. (3), relaxation of electron subsystem inside the dots will be suppressed, and the density of charge initially localized within one of the dots will stay there.

Evidently, the choice of F corresponding to one of the values in set F_j maintains the dynamic localization of the electron wave packet even when the energy exchange between the electron subsystem and the phonon environment is possible. Such the effect may be called "dynamic suppression of relaxation". It is important to notice that the phenomenon of dynamic suppression of relaxation is essentially nonlinear effect, which would never appear in a weak ac-field where $\lambda \ll 1$. The smallest value of amplitude F suitable for dynamical control over the dissipation equals to $3.832 \times \omega_0/2e\ell$, where numerical coefficient 3.832 is the first root of Bessel function $J_{-1}(\lambda)$.

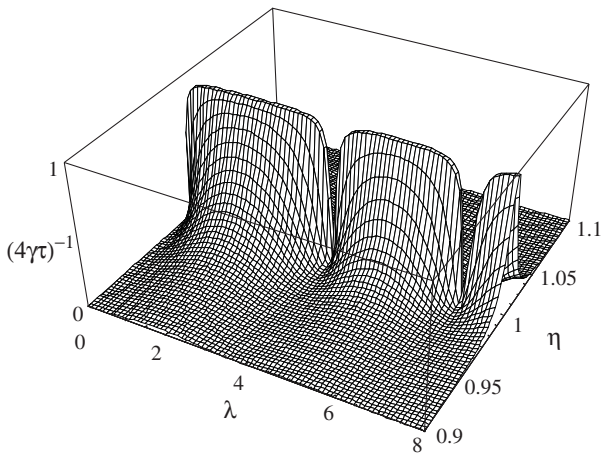

Fig. 1. Reciprocal relaxation time in units of 4γ as a function of dimensionless resonance detuning η and parameter λ, which is proportional to the ac-field magnitude F (see the text). $\omega_0/\Delta = 30$.

Acknowledgements

D. S. is thankful to Vladimir Privman for useful discussions and support. This work was financially supported in part by RFBR and CRDF.

References

[1] V. A. Burdov and D. S. Solenov, *Phys. E*, **24**, 217 (2004).
[2] R. Bavli, H. Metiu, *Phys. Rev. A*, **47**, 3299 (1993).
[3] V. A. Burdov, D. S. Solenov, *Phys. Lett. A*, **305**, 427 (2002).
[4] D. H. Dunlap and V. M. Kenkre, *Phys. Rev. B*, **34**, 3625 (1986).
[5] L. Fedichkin and A. Fedorov, *Phys. Rev. A*, **69**, 032311 (2004).
[6] G. Levine and V. N. Muthukumar, *Phys. Rev. B*, **69**, 113203 (2004).
[7] T. Brandes and T. Vorrath, *Phys. Rev. B*, **66**, 075341 (2002).

13th Int. Symp. "Nanostructures: Physics and Technology"
St Petersburg, Russia, June 20–25, 2005

Electron structure investigations of InGaP/GaAs(100) heterostructures with InP quantum dots

E. P. Domashevskaya[1], V. A. Terekhov[1], V. M. Kashkarov[1], S. Yu. Turishchev[1], S. L. Molodtsov[2], D. V. Vyalikh[3], I. N. Arsentyev[4], I. S. Tarasov[4] D. A. Vinokurov[4] and A. L. Stankevich[4]

[1] Voronezh State University, Universitetskaya pl., 1394693, Voronezh, Russia
[2] Institut für Oberflachen- und Mikrostrukturphysik, TU Dresden, Germany
[3] Institut für Experimentalphysik, Freie Universität Berlin, Arnimallee 14, Berlin, Germany
[4] Ioffe Physico-Technical Institute, St Petersburg, Russia

Abstract. Ultrasoft X-ray emission spectra (USXES) and X-ray absorption near-edge structure (XANES) spectra with the use of synchrotron radiation in the range of $PL_{2,3}$-edges were obtained for the first time for nanostructures with InP quantum dots grown on GaAs ⟨100⟩ substrates by vapour-phase epitaxy from metal-organic compounds. These spectra represent local partial density of states in the valence and conduction bands. All nanostructures demonstrate quantum-size effects and dependence of the band gap in the investigated materials on these effects. Assumptions are made on the band-to-band origin of luminescence spectra in the studied nanostructures.

Introduction

The purpose of this work is to obtain electron yield spectra of samples containing quantum dots applying synchrotron radiation (SR) for investigating the electron energy structure of unoccupied electron states in III-V heterostructures with InP quantum dots buried in InGaP matrix grown on GaAs substrates.

Total electron yield spectra are known to correspond those ones of X-ray absorption near-edge structure (XANES) [1] and they represent distribution of local partial density of states (LP DOS) corresponding to unoccupied states in conduction band of a material to within probability multiplier equal to the square of matrix element of electron transition from the core level to unoccupied states in the conduction band [2].

The obtained XANES spectra were associated with the spectra obtained by ultrasoft X-ray emission spectroscopy technique. Ultra-soft X-ray emission spectra (USXES) allow to determine LP DOS of occupied states in the valence band of the investigated material.

1. Experimental

XANES investigations in the range of $PL_{2,3}$-edges were made at Russian-German beamline of BESSY II synchrotron radiation facility. X-ray optic scheme of XANES measurements involved four mirrors coated with platinum and gold-coated plane grating with 600 lines/mm. Energy resolution was of 0.03 eV. The depth of analysis was about 5 nm.

USXES were obtained with X-ray laboratory spectrometer-monochromator RSM-500 with cylindrical mirror and cylindrical grating having 600 lines/mm and electron beam excitation. Energy resolution of spectrometer was 0.3 eV in the range of $PL_{2,3}$-spectra. The depth of analysis for electron energy in the beam 1–2 keV was about 10 nm.

Samples with quantum dots of InP were grown by vapour phase epitaxy from metal-organic compounds with Epiquip VP 50-RP unit under reduced pressure (100 mbar) at RF heat-ing of substrate. Self-organized nano-sized InP clusters were grown in $In_{0.5}Ga_{0.5}P$ matrix on GaAs ⟨100⟩ substrate [3]. Schematic pattern of such structure is given in the insert to Fig. 1. The structures contained InP nanocrystalline layer and its effective thickness varied from 3 to 10 monolayers. Nanocrystalline layers with quantum dots were capped with wide-band layer of $In_{0.5}Ga_{0.5}P$ of 20 nm thickness.

2. Results and discussion

All of the spectra presented in Fig. 1 are very alike as by energy position of its features as by the ratio of intensities between two peaks connected with spin-orbit splitting of core P 2p-level. The main difference of nanostructures with quantum dots XANES from $In_{0.5}Ga_{0.5}P$ alloy one is the appearance of weak additional peak at the energy of 133.5 eV in spite of 20-nm $In_{0.5}Ga_{0.5}P$ film protecting InP quantum dots. Its intensity increases with the growth of the number of InP monolayers from 3 to 10. One can assume that appearance of additional peak at $\sim$ 133.5 eV arranged at the distance of $\sim$ 3.3 eV from conduction band bottom E_c is connected with stresses at the border of InP quantum dots spreading through all capping $In_{0.5}Ga_{0.5}P$ layer.

$PL_{2,3}$ USXES of $In_{0.5}Ga_{0.5}P$ alloy and heterostructure with 4 ML quantum dots presented in Fig. 2 give the local partial density of occupied states in the valence band of investigated

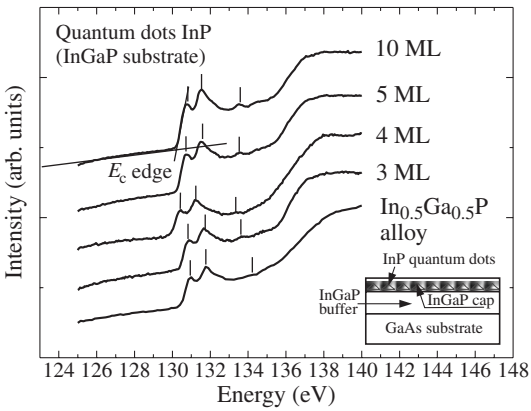

Fig. 1. $PL_{2,3}$ XANES of nanostructures with InP quantum dots with different number of monolayers (E_c is the bottom of conduction band). Insertion — schematic pattern of structure contained InP quantum dots in $In_{0.5}Ga_{0.5}P$ matrix on GaAs ⟨100⟩ substrate. Energy scale relative to core P 2p-level.

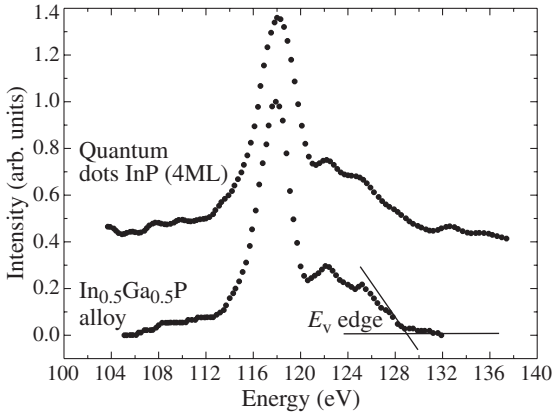

Fig. 2. $PL_{2,3}$ USXES of $In_{0.5}Ga_{0.5}P$ alloy and heterostructure with 4 ML quantum dots (E_v is the valence band top). Energy scale relative to core P 2p-level.

material (E_v is the valence band top).

These data show that width of the $PL_{2,3}$ USXES main maxima in heterostructures with quantum dots are larger that in case of $In_{0.5}Ga_{0.5}P$ alloy.

Fig. 3 represents photoluminescence spectra of the same nanostructures. The left more broad peak of photoluminescence is related to InP quantum dots while the right more narrow one is connected with a thin capping layer of $In_{0.5}Ga_{0.5}P$. The energy position of the right peak ~ 2 eV coincides quite well with the energy gap determined as a difference between the edges of conduction band Ec (XANES) (Fig. 1) and valence band E_v (USXES) (Fig. 2). It means band-to-band origin of photoluminescence spectra as in the alloy as in InP quantum dots. Unfortunately, we do not have information on the values of E_v for nanostructures with quantum dots because of the presence of protecting $In_{0.5}Ga_{0.5}P$ layer. However, the shift of XANES edges to-wards the lower energies in average by 0.2 eV as compared with epitaxial GaInP alloy should result in a decrease of the band gap in these structures at least by this value. In its turn, it must lead to the shift of luminescence peak in quantum dots towards lower energies as well. Just this effect is observed in photoluminescence spectra represented in Fig. 3.

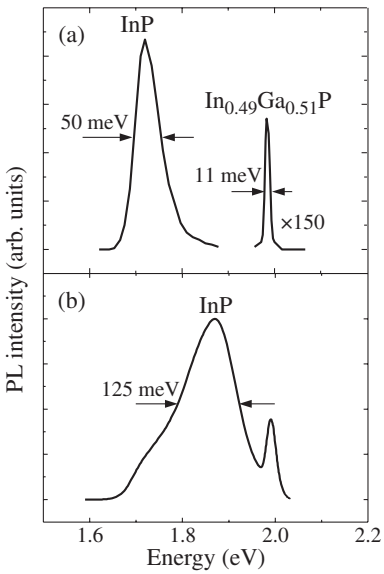

Fig. 3. Photoluminescence spectra ($T = 77$ K) of nanostructure with InP quantum dots (3 ML). Injection power: 100 W/cm^2 (a) and 5 kW/cm^2 (b) [3].

3. Conclusion

For the first time with the use of SR electron yield spectra near $PL_{2,3}$-edge were obtained in nanostructures with InP quantum dots and in $In_{0.5}Ga_{0.5}P$ alloy. XANES and USXES data are in a good agreement with photoluminescence spectra meaning band-to-band origin of the latter ones.

X-ray absorption fine structure with two distinguished peaks is observed for all of the samples. This is connected with spin-orbit splitting of core P 2p-level.

An additional XANES peak at $\sim$ 133.5 eV arranged by $\sim$ 3.3 eV from the bottom of conduction band in nanostructures with InP quantum dots is most likely due to quantum-size effects [4].

Acknowledgement

We are grateful for support of this work to the Director, official BESSY administration, BESSY Beamtime Allocation Committee and Coordinators of Russian-German Beamline facility.

References

[1] T. M. Zimkina *et al*, *Ultrasoft X-ray spectroscopy (Izd-vo LGU Leningrad)*, 153 (1971).
[2] A. S. Vinogradov *et al*, *Pis'ma v JETF*, **15**, 84 (1989).
[3] D. A. Vinokurov *et al*, *Semiconductors* **33**, 707 (1999).
[4] D. R. Yakovlev *et al*, *Semiconductors* **37**, 992 (2003).

13th Int. Symp. "Nanostructures: Physics and Technology"
St Petersburg, Russia, June 20–25, 2005

Modeling of excitation dependences of the photoluminescence from InAs quantum dots

A. G. Gladyshev[1], A. V. Savelyev[1], N. V. Kryzhanovskaya[1], S. A. Blokhin[1], A. P. Vasil'ev[1], E. S. Semenova[1], A. E. Zhukov[1], R. P. Seisyan[1], M. V. Maximov[1], N. N. Ledentsov[1,2] and V. M. Ustinov[1]

[1] Ioffe Physico-Technical Institute, St Petersburg, Russia
[2] Institut für Festkörperphysik, Technische Universität, D-10623, Berlin, Hardenbergst. 36, Berlin, Germany

Abstract. A theoretical simulation of excitation density dependent photoluminescence spectra of samples with InAs/InGaAs/GaAs quantum dots is presented. The modeling is based on a theory well-developed for ideal quantum dots structure. To interpret experimental data the mechanism of non-radiative recombination of carriers is taken into account. It is shown that non-radiative carrier lifetime is roughly constant while excitation power changes by 4 orders of magnitude.

Introduction

Light-emitting devices with self-organized quantum dots are an exciting and rapidly developing area of semiconductor physics. Quantum dots (QD) lasers demonstrate unique characteristics that were earlier predicted by theory: a low threshold current density and high differential efficiency and temperature stability (for review, see [1]). One of the specific properties of QDs compared to quantum well (QW) structures is the possibility to attain longer emission wavelengths in a given material system, for example, InGaAs-GaAs. To increase the emission wavelength, special growth techniques are used, such as activated alloy phase separation [2]. The growing of large QDs can be followed by the formation of dislocations in QDs and large clusters with dislocations, which gives rise to non-radiative recombination. These entities significantly deteriorate the characteristics of QD devices. Despite the fact that some works were devoted to theoretical studies of excitation dependent photoluminescence (PL) spectra for ideal QD samples, only a small number of publications focused on studying non-radiative processes and precise modeling of experimental data for realistic samples [3]. Experimental and theoretical investigation of excitation density dependent PL spectra is very important to understand the radiative and nonradiative recombination mechanisms and improve internal quantum efficiency of QD devices.

In this work we offer method of modeling of PL spectra excitation dependences for QD's structure. The method is based on a theory developed in works [4, 5]. We have added mechanism of non-radiative recombination of carriers [6], to make theoretical model more suitable for experimental data explanation. To test the model the room temperature (RT) PL spectra of self-assembled InAs QD's structure were measured at different excitation density.

1. Experiment

The structure studied in this work was grown by a molecular beam epitaxy (MBE), on (001)-oriented GaAs substrate followed by an undoped GaAs buffer layer at 600 °C. Three layers of self-assembled InAs QDs (2.4 ML) in 50 Å thick InGaAs quantum wells (QW) and 50 Å thick GaAs spacers between them were grown at 480 °C. This active region was embedded in the middle of 2000 Å thick GaAs layer. Two 1000 Å thick AlGaAs barriers were grown on both sides of the GaAs layer to prevent carrier leakage to the substrate and the surface. A 100 Å GaAs cap layer was grown at 600 °C on the top of the structure.

The PL spectra were excited with second harmonic of CW YAG:Nd laser (532 nm). The power density was varied in 0.01–350 W/cm^2 range, the laser spot diameter was about 200 μm. PL signal was measured by a grating monochromator operating with a cooled Ge photodiode. The spectra were recorded using standard lock-in technique.

2. Results and discussion

Figure 1a shows the PL spectra at different excitation densities. The ground state QD's emission at RT is centered at 0.993 eV. By increasing the excitation power density (P_{exc}) in the 0.01–350 W/cm^2 range a clear band filling effect is observable. Two additional excited state recombination peaks at 1.055 eV and 1.105 eV as well as two peaks at 1.274 eV and 1.42 eV are clearly distinguishable at the high P_{exc} and attributed to QW and GaAs matrix emission, respectively.

Dependence of integrated PL intensity (IPL) on excitation density is shown in Fig. 2. Three regions with different slops

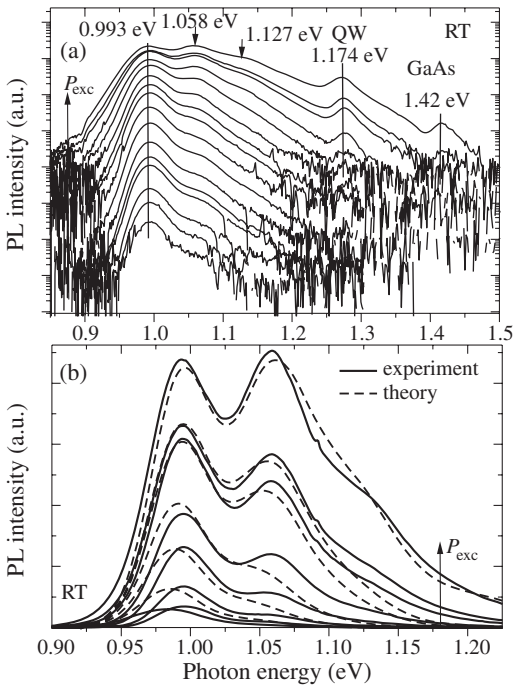

Fig. 1. (a) PL spectra of QD's structure at different excitation density at room temperature. The power density increased from 0.01 to 350 W/cm^2. (b) Comparison between experimental (continuous lines) and calculated (dashed lines) PL spectra at different (from 6 to 350 W/cm^2) power densities.

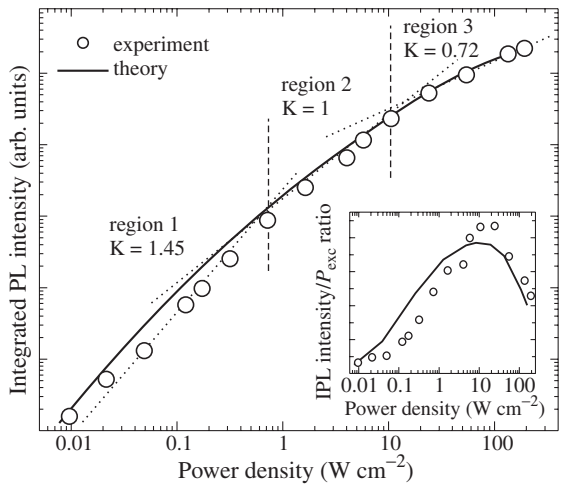

Fig. 2. Dependence of IPL intensity on excitation density. Circles represent experimental data, the continuous line is calculation. The inset shows ratio between IPL intensity and $P_{\rm exc}$ at different power densities.

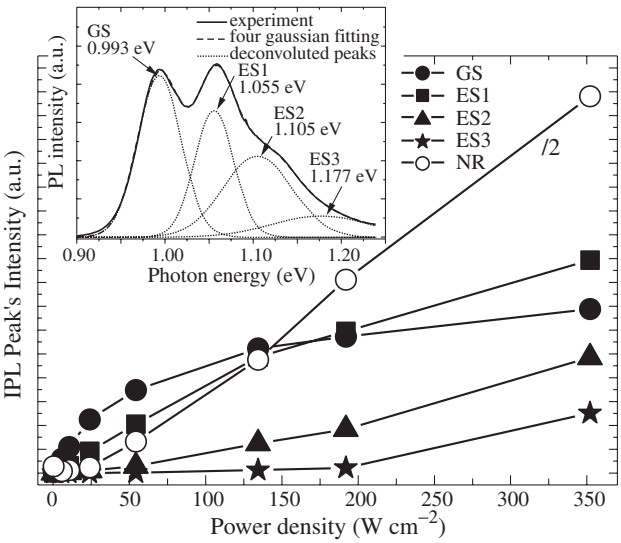

Fig. 3. IPL peak's intensity at different power density. Circles, squares, triangles and stars correspond to the experimental data on the ground state, the first, second and third excited states, respectively. The hollow circles represent non-radiative losses divided by 2.The inset shows the four gaussian fitting of the PL spectrum measured at $P_{\rm exc} = 350\,{\rm W/cm^2}$.

can be marked out on this dependence. The slope (k) of the first one, where $P_{\rm exc}$ changes from 0.01 to 0.7 W/cm^2, is equal to 1.45, i.e. dependence shows superlinear behavior. Earlier this superlinearity was explained by presence of saturated non-radiative centers near or inside QDs (for example, point defects) [6]. The assumption was related to the fact that superlinearity becomes weaker as the power increases and approaches linearity ($k = 1$) at the higher power (region 2). The third region is characterized by appearance of QW and GaAs matrix emissions and changing of the slope from 1 to 0.72. Such behavior of PL excitation dependence indicates the escaping of carriers from QDs states and nonradiative recombination in QW or/and GaAs matrix.

Assumptions of an equilibrium carrier distribution between QD's states, QW and GaAs matrix makes possible to study radiative and non-radiative processes independently. To determine energies of optical transitions and inhomogeneous broadening of QD's energy states PL spectra measured at the high power ($P_{\rm exc} = 110\,{\rm W/cm^2}$) were deconvoluted on four Gaussian peaks (see inset in Fig. 3). The last necessary optical parameters are effective reciprocal radiative lifetimes (g/τ_r, where g is the level degeneracy) which were reconstructed by fitting calculated spectra to experimental ones. Confinement energies of electrons and holes were taken from work of O. Stier *et al* [7]. Calculated PL spectra (see Fig. 1b) demonstrate good agreement with experiment in wide range of excitation power density. To the best of our knowledge this is the first detailed experimental verification of the well-known theory [3,4] of QD PL using wide range of injection powers. As a result of fitting the position of quasi-Fermi energy levels was obtained for each excitation power density. After that one can test models of non-radiative recombination by comparing predicted efficiency dependence with an experimental one.

As it was proposed earlier [6] there are two types of non-radiative recombination: recombination in defects that saturates at low injection current and recombination in lattice defects in a surrounding matrix that plays major role at the high injection. Here we use following expressions for current density of matrix recombination: $J_{\rm NR} = n_m/\tau_{\rm NR}$, where n_m — total surface density of non-localized carriers in InGaAs QW and GaAs matrix, $\tau_{\rm NR}$ — non-radiative lifetime. Results of calculation are presented in Fig. 2 and a good agreement between calculation and experiment can be seen. The best agreement corresponds to $\tau_{\rm NR} = 1.1\,{\rm ns}$ what agrees well with previous results [8] obtained from temperature PL dependencies. Power of radiative recombination through ground and excited states of QD's and total power of non-radiative recombination are presented in Fig. 3. It should be noted here that radiative recombination in QW and GaAs is much less than non-radiative component and is not considered here. In the inset to Fig. 2 the ratio between IPL intensity and $P_{\rm exc}$ (external efficiency) is shown. In the present calculations this ratio remarkably decreases with excitation decreases at low densities though centers that can be saturated are not included in the model. This fact can be explained by the presence of thermally activated carriers escaping from QD's states to matrix that control non-radiative recombination both at the low and high power densities. Therefore non-radiative recombination in the InAs/InGaAs/GaAs self-organized QD ensemble can be roughly described by only one time constant $\tau_{\rm NR}$.

Acknowledgements

This work was supported by the Russian Foundation of Basic Research and Physics of Solid State Nanostructures program, SANDiE.

References

[1] M. V. Maximov and N.N. Ledentsov, *Quantum Dots Lasers*, in Dekker Encyclopedia of Nanoscience and Nanotechnology, James A. Schwarz, Cristian I. Contescu and Karol Putyera, Eds.; Marcel Dekker, (New York), pp. 3109–3126, 2004.
[2] B. V. Volovik *et al*, *Semiconductors*, **33**, 901 (1999).
[3] E. C. Le Ru *et al*, *Phys. Rev. B*, **67**, 245318 (2003).
[4] L. V. Asryan and R. A. Suris, *Semicond. Sci. Technol.*, **11**, 554 (1996).
[5] L. V. Asryan *et al*, *IEEE J. Quantum Electron.*, **37**, 418 (2001).
[6] M. V. Maximov *et al*, *Semiconductors*, **38**, 1207 (2004).
[7] O. Stier *et al*, *Phys. Rev. B*, **59**, 5688 (1999).
[8] M. V. Maximov *et al*, *ICPS-26*.

13th Int. Symp. "Nanostructures: Physics and Technology"
St Petersburg, Russia, June 20–25, 2005

Application of symmetry in $k \cdot p$ calculations of the electronic structure of pyramidal self-assembled InAs/GaAs quantum dots

N. Vukmirović, D. Indjin, V. D. Jovanović and *P. Harrison*
School of Electronic and Electrical Engineering, University of Leeds, Leeds LS2 9JT, United Kingdom

Abstract. A method for the calculation of the electronic structure of pyramidal self-assembled quantum dots is presented. The plane wave method was used to solve the 8-band $k \cdot p$ Hamiltonian taking strain into account via continuum mechanical model. $\overline{C}_4$ symmetry of the Hamiltonian was used to block diagonalize the corresponding Hamiltonian matrix into four matrices of approximately equal size and therefore significantly reduce the computational time. The method was applied to calculate electron and hole quasibound states in a periodic array of vertically stacked pyramidal self-assembled InAs/GaAs quantum dots.

Introduction

Semiconductor quantum dots made by Stranski-Krastanow growth have attracted great interest over the past years due to their application in optoelectronic and microelectronic devices. In order to model and design such devices the electronic structure needs to be accurately known. The large lattice mismatch between InAs and GaAs has enabled the fabrication of quantum dots putting it at the forefront of both theoretical and experimental research. Different quantum dot shapes (such as pyramid, lens, cone and cylinder) of InAs/GaAs self-assembled quantum dots are often reported. A range of theoretical approaches has been used so far to calculate the energy levels in self-assembled quantum dots — effective mass [1,2], $k \cdot p$ [3,4] and empirical pseudopotential method [5]. In quantum dots with cylindrical symmetry, symmetry considerations have been applied to effectively reduce the geometry of the problem from a three dimensional to a two dimensional, both in the effective mass and the $k \cdot p$ method (within the axial approximation) [6]. C_{4v} symmetry of the pyramid has been used in the effective mass calculation [7] to reduce the size of the corresponding Hamiltonian matrix, however in none of the $k \cdot p$ calculations of pyramidal quantum dots has the explicit use of symmetry of the Hamiltonian been reported. The aim of this paper is to develop a method, based on symmetry considerations, for faster calculation of the electronic structure of pyramidal InAs/GaAs quantum dots. The method was then applied to calculate electron and hole quasibound states in a periodic array of vertically stacked pyramidal self-assembled InAs/GaAs quantum dots.

1. Theory

The 8-band $k \cdot p$ Hamiltonian [8] is used to calculate the energy levels both in the conduction and the valence band. The strain distribution is taken into account via the continuum mechanical model. The plane wave method [9] was used to solve the eigenvalue problem of the Hamiltonian matrix, therefore only Fourier transforms of the strain components are necessary and they are given by analytical formulae [10]. The number of plane waves taken is

$$N = 8(2n_x + 1)(2n_y + 1)(2n_z + 1)\,,$$

where $n_x = n_y$ and $2n_t + 1$ is the number of plane waves per dimension t ($t \in \{x, y, z\}$). The $k-$th element of the 8-component state spinor was thus taken as a linear combination of plane waves:

$$\psi_k(x, y, z) = \sum_{m_x=-n_x}^{n_x} \sum_{m_y=-n_y}^{n_y} \sum_{m_z=-n_z}^{n_z} A_{k,m_x,m_y,m_z} \times \exp\left[2i\pi\left(\frac{m_x x}{L_x} + \frac{m_y y}{L_y} + \frac{m_z z}{L_z}\right)\right].$$

The direct application of this approach would lead to an eigenvalue problem of a matrix of size $N \times N$. However, it is possible to exploit the symmetry of the system to block diagonalize the corresponding matrix.

The symmetry group of the system is the double group $\overline{C}_4$ [11]. The generator of the group is the total angular momentum $\hat{F}_z$ and therefore the representations of the elements of the group are given by $\hat{D}(R(\varphi)) = \exp(-i\varphi\hat{F}_z)$, where $\varphi \in \{k\pi/2\}$ ($k \in \{0, 1, \ldots, 7\}$) and $R(\varphi)$ is a rotation by an angle φ. The representation of the element $\hat{D}(R(\pi/2))$ acts on each component of the eight component state spinor as:

$$\hat{D}(R(\pi/2))\psi_k(x, y, z) = \exp(-iJ_z(k)\pi/2)\psi_k(y, -x, z)\,,$$

where $k \in \{1, 2, \ldots, 8\}$ and J_z is the z-component of the total angular momentum of Bloch basis state for the k-th component of the spinor ($J_z(1) = -1/2$, $J_z(2) = 1/2$, $J_z(3) = 1/2$, $J_z(4) = 3/2$, $J_z(5) = -3/2$, $J_z(6) = -1/2$, $J_z(7) = -1/2$, $J_z(8) = 1/2$).

Knowing how a representation of the generating element $R(\pi/2)$ acts on the states, it is straightforward to find the characters [11] of the representation D. The characters obtained were then used to reduce the representation into its irreducible constituents. It was found that

$$D = N_1 A_{1/2} + N_1 A_{-1/2} + N_2 A_{3/2} + N_2 A_{-3/2}\,,$$

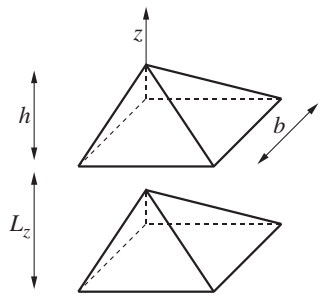

Fig. 1. Quantum dot geometry. The width of the base is b, the height h, the period of the structure is L_z.

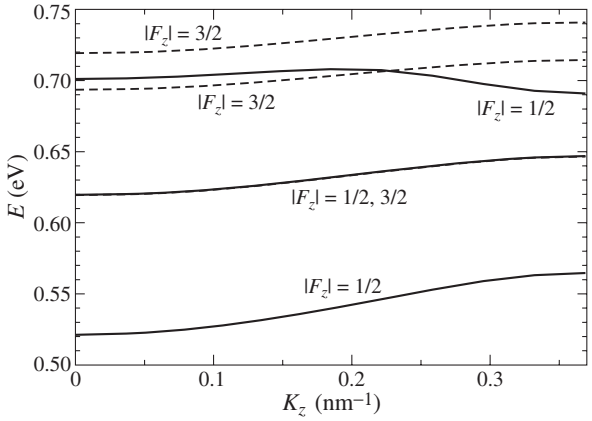

Fig. 2. Miniband structure of electron levels of the periodic array of vertically stacked InAs/GaAs quantum dots. The states with total quasi-angular momentum $|F_z| = 1/2$ are denoted by full lines and the states with $|F_z| = 3/2$ by dashed lines.

where

$$N_1 = 8n_x(n_y + 1)(2n_z + 1) + 3(2n_z + 1)\,,$$

$$N_2 = 8n_x(n_y + 1)(2n_z + 1) + 2n_z + 1$$

and $A_{F_z}(R(k\pi/2)) = \exp(ikF_z\pi/2)$ are the irreducible representations of the double group $\overline{C}_4$. Projection operators [11] were then used to find the symmetry adapted basis. In this basis the Hamiltonian matrix is block diagonal with four blocks of sizes $N_1 \times N_1$, $N_1 \times N_1$, $N_2 \times N_2$ and $N_2 \times N_2$, respectively. The corresponding matrices were diagonalized using the standard EISPACK routines.

2. Results

The method presented was applied to the calculation of the electronic structure of periodic array of vertically stacked pyramidal self-assembled quantum dots (Fig. 1). The width of the pyramid base was taken to be $b = 15\,\text{nm}$, the height $h = 7.5\,\text{nm}$, the wetting layer width $d_{WL} = 2.1\,\text{ML}$ and the period of the structure in z-direction $L_z = 8.5\,\text{nm}$. The piezoelectric effect that breaks the $\overline{C}_4$ symmetry of the Hamiltonian was neglected since our calculations have shown that its influence on the energy levels is of the order of 1 meV.

According to Bloch's theorem, the k-th component of the state spinor is given by

$$\Psi_k(x, y, z) = \exp(iK_z z)\psi_k(x, y, z)$$

and the K_z-dependence of the energy levels is shown in Fig. 2 for electrons and Fig. 3 for holes. In both figures the bottom of the unstrained InAs conduction band is taken as the energy reference level. In the calculation, the values $L_x = L_y = 2b$ were taken. Each state is characterized by two quantum numbers K_z and F_z. The quantum number F_z is a consequence of $\overline{C}_4$ symmetry and can be interpreted as the total quasi-angular momentum. It can be proved by considering the two dimensional irreducible representations of the more general double group $\overline{C}_{4v}$ [11] that states with the same absolute value of total quasi-angular momentum (and the same K_z) are degenerate, as confirmed by our calculation.

As seen from Fig. 2, the energies in the conduction band are increasing functions of K_z except for the second excited $|F_z| =$

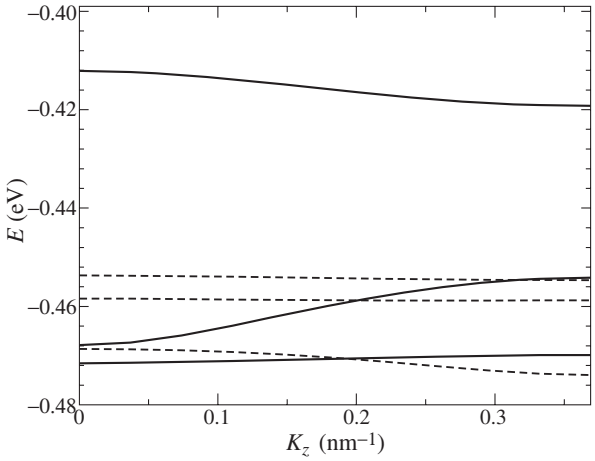

Fig. 3. Miniband structure of hole levels of the periodic array of vertically stacked InAs/GaAs quantum dots. The states with total quasi angular momentum $|F_z| = 1/2$ are denoted by full lines and the states with $|F_z| = 3/2$ by dashed lines.

$1/2$ miniband which has a maximum at approximately $K_z = \pi/2L_z$ and crosses with the first excited $|F_z| = 3/2$ miniband for slightly larger K_z. The ground $|F_z| = 3/2$ miniband and the first excited $|F_z| = 1/2$ miniband are nearly degenerate. If the piezoelectric effect that we have neglected were included, it would lead to a small splitting (of the order of 2 meV) of these two minibands. The miniband energy widths are of the order of 20–30 meV.

The hole minibands exhibit a more complicated structure (Fig. 3). There is an energy gap of approximately 30 meV between the ground $|F_z| = 1/2$ miniband and the other minibands, which lie very close to each other and often exhibit crossings.

References

[1] J. Y. Marzin *et al*, *Solid State Commun.*, **92**, 437 (1994).
[2] M. Califano *et al*, *Phys. Rev. B*, **61**, 10959 (2000).
[3] O. Stier *et al*, *Phys. Rev. B*, **59**, 5688 (1999).
[4] C. Pryor *et al*, *Phys. Rev. Lett.*, **80**, 3579 (1998).
[5] L. W. Wang *et al*, *Phys. Rev. B*, **59**, 5678 (1999).
[6] M. Tadić *et al*, *Phys. Rev. B*, **65**, 165333 (2002).
[7] M. Roy *et al*, *Phys. Rev. B*, **68**, 235308 (2003).
[8] T. B. Bahder *et al*, *Phys. Rev. B*, **41**, 11992 (1990).
[9] A. D. Andreev *et al*, *Phys. Rev. B*, **62**, 15851 (2000).
[10] A. D. Andreev *et al*, *J. Appl. Phys.*, **86**, 297 (1999).
[11] J. P. Elliott *et al*, *Symmetry in Physics*, London, UK 1979.

13th Int. Symp. "Nanostructures: Physics and Technology"
St Petersburg, Russia, June 20–25, 2005

Temperature stability of optical properties of InAs quantum dots overgrown by AlAs/InAlAs layers

N. V. Kryzhanovskaya[1], A. G. Gladyshev[1], S. A. Blokhin[1], A. P. Vasil'ev[1], E. S. Semenova[1], A. E. Zhukov[1], M. V. Maximov[1], V. M. Ustinov[1], N. N. Ledentsov[1,2] and D. Bimberg[2]

[1] Ioffe Physico-Technical Institute, St Petersburg, Russia
[2] Institut für Festkörperphysik, Technische Universität Berlin, Germany

Abstract. The work is focused on the optical properties of quantum dots formed in GaAs or AlGaAs matrixes by overgrowth of initial Stransky-Krastanov InAs islands with thin AlAs/InAlAs layers. The quantum dots emit at 1.27 μm at room temperature. It is shown that transport of carriers between neighbouring quantum dots in the temperature range 10–300 K is absent, and, correspondingly, the carrier distribution remains non-thermal. Suppression of the thermal escaping of the carriers is conditioned by high energy separation between ground- and first excited-state, absence of wetting layer level, and increase of carrier localization energy in quantum dots in case of $Al_{0.3}Ga_{0.7}As$ matrix.

Introduction

Self-assembled quantum dots (QDs) are of great interest because of their technological importance. Lasers with quantum dot active region have many attractive properties that originate in the three dimensional confinement of the QDs [1]. On the other hand, as it known, an InAs medium has relatively poor thermal stability, and this has been attributed to the thermal excitation of carriers into excited dot states. To improve the thermal stability of the QDs lasers ground-to-first-state energy separation should be increased. Thus, development of the growth methods allowing controlling of the energetic spectrum of the QDs, is of great importance. As have been shown, appropriate choice of the growth methods provides a means of tuning the properties of the QDs in a controlled way. Recently it has been shown that the deposition of a thin Al-containing layers after the growth of InAs QDs lead to longer wavelength emission, narrower linewidth and increased separation between the confined QD electronic states [2, 3]. At this work, comparative studies of the optical properties of InAs quantum dots covered by thin AlAs/InAlAs layers and InAs quantum dots overgrown by thin $In_{0.15}Ga_{0.75}As$ layer are done. Carrier transfer phenomena are studied in the expanded temperature range 10–500 K.

1. Experiment

Structures were grown by molecular beam epitaxy on GaAs (100) substrates. The QDs were embedded in a 0.2-μm-thick GaAs (structures A, B, C) or $Al_{0.3}Ga_{0.7}As$ (structures D) matrix layer confined by wide-gap barriers. The QDs were grown using the following sequence: first original InAs islands were formed by depositing 2.3 monolayers (ML) of InAs that was then overgrown with various capping layers at 485 °C. The rest epitaxial layers were grown at 600 °C. In sample A the dots were capped by GaAs, in sample B — by traditional 4 nm-thick $In_{0.15}Ga_{0.85}As$ layer, in sample C — 2 ML of AlAs and 4 nm-thick $In_{0.25}Al_{0.75}As$ with. The sample D is analogues to sample C, but the matrix was $Al_{0.3}Ga_{0.7}As$.

The photoluminescence (PL) was excited by cw Ar^+ laser ($W = 1500\,W/cm^2$, $\lambda = 514$ nm) or cw YAG:Nd laser, ($W = 1500\,W/cm^2$, $\lambda = 532$ nm) and detected by a cooled Ge photodiode. Low-temperature PL measurements were carried out by mounting the samples in a closed-cycle He cryostat. For high temperature measurement samples were mounted in the thermostat. For the measurements of the photoluminescence excitation (PLE) spectra and resonant PL (RPL), the tunable excitation source was provided by a 250 W tungsten halogen lamp, dispersed by a monochromator. The samples were mounted in a helium flow cryostat.

2. Results and discussion

Figure 1 shows room temperature PL spectra of the QDs. Except for the lines attributed to the ground QD state and excited QD states, peaks attributed to the matrix and, in case of structures A and B, to the wetting layer and $In_{0.15}Ga_{0.85}As$ layer are seen. Redshift of the PL line of the QDs overgrown by $In_{0.15}Ga_{0.85}As$ layer (structure B) is well studied and attributed to the several reasons. The main reason is activated alloy phase separation, increasing the QDs size [3]. The possibility to shift the QDs emission to 1.3 μm by deposition of a thin Al-containing layers after the growth of InAs QDs was described in several works [2, 3]. It was shown in work [2] that deposition of AlAs layer on top of the InAs QDs results in the increase of QDs height owing to replacement of In atoms from the wetting layer by Al atoms. As well as deposition of thin $In_xAl_{1-x}As$ layer increases the QD volume due to directional migration of In adatoms toward islands [3]. As a result, PL emission energy decreases and ground-to-first-state energy

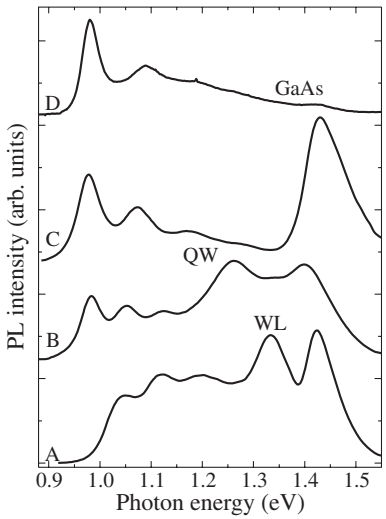

Fig. 1. Room temperature PL spectra of samples A–D.

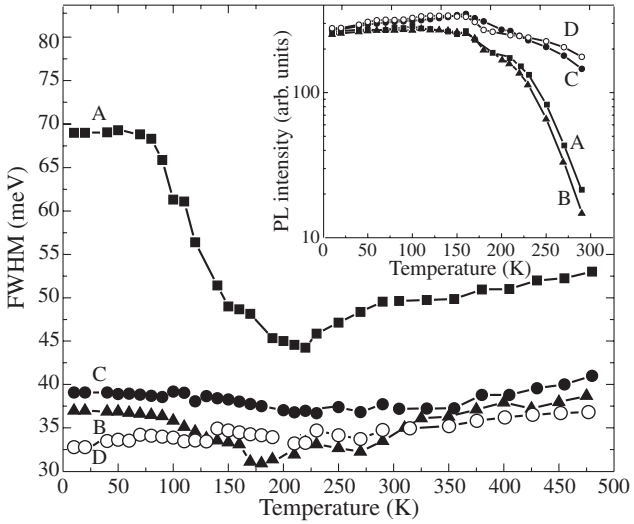

Fig. 2. Temperature dependencies of FWHM of structure A, B, C, D. Inset: temperature dependencies of the integral intensities.

increases.

Figure 2 shows the full width at half maximum (FWHM) of the QD peak plotted as function of temperature. PL was excited by Ar^+ laser ($3\,W/cm^2$). The dependence for samples A and B are typical and explained by the model of the temperature driven carrier dinamics. At low temperatures carrier population of QD anssemble is nonequilibrium and they distributed randomly. With the temperature going up carriers are thermaly activated out of the dots into the matrix and relax into the dots which provide higher localization, resulting in narrowing of the FWHM increases. At the higher temperatures quasiequilibrium in carrier distribution between QDs is established and PL linewidth becomes independent of temperature. As can be seen in the structures with Al-containing layers (samples C and D) FWHM is practically unchangeble with temperature, indicating absence of the carrier redistribution processes.

The inset in Fig. 2 compares dependencies of the PL intensity of the Al-containing samples with reference structure A. Although at low temperature the intensities are comparable, at high temperatures the PL intensities of the Al-capped structures are approximately an order of magnitude greater than that of the Al-free reference structure. The reason for this enhancement of the high temperature optical efficience is supression of the thermal carrier escape from QDs to matrix due to high energy separation between ground and excited QD states, absence of the wetting layer level and presence of AlAs/InAlAs barriers.

PLE spectra of samples B, C, D, obtained at different temperatures are shown at Fig. 3. Detection energy corresponds to QD PL maximum at the temperature. Spectra are shifted for clarity. At low temperature all spectra reveal features due to absorption in the barrier,excited states and in the InGaAs layer in structure B and LO-phonon resonances. At the PLE spectra of sample B all resonant lines quenches with temperature increase and disappear at 270 K. At RT PLE spectra any features are absent. That signifies that excitation is not selective for a QDs with ground state energy E_{DET} and carriers are in quasiequilibrium. At the PLE spectra of the sample C, resonant line associated with first excited state absorption remains at RT. That fact signifies suppression of the carrier escape mechanism up to 300 K and conservation of selective excitation

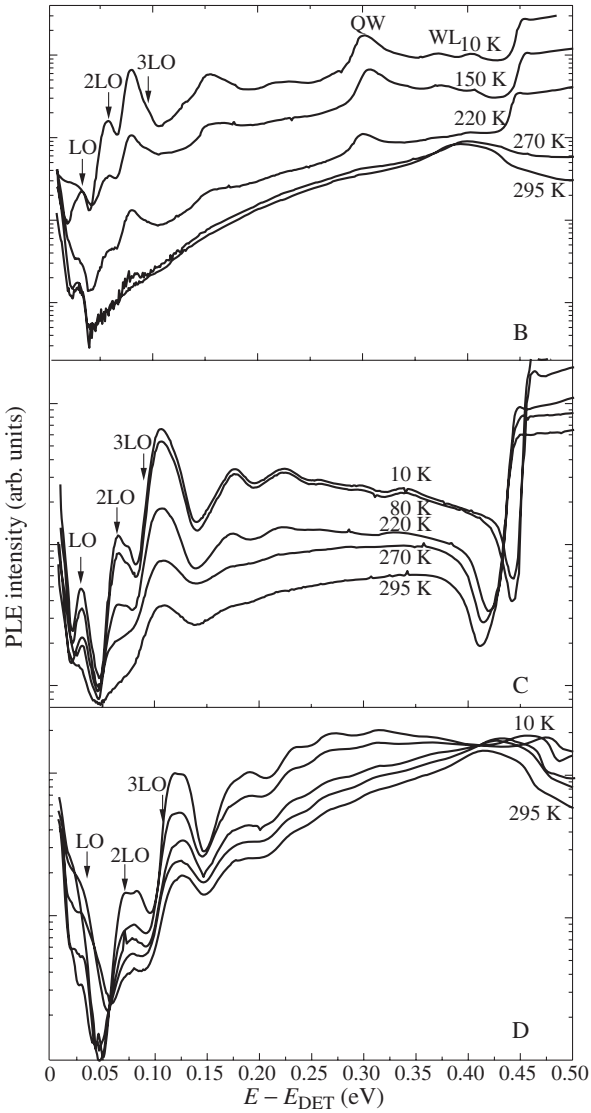

Fig. 3. PLE spectra of the structures B, C, D obtained at different temperatures.

conditions. Features corresponding to phonon-assisted carrier relaxation are observed also at resonant PL spectra (not shown) of the quantum dots up to room temperature, that signifies the absent of the thermal carriers distribution between quantum dots states.Thus at RT carriers captured in QDs are isolated and carrier distribution between QDs states is nonequilibrium.

Acknowledgement

This work was conducted in the frame of joint scientific program between Ioffe Institute (Russia) and NL-Nanosemiconductor-GmbH (Germany). The work is supported by RFBR, SANDiE. N. V. Kryzhanovskaya thanks INTAS Young Scientist Fellowship programm 03-55-882 for support.

References

[1] N. N. Ledentsov, M. Grundmann, N. Kirstaedter, *et al*, *Solid State Electron.* **40**, 785 (1996).

[2] A. F. Tsatsul'nikov, A. R. Kovsh, A. E. Zhukov, *et al*, *J. Appl. Phys.* **88**, p. 6272, (2000).

[3] M. V. Maximov, A. F. Tsatsul'nikov, B. V. Volovik, *et al*, *Phys. Rev. B*, **62**, p. 16671, (2000).

13th Int. Symp. "Nanostructures: Physics and Technology"
St Petersburg, Russia, June 20–25, 2005

Spatial structure of an individual deep acceptor in a cubic crystal

A. M. Monakhov, K. S. Romanov, I. E. Panaiotti and N. S. Averkiev
Ioffe Physico-Technical Institute, St Petersburg, Russia

Abstract. The wave-function of a hole localized on deep acceptor is considered. The cubic symmetry of the crystal has been taken into account. The obtained pictures qualitatively agree with STM image of Mn in GaAs.

Introduction

The development of STM and ATM methods stimulated the investigations of defects and nanoobjects in semiconductors. These methods allow to visualize the space charge distribution of the localized carriers. So, the quantum-mechanical calculation of the space charge distribution near the impurity atom which takes into account the actual crystal symmetry becomes an urgent problem.

It was shown that STM image of Mn in GaAs have a clear cubic symmetry [1]. Therefore the localized hole space charge distribution has the same symmetry. This result is very important because up to now the calculations of various parameters of deep and hydrogen-like acceptors in cubic crystals have been provided in the spherical approximation. This approximation describes such parameters as g-factor, deformation potential coefficients and dipole momentum value quite well. So, it is important to check out whether the spherical approximation is correct enough to describe such systems.

We propose the calculation of the space charge distribution of the hole localized on the deep acceptor in the effective mass approximation using the zero-range potential method. We took into account both the symmetry and degeneration of the GaAs valence band. The results of the simulation were compared with the STM experimental data in [1,2].

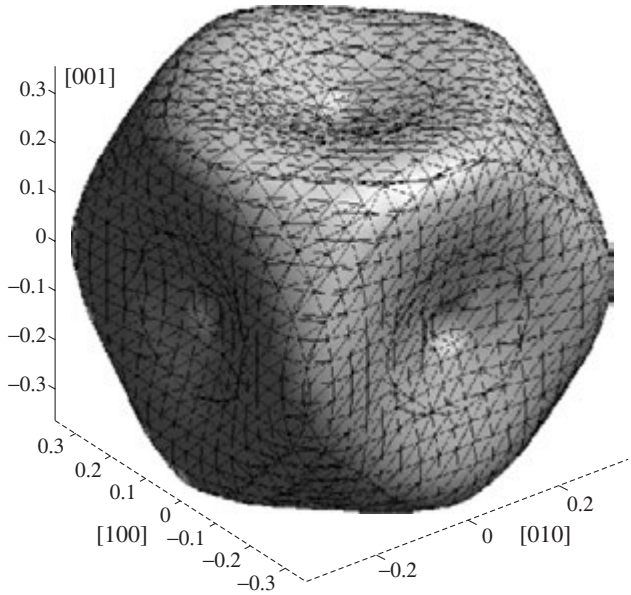

Fig. 1. The isosurface of the calculated wave-function squared module of the hole bounded on Mn in GaAs.

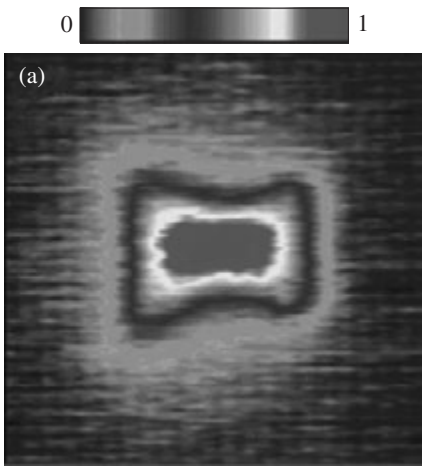

Fig. 2. The STM image of Mn in GaAs in [110] plane (from [2]).

1. Discussion

To calculate the wave-function of a deep center in cubic crystal it is convenient to use the zero-range potential method. This method is most appropriate for the deep enough acceptor. For instance it can be used for the description of the point defect in the heterostructure based on GaAs with the binding energy about 100 meV. The zero-range potential method allows one to take into account the Hamiltonian symmetry and gives the correct wave-function asymptotics far from the center.

Magnetic properties of Mn are known to reveal themselves clearly at the helium temperature, but in the experiments [1, 2] the temperature was $T = 300\,\mathrm{K}$ [3]. So, the exchange interaction between the bounded hole and Mn's 3d5 electron can be neglected.

The Shredinger equation for the hole localized on acceptor in the zero-range potential model is:

$$\hat{H}\psi(\vec{r}) = E\psi(\vec{r}) + V\delta(\vec{r} - \vec{r}_0) ,$$

where ψ and V are the 4 component spinors and $\hat{H}$ is:

$$\hat{H} = \Big[\Big(\gamma_1 + \frac{5}{2}\gamma_2\Big)\frac{p^2}{2} - \gamma_2\Big(\vec{p}\vec{J}\Big)^2 - 2\gamma_3\Big(\{p_x p_y\}\{J_x J_y\} + \{p_y p_z\}\{J_y J_z\} + \{p_z p_x\}\{J_z J_x\}\Big)\Big] ,$$

where γ_1, γ_2 and γ_3 are the Luttinger parameters and J are the matrices of the 3/2 momentum.

In the p-representation the equation (1) becomes an algebraic set of equations which can be solved analytically. To determine the space charge distribution is it necessary to obtain the Fourier transformation of the set of solutions. This problem has been solved numerically using discrete Fourier transform.

2. Results

The isosurface of the space charge distribution of the hole localized on a Mn acceptor is shown in Fig. 1. The STM image of such a center is shown in Fig. 2. It can be seen that there is qualitative agreement between the cross-section of Fig. 1 and Fig. 2, but for the quantitative comparison it should be taken into account that STM image is not the exact image of the wave-function squared module.

Acknowledgement

This work was supported in part by INTAS, RFBR, Ministry of Sciense and Education of Russia and scientific programs of RAS. K. S. Romanov acknowledges partial support from Dynasty foundation — ICFPM.

References

[1] A. M. Yakunin, A. Yu. Silov, P. M. Koenraad, J. H. Wolter, W. Van Roy, J. De Boeck, J.-M. Tang and M. E. Flatté, *Proc. of Nanostructures: Physics and Technology (St Petersburg, Russia, 2004)*, Ioffe Institute, 146 (2004).

[2] A. M. Yakunin, A. Yu. Silov, P. M. Koenraad, J. H. Wolter, W. Van Roy, J. De Boeck, J.-M. Tang and M. E. Flatte, *Phys. Rev. Lett.*, **92**, 216806 (2004).

[3] N. S. Averkiev, A. A Gutkin, E. B. Osipov and M. A. Reshchikov, *Sov. Phys. Sol. St.*, **30**, 1119 (1987).

13th Int. Symp. "Nanostructures: Physics and Technology"
St Petersburg, Russia, June 20–25, 2005

Recombination processes in systems based on ionic crystals with embedded self-organized nanocrystals

N. G. Romanov, A. G. Badalyan, D. O. Tolmachev, V. L. Preobrazhenski and P. G. Baranov
Ioffe Physico-Technical Institute, St Petersburg, Russia

Abstract. The recombination processes leading to tunnelling afterglow and photostimulated luminescence were studied in systems based on ionic host crystals with low-dimensional structures (semiconductor quantum dots) formed as a result of the self-organized growth. The systems of AgBr nanocrystals embedded into KBr crystal lattice and $CsPbBr_3$ or $CsEuBr_3$ nanocrystals embedded into the CsBr crystal lattice were investigated. The energy of electron-hole recombination in matrices was shown to transfer through the interface to quantum dots. To identify the structure of recombining electron and hole centers magnetic resonance detected optically by monitoring photoluminescence, tunnelling afterglow and photostimulated luminescence was used.

Introduction

In the last years, nanostructures have been successfully fabricated using self-organization effects common to strained heterosystems [1]. Semiconductor nanocrystals are of interest because of their high radiation efficiency due to quantum confinement effects. In addition to the scientific interest, their strong luminescence has also attracted attention for many applications including X-ray computer radiography [2].

Nanocrystals can be formed inside ionic crystals as a result of the self-organized growth. This was first demonstrated for copper and silver halide nanocrystals embedded in face-centered cubic alkali halide matrices with NaCl structure [3, 4 and refs. therein] and for $CsPbCl_3$ — like nanocrystals in body-centered alkali halide crystals with CsCl structure [5]. The embedded nanocrystals have the energy gaps which are by more than 5 eV narrower than those of the host crystals and can be considered as an array of self-organized quantum dots in a strained heterosystem.

In KCl/AgCl and KBr/AgBr, similar to InAs/GaAs the atoms of the same group are replaced. Therefore, the driving force of nanocrystal growth is strain on heterojunction. A different situation takes place in formation of nanostructures in alkali halides doped with impurity ions which have an excess charge, for example, doubly charged Mn^{2+}, Pb^{2+}, Eu^{2+} etc. ions. In this case cationic vacancies are formed to compensate the excess charge and at high enough temperatures nanometer size aggregates of impurity ion — cationic vacancy are formed. Such aggregates exist as a so called Suzuki phase in NaCl type crystals and as nanocrystals in CsCl type crystals (for example, $CsPbCl_3$ in CsCl:Pb [5]).

In this communication we report on the study of recombination processes leading to tunnelling afterglow and photostimulated luminescence in systems based on ionic host crystals with impurity-related low-dimensional structures, which are formed as a result of the self-organized growth.

1. Results and discussion

KBr:Ag, CsBr:Pb and CsBr:Eu crystals were grown by the Stockbarger technique. Tunnelling recombination afterglow was detected for many hours after X-ray irradiation of these crystals. Optical excitation in the long wavelength absorption bands of radiation centers leads to photostimulated luminescence PSL), which is higher in energy and originates from various recombination processes. Due to spin dependence of the afterglow and PSL optically detected magnetic resonance (ODMR) of the recombining defects and excitons can be studied as was discovered in [6, 7].

Figure 1 shows the tunnelling afterglow spectra and photostimulated luminescence excited by 650 nm light in CsBr:Pb (0.2%) crystals after quenching from 800 K (solid lines) and subsequent 20 min annealing at 450 K (dashed lines). The X-ray irradiation and the luminescence measurements were performed at 77 K. The afterglow spectrum consists from a broad band assigned to the electron-hole recombination in the host CsBr crystal and a narrow band, which is similar to that detected in the absorption and photoluminescence spectra and ascribed to excitons in $CsPbBr_3$ nanocrystals. The intensity of the broad bands in the quenched sample are larger by a factor of three. The additional broad band due to emission of self-trapped excitons (STE) in CsBr is observed in the PSL spectra.

A narrow emission band ascribed to the excitons seems to be a common property for nanocrystals. Fig. 2 shows the photoluminescence (PL) and 35 GHz ODMR spectra of AgBr nanocrystals in KBr:AgBr (2 mol% of Ag in melt) and in bulk AgBr (full and dashed lines, respectively). The marks show the resonance fields for the localized holes (h), shallow electron

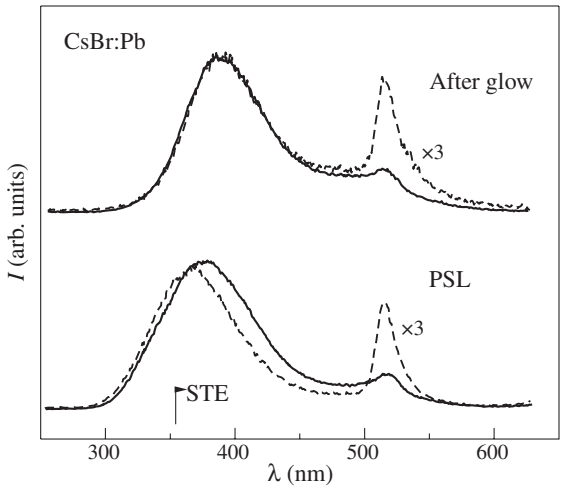

Fig. 1. Tunnelling afterglow and photostimulated luminescence (PSL) at 77 K in CsBr:Pb (0.2%) after quenching from 800 K (solid lines) and after subsequent 20 min annealing at 450 K (dashed lines). The arrow shows emission of self-trapped excitons (STE).

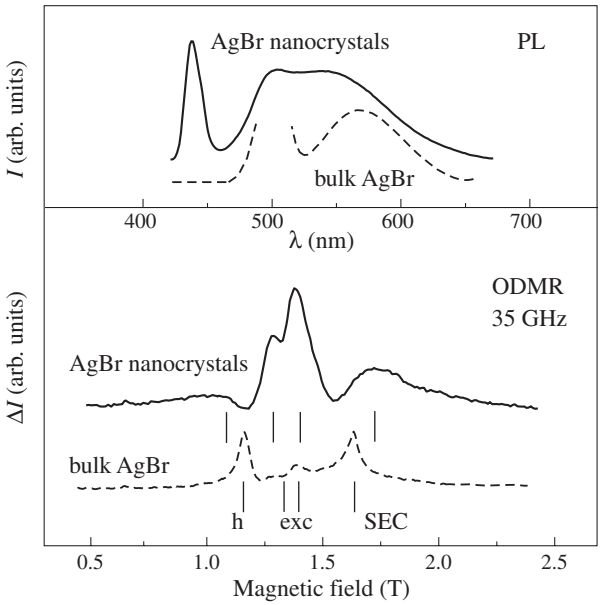

Fig. 2. The photoluminescence (PL) and ODMR spectra recorded in KBr:AgBr (2 mol% of AgBr in the melt) and in bulk AgBr (dashed lines). $\nu = 35.2$ GHz, $T = 1.7$ K, $\lambda = 587$ nm. The marks show the resonance fields for the localized holes (h), shallow electron centers (SEC) and triplet excitons (exc) for bulk AgBr and AgBr nanocrystals.

centers (SEC) and triplet excitons (exc). The PL and ODMR spectra obtained in the AgBr nanocrystals significantly differ from those observed in the bulk AgBr. In contrast to bulk AgBr the PL spectrum of the AgBr nanocrystals exhibits a narrow exciton band around 440 nm, and ODMR lines of electron and hole centers are changed in position and shape due to the confinement of electron-hole recombination [8].

Figure 3 presents PSL spectra recorded at 77 K in CsBr:Eu crystals as received (1) and after quenching from 800 K, X-ray irradiation and 1 hour annealing at 450 K (2). The photoluminescence spectra are shown by dashed lines for comparison. A narrow band around 520 nm appears after annealing at the expense of the 445 nm band of Eu. Its position and behavior are similar to those of $CsPbBr_3$ nanocrystals in CsBr:Pb. The same variations are also observed in the tunnelling afterglow spectra.

Divalent ions are known to tend to aggregate in alkali halides even at room temperature. Nanometer size aggregates of regular $CsPbBr_3$-like and $CsEuBr_3$-like structures can be created in as-grown CsBr:Pb and CsBr:Eu crystals [2, 9]. The narrow luminescence bands in the green region seem to be connected with the aggregation of Pb^{2+} ions and Eu^{2+} in the CsBr lattice, for instance, the PL spectra of the CsBr:Pb crystals are very similar to those of the bulk $CsPbBr_3$ crystals [2]. According to Ref. 2 the process of the creation of $CsPbBr_3$ (and probably $CsEuBr_3$) structure is initiated when several Pb^{2+} (Eu^{2+}) ions are close to each other, and the presence of the charge compensating cationic vacancies might make such a Pb^{2+} (Eu^{2+}) pre-aggregate energetically unstable. As a result the growth of a $CsPbBr_3$ ($CsEuBr_3$)-like phase in the volume of the CsBr host starts.

Sharp bands around 520 nm in CsBr:Pb (Fig. 1) and CsBr:Eu (Fig. 2) seem to belong to the emission of $CsPbBr_3$ and $CsEuBr_3$ nanocrystals, respectively. Since this is long lasting afterglow

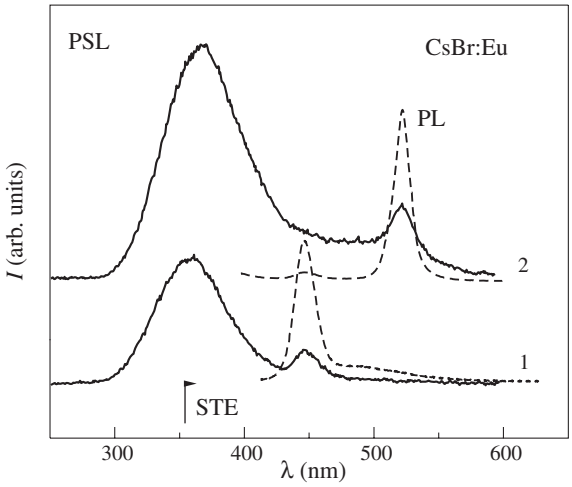

Fig. 3. The PSL spectra of CsBr:Eu recorded at 77 K in as received crystal (1) and after quenching from 800 K and 1 h annealing at 450 K (2). The PL spectra are shown by dashed lines for comparison.

it is doubtful that it were recombination of radiation defects inside the nanocrystals. Thus it is excited by the recombination in the matrix, the recombination energy being transferred through the interface into the quantum dot. ODMR by monitoring the afterglow, PSL and PL was used for identification of recombining centers in the systems under investigation. Magnetic quenching of the recombination bands was found in the afterglow spectra and ODMR of recombining centers was obtained. ODMR by monitoring the PSL provides new possibilities to study photostimulated processes, STE and impurity-bound excitons, as compared with the traditional ODMR by monitoring PL. It is important that the X-irradiation and the photostimulated recombination of defects are separated in time. This makes it possible to transform the radiation-induced centers before performing ODMR and also to excite selectively different recombination processes.

Acknowledgement

This study was supported by the RFBR under grants 03-02-17645 and 04-02-17632 and by Project of RAS "Spin-dependent effects in solids and spintronics."

References

[1] D. Bimberg, M. Grundmann and N. N. Ledentsov, *Quantum Dot Heterostructures*, John Wiley and Sons Ltd., Chichester (1998).
[2] P. Hackenschmied *et al*, *J. Appl. Phys.*, **93,** 5109 (2003).
[3] H. Vogelsang *et al*, *Phys. Rev.*, **B 61**, 1847 (2000).
[4] P. G. Baranov and N. G. Romanov, *Appl. Magn. Resonance*, **21**, 165 (2001).
[5] M. Nikl *et al*, *Phys. Rev.*, **B 51**, 5192 (1995); M. Nikl *et al*, *J. Luminescence*, **72–74**, 377 (1997).
[6] P. G. Baranov, Yu. P. Veshchunov and N. G. Romanov, *Sov. Phys.- Solid State*, **22**, 2186 (1980).
[7] N. G. Romanov, V. A. Vetrov and P. G. Baranov, *JETP Lett.*, **37**, 386 (1983).
[8] P. G. Baranov, *et al*, *JETP Letters*, **76**, 542 (2002).
[9] Yu. V. Zorenko, R. M. Turchak, I. V. Konstankevich, *Fizika Tverdogo Tela*, **46**, 1189 (2004).

13th Int. Symp. "Nanostructures: Physics and Technology"
St Petersburg, Russia, June 20–25, 2005

Rectification in ballistic quantum wires and quantum contacts

V. A. Sablikov, V. I. Borisov and A. I. Chmil'
Institute of Radio Engineering and Electronics, RAS, Moscow District, Fryazino, 141190 Russia

Abstract. We report on rectification properties of ballistic quantum wires caused by an asymmetry of the potential relief. The main effect is the presence of sharp peaks of the rectified current which appear as the potential of the wire is varied. The peak positions correlate with conductance quantization steps.

1. Introduction

Quantum structures with asymmetric conductance (ratchets) are currently of considerable interest. One of the major properties of such systems is the rectification of alternating current (for a review see [1]). Rectification is widely studied on multiterminal ballistic structures, created on the basis of semiconductor heterostructures, but the rectification mechanism remains poorly understood to date.

In this paper we show that the rectification effect occurs in a much simpler structure, containing only one quantum contact. Multiterminal structures contain many such contacts, which can contribute to the observed effect. We present experiments demonstrating the rectification and develop a model describing it. The rectification is observed on a quantum wire connecting electron reservoirs in the case when a potential relief in the wire is asymmetric with respect to reservoirs. The asymmetry is caused a charge piled up in the wire, or even simply by a charge of nearby random impurities.

2. Rectification mechanism

The rectification effect is explained as follows. Let a potential maximum in the wire is located asymmetrically with respect to the reservoirs as shown in Fig. 1, and an alternating voltage $V(t) = V\sin(\omega t)$ is applied across the reservoirs. The potential of the left reservoir is fixed, while the potential of the right reservoir oscillates with amplitude V. The electrochemical potential in the right reservoir varies with the same amplitude eV, but the barrier height u_m changes with a smaller amplitude βeV, where $\beta < 1$ is an asymmetry parameter showing what part of the applied voltage drops between the potential maximum and the source. If the equilibrium chemical potential μ is close to the maximum of the undisturbed potential relief, the transmission of electrons from left to right differs from the transmission in the opposite direction. As a result the electrons of one of the reservoirs (the left one, in the case shown in Fig. 1) are shut in by the barrier for a longer time than the electrons in the other reservoir. This is the situation in which the rectification occurs.

The rectified current is calculated using the standard approach by Landauer-Büttiker, disregarding effects of electron-electron interaction. This approach describes correctly the conductance quantization, though it does not explain details of the quantization steps (such as $0.7(2e^2/h)$ plateau) caused by the interaction. This calculation is helpful to demonstrate the rectification effect and to determine how the dc current depends on the chemical potential, temperature and the barrier shape. Deviations from these dependencies in the experiment can be used in studying the form of the potential relief in the structure as well as the effects of inter-electron interaction.

The time-dependent current through the wire is found as a sum of partial currents flowing from the left and right reservoirs in all subbands of transverse quantization. It is essential to take into account the oscillation of the barrier height. The rectified current $\bar{j}$ is calculated for an applied voltage of arbitrary amplitude by averaging over the period. Finally, $\bar{j}$ is expressed via the transmission coefficients T_n for n-th subband and the Fermi distribution function.

The rectified current $\bar{j}$ is found to depend strongly on the chemical potential μ. The current has a sequence of sharp peaks appearing when μ coincides with the maximums $u_n^{(m)}$ of potential shape in each subbands. The form of the peak depends on the ac voltage amplitude V, the temperature T and the tunneling energy Δ, which is determined by the curvature of the barrier shape.

For the limiting case of zero temperature and extremely smooth barrier shape ($\Delta \to 0$), the dependence of $\bar{j}$ on μ is shown on Fig. 2a. The rectified current is non-zero only in a strip $|\mu - u_n^{(m)}| \le eV \times \max[\beta, (1-\beta)]$. The maximum of the current $\bar{j}_m = (2e^2V/h) \times (2\beta - 1)/\pi$ is achieved at $\mu = u_n^{(m)}$. The form of the current peak is described by an universal function, its width being of the order of the applied voltage amplitude, eV.

For finite temperature and $\Delta \neq 0$, the peak is diffused in width to a value of about $\max[T, \Delta]$ and its maximum decreases. The largest value of the current $\bar{j}_m$ is achieved at $\mu = u_n^{(m)}$, as before. The dependence of the rectified current on the chemical potential is illustrated by Fig. 2b for a variety of temperatures.

With increasing temperature the maximum current $\bar{j}_m$ decreases as T^{-1} for $T \gg eV, \Delta$. A similar dependence takes place for $\bar{j}_m$ versus the tunneling energy Δ.

The direction of the current depends on the spatial position of the maximum of the potential relief: electrons are pumped into the reservoir that is further from the maximum of the potential relief.

The rectification mechanism is connected with a nonlinear

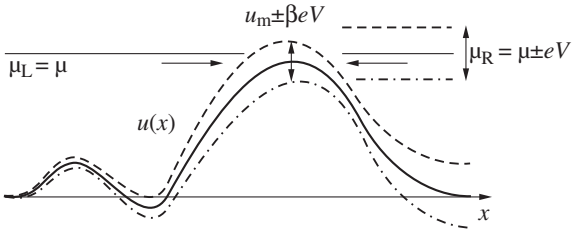

Fig. 1. Potential landscape of a quantum channel for zero (solid line), negative (dash line) and positive (dash-dot line) bias potential of the right reservoir.

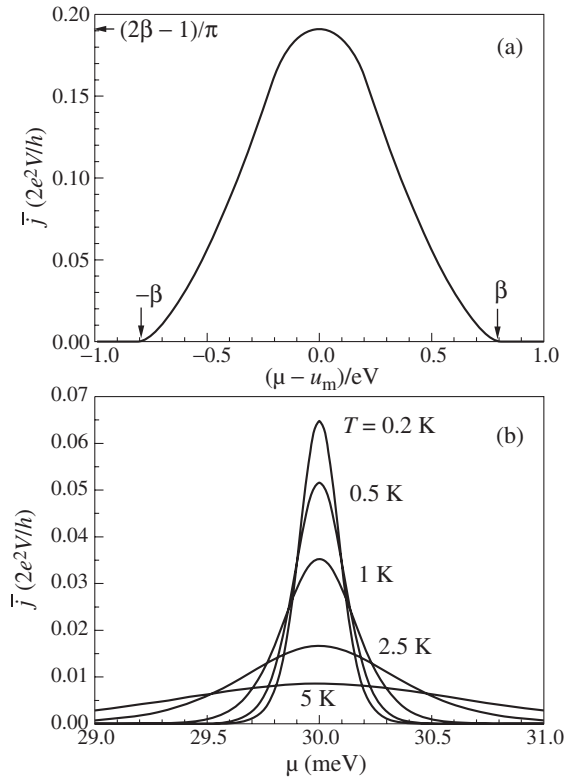

Fig. 2. Rectified current as a function of μ. (a) $T = \Delta = 0$, $\beta = 0.8$. (b) Temperature is varied from 0.2 to 5 K, at $V = 0.1$ mV, $\Delta = 0.05$ meV, $u^{(m)} = 30$ meV, $\beta = 0.8$.

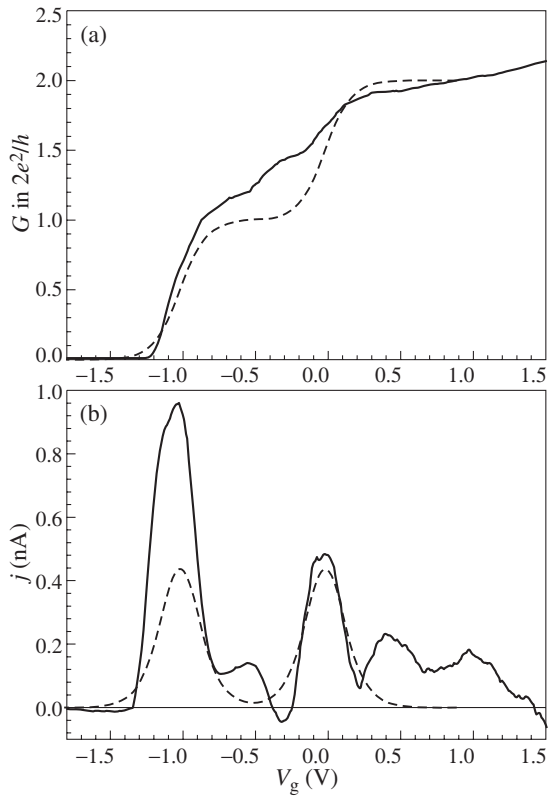

Fig. 3. Conductance (a) and rectified current (b) as a function of gate voltage at temperature 4.2 K. Solid lines — the experiment, dashed lines — the calculation for two subbands with following parameters: $\beta = 0.8$, $\Delta = 0.05$, $V = 0.3$ mV, intersubband energy 4 meV.

dependence of the current on voltage. The nonlinearity of the current-voltage characteristic is extremely strong if the chemical potential is close to the maximum of the potential relief. The characteristic voltages for the nonlinearity are $(\mu - u_n^{(m)})$, T and Δ. If $(\mu - u_n^{(m)}) \ll T, \Delta$, the only characteristic voltage remains $eV_1 = \max[T, \Delta]$, below which the current-voltage dependence is close to linear one. At low voltage $V < V_1$, the rectified current is quadratic in V, but at $V > V_1$, $\bar{j}$ becomes a linear function of V.

3. Experiment

Experiments were carried out on quantum channels formed on the basis of heterostuctures GaAs/AlGaAs with 2D electron gas. Transistor structures with a quasi-one-dimensional channel and side gates in the plane of the 2D electron gas were created using electron lithography and ion etching. [2] The channel length (of about 0.6 μm) was chosen such that it was short enough for the transport to be ballistic, but it was long for an asymmetric potential landscape to occur accidentally. The mean free path of electrons is about 2 μm. The conductance G of the channel demonstrates quantization plateaus observed with increasing the gate voltage, as shown in Fig. 3a. The conductance was measured using a small ac voltage (amplitude 30–150 μV, frequency 130 Hz), which was applied without dc bias. Simultaneously the dc component of the current $\bar{j}$ was measured. It was found that $\bar{j}$ has pronounced maximums at the points where the gate voltage corresponds to the values of G close to a half-integer number of $2e^2/h$ quanta.

This behavior of the rectified current can be explained qualitatively by the above theory. Two peaks of the rectified current in Fig. 3 correspond to the coincidence of the chemical potential with the maximums of the potential relief in the first and second subbands. Under this condition, the conductance is known to be close to half-integer number of $2e^2/h$, as in the experiment. More detailed quantitative analysis shows that the theory allows one to describe correctly the position of the observed peaks of the current. The results of the fitting of the theory to the experiment are depicted in Fig. 3. The describes the second peak rather well, but the value of the first peak (that corresponds to the first step of the conductance quantization) in experiment is higher than in the theory by a factor of about 3–4. This discrepancy may be connected with electron-electron interaction effects, which are known to be important in the region of the first step. As a possible mechanism of the interaction effect on the rectified current, we consider the electron scattering by Friedel oscillations.

Acknowledgements

This work was supported by RFBR, the Programs of RAS, Russian Ministry of Science and the Program "Integration".

References

[1] P. Reimann, *Physics Reports*, **361**, 57 (2002).
[2] V. A. Sablikov, V. I. Borisov and A. I. Chmil', *JETP Lett.*, **81**, 75 (2005).

13th Int. Symp. "Nanostructures: Physics and Technology"
St Petersburg, Russia, June 20–25, 2005

Efficient lateral inter-dots transport in array of InAs/AlAs quantum dots

T. S. Shamirzaev, A. M. Gilinsky, A. K. Kalagin, A. I. Toropov, A. K. Gutakovskii and K. S. Zhuravlev
Institute of Semiconductor Physics, 630090 Novosibirsk, Russia

Abstract. In contrast to the system of InAs/GaAs QDs, a considerable decrease of the PL intensity and decay duration with the formation of relaxed dislocated clusters with density of order of magnitude than that of QDs was observed. This difference in luminescence properties of InAs/GaAs and InAs/AlAs QD systems arises from the very large exciton lifetimes in InAs/AlAs quantum dots, which are longer than the lateral carrier transfer time from QDs to the nonradiative recombination centers of the dislocated clusters. Additional evidence for lateral carrier transfer was determine from study of PL decay duration of the structures with different QDs densities.

Introduction

The system of InAs QD's embedded in an AlAs matrix is very close to the system of InAs/GaAs QD's from the point of view of the Stranski–Krastanov growth mode, since AlAs has practically the same lattice constant as GaAs. Nevertheless, the system of InAs QDs embedded in an AlAs (or AlGaAs) matrix exhibits a decrease in QD size with increased QD densities, as compared with the InAs/GaAs QD system. The decrease in QD size together with the higher barrier energy leads to a stronger electronic confinement in the InAs/AlAs dots, and to significant changes in their electronic and optical properties [1–3]. Recently microsecond [2] and even millisecond-scale [3] nonexponential PL decays have been observed in InAs/AlAs QDs at low temperatures, while InAs/GaAs QDs display exponential nanosecond-scale decay times, which indicate a considerable difference in the recombination mechanisms in these two systems.

Recently we gave a guess that nonexponential PL decays of InAs/AlAs QD's is a result of inter-dots carrier transport. In this work in order to further attest the assumption we study InAs/AlAs structures with different QDs densities, and investigate the effect of introduction of lattice defects in InAs/AlAs QDs on excitonic recombination.

1. Experimental

The samples of InAs QDs in an AlAs matrix studied in this work were grown by molecular beam epitaxy in a Riber-32P system. The samples consisted of one layer of InAs QDs sandwiched between two 25 nm thick layers of AlAs. As it is shown in Fig. 1 sample A is dislocation free and has an average QDs lateral size of 20–23 nm and a QD density of 5×10^{10} cm^{-2}. Sample B has the same QDs size and density but contains dislocated clusters of InAs with a density of about 2×10^9 cm^{-2}.

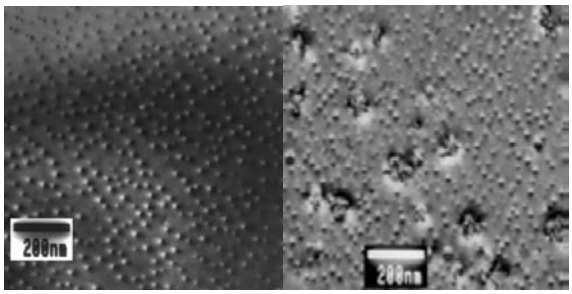

Fig. 1. TEM plan view images for structures: A (right), and B (left).

2. Results and discussions

Using time-resolved PL we demonstrate that in contrast to the InAs/GaAs QDs, the low temperature excitonic PL intensity and decay duration in the InAs/AlAs QDs drastically decrease with the formation of large relaxed clusters of InAs containing dislocations, manifesting a much higher sensitivity of the InAs/AlAs QD recombination mechanism to the presence of competing recombination channels. It is seen from Fig. 2 that in both the samples the decay kinetics is essentially nonexponential and after an initial pulse is described by a power-law function $I_{\mathrm{PL}}(t) \sim 1/t^{\gamma}$, which cannot be characterized by a single lifetime. For quantitative comparison of the PL kinetics we will use the length of period of time during which the PL intensity decreases by three orders of magnitude, τ. It was found that in dislocation-free sample A τ amounts to 40 ms, which is by 40 times longer than that in sample B. Since the samples have similar QD sizes and densities, we can attribute the strong difference in τ's in these samples to the effect of recombination centers located at or near the dislocated clusters. The reason for the high sensitivity is attributed to the long exciton lifetime in the QDs in an AlAs matrix resulting in a large rate of carrier transfer from the QDs to dislocations. The mechanism of carrier transport can be assessed using geometrical considerations. For samples with a cluster density of 2×10^9 cm^{-2} the average distance between the clusters is about 220 nm. Since the carrier tunneling length in AlAs is about 5 nm [4], the majority of the QDs reside too far from the

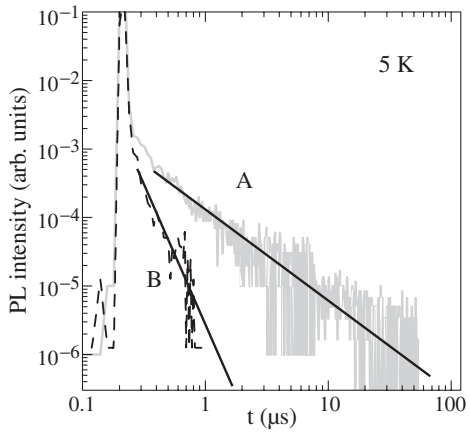

Fig. 2. Transient PL decay curves for samples A and B.

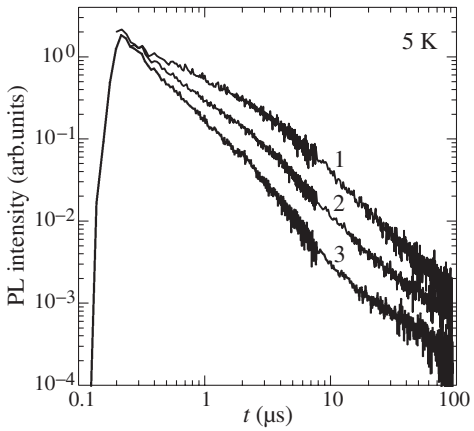

Fig. 3. Transient PL decay curves for defect free samples with a QDs density of: 1 — 9×10^9 cm^{-2}, 2 — 2×10^{10} cm^{-2}, and 3 — 2.5×10^{11} cm^{-2}.

nearest cluster for carriers to tunnel directly from the QD to the cluster. Therefore, the transport of carriers from the QDs towards the dislocated clusters proceeds as a sequential inter-dot transfer, or hopping.

Additional evidence for inter-dot transport was found from compare of the PL decay curves measured for defect free samples with different QDs density depicted in Fig. 3. One can see that decay duration decrease with increasing in QDs density. This experimental data is a result of increase inter-dot transfer to large size dots with smaller exciton lifetime with increasing in QDs density and be in a good agreement with model of exciton recombination in InAs/AlAs QD proposed in our previous work [3].

Acknowledgement

This work was supported by the Russian Foundation for Basic Research (grants no. 04-02-16653 and 04-02-16286).

References

[1] P. Ballet *et al*, *J. Appl. Phys.*, **90**, 481 (2001).
[2] P. Dawson *et al*, *Appl. Phys. Lett.*, **82**, 2349 (2002).
[3] T. S. Shamirzaev *et al*, *Physica E*, **20**, 282 (2004).
[4] S. R. Andrews *et al*, *Phys. Rev. B*, **47**, 15705 (1993).

13th Int. Symp. "Nanostructures: Physics and Technology"
St Petersburg, Russia, June 20–25, 2005

Lifetime of non-equilibrium charged carriers in semiconductor InAs/GaAs quantum dots

A. S. Shkolnik[1], L. Ya. Karachinsky[1], N. Yu. Gordeev[1], G. G. Zegrya[1], K. A. Kupriyanov[1], V. P. Evtikhiev[1], S. Pellegrini[2] and G. S. Buller[2]

[1] Ioffe Physico-Technical Institute, St Petersburg, Russia
[2] School of Engineering and Physical Sciences, Heriot-Watt University, Riccarton, Edinburgh EH14 4AS, United Kingdom

Abstract. The lifetime of nonequilibrium charged carriers in semiconductor InAs/GaAs quantum dots at different levels of excitation is investigated both experimentally and theoretically. It is shown that, depending on the level of excitation, four recombination processes control the charged carriers lifetime: (1) radiative recombination; (2) non-threshold Auger recombination inside a quantum dot; (3) quasi-threshold Auger recombination inside a quantum dot; and (4) Auger recombination due to Coulomb interaction with charged carriers in the barrier region.

Introduction

By virtue of the strong localization of the charged carriers in quantum dots (QDs), arrays of QDs represent the ideal systems for the non-radiative Auger processes (AP) realization. In a detailed theoretical investigation of the size quantization influence on the AP in heterostructures, the probability of displaying new AP was predicted — non-threshold and quasi-threshold ones [1–3]. In recent experimental papers devoted to the QDs laser diodes investigation some calculations denoted the necessity of the Auger recombination to be taken into account. For a detailed investigation of the AP influence on the QDs luminescence characteristics, we have performed detailed measurements of the charged carriers lifetime in QDs.

1. Experimental

An InAs QD single layer array was grown using the Stransky-Krastanow method by molecular beam epitaxy (MBE) on GaAs (001) substrate misoriented relatively to the [010] direction by 2°. The average thickness of the InAs layer was 2.9 monolayer (ML) and was grown at a temperature of 470 °C. The InAs QD array was confined by GaAs barriers (20 nm) surrounded by 250 nm thick AlAs/GaAs graded band-gap superlattices and by $Al_{0.7}Ga_{0.3}As$ cladding layers (200 nm). The structure was completed by a GaAs cap layer (5 nm). The size of the QDs, calculated from atomic force microscopy (AFM) images [4], was found to be about 15 nm laterally and 3 nm in height.

Steady state photoluminescence (PL) measurements of the internal quantum efficiency were performed with an Ar^+ ion laser ($\lambda = 514.5$ nm) in a wide range of excitation energy densities (0.5–4000) pJ·cm^{-2}. A detailed description of the time-resolved photoluminescence (TRPL) measurements is presented in [5]. The TRPL measurements of the ground state (GS) QD emission were performed in a wide incident energy density range (0.7–47,000) pJ·cm^{-2}. Narrow bandpass filters (a few nanometres width) were used to spectrally discriminate the luminescence signal. The measurements were performed at wavelengths coinciding with the maxima of the PL spectra, which correspond to the recombination of the charged carriers from the ground state.

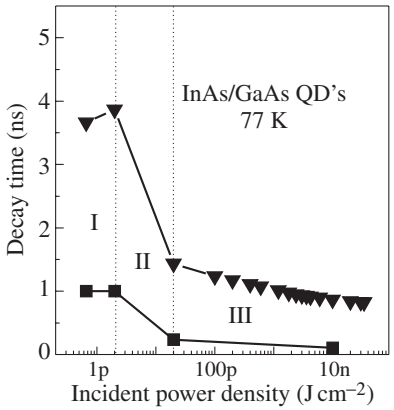

Fig. 1. Experimental (triangles) and theoretical (squares) values of the charge carriers lifetime on the QD ground state versus excitation energy density.

2. Results and discussion

The PL lifetime dependence on the incident energy density for this sample was investigated, and the results are shown in Figure 1. The lifetimes of the carriers were calculated from the TRPL traces. The dependence of the lifetime (τ) on incident energy density can be described in three parts: τ remains practically constant at low excitation power densities (part I); a rapid decrease of τ at power densities of 2 pJ·cm^{-2} (part II) and the following slight decrease of τ with increasing energy density (part III).

Such behavior cannot be explained by the influence of stimulated radiation because of the small diameter of the excitation spot and the low values of the modal gain. Additional measurements of the PL spectra in the full range of the excitation did not exhibit PL spectra sharpening connected to the stimulated radiation. A simple explanation of the lifetime reduction with the increase of the radiative recombination rate, due to the increase of the filling factor [5, 6], is not enough. In the case of strong localization of the charged carriers in the QDs, their Coulomb interaction should lead to the appearance of a much faster non-radiative Auger processes.

To explain the observed behavior of the lifetime dependence on the excitation level, we provide a theoretical analysis of the mechanisms responsible for the lifetime in the QDs at low temperatures. In Figure 2 the basic recombination processes of the

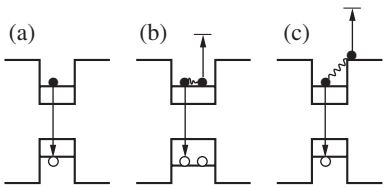

Fig. 2. Mechanisms responsible for the lifetime of the charge carriers: a) radiative recombination; b) non-radiative quasi-threshold and non-threshold Auger recombination in the QD and c) non-radiative Auger recombination due to Coulomb interaction with charged carriers in the barrier region.

charged carriers localized in the QDs are presented: 1) spontaneous radiative recombination ($\tau_{\mathrm{QD}}^{\mathrm{SP}}$); 2) non-radiative Auger recombination in the QDs ($\tau_{\mathrm{QD}}^{\mathrm{A}}$); 3) non-radiative Auger recombination with participation of charged carriers in the barrier ($\tau_{\mathrm{QD}}^{\mathrm{B}}$).

As it could be seen on Fig. 1, in part I the charged carriers' lifetime is slightly increasing with the increase of the excitation energy density. This part is mainly controlled by the radiative recombination process. Preliminary investigations have shown that the internal quantum efficiency at the level of excitation corresponding to part I is close to 100%.

At the excitation energy densities providing QD ground state occupancy by more than 1 carrier of the same charge — either two electrons or two holes (part II) [6], the lifetime of the charged carriers could change due to the switching on of the two non-radiative Auger recombination processes in the QDs (Fig. 2b). The quasi-threshold Auger process is closely connected to the limitation of the wave-function overlap area imposed by the QD volume. In accordance with the Heisenberg rule, this phenomenon leads to the replacement of δ-function in the law of quasi-pulse conservation with a function approaching to the δ-function within the limits of an infinite QD radius. The non-threshold Auger process is conditioned by the scattering of the electron (hole) at the heteroboundaries. In this process the excited carrier receives a big angular momentum. The ratio between the probabilities of these processes depends on the QD radius as follows:

$$\frac{W^{\mathrm{NTA}}}{W^{\mathrm{QTA}}} = \left(\frac{V_{\mathrm{C}}}{E_{\mathrm{g}}^{\mathrm{eff}}}\right)^2 \cdot \left(\frac{1}{k^2 a^2 \sin^2(ka)}\right) . \qquad (1)$$

where a is the QD radius, k the wave vector, V_{C} the barrier height for the electrons and $E_{\mathrm{g}}^{\mathrm{eff}}$ the ground state transition energy. In the case of the InAs QDs with height of 30 Å experimentally investigated, the quasi-threshold Auger process plays a key role. The estimated characteristic time of the quasi-threshold Auger process for the spherical shaped QDs (radius 30 Å) [7] is $2.5 \cdot 10^{-10}$ s. It is evident that the following increase in the excitation level does not increase the probability of quasi-threshold Auger process; all the states in the QDs are occupied. However the increase in the excitation energy (part III in Fig. 1) should lead to an increase in the concentration of charged carriers in the barriers. This effect starts another Auger process, with the participation of the carriers in the barriers (Fig. 2c). The probability for this process to occur is proportional to the carriers' concentration in the barriers. The estimated [8] probability for this process to take place in the case of a spherical shaped QD (radius 30 Å) and a carrier concentration in the barriers of $N_{3\mathrm{D}} = 10^{18}$ cm^{-3} gives a characteristic time of $4 \cdot 10^{-10}$ s.

The lifetime for the nonequilibrium of the carriers localized in the QDs is determined by the sum of the three recombination processes probabilities:

$$\frac{1}{\tau} = \frac{1}{\tau_{\mathrm{QD}}^{\mathrm{SP}}} + \frac{1}{\tau_{\mathrm{QD}}^{\mathrm{A}}} + \frac{1}{\tau_{\mathrm{QD}}^{\mathrm{B}}} . \qquad (2)$$

When all the processes mentioned above are taken into account the carriers' lifetime can be estimated, and the results are presented in Fig. 1. As it can be seen in Fig. 1, all the estimated values are smaller than the ones obtained experimentally, but the behavior of the curve is similar. However taking into account the real shape of the QDs, it is necessary to consider the change of the electron-hole wave-function overlap integral. Using the value of the wave-function overlap integral for the pyramidal shaped QDs taken from *Bimberg et al* [9] with a characteristic lateral size of 150 Å and a height of 30 Å, we can obtain a complete agreement between the experimental data and the calculated values for the non-equilibrium charged carriers' lifetime in the QDs across the whole range of excitation energy density.

Conclusion

In the present work the detailed analysis of the basic recombination mechanisms determining the lifetime of the charged carriers localized in the QDs was presented. It was shown that the charged carriers' lifetime, depending on the excitation energy density, is defined by three recombination channels. At low excitation power densities, the charged carriers' lifetime is determined by radiative recombination. When the excitation energy density increases, the charged carriers' lifetime is controlled by Auger recombination inside the QDs. With a further increase in the excitation energy density, the charged carriers' lifetime is determined by the Auger recombination process with assistance from the charged carriers in the barrier region.

The peculiarity of the charged carriers' lifetime behavior should be taken into account in the design of devices based on heterostructures containing QDs.

Acknowledgement

This work was provided with the partial support of the RFBR grants 04-02-16786 and 04-07-90148.

References

[1] G. Zegrya, V. Kharchenko, *JETF*, **101**, 327 (1992).

[2] G. Zegrya, A. Polkovnikov, *JETF*, (1998).

[3] G. Zegrya *et al*, *Phys. Rev. B*, **58**, 4039 (1998).

[4] V. P. Evtikhiev *et al*, *J. Cryst. Growth*, **201/202**, 1154 (1999).

[5] L. Ya. Karachinsky *et al*, *Appl. Phys. Lett.*, **84**, 7 (2004).

[6] S. Pellegrini *et al*, *Proc. of SPIE Int. Symp. "Photonic west"*, San Jose, USA (2005).

[7] E. V. Dogonkin *et al*, *Proc. of 8th Int. Symp. Nanostructures: Physics and Technology*, St Petersburg, Russia, 399 (2000).

[8] I. Solov'ev, G. Zegrya, *Appl. Phys. Lett.*, **82**, 2571 (2003).

[9] O. Stier, M. Grundmann, D. Bimberg, *Phys. Rev. B*, **59**, 5688 (1999).

13th Int. Symp. "Nanostructures: Physics and Technology"
St Petersburg, Russia, June 20–25, 2005

Effect of strain relaxation on photoluminescence spectra of nanostructures with InAs quantum dots

N. M. Shmidt, V. N. Petrov, V. V. Ratnikov, A. N. Titkov, A. G. Gladyshev, N. V. Kryzhanovskaya, *E. S. Semenova*, A. P. Vasil'ev, A. E. Zhukov and V. M. Ustinov
Ioffe Physico-Technical Institute, St Petersburg, Russia

Abstract. Strain relaxation in nanostructures with overgrown InAs quantum dots (QD) synthesized by MBE on either $Al_{0.85}Ga_{0.15}As$ or metamorphic InGaAs buffer layers is investigated. Three mechanisms of strain relaxation were found in case of the metamorphic buffer: the tetragonal distortion of the unit cell, the dislocation injection, and the surface roughening mechanism that results in the formation of strain relief on surface of the QD structure. The last mechanism dominates in the QD structures grown on the $Al_{0.85}Ga_{0.15}As$ buffer. Typical values of the stress resulting in strain relief for the studied QD structures were estimated to be 0.01–0.1 GPa. The relaxation of this weak stress noticeably affects the wavelength of QD photoluminescence (1200-1300 nm) and even the shape of the spectrum.

Introduction

Strain relaxation and its influence on formation of InAs self-organized quantum dots (QDs) and their optical properties have not been studied in detail yet. In the present paper the effect of strain relaxation on photoluminescence (PL) properties of two types of nanostructures with InAs QDs grown on either thick $Al_{0.85}Ga_{0.15}As$ layer or thick $In_{0.2}Ga_{0.8}As$ metamorphic layer are investigated.

1. Experimental

Two types of structures grown by molecular beam epitaxy on GaAs (100) substrates were investigated. The first type comprises a 1.2 μm-thick $Al_{0.85}Ga_{0.15}As$ layer followed by a 0.2 μm-thick GaAs matrix. Three layers with QDs were embedded in the middle of the matrix. The second type of the structures comprises a 0.5 μm-thick metamorphic $In_xGa_{1-x}As$ (x 20%) buffer deposited at 400 degC (the rest of epitaxial layers were grown at 500 degC). The QDs were embedded in a 0.2 μm-thick $In_{0.2}Ga_{0.8}As$ matrix layer confined by short-period $In_{0.2}Ga_{0.8}As/In_{0.2}Al_{0.8}As$ superlattices.

The QDs in both types were grown using the following sequence: initial InAs islands were first formed by depositing 2.6 monolayers of InAs then overgrown by 5 nm $In_yGa_{1-y}As$ ($y = x + 0.2$, where $x = 0$ or 0.2 for the first and the second type of the structures, respectively).

Transmission electron microscopy (TEM) imaging was carried out using a 100 keV Philips CM microscope. Photoluminescence (PL) was excited using YAG:Nd laser ($\lambda = 532$ nm) and detected with a cooled Ge photodiode. X-ray diffraction was used for evaluating material quality of the structures.

2. Results and discussion

For QD structures grown on thick $Al_{0.85}Ga_{0.15}As$ layer it was found from AFM studies and X-ray diffractometry that the main mechanism of strain relaxation is the surface roughening. This mechanism results in the formation of strain relief on the surface of the overgrown QD structure. Typical strain relief appeared on the surface of $Al_{0.85}Ga_{0.15}As$ buffer layer is shown in Fig. 1. Our previous investigation has shown that the strain relief formed in the buffer layer either remains on the surface of overgrown QD structure even after deposition of the active QD region and all subsequent layers, or spreads out, or completely disappears after different stages of nanostructure technological process.

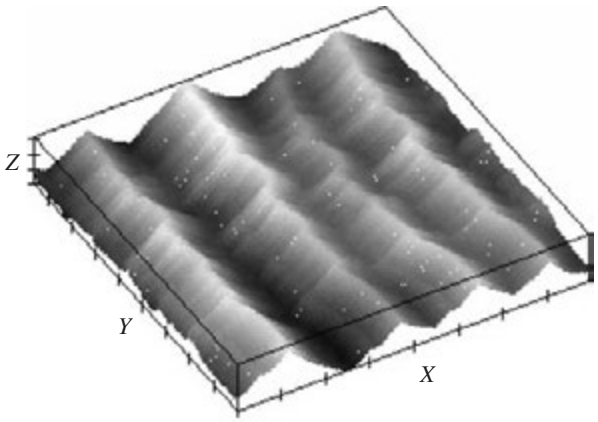

Fig. 1. AFM image of typical surface structure of $Al_{0.85}Ga_{0.15}As$ buffer layer. The X and Y multiplying factor is 100 nm, Z multiplying factor is 5 nm.

To clarify the effect of the stain relief on PL characteristics of overgrown QD structure we studied PL spectra of the structure of the first type having a small irregular deformation. In this case regions with different height of strain relief coexist on the surface. The AFM cross sections of these regions and corresponding PL spectra taken at room temperature are presented in Fig. 2. The same variety of strain relieves was observed in structures grown on $Al_{0.85}Ga_{0.15}As$ buffer layer with some variations of technological conditions (such as the buffer growth temperature, the introduction of thin GaAs layer inside the buffer).

The stress resulting in the strain relief was evaluated from the equation and the data of AFM instigations:

$$\sigma = \frac{2Gh^2}{L_d L_0}, \tag{1}$$

where G is the shear modulus, h is the relief height, L_d is the crest relief width at the base, L_0 is the distance between the relief crests. Typical value of stress resulting in strain relief for the structures under study was estimated to be 0.01–0.1 GPa.

The relaxation of this weak stress noticeably affects the shape of PL spectrum and shifts the PL peak position (1200–1300 nm for the QD ground-state) as shown in Fig. 2. Shift

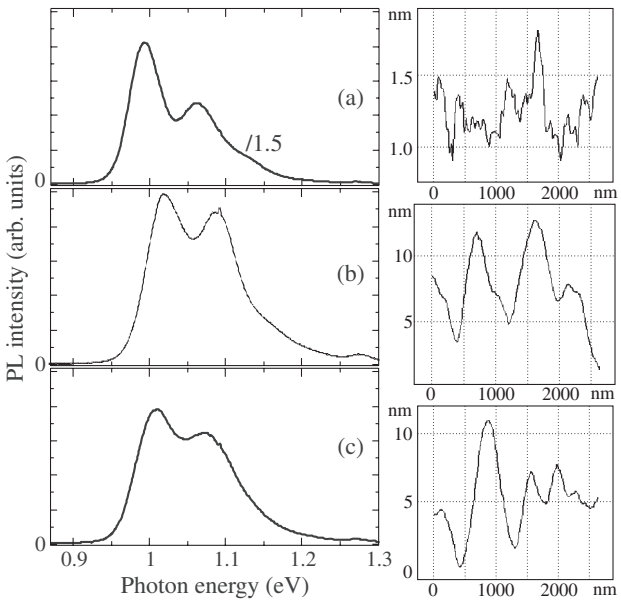

Fig. 2. AFM cross-sections (right-hand panels) and room-temperature PL spectra (left-hand panels) taken from regions: (a) without strain relief; b) with the highest strain relief; and (c) with strain relief 3 times smaller as compared to the (b).

to shorter wavelengths for higher strain relief is usual for all the structures investigated. The results obtained allow us to suppose that weak stress can affect the QD formation and cooperative phenomena in the QD-matrix layer system changing some optical properties.

The competition and cooperation of three mechanisms of strain relaxation were found in structures grown on the metamorphic buffer. In addition to strain relief, the injection of misfit dislocations with formation of the extended defect system (EDS) was detected using X-ray diffractometry. Elastic accommodation with tetragonal distortion of the unit cell was revealed from measurements of the wafer curvature. The typical curvature was 11–20 m.

The initial bend of the substrate affects PL spectra and peak position for QD structures grown under same technological conditions (fig.3). Initial bend of substrate also modifies the strain relaxation changing the optical properties of the buffer layer (fig.4). Comparative X-ray diffractometry investigations of buffer layers grown on substrates of different thicknesses (440 or 390 μm) showed that the strain relaxation of the buffer

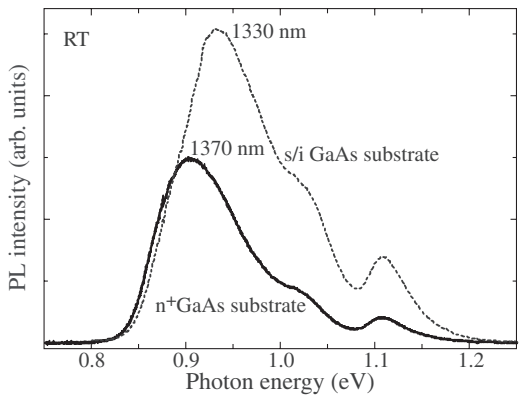

Fig. 3. Room-temperature PL spectra of QD structures of the second type grown on either semi-insulating or *n*-type doped GaAs substrates.

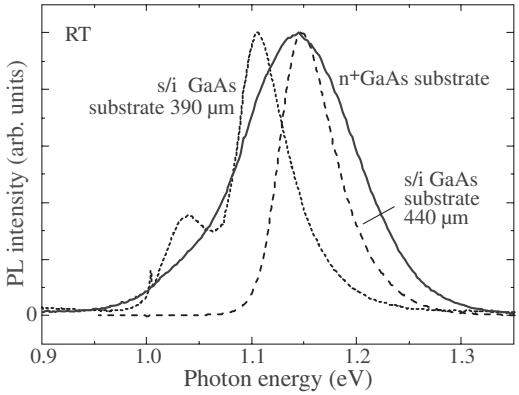

Fig. 4. Room temperature PL spectra of metamorphic InGaAs buffers grown on either n-type doped or semi-insulating GaAs substrates of different thickness.

layer may cause the formation of two layers with different In composition on the thinner substrate. This result is in a good agreement with the PL data (fig.4).

The strain relaxation resulting in formation of strain relief, biaxial stress in substrate and buffer can be the reasons of non-reproducibility of optical properties of QD structures.

Acknowledgements

This work was conducted in the frame of joint scientific program between Ioffe Physico-Technical Institute (Russia) and NL-Nanosemiconductor-GmbH (Germany). This work was also supported in different parts by Grant of the Russian Academy of Science "New Materials and Structures" No. 9.8A220 and Russian Foundation for Basic Research (Project 04-02-16282).

N. V. Kryzhanovskaya thanks INTAS Young Scientist Fellowship program for support (03-55-882). AEZ thanks the Grant (MD-4277.2004.2) of the President of the Russian Federation for the support of young scientists.

13th Int. Symp. "Nanostructures: Physics and Technology"
St Petersburg, Russia, June 20–25, 2005

Optical probing the spin states of a single magnetic ion in an individual quantum dot

L. Besombes[1], J. Cibert[2], D. Ferrand[1], Y. Leger[1], L. Maingault[1] and *H. Mariette*[1]

[1] CEA-CNRS group "Nanophysique et Semiconducteurs", Laboratoire de Spectrométrie Physique, Université J. Fourier-Grenoble I, and Département de Recherche Fondamentale sur la Matière Condensée/SP2M, CEA-Grenoble, 17 avenue des Martyrs, F-38054, Grenoble, France
[2] Laboratoire Louis Neel, CNRS, BP166X, F-38042, Grenoble, France

Precise control of electronic spins in semiconductors should lead to development of novel electronic systems based on the carriers' spin degree of freedom. Magnetic semiconductor quantum dots (QDs), where excitons can interact strongly with the magnetic atoms, hold particular promise as building blocks for such spin-based systems. This requires the ability to detect and manipulate individual spins. We will show in this presentation how we can optically probe the magnetic state of a single Mn^{2+} ion embedded in an individual QD.

In the case of a quantum dot incorporating a single magnetic atom (spin S) and a single confined exciton, the exchange interaction between the exciton and the magnetic atom acts as an effective magnetic field, so that the atom's spin levels are split even in the absence of any applied magnetic field [1]. A set of $2S+1$ discrete emission lines can be resolved, providing a direct view of the atom's spin state at the instant when the exciton annihilates.

Magneto-optic micro-spectroscopy was used to study the optical properties of individual Mn-doped self-assembled CdTe/ZnTe QDs. The fine structure of a confined exciton in the exchange field of a single Mn^{2+} ion ($S = 5/2$) is analyzed in detail. The exciton-Mn^{2+} exchange interaction shifts the energy of the exciton depending on the Mn^{2+} spin component and six emission lines are observed at zero magnetic field. Magneto-optic measurements reveal that the emission intensities in both circular polarizations are controlled by the Mn^{2+} spin distribution imposed by the exchange interaction with the exciton, the magnetic field and an effective manganese temperature which depends on both the lattice temperature and the density of photo-created carriers.

The influence of the number of confined carriers on the spin splitting will be then considered by investigating both the biexciton and exciton transitions in the same Mn-doped QD. The injection of the second electron-hole pair cancel the exchange interaction with the Mn ion and the spin degeneracy is almost restored. The biexciton level is found to be split by the perturbation of the carriers orbital wave functions induced by the interaction with magnetic ion.

Finally the influence of the system geometry, namely the QD in-plane asymmetry and the position of the Mn atom, will be demonstrated: the observed behaviour can be explained by the interplay between the exciton-manganese exchange interaction (dependent on the Mn position) and the anisotropic part of the electron-hole exchange interaction (related to the QD asymmetry).

References

[1] L. Besombes *et al*. *Phys. Rev. Lett.* **93**, 207403 (2004).

13th Int. Symp. "Nanostructures: Physics and Technology"
St Petersburg, Russia, June 20–25, 2005

Probing and manipulating spin effects in quantum dot

S. Tarucha

ICORP-JST & Department of Applied Physics, University of Tokyo, Tokyo 113-8656, Japan

Abstract. Strain relaxation in nanostructures with overgrown InAs quantum dots (QD) synthesized by MBE on either $Al_{0.85}Ga_{0.15}As$ or metamorphic InGaAs buffer layers is investigated. Three mechanisms of strain relaxation were found in case of the metamorphic buffer: the tetragonal distortion of the unit cell, the dislocation injection, and the surface roughening mechanism that results in the formation of strain relief on surface of the QD structure. The last mechanism dominates in the QD structures grown on the $Al_{0.85}Ga_{0.15}As$ buffer. Typical values of the stress resulting in strain relief for the studied QD structures were estimated to be 0.01–0.1 GPa. The relaxation of this weak stress noticeably affects the wavelength of QD photoluminescence (1200-1300 nm) and even the shape of the spectrum.

Control over spin effects is the central to the relevance of semiconductor nanostructures for applications to spintronics and quantum information technologies. Novel concepts of probing and manipulating spin information arise from interactions between electrons, nuclei, and magnetic field, and are embodied in recent experiments with semiconductor quantum dots such as spin filtering [1] and current rectification by Pauli effect [2]. In this talk I will review recent experimental studies on such spin effects in quantum dot devices: robustness of spin states, spin blockade, and hyperfine coupling to nuclear spin.

1. Robust spin state and spin blockade

There are only a few mechanisms causing spin relaxation in nonmagnetic compound semiconductor materials: spin-orbit interaction and hyperfine coupling to nuclear spin. Both of these effects are significantly reduced in quantum dots because of the spectral discreteness. We have used an electrical pump and probe technique to measure the lifetime (T_1) for a single spin state in an InGaAs vertical quantum dot [3]. The measured T_1 is longer than 0.2 ms, much longer than that for an orbital state [4]. More recently the same technique is applied for Zeeman sublevels by a Delft group [5], and T_1 of 0.8 ms is derived. These time scales are well accounted for by theory of spin-orbit coupling.

Note thus derived T_1 is sufficiently longer than a typical transport time for electrons throughout the dot system that the spin effect can significntly influence the transport properties. Spin blockade is such example. In the scheme of Coulomb blockade the number, N, of electrons in quantum dots is varied one-by-one just by adding one electron to the $N-1$ electron ground state (GS) to form the N-electron GS in the dot. This usually accompanies a change in the total spin by either $+1/2$ or $-1/2$ between the N and $N-1$ GSs. However, in the presence of strong correlation effect, the total spin, $S(N)$, for the N electron GS can differ from that for the $N-1$ electron GS by more than 1/2. This leads to suppression of single electron tunneling current through the dot or transition from the $N-1$ to N electron GS [6, 7]. We use a 2D harmonic vertical quantum dot holding just a few electrons and apply such a high magnetic field that the GS undergoes a transition to the fully spin-polarized state. We observe spin blockade for a transition between the fully spin-polarized $N-1$ electron GS and partially spin polarized N electron GS, for example, between the four-electron GS having $S(4) = 2$ and five-electron GS having $S(5) = 1/2$. We identify the electronic configuration stabilized by the correlation effect from measurements of excitation spectra evolving with magnetic field.

2. Control of hyperfine coupling

For GaAs quantum dots all of the constituent atoms of ^{71}Ga, ^{69}Ga, and ^{75}As have the nuclear spin of $I = 3/2$, and can interact with electronic spins via hyperfine interaction. The interaction Hamiltonian includes a flip-flop term between an electronic spin and nuclear spin, conserving energy as well as spin. However, the energy conservation is usually not maintained for the Zeeman sublevels, because the Zeeman energy is much greater for the electron spin than for the nuclear spin, and this difference cannot be managed at all due to the discreteness of electron energy.

However, this is not the case for two-electron spin states in a coupled two dot system, i.e. spin singlet and triplet states. The energy separation between these two states is a few tens of μeV. Application of a small magnetic field therefore leads to degeneracy of the singlet and one of the triplet sublevels. Near this degenerate point the transition between the singlet state and the triplet sublevel costs a small energy comparable to the nuclear Zeeman energy. We have used this technique to manipulate the hyperfine coupling [8]. One key ingredient in our work is to prepare an excited but long-lived electron-spin triplet state in a double dot system. Formation of such an electron spin triplet state blocks single electron tunneling current through the double dot system by Pauli exclusion [2]. Current can flow when the spin triplet state undergoes a spin-flip transition, mediated by hyperfine interaction with nuclear spins. We observe lifting of Pauli spin blockade or increased leakage current in the Pauli spin blockade region by application of in-plane magnetic field of 0.5 to 0.9 T. Contributions from nuclei of ^{71}Ga and ^{69}Ga to this finding are explored using a technique similar to NMR.

The hyperfine coupling effect or singlet-triplet degeneracy is tunable with bias voltage as well as magnetic field. While the hyperfine coupling is turned off, we can use a pulsed-NMR technique to rotate the nuclear spin polarization. Thus rotated nuclear spin polarization can be read out by turning on the hyperfine coupling. We use this technique to demonstrate coherent nuclear-spin rotation or Rabi oscillation. From experiments of Rabi oscillations and spin echo we are able to derive the decoherence time and dephasing time for nuclear spins in quantum dots.

Acknowledgements

This work has been performed in collaboration with K. Ono, Y. Nishi and D. G. Austing, and financially supported in part from SORST-JST, from a Grant-in-Aid for Scientific Research A (No. 40302799) from the Japan Society for the Promotion

of Science, from Focused Research and Development Project for the Realization of the World's Most Advanced IT Nation, IT Program, MEXT and from the DARPA grant number DAAD19-01-1-0659 of the QuIST program.

References

[1] J. A. Folk *et al*, *Science*, **299**, 679 (2003).
[2] K. Ono *et al*, *Science*, **297**, 1313 (2002).
[3] S. Tarucha *et al*, *Phys. Rev. Lett.*, **77**, 3613 (1996).
[4] T. Fujisawa *et al*, *Nature*, **419**, 278 (2002).
[5] J. M. Elzerman *et al*, *Nature*, **430**, 431 (2004).
[6] D. Weimann *et al*, *Phys. Rev. Lett*, **74**, 984 (1995).
[7] H. Imamura *et al*, *Phys. Rev. B*, **57**, 2574 (1997).
[8] K. Ono *et al*, *Phys. Rev. Lett*, **92**, 256803 (2004).

13th Int. Symp. "Nanostructures: Physics and Technology"
St Petersburg, Russia, June 20–25, 2005

Coherence and spin relaxation of interwell excitons in GaAs/AlGaAs coupled quantum wells

A. V. Larionov and V. B. Timofeev
Institute of solid state physics RAS, 142432 Chernogolovka, Russia

Abstract. The kinetics of spin aligned interwell excitons gas has been investigated in GaAs/AlGaAs coupled quantum wells (n-i-n heterostructures). The temporal formation of collective excitons phase and the temperature dependence of its spin relaxation rate have been studied. It was observed that radiative recombination time and spin relaxation rate of interwell excitons in the collective phase is strongly reduced. The observed effect is an evidence of the coherence of indirect excitons collective phase at the temperatures below critical one.

Introduction

In n-i-n types GaAs/AlGaAs CQW's with tilted bands due to bias, excitons can be excited with electron and hole confined in adjacent quantum wells separated by a tunneling barrier. These excitons are called spatially indirect or interwell excitons (IE's) and differ from the direct intrawell excitons (DE's), for which electron and hole are in the same QW. In contrast to intrawell excitons, interwell excitons are long-lived because the electron and hole wave functions overlap is very weak through the tunneling barrier. A large number of interwell excitons can be easily accumulated and a gas of these excitons can be cooled down to rather low temperatures. Various possible scenarios of collective behavior of a dense system of spatially separated electrons and holes have been considered theoretically [1, 2] and observed experimentally [3, 4].

Earlier, we found that in CQW's structures a gas of interwell excitons shows a critical behavior with the increasing density and at low enough temperatures [5]. We have assumed that strong narrowing of the IE's photoluminescence line, a drastic increasing of it circular polarisation degree and sensitivity of this effect with respect to exciton density and temperature are associated with the condensation of interwell excitons to the collective dielectric exciton phase. Later it has been shown that if critical conditions are satisfied the collective phase of the interwell excitons is most likely to occur in regions with lateral confinement — domains [6]. According to our experiments such condensation occurs at $T < 4\,\mathrm{K}$ and an average exciton concentration of $n_{\mathrm{th}} \sim 3 \times 10^{10}\,\mathrm{cm}^{-2}$.

Collective excitonic phase, corresponding to macroscopic exciton occupation of the lower state in domain, should be coherent. In considered case the coherent length scale is expected to be equal to domain size, connected with long range potential fluctuations (around one micron), where interwell excitons are accumulated. It means that within coherent length condensed excitons are described by common wave function. Expected consequences of that are increasing of the radiative decay rate of excitons and reducing of the exciton spin relaxation rate. All of these give unique opportunity for resonant photoexcitation of spin aligned collective interwell excitonic phase.

In below we will concern on study of spin relaxation rate by means of measurements and analysis of circular polarization degree under resonant pulsed laser photoexcitation.

1. Experimental

The CQW's system studied here consists of two GaAs quantum wells (the width $\approx 120\,$Å) separated by a narrow (4 monolayers) AlAs barrier. QW's are isolated from Si-doped ($10^{18}\,\mathrm{cm}^{-3}$) GaAs layers by $0.15\,\mu$ thick AlGaAs ($x = 0.33$) barriers. Details of architecture one can find in [5].

The photoluminescence (PL) of indirect excitons was excited by 120-femtosecond laser pulses with a repetition rate of 80 MHz. To organize resonant excitation a holographic grating with optical slits were used. The detection of the signal was provided by a Hamamatsu streak-camera (Model 5680-24) with a Si CCD-detector combined with a 0.5-m spectrometer (Acton SP-500i). The systems resolution was about 70 psec. Peak power excitation was about $30\,\mathrm{kW/cm}^2$ which corresponds to IE's concentration $n_{\mathrm{th}} \sim 3 \times 10^{10}\,\mathrm{cm}^{-2}$.

Detected by streak-camera signal is a three-dimensional image in energy-time-intensity coordinates. It allows to observe a time evolution for whole PL line. For the temporal data analysis this image was profiled along a time-scale. As a result PL decay curves at a fixed energy interval have been received. We have measured interwell excitons PL decay curves at different temperatures and bias.

First of all we were interested in a time evolution of IE's PL line. As the time delay increases, the PL line intensity increases as well and the line narrows and a bit displaces toward the long-wavelength part of the spectrum. With delays of 5-6 ns, its width is a minimum and is equal to 1.2 meV. The maximum intensity of the IE PL line is reached at delays of about 3 ns. This time is necessary for the formation of IE's upon the resonance

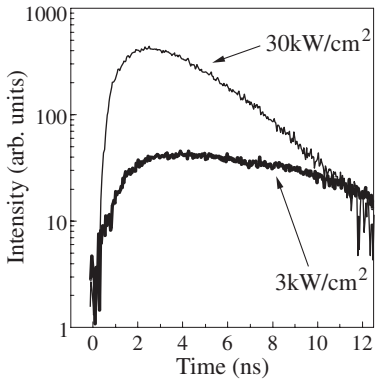

Fig. 1. Interwell exciton PL decay curves measured under pulsed photoexcitation at different excitation power and detected at PL line maximum ($T = 2\,\mathrm{K}$, $U = 0.6\,\mathrm{V}$).

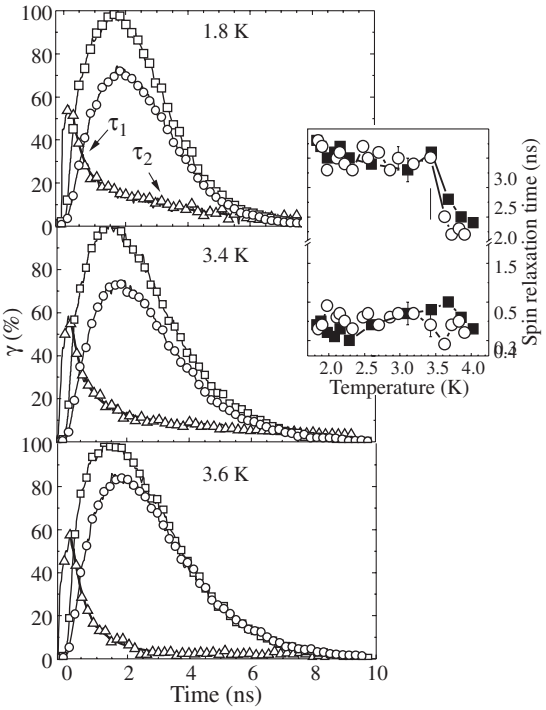

Fig. 2. Decay curves and circular polarization degree of interwell exciton PL measured at different temperatures. Insert presents the temperature dependencies of a spin relaxation time. Circular symbols correspond to the fast τ_1 and the slow τ_2 relaxation times at $U = 0.6$ V, square symbols — to the fast τ_1 and the slow τ_2 relaxation times at $U = 0.55$ V. The arrow indicates a temperature region where a rapid change of a spin relaxation rate occurs.

tunneling of electrons and holes to the neighboring quantum wells and their relaxation in energy scale to the equilibrium values of density and temperature. We believe that this behavior corresponds to IE's collective phase creation which is confirmed by results presented in Fig. 1. Two decay curves here correspond to different power of excitation and measured at a PL line maximum at $T = 2$ K and $U = 0.6$ V. One can see that decay time for larger power is much shorter (3 ns against 7 ns) than for smaller one. So, a radiative recombination time of IE's in collective phase is much shorter than the radiative recombination time of localized excitons.

For the IE's spin alignment we used circular polarized (for example, σ^+) pulsed laser excitation resonant with respect to the ground state of intrawell 1sHH excitons. Spin relaxation time was determined by analysis of measured circular polarization degree ($\gamma = (I_{\sigma^+} - I_{\sigma^-})/(I_{\sigma^+} + I_{\sigma^-})$, where I_{σ^+}, $_{\sigma^-}$ — PL signal intensity for σ^+ and σ^- components). Fig. 2 demonstrates IE's PL decay curves at different temperatures and $U = 0.6$ V for σ^+ and σ^- components, circular and square symbols, correspondingly. Triangular symbols correspond to IE's circular polarization degree, and solid lines are two-exponential decay fits by least-squares method. The temporal evolution of IE's circular polarization degree is governed by two kind of relaxation processes. Fast process (τ_1 time) is responsible for electron spin relaxation while carries relaxation to the equilibrium values of density and temperature occurs. It does not temperature dependent up to 15 K and τ_1 is equal to 0.35 ns. Slow process (τ_2 time) is IE's spin relaxation feature. It is determined by an electron-hole exchange interaction and τ_2 time drops above 3.5 K, which corresponds to the critical temperature of collective interwell exciton phase.

2. Discussions and summary

We believe that the presented experimental results are an evidence of the coherence of the IE's collective phase at low temperatures. Observed increased radiative recombination rate and reduced spin relaxation rate of IE's below critical temperature are an exhibition of the IE's collective phase coherence. Qualitatively, it is explained that interwell excitons in a collective state have the common wave function on the scales of the de Broglie wavelength. Our claim is based on work [7], where the spin relaxation rate of Bose-condensates atoms in traps was studied. It has been shown that the spin relaxation rate of the atoms in Bose-condensate is in N! times lower than for the atoms in usual classical gas (N — number of forming boson particles). Experimentally it confirms by work [8], where the atoms spin dynamics in Bose-condensate state has been investigated. In our case the τ_2 time, responsible for the exciton spin relaxation feature, changes around 2 times. It is in a good qualitative agreement with results [7].

In conclusion, for the first time the temperature dependence of a temporal dynamic of a dense interwell excitons gas has been investigated in GaAs/AlGaAs CQW's. It was found the drastic increase of the IE's spin relaxation time and strong decrease of the radiative recombination time at $T < T_c \leq 4$ K. The observed phenomenon is a sequence of the interwell excitons collective phase coherence at the temperatures below the critical one.

Acknowledgement

The authors express one's thanks Yu. Kagan for the fruitful and interesting discussions. This research was supported by DFG (Grant No. 436 RUS 17/95/03) and RFBI (Grants No. 04-02-17348 and No. 03-02-16920).

References

[1] Xuejun Zhu, P. L. Littlewood, M. S. Hybersten and T. Rice, *Phys. Rev. Lett.*, **74**, 1633 (1995).
[2] Yu. E. Lozovik and O. L. Berman, *JETP*, **84**, 1027 (1997).
[3] A. V. Larionov and V. B. Timofeev, *JETP Lett.*, **73**, 301–308 (2001).
[4] L. V. Butov, *J. Phys.: Condens. Matter*, **16**, R1577–R1613 (2004).
[5] A. V. Larionov, V. B. Timofeev, J. Hvam and C. Soerensen *JETP Lett.*, **71**, 117–1228 (2000).
[6] A. V. Larionov, V. B. Timofeev *et al*, *JETP Lett.*, **75**, 570–574 (2002).
[7] Yu. Kagan, V. A. Kashurnikov *et al*, *Phys. Rev. A*, **61**, 043608 (2000).
[8] E. A. Burt, R. W. Ghrist *et al*, *Phys. Rev. Lett.*, **79**, 337–340 1997.

13th Int. Symp. "Nanostructures: Physics and Technology"
St Petersburg, Russia, June 20–25, 2005

Low-field magnetoresistance and spin splitting in high-mobility heterostructures

L. E. Golub
Ioffe Physico-Technical Institute, St Petersburg, Russia

Abstract. Theory of weak antilocalization is developed for high-mobility two-dimensional systems. Linear in the wavevector spin-orbit interaction is taken into account. Anomalous magnetoresistance is calculated in the whole range of classically weak magnetic fields and for arbitrary strength of spin-orbit splitting. Obtained expressions are valid for both ballistic and diffusive regimes of weak localization. Proposed theory includes backscattering and non-backscattering interference contributions to the conductivity.

Introduction

Anomalous behavior of sample resistance in weak magnetic fields is a bright phenomenon observed at low temperatures on a wide class of conducting two-dimensional systems. Study of low-field magnetoresistance serves as a powerful tool for extracting kinetic and band-structure parameters of heterostructures.

The physical reason for the anomalous magnetoresistance is a *weak localization* effect. It consists in enhancement of backscattering from impurities due to quantum interference processes. Backscattering of particles appears on trajectories with self-crossing, Fig. 1. A particle has a possibility to pass a loop on such trajectory both clockwise and counter-clockwise. It acquires the same phase on both paths which leads to constructive interference of two electron waves. Enhancement of backscattering increases resistance of the system in comparison to its classical value. The length of closed paths contributing to the interference of backscattered waves is limited by the phase coherence time τ_ϕ. Low magnetic field destroys this interference which results in *negative* magnetoresistance.

In experiments, however, the anomalous resistance is an alternating function of magnetic field in two-dimensional semiconductor systems. In particular, in low fields it is *positive* and cannot be described by the simple picture given above. The reason for positive magnetoresistance is a spin-orbit interaction. In semiconductor heterostructures it is described by the following Hamiltonian

$$H_{SO}(\mathbf{k}) = \hbar\boldsymbol{\sigma}\cdot\boldsymbol{\Omega}(\mathbf{k})\,, \qquad (1)$$

where $\mathbf{k}$ is the electron wave vector, $\boldsymbol{\sigma}$ is the vector of Pauli matrices, and $\boldsymbol{\Omega}$ is an odd function of $\mathbf{k}$.

There are two $\mathbf{k}$-linear contributions to the spin-orbit interaction Hamiltonian (1) in two-dimensional semiconductor systems: the Rashba and the Dresselhaus terms. The anomalous magnetoresistance is the same if one takes into account the Rashba or the Dresselhaus contribution. Therefore we consider below only one term in $\boldsymbol{\Omega}$ with an isotropic spin splitting $2\hbar\Omega \sim k$.

In the limit of strong Rashba spin-orbit interaction the backscattering picture is shown in Fig. 1. An electron has a spin directed perpendicular to its wavevector $\mathbf{k}$. After passing the trajectory clockwise (counter-clockwise) the particle acquires the phase equal to $-\pi$ (π) [1]. Because of this difference, the interference is destructive. This leads to suppression of backscattering, i.e. the situation occurs opposite to spinless

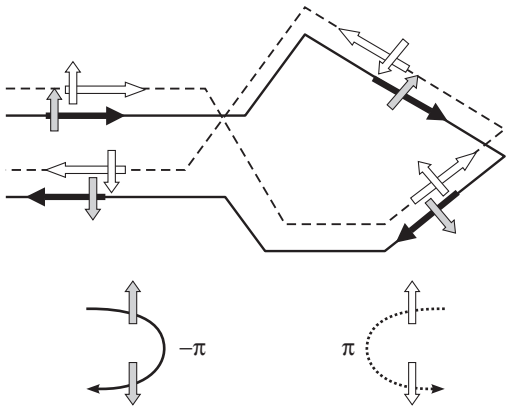

Fig. 1. Backscattering in the presence of strong Rashba spin-orbit interaction. The phase acquired after passage the loop clockwise (counter-clockwise) equals to $-\pi$ (π).

case. Therefore the effect in such systems is called *weak antilocalization*. Magnetic field destroying the interference increases the backscattering probability to its classical value which leads to *positive* magnetoresistance.

Elastic scattering results in that direction of electron spin is not directed along the vector $\boldsymbol{\Omega}$ (not perpendicular to $\mathbf{k}$ for the Rashba spin-splitting). At arbitrary $\Omega\tau$ where τ is the scattering time, the electron spin can rotate by the angle less than π after passing a loop. Therefore the sign of anomalous magnetoresistance can be both positive and negative.

Theory of anomalous magnetoresistance in systems with spin-orbit interaction (1) was developed in [2]. However the obtained expressions are valid only for i) weak spin-orbit interaction and ii) very low magnetic fields. The first assumption means that $\Omega\tau \ll 1$. The second condition reads as $l_B \gg l$, where $l_B = \sqrt{\hbar/eB}$ is the magnetic length, and l is the mean free path. This so-called "diffusion" regime takes place in fields $B \ll B_{tr}$, where $B_{tr} = \hbar/2el^2$ is the "transport" field.

In high-mobility structures both these conditions fail. Due to long scattering times the product $\Omega\tau$ can be even larger than unity [3,4,5]. Besides, the transport field is often less than 1 mT [3,4,6], that is too small range of magnetic fields. This means that particle motion is rather ballistic than diffusive. Therefore fitting experimental data by the theory [2] is unsuccessful [6].

The aim of the present work is to develop the weak-antilocalization theory for systems with strong spin-orbit interaction valid for both ballistic and diffusion regimes. The magnetic field dependence of the conductivity is calculated for arbi-

trary values of B/B_{tr} and $\Omega\tau$, opening a possibility to describe anomalous magnetoresistance experiments and to extract spin-splitting and kinetic parameters of high-mobility two-dimensional systems.

Anomalous magnetoconductivity

In order to calculate the anomalous magnetoconductivity $\sigma(B)$ we consider a particle in a state $|\alpha\rangle$ falling after backscattering within a state $|\beta\rangle$, where $\alpha,\ \beta = \pm 1/2$ are the particle spin projections onto the growth axis. Altogether there are four pairs of states which are useful to choose as a singlet and a triplet. The consideration shows that the singlet interferes always constructively, and its positive contribution to $\sigma(B)$ is independent of $\Omega\tau$. The triplet contribution is negative, however its magnitude changes drastically with $\Omega\tau$.

Calculation of the backscattering probability for electrons with spin splitting (1) in a magnetic field is performed [7] by the Green function method. The approach is to expand the backscattering probability in series over wavefunctions of a particle with the charge $2e$ in a magnetic field. As a result, the expression for the backscattering-induced conductivity correction has the form

$$\sigma(B)=\frac{e^2}{2\pi^2\hbar}\left(\frac{l}{l_B}\right)^2\sum_{N=0}^{\infty}\left\{\frac{P_N^3}{1-P_N}-\mathrm{Sp}\left[A_N^3(I-A_N)^{-1}\right]\right\}, \tag{2}$$

where I is a 3×3 unit matrix. The second term is the triplet part which is described by the matrix

$$A_N=\begin{pmatrix} P_{N-2}-S_{N-2}^{(0)} & R_{N-2} & S_{N-2}^{(2)} \\ R_{N-2} & P_{N-1}-2S_{N-1}^{(0)} & R_{N-1} \\ S_{N-2}^{(2)} & R_{N-1} & P_N-S_N^{(0)} \end{pmatrix}. \tag{3}$$

Here $P_N=\frac{l_B}{l}\int\limits_0^\infty dx\,\exp\left[-x\frac{l_B}{l}\left(1+\frac{\tau}{\tau_\phi}\right)-\frac{x^2}{2}\right]L_N(x^2)$,

$$S_N^{(m)}=\frac{l_B}{l}\sqrt{\frac{N!}{(N+m)!}}$$
$$\times\int\limits_0^\infty dx\,\exp\left(-x\frac{l_B}{l}-\frac{x^2}{2}\right)x^m L_N^m(x^2)\sin^2\left(\Omega\tau\frac{l_B}{l}x\right),$$

$$R_N=\frac{l_B}{l}\frac{1}{\sqrt{2(N+1)}}$$
$$\times\int\limits_0^\infty dx\,\exp\left(-x\frac{l_B}{l}-\frac{x^2}{2}\right)xL_N^1(x^2)\sin\left(2\Omega\tau\frac{l_B}{l}x\right),$$

with L_N^m being the Laguerre polynomials. Note that zeros should be taken instead of the values with negative indices in the matrix (3) for $N=0,\,1$.

In Fig. 1 the conductivity correction is plotted for different strengths of the spin-orbit interaction. There is also a non-backscattering contribution to the conductivity which is taken into account in the calculation (see [7] for details). One can see that the spin-orbit interaction changes dramatically the anomalous magnetoconductivity: its minimum shifts to higher fields. The positions of minima in the curves, $B_{\min}$, are shown in the inset. One can see that $B_{\min}$ almost linearly depends on the spin splitting at $\Omega\tau > 0.8$. Fitting yields the following approximate law

$$B_{\min}\approx(3.9\,\Omega\tau-2)B_{tr}\,.$$

In high fields, when $B\gg(\Omega\tau)^2B_{tr}$, the conductivity becomes independent of Ω. The reason is that in so strong field the dephasing length due to magnetic field $\sim l_B$ is smaller than one due to spin-orbit interaction, $l/\Omega\tau$. As a result, the particle spins keep safe at a characteristic trajectories. The conductivity for any finite $\Omega\tau$ has the high-field asymptotic

$$\sigma_{hf}(B)=-0.25\sqrt{\frac{B_{tr}}{B}}\,\frac{e^2}{\hbar}\,. \tag{4}$$

One can see that the asymptotic $\sigma_{hf}(B)$ is reached at $B\approx 100\,B_{tr}$ for all presented values of $\Omega\tau$.

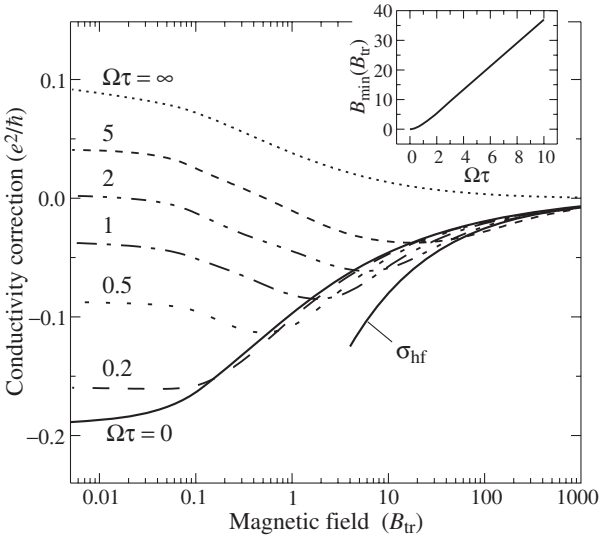

Fig. 2. Conductivity correction for different strengths of spin-orbit interaction at $\tau/\tau_\phi=0.01$. $\sigma_{hf}(B)$ is the high-field asymptotic (4). The inset represents the positions of minima in the magnetoconductivity.

In conclusion, the theory of weak antilocalization is developed for high-mobility two-dimensional systems. Anomalous magnetoconductivity is calculated in the whole range of classically weak fields and for arbitrary values of spin-orbit splitting.

Acknowledgement

This work is financially supported by RFBR, INTAS, and "Dynasty" Foundation — ICFPM.

References

[1] J. S. Meyer, V. I. Fal'ko and B. L. Altshuler, in: NATO Science Series II, Vol. 72, edited by I. V. Lerner *et al*. (Kluwer Academic Publishers, Dordrecht, 2002) .
[2] S. V. Iordanskii, Yu. B. Lyanda-Geller and G. E. Pikus, *JETP Lett.*, **60**, 206 (1994).
[3] T. Koga, J. Nitta, T. Akazaki and H. Takayanagi, *Phys. Rev. Lett.* **89**, 46801 (2002).
[4] J. B. Miller *et al*, *Phys. Rev. Lett.*, **90**, 076807 (2003).
[5] C. Schierholz, T. Matsuyama, U. Merkt and G. Meier, *Phys. Rev. B*, **70**, 233311 (2004).
[6] S. A. Studenikin, P. T. Coleridge, N. Ahmed, P. J. Poole and A. Sachrajda, *Phys. Rev. B*, **68**, 035317 (2003).
[7] L. E. Golub, cond-mat/0412047, submitted to *Phys. Rev. B*.

13th Int. Symp. "Nanostructures: Physics and Technology"
St Petersburg, Russia, June 20–25, 2005

Long-lived electron spin polarization in negatively charged InGaAs QDs

S. Yu. Verbin[1,2], A. Greilich[2], D. R. Yakovlev[2,3], M. Bayer[2], V. Stavarache[4], D. Reuter[4] and A. Wieck[4]

[1] V.A.Fock Institute of Physics, St Petersburg State University, 198504 St Petersburg, Russia
[2] Fachbereich Physik, Universität Dortmund, 44221 Dortmund, Germany
[3] Ioffe Physico-Technical Institute, St Petersburg, Russia
[4] Angewandte Festkörperphysik Ruhr-Universität Bochum, 44780 Bochum, Germany

Abstract. Light-induced spin orientation in negatively charged InGaAs quantum dots is shown experimentally to be conserved during milliseconds.

Introduction

The long-term orientation of spin systems in semiconductor structures attracts in recent years considerable attention as a promising way for recording and storing of optical information [1]. Most interesting, from this point of view, are structures with quantum dots (QD), where, due to confinement of the carrier motion, the main spin-relaxation processes appear to be suppressed. According to theoretical estimates [2], the spin lifetime in such structures may reach milliseconds and more. So long lifetimes of optically oriented electron spins in QDs have not been observed thus far. The longest lifetime of the electron spin orientation (during at least hundreds of microseconds) was found experimentally in the work of Ikezawa et al. [3] for n-doped InP QDs. In this communication, we present the results of experiments demonstrating conservation of the spin orientation for much longer times.

1. Experiment and discussion

We studied the kinetics of circularly polarized photoluminescence (PL) of negatively charged InGaAs QDs at helium temperatures.

The studied sample contains 20 layers of InGaAs/GaAs quantum dots separated by 60 nm barriers, with dot density 10^{10} cm^{-2}. The structure was n-doped 20 nm below each dot layer with a density to provide occupation of each dot with a single electron. The sample was thermally annealed after growth at a temperature of 945 °C. An undoped sample has been tested as a reference structure.

It was found that the degree of circular polarization, $\rho_{\rm circ}$, of the QDs ground state emission is negative (Fig. 1a) for excitation of QDs by σ^+ circularly polarized light in the wetting layer ($h\nu_{\rm exc}$=1.476 eV). For excitation in excited states of the QDs (intra-dot excitation) the PL is negatively polarized too, but with a lower value of $|\rho_{\rm circ}|$.

PL kinetics measurements show that $\rho_{\rm circ}(t)$ decays during hundreds of picoseconds after the exciting pulse and then $\rho_{\rm circ}(t)$ has a nearly constant negative value (Fig. 1b). This value is referred hereafter as the amplitude of degree of the negative circular polarization (NCP), $\rho_{\rm NCP}$ (Fig. 2b). The maximum of the observed $|\rho_{\rm NCP}|$ reaches 0.75 (Fig. 1b).

In conformity with conclusions of [3], the negatively polarized PL is observed for QDs occupied by a single resident electron. The NCP results from the flip-flop process of the electron and hole spins during their energy relaxation to the ground states [3]. The amplitude of the degree of NCP increases, when the resident electron spin is preferentially oriented along that of the photoexcited electron.

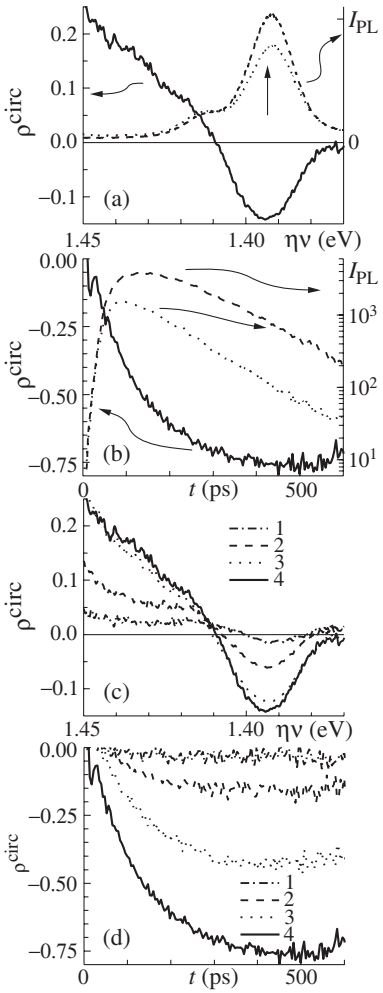

Fig. 1. Spectra and kinetics of PL intensity and of circular polarization degree $\rho_{\rm circ}$ ($h\nu_{\rm exc}$ = 1.476 eV). Dotted, dashed and solid lines in panels a) and b) show σ^+ and σ^- polarizations of PL and $\rho_{\rm circ}$ measured at the excitation intensity $I_{\rm exc} = I_0$. Kinetics was measured at the spectral position marked by the arrow on a). (c-d) — the dependencies of $\rho_{\rm circ}$ on the $I_{\rm exc}$: 1 — $I_{\rm exc} = 0.04I_0$, 2 — $I_{\rm exc} = 0.13I_0$, 3 — $I_{\rm exc} = 0.36I_0$, 4 — $I_{\rm exc} = I_0$.

An increase of $\rho_{\rm NCP}$ was observed with the rise of the exciting light intensity $I_{\rm exc}$ (Fig. 1, c, d). Using the amplitude of the NCP as a measure for the degree of orientation of the

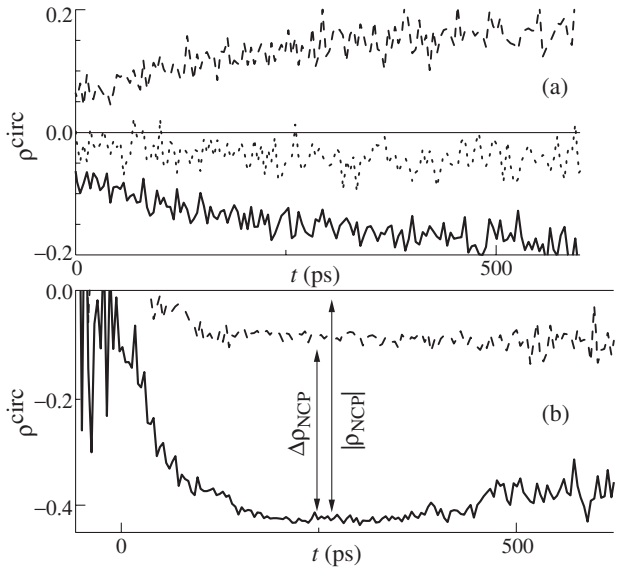

Fig. 2. Dependence of $\rho_{\rm circ}$ of PL by the σ^+ polarized probe on the pump polarization. Solid, dashed, and dotted lines correspond to σ^+, σ^- and linear polarization of the pump. (a) — $I_{\rm pump} \gg I_{\rm probe}$; (b) — $I_{\rm pump} = I_{\rm probe}$.

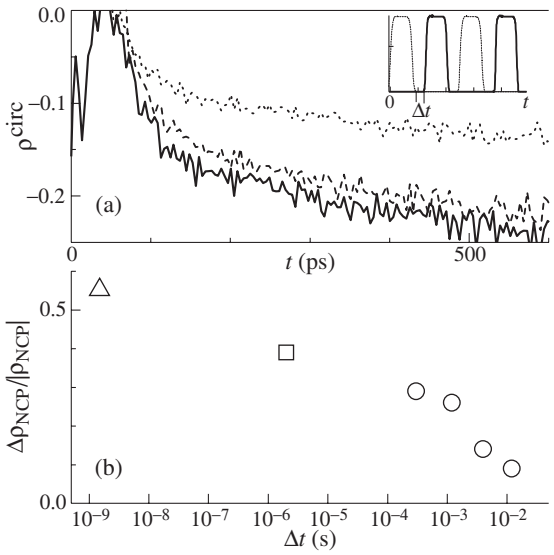

Fig. 3. Dependence of $\rho_{\rm circ}$ of PL excited by the probe pulse on the time delay Δt between pump and probe pulses: a) Dotted and dashed lines show kinetics of $\rho_{\rm circ}$ at σ^- polarized pump and at Δt = 0.3 and 12 ms, correspondingly; solid — at σ^+ polarized pump; inset shows the shape of probe (solid) and pump (dashed) pulse trains. b) dependence of ratio $\Delta\rho_{\rm NCP}/|\rho_{\rm NCP}|$ on Δt; triangle, square and circles correspond to time-shifted pump and probe pulses and to trains of these pulses formed by PEM or chopper, correspondingly.

electron spin, we have carried out a series of experiments to determine the spin orientation lifetime.

In the experiments, the PL was excited by two laser pulse trains obtained by splitting the beam of a mode-locked Ti:sapphire laser. One of these trains was shifted in time using an optical delay line. The time delay was about 1.5 ns. The probe beam was σ^+ polarized while the pump beam polarization could be varied independently.

Figure 2 shows the kinetics of the degree of polarization of the PL excited by the second (probe) beam for different polarizations of the first pump beam. As is seen, a change of the pump polarization results in a change ($\Delta\rho_{\rm NCP}$) of the NCP created by the probe pulse. This means that the spin orientation created by the first beam is held until the arrival of the second beam, i.e., for about 1.5 ns.

To strongly increase the time interval between the two beams, we have used photo-elastic modulator (PEM) or mechanical chopper which alternatively blocked the pump and the probe beams with various frequencies. In the experiments with mechanical chopper, the time interval Δt between the end of the train of pump pulses and beginning of the train of probe pulses (inset at Fig. 3a) was used as a measure of time delay between these trains.

A typical result of the experiment at nearly equal $I_{\rm pump}$ and $I_{\rm probe}$ is presented in Fig. 3a. It is seen that the NCP of the PL following the probe pulse still reveals a well reproducible change caused by the change of polarization of the pump pulse even at Δt = 12 ms. Fig. 3b shows the dependence of $\Delta\rho_{\rm NCP}/\rho_{\rm NCP}$ on the time interval between pump and probe pulses or between their trains. This result demonstrates in a straightforward way conservation of the spin orientation during the modulation period which exceeds 10^{-2} s.

So long conservation of the orientation in principle may be due to intrinsic property of electron spins in QDs [2, 3] or results from some stabilizing factor. The role of this factor is likely to be played by the field of the dynamic nuclear polarization [4] or by the fluctuating exchange field produced by nuclear spins [5]. The possible role of these mechanisms could be studied by the research of the NCP behavior in magnetic fields which is in progress.

From the above experimental data that the light-induced spin orientation in the negatively charged InGaAs QDs is hold during the time of about 10^{-2} s.

Acknowledgements

Authors are thankful to Dr. I. Ignatev and Dr. I. Gerlovin for fruitful discussions. The work is supported in part by the Deutsche Forschungsgemeinschaft through 436 RUS 17/102/04, by INTAS (1B 2167) and by RFBR (03-02-16858).

References

[1] D. D. Awschalom, J. M. Kikkawa, *Phys.Today* **52**, 33 (1999).
[2] A. V. Khaetskii, Yu. V. Nazarov, *Phys. Rev. B* **61**, 12639 (2000).
[3] M. Ikezawa *et al*, *Phys. Rev. Lett.* (submitted).
[4] D. Gammon *et al*, *Phys. Rev. Lett.* **86**, 5176 (2001).
[5] A. Merkulov *et al*, *Phys. Rev. B* **65**, 205309 (2002).

13th Int. Symp. "Nanostructures: Physics and Technology"
St Petersburg, Russia, June 20–25, 2005

Spin quantum beats and hole g-factor in GaAs quantum wells

I. A. Yugova[1,2], I. V. Ignatiev[1,2], A. Greilich[2], Yu. P. Efimov[1], Yu. K. Dolgikh[3], I. Ya. Gerlovin[3], V. V. Ovsyankin[3], D. R. Yakovlev[2,4] and M. Bayer[2]

[1] V. A. Fock Institute of Physics, St Petersburg State University, 198504 St Petersburg, Russia
[2] Fachbereich Physik, Universität Dortmund, 44221 Dortmund, Germany
[3] Vavilov State Optical Institute, St Petersburg, 199034, Russia
[4] Ioffe Physico-Technical Institute, St Petersburg, Russia

Abstract. The spin dynamics of the carriers in the GaAs quantum wells was studied by photo-induced linear birefringence and Kerr rotation technique. The oscillations of the signal resulting from excitonic spin quantum beats and free electron spin precession in the magnetic field are observed. The dependence of the electron and hole g-factors on the quantum well thickness are determined

The main way to determine the excitonic g-factor in semiconductor nanostructures was based, until recently, on the measurements of Zeeman splitting of the excitonic states. As a rule, the splitting was much smaller than inhomogenious width of the excitonic line, and to determine its value one needed to use very complicated and sometime ambiguous fitting procedures [1]. Significant progress in this field was achieved by use of the modern kinetic methods capable of detecting spin precession of the carriers in a magnetic field. One of them is the polarization-sensitive pump-probe pulsed method. The method is based on measuring the polarization changes in the probe beam induced by the pump pulses. In this report, we present the results of the experimental study of electron and hole g-factors in GaAs quantum wells using this method.

We studied an MBE-grown structure with 4 GaAs quantum wells, 5.1, 8.8, 13, and 17 nm thick, sandwiched between 50-nm AlGaAs barrier layers with the 34% of aluminum. The sample was mounted in a cryostat with a superconducting magnet, which allowed us to make the measurements both in longitudinal and transverse magnetic fields. We have used the pump-probe technique with polarization sensitivity for detection of the spin orientation. Ti:Sapphire laser with 1.8 ps pulses at a frequency of 76 MHz was tuned in the resonance with the QW excitonic transition. The polarization of the pump beam was modulated by means of photo-elastic modulator operating at 50 kHz. The probe beam was linearly polarized, its intensity being 10-20% of the pump beam. The reflected probe beam was detected by a balanced diode detector and a lock-in amplifier. The signal was detected either at the frequency of the pump beam modulation, or at the double frequency. In the first case, the signal resulted from the rotation of the polarization plane of the probe beam induced by the circularly polarized pump (photo-induced Kerr rotation) [2]. In the second case, we detected a linear birefringence induced by the linearly polarized pump [3]. The magnitude of the signal was measured as a function of the time delay between the pump and probe pulses and of the laser beam frequency.

As was shown in the preliminary experiments, the excitonic peaks in the photoluminescence spectra of the sample under study are characterized by a well-pronounced doublet structure. The short-wavelength components of the doublets, coincident in energy with the HH-peaks of the reflectivity spectra in each quantum well, are related to the excitonic luminescence. The long-wavelength components, spaced by 0.8–1 nm, are presumably related to the trionic luminecence [4].

To study the dynamics of the excitonic spin, we have measured the dependence of the linear birefringence signal on time delay between the pump and probe pulses. The experiments were made in a longitudinal magnetic field (Faraday configuration). In this configuration, the linearly polarized pump creates a coherent superposition of the optically active excitonic states with spin projections $+1$ and -1 (alignment of the excitonic spin). This gives rise to an ellipticity of the reflected probe beam, which can be detected as a birefrigence signal. The longitudinal magnetic field splits the optically active excitonic doublet and the ellipticity induced by pump becomes oscillating in time due to quantum beats between the doublet components. The oscillation frequency, ω, can be connected with the splitting, ΔE, by the equation: $\hbar\omega = \Delta E$, where $\Delta E = g_{\text{th}}\mu_B B$ (g_{th} is the excitonic g-factor, μ_B is the the

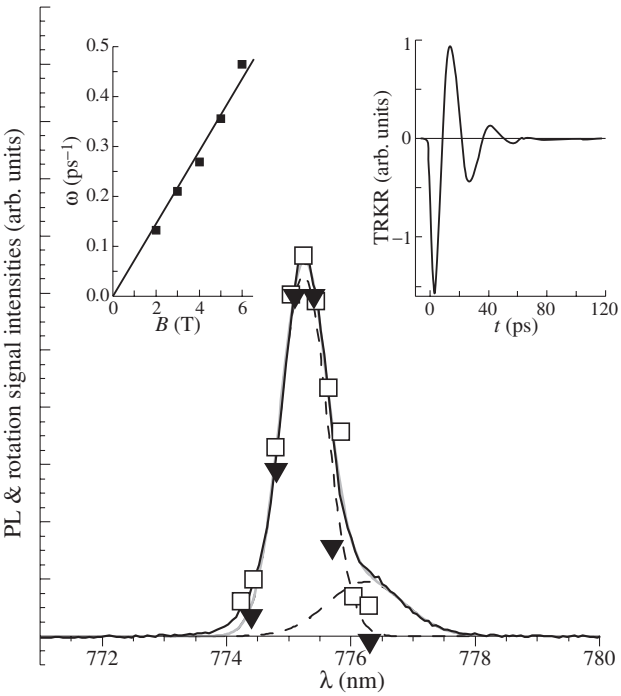

Fig. 1. Spectra of signals from 5 nm quantum well. Solid lines — PL spectrum (black) and theoretical fit by two gaussians (grey). Open squares — the amplitude of the linear birefringence signal in zero magnetic field. Full triangles — oscillations amplitude in the magnetic field 6 T. Left inset — field dependence of the oscillations frequency. Right inset — oscillating signal in the magnetic field 6 T. $T = 2$ K.

Bohr magneton and B is the magnetic field strength).

The results of the study of the birefrigence signal in the region of the excitonic peak in 5 nm quantum well are shown in Fig. 1. The spectrum of the signal is seen to reproduce almost exactly the profile of the exciton luminescence line. With no magnetic field, the dependence of the signal amplitude on the time delay is characterized by an exponential decay with the time constant 20 ps. In the longitudinal magnetic field, the dependence of the signal on time delay acquires the shape of damping oscillations (see right insert in Fig. 1). The decay time determined by dephasing of the exciton spin equals 18 ps and practically does not depend on the field strength. Spectral dependence of the initial oscillation amplitude coincides with the spectrum of the signal at zero field (see Fig. 1). As was shown in the experiments (see left inset in Fig. 1), the oscillation frequency linearly increases with the field. The slope of the field dependence corresponds to $|g_{\rm th}| = 0.8 \pm 0.05$.

The oscillating birefrigence signal was also seen on the excitonic peaks in other quantum wells (see Fig. 2), but the oscillation frequency for these peaks revealed nonlinear dependence on the magnetic field strength (a nonlinear field dependence of Zeemann splitting in 11.3 nm GaAs quantum well has been described in Ref. [1]). Because of the nonlinearity, the oscillation frequency cannot be determined reliably in magnetic fields smaller than 4 T. The frequency of the oscillations measured in the field of 6 T depends nonmonotonically on the quantum well thickness, as it can be seen from Fig. 2. This is the result of the sign inversion of the excitonic g-factor theoretically predicted for the GaAs quantum wells thicker than 10 nm [5].

Dependence of the g-factor on the quantum well thickness determined from the oscillation frequency in the field of 6 T is shown in the inset in Fig. 2. Sign of the g-factor was not determined in the experiment therefore this dependence is drawn in accordance with the results by Worsley *et al*. [3]. One can see that for the 5 nm quantum well our data correspond well to the data presented in Ref. [1], but for thicker quantum wells there are large discrepancies. The values of g-factor in Ref. [1] are determined in smaller magnetic field, so the most likely reason for the discrepancy is a nonlinear field dependence of the Zeeman splitting, mentioned above.

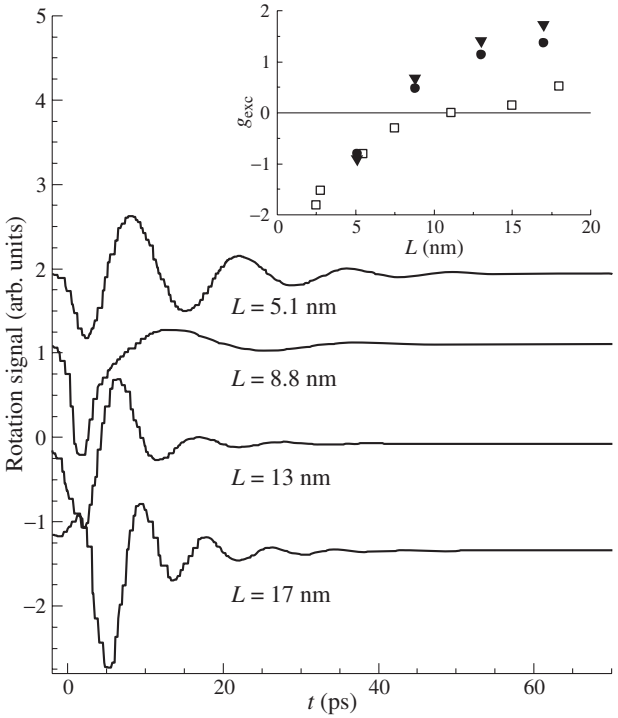

Fig. 2. Time delay dependence of the linear birefringence signal in different quantum wells. Thickness of the well is displayed near each curve. $B = 6$ T, $T = 2$ K. Inset — quantum well thickness dependence of the g-factor value. Full circles — excitonic g-factor, full triangles — hole g — factors (see in text), open squares excitonic g-factors from Ref. [1]

To determine the hole g-factor, one needs to know not only g-factor of the optically active excitonic state but also the longitudinal component of the electron g-factor. The last value was determined using the values of the transverse component of electron g-factor [6] and the difference between longitudinal and transverse components calculated theoretically in Ref. [7]. The hole g-factors calculated using these data are also demonstrated in Fig 2.

In conclusion, we have measured experimentally quantum beats of the fine structure components of the excitonic states in GaAs quantum wells. The values of the electron and hole g-factors and their dependence on the quantum well thickness are determined from the experimental data.

Acknowledgements

Authors thank Prof. V. S. Zapasskii for critical reading of the manuscript. The work is partly supported by ISTC, grant 2679, by the Deutsche Forschungsgemeinschaft through 436 RUS 17/39/04, 436 RUS 17/102/04.

References

[1] M. J. Snelling, E. Blackwood, C. J. McDonagh, R. T. Harley, C. T. B. Foxon, *Phys. Rev. B* **45**, 3922 (1992).

[2] S. A. Crooker, D. D. Awschalom, J. J. Baumberg, F. Flack, N. Samarth, *Phys. Rev. B* **56**, 7574 (1997).

[3] R. E. Worsley, N. J. Trainor, T. Grevatt, R. T. Harley, *Phys. Rev. Lett.* **76**, 3224 (1996).

[4] R. V. Cherbunin, Yu. K. Dolgikh, S. A. Eliseev, Yu. P. Efimov, I. Ya. Gerlovin, I. V. Ignatiev, V. V. Ovsyankin, V. V. Petrov, V. Stroganov, E. V. Ubyivovk, in *Nanostructures: Physics and Technology*, Proc. 12th Int. Symp. June 21–25, 2004, Ioffe Institute, St Petersburg, Russia, p. 326-327

[5] A. A. Kiselev, L. V. Moiseev, *Fiz. Tverd. Tela* **38**, 1574 (1996); [Phys. Solid State 38 (1996) 866].

[6] The transverse components of the electron g-factor in the quantum wells under study were measured using the oscillations of the Kerr-effect signal in the transverse magnetic field. The results of these experiments are in preparation for publication.

[7] E. L. Ivchenko, A. A. Kiselev, *Fiz. Tekh. Poluprovodn.* **26**, 1471, 1992 [Sov. Phys. Semicond., **26**, 827, 1992].

13th Int. Symp. "Nanostructures: Physics and Technology"
St Petersburg, Russia, June 20–25, 2005

In-plane anisotropy of spin relaxation in asymmetrical quantum wells

A. V. Platonov, A. S. Gurevich, V. P. Kochereshko, A. S. Shkolnik, M. G. Rastegaeva, V. P. Evtikhiev, L. E. Golub and N. S. Averkiev

Ioffe Physico-Technical Institute, St Petersburg, Russia

Abstract. An effect of optical orientation of electrons and Hanle effect was studied in GaAs-based asymmetrical quantum well structures. It has been found that the width of Hanle depolarization curve in the asymmetrical quantum well depends strongly on the orientation of magnetic field relatively to the crystallographic axes of the sample. An explanation of the observed effect is proposed in the framework of the D'yakonov-Perel spin relaxation mechanism.

Introduction

Reduction of symmetry due to carrier confinement in one or several directions gives rise to essentially new optical effects in nanostructures. In quantum wells such a reduction of symmetry causes the appearance of linear in wave vector terms in the Hamiltonian, which describes the energy spectrum of the two-dimensional (2D) carriers. It is essential that the linear contributions can originate either from the asymmetry of the quantum well itself (Rashba term), or from the absence of the inversion symmetry in the initial material (Dresselhaus term). The existence of terms odd in the wave vector in the energy spectrum leads to the relaxation of the carrier spin of and to the anisotropy of the magnetic properties of the quantum wells. In undoped GaAs- and GaAlAs-based structures at low temperatures the dominating mechanism of electron spin relaxation is the precession mechanism of D'yakonov-Perel [1], caused by odd in wave vector terms.

The presence of two types of linear terms becomes most brightly apparent in the dependence of electron spin relaxation on its orientation in the plane of the quantum well grown along the [100] direction. Such dependence means that the width of the Hanle curve for free carriers will depend on the direction of the magnetic field relatively to the crystallographic axes of the sample in the quantum well plane. It was theoretically shown [2] that for GaAs-based heterostructures the degree of the anisotropy depends on the magnitude of the built-in electric field. For quantum wells grown along the [100] axis it can reach tens percent. The aim of this work is an experimental observation of the electron spin relaxation rate dependence on the orientation of spin relatively to the crystallographic axes in the plane of the quantum well grown along the [100] direction.

1. Experimental

In order to observe the expected effect a set of triangular and rectangular quantum wells has been grown. The structures were MBE grown on semi-insulating (001) GaAs substrates and contained a 300 nm $Al_{0.36}Ga_{0.64}As$ buffer layer, a 250 nm $Al_{0.3}Ga_{0.7}As$ barrier layer, a quantum well, a second barrier layer, and a 5 nm cap layer. Both triangular GaAs quantum well structures with the well width of the order of 10 nm and asymmetrical quantum well structures, schematically shown on the inset to Figure 1, have been studied. The asymmetrical $Al_{0.05}Ga_{0.95}As$ triangular quantum well was confined from one side by the $Al_{0.3}Ga_{0.7}As$ barrier. The other inclined barrier was grown with linearly changing from 5 to30% content of Al on the width of 180Å. To keep the composition of the barrier a method of sup-monolayer epitaxy was used. The structures were not attentively doped being weakly p-type at temperature of 77 K.

Photoluminescence (PL) has been studied spectra under circularly polarized excitation. The measurements were performed at temperature 77 K. The nitrogen cryostat was placed in the cut of the electromagnet with maximal field of 0.5 T. The sample was excited by a He-Ne laser with wave length of 6328Å.

Figure 1 shows PL spectrum in zero magnetic field and optical orientation signal. The magnitude of the optical orientation signal amounts to 10% and is virtually constant within the PL contour.

Figure 2 shows the dependence of the magnitude of the optical orientation signal on the magnetic field in Voight geometry at the maximum of the PL line with the direction of the magnetic filed along the [110] and [1$\bar{1}$0] axes. Both dependencies are symmetrical relatively to the change of the magnetic field sign. It is evident that when the magnetic field is directed along the [110] axis the Hanle curve is more than two times wider than the depolarization curve for [1$\bar{1}$0] direction. Such an asymmetry of the Hanle effect was not observed for the structure with symmetrical GaAs QW.

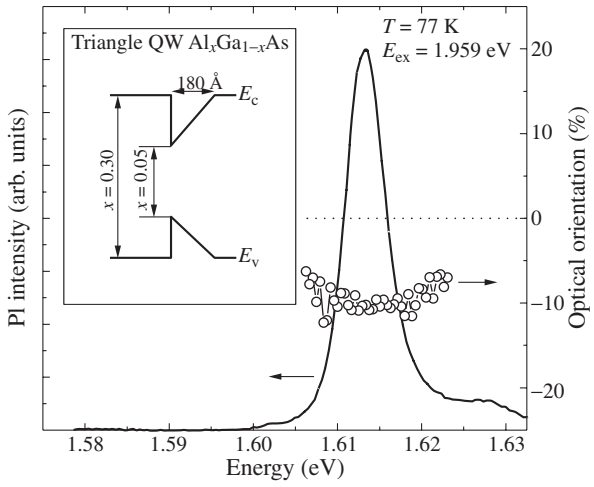

Fig. 1. Photoluminescence spectrum (solid curve) taken under He-Ne laser excitation with $\lambda_{exc} = 6328$ Å and optical orientation signal (open circles). The inset represents a scheme of the triangular QW structure.

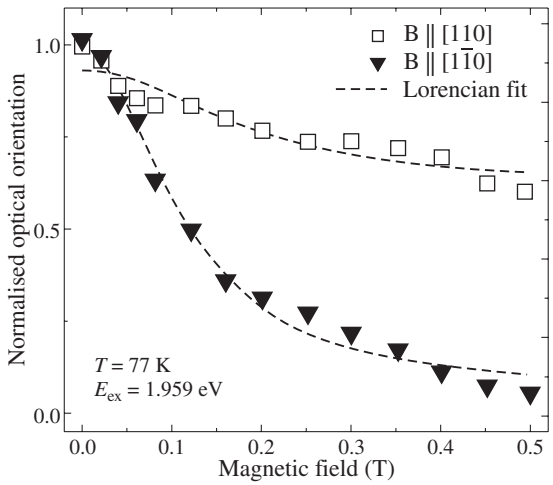

Fig. 2. Hanle depolarization curves taken from the sample with an asymmetrical QW for two magnetic field orientations: along the [110] (squares) and [1$\bar{1}$0] (triangles) axes. Dotted lines represent Lorentzian fit of the curves.

Discussion

The width of the Hanle curve is determined by the ratio of the electron Zeeman splitting to the lifetime of the electron spin. It is natural to expect [3] that the anisotropy of the electron Zeeman splitting should not exceed 10%. Thus the observed anisotropy of the Hanle effect should be related to anisotropy of the electron spin relaxation, caused by the mutual compensation of the Rashba and Dresselhaus terms [2].

We can estimate the value of the electron spin relaxation time from these Hanle curves if the electron g-factor is known. Assuming the g-factor $|g_e| \approx 0.2$ we will get for the electron spin relaxation time $\tau_s \approx 0.6$ ns. This means that at 77 K the spin relaxation is faster the electron lifetime $\tau_s \ll \tau_0$. This is in a good agreement with the initial value of the optical orientation signal at zero magnetic fields and with expected exciton lifetime [4].

Acknowledgement

This work was partially supported by the RFBR, INTAS, and the program of the presidium of RAS, the programs of DPhS of RAS and the Russian Ministry of Science and Education. Work of L. E. G. is supported by the "Dynasty" Foundation-ICFPM.

References

[1] E. L. Ivchenko, P. S. Kop'ev, V. P. Kochereshko, *et al*, *JETP Lett.*, **47**, 407 (1988).

[2] N. S. Averkiev, L. E. Golub and M. Willander, *J. Phys. Cond. Matter*, **14**, R271 (2002).

[3] S. Hallstein, M. Oestreich, W. W. Ruhle *et al*, *"High Magnetic Fields in the Physics of Semiconductors II"*, Vol 2, p. 593, World Scientific, Eds. G. Landwehr and W. Ossau (1997).

[4] J. Feldmann, G. Peter, E. O. Gobel, *et al*, *Phys. Rev. Lett.*, **60**, 243 (1988).

13th Int. Symp. "Nanostructures: Physics and Technology"
St Petersburg, Russia, June 20–25, 2005

Direct observation of the electron spin dephasing induced by nuclei in InAs/GaAs quantum dots

P.-F. Braun[1], X. Marie[1], L. Lombez[1], B. Urbaszek[1], *T. Amand*[1], P. Renucci[1], V. K. Kalevich[2], K. V. Kavokin[2], O. Krebs[3], P. Voisin[3] and Y. Masumoto[4]

[1] Laboratoire de Nanophysique, Magnétisme et Optoélectronique, F-31077 Toulouse, France
[2] Ioffe Physico-Technical Institute, St Petersburg, Russia
[3] Laboratoire de Photonique et Nanostructures, 91460 Marcoussis, France
[4] Institute of Physics, University of Tsukuba, Tsukuba 305-8571, Japan

Abstract. We have studied the electron spin decay in semiconductor InAs/GaAs quantum dots by time-resolved optical spectroscopy. The average spin polarisation of the electrons in an ensemble of p-doped quantum dots decays down to 1/3 of its initial value with a characteristic time $T_\Delta \approx 500$ ps, which is attributed to the hyperfine interaction with randomly oriented nuclear spins. We show that this efficient electron spin dephasing mechanism can be suppressed by an external magnetic field as small as 100 mT.

Introduction

Spins of localised electrons in semiconductor quantum dots (QD) are attractive for future spintronic and quantum information devices since they are not subject to the classical spin relaxation mechanisms known for free carriers. Recent theoretical studies have predicted that the dominant mechanism of electron spin relaxation in QD at low temperature is due to the hyperfine interaction with nuclear spins [1, 2]. An electron spin in a quantum dot interacts with a large but finite number of nuclei $N_L \approx 10^3$ to 10^5. In the frozen fluctuation model, the sum over the interacting nuclear spins gives rise to a local effective hyperfine field $\mathbf{B}_N$ [1]. The electron spin can thus coherently precess around $\mathbf{B}_N$ [1, 2]. However, the amplitude and direction of the effective nuclear field vary strongly from dot to dot. The average electron spin $\langle \mathbf{S}(t) \rangle$ in an ensemble of dots will thus decay as a consequence of the random distribution of the local nuclear effective field. The ideal configuration to probe the electron spin relaxation mediated by nuclei in QD with optical experiments presents itself in the form of positively charged excitons X^+ (consisting of one electron and two holes forming a spin singlet) [3]. As in the case of X^- [4] the exchange interaction between the electron and the two holes cancels in the X^+ ground state. The analysis of the circular polarisation of the X^+ luminescence in p-doped QD following a circularly polarised laser excitation will thus probe *directly* the spin polarisation of the electron. A large spin polarisation of the X^+ luminescence has indeed been observed recently in InAs/GaAs and GaAs/AlGaAs quantum dot photoluminescence (PL) spectra [5,6].

1. Experiments

We have studied three p-modulation doped QD structures grown by molecular beam epitaxy on (001) GaAs substrates. Very similar results have been obtained for all three samples. We present here the experimental data obtained in one of them which consists of 10 planes of lens shaped self assembled InAs/GaAs QD separated by a 30 nm GaAs layer; a Beryllium delta doping layer is located 15 nm below each wetting layer (WL). The nominal acceptor concentration is $N_A = 15 \times 10^{10}$ cm^{-2} per layer in this sample. The QD density is about 15×10^{10} cm^{-2} per plane. The observation of QD ground state PL under strictly resonant excitation (not shown here) proves that this structure contains on average less than two resident holes on the QD ground state. We have investigated the spin properties in these structures by continuous wave (cw) and time-resolved PL experiments. In the time resolved experiments the samples are excited by 1.5 ps pulses generated by a mode-locked Ti-doped sapphire laser with a repetition frequency of 82 MHz. The time resolved PL of the QD ground state is then recorded using a S1 photocathode Streak.

Camera with an overall time resolution of 30 ps. The excitation pulses are circularly polarized (σ^+). The luminescence intensity co-polarised (I^+) and counter-polarized (I^-) with the excitation laser are recorded. A magnetic field B_z is eventually applied along the sample growth axis Oz.

2. Spin dynamics of positively charged excitons in InAs/GaAs quantum dots

Figure 1(a) displays the cw PL spectrum of the QD ground states at $T = 10$ K. It is characterised by a full width at half maximum of about 50 meV due to the fluctuations of size, shape and strain in the ensemble of dots. Figure 1.b presents the circular polarisation of the time integrated PL after a circularly polarised picosecond excitation. The excitation energy is 1.44 eV; this corresponds to photon absorption in the low

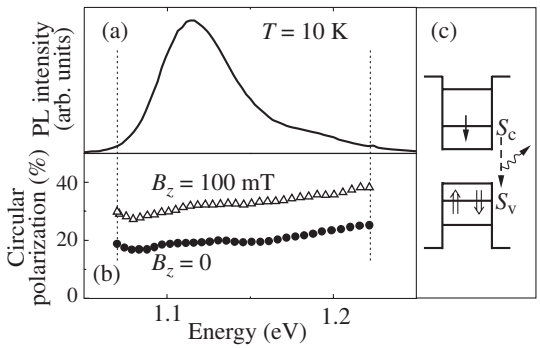

Fig. 1. (a) Cw photoluminescence spectrum of the QD. (b) Circular polarisation of the QD ground state luminescence for (•) $B_z = 0$ and (△) $B_z = 100$ mT. (c) Scheme of a positively charged exciton X^+ formed by a spin polarised electron and two holes with opposite angular momentum projection.

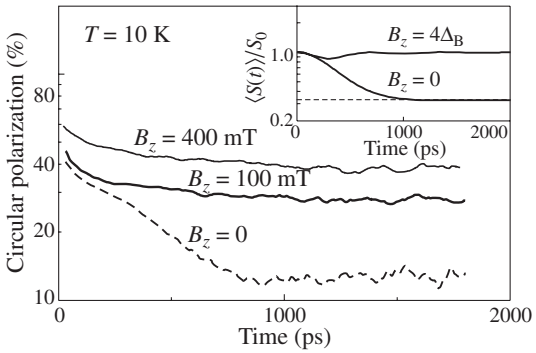

Fig. 2. Circular polarization dynamics of the QD ground state luminescence (semi-log. scale) after a σ^+ excitation for $B_z = 0$, 100 and 400 mT. The detection energy is centered at 1.11 eV. The inset displays the calculated time dependence of the average electron spin $\langle \mathbf{S}(t) \rangle / \mathbf{S}_0$ (see text).

energy part of the WL (because of the strain and the quantum confinement this absorption corresponds to an heavy-hole to electron like transition [7]). We measure a circular polarization degree of $\approx 19\%$ of the QD ground state emission ($B_z = 0$). The excitation intensity is about 1 mW; this corresponds to the photo-generation of less than one electron-hole pair per QD. All the samples studied present circular polarisation degrees larger than 10%. In contrast, the same experiment performed in nominally undoped QD samples (not shown here) yields a very small circular polarisation $P_c < 3\%$. This weak circular polarisation in undoped QD under these non-resonant excitation conditions is a direct consequence of the linearly-polarised neutral exciton eigenstates due to the Anisotropic Exchange Interaction (AEI) between the electron and the hole [8, 9]. The measurement of a significant circular polarisation in Fig. 1 is a strong indication of the successful chemical doping of the QD. For simplicity, we consider for the interpretation that (i) the dots contain a single resident hole and (ii) a single electron-hole pair is optically injected into the dot. Following excitation into the WL, it is commonly assumed that the electron spin does not relax during the capture and energy relaxation process in the QD whereas the initial hole spin orientation is lost due to effcient spin relaxation processes in the WL [5, 7]. The recorded PL in the p-doped QD samples corresponds essentially to the radiative recombination of positively charged exciton X^+ formed with a spin polarised electron and two holes with opposite spin (see Fig. 1c): $\left|X^+\right\rangle = 1/\sqrt{2}\,(|\Uparrow, \Downarrow, \downarrow\rangle - |\Downarrow, \Uparrow, \downarrow\rangle)$, where the arrows $\downarrow$,$\uparrow$ characterise the spin projection on Oz of the electron ground states (labelled S_c) and $\Uparrow$,$\Downarrow$ the heavy hole pseudo-spin in the valence ground state (labelled S_v) [7].

Figure 2 displays the circular polarisation dynamics of the QD ground state luminescence (same excitation conditions as Fig. 1.b). The circular polarisation dynamics at $B_z = 0$ presents two regimes. The polarisation decays within the first 800 ps down to a value of about 12%; then it remains stable with no measurable decay on the radiative lifetime scale. We can infer that the spin decay in this second regime is longer than 10 ns. This specific circular polarisation dynamics has been observed for any detection energy in the PL spectrum of the QD ground state ensemble.

A key argument for the hyperfine interaction being responsible for the initial polarization decay comes from magnetic field dependent measurements. Merkulov *et al.* predicts that the electron spin dephasing induced by hyperfine interaction can be strongly suppressed in an external magnetic field [1]. The required magnetic field must be larger than the typical fluctuation of the hyperfine field B_N , characterised by $\Delta_B = 2/3\langle (B_N)^2 \rangle$ ($\Delta_B \sim 10$ mT) [1, 2], to ensure that the Zeeman interaction on the electron spin is stronger than the interaction with the nuclei. We see in Fig. 1(b) that the time-integrated circular polarisation is almost doubled at the peak of the spectrum when a magnetic field of $B_z = 100$ mT is applied. This strong increase in circular polarisation for such a weak external magnetic field is very unusual in non-magnetic semiconductors. Note that the Zeeman splitting energy of the electron in this weak magnetic field is at least 50 times smaller than $k_B T$ at $T = 10$ K [10]. We see on Fig. 2 that, by applying a field of $B_z = 100$ mT, we drastically increase the initial decay time to ≈ 4000 ps as compared to ≈ 500 ps at $B_z = 0$. This pronounced effect of the small external magnetic field observed in Fig. 2 agrees very well with the expected influence of the external magnetic field on the QD electron spin relaxation by nuclei [1]. The effect observed here is similar to the suppression of the nuclear hyperfine interaction measured recently for localised electrons in lightly doped bulk n-GaAs [11,12]. We see in Fig. 2 that the time evolution of the circular polarization at $B_z = 400$ mT is very similar to the behaviour at $B_z = 100$ mT. Finally, it can be shown that the observed initial decay time $T_\Delta \approx 500$ ps is in agreement with the theoretical estimate deduced from Ref. [1] as shown in the inset of Fig. 2. This leads in turn to $\Delta_B \approx 28$ mT, smaller than 100 mT [3].

In conclusion, we have presented measurements of the electron spin dynamics in p-doped InAs/GaAs quantum dots using optical orientation experiments. We find that the time dependence of the electron spin polarisation exhibits two regimes: the polarisation decays within the first 800 ps down to $1/3$ of its initial value; then it remains stable with no measurable decay on the radiative lifetime scale. We also show experimentally that this efficient spin decay mechanism can be suppressed by the application of a small external magnetic field ($B \approx 100$ mT). We interpret these results as experimental evidence of electron spin dephasing mediated by the hyperfine interaction with nuclei in an ensemble of QD.

Acknowledgements

We gratefully thank A. E. Zhukov and V. M. Ustinov for the sample growth. P.-F.B. acknowledges financial support from FSE.

References

[1] I. A. Merkulov *et al.*, *Phys. Rev. B* **65**, 205309 (2002).
[2] A. Khaetskii *et al.*, *Phys. Rev. Lett.* **88**, 186802 (2002).
[3] P.-F. Braun *et al.*, *Phys. Rev. Lett.* **94**, 116601 (2005).
[4] T. Amand *et al.*, *Superlatt. and Microstruct.* **32**, 157 (2002).
[5] A. Bracker *et al.*, *Phys. Rev. Lett.* **94**, 047402 (2005).
[6] S. Laurent *et al.*, *Acta Physica Polonica A* **106**, 185 (2004).
[7] S. Cortez *et al.*, *Phys. Rev. Lett.* **89**, 207401 (2002).
[8] M. Paillard *et al.*, *Phys. Rev. Lett.* **86**, 1634 (2001).
[9] A. S. Lenihan *et al.*, *Phys. Rev. Lett.* **88**, 223601 (2002).
[10] M. Bayer *et al.*, *Phys. Rev. Lett.* **82**, 1748 (1999).
[11] R. I. Dzhioev *et al.*, *Phys. Rev. B* **66**, 245204 (2002).
[12] J. S. Colton *et al.*, *Phys. Rev. B* **69**, 121307 (2004).

13th Int. Symp. "Nanostructures: Physics and Technology"
St Petersburg, Russia, June 20–25, 2005

Effect of nuclear spins on the electron spin dynamics in negatively charged InP quantum dots

I. V. Ignatiev[1,2], I. Ya. Gerlovin[3], S. Yu. Verbin[1,2], W. Maruyama[2] and Y. Masumoto[2]

[1] Fock Institute of Physics, St Petersburg State University, St Petersburg, 198504, Russia
[2] Institute of Physics, University of Tsukuba, Tsukuba 305-8571, Japan
[3] Vavilov State Optical Institute, St Petersburg, 199034, Russia

Abstract. Kinetics of polarized photoluminescence of the negatively charged InP quantum dots in weak magnetic field is studied experimentally. Effect of both the nuclear spin fluctuations and the dynamical nuclear polarization on the electron spin orientation is observed.

Strong localization of electrons in quantum dots (QDs) may considerably enhance hyperfine interaction of electron spins with those of nuclei [1]. Two effects of the interaction are possible. First, due to limited number of nuclear spins interacting with the electron spin in a QD, typically $n \sim 10^5$, random correlation of nuclear spins may create a fluctuating nuclear polarization, $\Delta S_N \propto S_N/\sqrt{n}$, where S_N is the total spin of the polarized nuclei. Fluctuation ΔS_N acts on the electron spin as an effective magnetic field (referred hereafter to as nuclear field), δB_N, with random magnitude and orientation [2]. Electron spin precession in this field results in the relatively fast dephasing of the electron spins in ensemble of QDs and in the three-fold decrease in magnitude of the total electron spin. Theoretical estimates for the GaAs QDs give rise to subnanosecond dephasing times [2]. This dephasing may hinder in realization of the spin memory devices proposed by the so-called "Spintronics" [3]. The fluctuating nuclear polarization may also hinder in studying of the electron spin relaxation in steady-state conditions by means of Hanle effect [2,4]. Problem is that the electron spin does not "feel" any external magnetic field while the field is weaker than the effective magnetic field of the fluctuations [2].

Second effect of the hyperfine interaction appears when the nuclear spins are polarized, e.g., by means of optical orientation of the electron spin in presence of external magnetic field [5]. The dynamic nuclear polarization may act as a relatively strong effective magnetic field, B_N, causing Zeeman splitting of the electronic sub-levels [1]. Thermalization of the electron spin to the lowest sub-level at the low temperature (freezing effect) may create the electron spin polarization which lives as long as the nuclear spin polarization lives. In this case, the long-lived spin memory can be realized due to the freezing effect rather than to slow electron spin relaxation theoretically predicted for QDs by Khaetskii and Nazarov [6].

In this work, we present an experimental study of influence of the nuclear field effects on long-lived spin polarization observed recently for singly charged InP QDs [7]. We have studied a sample with the single layer of the QDs grown between the InGaP barrier layers on the n-doped GaAs substrate by the gas source MBE technology. Semi-transparent indium-tin-oxide electrode was deposited on top of the sample to control the charged state of the dots by means of applied bias. It was found previously [8] that the QDs contain one resident electron per dot (in average) at $U_{bias} = -0.1$ V.

To polarize spins of the resident electrons, we have used an excitation by the circularly polarized light at the energy which is slightly larger (~ 40 meV) the energy of the lowest optical transition in the QDs (intra-dot excitation). Such excitation creates an electron-hole pair at an excited state. After energy relaxation followed by electron-hole recombination, spin orientation of the pair can be transferred to spin of the resident electron and conserved for a time interval much longer than the recombination time. Mechanisms of the spin orientation are widely discussed in literature (see, e.g., [5]).

For the QDs under study, spin polarization of the resident electrons can be detected by means of negative circular polarization of photoluminescence (PL) observed in the PL spectrum and kinetics [7]. An example of the polarization kinetics is shown in Fig 1. As it is seen, the polarization degree approaches some constant negative value referred hereafter to as the amplitude of the negative circular polarization (NCP) of the PL. Mechanism of the NCP formation is discussed in Ref. [7] where it is shown that the NCP amplitude reflects spin orientation of the resident electrons.

Inset in Fig. 1 shows dependence of the NCP amplitude on the magnetic field applied along to the optical axis of the excitation (Faraday configuration). The curve has a pronounced maximum at $B \sim 0$ which is well fitted by Lorentzian with the full width at half maximum (FWHM), $\Delta = 30$ mT. The NCP amplitude at moderate magnetic field ($B > 0.1$ T) is three

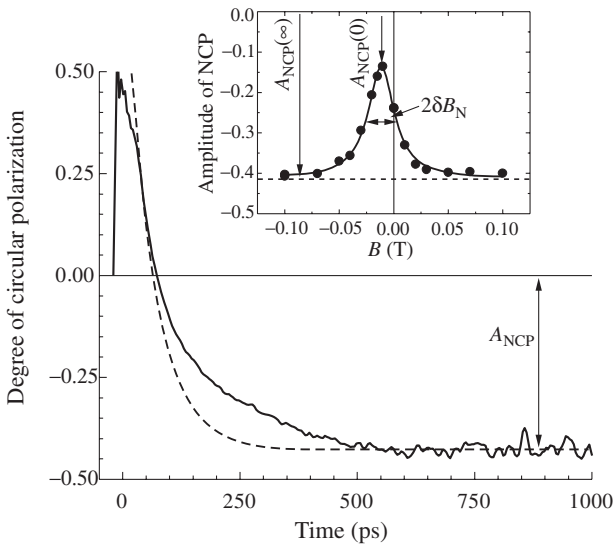

Fig. 1. Kinetics of degree of circular polarization. Dashed line is the fit in framework of a model of the NCP formation. Inset: dependence of the NCP amplitude on longitudinal magnetic field.

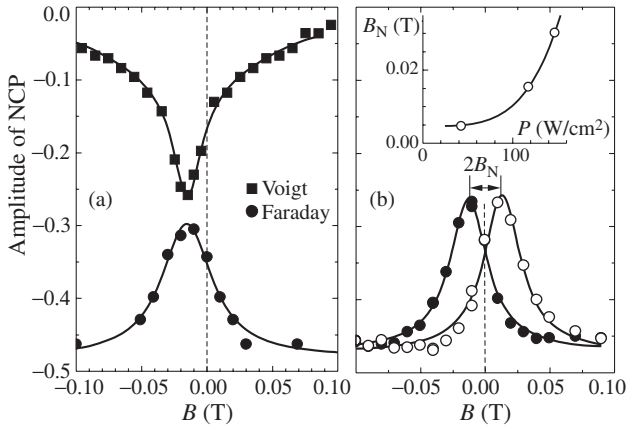

Fig. 2. (a) Dependence of the NCP amplitude on the longitudinal (circles) and transverse (squares) magnetic field. Solid lines are fits by Lorentzians. (b) Magnetic field dependence of the NCP amplitude measured at σ^+ (filled circles) and σ^- (empty circles) polarized excitations. Inset shows power dependence of the effective nuclear magnetic field.

times larger in absolute value than that in maximum of the dependence. Similar behavior of circular polarization of PL was observed in Refs. [4,9,11].

In accordance with the theory [2], three-fold decrease in the NCP amplitude at $B \sim 0$ can be caused by the fluctuating nuclear polarization. For simple explanation of the of the NCP decrease, random orientation of the nuclear spin fluctuations can be replaced by three types of the fluctuations directed along x, y, and z axes with equal probabilities. Electron spins directed along z axis are dephased due to precession in the nuclear fields, δB_N, directed along x and y axes and are conserved in z component of the field.

In presence of an external magnetic field directed along z-axis, B_{ext}, electron spin "feels" the total field which is the vector sum of δB_N and B_{ext} therefore effect of the nuclear spin fluctuations becomes negligible with the B_{ext} rise. So, dependence $A_{NCP}(B_{ext})$ must reveal a singularity near zero value of (B_{ext}) with full width at half maximum (FWHM) of the singularity determined by δB_N. As it is shown in the inset in Fig. 1, in our case, value of the fluctuating nuclear field $\delta B_N \approx 15$ mT.

In Fig. 2(a), dependence of the NCP amplitude on the magnetic field in the Faraday configuration is compared with that in the Voigt configuration. One can see that, in the latter case, FWHM of the dependence (Hanle effect) is close to that in the former case. This means that both of the dependences are of the same nature and result from suppression of the nuclear spin fluctuations by the external magnetic field. It should be pointed out that electron spin lifetime determined in kinetics experiments [7] is very long and cannot be responsible for the measured Hanle curve .

In Fig. 2(b), two dependences of the NCP amplitude on the longitudinal magnetic field measured for σ^+- and σ^--polarized excitations are shown. Relative shift of the curves allows us to estimate an effective magnetic field created by the dynamical nuclear polarization: $B_N = 15$ mT. This value is the same order of magnitude as that obtained in Refs. [9,11]. As it is seen from inset in Fig. 2(b), B_N increases with increasing pump power density, i.e., the nuclear field is really created by the optical pumping. At the same time, values of B_N optically created in the InP QDs is in orders of magnitude smaller than that observed for GaAs QDs [1,12]. Further studies are needed to understand this strong distinction between two types of QDs.

In conclusion, we have studied experimentally the dependence of the electron spin orientation in InP QDs on the magnetic field. The abrupt increase of the spin orientation was found in the longitudinal fields larger than 0.015 T. This behavior was explained as a result of suppression of the nuclear spin fluctuation effect by the external magnetic field. Mean value of the fluctuations of the nuclear field and the strength of the effective magnetic field created by dynamical nuclear polarization are estimated.

Acknowledgement

This work was supported by Grant-in-Aid for Scientific Research No. 13852003 and No. 16031203 from the MEXT of Japan, by the Russian Foundation for Basic Research (project No. 0302-16858), and by INTAS (project No. 1B 2167).

References

[1] D. Gammon, Al. L. Efros, T. A. Kennedy, M. Rosen, D. S. Katzer, D. Park, S.W. Brown, V. L. Korenev and I. A. Merkulov, *Phys. Rev. Lett.*, **86**, 5176 (2001).

[2] I. A. Merkulov, Al. L. Efros and M. Rosen, *Phys. Rev. B*, **65**, 205309 (2002).

[3] *Semiconductor Spintronics and Quantum Computation*, edited by D. D. Awschalom, D. Loss and N. Samarth, Nanoscience and Technology (Springer, Berlin, 2002).

[4] R. I. Dzhioev, V. L. Korenev, I. A. Merkulov, B. P. Zakharchenya, D. Gammon, Al. L. Efros and D. S. Katzer, *Phys. Rev. Lett.*, **88**, 256801 (2002).

[5] *Optical Orientation. Modern Problems in Condensed Matter*, edited by F. Meier and B. P. Zakharchenya (North-Holland, Amsterdam, 1984).

[6] A. V. Khaetskii and Yu. V. Nazarov, *Phys. Rev. B*, **61**, 12639 (2000).

[7] M. Ikezawa, B. Pal, Y. Masumoto, I. V. Ignatiev, S. Yu. Verbin, I. Ya. Gerlovin, *Phys. Rev. B.*, (submitted).

[8] I. E. Kozin, V. G. Davydov, I. V. Ignatiev, A. V. Kavokin, K. V. Kavokin, G. Malpuech, Hong-Wen Ren, M. Sugisaki, S. Sugou and Y. Masumoto, *Phys. Rev. B*, **65**, 241312(R) (2002).

[9] R. I. Dzhioev, B. P. Zakharchenya, V. L. Korenev, P. E. Pak, D. A. Vinokurov, O. V. Kovalenkov and I. S. Tarasov, *Phys. Solid State*, **40**, 1587 (1998) [Fiz. Tv. Tela, **40**, 1745 (1999)].

[10] R. I. Dzhioev, B. P. Zakharchenya, V. L. Korenev, P. E. Pak, M. N. Tkachuk, D. A. Vinokurov and I. S. Tarasov, *JETP. Lett.*, **68**, 745 (1998) [Pis'ma ZETF **68**, 711 (1998)].

[11] R. I. Dzhioev, B. P. Zakharchenya, V. L. Korenev and M. V. Lazarev, *Phys. Solid State*, **41**, 2014 (1999) [Fiz. Tv. Tela, **41**, 2193 (1999)].

[12] A. S. Bracker, E. A. Stinaff, D. Gammon, M. E. Ware, J. G. Tischler, A. Shabaev, Al. L. Efros, D. Park, D. Gershoni, V. L. Korenev and I. A. Merkulov, *Phys. Rev. Lett.*, **94**, 047402 (2005).

13th Int. Symp. "Nanostructures: Physics and Technology"
St Petersburg, Russia, June 20–25, 2005

Linearly polarized emission of the quantum wells subject to an in-plane magnetic field

N. S. Averkiev[1], *A. V. Koudinov*[1], Yu. G. Kusrayev[1], D. Wolverson[2], G. Karczewski[3] and T. Wojtowicz[3]

[1] Ioffe Physico-Technical Institute, St Petersburg, Russia
[2] Department of Physics, University of Bath, Bath BA2 7AY, United Kingdom
[3] Institute of Physics, Polish Academy of Sciences, 02-668 Warsaw, Poland

We present a combined experimental and theoretical study of linearly polarized photoluminescence (PL) of quantum wells (QWs). We are concerned here with PL that was partially linearly polarized, but *without any correlation* with the polarization of the exciting light (that is, optical alignment effects were not relevant to the present study). The experiments were performed on numerous heterostructures based on CdTe/(Cd,Mn)Te or (Cd,Mn)Te/(Cd,Mg,Mn)Te. Typically each heterostrucure contained several QWs of different thicknesses. The PL emission from the QWs was spectrally resolved and could be analyzed independently. A magnetic field parallel to the plane of the QWs was produced by a superconducting magnet and, in addition to the photoluminescence itself, we measured spin-flip Raman spectra in order to quantify the relevant spin splittings.

We have carefully analyzed the contributions of different symmetries to the linear polarization of the PL of the QWs, as well as the underlying physical mechanisms. The magnetic field, angular and spectral dependences of the PL polarization, along with the data on the spin-flip Raman scattering, were used for the formulation and verification of a theoretical model. We have shown that in real QWs, effects related to the breakdown of the in-plane symmetry are essential for the linear polarization of the PL and also determine the spin splitting of the valence band states by the in-plane magnetic field. On the contrary, the semi-magnetic nature of the QWs under study has not resulted in any qualitatively new effects (though it was useful in experiments, shifting the observed phenomena towards smaller magnetic fields). Thus, the conclusions of the present paper apply fully to non-magnetic QWs.

In most of the QWs, the zero-field PL revealed a weak linear polarization (which we term built-in polarization) whose direction is linked to the crystal axes while its value changes only weakly through the PL spectrum. The *mixing* of the valence band states *by in-plane distortions* is responsible for this polarization. With a magnetic field lying in the plane of the QW, there appear several field-induced contributions to the linear polarization, which differ in how they vary with the rotation of the crystal around the growth axis. The first contribution (the zero-th angular harmonic) corresponds to the polarization component whose direction is linked to the magnetic field with only a weak spectral dependence. This polarization component mainly originates from a Van Vleck type term, representing the *mixing* of the valence band states produced *by the magnetic field*. The second contribution (the second harmonic) corresponds to the polarization component whose direction is related to the crystal axes, similar to the built-in polarization, but, in contrast to the latter, its value has a sharp spectral dependence. Similar to the built-in polarization, this contribution is totally due to the in-plane distortion, but, unlike the built-in polarization, it mainly originates from the *splitting* of the electron and hole sublevels *by the magnetic field*. The third contribution (the fourth harmonic) has 90-degree symmetry and the most debatable nature. We have shown that a contribution of such type can be obtained in the quadratic approximation in the magnetic field with no explicit account of the cubic elements of symmetry of the crystal.

We also addressed the question of the origin of the in-plane distortion in the heterostructures under study and discovered a correlation between the presence of such distortions in the QWs and in the barrier layers, as well as some effects of the type of substrate and of buffer layer. Quantitative analysis of the results, especially the inconsistency between the values of the built-in polarization and the transverse g-factor of holes, has led us to the conclusion that the distortions are directed randomly on a mesoscopic scale.

In general, the theory we have developed is supported by the experimental tests and explains reasonably well the large amount of data on the linearly polarized luminescence in CdTe/(Cd,Mn)Te and (Cd,Mn)Te/(Cd,Mg,Mn)Te QWs.

Acknowledgements

This work was supported by INTAS (03-51-5266) and RFBR (04-02-17636). A.K. gratefully acknowledge the support from the Russian Science Support Foundation.

13th Int. Symp. "Nanostructures: Physics and Technology"
St Petersburg, Russia, June 20–25, 2005

Spin-dependent resonant electron coupling in a III–V/II–VI:Mn heterovalent double quantum well

A. A. Toropov, I. V. Sedova, S. V. Sorokin, Ya. V. Terent'ev, E. L. Ivchenko, D. N. Lykov and S. V. Ivanov
Ioffe Physico-Technical Institute, St Petersburg, Russia

Introduction

Physical realization of semiconductor spintronics relies at present on the heterostructures of either III–V group or II–VI group. Different semiconductor structures have been used to implement selected spin functionalities. Relatively long spin conservation was observed in weakly doped n-type GaAs [1]. Spin injection was demonstrated in the diluted magnetic semiconductor (DMS) structures, based on either paramagnetic compounds II–VI:Mn [2], or a ferromagnetic semiconductor GaMnAs [3]. In the former case, an efficient spin polarization of electrons was achieved. Nevertheless, low carrier mobility and fast spin relaxation inherent to II–VI compounds hinder the development of all-II–VI spintronic devices. On the other hand, the structures based on GaMnAs can provide only hole spin polarization, since Mn in GaAs acts as an acceptor. Extremely fast hole spin relaxation prevents simultaneous implementation of spin polarization and spin conservation in all-III–V structures.

Recently we have proposed the concept of heterovalent resonant-tunnelling structures combining in the active region both III–V ((Al,Ga)As) and II–VI:Mn ((Zn,Cd,Mn)Se) compounds [4]. In principle, such hybrid III–V/II–VI heterostructures could join together useful properties of both types of materials, namely, the magnetically tunable spin-dependent electron confining potential in the II–VI DMS part and high electron mobilities as well as long electron spin relaxation times in a non-magnetic III–V part. Realization of this idea relies on the controlled fabrication of a high-quality interface between the III–V and II–VI parts. Unlike a conventional isovalent interface separating compounds of the same chemical groups, all basic properties of a heterovalent interface drastically depend on the detail of its atomic structure [5]. Particularly discouraging is unavoidable presence of donor and acceptor interface chemical bonds resulting in emergence of a dipole moment with the value and direction depending on the microscopic structure of the interface layers. As a consequence, the average band offsets at the interface also depend on the interface structure. Besides, strong electric field can arise near the interface, penetrating inside the neighboring layers. These peculiarities appreciably complicate the design and growth of nanostructures including a heterovalent interface. Nicolini *et al*. have shown that valence band offset (VBO) at the GaAs/ZnSe junction grown by molecular beam epitaxy (MBE) can be tuned between 0.58 and 1.2 eV by changing Zn/Se flux intensity ratio [6]. However, little is known about the actual distribution of dipole moments and electric fields around such interfaces.

In this paper we report on the growth and magneto-optical studies of double heterovalent QW structures, where a non-magnetic GaAs/AlGaAs QW is electronically coupled with a DMS ZnCdMnSe/ZnSe quantum well (QW) through a thin barrier containing a heterovalent AlGaAs/ZnSe interface. This design has pursued two purposes. Firstly, an exciton in the GaAs/AlGaAs QW placed in the vicinity of the AlGaAs/ZnSe heterovalent interface can be considered as a sensitive indicator of both local electric fields (due to the quantum confined Stark effect) and disorder introduced by the heterovalent interface, since this disorder influences the width of the exciton resonance. Therefore optical excitonic spectroscopy applied to such samples gives valuable information about the interface microstructure. Furthermore, when the electron levels in the two QWs are in resonance, one can expect efficient inter-well mixing of the electron wave functions, which drastically enhances the electron penetration from the nonmagnetic QW into the DMS QW. Under these conditions, application of a relatively weak external magnetic field should result in giant Zeeman splitting of both mixed electronic states and hence in the efficient spin polarization of electrons in the III–V QW.

1. Experimental results and discussion

The samples were grown by MBE on GaAs(001) in a two-chamber set up. The GaAs/$Al_{0.3}Ga_{0.7}As$ QW was grown at a substrate temperature $T_S = 580\,^{\circ}C$. The top barrier was as thin as 2 nm. The grown AlGaAs/GaAs QW structure was cooled down with the (2×4)As surface reconstruction. Thereafter the structure was transferred to the II–VI chamber where it was heated up to 280 °C. The II–VI growth was initiated under the surface exposure to Se flux, as short as necessary to change the (2×4)As surface reconstruction to a (2×1) pattern. The latter was stable during the following 30-seconds-long exposure to Zn flux. According to this procedure, one could expect the formation of a Zn-reach interface with slight admixture of selenium. The II–VI part contained a $Zn_{0.87}Cd_{0.08}Mn_{0.05}Se$ 9-nm-wide QW embedded between 1.2- and 20-nm-thick ZnSe barriers on bottom and top, respectively.

The schematic view of the conduction band of the sample is shown in Fig. 1(a). The thickness of the combined AlGaAs/ZnSe barrier between the GaAs and ZnCdMnSe QWs totals 3.2 nm. The AlGaAs layer is inserted in order to move the heterovalent interface with presumably enhanced density of defects aback from the GaAs QW. The ZnSe spacer is needed for proper II–VI growth initiation and for preventing Mn diffusion in the III–V part, since even low content of Mn in III–V compounds damages their optical quality. A set of structures was grown with different widths of the GaAs QW, fixing the interface growth conditions, as described above. Most interesting results have been obtained in the double-QW structure with a 3.4-nm-thick GaAs QW, where the single-QW electron levels are close to the resonance at zero magnetic field.

Temperature-dependent PL spectra were measured in the spectral region of the GaAs QW exciton in a magnetic field

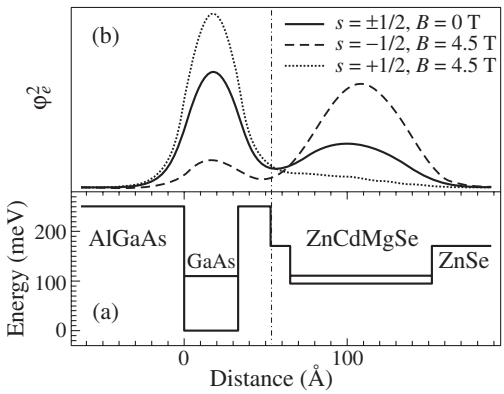

Fig. 1. (a) Conduction band lineup of the double QW sample. Geometrical parameters correspond to the experimental sample with the 3.4-nm-wide GaAs QW. (b) Spin-up (dotted curve) and spin-down (dashed curve) squared electron wave functions calculated for the magnetic field 4.5 T.

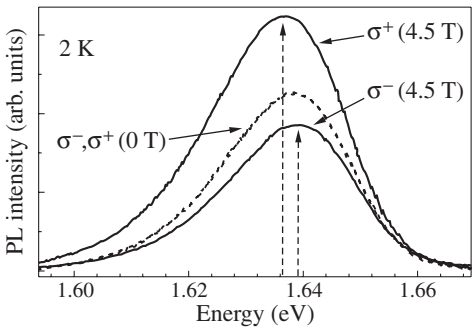

Fig. 2. σ^+ and σ^- polarized PL spectra measured at 0 T (dashed curves) and 4.5 T (solid curves) in the sample with a 3.4 nm wide GaAs QW.

applied in the Faraday geometry. Figure 2 shows the spectra of circularly polarized emission components measured at 2 K in the sample with a 3.4-nm-wide GaAs QW at 0 T (dashed curves) and 4.5 T (solid curves). The PL linewidth amounts to 26 meV and does not depend on the magnetic field. This value is about twice more than the change of exciton energy, corresponding to a single-monolayer variation of the QW width. Therefore the enhanced PL linewidth observed in the heterovalent double QW implies the presence of some additional broadening mechanism.

To elucidate the issue of exciton broadening we have measured in this sample the PL peak energy and integral intensity as a function of temperature (Figs. 3a and 3c, respectively). With the temperature rise the PL peak firstly shifts to lower energies, then near 50 K the direction of the shift changes. At even higher temperatures above 80–90 K the PL peak shifts towards lower energies again, approaching in the limit of high temperatures the curve reflecting the GaAs band gap temperature dependence (dashed curve in Fig. 3a). This behavior is typical for the emission of deeply localized excitons in highly disordered QWs or dense arrays of quantum dots [7]. At relatively low temperatures the emission peak energy is determined by the kinetics of exciton hopping accompanied by either emission or absorption of acoustic phonons. In the limit of high temperatures the PL peak tends to match the resonant energy of nearly free excitons. Figure 3b shows the difference (Stokes shift) between the expected temperature dependence of the exciton resonance energy and the experimental energies of the emission peak. The initial shift of the PL peak to lower energies is stronger than the shift due to the temperature induced shrinkage of the band gap, which confirms the important contribution from the processes of exciton localization. Usually this behavior is indicative of temperature induced redistribution of the metastable localized excitons in favor of deeper states [7].

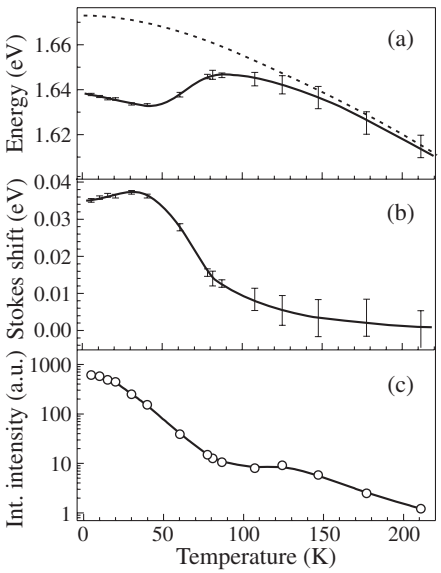

Fig. 3. PL peak energy (a), Stokes shift (b), and integral intensity (c) versus temperature, measured in the double QW sample with the 3.4-nm-wide GaAs QW. The dotted curve in Fig. (a) represents the band gap temperature dependence of GaAs, arbitrarily shifted along the vertical axis.

Figure 3c demonstrates the PL integral intensity plotted as a function of temperature. The process responsible for the PL quenching is quite complicated and can not be characterized by a single activation energy. As can be seen from the respective Arrehnius plot, shown in Fig. 4, at least two specific activation energies can be extracted — 22 and 65 meV. The latter energy is comparable with the height of the barriers confining QW electrons in the direction along the growth axis. Therefore, we attribute this process to the thermal escape of carriers from the QW. The other characteristic energy (22 meV) is much smaller. It describes activation of excitons localized by lateral traps generated most probably by the heterovalent interface. One can propose two mechanisms responsible for the interface-induced exciton broadening. Firstly, there could be broadening due to the random electric fields produced by interface electric dipoles. This mechanism should be enhanced in wider QWs, due to the increased sensitivity of the exciton energy to the electric fields, which contradicts experimental observations. For example, the PL linewidth in the double-QW sample with a 5.5-nm-wide GaAs QW is noticeably smaller — 16 meV. Therefore we suggest that the dominant contribution to the exciton broadening arises from the fluctuations of CBO value at the AlGaAs/ZnSe interface, induced by random variation of the interface microscopic structure.

The energy position of the PL peaks observed in the double-QW sample with the 3.4-nm-wide QW is plotted versus magnetic field in Fig. 5a. These dependencies reflect neither the Zeeman splitting expected for a conventional GaAs/AlGaAs QW nor the symmetrical giant splitting typical for a single DMS QW. Indeed, for a single 3.4-nm GaAs-based QW, the expected spin splitting at 4.5 T would be as small as $\sim$0.3 meV.

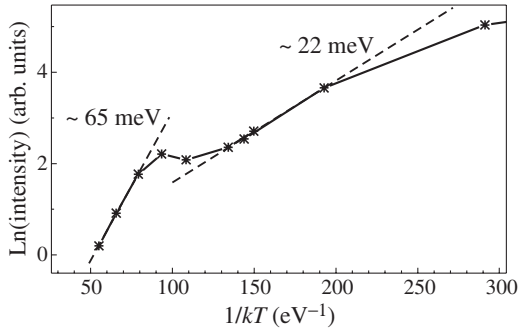

Fig. 4. Arrehnius plot for the dependence shown in Fig. 3c.

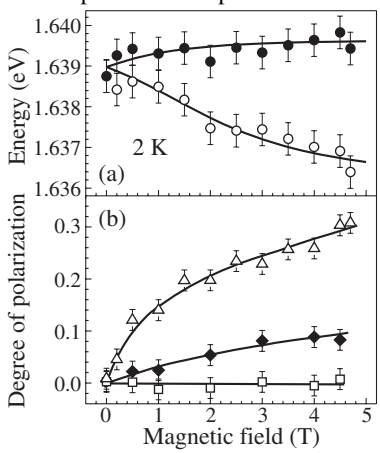

Fig. 5. (a) Energy of the PL peaks corresponding to $|-1/2, 3/2\rangle$ (open circles) and $|1/2, -3/2\rangle$ (solid circles) excitons. (b) Degree of σ^+ circular polarization of PL, measured in a resonant double-QW (open triangles), off-resonant double-QW (solid diamonds), and isolated GaAs QW (open squares).

The observed splitting is about one order of magnitude larger. Moreover, according to the known signs of g_e and g_{hh}, the lowest-energy exciton should be $|1/2, -3/2\rangle$, which is active in the σ^- polarization. The experimentally observed ordering of the spin-split excitons is opposite (see Fig. 5b). Therefore we have attributed the character of the observed PL band splitting to the effect of resonant coupling between electronic states in the nonmagnetic and DMS QWs. This interpretation explains the fact that no remarkable splitting has been observed in the off-resonant double-QW sample with a 5.5-nm-wide GaAs QW. The electron level in this QW lies 45 meV below the electron level in the 3.4-nm-wide QW. Therefore the levels in the nonmagnetic and magnetic QWs are remote far enough to prevent a remarkable effect of interwell coupling on the exciton energy. To describe the experimental data quantitatively, we have calculated the exciton spin-dependent energies as a function of magnetic field in the coupled QW system. More details of the calculation will be published elsewhere [8]. Very accurate fit, shown in Fig. 5a by solid curves, was obtained using CBO at the GaAs/ZnSe interface as the only fitting parameter. The best fit involves the CBO value 170±10 meV.

2. Conclusions

In conclusion, we have obtained resonant electronic coupling in a III–V/II–VI heterovalent double QW with the DMS II–VI part. The structure design has allowed one to enhance the GaAs QW electron g factor by more than one order of magnitude due to the enhanced penetration of the nonmagnetic QW electron wave function into the DMS region at resonance conditions. Such structures are especially beneficial for optical studies, since the electron wave function at resonance has a minimum at the heterovalent interface with a presumably large density of defects and electrical dipoles (see the dashed curve in Fig. 1b). Nevertheless the presence of the heterovalent interface manifests itself in an additional inhomogeneous broadening of the QW excitonic resonance. The performed studies of temperature-dependent PL revealed a localization potential with the characteristic activation energy ∼22 meV, resulting most probably from random variation of the interface atomic structure. Potential advantage of these hybrid DMS structures is a possibility to establish an electric control over the spin polarization in a p-i-n diode with the inserted heterovalent double QW.

Acknowledgements

This work was supported by the Program of the PS department of RAS and RFBR (03-02-17566). S.V.I. is grateful to RSSF.

References

[1] J. M. Kikkawa *et al*, *Phys. Rev. Lett.* **80**, 4313 (1998).
[2] R. Fiederling *et al*, *Nature* **402**, 787 (1999).
[3] Y. Ohno *et al*, *Nature* **402**, 790 (1999).
[4] A. A. Toropov *et al*, Proceedings of the 3rd International Conference on Physics and Applications of Spin-Related Phenomena in Semiconductors, 2004, Santa Barbara, USA, to be published in Journal of Superconductivity, 2005.
[5] W. A. Harrison *et al*, *Phys. Rev. B* **18**, 4402 (1978).
[6] R. Nicolini *et al*, *Phys. Rev. Lett* **72**, 294 (1994).
[7] S. A. Tarasenko *et al*, *Semicond. Sci.Technol.* **16**, 486 (2001).
[8] A A. Toropov *et al*, *Phys. Rev. B* (2005) to be published.

13th Int. Symp. "Nanostructures: Physics and Technology"
St Petersburg, Russia, June 20–25, 2005

Electric current induced spin orientation in quantum well structures

S. N. Danilov[1], S. D. Ganichev[1,2], P. Schneider[1], V. V. Bel'kov[2], L. E. Golub[2], V. A. Shalygin[3], S. Giglberger[1], J. Stahl[1], W. Wegscheider[1], D. Weiss[1] and W. Prettl[1]

[1] Fakultät Physik, University of Regensburg, 93040, Regensburg, Germany
[2] Ioffe Physico-Technical Institute, St Petersburg, Russia
[3] Politechnical State University, St Petersburg, Russia

Abstract. A longstanding theoretical prediction is the orientation of spins by an electrical current flowing through low-dimensional carrier systems of sufficiently low crystallographic symmetry. Here we show by means of terahertz and infrared transmission experiments through two-dimensional hole systems a growing spin orientation with an increasing current.

Introduction

The feasibility to orient the spin of charge carriers in GaAs based quantum wells by driving an electric current through the device was theoretically predicted more than two decades ago. [1,2,3]. A first direct experimental proof of this effect was obtained just recently [4,5]. In this paper we demonstrate by means of terahertz and infrared transmission experiments that an electric current which flows through a low-dimensional electron or hole system leads to a stationary spin polarization of free charge carriers. Microscopically the effect is a consequence of spin-orbit coupling which lifts the spin-degeneracy in **k**-space of charge carriers together with spin dependent relaxation and represents the inverse spin-galvanic effect [6].

1. Spin orientation by electric current

If an external electric field is applied to QWs, the charge carriers drift in the direction of the resulting force. The carriers are accelerated by the electric field and gain kinetic energy until they are scattered. A stationary state forms where the energy gain and the relaxation are balanced resulting in a non-symmetric distribution of carriers in **k**-space. This situation is sketched in Fig. 1a for holes. The holes acquire the average quasi-momentum

$$\langle \mathbf{k} \rangle = \frac{e\tau_p}{\hbar}\mathbf{E} = \frac{m^*}{e\hbar p}\mathbf{j}, \qquad (1)$$

where $\mathbf{E}$ is the electric field strength, τ_p is the momentum relaxation time, $\mathbf{j}$ is the electric current density, m^* is the effective mass, p is the hole concentration and e is the elementary charge. As long as spin-up and spin-down states are degenerate in **k**-space the energy bands remain equally populated and a current is not accompanied by spin orientation. In QWs made of zinc-blende structure material like GaAs, however, the spin degeneracy is lifted due to lack of inversion symmetry and low-dimensional quantization. The resulting dispersion reads $\varepsilon = \hbar^2 k^2/2m^* + \beta_{lm}\sigma_l k_m$, with the spin-orbit pseudotensor β and the Pauli spin matrices σ_l. The corresponding dispersion is sketched in Fig. 1b. To be specific for the coupling constant β and the mechanism depicted in Fig. 1b we consider solely spin-orbit interaction due to a Hamiltonian of the form $H_{SO} = \beta\sigma_z k_x$. This corresponds to a subband splitting for eigenstates with spins pointing in z-direction, normal to the quantum well plane and detectable in experiment. In our QWs of C_s symmetry the x-direction lies along $[1\bar{1}0]$ in the QW plane. In the presence of an in-plane electric field the **k**-space distribution of carriers gets shifted yielding an electric current. Due to the band splitting carrier relaxation becomes spin dependent. Relaxation processes including spin flips are different for the two subbands because the quasi-momentum transfer from initial to final states are different [7]. In Fig. 1b the **k**-dependent spin-flip scattering processes are indicated by arrows of different lengths and thicknesses. As a consequence different numbers of spin-up and spin-down carriers contribute to the current causing a stationary spin orientation. Here we assumed that the origin of the current induced spin orientation is, as sketched in Fig. 1b, exclusively due to scattering and hence dominated by the Elliott-Yafet spin relaxation process [7]. The other possible mechanism of the current induced spin orientation is due to D'yakonov-Perel spin relaxation, so named "precessional".

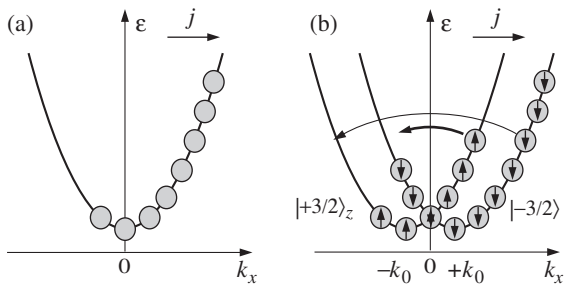

Fig. 1. Comparison of current flow in (a) spin-degenerate and (b) spin-split subbands. (a) Electron distribution at a stationary current flow due to acceleration in an electric field and momentum relaxation. (b) Spin polarization due to spin-flip scattering.

2. Experimental

In order to observe current induced spin polarization we study Faraday rotation of terahertz radiation transmitted through samples containing multiple p-type QWs (for n-type QWs we used mid-infrared radiation). As material we have chosen GaAs QWs of C_s point group symmetry. This was achieved in p-type samples by growing modulation Si-doped QWs on (113)A- or miscut (001)-oriented GaAs substrates. Two kinds of p-type samples were prepared. Sample A: (113)A with QWs of width L_W = 10 nm, and sample B: miscut (001) with L_W = 20 nm. Samples of n-type were prepared on (110)-oriented substrates. They contain asymmetric doped QWs of 8.2 nm width. To cope with the small Faraday rotation angles of an individual quantum well, we fabricated multiple QW structures containing 100 or 400 QWs. The sample edges were oriented

along $[1\bar{1}0]$ in the QW plane (x-axis) and perpendicular to this direction (y-axis). Two pairs of ohmic contacts were centered along opposite sample edges of 5 mm width. In addition structures containing 100 QWs and having very thin barriers were taken as quasi-bulk reference samples.

A spin polarization is not expected for both current directions. For materials of the symmetry used here only an electric current along $x \parallel [1\bar{1}0]$-direction is expected to align spins. By symmetry arguments it is straightforward to show that a current density j_x, in the plane of the QW yields an average spin polarization S_z normal to the QW plane according to $S_z = R_{zx} j_x$, where $\mathbf{R}$ is a second rank pseudo-tensor [8]. However, for a current flowing along y-direction, $S_z = 0$ holds since, due to symmetry, $R_{zy} = 0$. Thus a spin polarization may occur for current flow in one but not in the other direction. Below we denote these directions as active and passive, respectively.

The transmission measurements were carried out at room temperature and at $T = 80\,\mathrm{K}$ using linearly polarized $\lambda = 118\,\mu\mathrm{m}$ radiation for p-type samples and mid-IR light with $\lambda \approx 9\,\mu\mathrm{m}$ for n-type samples. The electric current was applied as $10\,\mu\mathrm{s}$ long pulses with a repetition rate of 20 kHz. The schematic experimental set up is shown in Fig. 2a: the sample was placed between two metallic grid polarizers and the cw terahertz radiation was passed through this optical arrangement. The transmitted radiation was detected in-phase with the current modulation frequency using a highly sensitive Ge:Ga extrinsic photodetector operated at 4.2 K.

The signal ΔV caused by rotation of polarization plane was observed only for currents flowing in the active direction. The spin polarization induced signals for samples A and B are shown in Fig. 2b. At room temperature and current $I = 150\,\mathrm{mA}$ we obtain a Faraday rotation angle per quantum well of 0.4 mrad for sample A and 0.15 mrad for sample B. Lowering the temperature of sample B to 80 K we obtain two times larger Faraday rotation. While the experiment displays clear spin polarization due to the driving current, there is not yet a straightforward way at hand to extract the value of the spin polarization from the Faraday rotation angle.

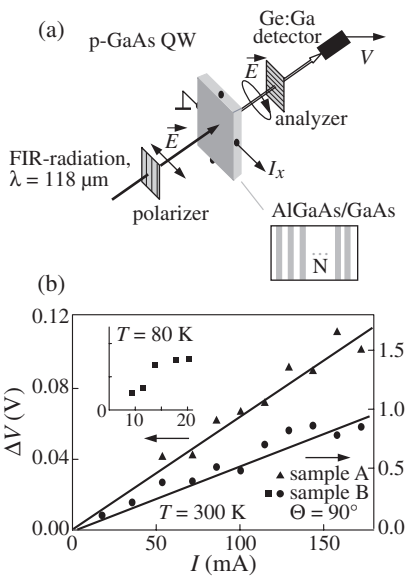

Fig. 2. (a) Experimental set-up. (b) polarization dependent signal for current in active direction as a function of current strength for two samples. Inset shows the same dependence ($\Delta V(I)$) for sample B at $T = 80\,\mathrm{K}$.

According to the theory of Aronov and Lyanda-Geller [1], a current should yield a spin polarization of the order of $\langle S\rangle \approx \beta \cdot \langle k\rangle / k_\mathrm{B}T$. Using Eq. (1) we estimate this value as $\langle S\rangle = \frac{Q\beta}{k_\mathrm{B}T} \cdot \frac{m^*}{e\hbar p} j$, where $Q \simeq 1$ is a constant determined by momentum scattering and the spin relaxation mechanism [9]. For a situation where Fermi statistic applies the factor $k_\mathrm{B}T$ needs to be replaced by $2E_\mathrm{F}/3$. Calculating $\langle S\rangle$ with the experimental parameters $p = 2 \cdot 10^{11}\,\mathrm{cm}^{-2}$, $m^* = 0.2m_0$ and spin splitting constant $\beta = 5\,\mathrm{meV\cdot nm}$ [10], we obtain an average spin polarization of $3.2 \cdot 10^{-4}$ and $0.8 \cdot 10^{-4}$ for the experimentally relevant current densities 3 mA/cm and 0.75 mA/cm per QW, respectively.

Finally, we discuss our results in the light of related experiments. Based on theoretical predictions made by Ivchenko and Pikus [11], Vorob'ev *et al* [12] observed a current induced spin polarization in bulk tellurium. This is a consequence of the unique band structure of tellurium with hybridized spin-up and spin-down bands and is, other than in our experiment, not related to spin relaxation. We would also like to note that, Kalevich and Korenev [13] reported an influence of an electric current on the spin polarization achieved by optical orientation. The current itself does not align spins, but the effective magnetic field due to the current causes a spin depolarization like the Hanle effect in an external magnetic field. Most recently spin orientation by current was also obtained on strained InGaAs bulk material [14].

Acknowledgement

We thank E. L. Ivchenko and A. Ya. Shul'man for helpful discussions. We acknowledge financial support from the DFG, RFBR, INTAS, and "Dynasty" Foundation — ICFPM.

References

[1] A. G. Aronov, Yu. B. Lyanda-Geller, *JETP Lett.*, **50**, 431 (1989).
[2] V. M. Edelstein, *Solid State Commun.*, **73**, 233 (1990).
[3] F. T. Vas'ko, N. A. Prima, *Phys. Solid State*, **21**, 994 (1979).
[4] S. D. Ganichev, S. N. Danilov, Petra Schneider, V. V. Bel'kov, L. E. Golub, W. Wegscheider, D. Weiss, W. Prettl, cond-mat/0403641 march (2004).
[5] A. Yu. Silov, P. A. Blajnov, J. H. Wolter, R. Hey, K. H. Ploog and N. S. Averkiev, *Appl. Phys. Lett.*, **85**, 5929 (2004).
[6] S. D. Ganichev, E. L. Ivchenko, V. V. Bel'kov, S. A. Tarasenko, M. Sollinger, D. Weiss, W. Wegscheider and W. Prettl, *Nature* (London) **417**, 153 (2002).
[7] N. S. Averkiev, L. E. Golub and M. Willander, *J. Phys.: Condens. Matter*, **14**, R271 (2002).
[8] S. D. Ganichev and W. Prettl, *J. Phys.: Condens. Matter*, **15**, R935 (2003).
[9] A. G. Aronov, Yu. B. Lyanda-Geller and G. E. Pikus, *Phys. JETP*, **73**, 537 (1991).
[10] P. Schneider *et al*, *J. Appl. Phys.*, **96**, 420 (2004).
[11] E. L. Ivchenko and G. E. Pikus, *JETP Lett.*, **27**, 604 (1978).
[12] L. E. Vorob'ev, E. L. Ivchenko, G. E. Pikus, I. I. Farbstein, V. A. Shalygin and A. V. Sturbin, *JETP Lett.*, **29**, 441 (1979).
[13] V. K. Kalevich, V. L. Korenev, *JETP Lett.*, **52**, 859 (1990).
[14] Y. Kato, R. C. Myers, A. C. Gossard and D. D. Awschalom, *Phys. Rev. Lett.*, **93**, 176601 (2004).

13th Int. Symp. "Nanostructures: Physics and Technology"
St Petersburg, Russia, June 20–25, 2005

Photo-induced pure spin currents in quantum wells

S. A. Tarasenko and E. L. Ivchenko
Ioffe Physico-Technical Institute, St Petersburg, Russia

Abstract. As is well known the absorption of circularly polarized light in semiconductors results in optical orientation of electron spins and helicity-dependent electric photocurrent, and the absorption of linearly polarized light is accompanied by optical alignment of electron momenta. Here we show that the absorption of unpolarized light in a quantum well (QW) leads to generation of a pure spin current, although both the average electron spin and electric current are vanishing.

Introduction

Spin and charge are among the basic properties of elementary particles such as an electron, positron and proton. The perturbation of a system of electrons by an electric field or light may lead to a flow of the particles. The typical example is an electric current that represents the directed flow of charge carriers. Usually the electric currents do not entail a considerable spin transfer because of the random orientation of electron spins. However, the charge current can be accompanied by a spin current as it happens, e.g., under injection of spin-polarized carriers from magnetic materials or in the optical-orientation-induced circular photogalvanic effect. Furthermore, there exists a possibility to create a pure spin current which is not accompanied by a net charge transfer. This state represents a non-equilibrium distribution when electrons with the spin "up" propagate mainly in one direction and those with the spin "down" propagate in the opposite direction. In terms of the kinetic theory, it can be illustrated by a spin density matrix with two nonzero components, $\rho(s, \mathbf{k}; s, \mathbf{k}) = \rho(\bar{s}, -\mathbf{k}; \bar{s}, -\mathbf{k})$, where s and $\mathbf{k}$ are the electron spin index and the wave vector, and $\bar{s}$ means the spin opposite to s. Spin currents in semiconductors can be driven by an electric field acting on unpolarized free carriers which undergo a spin-dependent scattering. This is the so-called spin Hall effect where a pure spin current appears in the direction perpendicular to the electric field. The spin currents can be induced as well by optical means as a result of interference of one- and two-photon coherent excitation with a two-color electro-magnetic field or under interband optical transitions in non-centrosymmetrical semiconductors [1].

Here we show that pure spin currents, accompanied neither by charge transfer nor by spin orientation, can be achieved under absorption of linearly polarized or unpolarized light in semiconductor low-dimensional systems. Particularly, the effect is considered for interband and free-carrier optical transitions in semiconductor QWs.

In general, the flux of electron spins can be characterized by a pseudo-tensor $\hat{\mathbf{F}}$ with the components F_β^α describing the flow in the β direction of spins oriented along α, with α and β being the Cartesian coordinates. In terms of the kinetic theory such a component of the spin current is contributed by a non-equilibrium correction $\propto \sigma_\alpha k_\beta$ to the electron spin density matrix, where σ_α is the Pauli matrix. We demonstrate that the appearance of a pure spin current under optical pumping is linked with two fundamental properties of semiconductor QWs, namely, the *spin splitting* of energy spectrum linear in the wave vector and the spin-sensitive *selection rules* for optical transitions.

1. Interband optical transitions

The effect is most easily conceivable for direct transitions between the heavy-hole valence subband $hh1$ and conduction subband $e1$ in QWs of the C_s point symmetry, e.g. in (113)- or (110)-grown QWs. In such structures the spin component along the QW normal z is coupled with the in-plane electron wave vector. This leads to $\mathbf{k}$-linear spin-orbit splitting of the energy spectrum as sketched in Fig. 1, where heavy hole subband $hh1$ is split into two spin branches $\pm 3/2$. As a result they are shifted relative to each other in the $\mathbf{k}$ space. In the reduced-symmetry structures, the spin splitting of the conduction subband is usually smaller than that of the valence band and not shown in Fig. 1 for simplicity. Due to the selection rules the direct optical transitions from the valence subband $hh1$ to the conduction subband $e1$ can occur only if the electron angular momentum changes by ± 1. It follows then that the allowed transitions are $|+3/2\rangle \to |+1/2\rangle$ and $|-3/2\rangle \to |-1/2\rangle$, as illustrated in Fig. 1 by vertical lines. Under excitation with linearly polarized or unpolarized light the rates of both transitions are equal. In the presence of spin splitting, the optical transitions induced by photons of the fixed energy $\hbar\omega$ occur in the opposite points of the $\mathbf{k}$-space for the spin branches $\pm 1/2$. The asymmetry of photoexcitation results in a flow of electrons within each spin branch. The corresponding fluxes $\mathbf{j}_{1/2}$ and $\mathbf{j}_{-1/2}$ are of equal strengths but directed in the opposite directions. Thus, this non-equilibrium electron distribution is characterized by the nonzero spin current $\mathbf{j}_{\rm spin} = (1/2)(\mathbf{j}_{1/2} - \mathbf{j}_{-1/2})$ but a vanishing charge current, $e(\mathbf{j}_{1/2} + \mathbf{j}_{-1/2}) = 0$.

The direction β of the photo-induced spin current and the orientation α of transmitted spins are determined by the form of spin-orbit interaction. The latter is governed by the QW symmetry and can be varied. For QWs based on zinc-blende-lattice semiconductors and grown along the crystallographic

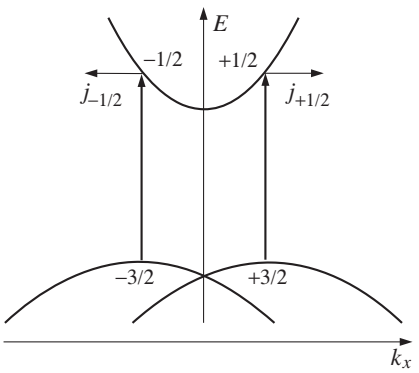

Fig. 1. Microscopic origin of pure spin current induced by interband photoexcitation.

direction [110] $\parallel z$, the light absorption leads to a flow along $x \parallel [1\bar{1}0]$ of spins oriented along z. This component of the electron spin flow can be estimated as

$$F_x^z = \gamma_{zx}^{(hh1)} \frac{\tau_e}{2\hbar} \frac{m_h}{m_e + m_h} \frac{\eta_{cv}}{\hbar\omega} I \,, \tag{1}$$

where $\gamma_{zx}^{(hh1)}$ is a constant describing the $\mathbf{k}$-linear spin-orbit splitting of the $hh1$ subband, τ_e is the relaxation time of the spin current, m_e and m_h are the electron and hole effective masses in the QW plane, respectively, η_{cv} is the light absorbance, and I is the light intensity. Note that the time τ_e can differ from the conventional momentum relaxation time that governs the electron mobility.

In (001)-grown QWs the absorption of linearly- or unpolarized light results in a flow of electron spins oriented in the QW plane. In contrast to the low-symmetry QWs considered above, in (001)-QWs the $\mathbf{k}$-linear spin splitting of the valence subband $hh1$ is small and here, for the sake of simplicity, we assume the parabolic spin-independent dispersion in the $hh1$ valence subband and take into account the spin-dependent contribution $\gamma_{\alpha\beta}^{(e1)} \sigma_\alpha k_\beta$ to the electron effective Hamiltonian. Then, to the first order in the spin-orbit coupling, the components of the pure spin current generated in the subband $e1$ are derived to be

$$F_\beta^\alpha = \gamma_{\alpha\beta}^{(e1)} \frac{\tau_e}{2\hbar} \frac{m_e}{m_e + m_h} \frac{\eta_{cv}}{\hbar\omega} I \,. \tag{2}$$

2. Free-carrier absorption

Light absorption by free carriers, or the Drude-like absorption, occurs in doped semiconductor structures when the photon energy $\hbar\omega$ is smaller than the band gap as well as the intersubband spacing. Because of the energy and momentum conservation the free-carrier optical transitions become possible if they are accompanied by electron scattering by acoustic or optical phonons, static defects etc. Scattering-assisted photoexcitation with unpolarized light also gives rise to a pure spin current. However, in contrast to the direct transitions considered above, the spin splitting of the energy spectrum leads to no essential contribution to the spin current induced by free-carrier absorption. The more important contribution comes from asymmetry of the electron spin-conserving scattering. In semiconductor QWs the matrix element V of electron scattering by static defects or phonons has, in addition to the main contribution V_0, an asymmetric spin-dependent term [2]

$$V = V_0 + \sum_{\alpha\beta} V_{\alpha\beta}\, \sigma_\alpha (k_\beta + k'_\beta) \,, \tag{3}$$

where $\mathbf{k}$ and $\mathbf{k}'$ are the electron initial and scattered wave vectors, respectively. Microscopically this contribution is caused by the structural and bulk inversion asymmetry similar to the Rashba/Dresselhaus spin splitting of the electron subbands. The asymmetry of the electron-phonon interaction results in non-equal rates of indirect optical transitions for opposite wave vectors in each spin subband. This is illustrated in Fig. 2, where the free-carrier absorption is shown as a combined two-stage process involving electron-photon interaction (vertical solid lines) and electron scattering (dashed horizontal lines). The scattering asymmetry is shown by thick and thin dashed lines: electrons with the spin $+1/2$ are preferably scattered into the states with $k_x > 0$, while particles with the spin $-1/2$ are scattered predominantly into the states with $k_x < 0$. The asymmetry causes an imbalance in the distribution of photoexcited carriers in each subband $s = \pm 1/2$ over the positive and negative k_x states and yields oppositely directed electron flows $\mathbf{j}_{\pm 1/2}$ shown by horizontal arrows. Similarly to the interband excitation considered in the previous section, this nonequilibrium distribution is characterized by a pure spin current without charge transfer.

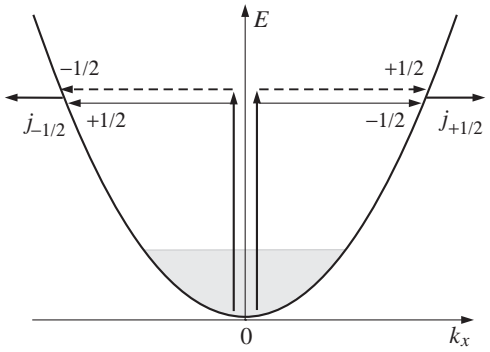

Fig. 2. Microscopic origin of pure spin current induced under light absorption by free electrons. The free-carrier absorption is a combined process involving electron-photon interaction (vertical solid lines) and electron scattering (dashed horizontal lines).

Let us assume the photon energy $\hbar\omega$ to exceed the typical electron kinetic energy, E_F for degenerate and $k_B T$ for nondegenerate electron gas. Then the pure spin current induced by free-carrier light absorption is given by

$$F_x^\alpha = \frac{\tau_e}{\hbar} \left[\frac{V_{\alpha x}}{V_0} \left(1 + \frac{|e_x|^2 - |e_y|^2}{2} \right) + \frac{V_{\alpha y}}{V_0}\, e_x e_y \right] \eta_{e1} I \,, \tag{4}$$

where $\mathbf{e} = (e_x, e_y)$ is the light polarization unit vector, and η_{e1} is the light absorbance in this spectral range.

In addition to the free-carrier absorption, the spin-dependent asymmetry of electron-phonon interaction can also give rise to a pure spin current in the process of photoelectron energy relaxation. In this relaxational mechanism the spin current is generated in a system of hot carriers, independently of heating means.

Besides the spin, free charge carriers can be characterized by another internal property, e.g., by the valley index in multivalley semiconductors. Thus, one can consider pure orbit-valley currents in which case the net electric current vanishes but the partial currents contributed by carriers in the particular valleys are nonzero.

Acknowledgements

We acknowledge helpful discussions with V.V. Bel'kov and S.D. Ganichev. This work was supported by RFBR, INTAS, programs of the RAS and Foundation "Dynasty"-ICFPM.

References

[1] R. D. R. Bhat, F. Nastos, A. Najmaie, and J. E. Sipe, arXiv:cond-mat/0404066.

[2] E. L. Ivchenko and S. A. Tarasenko, *Zh. Eksp. Teor. Fiz.* **126**, 476 (2004) [*JETP* **99**, 379 (2004)].

13th Int. Symp. "Nanostructures: Physics and Technology"
St Petersburg, Russia, June 20–25, 2005

In-plane and out-of-plane spin polarization by a lateral current in nonmagnetic heterojunctions

A. Yu. Silov[1], P. A. Blajnov[1], J. H. Wolter[1], R. Hey[2], K. H. Ploog[2] and N. S. Averkiev[3]

[1] COBRA Inter-University Research Institute, Eindhoven University of Technology, PO Box 513, NL-5600 MB Eindhoven, The Netherlands
[2] Paul-Drude-Institut für Festkörperelektronik, Hausvogteiplatz 5-7, 10117 Berlin, Germany
[3] Ioffe Physico-Technical Institute, St Petersburg, Russia

Abstract. Spin-polarization by a lateral current has been experimentally achieved in the single non-magnetic semiconductor heterojunctions grown both on the (001) and (113) substrates. The effect does not require an applied magnetic field. The (001) structures provide the mean spin density with only planar components. The (113) heterojunctions also allow the out-of-plane spin polarization. The effect can be used to manipulate the spin density: the nonequilibrium spin changes its sign as the current reverses.

Introduction

We have experimentally achieved the spin-polarization that is induced by an electrical current alone, in the absence of applied magnetic field and does not require ferromagnetic contacts. Such method of creating spin polarization differs radically from those employed so far [1,2]. The current-induced spin polarization can be seen as the inverse of the circular photo-galvanic effect. The photo-galvanic effect is allowed in quantum wells of III–V compounds due to the removal of the spin degeneracy. The extensive literature on spin photocurrents in low-dimensional structures is reviewed in Ref. [3].

Previously, the current-induced spin polarization in low-dimensional systems was theoretically considered only for the conduction electrons [5-6l. The effect is due to a spin-orbit interaction that is linear in the wave vector, $\boldsymbol{k}$, of charge carriers and manifests itself in lifting the spin degeneracy away from the zone centre (see, for instance, Ref. [7]). This can be caused either by *(i)* the inversion asymmetry of host material (Dresselhaus mechanism of spin splitting) or *(ii)* by the asymmetry of the confinement in low-dimensional systems (Bychkov–Rashba effect). However, the **k**-linear terms are not unique for the conduction band only, and, in zinc-blende semiconductors, are significantly larger in the valence band: the two-dimensional holes display much more pronounced removal of the spin degeneracy as compared to the electron gas in GaAs.

1. Experiment

All our samples contain a single modulation-doped heterojunction to form the two-dimensional hole gas(2DHG). The samples were MBE grown on either (001) or (113) GaAs substrates. Annealed Ni/ZnAu contacts were made to the 2DHG. The hole concentration at the (001) heterojunctions ($N_{\rm Hall}$) was 4.15×10^{11} cm^{-2} with the mobility ($\mu_{\rm Hall}$) of 46500 cm^2/V s at 5.8 K. For the (113) heterojunctions we have measured $\mu_{\rm Hall} = 610000$ cm^2/V s and $N_{\rm Hall}$ of 2.1 × 1011 cm^{-2} at 0.3 K.

We detect the spin-polarization by measuring the degree of circular polarization, P [8]. The samples were cleaved into bars of about 1×2.5 mm^2 with the current flowing along the long side, which was always in the $[1\bar{1}0]$ direction.

For the heterojunctions on (001)-surface (in the case of C_{2v} symmetry) the spin density may only have planar components perpendicular to the current flow [6]. This necessarily means that the polarized PL has to be collected from the cleaved (110) edge of the sample.

On the other hand, at the (311) heterojunctions (that is in the case of C_s symmetry) the mean spin density will have a component along the growth direction. That makes it possible to detect the circularly polarized PL in the backscattering geometry.

2. Results and discussion

2.1. (001) samples

Figure 1 shows the low-temperature PL spectra both with a current flow turned on or switched off. The PL contains a strong radiative band centred at about 1.52 eV. This band originates from recombination of the two-dimensional holes with electrons photoexcited into the GaAs conduction band [9]. The PL intensity is decreased by passing the current through the sample, while the emission wavelength is blueshifted. This spectral shift towards the higher energy side is explained by the extra energy acquired by the 2DHG in the lateral electric field.

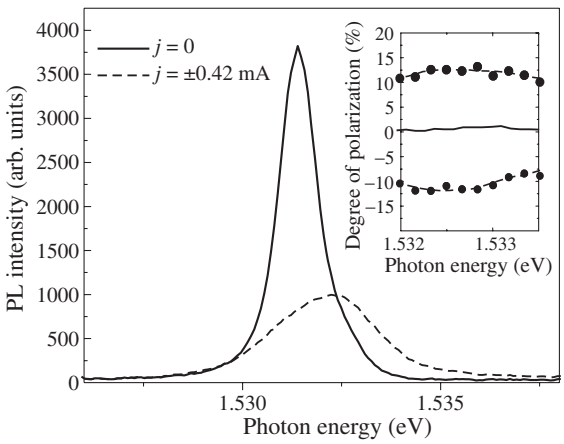

Fig. 1. Photoluminescence spectra of the (001) 2DHG at 5.1 K in absence of a current (gray line) and with current of ±0.85 mA (black line). Inset shows a degree of circular polarization as measured in the [110] direction for the two opposing currents. The solid lines are a guide for the eye.

The inset in Fig. 1 shows the observed P with the dotted line representing a baseline of the circular polarization. The baseline of the circularly polarized PL was carefully checked by recording a difference between PL_{σ^-} and PL_{σ^+} spectra when no current was delivered through the sample. The observed degree of polarization yields a maximum of 2.5%. It is the important feature of the data that the degree of polarization inverses its sign as the electric current reverses. This is a direct prove of the current-induced spin orientation, in complete agreement with the results on the spin photocurrents in quantum wells [10].

The spin orientation, S, can be estimated following calculations for 2D electrons from Ref. [5]:

$$S = 6Q\frac{\gamma F e \tau_p}{\hbar E_F}, \qquad (1)$$

where Q is a coefficient of approximately unity depending of the scattering mechanism, E_F is the DHG Fermi energy, F is an electric field, e is elementary charge, τ_p is the momentum relaxation time, and γ describes the $\mathbf{k}$-linear spin splitting. In a field of 6.5 V/cm, with $\gamma = 7 \times 10^{-2}$ eV Å (from linear interpolation of data [12], $\tau_p = 10^{-11}$ s and $E_F = 2$ meV from our transport measurements, the spin polarization is estimated to be 10%. Although in some cases the degree of circular polarization can be quantitatively linked to the spin polarization [13], for the 2DHG recombination the link is not straightforward. A strong admixture of the light-hole character to the ground (heavy-hole) state of the 2DHG reduces the value of the circular polarization degree. The experimentally observed P of 2.5% yields only a low-limit estimate of the nonequilibrium spin-polarization. Nonetheless, even $S = 2.5\%$ exceeds the spin polarization that has been initially achieved by the spin injection from ferromagnetic metals into GaAs [13].

2.2. *(113) samples*

Figure 2 summarizes our experimental data for the (113) samples. The experimental arrangements are identical to that for Fig. 1 with the exception of the detection: the polarized PL has been collected from the front facet of the sample now, i.e. along the growth direction. The observed degree of circular polarization now exceeds 12% at 5.1 K and has a different sign for the opposing currents. It is apparent that the spin polarization detected in the (113) heterojunctions resembles the (001) results in every detail. However, as was to be expected from symmetry considerations, the (113) 2DHG displays the out-of-plane spin density. It is worth noting that the lowest subband of the (113) 2DHG shows a pronounced admixture of the light-hole states already at $\mathbf{k} = 0$. This weakens the one-to-one correspondence between the degree of circular polarization and the spin orientation, which is unique for the undoped (001)-quantum wells. In contrast to the (001)-2DHG recombination as detected in the cleaved-side arrangements, the light-hole admixture is not indispensable for the detection of spin polarization in the [113] backscattering.

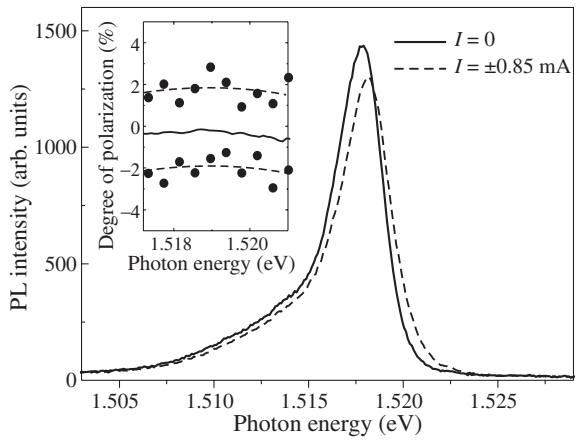

Fig. 2. Photoluminescence spectra of the (113) 2DHG at 5.1 K in absence of a current (gray line) and with current of ±0.42 mA (black line). Inset shows a degree of circular polarization as measured in the [113] direction for the two opposing currents. The solid lines are a guide for the eye.

Acknowledgements

This work was financially supported by the Dutch Organization for Advancement of Research (NWO). The research at the Ioffe Institute was also supported by INTAS, RFBR, scientific programs of RAS and Russian Ministry of Industry, Science and Technology.

References

[1] Meier, F., and Zakharchenya, B., editors, *Optical orientation*, North–Holland Physics, Amsterdam, 1984.
[2] Awschalom, D., Loss, D., and Samarth, N., editors, *Semiconductor spintronics and quantum computation*, Springer, Berlin, 2002.
[3] Ganichev, S. D., and Prettl, W., *J. Phys.: Condens. Matter*, **15**, R935 (2003).
[4] Edelstein, V. M., *Solid State Communications*, **73**, 233 (1990).
[5] Aronov, A. G., Yu. B. Lyanda-Geller, and Pikus, G. E., *Sov. Phys. JETP*, **73**, 537 (1991).
[6] Chaplik, A. V., Entin, M. V., and Magarill, L. I., *Physica E*, **13**, 744 (2002).
[7] Rashba, E. I., and Sheka, V. I. in *Landau Level Spectroscopy*, edited by G. Landwehr and E. I. Rashba, North–Holland, Amsterdam, 1991, vol. 1, p. 178.
[8] Pikus, G. E., and Aronov, A. G., *Sov. Phys. Semicond.*, **10**, 698 (1976).
[9] A. Yu. Silov, Haverkort, J. E. M., Averkiev, N. S., Koenraad, P. M., and Wolter, J. H., *Phys. Rev. B*, **50**, 4509 (1994).
[10] Ganichev, S. D., Ivchenko, E. L., Danilov, S. N., Eroms, J., Wegscheider, W., Weiss, D., and Prettl, W., *Phys. Rev. Lett.*, **86**, 4358 (2001).
[11] Störmer, H. L., Schlesinger, Z., Chang, A., Tsui, D. C., Gossard, A. A., and Wiegmann, W., *Phys. Rev. Lett.*, **51**, 126 (1983).
[12] Jonker, B. T., Hanbicki, A. T., Park, Y. D., Itskos, G., Furis, M., Kioseoglou, G., Petrou, A., and Wei, X., *Appl. Phys. Lett.*, **79**, 3098 (2001).
[13] Jonker, B. T., *Proc. IEEE*, **91**, 727 (2003).

13th Int. Symp. "Nanostructures: Physics and Technology"
St Petersburg, Russia, June 20–25, 2005

Extraordinary Hall effect in III-Mn-V thin films and quantum well structures

B. A. Aronzon[1], A. B. Davydov[1], V. V. Rylkov[1], Yu. A. Danilov[2], B. N. Zvonkov[2] and V. V. Podolskii[2]

[1] Russian Research Center "Kurchatov Institute" Moscow 123182, Russia
[2] NIFTI N. Novgorod State University, N. Novgorod 603950, Russia

Abstract. Results of magnetotransport and magnetic properties studies of GaMnSb films and InGaAs quantum wells placed in GaAs δ-doped with Mn are presented. The effect of disorder peculiar to these systems on Extraordinary Hall Effect and magnetoresistance is discussed.

1. Introduction

Diluted magnetic semiconductors (DMS) are candidates for spin-injectors and other spintronic devices, which could be easily combined with structures for common electronics [1]. $A_{III}B_V$ semiconductors doped with Mn (for example, GaMnAs and GaMnSb) are the most widely studied DMS [2]. It is known [3], that to get high temperature DMS Mn concentration should exceed $10^{21}\,\mathrm{cm}^{-3}$. In that case DMS is highly disordered system. The disorder is due not only to random distribution of Mn ions, but also is result of the formation of ferromagnetic nanograins like MnAs or MnSb. The effect of disorder on DMS properties start to be discussed very recently and is of grate importance [4]. On the other hand there is only a very few papers discussing properties of 2D structures based on this material. We report on the transport, magnetotransport and magnetic properties of GaMnSb films and InGaAs quantum wells placed in GaAs δ-doped with Mn. Mainly we concentrate ourselves on the discussion of peculiarities of the Extraordinary Hall Effect (EHE), which could be the sign of carrier spin-polarization.

2. Thing GaMnSb films

GaMnSb films with the approximately same Mn concentration (10 at %) were grown by laser plasma deposition method. Film thickness d is in the range 40–140 nm. The substrate temperature varied in the range 440−200 °C that results in carrier concentration ranging from $3\times10^{19}\,\mathrm{cm}^{-3}$ up to $5\times10^{20}\,\mathrm{cm}^{-3}$. Structural studies showed that additional to Mn ions substituting Ga atoms GaMnSb films contain ferromagnetic nanograins and Ga_{Sb} defects, acting as acceptors and responsible for high hole concentration. The saturated magnetization is roughly the same for all films, $M_s = 3.6$–$5.3\,\mathrm{mT}$.

For single-phase GaMnSb the Curie temperature is less 30 K, and the EHE sign is negative [5]. Unlike that in our samples EHE show magnetic hysteresis up to room temperature and its sign is positive. Fig. 1 depicts magnetic field dependences of Hall resistance $R_H(B)$ at $T = 77\,\mathrm{K}$ (Fig. 1a) and $T = 293\,\mathrm{K}$ (Fig. 1b) for GaMnSb samples with the hole concentrations $p = 5\times10^{20}\,\mathrm{cm}^{-3}$ (curve 1), $p = 1.5\times10^{20}\,\mathrm{cm}^{-3}$ (curve 2) and $p = 3\times10^{19}\,\mathrm{cm}^{-3}$ (curve 3), respectively.

The carrier concentration was evaluated from slope of the linear part of the $R_H(B)$ curve at $B > 0.4$–$0.5\,\mathrm{T}$. Linear character of the dependence for the sample 1 in this range of magnetic fields is demonstrated by the upper insert of Fig. 1b. Fig. 1 shows that EHE is the main contribution to the Hall effect in samples 1 and 2 at $T = 77$–$300\,\mathrm{K}$, while for sample 3 with the smallest hole concentration EHE was not detected. A comparison of data for samples 1 and 2, demonstrates that a decrease of the hole concentration suppresses the EHE hysteresis. For sample 1 ($p = 5\times10^{20}\,\mathrm{cm}^{-3}$) the coercive force $B_c = 0.29\,\mathrm{T}$ at $T = 77\,\mathrm{K}$ and hysteresis in EHE was observed up to room temperature (see lower insert in Fig. 1b). At the same time, for sample 2 ($p = 1.5\times10^{20}\,\mathrm{cm}^{-3}$) $B_c = 0.058\,\mathrm{T}$ at $T = 77\,\mathrm{K}$, and EHE hysteresis was not detected at $T = 300\,\mathrm{K}$.

For the spontaneous Hall resistance R_H^S determination the procedure developed by Arrott was proposed [6]. To get that we plot the R_H^2 dependence versus B/R_H and extrapolate its

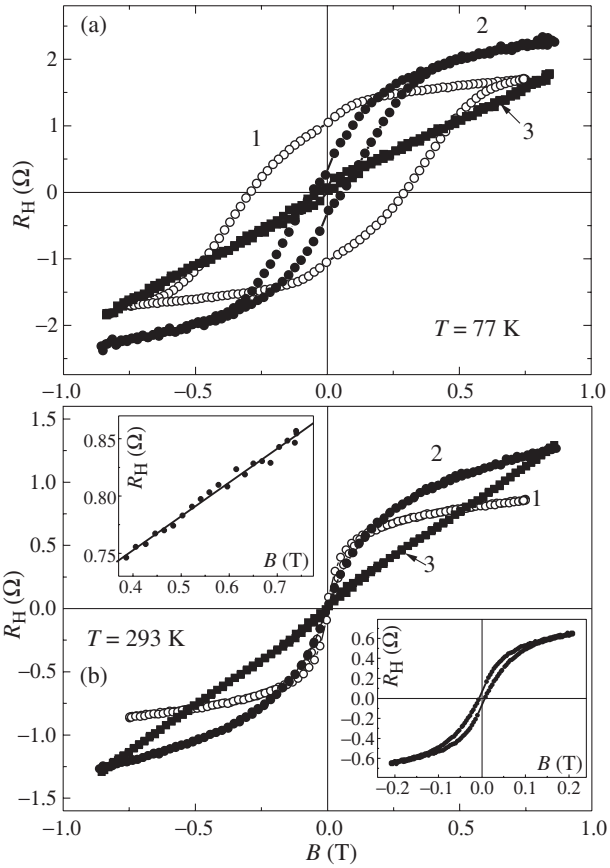

Fig. 1. Dependencies of the Hall resistance on a magnetic field for GaMnSb films: 1 — $p = 5\times10^{20}\,\mathrm{cm}^{-3}$, $T_s = 200\,^\circ\mathrm{C}$; 2 — $p = 1.5\times10^{20}\,\mathrm{cm}^{-3}$, $T_s = 200\,^\circ\mathrm{C}$; 3 — $p = 3\times10^{19}\,\mathrm{cm}^{-3}$, $T_s = 440\,^\circ\mathrm{C}$. Measurement have been performed at temperatures: (a) 77 K; (b) 293 K. At (b) the upper inset shows $R_H(B)$ for the sample 1 at $B > 0.4\,\mathrm{T}$; the bottom inset shows $R_H(B)$ at $-0.2 < B < 0.2\,\mathrm{T}$ for the same sample.

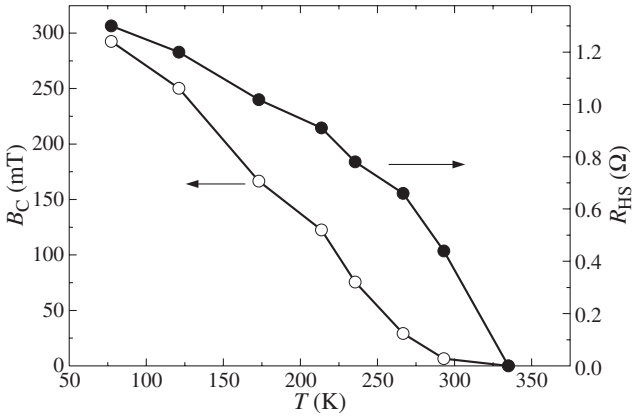

Fig. 2. Temperature dependencies of coercive force B_c (left curve) and spontaneous Hall resistance component R_H^S (right curve) for the sample 1.

linear part to intersection with ordinate axis. The temperature dependences of coercive field B_c and spontaneous Hall resistance R_H^S are shown in Fig. 2 for sample 1. The hysteresis loss temperature $T_c \approx 330$ K. Analogous procedure gives $T_c \approx 180$ K for sample 2.

The peculiar behavior of the Hall effect is due to the carrier interaction with ferromagnetic grains, which is strongly affected by Shottky barriers at the interface between the grain and the host semiconductor. These barriers prevent carrier from interacting with the ferromagnetic grain. With the carrier concentration increasing barriers become thinner and the interaction is strengthened. That is why EHE could be observed at high carrier concentration only. It is the reason for widely discussed the absence of the EHE in previous studies of III-V semiconductors with MnSb or MnAs inclusions and with low carrier concentrations, while on the other hand these measurements show the strong hysteresis of the magnetization.

3. InGaAs/GaAs quantum well with $\delta\langle$Mn$\rangle$-doped layer in GaAs

Quantum well (QW) samples were prepared by MOC-hydride epitaxy method. Samples contain $In_xGa_{1-x}As$ quantum well, carbon δ-layer and laser-deposited Mn δ-layer separated by GaAs spacers, x varied from 0.11 up to 0.17, while Mn concentration was controlled by laser-deposition duration time ranged in the interval 6–24 s. The thickness of the spacer between quantum well and Mn δ-layer ranged from 3 up to 6 nm.

The magnetoresistance and Hall effect measurements were performed at $T = 4.2$–77 K and in magnetic fields up to 3 T. Samples demonstrated mainly positive magnetoresistance, but in some cases at low temperatures the magnetoresistance reversed to the negative that. At low temperatures additionally to the normal Hall effect the EHE was observed (Fig. 3).

We believe that EHE is due to interaction of Mn ions in GaAs with holes in the quantum well. In the temperature range, where EHE was observed, the nonmonotonous temperature dependence of the sample resistance was detected. Such behavior is common for transitions to the ferromagnetic state. The results of our experiments also show (see Fig. 4, curve 1) that for the longitudinal geometry the negative magnetoresistance (NMR) is noticeably smaller, than that for field normal to the film (curve 2). Note that for DMS films the axis of light magnetization usually is in the film plane, i.e. NMR should more pronounced for the longitudinal field orientation. To explain

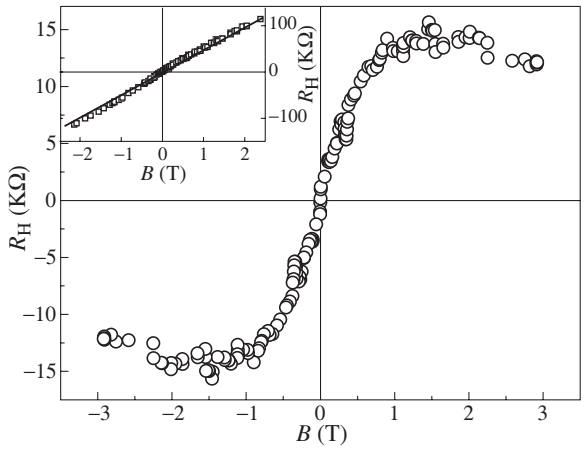

Fig. 3. Magnetic field dependence of the extraordinary Hall effect component for quantum well structure at $T = 30$ K. The insert shows the dependence of Hall resistance R_H (both ordinary and extraordinary components) on magnetic field.

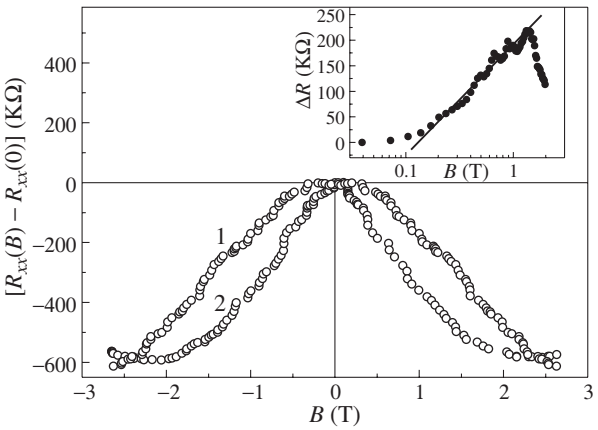

Fig. 4. Magnetoresistance curves for quantum well structure at $T = 30$ K: 1 — longitudinal geometry (field is parallel to the 2D channel and perpendicularly to current); 2 — cross geometry (field perpendicularly to film). The insert demonstrates the magnetic field dependence of the difference between magnetoresistance values for longitudinal and cross geometries: ΔR vs ln B.

these features of NMR in those structures additionally to the magnetic field controlled spin-dependent scattering of carriers the quantum corrections of conductivity should be taken into account.

Acknowledgement

This work supported by the RFBR, projects 04-02-16158, 04-02-19964 and 05-02-17021.

References

[1] G. Schmidt, L. W. Molenkamp (review), *Semicond. Sci. Technol.* **17**, 310 (2002).
[2] X. Chen, M. Na, M. Cheon *et al*, *Appl. Phys. Lett.* **81**, 511 (2002).
[3] T. Dietl, H. Ohno, F. Mutsukura, *Phys. Rev. B* **63**, 195205 (2001).
[4] C. Timm, *J. Phys.: Condens. Matter* **15**, R1865 (2003).
[5] E. Abe, F. Matsukura, H. Yasuda *et al*, *Physica E* **7**, 981 (2000).
[6] H. Ohno, F. Matsukura, *Sol. State Commun.* **117**, 179 (2001); F. Matsukura, D. Chiba, T. Omiya *et al*, *Physica E* **12**, 351 (2002).

13th Int. Symp. "Nanostructures: Physics and Technology"
St Petersburg, Russia, June 20–25, 2005

Magneto-gyrotropic photogalvanic effects in semiconductor quantum wells

W. Weber[1], *V. V. Bel'kov*[2], S. D. Ganichev[1,2], E. L. Ivchenko[2], S. A. Tarasenko[2], S. Giglberger[1], M. Olteanu[1], H.-P. Tranitz[1], S. N. Danilov[1], Petra Schneider[1], W. Wegscheider[1], D. Weiss[1] and W. Prettl[1]

[1] Fakultät Physik, University of Regensburg, 93040, Regensburg, Germany
[2] Ioffe Physico-Technical Institute, St Petersburg, Russia

Abstract. We show that free-carrier (Drude) absorption of both polarized and unpolarized terahertz radiation in quantum well (QW) structures causes an electric photocurrent in the presence of an in-plane magnetic field. Experimental data and theoretical analysis evidence that the observed photocurrents are spin-dependent and related to the gyrotropy of the QWs. Microscopic models for the photogalvanic effects in QWs based on asymmetry of photoexcitation and relaxation processes are proposed.

Introduction

Much current interest in condensed matter physics is directed towards understanding of spin dependent phenomena. Recently spin photocurrents generated in QWs have attracted considerable attention. A natural way to generate spin photocurrents is the optical excitation with circularly polarized radiation. It results in optical spin orientation of free carriers due to a transfer of photon angular momenta to the carriers [1]. Because of the spin-orbit coupling such excitation may result in an electric current.

However, in an external magnetic field photocurrents may be generated even by unpolarized radiation as it has been proposed for bulk gyrotropic crystals [2]. Here we report on an observation of such photocurrents in QW structures caused by the Drude absorption of terahertz radiation. We show that, microscopically, the effects under study are related to the gyrotropic properties of the structures. Photocurrents which require simultaneously gyrotropy and the presence of a magnetic field may be gathered in a class of magneto-optical phenomena denoted as magneto-gyrotropic photogalvanic effects. In most of the investigated structures, the photogalvanic measurements reveal a magneto-induced current which is independent of the direction of light in-plane linear polarization and related to spin-dependent relaxation of non-equilibrium carriers.

1. Phenomenological theory

Illumination of gyrotropic nanostructures in the presence of a magnetic field may result in a photocurrent. There is a number of contributions to the magnetic field induced photogalvanic effect (MPGE). They are characterized by different dependencies of the photocurrent on the radiation polarization state and the orientation of the magnetic field. A proper choice of experimental geometry allows one to investigate each contribution separately. We consider (001)-grown QWs based on zinc blende lattice compounds of C_{2v} symmetry in the coordinate system with $x' \parallel [1\bar{1}0]$ and $y' \parallel [110]$. For normal incidence of the light and the in-plane magnetic field $\mathbf{B} \parallel y'$, the MPGE is given by

$$j_{x'} = S_1 B I + S_2 B \left(|e_{x'}|^2 - |e_{y'}|^2 \right) I \,, \qquad (1)$$

$$j_{y'} = S_3 B \left(e_{x'} e_{y'}^* + e_{y'} e_{x'}^* \right) I + S_4 B I P_{\mathrm{circ}} \,, \qquad (2)$$

where I is light intensity, $\mathbf{e}$ is the light polarization unit vector. The first term on the right hand side of Eq. (1) yields a current in the QW plane which is independent of the radiation polarization. This current is induced even by unpolarized radiation. Each other contribution has a special polarization dependence.

The terms described by parameters S_2 and S_3 vanish if the radiation is *circularly* polarized. For *linearly* polarized light they depend on the azimuthal angle of the polarization. In contrast, the last term in Eq. (2), being proportional to the radiation helicity, vanishes for *linearly* polarized excitation. Charateristics of the polarization dependencies permit to separate each contribution experimentally from the others.

2. Experimental results

The experiments were carried out on MBE-grown (001)-oriented n-type GaAs/$Al_{0.3}Ga_{0.7}As$ and InAs/AlGaSb QW structures. The InAs/AlGaSb structure (sample A1) was grown on a GaAs substrate. The QW is nominally undoped, but contains 2D electron gas with the carrier density of $8 \cdot 10^{11}$ cm^{-2} at 4.2 K located in the InAs channel. All GaAs samples are modulation-doped. For samples A2–A4 Si-δ-doping with spacer layer thicknesses of 70 nm (A2, A3) and 80 nm (A4) has been used. In contrast, for sample A5 the AlGaAs barrier layer separating the QWs has been homogeneously Si-doped on a length of 30 nm. This results in a spacer thickness of only 5 nm. Therefore, in addition to the different impurity distribution compared to the samples A2–A4, the sample A5 has much lower mobility.

A pulsed terahertz laser was used for optical excitation. With NH_3 as active gas 100 ns pulses of linearly polarized radiation with $\sim$ 10 kW power were obtained at wavelength 148 μm. The samples were irradiated along the growth direction. Quartz $\lambda/4$-plate and metal mesh polarizer were used to vary the polarization state of terahertz radiation. The terahertz radiation induces free carrier absorption in the lowest conduction subband $e1$ because the photon energy is smaller than the subband separation and much larger than the $\mathbf{k}$-linear spin splitting.

All samples have ohmic contacts corresponding to the $\langle 100 \rangle$ and $\langle 110 \rangle$ in-plane directions. The photocurrent $\mathbf{j}$ was measured in unbiased structures. The external magnetic field B up to 1 T was applied parallel to the interface plane.

In all investigated QW structures, an illumination with terahertz radiation in the presence of an in-plane magnetic field

results in a photocurrent in full agreement with the phenomenological theory described by Eqs. (1, 2).

The experimental data obtained on the samples A1 to A4 show that in these QW structures only current contributions proportional to S_1 and S_4 are detectable, whereas other contributions are vanishingly small. These samples are denoted as type I below. The results obtained for type I samples are valid in the wide temperature range from 4.2 K up to room temperature. The transverse photocurrent observed in the direction normal to the magnetic field $\mathbf{B}$ applied along $\langle 110 \rangle$ is independent of the light polarization (see Fig. 1). It corresponds to the first term on the right side of Eq. (1). The longitudinal photocurrent component parallel to $\mathbf{B}$ describing by the last term of Eq. (2) appears under excitation with circularly polarized radiation only.

In contrast to the samples of type I, the experimental results obtained on the sample A5 (in the following denoted as type II) has characteristic polarization dependencies corresponding to the S_2 (see Fig. 2) and S_3 terms in Eqs. (1, 2). The photocurrent exhibits a pronounced dependence on the azimuthal angle of the linear polarization, but it is equal for the right and left circular polarized light.

3. Microscopic models

Mechanisms of MPGE in bulk non-centrosymmetric semiconductors are based on the cyclotron motion of free carriers in both the real and $\mathbf{k}$ spaces. Since, in a QW subjected to an in-plane magnetic field, the cyclotron motion is suppressed one needs to seek for alternative mechanisms. We demonstrate that the generation of magneto-induced photocurrent in QWs is related to gyrotropy and therefore the effects belong to the magneto-gyrotropic class.

Our microscopic treatment shows that there are two classes of mechanisms which contribute to the magneto-gyrotropic effects. The current may be induced either by an asymmetry of optical excitation and/or by an asymmetry of relaxation. The photocurrent depends on polarization for the first class of the mechanisms but is independent of the direction of linear light polarization for the second class. Thus the polarization dependence of the magneto-gyrotropic photocurrent signals allows us to distinguish between the above two classes. The asymmetry of photoexcitation may contribute to all terms in Eqs. (1, 2). Therefore, such photocurrent contributions should demonstrate a characteristic polarization dependencies given by the terms with the coefficients S_2, S_3. In contrast, the asymmetry of relaxation processes contributes only to the coefficients S_1, S_4.

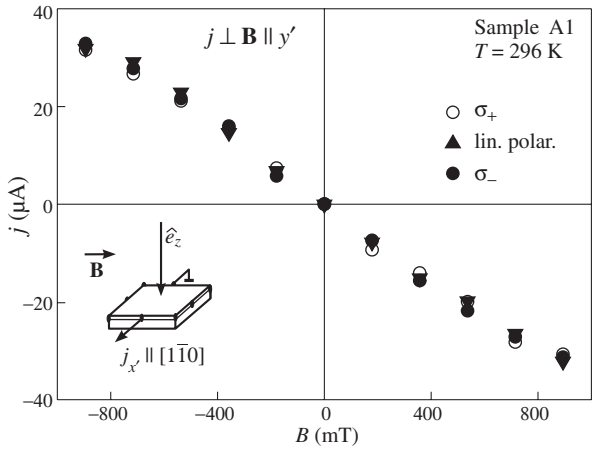

Fig. 1. Magnetic field dependence of the photocurrent measured in sample A1 Data are given for *linear*, right- (σ_+), and left-handed *circular* (σ_-) polarization. The current is measured in the direction x' *perpendicular* to $\mathbf{B}$.

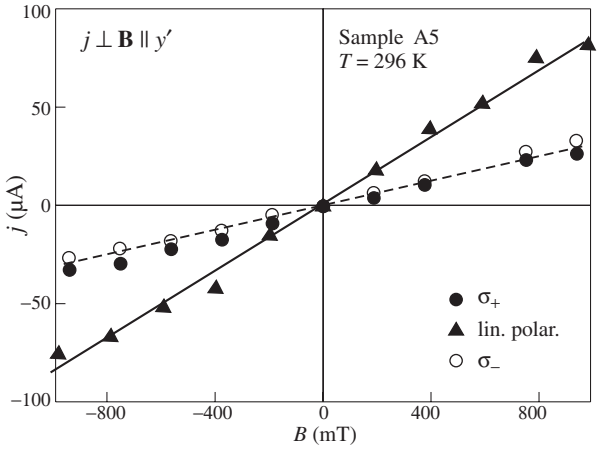

Fig. 2. Magnetic field dependence of the photocurrent measured in sample A5. Data are given for *linear*, right- (σ_+), and left-handed *circular* (σ_-) polarization. The current is measured in the direction x' *perpendicular* to $\mathbf{B}$.

Hence, the current obtained for the samples of type I is caused by the Drude absorption-induced electron gas heating followed by energy relaxation and/or spin relaxation.

Polarization dependencies of the photocurrent in type II sample prove that the main mechanism for current generation in the sample is the asymmetry of photoexcitation.

The question concerning the difference of type I and type II samples remains open.

The samples only differ in the type of doping and the electron mobility. The influence of impurity potentials (density, position, scattering mechanisms etc.) on microscopic level needs yet to be explored. In addition, the doping level of the type I samples is significantly lower and the mobility is higher than those in the type II samples. This can also affect the interplay between the excitation and relaxation mechanisms.

Finally we note, that under steady-state optical excitation, the contributions of the relaxation and photoexcitation mechanisms to MPGE are superimposed. However, they can be separated in time-resolved measurements. Indeed, under the ultra-short pulsed photoexcitation the current should decay, for the mechanisms considered above, within the energy, spin and momentum relaxation times times.

Acknowledgement

This work was supported by the DFG, RFBR, programs of RAS, and Foundation "Dynasty" — ICFPM.

References

[1] *Optical orientation*, F. Meier and B. P. Zakharchenya, Eds. (Elsevier Science Publ., Amsterdam, 1984).

[2] E. L. Ivchenko and G. E. Pikus, *Pis'ma Zh. Eksp. Teor. Fiz.*, **27**, 640 (1978) [*JETP Lett.* **27**, 604 (1978)].

13th Int. Symp. "Nanostructures: Physics and Technology"
St Petersburg, Russia, June 20–25, 2005

Spin relaxation in magnetic field for InP quantum dots

I. Ya. Gerlovin[1], I. V. Ignatiev[2,3], B. Pal[2], S. Yu. Verbin[2,3] and Y. Masumoto[2]

[1] Vavilov State Optical Institute, St Petersburg, 199034, Russia
[2] Institute of Physics, University of Tsukuba, Tsukuba 305-8571, Japan
[3] V.A. Fock Institute of Physics, St Petersburg State University, 198504 St Petersburg, Russia

Abstract. Effect of external magnetic field on the optical orientation of electron spins in negatively charged InP quantum dots is studied experimentally using the PL pump-probe method.

Recently, we have found that electron spin polarization in the InP quantum dots (QDs) exists for a long time, up to hundred microseconds [1], in accordance with the theoretical predictions of very long spin lifetime for electrons in QDs [2]. In this paper, we discuss specific peculiarity of the phenomenon, namely the dynamics of the electron spin in strong longitudinal magnetic field.

We have studied an ensemble of the negatively charged InP QDs grown between the InGaP barrier layers on a GaAs substrate by the gas source MBE technology. The base diameter of the QDs is about 40 nm and the height is about 5 nm. Further details of the structure are described in Ref. [3]. The lowest electron level in the QDs is close to the Fermi level of the n-doped substrate that allowed us to control the amount of the resident electrons in the QDs by means of external voltage.

Singly charged QDs have been studied in details. In these dots, optical excitation by the circularly polarized light creates electron-hole pairs which interact with the resident electrons and form trions. Spin orientation of the photocreated carriers can be transferred to spin of the resident electron and conserved after the electron-hole recombination. This process allows to polarize the resident electrons and to study their spin memory at the time scale much longer than the electron-hole pair lifetime.

As an indication of the spin orientation, we have used the effect of negative circular polarization (NCP) of photoluminescence (PL) observed in the singly charged QDs at quasi-resonant excitation in the PL spectrum and kinetics of degree of circular polarization (Fig. 1). Mechanism of the NCP formation is described in Ref. [1]. In short, polarization of the trionic PL is determined by spin orientation of the hole. The NCP results from the flip-flop process of the electron and hole spins during their energy relaxation to the ground states. This process, which occurs due to anisotropic component of exchange coupling [4], is an efficient way to overcome the Pauli blocking for energy relaxation of the photocreated electrons.

To study spin dynamics of the resident electrons, we have used the so-called PL pump-probe method [1]. In this method, a sample is excited by two beams which polarization can be varied independently. Pulses of one beam (pump) create polarization of the resident electrons. Time evolution of the polarization can be

detected by measuring polarization of the PL excited by the probe pulses delayed in time relatively to the pump pulses. As it seen from Fig. 1, amplitudes of the NCP differ for co- and cross-polarized pump and probe beams of equal intensities. This is an indication that polarization of the resident electrons is accumulated in the case of the co-pump-probe excitation and becomes large [6]. At the same time, for the cross-pump-probe excitation, the polarization created by the pump pulses is

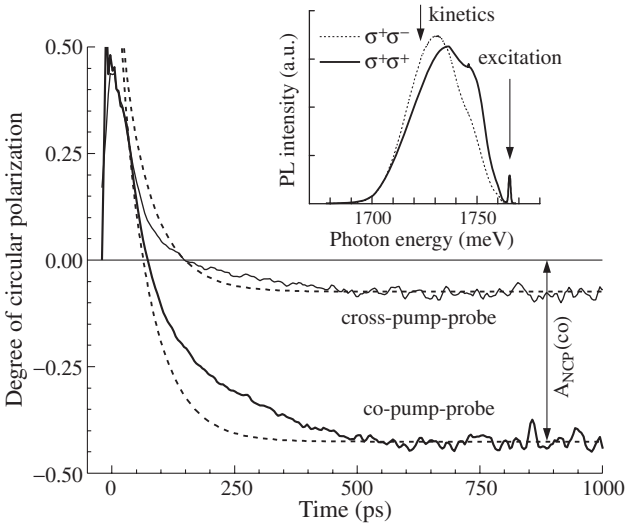

Fig. 1. Kinetics of degree of circular polarization for the co-and cross-polarized pump and probe beams. Sample temperature $T = 5$ K. Applied bias $U_{bias} = -0.1$ V. Longitudinal magnetic field $B = 0.1$ T [5]. Delay between the pump and probe pulses $\Delta t = 11$ ns. Dashed lines are the fits in framework of a NCP generation model. Inset shows PL spectra in co- and cross-polarizations under σ^+-excitation.

destroyed by the probe pulses and, therefore, there is no optical orientation of the spins (in average). For further study of the spin polarization, we have used a relatively weak probe beam with intensity of about 10 times smaller than that of the pump beam to avoid destroying of spin memory by the probe pulses.

In Fig. 2 we present delay dependence of the NCP amplitude at cross-polarized pumping for different values of magnetic field. Polarization of the pump beam was chosen so that the polarized resident electrons occupied the upper Zeeman level. At weak magnetic field, we observed very slow relaxation of the resident electron spins. Discussion of this result can be found in Ref. [1]. When magnetic field increases, decay of spin orientation becomes faster. This fact can be explained qualitatively by acceleration of spin relaxation due to interaction with the acoustic phonons resonant to Zeeman splitting of the electron spin doublet. Density of such phonons increases with energy and probability of transitions from upper to lower Zeeman sub-level with emission of the phonons increases too. So, spin orientation of resident electrons in magnetic field is determined by competition of two processes: optical pumping of the spins and spin relaxation to the ground Zeeman level (freezing effect) dependent on the magnetic field strength.

For more detailed study of the processes, we have measured magnetic field dependence of the NCP amplitude at co- and

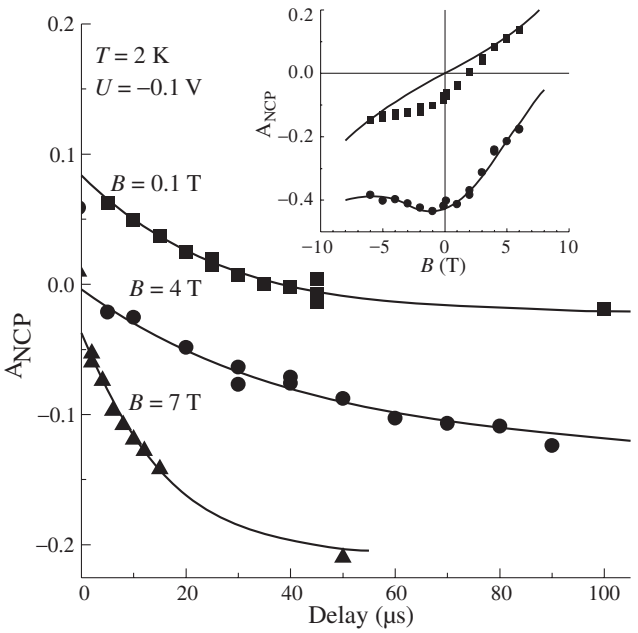

Fig. 2. Delay dependence of spin polarization at different magnetic fields under the circular cross-pump-probe excitation (solid symbols). Solid lines are the multi-exponential fits. The dependence for $B = 0.1$ T is shifted vertically by 0.1. Inset shows magnetic field dependence of the spin polarization under co- (circles) and cross- (squares) excitations at delay 11 ns. Solid lines are fits in framework of the freezing model (see text).

cross-polarized excitations by the pump and probe beams of equal intensities at small delay (see inset in Fig. 2). In the case of the cross-polarized pumping, when no optical orientation of the electron spins appears, the magnetic field dependence should reflect spin thermalization on Zeeman sublevels, that is freezing effect. Indeed, the dependence obtained experimentally is in good qualitative agreement with the theoretical curve described by equation:

$$A_{NCP} = \pm \frac{1 - \exp(\mp \Delta E_z / kT)}{1 + \gamma_P/\gamma_s(B) + \exp(\mp \Delta E_z / kT)},$$

where Zeeman energy $\Delta E_z = g\mu_B|B|$, factor $g = 1.5$ for the InP QDs, $\mu_B = 0.059\,\mu$eV/T is the Bohr magneton, γ_P and $\gamma_s(B)$ are the pumping and spin relaxation rates, respectively. Sign "-" is used for $B>0$ and "+" for $B<0$. A relatively small discrepancy between theory and experiment at B around zero is due to peculiarities of spin relaxation of holes in the QDs with parallel and anti-parallel electron spins [1].

For the co-polarized pumping, the dependence reflects both freezing effect and acceleration of the spin relaxation with magnetic field and can be described by equations:

$$A_{NCP} = \frac{Q - \gamma_P/\gamma_s(B) - \exp(-\Delta E_z / kT)}{1 + \gamma_P/\gamma_s(B) + \exp(-\Delta E_z / kT)},$$

for $B>0$, and

$$A_{NCP} = \frac{Q \cdot \exp(-\Delta E_z / kT) - \gamma_P/\gamma_s(B) - 1}{1 + \gamma_P/\gamma_s(B) + \exp(-\Delta E_z / kT)},$$

for $B<0$.

Optical orientation of the electron spins occurs when the photocreated holes loose their spin orientation and recombine with the non-polarized resident electrons. The efficiency of this process is described in equations given above by the factor $Q = (\tau_h - \tau_r)/(\tau_h + \tau_r)$, where τ_h and τ_r are the energy relaxation times of the holes with and without spin flip, respectively. Magnetic field dependence of the electron spin relaxation rate is modeled by equation $\gamma_s(B) = \gamma_{s0}[1 + (\alpha B)^2]$ assuming that acceleration of the relaxation is proportional to the density of the phonons with energy ΔE_z, which quadratically depends on energy and, therefore, on the magnetic field. Values of the fitting parameters $\gamma_P/\gamma_{s0} = 1.23$, $Q = 0.85$ for all the curves. Parameter α is slightly varied for different curves: $\alpha = 0.25$ in the case $B<0$ and co-pump-probe excitation and $\alpha = 0.2$ in other cases. This is probably due to oversimplification of the model used. Temperature of the QDs is also considered as the fitting parameter to take into account possible heating of the dots by the excitation. It has been found that $T = 15$ K which considerably larger than the sample temperature $T = 2$ K in these experiments.

In conclusion, exploiting of the polarized PL pump-probe method, we have studied dynamics of the resident electron spins in external magnetic field. We have found that effect of the magnetic field on the electron spin orientation is determined by two main factors: increase of the spin relaxation rate and the freezing effect.

Acknowledgements

This work was supported by Grant-in-Aid for Scientific Research No. 13852003 and No. 16031203 from the MEXT of Japan, by the Russian Foundation for Basic Research (project No. 0302-16858), and by INTAS (project No. 1B 2167).

References

[1] M. Ikezawa, B. Pal, Y. Masumoto, I. V. Ignatiev, S. Yu. Verbin, I. Ya. Gerlovin, *Phys. Rev. Lett.*, (submitted).

[2] A. V. Khaetskii and Yu V. Nazarov, *Phys. Rev. B*, **61**, 12639 (2000).

[3] I. E. Kozin, V. G. Davydov, I. V. Ignatiev, A. V. Kavokin, K. V. Kavokin, G. Malpuech, H. W. Ren, M. Sugisaki, S. Sugou and Y. Masumoto, *Phys. Rev. B*, **65**, 241312(R) (2002).

[4] K. V. Kavokin, *Phys. stat. solidi (a)*, **195**, 592 (2003).

[5] Small magnetic field is used to suppress effect of the nuclear spin fluctuations discussed in papers by Merkulov *et al*, *Phys. Rev. B*, **65**, 205309 (2002) and Ignatiev *et al*, NANO2005 (submitted).

[6] Dynamical nuclear polarization which appears under these experimental conditions does not affect the electron spin dynamics as it is shown in Ref. [1].

13th Int. Symp. "Nanostructures: Physics and Technology"
St Petersburg, Russia, June 20–25, 2005

Gate voltage controlled spin photocurrents in heterojunctions

S. Giglberger[1], S. D. Ganichev[1,2], V. V. Bel'kov[2], M. Koch[3], T. Kleine-Ostmann[3], K. Pierz[4], E. L. Ivchenko[2], L. E. Golub[2], S. A. Tarasenko[2] and W. Prettl[1]

[1] Fakultät Physik, University of Regensburg, 93040, Regensburg, Germany
[2] Ioffe Physico-Technical Institute, St Petersburg, Russia
[3] Institut für Hochfrequenztechnik, Technische Universitst Braunschweig, 38106 Braunschweig, Germany
[4] Physikalisch-Technische Bundesanstalt, D-38116 Braunschweig, Germany

Abstract. The spin-galvanic effect and the recently observed magneto-gyrotropic are investigated in GaAs heterojunctions as a function of voltage applied by a semitransparent gate electrode. It is shown that in a certain experimental geometry, the spin-galvanic current can be tuned by the variation of the gate voltage over a wide range providing an experimental access to the Rashba spin-orbit coupling. Furthermore in response to linear polarized radiation the magento-gyrotropic effect is detected and by control of the gate voltage a sign inversion of the magneto-gyrotropic current is observed.

Introduction

The manipulation of the spin of charge carriers in semiconductors is one of the key problems in the field of spintronics. Spin polarization may be tuned applying gate bias voltage by means of the Rashba spin-orbit coupling [1] in low dimensional structures. Here we demonstrate that a gate voltage applied to heterojunctions strongly affects the formation of spin photocurrents [2] excited by terahertz radiation. The most striking influence of the gate voltage is observed in GaAs heterojunctions excited by linearly polarized radiation in the presence of external magnetic field. The current caused by the magneto-gyrotropic effect [3] at positive biases reverses its direction. In additional we show that the strength of the spin-galvanic effect [4] excited in GaAs heterojunctions by circularly polarized radiation for a certain experimental geometry depends linearly on the gate voltage as expected from Rashba-like spin splitting.

1. Experimental

The experiments are carried out at room temperature on (001)-oriented n-type GaAs heterojunctions having C_{2v} point group symmetry. All samples have two pairs of ohmic contacts at the corners corresponding to the $x \parallel [100]$ and $y \parallel [010]$ directions. A semitransparent metallic gate electrode was prepared on the top of the structure a shown in the inset of Fig. 1. The voltage in the range between -17 V and $+5$ V was applied between the gate and the two-dimensional channel. For optical spin orientation we use a high power pulsed molecular far-infrared NH_3 laser operating at 148 μm wavelength. Radiation is linearly or circularly polarized. The terahertz radiation induces free carrier absorption in the lowest conduction subband $e1$ because the photon energy is smaller than the subband separation and much larger than the **k**-linear spin splitting. The samples are irradiated along the growth direction. The in-plane external magnetic field $B = 0.3$ T is applied parallel to the [100]-axis. The photocurrent **j** was measured at room temperature in unbiased structures via the voltage drop across a 50 Ω load resistor in closed circuit configuration with a fast storage oscilloscope. The measured current pulses of 100 ns duration reflected the corresponding laser pulses.

Irradiation of the samples subjected to an in-plane magnetic field with normally incident *circularly* polarized radiation yields a helicity dependent current. The polarity of the current changes upon reversal of the applied magnetic field as well as upon changing the light helicity from right- to left-handed indicating the spin-galvanic effect [4]. The effect is caused by the optical orientation of carriers, subsequent Larmor precession of the oriented electronic spins, and an asymmetric spin relaxation processes. Though, in general, the spin-galvanic current does not require an application of magnetic field, it may be considered as a magneto-photogalvanic effect under the above experimental conditions. Fig. 1 shows the dependence of the spin-galvanic effect on the bias voltage. It is measured along the magnetic field. The current depends almost linearly on the bias voltage. As we showed previously [5] for the $j \parallel B \parallel [100]$ geometry the spin-galvanic effect is due to the Rashba spin splitting of the band only as the Dresselhaus contribution to the current vanishes. The strength of the Rashba contribution depends linearly on the gate voltage. On the other hand the spin-galvanic current is proportional to the strength of spin-splitting. Therefore the observed gate voltage dependence is in fully agreement with the expected current behaviour. The gate voltage dependence of spin-galvanic current reflects the modulation of the strength of spin-orbit coupling in the low dimensional structure providing a direct experimental access to this important parameter.

Applying linearly polarized radiation a current parallel as well as perpendicular to the magnetic field is observed. The

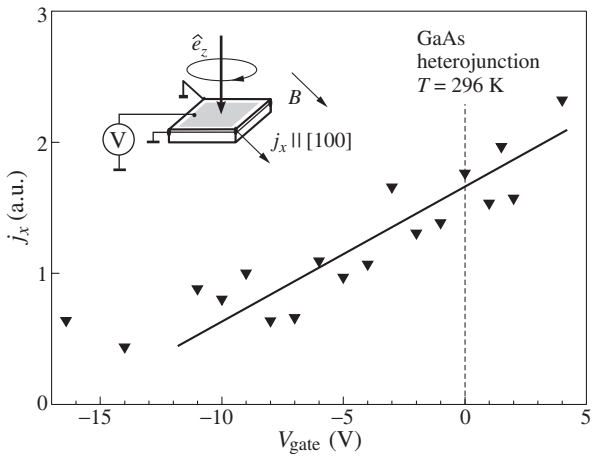

Fig. 1. Dependence of the spin-galvanic effect on the gate bias voltage. Inset shows the geometry of the experiment. Circularly polarized radiation of the wavelength 148 μm is normally applied through a semitransparent gate to GaAs heterojunction.

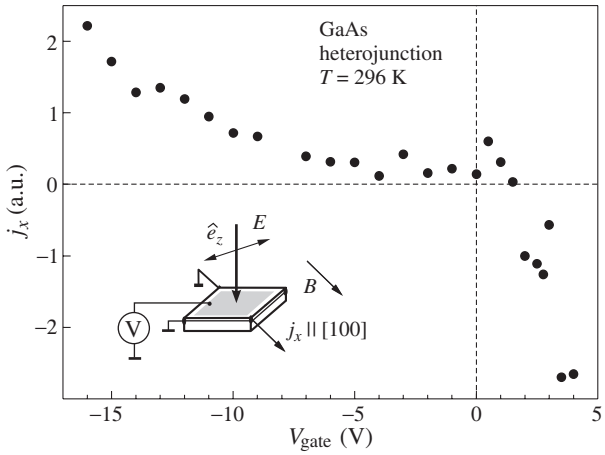

Fig. 2. Bias voltage dependence of the magneto-gyrotropic effect excited by linearly polarized radiation. Inset shows the geometry of experiment.

current changes its direction upon the magnetic field reversal. It is due to the recently observed magneto-gyrotropic effect caused by Drude absorption of terahertz radiation [3]. This current may be induced either by an asymmetry of optical excitation and/or by an asymmetry of relaxation.

On the bases of polarization dependences we conclude that in our samples the magneto-gyrotropic current is dominated by an asymmetry of relaxation of photoexcited carriers. In this mechanism the current is caused by the asymmetric part of electron-phonon interaction [6]. The light absorption by free electrons leads to an electron gas heating, i.e. to a non-equilibrium energy distribution of electrons. Due to the asymmetry of the electron-phonon interaction hot electrons with opposite $\mathbf{k}$ have different relaxation rates. As a result, an electric current is generated. Whether $-k$ or $+k$ states relax preferentially, depends on the spin direction. It is because the electron-phonon asymmetry is spin-dependent. The currents in spin-up and spin-down subbands flow in opposite directions. For $B = 0$ the currents cancel each other exactly. In the presence of a magnetic field the currents moving in the opposite directions do not cancel due to the non-equal population of the spin subbands and a net electric current flows. This current is spin polarized and can be independent of light polarization.

In additional to the current due to asymmetry of relaxation a small contribution (about 30 percent) of a magneto-gyrotropic effect due to an asymmetry of optical excitation [3] was also detected. This contribution yields a characteristic polarization dependences being in agreement with the phenomenological theory.

Fig. 2 shows the gate voltage dependence of the magneto-gyrotropic current for longitudinal and parallel to magnetic field geometry. It is seen that the current reverses its sign at small positive bias voltages. Measurements of polarization dependences showed that the ratio and the relative sign of both, "relaxation" and "excitation" contributions, remains unchanged. The microscopic mechanism of this striking feature is not well understood as yet.

Acknowledgement

We thank B. Hacke for technical assistance. We acknowledge financial support from the DFG, RFBR, and INTAS.

References

[1] Y. A. Bychkov and E.I. Rashba, *Pis'ma ZhETF*, **39**, 66 (1984) [*Sov. JETP Lett.*, **39**, 78 (1984)].

[2] S. D. Ganichev and W. Prettl, *J. Phys.: Condens. Matter*, **15**, R935 (2003).

[3] V. V. Bel'kov, S. D. Ganichev, E. L. Ivchenko, S. A. Tarasenko, W. Weber, S. Giglberger, M. Olteanu, H.-P. Tranitz, S. N. Danilov, Petra Schneider, W. Wegscheider, D. Weiss and W. Prettl, submitted to *J. Phys.: Condens. Matter*.

[4] S. D. Ganichev, E. L. Ivchenko, V. V. Bel'kov, S. A. Tarasenko, M. Sollinger, D. Weiss, W. Wegscheider and W. Prettl, *Nature* (London) **417**, 153 (2002).

[5] S. D. Ganichev, V. V. Bel'kov, L. E. Golub, E. L. Ivchenko, P. Schneider, S. Giglberger, J. Eroms, J. De Boeck, G. Borghs, W. Wegscheider, D. Weiss and W. Prettl, *Phys. Rev. Lett.*, **92**, 256601 (2004).

[6] E. L. Ivchenko and S. A. Tarasenko, *Zh. Eksp. Teor. Fiz.*, **126**, 476 (2004) [*JETP* **99**, 379 (2004)].

13th Int. Symp. "Nanostructures: Physics and Technology"
St Petersburg, Russia, June 20–25, 2005

Suppression of spin beats by magnetic breakdown in 2D systems

M. M. Glazov, N. S. Averkiev and S. A. Tarasenko
Ioffe Physico-Technical Institute, St Petersburg, Russia

Abstract. Zero-field spin splitting induced by Rashba or Dresselhaus spin-orbit coupling gives rise to beats in magneto-oscillations in 2D electron systems. Here we show that the pattern of the Shubnikov-de Haas oscillations depends drastically on the explicit form of the spin-orbit coupling. Depending on the ratio between the Rashba and Dresselhaus terms, the spectrum of the magneto-oscillations contains one, two, or three harmonics. Such a behavior is caused by magnetic breakdown between spin branches of the spin-split level.

Introduction

Spin-related transport phenomena in two-dimensional (2D) systems is of broad interest at present time. The peculiar property of 2D systems based on quantum wells is a linear in the wave vector $\mathbf{k}$ spin splitting of the electron spectrum. The splitting is caused by spin-orbit interaction that couples spin states and space motion of conduction electrons and governs the wide class of spin phenomena.

Experimentally, one of the most efficient methods for determination of spin splitting in 2D conducting structures is measurements of the conductivity oscillations (Shubnikov–de Haas effect). The quantum oscillations are highly sensitive to the fine structure of the energy spectrum of carriers, so that even small, comparing to the Fermi energy, spin splitting qualitatively modifies the oscillation behavior. The $\mathbf{k}$-linear terms in the effective Hamiltonian remove the spin degeneracy and give rise to magneto-oscillations with close frequencies, i.e. to beats [1]. Such a behavior was observed and attributed to the zero-field spin splitting in 2D electron gas under study of the Shubnikov-de Haas oscillations in various semiconductor heterostructures. An analysis of the oscillations was applied for determination of the spin splitting at the Fermi level. However, recently it was pointed out that the simple analysis of the beating pattern may lead to an incorrect conclusion on the spin splitting [2,3]. In particularly, in [001]-grown quantum wells it was shown that the $\mathbf{k}$-linear contributions originated from the lack of the inversion center in the bulk material (Dresselhaus term)

$$\mathcal{H}_D = \alpha(\sigma_x k_y + \sigma_y k_x)\,, \tag{1}$$

and induced by heteropotential asymmetry (Rashba term)

$$\mathcal{H}_R = \beta(\sigma_x k_y - \sigma_y k_x)\,, \tag{2}$$

interfere in magneto-oscillation phenomena [3]. Here σ_i ($i = x, y$) are the Pauli matrices and the axes x, y are assumed to be parallel to the crystallographic axes $[1\bar{1}0]$, $[110]$, respectively. It was found that spin beats disappear and oscillations occur only at a single frequency if the strengths of the Rashba and Dresselhaus contributions are equal.

Here we show that the pattern of magneto-oscillations depends drastically on the ratio between the above terms. The presence of only one type of the $\mathbf{k}$-linear terms gives rise to the beats, i.e. two close harmonics corresponding to spin branches of the spin-split subband. However, if the strengths of both contributions are comparable, the third (central) harmonic appears in the spectrum of the magneto-oscillations. For equal strengths of the contributions, only the central harmonic survives, and the oscillations occur at a single frequency, although the $\mathbf{k}$-linear terms remain in the Hamiltonian. We argue that such behavior is caused by magnetic breakdown between the spin subbands.

Theory

Magneto-oscillations at low temperature are determined by an arrangement of the Landau levels at the Fermi energy. Analysis of the energy spectrum allows one to ascertain the pattern of the oscillations. In the presence of one type of the linear terms, either Dresselhaus or Rashba, the electron spectrum in a magnetic field consists of two set of the Landau levels. For Dresselhaus splitting, e.g., the levels are given by

$$E_{n,\pm} = \hbar\omega_c n \pm \sqrt{4\alpha^2 n/\lambda_B^2 + (\hbar\omega_c)^2/4}\,, \tag{3}$$

where ω_c is the cyclotron frequency and $\lambda_B = \sqrt{\hbar/m^*\omega_c}$ is the magnetic length, with m^* being the effective electron mass. It is the spin splitting $E_{n,+} - E_{n,-}$ that gives rise to the beats in magneto-oscillations. In the other limiting case, $|\alpha| = |\beta|$, electron levels become spin-degenerate

$$E_{n,\pm} = \hbar\omega_c(n + 1/2) - 2m^*\alpha^2/\hbar^2\,. \tag{4}$$

The $\mathbf{k}$-linear terms, although being present in the Hamiltonian, do not lead to a splitting of the Landau levels, and the beats in magneto-oscillations do not occur. For arbitrary strengths of the Dresselhaus and Rashba terms the electron spectrum in the magnetic field can be calculated numerically only. Knowledge of the energy spectrum allows us to calculate the electron Green's function and analyze the effect of the spin splitting on magneto-oscillations. We demonstrate it taking the Shubnikov-de Haas effect as an example.

Results and discussion

Fig. 1 shows the magnetic-field dependence of the resistivity

$$\rho_{xx} = \frac{\sigma_{xx}}{\sigma_{xx}^2 + \sigma_{xy}^2}$$

calculated numerically for different ratios of Rashba to Dresselhaus spin-splitting constants, β/α. The insets in the Figures present the Fourier spectra of the corresponding dependencies ρ_{xx} on $1/\omega_c\tau$, where τ is the scattering time.

For the case of only one type of the $\mathbf{k}$-linear terms ($\beta = 0$, Fig. 1a) the oscillations demonstrate the pronounced beats. The phase of the oscillations reverses at node points. The spectrum of the oscillations consists of two harmonics.

In the presence of both Rashba and Dresselhaus contributions of comparable strengths the pattern of the magneto-oscillations modifies (Figs. 1b, 1c). The beats become irregular and the reverse of the oscillation phase at nodes disappears. The Fourier spectrum shows clearly the mixture of *three* harmonics. In the case of the equal strengths of the Rashba and Dresselhaus terms, the beats vanish completely. Magneto-oscillations occur at a single frequency in accordance with the spectrum (4), although the $\mathbf{k}$-linear spin splitting remains for the most of the directions of the wave vector $\mathbf{k}$.

Such a behavior of the magneto-oscillations at various β/α can be qualitatively understood in a semiclassical picture, implying that frequencies of the magneto-oscillations correspond to the Bohr-Sommerfeld quantization of electron motion along the classical cyclotron obits (Fig. 2). For the case when the spin-orbit splitting exceeds the cyclotron energy $\hbar\omega_c$, electrons move over the cyclotron obits, with their spins being adiabatically oriented parallel or antiparallel to the effective magnetic field $\mathbf{B}_{so}$ induced by the spin-orbit coupling [2]. The orbits corresponding to the spins oriented along and opposite to $\mathbf{B}_{so}$ are split in the $\mathbf{k}$-space. In the presence of the Dresselhaus term only (Fig. 2a), quantization of cyclotron orbits corresponding to the spins oriented parallel and antiparallel to $\mathbf{B}_{so}$ gives rise to two harmonics in the magneto-oscillations, i.e. the beating

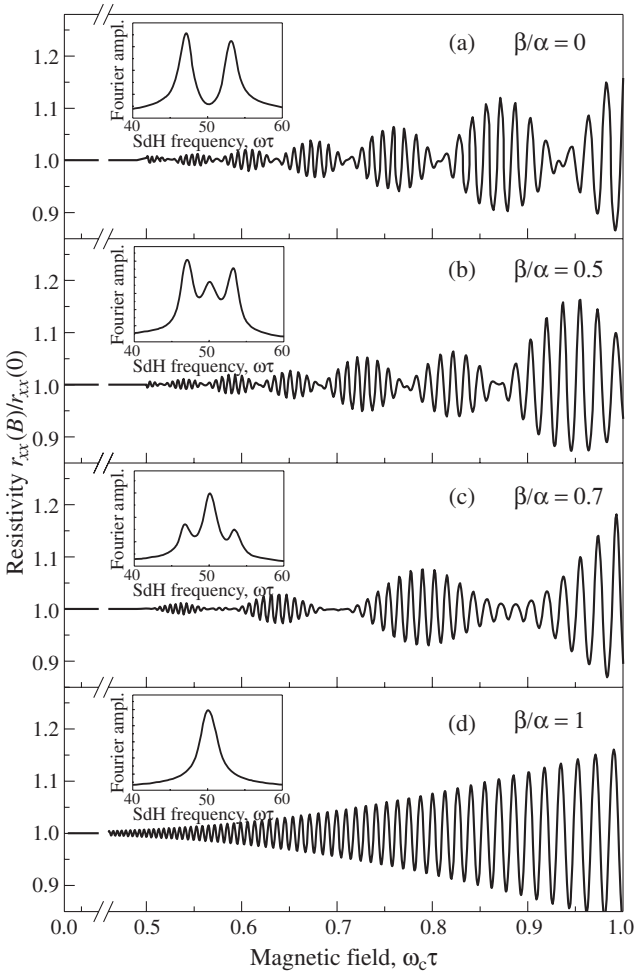

Fig. 1. The magnetic-field dependence of the resistivity ρ_{xx} for different ratios of Rashba to Dresselhaus terms, $\alpha/\beta = 0$, 0.5, 0.7, 1, at fixed Fermi energy $E_F\tau/\hbar = 50$ and fixed Dresselhaus splitting $\alpha k_F\tau/\hbar = 3$.

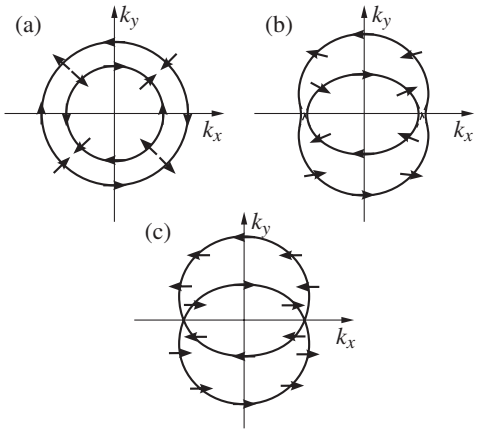

Fig. 2. Fermi contours for electrons in (001)-grown quantum wells in the presence of (a) Dresselhaus term only, (b) Rashba and Dresselhaus terms, (c) both contributions of the equal strengths. Arrows indicate the orientation of spins.

pattern.

In the presence of both Rashba and Dresselhaus contributions of comparable strengths (Fig. 2b) the condition of adiabatic spin orientation is broken at certain points in the $\mathbf{k}$-space there the spin splitting is small. In the vicinity of the points the electron spin does not follow adiabatically the effective field $\mathbf{B}_{so}$, and the magnetic breakdown becomes possible, i.e. electron tunneling between the close orbits [4]. Transitions corresponding to the magnetic breakdown between the orbits are shown in Fig. 2b with dashed lines. They result in the appearance of the third (central) harmonic in the magneto-oscillations. Increase of the ratio β/α leads to increase of the tunneling probability between the orbits, i.e. to an enhancement of the central peak and suppression of the low- and high-frequency harmonics.

In the particular case of $\alpha = \beta$ the zero-field Fermi surface consists of two identical circles shifted relative to each other along k_y and characterized with the spin states $|\pm 1/2\rangle$ onto the x-axis (Fig. 2c). Carriers within each spin subband are quantized identically in the external magnetic field, and only one (central) harmonic remains in the spectrum of the magneto-oscillations. Semiclassically, the electron spin initially oriented parallel or antiparallel to $\mathbf{B}_{so}$ keeps its orientation because the effective magnetic field is directed along x-axis independent of the wave vector, and the magnetic breakdown between the subbands do not occur.

Acknowledgements

This work was supported by the RFBR, the INTAS, programs of the RAS, Scientific Schools Support (2200.2003.2), the Russian Ministry of Science and Education, and Foundation "Dynasty" — ICFPM.

References

[1] Yu. A. Bychkov and É. I. Rashba, *J. Phys. C: Solid State Phys.*, **17**, 6039 (1984).
[2] S. Keppeler and R. Winkler, *Phys. Rev. Lett.*, **88**, 046401 (2002).
[3] S. A. Tarasenko and N. S. Averkiev, *Pis'ma Zh. Eksp. Teor. Fiz.*, **75**, 669 (2002) [*JETP Lett.*, **75**, 552 (2002)].
[4] E. A. de Andrada e Silva, G. C. La Rocca and F. Bassani, *Phys. Rev. B*, **50**, 8523 (1994).

13th Int. Symp. "Nanostructures: Physics and Technology"
St Petersburg, Russia, June 20–25, 2005

Suppression of spin-orbit effects in 1D system

M. V. Entin and *L. I. Magarill*

Institute of Semiconductor Physics, Siberian Branch of Russian Academy of Sciences, 13 Lavrent'eva, Novosibirsk, 630090, Russia

Abstract. We report the absence of spin effects such as spin-galvanic effect, spin polarization and spin current under static electric field and inter-spin-subband absorption in 1D system with spin-orbit interaction of arbitrary form. It was also shown that the accounting for the direct interaction of electron spin with magnetic field violates this statement.

Introduction

The spin-orbit (SO) interaction in a 2D system underlies various spin control methods owing to the coupling between translational and spin degrees of freedom. Such effects have been studied as spin-galvanic effect [1], spin polarization [2] and spin current [3,4] under static electric field, spin polarization under action of electromagnetic wave [5]. The one dimensional system seems to be more suitable for this purpose due to more strong correlation between the spin and the wire direction. This stimulates to examine the similar problems in 1D systems.

We consider the 1D Hamiltonian

$$\mathcal{H} = \frac{p^2}{2m} + V(x) + \mathcal{H}_{SO} \tag{1}$$

with the most general form of SO interaction

$$\mathcal{H}_{SO} = \{(\mathbf{a}(x)\boldsymbol{\sigma}),\, p\}\,, \tag{2}$$

where $\boldsymbol{\sigma}$ are the Pauli matrices, the figure brackets denote the symmetrization procedure, vector $\mathbf{a}(x)$ is an arbitrary function of coordinate x along the wire. The Hamiltonian (2) originates from different approaches related with SO interaction in 1D systems. In particular, it follows from 1D quantization of the 2D Rashba Hamiltonian [6,7]

$$\hat{\mathcal{H}}_{SO} = \alpha_R(\boldsymbol{\sigma}[\mathbf{p}\times\mathbf{n}])\,, \tag{3}$$

where $\mathbf{p}$ is the 2D electron momentum, and $\mathbf{n}$ is the normal to the plane of the system (axis z), x is the direction of the wire. The Hamiltonian obtains more general form (2) if the wire is curved or not homogeneous. The same Hamiltonian results from 1D quantization of the Dresselhaus SO Hamiltonian of the 3D crystal. Another example is the curvature-induced SO interaction [10].

In general, the Hamiltonian (2) does not conserve the spin and hence one can expect the above mentioned effects in the frameworks of this Hamiltonian. However, we have found that in a strictly 1D system with the SO Hamiltonian (2) these effects vanish.

1. Unitary transform

We shall demonstrate, that the Hamiltonian (1) can be unitary transformed to the form with no Pauli matrices. Let us consider an operator $U(x)$:

$$U(x) = T_x\left(\exp\left(-i\int_0^x dx\,(\mathbf{a}(x)\boldsymbol{\sigma})\right)\right)\,. \tag{4}$$

The the x-ordering operation T_x means that all operators should be placed in the decreasing order of x_k. Using this unitary transform we find

$$\mathcal{H}' = U^{-1}\mathcal{H}U = \frac{p^2}{2m} + V(x) - m\frac{a^2(x)}{2}\,. \tag{5}$$

Thus, the transformation excludes the spin from the Schrödinger equation. By means of the operator U the wave function transforms as $\psi(x) = U(x)\phi(x)$. This immediately yields the spin degeneracy of electron states, unless the boundary conditions depend on spin explicitly. In particular, this is the case for localized states in an infinite in both direction simple-connected quantum wire, where the boundary conditions are $\psi \to 0, x \to \pm\infty$.

2. Responses

The unitary transformation of the Hamiltonian to the form (5) has strong impact on different response functions. For example, consider linear responses of electric current $J = \sigma E$, spin polarization $S_i = \langle\sigma_i\rangle/2 = \gamma_i E$ and spin current $J_i^S = \langle\{\sigma_i, v\}\rangle/2 = \sigma_i^S E$. The electric field (tangent component) is assumed to be constant along the wire. These linear responses are expressed by the Kubo formula via the velocity or velocity-spin correlators $\mathrm{Tr}\left(\delta(\epsilon-\mathcal{H})v\delta(\epsilon'-\mathcal{H})\mathcal{A}_i\right)$, where in the case of conductivity $\mathcal{A}_i$ stands for the velocity operator v, for the spin orientation and spin current $\mathcal{A}_i = \sigma_i/2$ and $\mathcal{A}_i = \{v, \sigma_i\}/2$, respectively.

More general expressions for responses in arbitrary order on the electric field are determined by the velocity correlators

$$\mathrm{Tr}(v\delta(\epsilon_1-\mathcal{H})v\delta(\epsilon_2-\mathcal{H})\ldots v\delta(\epsilon_3-\mathcal{H})) \tag{6}$$

or spin-velocity correlators

$$\mathrm{Tr}(v\delta(\epsilon_1-\mathcal{H})v\delta(\epsilon_2-\mathcal{H})\ldots \sigma_i\delta(\epsilon_3-\mathcal{H}))\,. \tag{7}$$

Instead of the spin operator one can write the spin current operator $\{\sigma_i, v\}/2$.

After the transformation the expressions (6) and (7) reduce to

$$\mathrm{Tr}((p/m)\delta(\epsilon_1-\mathcal{H}')\ldots(p/m)\delta(\epsilon_3-\mathcal{H}'))\,, \quad \text{and} \tag{8}$$

$$\mathrm{Tr}((p/m)\delta(\epsilon_1-\mathcal{H}')\ldots\sigma_i(x)\delta(\epsilon_3-\mathcal{H}')) = 0\,. \tag{9}$$

As a result of (8), the conductivity of the system with SO interaction converts to that of the system with no SO interaction. The Eq. (9) follows from the identity $\mathrm{Tr}_\sigma(\boldsymbol{\sigma}(x)) \equiv 0$, where Tr_σ denotes the trace in the spin space. It proves that both coefficients of spin polarization γ_i and spin current σ_i^S

vanish. Similar conclusions can be done with respect to electrical responses of higher orders (e.g., the photogalvanic effect) which are not subjected to SO interaction and spin responses on the electric field (e.g., stationary spin orientation by alternating electric field) which vanish.

Note, that for proof of (9) it is essential the presence of *the only* spin operator under the trace; the similar correlators, containing two or more spin operators do not vanish.

Let us consider possible generalizations of the Hamiltonian (1-2) which conserve the main conclusions. First, we can include the electric field into the potential $V(x)$, hence all conclusions remain valid in presence of it in any order of magnitude. Second, we can consider the potential as periodic (or containing periodic part together with random one). Such potential without the SO interaction forms the energy bands $\epsilon(p)$, where p is now quasimomentum. The operator p/m in SO part goes to $\partial\epsilon/\partial p$. Hence the resulting new Hamiltonian can be also converted to the form with no spin operators. Third, the spin can be treated as a quantum number, counting any pair-degenerate levels. For example, they can be subbands, originated from two equivalent valleys of bulk semiconductor. The Hamiltonian (1) in that case refers to the system with valley degeneracy without spin. According to the found transform, the valley degeneracy will not be lifted. Fourth, we can include spin-independent e-e interaction. As such Hamiltonian does not touch the spin, the transformation can be done also.

3. What limits the spin elimination?

From said above it does not follow that there is no spin-orbit interaction in 1D system. In fact, the spin does not commute with the Hamiltonian (2). In the systems with magnetic spin injectors/spin-selective drains [9], an electron with a preset spin, once injected into the wire, will change the spin during propagation along the wire. Thus, the total system does not obey the conditions of the proof and the conductance of the wire senses the SO interaction.

The same is valid for cyclic systems, e.g. a ring. The periodic boundary condition in the ring of length L, $\psi(L) = \psi(0)$ converts into an equation, containing the spin via the operator U. Hence, the spin operator, being eliminated from the Schrödinger equation, appears in the boundary conditions that produces the spin splitting of levels.

We have neglected the relativistically weak direct interaction of spin with the magnetic field. This term actually leads to the spin-flip transitions caused by the alternating magnetic field. An example of such effect, namely EPR-induced photogalvanic effect in spiral quantum wire has been studied in [10].

In conclusion, we have found that in 1D systems different response functions, which do not include the spin degree of freedom are not influenced by spin-orbit interaction. The responses connecting the spin and translational degrees of freedom are nonexistent unless the direct magnetic-field spin-flip processes are taken into account. On the contrary, the inclusion of such interaction leads to the magnetic-field-induced resonant steady current.

In contrast to 2D systems, where SO interaction plays determinative role for phenomena involving charge transfer and spin, in 1D systems the influence of SO interaction is suppressed. The transition from 2D to 1D due to lateral quantization results in the sequential decrease of SO-induced effects.

Acknowledgements

The work was supported by grants of RFBR No 02-02-16398, Program for support of scientific schools of Russian Federation No 593.2003.2 and INTAS No 03-51-6453.

References

[1] S. D. Ganichev, E. L. Ivchenko *et al*, *Nature*, **417**, 153 (2002).
[2] V. M. Edelstein, *Solid State Comm.*, **73**, 233 (1990).
[3] J. Schliemann and D. Loss, *Phys. Rev. B*, **69**, 165315 2004.
[4] E. I. Rashba, *Phys. Rev. B* **70**, 161201 (2004).
[5] V. M. Edelstein, *Phys. Rev. Lett.*, **50**, 5766 (1998).
[6] Yu. A. Bychkov and E. I. Rashba, *JETP Lett.*, **39**, 78 (1984).
[7] E. I. Rashba and V. I. Sheka, *Landau Level Spectroscopy*, (ed. by G. Landwehr and E. I. Rashba, Elsevier, Netherlands), 178 (1991).
[8] L. I. Magarill and M. V. Entin, *JETP*, **96**, 766 (2003); M. V. Entin and L. I. Magarill, *Phys. Rev. B*, **64**, 085330 (2001).
[9] G. Schmidt, L. W. Molenkamp, A. T. Filip and B. J. van Wees, *Phys. Rev. B*, **62**, R4790 (2000).
[10] M. V. Entin, L. I. Magarill, *Europhys. Lett*, **68**, 853 (2004).

13th Int. Symp. "Nanostructures: Physics and Technology"
St Petersburg, Russia, June 20–25, 2005

Bichkov–Rashba spin-orbit splitting in kinetic binding regime in HgCdTe accumulation layers

V. F. Radantsev, V. V. Kruzhaev and G. I. Kulaev
Institute of Physics & Applied Mathematics. Ural State University, Ekaterinburg 620083, Russia

Abstract. The Rashba effect peculiarities in gated accumulation layers on zero-gap HgCdTe are studied theoretically and experimentally. It shown that the kinetic binding are strongly affected by spin-orbit interaction. Although the spin-orbit splitting is smaller in accumulation layers as compared with inversion ones, the "Rashba polarization" $\Delta n/n$ can achieve 100% in kinetic confinement regime.

Introduction

The investigations of spin-related phenomenons in semiconductors are of hight present-day interest because of potential applications in the growing field of spintronics. Mechanisms of spin-orbit (SO) coupling are most promising for the gate voltage V_g controls of spin dinamics, especially in narrow-gap and zero-gap semiconductors (NGS) [1]. In gated surface quantum wells (SQW) on these materials, the achieved values of Rashba SO splitting ΔE_R are almost one order of magnitude higher than these in InCaAs heterostructures [2]. However, in SQWs on low-doped substrates the Rashba polarization $P_R = (n^- - n^+)/(n^- + n^+)$ ($n^\pm$ are concentrations in different Rashba branches of spectrum) is weakly sensitive to V_g. By investigations of the Rashba effect in inversion layers it was recently shown that the increase doping of substrate not only enlarges the magnitude of the effect but also strengthens the V_g dependence of P_R [2].

In this work we report on an theoretical and experimental investigation of Rashba effect in accumulation layers. In this system the several specific features are exhibited. The contribution of the degenerated electron gas of continuum to the screening leads to such specific effect as the "two-dimensionalization" of electrons at zero surface electric fields [3,4]. Because of strong non-parabolicity the electron motion in SQWs on NGS in confinement direction are mixed with *in-2D plane* motion that leads to another specific effect — to the kinetic confinement [5,6] (the appearance of bound states at large enough 2D wave-vector $k_{2D} > k_{ci}$ although there are no the states bounded at zero or small k_{2D}). Such kinetically bound states (KBS) exist in both accumulation and inversion layers, but in former case the KBS may be occupied and thus they can be manifested experimentally in the usual magneto-oscillation effects. Because the cutoff wave-vector k_{ci} is strongly sensitive to the details of energy spectrum and confinement potential there is reason to hope that kinematic bounding is strongly affected by spin-orbit interaction also.

1. Experimental and theoretical remarks

The zero-gap $Hg_{0.88}Cd_{0.12}$ Te ($N_D - N_A = 5 \times 10^{16}\,\mathrm{cm}^{-3}$) MOS structures with a 70-nm thick anodic oxide film was investigated. Because the traditional Shubnikov-de Haas measurements cannot be used in accumulations layers on degenerate semiconductors (on account of the shunting of surface conductance by the bulk) the magneto-oscillations of differential capacitance of MOS structures were measured. In framework of this method the above drawback (strong charge exchange between the sates of 2D layer and substrate) turn into advantage because it ensures equilibrium regime of capacitance measurements. For the theoretical analysis, we used for the 8×8 Kane Hamiltonian a concept based on the transformation of matrix equation into Schrödinger-like equation [7].

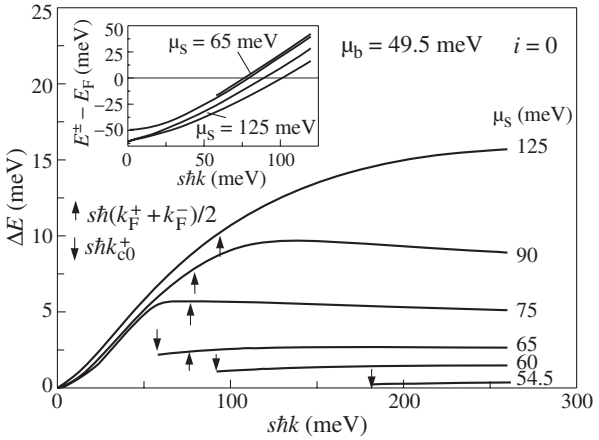

Fig. 1. The calculated dispersions $E^\pm(k)$ (insert) and spin-orbit splitting ΔE as a function of wave-vector k_i (in energy units $s\hbar k_i$, where s is Kane velocity).

2. Results and discussion

The dispersion relations $E^\pm(k_i)$ and SO splitting ΔE as a function of wave-vector k_i are shown in Fig. 1 for ground subband $i = 0$. At small surface potential μ_s (see Fig. 2) corresponding to the beginning of ground subband occupation, the subband dispersions are terminated at small k_i that is inherent to kinetic binding regime. At large k_i, the dispersions in two Rashba sub-subbands are very close to each other (ΔE is small) and to dispersion in bulk, however the k_{ci} values are indeed essentially different. In this regime, ΔE is practically k_i independent. The above behavior refer equally to excited subbands near their start. Thus the simple Rashba model with linear in k term is not applicable to describe the SO splitting in system we investigated.

By magneto-oscillation methods the values of wave vector at Fermi energy k_{Fi} are measured experimentally. In case of usually occupied states ($k_{ci} = 0$) this quantity at low temperature directly related to subband occupation $n_i^\pm = (k_{Fi}^\pm)^2/4\pi$. However, in kinetic binding regime $n_i^\pm$ is given by $((k_{Fi}^\pm)^2 - (k_{ci}^\pm)^2)/4\pi$. These values are plotted in Fig. 2 as a function of μ_s and total electron concentration N_s. The experimental values of $k_{Fi}^\pm$ determined from Fourier spectra of capacitance

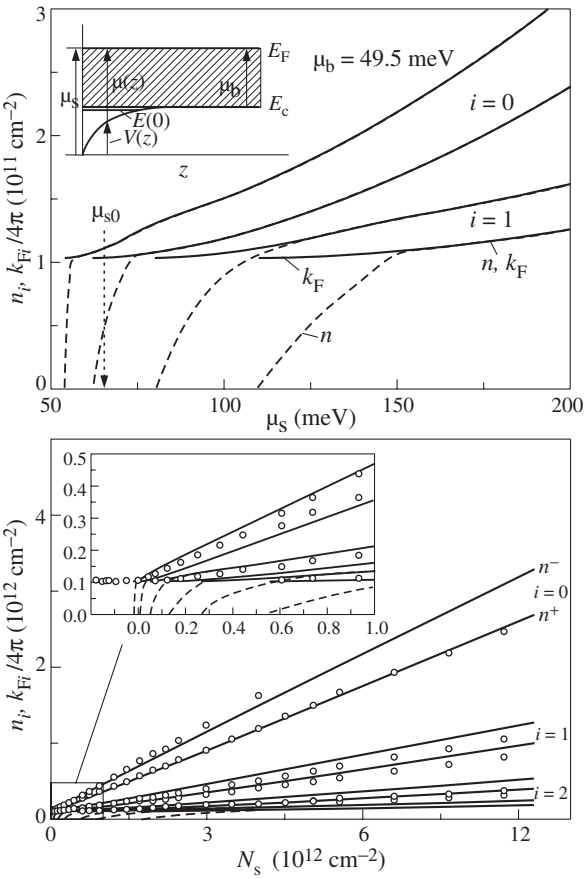

Fig. 2. Calculated subband concentrations n_i and $k_{Fi}^2/4\pi$ values vs μ_s and N_s. Measured values of $k_{Fi}^2/4\pi$ are shown as circles.

oscillations are shown in Fig. 2 also. Unfortunaly, in the accumulation layers the Rashba polarization cannot be measured at high and low subband occupations. At large n_i the only high-energy Rashba branch $E^+(k)$ of spectrum is manifested in the oscillations as is seen in Fig. 2. It is due to the large values of cyclotron mass in $E^-(k)$ branch at large n_i. In n_i ranges, where the 2D states appear, the Rashba splitting is non resolved in oscillations because of (i) small numbers of oscillations experimentally observed at low n_i, and (ii) large numbers of oscillations between beating nodes that is caused by extremely small difference in the values k_{Fi}^+ and k_{Fi}^- (Fig. 1). As a result, the beats of oscillations are not observable in the KBS occupation regime.

For large enough n_i the calculated Rashba polarization is practically N_s independent (see Fig. 3) and is close to its value in inversion layers at moderate doping level. At the same times, it can be seen in Fig. 1–3 that, in N_s range near 2D subband starts, the $\Delta E/E_F$ value as well as the $P_{RF} = ((k_{Fi}^-)^2 - (k_{Fi}^+)^2)/((k_{Fi}^-)^2 + (k_{Fi}^+)^2)$ ratio (beyond KBS filling regime this quantity coincides with P_R) are decreasing at decreasing N_s (μ_s), especially in the kinetic binding regime. Thus, in accumulations layer as well as in inversion one, the P_{RF} becomes to be V_g-sensitive at small enough n_i.

However, the gate-voltage dependence of P_{RF} is essentially different in two cases. In inversion layers, the additional electric field due to the charge in depletion layer magnifies the SO splitting. Because this contribution is particularly significant at small n_i, the Rashba polarization at low n_i is higher than in SQWs on non-doped substrate and P_{RF} decreases with n_i [2]. In contrast, in accumulations layer P_{RF} is lower as compared

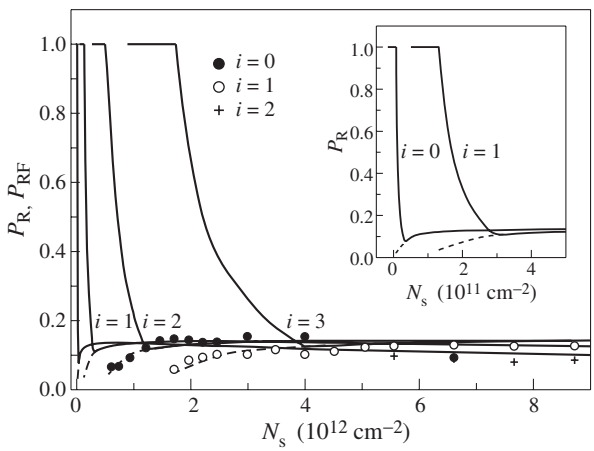

Fig. 3. Calculated values of P_R (solid lines) and P_{RF} (dashed lines) as a function of N_s. Measured values of P_{RF} are shown as the symbols.

with SQWs on non-doped substrate because of contribution in screening arising from mobile charge of continuum electron and P_{RF} increases with n_i. This behavior agrees qualitatively with experiment. However, the theory overestimates the SO splitting at small n_i. Experimentally, the decreasing of P_R and P_{RF} fall on the range of N_s values, which is higher than it predicted by the theory (Fig. 3). It may be noted that in inversion layers the theory underestimates splitting at low n_i [2].

At first sight, the above results show that the inversion layers are more preferable for spintronics devices because of larger values of Rashba splitting and P_R. However, if we take into account the distinctive features of occupation in kinetic binding regime, the situation changes. In KBS filling regime, the subband concentration increases with deepening of SQW mainly because of decreasing of k_{ci} whereas k_{Fi} in this regime is practically pinned to its value in bulk (see Fig. 2). Because $k_{ci}^+ > k_{ci}^-$, the populating of high-energy Rashba sub-subband $E^+(k)$ occurs at higher N_s values. As a result, although ΔE and P_{RF} decrease with decreasing N_s, the Rashba polarization P_R increases (Fig. 3) owing to depopulation of $E^+(k)$ spin branch at near-constant population n^- of low-energy branch. When termination energy $E^+(k_{ci}^+)$ ascends above the Fermi level, the states of this branch are entirely depopulated and Rashba polarization reaches 100%. As is seen from Fig. 2, 3, 100% Rashba polarization takes place in wide enough N_s range.

Acknowledgement

This work has been supported by the Grant RFBR (03-02-16305) and Award of the U. S. CRDF (REC-005).

References

[1] W. Zawadzki *et al*, *Semicond. Sci. Technol.*, **19**, R1 (2004).
[2] V. F. Radantsev *et al*, *Physica E*, **20**, 396 (2004).
[3] O. V. Konstantinov *et al*, *Sov. Phys. JETP*, **31**, 891 (1970).
[4] G. A. Baraff *et al*, *Phys. Rev. B*, **5**, 475 (1972).
[5] R. Doezema *et al*, *Phys. Rev. Lett.*, **57**, 762 (1986).
[6] M. Kubisa *et al*, *Semicond. Sci. Technol.*, **57**, S246 (1993).
[7] V. F. Radantsev *et al*, *Sov. Phys. JETP*, **95**, 491 (2002).

13th Int. Symp. "Nanostructures: Physics and Technology"
St Petersburg, Russia, June 20–25, 2005

Coherent control of ac spin currents via excitonic quantum interference in semiconductor quantum wells

I. Rumyantsev and J. E. Sipe
Department of Physics, University of Toronto, 60 St George Street, Toronto, Ontario, M5S 1A7, Canada

Abstract. We show theoretically how spin-polarized and pure spin AC currents can be optically injected in semiconductors via quantum interference between excitonic 1s and 2p states. Controllable by a choice of the polarizations of the corresponding optical pulses, a linear pure spin current, a linear spin-polarized charge current, or a circular spin-polarized charge current can be excited. The electrical currents may be observed by their THz radiation.

Introduction

Effective control and manipulation of the spins and spin currents is one of the central aims of spintronics [1]. There have been a number of recent theoretical proposals and experimental realizations of spin-polarized charge currents [2]. Spin-polarized carriers can be generated optically and then swept by an applied external electric field, injected through contacts with magnetic materials, or manipulated all-optically. Pure spin currents, with no charge transport, have also been observed experimentally [3,4]. All these experiments have dealt with what is essentially a DC spin current. A natural question is whether or not it is possible to produce a pure spin analog of AC current. We are aware of one proposal [5] for such a current, in which the spin current is generated by modulating the Rashba spin-orbit coupling using an applied voltage. In this scheme both the generation and detection are all-electric.

Here we show theoretically how an AC pure spin current can be generated all-optically. Our method relies on quantum intereference in a semiconductor 3-level system, in both time and space. As far as the optical excitation is concerned, our method of optical current injection is reminiscent of one used earlier [3,4]. There a quantum interference between one- and two-photon processes, involving light at frequencies 2ω and ω respectively, leads to constructive or destructive interference in the promotion of an electron from valence to conduction band at a given crystal momentum $\mathbf{k}$, depending on a relative phase parameter of the two beams. Constructive interference at $\mathbf{k}$ can be accompanied by destructive interference at $-\mathbf{k}$, and an asymmetry in the $\mathbf{k}$-space distribution of generated carriers then results. Large net currents, on the order of some KAmp/cm^2, can be optically injected even in bulk semiconductors at room temperature. By a clever choice of the phases and polarizations of the exciting optical pulses the currents can be spin-polarized, or pure spin currents without accompanying electrical currents can be injected. Most experiments to date have been done on GaAs, which is the material we consider here.

Rather than exciting carriers in the continuum [3,4], we propose a scheme in which optical coupling is used to connect the crystal ground state to bound excitonic states. In such an experiment the 2ω field would excite exciton states of s-symmetry through a one-photon processes, and the ω field would excite exciton states of p-symmetry through a two-photon process [6]. Note that while in most quantum interference processes the two transition amplitudes connect the same initial and final states, here the two final states, one of s-symmetry and one of p-symmetry, are distinct and indeed at different energies. Yet if pulses of the combined light at ω and 2ω are short enough, a relative phase parameter of the optical beams will be imprinted on the final superposition of the two states, and the resulting phase of the oscillation of the dipole moment of the final state will bear witness to that relative phase parameter.

1. Model and results

In order to obtain a quantitative estimate of this effect we consider here a quantum well geometry, including in the calculation only the heavy hole valence bands. Thus our single-particle energies are limited to the doubly degenerate conduction and valence bands labelled respectively by the z component of spin $s = \pm 1/2$ and $j = \pm 3/2$. The first order Coulomb correlations lead to the formation of an excitonic manifold. In our analysis we keep only the $1s$ and $2p$ states, as the rest of the excitons and the continuum states can only change some quantitative features of the effect, but will not affect our results qualitatively. Thus our model reduces two degenerate 3-level systems made up of semiconductor vacuum, $1s$, and $2p$ states; the degeneracy is associated with spin. This situation is schematically shown in Fig. 1.

We will show that, since the $1s$ and $2p$ excitonic states have different radial symmetry, the excitation of a superposition of these states leads to an asymmetry of the electron and hole distributions in $\mathbf{k}$-space. As in earlier works [3,4], this will lead to a controllable current, which can be an electrical current or a spin current depending on the choice of polarizations of the light pulses. Since the energies of the exciton states are different, the resulting current will oscillate with a difference

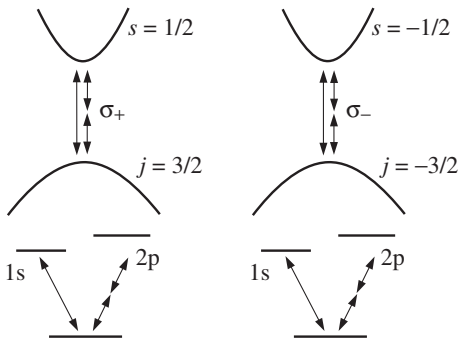

Fig. 1. Schematic of the model lateral band structure of the GaAs quantum well. The lowest conduction and heavy-hole subbands are shown for the two spin subsystems. Respective excitonic 3-level systems involving 1s and 2p states are show at the bottom of the figure.

different, the resulting current will oscillate with a difference of the $1s$ and $2p$ frequencies.

To put this simple picture in a quantitative framework we use the dynamically controlled truncation (DCT) technique. This microscopic approach has been used numerous times (see, *e.g.,* Axt and Kuhn [7] for a related recent review and further references) to treat coherent optical effects in semiconductors. To find the optically injected electrical (or spin) current we calculate the wave vector dependent populations of the electrons $f_s(\mathbf{k})$, where the subscript s labels the spin, within the second order limit of DCT. Anticipating that the $1s$ and $2p$ excitonic states are going to dominate the dynamics, it is convenient to project the equations of motions for the densities onto the excitonic eigenstates and truncate the expansion at the $2p$ level.

In this case the populations may be written (schematically) as $f_s(\mathbf{k}) \propto \left| p_s^{(1s)} + p_s^{(2p)} \right|^2$, $p_s^{(1s,2p)}$ being the amplitude of the respective transitions. The interference term in this expression is a contribution due to the Raman coherence between the $1s$ and $2p$ states carrying the phase information of the optical pulses; it is responsible for the quantum interference effects.

In our calculation, 100 fs gaussian pulses are considered with various polarization combinations: the ω and 2ω fields are taken to be collinearly, cross-linearly, or co-circularly polarized. Both the spectrum of the 2ω pulse, and the spectrum of the ω pulse evaluated at double its frequency argument, are taken to be centered on the transition from the ground state to the $1s$ exciton. Nonetheless, the use of these short pulses means that both spectra will extend to the transition from the ground state to the $2p$ exciton as well. The intensities of the pulses are chosen so that, square root of the product of the exciton densities $\sqrt{n^{(1s)} n^{(2p)}}$ is equal to $10^{16}/\mathrm{cm}^3$. The decay constants of the excitonic polarizations are chosen to be $\gamma^{(1s)} = \gamma^{(2p)} = 0.7/ps$ and the Raman coherence decay rate $\gamma^{(1s2p)} = 1/ps$.

We calculate the electronic current density associated with a spin compone s,

$$\mathbf{J}_s = \frac{e\hbar}{l m_e (2\pi)^2} \int d^2k \mathbf{k} f_s(\mathbf{k}),$$

where e is electron charge, l is the quantum well width, m_e is the effective electron mass. Corresponding results for our polarization combinations are presented in Fig. 2 separately for two spin subsystems. The currents both in x and y direction are plotted respectively with solid and dashed lines. In the case of collinearly polarized beams (x polarized) an electrical current in the same direction is generated. When the beams are cross polarized the charge currents of two spin subsystems is out of phase by π, thus there is no charge current. There is however a pure spin AC current defined as $\mathbf{J}_{1/2} - \mathbf{J}_{-1/2}$. Finally, when the laser pulses have same circular polarization only one subsystem is coupled with the light (in our approximation without light holes) we observe a circular spin-polarized charge current. These currents should of course lead to light emission on a $1s - 2p$ frequency, *i.e.* the THz range. The estimated peak emitted THz power for our model parameters is on the order of 100 μW.

In summary, it is shown theoretically how an AC spin current can be optically injected in a semiconductor. The effect is based on the quantum interference between coherent excitonic states of different spatial symmetry ($1s$ and $2p$ states in our example). These excitons are generated by the one- and two-photon absorption. Depending on the choice of the polarizations of the corresponding optical pulses, a linear pure spin current, a linear spin-polarized charge current, or a circular spin-polarized charge current can be excited.

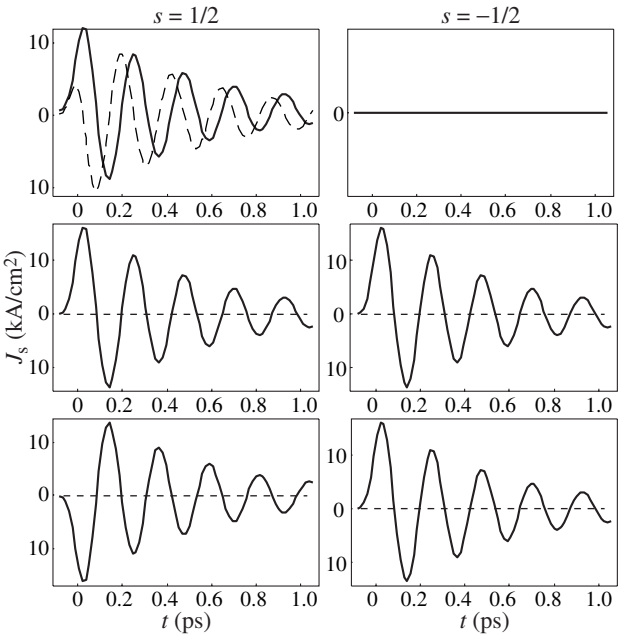

Fig. 2. Calculated currents versus time for the to spin subsystems are plotted in the respective columns (as labelled on top of each column). The three rows of plots correspond respectively to the co-circular, co-linear, and cross-linear polarizations of the ω and 2ω beams. The currents in x and y-direction are plotted respectively with solid and dashed lines.

Acknowledgements

This work was supported by the DARPA SpinS program and the Natural Sciences and Engineering Research Council of Canada. We thank Henry van Driel and Art Smirl, and members of their research groups, for many helpful conversations.

References

[1] S. A. Wolf, D. D. Awschalom, R. A. Buhrman, J. M. Daughton, S. von Molnar, M. L. Roukes, A. Y. Chtchelkanova, and D. M. Treger, *Science* **294** (2001), 1488.

[2] Igor Zutic, Jaroslav Fabian, and S. Das Sarma, *Reviews of Modern Physics* **76** (2004), 323.

[3] J. Hubner, W. W. Ruhle, M. Klude, D. Hommel, R. D. R. Bhat, J. E. Sipe, and H. M. van Driel, *Phys. Rev. Lett.* **90** (2003), 216601/1–4;

[4] M. J. Stevens, A. L. Smirl, R. D. R. Bhat, A. Najmaie, J. E. Sipe, and H. M. van Driel, *Phys. Rev. Lett.* **90** (2003), 136603/1–4.

[5] A. G. Mal'shukov, C. S. Tang, C. S. Chu, and K. A. Chao, *Phys. Rev. B* **68** (2003), 233307

[6] G. D. Mahan, *Phys. Rev.* **170** (1968), 825.

[7] V. M. Axt and T. Kuhn, *Reports on Prog. Phys.* **67** (2004), 433.

13th Int. Symp. "Nanostructures: Physics and Technology"
St Petersburg, Russia, June 20–25, 2005

Spin splitting of donor-bound electrons in InAs-based heterostructures under electrical injection condition

Ya. V. Terent'ev, O. G. Lublinskaya, A. A. Toropov, V. A. Solov'ev, S. V. Sorokin and S. V. Ivanov
Ioffe Physico-Technical Institute, St Petersburg, Russia

Abstract. Photo- and electro- luminescence (PL and EL) of InAs bulk layers manufactured by molecular-beam epitaxy (MBE) have been measured in an external magnetic field in Faraday geometry. PL spectra exhibit peaks attributed to donor–valence band and donor–acceptor pair recombination. The peaks are slightly-polarized and are not split by magnetic field within the experimental accuracy. EL demonstrates only one significantly broadened peak with its maximum located close to a donor-bound electron–valence band transition energy. The EL contour is characterized by strong splitting into two polarized components. In the magnetic fields below 2T the observed splitting is about twice as much as the expected Zeeman splitting of conduction electrons, but in higher fields it saturates. The conjecturable mechanism of the phenomenon is based on the model of spin-triplet states of double-donors excited by electric field, whereas their ground states are spin singlets.

During the last decade spin-related phenomena in semiconductors have been extensively studied due to their potential application for spin devices. Most of semiconductors have a small value of g factor and one needs to strengthen the phenomena dependent on a magnetic field by doping them with magnetic ions. Exchange interaction between conduction electrons and the magnetic ions in diluted magnetic semiconductors (DMS) can enhance the effect of the magnetic field on electron spins by two orders of magnitude. However, the spin splitting in DMS dramatically vanishes with temperature, which limits appreciably the practical applications of DMS-based spintronic devices. Alternatively, one can involve narrow band compounds such as InSb or InAs having rather large intrinsic g-factors (-48 and -14.8, respectively) together with extremely small electron effective masses and high carrier mobility.

In this paper we report on the new spin-related phenomena experimentally observed in InAs under electrical injection conditions. Experimental samples were grown by molecular beam epitaxy. Two sorts of structures have been studied — the bulk InAs layers (for photoluminescence (PL) experiments) and diode structures (for electroluminescence (EL) measurements). In the latter samples the active region is formed by bulk InAs (the layer thickness is 0.3 μm) bordered by p-AlGaAsSb:Be ($p \sim 10^{18}$ cm^{-3}) and n-CdMg(Mn)Se:Cl ($n \sim 10^{18}$ cm^{-3}) regions. InAs was not doped intentionally, but its background electron concentration was as high as $n \sim 510^{16}$ cm^{-3} at $T = 78$ K as deduced from Hall measurements. A thin (300 Å) InAs layer adjacent to p-AlGaAsSb also was heavily p-type doped to move the p-n junction away from the heterointerface. The AlGaAsSb and CdMg(Mn)Se border layers form high potential barriers for electrons and holes respectively (see Fig. 1), well confining injected carriers within the active region. Furthermore, such design allows one to increase the injection efficiency due to the suppression of a "nonradiative" leakage current [1]. The part of cathode doped with Mn is separated from InAs with a 40 Å nonmagnetic buffer CdMgSe to eliminate the exchange interaction between the magnetic ions Mn^{2+} and charge carriers in InAs[1]. The circular 200 μm mesa with a ring ohmic contact was fabricated by conventional photolithography and wet chemical etching. The sample produced for PL

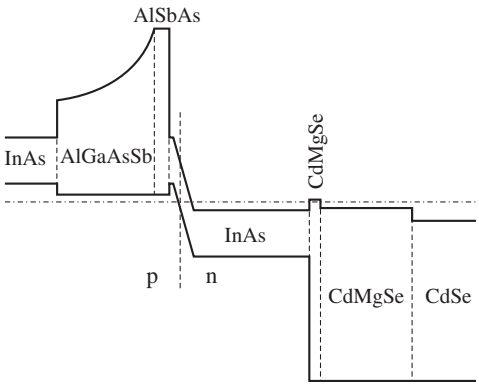

Fig. 1. Design of the diode structure for EL studies.

experiments differs mainly by the absence of a heavily doped CdMg(Mn)Se cap layer. Circularly polarized PL and EL spectra have been measured in magnetic fields up to 4 T in Faraday geometry at $T = 2$ K.

The emission of a semiconductor laser with $\lambda = 809$ nm was used for the excitation of PL. Light with power 50 mWt,â has been focused in a spot with the sizes 0.5×2 mm. Injection current in EL experiments was equal to 50 mA. The PL and EL experimental spectra for several values of a magnetic field are presented In Fig. 2. At zero field the PL spectrum contains two peaks with their energy smaller than the InAs band gap ($E_g = 416.8$ meV [2]). Peak D answers recombination through the ground state of shallow donors, and peak DA is red-shifted by 1.5 meV, which corresponds to the donor-acceptor pair (DAP) mechanism of recombination. In the EL spectra, there is one wide asymmetric contour, which is well described by the superposition of peak D and one more spectral component C with its energy above the InAs band edge. This implies that free electrons also give the appreciable contribution to the EL signal. Note that the zero field PL peak also has a high-energy shoulder attributed to the recombination of free electrons, but its contribution is much weaker. Peak DA is practically invisible in the EL spectra that is explained by easy saturation of the DAP transitions. When the external magnetic field is applied, the PL and EL spectra alter differently. As to PL, the free-electron shoulder vanishes with the field increase and the emission peak moves to higher energies, first much slower than the cyclotron energy of free electrons does. It means that the respective ionization energy increases with

[1]The initial sample design has been focused on the studies of spin injection from CdMnSe to InAs.

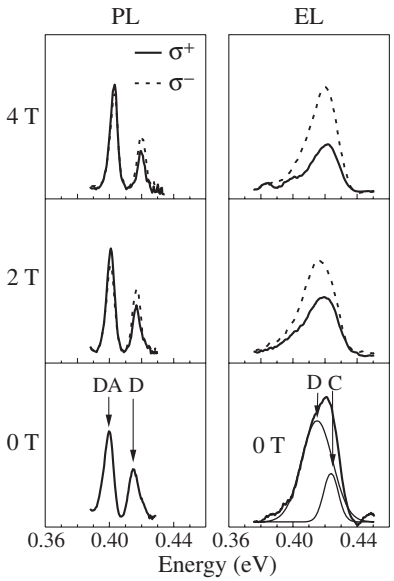

Fig. 2. Circularly polarized photo- and electroluminescence spectra recorded in an external magnetic field.

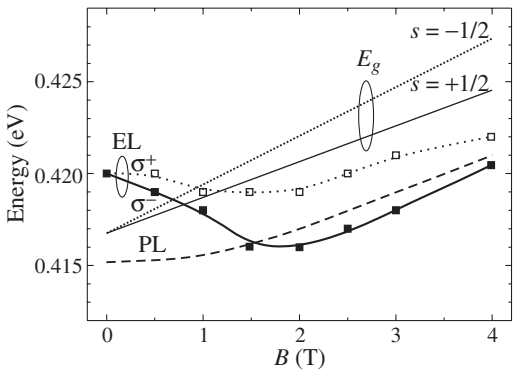

Fig. 3. Photo- and electroluminescence peaks position and calculated ground Landau level free-electron states with s=±1/2 vs magnetic field. For EL both circularly polarized components are presented as they are split by magnetic field; The PL contour has not been split and its energy dependence is shown by one curve.

the magnetic field. At higher magnetic fields the peak position aspires to the $\hbar\omega_c/2$ dependence. (see Fig. 3). This behavior evidences the effect of magnetic freeze-out, well pronounced usually in semiconductors with small effective masses.

The unexpected observation is that the peak is not split by the magnetic field into polarized components, though emission has a small degree of circular polarization (about -15%). FWHM of the PL contour totals 6 meV and does not vary with the field up to 4 T.

The behavior of EL is more complex. At zero field the recombination of hot electrons (component C, EL in Fig. 2) constitutes a large additive to donor-bound electrons (peak D) so that "centre of gravity" of the EL spectrum lies 3 meV higher than E_c. Application of the magnetic field firstly, modifies density of states, concentrating free electrons near the bottom of the conduction band and secondly, increases the Bohr energy of a donor (the effect of magnetic freeze-out). As a result, the component C disappears due to redistribution of electrons between conduction band and donors and "centre of gravity" shifts below E_c. Note that the EL peak is much wider than the PL one. When the magnetic field increases from 0 up to 4', the peak FWHM decreases from 24 to 20 meV. Furthermore, the EL peak undergoes strong splitting into two components demonstrating a high degree of σ- polarization (up to 38% at $B = 4$ T), the σ- polarized peak being the lowest one. This evidences that the electron g factor is negative. Note that if the injected carriers kept the spin orientation got as the result of exchange interaction with Mn^{2+} ions, they would contribute to the opposite sign of polarization. Thus, the role of spin injection in these experiments is negligibly small due to, most probably, sufficiently fast spin relaxation in InAs.

We attribute the distinctive features observed in PL and EL spectra of InAs in a magnetic field to the effects caused by the high concentration of donors. Indeed, in our samples $a_B \cdot N_D^{1/3} \sim 1$, which means that the average distance between donors is comparable with the electron Bohr radius a_B. Even at smaller concentrations, due to strong correlation in donors distribution, the two-donor complexes can be formed [3]. The ground state of such complex is spin singlet whereas the excited one is triplet. Apparently, the ground donor states contribute mainly to the unsplit PL emission, whereas the excited energy levels can be involved in the EL process. In the latter case, the electric field of the order of 3×10^3 V/cm is applied to the InAs region, which is strong enough to excite the donor-bound electron via impact ionization or direct excitation. Furthermore, the electron localization volume is significantly larger for the excited states than for the ground one. It looks very plausible that the luminescent peak broadening is inhomogeneous and is caused by electron scattering on charged impurities (our samples contain about 10^{16} cm^{-3} of ionized impurities). Then the large FWHM of the EL contour as compared to the PL line is consistent with the general reasons stated above. The detailed theoretical analysis of the considered recombination processes has not been performed yet, which is connected to difficulty of the analytical description of multinuclear complexes. Work in this direction is currently in progress.

Acknowledgements

This work was supported partly by RFBR 03-02-17566, PS Department of RAN and Volkswagen Foundation I77/856. S.V.I acknowledges the support of RSSF.

References

[1] S. V. Ivanov *et al*, *Applied Phys. Lett.* **78**, 1655 (2001).
[2] Y. Lacroix, C. A. Tran, S. P. Watkins, and M. L. W. Thewalt, *J. Appl. Phys.* **80**, 6416 (1996).
[3] I. V. Ponomarev and V. V. Flambaum, A. L. Efros, *Phys. Rev. B* **60**, 5485 (1999).

13th Int. Symp. "Nanostructures: Physics and Technology"
St Petersburg, Russia, June 20–25, 2005

Spin interaction effect in quasi-one-dimensional GaAs-AlGaAs quantum wires array observed in high field Zeeman

Jong-Chun Woo[1], In-Taek Jeong[1], Sungmin Ahn[1], Tae-Suk Kim[1] and Xing Wei[2]

[1] School of Physics, Seoul National University, Seoul 151-747, S. Korea
[2] NHMFL, Florida State University, Tallahassee, FL 32310, U.S.A.

Abstract. The Zeeman splitting in GaAs/AlGaAs quantum wire array has been measured by polarization dependent photoluminescence at high magnetic field. It shows an abrupt change in its field dependence at the field the Landau orbit approaches to the array period. This anomalous change is explained with the presence of electron-electron coupling with its orbital motion.

Introduction

In recent years, the electronic spin property in low dimensional semiconductors, especially one-dimensional (1-D) quantum wire (QWR) [1-3] and zero-dimensional (0-D) quantum dot [4, 5] attracts great attention in recent years due to its cause being related to spin degeneracy, which is closely related to possible application in quantum computation and spin memory device.

So far, for the 0-D and 1-D semiconductor structures, most of available information related to the spin interaction is through the conductance measurement, and the direct measurement on the field-dependent energy of spin state is rarely available. [6-8] In this work, presented is the direct observation of field dependent energy level of the spin states in quasi-1-D electronic system from the circular polarization dependent magneto-photoluminescence (PMPL) measurement. An anomalous and abrupt change of Zeeman separation at the Landau orbit approaching to the QWR period is observed. Also noticed is the field dependent oscillatory behavior. One of the possible interpretations is the effect caused by electron-electron interaction due to the many body effect.

Experiment

The GaAs-$Al_{0.5}Ga_{0.5}As$ QWR array sample was grown on vicinal cut GaAs substrate by migration enhanced molecular beam epitaxy with the layer thickness control of fraction of monolayer (ML). Its typical size is QWR width of 8 nm and the array period of 16 nm with the QWR height of 8 and 16 nm with a single layer of QWR. The TEM image of the array is shown in Fig. 1, where the dark image represents the QWR. The PMPL has been performed using Ar-ion laser excitation and circular polarizers of $\lambda/4$ and $3\lambda/4$ at LHe temperature. This is to detect the radiative recombination of the ground state excitions, i.e. those coupled between conduction electrons (CE) of $m_s = \pm 1/2$ states and heavy holes (HH) of $m_j = \pm 3/2$ states. The magnetic field (B) of 0 to 32 T was applied perpendicular to the plane of QWR array, i.e., Faraday geometry. The spin up and down states was also measured by reversing the field direction

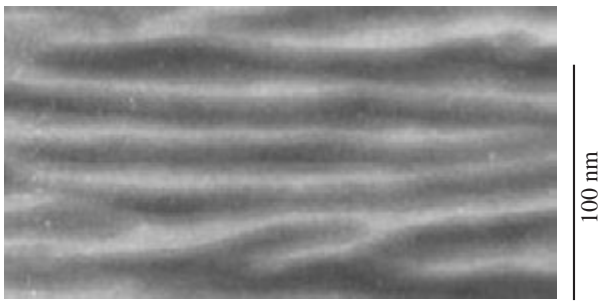

Fig. 1. TEM image of QWR cross-section.

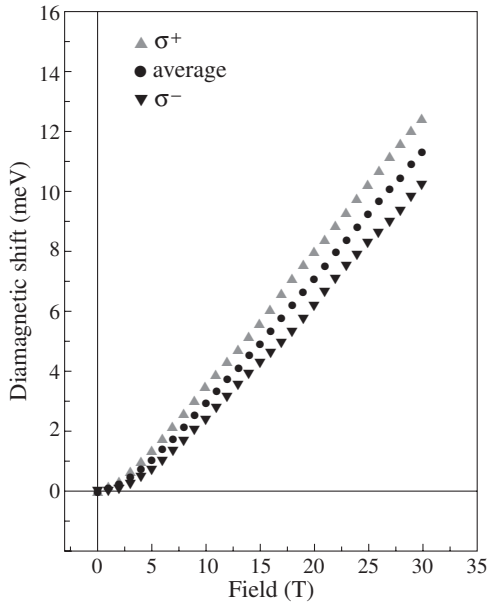

Fig. 2. Field-dependent PMPL peak position of $\sigma+$ and $\sigma-$ spectra.

Results

The Zeeman separation has been obtained from the photon energy difference between $m_s = 1/2$ to $m_j = 3/2$ transition ($\sigma+$) and $m_s = -1/2$ to $m_j = -3/2$ ($\sigma-$). The B-dependent peak positions of PMPL spectra, $\sigma+$ and $\sigma-$, and Zeeman, their difference, are summarized in Fig. 2 and Fig. 3, respectively. In Fig. 2, the B-dependent change of $\sigma+$ and $\sigma-$ peak positions is significant. The observed $\sigma+$ and $\sigma-$ peak positions are well fit to quadratic in B at low field region showing diamagnetic shift and becomes linear in B at the high field region indicating formation of Landau orbit. The noticeable diamagnetic shift could be understood introducing harmonic potential for the 1-D confinement. From the diamagnetic shift and the Landau rela-

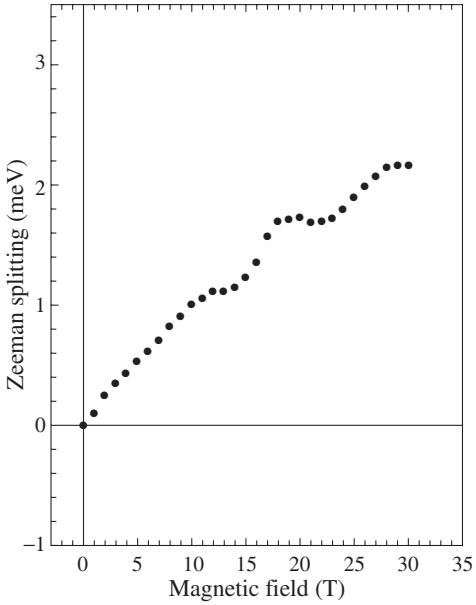

Fig. 3. Zeeman Separation obtained from the difference of $\sigma+$ and $\sigma-$.

tion, we could extract out the effective mass of electrons. Since the effective mass of CE is much smaller than that of HH, it is assumed that the B-dependence is dominated by the electron. In the Zeeman results shown in Fig. 3, two points are noticed. The first point is the obtained g-value is unusually large and positive, which is contracting to that of electronic g-value in bulk GaAs and GaAs quantum well (QW) of this QW height. The second point is that an anomalous and abrupt change of B-dependent Zeeman separation occurs at B where $D_c \approx L_p$. Here D_c and L_p are the diameters of cyclotron orbit and the period of QWR array, respectively. The extrapolation of the B-dependence for $D_c > L_p$ and $D_c < L_p$ region convincingly shows the presence of zero-field splitting in the high magnetic field where $D_c < L_p$. In addition to the abrupt discontinuity of the slope, clearly apparent is the B-dependent oscillatory behavior.

Discussion

The QWR result was cross-checked with two samples of 2-D confinement; the one is multiplayer GaAs-AlGaAs QW superlattice of 20 nm period. We observed Zeeman in Voigt geometry simulating the cyclotron orbit experiencing 1-D like array potential. Another is the $Al_{0.25}Ga_{0.75}As$-$Al_{0.5}Ga_{0.5}As$ QW in Faraday geometry for alloy and/or possible band crossing effect. Both observations support that the observed Zeeman results accompanying zero-field splitting in the QWR SL is genuinely from the1-D effect.

The occurrence of the zero-field splitting caused with increasing electronic localization in 1-D constriction can be explained electron spin coupled with cyclotron orbital motion whose orbital angular momentum is quantized.

Acknowledgements

This work is supported in part by KRF of Korea. The PMPL measurement is performed with the facility and technical help of NHMFL at Florida State University, U.S.A.

References

[1] K. J. Thomas *et al*, *Phys. Rev.* **B 58**, 4484 (1998).
[2] K. S. Pyshikin *et al*, *Phys. Rev.* **B 62**, 15942 (2000).
[3] N. T. Bagraev *et al*, *Phys. Rev.* **B 70**, 155315 (2004).
[4] B. I. Halperin *et al*, *Phys. Rev. Lett.* **86**, 2106 (2001).
[5] D. M. Zumbuhl *et al*, *Phys. Rev. Lett.* **89**, 276803-1 (2002).
[6] R. Rinaldi *et al*, *Phys. Rev. Lett.* **77**, 342 (1996).
[7] W. Heller and U. Bockelmann *Phys. Rev.* **B 55**, R4871 (1997).
[8] M. Notomi *et al*, *Physica* **B 249-251**, 171 (1998).

13th Int. Symp. "Nanostructures: Physics and Technology"
St Petersburg, Russia, June 20–25, 2005

10 Gb/s data modulation and 50 GHz mode locking using 1.3 μm InGaAs quantum dot lasers

M. Kuntz[1], G. Fiol[1], M. Lämmlin[1], D. Bimberg[1], A. R. Kovsh[2], S. S. Mikhrin[2], A. V. Kozhukhov[2], N. N. Ledentsov[1,2], C. Schubert[3], V. M. Ustinov[4], A. E. Zhukov[4], Yu. M. Shernyakov[4], A. Jacob[5] and A. Umbach[5]

[1] Institut für Festkörperphysik, Technische Universität Berlin, Hardenbergstr. 36, 10623 Berlin, Germany
[2] NL Nanosemiconductors GmbH, Von-Fraunhofer-Str. 13, 44227 Dortmund, Germany
[3] Fraunhofer-Institut für Nachrichtentechnik Heinrich-Hertz-Institut, Einsteinufer 37, 10587 Berlin, Germany
[4] Ioffe Physico-Technical Institute, St Petersburg, Russia
[5] u2t photonics AG, Reuchlinstrasse 10/11, 10553 Berlin, Germany

Abstract. Error free 8 and 10 Gb/s data modulation with InGaAs quantum dot lasers emitting at 1.3 μm is presented. 12 Gb/s open eye patterns are observed. An integrated fiber-optic QD laser module yields error free data modulation at 10 Gb/s at a receiver power of –2 dBm. Passive mode-locking is achieved from very low frequencies up to 50 GHz, hybrid mode-locking is achieved up to 20 GHz. The minimum pulse width of the Fourier-limited pulses at 50 GHz is 3 ps.

Introduction

The development of InGaAs quantum dot (QD) lasers [1,2] with 1.3 μm emission wavelength [3,4] showing very low threshold current, T_0 of 200–300 K at room temperature, suppressed beam filamentation, and feasibility of 10 Gb/s data modulation [59] presents a break-through towards the exploitation of nanotechnology for novel data- and telecom low cost, high performance systems. P-doping of the active region [10] and resonant tunnel injection of carriers [11] have partly contributed to this success.

For high frequency applications optical comb generators operating in the 10–40 GHz range and direct modulation at 10 Gb/s are needed. Mode-locking of quantum dot lasers at 1.3 μm with repetition rates up to 35 GHz and cut-off frequencies of 7.4 GHz upon direct modulation were previously reported by us [8, 12–14].

In this work we report on mode-locking with frequencies up to 50 GHz and on the first measurements of 10 Gb/s error free data modulation of 1.3 μm InGaAs QD lasers.

Data modulation of QD lasers

The $Al_{0.35}Ga_{0.65}As$/GaAs laser structures incorporating a tenfold stack of InGaAs quantum dots were grown by molecular beam epitaxy. 1.3 μm wavelength emission was achieved by overgrowth of the QDs with an InGaAs layer and by subsequent activated phase alloy separation [15]. The wafers were then processed into ridge waveguide (RW) structures with stripe widths from 1 to 4 μm by dry etching through the active layer [16].

A 1000 μm long, 1 μm width RW diode with 95% HR coating on the rear facet and backside n-contact was mounted in a fiber-optic module comprising a temperature controlled heat sink, a microwave port with an integrated impedance-matching bias network, and a SMF pigtail. At room temperature, the QD laser module has a threshold current density of 270 A/cm^2, emission wavelength of 1280 nm and a small-signal modulation bandwidth of about 7 GHz.

Eye pattern measurements were carried out back-to-back with the QD module biased at $5-7I_{thr}$ and a non-return-to-zero (NRZ) pseudo-random binary sequence (PRBS, word length of $2^{15}-1$) with 2.5 V_{p-p} amplitude (12 dBm). The average output power into fiber was 1–3 mW. The inset of Fig. 1 shows clearly open 10 Gb/s eye patterns, with a S/N ratio of 6.8, an extinction ratio of 4.9 dB and a peak-to-peak timing jitter of 30 ps. Open eye patterns were observed up to 12 Gb/s. Due to the strong damping of relaxation oscillations in QD lasers, all eye patterns show very little overshoot.

BER measurements were carried out at data rates of 8, 10, 11 and 12 Gb/s, keeping the eye pattern measurement settings. We inserted a semiconductor optical amplifier between laser and BER tester to compensate for optical losses due to a low laser-to-fiber coupling efficiency of 10 %. Fig. 1 shows the BER measurements for the QD laser module. Both for 8 and 10 Gb/s, we achieve error free operation (BER $< 10^{-11}$) at -4.5 dBm and -2 dBm receiver power, respectively. No error floor could be detected. There is a considerable power penalty of 2.5 dB when moving from 8 to 10 Gb/s data rate in agreement with the moderate bandwidth of 7 GHz.

The BER curve at 8 Gb/s follows more or less straight line whereas the data for 10 Gb/s show a curvature that is unexpected. A possible reason for this effect might be a saturation of the RF-amplifier used to amplify the electrical signal at the BER tester.

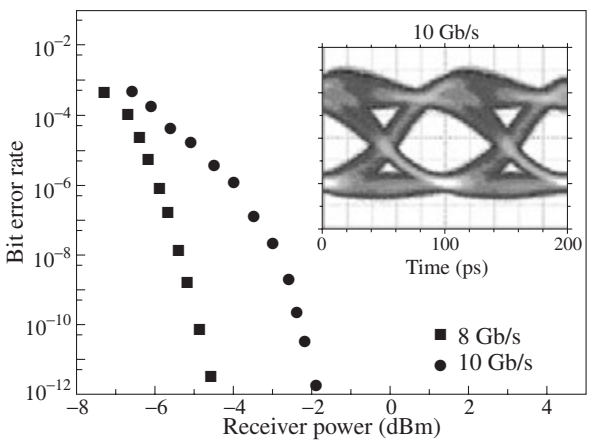

Fig. 1. BER measurement of QD laser module at 8 Gb/s and 10 Gb/s, inset shows the corresponding eye pattern at 10 Gb/s.

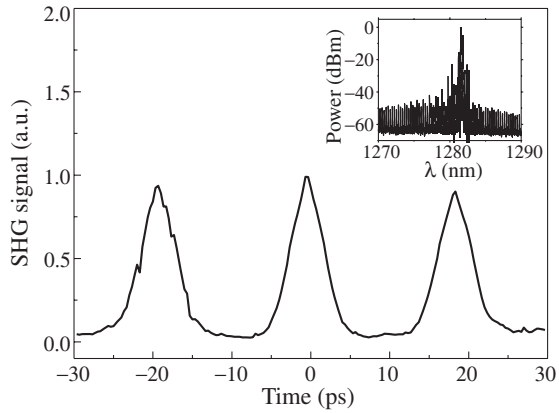

Fig. 2. Autocorrelation trace and wavelength spectrum of a passively mode-locked QD laser at 50 GHz repetition rate.

Passive mode locking

The $Al_{0.80}Ga_{0.20}As$/GaAs laser structure incorporating a five-fold stack of InGaAs quantum dots was grown and processed similar to the aforementioned samples. The samples for mode-locking were processed into two-sectional devices by defining a metallization gap of 20 μm between the sections yielding an electrical insulation above 1 kΩ. Lasers with as-cleaved facets were mounted p-side up on a copper heat sink and were electrically connected to two SMA ports via stripe lines and short (< 400 μm) bond wires.

The samples had 4 μm width RW and lengths between 800 and 8000 μm corresponding to round trip frequencies of 5 to 50 GHz. All samples with length of 1 mm or below were HR coated (95% reflectivity) on the rear facet. All measurements were carried out at room temperature (297 K) and continuous wave.

The two-section devices for mode-locking consisted of a long gain and a short absorber (typically 10–20% of the total length) section operated at reverse bias levels between 0 and -6 V. Time-domain measurements were carried out with an autocorrelator.

Figure 2 shows the autocorrelation (middle peak) and the cross correlation (side peaks) of the pulses from the 800 μm device. The autocorrelation trace was deconvoluted assuming a Gaussian pulse shape, the FWHM pulse width at –6 V absorber bias was 3 ps. This value is in good agreement with the Fourier limit ($\Delta\tau\Delta\nu = 0.44$) estimated from the spectral FWHM. The inset of Fig. 2 shows the spectrum of the mode-locked laser centred at a wavelength of 1280 nm. The peak power from one facet of the mode-locked laser was 6 mW. Comparison of autocorrelation and cross correlation allowed us to estimate the uncorrelated jitter to be less than 1 ps. However, we expect the main jitter contribution to be correlated jitter. Further investigations are required to clarify this question.

Similar Fourier limited characteristics were also found for all other devices at frequencies 5, 10, 20, and 40 GHz. The pulse width to period ratios we achieved at frequencies between 5 and 50 GHz were in the range between 5 and 16%. The minimum pulse width was limited by the maximum reverse bias voltage we estimated to be not harmful for the device.

In order to characterize the dependence of the pulses on parameters like reverse bias, gain current and RF power, we performed series of autocorrelation scans. The lasers were passively mode-locked at currents between I_{thr} and $2{*}I_{thr}$ using reverse bias voltages between 6 and 0 V.

With increasing reverse bias, the onset of lasing shifts to larger currents, due to the increasing absorption within the waveguide. The onset of lasing occurred abruptly as mode-locking, we observed no transition region. With increasing current, the pulses became broader, until we observed a cw offset, i.e. incomplete mode-locking. At even higher currents, we observed a transition region with all kinds of complex pulse patterns until all intensity fluctuations flattened out to cw lasing. The mode-locking range typically lies between I_{thr} and 1.2 I_{thr}, I_{thr} being the threshold at a particular absorber voltage.

As we are yet using only 2% of the intrinsic spectral width of the QD gain medium, there is still plenty of room for reducing the pulse width to levels in the range or below 1 ps. Stacking of more QD layers or the insertion of an ion implanted absorber for stronger absorption are the means to achieve this goal.

1. Conclusion

First error free 8 and 10 Gb/s data modulation with quantum dot lasers emitting at 1.3 μm has been presented. Open 12 Gb/s eye patterns were found. Careful electrical packaging of QD laser diodes yields error free data modulation at 10 Gb/s (BER = 10^{-12}) at a receiver power of –2 dBm. QD laser thus show their suitability for 10 Gb/s ethernet applications. Passive mode-locking of quantum dot lasers at 1.3 μm between 5 and 50 GHz repetition rate show Fourier limited pulses. The minimum pulse width we achieved was 3 ps.

Acknowledgements

Parts of this work are funded by the German Ministry for Education and Research, by the SANDiE NoE of the European Commission (contract no. NMP4-CT-2004-500101) and by the European IST DOTCOM Project.

References

[1] N. Kirstaedter *et al*, *Electron. Lett.* **30**, 1416 (1994).
[2] D. Bimberg *et al*, *Quantum Dot Heterostructures*, John Wiley & Sons, Chichester, 1999; D. Bimberg, *J. Phys.D* **38**, 1 (2005).
[3] D. L. Huffaker *et al*, *Appl. Phys. Lett.* **73**, 2564 (1998).
[4] Yu. M. Shernyakov *et al*, *Electron. Lett*. **35**, 898 (1999).
[5] C. Ribbat *et al*, *Appl. Phys. Lett.* **82**, 952 (2003).
[6] S. M. Kim *et al*, *IEEE Phot. Technol. Lett.* **16**, 377 (2004).
[7] K. Otsubo *et al*, *Japan. J. Appl. Phys*, **43**, L1124 (2004).
[8] M. Kuntz *et al*, *New J. Phys.* **6** (2004).
[9] M. Kuntz *et al*, *Electron. Lett.*, to be published
[10] D. G. Deppe *et al*, *IEEE J. Quantum Electron.* **38**, 1587 (2002).
[11] P. Bhattacharya *et al*, *IEEE J. Quantum Electron.* **39**, 952 (2003).
[12] M. Kuntz, *Integrated Photonics Research Conference IPRC San Francisco*, IThD4, OSA (2004).
[13] M. G. Thompson *et al*, *Electron. Lett.* **40**, 346 (2004).
[14] M. Kuntz *et al*, *Appl. Phys. Lett.* **85**, 843 (2004).
[15] V. M. Ustinov *et al*, *J. Crystal Growth* **227-228**, 1155 (2001).
[16] D. Ouyang *et al*, *Semicond. Sci. Technol.* **18**, L53-L54 (2003).

13th Int. Symp. "Nanostructures: Physics and Technology"
St Petersburg, Russia, June 20–25, 2005

Self-slowdown and -advancement of fs pulses in a quantum-dot semiconductor optical amplifier

M. van der Poel, J. Mørk and J. M. Hvam
Research Center COM, NanoDTU, Technical University of Denmark, DK-2800 Kgs. Lyngby, Denmark

Abstract. We demonstrate changes in the propagation time of 180 femtosecond pulses in a quantum-dot semiconductor optical amplifier as function of pulse input power and bias current. The results interpreted as a result of pulse reshaping by gain saturation but are also analogous to coherent population oscillations. Relative pulse delays (i.e. pulse time delay to pulse FWHM ratio) up to 40% and relative advancements up to 15% are observed when the amplifier is biased at zero current and at currents well above transparency, respectively. Under gain conditions, no pulse distortion is seen while a considerable pulse distortion occurs at zero bias.

Introduction

Tunability of pulse propagation time through an optical medium by means of Coherent Populations Oscillation (CPO) has been proposed as a technique for realizing optical components with storage capability [1,3]. One advantage of CPO compared to other slow-light techniques, such as e.g. electromagnetic induced transparency [2], is its insensitivity to the quantum mechanical coherence of the optical dipoles in the optical medium interacting with the signal light. CPO has been demonstrated to slow down light to 59 m/s at room-temperature in a Ruby crystal [1].

In this paper we demonstrate self-delay and -advancement of a femtosecond optical pulse in a Quantum-Dot (QD) Semiconductor Optical Amplifier (SOA) at room temperature. We interpret the results as a reshaping of the pulse envelope due to gain saturation. We believe, however, that the observed effect is similar to the CPO effect reported by Bigelow *et al.* [1]. The relative pulse shift is found to be up to 40% and 15% when the SOA is run below and above transparency, respectively. These values are comparable to the relative pulse shifts due to CPO reported in literature [1] where, however, pulsewidths on the order of 10 ms were considered.

1. Experiment and sample details

A ridge-waveguide SOA (length 2 mm, width 7 μm) with 5 sheets of self-assembled InAs/GaAs QDs as active layer [4] was used in the experiments. The QD ensemble showed a GS emission wavelength of 1260 nm and was probed with a laser pulse of 180 fs duration and wavelength of 1262 nm from a Ti:Sapphire laser + regenerative amplifier + optical parametric amplifier cascade. The probe pulse was derived from the laser source by an acousto-optic modulator (AOM) and coupled in and out of the SOA by means of microscope objectives. The total insertion loss of the QD SOA when operated at transparency was found to be 18 dB. The probe intensity could be changed over two orders of magnitude by varying the AOM drive voltage without changing its absolute temporal position. The probe propagation time and pulse distortion as function of probe power and SOA bias current were characterized by performing cross-correlation with the probe pulse and a reference pulse in a heterodyne detector.

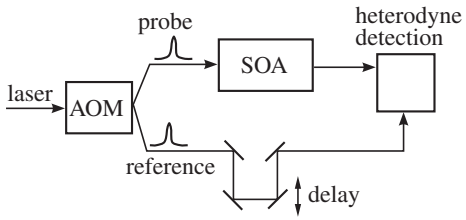

Fig. 1. Schematic overview of the experimental setup.

2. Results and discussion

Fig. 2a shows how the pulse propagation time through the SOA changes as function of pulse power and bias current. At injection currents well above the transparency point of 15 mA, a gradual relative pulse advancement up to 15% (absolute pulse advancement of 30 fs) is seen as the pulse power is increased to the highest available power. Oppositely we observe below transparency a gradual relative pulse slow-down of up to 40% (absolute slow-down of 70 fs) with increasing probe power. The onset of pulse slowdown or advancement is closely connected to saturation of the SOA. The right axis in Fig. 1a shows the zero-bias gain. In the small pulse power regime, the absorption stays constant. At higher pulse powers the absorption is bleached due to saturation of the QDs. At the very high-

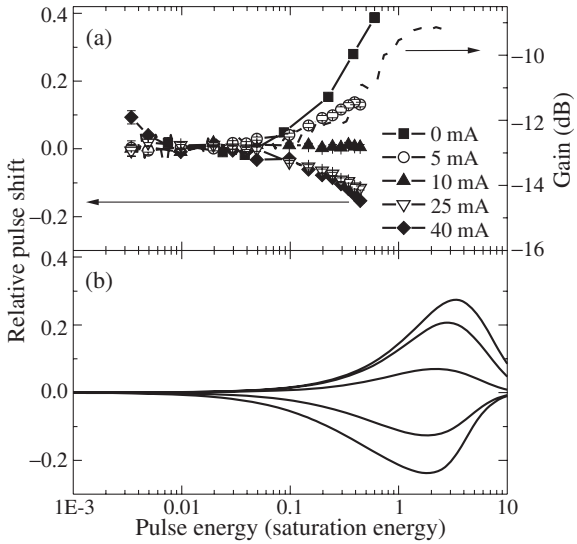

Fig. 2. a) Change in propagation time of a 180 fs pulse in a QD SOA for different pulse energies and bias currents. Absorption at zero bias is shown on the right y-scale. b) Results of pulse delay modelling under conditions corresponding to the data shown in a).

est pulse powers the bleaching is seen to level off due to an increased two-photon absorption.

The observed shift in pulse propagation time can be understood as a result of gain saturation in the SOA: In the gain regime the rising edge of the pulse burns a spectral hole in the carrier distribution so that the back side of the pulse experiences less gain. During its propagation through the SOA it's center of mass is therefore shifted forward. The opposite happens in the absorption regime. The absorption is bleached by the rising edge of the pulse so that the back side of the pulse is less absorbed. This picture was tested in a simple model of pulse propagation taking into account the intensity-dependent gain. The gain response is assumed to be slow compared to the pulse duration and the gain is characterized by the 3 dB pulse saturation energy E_{sat} and small signal gain G. The latter two quantities were measured independently for different currents. In the limit of small pulse energies E relative to E_{sat} one finds the following expression for the relative time shift $\Delta t/\tau$

$$\frac{\Delta t}{\tau} \approx -\frac{1}{2}(G-1)\frac{E}{E_{\mathrm{sat}}}. \qquad (1)$$

A slightly more sophisticated model, however, allowing one to calculate the relative time shift without the assumption of small pulse energies was used for comparison with the experiment. The result is shown in Fig. 2b. A reasonably good agreement with experiment is seen. Three input power regimes can be identified. At low pulse powers the number of carriers engaged in amplification is so small that no pulse reshaping takes place. In the intermediate spectral-hole burning regime we see a pulse advancement and delay in the amplification and absorption regime respectively. At very high input powers this time shift decreases again toward zero since in this regime the gain is saturated already by the very front of the pulse.

The absolute pulse delay change observed in the experiments is larger for zero bias current (absorption regime) than for high bias currents (gain regime). This feature is not explained by the above theoretical model and we suggest that it can at least be partially explained by the very different gain dynamics occurring in the gain and absorption regimes. Above transparency, the QD gain recovery occurs on a timescale of a few hundred fs due to intradot relaxation, while below transparency the absorption bleaching is long-lived and extends for tens of ps [5]. This implies that a partial gain recovery may be possible during the pulse in the gain regime while this is not so in the absorption regime. From this, one might expect to see a larger pulse distortion and a larger relative time shift of the pulse in absorption than in gain.

Actual amplitude cross correlation traces for two different pulse powers and for a bias current well above transparency and at zero bias are shown in Fig. 3. In the gain regime, a small pulse distortion, is seen, while considerable pulse distortion is clearly observed at zero bias. The relatively longer pulse delay times seen in Fig. 1a are therefore connected to a pulse distortion which is not taken into account in the theoretical results of Fig. 2b.

3. Conclusion

We have demonstrated self-slowdown and -advancement of an optical fs pulse in a QD SOA at room temperature. A simple model of pulse propagation taking into account gain saturation has been seen to provide a reasonably good explanation

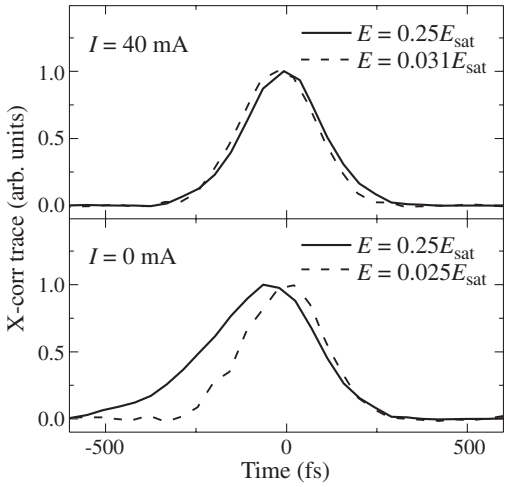

Fig. 3. Change in propagation time of a 180 fs pulse in a QD SOA for different pulse powers and bias currents. Pulse power is measured before incoupling into the SOA waveguide. Absorption at zero bias is shown on the right y-scale.

of the observed phenomenon. At the same time this kind of tuning of pulse propagation time in an absorbing or amplifying optical medium is analogous to CPO. The maximum relative pulse delay of 40% and relative pulse advancement of 15% are comparable to relative pulse shifts seen in other experiments.

Acknowledgements

Alexey Kovsh of the Ioffe Institute (now at NL semiconductor) is acknowledged for growing the QD sample. Matthias Laemmlin and Dieter Bimberg of Technische Universität Berlin is acknowledged for wafer processing. This project was supported by the EU-IST project DOTCOM.

References

[1] M. S. Bigelow, N. N. Lepeshkin and R. W. Boyd, *Phys. Rev. Lett.* **90**, 113903 (2003).

[2] L. V. Hau, S. E. Harris, Z. Dutton and C. H. Behroozi, *Nature* **397**, 594-598 (1999).

[3] P.-C. Ku, F. Sedgwick, C. J. Chang-Hasnain, P. Palinginis, T. Li, H. Wang, S.-W. Chang and S.-L. Chuang, *Opt. Lett.* **19**, 2291 (2004).

[4] A. R. Kovsh *et al.*, *J. Crystal Growth* **250**, 729 (2003)

[5] M.v.d. Poel, E. Gehrig, O. Hess, D. Birkedal and J. M. Hvam, submitted to *J. Quant. Elec.*

13th Int. Symp. "Nanostructures: Physics and Technology"
St Petersburg, Russia, June 20–25, 2005

Q-switching and mode-locking in QD lasers at 1.06 μm

I. M. Gadjiev[1], *A. E. Gubenko*[1], M. S. Buyalo[1], E. L. Portnoi[1], A. R. Kovsh[2], S. S. Mikhrin[2], I. L. Krestnikov[2] and N. N. Ledentsov[2]

[1] Ioffe Physico-Technical Institute, St Petersburg, Russia
[2] NL Nanosemiconductor GmbH, Dortmund, Germany

Abstract. Q-switching (QS) and mode-locking (ML) were studied in 1.06 μm Fabry–Perot QD lasers with a reverse biased section. A broad frequency tuning range of 200–750 MHz was demonstrated by changing the CW pumping level at QS. A pulse peak power of up to 130 mW per facet has been achieved at a single spatial mode. The transition from QS to ML occurred with an increase of absorption section reverse bias. Pulses of 3.4 ps were observed at the repetition frequency of 35.4 GHz at ML.

Introduction

QS and ML QD lasers with a wavelength of 1060–1070 nm are very attractive due to the possibility of further amplification in Yt-doped optical fiber amplifiers to create high-power optical pulse generators. Usually the QS regime is not observed in QD lasers [1–3]. Only a few conference papers on QS exist by this time [4, 5] which report pulses as long as 450 ps with a very narrow repetition frequency tuning range. Mode-locking of monolithic QD lasers at 1.3 μm was reported by several groups [1–3, 6, 7]. The purpose of this work was the creation of high quality Q-switched and mode-locked lasers at $\lambda = 1.06\,\mu$m.

1. Samples

Samples were fabricated in Ioffe Institute using NL Nanosemiconductor's QD laser structures. Wafers were grown by MBE technique with an active layer consisting of 5 layers of InAs/GaAs QDs placed in a 340 nm GaAs waveguide. Two-section 8 μm stripe lasers were processed with one of the sections operating as a saturable absorber (Fig. 1). The cavity length was varied within a range of 0.4–2 mm with an absorber share of 5–15%. Samples were mounted on a copper heatsink and measured at 20 °C.

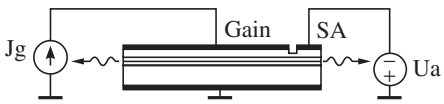

Fig. 1. Schematic image of two-contact laser samples.

2. Experimental

The gain section of laser was DC pumped. The absorber section bias was varied to achieve different dynamic regimes of lasing. Self-pulsations due to passive Q-switching were observed in ∼ 1 mm cavity length lasers at the positive or slightly negative absorber section bias. Pulsations frequency as low as 200 MHz took place at threshold, then grew to a maximum of 780 MHz as the pumping rate was increased. After that, the pulsation regime disappeared. The high-frequency cut-off at QS was earlier attributed to the gain compression at high optical power [8]. In QS DH lasers, this frequency was higher than 10 GHz due to the much lower gain compression factor as compared to QD lasers. Probably the absence of QS in 1.3 μm QD lasers is due to an even higher gain compression in comparison with 1.06 μm lasers. The pulse energy remains

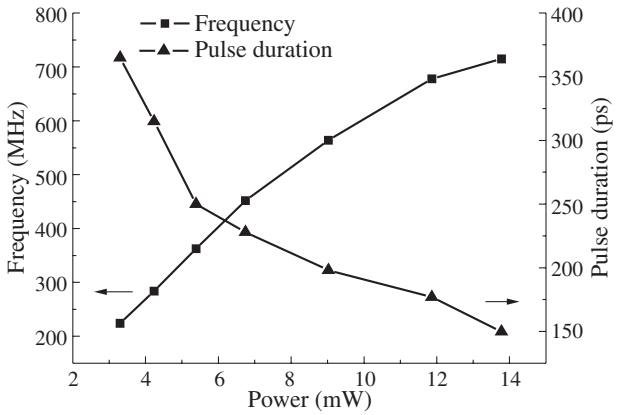

Fig. 2. Pulse duration and frequency as function of optical power, $V_a = 0.7$.

constant at ∼ 15 pJ/per facet within the frequency range of 200–450 MHz, then increases gradually up to 19 pJ. The pulse duration varies from 350 to 145 ps as pumping increases (Fig. 2). The highest peak power of 130 mW was reached at 195 mA and 740 MHz. As the absorber section reverse bias increases, the QS mode transitions to ML. Pure Q-switching takes place at 0.7 V (Fig. 3a) whereas at -2 V, both QS and ML exist simultaneously(Fig. 3b). Further reverse bias increasing makes QS to disappear. ML was achieved at different conditions. Pulses of 3.4 ps were generated with a repetition frequency of 35.4 GHz and an average power of 4 mW per facet at ML (Fig. 4.). Under those conditions, the bandwidth to pulse duration product was $\Delta\nu\Delta t$=1.2 and decreased at lower power.

3. Conclusion

The main results of this work are:

1. The world first demonstration of passive mode-locking at 1.06 μm in QD lasers;
2. Broad frequency range tunable Q-switching in QD lasers;
3. High energy of 19 pJ Q-switched pulses per each facet at single spatial mode.

References

[1] A. E. Gubenko *et al*, *IEEE 19th International Semiconductor Laser Conference Digest*, 2004, pp. 51–52.
[2] A. E. Gubenko *et al*, *12th Int. Symp. "Nanostructures: Physics and Technology"*, St Petersburg, Russia, June 21–25, 2004, pp. 69–70.

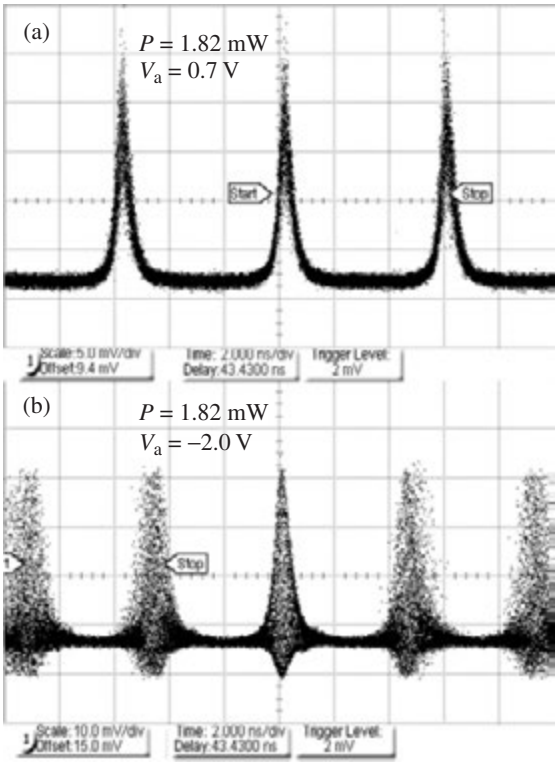

Fig. 3. Transition from QS to ML with increased absorber voltage: a) $V_a = 0,7\,\mathrm{V}$, b) $V_a = -2,0\,\mathrm{V}$. The optical power is the same for both cases.

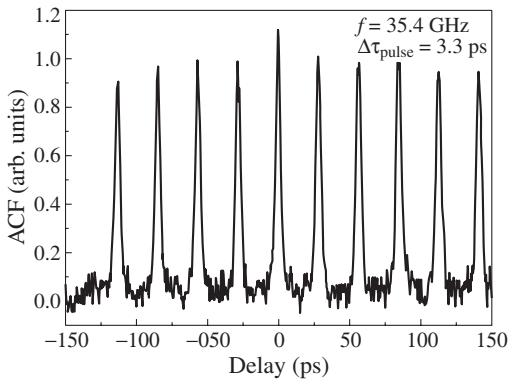

Fig. 4. Second order autocorrelation trace of radiated power at ML.

[3] Xiaodong Huang *et al*, *Appl. Phys. Lett.* **78**, 2825 (2001).
[4] Xiaodong Huang *et al*, *CLEO '01. Technical Digest*, 6–11 May 2001, p. 359.
[5] D. R. Matthews *et al*, *IEEE 18th International Semiconductor Laser Conference Digest*, 2002, pp. 75–76.
[6] M. Kuntz *et al*, *Appl. Phys. Lett.*, **85**, 843 (2004).
[7] Mark G. Thompson *et al*, *Proc. SPIE Int. Soc. Opt. Eng.*, 5452, 117 (2004).
[8] E. L. Portnoi *et al*, *AIP Conference Proceeding*, **240**, Leningrad USSR 1991, pp. 58–66.

13th Int. Symp. "Nanostructures: Physics and Technology"
St Petersburg, Russia, June 20–25, 2005

The development and study of 1.3 μm quantum dot lasers

D. Mowbray
Department of Physics and Astronomy, University of Sheffield, Sheffield S3 7RH U.K.

Abstract. InAs self-assembled quantum dots (QDs) allow the fabrication of 1.3 μm emitting lasers on GaAs substrates. In addition their unique QD density of states results in reduced threshold current densities (J_{th}) and decreased temperature sensitivity of J_{th} in comparison to conventional quantum well lasers. In my talk I will discuss the optimisation and characterisation of 1.3 μm InAs-GaAs QD lasers. In particular I will describe the use of a high growth temperature spacer layer (HGTSL), grown between the InAs QD layers, which significantly improves the performance of multi-layer devices. Such devices demonstrate world-record low J_{th} values at room temperature and permit operation above 100 °C. In addition I will discuss carrier recombination processes in optimised QD lasers and the use of AlInAs and GaAsSb cap layers to modify the nature of the dot confinement potential, with the aim of improving the high temperature performance. Finally preliminary studies of p-type modulation doped devices, which exhibit a negative temperature sensitivity of J_{th} at room temperature, will be reported.

InAs dot-in-a-well (DWELL) devices were grown by solid-source molecular beam epitaxy on n^+ (100) GaAs substrates. Devices consisted of three or five dot layers, with each layer containing 3.0 monolayers (MLs) of InAs grown on 2 nm of $In_{0.15}Ga_{0.85}As$ and capped by 6 nm of $In_{0.15}Ga_{0.85}As$. 50 nm GaAs barriers separated the DWELLs. The growth temperatures was 510 °C for both the In containing layers and GaAs. In a second set of devices, following each DWELL and initial 15 nm of GaAs the temperature was increased to 580 °C for the remaining 35 nm GaAs, being reduced back to 510 °C for the growth of the next DWELL. The inclusion of these HGTSLs is found to considerably improve the laser device performance.

Fig. 1a shows a cross-sectional TEM image of a three layer non-HGTSL device. Threading dislocations are clearly visible, in the present case starting in a large, defective dot in the second layer and extending through subsequently deposited layers. Fig. 1b shows an image of a five layer non-HGTSL structure. Again threading dislocations are observed, here extending from a pair of defective dots in the second layer. It is found that a defective dot in one layer generally causes the nucleation of an even larger, more defective dot in the next layer, with the consequence that the threading dislocation density increases as the total number of DWELL layers increases. Dislocation densities of $\sim 10^7$ and $\sim 10^9\,\mathrm{cm}^{-2}$ are estimated for three and five layer devices respectively. In contrast the introduction of the HGTSLs suppresses threading dislocation formation. No dislocations are observed for a five layer device grown with HGTSLs (see Fig. 1c), allowing an upper limit of $1 \times 10^6\,\mathrm{cm}^{-2}$ to be placed on their density in this device.

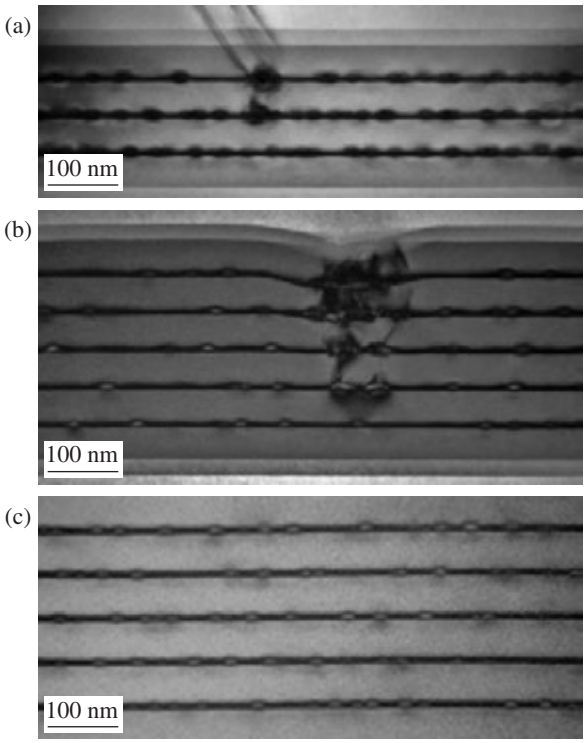

Fig. 1. Dark field (200) TEM cross-sectional images of a) and b) three and five layer devices grown without HGTSLs respectively and c) a five layer device grown with HGTSLs. The growth direction is vertically upwards for all three images.

Fig. 2 compares the J_{th} temperature dependence of three devices. For the devices with three DWELL layers, J_{th} is smaller for the HGTSL device at all temperatures, at room temperature a factor of ~ 5 lower. At room temperature (300 K) the pulsed

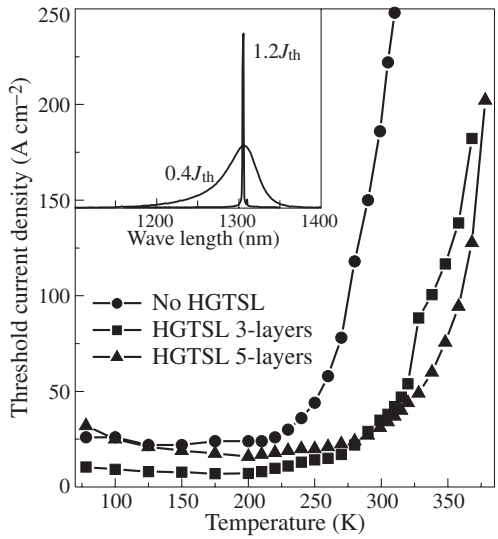

Fig. 2. Temperature variation of the pulsed threshold current densities for two three-DWELL laser devices, grown with and without HGTSLs and a five-DWELL device with HGTSLs. The cavities lengths are 5 mm. The inset shows room temperature below and above threshold spectra for the five-DWELL HGTSL device.

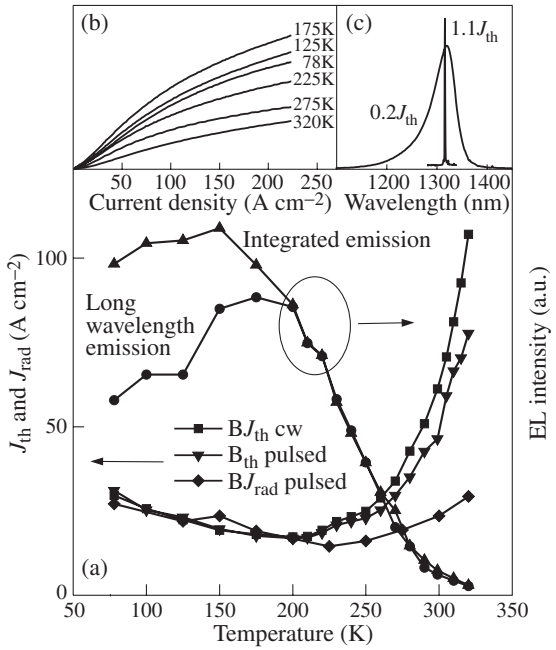

Fig. 3. (a) Comparison of the temperature dependence of the spontaneous emission and threshold current density. The spontaneous emission intensities are normalised to a common value at 200 K. The radiative current at threshold, J_{rad}, is also plotted. (b) Integrated spontaneous emission from a mesa device for pulsed current injection. (c) Emission spectra for a 5 mm cavity laser device.

J_{th} for the HGTSL device has a very low value of 35 Acm^{-2}, with lasing at 1.296 μm. Without HGTSLs the dislocation density in five layer devices is too high to permit lasing at room temperature, only pulsed operation up to 190 K is possible. With HGTSLs lasing significantly above room temperature is possible. The additional gain provided by the five layers results in improved temperature stability and longer wavelength lasing, with room temperature J_{th}, lasing wavelength and T_0 values of 31 Acm^{-2}, 1.307 μm and 111 K respectively for a 5 mm long cavity. A cw room temperature J_{th} of 39 Acm^{-2} is obtained, with both pulsed and cw lasing up to 105 °C (limited by the measurement system). Ground state lasing at room temperature is obtained for cavity lengths down to 1.5 mm, for shorter cavities excited state lasing occurs. To the best of our knowledge a room temperature J_{th} of 31 Acm^{-2} represents the lowest reported value for a $> 1.3\,\mu$m DWELL laser. HR coated facet devices demonstrate a room temperature J_{th} as low as 17 Acm^{-2} for a 2 mm long device.

Fig. 3a shows the temperature variation of the spontaneous emission and J_{th}, the former recorded from a mesa structure. At low temperature emission from the lasing subset of QDs increases as carriers are transferred from a non-lasing subset of smaller dots. Commensurate with this behaviour is a decrease of J_{th}. Also plotted in Fig. 3a is the temperature dependence of the radiative current density, J_{rad}, which is proportional to the spontaneous emission intensity at threshold. The latter is extracted from integrated spontaneous emission *vs* current characteristics, as shown in Fig. 3b. J_{rad} is normalised to J_{th} at low temperatures (< 200 K); in this temperature range non-radiative processes are assumed to be negligible. J_{rad} decreases between 78 and ~ 200 K, reflecting the concentration of carriers in the lasing subset of QDs. From 225 to 320 K J_{rad} increases by a factor of ~ 2.2, compared to an increase in J_{th}

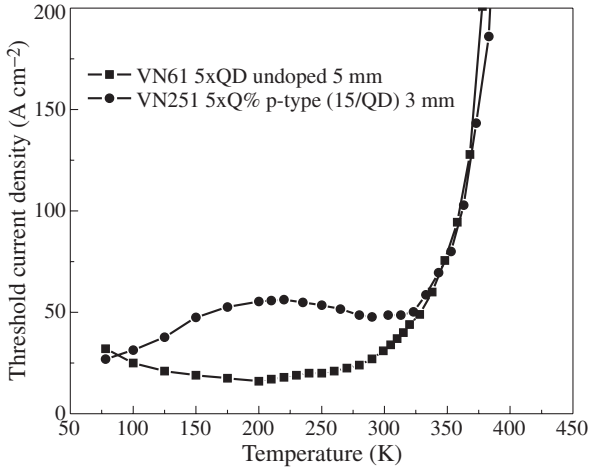

Fig. 4. Comparison of the temperature dependence of J_{th} for a p-type modulation doped device with an undoped reference device.

of ~ 4. At 320 K J_{rad} is 38% of J_{th}. This high-temperature increase of J_{rad} most likely reflects the excitation of carriers out of the lasing states to excited dot states. It has been shown previously that with increasing temperature the loss of carriers to excited QD states requires an increase in J_{rad} to maintain the ground state carrier density necessary to achieve the threshold gain.

The fact that the integrated QD emission decreases with increasing temperature above 200 K however, (see Fig. 3a&b) indicates that the corresponding increase in J_{th} is not entirely due to the thermal excitation of carriers into higher energy, non-lasing dot states, as such a process would conserve the integrated dot emission. As the total dot emission is not conserved, carriers must either recombine non-radiatively in the dots or be lost from the dots. In the latter case they must subsequently recombine non-radiatively as negligible emission is observed from the regions surrounding the quantum dots. Hence the decrease in the optical efficiency at high temperatures indicates the increasing importance of non-radiative carrier recombination. However, the present results do not allow the nature of the dominant non-radiative process (defect or Auger) to be identified.

Finally Fig. 4 shows data recorded from a five layer device where the QDs are p-type modulation doped with ~ 15 acceptors per dot. In comparison to an undoped reference device improved temperature stability is achieved in the region around room temperature, in the present device J_{th} decreases with increasing temperature over the range 225 to 300 K.

13th Int. Symp. "Nanostructures: Physics and Technology"
St Petersburg, Russia, June 20–25, 2005

220 mW single mode CW operation of InAs/InGaAs quantum dot lasers on GaAs substrates emitting at 1.5 μm

T. Kettler[1], L. Ya. Karachinsky[1,2], A. Lochmann[1], O. Schulz[1], L. Reissmann[1], N. Yu. Gordeev[2], I. I. Novikov[2], M. V. Maximov[2], Yu. M. Shernyakov[2], N. V. Kryzhanovskaya[2], A. E. Zhukov[2], A. P. Vasil'ev[2], E. S. Semenova[2], V. M. Ustinov[2], N. N. Ledentsov[1,2,3], A. R. Kovsh[3], V. A. Shchukin[3], S. S. Mikhrin[3] and D. Bimberg[1]

[1] Technische Universität Berlin, Institut für Festkörperphysik and Center of Nanophotonics, PN 5-2, 10623 Berlin, Germany
[2] Ioffe Physico-Technical Institute, St Petersburg, Russia
[3] NL-Nanosemiconductor GmbH, 44227 Dortmund, Germany

Abstract. Metamorphic InAs/InGaAs Quantum Dot (QD) lasers grown on GaAs substrates by Molecular Beam Epitaxy (MBE) emitting at 1.5 μm have been studied. Narrow ridge stripe lasers demonstrated single transverse mode operation and differential quantum efficiency up to 50%. Total optical output power in CW mode was up to 220 mW limited by thermal roll-over. Absence of beam filamentation of the TEM00 mode is demonstrated up to the highest power level studied.

Introduction

For many applications, e.g. data communication through optical fibers, lasers with long emission wavelengths in the 1.3 and 1.5 μm range are needed. GaAs-based lasers with self-assembled quantum dots (QDs) as active media are of particular interest, because of their superior properties compared to quantum well-lasers, e.g. their low threshold current densities, improved temperature stability, low chirp and suppressed beam filamentation [1, 2, 3]. High performance 1.3 μm GaAs-based InAs QD lasers, including VCSELs have already been realized [4], and interest is shifting towards QDs emitting in the 1.5 μm range. Two approaches are currently applied for 1.5 μm GaAs-based lasers. In the frame of the first approach GaInAsN/GaAsN [5] or GaInNAsSb/GaNAsSb quantum wells [6] are used as active region. The second approach has been recently developed [7, 8]. It was shown that thick metamorphic InGaAs layers with high structural and optical quality can be grown on GaAs substrate. Quantum dots grown on top of such a metamorphic buffer showed larger emission wavelengths as compared to those grown directly on GaAs. Broad area lasers based on tenfold stacked metamorphic InAs/InGaAs QDs demonstrated an emission wavelength of 1.52 μm at 80 °C. At room temperature lasing at 1.488 μm was obtained with threshold current density about 1.5 kA/cm^2 and external quantum efficiency up to 52%. Output power exceeding 7 W was achieved under pulsed excitation [8, 9].

In this work we report about realization of the first single mode continuous wave (CW) lasers based on metamorphic InAs/InGaAs QDs on GaAs substrate with high optical output power of 220 mW.

1. Experiment

The laser structure was grown by solid-source molecular-beam epitaxy on n+ GaAs (100) substrate. The active region consists of tenfold stacked InAs self-organised QD layers that are deposited in the center of an 0.8-μm thick $In_{0.21}Ga_{0.79}As$ waveguide layer. Each plane of QDs is further capped with an $In_{0.41}Ga_{0.59}As$ quantum well. The QD-containing waveguide layer is confined by $In_xAl_zGa_{1-z-x}As$ cladding layers doped with n- and p-type dopants, respectively. The Metamorphic transient layer comprises a 1-μm-thick $In_xGa_{1-x}As$ buffer followed by a 1.5-μm thick $In_xAl_zGa_{1-z-x}As$ ($z \sim 30\%$) cladding [8]. Defect reduction technique was used to suppress threading dislocations [10].

The structure was processed into narrow-stripe ridge waveguide lasers with stripe widths of 6, 7 and 8 μm. The ridges were etched down to 750 nm above the waveguide. Ni/AuGe/Au n-type and Ti/Pt/Au p-type contacts were deposited. Samples were mounted p-side down. No facet coatings were deposited. The lasers were characterised at 20 and 10 °C in pulsed mode (200 ns, 1 kHz) and CW mode, respectively. For measuring near fields, the laser front facet was imaged by a microscope objective on a CCD camera. For attenuation, gray-glass neutral filters were used. Electroluminescence was detected using a Ge photodiode.

2. Results and discussion

The laser performance and the output characteristics in pulsed mode of the fabricated lasers were investigated first. Threshold currents (I_{th}) of 380–420 mA were obtained for lasers with cavity length of 1.4 mm and ridge widths of 6, 7 and 8 μm. The emission wavelength was 1460 nm at room temperature. For a 7-μm-stripe laser with I_{th} = 390 mA maximum output power was about 440 mW. Differential quantum efficiency (η_d) was found to be 50%. This value corresponds to the best results reported for metamorphic InAs/InGaAs QD lasers on GaAs substrates [8, 9].

The distribution of the near field intensity along the facet of a 6-μm-stripe laser for pump currents of 1.03 I_{th}, 1.3 I_{th}, 2 I_{th} and 3 I_{th} are presented in Fig. 1. The absence of extra features or spikes at higher currents clearly shows that no new optical modes or beam filamentation appear. 7-μm and 8-μm stripes demonstrated similar behaviour.

Fig. 2 shows lateral far field pattern of 6-μm laser versus pump current. FWHM was found to be in 5.6–7.1 ° range. The profile is Gaussian and agrees with the extension of the near-field pattern, as also in case of 7-μm and 8-μm stripes. Fig. 2 also shows lateral far field pattern of a 6-μm laser. In this direction the far field pattern did not change with pump current. FWHM was found to be about 43 ° in agreement with

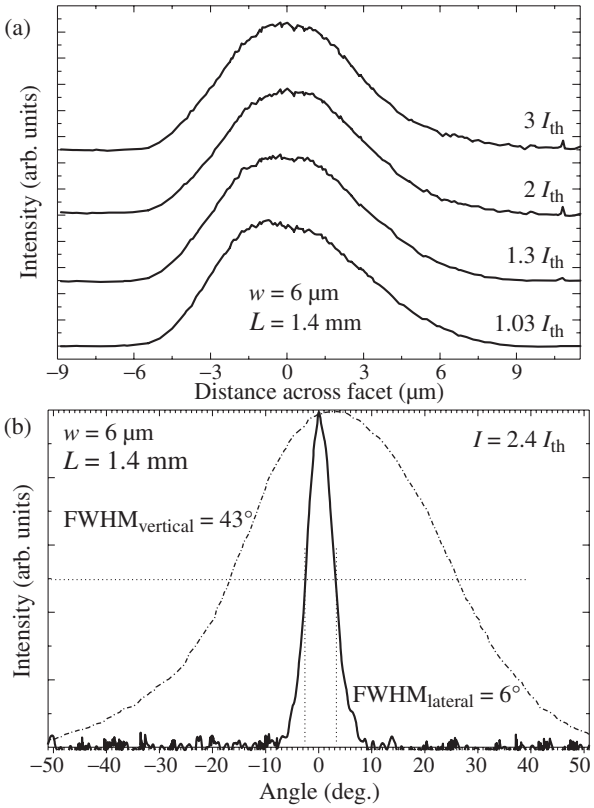

Fig. 1. (a) Near field cross sections in lateral direction of 6-μm-stripe laser ($L = 1.4$ mm) versus pump current. (b) Lateral and vertical far field patterns of 6-μm laser ($L = 1.4$ mm) versus pump current.

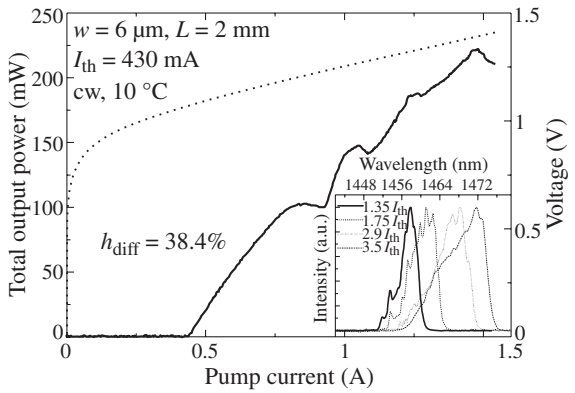

Fig. 2. CW light-current (solid line) and voltage current (dashed line) characteristics of 6 μm-lasers ($L = 2$ mm) at 10 °C. The inset shows CW spectra of the same laser.

the calculated far field according to the waveguide geometry.

Fig. 2 shows CW light-current and voltage-current characteristics of a 6 μm-laser with 2 mm cavity length at 10 °C. Maximum optical output power was as high as 220 mW limited by thermal roll-over. Differential quantum efficiency was 38.4%. Corresponding CW spectra are presented in the inset. The observed kinks in the L-I-curve at powers above 100 mW are believed to be due to switching between different longitudinal mode groups, revealed in the emission spectrum [11]. The observed red shift of emission wavelength is attributed to heating of the active region with increasing current.

3. Conclusion

We have studied metamorphic quantum dot lasers grown on GaAs substrate with lasing wavelength at 1.5 μm. Single mode operation with high differential efficiency (up to 50%) and CW optical output powers up to 220 mW has been realised. Absence of beam filamentation was demonstrated. We believe that the results clearly indicate that metamorphic InAs/InGaAs quantum dot lasers are promising candidates for high-performance 1.3 μm–1.5 μm edge- and surface emitting lasers on GaAs or Si substrates.

Acknowledgements

The authors are grateful to S. Rodt for expert technical assistance and to Dr. N. D. Il'inskaya and I. N. Kaiander for fruitful discussions. This work was supported in different parts by EU projects SANDiE (contract number NMP4-CT-2004-500101) and DOTCOM, RFBR, DLR and INTAS, and also by Joint Research Project between Ioffe Physico-Technical Institute (St Petersburg, Russia) and NL-Nanosemiconductor-GmbH (Dortmund, Germany). A.E.Z. thanks the Grant (MD-4277.2004.2) of the President of the Russian Federation for the support of young scientists. N.V.K. acknowledges financial support received from INTAS (YSF No 03-55-882). L.Ya.K. gratefully acknowledges financial support received from DFG.

References

[1] D. Bimberg *et al*, *Quantum Dot Heterostructures*, (Chichester: Wiley) 1998.
[2] C. Ribbat *et al*, *Appl. Phys. Lett.*, **82**, 952 (2002).
[3] D. Bimberg *et al*, *J. Phys. D: Appl. Phys.*, **38**, 1 (2005).
[4] N. N. Ledentsov *et al*, *IEEE J. Sel. Top. Quantum Electron.*, **8**, 1015 (2002).
[5] D. Gollub *et al*, *Electron. Letters*, **38**, 1183 (2002).
[6] L. H. Li *et al*, *Electron. Letters*, **39**, 519 (2003).
[7] A. E. Zhukov *et al*, *Semiconductors*, **37**, 1119 (2003).
[8] N. N. Ledentsov *et al*, *Electron. Letters*, **39**, 1126 (2003).
[9] M. V. Maximov *et al*, *Semiconductors*, **38**, 732 (2004).
[10] N. N. Ledentsov *et al*, *SPIE Asia-Pacific Optical Communication APOC* (Beijing, China, 2004).
[11] D. Ouyang *et al*, *Appl. Phys. Lett.*, **81**, 1546 (2002).

13th Int. Symp. "Nanostructures: Physics and Technology"
St Petersburg, Russia, June 20–25, 2005

High power 645 nm lasers with narrow vertical beam divergence (8° FWHM)

M. V. Maximov[1], Yu. M. Shernyakov[1], I. I. Novikov[1], S. M. Kuznetsov[1], L. Ya. Karachinsky[1], N. Yu. Gordeev[1], V. P. Kalosha[3], I. Samid[3], V. A. Shchukin[2,4] and N. N. Ledentsov[2,4]

[1] Ioffe Physico-Technical Institute, St Petersburg, Russia
[2] Institut für Festkörperphysik, Technische Universität Berlin, PN5-2, Hardenbergst. 36, D-10623 Berlin, Germany
[3] PBC-Lasers Ltd., Technology Incubator D.N., Misgav 20179, Israel
[4] NL Nanosemiconductor GmbH, Josef-von-Fraunhofer Str. 13, 44227 Dortmund, Germany

Abstract. We report on the red (646 nm) GaInP-AlGaInP lasers with a one-dimensional longitudinal photonic bandgap crystal waveguide. Very small vertical divergence of 8° (full width at half maximum), high differential quantum efficiency up to 85% and pulsed output power of 20 W were obtained. Such value of output power is 2.5 higher with respect to the number obtained for the lasers fabricated from the state-of-the-art epiwafers for commercial 650 nm DVD lasers.

Introduction

Read-write optical storage systems have become a major application for red GaInP-AlGaInP semiconductor lasers. In such systems, narrow far-field divergence in vertical direction is required. Several approaches to waveguide engineering have been proposed to increase the modal spot size [1, 2]. Two major schemes can be distinguished: either a low-index layer is inserted into the confinement layer or a high-index layer is inserted into the cladding layer. However such designs use traditional waveguides and the vertical divergence of the lasers is still above 13–18°. More recently, an idea of using an a longitudinal photonic bandgap crystal (PBC) structure has been proposed to realize stable single-mode lasing with an arbitrary narrow modal spot size [3]. A longitudinal PBC with an irregularity (an optical defect) can be designed in such a way that only one optical mode, e.g. the fundamental one, is localized at the defect and decays away from it, whereas all other (high-order) optical modes are extended over the entire photonic band gap crystal due to the effective "resonant tunnelling effect" and show order (orders) of magnitude higher leakage losses. In a similar manner in our waveguide only one (the fundamental) mode is localised at the PBC waveguide region having a maximum intensity in the gain region (multiple quantum wells (QWs)) while all extended high-order modes are leaky and penetrate into the substrate or the contact layers. Our results on 980 nm PBC lasers with ultrabroad ($> 10\,\mu$m) waveguide and narrow field divergence (< 5 degrees) were described in [4, 5]. In this work we study the properties of a red PBC GaInP-AlGaInP semiconductor laser and compare its performance with that for conventional red DVD lasers currently used for commercial applications.

1. Experimental

Fig. 2 compares the dependence of lasing wavelength, threshold current density and reciprocal differential efficiency on stripe length for the PBC and conventional laser. Note that lasing wavelength for the PBC laser is shorter (646 nm) as compared to the case of conventional laser (659 nm).

The epitaxial structures were grown by IQE (Europe) Ltd using metal-organic chemical vapor deposition (MOCVD) on misorientated GaAs substrates tilted 10° off the (100) toward [111]A. The conventional red laser was based on 3 InGaP QWs placed in the centre of $(Al_{0.5}Ga_{0.5})_{0.51}In_{0.49}P$ waveguide, which was clad with $(Al_{0.7}Ga_{0.3})_{0.51}In_{0.49}P$ layers. The design is optimized for far field divergence in vertical direction 16 degrees and currently used for commercial DVD lasers. The PBC structure was grown according to the concept described in [3–5]. The total thickness of the PBC waveguide with the core layer containing two InGaP QWs was about 5 μm to provide narrow vertical divergence 8 degrees (Fig. 1). The period of the PBC $(Al_{0.5}Ga_{0.5})_{0.51}In_{0.49}P$-$(Al_{0.7}Ga_{0.3})_{0.51}In_{0.49}P$ structure was about 600 nm to completely localize the fundamental mode and provide filtration of all high-order modes (Fig. 1a). The PBC structure as well as the conventional was doped using Zn on the p side and with Si on the n side.The structures were processed into 100 μm-wide stripe lasers. Samples were mounted p-side down. No facet coatings were deposited.

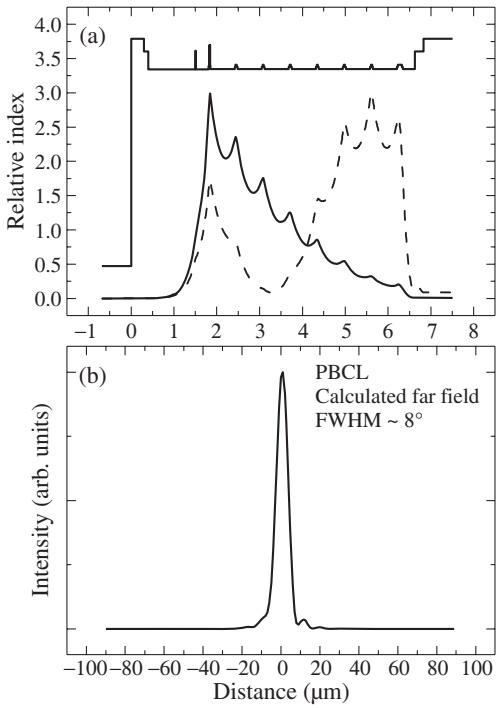

Fig. 1. Schematics of the PBC laser design (refractive index profile) and the calculated profile of the electric field for the fundamental (solid line) and the first-order modes (dash line) (a); simulated far field (b).

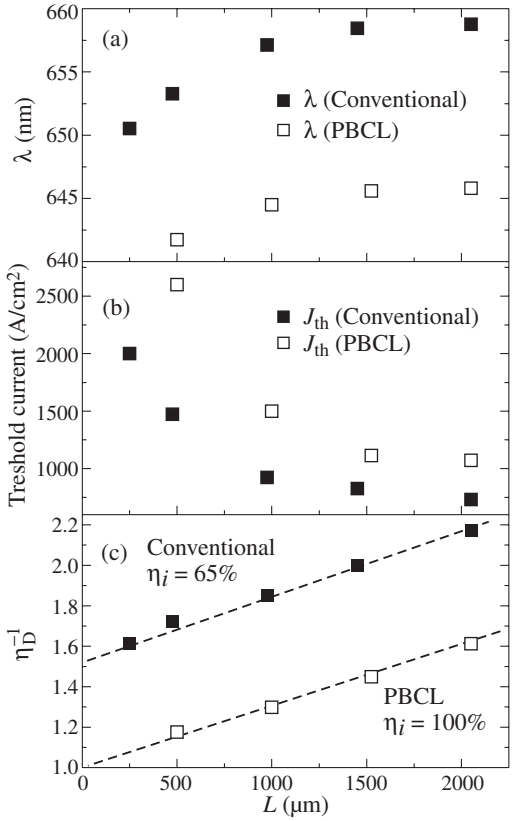

Fig. 2. Dependence of lasing wavelength (a), threshold current density (b) and reciprocal differential efficiency (c) on stripe length for the PBC and conventional lasers.

The lasers were characterized at 20 °C in the pulsed (300 ns, 1 kHz) mode.

2. Results and discussion

The PBC laser shows much better differential efficiency as compared to that for the conventional design. For 1000 and 500 μm long cavities deferential quantum efficiencies are 77 and 85%, respectively. To the best of our knowledge these are the highest values for 650 nm range red GaInP-AlGaInP lasers. The somehow higher threshold current density of the PBC laser can be explained by shorter lasing wavelength and lower optical confinement factor. Fig. 3 compares light-current characteristics for the PBC and conventional laser. In the latter case output power is below 8 W and limited by the catastrophic optical mirror degradation (COMD).

The waveguide of the PBC laser is broader which reduces power density per facet area. Facet degradation was not observed up to output power about 20 W limited by the current source. The wall-plug efficiency of PBCL was 1.25 times higher as compared to the conventional structure and maximum was shifted to a twice higher values of the drive current. Characteristic temperature for 2 mm-long PBC laser in the temperature range 20–60 °C is 100 K.

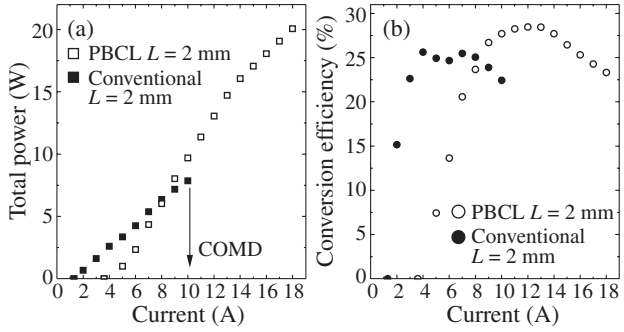

Fig. 3. Light-power characteristics for the PBC and conventional lasers.

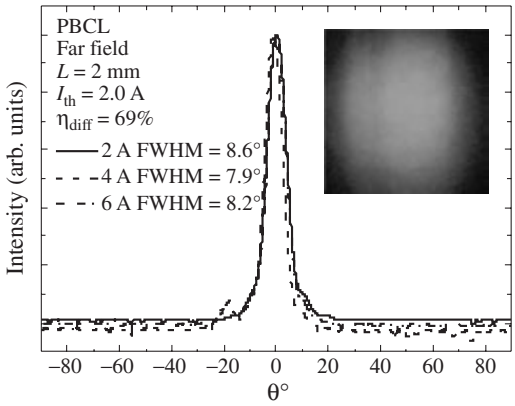

Fig. 4. Vertical far field patterns at various drive currents for the PBC laser. The inset shows 2D image of far field pattern.

The full width at half maximum (FWHM) of the far field pattern of the PBC laser is 8 degree and remains very stable with increase of injection current (Fig. 4). This value is in a very good agreement with the theoretical simulations (Fig. 1b). Lateral far-field pattern is multimode with total FWHM of 7–8 degrees up to the highest currents applied. Thus, far field pattern of the PBC laser is round shaped (see inset in Fig. 4a). The far field of the conventional structure is twice boarder with FWHM 16 degrees, which is typical for the state-of-the-art commercial red DVD lasers.

Acknowledgements

This work is supported by PBC Lasers, Israel and joint project between RFBR and the Israeli Center for Academic Relations with the CIS and Baltic States.

References

[1] J. Temmyo *et al*, *Electronics Letters*, **31**, 642 (1995).
[2] P. M. Smowton *et al*, *IEEE Journal of Quantum electronics*, **5**, 735 (1999).
[3] N. N. Ledentsov *et al*, *SPIE Optical Engineering*, **41**, 3193 (2002).
[4] M. V. Maximov *et al*, *Electronics Letters*, **39**, 1729 (2003).
[5] M. V. Maximov *et al*, *Physica status solidi (c)*, **2**, 919 (2005).

13th Int. Symp. "Nanostructures: Physics and Technology"
St Petersburg, Russia, June 20–25, 2005

Quantum cascade lasers: widely tailorable light sources for the mid- and far infrared

F. Capasso
Division of Engineering and Applied Sciences, Harvard University, Cambridge, MA 02138

Abstract. The unipolar nature of QC lasers combined with the capabilities of electronic and photonic bandstructure engineering leads to unprecedented design flexibility and functionality compared to other lasers. State-of-the-art performance in the mid-ir and far-ir will be reviewed. I will also discuss recent exciting developments such newligh-sources that uses the giant resonant nonlinear susceptibilities of intersubband transitions in quantum wells and internal optical pumping in QC lasers to achieve high conversion efficiency and its application in the first Raman injection lasers, new modelocking regimes associated with such large nonlinearities, Terahertz QCLs, ultrabrodband lasers, "bow tie" lasers and photonic crystal QCLs.

13th Int. Symp. "Nanostructures: Physics and Technology"
St Petersburg, Russia, June 20–25, 2005

Quantum cascade lasers in magnetic fields

I. Savić[1], V. Milanović[2,1], Z. Ikonić[1], D. Indjin[1], V. D. Jovanović[1] and *P. Harrison*[1]

[1] School of Electronic and Electrical Engineering, University of Leeds, Leeds LS2 9JT, United Kingdom
[2] Faculty of Electrical Engineering, University of Belgrade, 11120 Belgrade, Serbia and Montenegro

Abstract. A model of the active region of a quantum cascade laser (QCL) subjected to an externally applied magnetic field is presented, based on a solution of the coupled rate equations, assuming unity injection. Landau quantization induced by magnetic confinement imposes a need for a modification of the well-established active region model in order to accurately describe the processes occurring in an entirely discrete spectrum. Landau level (LL) configuration has major consequences for scattering processes, enhancing or inhibiting them depending on the inter-LL energy separation, and strongly modifies the population inversion and optical gain that can be estimated from the presented model. Numerical calculations were performed for a GaAs/AlGaAs QCL emitting at $\lambda \approx 11.4\,\mu$m in a magnetic field of 10–60 T.

Introduction

In zero magnetic field the energy spectrum of a quantum cascade laser (QCL) in an externally applied electric field is formally continuous, but to a very good approximation can be considered as consisting of quasi-discrete states (resonances) having plane wave-like energy dispersion in the direction parallel to the layers. An external magnetic field applied to a quantum well system parallel to the confinement direction splits the in-plane continuum of quantized subbands into LLs, each subband producing a set of LLs, described by a Landau index and additionally by a spin index (gyromagnetic spin splitting within the LLs). Due to the quantization of the energy spectrum, the scattering rate greatly increases whenever the energy spacing between two LLs associated with separate subbands is equal to one LO phonon energy (resonance). In contrast, when the LLs are off resonance, the transition is forbidden because the scattering of electrons with phonons can not conserve energy and the scattering rate is strongly reduced. Hence, a magnetic field represents an effective means for the modulation of the scattering rates of the LLs stemming from the upper laser state [1, 2, 3], which translates into the modulation of the population inversion and optical gain.

1. Theoretical considerations

The application of a perpendicular magnetic field to a QCL system alters the energy spectrum to a discrete one in which the ith state represents the j_ith LL stemming from the m_ith subband ($i = |m_i, j_i\rangle$) with energy E_i ($E_i > E_j$, $j = 0, \ldots i-1$ and $E_i < E_j$, $j = i+1, \ldots N$) approximately given as

$$E_i = E_{m_i,j_i} = E_{m_i} + \left(j_i + \frac{1}{2}\right)\frac{\hbar e B}{m^*}, \qquad (1)$$

where E_{m_i} is the energy of the subband in the absence of a magnetic field and m^* is the electron effective mass. The values of the magnetic field giving rise to resonant LO emission are the solutions of the following equations $E_{3,j_i} - E_{m_j,j_j} = \hbar\omega_{\mathrm{LO}}$ with $m_j = 1, 2$.

In optical transitions the Landau index and spin are conserved, and absorption occurs only on transitions between LLs associated with different subbands. The fractional absorption on such a transition is [4]

$$a_{i,f} = \frac{\pi e^2 \omega}{n\epsilon_0 c} M^2_{m_i,m_f}\delta(E_f - E_i - \hbar\omega)(n_f - n_i), \qquad (2)$$

where n is the refraction index, ω is the frequency of incident radiation, E_i and E_f are Landau energies with the corresponding wavefunctions ψ_{m_i} and ψ_{m_f}, M_{m_i,m_f} is the matrix element, and n_i and n_f are the electron sheet densities of $i = |m_i, j_i\rangle$ and $f = |m_f, j_f\rangle$ LLs. The total absorption between subbands m_i and m_f is a sum of contributions of all the LLs stemming from them. State broadening can be given by a Gaussian distribution with $\sigma(0) = \Gamma\sqrt{\pi/2}$ where Γ is the transition linewidth if $m_i = m_j$, $\sigma(B) = \sigma_0\sqrt{B}$ if $m_i \neq m_j$ but $j_i = j_j$, and $\sigma_{\mathrm{eff}} = \sqrt{\sigma^2(0) + \sigma^2(B)}$ if $m_i \neq m_j$ and $j_i \neq j_j$. In the analysed GaAs/AlGaAs QCL structure [5], instead of absorption, one analyses the optical gain as the negative value of absorption between subbands $m_i = 3$ and $m_f = 2$.

In the absence of a magnetic field, it is assumed that the electrons from the collector are injected completely into the uppermost state of the active region and all of them are removed from the lowest state to be recycled, constituting quantitatively the same injected current in an additional stage. Upon an applied magnetic field, the assumption is that the current is completely injected into LL $|3, 0\rangle$ and entirely extracted from the lowest $|1, 0\rangle$ LL (Fig. 1a). A more refined model accounts for thermal distribution of injected current (see Fig. 1b). In a magnetic field, the injector state and the upper laser level split into LLs preserving the same energy separation of the corresponding LLs as in zero magnetic field. Therefore, if the ith LL associated with the injector state is populated, those electrons are injected into the ith LL originating from the upper laser level. The same conclusion applies to the active region-collector cross-section. Electrons occupying LLs originating from the same subband are thermally distributed over them, contributing to the injection current proportionally to their pop-

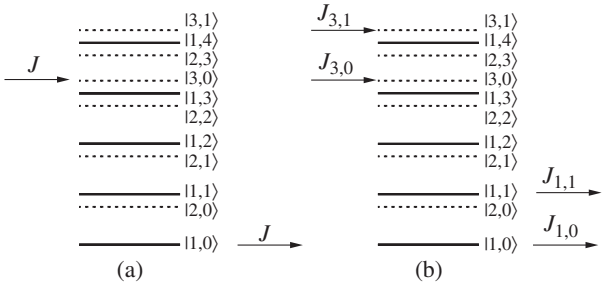

Fig. 1. Schematic diagram of the considered active region models in magnetic field assuming (a) injection into Landau level $|3, 0\rangle$, (b) thermal distribution of injected current.

ulation.

If the largest Landau indices of the upper $m_i = 3$ and ground state $m_i = 1$ LLs whose population is not negligible are $j_{3,\max}$ and $j_{1,\max}$, the current injected into the upper state LLs and extracted from the ground ones is given by the expression

$$J_i = J_{m_i,j_i} = J \sum_{j_j=0}^{j_{m_i,\max}} e^{-(E_{m_i,j_j} - E_{m_i,j_i})/kT}$$

where J is the total injection rate at equilibrium. Other LLs do not participate in injection and extraction and $J_i = 0$. The unity injection approximation is valid only when the rate equations system is linear i.e. neglecting the Pauli exclusion principle and electron-electron scattering that both introduce nonlinearity into the system. Electron-LO and LA phonon scatterings are incorporated into the model and calculated as in [6, 7]. The scattering rate equations in the steady-state are

$$\frac{dn_f}{dt} = 0 = \frac{J_f}{e} + \sum_{i=1, i\neq f}^{N} n_i W_{i,f} - n_f \sum_{i=1, i\neq f}^{N} W_{f,i}\,, \quad (3)$$

where $N = |3,\, j_{3,\max}\rangle$ is the uppermost LL and $1 \leq f \leq N$. Out of the total of N, there are $N-1$ linearly independent equations, so one of them is replaced by the particle conservation law.

2. Numerical results

A detailed description of the analysed active region based on GaAs/$Al_{0.33}Ga_{0.67}$As is given in Ref. [5]. The total scattering rate from the upper state as a function of the magnetic field imposed by electron-LO phonon scattering is presented in the inset of Fig. 2, obtained as a sum of the contributions arising from two of the LLs associated with the upper and one of the lower states respectively. As expected, it oscillates with increasing magnetic field which translates into strong modulations of the gain and gain coefficient as a function of the magnetic field (given in Fig. 2).

The local maxima of the total scattering rate are associated with minima in the gain coefficient and vice versa. Peaks in the scattering rate from the upper laser state (minima in modal gain) occur at $B \approx 11.4$, 19.6, 28 and 41 T. These peaks correspond to situations when $E_{2,4} = E_{1,6} = E^{\rm res}_{3,0}$, $E_{2,2} = E_{1,3} = E^{\rm res}_{3,0}$, $E_{1,2} = E^{\rm res}_{3,0}$ and $E_{2,1} = E^{\rm res}_{3,0}$, where $E^{\rm res}_{3,0} = E_{3,0} - \hbar\omega_{\rm LO}$. LLs lying one LO energy below $|3,\, 0\rangle$ allow resonant LO emission. Therefore, the scattering rate increases, which decreases the population inversion and gain in the case of constant current injection. At $B = [13.8,\ 15.9]$ T, a broad maximum in the scattering is observed, together with a minimum in gain. Considering the line broadening, these features correspond to intercepts of the resonances between $E_{3,0}$ and the $E_{1,5}$, $E_{2,3}$ and $E_{1,4}$ states. In contrast, for intermediate magnetic fields there are no LLs situated one LO energy below an upper state LL, hence electrons injected into it cannot lose their energy by LO emission since the energy cannot be preserved. Thus the scattering is strongly reduced and consequently, the optical gain is enhanced.

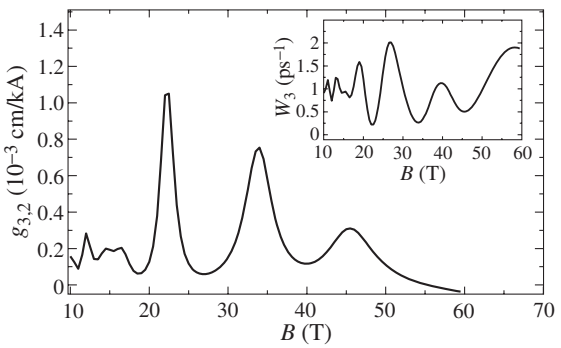

Fig. 2. Gain coefficient versus magnetic field dependence. Inset: The total scattering rate from the upper laser state versus magnetic field dependence.

3. Conclusion

An active region model of QCLs operating under an applied magnetic field, determined by Landau discretization of the energy spectrum, was developed, representing a tool for controlling the population inversion via modulation of the phonon assisted transfer. The calculation of the optical gain in a mid-infrared QCL based on GaAs/AlGaAs exposed to magnetic field was performed in order to illustrate the application of the model.

References

[1] C. Becker *et al*, *Appl. Phys. Lett.*, **81**, 2941 (2002).
[2] D. Smirnov *et al*, *Phys. Rev. B*, **66**, 125317 (2002).
[3] J. Alton *et al*, *Phys. Rev. B*, **68**, 081303 (R) (2003).
[4] S. Živanović *et al*, *Phys. Rev. B*, **52**, 8305 (1995).
[5] P. Kruck *et al*, *Appl. Phys. Lett.*, **76**, 3340 (2000).
[6] P. J. Turley *et al*, *Phys. Rev. B* **72**, 2356 (1993).
[7] C. Becker *et al*, *Phys. Rev. B*, **69**, 115328 (2004).

13th Int. Symp. "Nanostructures: Physics and Technology"
St Petersburg, Russia, June 20–25, 2005

Control of the population of the upper laser level in quantum well structures with strongly asymmetric barriers by the electric field

Yu. A. Aleshchenko[1], *V. V. Kapaev*[1], Yu. V. Kopaev[1], P. S. Kop'ev[2], V. M. Ustinov[2] and A. E. Zhukov[2]

[1] Lebedev Physical Institute, RAS, 119991 Moscow, Russia
[2] Ioffe Physico-Technical Institute, St Petersburg, Russia

Abstract. We propose a means of controlling the population of the upper laser level in triple quantum well (QW) structures with strongly asymmetric (in height) barriers. Both the theoretical calculations and the photoluminescence (PL) results indicate that our approach based on the application of an external electric field to the structure allows one to increase the nonradiative relaxation time to the lower laser state by several fold.

Introduction

We have proposed [1] an original design of the active element of a quantum unipolar semiconductor laser. In such an active element, the lower laser subband ε_{l1} belongs to the QW with strongly asymmetric barriers and thus exists only within the restricted range of the 2D wavevector ($0 < k < k_c$), while the upper laser subband ε_{l2} is in QW with symmetric barriers. This prevents the nonradiative relaxation to the ε_{l1} subband and facilitates the population inversion. This structure has been modified recently [2] to increase the electron localization in the ε_{l1} subband at $k = 0$ and to decrease k_c. In this paper, we report a significant increase in the nonradiative relaxation time between the laser levels of this structure in the external electric field.

1. Experimental results

The structures were grown by MBE. The nominal layer sequence in their active region designed for operation under the flat band conditions (in nanometers; in the growth direction) was as follows: *34.0*/**2.5** (QW1)/3.0/**5.1** (QW2)/1.4/ **8.2** (QW3). GaAs layers are in bold, $Al_{0.35}Ga_{0.65}As$ barriers are in regular typeface, and the lower barrier $Al_{0.09}Ga_{0.91}As$ is in italics. The active region was surrounded by the $Al_{0.35}Ga_{0.65}As$ barriers. The parameters of the structures were chosen to reduce significantly the single-phonon nonradiative intersubband transitions to the ε_{l1} subband. The n^+GaAs contact layers were provided to apply an external electric field to the structure. The PL spectra were excited at 80 K by the 514.5 nm line of an Ar^+ laser and analyzed with an Jobin Yvon T64000 spectrometer equipped with a cooled CCD camera.

There are two closely spaced strong PL peaks at $\mathcal{E}_1 = 1.557$ and $\mathcal{E}_2 = 1.565$ eV in the spectra of sample No. 4-399 taken in zero electric field. In the PL spectra of sample No. 4-727 grown in different growth run these peaks manifest themselves at 1.562 and 1.569 ev, respectively. A weak peak at $\mathcal{E}_3 = 1.61$ eV is also observed in the spectrum of this sample. In addition to the peaks $\mathcal{E}_1$–$\mathcal{E}_3$ resulting from the active region of the structures studied the weak contributions of the barrier layers are observed in both spectra. The positions of the latter peaks correlate with the nominal composition of the barrier layers. Figure 1 shows the behavior of the strong PL peaks $\mathcal{E}_1$ and $\mathcal{E}_2$ with applied bias for both structures. One can see the monotonic bias dependences for sample No. 4-727 in Fig. 1b. In contrast,

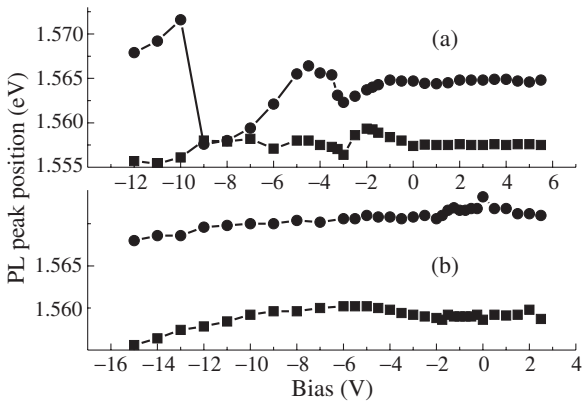

Fig. 1. Bias dependences of the strong PL peaks for samples No. 4-399 (a) and No. 4-727 (b).

the bias dependences for sample No. 4-399 exhibit strong irregularities, which can be attributed to the anti-crossings of the laser subbands with the states of the quasi-continuous spectrum localized in the region of the low barrier. It should be noted that the bias dependences of the intensities of the stronges PL peaks also exhibit nonmonotomic behavior.

2. Theory

The electron spectrum of the structures was calculated by the technique developed by us [2]. The QW and barrier widths were varied to fit the bias dependences of the peaks $\mathcal{E}_1$ and $\mathcal{E}_2$. The overlap integrals for the wave functions of electrons and holes participating in the corresponding transitions were calculated to correlate with the PL intensity. The best fit was observed for the structures *34.0*/**5.0**/4.0/**4.5**/3.0/**7.0** (I, sample No. 4-399) and *34.0*/**5.8**/4.0/**4.5**/ 3.0/**6.4** (II, sample No. 4-727). The strong difference of the width of the QW with asymmetric barriers (QW1) from the nominal value can be explained by the smearing of the interface between the lower barrier ($x = 0.09$) and GaAs.

The transition of states to the quasi-continuous spectrum with field results in the strong variation in the overlap integrals $I(E)$ of the electron and hole states and their dependence on the wave vector k. We calculated $I(E)$ for various k. The strong dependence $I(k)$ was shown to be within the relatively narrow field domains. However, by proper choosing the external bias the phonon relaxation can be significantly suppressed even in the structures with the parameters different from the

nominal ones.

The field dependences of the nonradiative relaxation time τ_{21} from the ε_{l2} subband localized in QW3 to the ε_{l1} subband in QW2 were calculated for the structure with nominal parameters and for the structures I and II. For the nominal structure along with the maximum $\tau_{21} = 9$ ps in zero field (associated with the dimesionality transformation of the ε_{l1} subband with k) the second maximum $\tau_{21} = 57$ ps is observed at $E = -10^4$ V/cm. The latter is due to the anticrossing of subbands and exit of the state ε_{l1} localized in QW2 at $k = 0$ to the quasi-continuous spectrum at $k = k_c$.

The suppression of relaxation with the optical phonon emission between the laser subbands of the structure is not the only prerequisite to the maximum τ_{21}. One should also minimize the time of stay in the ε_{l1} subband (for this purpose the distance between this subband and the lowest one ε_{l0} localized in QW3 should be close to the optical phonon energy) and obtain a reasonably large product of the dipole matrix elements $Z_{02}Z_{12}$ (for a high gain). These requirements are met simultaneously in the nominal structure under the flat band conditions. In this case, $Z_{02}Z_{12} = 250\,\text{Å}^2$.

In Fig. 2 are shown the field dependences of τ_{21} and τ_2 (the total life time for the ε_{l2} subband) for the structure II. A similar behavior is also characteristic for the structure I. The fact that τ_{21} exceeds that for the nominal structure throughout the field range studied is mainly due to the wider barrier between the QW3 and QW2 and is not directly related to the effect of dimensionality transformation of the subbands. The sharp spikes of τ_{21} at some field strengths are of prime interest for us. For the structure II at $E = 0$ and $E = 10^3$ V/cm the distance between the ε_{l1} and the ε_{l0} subbands is close to the optical phonon energy $\hbar\omega_{\text{opt}}$. This provides the rapid escape of electrons from the ε_{l1} subband. The dashed lines in Fig. 2 represent the change in the actual subband number of the laser subbands ε_{l1} and ε_{l2} as they cross the states of the quasi-continuous spectrum with field. Our calculations show that the drastic increase in τ_{21} occurs at the field strengths corresponding to the anticrossing of the ε_{l1} state with one of the states n_c of the quasi-continuous spectrum. This is due to the strong k dependence of the wave functions of this state. At $k = 0$ the wave function of the ε_{l1} state is localized in QW2, while at k corresponding to the energy $\varepsilon_{l2} - \hbar\omega_{\text{opt}}$ it is localized in the region of lower barrier. In this case, τ_{21} formally increases by more than one order of magnitude. However, for this resonance the state of quasi-continuous spectrum is localized in QW2. As a result the relaxation time to this state is of the order of τ_{21} outside the resonance. Owing to the proximity of the ε_{l1} and n_c states the further loss of energy by the electron is possible both through the intraband relaxation and interband transition between these states. In this case, the total time of transition between the laser levels can be substantially below the time of direct transition τ_{21}. The fact that the intraband relaxation for the n_c subband finally results in the electron escape from QW2 to the region of the lower barrier allows one to conclude without an exact calculation that the total relaxation time to the ε_{l1} state can be increased by several fold under the condition of resonance of this state with one of the states n_c.

The total life time in the ε_{l2} subband varies weakly with field but has sharp minima in the vicinity of the resonances τ_{21}. In this case, the higher laser state smeared out over the structure resulting in the efficient relaxation to the states of the quasi-continuous spectrum. Moreover, the minima arise under the condition $\varepsilon_{\text{nc}} \sim \varepsilon_{l2} - \hbar\omega_{\text{opt}}$, i.e., when the state separated from the higher laser state by the optical phonon energy is available. The life time τ_2 in this case is several times less. This can affect the intensity of the interband PL.

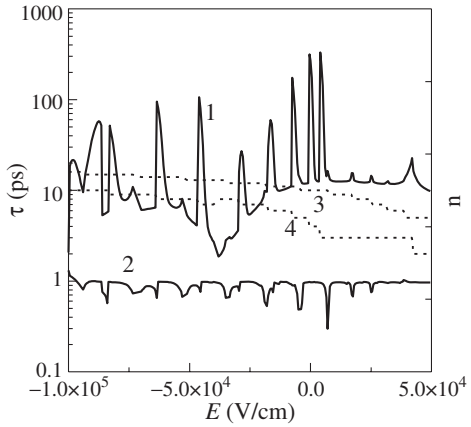

Fig. 2. Field dependences of τ_{21} and τ_2 (curves 1 and 2, respectively) and variation of the actual subband number of the laser subbands ε_{l2} and ε_{l1} with field (curves 3 and 4) for the structure II.

3. Conclusions

Thus, the application of an external electric field to the structures under study allows one to achieve the effect similar to that of dimensionality transformation of states in the structure with optimum parameters. In spite of the significant increase in the barrier widths in structures I and II the product of dipole matrix elements defining the gain remains reasonably large ($\sim 150\,\text{Å}^2$ vs. $250\,\text{Å}^2$ for the structure with optimum parameters) within the broad field domain.

Acknowledgements

This work was supported in part by the Program of Presidium of the Russian Academy of Sciences "Low-Dimensional Quantum Structures", the Program of Basic Research of the Division of Physical Sciences of the Russian Academy of Sciences, and the Program of the Ministry of Education and Science "Physics of Solid-State Nanostructures".

References

[1] Yu. A. Aleshchenko, V. V. Kapaev, Yu. V. Kopaev and N. V. Kornyakov, *Nanotechnology*, **11**, 206 (2000).

[2] Yu. A. Aleshchenko, A. E. Zhukov, V. V. Kapaev, Yu. V. Kopaev, P. S. Kop'ev and V. M. Ustinov, *JETP*, **98**, 770 (2004).

13th Int. Symp. "Nanostructures: Physics and Technology"
St Petersburg, Russia, June 20–25, 2005

InAs/AlSb quantum cascade structures for short wavelength emission

D. Barate, R. Teissier and *A. N. Baranov*

Centre d'Électronique et de Microoptoélectronique de Montpellier, UMR 5507 – CNRS/Université Montpellier 2, 34095 Montpellier, France

Abstract. The InAs/AlSb material system is well suited for the development of short wavelength quantum cascade lasers due to the large conduction band offset of 2.1 eV. We present a study of evolution of electroluminescence spectra of InAs/AlSb quantum cascade structures with decreasing emission wavelength. Intersubband emission near 2.5 μm at room temperature has been obtained. The measured optical power of the intersubband emission increases with decreasing wavelength reaching several microwatts for the structures operating near 2.5 μm.

Quantum cascade lasers (QCLs) are widely used now to produce coherent radiation in the mid- and far-infrared. For short wavelength QCLs emitting below 4.5 μm the choice of a material system with sufficiently large conduction band discontinuity becomes a key issue. The use of strained materials in the conventional InP-based system made it possible to realise the shortest wavelength QCL with emission at 3.5 μm [1]. A similar approach based on strain compensated structures with AlAs barriers on InP has been used in QCLs emitting at 3.8 μm [2]. The alternative solutions are based on antimonide systems, either employing AlSbAs barriers and InGaAs quantum wells in structures lattice matched to InP [3], or InAs/AlSb structures grown on InAs or GaSb [4].

The InAs/AlSb material system is a very promising candidate for the development of short wavelength QCLs due to the large conduction band discontinuity of 2.1 eV. InAs/AlSb QCLs operating at room temperature (RT) near 4.5 μm have been reported [5]. In this paper we present a study of RT electroluminescence of InAs/AlSb quantum cascade structures emitting below 4.5 μm aiming to explore the short wavelength limit of their operation.

The main difficulty in designing short wavelength InAs/AlSb QCLs is the lack of reliable information on band parameters for accurate modelling of the required high energy levels. An especially important issue is the precise alignment of the injector ground state eL with the upper state of the lasing transition $e3$ (see Fig. 1), situated at about 800 meV above the bottom of conduction band of the active quantum well of the structures designed to emit near 3 μm. A small inaccuracy of the electron effective mass or band non-parabolicity used for modelling can provoke a dramatic shift of injector states with respect to the active quantum well states and prevent efficient electron injection in a real structure. Multilayer structures always have more or less gradual interfaces depending on the material system and growth conditions. For accurate modelling one can use known band parameters applied to the real band profile of the structure which is difficult to predict. Another way is to consider the structure as an ideal one with abrupt interfaces, but to use effective band parameters which describe the real structure. Our approach was to find, first, the best empirical set of parameters that describes the experimental intersubband emission energies for a large number of samples emitting at different wavelength. Then, for a given active region design, the best injection conditions were searched by slightly varying injector levels with respect to active quantum well levels, and looking for the smallest turn-on voltage and the highest resonant current density. Finally, the band parameters were refined in order to obtain in modelling an exact $eL-e3$ alignment for the optimized structures. One period of a typical structure, modelled with the optimised set of parameters and designed to emit at 2.5 μm, is shown in Fig. 1.

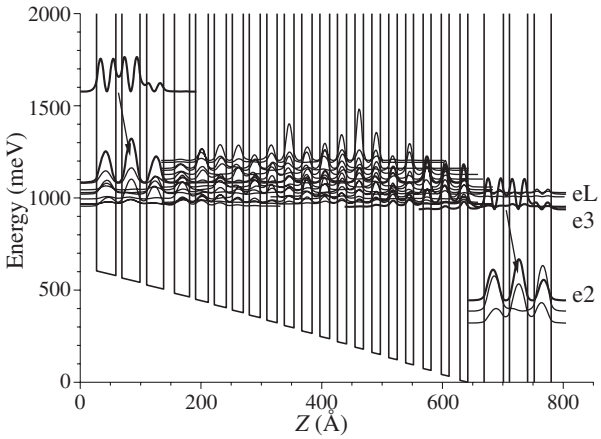

Fig. 1. Calculated conduction band profile and moduli squared of the relevant wave functions for sample C emitting at 2.55 μm under an applied field of 90 kV/cm. The photon emission occurs between the levels labelled $e2$ and $e3$.

The studied samples were grown by molecular beam epitaxy on n-GaSb (100) or n-InAs (100) substrates in a RIBER Compact 21 machine equipped with valved cracker cells producing As_2 and Sb_2 molecules. Structures emitting beyond 4 μm were grown on InAs substrates, whereas GaSb substrates were used for shorter wavelengths. Formation of InSb-like interfaces between InAs and AlSb layers was favoured during the growth on GaSb substrates in order to improve lattice matching. For the same reason formation of AlAs-like interfaces was forced in the wafers grown on InAs substrates. The structures consisted of 10 periods of the active zone enclosed between digital grading regions providing band matching with the buffer and contact layer made of the same material as the substrate. For each sample presented in this paper, the period of the structure, extracted from X-ray diffraction rocking curves, corresponded to the desired value with accuracy better than 3%.

The wafers were processed into 160×160 μm^2 square deep etched mesas. Device bars with one edge polished at 45° were soldered with In onto copper heatsinks. The measurements

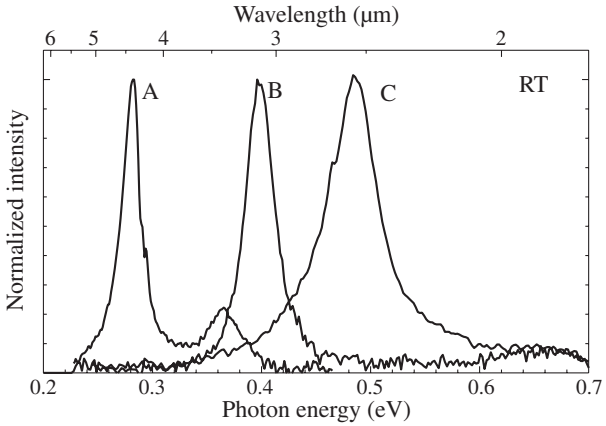

Fig. 2. Normalized emission spectra of different samples at room temperature.

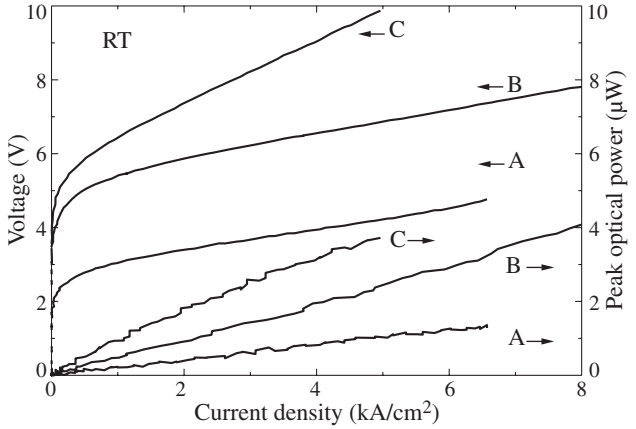

Fig. 3. Voltage–current and light–current characteristics of samples A, B and C (Fig. 2) at room temperature.

were carried out in pulse regime, using typically 200 ns long current pulses at a repetition rate of 20 kHz. Electroluminescence spectra of the samples were measured from the polished edges of the device bars in step scan regime using a Nicolet Nexus 810 Fourier spectrometer with a cooled InSb detector.

Room temperature emission spectra of some studied structures are presented in Fig. 2. RT emission has been obtained at wavelengths as short as 2.55 μm. For all samples, the measured peak energy corresponded to the intersubband transition energy, calculated with the above described band parameters, within 10 meV accuracy. On most devices a second peak is observed at higher energy (650–700 meV for GaSb substrates, 360–380 meV for InAs substrates) due to interband emission in the layers close to the active region, GaSb or InAs depending on the substrate type. The nature of the observed emission bands is clearly identified from their polarization. The low energy peak is TM polarized (>90%), characteristic of intersubband emission, while the higher energy peak is not polarized, as expected for interband recombination.

The absolute optical power of the room temperature intersubband emission was measured after calibration of the FTIR detector. For a given current density of 5 kA/cm^2, it increases from 1 μW for the structure emitting near 4.5 μm to 4 μW for the one emitting at 2.55 μm. This increase is consistent with calculated values of the relative change of oscillator strength for these structures.

The width of the emission spectra of many samples has been analyzed. For the structures emitting near 3 μm the RT electroluminescence spectra were as narrow as 30 meV. For λ=2.55 μm the full width at half maximum (FWHM) increases to 57 meV. Contribution of phonon scattering and nonparabolicity to the linewidth of intersubband emission has been calculated following ref. [6]. Inhomogeneous broadening has been estimated as the shift of the level positions due to one monolayer (3 Å) fluctuations of the InAs well widths. The measured FWHM of the emission spectra agree with the total effect of these three mechanisms. The inhomogeneous broadening appears to be a major contribution to the emission linewidth in the structures emitting at near 3 μm and below. This finding, however, is not a specific characteristic of the InAs/AlSb system, it is rather due to the small layer thicknesses required to obtain short wavelength intersubband emission in general.

Electrical characteristics are shown in Fig. 3. The samples emitting at 4.5 and 3.1 μm exhibited low differential resistance and maximum current densities of 7 and 8 kA/cm^2, respectively. In the shorter wavelength devices, which have not yet been optimized, the series resistance is higher.

In conclusion, we have demonstrated InAs/AlSb quantum cascade structures operating at room temperature with peak emission wavelength down to 2.55 μm. The obtained results do not show any fundamental limitation for realization of InAs/AlSb short wavelength QCLs emitting at least down to 3 μm.

Acknowledgement

This work has been carried out within the framework of the European Marie Curie research training network POISE.

References

[1] J. Faist, F. Capasso, D. L. Sivco, A. L. Hutchinson, S. N. G. Chu and A. Y. Cho, *Appl. Phys. Lett.*, **72**, 680 (1998).

[2] M. P. Semtiv, M. Ziegler, S. Dressler, W. T. Masselink, N. Georgiev, T. Dekorski and M. Helm, *Appl. Phys. Lett.*, **85**, 1478 (2004).

[3] D. G. Revin, L. R. Wilson, E. A. Zibik, R. P. Green, J. W. Cockburn, M. J. Steer, R. J. Airey and M. Hopkinson, *Appl. Phys. Lett.*, **85**, 3992 (2004).

[4] C. Becker, I. Prevot, X. Marcadet, B. Vinter and C. Sirtori, *Appl. Phys. Lett.*, **78**, 1029 (2001).

[5] R. Teissier, D. Barate, A. Vicet, C. Alibert, A. N. Baranov, X. Marcadet, C. Renard, M. Garcia, C. Sirtori, D. Revin and J. Cockburn, *Appl. Phys. Lett.*, **85**, 167 (2004).

[6] B. Gelmont, V. Gorfinkel and S. Luryi, *Appl. Phys. Lett.*, **68**, 2171 (1996).

13th Int. Symp. "Nanostructures: Physics and Technology"
St Petersburg, Russia, June 20–25, 2005

Vertically emitted leaking whispering gallery mode semiconductor lasers and laser systems

A. Andronov

Institute for Physics of Microstructures Russian Academy of Sciences 603950 GSP-105 Nizhny Novgorod Russia

Abstract. New approach to vertically emitted semiconductor lasers and the laser system based on the leaking whispering gallery mode (WGM) is put forward and elaborated. The approach is appropriate to all of the semiconductor lasers: both interband and intraband (cascade) heterolasers and bulk germanium and silicon lasers. It is important that in such approach a lot of lasers can be fabricated at one wafer in single technological process.

Introduction

Cavity system of the both interband and intraband cascade heterolasers are grown on the substrate with refractive index higher than the index of the laser emission modes. As a results the mode can leak to the substrate the degree of the leaking depending on optical thickness of the waveguiding layer between the active layers and substrate. This leaking was used by Zvonkov *et al* [1] in an attempt to improve the output beam quality of semiconductor laser.

With use of WGM in circular laser diodes with penetration its cavity system into substrate in the form of a cone (a trumpet) it is possible to direct the leakage into vertical direction to the back side of substrate. Also by arranging proper barrel-like form of the active region with WGM it is possible to exclude completely from the laser structure the waveguiding layers. This scheme is attractive for intraband germanium and silicon lasers. This approach opens also simple way of integration of vertically emitted lasers on one wafer and to produce the integrated laser system in a single technological process. The laser beam reaching the back side of substrate are higher order gaussian beams. If necessary the structure of the beam may be changed (improved) by producing appropriate beam phase corrector on the back of substrate. Modified similar approach can be used for narrow gap semiconductor lasers with the laser active layers grown on wide gap substrate.

WGM semiconductor lasers are well known both for the interband [2] and intraband (cascade) [3] lasers. Also WGM p-Ge laser was fabricated . Still the WGM laser have not found wide use. And the reason is: no ways for effective directional extraction of the laser emission out of the WGM cavity were found.

There exist vertically emitted semiconductor lasers based on the multilayer Bragg reflectors fabricated on the both side of the laser active region. Still they also have not found wide use because of cost of the reflector producing and depression of carrier injection through reflectors.

To the best of my knowledge the present quite simple approach to produce directional emission from WGM lasers have not been discussed. On the other hand the approach in its essence is just a modified transfer of the approaches to cavity electrodynamics and output systems of vacuum tube microwave and millimeter wave generators (gyrotron and alike) which have been developing for almost 40 years in Nizhny Novgorod by Michael Petelin, his colleagues and followers (see e.g. [4]).

1. Schemes of semiconductor lasers based on leaking whispering gallery modes

Fig. 1 gives (not to scale) scheme of proposed WGM interband heterolaser integrated on one wafer. The active region is a circular diode heterostructure with waveguiding layers between which the laser mode moves in circles occupying a narrow region (5–10 of the wavelength in the material) near rim of the diode. The mode leaks to the cone below and by reflecting from the cone sides starts moving to the back side of the substrate in vertical direction. To achieve vertical movement the mode dimension in the cone should increase two or three fold. In this case as estimate in the framework of geometrical optics approximation shows the length of the cone should be the cone initial radius multiplied by square of the mode diameter ratio the mode to proceeds adiabatic. As a representative example one have for a laser diode diameter 20 micron the length of the cone should be 40–60 microns.

On the back side of the substrate to transform the electromagnetic field originated from WGM with high azimuthal 30–300 index number to a beam with azimuthally symmetry one can etch phase corrector which suppress azimuth dependence of the laser beam.

Fig. 2 shows the laser without waveguiding layers (laser without cladding) in the active region WGM guiding around

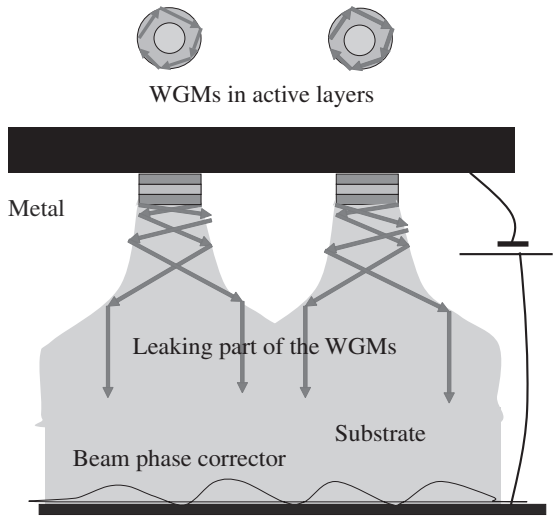

Fig. 1. Scheme (not to scale) of a portion of wafer with multiple WGM lasers leaking to and made on the same substrate with waveguide layers, active layers, metal contacts, leaking wave beam and phase correctors shown.

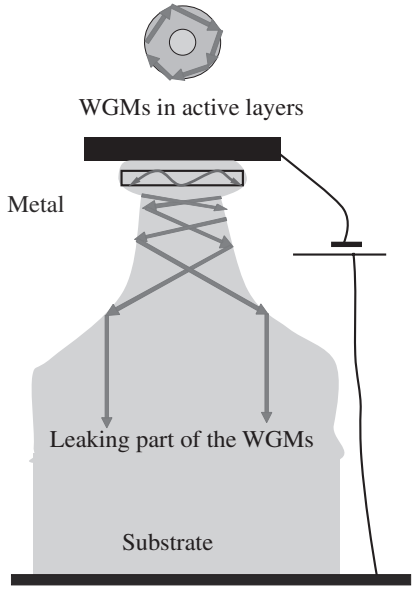

Fig. 2. Scheme of the WGM laser without cladding.

active layer is achieved here due to formation of caustic produced by barrel-like form of the active region. It is an intriguing possibility to produce interband QW laser without waveguiding layers because in this case carrier injection to active QW layer can improve. On the other hand such a scheme looks the ideal way to fabricate miniature cw intraband lasers on silicon and germanium.

Fig. 3 gives scheme of WGM laser with narrow gap (high dielectric constant) active layers grown on wide gap (low dielectric constant) substrate. WGM in this case is low leaking one. The degree of the leak can be increased if one produce trapezoidal-like form of the active layers.

2. Conclusion

We believe that the discussion given show a lot of different and flexible possibilities for fabrication of vertically emitted lasers of different type and of systems of such lasers. Many details of their design should be elaborated yet. Here one should take experience of people of Nizhny Novgorod (now with IAP RAS) in design, understanding, simulation and calculation for similar system of vacuum electronics. It is likely that with proper choice of the cone form and parameters of the phase corrector at the back side of substrate it is possible to produce vertically propagating gaussian beam. Also in the case of small diameter single mode lasers fabricated on single wafer by proper choice of inter laser distance and, say, coupling elements on the substrate back side it is possible to organize synchronization of the whole laser system. Surely one of the crucial problem is developing of the appropriate fabrication methods for such lasers.

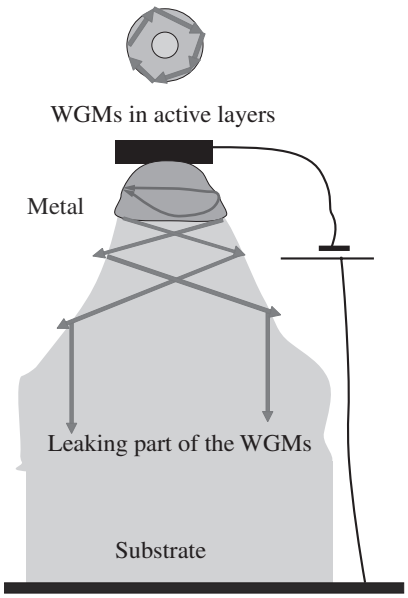

Fig. 3. Scheme of the WGM laser with narrow gap active layer grown on wideband substrate.

Acknowledgements

This work is supported in part by RFBR grant N 03-02-17318, by RAS Programs "Problems of Radiophysics" and "Semiconductor Lasers".

The author is indebted to M. I. Petelin, B. N. Zvonkov and N. B. Zvonkov, V. I. Shashkin and F. Yu. Klimov for encouragement, fruitful discussions and important remarks.

References

[1] B. N. Zvonkov, N. B. Zvonkov *et al*, *Quantum Electronics* **25**, N 7, 622 (1998).
[2] Y. Yamamoto and E. Slusher, *Physics Today* **46**, 66 (1993).
[3] C. Gmachl, F. Cappaso *et al*, *Science* **280**, 1556 (1998).
[4] M. Petelin *et al*: In Proceedings of the Institute of Applied Physics RAS, published in 70s and 80s.

13th Int. Symp. "Nanostructures: Physics and Technology"
St Petersburg, Russia, June 20–25, 2005

Matrix of vertical-cavity surface-emitting lasers with combined AlGaO/GaAs–AlGaAs/GaAs DBRs

S. V. Chumak[1], N. A. Maleev[2], A. G. Kuzmenkov[2], A. S. Shulenkov[1], A. E. Zhukov[2], A. P. Vasil'ev[2], S. A. Blokhin[2], M. M. Kulagina[2], M. V. Maximov[2] and V. M. Ustinov[2]

[1] Minsk R&D Institute of Radiomaterials, Minsk, Belarus
[2] Ioffe Physico-Technical Institute, St Petersburg, Russia

Abstract. Design features and fabrication technology of integrated matrix of vertical-cavity surface-emitting lasers (VCSELs) with oxidized top AlGaO/GaAs and semiconductor AlGaAs/GaAs bottom distributed Bragg reflectors (DBRs) are discussed. Matrix emitters contain 8x8 bottom-emitting VCSELs and are based on double quantum well InGaAs active region. Individual emitters with 8–10 micron oxidized apertures demonstrate lasing at 960–975 nm with room-temperature threshold current of 1–2 mA, external efficiency > 0.3 mW/mA and maximum CW output power 2–3 mW.

Introduction

Large-scale individually addressable VCSEL matrix are key active elements for future high aggregate rate short range optical data links and free space interconnects [1,2]. Matrix based on bottom-emitting VCSELs with InGaAs quantum well (QW) active region are good choice since they are suitable for flip-chip bounding [3]. Usually these devices utilize either standard p- and n-doped AlGaAs/GaAs DBRs or undoped AlGaAs/GaAs DBRs and intracavity contacts. In this work we discuss design, MBE growth and fabrication technique of integrated VCSEL matrix based on bottom-emission intracavity-contacted structures with combined AlGaO/GaAs–AlGaAs/GaAs DBRs.

Intracavity-contacted VCSEL matrix with combined AlGaO/GaAs-AlGaAs/GaAs DBRs

The VCSEL design with combined AlGaO/GaAs–AlGaAs/GaAs DBRs and oxidized apertures was verified by fabrication of InGaAs QW intracavity-contacted bottom-emission VCSELs [4]. In this work VCSEL structure was adopted for matrix application by using individual contact pads on the top of AlGaO/GaAs DBRs and common integrated intracavity n-contact for all emitters. Individual VCSEL structure is shown schematically in Fig. 1. The 5λ cavity with two aperture layers is placed between top AlGaO/GaAs DBR (7 pairs) and bottom output $Al_{0.92}Ga_{0.08}As$ DBR (19 pairs). 1λ GaAs active region with two InGaAs quantum wells is sandwiched between p-doped and n-doped AlGaAs aperture layers with graded interfaces.

All epitaxial layers are grown on a semi-insulating GaAs substrate by molecular-beam epitaxy in Riber 32 chamber. Preliminary calibration for the layer thickness/compositions were applied. To obtain better exactness the MBE system was additionally equipped with optical system for reflection spectra measurements in high-vacuum loading chamber. The reflection spectra for real VCSEL structures were measured after bottom DBR and cavity growth. Necessary correction in MBE-growth regimes was done basing on comparison of measured and calculated reflection spectra. The key point to obtain mechanically-stable VCSEL structure with oxidized DBRs/apertures is careful optimization of layer compositions and oxidation regimes. Optimized technology provides reproducible oxidation of the both aperture layers and top DBR in one process [4].

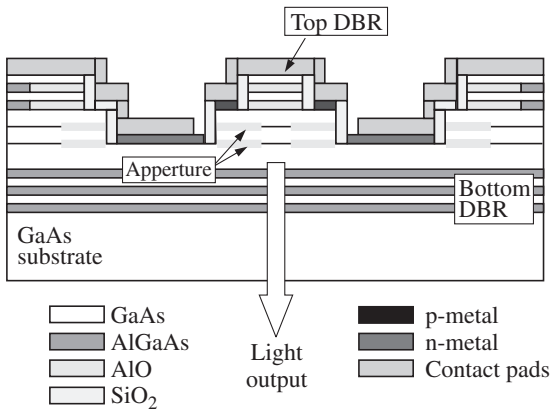

Fig. 1. Schematic cross-section of individual VCSEL structure.

After p- and n-contact deposition, device passivation, contact pads formation and substrate thinning individual VCSELs characteristics were measured directly on wafer in CW operation mode. Measured L–I and I–V curves are shown in Fig. 2. Device demonstrates threshold voltage of ∼2 V and threshold current of ∼1 mA at room temperature. Output power of 3.0 mW was obtained before laser output roll-over was observed. Device series resistance (115 Ω at 10 μm aperture) is a quite low for double intracavity-contacts design.

Fabricated emitters with aperture sizes 8–10 micron demonstrate multi-mode behavior. However this is not limitation

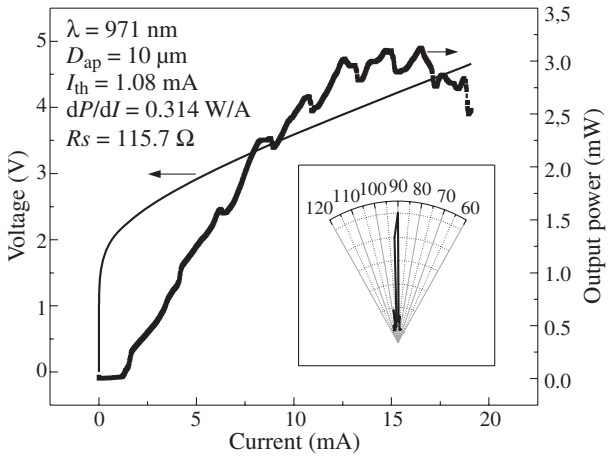

Fig. 2. Measured L–I and I–V curves for individual VCSEL emitter measured on-wafer without temperature stabilization. Insert shows far-field pattern.

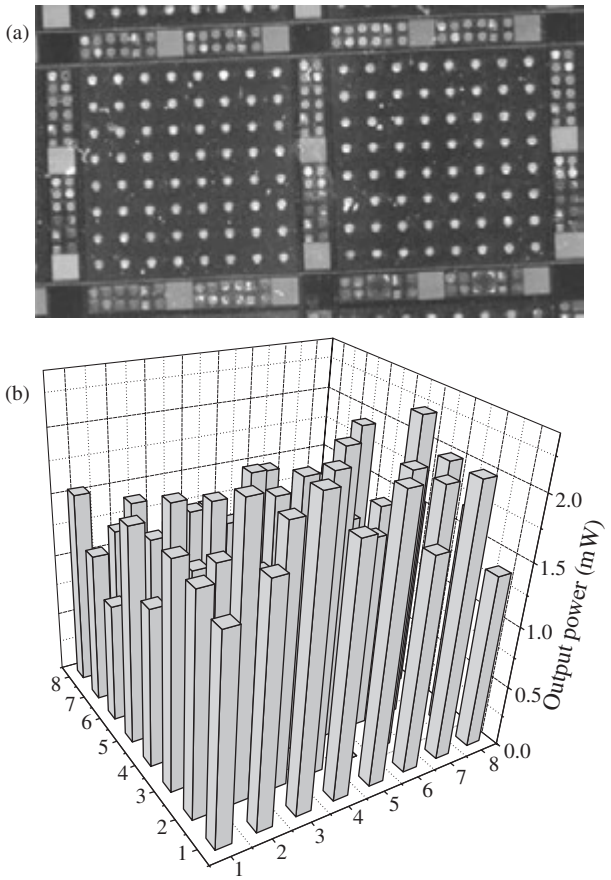

Fig. 3. Photograph of matrix chip (a) and output power distribution of individual VCSELs at drive current of 10 mA (b).

for many applications such as inter-board connection systems. Measured VCSEL far-field pattern is shown in insert of Fig. 2.

Photograph of VCSEL matrix chips (top-view) is shown in Fig. 3. Neighboring matrix are separated by region with test elements. Fig. 3b illustrates spatial distribution of output optical power for individual VCSEL emitters. CW output power was measured on-wafer at drive current of 10 mA without temperature stabilization. All emitters demonstrate output power more than 1 mW. Sufficient non-uniformity are mainly caused by variation in aperture sizes. Further improvements in aperture sizes control may be obtained by using low-pressure oxidation technique, careful surface cleaning before oxidation and smaller mesa sizes [5].

References

[1] *Vertical-Cavity Surface-Emitting Lasers*, Eds. C. W. Wilmsen, H. Temkin and L. A. Coldren, Cambridge Univ. Press, 1999.
[2] O. Kibar, D. A. Van Blerkom, F. Chi, S. C. Esner, *J. Lightwave Techn*. **17**, 546 (1999).
[3] K. D. Choquette and H. Q. Hou, *Proc. IEEE* **85**, 1730 (1997).
[4] N. A. Maleev, A. G. Kuzmenkov, A. E. Zhukov, A. P. Vasil'ev, A. S. Shulenkov, S. V. Chumak, E. V. Nikitina, S. A. Blokhin, M. A. Kulagina, E. S. Semenova, D. A. Livshits, M. V. Maximov, V. M. Ustinov, *Semiconductors* **37**, 1234 (2003).
[5] P. C. Ku, C. J. Chang-Hasnain, *IEEE J. Quantum Electron*. **39**, 577 (2003).

13th Int. Symp. "Nanostructures: Physics and Technology"
St Petersburg, Russia, June 20–25, 2005

Light emission, absorption and amplification in InAs/GaAs quantum dots and GaAs/AlGaAs quantum wells resulting from optical pumping

D. A. Firsov[1], L. E. Vorobjev[1], M. A. Barzilovich[1], V. Yu. Panevin[1], I. V. Mikhaylov[1], N. K. Fedosov[1,5], V. A. Shalygin[1], A. A. Tonkikh[2], N. K. Polyakov[2], Yu. B. Samsonenko[2], G. E. Cirlin[2], A. E. Zhukov[3], N. A. Pikhtin[3], I. S. Tarasov[3], V. M. Ustinov[3], F. H. Julien[4], M. Sekowski[5], S. Hanna[5] and A. Seilmeier[5]

[1] St Petersburg State Polytechnic University, 195251 St Petersburg, Russia
[2] Institute for Analytical Instrumentation, 198103 St Petersburg, Russia
[3] Ioffe Physico-Technical Institute, St Petersburg, Russia
[4] Universite Paris-Sud, 91405 Orsay, France
[5] Experimentalphysik III, Universität Bayreuth, D-95447 Bayreuth, Germany

Abstract. Optical phenomena in quantum dot and quantum well nanostructures aimed at the development of mid-infrared lasers based on intraband electron transitions are investigated in the conditions of interband optical pumping. Evolution of photoluminescence spectra and interband light absorption are investigated in InAs/GaAs quantum dot structures. Optically induced intersubband mid-infrared light absorption is studied in undoped tunnel-coupled GaAs/AlGaAs quantum wells. Intensities of interband optical pumping necessary for filling the quantum dot ground states and lasing in structures with quantum wells are estimated.

Introduction

The present paper is devoted to the investigation of optical phenomena in nanostructures induced by optical pumping. Photoluminescence spectra, absorption and amplification of near-infrared (NIR) light related to the interband electron transitions were studied in InAs/GaAs quantum dot (QD) structures. The absorption of mid-infrared light due to intersubband electron transitions was studied in GaAs/AlGaAs tunnel-coupled quantum wells (QWs). Results of the present investigations will be useful for the development of MIR lasers based on intraband electron transitions in nanostructures with QDs and QWs [1, 2].

1. Experiments on QDs

QD structures of two types were used. In the structure F173 15 layers of InAs/GaAs QDs were embedded into a wide (approximately 8 μm) graded AlGaAs waveguide providing optical confinement both for MIR and NIR radiation what is important for two-color laser operation [1, 2]. The evolution of PL spectra was studied in the structures with a Fabry-Perot resonator under increasing intensity of a 100 fs pulse optical pumping at a wavelength of $\lambda = 0.8\,\mu$m. Superluminescence and NIR lasing corresponding to carrier transitions between excited QD states were found. NIR lasing is a necessary condition of MIR stimulated emission due to intraband electron transitions in QDs [1, 2].

Occupation of the ground QD states under interband optical pumping was studied in the structures F140 with 15 InAs/GaAs QD layers without waveguide. NIR probe polarized light absorption technique was used. The input and output edges of the sample were polished at an angle of 45°. The structure was pumped with pulses ($\Delta t \simeq 0.4\,\mu$s) of a frequency doubled YAG laser radiation ($\lambda = 0.532\,\mu$m).

Two semiconductor lasers ($\lambda_1 = 1.15\,\mu$m, $\lambda_2 = 1.25\,\mu$m) were used as a NIR probe sources. Operating wavelength of the first laser λ_1 corresponded to the NIR light absorption peak for electron transitions hh1→e1, while the second laser was tuned out of the absorption peak. Photon energies for both lasers are shown by arrows in Fig. 1 where the interband light absorption spectrum is shown.

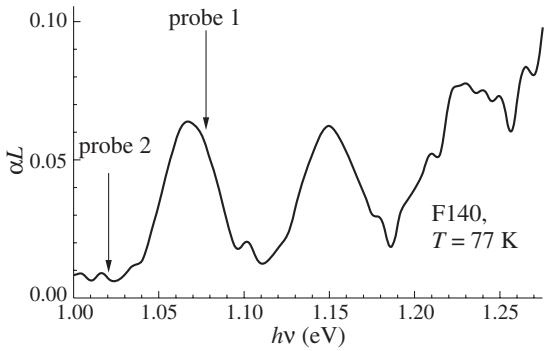

Fig. 1. Interband light absorption in QD sample F140 (α is absorption coefficient, L is optical path).

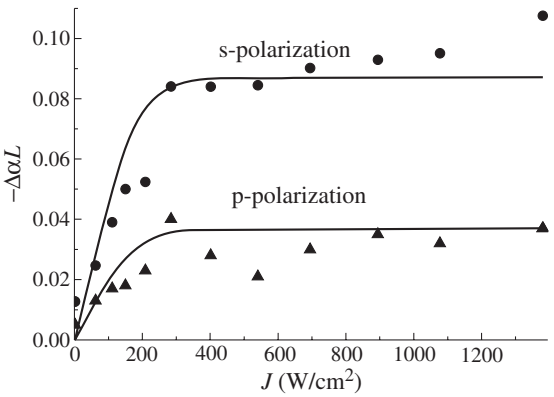

Fig. 2. The change of light absorption in QDs at wavelength $\lambda_1 = 1.15\,\mu$m for s- and p-polarized probe light as a function of optical pumping intensity. $T = 77$ K.

Absorption of probe light at $\lambda_1 = 1.15\,\mu$m decreases with increasing pump level (see Fig. 2) due to filling QD states with electrons and holes (Pauli blocking). Probe light absorption converted to light amplification at high pump intensities and strong occupation of ground QD states.

Optical hh1→e1 transitions in InAs/GaAs QDs are allowed only for s-polarized light (polarization vector lyes in the plane

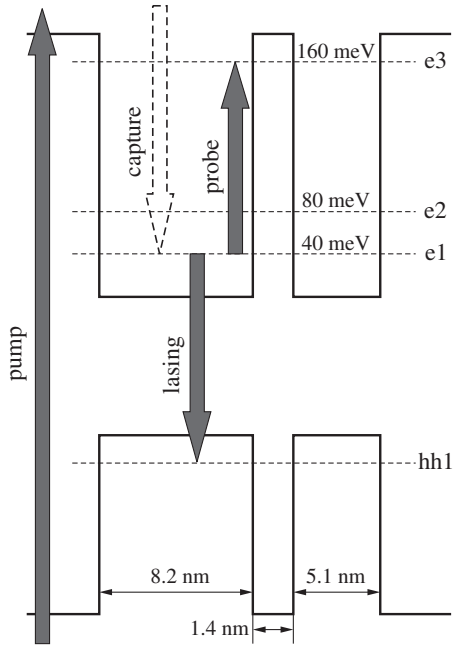

Fig. 3. Diagram of photoinduced intersubband MIR light absorption in tunnel-coupled GaAs/AlGaAs QWs.

of QD layers). Therefore, the change of absorption for p-polarized light containing a component parallel to the growth axis has to be two times less. This is confirmed by experimental data (Fig. 2). At the same time, the transmission of light at $\lambda_2 = 1.25\ \mu$m (outside of absorption peak) is weekly affected by optical pumping both for p- and s-polarizations. The observed data allow to evaluate the level of optical pump needed to fill the ground states of QDs by electrons and holes.

2. Experiments on QWs

Intraband (intersubband) MIR light absorption connected with electron transitions between ground and excited states e1→e3 was studied in undoped tunnel-coupled GaAs/AlGaAs QWs under interband optical pumping (see Fig. 3).

The structure contained 18 layers of asymmetrical pairs of tunnel-coupled QWs separated by wide 12 nm barriers. These active layers were surrounded by a graded NIR waveguide. Cleaved edges of the sample formed a 2 mm resonator. This system of tunnel-coupled QWs is analogous to funnel shape QWs described in [1, 2], so intraband population inversion between excited levels e2 and e3 is possible in this structure under interband optical or current pumping.

Optical pumping was realized with the same YAG laser ($\Delta t \simeq 0.4\,\mu$s, $\lambda = 0.532\ \mu$m). The wavelength of probe MIR light was $10.6\,\mu$m. Intersubband optical transitions in QWs are allowed only for light polarized along growth axis. That is why we observed the increase of MIR light absorption with the increase of optical pumping intensity only for p-polarized light. Light absorption corresponding to e1→e3 transitions and consequently the electron concentration at the ground level e1 saturate after starting NIR lasing due to interband e1→hh1 transitions. Stabilization of the ground state electron concentration is one of the necessary conditions of MIR stimulated emission in a bi-color laser [1, 2]. The intensity of optical pumping necessary for NIR interband lasing is estimated.

Acknowledgements

This work was supported by grants of INTAS, RFBR, ISTC and Russian Ministry of Education and Science. One of the authors is grateful for support to DAAD and Russian Ministry of Education and Science "Michael Lomonosov" program.

References

[1] A. Kastalsky, L. E. Vorobjev, D. A. Firsov, V. L. Zerova, E. Towe, *IEEE Journal of Quantum Electronics*, **37**, 1356 (2001).

[2] L. E. Vorobjev, D. A. Firsov, V. A. Shalygin, V. N. Tulupenko, N. N. Ledentsov, P. S. Kop'ev, V. M. Ustinov, Yu. M. Shernyakov, Zh. I. Alferov, *Physics-Uspekhi*, **42**, 391 (1999).

13th Int. Symp. "Nanostructures: Physics and Technology"
St Petersburg, Russia, June 20–25, 2005

Silicon quantum dot assemblies with erbium: toward Si-based optical amplifiers and lasers

P. K. Kashkarov[1], O. A. Shalygina[1], D. M. Zhigunov[1], S. A. Teterukov[1], V. Yu. Timoshenko[1], M. Zacharias[2], M. Fujii[3] and Sh. Hayashi[3]

[1] Moscow State Lomonosov University, Physics Department, 119992 Moscow, Russia
[2] Max-Planck-Institute of Microstructure Physics, Weinberg 2, 06120 Halle, Germany
[3] Kobe University, Faculty of Engineering, Department of EEE, 657-8501 Kobe, Japan

Abstract. Structures of assembled Si quantum dots in SiO_2 matrix are characterized by efficient photoluminescence whose spectral position is tuneable from 1.3 to 1.7 eV depending on nanocrystals size varied from 4.5 to 1.5 nm. Er-doped structures exhibit luminescence of Er-ions at 0.81 eV, which are excited by energy transfer from excitons confined in Si quantum dots. Under strong optical pumping the energy transfer to Er^{+3} ions results in the population inversion, which is promising for future applications of such kind of structures in optical amplifiers and lasers compatible with Si-based technology.

Introduction

It is known that Er^{+3} ions in a solid matrix can emit at 1.5 μm due to ${}^4I_{13/2} \rightarrow {}^4I_{15/2}$ transitions in their internal $4f$-shell [1]. Since this wavelength corresponds to a transparency window of silica fiber communication systems, Er-doped materials are promising for applications [1, 2]. It was recently demonstrated that Er-doped SiO_2 layers containing Si quantum dots (QDs) exhibit efficient room temperature PL at 1.5 μm (0.8 eV), which is caused by energy transfer from excitons confined in Si QDs [3–8]. In the present work we investigate the PL transients and spectra of undoped and Er-doped nc-Si/SiO_2 structures at different temperatures and pump intensities. It is shown that at high excitation level the population inversion of Er^{+3} ions could be achieved because of the efficient energy transfer from excitons in Si QDs.

1. Experimental

Two kinds of nc-Si/SiO_2 structures are investigated. Series 1 consists of the structures of quasi-ordered Si nanocrystals prepared by thermal crystallization of amorphous SiO/SiO_2 superlattices [5]. Samples of series 2 were formed by co-sputtering c-Si, SiO_2 and Er_2O_3 targets in plasma of rf-discharge and then thermally annealed [3]. For series 1 the nanocrystals size d was varied from 1.5 to 4.5 nm by changing the SiO layer thickness d_{SiO} from 2 to 6 nm with a step of 1 nm. The inset of Fig. 1 shows a transmission electron microscopy (TEM) cross-sectional image of the nc-Si/SiO_2 structure of series 1 with $d_{SiO} = 3$ nm. Dense arrays of nearly spherical Si nanocrystals (black fields) embedded in the SiO_2 matrix are well distinguished. The average nanocrystal diameter extracted for this sample from its TEM image is $d = (3.5 \pm 0.5)$ nm. Pieces of the samples of series 1 were implanted by Er ions at 300 keV with doses of $2 \cdot 10^{15}$ cm^{-2} (average Er concentration $N_{Er} \sim 10^{20}$ cm^{-3}). The samples of series 2 contain 0.1 at.% Er ($N_{Er} \sim 10^{19}$ cm^{-3}). The layers thickness dependent on d_{SiO} was 0.1–0.3 μm (series 1) and ~ 1 μm (series 2).

The PL was excited by using a N_2-laser ($E_p = 3.7$ eV, pulse duration $\tau_p = 10$ ns, repetition rate $\nu \sim 10$ Hz) or a Cu-laser ($E_p = 2.1$ and 2.4 eV, $\tau_p = 20$ ns, $\nu \sim 12$ kHz). The PL signal was detected by an InGaAs photodiode (spectral range 0.7–2.2 eV) with a preamplifier or by a CCD array (spectral range 1.1–2.2 eV). The PL spectra under pulsed excitation were measured by a photomultiplier or photodiode operating in time integrating regime. PL spectra were corrected for spectral response of the measurement system. Transients of the Er-related PL under pulsed laser excitation were detected by an InGaAs photodiodes with preamplifiers, which possess time resolution of about 0.2 ms.

2. Results and discussion

The PL spectra of the undoped nc-Si/SiO_2 structures of series 1 with different nanocrystal size d are shown in Fig. 1. The intrinsic PL represents a broad band with maximum at 1.3–1.6 eV depending on d: a blue shift of the PL band is observed with decreasing d_{SiO}. The intrinsic PL of nc-Si can be assigned to the radiative recombination of excitons confined in Si nanocrystals, while the size dependent spectral shift is usually attributed to the quantum confinement effect. A considerable halfwidth of the PL band is explained by nanocrystal size distribution and by phonon-assistant electron-hole recombination. The external quantum yield of the exciton PL is found to reach $\sim 1\%$ for the samples of series 1 with $d = 3 - 4$ nm. This high quantum yield indicates a low efficiency of nonradiative recombination processes. However the PL intensity of nc-Si/SiO_2 structures with $d_{SiO} = 2$ nm (nanocrystal size 1.5 nm) was essentially

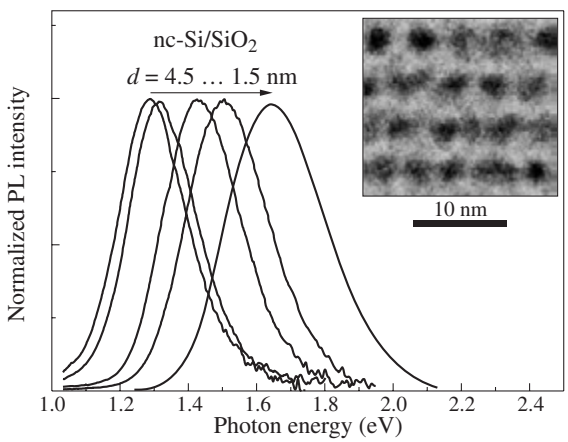

Fig. 1. PL spectra of undoped nc-Si/SiO_2 structures with different nanocrystal size d. Inset: TEM cross-sectional image of the structure with $d = 3.5$ nm.

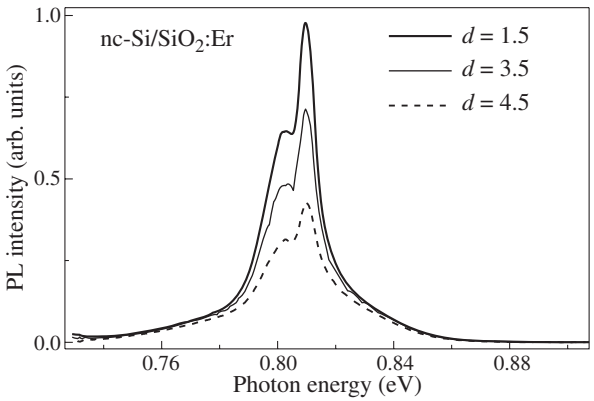

Fig. 2. Spectra of the Er^{+3} PL of nc-Si/SiO_2:Er structures with different d.

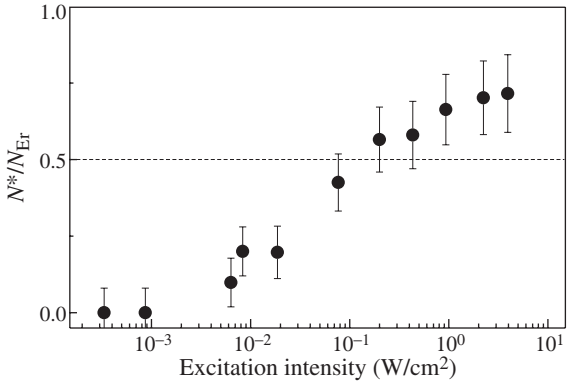

Fig. 3. Relative concentration of the excited Er^{+3} ions *vs* laser pump intensity for nc-Si/SiO_2:Er structure with $d = 4$ nm. Dashed line indicates the level of $N^*/N_{\rm Er} = 0.5$, i.e. the population inversion.

weaker. This fact can be explained by decreasing the optical absorption cross-section of the small Si nanocrystals. However, an increase of the nonradiative recombination rate can not be ruled out because the smallest nanocrystals have largest specific surface area and then the defect density.

The Er-doping leads to a strong quenching of the exciton PL and an appearance of the Er^{+3} emission at 0.81 eV. The room temperature spectra of the Er-related PL of nc-Si/SiO_2:Er structures with different nanocrystal size are plotted in Fig. 2. One can see that the Er^{+3} PL intensity increases when the nanocrystal size decreases. The strongest Er^{+3} PL yield is observed in the structure composed from Si nanocrystals of 1.5–2 nm size. This fact demonstrates that the Er^{+3} sensitization efficiency is maximal in the structures with smallest Si QDs.

In order to analyze qualitatively the role of the limited number of the ions and possibility to reach the population inversion, we investigated transients of the Er^{+3} PL at 0.8 eV, which were excited by chopped laser radiation. The ratio of $N^*/N_{\rm Er}$, where N^* is the ion concentration in the first excited state and $N_{\rm Er}$ is the total ion concentration, can be easily derived from the PL times. Indeed, the following equation governs the dynamics of the population and depopulation of ions:

$$\frac{dN^*}{dt} = g\left(N_{\rm Er} - N^*\right) - N^*\tau_{decay}^{-1}\,, \qquad (1)$$

where g is the generation rate, which can depend on nanocrystals size, temperature, excitation intensity and photon energy, and etc. However, at continuous pump one can assume that $g = \text{const}$. Thus, from Eq. (1) the following expression for the rise and decay times can be written:

$$\tau_{\rm rise}^{-1} = g + \tau_{\rm decay}^{-1}\,. \qquad (2)$$

According to expressions (1) and (2) the number of excited ions in steady state conditions is given by the following equation:

$$N^* = \frac{gN_{\rm Er}}{g + \tau_{\rm decay}^{-1}} = gN_{\rm Er}\tau_{\rm rise}\,. \qquad (3)$$

Thus, $N^*/N_{\rm Er}$ ratio is as follows:

$$\frac{N^*}{N_{\rm Er}} = 1 - \frac{\tau_{\rm rise}}{\tau_{\rm decay}}\,. \qquad (4)$$

Typical dependence of $N^*/N_{\rm Er}$ ratio on excitation intensity is shown in Fig. 3. The population inversion ($N^*/N_{\rm Er} > 0.5$) for samples of series 2 is achieved at pump intensity $I_{\rm p} > 0.1$ W/cm^2. To achieve the population inversion for the samples of series 1 a stronger pump is needed because $N_{\rm Er}$ is higher than for series 2. It should be noted that at low temperatures the population inversion for the samples of both series is achieved at lower pump intensities because the nonradiative recombination rate decreases with temperature lowering in the structures investigated [8].

It has been found that the decay time becomes shorter at excitation intensities, which lead to the deeper population inversion. This fact can be caused by a contribution of the stimulated optical transitions at 0.8 eV. Another possible reason of the lifetime decrease is the energy back transfer from Er^{+3} to the matrix. In particular, the Er^{+3} PL can be absorbed by the ions in the first excited state followed the transition to the third excited state [1]. The ions in the third and second excited states can transfer fast their energy back to the excitons in Si quantum dots. This process seems to be rather efficient under the population inversion conditions. It should be noted that the decrease of the decay time under strong laser excitation was observed for the samples of both series, i.e. for different $N_{\rm Er}$. Further experiments are needed to completely understand the lifetime shortening of the Er^{+3} emissions at high excitation intensity. A contribution of the stimulated optical transitions can be obviously enhanced by optimizing the sample properties (e.g., Si nanocrystal size, layer thickness, $N_{\rm Er}$, and etc.) as well by forming waveguide structures.

Acknowledgements

This work was supported by INTAS (grant No. 03-51-6486), Russian Foundation for Basic Research (grants Nos. 03-02-16647, 04-02-08083), and Ministry of Education and Science of the Russian Federation.

References

[1] A. Polman, *J. Appl. Phys.*, **82**, 1 (1997).
[2] S. Coffs *et al*, *MRS Bulletin*, **4**, 25 (1998).
[3] M. Fujii *et al*, *J. Appl. Phys.*, **84**, 4525 (1998).
[4] P. G. Hansen *et al*, *Appl. Phys. Lett.*, **76**, 2325 (2000).
[5] J. Heitmann *et al*, *Mat. Sci. Engin.*, **B105**, 214 (2003).
[6] P. K. Kashkarov *et al*, *JETP*, **97**, 1123 (2003).
[7] V. Yu. Timoshenko *et al*, *Appl. Phys. Lett.*, **84**, 2512 (2004).
[8] V. Yu. Timoshenko *et al*, *J. Appl. Phys.*, **96**, 2254 (2004).

13th Int. Symp. "Nanostructures: Physics and Technology"
St Petersburg, Russia, June 20–25, 2005

Generation of sum harmonic in two-chips GaAs/InGaAs/InGaP laser with composite resonator

K. V. Maremyanin[1], S. M. Nekorkin[2], A. A. Biryukov[3], *S. V. Morozov*[1], V. Ya. Aleshkin[1], V. I. Gavrilenko[1] and Vl. V. Kocharovsky[4]

[1] Institute for Physics of Microstructures RAS, Nizhny Novgorod, Russia
[2] Research Physical-Technical Institute of the N. Novgorod State University, Nizhny Novgorod, Russia
[3] Institute for Quantum Studies and Department of Physics, Texas A&M University, College Station, USA
[4] Institute of Applied Physics RAS, Nizhny Novgorod, Russia

Abstract. Parametric generation of sum harmonic has been discovered in "two-chips" CW laser with the compound resonator at room temperature.

Introduction

Semiconductor heterolasers based on GaAs and other semiconductor A_3B_5 compounds, are promising devices from the point of view of nonlinear optics. Indeed, the electric field of a lightwave inside the laser is very high: 10^4–10^5 V/cm. Besides, the value of the 2nd order lattice nonlinear permittivity in GaAs is sixfold that in the commonly used nonlinear crystal $LiNbO_3$ [1]. These factors allow to reckon on essential nonlinear effects, in particular, the parametric generation of difference and sum harmonics in near IR GaAs/InGaAs/InGaP injection semiconductor lasers with InGaAs quantum wells.

1. Experimental

In Ref. [2] in two-frequency semiconductor laser a mid IR radiation was detected, the radiation being attributed to the parametric generation of the difference harmonic. However the radiation intensity was so weak that it was observed at liquid helium temperature only when the laser and the detector were situated close by each other. Evidently it results from the absence of the phase matching between nonlinear polarization wave and the difference harmonic and from a small factor of space overlapping of the fundamental laser modes. Note that up to the present in such lasers a sum harmonic has not been observed.

In the present work we demonstrate the design of a "two-chips" laser with the composite resonator, consisting of two single-frequency injection GaAs/InGaAs/InGaP quantum wells lasers mounted on the one and the same platform just next to each other. The wavelengths of fundamental modes of the both lasers (in the range of 1 μm) are a little bit different. The design makes it possible to bring an appreciable part of one laser radiation in the resonator of another one. Actually, one of lasers (more long-wavelength) is used only for pumping while the second serves simultaneously as a nonlinear element. To our experience it is possible to get up to 50% of radiation power of long-wavelength laser in the waveguide of another one. The two-chips laser design has a series of advantages in comparison with the two-frequency one, such as separate pumping of each laser, expansion of the range for difference harmonic generation due to independent growth of two separate structures; use of the combined pumping mode, independent temperature control of two separate chips. The most important one seems to be the increase of space overlapping between the fundamental modes that greatly enhance the nonlinear effects. As a result

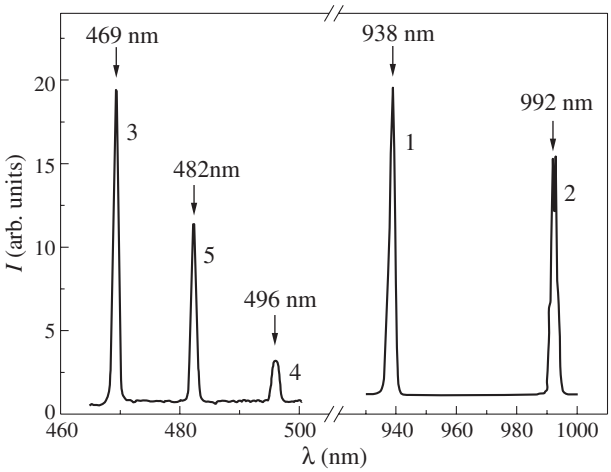

Fig. 1. Emission spectra of two-chips laser: fundamental modes (1, 2), second (3, 4) and the sum (5) harmonics at room temperature.

we have succeeded to observe for the first time the parametrical generation of the sum harmonic. Typical measures spectra of the fundamental modes as well as the second and the sum harmonics are given in Fig. 1.

Essential intensity of the sum harmonic testifies the efficiency of nonlinear interaction of the two near IR modes inside the laser resonator and, as consequence, point out on a possibility of difference harmonic generation. Since the observation of sum harmonic is much easier to realize if compared with the difference frequency one the sum harmonic measurements are useful as an indicator of the efficiency of nonlinear interaction in the laser waveguide.

By means of polarization measurements the sum harmonic is shown to be a TM mode (the electric field is directed normally to the structure). At the same time the laser fundamental modes are TE modes. The polarizing restudies have confirmed that the sum harmonic generation is due to the lattice nonlinearity. Since the fundamental modes are propagating in the laser resonators along [110] direction, the lattice nonlinearity results in the electric induction along [001] direction that corresponds to excitation of a TM mode.

Acknowledgements

The work has been financially supported by Program Jointly by Russian Ministry of Education and US Civilian Research Development Foundation (CRDF) and Basic Research and Higher

Education (BRHE) (REC NN #001), RFBR (# 04-02-17432), ISTC (# 2293), NATO (SfP-973799 Semiconductors), RAS and Ministry of Education and Science of Russian Federation.

The authors are thankful to B. N. Zvonkov, N. B. Zvonkov and L. P. Kulikova for growth and manufacturing “two-chips” lasers.

References

[1] Y. S. Lee *et al*, *Appl. Phys. Lett.*, **78**, 3583 (2001).
[2] V. Ya. Aleshkin *et al*, *Proc. of 12th Int. Symp. Nanosructures: Physics and Technology*, St Petersburg, Russia, 54 (2004).

13th Int. Symp. "Nanostructures: Physics and Technology"
St Petersburg, Russia, June 20–25, 2005

Analysis of bistable quantum dot injection laser

N. S. Averkiev, *V. V. Nikolaev*, M. Yu. Poliakov, A. E. Gubenko, I. M. Gadjiev and E. L. Portnoi
Ioffe Physico-Technical Institute, St Petersburg, Russia

Abstract. We developed a theoretical model of bistable operation of a two-sectional injection laser based on quantum dot heterostructure. In such a laser one of the sections is pumped by direct current (works as an amplifier) and the other section is reverse biased (works as a saturated absorber). We have established the region of variation of the ratio between the lengths of the amplification and absorption sections in which the bistable behaviour exists. The comparison between the theoretical model and experimental data is presented.

Introduction

It was predicted as early as in 1960s [1] that a semiconductor injection laser with a saturable absorber can exhibit bistable behaviour. The power output from a bistable laser experiences an abrupt jump with the increase of the pumping current; the value of the current at which this jump occurs can be called a *turn-on threshold current*, J_{thON}. When the pumping current is decreased, the lasing stops at the *turn-off threshold current* J_{thOFF}, less than the turn-on current $J_{\mathrm{thOFF}} < J_{\mathrm{thON}}$. Hence the light-versus-current curve of such a device features a hysteresis loop. Such a bistable behaviour could have important applications in optical switching and modulation. On the other hand, such an effect could be damaging for quantum-dot lasers operating in the mode-locked regime.

Despite the early theoretical prediction, the full bistable operation has never been observed in double-heterostructure or quantum-wells lasers. Recently, room-temperature bistability in two-section injection lasers which utilise quantum dots (QDs) as an active medium has been reported [2,3]. The bistability is observed in structures with the absorber lengths less than 20 percent of the total length of the device. This contradicts to the Lasher's prediction [1] that realisation of bistable operation is possible only when the absorbing section is comparable or even larger when the gain section. These experimental results suggest that the quantum-dot layers, used as an active medium of a laser system, are qualitatively different from conventional semiconductor or quantum wells with respect to bistability. In this paper we present theoretical model which is able to describe laser bistability in quantum-dot systems.

1. The model

The model is based on rate equations which couple the occupation probabilities of the levels of the quantum dots in gain and absorption sections with the number of photons S (reduced to the area of the device) in the lasing mode.

Consider a quantum dot in which the energy difference E between the ground electron and hole quantised levels is equal to one of the laser cavity modes. For the gain section of the device, one can write the following rate equation for the occupation number f_g^e of the electron level in this QD

$$\frac{d}{dt} f_g^e(E) = k_e n_{\mathrm{QW}} \left(1 - f_g^e(E)\right) - k_e N_{2D}^c \exp\left(\frac{\varepsilon_g^e(E) - E_{\mathrm{QW}}^c}{T}\right) f_g^e(E) - \frac{1}{\tau_{\mathrm{QD}}} f_g^e(E) f_g^h(E) - \frac{g_0}{\pi\hbar\gamma_H}\left(f_g^e(E) + f_g^h(E) - 1\right) S\,. \quad (1)$$

The first and second terms in the right-hand side of Eq. (1) describe electron capture and escape, correspondingly; k_e is the temporal cross-section of electron capture from the wetting layer to a quantum dot, n_{QW} is the electron density in the wetting layer, and $N_{2\mathrm{D}}^c$ is the effective density of states of the lowest electron band in the wetting layer. It is assumed that the energy interval between different quantised levels in quantum dots is larger than their inhomogeneous broadening, in which case the values of electron and hole quantum-dot energy levels $\varepsilon_g^{e(h)}$ are well-defined functions of the transition energy E [4]. In this work we consider only the ground QD optical transition. The third term describes the spontaneous recombination in a QD; τ_{QD} is the electron-hole radiative lifetime. The last term is due to stimulated emission into the resonant cavity mode; coefficient g_0 accounts for the coupling between the QD optical transition and the cavity mode and can be described through τ_{QD}, the average transition energy E_0, and the optical confinement factor reduced to the QD layer width Γ/a_{QD}:

$$g_0 = 2\left(\frac{c\hbar}{n_c}\right)^3 \frac{1}{E_0^2}\frac{1}{\tau_{\mathrm{QD}}}\frac{\Gamma}{a_{\mathrm{QD}}}\,. \quad (2)$$

Here n_c is the cavity refractive index. The quantity $\hbar\gamma_H$ in Eq. (1) is the homogeneous broadening of the QD-to-lasing mode transition.

The equation for the hole occupation number f_g^h in the gain section is similar to Eq. (1). To obtain the corresponding equations for the occupation numbers in the absorption section $f_a^{e(h)}$ one should omit the carrier capture term (recapture is neglected). Furthermore, the escape coefficient may differ from that in Eq. (1) since, in the absorber case, the carriers in quantum dots and in the wetting layer are far from equilibrium. The carrier escape time from a QW in the absorber section is strongly dependent on the reverse bias.

The gain- and absorber-section rate equations are coupled by the equation for the photon number in the lasing mode:

$$\frac{d}{dt}S = N_{\mathrm{QD}} g_0 \Big[(1-\gamma_a) w_g(\hbar\omega_c)\left(f_g^e(\hbar\omega_c) + f_g^h(\hbar\omega_c) - 1\right) + \gamma_a w_a(\hbar\omega_c)\left(f_a^e(\hbar\omega_c) + f_a^h(\hbar\omega_c) - 1\right)\Big] S - r_c S. \quad (3)$$

Here N_{QD} is the surface density of QDs, γ_a is the ratio of the absorption-section length to the total length of the device (reduced absorber length). The function $w_{g(a)}$ is the distribution of the optical transitions per energy for gain (absorption)

section, normalised to unity. Here we use the Gauss distribution:

$$w_{g(a)}(E) = \frac{1}{\sqrt{2\pi}\,\Delta\varepsilon_{\text{inh}}} \exp\left(\frac{1}{2}\left(\frac{E - E_0^{g(a)}}{\Delta\varepsilon_{\text{inh}}}\right)^2\right). \quad (4)$$

The inhomogeneous broadening of the transition (ε_{inh}) is caused by the QD size fluctuations. The central transition energy in the absorber E_0^a is dependent on the applied bias, due to the quantum-confined Stark effect.

The last term in Eq. (3) gives cavity loss rate. The expression (3) is obtained with presumption that the inhomogeneous broadening is much larger than homogeneous one ($\varepsilon_{\text{inh}} \gg \hbar\gamma_H$), and the spontaneous radiative recombination into the lasing mode is neglected.

For a cavity length of a few millimetres generally there is a large number of modes within the broadened QD optical transition, which leads to a wide multimode lasing spectra at low temperatures. However, at room temperature the QD lasing linewidth is narrow, which can be explained by carrier thermolisation [5] or/and the increase of the homogeneous broadening. Here we consider a single homogeneously-broadened effective lasing mode, the position of which is established by the maximum of the gain spectra (i.e. we assume that there is always a cavity mode in the close vicinity of the gain maximum).

The above equations are solved in the steady-state regime, under condition of the charge neutrality of the gain section. The current in the gain section is the sum of the wetting layer recombination current $J_{\text{QW}} = B_{\text{QW}} n_{\text{QW}} p_{\text{QW}}$ and the quantum dot recombination J^r_{QD} and stimulated emission J^s_{QD} currents:

$$J^r_{\text{QD}} = e\frac{N_{\text{QD}}}{\tau_{\text{QD}}} \int f_g^h(E) f_g^e(E) w_g(E)\, dE \quad (5)$$

$$J^e_{\text{QD}} = e g_0 N_{\text{QD}} \left(f_g^h(\hbar\omega) + f_g^e(\hbar\omega) + 1\right) w_g(\hbar\omega) S\,. \quad (6)$$

By dividing the right-hand-side of Eq. (3) by S and multiplying by the group velocity v_g we can write the steady-state equation in the form

$$g_{mod}(\hbar\omega, J, S) = \beta_c\,, \quad (7)$$

where g_{mod} is the modal gain coefficient and $\beta_c = v_g r_c$ is the cavity loss coefficient. The modal gain is dependent on the light (i.e. cavity mode) frequency, the pumping current and the photon number. The laser output power is found through maximising the gain coefficient by frequency $\hbar\omega$ and then finding S from Eq. (7) under condition of a fixed pumping current. The bistable operation regime manifests itself by the two different roots of Eq(7), $S_1 > S_2$. It is possible to show that S_1 is a stable solution, whereas S_2 is always unstable. In such situation the system can reside either in the turn-on ($S = S_1$) or turn-off ($S = 0$) state, depending on the initial conditions.

2. Results and discussion

Figure 1 shows the calculation results of the laser light output versus the pumping current. The reduced length of the absorber γ_a is varied, and the total device length is kept constant (1.8 mm). The field applied to QDs in the absorber is set to zero which corresponds to an open circuit. One can see that

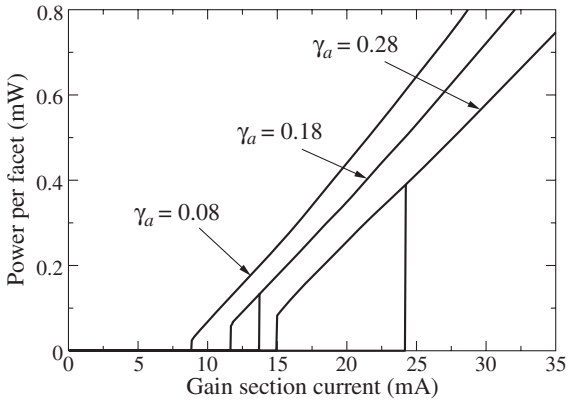

Fig. 1. Calculated light versus current curve for three different absorber reduced lengths. The total device length is 1.8 mm.

for the reduced absorber length of 0.18, corresponding to the experimental structure presented in [3], there is a pronounced hysteresis loop in the light-current curve. When the absorber occupies only 8 percent of the structure volume (corresponds to the actual structure measured in [6]) the hysteresis loop is clamped, but there is a jump in the output power at the start of the lasing. Such a behaviour is actually observed in experiment [3,6]. As the absorber percentage increases ($\gamma_a = 0.28$), the hysteresis loop is widening, and the both threshold current increase.

3. Conclusion

The theory of the quantum dot lasers with absorber sections was developed for the first time. The theory explains the occurrence of the bistable behaviour of the laser for some particular parameters of the structure. The change of the hysteresis in the light-current curve with the change of the length of the absorber is described. The results are in perfect qualitative and in good quantitative agreement with the experimental results.

References

[1] G. J. Lasher, *Solid-State Electronics*, **7**, 707 (1964).
[2] X. Huang *et al*, *IEEE J. Quantum Electron.*, **37**, 414 (2001); X. Huang *et al*, *Appl. Phys. Lett.* ,**78**, 2825 (2001).
[3] A. E. Gubenko *et al*, *Proc. of 12th Int. Symp., "Nanostructures: Physics and Technology"*, 69, 2004.
[4] L. V. Asryan and R. A. Suris, *Semicond. Sci. Technol.*, **11**, 554 (1996).
[5] H. Huang and D. G. Deppe, *IEEE J. Quantum Electron.*, **37**, 691 (2001).
[6] A. E. Gubenko *et al*, *Proc. of IEEE 19th Int. Semiconductor Laser Conf.*, 51 (2004).

13th Int. Symp. "Nanostructures: Physics and Technology"
St Petersburg, Russia, June 20–25, 2005

Perspectives of acceptor lasing in strained SiGe structures

E. E. Orlova[1], D. V. Kozlov[1], A. V. Antonov[1], J. N. Hovenier[2], T. O. Klaassen[2], A. J. L. Adam[2], M. S. Kagan[3], I. V. Altukhov[3], Q. V. Nguyen[4], D. A. Carder[4], P. J. Phillips[4] and B. Redlich[4]

[1] Institute for Physics of Microstructures of the Russian Academy of Sciences, GSP-105, 603950 Nizhny Novgorod,Russia
[2] Institute of Radioengineering and Electronics of the Russian Academy of Sciences, Mokhovaya 11-7, GSP-9, 101999, Moscow, Russia
[3] Kavli Institute of Nanosciences Delft, Faculty of Applied Sciences, Delft University of Technology, P.O. Box 5046, 2600 GA Delft, The Netherlands
[4] FOM Institute for Plasma Physics, Niewegein, The Netherlands

Abstract. The possibility of inverse population and lasing on acceptor transitions in strained SiGe structures is investigated. Intra-acceptor relaxation is studied using pump-probe method and the life time of the first excited state of boron acceptor in silicon is found to be about 0.5 ns. Acceptor spectrum in strained silicon is calculated. Strain values providing depletion of 1s state split off the ground state due to fast phonon assisted transitions and corresponding range of frequency tuning are determined.

Introduction

Impurities in semiconductors are attractive as an active THz medium because of relatively long life times of impurity states, large optical cross sections and the cascade character of the relaxation processes. Incorporation of impurity delta-layers in quantum well structures provides the possibility of cascade pumping of impurity transitions due to resonance tunnelling from bound impurity states [1]. Impurity lasers based on Si/SiGe structures can potentially be integrated with silicon-based electronic devices.

Lasing on impurity transitions has been experimentally observed in n-Si under optical excitation [2], however the high threshold of lasing in n-Si leads to pulsed operation and limits applications. Investigation of non-equilibrium population of impurity states in silicon under optical pumping [3] has led to a progress in the understanding of intra-center relaxation processes. It was found out that high lasing threshold is caused by the fast (10^{-10} s) inter-valley phonon assisted transitions reducing the life times of donor states [4].

Inter-valley transitions are excluded in acceptors, while intra-valley relaxation is suppressed due to momentum conservation law. The life times of impurity states in silicon based structures are not shorter than that in bulk material provided the parameters of the structure satisfy relations derived in [5]. Depletion of the lower state of the lasing transition can be reached by splitting of the ground acceptor state in strained material leading to fast acoustic phonon assisted relaxation from the split off s-state [6]. Moreover, the lasing frequency can be tuned by internal strain. We present here results of experimental and theoretical investigations of acceptor states in silicon aimed at the analysis of the conditions of acceptor lasing in strained SiGe structures.

1. Experimental investigation of intra-acceptor relaxation

Intra-acceptor relaxation in silicon doped with boron was investigated using pump-probe method with excitation to different acceptor states and to the valence band by radiation of free electron laser. The time of relaxation from the first excited p-state of acceptor was found to be about 0.5 ns which is much longer than that in donors and the times of relaxation on inter-subband transitions. This time is longer than the time of energy relaxation for free carriers and recombination time (0.2 ns) and thus can be attributed to the acoustic phonon assisted transition from the first excited state.

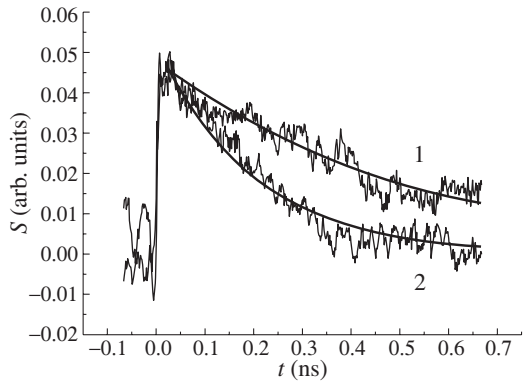

Fig. 1. Relaxation of modulation of absorption by laser excitation of Si:B $Na = 10^{15}\,\mathrm{cm}^{-3}$, 1 — excitation to the first excited p-state at 40.8 μm, 2 — excitation to the continuum at 27 μm.

2. Calculations of acceptor states in silicon under uniaxial deformation

The measured relatively long life time of the first excited acceptor p-state shows that acceptors in silicon and silicon structures are promising as a possible THz active medium. However degeneracy of the ground acceptor state does not allow realization of four-level inversion scheme which was used in donors. This produces complications in depletion of the lower state of lasing transition. This problem can be solved by using uniaxial deformation of the lattice to produce a short living s-state below the first excited p-state due to the splitting of the ground acceptor state.

We have calculated acceptor states in Si:B under uniaxial deformation using non-variational procedure based on diagonalization of the matrix for the effective mass equation. The 6×6 hamiltonian is the sum of Lattinger hamiltonian with the terms describing strain, Coulomb potential, and the short range potential describing chemical shift. The latter was taken in the form proposed in [7]. Acceptor wave function have been expressed in terms of the free holes envelope function

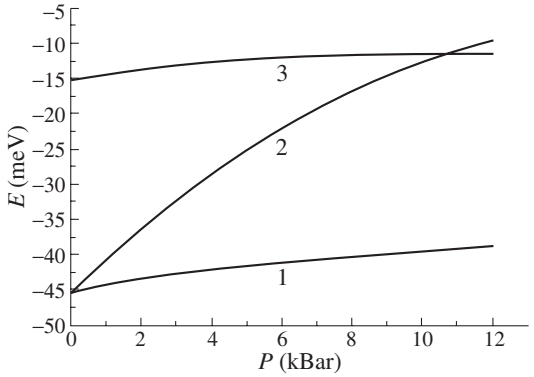

Fig. 2. Acceptor levels in strained silicon, 1 — ground state, 2 — split off s-state, 3 — the first excited p-state.

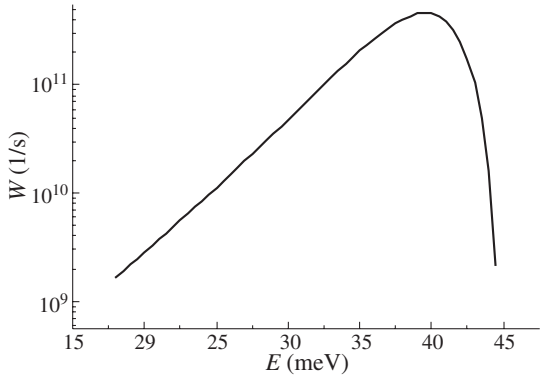

Fig. 3. Dependence of the rate of acoustic phonon assisted transition from split off s-state on the energy of the state.

in unstrained silicon. Results presented on Fig. 2 show that the energy of splitting of the ground acceptor state grows fast with equivalent stress values, while the energy of the first excited p-state does not change much within the range of strain achievable in SiGe structures.

Relaxation rate from the split off state due to emission of acoustic phonons depends strongly on the energy gap between this state and the ground acceptor state, and thus can be controlled by strain (Fig. 3). It has a maximum when the wave vector of phonon correspondent to the energy of transition is of the order of inverse Bohr radius and decreases fast for bigger energies due to the momentum conservation law. However for the wide range of splitting energies it exceeds the rate of relaxation from the first p-state thus providing conditions for population inversion on these states. Correspondingly energy of inverted transition can be tuned in the wide range $50-80\ \mu$m by varying equivalent strain in the range $1.5-4.5$ kBar.

Acknowledgements

The work was supported by RFBR grant 03-02-16586. M. S. Kagan and I. V. Altukhov acknowledge support by European office of Aerospace Research and Development (ISTC grant 2206p), and CRDF (grant RP2-2552-MO-03). The authors acknowledge discussions with I. N. Yassievich, S. G. Pavlov, P. Harrison. We gratefully acknowledge the support by the Stichting voor Fundamenteel Onderzoek der Materie (FOM) in providing the required beam time on FELIX and highly appreciate the skilful assistance by the FELIX staff.

References

[1] E. E. Orlova, *Proceedings of 19 CMD — CMMP Conference, Brighton, UK*, 201 (2002).

[2] S. G. Pavlov, R. Kh. Zhukavin, ... and H. Riemann, *Phys. Rev. Lett.*, **84**, 5220 (2000).

[3] V. N. Shastin, R. Kh. Zhukavin, ... and A. F. G. van der Meer, *Appl. Phys. Lett.*, **80**, 3512 (2002).

[4] E. E. Orlova, *Poceedings of 26 International Conference on Physics of Semiconductors, Edinburgh, UK* 61 (2002).

[5] E. E. Orlova, P. Harrison, *Appl. Phys. Lett.*, **85**, 5257 (2004).

[6] E. E. Orlova, *Abstracts of 12th International Symposium on Ultrafast Phenomena in Semiconductors, Vilnius, 22–25 August*, 32 (2004).

[7] N. O. Lipary, A. Baldereschi, M. L. W. Thewalt, *Solid State Communications*, **33**, 277 (1980).

13th Int. Symp. "Nanostructures: Physics and Technology"
St Petersburg, Russia, June 20–25, 2005

Focused output from 100 μm aperture QW laser diode with curved-grating

G. S. Sokolovskii[1], V. V. Dudelev[1], I. M. Gadjiev[1], S. N. Losev[1], A. G. Deryagin[1], V. I. Kuchinskii[1], E. U. Rafailov[2] and W. Sibbett[2]

[1] Ioffe Physico-Technical Institute, St Petersburg, Russia
[2] 2 School of Physics and Astronomy, University of St Andrews, North Haugh, St. Andrews, Fife KY16 9SS UK

Abstract. We report theoretical and experimental assessments of prototype broad-area curved-groove distributed Bragg reflector laser diodes (c-DBR) and demonstrate their single-mode and focusing operation. These laser sources will be suitable for applications requiring both spectrally and spatially enhanced optical beam quality.

Introduction

Good quality optical beams are a critical requirement in many applications for high-power semiconductor lasers, such as telecommunications, photo-medicine, and optical pumps for lasers/amplifiers and in nonlinear crystals for frequency up/down conversion. For these applications, a range of output characteristics that includes high cw/average power and good spectral and spatial quality, often required.

Single-element diode lasers based on narrow index-guiding stripes and ridge waveguides can presently deliver 100–200 mW of output power in a single lateral mode. These narrow-stripe devices are limited in power to less than 500 mW by either catastrophic optical damage or thermal overheating of the facets. Both of these failure modes are associated with the small stripe width of $\leq 5\ \mu$m required to maintain a single lateral mode. Other approaches aimed at increased diffraction-limited output powers include arrays of anti-guided narrow-stripe lasers, unstable resonators and master oscillator/power amplifier (MOPA) structures, in either discrete or monolithic configurations. Of these, only MOPA's have demonstrated diffraction-limited operation to output powers of 1 W or greater, but the technology required to fabricate them is quite complex. One of the proposed solutions to this problem involves the use of "curved-groove" diffraction gratings to control the divergence and spectrum of the emitted light.

The work presented here relates to research into a novel type of "curved-groove" distributed Bragg reflector laser (c-DBR). In theoretical studies [1,2], novel curved-groove DFB lasers (c-DFB) were proposed, and their spatial and spectral beam characteristics were shown. However, the technology of all DFB devices is inherently complex, because it involves a re-growth step. Unlike a DFB laser, the Bragg mirrors in a DBR device can be etched through the cap layer and thus do not require regrowth.

1. C-DBR laser design and formalism

This presentation represents an update on the theoretical analyses and experimental assessments of prototype devices in a curved-groove DBR (c-DBR) configuration that supports single-mode and self-focusing operation. The c-DBR configuration has the potential of combining the high-power capability of a broad-stripe device with the spatial and spectral control provided by an appropriately designed curved grating structure [1–3].

A simplified schematic of a c-DBR laser is shown in Fig. 1. The confocal device geometry causes the output emission in the plane of the p-n junction to be focused at a focal point that is defined by the grating curvature. Theoretical studies of c-DBR structures have shown that the spectral properties of these lasers are the same as for the conventional DBR-laser with the same coupling parameter and length. It was predicted that a diffraction grating with curved-grooves could be designed to concentrate the output emission to a focus that is predetermined by the curvature of the grating. Fig. 1 shows the calculated intensity distribution in plane of p-n-junction near the focal point of a c-DBR laser.

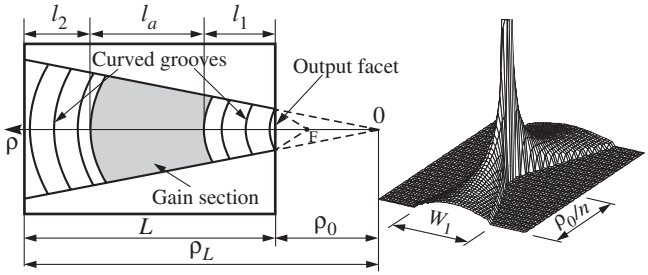

Fig. 1. Simplified schematic of the c-DFB laser and calculated intensity distribution near the focal point.

2. Beam focusing mechanism

We have also obtained significant results concerning the parameters affecting the focal distance and beam-waist size which is one of the main goals of our ongoing research. According to our results to date, the c-DFB/c-DBR laser design allows adjustment of the structural parameters to obtain the beam properties necessary for different applications. For example, one can have a minimal beam waist size and short focal distance for coupling with single-mode optical fibres or long beam waist for frequency conversion in nonlinear crystals.

According to our theoretical investigations there are three main mechanisms defining the beam waist size of the c-DFB/c-DBR laser diode:

1. Paraxial beam focusing due to the cylindrical symmetry of the laser resonator. For this focusing mechanism (similarly to conventional optical lens) beam waist size is proportional to the ratio of focal length ρ_0/n to the effective width of the grating W_1 [2,3] and, hence, defined by the numerical aperture NA of the device.

2. Focus "smearing" due to refraction of the cylindrical laser beam on the planar output facet of the device. This effect is negligible for the paraxial beams (small NAs) and significant beyond the paraxial limit [2, 3].

3. Beam focusing due to the spectral selectivity of the curved

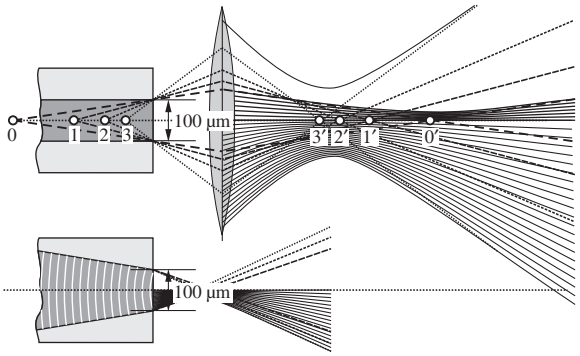

Fig. 2. Illustration of focusing of the multi-mode laser beam for the conventional DBR and for the c-DBR laser diode.

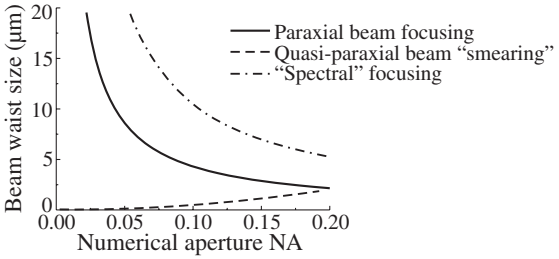

Fig. 3. Beam waist size of the 0.1nm linewidth c-DBR laser with 100 μm output facet due to paraxial beam focusing (solid), quasi-paraxial beam smearing (dash) and "spectral" focusing (dash-dot).

grating. In the conventional broad-area laser diode, multiple lateral modes have different beam curvatures due to different mode divergence with (Fig. 2a). This makes focusing of the multimode laser beam inefficient. In the c-DBR resonator, all the modes of distributed feedback nature have the same beam curvature that stems from the cylindrical symmetry of the device (Fig. 2b). Moreover, non-cylindrical propagation of the beam in a c-DFB/c-DBR resonator causes a change in the effective Bragg period of the cylindrical grating with distance and, hence, decrease of the reflection from the Bragg mirror. Competition of the spectral line broadening with spectral selectivity of Bragg reflector defines the beam waist size.

Fig. 3 represents the results of calculation of the beam waist size of the 0.1 nm linewidth c-DBR laser with 100 μm output facet defined by the paraxial beam focusing, quasi-paraxial beam smearing and "spectral" focusing.

3. The experiment

Curved-grating distributed-Bragg-reflector lasers operating at a wavelength of 860 nm were fabricated from a GaAs/AlGaAs double quantum well structure. The third-order (385 nm period) c-DBR gratings were defined by e-beam lithography and dry-etched to a depth of 0.6 μm (estimated coupling strength $\kappa = 17.5$ cm^{-1}). AR coated devices exhibited a threshold currents of ~1.2–1.7 A being the function of laser aperture and, hence, pumping area. The thresholds were high due to the broad pumping area and because only a third of the device was pumped, and the two passive c DBR sections suffered high absorption loss.

Fig. 4 represents the near-field transformations measured from the c-DBR laser diode with output facet 100 μm and focal length 0.8 mm at threshold and above threshold. This figure demonstrates that the beam waist size can be focused to ~15–20 μm. Comparison of near-fields and emission spectra on Figs 4a and b support the predicted feature of the "spectral" focusing of the output beam in a c-DBR laser.

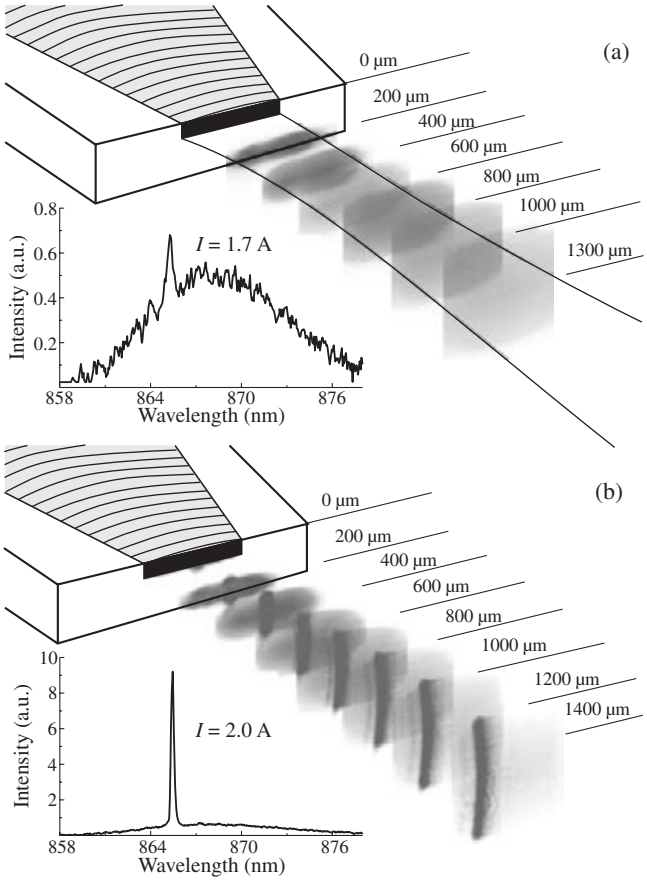

Fig. 4. Near-field distributions from c-DBR laser diode with output facet of 100 μm and focal length 0.8 mm at threshold and above threshold.

We believe that improvement of the c-DBR laser aperture and grating coupling strength together with reductions in the extent of the unpumped regions will enhance further the lasing efficiency and grating focusing effect and facilitate efficient direct coupling of the c-DBR laser radiation to single-mode optical fibers.

Summary

In this paper evaluations of distributed feedback laser diodes having a "curved-groove" diffraction grating (c-DBR) to produce enhanced spectral and spatial characteristics are described. Spectral and spatial characteristics of the c-DBR laser diodes were studied both theoretically and experimentally. Beam focusing and the effects of different structure parameters on beam focusing were also investigated.

References

[1] G.S. Sokolovskii, E.U. Rafailov, D.J.L. Birkin and W. Sibbett, *J. Opt. and Quant. El.* **31**, 215 (1999).

[2] G.S. Sokolovskii, E.U. Rafailov, D.J.L. Birkin and W. Sibbett, *IEEE J. Quant. El.* **36**, 1412 (2000).

[3] D.A. Yanson, E.U. Rafailov, G.S. Sokolovskii, V.I. Kuchinskii, A.C. Bryce, J.H. Marsh and W. Sibbett, *J. of Appl. Phys.* **95**, 1502 (2004).

[4] Y.G. Boucher, A.G. Deryagin, V.I. Kuchinskii and G.S. Sokolovskii, *Nanotechnology* **14**, 615 (2003).

[5] Y.G. Boucher, A.G. Deryagin, V.I. Kuchinskii and G.S. Sokolovskii, *Semicond. Sci. Technol.* **19**, 1010 (2004).

13th Int. Symp. "Nanostructures: Physics and Technology"
St Petersburg, Russia, June 20–25, 2005

MBE grown ZnSSe/ZnMgSSe MQW structure for blue VCSEL

I. P. Kazakov[1], V. I. Kozlovsky[1], V. P. Martovitsky[1], Ya. K. Skasyrsky[1], M. D. Tiberi[2],
A. O. Zabezhaylov[3] and E. M. Dianov[3]

[1] P.N.Lebedev Physical Institute, Russian Academy of Sciences, Moscow, Russia
[2] Principia LightWorks, Inc. CA, USA
[3] Fiber Optics Research Center at A.M. Prokhorov General Physics Institute RAS, Moscow, Russia

Abstract. ZnSSe/ZnMgSSe MQW structures were grown by molecular beam epitaxy on GaAs substrates. The band gap of ZnMgSSe barriers was approximately 3 eV at room temperature. Cathodoluminescence, X-ray diffraction, optical, scanning electron beam and atomic force microscopy were all used for structure characterization. Decay of the ZnMgSSe solid solution in at least two phases was observed. Improvement in the quality of the crystal lattice and surface morphology was achieved by mismatching the ZnMgSSe from the GaAs substrate by increasing the lattice period by 0.5 %.

Introduction

To obtain blue (455 – 465 nm) lasers in MQW structures it is necessary to use compounds with a wide band gap. ZnMgSSe with $E_g \sim 3.0$ eV is a suitable material for barrier layers while ZnSSe or ZnSe may be used as the QW material in the blue spectral range. ZnMgSSe has been used in injection lasers emitting in green (525 – 535 nm) but as cladding layers for the formation of waveguides mainly [1]. An attempt has been made to apply this alloy for the blue range also [2]. They have found a big problem relating to p-type doping for ZnMgSSe with high Mg and S content. However, with optical or electron beam pumping, undoped ZnSSe/ZnMgSSe structures can be used for vertical cavity surface emitting lasers (VCSEL). This type of laser can be used for large screen projection display as well as a light source for rear projection television [3]. Another alternative is to use an external cavity mirror to transform a high efficiency GaN-based laser diode into high quality blue laser [4]. UV laser emission is also possible using intracavity second harmonic transformation.

A significant issue using ZnMgSSe with high Mg and S content is that the crystal lattice in solid solution is predicted to have extended instability and immiscibility regions at typical MBE growth temperatures [5]. According to this prediction, the ZnMgSSe composition matched to GaAs and having $E_g \sim 3.0$ eV is in the region of its metastable phase and is close to the instability region boundary. Unfortunately, only a few experimental efforts have studied this problem [6-8]. These results were insufficient to support using wide band gap ZnMgSSe compounds in VCSEL structures. This work studies undoped molecular beam epitaxy grown ZnSSe/ZnMgSSe MQW structures suitable for lasers with resonant periodic gain. The main purpose of this study is to find the growth conditions necessary to obtain intense blue emission at RT.

1. Experimental

Periodic ZnSe/ZnMgSSe and ZnSSe/ZnMgSSe MQW structures were grown by MBE on GaAs substrates misoriented by 3° or 10° from (001) to (111)A. The period was equal to λ/N where λ is the desired laser wavelength and N is the average refractive index along the period. Several different structures were grown having from 5 to 30 periods. The MQW region was grown on a 60 nm thick ZnSe buffer. The QW thickness was about 6 nm and the ZnMgSSe barrier had a band gap of about 3 eV at room temperature (RT). These structures were completed with a ZnMgSSe layer equal to the thickness of the ZnMgSSe barrier layer and was followed by a 6 nm thick ZnSe cap layer. The ZnMgSSe lattice period was close to that of GaAs substrate although not precisely matched. The growth was carried out in an MBE chamber of TSNA–18 set-up (Russian setting). The substrate temperature was 280 °C.

As-grown structures were studied by cathodoluminescence (CL), photoreflection (PR), X-ray diffraction, optical microscope, scanning electron microscope (SEM) and atomic force microscope (AFM). CL was measured at $T \approx 14$ K and RT, electron energy $E_e = 3$, 10 and 30 keV, continuous current $I_e = 1$ μA and e-beam spot diameter $d_e = 1$ mm. Graphite monochromator and CuK_α emission were used for the X-ray diffraction study.

2. Results and discussion

Low temperature CL spectra of the structures with different E_g and having a close lattice period to that of GaAs are presented in Fig. 1. At $E_g < 3$ eV (about 2.9 eV at RT) the intensity of the QW emission is noticeably higher than the ZnMgSSe emission which has only one narrow line. This demonstrates adequate transport of nonequilibrium carriers into the QWs. At $E_g > 3.1$ eV (about 3 eV at RT), the ZnMgSSe emission is evidenced by two or more broad lines, whereas the QW emission line intensity is small and the additional emission

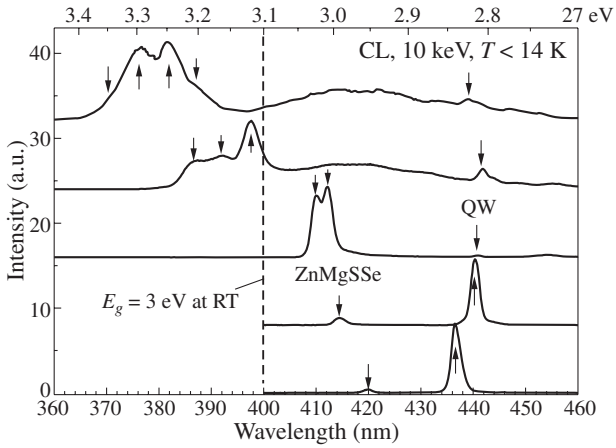

Fig. 1. CL spectra of different ZnSSe/ZnMgSSe MQW structures at $T < 14$ K, $E_e = 10$ keV.

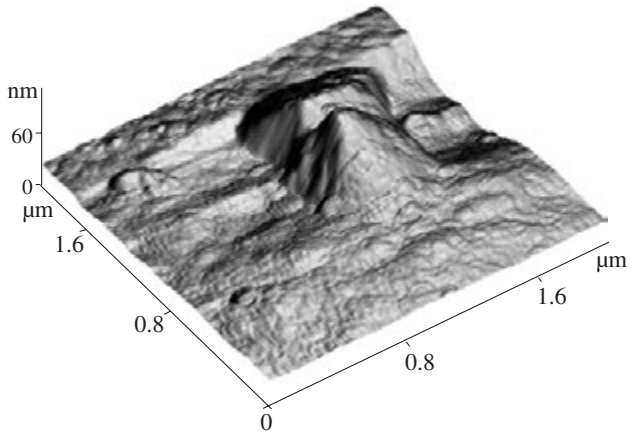

Fig. 2. AFM image of surface defects of a ZnSe/ZnMgSSe MQW structure.

appears in the range between the ZnMgSSe emission lines and the QW emission line. In the range from 3 eV to 3.1 eV, the ZnMgSSe may have one or more lines depending on the stoichiometry of the molecular flows and lattice mismatching. In this instance carrier transport becomes noticeably worse.

The surface of the structures may be mirror-like, especially at $E_g < 3$ eV. Surface defects resemble a double pyramid as seen in the AFM image in Fig. 2. The cross section SEM image of a pyramid is presented in Fig. 3. In this structure, the pyramid grows from the GaAs–ZnSe interface, however, some structures show pyramids of various sizes propagating from the internal interfaces. A proliferation of pyramids is observed with increasing of the lattice period. Pyramid concentrations of higher than 10^5 cm^{-2} leads to a decrease of intensity of all CL spectra lines.

All ZnMgSSe structures with $E_g > 2.9$ eV at RT found by X-ray diffraction analysis shows two or more diffraction peaks. This demonstrates that the structure decays in two or more phases having different compositions and/or different elastic deformation. The intensities of the diffraction peaks remain comparable to samples with different pyramid concentrations. This is interpreted to mean that the decay is not due to pyramid formation. One of the peaks occurs in the diffraction pattern for all structures. A relaxed crystal phase corresponding to this peak have a larger lattice period by about 0.24 % than that of GaAs. If the ZnMgSSe composition is close to the 0.24 % mismatch then the phase has a narrow diffraction peak and shows tetragonal and monoclinic deformation. For structures matched to GaAs or having a negative mismatch, the diffraction peaks become wider and the quality of the crystal lattice worsens as a whole in comparison with structures under small compressive strain.

We can therefore conclude that ZnSe/ZnMgSSe structures with $E_g > 2.9$ eV at RT have characteristics unsuitable for lasers. The main reason is the decay of ZnMgSSe solid solution in several phases because of its low thermodynamic stability [5]. However, we believe that the most stable lattice can be found with a composition of $(ZnSe)_{1-x}(MgS)_x$. At small values of x, the lattice period should be close to that of ZnSe. Therefore, we believe that a stable phase with 0.24 % mismatching observed by X-ray diffraction has just this composition. Unfortunately, the $(ZnSe)_{1-x}(MgS)_x$ layer will be relaxed if its thickness exceeds the critical value due to relatively large mismatching. This relaxation results in the formation of twins and dislocations with preference along the (111) crystal planes. Therefore, we observed only a minimal improvement in the luminescence characteristics for structures with ZnMgSSe compositions close to $(ZnSe)_{1-x}(MgS)_x$. Better results may be achieved by using ZnSe substrates.

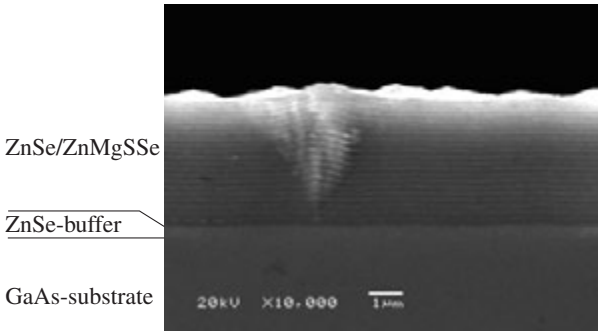

Fig. 3. SEM image of cleaved (1-10) surface of a ZnSe/ZnMgSSe structure.

3. Conclusion

The decay of ZnMgSSe solid solution with $E_g \approx 2.9$ eV at RT in two or even more phases has been observed. This decay leads to a significant decrease in the transport of nonequilibrium electrons and holes generated in the ZnMgSSe barrier layers to the QWs in the ZnSe/ZnMgSSe MQW structures. Improved quality of the crystal lattice is achieved by mismatching the ZnMgSSe from the GaAs to a larger lattice period by 0.24 %. Intense cathodoluminescence may be obtained with the ZnMgSSe composition having $E_g \approx 2.85$ eV at RT.

Acknowledgements

This work was supported in part by Russian Foundation of Basic Researches, Grants 04-02-16877, 04-02-17262 and 05-02-16390, Program "Scientific Schools of Russia", Grant 1466-2003-2 and Principia LightWorks, Inc.,CA.

References

[1] S. Itoch *et al*, *J. Cryst. Growth* **214/215**, 1029 (2000).
[2] D. C. Grillo *et al*, *Electron. Lett.* **30**, 2131 (1994).
[3] M. D. Tiberi, *et al*, *Proceedings of SPIE* 5740 (2005).
[4] A. C. Tropper *et al*, *J. Phys. D: Appl. Phys.* **37**, R75 (2004).
[5] V. S. Sorokin *et al*, *J. Cryst. Growth* **214/215**, 130 (2000).
[6] B. J. Wu *et al*, *Appl. Phys. Lett.* **66**, 3462 (1995).
[7] H. Kalisch *et al*, *J. Cryst. Growth* **184/185**, 129 (1998).
[8] G. C. Hua *et al*, *J. Cryst. Growth* **138**, 367 (1994).

13th Int. Symp. "Nanostructures: Physics and Technology"
St Petersburg, Russia, June 20–25, 2005

Light matter interaction effects in quantum dot microcavities

Alfred Forchel
Technische Physik, Universität Würzburg Am Hubland, D 97074 Würzburg, Germany

Engineering the interaction of light with matter allows one to tune important properties of solids like e.g. the spontaneous emission rate or the spontaneous emission coupling factor into a laser mode. In the frame of cavity quantum electro dynamics light matter interaction phenomena are divided into weak and strong interaction effects. Weak interaction effects result e.g. in an enhancement of the spontaneous emission rate of an emitter in a cavity when on resonance with the cavity modes. Strong interaction effects can be observed when the rate describing the coupling of the emitter and the light becomes stronger than dissipative processes in the system. Then emission becomes a reversible process.

We have investigated weak and strong coupling effects in semiconductor microcavities with InGaAs quantum dots. The cavities are based on undoped GaAs/AlAs VCSEL structures from which micropillars with diameters between 1.0 μm and 4 μm are realized by reactive etching. In combination with the vertical optical confinement the etching of pillars allows to obtain discrete photon modes. The microcavities have quality factors Q of about 5.000 to 35.000Q which correspond to photon cavity lifetimes between 2 and 18 ps. The quantum dot energy range has been optimized in order to locate only individual a small number of exciton transitions close to the cavity resonance. By using low excitation powers these structures can therefore be used to investigate the interaction of a single quantum dot exciton with vacuum field fluctuations. In the weak coupling regime we observe e.g. an enhancement of the exciton and biexciton emission probability due to the Purcell effect.

By using dots with large dipole moment we observe clear anticrossing effects due to strong interaction of QD excitons with vacuum field fluctuations characterized by a vacuum Rabi splitting of up to 140 μeV. The anticrossing is investigated by using temperature tuning, which allows one to move individual quantum dot excitons into resonance with the cavity mode. In addition to anticrossing effects of the dispersion relations of exciton and cavity mode we observe an exchange of the emission linewidths and of the intensities of the cavity mode and the single quantum dot exciton transition, as expected for strong coupling.

Investigations of a number of different cavities with typical diameters of 1.5 to 2 μm yield a wide variety of strong coupling situations. We observe e.g. sequential strong and weak coupling effects by two different single dot excitons as well as several sequential strong coupling effects in micropillars. Of particular interest are cases in which the cavity is seen to strongly interact simultaneously with two quantum dots with an energetic separation below the cavity linewidths. This results in coherent coupling of both excitons with the mode characterized by a particularily large vacuum Rabi splitting (250 μeV).

At higher excitation powers interaction effects between quantum dot excitons and cavity fields represented by one or more photons are investigated. Here we observe for example lasing in micropillars with < 50 quantum dots as well as indications for single dot related effects in lasing.

13th Int. Symp. "Nanostructures: Physics and Technology"
St Petersburg, Russia, June 20–25, 2005

Fabrication and optical properties of 2D PhCs with active area based on InAs/InGaAs QDs

A. V. Nashchekin, E. M. Arakcheeva, S. A. Blokhin, M. V. Maximov, E. M. Tanklevskaya, O. A. Usov, S. A. Gurevich, S. G. Konnikov, N. N. Ledentsov, A. E. Zhukov and V. M. Ustinov
Ioffe Physico-Technical Institute, St Petersburg, Russia

Abstract. A two-dimensional photonic crystal with hexagonal lattice of air-holes is patterned into an active planar waveguide containing InAs/InGaAs quantum dots. Variable-angle reflectivity method is used to map out the photonic band structure. Specific for photonic crystals inflection points are revealed in optical reflectance spectra. Photoluminescence measurements are performed in the same geometry. Peculiarities in photoluminescence spectra are in a good agreement with those at the reflectivity spectra.

Introduction

Photonic crystals (PhCs) are compounds with spatially periodic dielectric function and lattice periods compared with wavelength of propagating light. In such structures Bragg-scattering of electromagnetic waves leads to the formation of the photonic bands (PB). The engineering of PhCs permits to control the spontaneous emission, light propagation and offers enormous potential for optoelectronic device application such as lasers, light emitting diodes and photonic integral circuits.

We describe optical properties of 2D PhCs with active area based on InAs/InGaAs QDs. PhCs are fabricated by using electron lithography and reactive ion etching [1]. A 2D hexagonal lattice of air-holes is etched in a planar GaAs-AlGaAs waveguide with QDs. The optical properties of PhCs are experimentally analyzed by external coupling reflectivity spectroscopy and angle-resolved photoluminescence. The TE and TM polarized light reflection is measured in $\Gamma - K$ direction of Brillouin zone and used to map out the PB structure [2, 3]. Photoluminescence measurements performed in the same geometry show good agreement with the results obtained by reflectivity studies.

Technology

The technology of mesa fabrication included optical and electron beam lithography, wet chemical etching and reactive ion etching (RIE).

First, the whole structure was etched down to the substrate except 300×300 μm^2 square areas. A mask for RIE of mesas was formed on the surface of each square area by deposition of a thin Ni layer (20 nm), followed by spinning-on positive electron resist (PMMA) with thickness as large as 350 nm and electron lithography process. Argon etching of the Ni layer was applied after PMMA development. This procedure is required because of low durability of the PMMA to the reactive ion etching. Further, RIE was used for drilling the active region in GaAs through the Ni mask. In such a way, hexagonal photonic structures with set of the geometrical parameters with period 600–1200 nm, hole diameters 360–700 nm were obtained. The etching was done through the active region (etching depth 500 nm) with very good verticality of the walls. A typical SEM image of PhC is shown in Fig. 1. The air-hole radius is equal to 0.3 times the lattice period.

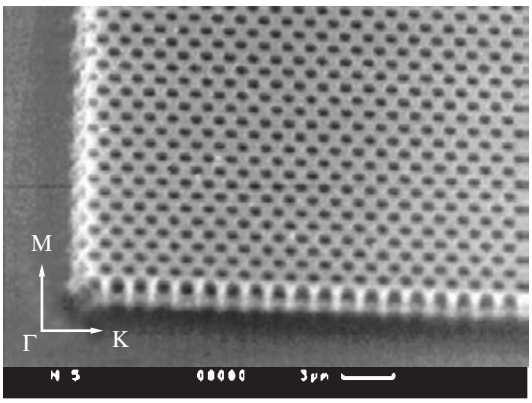

Fig. 1. SEM image of the PhC with period 1 μ and holes diameter 600 nm.

Experimental results and discussion

Figures 2(a) and 3(a) show variable-angle reflectivity spectra for TM and TE polarized light incident along the $\Gamma - K$ orientation in the angle range $5^\circ - 35^\circ irc$ for the sample with period 1170 nm and hole diameter 670 nm. The variable-angle reflectance was measured in the spectral range 1000–1600 nm. By varying the angle of incidence light along symmetry direction at selected frequency we can match the parallel wave vector of incoming beam to those of photonic mode propagating in the plane of the sample.

Due to coupling between discrete irradiated modes of PhCs and continuum incidence beam a corresponding Fano-type resonance structure appears in reflectance. This inflection points are used to map out the PB structure. The experimental PB structures are partially confirmed by plane wave (truncated to 361 plane waves) transfer matrix method calculations, used for analyzes of experimental data (Fig. 2(b) and Fig. 3(b)). The presence of the oxide layer (with refractive index 1.5 and thickness about 30 nm) on the inside surfaces of the holes was taken into account in calculation. This oxide layer lowers the average index of the lattice and shifts the calculated band structure to higher energy.

The photoluminescence spectra were measured in the registration angle range from $5^\circ - 35^\circ$ at room temperature for reference (without PhCs) and PhC samples. The structures were optically pumped by Ar^+ laser (514 nm) with power density 630 W/cm^2. For the PhC structure the emission exhibits features, which are not observed in PL spectra of the reference sample (Fig. 4). These peculiarities correlate with the resonances observed in the reflectivity spectra. We think that

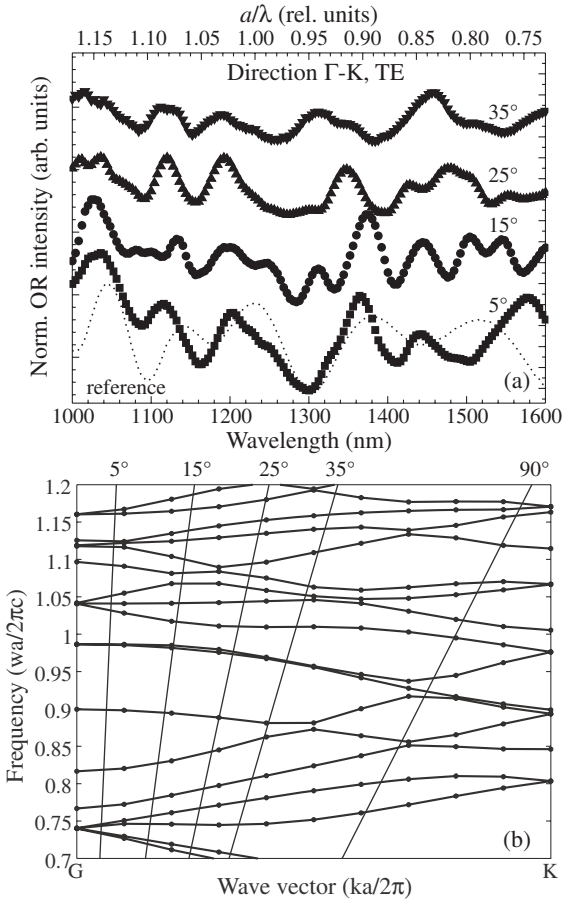

Fig. 2. Angle-variable reflectivity of the PhC (a) and calculated photonic bands (b) for TM polarization.

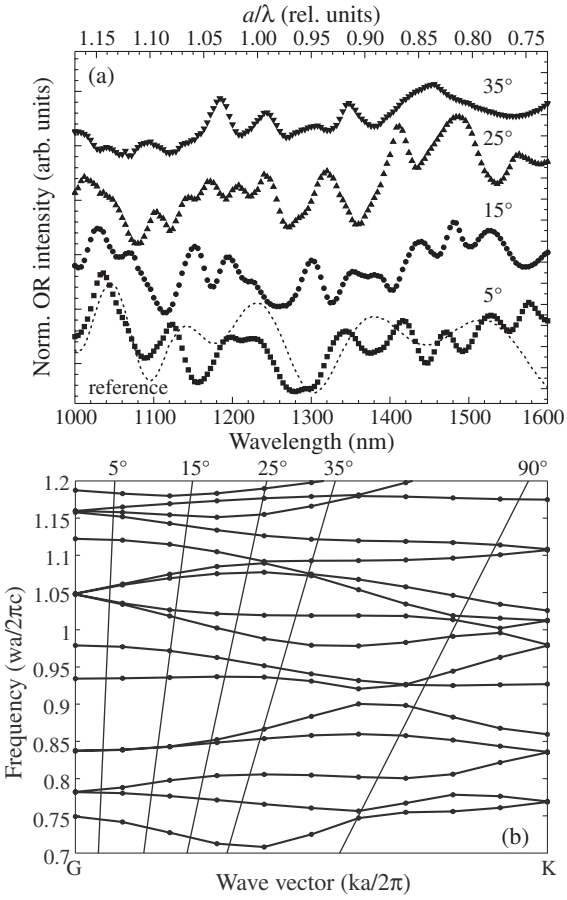

Fig. 3. Angle-variable reflectivity of the PhC (a) and calculated photonic bands (b) for TE polarization.

the features at PL spectra are due the overlap of high density dielectric modes with active material in the PhC structure.

Conclusions

The technology of fabrication of 2D PhCs employing InAs/InGaAs QDs as active material has been developed. Obtained photonic structures have been characterized by optical methods. The experimental variable-angle reflectivity and photoluminescence results in the selected 1000–1600 nm wavelengths range were found to be in a good agreement with photonic band dispersion obtained by using numerical calculations by transfer matrix method.

Acknowledgements

This work is supported by the program of physical department of RAS "Novel materials and structures" and CRDF. The authors are grateful to S. I. Troshkov for useful discussion and also to Interface company for given equipment for electron lithography process realization.

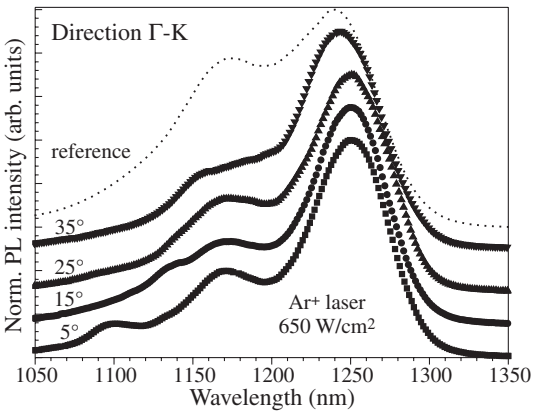

Fig. 4. Angle-resolved PL spectra of the PhC.

References

[1] E.M. Arakcheeva, A.V. Nashchekin, V.A. Solovev, E.M. Tanklevskaya, M.V. Maximov, S.G. Konnikov, S.A. Gurevich, N.N. Ledentsov, vol.75, 78-81 (2005). *Zh.Tech.Phys.* **75**, 78-81 (2005).

[2] T. Fujita, Y. Sato, T. Kuitani, T. Ishihara, *Phys. Rev.*, **57**, 12428 (1998).

[3] D.M. Whittaker, I.S. Calshaw, *Phys. Rev.* **60**, 2610 (1999).

13th Int. Symp. "Nanostructures: Physics and Technology"
St Petersburg, Russia, June 20–25, 2005

Quantum beats between quantum well polarization states in semiconductor microcavity in magnetic field

M. N. Makhonin, A. A. Demenev, D. N. Krizhanovskii and V. D. Kulakovskii
Institute of Solid State Physics, RAS, 142432 Chernogolovka, Russia

Abstract. The spin properties of quantum well excitons in the active layer of a planar microcavity have been analyzed using pump-and-probe technique in a wide range of magnetic fields normal to the cavity plane. When exciting the cavity polaritons with linearly polarized ps pulses the differential transmission (DT) spectra show time oscillations both in the DT signal and spectral position of lower polariton (LP) states. The oscillations in the DT signal and energy gap between σ^+ and σ^- LP components are shown to be controlled by rotating the LP polarization plane due to the difference in the σ^+ and σ^- LP energies. The oscillation period is inversely proportional to the magnitude of the magnetic field and coincides for the DT signal and energy gap whereas the phases of their oscillations differs from each other by $\pi/4$. The decay time of quantum beats decreases with excitation density due to an enhanced interparticle scattering.

Introduction

The investigation of the spin properties of electrons and excitons has become a main focus of the semiconductor nanostructures research. The interest arises due to much longer spin coherence as compared to the conventional charge degrees of freedom [1–4]. This opens perspectives for a fundamental research and possibly also for future applications in the field of quantum information processing [5]. One of the system with the promising perspectives is excitons in quantum wells (QW) embedded in a planar microcavity (MC). Strong coupling between QW excitons and a high finesse cavity mode results in formation of quasi-two-dimensional excitonic polaritons [6] with an extremely small effective mass and an unique dispersion law resulting in a variety of interesting nonlinear effects. Because of the promising perspectives the spin properties of excitons in the strong coupling regime in semiconductor microcavities require more extensively investigations.

Here we study excitons in QWs embedded in the active layer of a high finesse planar microcavity in magnetic field normal to the cavity plane. Magnetic field splits polaritons into circularly polarized σ^+ and σ^- states. Excitation of the cavity polaritons with linearly polarized picosecond pulses with a pulse spectral width exceeding Zeeman splitting of LPs results in the coherent superposition of the two (σ^+ and σ^-) oscillators where the relative phase changes with time due to difference in the oscillator frequencies. In this work we use pump-and-probe technique to test the time behavior of photoexcited polarization states and to control spin properties of the photoexcited system. That allows us to observe the quantum beats between polarization states split by magnetic field and to determine the spin decoherence time.

1. Experimental details

The sample is a microcavity structure grown by a metal organic vapor phase epitaxy. It consists of two Bragg reflectors with 17(20) repeats of $\lambda/4$ $Al_{0.13}Ga_{0.87}As$/AlAs layers in the top(rear) mirrors and $3/2\lambda$ GaAs cavity that contains six 10-nm thick $In_{0.06}Ga_{0.94}As$/GaAs QWs. Rabi splitting of coupled exciton-cavity modes is $\Omega \approx 6$ meV. The sample was placed into the magneto-optical cryostat at temperature of 2 K. Magnetic field was orientated normal to the cavity plane.

Pump-and-probe experiments were performed in transmission geometry using a mode-locked Ti:Sapphire laser. The duration of the probe pulse of 100 fs corresponds to a spectral width of ~ 25 meV. The probe beam was directed normal to the MC probing the polariton population at $k = 0$. The pump beam excites the sample under an angle of 15° relative to the cavity normal (lateral wavevector $k = 2.1 \cdot 10^4\,\mathrm{cm}^{-1}$).The pump pulse was spectrally tailored using a grating and a slit for selective resonant excitation into the LP mode at chosen angle and had a duration of ~ 1 ps at a spectral width of ~ 2.5 meV. Both beams were focused onto the same spot of the sample, having a diameter of roughly $\approx 50\,\mu$m. The transmission signal was spectrally analyzed by a monochromator with a spectral resolution of $\approx 30\,\mu$eV and detected by a liquid nitrogen cooled CCD camera for various delay times ($\tau_d = t_{\mathrm{probe}} - t_{\mathrm{pump}}$) between probe and pump.

2. Experimental results

The time dependence of the DT signal at the LP energy recorded at magnetic field of 5 T under co-linear and cross-linear polarizations of the pump and probe pulses is illustrated in Fig. 1 for low (c) and high (d) pump powers. At low excitation power the DT signal shows well pronounced time oscillations in the intensity both in co- and cross-linear polarizations. With increasing excitation power the oscillations become less pronounced(see Fig. 1d). This occurs due to an increased scattering in the dense system. Fig. 1c shows as well that the oscillations in geometries of co- and cross-linear pump and probe polarizations are in antiphase.

In addition to the changes in the transmission signal the pump pulse causes changes in the polariton energies. The changes are observed in the energies of both upper polariton (UP) (Fig. 1a, b) and LP (Fig. 1e, f) branches. Fig. 1a shows that the pump pulse results in $\sim 20\,\mu$eV red shift in the UP energy. The shift decreases exponentially with τ_d without any marked oscillation. In contrast, both σ^+ and σ^- LP lines exhibit well pronounced oscillations resulting in oscillations in the energy gap between σ^+ and σ^- LP components, Δ, shown in Fig. 1e. The oscillation period is equal to that in the DT signal whereas its phase is different. A comparison of oscillations in Figs. 1c and e shows that the lagging is equal to $-\pi/4$ both for co-linear and cross-linear pump and probe polarizations.

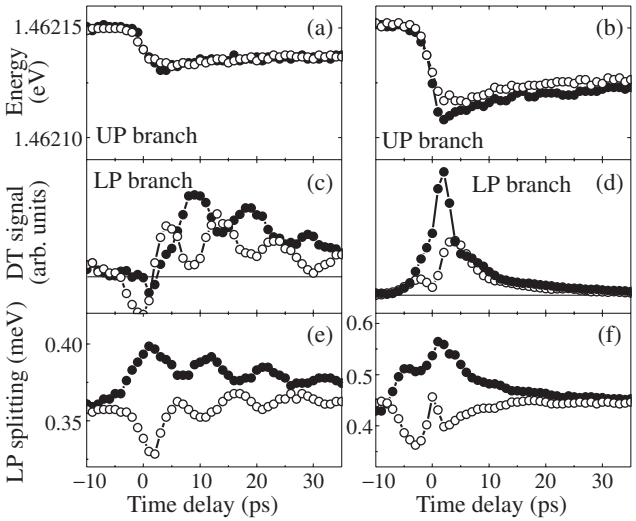

Fig. 1. Experimental dependencies of UP line shift (a, b),integral DT signal of the LP line (c, d), and energy gap between $\sigma+$ and $\sigma-$ LP components (e, f) on τ_d. The left and right panels display the dependencies recorded at 130 and 260 W/cm^2 excitation density, respectively. Open and full symbols correspond to co- and cross-linear configurations of the pump and probe polarizations.

Experiments in a wide range of magnetic fields have shown that the oscillation period decreases with magnetic field $\propto 1/B$ Fig. 2. No oscillations are observed in the DT signal at zero magnetic field. Quantum beats appear in magnetic field and can be measured at $B \gtrsim 0.5$ T.

3. Discussion

Comparison of the magnetic field dependence of the oscillation frequency with the energy gap Δ between σ^+ and σ^- LP components in Fig. 2 shows that $1/T$ coincides with Δ. This indicates the correlation between the observed quantum beats and Zeeman splitting of LP components. The linearly polarized pump excites the linear combination of σ^+ and σ^- states, $|x\rangle = (|x + iy\rangle + |x - iy\rangle)/2$. The difference in the energies of σ^+ and σ^- states results in a linear increase of phase difference between these state with delay time equal to $\phi = \tau_d \Delta/\hbar$, which leads to the rotation of linear polarization of the photoexcited $|x\rangle$ state with a period of $T = 2\pi\hbar/\Delta$.

At low pump powers the non-linear response of the cavity is mainly determined by photoexcited excitons trapped in localization sites. Due to the Pauli-blocking these electron-hole pairs enhance the DT of the cavity [7]. The difference in the absorption of $|x\rangle$ and $|y\rangle$ polarized light is connected with the fact that the selection rules allow the light induced transition from the excited to ground state only for the light with the same polarization. That means that the DT signal oscillation for the $|x\rangle$ and $|y\rangle$- polarized pump is proportional to $\langle x|(|x + iy\rangle \exp(i\phi(t)) + |x - iy\rangle) \propto +\cos(\phi(t))$ and $\langle y|(|x + iy\rangle \exp(i\phi(t)) + |x - iy\rangle) \propto -\cos(\phi(t))$, respectively. That explains the occurrence of quantum beats in the DT and the opposite phase of the oscillation in co- and cross-linear polarizations.

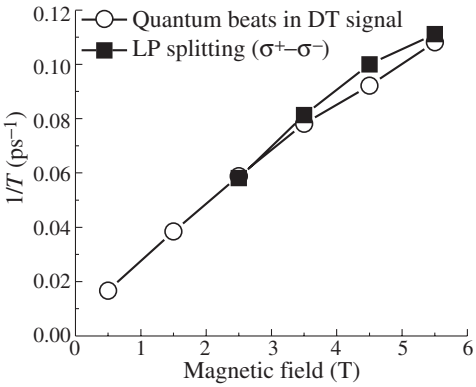

Fig. 2. Inverse quantum beats oscillation period (circles) as a function of the magnetic field in comparison with the energy gap between σ^+ and σ^- LP components (squares) extracted from the transmission spectra.

The oscillations in energy gap between Zeeman components are related with a renormalization of transition energies. The latter appears due to the interference of exciton polarization and the probe electric field and depends both on the x and y components of the exciton polarization. The phase shift between them leads to the lagging between DT signal and transition energy oscillations.

The decay of DT signal is determined by two characteristic times namely, recombination time τ and spin coherence decay time τ_{coh}

$$I_{\text{co/cross}} \sim \exp(-\tau_d/\tau) \pm \exp(-\tau_d/\tau_{\text{coh}}) \cdot \cos(2\pi t_d/T)\,.$$

The time τ determines the decay of the signal whereas τ_{coh} describes the decay of oscillations. This expression describes the experimental dependence very well in the whole range of $\tau_d = 5$–50 ps. That allows us to determine both τ and τ_{coh}: $\tau \sim 30$ ps and $\tau_{\text{coh}} \sim 10$ ps.

Acknowledgements

The authors thank N. A. Gippius and S. G. Tikhodeev and A. I. Tartakovskii for fruitful discussions, M. S. Skolnick for the samples, and RFBR and INTAS for financial support.

References

[1] J. M. Kikkawa *et al*, *Science*, **277**, 1284 (1997); J. A. Gupta *et al*, *Phys. Rev. B*, **59**, R10421 (1999).
[2] M. Paillard *et al*, *Phys. Rev. Lett.*, **86**, 1634 (2001).
[3] I. Malajovich *et al*, *Phys. Rev. Lett.*, **84**, 1015 (2000).
[4] R. Fiederling *et al*, *Nature*, **402**, 6763 (1999).
[5] A. Imamoglu *et al*, *Phys. Rev. Lett.*, **83**, 4204 (1999).
[6] C. Weisbuch *et al*, *Phys. Rev. Lett.*, **69**, 3314 (1992).
[7] D. N. Krizhanovskii *et al*, *Solid. State. Comm.*, **119**, 435–439 (2001).

13th Int. Symp. "Nanostructures: Physics and Technology"
St Petersburg, Russia, June 20–25, 2005

Resonant Rayleigh Scattering of light by semiconductor microcavity

M. V. Lebedev, A. A. Demenev and V. D. Kulakovskii
Institute of Solid State Physics RAS Chernogolovka, Moscow distr., 142432, Russia

Abstract. Experimental study of Resonant Rayleigh Scattering of light by a semiconductor microcavity was carried out on a double cavity sample. The shifts of RRS lines spectral positions with sample rotation demonstrate clearly polariton dispersion. The shape of the lines depends strongly on the position of the excitation spot on the structure surface and temperature. The treatment of experimental data in terms of Fano quantum mechanical interference between a discreet state and continuum gives a direct method to study polariton scattering probabilities.

Introduction

Resonant Rayleigh Scattering (RRS) of light by semiconductor quantum well structures attracted much attention recently and turned out to be a powerful tool for study random potential fluctuations in quantum wells [1–4] and microcavities [5–7]. Rayleigh scattering is an elastic scattering process, that is energy of the scattered photon is not changed by the scattering medium but the direction of its propagation differs from that of the incoming one. The RRS process is closely connected to resonance luminescence, because it can be understood as a resonant absorbtion of a photon followed by its reemission in a different direction. The main feature of the RRS is its coherent character which means that the phase correlation between incoming and outgoing light is conserved during the scattering process. Light in microcavities (MC) interacts usually strongly with excitons in quantum wells embedded in a MC forming a new elementary excitation, the so called cavity polariton. In the case when the incoming and outgoing photons belong inside the MC to polariton dispersion curves the overall scattering process may be treated in terms of RRS of cavity polaritons [8]. In a more general case the photons taking part in a scattering process may not belong to polariton dispersion curves, so that RRS of light can not be regarded as polariton-polariton RRS. Just this case is analyzed in the present work. We show that RRS of light in a MC gives a possibility to study polariton dispersion, random potential fluctuations and polariton-phonon interaction in a rather simple way and at very low excitation levels. Our experimental measurements carried out on a double MC structure demonstrate a variety of RRS spectra all of which can be described into a common frame of Fano theory of quantum mechanical interference between a discrete state and a continuum [9]. The main advantage of such description is the ability to characterize the complicated disorder in a MC and polariton-phonon interaction with only three parameters, which determine the shape of the Fano antiresonance curve, namely the background scattering level, polariton damping and Fano parameter q. All this parameters can be directly determined from the fitting of experimental spectra and have clear physical meaning.

1. Experiment

Measurements were carried out on a double MC GaAs/ AlGaAs structure at helium temperatures under resonant broad band illumination of the sample by a cw light emitting diode (LED). The light of the LED was well collimated and the scattered light was detected with high spectral and angle resolution by means of a Ramanor U 1000 spectrometer and a CCD camera.

2. Experimental Results

The RRS spectrum demonstrates sharp spectral lines corresponding to different polariton modes excited in the sample. The shape, intensity and spectral positions of this lines depend on the angles of excitation and observation. Shape and intensity are in addition strongly dependent on the position of the excitation spot on the crystal surface. When rotating the sample, we observe shifts of the spectral positions of RRS lines accompanied by the change of their intensities and shapes. The origin of this shifts is polariton dispersion. Fig. 1. shows the polariton dispersion curves of our double cavity structure measured from RRS lines positions when rotating the sample.

The two modes labeled MC1 and MC2 corresponding to polaritons of two cavities of our double cavity structure are clearly seen. The additional mode lying between the MC1 and MC2 modes demonstrates splitting. This mode is the closest one to the unperturbed exciton level of quantum wells and under certain conditions the corresponding RRS line demonstrates a typical asymmetric shape known as Fano antiresonance (see Fig. 2). The shape of the Fano antiresonance curve is determined by only three parameters, namely the background level, the polariton damping constant and Fano parameter q, which is proportional to the ratio of scattering probabilities of the incoming photon into discreet spectrum state and a continuum of states. The discreet state corresponds in our case to the cavity polariton mode, while the continuum of states is excited due to nonresonant Rayleigh scattering of light on the surface of the structure and in the Bragg reflectors.

The Fano antiresonance curve of the RRS exhibits a dis-

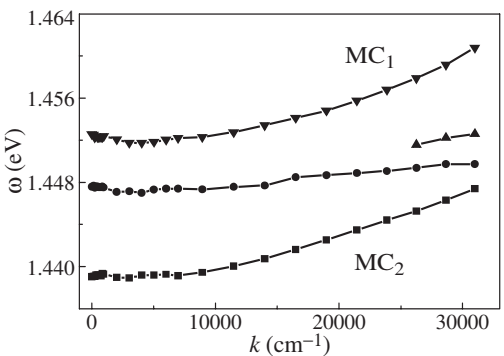

Fig. 1. Polariton dispersion measured from the RRS lines positions.

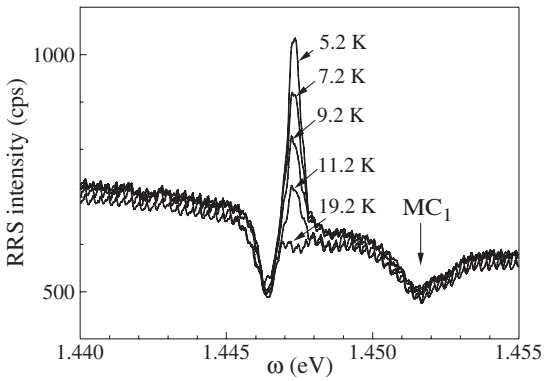

Fig. 2. RRS signal temperature dependence.

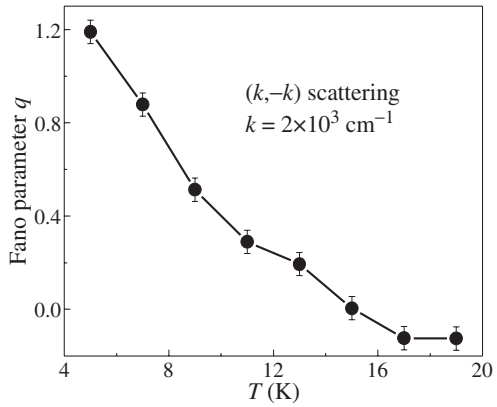

Fig. 3. Fano parameter q temperature dependence observed for the central polariton mode (1,447 eV).

tinct temperature dependence (see Fig. 2) and changes with displacement of the excitation spot on the crystal surface. This finds a natural explanation in terms of increasing of polariton damping and alteration of the parameter q, which should depend strongly on the local random potential fluctuations. The sign of this parameter determines the phase shift of the scattered light and sign inversion is accompanied by the inversion of the antiresonance curve. We do observed the RRS line shape inversion under certain experimental conditions. Temperature increase leads to reduction of the absolute value of the Fano parameter (see Fig. 3).

By scanning the sample surface with the excitation spot one can get out the map of polariton damping and polariton scattering probability in the structure. This is a direct method of sample quality characterization, which may be useful for applications. This method can be used to study random potential fluctuations directly under conditions of experiment, that is when the sample is positioned into the cryostat, cooled down to helium temperatures and excited with some laser beam. This is important, because random potential fluctuations may be very sensitive to temperature, cooling down regime and additional excitation of the sample. Our measurements showed that the RRS scattering by the MC changes when additional over barrier excitation of the sample takes place. This may play important role for polariton relaxation investigations.

3. Discussion and conclusions

Our results show that the concept of Fano quantum mechanical interference gives a convenient frame for describing RRS of light in microcavities. The main advantage of this description is a possibility of direct determination of polariton scattering probabilities from experimental spectra. This opens a new way for investigation polariton relaxation, random potential fluctuations and polariton-polariton scattering in MC. The most intriguing is the ability to observe RRS of light in the presence of a macrooccupied polariton mode inside the cavity. One can expect to find at this conditions an increase of the scattering probability from the initial polariton state to the macrooccupied one due to bosonic nature of polaritons. All our measurements were carried out at very low excitation levels (our LED had an integral output power less than 0,5 mW) and the RRS process itself does not leads to crystal excitation. This gives a possibility to measure polariton dispersion in a rather simple way at a certain place of the sample without disturbing the polariton distribution formed with excitation by a powerful laser. This can be used in studying of nonequilibrium polariton dynamics which may be accompanied by renormalization of the polariton dispersion curve .

References

[1] M. Gurioli *et al*, *Phys. Rev. Lett.*, **78**, 3205 (1997).
[2] D. Birkedal and J. Shah, *Phys. Rev. Lett.*, **81**, 2372 (1998).
[3] W. Langbein *et al*, *Phys. Rev. Lett.*, **82**, 1040 (1999).
[4] V. Savona *et al*, *Phys. Rev. Lett.*, **84**, 183 (2000).
[5] F. Bogani *et al*, *Phys. Stat. Sol. (b)*, **221**, 137 (2000).
[6] M. Gurioli *et al*, *Phys. Rev. B*, **64**, 165309–1 (2001).
[7] G. Gassabonis *et al*, *Phys. Rev. B*, **64**, 045321 (2001).
[8] T. Freixanet *et al*, *Phys. Rev. B*, **60**, R8509 (1999).
[9] U. Fano, *Phys. Rev.*, **124**, 1866, (1961).

13th Int. Symp. "Nanostructures: Physics and Technology"
St Petersburg, Russia, June 20–25, 2005

Optical polarization-resolved studies of photonic bandgap structure in synthetic opals

A. V. Baryshev[1,2], M. Inoue[2,3], A. A. Kaplyanskii[1], V. A. Kosobukin[1], *M. F. Limonov*[1], M. V. Rybin[1], A. K. Samusev[1], A. V. Sel'kin[1] and H. Uchida[2]

[1] Ioffe Physico-Technical Institute, St Petersburg, Russia
[2] Toyohashi University of Technology, Toyohashi, Aichi 441-8580, Japan
[3] CREST, Japan Science and Technology Corporation, Tokyo 113-0033, Japan

Abstract. The photonic bandgap structure of synthetic opals has been investigated by measuring optical polarization-resolved diffraction patterns and polarization- and angle-resolved transmission spectra. For special crystallographic directions, we found that the intensity of both diffracted and transmitted light strongly depends on polarization. The transmission spectra are discussed in terms of the two-band mixing formalism for the Bloch states in a photonic crystal. The measured energy positions of the photonic bandgaps were found to be in good agreement with the calculated data.

Introduction

Photonic crystals [1] have attracted close attention owing to possible complete band gap that were predicted to exist in three dimensional structures. The complete photonic band gap occurs when photons of a particular energy cannot propagate through the structure for all directions and all polarizations. Whereas much effort has been made to investigate the photonic bandgap for different spatial directions, there are only few papers devoted to polarization-resolved spectroscopy of photonic bandgaps [2–4]. As a result, available experimental data are rather poor and their interpretation is incomplete. This work is aimed at settling this problem by measuring the polarization-resolved optical diffraction patterns and polarization- and angle-resolved transmission spectra of synthetic opals. We found strong anisotropy in intensity of the diffracted and transmitted light with different polarizations along special crystallographic directions. The polarization-resolved transmission spectra are discussed in terms of the two-band mixing formalism [5] for Bloch states in a photonic crystal taking into account the relative orientation of different crystallographic planes {hkl} in the opal structure.

1. Experimental

Opals are made up of uniformly sized amorphous silica (α-SiO_2) spheres closely packed in rather perfect hexagonal growth layers (111) forming twinned fcc structure. All samples were of high quality, well characterized and oriented previously [6, 7]. The selected diameter and scanning path allow us to investigate the light coupling to (111), ($\bar{1}11$), (200), and (020) planes in the measured spectral range of 365–825 nm (a Shimadzu UV-3100 spectrophotometer) [7]. An opal sample was fixed at the center of a spherical cell. To minimize diffuse scattering of light from the sample surface of the sample, the latter was immersed in a mixture of propylene-glycrol and water ($n_{\text{opal}}/n_{\text{liquid}} \approx 0.98$).

The transmission spectra were investigated experimentally [7, 8] by varying the angle of incidence q onto the sample along different paths $L_g \to K \to L$, $L_g \to U \to X$ and $L_g \to W$ on the Brillouin zone (BZ) surface of the fcc crystal lattice (Fig. 1a). In diffraction experiments (Fig. 1b), a translucent frosted glass screen was placed in between the sample and the light source (Ar-laser, $\lambda = 514$ nm). A detailed description of the optical setup can be found elsewhere [6].

2. Results and discussion

The transmission spectra show characteristic deeps (Fig. 2) corresponding to the photonic bandgaps and a pronounce variation in the position and the intensity of the deep minima with the angle θ (see Fig. 1). Moreover, strong anisotropy in intensity of the transmitted light was reported [7, 8] for polarizations $E_\parallel$ and $E_\perp$ which are parallel and perpendicular to the scanning plane S respectively. Only for the $G \to L$ incidence direction, the transmission spectra are nearly polarization independent ($T_\parallel \approx T_\perp$). The most pronounce polarization dependence is clearly seen for the $G \to K$ incidence. Experimentally observed differential transmissivity $T_\parallel - T_\perp$ changes its sign being positive in the energy range of the {111} photonic bandgap and negative in the energy range of the {200} bandgap.

To describe the transmittance spectra observed we developed a theoretical model with an allowance of the fact that the samples under study are characterized by low dielectric contrast between silica spheres and the immerse liquid. In such a case, it is possible to simplify the approach [5] based on the two-band mixing formalism for the Bloch states in a photonic crystal and discuss the problem in terms of the effective index of refraction of the crystal. This index obeys the formula similar to the Lorentz one and shows resonant behavior due to Bragg diffraction of light from the appropriate crystal planes.

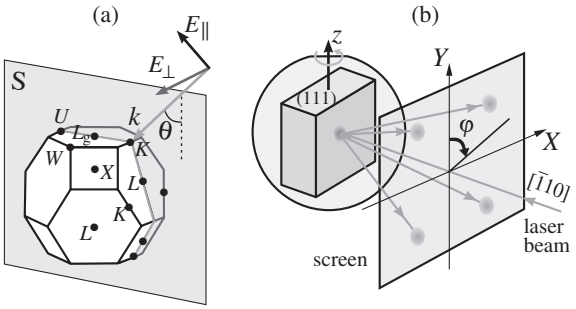

Fig. 1. (a) The BZ for the fcc crystal lattice and the scanning plane S for the $L_g \to K \to L$ path. The incidence angle θ is shown. (b) Sketch of the diffraction experiments setup.

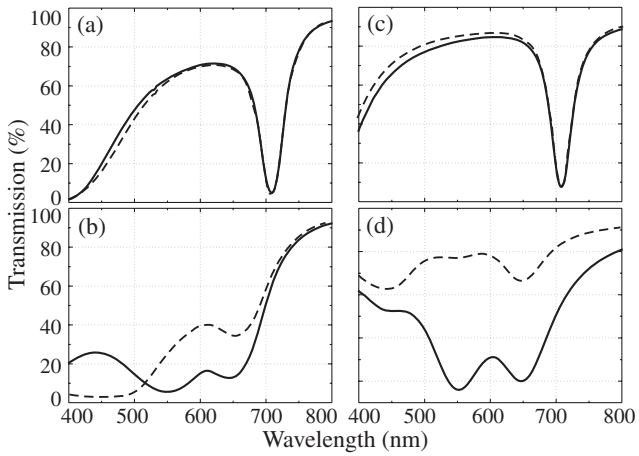

Fig. 2. Measured transmission spectra at $\theta = 0^\circ$ (a) and 40° (b) and calculated spectra for $\theta = 0^\circ$ (c) and 40° (d). Solid (dashed) lines correspond to the $E_\perp$ ($E_\parallel$) polarization.

The imaginary part of the refractive index is the parameter that is responsible for the formation of the transmittance spectra and is determined by mechanisms of damping for Bloch modes.

It should be noted that our theoretical consideration involves also the effects of polarization of light and allows us to describe corresponding experimental data.

Figure 2(c, d) shows the results of numerical calculations performed in the framework of the discussed theory. It is clearly seen that the principal spectral features observed experimentally are well reproduced in the fit. At the angle of incidence $\theta = 40^\circ$, three bands, located at about 650, 550 and 450 nm, appear in the spectra, which are due to the resonant Bragg diffraction on the $(\bar{1}11)$, (111) and (200) crystal planes, respectively. The spectra demonstrate strong inhibition of the bands depending on the angle of incidence and on the light polarization. At oblique incidence, the {111} bands are manifested in the $E_\perp$ polarization at any angle θ, while in the $E_\parallel$ polarization these bands are inhibited at certain angles, including $\theta = 40^\circ$ (Fig. 2d).

It noteworthy that there exists some analogy between the observed inhibition of Bragg resonance features at certain angles of incidence and the familiar Brewster effect, which gives some critical value θ_c for p-polarized light. However the principal difference in the two discussed phenomena takes place: the Brewster effect is accompanied by the reflection coefficient phase jump (on $\pm\pi$), whereas the Bragg reflection coefficient does not exhibit such jump of the phase.

Figure 3 presents the results of diffraction experiments. The top panel shows the diffraction patterns depending on the azimuth polarization angle φ, see Fig. 1(b). In the case of $[\bar{1}11]$ - incidence, the monochromatic incident beam produces diffraction pattern consisting of four spots located symmetrically relative to the beam. These spots are due to the Bragg diffraction from the {111} planes belonging to the twinned fcc opal structure (fccI and fccII in terms of [6]). One diagonal pair of the spots is due to diffraction from the fccI lattice and the other pair is associated with diffraction from the fccII lattice. From Fig. 3, it is evident that intensities of these pairs of spots show anti-phase dependence on the angle of polarization φ. This is because the {111} planes responsible for the observed diffraction are nearly perpendicular to each other in fcc — twins.
In summery, both polarization-resolved diffraction patterns and transmission spectra can be understood taking into account the relative orientation of different crystallographic planes {hkl} in the opal structure.

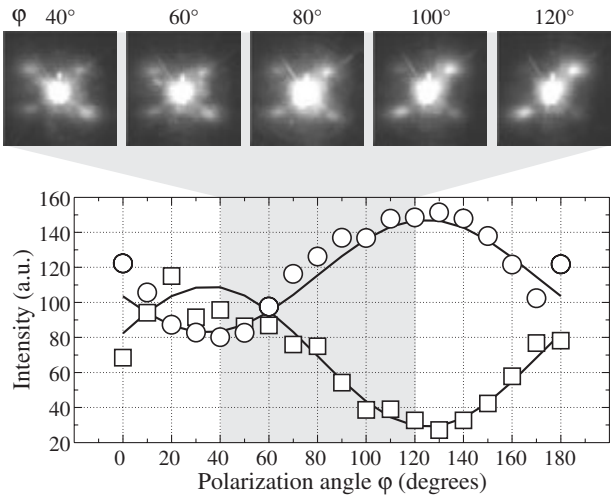

Fig. 3. Photographs of diffraction patterns for the $[\bar{1}10]$-incidence and dependence of the spot intensity on the polarization angle φ for two pairs of diagonal spots.

Acknowledgements

We thank M. I. Samoylovich for the preparation of the opal samples and A. V. Moroz for experimental assistance. This work was supported in parts by the Russian Foundation for Basic Research (grants 05-02-17809, 04-02-17592, 05-02-17776), Grant-in-Aid for Scientific Research (A) Nos. 14205045, 14655119 and Grant-in-Aid for JSPS Fellows No. 03042.

References

[1] Photonic Band Gap Materials, ed. by C. M. Soukoulis, *NATO ASI Ser. E*, **Vol. 315** (1996).
[2] I. I. Tarhan and G. H. Watson, *Phys. Rev. Lett.*, **76**, 315 (1996).
[3] H. M. van Driel and W. L. Vos, *Phys. Rev. B*, **62**, 9872 (2000).
[4] J. F. Galisteo-Lopez, F. Lopez-Tejeira, S. Rubio, C. Lopez and J. Sanchez-Dehesa, *Appl. Phys. Lett.*, **82**, 4068 (2003).
[5] D. A. Mazurenko, R. Kerst, J. I. Dijkhuis, A. V. Akimov, V. G. Golubev, D. A. Kurdyukov, A. B. Pevtsov and A. V. Sel'kin, *Phys. Rev. Lett.* **91**, 213903 (2003).
[6] A. V. Baryshev, A. A. Kaplyanskii, V. A. Kosobukin, K. B. Samusev, D. E. Usvyat and M. F. Limonov, *Phys. Rev. B*, **70**, 113104 (2004).
[7] A. V. Baryshev, K. Nishimura, H. Uchida and M. Inoue, *Proc. 12th Int. Conf. Nanostructures: Physics and Technology*, p. 105, St Petersburg, 2004.
[8] A. V. Baryshev, A. B. Khanikaev, H. Uchida, M. Inoue and M. F. Limonov, *(unpublished)*.

13th Int. Symp. "Nanostructures: Physics and Technology"
St Petersburg, Russia, June 20–25, 2005

Nonlinear magneto-optics in garnet magnetophotonic crystals

O. A. Aktsipetrov[1], T. V. Dolgova[1], A. A. Fedyanin[1], R. V. Kapra[1], T. V. Murzina[1], M. Inoue[2], K. Nishimura[2] and H. Uchida[2]

[1] Department of Physics, Moscow State University, 119992 Moscow, Russia
[2] Toyohashi University of Technology, 441-8580 Toyohashi, Japan

Abstract. Nonlinear magneto-optical Kerr effect (NOMOKE) both in magnetization-induced second-harmonic generation (MSHG) and magnetization-induced third-harmonic generation (MTHG) is observed in garnet magnetophotonic crystals and microcavities. Magnetization-induced variations of MSHG and MTHG intensity as well as magnetization-induced shift of phase and rotation of polarization of second-harmonic and third-harmonic waves are observed in proper transversal, longitudinal or polar-NOMOKE configurations.

Introduction

The studies of nonlinear magneto-optical effects in magnetophotonic crystals (MPC) are two-fold motivated as both photonic band gap (PBG) materials and nonlinear magneto-optics separately attract recently considerable attentions. One of the potential advantages of PBG materials is significant enhancement of the nonlinear-optical effects such as second-harmonic (SHG) and third-harmonic (THG) generation in photonic crystals. New domain of nonlinear optics appears as the second- and third-order structural nonlinearities are combined with the broken time reversal symmetry due to the magnetization of ferromagnetic materials. Due to this combination, SHG and THG become very sensitive to the control by external magnetic impact.

Samples

Magnetophotonic microcavities (MMC) are formed from two dielectric Bragg reflectors and a ferromagnetic cavity spacer. Reflectors consist of five pairs of alternating quarter-wavelength-thick SiO_2 and Ta_2O_5 layers. The cavity spacer is a Bi-substituted yttrium-iron-garnet layer, $Bi_{1.0}Y_{2.5}Fe_5O_x$. The spacer optical thickness is a half of wavelength. Magnetophotonic crystals (MPC) are fabricated from a stack of four repeats of $3\lambda_{PC}/4$-thick Bi:YIG layers and $\lambda_{PC}/4$-thick SiO_2 layers with $\lambda_{PC} \simeq 950$ nm [1]. Cleavage of MMC and MPC is studied using field-emission scanning electron microscope (FESEM). The FESEM images are shown in Fig. 1.

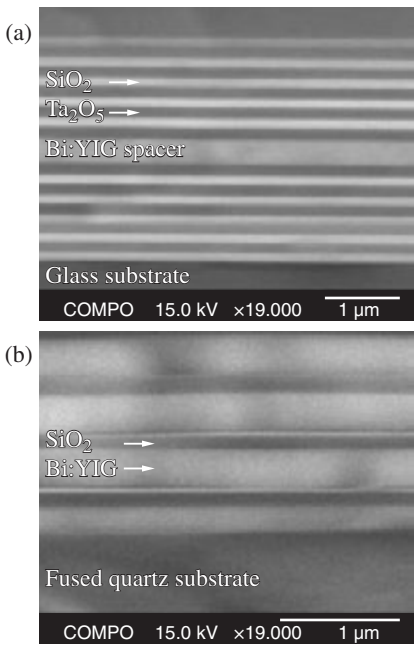

Fig. 1. The FESEM images of the MMC (upper panel) and MPC (lower panel) cleavages.

Experimental results

Magnetization-induced SHG in MMC

Figure 2 shows the SHG intensity as a function of the fundamental wavelength measured in the spectral vicinity of the microcavity mode for opposite directions of the dc-magnetic field applied in the transversal configuration, $\mathbf{M} = (0, M_Y, 0)$ [2].

The SHG intensity is enhanced as the fundamental wave is tuned across the microcavity mode. The ratio of the intensities for opposite directions of the magnetic field is almost 2. Insert in Fig. 2 shows the spectral dependence of the magnetic contrast in the SH intensity, $\rho = (I_+ - I_-)/(I_+ + I_-)$, where $+$ and $-$ denote directions of the magnetization. ρ achieves values of 0.3 and appears to be almost spectrally independent. The changing of the magnetic field direction varies only the SH intensity and no spectral shifts of SHG resonances are observed.

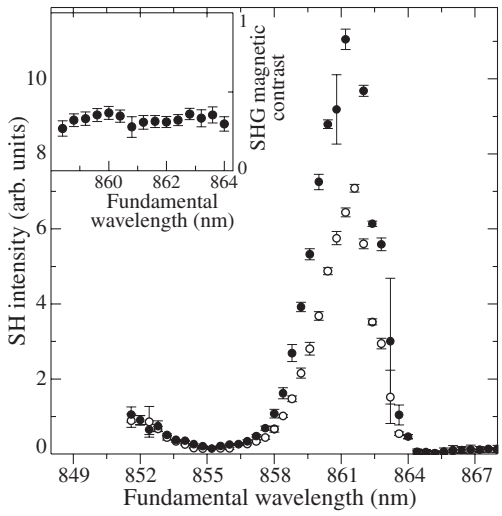

Fig. 2. Intensity effects in MSHG: (a) The spectrum of the SHG magnetic contrast in the spectral vicinity of the micro-cavity mode. (b) Transversal NOMOKE in SHG measured in the p-in, p-out polarization combination for opposite directions of magnetic field, solid and open circles, respectively.

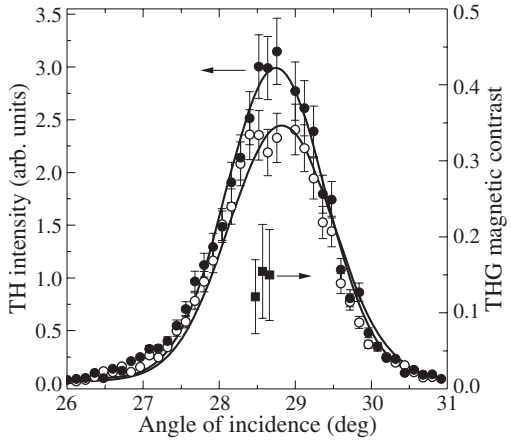

Fig. 3. Intensity effects in MTHG: Angular spectra of transversal NOMOKE in THG measured in MMC with with $\lambda_{MC} \simeq 900$ nm for opposite directions of magnetic field, solid and open circles, respectively. The spectrum of the THG magnetic contrast in the angular vicinity of the microcavity mode.

Magnetization-induced THG in MMC

The magnetization-induced effects in the intensity of third-harmonic generation are studied for the transversal NOMOKE configuration. Fig. 3 shows the THG intensity spectra measured in the wave-vector domain (k-domain spectra) for the oppositely directed magnetic

Field for the transversal NOMOKE con?fiuration. Similar to the magnetization-induced SHG, the THG magnetic contrast is determined by the expression $\rho_{3\omega} = (I_{-}^{3\omega} I^{3\omega} + I_{-}^{3\omega})/(I_{-}^{3\omega})$, where $I^{3\omega}$ and $I^{3\omega}$ are the THG intensities for the oppositely directed magnetic fields. The measured value of the magnetic contrast in the THG intensity is found to be about 0.1 for the angles of incidence corresponding to the resonance with the microcavity mode.

Phase-matched MSHG in MPC

Figure 4 shows the SHG spectra measured in MPC for two directions of saturated magnetic field in the transversal NOMOKE configuration. The SHG intensity is enhanced manyfold in the vicinity of 1050 nm corresponding to the phase-matched conditions for SHG at the long-wavelength PBG edge of MPC. Changing the magnetic field direction varies the SHG intensity approximately by a factor of seven at $\lambda_\omega \simeq 1055$ nm that indicates the noticeable interference between the $E_{2\omega}^{\mathrm{NM}}$ and $E_{2\omega}^{M}$ fields. At $\lambda_\omega \simeq 1025$ nm the SHG intensity for one of the magnetic field direction is close to zero. It means that the contrast of the magnetization-induced variations in the SH intensity is close to unit, which the upper limit for SHG magnetic contrast.

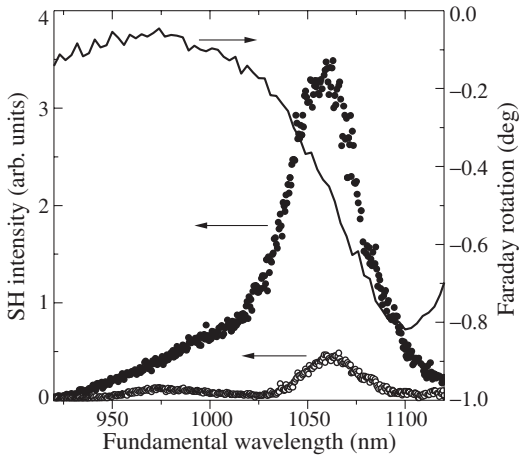

Fig. 4. The SHG spectra of MPC in the p-in, p-out polarization combination and in transversal magnetic-field configuration measured for opposite directions of the dc-magnetic field, open and filled circles, respectively. Line, the Faraday rotation spectrum at the normal incidence.

References

[1] A. A. Fedyanin, O. A. Aktsipetrov, D. Kobayashi, K. Nishimura, H. Uchida and M. Inoue, *J. Magn. Magn. Mater.* **282**, 256 (2004).

[2] T. Murzina, T. Dolgova, R. Kapra, A. Fedyanin, O. Aktsipetrov, K. Nishimura, H. Uchida and M. Inoue, *Phys. Rev. B* **70**, 012407 (2004).

13th Int. Symp. "Nanostructures: Physics and Technology"
St Petersburg, Russia, June 20–25, 2005

Electro-optical effect in composite photonic structures based on grooved silicon and liquid crystal

J. A. Pilyugina[1], E. V. Astrova[1] and T. S. Perova[2]

[1] Ioffe Physico-Technical Institute, St Petersburg, Russia
[2] Department of Electronic and Electrical Engineering, University of Dublin, Trinity College, Dublin 2, Ireland

Abstract. One-dimensional periodic structures with deep vertical grooves were obtained by wet anisotropic etching of a 40 μm thick Si layer oriented in (110) plane. Inter-digital electrodes formed by silicon ribs were isolated from the substrate by a 2 μm thick SiO_2 film. The grooves of various widths were infiltrated with nematic liquid crystal (LC) E7. Electro optical effect in the LC was registered with visible polarized light. The threshold voltage was found to be in the range 2.5 . . . 3.0 V.

Introduction

Narrow grooves with deep vertical walls can be obtained by means of wet anisotropic etching of (110)-oriented silicon [1]. Periodic structures of grooved silicon with lattice period comparable to the wavelength of infrared range suit well for the various elements of integrated optics such as 1D photonic crystals (PC) [2], microcavities, wave-guides and diffractive gratings. These structures can also be used to fabricate an optical media with anisotropy of form [3]. The composites, obtained by infiltration of nematic liquid crystal (LC) into the voids of periodic semiconductor matrices, are of special interest [4]. The optical properties of such composites can be tuned by altering of the LC's refractive index. The simplest way to obtain the effect is to raise the temperature above the phase transition point, i.e. use thermo-optical effect. However, the application of an external electric field is more attractive from the practical point of view. Serious problems arise when one tries to apply a voltage to a LC inside the composite based on electro-conductive matrices, such as 2D PC made on macro-porous silicon, for example. Being conductive, grooved silicon nevertheless suits for planar electro-tuned structures. The aim of the work was to design and to fabricate the model periodic structures with the ability to tune its optical properties by means of an external electric field.

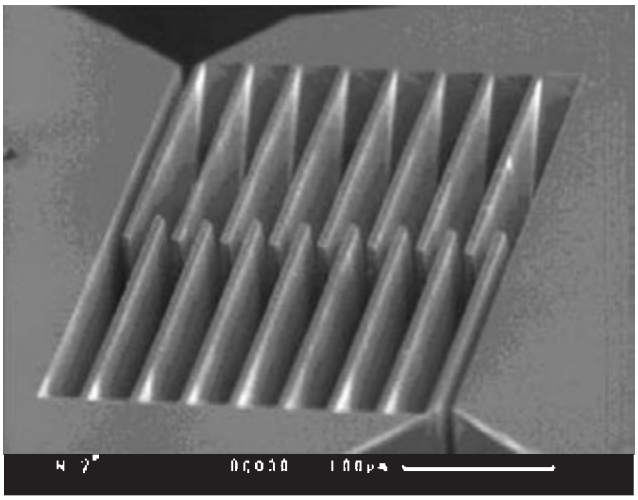

Fig. 1. SEM image of the inter-digital electrode structure.

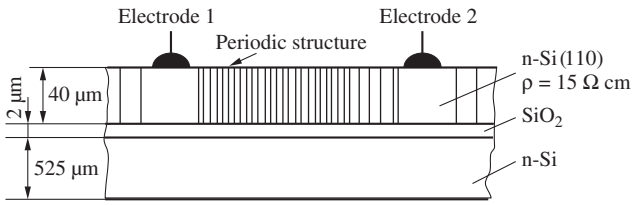

Fig. 2. Cross section sketch of the sample fabricated on SOI substrate.

1. Experimental

The topology of inter-digital silicon electrodes has been chosen as a basis (Fig. 1) for model structures. The fabricated photo mask allows one to obtain the elements with various grooves width, w, ranging from 2 to 100 μm, on the same wafer. The structures with the lattice period of $A = 4$; 8; 16 and 32 μm were fabricated. Around each of the chips there was a trench and a vessel connected to the grooves. This allows the formation of a confined volume and prevents LC leakage from the structure. Different techniques of isolating the electrodes from the substrate such as p-n junction, epoxy glue and silicon dioxide (SOI substrate) (Fig. 2) have been tested. The latter was found to be the optimal one due to the flat and smooth bottoms of the grooves, and the possibility to check visually the etch depth and the electric isolation.

To infiltrate the grooves we have chosen the mixture E7 from Merck. It possesses high birefringence and has the mesophase at room temperature. The electro-optical effect was studied under DC or saw-shaped voltage of frequency 50 Hz. Freedericks transition was registered with polarized light of a microscope in the reflection mode when polarizer and analyzer were crossed. At $V = 0$ LC was bright in the region of overlapping electrodes, and it became dark under a voltage higher than the threshold voltage V_c, and turned bright again when the voltage was turned off (Fig. 3). The V_c value was 2.5–3.0 V and practically did not depend on the groove width. The obtained V_c is close to the value known for this LC (2 V) and is much lower if compared to the voltage required to align LC rod-like molecules along the field in the same structures isolated with a p-n junction [5].

Acknowledgements

This work has been supported by Science Foundation Ireland Basic Research Program (Grant 04/BR/P0698) and Russian Programs "Physics of Solid-State Nanostructures", Laser Physics and Scientific school — 758.2003.2.

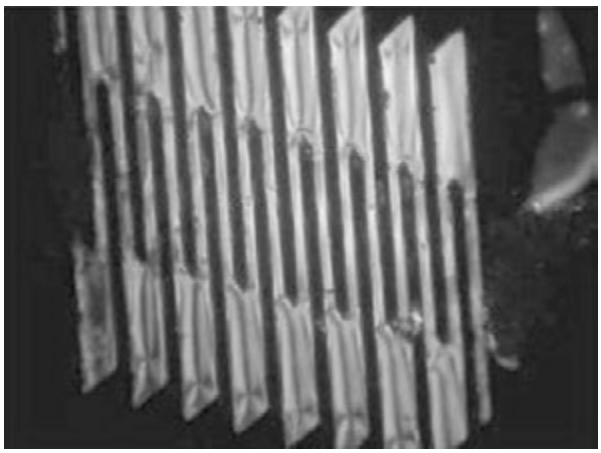

$V = 0$

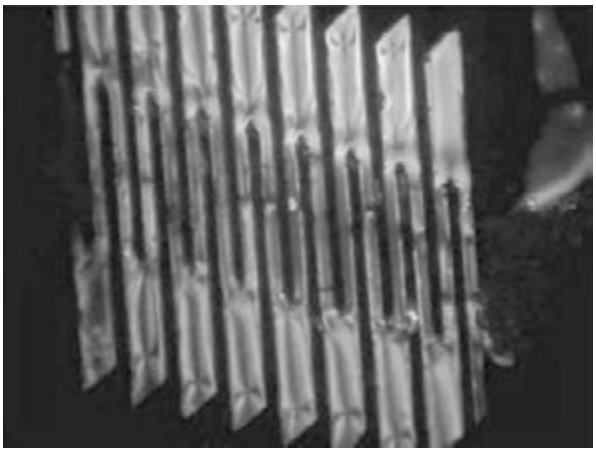

$V = 5$

Fig. 3. Optical microscope image of the composite structure under crossed polarizers. Black stripes are silicon electrodes, bright regions are grooves filled with LC.

References

[1] D. L. Kendall, *Ann. Rev. Mat. Sci.* **9**, 373 (1979).
[2] V. Tolmachev, E. Astova, T. Perova. *Proceeding SPIE*, **5401**, 192 (2004).
[3] E. V. Astrova, T. S. Perova, V. A. Tolmachev, A. D. Remenyuk, J. Vij and A. Moore, *Semiconductors*, **37**, 399 (2003).
[4] K. Busch, S. John, *Phys. Rev. Lett.* **83**, 967 (1999).
[5] E. V. Astrova, T. S. Perova, S. A. Grudinkin, V. A. Tolmachev, J. A. Pilyugina, V. B. Voronkov, J. K. Vij, *Semiconductors*, **39**, (2005) (to be published).

13th Int. Symp. "Nanostructures: Physics and Technology"
St Petersburg, Russia, June 20–25, 2005

Reflection spectroscopy of the exciton-mediated resonant Bragg GaAs/AlGaAs nanoheterostructures

V. P. Evtikhiev[1], A. B. Pevtsov[1], A. V. Sel'kin[1], A. S. Shkolnik[1], E. L. Ivchenko[1], V. V. Chaldyshev[1], L. I. Deych[2], A. A. Lisyansky[2], D. R. Yakovlev[1,3] and M. Bayer[3]

[1] Ioffe Physico-Technical Institute, St Petersburg, Russia
[2] Queens College of the City University of New York, Flushing, New York 11367, USA
[3] Fachbereich Physik, Universität Dortmund, 44221 Dortmund, Germany

Abstract. An exciton-mediated resonant Bragg structure (RBS) were designed, grown and characterized in order to reveal sharp resonant features in the reflection spectra by variation of an angle of incidence of light and the sample temperature. The RBS consisting of 36 GaAs quantum wells (QW's) separated by 104 nm thick AlGaAs barriers was grown by molecular-beam epitaxy. In the periodic sequence of the 15 nm thick QW's we introduced four "defect" (DQW's), which were as thick as 20 nm. We analyze the measured optical properties of such RBS in terms of theoretical model which takes into account the exciton-photon coupling.

Introduction

The resonant Bragg structure (RBS) is a specific type of one-dimensional photonic crystals, where the electro-magnetic waves interact with shallow eigenexcitations in periodic nanostructures such as multiple quantum wells (MQW). When the frequency of light coincides with that of excitons in quantum wells, both photons and excitons loose their identities transforming into exciton-polaritons. These quasi-particles are normal waves, multiple diffraction of which determines optical properties of the medium in the vicinity of the resonant frequency.

Optical properties of a resonant Bragg structure were first theoretically considered in Ref. [1]. It has been shown that the large number of quantum wells gains the light-matter interaction and significantly increases the width of the polariton band gap. The experimental research has been done on the base of CdTe/CdMgTe [2] and GaAs/InGaAs [3, 4] MQW structures with identical quantum wells. This research evidenced the experimental feasibility of the coherent exciton-photon coupling in MQW with large number of periods.

So, the RBS seems to be an attractive object for applications to a variety of photonic devices. It should be noted, however, that growth of the MQW with desirable parameters and quality is a challenging technological task, since the inhomogeneous broadening and deviation from prescribed geometry and exciton energies are crucial for the phenomenon.

In this paper we first demonstrate the results of optical study of a novel resonant Bragg structure based on MQW in the GaAs/AlGaAs system. As distinct from previous data we focus on the structures with the one-dimensional photonic band gaps covering resonant excitonic frequencies for the case of oblique incidence of light. The RBS was specifically designed to have "defects" in resonant excitonic frequencies, which manifest themselves as a sharp features in the reflection spectra.

1. Theory

It has been shown in Ref. [5] that a defect layer placed in the middle of a sufficiently long MQW structure leads to an appearance of a special mode of the electromagnetic field localized near the defect. The resonant transmission at the frequency of this mode results in an essential modification of the reflection and transmission spectra of such structures. Later, it was demonstrated [6, 7] that the resonant suppression of the reflection should also sustain in short structures. Such structures are characterized by the exciton frequencies of the host, ω_h, and the defect, ω_d, layers. The width of the host layers should satisfy the Bragg condition, $\omega_h n d/c = \pi$, where d is the period of the structure and n is the background index of refraction. If this condition is met, the reflection near the defect frequency ω_d is given by

$$r = r_N \frac{(\omega_d - \omega_h)/N - \chi_d^{-1}}{i - \chi_d^{-1}}, \qquad (1)$$

where r_N is the reflection coefficient of a structure without a defect, N is the number of layers and χ_d is the exciton susceptibility of the defect layer. The specific feature of the reflection is the resonant drop near the frequency $\omega_d - (\omega_d - \omega_h)/N$.

This effect can be amplified by building a special multiple defect superstructure. Such a structure is built of M blocks such that each individual block has a form of an N-layer MQW structure with a defect layer at the middle.

2. Experiment

The design of the experimentally realized MQW structure is based on the theoretical calculations. The building block of the structure consists of 20 nm thick "defect" quantum well (DQW) in the middle and four 15 nm thick quantum wells (QW) to the left and right of it. Schematic band diagram of two adjacent blocks of the MQW is shown in Fig. 1.

The barriers were designed as short-period AlAs/GaAs superlattices with the effective height corresponding to the $Al_{0.3}Ga_{0.7}As$ alloy. The barrier width was adjusted to meet the Bragg condition for the excitons in the quantum wells:

$$\frac{\omega_h}{c}(n_b d_b + n_w d_w) = \pi, \qquad (2)$$

where indices b and w indicate the barrier and well (QW or DQW). For the chosen QW and DQW parameters the barrier width was of 104 nm and 101.5 nm, respectively.

The MQW structure was grown by molecular beam epitaxy in a TsNA-13 system. The substrate was a 2-inch n-GaAs wafer with (001) orientation. The MQW was grown at 690 °C and

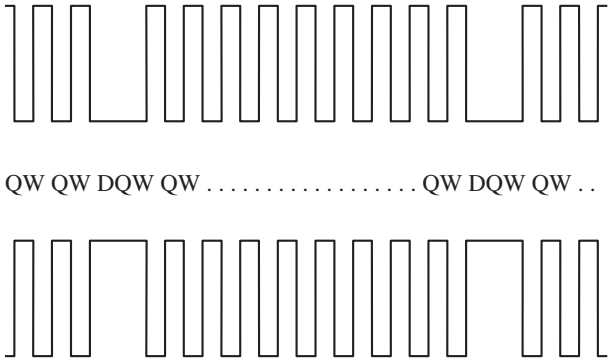

Fig. 1. Schematic band diagram of two adjacent blocks of the MQW structure. DQW denote 20 nm thick "defect" quantum wells, whereas QW stand for 15 nm regular quantum wells. The barriers are AlGa-GaAs short period superlattices. Their effective height corresponds to AlGaAs alloy with Al content of 0.3.

under the V/III flux ratio of 4. The growth rate was monitored by using the RHEED oscillations, which showed 0.6 μm/h for GaAs and 0.35 μm/h for AlAs layers.

The reflectance spectra of the fabricated RBS were explored at various angles of incident light in the temperature range from 7 to 140 K. The grating monochromator equipped with InGaAs CCD was used as a photodetector.

Fig. 2 shows the reflectance spectra recorded at 7 K for the TE mode for two different angles of incidence of light (0° and 70°).

The spectra demonstrate one pronounced reflectance peak (with FWHM being equal to ~ 25 nm) and a number of satellites. In the wider wavelength scale there are a lot of interference fringes indicating a high planarity of the structure as a whole.

The major reflectance peak originates from the periodic modulation of the refractive index that is different in the wells and barriers. The corresponding one-dimensional photonic band gaps are indicated approximately in Fig. 2 by horizontal arrow bars. The shift of the reflectance band center, λ_m, with changing an angle of incidence from normal to oblique is given by the Bragg diffraction low:

$$\lambda_m = 2d(\varepsilon_0 - \sin^2\theta)^{1/2}, \qquad (3)$$

where d is the period in the RBS, $\varepsilon_0 = n^2$ is the average dielectric constant.

Several specific features are observed in the reflectance spectra, which may be due to the polariton modes of the RBS. At 7 K, these features are situated at the wavelengths of 807 and 813 nm and are originated from the host and defect QW's, respectively. In the case of the normal incidence the features appear weakly on the short-wave shoulder of the reflectance spectrum. When the oblique incidence is used the excitonic features became more clear owing to increasing the excitonic time of life (see insert in Fig. 2) under the PBG effect. It should be noted that the "defect" peculiarity shifts to the long-wave range on about 8 meV with respect to the host exciton frequency. This fact is good accordance with our numerical estimations.

For each of temperatures between 7 and 140 K we can find the angle of incidence, which provides the overlapping of the excitonic resonant frequencies and the photonic band gap. However our experimental data demonstrate rather strong

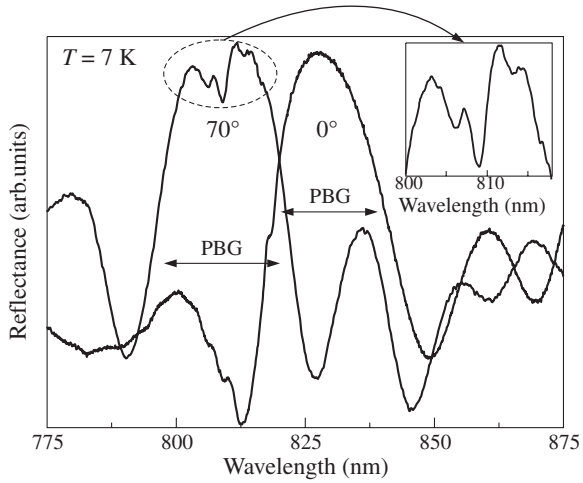

Fig. 2. Reflectance spectra of the GaAs/AlGaAs periodic MQW structure at normal and oblique angles of incidence for the TE mode. Arrow bars show the photonic band gaps related to the periodic modulation of the refractive index. The reflection features related to the resonant states are magnified in the insert for better observation.

broadening of the excitonic states as compared with Ref. [7, 8], which reflects the actual, not perfect, quality of the investigated samples.

To conclude, a MQW structure being theoretically designed has been grown by molecular-beam epitaxy. The structure contained four "defect" quantum wells within 36 periods. The geometrical and optical parameters of the MQW structure under study meet the demands of the RBS pointed above. Our investigations show that exciton-photon interaction in the RBS can be essentially enhanced by fine tuning the exciton frequency within the PBG spectral range.

Acknowledgements

This work has been supported in part by the Russian Foundation for Basic Research, by the Deutsche Forschungsgemainschaft through Grant 436 RUS 17/115/02, and by NATO Grant PST CLG 980399.

References

[1] E. L. Ivchenko, A. I. Nesvizhskii, and S. Jorda, *Phys. Solid State* **36**, 1156 (1994).

[2] E. L. Ivchenko, V. P. Kochereshko, A. V. Platonov, D. R. Yakovlev, A. Waag, W. Ossau, G. Landwehr, *Phys. Solid State* **39**, 1852 (1997).

[3] M. Hubner, J. P. Prineas, C. Ell, P. Brick, E. S. Lee, G. Khitrova, H. M. Gibbs, and S. W. Koch, *Phys. Rev. Lett.* **83**, 2841 (1999).

[4] J. P. Prineas, C. Ell, E. S. Lee, G. Khitrova, H. M. Gibbs, and S. W. Koch, *Phys. Rev. B* **61**, 13863 (2000).

[5] L. I. Deych, A. Yamilov, and A. A. Lisyansky, *Phys. Rev. B* **64**, 075321 (2001).

[6] L. I. Deych, M. V. Erementchouk, and A. A. Lisyansky, *Appl. Phys. Lett.* **83**, 4562 (2003).

[7] L. I. Deych, M. V. Erementchouk, A. A. Lisyansky, *Phys. Rev. B* **69**, 75308 (2004).

[8] E. L. Ivchenko, M. M. Voronov, M. V. Erementchouk, L. I. Deych, A. A. Lisyansky, *Phys. Rev. B* **70**, 195106 (2004).

13th Int. Symp. "Nanostructures: Physics and Technology"
St Petersburg, Russia, June 20–25, 2005

Enhancement of second- and third-harmonic generation in single and coupled porous silicon microcavities

M. G. Martemyanov[1], D. G. Gusev[1], I. V. Soboleva[1], T. V. Dolgova[1], *A. A. Fedyanin*[1], G. Marowsky[2] and O. A. Aktsipetrov[1]

[1] Department of Physics, M.V.Lomonosov Moscow State University, 119992 Moscow, Russia
[2] Laser-Laboratorium Göttingen, D-37077 Göttingen, Germany

Abstract. Second- and third-harmonic generation (SHG and THG) is studied in single and coupled porous silicon microcavities in both frequency and wave vector domains. For the fundamental field resonant to the microcavity mode the second-harmonic intensity is enhanced by 10^2 times in comparison with that outside the photonic band gap, while the third-harmonic intensity reveals more than 10^3-times enhancement. SHG and THG spectroscopy in identical microcavities coupled through the intermediate Bragg reflector reveals the peaks in the second- and third-harmonic intensity spectra if the fundamental field is in resonance with the splitted modes of coupled microcavities. The peaks are caused by the combination of the resonant enhancement of the fundamental radiation and constructive interference of the second-(third)-harmonic fields induced in the microcavity spacers.

Introduction

One of the issues regarding the application of photonic crystals and microcavities is the control of the nonlinear-optical response enhancement in a preset spectral region [1]. For instance, the multiple reflection interference of forward- and backward-propagating waves can compensate the phase mismatch between the fundamental and second-harmonic (SH) waves and fulfills the phase-matching conditions in the spectral ranges of the edges of the photonic band gap (PBG) [2]. Additional enhancement mechanism can be realized in the planar photonic crystal microcavities (MC) constituted of two Bragg reflectors separated by a submicron-thick spacer. The cavity mode located inside PBG manifests as a sharp drop at the high reflectivity plateau of the linear reflection spectrum. The optical field is strongly confined inside MC as the wavelength of the incident field is in resonance with the cavity mode. Macroporous and mesoporous silicon MC and photonic crystals [3] are attractive for all-silicon-based optoelectronic applications being easily incorporated in the semiconductor technology.

In this paper the experimental study of the second- and third-harmonic generation (SHG and THG) enhancement in porous-silicon-based microcavities is presented. SHG and THG spectroscopy in both frequency and wave vector domains reveals the giant SHG enhancement in MC with the half-wavelength-thick porous silicon spacer and the Bragg reflectors consisted of alternating quarter-wavelength-thick porous silicon layers of different porosities and, as a consequence, different refractive indices. The intensity enhancement of SHG and THG in coupled microcavities (CMC) upon the fundamental wave resonance with splitted modes is studied. The angular spectra of the second-harmonic (SH) and third-harmonic (TH) intensities measured on the series of the CMC samples formed from mesoporous silicon with varied reflectivity of the intermediate Bragg reflector show the strong dependence on the electromagnetic coupling between two identical spacers.

1. Experimental

The MC samples are fabricated by conventional electrochemical technique [3]. Briefly, the Si(001) wafer etching in the HF:C_2H_5OH solution forms the mesoporous silicon layer. The porous silicon layers with different porosity and thickness are obtained by the variation of the current density and the etching time. MC with the mode centered at the wavelength of λ_{MC} for normal incidence are composed from two Bragg reflectors separated by the $\lambda_{MC}/2$-thick MC spacer. Each Bragg reflector has 5 or 5.5 pairs of $\lambda_{MC}/4$-thick PS layers with two different refractive indices. The CMC samples consist of three one-dimensional photonic crystals, separated by two identical $\lambda_{MC}/2$-thick spacers. External Bragg reflectors are formed from four pairs of $\lambda_{MC}/4$-thick layers of porous silicon. The number of layers in the intermediate Bragg reflector (IBR), N, is changed in series from three to nine. Porous silicon layers with high refractive index are etched with the current density of 25 mA/cm^2, the layers with low refractive index are formed with the current density of 83 mA/cm^2. Refractive indices of the porous silicon layers are found from the calibration reflection spectra of the single porous silicon layers. Porosities of layers are calculated using effective medium approximation. Layers with high refractive index have $n_H = 1.78$ and porosity of $f_H = 0.64$, and layers with low refractive index have $n_L = 1.42$ and $f_L = 0.77$. Refractive index of spacers is n_L.

The tuning of the fundamental radiation across the resonance of the fundamental wave with the microcavity mode, $k_z d_{MC} = \pi$, where k_z is the normal component of the fundamental wave vector inside the MC spacer, is achieved in both frequency and wave-vector domains. SHG and THG spectroscopy in the frequency domain is realized by tuning the fundamental wavelength, λ_ω, at fixed angle of incidence, θ. In wave-vector domain SHG and THG spectroscopy, θ is varied at fixed λ_ω. The 4-ns-pulsed output of the optical parametric oscillator tunable from 750 nm to 1300 nm and the 10-ns-pulsed infrared output of the Nd^{3+}:YAG laser with energy below 5 mJ/pulse are used. The TH and SH radiations are separated by a set of appropriate color filters and detected by a photomultiplier tube. A monochromator is used to check the spectral background.

2. Resonant SHG and THG in single porous silicon microcavities

Figure 1 shows the SHG and THG spectra measured in the wave-vector domain. The reflection spectrum shown for comparison has the plateau with almost full reflection corresponded

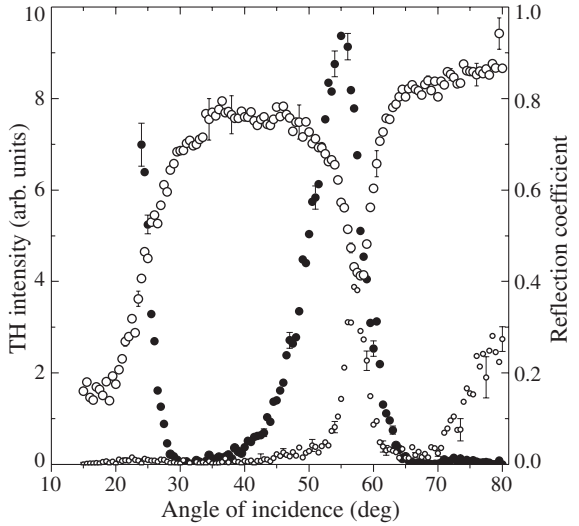

Fig. 1. Filled circles: the angular THG spectrum of the porous silicon MC measured in the p-in, p-out polarization combination. Open circles: the reflectance spectrum of the s-polarized radiation of 1064 nm. Small circles: the angular spectrum of the SH intensity measured in the s-in, p-out polarization combination.

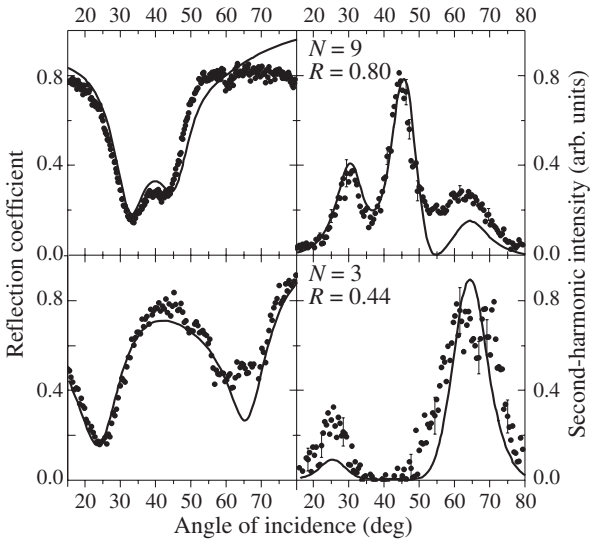

Fig. 2. Angular spectra of SH intensity (right panels) and linear reflection coefficient (left panels) of porous silicon CMC with $\lambda_{MC} = 1200$ nm and different reflection coefficient of intermediate Bragg reflector, R. Lines are the fit results by the transfer-matrix formalism.

to PBG and the dip related to the MC mode. The TH intensity reveals an enhancement at $\theta \simeq 55^\circ$, that is close to the MC mode, and resonance in SHG located at $\theta \simeq 58^\circ$. The THG peak is approximately 2 times broader than the MC mode drop of the linear reflection. This is apparently associated with smaller Q-factor value for the p-polarized fundamental radiation than the quality factor for the s-polarized one. The shift of the THG peak from the mode position and the SHG peak stems from different mode positions of the s- and p-polarized fundamental light. The TH intensity increases also at the short-wavelength PBG edge for $\theta < 30^\circ$.

The SHG and THG spectra are interpreted using the nonlinear transfer matrix formalism [4]. The peculiarities of the model and details of the fit are presented in [5]. Briefly, the SHG and THG resonances at the MC mode is caused by the spatial confinement of the fundamental field inside the spacer and the constructive interference of complex SHG(THG) contributions from each porous silicon layer which accounts for the phase-matching in the periodic MC structure [5]. The interference of the homogeneous and inhomogeneous SH waves at external and internal MC interfaces is described by the nonlinear transfer matrices [4].

3. SHG and THG enhancement in coupled porous silicon microcavities

The angular spectra of linear reflection, SH intensity and TH intensity are measured at the series of porous silicon CMC with different reflectivity of the intermediate Bragg reflector. Figure 2 shows spectra of linear reflection and SH intensity for two representative CMC with $N = 9$ and $N = 3$. The linear spectra have two dips, where reflection coefficient value decreases up to 0.2, corresponding to the resonance of the fundamental radiation with the CMC modes. In the other parts of spectra, reflection coefficient reaches the values up to 0.85 that corresponds to the PBG. For all CMC samples, the right dip in the spectra related to the long-wavelength-mode of CMC is smaller than the left one that can be attributed to the monotonous decrease of optical thickness of porous silicon layers with the depth [6].

The angular splitting of dips in reflection spectra and SHG peaks decrease gradually with the increase of the intermediate Bragg reflector reflectivity that characterizes the reduction of the coupling between microcavities. The basic mechanism of the SHG enhancement is localization of the fundamental field inside the spacers, which leads to the increase of the amplitudes of the SH fields induced inside them. Constructive interference of the outgoing SH fields from the various layers of CMC results in redistribution of amplitudes of SHG resonances and shift of peaks from angular positions corresponding to the maximal localization of the fundamental field.

Acknowledgement

This work has been supported in part by Russian Foundation of Basic Research.

References

[1] K. Sakoda, *Optical Properties of Photonic Crystals*, Springer, 2001.
[2] M. Scalora *et al*, *Phys. Rev A*, **56**, 3166 (1997).
[3] L. Pavesi, *Riv. Nuovo Cimento*, **20**, 1 (1997).
[4] D. S. Bethune, *J. Opt. Soc. Am B*, **6**, 910 (1989).
[5] T. V. Dolgova *et al*, *J. Opt. Soc. Am B*, **19**, 2129 (2002).
[6] A. G. Cullis *et al*, *J. Appl. Phys.*, **82**, 909 (1997).

13th Int. Symp. "Nanostructures: Physics and Technology"
St Petersburg, Russia, June 20–25, 2005

3D magneto-photonic crystals: magnetization induced second harmonic generation

R. V. Kapra[1], E. M. Kim[1], T. V. Murzina[1], D. A. Kurdyukov[2], V. G. Golubev[2], S. F. Kaplan[2], M. A. Bader[3] and G. Marowsky[3]

[1] Department of Physics, Moscow State University, 119992 Moscow, Russia
[2] Ioffe Physico-Technical Institute, St Petersburg, Russia
[3] Laser-Laboratorium Göttingen, D-37077 Göttingen, Germany

Abstract. Photonic crystals (PC) and especially magneto photonic crystals are perspective materials for photonics. In this paper 3D magneto photonic crystals fabricated on the base of artificial opals infiltrated by yttrium iron-garnet (YIG) are studied. 3D photonic crystals have the YIG filling factor of the composed structure being about 0.5. The nonlinear magnetic properties of 3D magneto photonic crystals are studied by magnetization-induced second harmonic generation technique. A large magnetic contrast of the SHG intensity of about 0.1 is observed at the edge of the photonic band gap.

Introduction

Photonic crystals (PC), which are one-, two- or three-dimensional artificial periodically ordered structures with a optical wavelength period, are a subject of intensive theoretical and experimental studies since the pioneering work of Yablonovich [1] because of perspective applications in optoelectronic and photonic devices. The main properties of PC originate from the existence of photonic band gap (PBG) which allows for the control over the flow of light, its propagation, dispersion and refraction. The functional properties of PC can be sufficiently enlarged as they are combined with the magnetic ones. The possibility to change the spectral position of the PBG by application of the DC magnetic field was discussed in [2,3].

In this paper, the composition and studies of 3D magneto photonic crystals fabricated on the base of artificial opals infiltrated by Bi-substituted yttrium iron-garnet (YIG) are presented. It is shown that a high nonlinear magneto-optical Kerr effect in the second harmonic generation (SHG) can be attained at the edge of the PBG of such a structure.

1. Experimental

Synthetic opals formed from close-packed monodisperse amorphous SiO_2 balls of 330 ± 5 nm in diameter are used as a template for the impregnation of YIG [5]. These opals have a regular interconnected sublattice of pores occupying about 26% of the whole volume of the sample. The opal templates have a polydomain structure, the size of a single domain with highly ordered SiO_2 spheres ranges from 30 to 100 μm. The experimental samples were cut parallel to the (111) opal plane. Bi-substituted YIG was impregnated in opals in two different ways. The first way was the soaking of opals by the colloidal solution of yttrium-iron hydroxides taken in stoichiometric proportion, when the mean size of the colloidal particles was about 5 nm. The subsequent annealing at 1300 K results in the formation of crystalline YIG inside the opal pores. We suppose that the yttrium oxide reacts mostly with silicon dioxide forming silicate and, therefore, only a small amount of yttrium iron garnet was formed. The filling factor of pores was 25–30% vol.

The second way was using a thin platinum layer [6] (with thickness of 2–3 nm) covering the inner surface of the opal matrix to prevent the chemical reactions between yttrium oxide and the silica matrix. Then the samples are infiltrated by an aqueous solution of yttrium and iron acetates and annealed as described above for the first way. The filling factor of pores with YIG was about 30% vol.

Optical characteristics of the composed samples are first studied by means of the linear reflectance spectroscopy in the spectral range 500–1100 nm. For the nonlinear optical spectroscopy, the output of a nanosecond OPO laser system with the pulse duration of 4 ns, the peak energy of 1 MW/cm^2 in the spectral range of the fundamental wavelength from 700 to 1100 nm is used as the fundamental radiation. Fresnel rhombus and a Glan polarizer select the polarization of the fundamental and SHG waves, respectively. The SHG signal in the direction of specular reflection is detected by a PMT and a boxcar integrator. The magnetic field of 2 kOe is applied to the sample in the transversal geometry, i.e. in the plane of the sample and perpendicular to the plane of incidence.

Figure 1a shows the linear reflectance spectrum of YIG-impregnated opals measured for the angle of incidence of 10°. The spectrum reveals a peak centered approximately at 780 nm, which corresponds to the photonic bandgap in this sample.

The SHG spectrum measured for 20° angle of incidence reveals a sharp peak in the SHG intensity at $\sim$ 768 nm, which corresponds to the left PBG wing. An increase of the nonlinear-optical response at the edge of the PBG of a photonic crystal has been previously observed for one-dimensional porous silicon PC [4] and should be attributed to the fulfillment of the phase-matching conditions for the effective second harmonic generation. The phase-matching can be expected due to anomalous high dispersion of the photonic crystal in the vicinity of the PBG.

For the studies of the magnetic properties of opals infiltrated by YIG, the magnetic contrast in the SHG intensity is measured for the geometry of the transversal Kerr effect. In this case, odd with respect to the magnetization, M, changes in the SHG intensity are expected. As a measure of these changes, the SHG magnetic contrast, $\rho_{2\omega}$, is commonly introduced as $\rho_{2\omega} = (I(M\uparrow) - I(M\downarrow))/(I(M\uparrow) + I(M\downarrow))$, where $I(M\uparrow)$ and $I(M\downarrow)$ are the SHG intensities measured for the opposite directions of the applied magnetic field. The SHG magnetic contrast is measured for the wavelengths corresponding to the SHG spectral maximum and the corresponding data are presented in Fig. 1b. The observed SHG magnetic contrast is about 4.5% for YIG opals without impregnated Pt.

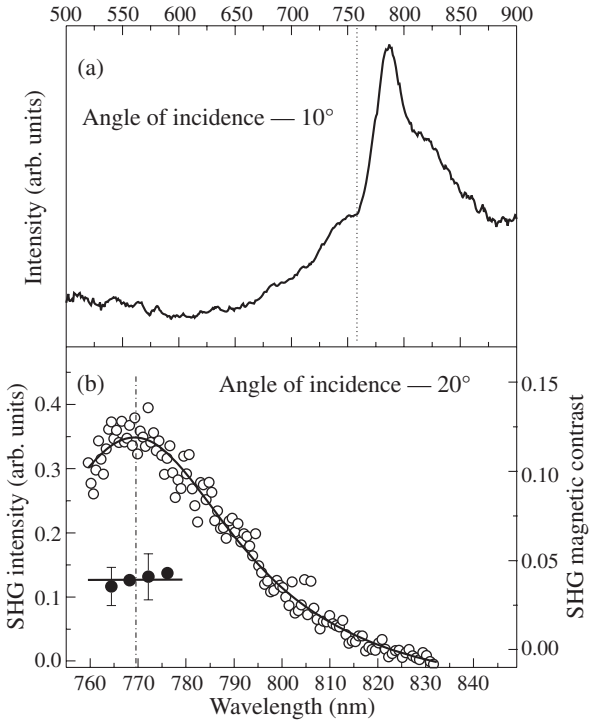

Fig. 1. Linear spectra (a) and the SHG spectra (b, open circles) of YIG-impregnated opals measured for the angle of incidence of 10° and 20°, respectively. The magnetic contrast of the SHG intensity is shown in Fig. 1b by solid circles.

Similar measurements were performed for opals with platinum, impregnated by YIG. The linear reflectance spectrum is observed nearly in the same spectral range. The SHG intensity in opals with Pt is greater than in opals without it.

The value of magnetic contrast in the SHG intensity obtained for the transversal nonlinear magneto-optical Kerr effect is about 7%. Larger values of both the SHG intensity at spectral edge of PBG, and of the SHG magnetic contrast are probably related to a better quality of the SiO_2-Pt-YIG interfaces as compared with the SiO_2-YIG sample as platinum prevents a chemical reaction between yttrium oxide and the silica opal matrix. It can be pointed out, that large values of nonlinear magneto-optical Kerr effect in SHG are by an order of magnitude larger as compared with the typical values of the linear magneto-optical Kerr effect.

2. Conclusion

The 3D magneto photonic crystals based on artificial opals infiltrated by yttrium iron-garnet are fabricated and their optical properties are studied by the linear spectroscopy and nonlinear second harmonic spectroscopy. Optical second harmonic generation technique is applied for the first time to study the nonlinear magneto-optical properties of YIG-infiltrated opals. The magnetic contrast of the SHG intensity of up to 7% is observed for the spectral edge of the photonic band gap of the composed magneto-photonic crystals.

Acknowledgements

This work is supported in part by the Russian Foundation for Basic Research Grants No. 04-02-16847, No. 04-02-17059, the Presidential Grant for Leading Russian Science Schools No. 1604.2003.2, INTAS Grants No. 03-51-3784, No. 04-83-3149 and EC-funded project PHOREMOST (FP6/2003/IST/2-511616).

References

[1] E. Yablonovitch, *Phys. Rev. Lett.*, **58**, 2059 (1987).
[2] A. Figotin, Y. A. Godin and I. Vitebskiy, *Phys. Rev. B.*, **57**, 2841 (1998).
[3] A. Figotin and I. Vitebskiy, *Phys. Rev. E*, **63**, 066609 (2001).
[4] T. V. Dolgova, A. I. Maidykovski, M. G. Martemyanov, A. A. Fedyanin, O. A. Aktsipetrov, G. Marowsky, V. A. Yakovlev, G. Mattei, N. Ohta and S. Nakabayashi, *J. Opt. Soc. Am. B.*, **19**, 2129 (2002).
[5] W. Stober, A. Fink and E. Bohn, *J. Colloid Interface Sci.*, **26**, 62 (1968).
[6] N. A. Feoktistov, V. G. Golubev, J. L. Hutchison, D. A. Kurduykov, A. B. Pevtsov, V. V. Ratnikov, J. Sloan and L. M. Sorokin, *Semicond. Sci. Technol.*, **16**, 955 (2001).

13th Int. Symp. "Nanostructures: Physics and Technology"
St Petersburg, Russia, June 20–25, 2005

Recovery dynamics of quantum-well saturable absorber

V. V. Nikolaev[1,2] and E. A. Avrutin[2]

[1] Ioffe Physico-Technical Institute, St Petersburg, Russia
[2] Department of Electronics, University of York, Heslington, York YO10 5DD, UK

Abstract. We propose a new numerically-efficient method for quantitative analysis of the recovery dynamics of a saturable absorber containing quantum wells, which we call the *delay-differential method*. The dynamical behavior of the main absorber parameters is analyzed and compared for two different material systems: GaAs/AlGaAs and InP/InGaAsP single-quantum well structures. The absorption saturation and recovery in single-pulse regime is modeled for different pulse energies, and the different factors leading to the recovery time increase are assessed. We model the passing of the pulse train through the saturable absorber and discuss the degradation of the absorber performance with the increase of the signal frequency.

Introduction

Semiconductor saturable absorbers currently attract increasing interest due to their use for optical pulse generation [1] as well as prospective application for all-optical signal processing. The recovery time of a saturable absorber (SA) is its major parameter which can potentially determine the dynamical range of the device or even the whole signal-processing network. The quantitative analysis of the SA recovery therefore is of major importance.

The absorption recovery is a result of a complex kinetic process, which leads to the transfer of optically-generated electrons and holes, initially confined in the quantum wells, out of the system. To describe this process theoretically, one has to employ suitable approximations. Currently, the most widely used theoretical method for the analysis of the dynamic processes in SA's combines the solution of the drift-diffusion equation with the assumption of thermal equilibrium at the heterointerfaces of the optical confinement layer (OCL) [2, 3]. This approach stems from similar methods for semiconductor amplifiers, and is well justified for the high excitation (as in the case for lasers) or for low enough biases. For significant biases (as in the case of saturable absorbers), this approach can ran into trouble, as this model can give large densities in the close vicinity (on the order of angstroms) of the OCL heterointerfaces, where the drift-diffusion approach is highly tenuous. Furthermore, for the large biases, the drift-diffusion method usually gives the large values of carrier density at the OCL heterointerfaces, which can lead to the overestimation of the current across the interface.

In this presentation, we propose a new theoretical approach, which is not restricted by the above-mentioned limitations, and, at the same time provides substantial enhancement of numerical efficiency, as compared to solving time-dependent drift-diffusion equation.

1. Method

We propose to calculate the carrier density at the hetorojunctions consistently with the assumption of quasi-equilibrium at the heterointerface, and, therefore, consistently with the current. We assume that the QWs are described by their own electron and hole quasi-Fermi levels. The main problem in this approach is to correctly describe the process of the transfer of the carriers after escaping QWs to the heterointerfaces. We propose to consider drift as the main mechanism of the carrier transfer and to ignore diffusion, which is justifiable for the fields of $\geq 10\,\mathrm{kV/cm}$ (including screening).

The main details of our approach are as follows. The electrons and holes in the absorber are described by 2-D densities, each of those, at a given time t, is divided into three parts, describing carriers confined in the QW ($n_{QW}(t)$ and $p_{QW}(t)$), the carriers at the heterointerfaces of the optical confinement layer (OCL) ($n_{OCL}(t)$ and $p_{OCL}(t)$) and the carriers drifting from the QW towards the heterointerfaces of the OCL ($n_{DR}(t)$ and $p_{DR}(t)$). Other dynamic variables are the energy densities of electrons and holes in the OCL, the values of the p- and n- impurity charges $Q^+(t)$ and $Q^-(t)$ (see Fig. 1), screening potentials $\phi_{DR}^{e/h}$ associated with the drifting electrons and holes, and the integrals of the effective drift velocities $Z^{e/h} = \int v_{dr}^{e(h)}\, dt$.

In our approach, these 14 dynamic variables are driven by a set of 14 coupled ODE rate equations with time-dependent parameters. These parameters are: the absorption coefficient, the five effective field parameters (fields applied to the QW on both sides, $F_{QW}^{e(h)}$, two fields applied to OCL heterobarrier, $F_{OCL}^{e(h)}$ and the effective field inside the QW, F_{QW}^{in}, see Fig. 1), the temperatures of electrons and holes at heterobarriers, and the four escape time parameters. As the processes of the carrier escape from QWs and across the OCL interfaces are the core of the problem, we use here the recently developed approach of calculation of escape times [4, 5], which is more accurate than commonly used methods.

Our approach allows us to investigate the contributions from

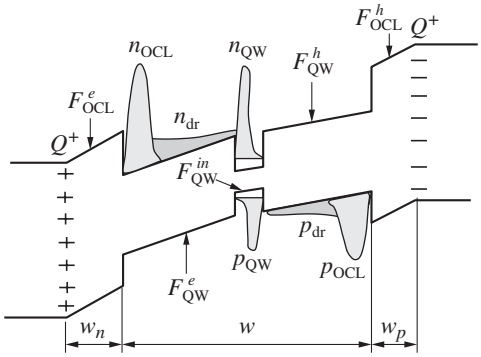

Fig. 1. Schematic representation of the single-quantum-well biased structure: band diagram, carrier-density, impurity-charge and effective-field parameters.

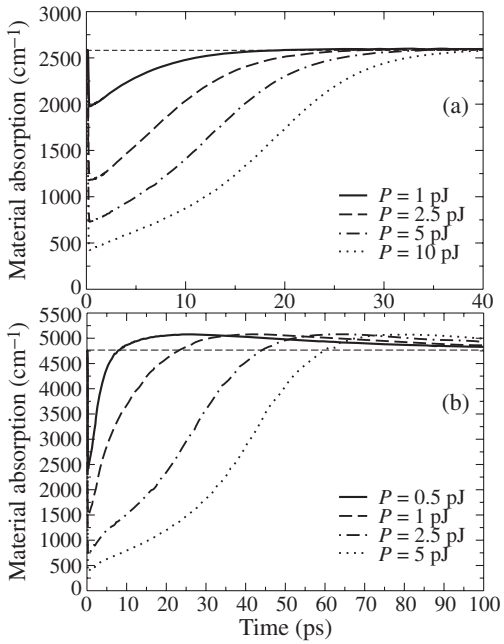

Fig. 2. Absorption recovery in the (a) GaAs/AlGaAs and (b) InP/InGaAsP structures for different pulse energies. Thin dashed lines denote the absorption in the unexcited structures.

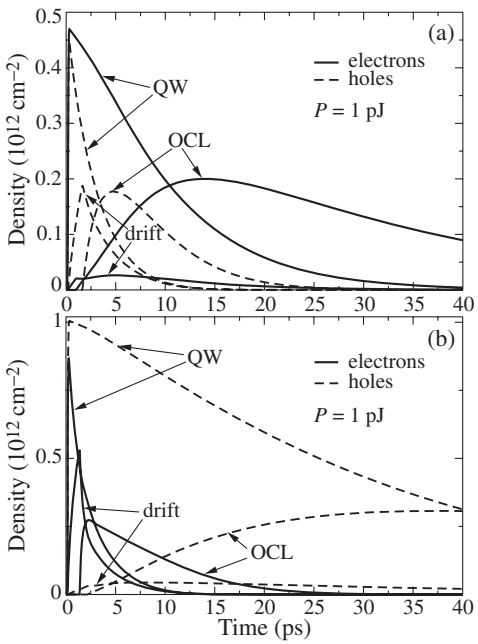

Fig. 3. Dynamics of the carrier-density parameters in the (a) GaAs/AlGaAs and (b) InP/InGaAsP structures excited by a 1-pJ pulse.

the main processes in the system (such as carrier escape, drift, heating by the electric field, and electric field screening by photo-generated carriers) separately.

2. Results and discussion

All the calculations are performed for the room temperature, and the applied electric bias is such that the internal field in the unexcited structures is 100 kV/cm. The Fig. 2 shows the calculated evolution of the QW absorption after the two structures were optically exited with a single short (FWHM of 100 fs) pulse. One can see that, together with the decrease of the minimal absorption value, both material systems feature substantial slowdown of the absorption recovery with the increase of the pulse energy. Furthermore, it is well seen for large pulse energies that the recovery dynamics is non-exponential.

For the InGaAsP structure, both tunneling and fermionic-escape factors lead to the fast electron escape, with the escape times much shorter than those for holes. This relation is the major reason for the occurrence of the "anomalous behavior" in absorption dynamics, Fig. 2. Indeed, as can bee seen from the Fig. 3, the decay of the QW hole density in the AlGaAs structure, although faster, takes place on the same time scale as the electron density decay. Quite oppositely, in the InGaAsP structure, electrons quickly escape the QW, leaving it charged with slowly escaping holes. This fast electron escape leads to sharp increase of the filling factor, facilitated by the small electron DOS, as compared to the hole one. At the same time, holes in the QW effectively screen the applied field, and the overlap integral decreases to its unexcited value with the slow hole escape time, τ^h_{QW}.

3. Conclusion

A new numerically efficient method of the calculation of the recovery time for the quantum-well saturable absorbers is developed. This method gives account for the carrier escape, drift, heating by the electric field, and electric field screening by photo-generated carriers. Calculation results for GaAs/AlGaAs and InP/InGaAsP single-quantum well structures are presented.

References

[1] E. A. Avrutin, J. H. Marsh and E. L. Portnoi, *IEE Proc. Optoelectron.*, **147**, 251 (2000).

[2] S. Højfeldt and J. Mørk, *IEEE J. Select. Topics Quantum Electron.*, **8**, 1265 (2002).

[3] A. V. Uskov, J. R. Karin, R. Nagarajan and J. E. Bowers, *IEEE J. Select. Topics Quantum Electron.*, **1**, 552 (1995).

[4] V. V. Nikolaev and E. A. Avrutin, *IEEE J. Quantum Electron.*, **39**, 1653 (2003).

[5] V. V. Nikolaev and E. A. Avrutin, *Phys. Rev. B*, **70**, 125319 (2004).

13th Int. Symp. "Nanostructures: Physics and Technology"
St Petersburg, Russia, June 20–25, 2005

Modification of spontaneous emission at the edge of photonic stop band in Bragg structures based on Er-doped amorphous silicon

A. B. Pevtsov[1], A. V. Sel'kin[1], N. A. Feoktistov[1], V. G. Golubev[1], D. R. Yakovlev[1,2] and M. Bayer[2]

[1] Ioffe Physico-Technical Institute, St Petersburg, Russia
[2] Fachbereich Physik, Universität Dortmund, 44221 Dortmund, Germany

Abstract. Both enhancement and inhibition of an erbium ion spontaneous emission near the photonic stop band edge in one-dimensional photonic crystal constituting a Bragg structure of 13 alternating quarter-wave layers of a-SiO_x:H and a-Si(Er):H have been found. From comparison of the transmittance and photoluminescence spectra the conclusion is made that the observed modification of photoluminescence intensity is originated from non-monotonic behavior of the optical mode density at the photonic stop band edge.

Introduction

It is well known that spontaneous emission depends strongly on surrounding environment through the density of optical states and local strength of the electromagnetic modes [1]. Photonic crystals are materials that are periodic on the photon wavelength scale. The most striking property of these materials is the existence of the photonic stop band, the energy range where photons cannot propagate in some direction inside the structure over a finite band of frequencies. Due to modification of the density of optical states in such structures it is possible to observe a number of quantum-electrodinamical phenomena such as enhancement or suppression of spontaneous emission, formation of cavity polariton branches, separated in energy by Raby splitting [2–4]. Studies of interaction effects of spatially-confined light with emitters introduced in the photonic crystals are promising for obtaining a new generation of optoelectronics devices [5, 6].

In the present work, we investigate the change in the intensity of spontaneous emission near the edge of photonic stop band due to the placement of emitting erbium-centers within a finite one-dimensional photonic crystal based on alternating quarter-wave amorphous silicon/amorphous silica layers.

1. Samples

The Bragg structures were fabricated by plasma-enhanced chemical vapor deposition technique [7]. The a-Si:H layers were deposited from 10% silane-argon mixture. Up to 10% of oxygen were added to the gas mixture to form a-SiO_x:H films. The average deposition rate was less than 0.2 nm/s. Erbium ions were introduced into a-Si:H films by magnetron sputtering of an erbium target which was placed in a technological reactor out of RF glow discharge. In-situ interferometric monitoring was fulfilled to control the layer thickness, deposition rate and optical characteristics of the structure. A slight thickness variation in the structure along lateral plane was used for fine tuning the photonic stop band edge around the spectral position of the 1.54 μm Er-emission peak. One of the structures consisting of 13 alternative layers is schematically shown in Fig. 1a. Here, λ is the light wavelength in vacuum, $n_a = 1.46$ is the refraction index of a-SiO_x:H layers $n_b = 3.46$ is the refraction index of a-Si:H layers. The optical parameters were calculated directly from the interferometric spectra during the growth of the structure. The reflection and emission spectra were investigated by diffraction grating monochromator equipped with

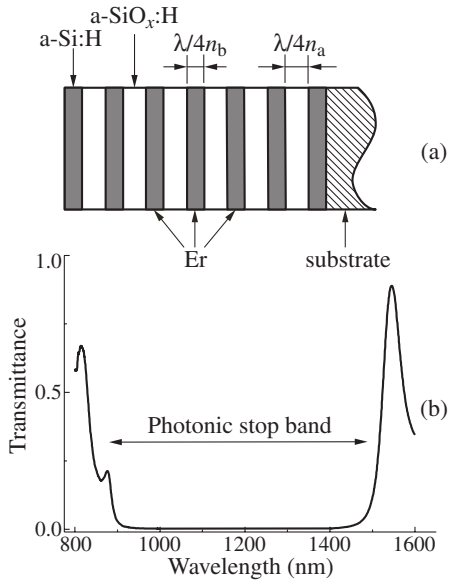

Fig. 1. a) Bragg structure composed of 13 quarter-wave alternating a-Si:H/a-SiO_x:H layers. Three central layers of a-Si:H were doped with erbium. b) The transmittance spectrum of the fabricated Bragg structure (one-dimensional photonic crystal) in wide wavelength range.

InGaAs photodiode. The photoluminescence spectra were excited by 640 nm line of a dye laser.

2. Experimental and discussion

As stated above, in the fabricated Bragg structures the high-refractive index layers (a-Si:H) were doped with erbium. According to the electromagnetic variational theorem [8], for modes in the lower energy photonic band, the power of modes is concentrated primarily in the high-refractive index regions. Therefore, to increase the light-matter coupling, the parameters of the structure were chosen so that the lower energy photonic band edge was tuned to the 1.5 μm spectral range corresponding to the frequency of the Er-ion main transition. The experimental transmittance spectrum of the a-Si:H/a-SiO_x:H Bragg structure is shown in Fig. 1b.

To demonstrate the effect of the photonic stop band edge on the Er spontaneous emission we measured carefully both the luminescence and transmittance spectra from the same point (area of about 100 μm^2) on the lateral face of the structure. Because of thickness variation of the structure along the lateral

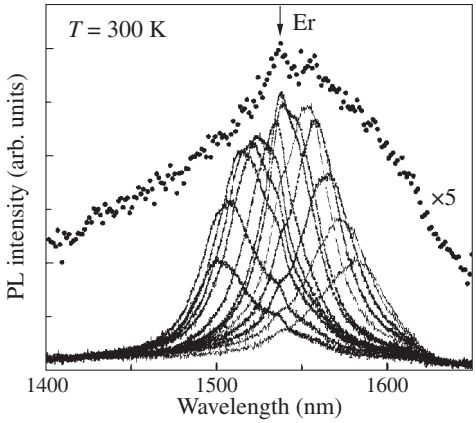

Fig. 2. Photoluminescence spectra of the a-Si:H/a-SiO_x:H Bragg structure at various position of the long-wave photonic stop band edge with respect to Er-emission peak (marked by vertical arrow) and Er photoluminescence spectrum from the cross-cut cleavage of the Bragg structure (dots, x5).

directions the different points under detection correspond to different spectral positions of the photonic stop band edge. In Fig. 2, the luminescence spectra measured from different points on the sample surface are depicted. It is seen that with shifting the photonic stop band edge the photoluminescence intensity increases at first, then passes over maximum and decreases. For comparison, the Er-photoluminescence spectrum taken from the cross-cut cleavage of the Bragg structure is shown (dots). This spectrum represents a rather wide contour with the spectral width determined by inhomogeneous broadening in the system of emitting Er centers incorporated in a-Si:H. Our results show a strong enhancement of the Er-emission intensity owing to the photonic stop band edge effect.

In Fig. 3, one of the luminescence spectrum from Fig. 2 is depicted together with the corresponding transmittance recorded at the long-wave photonic stop band edge. It is important to note that the luminescence peak intensity is remarkably shifted to the short wave side relative to the transmittance maximum. On the other hand, as shown elsewhere [7], the shape of luminescence spectrum due to Er-emission through a microcavity eigenmode coincides well with that of transmittance for the case when the conditions of weak coupling between an emitting center and electromagnetic field are fulfilled and the radiative lifetime of the center in an exited state is slowly depends on frequency within emission line contour. So, Fig. 3 clearly indicates that at least one of the above conditions breaks down near the photonic stop band edge.

This fact is expectable from qualitative considerations based on the density of states (DOS) behavior near the photonic stop band edge. Indeed, due to pronounced DOS increasing very strong decrease in the radiative lifetime should take place and this time should reach its minimum value immediately at the photonic stop band edge. As seen from Fig. 3, the luminescence intensity peak observed in our experiment is located close to the frequency where the short-wave shoulder transmittance demonstrates the contrary flexure point. It is the point that approximately corresponds to the photonic stop band edge.

In conclusion, a strong modification of spontaneous emission at the edge of photonic stop band has been demonstrated by direct comparison of luminescence and transmittance spectra of Er-doped amorphous silicon based Bragg structures.

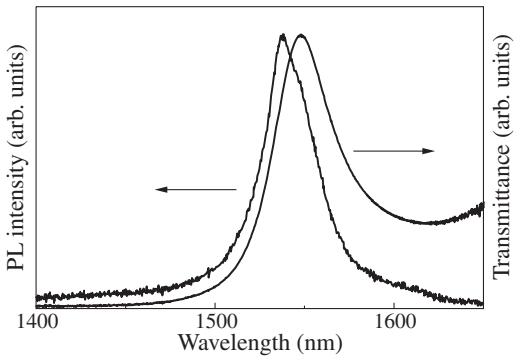

Fig. 3. Photoluminescence spectra of the a-Si:H/a-SiO_x:H Bragg structure as compared to the corresponding transmittance spectrum.

Acknowledgement

This work was partly supported by the MES program "Physics of Solid State Nanostructures", the RAS Program "Low-dimensional quantum structures", by the Deutsche Forschungsgemainschaft through Grant 436 RUS 17/115/02, by NATO Grant PST CLG 980399, and by contract PHOREMOST (FP6/2003/IST-2-511616).

References

[1] E. M. Purcell, *Phys. Rev.*, **69**, 681 (1946).
[2] M. Skolnick, T. A. Fisher and D. M. Whittaker, *Semicond. Sci. Technol.*, **13**, 645 (1998).
[3] C. Weisbuch, H. Benisty, R. Houdre, *Journal of Luminescence*, **85**, 271, (2000).
[4] M. Bayer, A. Forchel, Th. L. Reinecke, P. A. Knipp and S. Rudin, *phys. stat. sol. (a)*, **1**, 3 (2002).
[5] V. I. Kopp *et al*, *Opt. Lett.*, **23** 1707 (1998).
[6] J. Kalkman *et al*, *J. Appl. Phys.*, **96**, 2297 (2004).
[7] D. A. Dukin *et al*, *Appl.Phys.Lett*, **77**, 3009 (2000).
[8] J. D. Joannopoulos, R. D. Meade and J. N. Winn, *Photonic Crystals. Molding the Flow of the Light* Princeton, NY: Princeton University Press (1995).

13th Int. Symp. "Nanostructures: Physics and Technology"
St Petersburg, Russia, June 20–25, 2005

Bragg reflection spectroscopy of photonic crystals with high dielectric contrast

A. V. Sel'kin[1], A. G. Bazhenova[1], Yu. A. Pashkov[1], A. Yu. Bilibin[2], A. Yu. Menshikova[3] and N. N. Shevchenko[2]

[1] Ioffe Physico-Technical Institute, St Petersburg, Russia
[2] St Petersburg State University, Institute of Chemistry, St Petersburg, Russia
[3] Institute of Macromolecular Compounds of Russian Academy of Sciences, St Petersburg, Russia

Abstract. A new approach to analyzing Bragg diffraction spectra of photonic crystals (PhC) is proposed around which effective methods of structural characterization of opal-like PhCs are developed. Within the Bloch mode formalism, a physically clear picture is given which describes Bragg reflection spectrum formation in the case of 3D PhC. Optical reflectance spectra of polymer opal-like PhCs synthesized from mono-disperse polystyrene spheres are measured. The experimental spectra are obtained for polarized light at different angles of incidence and are well simulated in the theoretical calculations. New structural invariants are found which relate to each other multiple Bragg diffraction spectral features and angles of incidence.

Introduction

For more then ten years, the new class of spatially periodic solid state structures, the so called photonic crystals (PhCs), have been the subject of intense international research efforts [1]. More specific property of PhC is a periodically varying dielectric function $\varepsilon(\mathbf{r})$, the periodicity being of the same order of magnitude as the wavelength of electromagnetic radiation. This allows the control of the propagation of light, in particular, the creation of the photonic band gaps (PBGs), ranges of frequencies where such propagation is not permitted for certain or even for all directions [2, 3].

In this work, for the first time, the results of comprehensive experimental and theoretical studies are presented concerning the Bragg diffraction of light in 3D PhCs with fcc crystal structures. Considerable attention is given to the study of resonant, in PBG ranges, Bragg reflection spectra which are due to light scattering on two, non-parallel to each other, sets of crystal planes from the {111} family, e.g. on the lateral (111) and oblique $(\bar{1}11)$ planes.

1. Samples

As model experimental objects, we used thick (~ 0.1 mm) films of opaline PhC synthesized from mono-disperse polystyrene spheres [4]. For optical studies we chose the samples of a high structural quality, preliminary control of which was performed with the scanning electron microscopy (SEM). From micrographs obtained with SEM, spatial orientations of the sample were identified relative to the main crystallographic directions and the lattice constants for the lateral (growth) planes (111) were determined.

2. Experimental

Fig. 1 shows typical Bragg reflection spectra for one of the PhC samples investigated. The spectra were recorded for s-polarized light in the experimental geometry with the (111) plane being parallel to the reflecting surface of the sample. The wave vectors of incident and reflected light lay in the Γ-K-L-U plane of the first Brillouin zone of a *fcc* lattice. At rather low angles of incidence, $\theta \lesssim 45^\circ$, the Bragg reflection spectra are mainly due to diffraction of light on the (111) crystal planes.

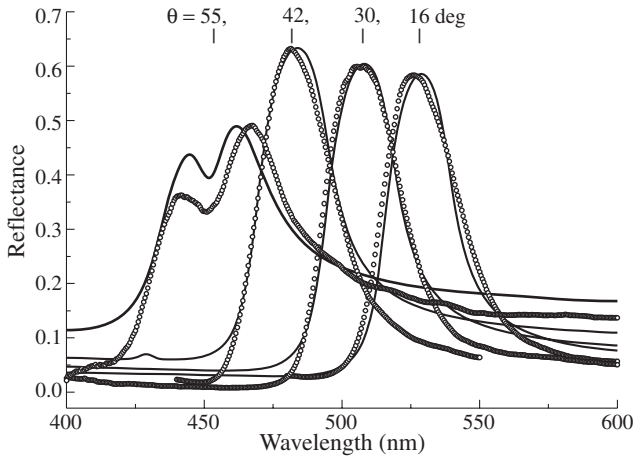

Fig. 1. Bragg reflection spectra of the polystyrene opaline photonic crystal at different angles of incidence θ, indicated in figure, for s-polarized light. Solid lines are calculated in the framework of the three-band mixing formalism for Bloch states, the open circles represent experimental data.

The doublet structure appearance at high angles of incidence can be ascribed to the effect of the multiple [5–7] Bragg diffraction of light on two or more sets of the crystal planes differing from each other in the Miller indices *hkl*. In the geometry of the experiment chosen by us, only two sets of the intersecting crystal planes, (111) and $(\bar{1}11)$, are responsible for the effect in the vicinity of the angle of incidence $\theta \approx 55^\circ$. In Fig. 2, wavelengths of the reflectance maxima (black triangles) and the deep (open circles) between them are plotted against the angle of incidence.

3. Theoretical

In order to clarify the physical mechanisms underlying the phenomena observed and describe the measured Bragg diffraction spectra qualitatively we utilized the basic idea of Ref. [8] when carrying out the appropriate theoretical analysis. This analysis is based on the Bloch mode formalism and uses the three band mixing approximation. The three bands of interest are determined by three reciprocal-lattice vectors $\mathbf{G}_{hkl} = \mathbf{G}_{000}$, $\mathbf{G}_{111}$ and $\mathbf{G}_{\bar{1}11}$ with the relevant indices *hkl*.

According to the model [8] an opaline PhC consists of spheroidal interpenetrating particles with the axes of rotational symmetry directed along the normal to the crystal surface. The aspect ratio of spheroids is η and can be considered as some anisotropic shrinkage coefficient of PhC, oblate spheroids being characterized by $\eta < 1$. The interpenetration of spheroids corresponds to their sintering and is assumed to reduce uniformly all the spheroid centre to centre distances by a factor $(1 - \chi)$ where χ is the sintering coefficient. As a result, the distance between the centres of nearest-neighbors spheroids placed in the lateral plane becomes equal to a_{00}, and the filling fraction, f, for spheroids is expressed in terms of χ (see [8]).

Dielectric properties of spheroids ("atoms") and background are involved in the corresponding dielectric constants ε_a and ε_b. Besides, an imaginary part, $i\varepsilon_0''$, was added to the average dielectric constant $\varepsilon_0 = f\varepsilon_a + (1 - f)\varepsilon_b$ in order to account for extinction effects due to additional scattering of light and absorption.

4. Discussion

Essentially new information of PhC structure can be obtained from an analysis of the curves depicted in Fig. 2. On the one hand, spectral location, λ, of the Bragg reflection maxima at the angles of incidence, $\theta < 45^\circ$, where the doublet structure does not appear, is well fitted by the familiar Bragg formula (the solid line 1 in Fig. 2). On the other hand, the wavelength, λ, of the reflectance deep as a function of the angle θ within the PBG is given by the solid line 2 (the relevant formula was derived in Ref. [8]). The intersection point (λ_*, θ_*) of the lines 1 and 2 in Fig. 2 obeys the relationship:

$$\frac{a_{oo}}{\lambda_*} \sin\theta_* = \frac{4\eta^2 - 1}{4\eta^2\sqrt{3}}\,, \qquad (1)$$

which represents a structural invariant relating to each other the lateral period a_{00} and the coefficient of anisotropy η.

From comparison of the computational results and experimental data presented in Figs. 1 and 2, we have found the values of structural parameters being characteristic of the investigated PhC sample. When fitting theoretical parameters we fixed the values $\varepsilon_a = 2.522$ for polystyrene and $\varepsilon_b = 1$ for background (air). Other parameters were variable. As determined from the theoretical fit, the centre to centre distance, a_{00}, in the lateral crystal plane (111) was found to be equal to 229.5 nm. This value is in good agreement with the data of SEM. The filling fraction for spheroids takes the value $f = 0.854$ ($> \pi/(3\sqrt{2}) \approx 0.74$ given for point-touched spheroids), suggesting that there exists a strong inter-particle sintering. As to the anisotropic shrinkage coefficient η, it equals 0.942, i.e. rather strong anisotropic deformation along the [111] direction takes also place for the sample under study. The shapes of the Bragg reflection spectral bands are well reproduced in the theory at $\varepsilon_0'' \approx 0.04$.

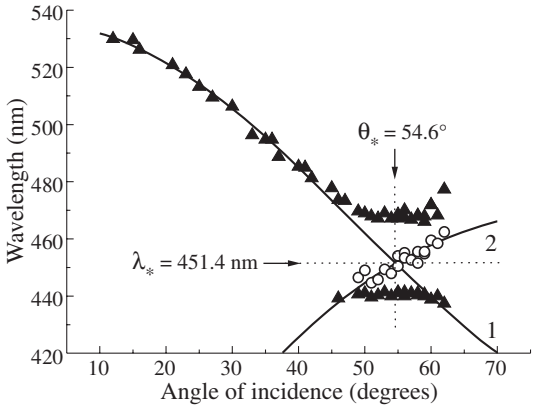

Fig. 2. Wavelengths of the reflectance maxima (black triangles) and the deep (open circles) between them against the angle of incidence θ for polystyrene opaline photonic crystal. Solid lines are fitted to the experimental data using the Bragg diffraction low (curve 1) and the formula (3) from Ref. [8] (curve 2).

It is noteworthy that in our calculations we used the Fourier coefficients ε_{hkl} of $\varepsilon(\mathbf{r})$ in Fourier series summed over reciprocal lattice vectors $\mathbf{G}_{hkl}$. These coefficients, governing widths of the Bragg peaks, were directly computed with an allowance of sintering effects. For the sample investigated, the values $\varepsilon_{000} \equiv \varepsilon_0 = 2.3$, $|\varepsilon_{\bar{1}11}| \approx |\varepsilon_{111}| = 0.1$ and $|\varepsilon_{200}| \approx 0.006$ have been found. Smallness of the coefficient $|\varepsilon_{200}|$ as compared with ε_0 and $|\varepsilon_{111}|$ allows us to take into account for the low-frequency modes relevant to us only two distinct sets of $\mathbf{G}_{hkl}$ with $\{hkl\} = \{000\}$ and $\{hkl\} = \{111\}$.

In conclusion, we draw attention to the fact that the multiple Bragg diffraction phenomenon discussed in this paper is due to spatial finiteness of a PhC and follows from breakdown of the Bragg conditions required for the stop-band formation. In such a situation, Bloch modes associated with both (111) and $(\bar{1}11)$ crystal planes propagate, and transfer energy, throughout the PhC at frequencies within the stop-band. The frequencies depend on the angles of incidence of light and appear as deeps in Bragg reflection spectra.

Acknowledgements

The work was supported by the Russian Foundation for Basic Research under Grants 05-02-17776 and 04-03-33080, by the contract IST-2-511616-PHOREMOST and the RAS Scientific Program "Nanostructures in polymer systems perspective for optoelectronics".

References

[1] C. López, *Adv. Matter.*, **15**, 1679 (2003).
[2] E. Yablonovich, *Phys. Rev. Lett.*, **58**, 2059 (1987).
[3] S. John, *Phys. Rev. Lett.*, **58**, 2486 (1987).
[4] A. Yu. Menshikova, B. M. Shabsels, T. G. Evseeva, N. N. Shevchenko and A. Yu. Bilibin, *Zh. priklad. chem.*, **78**, 161 (2005).
[5] H. M. van Driel, W. L. Vos, *Phys. Rev. B*, **62**, 9872 (2000).
[6] S. G. Romanov, T. Maka, C. M. Sotomayor Torres, M. Müller, R. Zentel, D. Cassagne, J. Manzanares-Martinez and C. Jouanin, *Phys. Rev. E*, **63**, 056603 (2001).
[7] G. Gajiev, V. G. Golubev, D. A. Kurdyukov, A. B. Pevtsov, A. V. Sel'kin and V. V. Travnikov, *Phys. stat. sol. (b)*, **231**, R7 (2002).
[8] A. V. Sel'kin, *Proc. of 12th Symp. "Nanostructures: Physics and Technology" (St Petersburg, Russia, 2004)*, Ioffe Istitute, 111 (2004).

13th Int. Symp. "Nanostructures: Physics and Technology"
St Petersburg, Russia, June 20–25, 2005

Second-and third-harmonic generation in birefringent silicon photonic crystals and microcavities

I. V. Soboleva, E. M. Murchikova, A. A. Fedyanin and O. A. Aktsipetrov
Department of Physics, Moscow State University, 119992 Moscow, Russia

Abstract. One-dimensional anisotropic photonic crystals and microcavities based on birefringent porous silicon are fabricated. The spectra of linear reflectance demonstrate the presence of photonic band gap and microcavity modes with spectral positions tunable upon the sample rotation around its normal and/or incident light polarization plane rotation. Simultaneous enhancement of second-and third-harmonic generation at the photonic band gap edge due to the phase matching is observed. The angular positions of the second-and third-harmonic peaks are controllable via the anisotropy of the refractive indexes of porous silicon layers.

Introduction

One of the issues regarding the possible application of photonic crystals in optoelectronics and intergrated optics is the fabrication of silicon-based microstructures possessing photonic band gap (PBG). Apart of intensive studies of linear optical properties of silicon photonic crystals, this generates much interest to their nonlinear properties as well [1]. For example, ultrafast tuning of the band edge of silicon photonic crystals due to the third-order optical susceptibility has been observed recently. The efficient up-conversion, such as second-and third-harmonic generation, has been also demonstrated as a result of the enhancement of photonic density of states and giant dispersion at the PBG edge. The effective fulfillment of the phase-matching conditions obtained as the fundamental radiation is tuned across the long-wavelength PBG edge leads to the manyfold increase of the second-harmonic (SH) and third-harmonic (TH) intensities [2]. Birefringence, which is directly attributed to the optical anisotropy of the medium, can also effectively control the gain of the up-conversion effects using the different dispersion properties of ordinary and extraordinary waves. The fabrication of silicon photonic crystals possessing birefringence can open up new prospectives to applications for integrated optics and on-chip devices of nonlinear photonics requiring the controllable manipulation of the up-conversion efficiency. Silicon crystal anisotropy is quite small due to cubic lattice structure, but porous modification of silicon can exhibit a strong in-plane anisotropy of the refractive index. The form anisotropy is achieved during etching of the (110) silicon wafers and introduced by the selective crystallographic pore orientation in equivalent [010] and [100] directions [3].

In this paper one-dimensional silicon photonic crystals Bragg reflectors, microcavities, are fabricated from the birefringent porous silicon. The presence of a single optical axis oriented along the [001] direction is shown. The spectral shifts of the PBG and the microcavity modes are observed for variation of the mutual orientation of the optical axis and the wave polarization. The simultaneous SH and TH enhancement is observed if the fundamental radiation is tuned across the long-wavelength PBG edge. The angular positions of the SH and TH peaks and the maximal intensity enhancement are shown to be controllable via the artificial birefrengence of the porous silicon layers.

Samples

Samples of anisotropic photonic crystals and microcavities are fabricated by electrochemical etching of heavily doped p^+-type silicon wafers of 50 mΩ cm resistance with (110) surface orientation in 22% HF aqueous solution with ethanol [4]. Porous silicon layers of different porosity and optical thickness are obtained by the variation of the current density and the etching time. Refractive indexes of the porous layers are determined from the linear reflectance spectroscopy of the single porous silicon layers. Photonic crystals consist of 24 pairs of quarter-wavelength-thick porous silicon layers with refractive indexes of $n_1 = 1.81$ and $n_2 = 2.17$, respectively, and optical thickness of $n_{1,2}d_{1,2} = 215$ nm. Microcavities are made of two Braggs reflectors of 12 pairs porous silicon layers separated by one microcavity spacer of doubled thickness λ_{MC}. Refractive index anisotropy for porous layers used is determined to be $\Delta n_1 = 0.03$ and $\Delta n_2 = 0.04$, respectively.

Results and discussion

Birefringence of photonic crystals appears in the dependence of the reflectance on the mutual orientation of the electric-field vector and the main plane formed by the wavevector and the optical axis of photonic crystal. Therefore, it can be probed by rotation of the wave polarization vector with fixed position of the main plane or the changing of the main plane orientation keeping fixed the light polarization. Figure 1(a) shows the reflectance spectra of porous silicon micro-cavity with $\lambda_{MC} = 860$ nm, where λ_{MC} denotes the spectral position of the microcavity mode at the normal incidence.

Spectra are measured for two values of the azimuthal angle ψ between the optical axis and the plane of incidence with $\psi = 0^\circ$ corresponding to the coincidence of the incident and $(1\bar{1}0)$ planes. The spectra reach reflectance up to 0.9 in the range from 770 to 840 nm corresponded to the PBG and dips near the 840 nm related to microcavity modes. The spectra show shifts of the PBG and microcavity mode spectral positions in accordance to sample azimuthal position change. The maximal shift is about 10 nm. The same shift is obtained reflectance spectra the porous silicon photonic crystal presented in the inset of Fig. 1(a). This indicates that anisotropic photonic crystals and microcavities can be considered as uniaxial negative birefringent crystals with optical axis along the [001] direction in the (110) plane. The refractive indexes of porous silicon layers are estimated to be $n_o = 2.21$, $n_e = 2.17$ and

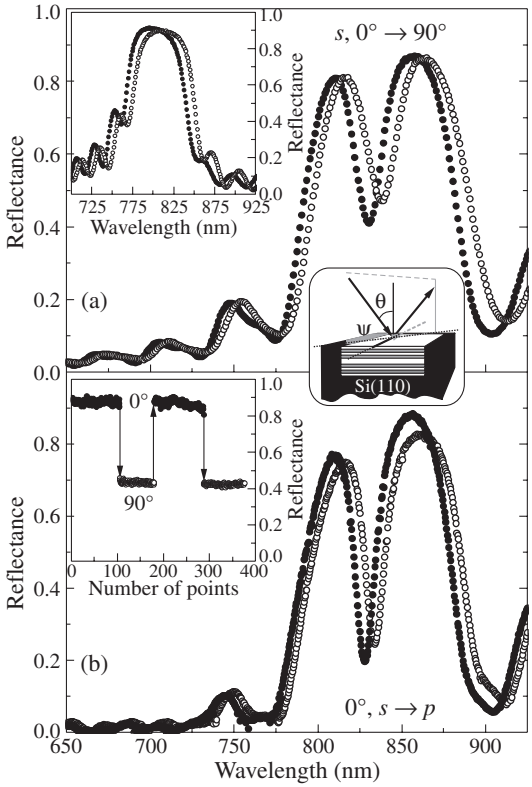

Fig. 1. (a) The spectra of the linear reflectance of the s-polarized light from the anisotropic microcavity measured for $\psi = 0^\circ$ (filled circles) and $\psi = 90^\circ$ (open circles). (b) The spectra of the linear reflectance of the s-(open circles) and p-polarized (filled circles) light from the anisotropic microcavity measured for $\psi = 90^\circ$. Angle of incidence is $\theta = 20^\circ$. Inset. The spectra of linear reflectance of s-polarized light from the anisotropic Bragg reflector measured for $\psi = 0^\circ$ (filled circles) and $\psi = 90^\circ$ (open circles).

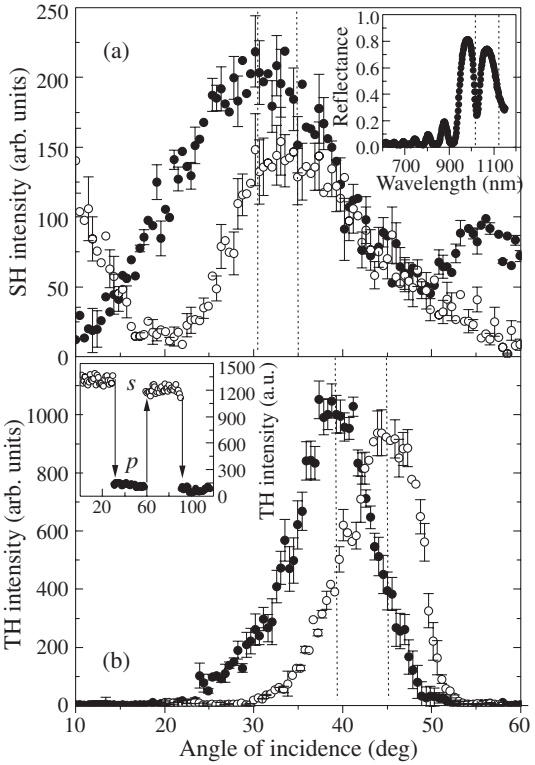

Fig. 2. (a) The SH intensity angular spectra of microcavity with $\lambda_{MC} = 1100$ nm for the s-(open circles) and p-polarized (filled circles) fundamental wave. Arrow emphasize the angular shift of the TH maxima. Inset. The linear spectrum of this microcavity. Band shows the part of the spectrum corresponding to the angular tuning range. (b). The TH intensity angular spectra of this microcavity for the s-(open circles) and p-polarized (filled circles) fundamental wave. Inset. The contrast of the TH magnitude measured for s-and p-polarized fundamental wave, $\theta = 43^\circ$, $\psi = 0^\circ$.

$n_o = 1.84$, $n_e = 1.81$ for low and high porosity layers, respectively. Figure 1(b) shows modification of the microcavity reflectance spectrum upon rotation of the light polarization. The spectral shifts of the PBG and mode is approximately the same as obtained for the sample azimuthal rotation.

The output of the YAG:Nd^{3+} laser with the wavelength of 1064 nm is used as the fundamental wavelength for wave vector domain SH and TH spectroscopy. The pulse duration is of the 10 ns with energy of 6 mJ per pulse and spot diameter of 1 mm.

Figures 2(a) and 2(b) shows the angular spectra of second-harmonic and third-harmonic intensity, respectively. The enhancement second-harmonic and third-harmonic generation is achieved at the microcavity PBG long-wavelength edge due to fulfillment of phase matching condition. The SH and TH intensity is enhanced by about 10^2 and 10^3 times, respectively, in comparison with that outside of the PBG. The SH angular spectra have two wide peaks at $\theta = 32^\circ$ shifted for 3° one from another for various polarizations of the fundamental wave. The TH spectra have peaks at $\theta = 38^\circ$ and $\theta = 44^\circ$. At the linear spectra the long-wavelength microcavity band gap edge [inset of the Fig. 2(a)] lies in the measured angular range. Thus, the obtained SH and TH enhancement results from the phase-matching confinement achieved at the band gap edge. But since the refractive indexes of the layers depends on the polarization of the fundamental light due to the in-plane anisotropy peaks are found to be shifted for different wave polarization. Besides, the different angular positions of SH and TH peaks are associated with different phase mismatch value. The largest contrast in the TH intensity of spectra is shown at the inset of Fig. 2(b). The contrast between s-in and p-in TH is measured. The 10 times changes of the TH intensity are attained for switch of fundamental wave from ordinary to extraordinary one due to anisotropy of the dielectric functions of porous silicon layers.

References

[1] K. Sakoda, *Optical Properties of Photonic Crystals*, Springer, 2001.
[2] M. Scalora *et al*, *Phys. Rev A* **56**, 3166 (1997).
[3] N. Kunzner *et al*, *Opt. Lett.* **26**, 1265 (2001).
[4] L. Pavesi, *Riv. Nuovo Cimento* **20**, 1 (1997).

13th Int. Symp. "Nanostructures: Physics and Technology"
St Petersburg, Russia, June 20–25, 2005

Thermo-optical effect in Si-liquid crystal photonic bandgap structures

V. A. Tolmachev[1,2], T. S. Perova[2], E. V. Astrova[1], J. A. Pilyugina[1] and R. A. Moore[2]

[1] Ioffe Physico-Technical Institute, St Petersburg, Russia
[2] Department of Electronic and Electrical Engineering, University of Dublin, Trinity College, Dublin 2, Ireland

Abstract. Periodically grooved silicon matrices and based on the above composite structures arising from the infiltration with liquid crystal (LC) E7 were fabricated using wet anisotropic etching of (110) Si. The calculated reflection spectra are in a good agreement with experimental data obtained with an FTIR spectrometer in conjunction with an IR microscope. A shift of the photonic bandgap edges by a factor $\Delta\lambda/\lambda = 2.5 - 3\%$ has been obtained as a result of the thermo-optical effect in LC.

Introduction

Silicon-based photonic bandgap (PBG) structures have received much attention in the research community as an established technology for fabricating high-performance optical elements [1-5]. Fabricating the structures on a silicon substrate provides the advantage of easier integration with current semiconductor processing technology. It has been shown recently [6, 7] that a periodic array of silicon stripes and air spaces (so called grooved Si) fabricated by wet anisotropic etching on (110) oriented Si wafers can serve as a one-dimensional (1D) photonic crystal (PC). Depending on the lattice constant, A, grooved Si structures possess a main photonic bandgap in the region of $\sim 10{-}30\,\mu$m and a number of secondary bandgaps extended to the near infrared range of the spectrum. Composite materials with optical properties different to the original matrix can be more easily obtained by infiltrating the grooves with liquid crystal. The optical properties of such composites can be tuned by altering the refractive index of the liquid crystal by any means. The purpose of this work was to design and fabricate a number of periodic grooved Si structures and to demonstrate the tuning of their optical properties by means of the thermo-optical effect.

1. Experimental

To simplify the task we started with simulation of a suitable matrix for demonstration of the thermo-optical effect. In order to reduce the influence of thickness non-uniformity and possible defects, in such a structure, on the optical properties, the minimal number of lattice periods, $m = 2$, has been chosen. Therefore the constructed 1D PC has a structure with five layers, Si-LC-Si-LC-Si. The reflection/ transmission spectra were calculated using 2×2 characteristic matrix method [8]. The following parameters of an empty matrix were used for calculation: $D_{\mathrm{Si}} = 1.2\,\mu$m; $D_{\mathrm{space}} = 1.6\,\mu$m; $A = 2.8\,\mu$m, $n_{\mathrm{Si}} = 3.42$ and $n_{\mathrm{space}} = 1$. It is well known that the reflection/transmission spectrum of a composite structure depends on the refractive index of the compound infiltrated into the grooves and on the type of incident light polarization. Therefore, after infiltration of the structure with the liquid crystal the refractive index of air, n_{space}, will be consequently changed to the ordinary, $n_0 = 1.49$, extraordinary, $n_{\mathrm{e}} = 1.69$, or isotropic, $n_{\mathrm{i}} = 1.54$, refractive indexes of liquid crystal depending on the type of alignment and the state of the phase [9].

From our previous investigation we have found that the homogeneous planar alignment, as shown in Fig. 1a, will normally be obtained during infiltration of the grooves [6,7]. Fig. 2 shows the calculated reflection spectra of a 1D PC composite

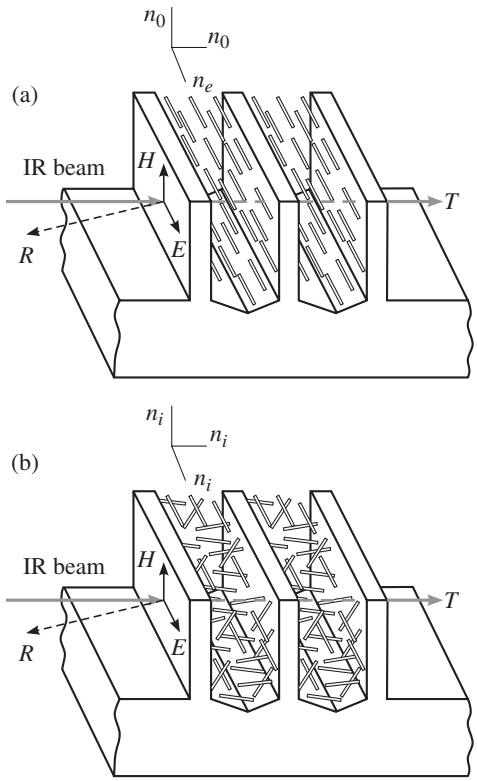

Fig. 1. The (a) homogeneous planar and (b) isotropic alignment of long molecular axis of liquid crystal molecules with respect to the Si walls in 1D composite photonic crystal.

structure corresponding to two orthogonally polarized beams of light, H and E (see Fig. 1a and b), at room temperature (LC in nematic phase) and at 70 °C (LC in isotropic phase). As can be seen from Fig. 2 the maximal change in the refractive index, from n_0 to n_{e}, results in a shift of the bandgap edge by $\Delta\lambda = 0.5\,\mu$m, while the thermooptical effect (thermo-tuning) leads to a shift, $\Delta\lambda$, of 0.4 μm. Fig. 3 shows the experimental reflection spectra in E-polarisation for the above-mentioned structure at room temperature and at $T = 70\,^{\circ}$C. The experimental result obtained for $\Delta\lambda$ in the main bandgap is 0.25 μm. We believe that the deviation of the experimental shift from the calculated one, $\Delta\lambda = 0.4\,\mu$m, is due to deformation of the edge of the interference band (see Fig. 3). However, we note that the results of the refractive index fitting are in a good agreement with the known values for n_0, n_{e} and n_{i} [9].

Acknowledgements

This work has been supported by Science Foundation Ireland Basic Research Program (Grant 04/BR/P0698) and Russian

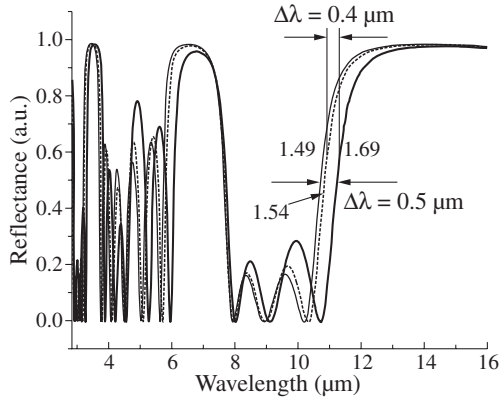

Fig. 2. Calculated reflection spectra of Si-LC composite photonic crystal with number of periods $m = 2$ and shift of the bandgap edge as a result of the thermo-optical effect ($\Delta\lambda = 0.4\,\mu$m) shown for E polarisation. The figures beside the curves show the corresponding refractive index value.

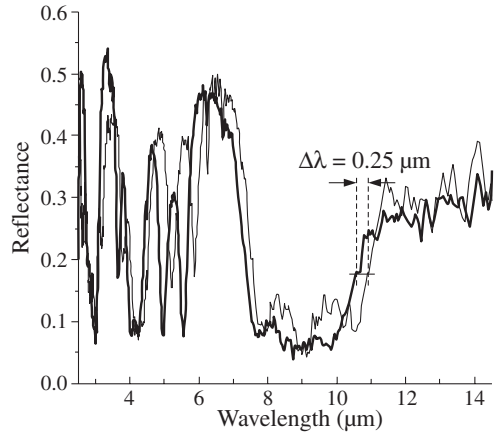

Fig. 3. Experimental reflection spectra of a Si-LC photonic crystal measured for E-polarised light at temperatures $T = 23\,^{\circ}$C (thin line) and $T = 70\,^{\circ}$C (solid line).

Programs “Physics of Solid-State Nanostructures”, Laser Physics and Scientific school –758.2003.2.

References

[1] A. Birner, R. B. Wehrspohn, U. M. Gõsele, K. Busch, *Adv. Mater.* **13**, 377 (2001).
[2] S.-S. Yun and J.-H. Lee, *J. Micromesh. Microeng.* **13**, 721 (2003).
[3] S. M. Weiss, P. M. Fauchet, *Phys. Stat. Sol.* **A197**, 556 (2003).
[4] G. Pucker, A. Mezzetti, M. Crivellari, P. Belluti, A. Lui, N. Daldosso, and L. Pavesi, *J. Appl. Phys.* **95** 767 (2004).
[5] M. Lipson, *Opt. Materials* **27**, 731 (2004).
[6] V. Tolmachev, T. Perova, J. Vij, E. Astrova, K. Berwick, and R. A. Moore, *Proceeding SPIE* **4876**, 196 (2003).
[7] V. Tolmachev, E. Astova, T. Perova, *Proceeding SPIE*, **5401**, 192 (2004).
[8] R. M. A. Azzam, N. M. Bashara, “Ellipsometry and polarized light”, North-Holland. Amsterdam, Netherlands, (1977).
[9] S.-T. Wu, *Opt. Eng.* **26**, 120-128 (1987).

13th Int. Symp. "Nanostructures: Physics and Technology"
St Petersburg, Russia, June 20–25, 2005

Photoluminescence of near-Bragg multiple quantum-well structures

M. M. Voronov and E. L. Ivchenko
Ioffe Physico-Technical Institute, St Petersburg, Russia

Abstract. We report on a theoretical study of photoluminescence (PL) of the resonant one-dimensional photonic crystals, the near-Bragg quantum-well (QW) structures. The PL spectral intensity is found by including random sources in the equations for the exciton dielectric polarization and introducing the discrete Green function. The position and width of peaks in the calculated PL spectra are in agreement with the real and imaginary parts of the exciton-polariton eigenfrequencies.

Introduction

The physics of photonic crystals, i.e. structures with periodically modulated dielectric function allowing for Bragg diffraction of light, is a rapidly developing field. Among one-dimensional photonic crystals, of particular interest are the so-called resonant Bragg structures with the period d satisfying the Bragg condition $d/\lambda(\omega_0) = 0.5$ at the exciton resonance frequency ω_0, see [1]. Experimentally, PL spectra of the resonant Bragg and near-Bragg quantum well structures were studied in Refs. [2,3]. In this work we propose a theory of secondary radiation of exciton-polaritons in multiple QW structures, derive the equations for the PL spectral intensity and present the preliminary quantitative results.

1. The photoluminescence spectral intensity: General equation

While considering the free-exciton photoluminescence in quantum well structures we should bear in mind that only excitons with the in-plane wave vector $k < \bar{k} \equiv (\omega_0/c)n_b$ can emit photons whereas those with $k > \bar{k}$ are "dark". Here ω_0 is the exciton resonance frequency and n_b is the barrier refractive index. In multiple-QW structures the bright excitonic states in different QWs are coupled via the electromagnetic field to form the exciton polaritons. We assume that the photoexcited dark excitons are characterized by the quasi-equilibrium distribution function $f(k)$ which can be calculated by using the conventional kinetic theory. The secondary photons are emitted following the acoustic-phonon-assisted scattering of dark excitons into the exciton-polariton states defined inside the circle $k < \bar{k}$. The latter have the alternative either to escape from the sample or be rescattered to one of the dark states. The scattering of exciton polaritons within the circle of bright states can be neglected. This allows to calculate the PL intensity although the criterion for validity of the Boltzmann kinetic equation for the bright states is not satisfied. The calculation procedure is similar to that used in [4] to describe the contribution to PL due to the upper branch of exciton-polariton dispersion curve.

Let us consider a structure consisting of N equidistant identical QWs, introduce the exciton polarization P_n in the nth QW ($n = 1, 2 \ldots N$) and limit ourselves to the vertical light emission connected to the exciton-polariton states with $\mathbf{k} = 0$. Values of P_n are interconnected by a set of linear equations

$$(\omega_0 - \omega - \mathrm{i}\Gamma)\, P_n + \sum_{n'} \Lambda_{nn'} P_{n'} = S_n \,,$$

$$\Lambda_{nn'} = -\mathrm{i}\Gamma_0\, e^{iqd|n-n'|} \,,\ q = \omega n_b/c \,.$$

Here d is the period, Γ_0 and Γ are the exciton radiative and nonradiative damping rates in a single QW structure, see, e.g., [1], and S_n is the random perturbation in the n-th QW making allowance for the phonon-induced scattering from the dark states with $k > \bar{k}$ into the state with $k = 0$. The perturbation average square is given by

$$\langle |S_n(\omega)|^2 \rangle = \frac{\varepsilon_b}{2\hbar q a^2} |M_0|^2 G_0(\omega; n) \,,$$

$$G_0(\omega; n) = \frac{2\pi}{\hbar} \sum_{\mathbf{k}} f_{\mathbf{k}}^{(n)} \, |V_{\mathbf{k}}|^2 \qquad (1)$$

$$\times [(N_{\mathbf{k}} + 1)\, \delta(\hbar\omega - E_{\mathbf{k}} + \hbar\Omega_{\mathbf{k}}) + N_{\mathbf{k}}\, \delta(\hbar\omega - E_{\mathbf{k}} - \hbar\Omega_{\mathbf{k}})] \,.$$

The notations used are as follows: $\varepsilon_b = n_b^2$, a is the QW width, $E_{\mathbf{k}}$ is the exciton energy, ω and $\Omega_{\mathbf{k}}$ are the photon and phonon frequencies, M_0 is the matrix element of emission of a photon by an exciton in a single QW, $f_{\mathbf{k}}^{(n)}$ is the exciton distribution function in the n-th QW defined outside the circle $k > \bar{k}$, $N_{\mathbf{k}}$ is the phonon occupation number, and $V_{\mathbf{k}}$ is the matrix element of the exciton-phonon interaction. In Eq. (1), two terms in the square brackets describe, respectively, the phonon emission and absorption processes.

2. Discrete Green's function in a periodic MQW structure

Enumerating the QWs in order from $n = 1$ to $n = N$ we define the discrete Green function $G_{nn'}$ in the following way

$$(\omega_0 - \omega - i\,\Gamma) G_{nn'} + \sum_{n''} \Lambda_{nn''} G_{n''n'} = \delta_{nn'} \,. \qquad (2)$$

The solution of (2) can be presented in the form

$$G_{nn'} = P_+^{(n')} e^{\mathrm{i}Kdn} + P_-^{(n')} e^{-\mathrm{i}Kdn} + \begin{cases} P_0 & \text{for} \quad n = n' \,, \\ P\, \mathrm{e}^{\mathrm{i}Kd|n-n'|)} & \text{for} \quad n \neq n' \,. \end{cases}$$

Here K is the wave vector of an exciton polariton in an infinite QW structure, it satisfies the dispersion equation [1]

$$\cos Kd = \cos qd + \frac{\Gamma_0}{\omega - \omega_0 + \mathrm{i}\Gamma} \sin qd \,, \qquad (3)$$

P_0, P determine the Green function for an infinite QW structure and are given by

$$P = \frac{\mathrm{i}\Gamma_0 \sin qd}{(\omega_0 - \omega - \mathrm{i}\Gamma)^2 \sin Kd} \,,$$

$$P_0 = P + \frac{1}{\omega_0 - \omega - \mathrm{i}\Gamma} \,,$$

$P_{\pm}^{(n')}$ result from the internal reflection of exciton polaritons from the first and last QWs,

$$P_{\pm}^{(n')} = rP\,\frac{e^{i\Phi_{\pm}} + re^{iKd(2N\mp n'-2)}}{1 - r^2 e^{2iKd(N-1)}}\,,$$

where

$$r = -\frac{1 - e^{-i(q-K)d}}{1 - e^{-i(q+K)d}}\,,$$

$\Phi_+ = Kd(n'-2)$, $\Phi_- = Kd(2N-n')$.

3. Photoluminescence spectrum of near-Bragg QW structures

The PL spectral intensity is derived to have the form

$$I(\omega) \propto \sum_{n'} |\mathcal{E}^{(n')}|^2 \langle |S_{n'}(\omega)|^2 \rangle\,.$$

Here $\mathcal{E}^{(n')}$ is the electric field of the secondary radiation arising due to the emission from n'th QW. For the semiinfinite outermost barriers, it is given by

$$\mathcal{E}^{(n')} = \frac{(\omega_0 - \omega - i\Gamma)G_{1n'} - \delta_{1n'}}{\xi\Gamma_0}\,,$$

where $\xi = \varepsilon_b/(2\pi qa)$. This equation can be reduced to

$$\mathcal{E}^{(n')} = \frac{ie^{-iKd}\sin qd}{\xi \sin Kd}\,\frac{1+r}{\omega - \omega_0 + i\Gamma}\,\frac{e^{iKdn'} + re^{iKd(2N-n')}}{1 - r^2 e^{2iKd(N-1)}}\,.$$

For the structure containing N QWs, a semiinfinite back barrier and a front barrier of the thickness $b = d - a$ between the first QW and vacuum, the expression for $\mathcal{E}^{(n')}$ is multiplied by the factor $\tau/(1 - \varrho r_N)$, where $\varrho = (n_b - 1)/(n_b + 1)$, $\tau = 2n_b/(n_b + 1)$ and r_N is the reflection coefficient from a set of N equidistant QWs.

The PL spectral peaks are expected to appear at the real parts of eigenfrequencies of exciton polaritons satisfying the following transcendental equation [5]:

$$\tan(NKd) = -i\mathcal{F}(\omega, K)\,,\ \mathcal{F}(\omega, K) = \frac{\sin qd \sin Kd}{1 - \cos qd \cos Kd}\,.$$

We remind that K and ω are related by Eq. (3). As soon as $|\sin qd| \ll \Gamma_0/|\omega - \omega_0 + i\Gamma|$ the complex eigenvalues K_j can be approximated by

$$K_j d = \frac{1}{N}\left(\pi j + \frac{i}{2}\ln\frac{1 - \mathcal{F}_j}{1 + \mathcal{F}_j}\right)\,, \qquad (4)$$

where j is an integer and $\mathcal{F}_j = \mathcal{F}(\omega_0, \pi j/N)$. We have considered a QW structure with $N = 100$. For the detuning parameter $d/\lambda(\omega_0) = 0.495$ and ratio $\Gamma/\Gamma_0 = 0.1$, the exact values $K_j d$ for $j = N-2, \ldots, N-5$ and those calculated by using Eq. (4) are listed below

$j = N-2 = 98$: 3.0771−i0.0099 and 3.0788−i0.0110,
$j = N-3 = 97$: 3.0468−i0.0067 and 3.0473−i0.0069,
$j = N-4 = 96$: 3.0157−i0.0050 and 3.0159−i0.0051,
$j = N-5 = 95$: 2.9844−i0.0040 and 2.9845−i0.0040.

and demonstrate a satisfactory coincidence. For $j = 99$ the exact eigenvalue is 3.1030−i0.0154, for this j the approximate equation (4) is invalid.

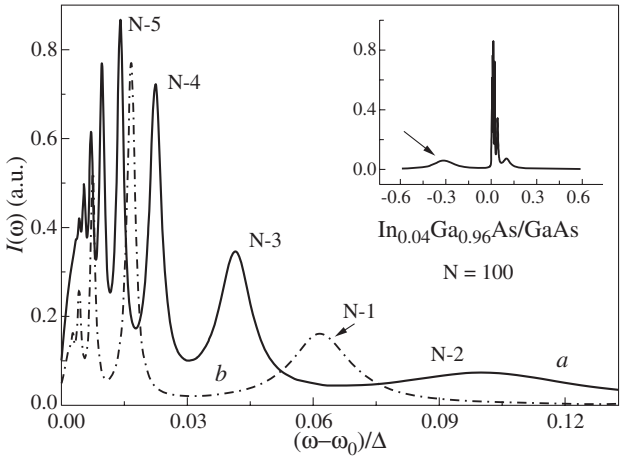

Fig. 1. Calculated PL spectra for the near-Bragg structures with the detunings $d/\lambda(\omega_0) = 0.495$ (a) and 0.499 (b). In the horizontal axis the difference $\omega - \omega_0$ is presented in units of Δ, where $\Delta = (2\omega_0\Gamma_0/\pi)^{1/2}$ is a half of the forbidden gap in the dispersion of exciton polaritons in the resonant Bragg structure. The other parameters of the system are as follows: $\varepsilon_b = 13$, $a = 85$ Å, $\hbar\omega_0 = 1.5$ eV, $\hbar\Gamma_0 = 27\,\mu$eV, $\Delta = 5.1$ meV. Inset shows the PL spectrum (a) in the wider region including negative values of $(\omega - \omega_0)/\Delta$.

The calculated PL spectra are shown in Fig. 1. There are several distinct peaks which correspond to polaritonic modes beginning from $j = N - 2, N - 3, \ldots$. In addition, there is a supplementary peak below the exciton resonance frequency ω_0 shown by an arrow in the inset. The corresponding value of Kd cannot be found by using Eq. (4) and equals $3.1196 - i0.0126$ which corresponds to the complex eigenfrequency $\omega = \omega_0 - (0.33 + i0.18)\Delta$.

In conclusion, we have developed a theory describing the PL spectra of multiple QW structures, in particular, near-Bragg QW structures. The spectral fine structure is quite sensitive to the geometrical parameters of the structure, the period d, the number of QWs N and the cap-layer thickness. The quantitative comparison with experiment [2,3] needs a thorough fitting of these parameters and, obviously, allowance for inhomogeneous broadening.

Acknowledgements

This work is financially supported by RFBR and the program of Russian Ministry of Science and Education.

References

[1] E. L. Ivchenko, *Optical spectroscopy of semiconductor nanostructures*, Alpha Science International, Harrow, UK, 2005.
[2] A. V. Mintsev, L. V. Butov, C. Ell, S. Mosor, G. Khitrova and H. M. Gibbs, *JETP Letters* **76**, 637 (2002).
[3] A. V. Mintsev, *Proc. 11th Int. Symp. "Nanostructures: Physics and Technology"*, Ioffe Institute, St. Petersburg, Russia, p. 195, 2003.
[4] A.V. Sel'kin, A.G. Abdukadyrov, M.I. Sazhin, N.Kh. Yuldashev, *Optika i Spectroscopiya* **67**, 845 (1989).
[5] M.R. Vladimirova, E.L. Ivchenko and A.V. Kavokin, *Semiconductors* **32**, 90 (1998).

13th Int. Symp. "Nanostructures: Physics and Technology"
St Petersburg, Russia, June 20–25, 2005

Magnetic resonance and photoluminescence in $Pb_xNb_yO_z$-ceramics as a system containing chemical nanoclusters

V. S. Vikhnin[1], *H. R. Asatryan*[1], R. I. Zakharchenya[1], A. B. Kutsenko[1] and S. E. Kapphan[2]

[1] Ioffe Physico-Technical Institute, St Petersburg, Russia
[2] FB Physik, Universität Osnabrück, 49069 Osnabrück, Germany

Abstract. The simulation of chemical fluctuation regions in the PMN-like relaxors by growth of the $Pb_xNb_yO_z$-ceramics was performed. Different $Pb_xNb_yO_z$-nanoclusters (chemically and structurally) coexist in such a ceramics. Hole polarons and "bi-polarons" and "Cr^{3+}-two polaronic holes" paramagnetic complexes were considered for an explanation of EPR spectra in $Pb_xNb_yO_z$ ceramics. Dynamical averaging and light induced effects, and significant effects of reduction treatment giving a co-existence of Nb^{5+} and Nb^{3+} ions as well as of strong internal magnetic field were discovered in such a ceramics. The latter could be related with antiferromagnetic phase realization in $Pb_xNb_yO_z$-nanoclusters containing high enough concentration of magnetic Nb^{3+} host lattice ions. Such a situation leads to antiferromagnetic resonance on Nb^{3+} ions as well as to EPR of Cr^{3+}-related paramagnetic complexes in Nb^{3+}-induced internal magnetic field. Charge transfer vibronic excitons (CTVE) in free and in CTVE-phase states were detected in $Pb_xNb_yO_z$-ceramics by photoluminescence studies.

Introduction

One of a significant source of the polar nanocluster formation in ferroelectric relaxors important for application could be chemical fluctuation nanoclusters with ferroordering. For example, these are Nb-rich regions with different Pb-Nb-O compositions in ferroelectric relaxor $PbNb_{2/3}Mg_{1/3}O_3$ (PMN). For study such a situation we have investigated the limiting case of $Pb_xNb_yO_z$-ceramics only consisting of different type of $Pb_xNb_yO_z$-nanoclusters.

The chemical analysis study achieved that average normalized concentration of O-ion for as grown $Pb_xNb_yO_z$-ceramics equals approximately to +3.5. That is, the Nb^{3+} ions have here relatively low concentration with respect to the main Nb^{5+} ion contribution. Nevertheless, a situation becomes principally different for the samples after reduction treatment. Indeed, such an average O-ion concentration becomes approximately +3 after essential sample reduction in the hydrogen atmosphere. It reflects the co-existence of different $Pb_xNb_yO_z$-nanoclusters with chemical compositions inclusive in average the Nb^{5+} as well as Nb^{3+} ions with approximately the same concentration. Note that corresponding Nb^{3+}-ion significant contribution could be responsible for an appearance of *magnetic behavior* for such a $Pb_xNb_yO_z$-ceramics. The latter is related with paramagnetic properties of Nb^{3+} ion ($S = 1$). As a result, antiferromagnetic ordering of Nb^{3+} ion spins will be predicted here due to antiferromagnetic exchange interaction between these ions. Co-existence of $Pb_xNb_yO_z$-*nanoclusters* with different chemical composition inclusive Nb^{5+} as well as Nb^{3+} ions in the reduced ceramic Pb-Nb-O samples will be the main suggestion of our model.

We assume that $Pb_xNb_yO_z$-ceramics consists of non-magnetic $Pb^{2+}Nb_2^{5+}O_6^{2-}$, $Pb_5^{2+}Nb_4^{5+}O_{15}^{2-}$, and $Pb_2^{2+}Nb_2^{5+}O_7^{2-}$ nanoclusters on the one hand, and of antiferromagnetic $Pb_2^{2+}Nb_2^{3+}O_5^{2-}$, $Pb^{2+}Nb_2^{3+}O_4^{2-}$, and $Pb^{2+}Nb_{1/2}^{3+}Nb_{1/2}^{5+}O_3^{2-}$ nanoclusters on the other.

Experimental results and interpretation

1. Hole polarons and "bi-polarons" and "Cr^{3+}-two polaronic holes" paramagnetic complexes in $Pb_xNb_yO_z$ nanoclusters. Light induced effects.

(a). Significant increasing of definite EPR-lines due to illumination (for instance, by mercury lamp during 0.5 h) takes place for as grown $Pb_xNb_yO_z$ ceramic samples. Indeed, characteristic doublet in low magnetic fields for $g>2$ (see also [1]) is essentially increased by such illumination. In contrast with it, a central line (with respect to such a doublet) at least is not increased by the same illumination. We assume that this behavior could be related with EPR manifestation of polaronic and bi-polaronic states in $Pb_xNb_yO_z$ nanoclusters. The doublet mentioned above could be considered as a result of $|0\rangle \rightarrow |\pm 1\rangle$ transitions for triplet spin state ($S = 1$). Here splitting between $|0\rangle \rightarrow |+1\rangle$ and $|0\rangle \rightarrow |-1\rangle$ lines formation could be explained as a result of uniaxial in-cluster field action. Such a photoinduced triplet could be related with pairs of self-localized carriers. These self-localized pairs of carriers in ferroelectric oxides become polaronic pairs. So, active here $|0\rangle$, $|+1\rangle$ and $|-1\rangle$ triplet spin states could be treated as the states of photoinduced triplet hole bi-polaron. The central line (with respect to the doublet discussed) could be interpreted as an effect of free polaronic hole. Its g-factor value ($g = 3.015$) could be explained due to direct contribution of orbital Zeeman effect in the ground double degenerating state of oxygen related hole ($2p_x$ and $2p_y$).

(b). In accord with our photoluminescence studies of the $Pb_xNb_yO_z$ ceramics under discussion these samples contain unwanted Cr^{3+} impurity. Its existence was confirmed by the detection of characteristic for $3d^3$ shall of Cr^{3+} ion very narrow R-lines of a luminescence. Note that some specific charge compensation for Cr^{3+} impurity on Nb^{5+} site is topical for the case of $Pb_xNb_yO_z$-clusters with Nb^{5+} ion state (for $PbNb_2O_6$-, $Pb_5Nb_4O_{15}$-, and $Pb_2Nb_2O_7$-clusters). Here extra (2-) charge on the Cr^{3+} site needs corresponding charge compensation. It is realized due to two oxygen hole trapping on the Cr^{3+} ion on the Nb^{5+} site. In reality we deal with Cr^{3+} ion extra-charge compensation under the conditions of hole-hole correlation as well as of essential hole — lattice polarization and hole — lattice deformation interactions. As a result, hole bi-polaron trapping to the first coordination sphere of Cr^{3+} impurity ion takes place here. We suppose that charge compensation of Cr^{3+} ion located on Nb^{5+} site is namely realised due to trapping of

two oxygen-related polaronic holes to the first coordination sphere of such Cr^{3+} ion. As a result, neutral "impurity — two polaronic hole" complex with related three-particle "Negative-U" effect is appeared. Namely such a "Cr^{3+} impurity — two polaronic hole "complex appearance explains the main EPR spectrum including dynamical averaging effect detected.

2. Antiferromagnetic phase realization in $Pb_xNb_yO_z$-nanoclusters with magnetic Nb^{3+} ions. Antiferromagnetic resonance on Nb^{3+} ions.

Strong reduction treatment of the $Pb_xNb_yO_z$ceramics under consideration leads to new situation with respect to contributions of Nb^{5+} and Nb^{3+} charge states of Nb-ion to such a ceramics. Namely, the contribution of Nb^{3+} ions is significantly increased and reaches the contribution of Nb^{5+} ions. Antiferromagnetic clusters are appeared here on the basis of above mentioned three type micro-regions containing Nb^{3+} paramagnetic ions with $3d^2$ shell and $S = 1$. The antiferromagnetic ordering is created there due to Nb^{3+}-O-Nb^{3+} super-exchange interaction via intermediate oxygen ion. Such clusters were detected in the present work by antiferromagnetic resonance (AFMR). Note that magnetic ordering mentioned above is accompanied by *internal local magnetic field appearance* with characteristic temperature dependence. Characteristic antiferromagnetic ordering features, namely, strong AFMR line shifts with temperature lowering up to an appearance of near zero field AFMR-lines on the one hand, and resonance line intensity decrease and line width increase with the same temperature lowering on the other support such an interpretation. Moreover we have to deal with the AFMR induced by two different Nb^{3+}-rich antiferromagnetic clusters (for example, by $Pb_2^{2+}Nb_2^{3+}O_5^{2-}$ and by $Pb^{2+}Nb_2^{3+}O_4^{2-}$ clusters) because two basic AFMR-doublets take place on the experiment. The EPR of Cr^{3+}-related paramagnetic complexes in temperature-dependent internal magnetic field induced by Nb^{3+}-ions was also detected.

3. Free charge transfer vibronic excitons (CTVE) and CTVE-phase states detected in $Pb_xNb_yO_z$-nanoclusters by photoluminescence.

CTVEs are characteristic long living dipole excitations in ferroelectric oxides (see [2]). They are polaronic electron-hole pairs or triads. In this work we have detected CTVEs in $Pb_xNb_yO_z$-nanoclusters. Here CTVEs with $O \rightarrow Nb^{5+}$ charge transfer were directly manifested by photoluminescence studies. We had detected a photoluminescence line related with recombination of $O \rightarrow Nb^{5+}$ *free CTVEs* at $\sim$ 500 nm. Special interest is caused by a detection of two red luminescence lines (at $\sim$ 740 nm and at $\sim$ 760 nm) which can be connected with recombination of $O \rightarrow Nb^{5+}$ CTVEs in the *CTVE-phase state*. Such a phase is related with an appearance of a system of strongly correlated CTVEs when in each cell the CTVE is appeared [2].

Acknowledgements

This work has been supported in part by RFBR (03-02-17589), RFBR (04-02-17632), and by Programs "Low dimension quantum structures", and Project of RAS "Spin-dependent effects in solids and spintronics".

References

[1] V. S. Vikhnin, H. R. Asatryan, R. I. Zakharchenya, A. B. Kutsenko, S. Kapphan, *Fizika Tverdogo Tela*, to be published (2005).

[2] V. S. Vikhnin, R. I. Eglitis, S. E. Kapphan, G. Borstel, E. A. Kotomin, *Phys.Rev.* **B**65, 104304 (2002).

13th Int. Symp. "Nanostructures: Physics and Technology"
St Petersburg, Russia, June 20–25, 2005

Study of magnetic clusters in the system ferromagnetic-nonmagnetic semiconductors (Zn,Mn)GeP_2/$ZnGeP_2$ by means of hole transport and magnetic resonance

G. A. Medvedkin[1], V. V. Popov[1], S. I. Goloshchapov[1], P. G. Baranov[1], H. Block[2], S. B. Orlinskii[2] and J. Schmidt[2]

[1] Ioffe Physico-Technical Institute, St Petersburg, Russia
[2] Hygens Laboratory, Leiden University, P.O. Box 9504, 2300 RA Leiden, The Netherlands

Abstract. Two different methods for studying magnetic effects in the heterojunction system ferromagnetic layer (Zn,Mn)GeP_2 on nonmagnetic $ZnGeP_2$ single crystal were applied to find manifestations of magnetic atomic-size defects, nano- and microclusters responsible for para- and ferromagnetic interactions. Giant electron spin echo, large negative magnetoresistance, low temperature hysteresis in magnetoresistance and anomalous Hall effect have been found and investigated in detail. Ferromagnetic ordering of nanocluster isles influenced on magnetic resonance phenomena in Mn doped $ZnGeP_2$ bulk, but not on the crystal structure of diamond-like chalcopyrite matrix. Percolate model approach is discussing as one of the non-discrepant mechanisms for explanation of features in charge carrier transport in magnetic field and magnetic resonance in Mn spin system.

Introduction

Nowadays clusters with an exactly determined number of atoms are considered as a base of new class materials [1]. Magnetic semiconductors can exhibit specific magnetically ordered quantum objects as ferromagnetic nanoclusters. Their size spans from several atoms to 10^9 atoms bonded by a strong magnetic coupling. These small particles have totally different magnetic structures and 'materials properties' than their bulk crystalline counterparts. Even more, these properties sometimes change drastically whenever a single atom is added to or removed from the cluster [1].

Novel Mn-doped chalcopyrites based on II-IV-V_2 ternary compounds were started to intense investigation [2–4]. They show high temperature (high T_C) ferromagnetism and the diamond-like crystal structure of chalcopyrite. Their electric resistance can be varied from isolator ($> 10^9\,\Omega$ cm) and down to metallic-like material in dependence on a concentration of magnetic impurity [5]. High-T_C ferromagnetism was shown in experiment to remain in both phases. This work studies magnetic clusters in high-T_C ferromagnet (Zn,Mn)GeP_2 by means of magnetoresistance (MR), anomalous Hall effect and electron paramagnetic resonance (EPR) detecting the electron spin echo (ESE) signals.

1. Experimental

(Zn,Mn)GeP_2 layers were grown on insulated $ZnGeP_2$ single crystals oriented in the isotropic direction [001]. The optically high-quality p-type crystals were processed for reactive diffusion of manganese at 550 °C in vacuum of 10^{-8} torr. The prepared heterostructures (Zn,Mn)GeP_2/$ZnGeP_2$ and $ZnGeP_2$:Mn single crystals containing 0.2 at.% and 2 at.% of Mn were studied.

Magnetic resonance techniques employed the pulsed EPR spectrometer operating at frequency of 275 GHz/J-band and a continuous wave (cw) spectrometer providing X-band regime at 9.3 GHz, $T = 4 \sim 300$ K. We detected signals of ESE using the J-band spectrometer with the finest spectral resolution at $T = 1.6 \sim 5$ K. Hall effect and MR measurements were performed using golden dot contacts in six-probe geometry. Magnetic field up to 30 kOe and $T = 1.8$ to 390 K were maintained for steady state and H-loop cycling experiments.

2. Result and discussion

Figure 1 demonstrates the chalcopyrite crystal structure $I\bar{4}2d$ of the Mn-doped $ZnGeP_2$ crystal, where Zn, Ge and P atoms situate at the diamond-like lattice sites regularly. Mn atoms are suggested to situate randomly at two different Zn-sites and at Ge-site (not shown).

Figure 2 presents EPR spectra at J-band (275 GHz) of the 2% Mn-doped $ZnGeP_2$ homogeneous single crystal measured at T=270 K (cw-EPR) and 5 K (ESE detected pulse EPR). Intensities of these fine-structure components differ strongly at 5 K due to an extreme population of the M_S sublevels and a large Zeeman splitting. The broad overlapped line is due to exchange coupled Mn clusters existing in ferromagnetic chalcopyrite along with isolated Mn^{2+} ions at Zn sites. Earlier EPR data established the main point defect in $ZnGeP_2$ is zinc vacancy V_{Zn} and according to the Hall effect, the undoped crystals take shape as p-type material owing to V_{Zn} acceptors, as well. Mn dopants compensate zinc vacancies that is confirmed by our EPR data on a high concentration of Mn^{2+}_{Zn} centers in both Mn-doped $ZnGeP_2$ and (Zn,Mn)GeP_2.

The local crystal structure in Fig. 1 shows Mn ions in clus-

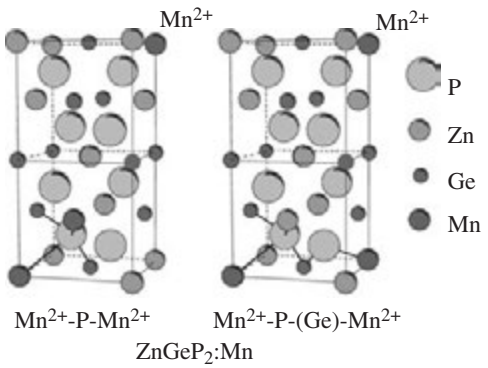

Fig. 1. Two type Mn-pairs which could be realized in $ZnGeP_2$:Mn.

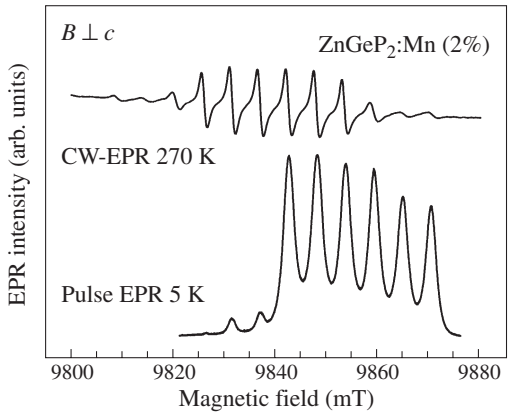

Fig. 2. cw-EPR and ESE detected EPR spectra of $ZnGeP_2$:Mn crystal at $T = 270$ K and 5 K, respectively.

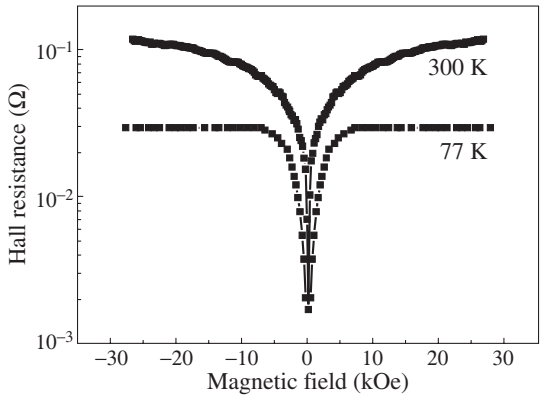

Fig. 3. Hall sheet resistance vs. magnetic field of (Zn,Mn)GeP_2 layer at $T = 300$ K and 77 K. The curve at 77 K is multiplied by the factor of 10.

ters are coupled in atomic-size chains through P atom or three atoms P-Ge-P. These motives can repeat in the neighborhood many times finally forming a magnetic nanocluster. EPR evidences the presence of magnetic nanoclusters in Mn-doped $ZnGeP_2$ at high manganese concentration. Because the completely Mn substituted compound $MnGeP_2$ has been recently prepared and [Mn] in (Zn,Mn)GeP_2 is expected to change in the wide range ($0 \sim 100\%$), one can suggest the size of clusters changes as [Mn] increases, resulting in absorption of detached ferromagnetic isles by the ferromagnetic sea. Such dimensional transition is known as a percolation in charge carrier transport.

Figure 3 gives a dependence of the Hall sheet resistance ρ_{xy}/d on magnetic field of a highly conductive p-(Zn,Mn)GeP_2 layer. The curves nonlinear clearly show the contribution of an anomalous Hall coefficient R_a is strong. The anomalous Hall effect increases with temperature, so a saturation of the Hall resistance observed at 77 K cannot be recorded at 300 K in these H-fields. The $\rho_{xy}(H)/d$ value achieves the state of saturation at fields $H > 5$ kOe because of magnetization saturation, since $(\rho_{xy})_a = R_a \mu_0 M$. Unlike magnetization, the anomalous Hall effect slackens with decreasing temperature, approximately is 50 times as low, see Fig. 3. The MR occurs to obey different mechanisms at high and low temperatures. It increases gradually from practically zero to the large magnitude of -8.5% in the range of $T = 300 \sim 2$ K. The dependences $\Delta\rho/\rho_0(H)$ remain linear with an increasing slope $\partial(\Delta\rho/\rho_0)/\partial(H)$ [5]. However, the next anomaly was observed as a hysteresis of

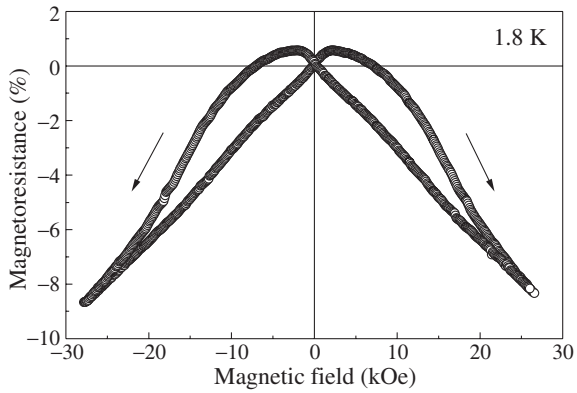

Fig. 4. Low temperature hysteresis of MR. Arrows indicate the detour direction of magnetic field.

MR vs. magnetic field only at low temperatures. The hysteresis loop at 1.8 K is shown in Fig. 4. Such a behavior is characteristic of cluster systems where freezing out of magnetic moments of clusters occurs due to either the dipole-dipole interaction or the presence of magnetic anisotropy. The magnetic cluster structure is a reasonable model for the highly conductive ferromagnetic (Zn,Mn)GeP_2 reaching the percolation level at the degenerate hole concentration in the ferromagnetic layer.

3. Conclusion

Properties of the nanoclusters are different from the host bulk semiconductor, at that, the crystal structure of samples remains equal (or similar) to the starting crystal with the diamond-like crystal structure, chalcopyrite. Above we described the present state of knowledge of properties of the clusters by atoms Mn-P-Mn and Mn-P-Ge-P-Mn which in their bulk form conventional doped semiconductor $ZnGeP_2$:Mn. Technological advances are expected using clusters in a specific support material in the areas of magnetic storage media and spin-dependent electronic materials.

Acknowledgements

The study was supported by the Innovation Fund FASIE (2398p/4716), the RF President and RFBR grants (NSh-2200.2003.2 and 04-02-17632), and the project of RAS "Spin-dependent effects in solids and spintronics".

References

[1] W. Eberhardt, Clusters as new materials, *Surface Science*, **500**, Issues 1–3, 242 (2002).
[2] G. A. Medvedkin *et al*, *Jpn. J. Appl. Phys.*, **39**, L949 (2000); G. A. Medvedkin *et al*, *J. Cryst. Growth*, **236**, 609 (2002).
[3] S. Cho *et al*, *Phys. Rev. Lett.*, **88**, 257203 (2002).
[4] P. G. Baranov *et al*, *Physica B*, **340–342**, 878 (2003); P. G. Baranov *et al*, *J. Supercond.*, **16**, 131 (2003).
[5] V. V. Popov *et al*, *Sol. St. Commun.*, **132**, 561 (2004).

13th Int. Symp. "Nanostructures: Physics and Technology"
St Petersburg, Russia, June 20–25, 2005

Kerr effect for FeNi film thickness below ∼ 6 nm and polar magnetization of FeNi-Si system

F. A. Pudonin[1], J. M. Talmadge[2], J. Gao[2], M. P. Riley[2], R. J. Roth[2], S.-O. Kim[2], J. G. Eden[2] and I. V. Mel'nikov[3]

[1] P.N. Lebedev Physical Institute, RAS, 119991 Moscow, Russia
[2] University of Illinois, Urbana, IL 61801,USA
[3] University of Toronto, Toronto, Canada M5S 3G4

Abstract. The magneto-optical Kerr effect has been observed in 1–80 nm thick FeNi films deposited onto Si(100), for an external magnetic field (variable in strength up to 800 G) oriented parallel or orthogonal to the magnetization axis of the film. Our data indicate the two-dimensional quantum behavior for films with $d < 6$ nm. The existence of a magnetic moment, perpendicular to the film surface was detected.

The discovery of the giant magnetoresistance effect has opened opportunity of creation new nanoscale magnetic film devices. The realization and optimization of this devices (multilayer spin valve, spin-tunneling or magnetic superlattice structures) require a detailed understanding of the electrical, structural, and optical characteristics of magnetic films having thicknesses in the range of ∼ 0.5–15 nm, an interval in which quantum confinement and domain wall structure exert a profound influence on the magnetic properties of a film. The magnetooptical Kerr effect (MOKE) of thin (1–80 nm) FeNi-films on Si-substrates are studied in this report [1].

FeNi films ranging in thickness (d) from 1 to 80 nm were deposited onto Si(100) substrates by RF sputtering. Laser ellipsometry, and optical interference and electron microscopy studies determined the film deposition rate, ∼ 4.7 nm/min, to be independent of film thickness. Analysis of the films by Auger Electron Spectroscopy (AES) verified that, the stoichiometry of the deposited films matched that of the FeNi target. Experimental measurements of the magneto-optical characteristics of the FeNi films were made at room temperature with a MOKE configuration that allowed for magnetic field strengths up to 400 G to be studied. Experiments have been conducted for optical probe wavelengths in the red (635 nm) and green.

For $d \geq 6$ nm the coercivity ($\lesssim 5$ G) varies little with film thickness and is similar to values in the literature for bulk FeNi and 10 nm FeNi films. Also, the shift of the hysteresis loops from zero field is virtually imperceptible, suggesting that the films are of high quality. The saturated MOKE response is constant for field strengths beyond 110 G.

For film thicknesses below ∼6 nm, the MOKE characteristics change dramatically. The field strength required to reach saturation, and the coercivity, rise quickly. These data display a clear difference of the FeNi film MOKE characteristics from bulk behavior and Fig. 1 provides another perspective of this transition to a two-dimensional structure. One concludes that our data indicate the onset of two-dimensional quantum behavior for d<6 nm. Approximately just the same quantum behaviour of MOKE response are observed for external magnetic field oriented parallel to the magnetization axis of the film.

Measurements of the MOKE response of the FeNi films with the magnetic field perpendicular to both the magnetization axis and the film surface demonstrate that the FeNi films have a component of the magnetic moment that is directed out of the plane of the film (polar magnetization). The physical nature of this polar magnetization can be connection with interface FeNi-Si or type of domain walls. It is well known that silicides such as Fe_nNi (n = 1–3) form readily at metal/Si interfaces. Both magnetic and non-magnetic phases (islands) can be produced, and the non-magnetic FeSi (or NiFe) phases has been identified as the origin of antiferromagnetic coupling between islands and FeNi film and polar magnetic moment. Other possibility connect with type of domain walls. Our data, in particular, are consistent with the calculations of Trunk *et al* [2] which predict the transition between Bloch and Neel wall domain structure to occur in FeNi films for $d \approx 30$ nm. As discussed in [2], vortex structure associated with Bloch wall domains gives rise to a magnetization component directed out of the plane of the film. In particular, the overshoot angle θ, which characterizes the orientation of the polar magnetization, was predicted to be small for $d < 30$ nm (Neel domain) and to rise abruptly for film thicknesses above 30 nm.

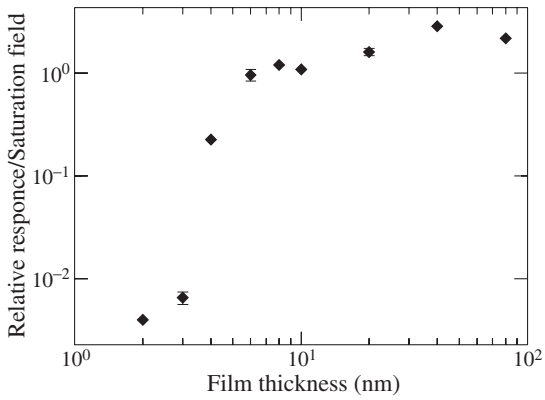

Fig. 1.

Acknowledgement

The technical assistance of K. Collier is gratefully acknowledged. This work was supported by the U.S. Air Force Office of Scientific Research (grant F49620-00-1-0372), the RFBR (grant 04-02-17428) and program in support Leading Scientific Schools (pr. NSh-19232003.2) and Nortel Institute for Telecommunication.

References

[1] J. M. Talmadge *et al*, *Appl. Phys. Lett.*, **84**, 4197 (2004).
[2] T. Trunk *et al*, *Appl. Phys. Lett.*, **89**, 7606 (2001).

13th Int. Symp. "Nanostructures: Physics and Technology"
St Petersburg, Russia, June 20–25, 2005

A continuous time QMC study of the correlated adatom trimer

V. V. Savkin[1], *A. N. Rubtsov*[2], M. I. Katsnelson[1] and A. I. Lichtenstein[1,3]

[1] Institute of Molecules and Materials, University of Nijmegen, 6525 ED Nijmegen, The Netherlands
[2] Department of Physics, Moscow State University, 119992 Moscow, Russia
[3] Institute of Theoretical Physics, University of Hamburg, 20355 Hamburg, Germany

Abstract. The problem of three interacting Kondo impurities is solved within a numerically exact continuous time quantum Monte Carlo scheme. A suppression of the Kondo resonance by interatomic exchange interactions for different cluster geometries is investigated. It is shown that a drastic difference between the Heisenberg and Ising cases appears for antiferromagnetically coupled adatoms. The effects of magnetic frustrations in the adatom trimer are investigated, and possible connections with available experimental data are discussed.

Introduction

The electronic structure of adatoms and clusters on surfaces constitutes one of the most fascinating subjects in condensed matter physics and modern nanotechnology [1]. The scanning tunneling microscopy (STM) allows the study of atomic structure, the electronic energy spectrum, and magnetic properties of different surfaces at an atomic scale. In particular, STM gives the unique opportunity of directly investigating an essentially many-body phenomenon, namely the Kondo effect. Recently STM studies of small transition metal nanoclusters on different surfaces have been performed, including Co dimers and Cr trimers on a Au surface, and Co clusters on carbon nanotubes. The electron spectrum of these nanosystems, in particular the existence of the Kondo resonance, turns out to be very sensitive to the geometry of the clusters as well as to the type of magnetic adatoms. The later can be important for nanotechnological fine tuning of surface electronic structure. At the same time, due to the extreme complexity of the problem, theoretical investigations of electronic structure for several Kondo centers usually involve some uncontrollable approximations, such as a replacement of the Heisenberg interatomic exchange interactions by the Ising ones or a variational approach based on a simple trial function.

In this communication we present results of a numerically exact solution of the three Kondo impurity problem within the recently developed continuous time quantum Monte Carlo (CT-QMC) method. For the antiferromagnetic (AFM) exchange interatomic interaction, in contrast to the ferromagnetic (FM) one, the results for the Heisenberg and Ising systems differ essentially. Based on our analysis, the recent paradoxical experimental results [2] where the Kondo resonance is observable for an isosceles magnetic triangle but not for the perfect Cr-trimer or individual Cr adatom will be discussed.

1. Model and methods

We start with the system of three impurity correlated sites with Hubbard repulsion U in a metallic bath and with an effective exchange interaction J_{ij} between them, a minimal model which however includes all relevant interactions necessary to describe magnetic nanoclusters on a metallic surface. The effective action for such cluster in a metallic medium has the form $S = S_0 + W$ with

$$S_0 = -\int_0^\beta \int_0^\beta d\tau d\tau' \sum_{i,j;\sigma} c^\dagger_{i\sigma}(\tau)\mathcal{G}^{-1}_{ij}(\tau-\tau')c_{j\sigma}(\tau'),$$

$$W = \int_0^\beta d\tau \left(U \sum_i n_{i\uparrow}(\tau)n_{i\downarrow}(\tau) + \sum_{i,j} J_{ij}\mathbf{S}_i(\tau)\mathbf{S}_j(\tau) \right).$$

The last term in the right-hand-side of Eq. (1) allows us to consider the most important "Kondo lattice" feature, that is, the mutual suppression of the Kondo screening and intersite exchange interactions. Another factor, the coherence of the resonant Kondo scattering, is taken into account by the introduction of inter-impurity hopping terms t_{ij} to the bath Green function which is supposed to be $\mathcal{G}^{-1}_{ij} = \mathcal{G}^{-1}_i\delta_{ij} - t_{ij}$. Here $\mathcal{G}^{-1}_i(i\omega_n) = \mu + i(\omega_n + \sqrt{\omega_n^2+1})/2$ corresponds to the semicircular density of states (DOS) with band-width 2 and t_{ij} are inter-impurity hopping integrals. For real adatom clusters the exchange interactions are mediated by conduction electrons (RKKY interactions) which are dependent on the specific electronic structure of both adatoms and host metal. To simulate this effect we will consider J_{ij} as independent parameters which is a common practice in the Kondo lattice problem; otherwise for the half-filled non-degenerate Hubbard model used in our calculations the exchange is always antiferromagnetic. In the model (1) the geometry of the problem is specified by the values of exchange integrals J_{ij} and hopping parameters t_{ij}. We will concentrate on the case of equilateral triangle when $J_{ij} = J$ and $t_{ij} = t$; to compare with the experimental situation in also an isosceles triangle will be considered. To check an approximation used previous works we will investigate the case when all spin-flip exchange terms are ignored and the Heisenberg (**SS**) form of interaction $J_{ij}\mathbf{S}_i(\tau)\mathbf{S}_j(\tau)$ is transformed into the Ising (S_zS_z) one $J_{ij}S^z_i(\tau)S^z_j(\tau)$.

We use the numerically exact CT-QMC method [3] for our computer simulations. Unlike the Hirsh-Fye discrete-time scheme it does not involve auxiliary Ising spins, but performs a random walk in the space of terms of the perturbation expansion for the Green function. One of the advantages of this novel approach is the opportunity it provides to study systems with non-local (in space and in time) interactions, which in the usual Hirsh-Fye approach would involve a huge increase in the required number of auxiliary fields and time slices.

2. Results and discussion

Let us discuss correlated adatom trimer in the metallic bath depending on type of the effective exchange interaction (S_zS_z or **SS**) for AFM and FM cases. First we show that **SS** type of interaction suppresses the resonance in AFM case. We study

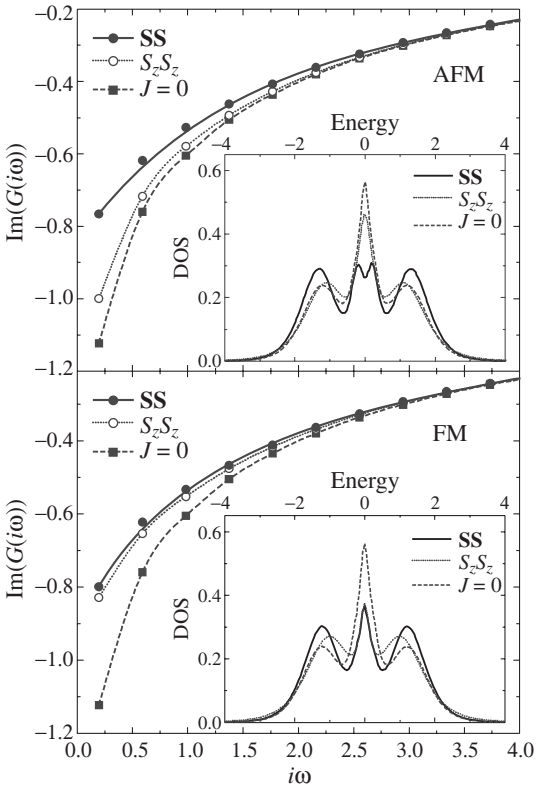

Fig. 1. Imaginary part of the Green functions at Matsubara frequencies for the correlated adatom equilateral triangle in the metallic bath for AFM (upper figure) and FM (lower figure) types of effective exchange interaction. Parameters: $U = 2$, $J = \pm 0.2$, $t = 0$, $\beta = 16$, $\mu = U/2$. There are three dependencies on each picture for **SS**, S_zS_z and $J = 0$ (which corresponds to single atom in the metallic bath) types of interaction. The insets show DOS.

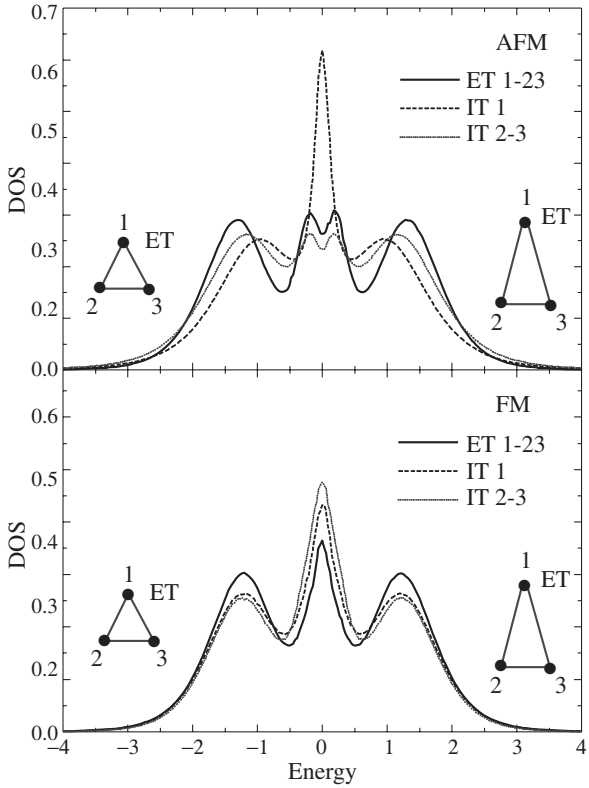

Fig. 2. DOS for equilateral triangle (ET) and isosceles triangle (IT) geometries with AFM (upper figure) and FM (lower figure) types of effective exchange interaction. Parameters are the same as in Fig. 1. Values of the effective exchange integrals for IT are as follows: $J_{23} = J$, $J_{12} = J/3$, $J_{13} = J/3$. There are two dependencies in case of IT: one for adatom 1 and another for equivalent adatoms 2 and 3. All adatoms are equivalent in the case of ET (one dependence).

the equilateral triangle at half-filling. The Green functions at the Matsubara frequencies obtained by the CT-QMC technique and corresponding DOS are presented in Fig. 1. The case of $J = 0$ corresponds to the single Kondo impurity in the bath. One can see that there is no essential difference between S_zS_z and **SS** types of interaction in FM but for the AFM one this difference is very important. The AFM **SS** interaction leads to pronounced suppression of the Kondo resonance at Fermi level (Fig. 1).

To explain these results we need to calculate the spectral density $D(\omega)$ of the on-site spin-flip operators $S_i^{\pm}$ for an AFM equilateral triangle $D_{\mathbf{SS}}(\omega) = \frac{2}{3}\delta(\omega) + \frac{1}{3}\delta(\omega - 3J)$, $D_{S^zS^z}(\omega) = \frac{1}{3}\delta(\omega) + \frac{2}{3}\delta(\omega - 2J)$. In both cases there is a part of the spectral density with zero frequency due to degeneracy of the ground state and spin-flip transitions between its components, but for the **SS** case this part is twice as large. For the case $J \gg T_K$ (T_K is one-site Kondo temperature) only this "soft" component of the spectral density will lead to Kondo screening which means that the suppression of the Kondo effect is twice more efficient for the **SS** case than for the S_zS_z one. Interactions shows that there is no difference between the S_zS_z and **SS** model there and $T_K^* \simeq T_K^3/J^2$ as in the AFM S_zS_z case.

In order to describe the experimental situation we changed the geometry of the adatom trimer. An observation of the Kondo resonance reconstruction was reported for one isosceles geometry of three Cr atoms on a gold surface. Thus we study the isosceles triangles for AFM and FM types of effective exchange interaction. We have chosen the following parameters of J_{ij} to imitate the experimental system: $J_{23} = J$, $J_{12} = J/3$, $J_{13} = J/3$. The computational results are presented in Fig. 2, where one can see the reconstruction of resonance in AFM and FM cases in accordance with experimental data. Note that the Kondo resonance appears only for the more weakly bonded adatom in AFM case.

The results are published in Physical Review Letters, **94** 026402 (2005).

Acknowledgements

The work was supported by FOM project N0703M, NWO project 047.016.005 and "Dynasty" foundation.

References

[1] For review, see special issue of Surf. Sci., **500** (2002), especially E. W. Plummer *et al*, *Surf. Sci.*, **500**, 1 (2002); J. Schen and J. Kirschner, *Surf. Sci.*, **500**, 300 (2002).

[2] T. Jamneala *et al*, *Phys. Rev. Lett.*, **87**, 256804 (2001).

[3] A. N. Rubtsov and A. I. Lichtenstein, *Pis'ma v ZHETF*, **80**, 67 (2004); A. N. Rubtsov, cond-mat/0302228.

13th Int. Symp. "Nanostructures: Physics and Technology"
St Petersburg, Russia, June 20–25, 2005

Nanostructure magnetism of polymerized C_{60}

E. F. Sheka[1], V. A. Zayets and I. Ya. Ginzburg[2]

[1] Russian Peoples' Friendship University, 117302 Moscow, Russia
[2] Institute of Problems of Chemical Physics of RAS, 142432 Chernogolovka, Russia

Abstract. The paper is devoted to disclosing the origin of magnetism of carbon crystals, formed by polymerized layers of covalently bound C_{60} molecules. The problem has been considered computationally. The calculations have been performed in the unrestricted SCF HF approximation by using AM1 semi empirical technique. As shown, exchange integrals J of both free molecule and C_{60} monomer unit of polymers are too big to provide magnetism of ideal crystals. However, those are shrinked by about $1/k$ for an oligomer of k C_{60} molecules so that at big kJ may approach value to be enough for magnetic behavior observation. The suggested "scaly" character of the observed phenomenon is well consistent with recent experimental findings concerning the importance of nanoclustering of magnetic samples.

Introduction

Since its discovery [1], the magnetism of carbon crystals, formed by polymerized layers of covalently bound C_{60} molecules, still has been an intriguing phenomenon of obscure origin. The list of works devoted to the problem counts tens but the problem is still far from a complete solution. The current paper presents one more attempt to throw light on the phenomenon.

The approach suggested in the paper stands from a convenient basic statement that magnetism of any crystalline solid is caused by peculiar electronic properties of its main building block. As known, this is necessary, but not always enough, so that the packing of the building blocks is important as well. The C_{60} molecule (monomeric molecule, MM, below) plays the role for polymerized C_{60} crystals. Until now it has been suggested that the molecule has no unpaired electrons. As a result, a thorough theoretical investigation of the ability to create such electrons under the molecule polymerization [2] gave a negative answer so that the ideal crystal consisting of C_{60} polymers should not have any magnetic behavior. The statement has contradicted to the experimental findings and a lot of theoretical suggestions on either radical [3,4] or topological [5] defects possessing unpaired electrons have appeared, but no convincing experimental proving of such defect structure has been obtained. Moreover, to provide the crystal magnetism, the defects should be orderly distributed through over the crystal body. And then a question arises, which mechanism is responsible for the regulated distribution of the defects. Simultaneously, experiment has revealed a new facet of the phenomenon. As shown, the magnetism is not a stable intrinsic property of perfect crystals but its observation is directly connected with the crystal imperfection [6-8]. These facts led the foundation of reconsidering the problem. We have tried to answer two following questions: 1) what might be the origin of unpaired electrons in such crystals and 2) how the magnetic behavior of these electrons is connected with the real structure of the crystalline samples.

1. Effectively non paired electrons of fullerenes

Recent theoretical study has shown [9] that the electronic properties of the fullerene molecules are determined by a non-trivial behavior of their odd electrons, equal by number to that of atoms. These electrons are not fully covalently paired so that there is a significant fraction of the effectively unpaired electrons, whose total number N_D constitutes 9 and 14 for the C_{60} and C_{70} molecules, respectively [10]. These quantities are distributed over the molecules atoms in a peculiar non-integer manner, and both molecules are partially radicals. Seemed, the answer to the first question was found. However, the exchange interaction between odd electrons occurs to be rather strong, so that the exchange integral J for the C_{60} species is of -1.86 kcal/mol. The value is too big to provide observable magnetic behavior of the molecule. Its ground state is singlet and the molecule is diamagnetic. As should be expected, the pristine C_{60} crystal, built of such molecules, is diamagnetic that is observed indeed.

An obvious question arises what is going with the N_D and J values under the molecule polymerization. To clear the point, quantum chemical calculations have been performed for a set of oligomers, which simulate three types of molecule packing in the crystalline C_{60} polymers. Below, the results will be given for rhombohedral $9{\cdot}C_{60}$ (Rh), tetragonal $9{\cdot}C_{60}$ (Tg), and linear $5{\cdot}C_{60}$ (L) oligomers.

2. Computational details

The calculations have been performed by using AM1 semi empirical technique implemented in CLUSTER-Z1 sequential [11] and NANOPACK parallel [12] codes. Among other standard characteristics, the main attention was given to the N_D and J values. According to [10, 13], the former quantity is determined as $N_D = \sum_A N_{DA}$, $N_{DA} = \sum_{i\in A}\sum_{B=1}^{NAT}\sum_{j\in B} D_{ij}$, where *Dij* are elements of the density matrix. The exchange integrals are calculated as [9, 14]

$$J = \frac{E^{UHF}_{S=0} - E^{UHF}_{S_{\max}}}{S^2_{\max}}, \quad \text{where} \quad E^{UHF}_{S=0} \quad \text{and} \quad E^{UHF}_{S_{\max}}$$

are the oligomer energies in the UHF singlet state and in the state with the highest multiplicity $2S_{\max}+1$ related to spin $S_{\max} = n/2$. Here n defines the total number of odd electrons [9], which takes values 60, 524, 492, and 284 for C_{60}, and the studied (Rh), (Tg), and (L) oligomers, respectively.

3. Results and discussion

The oligomer equilibrated structures, which correspond to the energy minima, are shown in Fig. 1. Central MMs are in the positions characteristic for macrosamples. Taking them out of the structures and calculating without changing the molecule geometry, one can obtain characteristics of the building blocks

Table 1.

Species	N_D (a.u.)	J (kcal/mol)
Molecules		
Free	9.8	−1.80
MM (Rh)	16.0	−2.00
MM (Tg)	14.0	−1.94
MM (Or)	12.0	−1.92
Oligomers		
9*C_{60} (Rh)	10.6[1]	−0.38
9*C_{60} (Tg)	12.3[1]	−0.26
5*C_{60} (Or)	11.5[1]	−0.27

[1] Obtained per one molecule from the oligomer calculations.

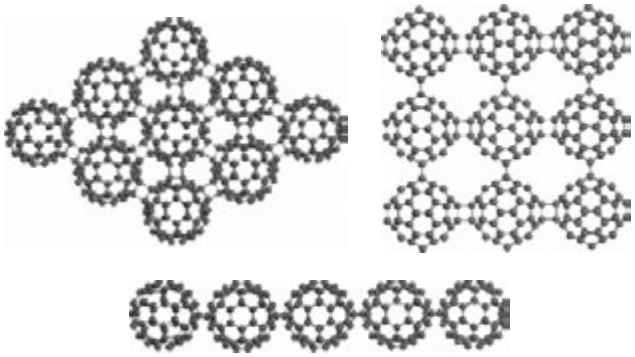

Fig. 1. Equilibrated structures of the 9*C_{60}, 9*C_{60}, 5*C_{60} oligomers; UHF singlet state.

of the considered polymeric structures. The relevant data are given in the upper part of Table 1.

As seen from the table, the polymerization causes a significant changing in the electronic structure of the individual molecules. A considerable growth of the N_D value is observed that means a weakening of covalent pairing of odd electrons in the MMs under polymerization. However, the exchange interaction between them becomes obviously stronger so that the polymerization itself does not favor the sample magnetism.

When looking at the characteristics for the whole oligomers, it should be pointed out that their exchange integrals significantly decrease by factor $\sim 1/k$, where k is the MM number. This evidences weakening the odd electrons interaction within the whole oligomer that is favorable for magnetism. Thus, oligomers with a few tens of MMs may exhibit magnetic behavior. Therefore, nanostructured polymeric samples may be expected to be magnetic. This is really observed experimentally at photogenerated linear oligomerization of the C_{60} molecules in the pristine crystal body with average k about 20 [15]. Nanostructuring seems to be responsible for magnetism of the carpet-like structures as well. Thus, Rh-magnetism is the best observed for samples, which are produced at high temperature and pressure close to the limit parameters of crystal destruction [7]. It occurred possible to form a whole family of magnetic carbons with varying degree of ferromagnetic content (and/or nanostructuring). Rh-magnetic samples have high mosaicity [8] and non-uniform magnetic structure, which constitutes not more than 30% of the sample [6]. No such features, as well as no magnetism have been observed for Tg crystals. Therefore nanostructuring of carbon materials with potentially non paired electrons can be a reasonable explanation of the phenomenon.

A scale-like model for the Rh-magnetism can be suggested. Obviously, graphite-like structure of the crystal favors "scaly" nanoclustering of the body under severe conditions [6-8]. The number and size of the scales undoubtedly depend on the technological treatment. However, consisting of a few tens of MMs, the scales are characterized by small exchange integrals. When the latter become small, primary negative due to domination of the Coulomb term, they may change sign due to interscale interaction, thus providing the growth of the potential exchange interaction contribution. Consequently, the antiferromagnetic behavior of the scale changes for the ferromagnetic one following to one of the proposed mechanisms, which describe inducing magnetic order in the systems with the singlet ground state [16].

Acknowledgement

The study was supported by the RFSF grant No. 03-07-90197.

References

[1] T. L. Makarova *et al*, *Nature* **413**, 716 (2001).
[2] S. Okada *et al*, *Phys. Rev. B* **59**, 1930 (1999).
[3] A. N. Andriotis *et al*, *Phys. Rev. Lett.* **90**, 026801 (2003).
[4] J. Ribas-Arino *et al*, *J. Phys. Chem. Sol.* **65**, 787 (2004).
[5] N. Park *et al*, *Phys. Rev. Lett.* **91**, 237204 (2003).
[6] K.-H. Han *et al*, *Carbon* **41**, 785 (2003).
[7] R. A. Wood *et al*, *J.Phys. Cond. Matt.* **14**, L385 (2002).
[8] M. Tokumoto *et al*, *Proc. AIP Conf.*, Melville, NY, USA 2002, p. 73.
[9] E. F. Sheka *Int. J. Quant. Chem*. **100**, 375 (2004).
[10] E. F. Sheka *Zh. Srukt. Khimii* (in press)
[11] V. A. Zayets *CLUSTER-Z1:* Inst. Surf. Chem. Nat. Ac. Sci. Ukraine: Kiev (1990).
[12] P. K. Berzigiyarov *et al*, *Int. J. Quant. Chem*. **88**, 449 (2002).
[13] K. Takatsuka *et al*, *Theor. Chim. Acta.* **48**, 175 (1978).
[14] L. Noodleman. *J. Chem. Phys.* **74**, 5737 (1981).
[15] F. J. Owens *et al*, *Phys. Pev. B* **69**, 033403 (2004).
[16] A. K. Zvezdin *et al*, *Rare Earth Ions in Magneto-Ordered Crystals* (Russian). Moskva: Nauka. 1985, Chapter 10.

13th Int. Symp. "Nanostructures: Physics and Technology"
St Petersburg, Russia, June 20–25, 2005

Interaction of localized and free plasmons on nanoporous metal surface

T. V. Teperik[1], V. V. Popov[1] and F. J. García de Abajo[2]

[1] Institute of Radio Engineering and Electronics (Saratov Division), Russian Academy of Sciences, Saratov 410019, Russia
[2] Centro Mixto CSIC-UPV/EHU and Donostia International Physics Center, Aptdo. 1072, 20080 San Sebastian, Spain

Abstract. We have theoretically studied the optical plasmonic properties of a planar nanoporous metal surface with periodic lattice of voids buried in metal just beneath the surface in the framework of a self-consistent electromagnetic multiple-scattering layer-KKR approach. We have investigated two types of plasmon excitations: surface plasmon-polaritons propagating at the planar surface of metal and Mie plasmons localized in voids. It is shown that the coupling between these two types of plasma oscillations leads to a huge enhancement of the surface plasmon-polariton resonances.

Introduction

The optical properties of planar metallic polaritonic crystals have been a subject of extensive research activities in recent years [1, 2]. Such polaritonic crystals have a two-dimensional ($2D$) periodic structure with complex unit cell, containing nanostructured metallic materials with inner material (plasmon) resonances. Nowadays, many efforts are devoted to investigate the metals with periodically arranged nanopores that is a prominent example of polaritonic crystal. The interest in such structures is based on considerable advances made in the template-assisted assembly of microporous and nanoporous metal structures [3-5].

Remarkable effects caused by excitation of plasmons in nanopores have been predicted theoretically for nanoporous metal films, such as extraordinary transmission [6] and absorption [7]. In [3] strong resonant dips in the reflectivity spectra of light have been observed from nanoporous metal surface formed by periodical arrangements of close-packed spherical segment voids (nanocups). All these effects are caused by excitation of Mie plasmons in voids (void plasmons). Apart from Mie plasmons localized in spherical cavities inside metal, the surface plasmon-polaritons propagating at the planar surface of porous metal can be also, in principle, excited if the period of the void lattice is comparable with the surface plasmon-polariton wavelength. This fact remarkably distinguishes porous metal polaritonic crystals, where a host medium (metal) is optically active, from polaritonic crystals [1, 2] containing active (metal) inclusions in (optically inactive) dielectric host medium. The lattice of voids buried beneath the planar surface of metal plays a two-fold role: (i) periodic lattice of voids forms a coupling element, which couples incoming light to surface plasmon-polaritons (it is well known that the surface plasmon-polaritons are non-radiative excitations and, therefore, they can not be excited on a planar surface of metal by incoming light without special coupling elements, e.g., grating or total reflection prism), (ii) localized Mie plasmons are exited in spherical voids. In contrast to the surface plasmon-polaritons, void plasmons are radiative excitations [8] and, therefore, they can be coupled to light effectively without using any special coupling device. Furthermore, it might be expected that the localized void plasmons and propagating surface plasmon-polaritons can be put into interplay by tuning the structure parameters. Surface plasmon-polaritons on metal surfaces are widely used for the sake of spectroscopy of surface epilayers and absorbates in optoelectronics and biophysics. Hence, the studying of new structures, in which surface plasmon-polaritons can be excited by incoming light in the most effective and practical way, is an important problem.

In this paper, we study the optical plasmonic properties of a hexagonal $2D$ lattice of spherical nanovoids buried inside metal at a distance less than skin depth from planar metal surface. We have calculated the reflectivity spectra of such a nanoporous metal surface in the framework of a self-consistent electromagnetic multiple-scattering layer-Korringa–Kohn–Rostoker (KKR) approach. We have investigated two types of plasmon excitations: surface plasmon-polaritons excited at the planar surface of metal and Mie plasmons localized in voids. The special attention is given to coupling effects between these two types of plasma oscillations. It is shown that the surface plasmon-polariton resonance can be considerably enhanced due to its interaction with Mie plasmons in nanovoids. This paves the way towards developing various sensors based on surface plasmon-polaritons operating with high sensitivity without special coupling elements.

Results and discussion

Let us consider the light is incident normally on a planar surface of metal that contains a $2D$ lattice of voids just beneath the surface with primitive lattice vectors $\mathbf{a}$ and $\mathbf{b}$, where $|\mathbf{a}| = |\mathbf{b}|$ and $\mathbf{a} \cdot \mathbf{b} = |\mathbf{a}|^2 \cos 60^\circ$. To calculate the light reflection spectra from such a porous surface we use a rigorous solution of Maxwell's equations based upon a multiple-scattering layer-Korringa-Kohn-Rostoker (KKR) approach that makes use of a re-expansion of the plane-wave representation of the electromagnetic field in terms of spherical harmonics (see [6, 7] and references therein). We describe the dielectric response of the metal to an electric field $\mathbf{E}\exp(-i\omega t)$ in the local Drude model as $\varepsilon(\omega) = 1 - \omega_p^2/\omega(\omega + i\nu_e)$, where ω_p is the bulk plasmon frequency and ν_e is a phenomenological bulk electron relaxation rate. For our calculations we choose the parameters $\omega_p = 7.9$ eV and $\nu_e = 90$ meV, which are characteristic for gold [9].

Fig. 1 shows the calculated reflection spectra of light incident normally onto a planar gold surface with a single hexag-

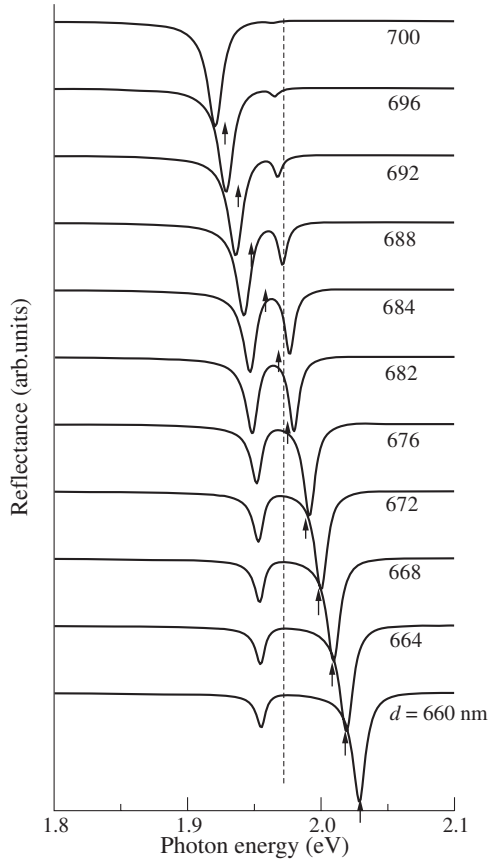

Fig. 1. Reflectivity spectra of light incident normally onto a planar gold surface with an hexagonal lattice of spherical voids of different diameters, d. Distance from the planar surface of metal to the tops of voids, h, is equal to 25 nm and $|\mathbf{a}| = |\mathbf{b}| = 705$ nm. The vertical arrows mark the energy of the second Mie plasmon mode of a single void in bulk gold. Dashed straight line indicates the energy of the surface plasmon-polaritons estimated in the "empty lattice approximation".

onal $2D$ lattice of voids buried in metal just beneath the surface for different void diameters, but the same void-lattice period, $|\mathbf{a}| = |\mathbf{b}| = 705$ nm. One can see two dips in every reflectivity spectra. One of them is associated with excitation of Mie plasmons in voids [7]. The frequency of Mie-plasmon resonance is close to the frequency of the second Mie-plasmon mode, the orbital quantum number $l = 2$, of a single void in bulk gold (marked by vertical arrows in Fig. 1), although they do not completely coincide due to the coupling of Mie plasmons in adjacent voids and/or disturbance of Mie-plasmon mode by proximity of the planar surface of metal [7]. The other dip in reflectivity spectra is related to the excitation of surface plasmon-polaritons at the planar surface of metal. The frequency of surface plasmon-polariton resonance is close to the frequency of surface plasmon-polaritons estimated in the "empty lattice approximation" (marked by dashed line in Fig. 1), $|\mathbf{k}_{\|} + \mathbf{g}|^2 = (\omega/c)^2\varepsilon(\omega)/(1 + \varepsilon(\omega))$, where $\mathbf{g} = p\mathbf{A} + q\mathbf{B}$ are the in-plane reciprocal lattice vectors, $\mathbf{A} = 2\pi(\mathbf{b} \times \mathbf{n})/|\mathbf{a} \times \mathbf{b}|$ and $\mathbf{B} = 2\pi(\mathbf{n} \times \mathbf{a})/|\mathbf{a} \times \mathbf{b}|$ are the primitive vectors of the reciprocal $2D$ lattice, p and q are integers, and $\mathbf{k}_{\|}$ is the in-plane reduced wavevector, which is equal to zero in the case of normal incidence.

Mie-plasmon resonance and surface plasmon-polariton resonance exhibit clear anticrossing when Mie-plasmon resonance passes by surface plasmon-polariton resonance with variation of the void diameter (see Fig. 1). This proves that these two types of plasmon resonances effectively interact with each other.

One can see in Fig. 1 that, in general, Mie plasmons excited in voids produce a stronger resonance dip in comparison with the surface plasmon-polariton resonance. The reason for this is that Mie plasmons in voids are radiative excitations [8] and, hence, they can couple to light effectively, while the surface plasmons are non-radiative excitations and can be coupled to light only via a coupling element, which is the lattice of voids itself in our case. Notice, however, that in the anticrossing regime (void radius is equal to 682 nm) Mie-plasmon resonance and surface plasmon-polariton resonance become comparable in amplitude. This is because in the interaction region these two types of plasmon resonances effectively exchange their oscillator strength, so that a stronger Mie-plasmon resonance supplies a weaker surface plasmon-polariton resonance with extra oscillator strength. As a result, the strength of the surface plasmon-polariton resonance increases considerably in the interaction region. The frequencies of Mie-plasmon resonance and plasmon-polariton resonance can be easily tuned by varying the diameter of the voids or by filling them with dielectric materials [7] and by varying the period of the void lattice, respectively. All this makes this type of nanoporous metals a very attractive choice for a variety of applications ranging from nanophotonics to biophysics.

Acknowledgements

We thank J. J. Baumberg, V. G. Golubev, and S. G. Tikhodeev for inspiring conversations. This work was supported by the Russian Foundation for Basic Research (Grant 02-02-81031) and the Russian Academy of Science Program "Low-Dimensional Quantum Nanostructures". T.V.T. acknowledges the support from the National Foundation for Promotion of Science, and also thanks the Donostia International Physics Center in San Sebastian, Spain, for hospitality during the preparation of this work. F.J.G.A. acknowledges help and support from the University of the Basque Country UPV/EHU (Contract No. 00206.215-13639/2001) and the Spanish Ministerio de Ciencia y Tecnología (Contract No. MAT2001-0946).

References

[1] A. Christ, T. Zentgraf, J. Kuhl *et al*, *et al*, *Phys. Rev. B* **70**, 125113 (2004).
[2] A. Christ, S. G. Tikhodeev, N. A. Gippius *et al*, *Phys. Rev. Lett.* **91**, 183901 (2003).
[3] S. Coyle, M. C. Netti, J. J. Baumberg *et al*, *Phys. Rev. Lett.* **87**, 176801 (2001).
[4] O. D. Velev, P. M. Tessier, A. M. Lenhoff *et al*, *Nature* **401**, 548 (1999).
[5] J. E. G. J. Wijnhoven, S. J. M. Zevenhuizen, M. A. Hendriks *et al*, *Adv. Mater.* **12** 888 (2000).
[6] N. Stefanou, A. Modinos, and V. Yannopapas, *Solid State Commun.* **118**, 69 (2001).
[7] T. V. Teperik, V. V. Popov, and F. J. García de Abajo, *Phys. Rev. B* [in press].
[8] T. V. Teperik, V. V. Popov, and F. J. García de Abajo, *Phys. Rev. B* **69**, 155402 (2004).
[9] M. Kreiter, S. Mittler, W. Knoll *et al*, *Phys. Rev. B* **65**, 125415 (2002).

13th Int. Symp. "Nanostructures: Physics and Technology"
St Petersburg, Russia, June 20–25, 2005

Possible realization of single-electron trap based on Cr granular film: experimental characterization and numerical simulation

V. A. Krupenin[1], *V. O. Zalunin*[1,4], V. S Vlasenko[1], D. E. Presnov[2] and A. B. Zorin[2,3]

[1] Laboratory of Cryoelectronics, Moscow State University, 119899 Moscow, Russia
[2] Nuclear Physics Institute, Moscow State University, 119899 Moscow, Russia
[3] Physikalisch-Technische Bundesanstalt, 38116 Braunschweig, Germany
[4] ST Microelectronics SA, Moscow Branch, 115114 Moscow, Russia

Abstract. We have studied possible realization of a single-electron trap on the basis of thin chromium granular films. These films function as chains of tunnel junctions in traditional trap structures. The films were formed by the evaporation of Cr in an atmosphere of pure oxygen. At 25 mK the value of Coulomb blockade threshold of our Cr trap structures varied in the range 10−30 mV. The parameters of the trap obtained from the measurements were used for a numerical simulation of the main device characteristics. In particular, the numerical simulations showed that the height of potential barrier of the trap is about 10 mV that is nearly one order of magnitude higher than corresponding value in traditional SET trap structures based on Al/AlO_x/Al tunnel junctions.

Introduction

Single-electron trap is probably the most interesting single-electron tunneling (SET) device functioning as a memory cell prototype. In this device information can be encoded by a presence or an absence of single electrons on the memory node. A single-electron memory cell consists of a SET trap capacitively coupled with SET transistor-readout electrometer. During the last two decades a number of experiments with single electron-traps of different kind had been carrier out (see [1,2] and references therein). Lithographic methods allow to fabricate nanostructures with excellent reproducibility, but the size of these structure elements can not be decreased below approximately 30 nm. For example, the element sizes of single-electron traps fabricated using this traditional shadow evaporation technique [1, 2] were about 100 nm and their operation temperature was limited by the level below approximately 100 mK. On the other hand, cluster-based and molecular-based single-electron structures enabling, in principle, operation at temperature up to 300 K are insufficiently reproducible and molecular single-electron traps have not been realized yet. Therefore, the application of granular thin film structures for implementation of SET devices seems very promising. The sizes of grains in these structures can be substantially smaller than the sizes of elements in lithographically patterned SET structures and, as a result, the working temperature can be much higher. At the same time granular structures can have reasonable reproducibility. In this paper we present a modified single-electron trap structure where the chromium granular films patterned by a lithographic method substitute the chains of tunnel junctions of traditional trap structures. These elements (one-dimensional chain or granular film stripe) form the controllable potential barrier for single charges entering or leaving the storage metallic island (node). Our design of a memory cell was based on numerical simulations and the experimental study of Cr granular films.

1. Fabrication of the samples

Our experimental structures consisted of a SET trap only (Fig. 1a), while a readout electrometer is planned to be fabricated in separate technological cycle with precision alignment of the storage island of the trap and a transducer (central island) of SET electrometer (see Fig. 1b). The trap structures were fabricated by double-shadow deposition technique [3] on Si substrate buffered by AlO_x layer 200 nm thick. The chromium films, aluminum counter electrodes and central (storage) island were formed in situ through a suspended mask

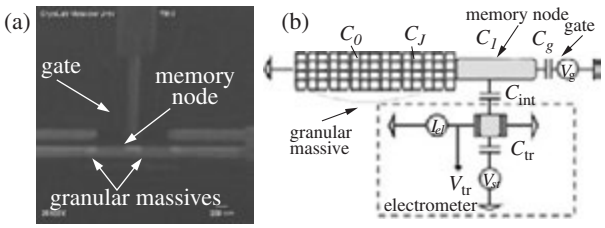

Fig. 1. (a) SEM Photo of the experimental trap structure with gate, storage island connected to two Cr films. (b) The electrical circuit diagram of SET trap based on Cr granular film with readout electrometer.

using e-gun evaporation system. The first (chromium) layer with a thickness of 7–8 nm was deposited in an atmosphere of pure oxygen at a pressure of 10^{-5} mbar. Secondly, the 30 nm thick aluminum electrodes and the storage island of the trap were formed. The electrodes had relatively large overlapping area (100 nm by 200 nm) to the chromium film (see Fig. 1a) that ensured the good electrical contact between granular structure and Al counter electrodes. The investigated groups of the samples had the different size of the storage central island (100 nm and 200 nm) and the identical width and length of chromium films (100 nm and 500 nm correspondingly).

2. Characterization of the samples

I–V characteristics of the samples were measured in a wide temperature range from 25 mK to 77 K. At temperature of 25 mK the experimental structures of SET trap exhibited a wide Coulomb blockade region (Fig. 2a). The threshold voltage for these samples varied in the range from 10−30 mV and slightly drifted in time by 2−3 mV.

It was shown in Ref. [4] that chromium granular films evaporated in the oxygen atmosphere have a granular structure, i.e. the film presents an array of conducting islands separated by thin chromium oxide layers ensuring tunnel conductivity. For this film we apply a model of two-dimensio-nal array of islands with stray capacitance to ground C_0. The islands are separated by tunnel junctions of capacitance C. In order to determine the value of C we have used the standard activation measurement technique. The Ahrenius plot for one of the investigated samples is given in Fig. 2b. Activation energy E_a of the samples varied in the range from 20 to 40 K. Assuming uniform array of tunnel junctions their mutual capacitance C can be calculated in following manner $C = e^2/8E_a$ [5]. Stray capacitance of a conducting island can be obtained from the value of threshold

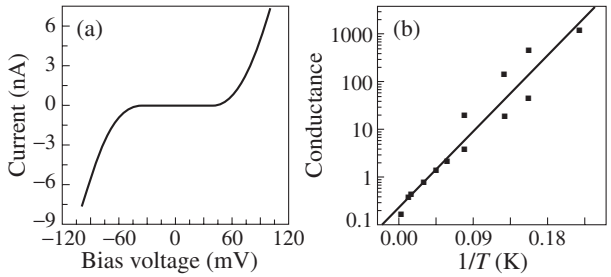

Fig. 2. Experimental characteristics of sample A1. (a) I–V curve of the trap (Fig. 1a) measured at 25 mK. Coulomb blockade threshold voltage is equal to 27 mV. (b) Ahrenius plot of the trap structure. Activation energy $E_a = 40.5$ K

Table 1. Experimental parameters of the fabricated chromium films.

Sample	E_a (K)	V_t (V)	C (aF)	C_0 (aF)
A1	40.5	27	5.72	0.20
A2	40.7	22	5.70	0.30
A3	22.8	10	11.26	0.75
A4	20.6	12	10.17	0.57

voltage V_t (see Ref. [6]), i.e. $C_0 = (1 - \frac{2}{\pi})^2 e^2/(4{V_t}^2 C)$. Values of E_a, C and C_0 for different samples are given in Table 1.

3. Numerical simulations

We have made some preliminary estimations towards fabrication of the fully functional device. Using the main electrical characteristics (C, C_0 and intergranular tunnel resistance R) of the granular array obtained from the experiment we have found the important parameters of the memory cell. These parameters are the required memory node stray capacitance C_s determined by the size of the storage island, the number of stable elementary charge states M in the trap, total capacitance C_M of the memory node. Values of the gate capacitance C_g and interaction capacitance C_{int} between the trap node and a readout SET electrometer were taken from consideration of technological convenience.

In the single-electron memory cell the information can be coded by the presence ("1") and the absence ("0") of one or several additional electrons on the storage island. The number of stable charge states M (maximum number of additional electrons for logical coding) on the memory node is determined by the height of the potential barrier and the charging energy of the electron on the node at $V_g = 0$. The more electrons encode logic state, the higher potential barrier has to be formed. The value of $M = 3-10$ provides a compromise between the desirable small number of electrons ensuring coding of the logic states and sufficiently large height of the barrier resulting in long storage time. According to preliminary numerical simulation using a Monte Carlo method, the trap structure with the memory node stray capacitance $C_s \sim 7$ aF (see Fig. 3a) demonstrated a reasonable number of stable states. Thus, the corresponding linear size of the storage island of the real structure should be about ~ 100 nm.

To compensate the exceeded charge of one electron on the memory node by the gate voltage $V_g \sim 2.5$ mV we took the corresponding capacitance $C_g = e/V_g = 50$ aF. To observe the charge dynamics in the trap a traditional Al SET transistor will be used as a readout electrometer. We took a coupling coefficient $K = 1/20$ which means that every entering/leaving electron on the memory node polarizes the transistor central island with a magnitude of $1/20e$. This value of a readout signal is more than one order higher then typical level of the background charge noise for Al SET transistor at low frequency. For the given value of K we estimated the interaction capacitance C_{int} to be about 3 aF. This value of C_{int} corresponds to the distance between the memory node and transistor central island to be about

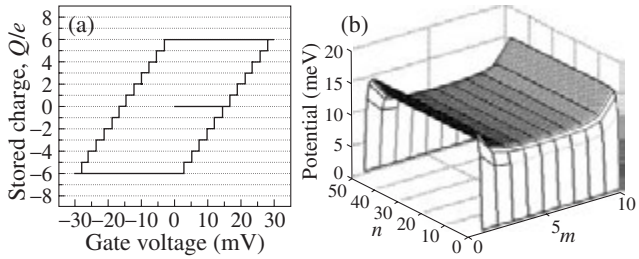

Fig. 3. Numerical simulation of single-electron trap characteristics for $C_s = 7$ aF, $C = 5.7$ aF and $C_0 = 0.7$ aF. (a) Charge hysteresis in the trap. The number of stable states is $M = 14$. (b) The shape of potential barrier formed by uniform array of metallic islands modeling the Cr granular film.

200−400 nm if the linear size of the island is equal to 100−200 nm. The available alignment technique can ensure such accuracy.

We had also found the shape of the barrier formed by the array of islands in the film. The plot has a saddle shape (see Fig. 3b). The important parameter of the trap is the barrier's height in the central part of the array, which corresponds to the main current channels in our case. For the studied sample the barrier's height obtained in simulations was about 11 mV. This value is more than 5 times higher than that of a typical SET trap in which the potential barrier is formed by the chain of Al/AlO_x/Al tunnel junctions [2] fabricated using traditional e-beam lithography technique. Therefore, we expect that the SET trap based on granular Cr film can have larger storage time allow further increase of operating temperature of this promising device.

4. Conclusion

The obtained results demonstrate the possibility to construct a single-electron trap based on granular Cr structures. The stand-alone trap structures were fabricated and studied at low temperatures. The parameters of the trap obtained from this experiment were used for a numerical simulation of the main device characteristics. These characteristics seem to be superior to those of traditional devices fabricated by e-beam lithography technique. Further investigation of Cr granular structures and SET devices on their basis is in progress.

Acknowledgements

This work has been supported by Russian Fund for Basic Research and Russian Ministry of Science.

References

[1] J. T. Lukens, P. D. Dresselhaus, S. H. L. Ji, K. K. Likharev and W. Zheng, *Physica B* **203**, 354 (1994).
[2] V. A. Krupenin, S. V. Lotkhov and D. E. Presnov, *JETP* **84**, 190 (1997).
[3] J. Niemeyer, *PTB Mitt.* **84**, 251 (1974); G. D. Dolan, *Appl. Phys. Lett.* **31**, 337 (1977).
[4] V. A. Krupenin, V. O. Zalunin and A. B. Zorin, *Proc. of 12th Int. Symposium "Nanostructures: physics and technology" (St Petersburg, 2004)*, Ioffe Institute, 352, 2004.
[5] P. Delsing, C. D. Chen, D. B. Haviland, Y. Harada and T. Claeson, *Phys. Rev. B* **50** (6), 3959 (1994).
[6] N. S. Bakhvalov, G. S Kazacha, K. K. Likharev and S. I. Serdyukova, *Physica B* **173**, 319 (1991).

13th Int. Symp. "Nanostructures: Physics and Technology"
St Petersburg, Russia, June 20–25, 2005

Impurity-induced metal-insulator transition in quasi-one-dimensional metals $TaSe_3$ and $NbSe_3$

A. V. Zavalko and S. V. Zaitsev-Zotov
Institute of Radioengineering and Electronics of the RAS, Moscow 125009, Mokhovaya St. 11/7, Russia

Abstract. Metal-insulator transition induced by impurity incorporation was observed in $TaSe_3$ and $NbSe_3$ samples. It was found out that conduction of nanometer-scale thickness $TaSe_3$ samples exhibits behavior expected for one-dimensional electron systems. Thick micrometer-scale $NbSe_3$ samples with impurities introduced by thermal diffusion show behavior similar to one observed earlier in nanoscale samples.

Introduction

Physical properties of one-dimensional (1D) electron systems differ dramatically from those of three-dimensional (3D) ones. Elementary excitations in one-dimensional electron systems are collective charge and spin boson modes, rather than fermion quasiparticles as in 3D metals. One of the widely-used models describing 1D electron systems is so-called Luttinger-liquid (LL) model [1]. The ground state of a LL is characterized by a power-law suppression of the tunneling density of states. Impurities in a LL act as tunneling barriers. Therefore, the conduction G of a LL with a single impurity is a power-law function of temperature, $G \propto T^{\alpha}$, and voltage, $G \propto V^{\alpha}$ [1]. In the Luttinger liquid the variable range hopping (VRH) conduction $G \propto \exp(C/T^{0.5})$ is expected in the presence of disorder [2].

The transition-metal trichalcogenides $NbSe_3$ and $TaSe_3$ are quasi-1D metals with chain-like structures [3]. X-ray study shows monoclinic crystal structures for both $NbSe_3$ and $TaSe_3$ [3]. Both materials grow as long thin fibrous ribbons or whiskers composed of trigonal prisms stacked along the fiber axis, which is parallel to b axis. Although the crystal structures are similar the transport properties show significant differences reflecting thereby the differences in the band structure and Fermi surfaces. $NbSe_3$ shows two Peierls transitions, which occur at 145 K and 59 K. Such anomalies are not observed in $TaSe_3$ which exhibits metallic behavior in the entire temperature range.

It was demonstrated that crystals of $NbSe_3$ with nanometer-scale-transverse sizes exhibit behavior expected for 1D electron systems [4]. It was also shown theoretically that introduction of impurities into quasi-1D conductors may stabilize there LL [5]. Here we demonstrate that introduction of impurities into both $NbSe_3$ and $TaSe_3$ crystals leads to a metal-insulator transition and produce a state very similar to one expected for 1D electron systems and observed earlier in nanoscale-sized $NbSe_3$ crystals [4].

1. Experimental

All studied crystals of $TaSe_3$ were picked up from a single growth batch, all studied $NbSe_3$ crystals were from one batch accordingly. Cross-sectional areas s were estimated from the resistance R at ambient temperature, taking the resistivity as 8 $\Omega\mu$m for $TaSe_3$ and 2 $\Omega\mu$m for $NbSe_3$. Crystals of $NbSe_3$ were quite pure with RRR $\equiv R(300\,\mathrm{K})/R(10\,\mathrm{K}) \approx 200$, RRR$\approx$ 30 for bulk $TaSe_3$ crystals.

$NbSe_3$ samples were prepared using mechanical cleavage technique [6]. Current and voltage terminals were made by In wires gently pressed to the surface of ribbon-like crystals. Introduction of indium impurities in $NbSe_3$ samples were made by thermal diffusion in the way described by J.C. Gill [7]. Namely, indium was incorporated in samples by heating to 400–420 K in vacuum (pressure = 0.03 torr) for hours. Indium atoms diffuse from terminals and presumably intercalate $NbSe_3$ chains. Effect of indium diffusion was detectable even in regions up to 2 mm apart the terminals. Expected atomic concentration of In exceeds 1% [7].

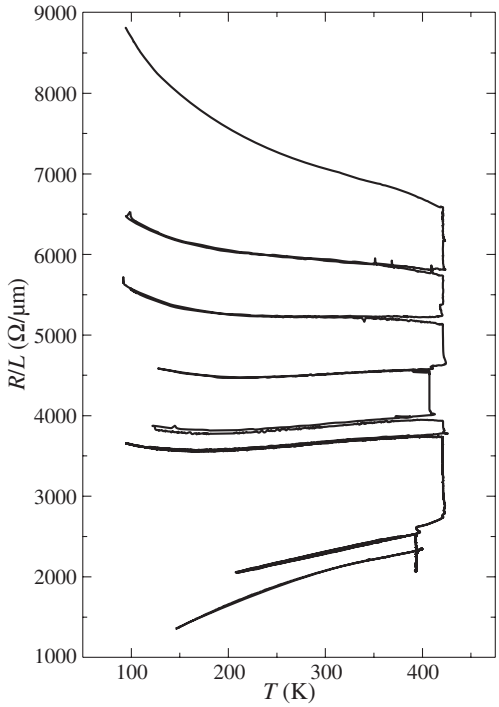

Fig. 1. Heating-induced evolution of temperature dependence of the unit length resistance R/L of $TaSe_3$ sample with nanoscale transverse dimensions. Initial sample resistance corresponds to $s = 4 \times 10^3$ nm^2.

For preparation of samples of $TaSe_3$, crystals were cleaved by electric field in vacuum [4,6]. Current terminals were prepared by vacuum deposition on In through a mask. Typical distance between the terminals was 10–30 μm. It was found, that resistance of a thin samples of $TaSe_3$ with $s < 10^{-2}$ μm^2 is growing during heating in vacuum or storage at room conditions. Growth of resistance during storage was observed earlier in thin $NbSe_3$ crystals [4,6]. Two-probe measurements were used for $TaSe_3$ samples, since influence of contact resistance in our thin crystals turned out to be negligible.

2. Results

Fig. 1 shows evolution of temperature dependence of the unit length resistance R/L of $TaSe_3$ sample with nanoscale transverse dimensions. The evolution is induced by heating in vacuum. Initially the sample shows metallic behavior of resistance R/L *vs* temperature, T, ($dR/dT < 0$). The heating changes the shape of $R(T)$ dependence and result in appearance of a minimum of R(T) and then nonmetallic low-temperature behavior ($dR/dT > 0$).

Samples of $TaSe_3$ with much higher R/L exhibit nonmetallic behavior. $R(T)$ dependencies for thinnest samples of $TaSe_3$ can be fitted by VRH dependence as shown on inset in Fig. 2. In addition, the resistance of such thin samples is found to depend on the voltage, V, changing R by orders of magnitude (see Fig. 2). $R(V)$ can be approximated by the power law $R \propto V^{-\beta}$ ($\beta = 1.25$). Nonlinear resistance is observed only in thinnest $TaSe_3$ samples at $T < 30$ K.

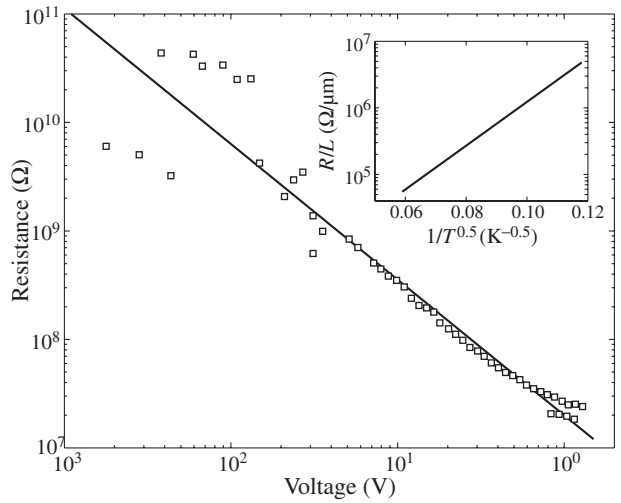

Fig. 2. Voltage dependence of resistance of $TaSe_3$ sample with $s = 140$ nm^2. $T = 13$ K. Inset shows temperature dependence of R/L. Straight line corresponds to 1D variable range hopping.

Fig. 3 shows a sequence of $R(T)$ dependencies of a bulk $NbSe_3$ sample after heating at $T = 400-420$ K. Total treatment time is 50 hours. As one can see from Fig. 3, the temperature dependence of resistance R of thick $NbSe_3$ sample also exhibits evolution similar to one shown in Fig. 1. Transition from metal-like to nonmetal-like behavior is observed.

3. Discussion

Transition from metallic to nonmetallic conduction behavior induced by increase of impurity concentration cannot be explained in conventional terms of 3D metal with impurities. Similar behavior of $R(T)$ curves for $TaSe_3$ samples with different thickness and similar R/L also cannot be explained just in terms of finite-size effects. As it was shown by Artemenko [5], the Luttinger liquid in linear-chain compounds can be stabilized by impurities and LL-like behavior reported earlier for thin $NbSe_3$ and TaS_3 samples [4] could be attributed to this mechanism. The results of the present study prove that diffusion of impurities in bulk samples have the same effect on the transport properties of q-1D metals as reduction of transverse sample sizes [4]. Observed VRH-like behavior of thinnest nanometer-scale $TaSe_3$ samples is consistent with properties of Luttinger liquid in the presence of disorder [2]. Thus, in general, our observations are in qualitative agreement with 1D models [1,2].

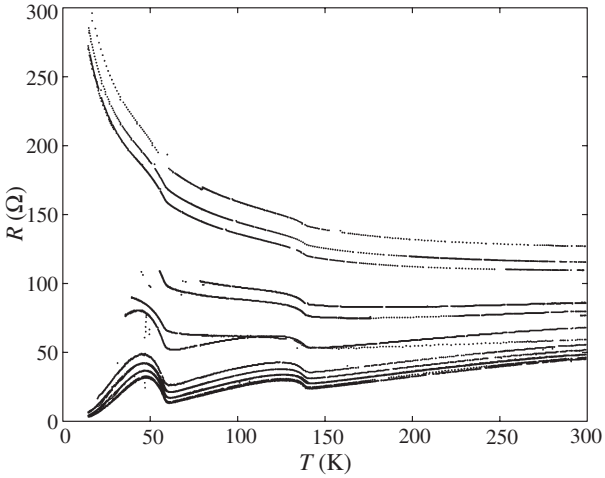

Fig. 3. Evolution of temperature dependence of the resistance of bulk $NbSe_3$ sample induced by heating. Initial sample resistance corresponds to $s = 20$ μm^2.

Acknowledgements

This research was performed in the frame of the CNRS-RAS-RFBR Associated European Laboratory "Physical properties of coherent electronic states in condensed matter" between CRTBT and IRE RAS. We are grateful to R. E. Thorne for providing batches of high-quality $NbSe_3$ crystals, Ya. S. Savitskaya and V. V. Frolov for high-quality $TaSe_3$ crystals, and S. N. Artemenko for duscussions. The work is supported by RFBR, CRDF and INTAS.

References

[1] J. Voit, *Rep. Prog. Phys.* 58 (1995) 977.
[2] S. V. Malinin, T. Nattermann, and B. Rosenow *Phys. Rev. B* **70**, 235120 (2004).
[3] For a review, see: P. Monceau, in: *Electronic Properties of Inorganic Quasi-one-dimensional Conductors*, Part 2. Ed. by P. Monceau. Dortrecht: D. Reidel Publ. Comp., 1985; G. Grüner, *Rev. Mod. Phys.* **60**, 1129 (1988).
[4] For a review see: S. V. Zaitsev-Zotov, *Pisma v ZhETF* **80**, 503 (2004) [*JETP Lett.* **80**, 445 (2004)]
[5] S. N. Artemenko, *Pisma v ZhETF* **79**, 335 (2004) [*JETP Lett.* **79**, 335 (2004)]
[6] S. V. Zaitsev-Zotov, *Uspekhi Fiz. Nauk* **174**, 585 (2004) [*Physics-Uspekhi* **47** 533 (2004)].
[7] J. C. Gill, *Phys. Rev. B*, **53**, 15586, (1996).

13th Int. Symp. "Nanostructures: Physics and Technology"
St Petersburg, Russia, June 20–25, 2005

Current driven instability in ferromagnetic junctions

R. J. Elliott[1], E. M. Epshtein[2], Yu. V. Gulyaev[2] and *P. E. Zilberman*[2]

[1] University of Oxford, Department of Physics, Theoretical Physics, Oxford OX1 3NP, United Kingdom
[2] Institute of Radio Engineering and Electronics of the Russian Academy of Sciences, Fryazino Branch, Fryazino, Moscow Region, 141190, Russia

Abstract. We consider theoretically a current flowing perpendicular to interfaces of a spin-valve type ferromagnetic metallic junction. For the first time a simultaneous action of the two current effects is investigated, namely, the nonequilibrium longitudinal spin injection and the transversal spin surface torque. Dispersion relations for fluctuations are derived and solved under the proper boundary conditions. Joint action of the two effects mentioned lowers the instability threshold, its typical value being $1 \times 10^6 - 3 \times 10^7$ A/cm^2. Spin wave excitations may soften near the threshold.

1. Motivation

Great attention is attracted now to features of current flowing through ferromagnetic junctions, i.e. structures with contacting ferromagnetic thin layers. As experiments showed, current effects substantially the layer magnetic state of such junctions that leads to resistance jumps [1], as well as microwave emission [2]. Two possible mechanisms of current effect are known: the spin injection [3, 4] and the surface torque [5, 6]. The mechanisms have been considered separately up to now. But in real experiments these two mechanisms coexist and influence each other. Therefore, both effects are to be taken into account simultaneously, in scope of a unified theory, to understand better the experimental situation. Such a theory is developed in the present work for the first time. We show the following principal results are valid: 1) the instability thresholds lower due to the joint action of the both current effects mentioned; the lowering may reach even more than one order of magnitude and 2) eigenfrequencies of the layer spin waves may become strongly current dependent and tend to zero as current rises to the threshold value.

2. Model and calculations

We consider a spin-valve type magnetic junction with current flowing perpendicular to the layer interfaces. Ferromagnetic metal layer **1** has pinned orientations of the lattice and mobile electron spins. Another ferromagnetic metal layer **2** with the lattice magnetization $\mathbf{M}$ and mobile electron magnetization $\mathbf{m}$ is assumed to contain free spins, so that the magnetization direction can be changed by an external magnetic field $\mathbf{H}$ or spin-polarized electric current density $\mathbf{j}$. There is a very thin nonmagnetic spacer between the layers **1** and **2**. To close the electric circuit, a nonmagnetic metal layer **3** is necessary.

Coupled system of equations is used to describe processes in the junction: Landau–Lifshitz–Gilbert equations for vector $\mathbf{M}$ and continuity equation for vector $\mathbf{m}$. The vectors mentioned interact due to *sd* exchange. Boundary conditions at the layer interfaces include longitudinal and transversal (with respect to $\mathbf{M}$) spin flux continuity. Dispersion equation for linear spin-wave fluctuations in the layer **2** may be presented in the form

$$q(\omega)L\tan(q(\omega)L) = -\Phi, \qquad (1)$$

where $\Phi \sim j$ and at $j = 0$ the equation transforms into standard dispersion relation for spin-wave resonance modes of the layer having thickness L and non-pinned surface spins, value $q(\omega)$ being the well-known wave number taken as a function of eigenfrequency ω [7]. The right-hand side Φ describes how the current influences the fluctuations. It contains real and imaginary contributions:

$$\mathrm{Re}\,\Phi = \frac{\alpha\mu_B Q L\tau}{AM}\left(\frac{j}{e}\right)\left[1 - \frac{\nu}{\sinh(L/l) + \nu\cosh(L/l)}\right],$$
$$\mathrm{Im}\,\Phi = \pm\frac{\mu_B Q L}{\gamma A M^2}\left(\frac{j}{e}\right), \qquad (2)$$

where μ_B is Bohr magneton, e is electron charge, γ is gyromagnetic ratio, $\alpha \sim 2 \times 10^4$ is dimensionless *sd* exchange constant, $\tau \sim 3 \times 10^{-13}$ s is spin relaxation time in metals at room temperature, $\sqrt{A} \sim 10^{-6}$ cm is intralattice direct exchange length, $0 < Q < 1$ is polarization degree of mobile electrons, $l \sim 3 \times 10^{-6}$ cm is spin diffusion length and $0 < \nu < 1$ is matching parameter between the layers **2** and **3**. The calculations show that the Re Φ contribution arises due to longitudinal spin injection effect whereas Im Φ is due to transversal spin surface torque.

3. Instability and spectrum of fluctuations

The condition of instability $\mathrm{Im}\omega \geq 0$ may be found from the equation (1) in the form

$$\kappa^2(\Omega_1 - \mathrm{Re}\,\Phi)(\Omega_2 - \mathrm{Re}\,\Phi) - (\mathrm{Im}\,\Phi)^2 < 0, \qquad (3)$$

where $\kappa \sim 10^{-3} - 3 \times 10^{-2}$ is Gilbert damping constant, dimensionless characteristic frequencies are: $\Omega_1 = L^2(H + H_a + 4\pi M)/AM$, $\Omega_2 = L^2(H + H_a)/AM$, H_a being an anisotropy field (typically: $H \sim H_a \sim 10 - 100$ Oe, $M \sim 10^3$ G and $\Omega_1 \gg \Omega_2$).

Two sources of instability are seen clearly from the condition (3): the spin injection, which is presented by Re Φ, and the surface torque, which is presented by Im Φ. The dissipation loss influences the sources in principally different ways. Dissipation is not substantial for injection type instability, because Re $\Phi > \Omega_2$ condition is sufficient. On the other hand, if only the torque retains, Re $\Phi \to 0$, then some threshold due to dissipation is to be overcome. At the same time, joint action of both mechanisms always decreases the left-hand part of (3) and, consequently, facilitates the instability appearance. Let us equate to zero the right-hand side of (3). We obtain then a quadratic equation for instability threshold current density j_{th}.

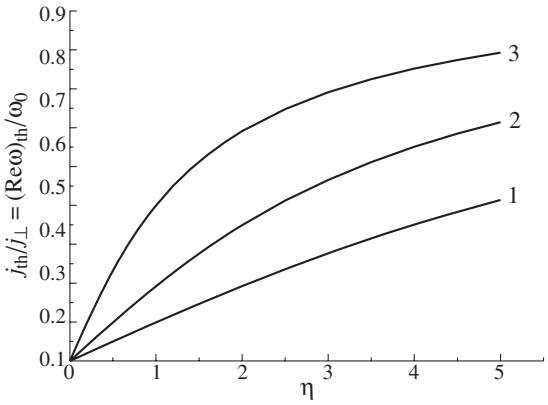

Fig. 1.

Fig. 1 shows the ratio $j_{\rm th}/j_\perp$ as a function of parameter $\eta = \mathrm{Im}\,\Phi/\kappa\mathrm{Re}\,\Phi$, current $j_\perp$ being the threshold for surface torque action only. The curves differ in the values of parameter $f = \sqrt{\Omega_2/\Omega_1}$: 1—$f = 0.1$; 2—$f = 0.2$; 3—$f = 0.5$. We see the injection always lowers threshold because the ratio becomes less than unity. The strongest lowering occurs at small values of η, when spin injection dominates. The lowering may be more than order of magnitude.

There is a very significant difference of the two instability mechanisms. Whereas surface spin torque inserts only an energy generation into the system, which should overcome dissipation loss, the spin injection effective field leads to reorientation phase transition. That is why the surface torque threshold depends strongly on the dissipation contrary to the spin injection threshold, which does not depend on it at all. Moreover, it is interesting to note that the spin injection influences not only the decrement but the spectrum of spin waves also. That is analogous to the well known common behavior near the point of phase transition. Eigenmodes become more and more soft, their frequencies tend to zero at the threshold. According to Fig. 1, the threshold ratio is equal to the ratio of frequencies ($\omega_0 = (\gamma AM/L^2)\sqrt{\Omega_1\Omega_2}$) and tends to zero when the spin injection dominates ($\eta \to 0$).

Acknowledgement

The work was supported by RFBR (Grant 03-02-17540).

References

[1] J. A. Katine, F. J. Albert, R. A. Buhrman et al., *Phys. Rev. Lett.* **84**, 3149 (2000).
[2] M. Tsoi, A. G. M. Jansen, J. Bass et al., *Phys. Rev. Lett.* **80**, 4281 (1998).
[3] C. Heide, P. E. Zilberman and R. J. Elliott, *Phys. Rev. B* **63**, 064424 (2001).
[4] Yu. V. Gulyaev, P. E. Zilberman, E. M. Epshtein and R. J. Elliott, *JETP Lett.* **76**, 155 (2002).
[5] J. C. Slonczewski, *J. Magn. Magn. Mater.* **159**, L1 (1996).
[6] L. Berger, *Phys. Rev. B* **54**, 9353 (1996).
[7] A. G. Gurevich and G. A. Melkov, *Magnetization Oscillations and Waves*, Boca Raton, FL: CRC Press, 1996.

13th Int. Symp. "Nanostructures: Physics and Technology"
St Petersburg, Russia, June 20–25, 2005

Shot noise in double barrier resonant diodes: a way to distinguish coherent from sequential tunneling

V. Ya. Aleshkin[1] and L. Reggiani[2]

[1] Institute for Physics of Microstructures, 603950 Nizhny Novgorod GSP-105 , Russia
[2] National Nanostructure Laboratory of INFM, Dipartimento di Ingegneria dell' Innovazione, Università di Lecce, Via Arnesano s/n, 73100 Lecce, Italy

Abstract. We implement a quantum approach to investigate current voltage characteristics and shot noise in double barrier resonant diodes. Theory applies to the region of low applied voltages up to the region of the current peak and considers the wide temperature range from zero to room temperature. It is shown that shot noise can be suppressed with a Fano factor well below the value of 0.5. This feature is a signature of coherent tunnelling since the standard sequential tunnelling predicts in general a Fano factor equal to or greater than the value of 0.5. This giant suppression is a consequence of Pauli principle as well as long range Coulomb interaction.

Introduction

The microscopic interpretation of electron transport in double barrier resonant diodes (DBRDs) is found to admit a coherent or a sequential tunneling approach [1]. The coherent approach [2] consists in considering the whole device as a single quantum system characterized by a transmission coefficient describing carrier transport from one contact to the other. This approximation is valid when the probability of electron scattering inside the quantum well is negligible in comparison with the probability of electron tunneling to the contacts. In the opposite case the sequential approach is used. The sequential approach [3] consists in considering tunneling through the diode as a two step process where carriers first transit from one contact into the well, then from the well to the other contact. The intriguing feature of these two approaches is that from the existing literature it emerges that both of them are capable to explain the I–V experimental data [4] as well as most of the shot noise characteristics. Therefore, to our knowledge there is no way to distinguish between these two transport regimes and the natural question whether the tunneling transport is coherent or sequential remains an unsolved one.

The coherent approach to shot noise in DBRD has received wide attention since the first experimental evidence by Li *et al* [5] of shot noise suppression with a minimum value of the Fano factor $\gamma = S_I/(2qI) = 0.5$, here S_I is the low frequency spectral density of current fluctuations and q the absolute value of the unit charge responsible of current. Remarkably, most of the coherent approaches developed so far (see bibliography in [1]) predict a maximum suppression $\gamma = 0.5$ even if there is clear experimental evidence of suppression below this value [6,7,8] down to values of $\gamma = 0.25$. To this purpose, some authors obtained theoretical values of the Fano factor just below the value of 0.5, [9,10]. However, the physical interpretation of these results remains mostly qualitative. We remark that the theory of shot noise in DBRDs under the sequential approach [11] provides a Fano factor of 0.5 as the minimum value of shot noise suppression.

The aim of this work is to report a coherent theoretical approach for current voltage and electronic noise in DBRDs accounting for Pauli principle and long range Coulomb interaction going beyond existing models. We anticipate that the main result of the present approach concerns with the prediction that suppression of shot noise with a Fano factor below 0.5 is a signature of coherent tunneling against sequential tunneling.

1. Model

The typical diode investigated here is the standard double well structure depicted in Fig. 1. We denote by $\Gamma = (\Gamma_L + \Gamma_R)$ the resonant states width, by ε_r the energy of the resonant level as measured from the center of the potential well and by $\Gamma_{L,R}$ the partial widths due to the tunnelling through the left and the right barrier, respectively. We consider the case of coherent tunnelling in the presence of only one resonant state and we assume that the diode has contacts with unit square surfaces. For convenience, calculations are carried out using the cgs system.

The kinetic model is developed by assuming that the electron distribution functions in the emitter and in the collector, f_α, are equilibrium-like, but with different electro-chemical potentials F_α:

$$f_\alpha(\varepsilon, F_\alpha) = \frac{1}{1 + \exp\left(\frac{\varepsilon - F_\alpha}{k_B T}\right)}, \qquad (1)$$

here $\alpha = L$ stands for the left contact (the emitter), $\alpha = R$ for the right contact (the collector), k_B is the Boltzmann constant, T the bath temperature and ε the carrier energy.

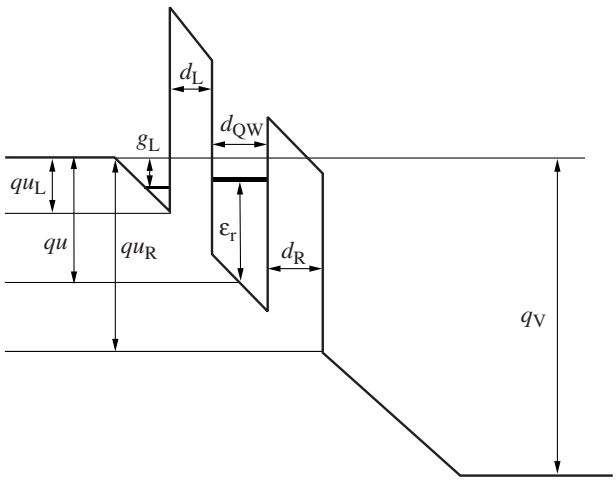

Fig. 1. Sketch of the band profile of the double barrier structure.

The full Hamiltonian of the structure is

$$H = H_L + H_R + H_{\rm res} + H_{\rm tun} \tag{2}$$

here

$$H_\alpha = \sum_{p_\perp}\sum_{p_\alpha}(E(p_\alpha) + p_\perp^2/2m)c_\alpha^+(p_\alpha, p_\perp)\, c_\alpha(p_\alpha, p_\perp)$$

are the Hamiltonians of the right and left contacts, c_α^+ and c_α the creation and annihilation operators of electrons in contact α, $p_\perp$ and p_α the momentum components perpendicular and parallel to the direction of the current, respectively, m is the effective electron mass in the conduction band, $E(p_\alpha) + p_\perp^2/2m$ the electron energy in the α contact,

$$H_{res} = \sum_{p_\perp}\left(E_r + p_\perp^2/2m\right) a^+(p_\perp)\; a(p_\perp)$$

is the Hamiltonian of the resonant states, $E_r = \varepsilon_r - qu$ with u the voltage drop between the emitter and the center of the quantum well, $-q$ the electron charge, a^+ and a the creation and annihilation operators of electrons in the resonant level, and

$$H_{\rm tun} = \sum_{p_\perp,\alpha}\left(T_\alpha a^+(p_\perp)\sum_{p_\alpha} c_\alpha(p_\alpha, p_\perp) + hc\right)$$

the part of the Hamiltonian describing the electron tunneling, with T_α the amplitude of tunneling between the resonant state and the αth contact.

The current operators for the left and right contacts $I_{L,R}$ and for the total current I are:

$$I_\alpha(t) = -\frac{iq}{\hbar}\sum_{p_\alpha,p_\perp}\left(T_\alpha a^+(t, p_\perp)c_\alpha(t, p_\alpha, p_\perp) - hc\right) \tag{3}$$

$$I = \eta I_L - (1-\eta)I_R \tag{4}$$

where $\eta = u/V$, V being the total applied voltage (see Fig. 1), $a^+(t, p_\perp)$, $c_\alpha(t, p_\alpha, p_\perp)$ are operators in the Heisenberg representation. From Eqs. (3) and (4) we find the usual expression for the average current

$$\langle I\rangle = \langle I_L\rangle = -\langle I_R\rangle = \frac{qm}{2\pi^2\hbar^3}\int_{-g_L}^{\infty} d\varepsilon_z D(\varepsilon_z) \times \int_0^\infty d\varepsilon_\perp\left[f_L(\varepsilon, F_L) - f_R(\varepsilon, F_R)\right] \tag{5}$$

where $\varepsilon_\perp = p_\perp^2/2m$ is the kinetic energy of the transverse motion, $\varepsilon = (\varepsilon_z + \varepsilon_\perp)$, g_L (u_L) the energy gap between the bottom of the conduction band and the first quantized level in the well before the left barrier (see Fig. 1), $D(\varepsilon_z)$ the transparency of the double barrier given by:

$$D(\varepsilon_z) = \frac{\Gamma_L\Gamma_R}{(\varepsilon_z - \varepsilon_r + qu)^2 + \frac{\Gamma^2}{4}}$$

To calculate the spectral density of current fluctuations at zero frequency under fixed voltage we use the expression:

$$S_I(0) = \int_{-\infty}^{\infty} dt\langle\delta I(0)\delta I(t) + \delta I(t)\delta I(0)\rangle. \tag{6}$$

We anticipate that the total current fluctuation consists of two sources. The first comes from the fluctuation of population states in the contacts and the second from the fluctuation of the electron charge in the quantum well $\delta Q_{\rm QW}$ [12] which changes structure transparency. Accordingly, $S_I(0)$ is found to be given by the sum of three terms as:

$$S_I(0) = S_1 + S_2 + S_3 \tag{7}$$

Expressions for S_1, S_2, S_3 are presented in [13]. It is possible to prove [13] that Eq. (7) satisfies the Nyquist theorem and $S_I(0) \to \infty$ on the border of instability region where $d\langle I\rangle/dV \to \infty$.

2. Results and discussion

We investigate the condition of high applied voltages, when $qV > F_R$, because more close to experiments. (We recall that typical magnitudes for the relevant parameters of DBRDs are: for Γ less than a few meV, for F_L less than 100 meV, and for the voltage at the peak current around 0.5 V.) Then, at zero temperature the expressions for the current and Fano factor become:

$$\langle I\rangle = \frac{qm\Gamma_L\Gamma_R}{4\pi^2\hbar^2}B(f,\xi) \tag{8}$$

$$\gamma = 1 - \frac{4\Gamma_L\Gamma_R}{\Gamma^2}\left\{1 - \lambda\frac{(\Gamma_L - \Gamma_R)}{\Gamma} - \lambda^2\frac{\Gamma_L\Gamma_R}{\Gamma^2}\right\}\frac{A(f,\xi)}{B(f,\xi)} \tag{9}$$

where

$$A = (f+\xi)\left[\frac{f+\xi}{1+(f+\xi)^2} + \arctan(f+\xi) - \frac{\xi}{1+\xi^2} - \arctan(\xi)\right] + \frac{1}{1+(f+\xi)^2} - \frac{1}{1+\xi^2},$$

$$B(f,\xi) = 2(f+\xi)\left[\arctan(f+\xi) - \arctan(\xi)\right] - \ln\left(\frac{1+(f+\xi)^2}{1+\xi^2}\right),$$

and for convenience we define dimensionless chemical potential f and voltage drop ξ as

$$f = \frac{2(F_L + g_L)}{\Gamma}, \quad \xi = \frac{2(qu - \varepsilon_r - g_L)}{\Gamma}$$

The Coulomb interaction is described by the dimensionless parameter λ

$$\lambda = \frac{\hbar\Gamma}{\Gamma_L\Gamma_R}\frac{1}{(C_L + C_R + C_{\rm QW})}\frac{\partial\langle I\rangle}{\partial u}.$$

where C_L, C_R, $C_{\rm QW}$ are the capacitances of the emitter, the collector and the quantum well, respectively. If $f \gg 1$ and the resonant level is located below the the Fermi level of the emitter far from its borders F_L and $-g_L$, i.e. $\xi \ll -1$, $f + \xi \gg 1$, then $A(f,\xi)/B(f,\xi) \approx 1/2$ and Eq. (9) recovers the expression given in [12]

$$\gamma = \frac{\Gamma_L^2 + \Gamma_R^2 + 2\Lambda(\Gamma_R - \Gamma_L) + 2\Lambda^2}{\Gamma^2}, \tag{10}$$

with $\Lambda = -\lambda\Gamma_L\Gamma_R/\Gamma$. As it will be shown below, when $f \gg 1$ the values taken by γ in Eq. (10) are practically constant and correspond to the plateau exhibited by $\gamma(f,\xi)$. On

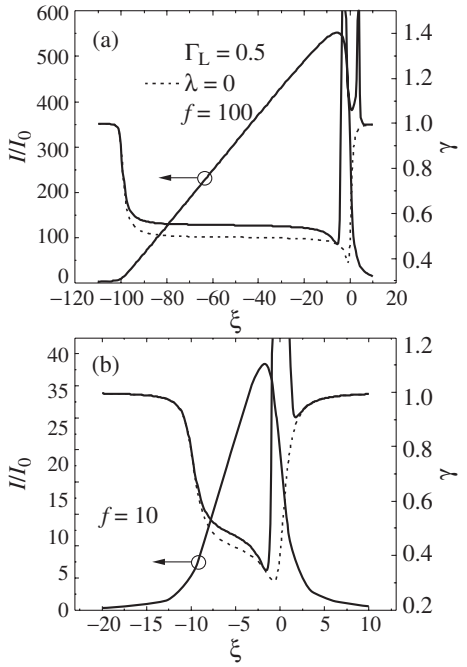

Fig. 2. Dependence of the Fano factor and of the dimensionless current on the dimensionless electrical potential $\xi = 2(qu - \varepsilon_r - g_L)/\Gamma$ at $T = 0$ K. Curves 1, 2, and 3 correspond, respectively, to dimensionless chemical potentials $f = 1, 15, \infty$. Here $f = 2(F_L + g_L)/\Gamma$ and $I_0 = qm\Gamma_L\Gamma_R/(2\pi^2\hbar^3)$.

this plateau, $1 \geq \gamma \geq 1/2$ and shot noise is suppressed. Now we demonstrate that at voltage values for which the resonant level is close to the band edge of the emitter the Fano factor can drop below the value 1/2. To this purpose, we first consider the simplified model by taking $\kappa = 12.9$ (GaAs), $C_L = C_R = \kappa/4\pi d$, $d = 5$ nm. Figure 2 reports the dependencies of current and Fano factor on ξ for the two values $f = 100$ (Fig. 2(a)), $f = 10$ (Fig. 2(b)) when $\Gamma_L = \Gamma_R$ and in the presence (continuous curves) or absence (dotted curves) of Coulomb interaction. The figure shows that for large values of the ratio between the Fermi energy and the resonant width ($f = 100$), $\gamma(\xi)$ exhibits a wide plateau region where $\gamma \approx 0.55$ followed by a minimum with $\gamma_{\min} \approx 0.46$. By further increasing the value of f ($f = 1000$) the plateau region is found to widen and $\gamma_{\min} \approx 0.49$. Note that, as it follows from Eq. (10), Coulomb interaction always increases the noise if $\Gamma_L = \Gamma_R$. With the decrease of f (see Fig. 2(b) where $f = 10$), the plateau region narrows and the value of $\gamma_{\min}$ decreases. Such a decrease of $\gamma_{\min}$ is due to two complementary reasons. The first is associated with the decreasing of the strength of Coulomb interaction. The second is associated with the increase of the effective barrier transparency near to the current peak and in turn with the further suppression of partition noise. For the ideal case $f \ll 1$, at the peak current the transparency $D \to 1$ and in turn $\gamma_{\min} \to 0$.

To confirm the possibility of evidencing the giant suppression $\gamma_{\min} < 0.5$ in a real structure, Fig. 3 presents the calculations performed with a set of parameters related to the experiments in [6] at $T = 4.2$ K and where both a symmetric (continuous curve) and an asymmetric (dashed curve) are considered. The structure parameters are $n = 2 \times 10^{16}\,\mathrm{cm}^{-3}$, $d_L = d_R = d_{\mathrm{QW}} = 5$ nm, squared area of contacts 50 $\mu\mathrm{m}^2$ and $L = 50$ nm, $m = 0.067\,m_0$, with m_0 the free electron mass and

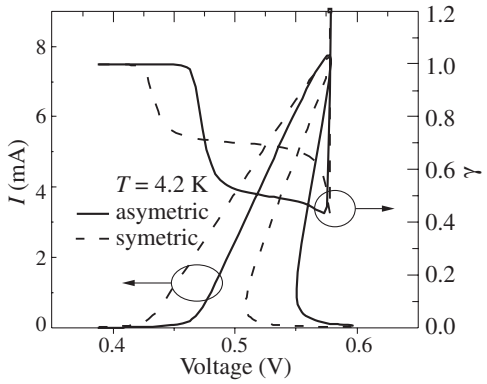

Fig. 3. Dependence of the current and Fano factor on applied voltage for the structure of [6] at $T = 4.2$ K. Values of $\Gamma_{L,R}$ and ε_r are chosen from the fitting current voltage characteristic at 77 K.

$\kappa = 12.9$. In the symmetric structure, the only two fitting parameters are $\Gamma_L = 0.5\Gamma = 0.48$ meV and $\varepsilon_r = 104$ meV. Their values control the location and the amplitude of the current peak, respectively, and are chosen by optimizing the agreement between the experimental and calculated I–V characteristics at 77 K. For the asymmetric structure there are three parameters and we take $\Gamma_L = 0.25\Gamma$, $\Gamma = 1.22$ meV, $\varepsilon_r = 112$ meV. Calculations give $\gamma_{\min} = 0.43$ in reasonable agreement with the value of 0.35 found in experiments [6]. From Fig. 3 we see that both the I–V and the noise characteristics are sensitive to the asymmetry of the structure, as expected. In any case, the main features of both characteristics are preserved.

Acknowledgements

This research was performed within the project "Noise models and measurements in nanostructures" supported by the Italian Ministery of Education, University and Research (MI UR) through the cofin03. Partial support from the NATO Science Programme (NATO LINKAGE grant PST. EAP. CLG 980629), and the SPOT-NOSED project IST-2001-38899 of the EC is gratefully acknowledged.

References

[1] Y. M. Blanter and M. Büttiker, *Phys. Rep.* **336**, 1 (2000).
[2] L. L. Chang *et alAppl. Phys. Lett.* **24**, 593 (1974).
[3] S. Luryi *Appl. Phys. Lett.* **47**, 490 (1985).
[4] S. Datta *Electronic transport in mesoscopic systems*. Cambridge University Press 1995.
[5] Y. P. Li *et alPhys. Rev. B* **41**, 8388 (1990).
[6] E. R. Brown *IEEE Trans. Electron. Dev.* **39**, 2686 (1992).
[7] A. Przadka *et alAppl. Phys. Lett.* **71**, 530 (1997).
[8] V. Kuznetsov *et alPhys. Rev. B* **58**, R10159 (1998).
[9] J.C. Egues *et alPhys. Rev. B* **49**, 13517 (1994).
[10] M. Jahan and A. Anwar *Solid-State Electron.* **38**, 429 (1995).
[11] G. Iannaccone *et alPhys. Rev. B* **55**, 4539 (1997).
[12] Y.M. Blanter and M. Büttiker *Phys. Rev. B* **59**, 10217 (1999).
[13] V.Ya. Aleshkin *et al*, *Phys.Rev.B* **70**, 115321 (2004)

13th Int. Symp. "Nanostructures: Physics and Technology"
St Petersburg, Russia, June 20–25, 2005

Resonant tunneling in strain compensated Si/SiGe quantum wells and superlattices

M. Scheinert[1], S. Tsujino[1], U. Gennser[2], C. V. Falub[1], G. Scalari[3], E. Müller[1], A. Weber[1], H. Sigg[1] and *D. Grützmacher*[1]

[1] Laboratory for Micro- and Nanotechnology, Paul Scherrer Institute, CH-5232 Villigen, Switzerland
[2] CNRS-LPN, F-91960 Marcoussis, France,
[3] Institute of Physics, University of Neuchâtel, CH-2000 Neuchâtel, Switzerland

Extending the possible device applications based on Si has lately drawn large attention in semiconductor electronics and opto-electronics. Popular approaches like quantum cascade lasers and even some ideas on spintronics employ vertical transport via tunnelling. Here, resonant tunnelling devices (RTDs) may be used in conjunction with the injection and detection of spin currents [1,2]. Strain compensated Si/SiGe structures with their large band offsets and pronounced strain splitting of light and heavy hole levels provide unique design freedom to perform experiments giving detailed insights into the physics of these systems. Moreover, the large band discontinuities (∼600 meV) in $Si_{0.2}Ge_{0.8}$/Si quantum well structures grown on $Si_{0.5}Ge_{0.5}$ virtual substrates is advantageous for designing p-SiGe quantum cascade devices [3].

In our present study resonant tunnelling diodes and superlattices have been deposited by low temperature (300˚C) molecular beam epitaxy (MBE) using e-beam evaporation for Si and Ge. The required p-type doping was achieved by Boron evaporation from a solid high temperature source. Three different diode structures have been deposited. The basic structure contains a $Si_{0.2}Ge_{0.8}$ quantum well sandwiched between Si barriers, and in the emitter and collector regions the Ge concentration is ramped from 50 to 80% towards the Si barriers (sample A). In the second type of samples an additional very thin Si barrier was placed in the centre of the $Si_{0.2}Ge_{0.8}$ well (sample B), while in the third structure the Ge concentration in the emitter and collector was only ramped to 65% (sample C). The superlattice structures contain 30 periods of closely spaced $Si_{0.2}Ge_{0.8}$ quantum wells and Si barriers. The dimensions of SiGe well and Si barrier width were chosen to achieve strain compensation and formation of minibands for the hole states at zero bias.

Figure 1 shows the schematic valence band diagram (top) and the IV characteristics (bottom) of samples A and B. Both curves show 3 clearly resolved resonances. The introduction of the 0.5 nm thick silicon spike into the 3.5 nm thick $Si_{0.2}Ge_{0.8}$ well in sample B results in a strong shift of the first peak, whereas the second and third peak are hardly affected. This indicates that the first resonance can be assigned to the heavy hole ground state (HH_1) and the second one to the first excited heavy hole state (HH_2), whose energy is less affected by the centre Si spike in the well due to the asymmetry of the wavefunction. This assignment agrees with the dependence of the confinement shift of these peaks with well width. The shifts due to a central potential spike in a well in combination with magnetotunnelling spectroscopy demonstrate that the first two resonances are due to tunnelling through heavy hole levels, whereas there is no trace of tunnelling through the first light hole state (LH_1), demonstrating for the first time the conservation of the total angular momentum in valence band resonant tunnelling.

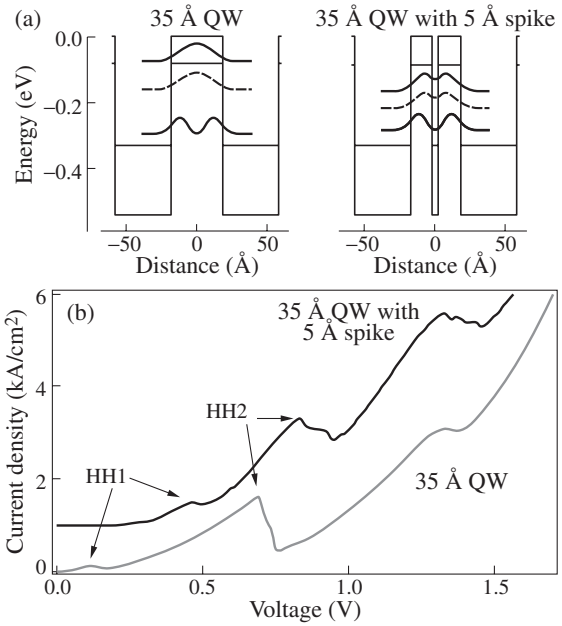

Fig. 1. a,b: Schematic band diagram and IV curves of Si/$Si_{0.2}Ge_{0.8}$ resonant tunneling structures grown on relaxed $Si_{0.5}Ge_{0.5}$ buffer layers.

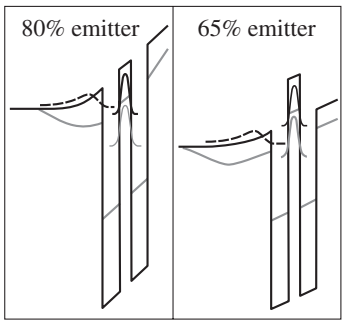

Fig. 2. Schematic view of the valence band structure of resonant tunneling diodes having 80% and 65% Ge in the emitter. Black and grey solid lines represent HH and LH band edge as well as the confined wavefunctions, respectively. The dashed line illustrates the confined emitter wavefunction.

The reduction of the Ge concentration in the emitter and collector state for sample C shifts the HH_1 state below the band edge in the emitter and reduces the splitting between heavy hole and light hole states in the emitter from ∼86 to ∼50 meV. Here

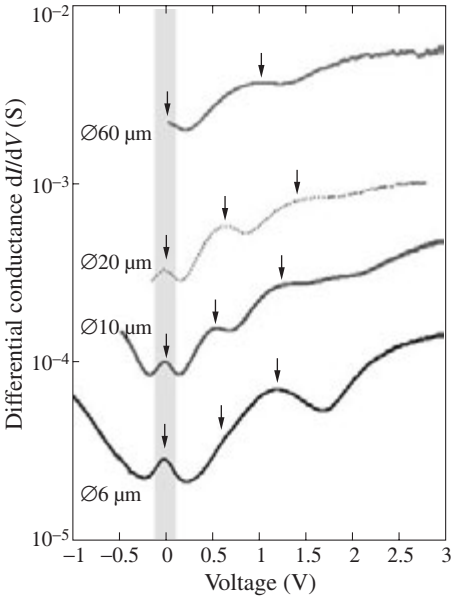

Fig. 3. Differential conductance of $Si/Si_{0.2}Ge_{0.8}$ superlattice resonant tunneling diodes with diameters ranging from 60 down to 6 μm.

the differential IV curve indicates that conduction through light hole states is possible and is assigned to tunnelling of carriers from bulk emitter states. This explanation is reasonable due to the change of the barrier for the light holes initiated by the reduced heavy to light hole splitting in the emitter. A schematic comparison of the valence band edge for the samples A and C is depicted in Fig. 2. Once again magneto-tunnelling experiments confirm this assignment.

Figure 3 shows the differential conductance vs. voltage for a strain compensated $Si/Si_{0.2}Ge_{0.8}$ superlattice with 1.2 nm wide barriers and 2 nm wide wells. Diodes with diameters from 60 to 6 μm have been fabricated. The resonance at zero bias is attributed to miniband transport via HH_1 states. The resonances found at higher voltages are assigned to tunnelling from localized HH_1 Wannier Stark states to spatially extended LH_1 Wannier Stark states. Thus tunnelling between HH states and LH states located in the second, third and fourth nearest neighbour QW could be obtained. Finally, it should also be noted that these results may have an additional relevance for the development of a Si/SiGe based quantum cascade laser, in they give insights into possible non-radiative conduction paths for the HH carriers in these structures.

Acknowledgements

We are grateful to STMicroelectronics for the supply of relaxed buffer layers. Financial support by the Swiss national science foundation and the European community (SHINE project) is highly acknowledged.

References

[1] K. C. Hall, *et al*., *Appl. Phys. Lett.* **83**, 2973 (2003).
[2] M. M. Glasov, *et al*., cond-mat 0406191 (2004).
[3] L. Diehl, *et al*., *Appl. Phys. Lett.* **81**, 4700 (2002).

13th Int. Symp. "Nanostructures: Physics and Technology"
St Petersburg, Russia, June 20–25, 2005

Tunnelling between two-dimensional hole layers in GaAs

E. N. Morozova[1], V. Renard[2], Yu. V. Dubrovskii[1], V. A. Volkov[3], L. Eaves[4], J.-C. Portal[2,5,6], O. N. Makarovskii[4], M. Henini[4] and G. Hill[7]

[1] Institute of Microelectronics Technology RAS, 142432 Chernogolovka, Russia
[2] Grenoble High Magnetic Field Laboratory, MPI-CNRS, BP166 38042 Grenoble Cedex 9, France
[3] Institute of Radioengineering and Electronics RAS, Moscow, Russia
[4] The School of Physics and Astronomy, University of Nottingham, Nottingham NG7 2RD, UK
[5] INSA, F31077 Toulouse Cedex 4, France
[6] Institute Universitaire de France, 103, Boulevard Saint-Michel, 75005 Paris, France
[7] Department of Electrical and Electronics Engineering, University of Sheffield, Sheffield S3 3JD, UK

Abstract. The studies of resonant tunnelling between identical parallel two-dimensional hole accumulation layers in GaAs at low temperatures down to 2 K are presented. To identify features in tunnelling spectra we take measurements in magnetic field normal to the layers. We reveal resonant tunnelling between "heavy hole 1" ground occupied subband and empty states of "light hole 1" and "heavy hole 2" subbands. The resonant tunnelling between "heave hole 1" subband states is suppressed. Resonant tunnelling into "light hole 1" is weak at lowest temperatures but becomes pronounced with temperature increase up to 7 K. We discuss our findings in terms of different tunnel coupling between hole states of different subbands and of intralayer Coulomb interaction.

The tunnelling spectroscopy provides a tool for direct measurements of a tunnelling density of states (TDOS), which is strongly sensitive to many-electron phenomena in low-dimensional electron systems. As a result of the intra- and interlayer electron-electron Coulomb interaction in double two-dimensional electron systems many phenomena were found recently by tunnelling spectroscopy. The most impressive ones were the following: induction of the hard gap in TDOS at the Fermi level of high quality 2DES by magnetic field [1]; development of the soft gap with magnetic field in the case of disordered 2DES's [2,3]; resonantly enhanced tunnelling in a double layer quantum Hall ferromagnet [4]; Fermi edge singularity at zero bias in tunnelling between strongly couple disordered 2DES's [5]. In all above works correlation effects were studied in electron systems. One should expect more pronounced many body phenomena in systems with higher effective mass, since the interaction parameter r_S is equal to the ratio of Coulomb to Fermi energy in the two-dimensional system. For GaAs the direct way would be the studies of tunnelling between parallel two-dimensional hole systems (2DHS).

In this work we present our studies of tunnelling between parallel near identical accumulation 2DHS at low temperatures (1.8–29 K) and in magnetic fields up to 15 T normal to the layers. In equilibrium only low energy heavy holes (HH1) subbands are occupied in the accumulation layers. Next light holes subband (LH1) are empty. We have not found any features related with resonant tunnelling between HH1 subbands. Resonant tunnelling from HH1 subband to LH1 subband is partially suppressed and associated features becomes more pronounced with temperature increase. We discuss our findings in terms of different tunnel coupling between different subbands in the layers and suppression of the tunnel current by intralayer Coulomb interaction.

The MBE-grown sample was a single barrier GaAs/$Al_{0.4}Ga_{0.6}As$/GaAs heterostructure with a 5.1 nm thick barrier. The barrier was separated from the highly-doped bulk contact regions by 24.3 nm thick undoped GaAs spacer layers. Si donor δ-layer sheets with concentration of $5 \times 10^{11}\,\mathrm{cm}^{-2}$ were located 3.9 nm from each side of the barrier. In our experiments we used two types of samples.

In our experiments, hole transport along the layers does not contribute to the measured current, which flows perpendicular to the plane of the barrier. The tunnelling transparency of the main barrier is much lower than that of the spacer regions, so that most of the applied voltage is dropped across the barrier. Samples were fabricated into mesas of diameter 50 or 100 μm.

To identify features in tunnelling spectra we take measurements in magnetic field normal to the layers. Figure 1 shows the differential tunnel conductance G versus external bias voltage V_b in various magnetic fields from 0 T to 15 T measured using standard lock-in techniques at $T = 7$ K for "type 1" sample. Both types of samples shows the same features on tunnelling spectra with magnetic field. The curves are near symmetrical for both polarities, so we present data for negative bias, which are slightly more pronounced. Figure 2 shows fan diagram of the peaks position versus magnetic field. Fan

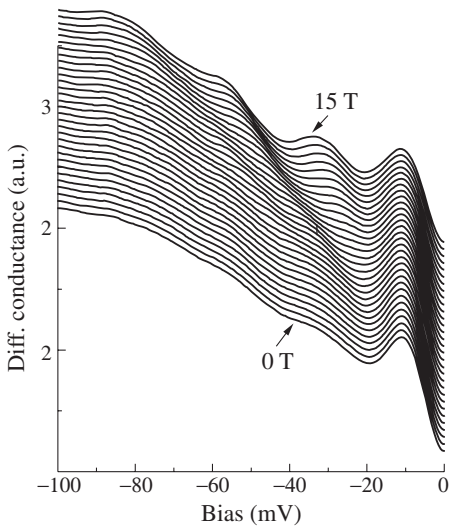

Fig. 1. The differential tunnel conductance G versus external bias voltage V_b in various magnetic fields from 0 T (lowest) to 15 T (top). Magnetic field step between curves $\Delta B = 0.5$ T. The curves are shifted for clarity in vertical direction. $T = 7$ K.

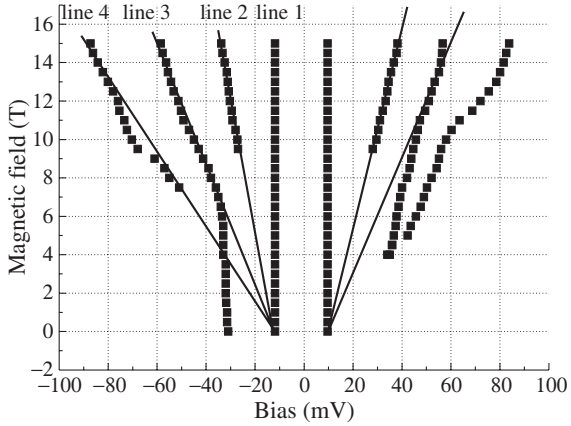

Fig. 2. Fan diagram of the peaks position versus magnetic field.

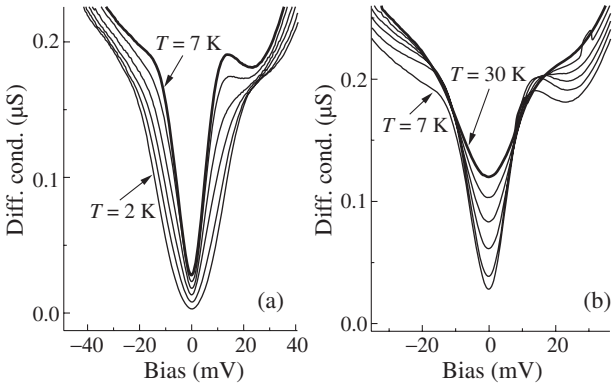

Fig. 3. The differential tunnel conductance G versus external bias voltage V_b in zero magnetic field at two temperature ranges: 2–7 K (Fig 3(a)) and 7–30 K (Fig 3(b)).

diagram is symmetrical about zero bias.

The data in Figure 2 have been compared with calculation of the energy levels in magnetic fields [6]. It should be noted that two-dimensional valence band in plane subbands dispersions are strongly non parabolic. All subbands are spin degenerated only at $k = 0$. At $k \neq 0$ all subbands (HH1, LH1 and others) are split to so called "spin subbands". In magnetic field line 1 corresponds to the tunnelling from unresolved occupied Landau levels states of HH1 subband into unresolved Landau level states with index $n = 0,\ 1,\ -1$ of LH1 subband. Line 2 corresponds to the tunnelling into unresolved Landau level states with index $n = 2,\ 3$ of LH1 subband. In fact this comparison is quite accurate. The slope of the line 2 in the Figure 2 equals to 1.5, when the theoretical value is 0.95. Identification of the lines 3 and 4 in magnetic field meet problems since we are not aware of theoretical calculations of energy levels of other subbands in a magnetic field. Simple comparison with calculations without magnetic field suggests that line 3 in low magnetic fields corresponds to tunnelling into HH2 states.

First of all we should emphasize that we have not detected any peak around zero bias that is the feature of resonant tunnelling between ground occupied subbands (HH1-HH1 resonance in our case) of near identical two dimensional systems [3]. Weak tunnel coupling of heavy mass states and Coulomb interaction in the layers could be the reasons. The latter is due to stronger localization of the hole states in 2D systems formed by δ-doping in comparison with similar electron systems. It is well known that strong localization leads to formation of the Coulomb gap in the density of states at the Fermi level [7]. Studies of tunnelling spectra variation with temperature strongly indicate the existence of the Coulomb gap.

Figure 3 shows tunnelling conductance versus external bias at different temperatures in zero magnetic field. The temperature range is from 2 K to 7 K for Figure 3(a) and from 7 to 30 K for Figure 3(b). The data are presented for "type 2" sample because they are more pronounced. Qualitatively the "type 1" sample demonstrates the similar transformation with temperature. It is evident that peaks around ± 15 mV associated with tunnelling between HH1 and LH1 subbands are recovered at 7 K (Figure 3(a)). With further temperature increase these peaks are smeared out.

In conclusion we have measured the tunnelling between near identical two-dimensional hole accumulation layers in GaAs. The features in tunnelling spectra in zero magnetic field are associated with tunnelling from occupied HH1 subband into LH1 and HH2 empty states. The resonant tunnelling between HH1 subbands is suppressed. The resonant tunnelling into LH1 states demonstrates unusual temperature dependence. We argue that our findings could be explained in terms of different tunnel coupling between hole states of different subbands and of intralayer Coulomb interaction.

Acknowledgements

This work was supported by RFBR, PICS, RAS programs "Quantum Macrophysics", and "Low-Dimensional Quantum Nanostructures", EPSRC, and RS (UK).

References

[1] J. P. Eisenstein *et al*, *PRL*, **69**, 3804 (1992).
[2] Yu. N. Khanin *et al*, *Physica E*, **6**, 602 (2000).
[3] Yu. V. Dubrovskii *et al*, *ArXiv: cond-mat/***0501074**.
[4] I. B. Spielman *et al*, *PRL*, **84**, 5808 (2000).
[5] Yu. V. Dubrovskii *et al*, *Proc. 11th Int. Symp. "Nanostructures: Physics and Technology" (St Petersburg, Russia 2003)*, Ioffe Institute, 249 (2003).
[6] U. Ekenberg and M. Altarelli, *Phys. Rev. B*, **32**, 3712 (1985).
[7] A. L. Efros and B. I. Shklovskii, *J. Phys. C: Solid State Phys.*, **8**, 49 (1975).

13th Int. Symp. "Nanostructures: Physics and Technology"
St Petersburg, Russia, June 20–25, 2005

Decrease of tunnelling conductance near LO-phonon emission threshold in Al/δ-GaAs junctions

I. N. Kotel'nikov, S. E. Dizhur and N. A. Mordovets
Institute of Radioengineering and Electronics of the RAS, Moscow 125009, Mokhovaya St. 11/7, Russia

Abstract. The Al/δ-GaAs tunnel junctions with different 2D subbands spectra in the 2D electron system (2DES) of delta-layer were studied. In each of the samples the intersubband energies and the subband spectrum in the 2DES can be changed by the diamagnetic shift or by the persistent tunnelling photoconductivity effect. For tunnelling into the 2DES the tunnelling conductance decreased at the LO-phonon emission threshold if the intersubband electron–LO-phonon coupling was possible. The increase of the conductance usually observed in tunnelling spectra was found for intrasubband inelastic processes only.

Introduction

Investigations of last years showed that electrons and LO-phonons interaction in two dimensional electron systems (2DES) in GaAs structures results in noticeable intersubband polaron effects. In the optical experiments on AlGaAs/GaAs heterostuctures with two quantum wells separated by tunnelling-transparent barrier [1, 2] the intersubband coupling electron–LO-phonon modes have been observed. It is justified in terms of the anticrossing effect [2]. The pinning and anticrossing of 2D levels which is specific for the intersubband polaron have been observed in tunnelling spectra (TS) of Al/δ-GaAs junctions [3]. The resonant conditions for interactions with LO-phonon was obtained by the diamagnetic shift. These conditions were complied when 2D levels, both empty and occupied, became $\pm\varepsilon_{\rm LO}$ off Fermi surface, where $\varepsilon_{\rm LO} = 36.5$ meV is LO-phonon energy in GaAs. Further experiments showed that LO-phonon lines (PhLs) observed in TS at $U = \pm\varepsilon_{\rm LO}/e$ demonstrated significant lineshape variations near the polaron resonance too [4]. In Al/δ-GaAs tunnel junctions a new type of the PhL was found [5]. This line, corresponding to decreasing of the tunnel conductance at the threshold, appeared with subbands filling in 2DES. Though the intersubband LO-phonons coupling seemed most probably reason of the new line appearance [5], it was not clear what kind of parameters of 2DES spectrum namely caused its occurrence. This report presents attempt to clarify a mechanism of the electron–LO-phonon interactions, leading to conductance decreasing beyond LO-phonon ejection threshold at tunnelling into 2DES.

Experiment, results and discussions

We investigated Al/δ-GaAs structures, prepared in IRE RAS by MBE method [3]. The distance between Al/GaAs interface and δ-doped layer was about 20 nm. The TS of the Al/δ-GaAs junctions were measured at temperature 4.2 K. The logarithmic derivative $S = d\ln\sigma/dU$ of the conductance $\sigma = dI/dU$ was used as the tunnelling spectrum. Such choice allows to unified scale for tunnelling characteristic curves of the junctions with different σ. Three types of the samples have been used in our experiments: under the tunnelling *into* 2DES ($U < 0$), when the Fermi energy in metal was above Fermi energy E_{F_δ} in δ-layer on $\varepsilon_{\rm LO} = 36.5$ meV (see Fig. 1), the electron can tunnel into one, two or three subbands. The energies of three low levels $E_{iF} = E_i - E_{F_\delta}$ of these samples, found from the TS [3], are cited in Table 1.

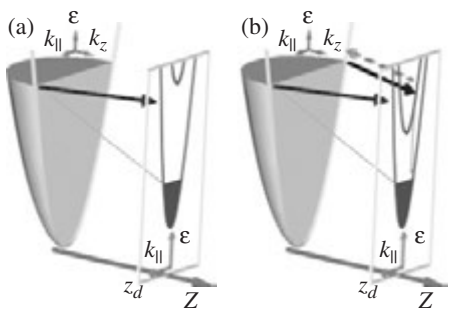

Fig. 1. Scheme of tunnelling from 3D metal to 2DES near LO-phonon emission threshold. (a) one subband tunnelling with inelastic LO-phonon assisted tunnelling channel (b) two subbands tunnelling with addition of intersubband LO-phonon emission in 2DES electrode.

Table 1.

Sample	E_{0F} (meV)	E_{1F} (meV)	E_{2F} (meV)
z6b1(dark)	−19	36	76
z6b1(PTPC)	−25	22	52
df2b1(dark)	−21	18	44
df2b1(PTPC)	−24	11.5	24.5
a7c1(dark)	−61	−7.5	28
a7c1($B_\| = 7.4$ T)	−57	6.0	44

The polynomial approximation of tunnelling spectrum $S_{\rm ph}$ near PhL, after cutting the region of singularity from TS, was used to get background curve $S_{\rm bkg}$ as on Fig. 2. A part of $S_{\rm ph}(U)$, included the singularity itself (±6 mV from line center), was excluded from approximation region. Whereupon $S_{\rm bkg}$ was determined by least-squares method (Fig. 2). The comparison this procedure with extracting technique of $S_{\rm bkg}$ by cubic splines-assisted yielded close results [6].

The phonon singularity $\Delta S_{\rm ph}$ was determined as $\Delta S_{\rm ph} = S_{\rm ph} - S_{\rm bkg} = d(\ln\sigma_{\rm ph} - \ln\sigma_{\rm bkg})/dU$. If $|\Delta\sigma_{\rm ph}| = |\sigma_{\rm ph} - \sigma_{\rm bkg}| \ll \sigma_{\rm bkg}$ then $\Delta S_{\rm ph} \simeq d(\Delta\sigma_{\rm ph}/\sigma_{\rm bkg})/dU$. Hence, the integral $\Delta S_{\rm ph}$ by dU gives the relative change of the tunnel conductance $\Delta\sigma_{\rm ph}/\sigma_{\rm bkg}$ in PhL region (Fig. 2). PhL on Fig. 2 corresponds to ordinary inelastic process with LO-phonon emission: the conductance increase at the threshold and its step $\Delta\sigma^* > 0$ on the $\Delta\sigma_{\rm ph}(U)/\sigma_{\rm bkg}(U)$ appears. Further we will consider the dependence of the $\Delta\sigma^*$ upon the position of the nearest to the energy $E_{F_\delta} + \varepsilon_{\rm LO}$ subband.

The energies of 2D-subbands in δ-layer can be changed by persistent photoconductivity (PTPC) effect [7]: unoccupied

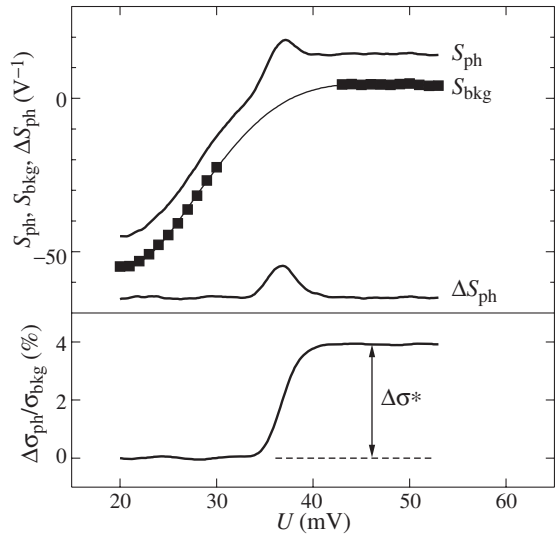

Fig. 2. Procedure of background subtraction to get phonon line and relative conductivity change near $eU = \varepsilon_{LO}$.

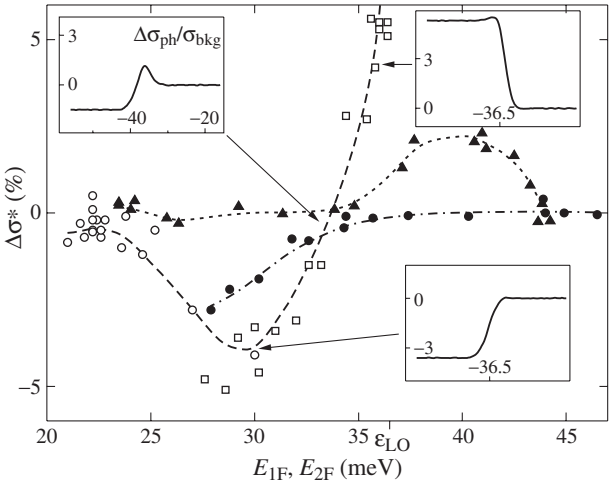

Fig. 3. Dependencies of the conductance steps $\Delta\sigma^*$ on subband energy E_{iF} for tunnelling to 2DES. Squares and triangles — PTPC regime for samples z6b1 ($\Delta\sigma^*(E_{1F}(t))$) and df2b1 ($\Delta\sigma^*(E_{2F}(t))$), respectively. Circles — diamagnetic shift in $B_\parallel$ for sample a7c1 ($\Delta\sigma^*(E_{2F}(B_\parallel))$).

subbands ($E_{iF} > 0$) "thickening" to the ground state after sample illumination by LED for time t. In accordance with Table 1, the bottom of the subband E_{1F} in the sample z6b1 (dark) equals ε_{LO}, i.e. at phonon emission threshold.

The dependence of $\Delta\sigma^*$ on $E_{1F}(t)$ for z6b1 is shown on Fig. 3. $\Delta\sigma^*$ becomes negative when $E_{1F}(t)$ go down to LO-phonon emission threshold (ε_{LO}). The same but weaker effect observed for sample df2b1 (similar curve $\Delta\sigma^*(E_{2F}(t))$ on Fig. 3). Moreover, the sign reversal of $\Delta\sigma^*$ for both samples occurs at the same value $E_{iF} \simeq 33$ meV$\simeq \varepsilon_{LO}$. The subband E_{2F} in the sample a7c1 is situated below the threshold (see Table 1 "a7c1 (dark)" row), so $\Delta\sigma^* < 0$. The in-plane magnetic field $B_\parallel$ gives rise to pushing subband E_{2F} from quantum well and at $E_{2F}(B_\parallel \simeq \varepsilon_{LO})$ the value of $\Delta\sigma^*$ becomes zero (see Fig. 3).

The results obtained demonstrate that new PhL appeared in TS of Al/δ-GaAs relates with joining of the next subband to the tunnelling process. These subbands are E_{1F} for the sample z6b1 and E_{2F} for df2b1. It seems rather obviously that tunnelling into this level leads to electrons transition from this subband onto empty states above Fermi energy of underlying subband (with LO-phonon emission). For both samples underlying subband is E_{0F}, since for df2b1 intersubband distance $E_{21} < \varepsilon_{LO}$.

Observed behaviour of $\Delta\sigma^*$ may be explained by using model from [8]. In the paper electron–phonon interaction is described by an electron self-energy Σ. Its imaginary part, $\mathrm{Im}\Sigma$, describes the phonon emission life-time. The contribution to the tunnel conductance from $\mathrm{Im}\Sigma$ is a step. Moreover, if the interaction is localized in an electrode (in our case in 2DES region), the contribution from $\mathrm{Im}\Sigma$ is a step decrease in conductance ($\Delta\sigma^* < 0$). This result can be understood that the reflection coefficient at the electrode–barrier interface increases, when electrons are tunnelling into dissipative medium (2DES region in our case), see Fig. 1b. On the other hand, if the interaction is in the tunnel barrier (in our case, between the metal and δ-layer), this contribution is a step increase in conductance due to to opening up to inelastic channels for tunnelling (Fig. 1a).

Conclusion

Thus, we observed in the first time the sign reversal of the step in conductance $\Delta\sigma^*$ by the change subbands spectrum in 2DES. In the frame of a model [8] the data obtained demonstrate that $\Delta\sigma^* < 0$ may be explained by intersubband electron transitions with LO-phonon emission in the 2DES. But $\Delta\sigma^* > 0$ is determined by intrasubband inelastic LO-phonon process under the condition of the interaction in the tunnel barrier.

Acknowledgements

This work is supported by RFBR and by programs of RAS. The authors thank S. N. Artemenko, V. A. Volkov and A. Ya. Shul'man for discussions and E. M. Dizhur for his method of background subtraction. We are grateful Yu. V. Fedorov and A. S. Bugaev for preparation of the samples.

References

[1] H. C. Liu *et al*, *Appl. Phys. Lett.*, **78**, 3580 (2001).
[2] H. C. Liu *et al*, *Phys. Rev. Lett.*, **90**, 077402 (2003).
[3] I. N. Kotel'nikov *et al*, *JETP Lett.*, **71**, 387 (2000).
[4] S. E. Dizhur *et al*, *Proc. of 26th ICPS (Edinburgh, Scotland, UK, 2002)*, Institute of Physics Publishing, 171, P158, 2002.
[5] I. N. Kotel'nikov, S. E. Dizhur, *Proc. of 12th Int. Symp. NANO2004 (St Petersburg, Russia, 2004)*, Ioffe Institute, 366, 2004.
[6] E. M. Dizhur *et al*, *JETP Lett.*, **80**, 433 (2004).
[7] S. E. Dizhur *et al*, *PLDS*, **11/12**, 233 (2001).
[8] J. A. Appelbaum, W. F. Brinkman, *Phys. Rev. B*, **2**, 907 (1970).

13th Int. Symp. "Nanostructures: Physics and Technology"
St Petersburg, Russia, June 20–25, 2005

Many-body induced enhancement of tunneling through InAs quantum dot in magnetic field

E. E. Vdovin[1], Yu. N. Khanin[1], *I. A. Larkin*[1], Yu. V. Dubrovskii[1], L. Eaves[2] and M. Henini[2]

[1] Institute of Microelectronics Technology RAS, 142432 Chernogolovka, Russia
[2] School of Physics and Astronomy, University of Nottingham, NG7 2RD, UK

Abstract. The current voltage characteristics of a single barrier tunneling device which contains self-organized InAs quantum dots within the barrier are studied in zero and strong magnetic fields at low temperatures. We observe the anomalous enhancement of the tunneling through quantum dot in a magnetic field both the parallel and the perpendicular to the current attributed to a many-body contribution which arises due to the strong interaction of a tunnelling electron with the Fermi sea in the emitter.

Artificially fabricated nanostructures, which contain only a few electrons, have proven to be excellent laboratories to study quantum size effects. The electron wave nature gives rise to the formation of zero-dimensional (0D) states when electrons are confined in all three spatial directions in a quantum dot. Resonant tunneling through a 0D state has been studied in detail by measuring the current through a quantum dot, but noninteracting electron picture cannot explain the behavior of this system at low temperatures. This is not very surprising, because the interaction phenomena of the Coulomb blockade, the Kondo effect and Fermi-edge singularities (FES) [1–5] are known to strongly influence the tunnel current through a quantum dot. However, what is surprising is that interaction effect can enhances in magnetic field rapidly. Recently, it has been observed that interaction-induced singularities (FES) in the tunneling current via InAs quantum dots show a considerable magnetic-field dependence in high magnetic fields parallel to the current [6].

In this paper we observe the anomalous enhancement of the tunneling through quantum dot in a magnetic field both the parallel and the perpendicular to the current and propose a description of the observed effect within the framework of adapted Matveev-Larkin theory, which predicted magnetic field — induced FES in the tunneling current via InAs quantum dots. The analyze of the temperature dependence of the current confirmed that the anomalous enhancement of the tunneling current has been attributed to FES independently. Moreover we experimentally demonstrated, that many-body character of the electron tunneling through zero dimensional states not only has strong influence on the shape of the tunnel resonance, but also limits the applicability of the magnetotunneling spectroscopy (MTS) rapidly.

The sample studied was a single-barrier 8 nm GaAs-$Al_{0.4}Ga_{0.6}As$-GaAs heterodiode, grown by molecular-beam epitaxy on (100)-oriented Si doped n-GaAs substrate. InAs quantum dots were grown on the center plane of the barrier using the Stranski-Krastanow growth mode, producing a dot density of $2 \times 10^{11}\,\mathrm{cm}^{-2}$ with a typical size 10 nm.

We now consider the magnetic field dependence of the transport characteristic of the experimental heterostructure as a function of magnetic field B. Figure 1 shows I-V characteristics of our sample at the perpendicular to the current magnetic field of 8 T at two different temperatures. Decreasing of the temperature to $T = 0.5$ K leads to sharp increasing of the front of the resonant feature at $V = 8$ mV (peak A) near the threshold of tunneling when lowest QD state is resonant with Fermi energy of emitter and slow increasing of other resonances. Full width half maximum (FWHM) values of the singularity near the first current peak as small as 0.3 mV has been measured that corresponded to 130 μeV in energy scale. We related the unexpected rapid enhancement of the low voltage resonance in magnetic field at low temperature with manifestation of the interaction-induced Fermi-edge singularity in the tunneling current via a localized state. A similar singularity in the tunneling current was observed in the transport characteristic in the parallel to the current magnetic field (not shown here). Let's note, that a singularity was not observed in absence of the magnetic field even at the lowest temperature of 0.4 K .

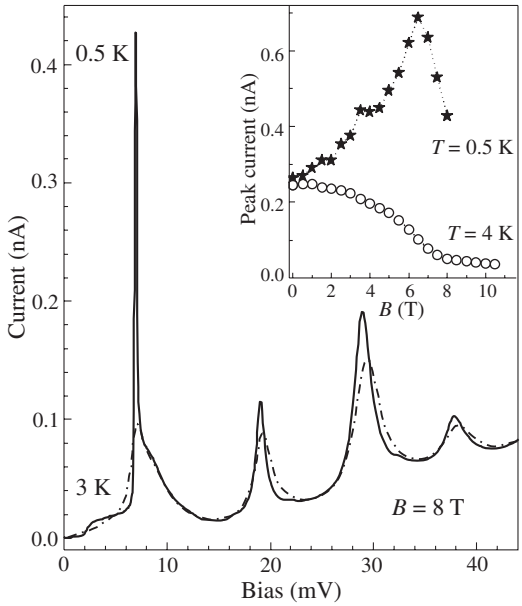

Fig. 1. I-V characteristics of the experimental sample at the perpendicular to the current magnetic field of 8 T at two different temperatures of 3 K (dash-dot) and 0.5 K (full curve). Inset: the magnetic field dependence of the amplitude of the peak A at temperatures of 4 K and 0.5 K.

The inset in Fig. 1 shows the magnetic field dependence of the amplitude of the first peak at temperatures 4 K and 0.5 K. We attribute the general fall in amplitude of the peak with increasing B at 4 K to a well-established effect that can be understood in term of a single-particle model for electron tunneling in the presence of the perpendicular to the current magnetic field. This effect is basis of the method of the magnetotun-

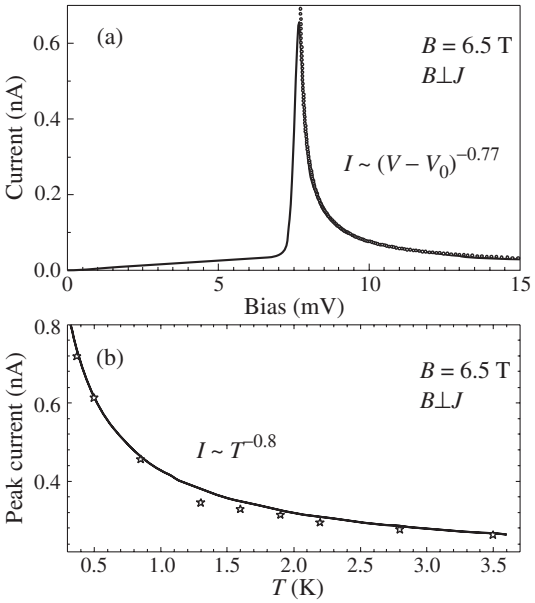

Fig. 2. (a) Detailed I-V characteristic of the experimental sample at the perpendicular to the current magnetic field of 6.5 T at low biases. (b) The amplitude of FES peak as a function of temperature.

neling spectroscopy (MTS) of the spatial form of the wave function and discussed in detail elsewhere [7, 8]. The strong extra interaction-induced tunneling channel at 0.5 K changes dependence of the amplitude of the resonant peaks on a magnetic field and distort the MTS results rapidly (as shown in the inset in Fig. 1.) and as a result does not allow to produce images of the probability density of the electron wave function as at temperature 4 K.

In order to analyze this many-body current we investigated the slope of the experimental peak. Figure 2(a) shows in detail the shape of the first current peak at the magnetic fields applied perpendicular to the current of $B = 6.5$ T at 0.5 K. We assume that the total current in Fig. 2(a) is provided mainly interaction-induced contribution because the relatively strong magnetic field suppresses the tunneling of the non-interacting electrons as it is clearly visible from the inset in Fig. 1. Its alloys as to analyze the slope of the experimental resonant peak and compare the result with theoretical predictions from Ref. [1, 2]. The decrease of the current for $V > V_0$ is described with the characteristic behavior for a Fermi-edge singularity, $I \sim (V - V_0)^{-\gamma}$, with the edge exponent $\gamma = 0.77$ where V_0 here is the voltage at the maximum peak current. The value γ received by us essentially exceeds theoretical value for similar experimental structure [1] without a magnetic field and is little bit more then magnetic field value from Ref. [6].

A different way to determination of the origin of the anomalous enhancement of the tunneling through quantum dot is a temperature-dependent experiment. As predicted in Ref. [4], the fact that the area under I-V curve around the resonance increases with decreasing temperature strongly indicates that the temperature dependence in this case has a many-body nature. A similar temperature behavior is demonstrated by our experimental curves clearly (Fig. 2). Moreover temperature dependent measurements offer an additional way to determine the edge exponent [3, 6]. As shown in Fig. 2(b) the amplitude of the first current peak decreases according to a power law $I \sim T^{-\gamma}$ with $\gamma \sim 0.8$. This value coincided with the observed decrease of the current for $V > V_0$ within experimental accuracy. Thus the analyze of the temperature dependences shown that the anomalous enhancement of the tunneling current has been attributed to a many-body contribution which arises due to the strong interaction of a tunnelling electron with the Fermi sea in the emitter.

The extreme values of the edge exponent of $\gamma \sim 0.8$ can't been explain by theory of the FES valid for $\gamma \ll 1$ [1] without additional modifications. A similar on observed by us strong enhancement of the FES has been reported in Ref. [6] in very high magnetic fields (up to 28 T) parallel to the current. In this paper was proposed the adapted model of FES and have shown that the interaction between a localized charge on the QD and the electrons in the Landau quantized emitter leads to FES due to dramatic Fermi phase shifts if only the lowest Landau level in the 3D emitter is occupied. This results in edge exponents $\gamma \sim 0.5$ in high magnetic fields when the electrons in the lowest Landau level of the emitter is mainly spin polarized. In our experiment the values of the Fermi energy in the 3D emitter at the bias near the first current peak is 2.4 meV and it is approximately in 6 times less when in Ref. [6]. As a consequence electrons in the emitter at 8 T is totally spin polarized and we can observed FES at relatively slow magnetic field.

Acknowledgements

The work is partly supported by RFBR (03-02-17693 and 04-02-16869) and EPSRC (UK). YVD gratefully acknowledge support from the Royal Society. The authors thank A. V. Khaetski for useful discussions, and V. V. Belov for technical assistance.

References

[1] K. A. Matveev and A. I. Larkin, *Phys. Rev. B*, **46**, 15337 (1992).
[2] G. E. W. Bauer *et al*, *Surface Science*, **305**, 358 (1994).
[3] D. H. Cobden and B. A. Muzykantskii, *Phys. Rev. Lett.*, **75**, 4274 (1995).
[4] C. Zhang, D. J. Fisher and S. M. Stewart, *Surface Science*, **361/362**, 231 (1995).
[5] K. A. Benedict *et al*, *Physica B*, **256/258**, 519 (1998).
[6] I. Hapke-Wurst *et al*, *Phys. Rev. B*, **62**, 12621 (2000).
[7] E. E. Vdovin *et al*, *Science*, **290**, 122 (2000).
[8] A. Patane *et al*, *Phys. Rev. B*, **65**, 165308, 1-12 (2002).

13th Int. Symp. "Nanostructures: Physics and Technology"
St Petersburg, Russia, June 20–25, 2005

Increase of current via quantum well by in-plane magnetic field

A. Yu. Serov and G. G. Zegrya
Ioffe Physico-Technical Institute, St Petersburg, Russia

Abstract. We have investigated I–V characteristics of resonant-tunneling diode and double quantum well system under in-plane magnetic field. It is shown for the first time that nonmonotonic dependence of peak current on magnetic field is caused by redistribution of electrons on its magnetic centres.

1. Introduction

Tunneling via quantum well has been the subject of much interest because of various physical effects and technical applications [1,2,3]. Tunneling into QW from 3D states was investigated in resonant tunneling diode (RTD) [1,2]. It was shown that in-plane magnetic field causes broadening of I–V characteristics [4]. This broadening usually causes decrease of peak current what was observed in [4]. However in the paper [4] nonmonotonic dependence of peak current on magnetic field was observed when second heterobarrier was wider than first. The explanation of this effect was not provided in literature. The increase of current was theoretically investigated in paper [5] in part. Tunneling into QW from 2D states at double quantum well system (DQW) was investigated in [7]. Tunneling in DQW under in-plane magnetic field was analyzed in paper [8]. But the influence of in-plane magnetic field on I–V characteristic and peak current was not analyzed there. In present paper we investigate tunneling into QW in RTD and DQW structures under in-plane magnetic field. We show that the number of unoccupied states can increase with increasing of in-plane magnetic field. So magnetic field can cause increase and decrease of peak current depending on electron concentration in QW.

2. Model

Let us consider a RTD with in-plane magnetic field and y-axis directed along the magnetic field vector. The tunneling current flows in the z-axis directions. The calibration of vector potential of magnetic field is assumed to be $\mathbf{A} = (Hz, 0, 0)$, where H is magnetic field. This calibration allows us to solve one-dimensional problem.

The potential for electrons has the form (Fig. 1)

$$U(z) = U_b + \frac{mw_c^2(z - z_0)^2}{2} \qquad (1)$$
$$z_0 = \frac{cp_x}{eH}, \quad w_c = \frac{eH}{mc}$$

where w_c is the cyclotron frequency of an electron in a magnetic field, and z_0 is the centre of the magnetic potential.

Magnetic field affects two aspects of tunneling via QW. At first it changes resonance conditions, because of mixing magnetic potential with potential of heterobarriers. We should note that magnetic potential depends on coordinate of magnetic centre z_0 and hence resonance conditions also depend on it. This effect causes broadening of resonance conditions.

At second magnetic field cause redistribution of electrons by its magnetic centre for profit in energy. And we will see that it causes the increase of peak current via QW.

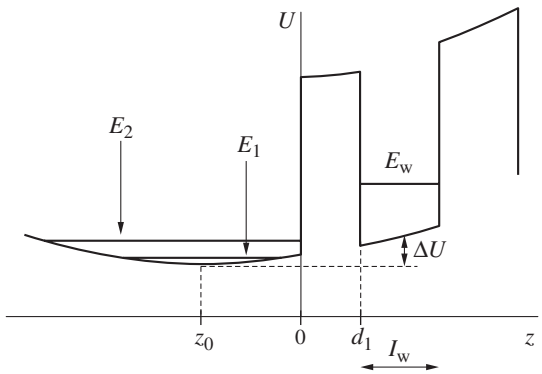

Fig. 1. Potential of RTD in magnetic field. z_0 is the centre of the magnetic potential; ΔU, the shift of the QW bottom relative to emitter bottom

After tunneling under in-plane magnetic field electron gets addition in magnetic energy (Fig. 1). It is due to conservation of magnetic centre in act of tunneling, and electron after tunneling "rolls" far from its magnetic centre. So final states in QW for tunneling electrons are not advantageous in energy. Because of scattering these states lose electrons by scattering time, which is less than tunneling time, and become unoccupied.

For calculation of current via quantum well we have to summarize contribution of electrons by all quantum numbers, i.e. centre of magnetic potential z_0, quasi-momentum parallel to magnetic field p_y, number of levels in emitter and quantum well N_1, N_2 respectively. To calculate the number of vacant final states, we have to count the number of electrons in QW which has the same centre of magnetic potential as tunneling electrons in emitter. So tunneling electrons have energy E_y in range

$$E_{y,\mathrm{em}} = E_{\mathrm{F,QW}} - \frac{mw_c^2}{2}\left(z_0 + d + \frac{l_\mathrm{w}}{2}\right)^2 \div E_{\mathrm{F,em}} - \frac{mw_c^2 z_0^2}{2} \qquad (2)$$

where d — barrier width, l_w — width of QW, $E_{\mathrm{F,QW}}$, $E_{\mathrm{F,em}}$ — Fermi levels in QW and emitter respectively. We can see that with the increase of magnetic field the energy range and hence number of tunneling electrons increase.

3. Peak current in RTD

Let us consider influence of in-plane magnetic field on current in case of RTD. We used the following structure parameters: GaAs quantum well is 56 Å wide, the asymmetric $Al_xGa_{1-x}As$ barriers are 85 Å wide and have Al mole fractions of $x = 0.4$ and $x = 0.5$. For our calculations we assume that electron concentration in QW is constant and independent of current. The self-consistent calculation with determination of electron concentration in QW is presented in [5,6]. The dependence

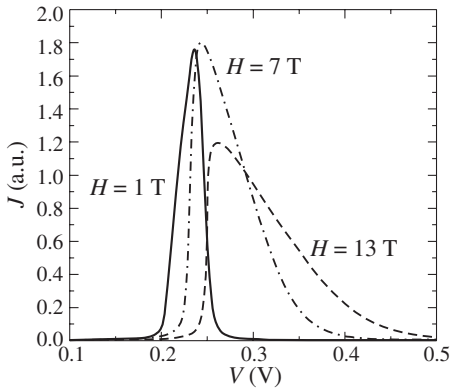

Fig. 2. Current from emitter to QW in RTD

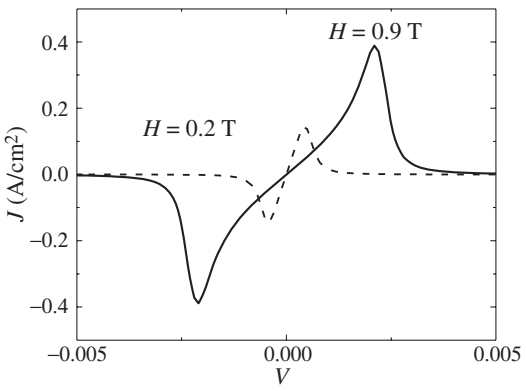

Fig. 3. Current in DQW.

of current on voltage with various values of in-plane magnetic field is presented on Fig. 2. We can see that I–V characteristics are broadened with nonmonotonic dependence of peak current on magnetic field.

Decrease of peak current in RTD by in-plane magnetic field was studied in several papers [4, 9]. This effect results from broadening of resonance conditions by in-plane magnetic field, because of electrons with various magnetic centre tunnel under various bias. So the number of initial states of electrons which are resonant decreases. This effect is strong and takes place independently of structural parameters.

However, as we could see, in-plane magnetic field can increase peak current. The reason of this effect is modifying number of vacant final states for tunneling electrons. This mechanism is usually weaker, but sometimes it can be stronger than decreasing mechanism. When all final states for tunneling electrons are vacant, the mechanism of current increasing does not work. This increasing mechanism is powerful in case of big electron concentration in QW, because big electron concentration respond to big number of occupied final states for tunneling electrons and suppression of current. In case of low electron concentration in QW the broadening mechanism suppresses increasing, that was also observed in [4].

We should note that electron concentration in QW does not strongly depend on bias, but is caused by the width of heterobarriers.

So we have two concurrent mechanisms of influence of in-plane magnetic field on current. The mechanism of current increasing works better in case of big concentration in QW. In this case the number of vacant states changes strongly by magnetic field. In case of low electron concentration in QW the main mechanism is current decreasing.

4. Peak current in DQW

Let us consider DQW structure with QW of 70 Å width and barrier of 60 Å width. Electron concentrations in both QW are equal 2×10^{11} cm^{-2}. I–V characteristics of this case is presented on Fig. 3. As we can see small increase of magnetic field cause big current increasing. It is due to strong dependence of number of unoccupied final states on magnetic field in such a structure. Mechanism of current increasing in DQW is the same as in RTD and our results are forecasts.

5. Conclusion

We have showed the mechanism of the increase of peak current via QW by in-plane magnetic field. We have studied current-voltage characteristics in RTD and DQW systems. Current increasing is caused by redistribution of electrons in QW by its magnetic centres. This mechanism works better in case of big electron concentration in QW, otherwise it is suppressed by broadening the resonance conditions.

Acknowledgements

This work was supported in part by Russian Foundation for Basic Research, Grants 05-02-16679, 04-07-90148, Federal Program on Support of Leading Scientific Schools, Grant 2160.2003.2

References

[1] L. L. Chang, L. Esaki, and R. Tsu, *Appl. Phys. Lett.* **24**, 593 (1974).
[2] V. J. Goldman, D. C. Tsui, and J. E. Cunningham, *Phys. Rev. Lett.* **58**, 1256 (1987).
[3] J. S. Moon, J. A. Simmons, M. A. Blount, *Appl. Phys. Lett.*, **74**, 314 (1999).
[4] A. Zaslavsky, Yuan P. Li, D. C. Tsui, M. Santos, and M. Shayegan, Phys. Rev. B **42**, 1374 (1990).
[5] A. Yu. Serov, G. G. Zegrya, *Appl. Phys. Lett.* **86**, 032108 (2005).
[6] A. Yu. Serov, G. G. Zegrya, *JETP* **99**, 147 (2004).
[7] J. P. Eisenshtein, L. N. Pfeiffer, and K. W. West, *Appl. Phys. Lett.* **58**, 1499 (1991).
[8] J. P. Eisenshtein, T. J. Gramila, L. N. Pfeiffer, and K. W. West, *PRB* **44**, 6511 (1991).
[9] H. Paredes Gutierrez, N. Porras-Montenegro, and A. Latge, *PRB* **68**, 045311 (2003).

13th Int. Symp. "Nanostructures: Physics and Technology"
St Petersburg, Russia, June 20–25, 2005

Electronic properties of few-layer thin films of graphite

K. S. Novoselov[1,2], S. V. Morozov[2], A. K. Geim[1], D. Jiang[1], Y. Zhang[1], S. V. Dubonos[2] and A. A. Firsov[2]

[1] Department of Physics & Astronomy, University of Manchester, Oxford Road, Manchester, M13 9PL, UK
[2] Institute for Microelectronics Technology, 142432, Chernogolovka, Russia

Abstract. We describe monocrystalline graphitic films, which are a few atoms thick but are nonetheless stable under ambient conditions, metallic, and of remarkably high quality. The films are found to be a two-dimensional semimetal with a tiny overlap between valence and conductance bands, and they exhibit a strong ambipolar electric field effect such that electrons and holes in concentrations up to $10^{13}\,\mathrm{cm}^{-2}$ and with room-temperature mobilities of $10{,}000\,\mathrm{cm}^2/\mathrm{V}\cdot\mathrm{s}$ can be induced by applying gate voltage.

Introduction

The ability to control electronic properties of a material by externally applied voltage is at the heart of modern electronics. In many cases, it is the electric field effect that allows one to vary the carrier concentration in a semiconductor device and, consequently, change an electric current through it. As the semiconductor industry is nearing the limits of performance improvements for the current technologies dominated by silicon, there is a constant search for new, nontraditional materials whose properties can be controlled by the electric field. The most notable recent examples of such materials are organic conductors [1] and carbon nanotubes [2]. It has long been tempting to extend the use of the field effect to metals (e.g., to develop allmetallic transistors that could be scaled down to much smaller sizes and would consume less energy and operate at higher frequencies than traditional semiconducting devices [3]). However, this would require atomically thin metal films, because the electric field is screened at extremely short distances ($< 1\,\mathrm{nm}$) and bulk carrier concentrations in metals are large compared to the surface charge that can be induced by the field effect. Films so thin tend to be thermodynamically unstable, becoming discontinuous at thicknesses of several nanometers; so far, this has proved to be an insurmountable obstacle to metallic electronics, and no metal or semimetal has been shown to exhibit any notable ($> 1\%$) field effect [4].

We report the observation of the electric field effect in a naturally occurring two-dimensional (2D) material referred to as few-layer graphene (FLG). Graphene is the name given to a single layer of carbon atoms densely packed into a benzene-ring structure, and is widely used to describe properties of many carbon-based materials, including graphite, large fullerenes, nanotubes, etc. (e.g., carbon nanotubes are usually thought of as graphene sheets rolled up into nanometer-sized cylinders) [5–7]. Planar graphene itself has been presumed not to exist in the free state, being unstable with respect to the formation of curved structures such as soot, fullerenes, and nanotubes [5–13].

We have been able to prepare graphitic sheets of thicknesses down to a few atomic layers (including single-layer graphene), to fabricate devices from them, and to study their electronic properties. Despite being atomically thin, the films remain of high quality, so that 2D electronic transport is ballistic at submicrometer distances. No other film of similar thickness is known to be even poorly metallic or continuous under ambient conditions. Using FLG, we demonstrate a metallic field-effect transistor in which the conducting channel can be switched between 2D electron and hole gases by changing the gate voltage.

1. Sample preparation

Our graphene films were prepared by mechanical exfoliation (repeated peeling) of small mesas of highly oriented pyrolytic graphite [14]. This approach was found to be highly reliable and allowed us to prepare FLG films up to $10\,\mu\mathrm{m}$ in size. Thicker films ($d \geq 3\,\mathrm{nm}$) were up to $100\,\mu\mathrm{m}$ across and visible by the naked eye. Figure 1 shows examples of the prepared films, including single-layer graphene (see also [14]). To study their electronic properties, we processed the films into multiterminal Hall bar devices placed on top of an oxidized Si substrate so that a gate voltage V_g could be applied. We have studied more than 60 devices with $d < 10\,\mathrm{nm}$. We focus on the electronic properties of our thinnest (FLG) devices, which contained just one, two, or three atomic layers [14]. All FLG devices exhibited essentially identical electronic properties characteristic for a 2D semimetal, which differed from a more complex (2D plus 3D) behavior observed for thicker, multilayer graphene [14] as well as from the properties of 3D graphite.

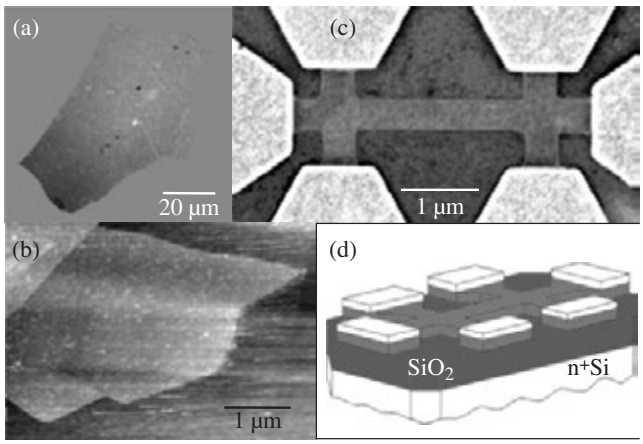

Fig. 1. Graphene films. (a) Photograph (in normal white light) of a relatively large multilayer graphene flake with thickness $\sim 3\,\mathrm{nm}$ on top of an oxidized *Si* wafer. (b) AFM image of single-layer graphene. Notice the folded part of the film near the bottom, which exhibits a differential height of $\sim 0.4\,\mathrm{nm}$. For details of AFM imaging of single-layer graphene, see [14]. (c) Scanning electron microscope image of one of our experimental devices prepared from FLG. (d) Schematic view of the device in (c).

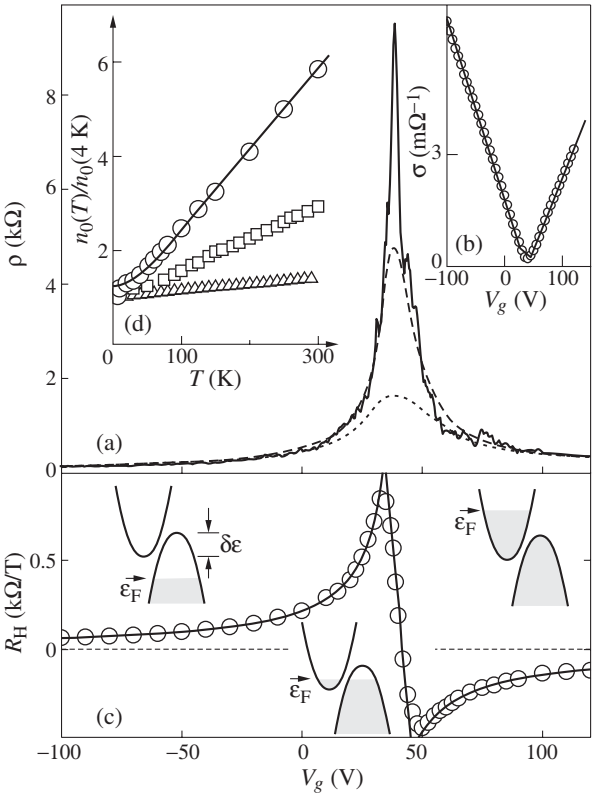

Fig. 2. Field effect in FLG. (a) Typical dependences of FLG's resistivity ρ on gate voltage for different temperatures ($T = 5$, 70, and 300 K for top to bottom curves, respectively). (b) Example of changes in the film's conductivity $\sigma = 1/\rho(V_g)$ obtained by inverting the 70 K curve (circles). (c) Hall coefficient R_H versus V_g for the same film; $T = 5$ K. (d) Temperature dependence of carrier concentration n_0 in the mixed state for the film in (a) (circles), a thicker FLG film (squares), and multilayer graphene ($d \approx 5$ nm; triangles). Solid curves in (b) to (d) are the dependences calculated from our model of a 2D semimetal illustrated by insets in (c).

2. Experimental results

In FLG, the typical dependence of its sheet resistivity ρ on gate voltage V_g (Fig. 2a) exhibits a sharp peak to a value of several kΩ and decays to $\sim 100\,\Omega$ at high V_g. Its conductivity $\sigma = 1/\rho$ increases linearly with V_g on both sides of the resistivity peak (Fig. 2b). At the same V_g where ρ has its peak, the Hall coefficient R_H exhibits a sharp reversal of its sign (Fig. 2c).

Our measurements can be explained quantitatively by a model of a 2D metal with a small overlap $\delta\varepsilon$ between conductance and valence bands [14]. The gate voltage induces a surface charge density $n = \epsilon_0\epsilon V_g/te$ and, accordingly, shifts the position of the Fermi energy ε_F. Here, ϵ_0 and ϵ are the permittivities of free space and SiO_2, respectively; e is the electron charge; and t is the thickness of our SiO_2 layer (300 nm). For typical $V_g = 100$ V, the formula yields $n \approx 7.2 \times 10^{12}\,\mathrm{cm}^{-2}$. The electric field doping transforms the shallow-overlap semimetal into either completely electron or completely hole conductor through a mixed state where both electrons and holes are present (Fig. 2). The three regions of electric field doping are clearly seen on both experimental and theoretical curves. For the regions with only electrons or holes left, R_H decreases with increasing carrier concentration in the usual way, as $1/ne$. The resistivity also follows the standard dependence $\rho = 1/ne\mu$ (where μ is carrier mobility). In the mixed state, σ changes little with V_g, indicating the substitution of one type of carrier with another, while the Hall coefficient reverses its sign, reflecting the fact that R_H is proportional to the difference between electron and hole concentrations.

Carrier mobilities in FLG were determined from field-effect and magnetoresistance measurements as $\mu = \sigma/en$ and $\mu = R_H/\rho$, respectively. In both cases, we obtained the same values of μ, which varied from sample to sample between 3000 and 10,000 cm^2/V·s. The mobilities were practically independent of temperature T, indicating that they were still limited by scattering on defects. For $\mu \approx 10,000\,\mathrm{cm}^2$/V·s and our typical $n \approx 5 \times 10^{12}\,\mathrm{cm}^{-2}$, the mean free path is $\sim 0.4\,\mu$m, which is surprising given that the 2D gas is at most a few Å away from the interfaces. However, our findings are in agreement with equally high μ observed for intercalated graphite [5], where charged dopants are located next to graphene sheets. Note that for multilayer graphene, we observed mobilities up to $\sim$ 15, 000cm^2/V·s at 300 K and $\sim$ 60, 000cm^2/V·s at 4 K.

3. Conclusions

Graphene may be the best possible metal for metallic transistor applications. In addition to the scalability to true nanometer sizes envisaged for metallic transistors, graphene also offers ballistic transport, linear current-voltage characteristics, and huge sustainable currents ($> 10^8\mathrm{A/cm}^2$) [14].

Acknowledgements

K. S. N. would like to acknowledge The Leverhulme Trust for support within Early Career Fellowship scheme. S. V. M. and S. V. D are grateful to RFBR for financial support.

References

[1] C. D. Dimitrakopoulos, D. J. Mascaro, *IBM J. Res. Dev.*, **45**, 11 (2001).
[2] R. H. Baughman, A. A. Zakhidov, W. A. de Heer, *Science*, **297**, 787 (2002).
[3] S. V. Rotkin, K. Hess, *Appl. Phys. Lett.*, **84**, 3139 (2004).
[4] A. V. Butenko, D. Shvarts, V. Sandomirsky, Y. Schlesinger, *J. Appl. Phys.*, **88**, 2634 (2000).
[5] M. S. Dresselhaus, G. Dresselhaus, *Adv. Phys.*, **51**, 1 (2002).
[6] I. L. Spain, *Chemistry and Physics of Carbon*, P. L. Walker, P. A. Thrower, Eds. (New York: Dekker) 119–304 (1981).
[7] O. A. Shenderova, V. V. Zhirnov, D. W. Brenner, *Crit. Rev. Solid State Mater. Sci.*, **27**, 227 (2002).
[8] A. Krishnan *et al*, *Nature*, **388**, 451 (1997).
[9] E. Dujardin, T. Thio, H. Lezec, T. W. Ebbesen, *Appl. Phys. Lett.*, **79**, 2474 (2001).
[10] H. Shioyama, *J. Mat. Sci. Lett.*, **20**, 499 (2001).
[11] A. M. Affoune *et al*, *Chem. Phys. Lett.*, **348**, 17 (2001).
[12] K. Harigaya, Y. Kobayashi, K. Takai, J. Ravier, T. Enoki, *J. Phys. Cond. Matter*, **14**, L605 (2002).
[13] T. A. Land, T. Michely, R. J. Behm, J. C. Hemminger, G. Comsa, *Surf. Sci.*, **264**, 261 (1992).
[14] K. S. Novoselov *et al*, *Science*, **306**, 666 (2004).

13th Int. Symp. "Nanostructures: Physics and Technology"
St Petersburg, Russia, June 20–25, 2005

Single electron transport in split gate structures containing InAs self-assembled quantum dots

E. E. Vdovin[1], Yu. N. Khanin[1], S. V. Dubonos[1], Yu. V. Dubrovskii[1], L. Eaves[2] and M. Henini[2]

[1] Institute of Microelectronics Technology RAS, 142432 Chernogolovka, Russia
[2] School of Physics and Astronomy, University of Nottingham, NG7 2RD, UK

Abstract. We report studies of single electron transport through InAs self-assembled quantum dots in a modulation-doped structure with split gates. By application of a source-drain voltage we observed the sharp current peaks at voltage correspondent of the energies of a InAs dot that is trapped within the 1D channel defined by the split gate.

Semiconductor quantum dots (QD) have attracted the attention of many researchers because of their both in physics and device applications. One of most promising materials are InAs self-assembled quantum dots embedded in a GaAs matrix [1, 2]. Although QD lasers based on this material system have been already commercialized, the electronic structure as well as the transport properties of this QD system is not exactly known.

The transport properties are extremely important for device application, such as a single-electron transistor. Electron transport in the growth direction was mainly investigated with capacitance [3, 4] and resonant tunneling spectroscopy [5-8]. So far, only a few resonant tunneling experiments via dot states were done in the lateral direction [9-11]. In lateral tunneling experiments a point contact was defined in the gate region of a high electron mobility transistor in order to observe electron transport through only a few InAs islands within the constriction. In this paper we investigate the electron transport properties through InAs self-assembled QDs in modulation-doped structures with split gates. By application of a source-drain voltage we observed the sharp current peaks at voltage correspondent of the energies of a InAs dot that is trapped within the 1D channel defined by the split gate. In addition, by increasing source-drain bias we were able to recover the resonant tunneling through QD located closer to the source contact.

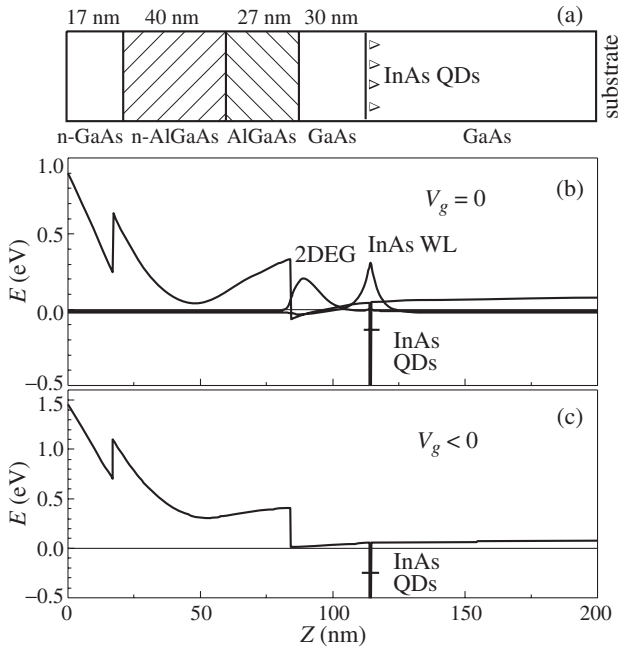

Fig. 1. Schematic illustration of (a) epitaxial structure, (b) corresponding band diagram with no gate bias, and (c) band diagram with gate bias lower than critical gate voltage. For no gate bias (b), electron exist both at the n-AlGaAs/GaAs interface and in InAs dots. For the gate bias (c), electrons exist only in the InAs dots.

The samples were grown by MBE on (100) GaAs semiinsulating substrate. The sequence of the layers for our sample and its schematic band diagram are shown in Figure 1. A 2-μm-thick GaAs layer was grown at 640 °C. After that the InAs self-assembled dots were grown at 500 °C with nominal thickness of 1.8 ML and subsequently embedded in 30 nm of GaAs. The average in-plane diameter and height of the InAs dot are 20 and 3 nm, respectively. The density of dots is $\sim 10^{11}$ cm^{-2}. For modulation doping, a 27 nm undoped $Al_{0.33}Ga_{0.67}As$ and a 40 nm n-$Al_{0.33}Ga_{0.67}As$ with doping density of 1.3×10^{18} cm^{-3} were grown at 600 °C. An undoped 17 nm GaAs cap layer was grown at 600 °C. After brief illumination with a red light emitting diode the carrier density of $n = 1.2\times10^{11}$ cm^{-2} and electron mobility of 4×10^4 cm^2/Vs of this structure was determined by Hall measurements at 4.2 K [12].

The sample arrangement is shown in Figure 2. To constrict electron transport path laterally we adopted a split gate structure. The AuNi split gate was fabricated by electron beam lithography and liftoff. The gate length was 0.3 μm. We fabricated two different samples with spacing between the split gates of 0.3 and 1 μm.

With no gate bias electrons exist both at the AlGaAs/GaAs interface and in the InAs dots (Fig. 1(b)). By applying a negative gate bias, we can create a condition where the electrons at the AlGaAs/GaAs interface are fully depleted and the only exiting electrons are in the InAs dots (Fig. 1(c)). This can be confirmed by the calculation of electron density at the interface and in the dots. In this calculation we solved numerically the Poisson equation and the Schrodinger equation self-consistently.

The two-terminal DC drain current I_{SD} vs. V_g split gate voltage at different DC source-drain voltage V_{SD} was measured at 4.2 K. By varying the split gate bias, the Fermi level μ can be moved through quantum levels in the InAs dots between the split gates. When the Fermi level is aligned with the quantum level of the InAs dots at a certain gate voltage, electrons will flow through that quantum level of the InAs dots. As a result, the current peak can be observed at the corresponding gate voltage in the I_{SD} vs. V_g characteristics. Thus conditions of opening and closing of the channel of tunneling (width of resonant peak on I_{SD} vs. V_g characteristics) will be defined by a difference of Fermi energies in the drain and the source. Figure 3 shows the typical I_{SD} vs. V_g characteristics in a sample

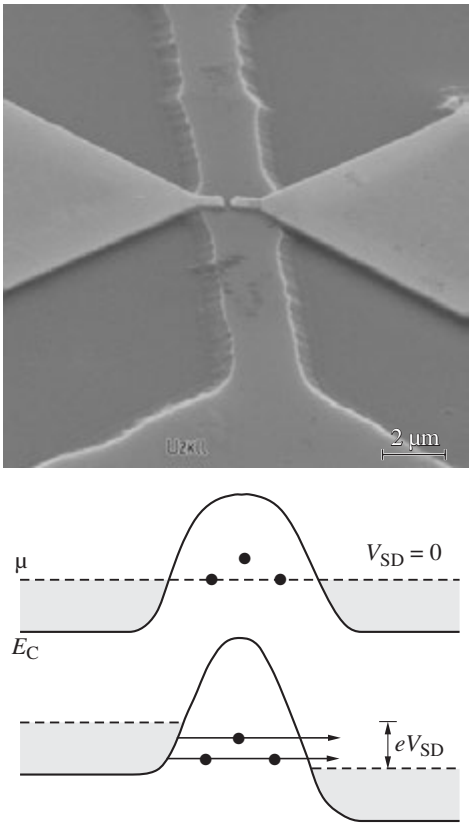

Fig. 2. The TEM micrograph of the split gate structure forming 1D constriction. The cross section of the our structure with 2D source and drain (shaded area) and the barrier between them.

with the split gates spacing of 0.3 μm. There are five distinctive peaks (numbered A, B, C, D and E in Fig. 3) in the voltage range from -1.2 to -0.8 V. Significant increasing of amplitudes of resonant features with increase of the source-drain voltage V_{SD} is caused by increasing of a transparency of a tunnel barrier. The insignificant increase in width of observed peaks with the source-drain voltage related to small change of Fermi energy in this interval of the V_{SD}.

The most interesting is the appearance of additional peaks A and B only at high source-drain bias. It is known that maximum resonant current flows through a zero-dimensional state located exactly in the center of the barrier. In our sample an increase of the source-drain voltage leads to the decreasing of the barrier thickness in the point-contact. But the barrier thickness decreases mainly from the drain side. It means that QD's located closer to the source contact at zero bias become "central" with application of the definite source-drain bias and the resonant tunneling through these dots could to be detected.

Note, that the part of observed peaks can be connected not only to tunneling through states of individual InAs QDs, but also with sequential tunneling through a pair of dots in comparatively long (0.3 μm) 1D channel. It can be the origin of distinction of shapes of observed resonant features.

In conclusion, we present two-terminal measurements through a 1D constriction created by a split gate. We observe resonant tunneling current peak through a quantum dot that is in, or close to, the 1D constriction. These conductance measurements provide information about the individual quantum dots formed by the self-assembled InAs dots.

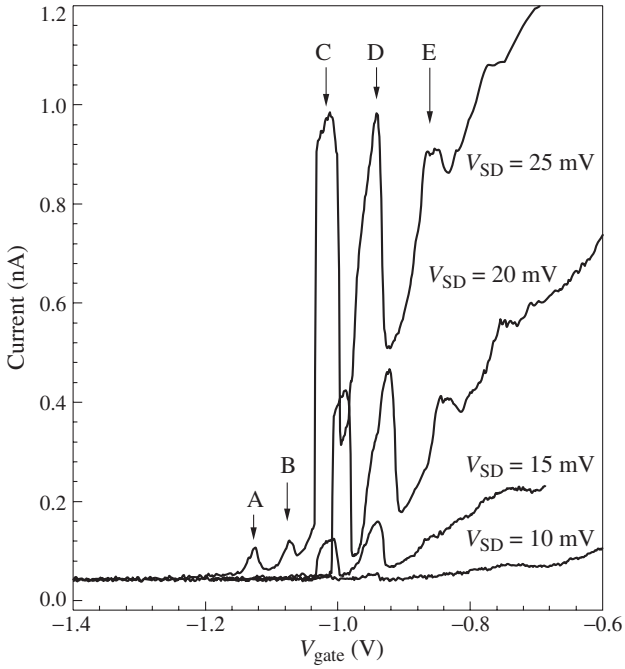

Fig. 3. Drain current vs. gate voltage characteristics at different source-drain voltages V_{SD} for sample with spacing between the split gates of 0.3 μm.

Acknowledgements

The work is partly supported by RFBR (03-02-17693), FTNS program and RAS programs "Quantum Macrophysics", and "Low-Dimensional Quantum Nanostructures". YVD gratefully acknowledge support from the Royal Society. We are gratefully to L.G. Maistrenko and R.N. Vydumkina for technical assistance.

References

[1] D. Leonard, K. Pond and P. M. Petroff, *Phys. Rev. B* **59**, 11687 (1994).
[2] D. Bimberg, M. Grundmann and N. N. Ledentsov, *Quantum Dot Heterostructures*, (New York: John Wiley & Sons) 1999.
[3] G. Medeiros-Ribeiro *et al*, *Appl. Phys. Lett.* **66**, 1767 (1995).
[4] K. H. Schmidt *et al*, *J. Appl. Phys.* **95**, 5715 (2004).
[5] M. Narihiro *et al*, *Appl. Phys. Lett.* **70**, 105 (1997).
[6] A. S. G. Thornton *et al*, *Appl. Phys. Lett.* **73**, 354 (1998).
[7] E. E. Vdovin *et al*, *Science* **290**, 122 (2000).
[8] I. Hapke-Wurst *et al*, *Phys. Rev. B* **62**, 12621 (2000).
[9] N. Horiguchi *et al*, *Appl. Phys. Lett.* **70**, 2294 (1997).
[10] G. H. Kim *et al*, *Phys. Rev. B* **61**, 10910 (2000).
[11] S. K. Jung *et al*, *Physica E* **7**, 430 (2000).
[12] P. Redkozubov *et al*, *Proc. 11th Int. Symposium "Nanostructures: physics and technology" (St Petersburg, Russia 2003)*, Ioffe Institute, 404–405, 2003.

13th Int. Symp. "Nanostructures: Physics and Technology"
St Petersburg, Russia, June 20–25, 2005

Experimental study of vertical transport in semiconductor superlattices with narrow barriers

A. A. Andronov[1], *D. I. Zinchenko*[1], E. P. Dodin[1], M. N. Drozdov[1], Yu. N. Nozdrin[1], V. I. Shashkin[1], A. A Marmalyuk[2] and A. A. Padalitsa[2]

[1] Institute for Physics of Microstructures, Russian Academy of Sciences, Nizhny Novgorod GSP-105 603600, Russia
[2] SIGM plus, Vvedenskogo Str, 3, 117342, Moscow, Russia

Abstract. Transport and current oscillations in GaAs–GaAlAs superlattices of 173 Å and 195 Å periods and with weak barriers and lowest miniband laying below optical phonon energy is studied at 4–300 K. The SLs demonstrate transition from single miniband transport to multiminiband transport and disappearance of NDC at $T > 200$ K. These studies is a first step to fabrication of Terahertz Bloch oscillator on such SLs, proposed earlier.

Introduction

Study of vertical transport in semiconductor superlattices (SL) with narrow minibands and narrow minigaps is of great interest from the point of view of studying transition from single miniband transport to multiminiband transport and also as a way of realization of negative differential conductivity (NDC) caused by Bloch oscillations of electrons at Terahertz frequency and construction of Terahertz oscillator on this basis [1]. In high quality superlattices (SLs) with narrow barriers and relatively wide wells, when the primary mechanism of scattering is the polar optical phonon scattering, coherent quasiballistic electron transport in conduction miniband needed for appearance of NDC can be realized at low temperatures, if the lowest miniband is below optical phonon energy. In this work transport properties just of such SL are investigated.

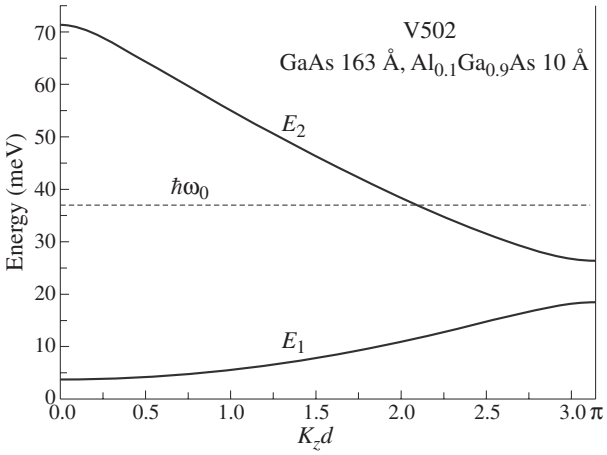

Fig. 1. First 2 minibands of V502 sample.

1. Transport properties

We have studied electron transport phenomena in undoped GaAs/$Al_xGa_{1-x}As$ ($x = 0.1$ is aluminium portion in AlGaAs barrier) superlattices grown by MOCVD on n+GaAs substrate with impurities concentration $N_i = (1-4)\times10^{18}$ cm^{-3} (Si) with parameters given in the Table 1. The SL is capped with similar n+GaAs layer with doping about $N_i = 1.5\times10^{18}$ cm^{-3} (Si).

Table 1. Sample parameters.

Sample	Period (Å) $d = b + w$	b (Å)	Number of layers
D426	196	10	100
V502	173	10	150

Studied samples are made in the form of circular diodes 500 and less micrometers in diameters. The ohmic contacts are provided by standard Au-Ni-Si deposition and thermal treatment.

Energy spectrum of first and second conduction minibands for V502 structure can be seen in Fig. 1. Here the optical phonon energy $\hbar\omega_0 = 36$ meV is higher then the first minigap. Acoustic scattering in the lowest miniband with width $\Delta E_1 \approx 15$ meV is small compared to polar optical phonon energy also shown in the figure. In this case electrons are easily heated up in the first miniband, so NDC appears caused by Bragg reflection on Brillouin zone boundary. In high electric fields electrons can perform cyclic ballistic motion (Bloch oscillations) inside the first miniband even out of NDC region. It is this oscillation in such field which could provide dynamic NDC [1] in THz range.

To our knowledge transport experiment on such SLs have not been performed so far. Static current-voltage curves for SL D426 and V502 at 4 K and 78 K are given in Fig. 2. For D426 there are two NDC regions (hatched). Similar current-voltage curves with less pronounced NDC regions are found for re-

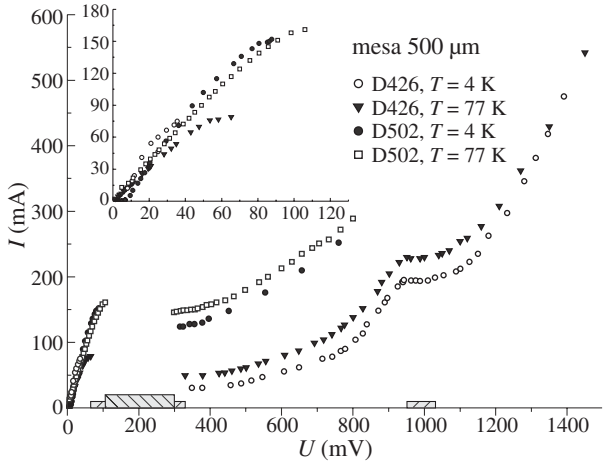

Fig. 2. Current-voltage curves for samples D426 and V502 at 4 and 77 K.

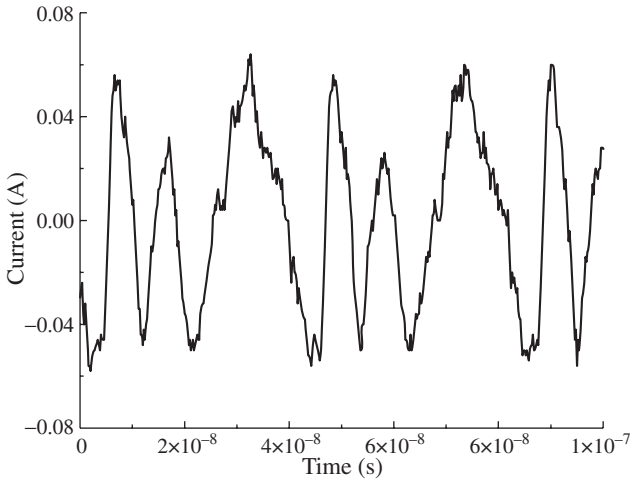

Fig. 3. Current oscillations in sample V502.

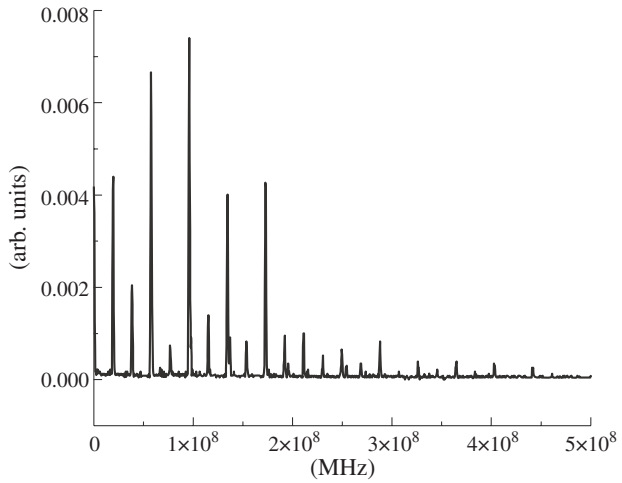

Fig. 4. Spectrum of oscillations shown in Fig. 3.

verse bias. Outside the NDC regions at higher fields current is a rising function of electric field. In this region multiminiband transport takes place produced by interminiband Zener tunneling (cf. [1].) The static NDC regions in all of the SL studied disappears at T above about 200 K. On the other hand at the temperatures where NDC exists in all of the SL studied both periodic and aperiodic current oscillation in the MHz band were observed. Depending on applied voltage, biasing and circuit the principal frequency of the oscillations (Fig. 3) can be from one to several MHz. The spectrum of the oscillations (Fig. 4) shows that harmonics up to 10th with frequency up to 300 MHZ are observed.

2. Conclusion

We have studied transport in GaAs-GaAlAs weak barrier SL and at low temperatures (below 200 K) observe transition from single miniband to muliminiband transport. At $T > 200$ K disappearance of nonlinearaty in current voltage curves and NDC there observed. This studies are the first step to find low temperature dynamic NDC in the THz range in such SLs. And in the report further results on transport, current oscillation and THz emission from these and other similar weak barrier GaAs-GaAlAs SL will be reported.

Acknowledgements

The work is supported by RAS Programm “Semiconductor Lasers” and by 2005 Grant from RFBR.

References

[1] A.A. Andronov, I.M. Nefedov, A.V. Sosnin *Semiconductors* **37**, 378 (2003).

13th Int. Symp. "Nanostructures: Physics and Technology"
St Petersburg, Russia, June 20–25, 2005

Quantum phase tunnelling in ultra-narrow superconducting channels

K. Yu. Arutyunov, M. Zgirski, K.-P. Riikonen and V. Touboltsev
University of Jyväskylä, Department of Physics, NanoCentre, PB 35, 40014 Jyväskylä, Finland

Abstract. Below a certain temperature T_c (typically cryogenic) some materials lose their electric resistance R entering a superconducting state. With the natural tendency of integration of greater number of electronic components it is desirable to use superconducting elements to minimize heat dissipation. It is expected that this basic property of a superconductor (dissipationless electric current) will be preserved at reduced scales required by modern nanoelectronics. Unfortunately, there are indications that there is a certain limit 10 nm below which a "superconducting" wire is not any more a superconductor in a sense that it acquires a finite resistance. Here we report an experimental evidence of such behaviour in ultranarrow aluminium nanowires.

Introduction

A superconducting wire can be considered as quasi-one dimensional (1D) if its characteristic transverse dimension $\sqrt{\sigma}$ (σ being the cross section) is smaller than the coherence length $\xi(T)$. The shape of the bottom part of the resistive transition $R(T)$ of a 1D superconducting strip is described by the model of phase slips activation [1]. If the wire is infinitely long, then there is always a finite probability that a "small" part of the sample is instantly driven normal: locally the modulus of the order parameter Δ goes to zero and its phase f "slips" by 2π. One can make a formal analogy with a "classical" jump of a particle (e.g. a gas molecule) over an energy barrier ΔF provoked by a thermal energy $k_B T$. However, keeping in mind that system is quantum, there should be an alternative mechanism attributed to tunnelling through the barrier.

1. Experimental

We have developed a method of progressive reduction of transverse dimensions of e-beam lift-off fabricated nanostructures by ion-beam sputtering [2]. The method enables galvanomagnetic measurements of the same sample in between the sessions of etching. Sputtering can be considered as an erosion of the surface due to bombardment of primary ions. The method is very promising, for it lets us directly follow changes in superconductive transition in a 1D superconductor along with successive reduction of its cross section. AFM control revealed that sputtering makes the sample surface smoother and more homogenous, eliminating inevitable imperfections while original lift-off process. Evolution of an aluminium wire shape and crossection is presented in Fig. 1.

2. Results and discussion...

Fig. 2 shows an evolution of the $R(T)$ dependencies of the same 10 μm long nanowire while a sequence of sputtering. It can be easily seen that for larger diameters (from $\sqrt{\sigma} \geq 17$ nm) the $R(T)$ dependencies follow the same qualitative behavior: relatively narrow transition with quasi-linear slope in logarithmic scale. These experimental data can be fitted with a reasonable accuracy by theoretical calculations explained in terms of the model of thermally activated phase slips [1]. The systematic shift of the mean critical temperature T_c to higher values with reduction of the wire cross section is not directly related to the effect under investigation.

When the wire effective diameter reaches 11 nm and the corresponding normal state resistance $R_N \sim 9k\Omega$, the shape

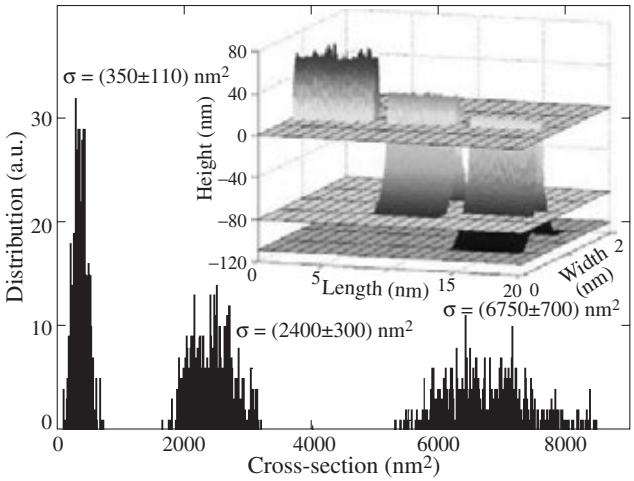

Fig. 1. Histograms showing the distribution of the wire cross section after a sequence of sputtering. Narrowing of the histograms is due to the "polishing" effect of ion sputtering. The inset shows the evolution of the sample shape while sputtering measured by SPM. Planes indicate Si substrate base levels after successive sessions of sputtering. As Si is sputtered faster then Al finally wire is situated at the top of Si pedestal. Plane (height = 0) separates Si from Al.

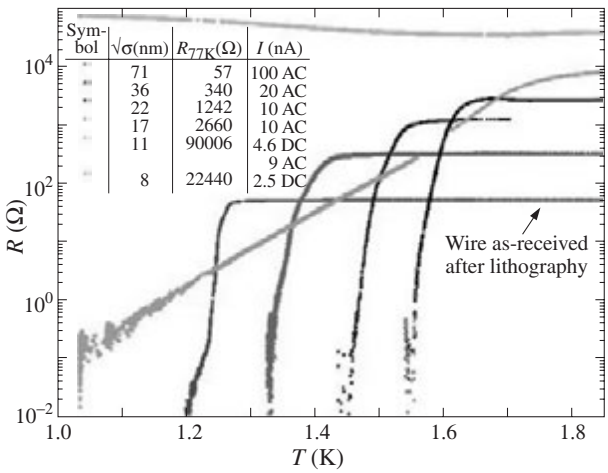

Fig. 2. Resistance vs. temperature for the same wire of length $L = 10\,\mu$m after several sputtering sessions. The sample and the measurement parameters are listed in the table. Note the qualitative difference of $R(T)$ dependencies for the two thinnest wires from the thicker ones.

of the $R(T)$ dependence dramatically changes: it suddenly becomes much "wider" (Fig. 2). Contrary to thicker wires, the shape of the transition cannot be fitted by the model of thermally activated phase slips [1] at any reasonable set of parameters. Much broader $R(T)$ transition for thinner wires we associate with the quantum phase tunnelling effect. There have been several approaches for theoretical description of this phenomenon. Here we present a comparison of our data with the renormalization theory [3]. If the wire is short enough that only one phase slip event can happen at a time, one can derive a simple phenomenological model utilizing results of the renormalization theory [3] for the rate of QPS activation . Taking into consideration the simplified "short wire" approach the correspondence between the model [3] and the experiment can be considered as satisfactory (Fig. 2).

In conclusion we have observed an evolution of the shape of $R(T)$ dependencies of ultrathin and homogeneous aluminum wires as a function of the effective diameter. With a high level of confidence the artifacts related to the structure inhomogeneity can be ruled out. We believe that our observations are related purely to a size phenomenon. Qualitatively similar results have been obtained on several sets of samples. It has been found that for effective diameters $\sqrt{\sigma} \geq 15\,\mathrm{nm}$ the $R(T)$ dependencies can be described by the model of thermally activated phase slips [1]. For thinner wires the width of $R(T)$ transition is dramatically wider, and the resistance may not tend to zero at $T \to 0$. We associate this phenomenon with manifestation of quantum phase fluctuations (quantum phase slips). The effect should have a universal validity for all superconducting materials. Apart from Al other materials (Sn, In, Pb) are in the list of our current research. The study of quantum fluctuations phenomenon suppressing superconductivity in ultranarrow wires is of a vital importance for future development of nanoelectronics. It puts a fundamental limitation to utilization of superconducting nanoelements designed to transport a dissipationless electric current.

References

[1] J. S. Langer and V. Ambegaokar, *Phys. Rev.* **164**, 498 (1967).
[2] M. Savolainen, V. Touboltsev, P. Koppinen, K.-P. Riikonen and K. Arutyunov, *Appl. Phys. A.* **79**, 1769 (2004).
[3] D. S. Golubev and A. D. Zaikin, *Phys. Rev. B* **64**, 014504 (2001).

13th Int. Symp. "Nanostructures: Physics and Technology"
St Petersburg, Russia, June 20–25, 2005

Lateral quasiballistic transport in nanostructures based on short-period $(GaAs)_n/(AlAs)_m$ superlattice under high electric field

V. T. Trofimov[1], M. V. Valeiko[1], N. A. Volchkov[1], K. S. Zhuravlev[2], E. V. Kiseleva[3], M. A. Kitaev[4], V. A. Kozlov[5], S. V. Obolenskii[3] and A. I. Toropov[2]

[1] P.N.Lebedev Physical Institute of RAS, 119991 Moscow, Leninskii pr. 53, Russian Federation
[2] Institute of Semiconductor Physics SD RAS, Novosibirsk, Russian Federation
[3] N.I.Lobachevskii Nizhegorodskii University, Russian Federation
[4] NPP "Salut", Nizhnii Novgorod, Russian Federation
[5] Institute of Microstructure Physics, Nizhnii Novgorod, Russian Federation

Abstract. Quasi-ballistic regime of electron motion was realized along heterointerface of undoped GaAs and short-period superlattice (SL) under high electric field. For the gallium arsenide, record high value of electric current per single carrier participating in charge transfer was obtained in nanostructures with planar length of ∼100 nm. We have found that in developed structures a mean value of electron velocity exceeds of 5×10^7 cm/s, while the time of electron pass through the structure equals to $\sim 2\times10^{-13}$ s. This regime was achieved due to injection of high energy electrons into the ballistic motion zone with an energy much higher than the thermal one, realization of sharp gradient of electric field and compression of trajectories of electron motion after sliding reflection from blocking superlattice.

Introduction

Fabrication of semiconductor nanostructures with high transport properties is one of the basic problems of nanotechnology. The maximum of specific current is achieved under high electric field due to overshoot effect when carrier motion in short-period structures becomes ballistic. To realize the ballistic motion it is necessary to accelerate an electron from Γ-valley up to extreme velocity as fast as possible without scattering in the higher valleys. That requires creation of sharp gradients of high electric field inside the structure.

In case of lateral transport it is difficult to create high electric field with large gradients (that needs high carrier concentration) and to prevent scattering of carriers. In the present paper a quasiballistic lateral transport of electrons is realized near the heterointerface of undoped GaAs and short-period superlattice $(GaAs)_n/(AlAs)_m$ in short-length nanostructures.

1. Experimental

Nanostructures with the lateral length of 0,1 μm and width of 50 μm were formed under V-like groove breaking heavy-doped contact layers of heterostructure (Fig. 1). The gate electrode was formed on the wall nearest to the source.

The base of the structure is short-period reflecting $(GaAs)_n/(AlAs)_m$ superlattice (SL) made of GaAs and AlAs layers with the thicknesses of 12 and 6 monolayers respectively. At the top heterointerface of SL the 35 nm thick i-GaAs layer was grown containing in the upper part δ-Si supply layer with sheet concentration of $\sim 2.0\times10^{12}$ cm^{-2}, which serves as conducting channel under weak electric field.

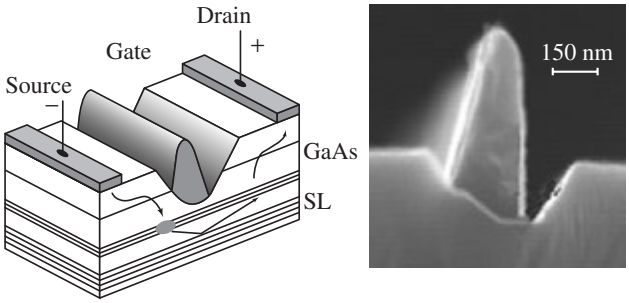

Fig. 1. Layout of $(GaAs)_n/(AlAs)_m$ short-period superlattice and SEM image of its split off.

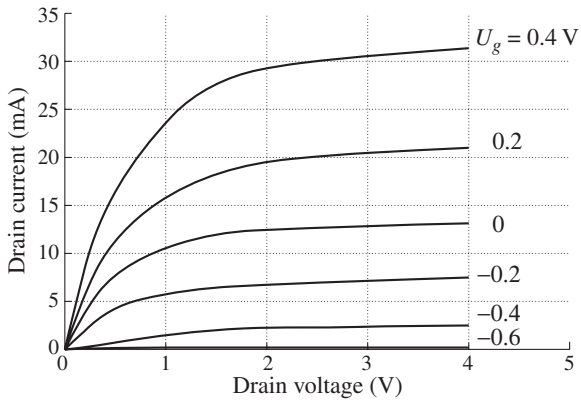

Fig. 2. The dependence of drain current on source-drain voltage at $T = 300$ K and various gate potentials. The value of transconductance achieves more than 1 Sm/mm.

Under the high electric field the whole i-GaAs layer acts as a conducting channel because of the energy diagram distortion and small De Broglie wavelength of electron. Carrier mobility in the GaAs layer was ∼ 8000 and ∼ 65000 cm^2/V s at 300 and 77 K, respectively. Conducting channel was covered by 1.5 nm thick barrier AlAs layer which is used as an injector of hot electrons. The presence of AlAs layer do not prevent electrons from penetrating to extractor zone located at the end of nanostructure close to the drain electrode. Effective scattering of hot electrons in the extractor leads to static negatively charged domain formation, that additionally increases electric field magnitude in the ballistic zone. The structure was finally covered by n^+-GaAs⟨Si⟩ contact layer.

Period of SL was optimized to reach a value of hot electrons reflection coefficient as high as 90%. That was achieved by means of small subband width of SL.

The proposed scheme of lateral transport allows to realize quasiballistic regime of electron motion with velocities close

to the overshoot at the length of more than 100 nm due to following reasons.

1. The region of high electric field is formed between heavily doped injector and extractor where depletion length is as low as 20 nm. It allows to realize a large gradient of the electric field. As a result the electrons acquire the energy close to X-valley edge at the time comparable with the momentum relaxation time ($\sim 10^{-13}$ s).

2. From the substrate side the motion of electrons is confined by reflector SL which forms effective potential barrier of $\sim$ 1 eV height both for cold and hot carriers of Γ-valley and minimizes the length of the trajectories of their motion.

3. Electrons are injected into the high electric field region after tunneling through 1.5 nm thick AlAs barrier, so their mean energy is much higher than the thermal one. The presence of barrier brings additional confinement of the electrons in the injection and extraction zones.

In Fig. 2 the current-voltage characteristics of nanostructure are shown for $T = 300$ K at various potentials of gate electrode. The drain current saturation for the most of samples starts at the gate voltage of 0.7 V due to intervalley scattering of electrons mainly into X-valley of GaAs.

The transconductance (the derivative of drain current by voltage on the gate electrode U_g, which controls transversal electric field) achieves the value as high as 1 S/mm which is absolute record for GaAs and can be compared to the best values for p-HEMT structures with InGaAs channel. The measured capacity of the gate electrode was $\sim$ 30 fF.

2. Modeling of electron transport

The nanostructure transconductance value S allows one to determine main transport properties of electron gas inside the channel. For a short-channel structure with length and width being equal to L^* and W respectively the transconductance can be written as follows:

$$S = \frac{\Delta J_d}{\Delta U_g} = \frac{\Delta(e \cdot n_s \cdot v \cdot W)}{\Delta U_g} = \frac{\Delta Q}{\Delta U_g} \cdot \frac{v}{L^*} = \frac{C_0}{\tau} \quad (1)$$

where $\Delta Q = (e \cdot n_s \cdot L^* \cdot W)$ is the net charge of carriers in the nanostructure, $\tau = L^*/v$ is time of electron pass through nanostructure, e — charge of electron, n_s — sheet carrier concentration and v — their mean velocity, C_0 — active part of input electric capacity which controls the dependence of electron concentration in nanostructure on transversal potential. The formula allows one to estimate time of flight $\tau \sim 2 \times 10^{-13}$ s which occurs to be purely comparable to momentum relaxation time τ_δ, and mean velocity of electron motion $v \sim 5 \times 10^7$ cm/s which exceeds almost five times the value for long samples.

Monte-Carlo simulation of electron motion inside the nanostructure showed that due to high starting velocity the most of carriers move quasiballistically participating only in 5–6 small angle scattering acts. As a result the trajectories shape is close to collisionless one and mean electron velocity exceeds the saturation one at least in 3–4 times. Relative contribution of non-sliding reflections from SL is negligible due to high quality of the interface and low incidence angles of electrons on heterointerface.

Figure 3 shows simulated trajectories of electron motion in the structure. The splitting of trajectories occurs due to scattering of carriers on donor impurities during crossing over

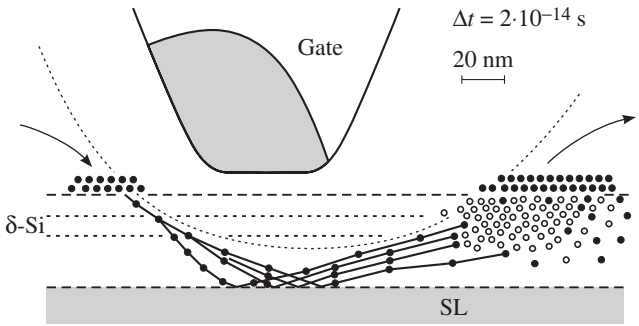

Fig. 3. Trajectories of electron motion in the vicinity of V-ditch. Dots denote the electron positions in time intervals of $\Delta t = 2 \times 10^{-14}$ s: • — electrons localized in Γ-valley, ○ — electrons in L- and X-valleys. Dashed line shows the boundary of depletion space around V-ditch surface.

GaAs⟨δ-Si⟩ layer and phonon scattering which at high electron energy also occurs at small angles only. The most of electrons pass the structure being located in Γ-valley, that provides their high mean velocity. Sharp increase of scattering probability into X-valley accompanied by intervalley high energy (0.55 eV) phonon emission limits the possible starting electron energy in the injector because further starting energy increase leads to reduction of free path length. As a result for the given effective nanostructure length L^* the optimum of starting energy exists. According to our estimations it is about 50 meV.

Time of flight value and mean velocity value averaged through the trajectories equal to $\sim 2 \times 10^{-13}$ s and $\sim 5 \times 10^7$ cm/s, being in an excellent agreement with the estimations made earlier. The proposed scheme of nanostructure could be used for semiconductor devices fabrication, particularly for gigahertz and terahertz frequency range devices.

Acknowledgement

The investigations were partially supported by RFBR, grant No. 04-02-17385.

13th Int. Symp. "Nanostructures: Physics and Technology"
St Petersburg, Russia, June 20–25, 2005

The Monte-Carlo simulation of transport in quantum well GaAs/AlGaAs heterostructure doped with shallow donors under impurity breakdown

L. V. Gavrilenko, V. Ya. Aleshkin and A. A. Dubinov
Institute for Physics of Microstructures RAS, Nizhny Novgorod, Russia

Abstract. The impurity breakdown was simulated in numerical calculations. The distribution function for an electron in the electric field was calculated using the Monte-Carlo method. The electron concentration in the impurity ground state and in the first subband was determined by solving the rate equations. It was found out that the population inversion between the 1s-level and the bottom of the first subband is likely arise. The requirements for population inversion to occur were determined.

Introduction

The states of shallow impurities in semiconductors is a very promising object from the point of view of laser generation in the far infrared region. Stimulated light emission has been observed for hole transitions between the resonant and localized states of shallow acceptors in axially stressed bulk Ge [1]. A likely mechanism behind appearance of the population inversion in this experiment is depopulation of the impurity state due to the impact ionization in the electric field. It is well known that the properties of a shallow impurity state in a quantum well (QW) are more flexible compared with those in a bulk semiconductor.

In this paper the modelling of the impurity breakdown in QWs GaAs/$Al_{0.3}Ga_{0.7}As$ under applied electric field was carried out. The distribution function for the electron momentum vector and energy was calculated using the Monte-Carlo method. The distribution function was formed due to scattering on the optical and acoustical phonons and impurity scattering. We sought the electron concentration in the impurity ground state and in the first subband by solving the rate equations. The modelling revealed a possibility for a population inversion to occur between the 1s-level and the bottom of first subband. We also found the population inversion requirements.

The donor ground state is depopulated due to the impact ionization, but is filled up by Auger-recombination processes and PO phonon scattering processes. The excess of the bottom subband population over the population of the 1s state is achieved under an electric field and PO phonon scattering forming a non-equilibrium electron distribution function.

The simulation was carried out for GaAs/$Al_{0.3}Ga_{0.7}As$ QW heterostructure, quantum well width was 200 A, the delta-doped layer was localized in the quarter of the QW width from heterointerface. The electric field was directed along the quantum well layer.

1. Modelling of impurity breakdown

The distribution function $f(k)$ was calculated for the case of a single quantum well in an electric field at liquid Helium temperature by the Monte-Carlo method. We regarded for the carriers transitions between three lower subbands only, because in an electric field up to 1000 V/cm the higher subbands are empty. As to the scattering processes, we took into account the carriers transitions due to the optical and acoustical phonon scattering. We also considered impurity scattering. It is assumed that the rates for both intra-subband and inter-subband transitions strongly exceed the rate of transitions involving the impurity states. The Monte-Carlo simulation determines the distribution function shape only. The variation of a steady-state carrier density and the absolute value of $f(k)$ with electric field can be described by the rate equations.

$$(N_\mathrm{d} - N)(a\nu_\mathrm{opt} + a^2\nu_\mathrm{Auger}) - Na\nu_\mathrm{imp} = 0\,,$$
$$N + a\frac{1}{(2\pi)^2}\int f(k)d^2k = N_\mathrm{d}\,, \qquad (1)$$

where a is the normalization factor for $f(k)$, N is the electron concentration in the 1s donor level, N_d is the donor concentration in the δ-doped layer. ν_opt, ν_imp, ν_Auger are the frequencies of PO phonon scattering, impact ionization and Auger-recombination involving the 1s state, respectively. By solving these equations we find the values of N and a. $a\,f(k)$ is the probability of electron occupation state with energy ε. Population inversion exists, if $max(af(\varepsilon)) > N/N_\mathrm{d}$.

2. Scattering mechanisms

An electron in the first subband may pass to the donor level with emission by a polar optical (PO) phonon, a deformation acoustical (DA) phonon, a piezoelectric acoustical (PA) phonon and due to Auger process. The frequencies of scattering on PA and DA phonons are negligible in comparison with the PO phonon scattering frequency [2]. We calculated the PO phonon scattering frequency using the method described in [3].

At low temperature in an electric field the impact ionization becomes a primary ionization mechanism. We calculated the probability of impact ionization and Auger process for the 1s donor level and the first subband, using the Born approximation. The process of Auger-recombination is exactly the opposite to impact ionization. The matrix elements for the electron-electron interaction are:

$$B_{i,j}^{l,m} = \int d^3r \int d^3r' \Psi_i(r)\Psi_j(r')\frac{e^2}{\kappa\sqrt{r^2 - r'^2}}\Psi_l^*(r)\Psi_m^*(r'), \quad (2)$$

here $\Psi_i(r)$ and $\Psi_j(r')$ are the wave functions of the initial states of system, $\Psi_l(r)$ and $\Psi_m(r')$ are the wave functions of the final states. It is obvious that in our case equation (2) is a double Fourier-transformation for the Colomb potential. Both of the triple integrals are solved analytically.

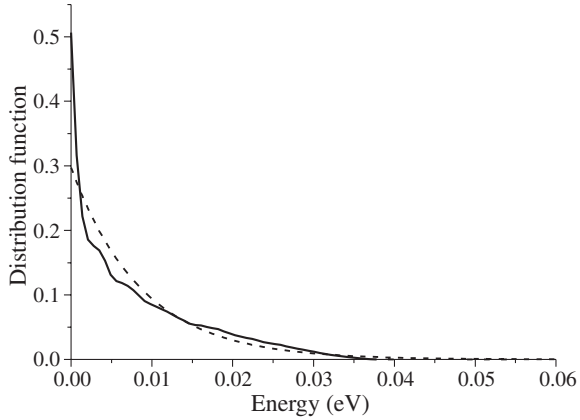

Fig. 1. The comparison of the calculated distribution function (solid line) and Maxwell distribution function for the same average electron energy (8,7 meV) (dashed line) for $N_d = 6 \cdot 10^{10}\,cm^{-2}$ and electrostatic intensity = 10 V/cm.

In this paper we do not consider the cascade Auger capture, i.e., an electron being captured in exited donor state and scattering on the acoustical phonons. But the acoustic phonon scattering is a very rare process in contrast to the Auger capture and impact ionization, so almost all captured electrons are being knocked back to the first subband. Moreover, if the donor excited level is occupied, transitions to the 1s-state are forbidden. Hence, consideration of the cascade Auger capture will only make the conditions for population inversion less stringent.

3. Distribution function and population inversion

A strongly non-equilibrium shape of the electron distribution function is the necessary condition for the population inversion to appear between the 1s donor level and the bottom of the first subband. A highly non-equilibrium electron distribution in an electric field is formed as a result of a PO phonons scattering. The impurity scattering and the acoustical phonons scattering are quasielastic processes, so they do not affect the distribution function shape very much. In Fig. 1 the calculated distribution function is shown versus the Maxwell distribution function for the same average electron energy. It is seen from the picture that the probability for an electron to be found at the bottom of the first subband is high for the non-equilibrium distribution function.

4. Results and discussion

The area of inversion depending on the electric field magnitude and donor concentration is shown in Fig. 2. It is obvious that in a small electric field the distribution function is almost equilibrium and there is no inversion. On the other hand in a strong electric field the distribution function becomes wide and the inversion disappears.

The PO phonon scattering is a fast process of filling up the 1s state, so one needs a rather high donor concentration (about $10^{10}\,cm^{-2}$) to increase the impact ionization frequency. But the Auger-capture frequency depends on N_d^2. This fact sets a limit on the donor concentration maximum.

Acknowledgements

This work has been supported by RFBR (grant 04-02-17178), Russian Science Support Foundation.

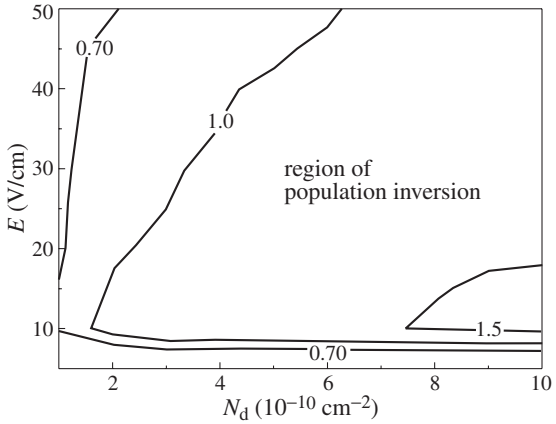

Fig. 2. The isolines of the ratio of the 1s state population N/N_d to the population of the first subband bottom $af(\varepsilon = 0)$ as a function of the electric field and the donor concentration.

References

[1] I. V. Altukhov, M. S. Kagan *et al*, *JETP*, **88**, 514 (1999).
[2] V. Ya. Aleshkin, L. V. Gavrilenko *Proc. 11th Phohons Scattering in Condensed Matter*, St Peterburg, Russia 2004.
[3] V. Ya. Aleshkin *et al*, *JETP*, **98**, 1340 (2004).

13th Int. Symp. "Nanostructures: Physics and Technology"
St Petersburg, Russia, June 20–25, 2005

Dephasing in presence of a magnetic field

A. V. Germanenko[1], I. V. Gornyi[2,3], G. M. Minkov[4] and V. A. Larionova[1]

[1] Institute of Physics and Applied Mathematics, Ural State University, 620083 Ekaterinburg, Russia
[2] Institute für Nanotechnologie, Forschungszentrum Karlsruhe, 76021 Karlsruhe, Germany
[3] Ioffe Physico-Technical Institute, St Petersburg, Russia
[4] Institute of Metal Physics RAS, 620219 Ekaterinburg, Russia

Abstract. Effect of the magnetic field on the rate of phase breaking is studied. It is shown that that magnetic field resulting in decrease of phase relaxation rate τ_ϕ^{-1} makes the negative magnetoresistance due to suppression of the electron interference to be smoother in the shape and lower in the magnitude than that found with constant τ_ϕ^{-1}-value. Nevertheless our analysis shows that experimental magnetoconductance curves can be well fitted by the Hikami-Larkin-Nagaoka expression [1]. The fitting procedure gives the value of τ/τ_ϕ, where τ is the quasimomentum relaxation time, which is close to the value of $\tau/\tau_\phi(B=0)$ with an accuracy of 25% or better when the temperature varies within the range from 0.4 to 10 K. The value of the prefactor α found from this procedure lies within the interval 0.9 . . . 1.2.

Introduction

The interference correction to the conductivity originates in the constructive interference of time-reversed electron trajectories. How can the dephasing time, τ_ϕ, be obtained experimentally? As a rule, the value of τ_ϕ (or the ratio τ/τ_ϕ referred further as γ) is extracted from an analysis of the negative magnetoresistance arising due to the suppression of the weak localization by a magnetic field. The experimental $\Delta\sigma(b)$-vs-b curves are often fitted to the well-known expression [1]:

$$\Delta\sigma(b) = \alpha G_0 \left[\psi\left(0.5+\gamma b^{-1}\right) - \ln\left(\gamma b^{-1}\right)\right], \quad (1)$$

where $\Delta\sigma(b) = 1/\rho_{xx}(b) - 1/\rho_{xx}(0)$, $\psi(x)$ is a digamma function, b stands for the magnetic field measured in units of transport magnetic field, $B_{tr} = \hbar/(2el^2)$ with l as the mean free path, $G_0 = e^2/(2\pi^2\hbar)$. Although the prefactor α must be equal to unity within the framework of the conventional weak-localization theory, it is always used by experimentalist as the second fitting parameter together with τ_ϕ. Other expression obtained within different approximations are used as well. The comparative analysis of all known formulas can be found in [2].

Generally, the value of τ_ϕ found from the magnetoresistance should not coincide with that for $b = 0$. It is due to the fact that all the expressions referred above do not take into account the magnetic field dependence of the phase relaxation rate. Physically, it can be understood as follows. It is clear that only the effects which result in phase shift between a pair of closed paths traversed in opposite directions of about π destroy the phase coherence. Therefore for the closed paths with length L only the inelastic processes with energy transfer higher than $\sim \hbar v_F/L$ contribute to the dephasing rate (v_F is the Fermi velocity). For the long trajectories, $L > \sqrt{D\tau_\phi}$, where D is the diffusion coefficient, all the inelastic processes determining the phase breaking time τ_ϕ contributes to the dephasing rate and, hence, it is determined by the value of τ_ϕ. For the short paths, $L < \sqrt{D\tau_\phi}$, the dephasing rate is determined by the length of the paths rather than τ_ϕ. Since a magnetic field puts the long trajectories with $L > l_B$, where $l_B = \sqrt{\hbar/eB}$ is the magnetic length, out of the interference, the inelastic processes with energy transfer less than $\sim \hbar v_F/l_B$ becomes to be inefficient. Thus, the increase of the magnetic field should decrease of the dephasing rate.

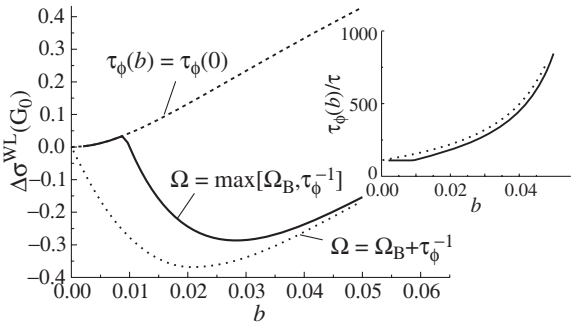

Fig. 1. The dependence $\Delta\sigma(b)$ calculated from Eqs. (2) and (4) with $\Omega = \max[\Omega_b, \tau_\phi^{-1}]$ (solid curve), $\Omega = \Omega_b + \tau_\phi^{-1}$ (doted curve), and with constant phase breaking time $\tau_\phi(b) = \tau_\phi(0)$ (dashed curve). Inset shows the corresponding dependences $\tau_\phi(b)$. The parameters used are $k_F l = 17.8$, $n = 4.5 \times 10^{15}\,\mathrm{m}^{-2}$, $\tau = 3.3 \times 10^{-13}\,\mathrm{s}$, $F_0^\sigma = -0.334$, and $T = 1.5\,\mathrm{K}$.

In present paper this problem is considered more comprehensively. In particular, we solved the problem of the influence of the magnetic field on the dephasing numerically.

As mentioned above, Eq. (1) has been derived in the assumption that the dephasing rate is independent of magnetic field. Let us firstly demonstrate analytically how delicate the problem of the low-B magnetoresistance is. Our consideration is based on the results published in [3]. In the diffusion regime, for which $T\tau \ll 1$, the magnetoconductivity $\Delta\sigma(B, T)$ is presented in the following form

$$\frac{\Delta\sigma(b,T)}{G_0} = \psi\left(\frac{1}{2}+\frac{1}{b}\frac{\tau}{\tau_\phi(T,b)}\right) - \ln\left(\frac{1}{b}\frac{\tau}{\tau_\phi(T,0)}\right), \quad (2)$$

where

$$\tau_\phi^{-1}(T,b) = I_2\left(T, \max\left[\Omega_b, \tau_\phi^{-1}(T,b)\right]\right), \ \Omega_b = b\tau^{-1}, \quad (3)$$

and

$$I_2(T,\Omega) = \left(1 + \frac{3(F_0^\sigma)^2}{(1+F_0^\sigma)(2+F_0^\sigma)}\right)\frac{T}{g}\ln\left(\frac{T}{\Omega}\right). \quad (4)$$

Here, $g = \sigma/(\pi G_0)$ and F_0^σ is the Fermi-liquid constant. Eq. (2) is very similar to Eq. (1). The only difference is that now the dephasing time in the digamma function appears to be magnetic field dependent through the b-dependence of I_2. The magnetic field dependence of $\tau_\phi(T, b)$ comes from the lower self-consistent cut-off in the frequency integral determining the

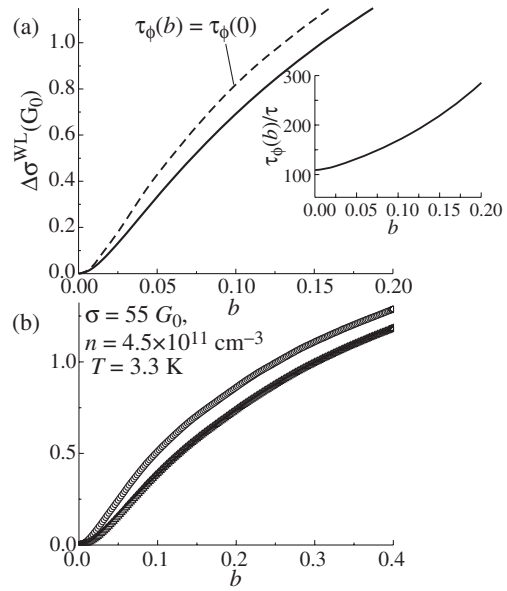

Fig. 2. (a) The dependence $\Delta\sigma(b)$ found from self-consistent solution of Eqs. (2) and (5) (solid curve). Dashed curve is Eq. (1) with constant phase breaking time $\tau_\phi = \tau_\phi(0)$. Inset shows the corresponding dependence $\tau_\phi(b)$. The parameters used in calculation are the same as in Fig. 1. (b) The magnetoconductance obtained from the simulation with a constant rate of the dephasing (circles) and taking into account its magnetic field dependence (triangles). Curve is the best fit to (1) carried out at $b \le 0.4$, the fitting parameters are $\alpha = 0.89$, $\gamma = 0.018$.

value of I_2. In [3] this cut-off was set to $\Omega = \max[\Omega_b, \tau_\phi^{-1}]$. Fig. 1 shows the result for magnetoconductivity obtained using Eqs. (2)–(4). As seen these expressions yield very strange behavior of $\Delta\sigma(b)$ in low magnetic fields which follows from the rough cut-off in I_2. It can be made smoother by choosing $\Omega = \Omega_b + 1/\tau_\phi$. Usually, this approach works perfectly, however this is not the case for the present problem of a low-B magnetoresistance. The substitution $\Omega = \Omega_b + 1/\tau_\phi$ does not improve the situation radically. As seen from Fig. 1, it results in a positive linear magnetoresistance in low magnetic field.

In principle, the situation can be improved if one does not use the artificial cut-off and calculate the dephasing rate more carefully. We propose the self-consistent equation for $1/\tau_\phi(T, b)$ which matches Eq. (3) in the limiting cases $\Omega_b = 0$ and $\Omega_b\tau_\phi \gg 1$ and does not lead to the spurious linear contribution,

$$\frac{1}{\tau_\phi(T,b)} = \mathcal{A}\frac{T}{g}\left[\ln\left(\frac{T}{\Omega_b}\right) - \psi\left(\frac{1}{2} + \frac{1}{\Omega_b\tau_\phi(T,b)}\right)\right], \qquad (5)$$

where $\mathcal{A}$ is multiplier in brackets in Eq. (4). As Fig. 2a illustrates the simultaneous solution of the equations (2) and (5) gives the significantly more realistic behavior of the magnetoconductance and, from our point of view, it reflects the physics of the b increase of the phase breaking time more adequately. It is seen that the magnetoconductance is positive in all magnetic fields and its magnitude is practically the same that that corresponding to B-independent dephasing rate. For the first sight it seems to be surprising since the phase breaking time appreciably increases with magnetic field increase (see inset in Fig. 2a). However, this fact is justified by the results of the computer simulation.

As shown in [4] the weak localization correction in two dimensions can be found as follows

$$\delta\sigma = -2\pi l^2 G_0 \int W(0,t)dt\,, \qquad (6)$$

where $W(r,t)$ obeys the equation

$$[\partial/\partial t - D\nabla^2 + U(r)]W(r,t) = \delta(t)\delta(r)\,. \qquad (7)$$

Here, $U(r)$ is given by [5]

$$U(r) = \tau_0^{-1}\ln\left(1 + |r|\sqrt{T/D}\right) \qquad (8)$$

with $\tau_0 = \hbar g/(2k_B T)$. Instead of finding the analytical solution of the problem we have analyzed the influence of the magnetic field on the dephasing using the simulation approach. Since this approach is thoroughly described in [6], we give here only the modifications. Earlier, the phase breaking in the simulation was taken into account by introducing the phenomenological parameter l_ϕ, which reduced the contribution of each closed path to the interference correction by a factor $\exp(-l_k/l_\phi)$, where l_k was the length of k-th closed path. So, such an approach corresponds to (7) with $U(r) = 1/\tau_\phi = v_F/l_\phi$. In order to simulate the situation corresponding to (7) with $U(r)$ from (8), the following replacement has been made

$$\exp\left(-\frac{l_k}{l_\phi}\right) \to \prod_{i=1}^{I_k}\frac{1}{1+\tau U(r_i^k - r_1^k)}\,, \qquad (9)$$

where production runs over the collisions, I_k stands for the number of collisions for k-th closed path, and $|r_i^k - r_1^k|$ is the distance between starting point and i-th collision. Fig. 2b shows a plot of the magnetoconductance calculated with parameters corresponding to the 2D system with $n = 4.5\times10^{15}\,\mathrm{m}^{-2}$, $\tau = 3.3\times10^{-13}\,\mathrm{s}$ and $\sigma = 55\,G_0$ at $T = 3.3\,\mathrm{K}$. For comparison, results for constant dephasing rate are also presented. For both cases the the interference corrections at zero magnetic field have been of the same value, $\delta\sigma = -3.75\,G_0$, that corresponds to $\tau/\tau_\phi(b=0) = 0.0235$. As seen taking into account the magnetic field dependence of the phase breaking rate leads to the smoother magnetoconductance curve that accords with the analytical consideration. Fig. 2b shows also that this curve can be fitted rather well by expression (1) with constant dephasing rate. The value of the fitting parameter $\gamma = 0.018$ differs from $\tau/\tau_\phi(b=0)$ by approximately 25%. Analogous results have been obtained in wide range of σ, τ and T.

Thus, the use of the Hikami-Larkin-Nagaoka formula (1) with constant dephasing rate for analyzing the experimental results gives an error in determination of τ_ϕ no more than a neglect of other factors, for instance, limitations of the diffusion approximation, the spin-orbit interaction.

Acknowledgements

This work was supported in part by the RFBR (grants 02-02-17688, 03-02-16150, and 04-02-16626), the CRDF (grants EK-005-X1 and Y1-P-05-11), the INTAS (grant 1B290), the Russian Program *Physics of Solid State Nanostructures*, the SPP *Quanten-Hall-Systeme* of the DFG, the Program Russian Science School 2192.2003.2.

References

[1] S. Hikami *et al*, *Prog. Theor. Phys.*, **63**, 707 (1980).
[2] S. McPhail *et al*, *Phys. Rev. B* **70**, 245311 (2004).
[3] B. N. Narozhny *et al*, *Phys. Rev. B*, **65**, 180202 (2002).
[4] B. L. Altshuler *et al*, *J. Phys. C*, **15**, 7367 (1982).
[5] I. L. Aleiner *et al*, *Phys. Rev. B*, **65**, 115317 (2002).
[6] G. M. Minkov *et al*, *Phys. Rev. B*, **61**, 13164 (2000).

13th Int. Symp. "Nanostructures: Physics and Technology"
St Petersburg, Russia, June 20–25, 2005

Weak-localization-induced anomaly in Hanle effect

I. S. Lyubinskiy and *V. Yu. Kachorovskii*
Ioffe Physico-Technical Institute, St Petersburg, Russia

Abstract. The influence of weak localization on the Hanle effect in a two-dimensional system with spin-split spectrum is considered. We show that weak localization drastically changes the dependence of stationary spin polarization $\mathbf{S}$ on external magnetic field $\mathbf{B}$. In particular, the non-analytic dependence of $\mathbf{S}$ on $\mathbf{B}$ is predicted for III-V-based quantum wells grown in [110] direction and for [100]-grown quantum wells having equal strengths of Dresselhaus and Bychkov-Rashba spin-orbit coupling. It is shown that in weakly localized regime the components of $\mathbf{S}$ are discontinuous at $B = 0$. At low B, the magnetic field-induced rotation of the stationary polarization is determined by quantum interference effects.

The ultimate goal of spintronics is to develop novel electronic devices that exploit the spin degree of freedom [1]. The effective manipulation of the spin requires that the characteristic spin lifetime be long compared to the device operation time. This is a challenging problem, especially for III-V-based semiconductor nanostructures where spin polarization relaxes rapidly due to Dyakonov-Perel spin relaxation mechanism [2]. This mechanism is based on the classical picture of the angular spin diffusion in random magnetic field induced by spin-orbit coupling. In two-dimensional (2D) systems, the corresponding spin-relaxation time τ_S is inversely proportional to the momentum relaxation time τ [3]. As a consequence, in high-mobility structures which are most promising for device applications, τ_S is especially short. However, in some special cases, the relaxation of one of the spin components can be rather slow even in a system with high mobility. In particular, a number of recent researches [4] are devoted to GaAs symmetric quantum wells (QW) grown in [110] direction. In such wells, the random field is perpendicular to the QW plane and the normal to the plane component of the spin does not relax [3]. Also, the random field might be parallel to a fixed axis in an asymmetric [100]-grown QW [5] due to the interplay between structural [6] and bulk [7] spin-orbit coupling.

We discuss the dependence of the spin polarization in such structures on external magnetic field $\mathbf{B}$. We assume that the spin is injected into the system with a constant rate, for example, by optical excitation [8]. The stationary spin polarization $\mathbf{S}$ is proportional to the product of injection intensity and the spin relaxation time. The Hanle effect is that the external field modifies the stationary polarization. In particular, $\mathbf{S}(\mathbf{B})$ deviates from $\mathbf{S}(0)$ by an angle θ which depends on the relation between spin precession frequency $\mathbf{\Omega} = g\mu_B\mathbf{B}/\hbar$, and the spin relaxation rate (here $\mu_B = e\hbar/2m_0c$ is the Bohr magneton, m_0 is the free electron mass and g is Landé g factor). We show that at low temperatures θ is very sensitive to weak localization (WL) effects. Usually such effects are discussed in context of quantum corrections to the conductivity [9]. Though the WL correction is small compared to the classical conductivity it has attracted much attention due to its fundamental nature and anomalous behavior with external parameters such as magnetic field. Remarkably, the influence of WL on Hanle effect can not be considered as a small correction to the classical result. We demonstrate that WL might give rise to a discontinuity in the dependence of θ on $\mathbf{B}$. As a result, at low B the Hanle effect is totally driven by WL.

Physically, the non-analytic dependence of θ on $\mathbf{B}$ is related to memory effects specific for WL. It is known that the

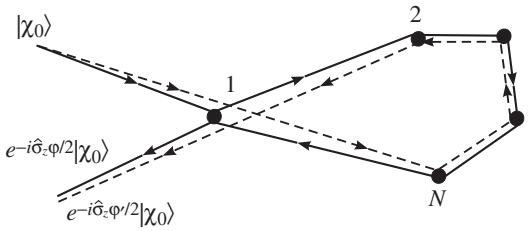

Fig. 1. A coherent scattering involving N impurities. At point 1 the electron wave splits into two parts propagating around the closed loop clockwise and counterclockwise. The initial electron spinor $|\chi_0\rangle$ is transformed to $|\chi\rangle = e^{-i\hat{\sigma}_z\varphi/2}|\chi_0\rangle$ and $|\chi'\rangle = e^{-i\hat{\sigma}_z\varphi'/2}|\chi\rangle$ for clockwise and counterclockwise paths, respectively.

WL is caused by interference of electron waves propagating along a closed loop in the opposite directions. Such interference process can be considered as a coherent scattering (additional to the Born scattering) involving a large number of impurities (see Fig. 1). The probability of the coherent scattering is proportional to the probability of the diffusive return $1/Dt$, where t is the time of the electron passage along the loop and D is the diffusion coefficient. In the absence of external magnetic field, such scattering does not change the direction of the spin [11]. Thus, electrons keep memory about initial spin polarization during the time much larger than τ_S and the long-living tail $1/t$ in the spin polarization appears [10, 11]. When the external magnetic field is applied, the electron spin rotates with a frequency $\boldsymbol{\omega}_\mathbf{p} + \mathbf{\Omega}$, where $\boldsymbol{\omega}_\mathbf{p}$ is the momentum-dependent frequency of the spin precession in the spin-orbit-induced magnetic field. In the special case under discussion, $\boldsymbol{\omega}_\mathbf{p}$ is parallel to a fixed axis (say z-axis) for any $\mathbf{p}$. Let us consider the simplest case, when $\mathbf{\Omega}$ also lies along z axis. In this case, spin rotation matrices, describing rotation of electron spin on the different segments of the closed loop, commute with each other and the spin rotation angles for clockwise and counterclockwise propagating waves are simply given by $\varphi = \Omega t + \int_0^t \omega_\mathbf{p} dt'$, $\varphi' = \Omega t + \int_0^t \omega_{\mathbf{p}'} dt'$. The initial electron spinor $|\chi_0\rangle$ is transformed to $|\chi\rangle = e^{-i\hat{\sigma}_z\varphi/2}|\chi_0\rangle$ and $|\chi'\rangle = e^{-i\hat{\sigma}_z\varphi'/2}|\chi_0\rangle$ for clockwise and counterclockwise paths, respectively. Here $\hat{\sigma}_z$ is the Pauli matrix. In 2D systems, $\boldsymbol{\omega}_\mathbf{p}$ is linear in $\mathbf{p}$. Since for any closed path $\int_0^t \mathbf{p}(t')dt' = 0$, we find $\varphi = \varphi' = \Omega t$. The interference contribution to the electron spin-density matrix after a coherent scattering is given by $|\chi\rangle\langle\chi'| = e^{-i\hat{\sigma}_z\Omega t/2}|\chi_0\rangle\langle\chi_0|e^{i\hat{\sigma}_z\Omega t/2}$. Hence, the electron spin after the coherent scattering is rotated by an angle Ωt with respect to the spin before scattering. The deviation of the spin from the initial direction is proportional to $\sin(\Omega t)$. The

integration over t weighted with the probability of the coherent scattering yields $\theta \sim \int dt \sin(\Omega t)/t \sim \Omega/|\Omega|$. In other words, the rotation frequency Ω should be multiplied by the effective rotation time $1/|\Omega|$, which is very long for small Ω. Rigorous calculations (see below) give an additional factor λ/l in this result, which reflects the quantum nature of the phenomena: $\theta \sim \lambda\Omega/l|\Omega|$ (here λ is the electron wave length and l is the mean free path). In contrast to coherent scattering, the classical rotation of spin is limited by the spin relaxation time τ_S, so that the classical contribution is $\theta \sim \Omega\tau_S$. For $\Omega\tau_S \ll \lambda/l$, this contribution can be neglected and the Hanle effect is totally driven by WL.

The Hamiltonian of a 2D system with a spin-split spectrum is given by

$$H = \frac{\mathbf{p}^2}{2m} + \frac{\hbar}{2}\left[\boldsymbol{\omega}_\mathbf{p} + \boldsymbol{\Omega}\right]\hat{\boldsymbol{\sigma}} + U(\mathbf{r}) \,. \tag{1}$$

Here $\mathbf{p}$ is the in-plane electron momentum, m is the electron effective mass, $\hat{\boldsymbol{\sigma}}$ is a vector consisting of Pauli matrices, and $U(\mathbf{r})$ is the impurity potential. The spin-orbit interaction is described by the term $\hbar\boldsymbol{\omega}_\mathbf{p}\hat{\boldsymbol{\sigma}}/2$. In 2D case the resulting spectrum splitting is linear in the electron momentum [6, 3]. We assume that

$$\boldsymbol{\omega}_\mathbf{p} = (\mathbf{p}\boldsymbol{\alpha})\hat{\mathbf{z}} \,. \tag{2}$$

Here $\hat{\mathbf{z}}$ is the unit vector along the direction of the random field and $\boldsymbol{\alpha}$ is a constant in-plain vector. Equation 2 implies that the spectrum splitting depends only on one component of momentum p_α. This happens in symmetric [110]-grown QWs. In this case, $\hat{\mathbf{z}}$ is normal to the QW plane [3]. For asymmetric [100] wells Eq. 2 can also take place if Bychkov-Rashba and Dresselhaus couplings have equal strengths [5]. For such wells vector $\hat{\mathbf{z}}$ lies in the QW plane.

To describe spin dynamics in the weakly localized regime we use the kinetic equation [11]. If the spin polarization is uniform in space, this equation looks as follows

$$\frac{\partial \mathbf{s}}{\partial t} = \left[\boldsymbol{\omega}_\mathbf{p} + \boldsymbol{\Omega}\right] \times \mathbf{s} - \frac{\mathbf{s} - \langle \mathbf{s} \rangle}{\tau} + \delta\hat{J}\mathbf{s} + \mathbf{I} \,, \tag{3}$$

where $\mathbf{s} = \mathbf{s}(\mathbf{p})$ is the spin density in the momentum space, related to the averaged spin by $\mathbf{S} = \int \mathbf{s} d^2\mathbf{p}/(2\pi)^2$, $\langle \ldots \rangle$ stand for averaging over directions of the electron momentum, $\mathbf{I}$ is the constant source, and $\delta\hat{J}$ is the WL-induced correction to the Boltzmann collision integral [11]

$$\delta\hat{J}\mathbf{s} = -\frac{\lambda l}{\pi\tau^2}\int_{-\infty}^{t} dt' \hat{W}(t-t')[\mathbf{s}(\mathbf{p},t') - \langle \mathbf{s}(\mathbf{p},t') \rangle] \,. \tag{4}$$

Here $\hat{W}(t)$ is the time-nonlocal scattering kernel. In the absence of the external field $W_{ik} = \delta_{ik}/4\pi Dt$ [11].

We calculate $\hat{W}$ in the presence of external magnetic field. For simplicity, we discuss only the QW grown in [100] direction and assume that $\mathbf{B}$ is parallel to z-axis. Since in this case $\hat{z}$ lies in the QW plane, the external field does not affect the orbital motion of the electrons and the Zeeman term $\hbar\Omega\hat{\sigma}_z/2$ commutes with the Hamiltonian. As a consequence, the solution of Eq. 3 with $I = 0$ and $B \neq 0$ can be obtained from solution at zero field: $\mathbf{s}_B(t) = \hat{T}(\Omega t)\mathbf{s}_{B=0}(t)$, where $\hat{T}$ is 3×3 matrix, describing rotation around z-axis by the angle Ωt.

In order that $\mathbf{s}_B(t)$ obeys Eq. 3, the scattering kernel has to be as follows:

$$\hat{W}(t) = \frac{\hat{T}(\Omega t)}{4\pi Dt} \,. \tag{5}$$

Equations 3, 4 and 5 allow us to find the relation between isotropic spin polarization $\mathbf{S}$ and $\mathbf{S}_0 = \int \mathbf{I} d^2\mathbf{p}/(2\pi)^2\Gamma$. For $\Omega\tau_S \ll 1$, the angle between $\mathbf{S}$ and $\mathbf{S}_0$ is

$$\theta(\Omega) \approx \Omega\tau_S + \frac{\lambda}{4\pi l}\frac{\Omega}{|\Omega|} \,. \tag{6}$$

In this equation, $\Omega\tau_S$ stands for the classical contribution, while the second term is due to WL effect (here τ_S is the spin relaxation time for the spin components perpendicular to the random field). At small fields the classical contribution can be neglected. We see that WL contribution to θ is a non-analytic function of the magnetic field. At zero field the function $\theta(\Omega)$ has a discontinuity

$$\theta(+0) - \theta(-0) = \lambda/2\pi l \,. \tag{7}$$

The discontinuity at $\Omega = 0$ is smeared by inelastic scattering, which destroys phase coherence between clockwise and counterclockwise propagating paths, thus limiting a time of the coherent spin rotation: $t < \tau_\varphi$, where τ_φ is the phase breaking time.

To conclude, the theory of Hanle effect in a 2D system is developed for the weakly localized regime. At low external magnetic fields the Hanle effect is totally driven by quantum interference effects. In the absence of inelastic scattering, the components of the spin polarizations are discontinuous as functions of the external field.

Acknowledgement

This work has been supported by RFBR, a grant of the RAS, a grant of the Russian Scientific School 2192.2003.2, and a grant of the foundation "Dinasty"-ICFPM.

References

[1] Semiconductor Spintronics and Quantum Computation, eds. D. D. Awschalom, D. Loss and N. Samarth (Springer-Verlag, Berlin, 2002).
[2] M. I. Dyakonov and V. I. Perel', *Sov. Phys. Solid State*, **13**, 3023 (1972).
[3] M.I. Dyakonov and V.Yu. Kachorovskii, *Sov. Phys. Semicond.*, **20**, 110 (1986).
[4] Y. Ohno *et al*, *Phys. Rev. Lett.*, **83**, 4196 (1999); T. Adachi *et al*, *Physica E*, (Amsterdam) **10**, 36 (2001); O. Z. Karimov *et al*, *Phys. Rev. Lett.*, **91**, 246601 (2003); K. C. Hall *et al*, *Phys. Rev. B*, **68**, 115311 (2003); S. Döhrmann *et al*, *Phys. Rev. Lett.*, **93**, 147405 (2004).
[5] F. Pikus and G. Pikus, *Phys. Rev. B*, **51**, 16928 (1995); N. Averkiev and L. Golub, *Phys. Rev. B*, **60**, 15582 (1999);
[6] Yu. Bychkov and E. Rashba, *JETP Lett.*, **39**, 78 (1984).
[7] G. Dresselhaus, *Phys. Rev.*, **100**, 580 (1955).
[8] *Optical orientation*, eds. F. Meier and B. P. Zakharchenya, (North Holland, Amsterdam, 1984).
[9] L. P. Gor'kov, A. I. Larkin and D. E. Khmelnitskii, *JETP Lett.*, **30**, 248 (1979).
[10] A. G. Mal'shukov, K. A. Chao and M. Willander, *Phys. Rev. B*, **52**, 5233 (1995).
[11] I. S. Lyubinskiy, V. Yu. Kachorovskii, *Phys. Rev. B*, **70**, 205335 (2004).

13th Int. Symp. "Nanostructures: Physics and Technology"
St Petersburg, Russia, June 20–25, 2005

Transport and anomalous Hall effect in p-type GaAs⟨Mn,Mg⟩ layers fabricated by ion implantation

V. A. Kulbachinskii[1], P. S. Gurin[1], R. A. Lunin[1], Yu. A. Danilov[2], A. V. Kruglov[3] and E. I. Malysheva[2,3]

[1] M.V. Lomonosov Moscow State University, Low Temperature Physics Dept., 119992, GSP-2, Moscow, Russia
[2] Physico-Technical Research Institute, University of Nizhny Novgorod, 603950, Nizhny-Novgorod, Russia
[3] Research and Education Center for Physics of Solid State Nanostructures, University of Nizhny Novgorod, 603950, Nizhny Novgorod, Russia

Abstract. Mn-doped GaAs structures have been fabricated by ion implantation. The implanted samples were annealed at temperatures in the range of $T_a = 700$–$800\,^\circ$C. At this temperatures MnAs clusters are formed in GaAs due to decay of supersaturated solid solution of Mn in GaAs. Additional Mg implantation was used to provide the enhancement of p-type doping in Mn layer. Temperature dependences of resistance and magnetoresistance were investigated in ion-implanted by Mn and Mg GaAs structures. Anomalous Hall effect and enhanced positive magnetoresistance were observed at $T > 30$ K.

Introduction

Diluted magnetic semiconductors (DMS) are alloys of semiconductors and magnetic ions (transition metals or rare-earths) that exhibit a variety of cooperative effects via spin-exchange interactions not present in nonmagnetic semiconductors [1]. The exchange interaction between the charge carriers and the localized moments of the magnetic ions can alter the transport, optical and magnetic properties of the host semiconductor. In the extreme case, the interaction may induce a ferromagnetic phase transition. The efforts to grow III–V-based DMS by low-temperature MBE were rewarded with successful epitaxial growth of uniform (In,Mn)As films on GaAs substrate, where partial ferromagnetic order was found, and ferromagnetic (Ga,Mn)As (for a thorough recent review see Ref. [2]).

Carrier induced ferromagnetism in DMS has generated intense interest, because it opens the prospect of developing devices, which combine charge and magnetic degrees of freedom. Hole induced ferromagnetism in transition metal doped III–V compounds offers integration of ferromagnetism with the existing nonmagnetic III–V heterostructures. These structures allow us to explore spin-dependent phenomena in semiconductor heterostructures, which may lead us to a new form of electronics, spin-electronics (spintronics), where both the spin and charge degrees of freedom play critical roles [3].

Ion implantation of Mn is one of methods to fabricate samples with carrier-mediated ferromagnetism. This method was used to produce ferromagnetic hole-doped GaP [4]. In the present study we investigated the influence of Mn ion implantation on transport and the galvanomagnetic properties of p-GaAs.

1. Samples and experimental

Investigated structures were fabricated on semi-insulating GaAs (100) surface by ion implantation by Mn^+ with the energy of 100 keV and dose of $10^{16}\,cm^{-2}$. Profile of the Mn atom distribution in GaAs, simulated by TRIM code [5], is shown in Fig. 1.

We can see that maximum of Mn concentration is located at ≈ 60 nm from the surface of the sample. To stimulate an enhancement of hole concentration in implanted layers, additional acceptor doping by Mg^+ ion implantation was performed. The energy of Mg^+ ions (45 keV) was selected for coincidence of peaks for Mg^+ and Mn^+ ions. Dose of Mg^+ ion implantation was varied from 1×10^{14} to $1\times10^{15}\,cm^{-2}$. Thus p-type conductivity layer in GaAs was formed by double implantation. All implantations were performed in conditions to avoid a canalization of incident ions. The implanted samples were submitted to rapid (10 s) thermal annealing (RTA). Temperature T_a of RTA was varied in the range from 700 to 800 °C. Some parameters of samples are listed in Table 1.

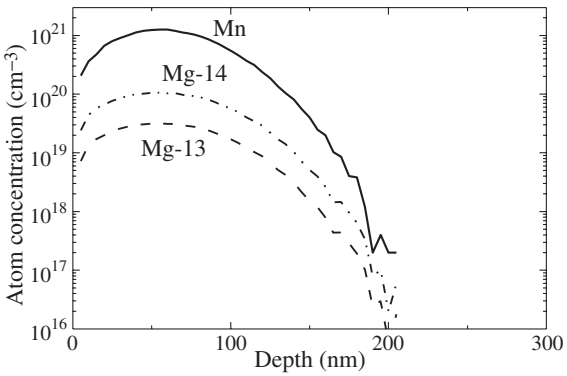

Fig. 1. Atom profiles, simulated by TRIM code for implantation of Mn (100 keV, $1\times10^{16}\,cm^{-2}$) and Mg (45 keV) into GaAs. Numbers on profiles of Mg correspond to the samples 13 and 14.

Table 1.

N	Mg iondose,	T_a	(ρ) (kΩ)		
	$(10^{14}/cm^2)$	(°C)	$T = 300$ K	$T = 77$ K	$T = 4.2$ K
13	3	800	1.270	9.05	—
14	10	700	5.070	29.5	—
15	10	725	2.900	8.66	—
16	10	750	2.380	20.5	29500
17	2300	800	0.910	0.648	0.547

Surface morphology of implanted and annealed samples was investigated by atom force microscope "Topometrix" in contact mode. Temperature dependences of resistance have been measured in the temperature range $4.2 \le T \le 300$ K. Magnetoresistance and Hall effect has been measured by a conventional four probe technique in the temperature range 4.2 K–200 K in magnetic field B up to 6 T.

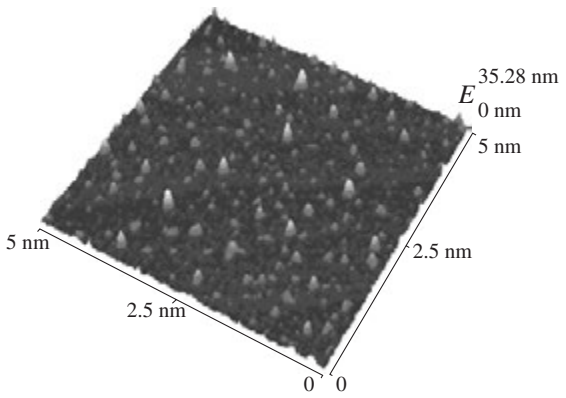

Fig. 2. AFM — image of the GaAs surface implanted by Mn^+ and Mg^+ ions and annealed at $T_a = 750\,^\circ$C (sample 16).

2. Results and discussion

Fig. 2 shows AFM image of Mn+Mg doped sample 16. We see formation of surface MnAs clusters with height up to 35 nm and diameter of about 200 nm.

All samples had p-type conductivity. When temperature decreased resistance of Mn implanted samples increased very rapidly and for some samples became not measurable at $T <$ 20 K except sample 17 with metallic temperature dependence of the resisistivity. Typical temperature dependencies of the resistivity for some samples with different densities of holes are shown in Fig. 3.

R_{Hall} can be expressed as

$$R_{Hall} = \frac{R_0}{d} B + \frac{R_a}{d} \mu_0^M , \qquad (1)$$

where R_0 is the ordinary (normal) Hall coefficient, R_a is the anomalous Hall coefficient due to magnetization M of the sample, B is magnetic field. The magnetic field dependence of R_{Hall} at different temperatures reflects that of M, confirming the dominating contribution of the anomalous Hall effect. In Fig. 4 we plot magnetic field dependence of R_{Hall} at different temperatures for sample 14. The anomalous part is the deviation of the Hall resistance in low magnetic fields from linear behavior (dashed line). The anomalous Hall effect is measurable up to 195 K and shows the hole-mediated ferromagnetism of $Ga_{1-x}Mn_xAs$ solid solution after Mn implantation and rapid annealing.

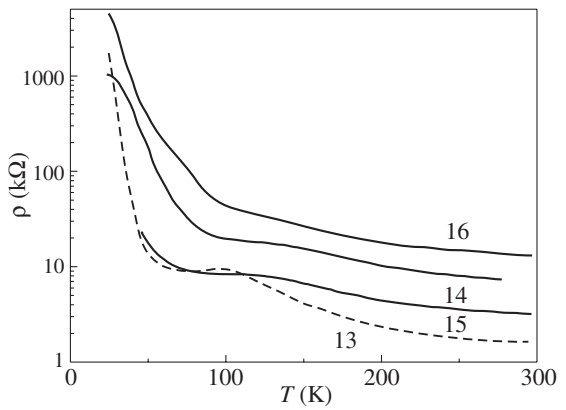

Fig. 3. Temperature dependencies of resistivity ρ for p-type structures with ion implanted Mn and Mg. Sample numbers correspond to Table 1.

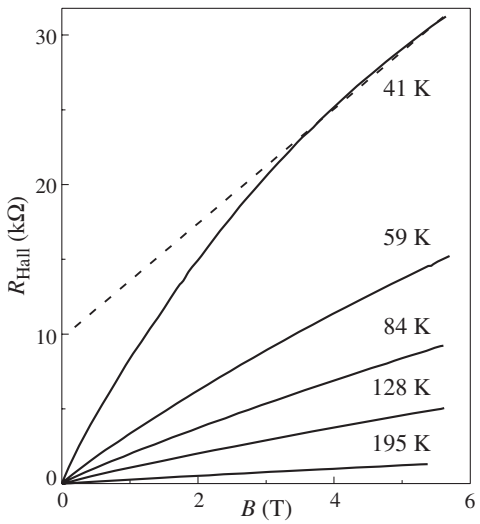

Fig. 4. Anomalous Hall effect in the sample 14 at 5 different temperatures.

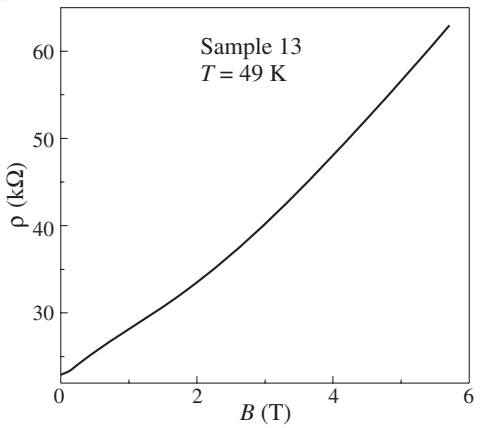

Fig. 5. Magnetoresistance of sample 13 at $T = 49$ K.

Positive magnetoresistance has been observed at temperatures 30–100 K in all structures. As an example magnetoresistance of sample 13 is shown in Fig. 5 for $T = 49$ K. The high value of positive magnetoresistance might be explained by the enhanced geometric magnetoresistance effect in inhomogeneous semiconductors [6].

Thus the ferromagnetic clusters were embedded into GaAs by Mn ion implantation and rapid thermal annealing. Ferromagnetism manifests itself in the anomalous Hall effect.

Acknowledgement

The work was supported by RFBR, grants 05.02.17029a and 03-02-16777a.

References

[1] For a reviews on DMS, see: a) J. K. Furdina, *J. Appl. Phys.*, **64**, R29 (1988); b) N. Samarth, *Solid State Physics*, **58** Solid State Physics-Advances In Research And Applications: 1–72 (2004).
[2] H. Ohno, *J. Magn. Magn. Mater.*, **200**, 110 (1999).
[3] H. Ohno, *Science*, **281**, 951 (1998).
[4] N. Theodoropoulou, A. F. Hebard *et al*, *Phys. Rev. Lett.* **89**, 107203 (2002).
[5] J. F. Ziegler, J. P. Biersack, U. Littmark. The Stopping and Range of ions in Solids, Pergamon Press, New York, 1985.
[6] Sh. U. Yuldashev, Y. Shon *et al*, *J. Appl. Phys.*, **90**, 3004 (2001).

13th Int. Symp. "Nanostructures: Physics and Technology"
St Petersburg, Russia, June 20–25, 2005

Photoconduction relaxation in the Peierls conductor TaS_3

V. E. Minakova and S. V. Zaitsev-Zotov

Institute of Radioengineering and Electronics of RAS, Moscow, Russia

Abstract. Kinetics of photoconduction in a quasi-one-dimensional conductor TaS_3 is studied. The photoconduction relaxation is slow with relaxation time distribution depending on the light intensity. The amplitude of photoconduction in the time scale $t \sim 1$ s is found to be proportional to the root squared of the light intensity, that implies the quadratic recombination mechanism. Deviation from the quadratic recombination is found on the time scale $t \gg 1$ s.

Introduction

The energy gap developing in quasi-one-dimensional (q-1d) conductors below the Peierls transition temperature makes them similar to narrow-band semiconductors [1]. As a result, many physical properties of q-1d conductors can be accounted in the framework of a semiconductor model, the doping level being dependent on the charge-density wave (CDW) deformation. On this analogy, one could expect that photoconduction is also intrinsic to CDW conductors and could be easily seen, like it happens in many semiconductors. On the other hand, there are predictions that energy relaxation time of nonequilibrium carriers in CDW conductors is very short, of the order of 10^{-12} s [2]. Indeed, experimental measurements of kinetics of reflection relaxation in the blue bronze, $K_{0.3}MoO_3$ by optical methods [3] demonstrate picosecond relaxation scale for photoexcited carriers. On this basis, detection of photoconduction in transport measurements would not be a simple task.

The first clear observation of photoinduced changes in transport properties of CDW conductors was reported by Ogawa *et al* [4] in $K_{0.3}MoO_3$. They found photoinduced suppression of CDW sliding, i.e. photoinduced changes of the *nonlinear* conduction. The origin of the effect was attributed to a local destruction of the CDW which leads to the photoinduced phase slip and the redistribution of the CDW phase. Similar behavior was observed in TaS_3 [5,6]. Moreover, illumination-induced growth of the *linear* conduction (photoconduction) was found as well [5,6]. It was also shown that photoinduced changes in CDW kinetics can be explained quantitatively if photoinduced changes of the CDW deformation screening length are taken into account.

Despite the success in explanation of photoinduced changes in the nonlinear conduction [5], the origin of photoconduction itself is still not clear. The value of photoconduction in TaS_3 corresponds to the relaxation time 10^{-10} s [5], but the measurements of relaxation kinetics clearly demonstrate relaxation with relaxation times up to 10^4 s [6]. Moreover, similar relaxation was also observed without illumination after application of the voltage pulse to a sample [6]. It was concluded that the CDW metastable states caused by illumination-induced changes of the total current carrier concentration are responsible for the long-time photoconduction relaxation [6].

Here we present the results of detailed study of photoconduction kinetics in TaS_3 crystals of submicrometer transverse sizes. Our results demonstrate quadratic recombination of the photoconduction on the time scale $t \lesssim 1$ s and deviation from this mechanism on $t \gg 1$ s.

1. Experimental and results

The conduction measurements were done in the voltage-controlled regime. The current was measured by a home-made current-to-voltage converter with a transient time 0.04 ms to a 50% level and 0.3 ms for an accuracy below 1%. Photoexcitation was provided by an IR LED placed near a sample. The results presented here were obtained for a representative sample with $R_{300} = 7\,\mathrm{k\Omega}$ and $s = 0.16\,\mu\mathrm{m}^2$.

Figure 1 shows temperature dependences of the linear conduction of TaS_3 crystal under illumination and in the dark. The noticeable photoconduction develops at $T \lesssim 60$ K.

Figure 3 shows a typical photoresponse to light pulses (1s duration) of different W for $T \geq 40$ K. Both front and rear parts of the response are characterized by a wide distribution

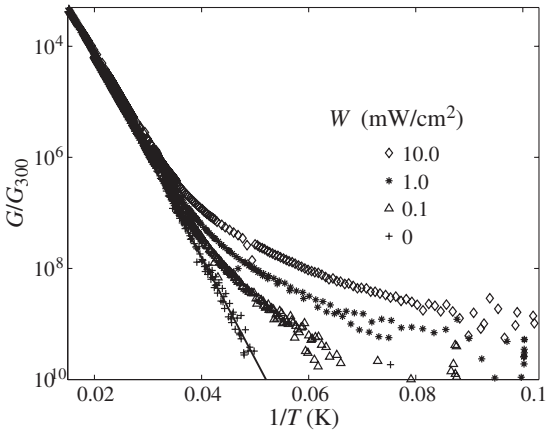

Fig. 1. Low-temperature part of the temperature variation of conduction of TaS_3 without (crosses) and with different level of illumination (other marks). The straight line corresponds to the activation energy 430 K.

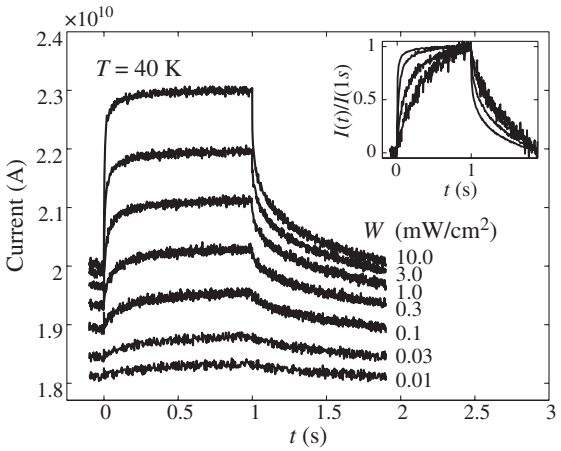

Fig. 2. Photoresponse of TaS_3 sample to a 1s light pulse (light is on at $t = 0$) at different light intensities. $V = 2$ V, $T = 20$ K. The inset shows photoconduction as a function of the light intensity at different temperatures.

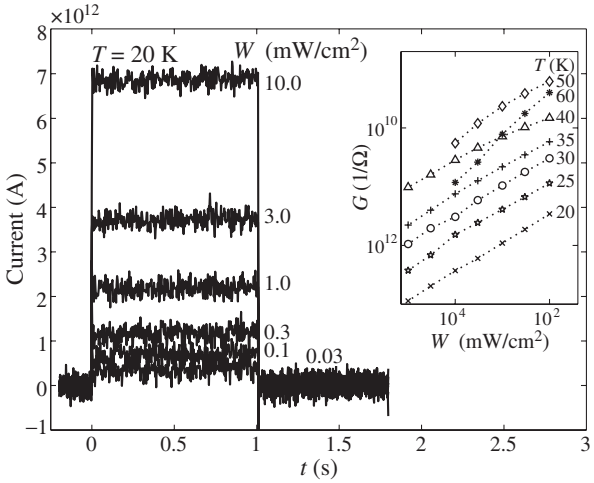

Fig. 3. Photoresponse of TaS_3 sample to a meander light pulse sequence (light is on at $t = 0$ and off at $t = 1$ s) at $T = 40$ K at different light intensities. $V = 200$ mV. Inset shows the shape of the pulse $\delta I(t)/\delta I(1\text{s}) = [I(t) - I(0)]/[I(1\text{s}) - I(0)]$.

of relaxation times at all W. The shape of the photoresponse depends on W and is more sharp for more intensive light (see inset).

Figure 2 shows a typical shape of the low-temperature photoresponse. In contrast to the hight-temperature data no noticeable relaxation is seen at least on the presented time scale, and the response appears immediately after illumination. Inset in Fig. 2 shows a temperature set of the photoconduction *vs.* W dependences. The photoconduction value was measured as a difference $\delta G = G(1\text{s}) - G(0)$ in the response to the meander ligh pulse sequence ($t = 0$ corresponds to the onset of the pulse, see Fig. 3). The dependences is nonlinear and can be approximated by the power law $\delta G \propto W^{\alpha}$, as it was reported earlier [5]. The value of α is close to 1/2 at $T \leq 40$ K, and starts to grow at higher temperatures. The pulse amplitude is found to follow the activation law with the activation energy 360 K comparable to one for the linear conduction (430 K, see Fig. 1).

Figure 4 shows a temperature set of photoresponse relaxation curves. Two different temperature ranges can be clearly distinguished. The response at $T > 40$ K starts at $t_0 = 0.2$–

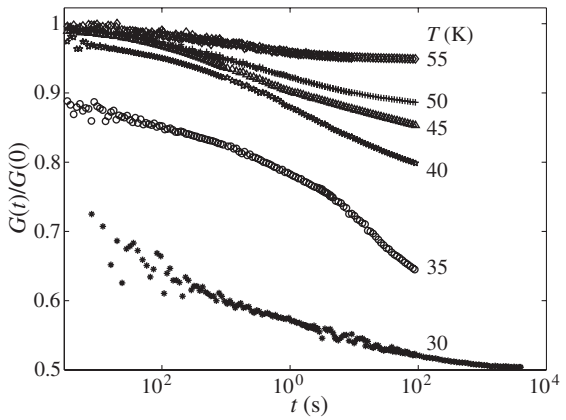

Fig. 4. Decay of photocurrent in TaS_3 sample after switching off the light pulse with $W = 10\,\text{mW/cm}^2$ intensity and 1 s duration at different temperatures. The conduction is normalized to $G(t = 0)$, where $t = 0$ corresponds to switching the light off.

0.3 ms (at $W = 10\,\text{mW/cm}^2$) and relaxes smoothly toward zero. Similar behavior is observed at the front of the light pulse. When the temperature is lower, or when the light intensity is higher, the initial part of both onset of the response and its relaxation is sharp and cannot be observed with our setup.

2. Discussion

The resutls presented above demonstrate that photoconduction at $T \leq 40$ K and $t \lesssim 1$ s corresponds to the quadratic recombination, $\delta G \propto \sqrt{W}$ [7]. Very sharp low-temperature response (Fig. 2) can also be explained, at least qualitatively, in terms of the quadratic recombination model, as the limiting case of very high light intensity. The long-time relaxation of photoconduction (Fig. 3) does not corresponds, however, $1/t$ relaxation expected for the quadratic recombination [7]. Instead, much slower relaxation is observed. Thus, two-component relaxation takes place.

The origin of the long-living component with a very wide distribution of the relaxation time is still an open question. It was suggested [6] that this long-time relaxation is a manifestation of metastability of the CDW that is caused by photoexited quasiparticles changing the equilibrium value of the CDW wave vector. The results of the present study does not contradict this point of view.

No expected fast component with the relaxation time $\tau \sim 10^{-12}$–10^{-10} s [3,5] is seen at least at $T > 40$ K. Instead, in this temperature region the relaxation proceeds entirely on the time scale $t > 1$ ms. Therefore there is a contradiction between the relatively small value of the photoconduction and its very long relaxation time. Further study is necessary to clarify details of the photoconduction mechanism.

Acknowledgements

This research was performed in the frame of the CNRS-RAS-RFBR Associated European Laboratory "Physical properties of coherent electronic states in condensed matter" between CRTBT and IRE RAS. We are grateful to R. E. Thorne for providing batches of high-quality crystals of TaS_3. The work was supported by CRDF, INTAS, and RFBR.

References

[1] For a review, see: P. Monceau, in: "Electronic Properties of Inorganic Quasi-one-dimensional Conductors", Part 2. Ed. by P. Monceau. Dortrecht: D. Reidel Publ. Comp., 1985; G. Grüner, *Rev. Mod. Phys.*, **60**, 1129 (1988).

[2] S. A. Brazovskii, *Zh. Exp. Teor. Fiz.*, **78** 677 (1980).

[3] J. Demsar, K. Biljakovic and D. Mihailovic, *Phys. Rev. Lett.*, **83**, 800 (1999).

[4] N. Ogawa, A. Shiraga, R. Kondo, S. Kagoshima, K. Miyano, *Phys. Rev. Lett.*, **87**, 256401 (2001).

[5] S. V. Zaitsev-Zotov, V. E. Minakova, *JETP Letters*, **79** 550 (2004).

[6] V. E. Minakova, S. V. Zaitsev-Zotov, 12th Int. Symp. "Nanostructures: Physics and Technology", p. 126 (2004).

[7] S. M. Ryvkin, *"Photoelectric phenomena in semiconductors"* (in Russian), Fiz. Mat. Giz., Moscow (1963).

13th Int. Symp. "Nanostructures: Physics and Technology"
St Petersburg, Russia, June 20–25, 2005

Temperature dependence of the Aharonov–Bohm effect in chiral Fermi-system

D. V. Nomokonov[1], A. A. Bykov[1], A. K. Bakarov[1], A. K. Kalagin[1], A. I. Toropov[1] and J. C. Portal[2]

[1] Institute of Semiconductor Physics, 630090 Novosibirsk, Russia
[2] Grenoble High Magnetic Fields Laboratory, F-38042 Grenoble, France

Abstract. The Aharonov–Bohm effect in submicron rings with narrow electron channels was studied in the range of magnetic fields from 0 to 15 T and temperatures from 0.1 to 10 K. It is found that the temperature dependences of the h/e-oscillation amplitude at low magnetic fields and in the situation of tunnel-coupled edge current states are different. The obtained experimental data are explained by the influence of Fermi-system chirality on the coherent transport in a ring interferometer.

Introduction

It is known that the coherent processes occurring in a ring interferometer placed in a uniform external magnetic field B are governed not only by the flux through the ring inner area but also by the flux through the electron channels of the interferometer. As a result, the magnetoconductance of metallic rings operating in the diffusion charge-carrier transport regime exhibits, apart from Aharonov–Bohm (AB) oscillations, universal conductance fluctuations [1]. The flux through the electron channels in semiconductor ballistic interferometers fabricated on the basis of a high-mobility two-dimensional electron gas (2DEG) modifies the ring energy spectrum and induces AB oscillation beats [2]. In a high magnetic field, the flux through the channels of a ballistic ring gives rise to edge current states, in which electrons can move only in one direction. In these conditions, the symmetry of charge-carrier transport breaks and the Fermi system becomes chiral.

According to [3], the influence of chirality on the coherent processes in the interferometer is as follows. The magnetic flux through the ring in a nonchiral system gives rise to both constructive and destructive interference of electron waves, whereas the chiral system allows only constructive interference. This distinction in the transport through the ring should primarily manifest itself in the temperature dependence of the AB effect. This follows from the fact that h/e oscillations in the nonchiral system are suppressed when the temperature length L_T becomes shorter than the circle half-length $L/2$, whereas, in the chiral system, this occurs when L_T is shorter than L, where $L_T = \hbar v/k_B T$ and v is the Fermi velocity. The interval of magnetic fields where the AB oscillations appear in the ballistic rings is determined by the width of electron channels; the narrower the channels, the broader this interval [4]. Because of this, ballistic rings with narrow electron channels allow the transition from the nonchiral to chiral system to be followed from its onset to its completion upon increasing B. The purpose of this work is to study the temperature dependence of the AB effect in such rings and to reveal experimentally the role of chirality in the suppression of the h/e-oscillation amplitude with increasing temperature.

1. Experimental

Interferometers for study were fabricated on the basis of 2DEG in single GaAs quantum wells with AlAs/GaAs superlattice barriers. Contrary to the gas in a GaAs/AlGaAs heterojunction, 2DEG in our structures can simultaneously be highly mobile and have high concentration, allowing the fabrication, on its basis, of ballistic rings of submicron sizes. The 2DEG concentration and mobility in the starting structure grown from molecular beam epitaxy were, respectively, $n_s = 1.8 \times 10^{12}$ cm^{-2} and $\mu = 4 \times 10^5$ cm^2/(Vs) at $T = 4.2$ K.

The schematic view of the interferometer is shown in Fig. 1a. Double bridges with a width of 50 μm and a separation between the potentiometric terminals of 100 μm were fabricated using optical lithography and liquid etching. The ring was placed between two pairs of potentiometric terminals and fabricated using electron beam lithography and dry etching. The ring effective radius determined from the period of h/e oscillations was $r_{\text{eff}} = 0.13-0.15\,\mu$m. Experiments were carried out in the range of magnetic fields from 0 to 15 T and temperatures from 0.1 to 10 K.

2. Results and discussion

In Fig. 1b, the magnetic-field dependences of the interferometer longitudinal (R_{23}) and transverse (R_{37}) resistances are presented. It is seen from this figure that the 2DEG transverse resistance (R_{37}) in magnetic fields above 5 T assumes quan-

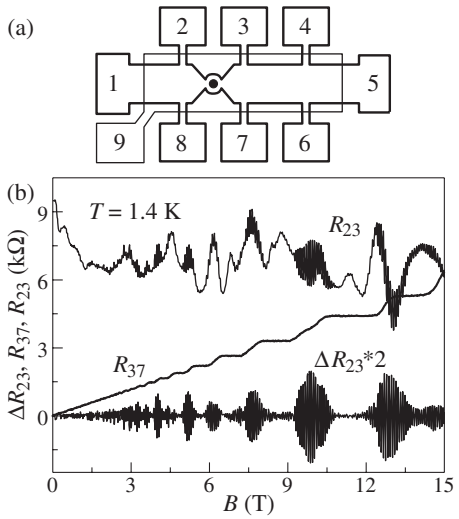

Fig. 1. (a) Schematic of the ring interferometer. (1, 5) Current terminals; (2, 3, 4, 6, 7, 8) potentiometric terminals; and (9) thin-film metallic gate. (b) Experimental $R_{23}(B)$ and $R_{37}(B)$ curves and the differences $\Delta R_{23}(B)$ between the experimental and smoothed curves at $T = 1.4$ K.

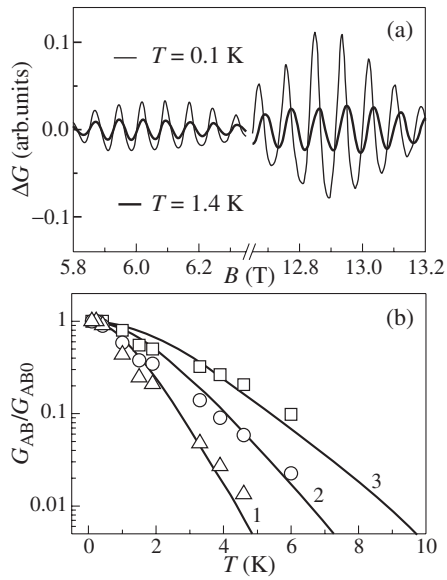

Fig. 2. (a) The $\Delta G(B)$ dependences in two different intervals of B at $T = 0.1$ and 1.4 K. (b) Temperature dependences of the relative amplitude G_{AB}/G_{AB0} of AB oscillations in different intervals of B: □ — 2.8−3.3, ◯ — 7.2−7.7, and △ — 12.7−13.2 T. Calculations by formula $G_{AB}/G_{AB0} = (T/T_0)/\sinh(T/T_0)$ from [3]. (1) $T_0 =$ 0.6, (2) 0.9, and (3) 1.2 K.

tized values. However, the quantization is not seen in the four-terminal ring resistance (R_{23}) up to 15 T. This implies that, in a high magnetic field, the situation of tunnel-coupled edge current states appears in the narrowest ring input/output regions of the interferometer and in the conducting channel constrictions [5].

The $G(B)$ dependence of the periodic component of ring conductance is shown in Fig. 2a for two different temperatures. One can see that the h/e-oscillation amplitude decreases with increasing temperature faster at high magnetic fields than at lower fields. Fig. 2b shows that the temperature dependences of the relative amplitude G_{AB}/G_{AB0} of AB oscillations, where G_{AB0} is the h/e-oscillation amplitude at $T = 0.1$ K, become steeper as the magnetic field increases. The temperature dependence of the AB effect in a chiral Fermi system was theoretically analyzed in [3]. The h/e-oscillation amplitude in such a system is determined by the lengths L and L_T. In our case, $L = 2\pi r_{\text{eff}}$. If $L_T \gg L$, the h/e-oscillation amplitude is maximal and independent of T. In the opposite case, $L_T \ll L$, the AB effect does not occur. The characteristic temperature separating these limiting cases is given by the expression $T_0 = \hbar v/\pi k_B L$. It is pointed out above that, in contrast to the situation with tunnel-coupled edge states, the Fermi system is nonchiral in a low magnetic field, and the value of T_0 in this case will be determined not by the full length L but by its half. This signifies that T_0 should change twofold upon the transition from low to high fields. In [3], it was shown that the AB oscillation amplitude normalized to its zero-temperature value is given by the relation $G_{AB}/G_{AB0} = (T/T_0)/\sinh(T/T_0)$. Curves 1, 2, and 3 in Fig. 2b are calculated by this formula for different T_0 values. One can see that the experimental temperature dependences are consistent with the theoretical curves. As the magnetic field increases, the fitting parameter T_0 decreases from 1.2 to 0.6 K; i.e., in the ring interferometers studied, T_0 in a low magnetic field differs approximately twofold from its value in the regime of tunnel-coupled edge current states, in accordance with the change in chirality of the Fermi system.

Summary

Thus, the temperature dependences of the AB effect in submicron rings with narrow conducting channels have been studied experimentally in the range of magnetic fields from 0 to 15 T. In the interferometers studied, not only the suppression of the AB oscillations but also their shift have been observed upon increasing temperature in a high magnetic field. It has been found that the slope of the temperature curve for the h/e-oscillation amplitude in a low magnetic field differs from that in the situation with the tunnel-coupled edge current states. The obtained experimental data are explained by the fact that the chirality of the Fermi system changes with increasing magnetic field.

Acknowledgements

This work was supported by RFBR, project no. 04-02-16789 and by the program "Physics of solid state nanostructures".

References

[1] R. A. Webb *et al*, *Phys. Rev. Lett.*, **54**, 2696 (1985).
[2] W.-C. Tan and J. C. Inkson, *Phys. Rev. B* **53**, 6947 (1996).
[3] M. R. Geller and D. Loss, *Phys. Rev. B* **56**, 9692 (1997).
[4] A. A. Bykov *et al*, *Physica E*, **12**, 778 (2002).
[5] A. A. Bykov *et al*, *JETP Lett.*, **71**, 434 (2000).

13th Int. Symp. "Nanostructures: Physics and Technology"
St Petersburg, Russia, June 20–25, 2005

Dynamic localization and electromagnetic transparency of semiconductor superlattice in biharmonic electric fields

J. Y. Romanova and Y. A. Romanov
Institute for Physics of Microstructures RAS,603950 Nizhny Novgorod, Russia

Abstract. We consider the dynamics of electrons in semiconductor superlattices in intense multifrequency electric fields. We examine the conditions for dynamic localization and electromagnetic transparency. We investigate processes of formation, destruction and stabilization of electromagnetic transparency in biharmonic field. The stable dc fields are founded.

Introduction

In the semiconductor superlattice (SL) with relatively narrow Brillouin minizone electrons perform complex Bloch oscillations under strong electric fields. For specific ratio of amplitude and frequency of applied harmonic field the value of average electron velocity (no scattering) vanishes independently of its initial momentum. This effect is called dynamic localization (DL) in literature. One of macroscopic manifestation of complex Bloch oscillations is nonmonotonic dependence of high-frequency conductivity on amplitudes and frequencies of fields. In particular, the effects of induced (IT) and self-induced transparencies (SIT) arise.

The conditions for SIT within the single τ-approximation for a one-dimensional superlattice sample with harmonic dispersion law are the same as for dynamic localization, but these effects have different physical origins [1,2].

As a rule transparency state is unstable to the generation of both static and additional harmonic fields. There are some scenarios of destruction of SIT. Which of them will dominate depended on which process — the dc field or the high-frequency field generation and amplification will proceeds with a faster-growing increment. In reality situation intrinsic SL field is multifrequency field even if the external field is harmonic. So for the better understanding of electromagnetic properties of the SL we have to investigate the behavior of SL in given multifrequency electric fields.

In the present paper we examine the effects of DL, electromagnetic transparency and current and voltage self-oscillations in SL, which arise under biharmonic fields. We used Boltzmann kinetic equation within τ-approximation and equation, which describe continuity of the total current in the broken circuit [3] (the dc current is zero).

1. Dynamic localization

Let's consider electric field of the type

$$E(t) = \sum_{\alpha=1}^{N} E_\alpha \cos(\omega_\alpha t + \delta_\alpha)\,, \qquad (1)$$

having dc component E_c and N harmonics with arbitrary frequencies ω_α and beginning phases δ_α. Under influence of the electric field (1) an electron executes nonlinear oscillations having velocity given by:

$$V(k_0, t_0, t) = V_m \sin[k_0 d + \Omega_c(t - t_0) \cdot \sum_{\alpha=1}^{N} g_\alpha(\sin(\omega_\alpha t - \delta_\alpha) - \sin(\omega_\alpha t_0 - \delta_\alpha))]\,, \qquad (2)$$

where $V_m = \Delta d/2\hbar$ is maximum longitudinal velocity, d and Δ are period and minizone width of SL, k_0 is the electron wave vector at initial time t_0, $\Omega_c = eE_c d/\hbar$ — Bloch frequency, $g_\alpha = eE_\alpha d/\hbar\omega_\alpha$ are dimensionless amplitudes of fields harmonics. In the biharmonic field with frequencies $\omega_2 = n_0\omega_1$, $\Omega_c = \lambda\omega_1$, ($n_0 = 2, 3, \ldots$, $\lambda = 0, 1, 2, \ldots$) the time averaged electron velocity is given by

$$\overline{V(k_0, t_0, t)} = V_m \sum_{\nu=-\infty}^{\infty} J_{-\lambda-n_0\nu}(g_1) J_\nu(g_2) \cdot \sin[k_0 d - \Omega_c t_0 - g_1 \sin(\omega_1 t - \delta_1) - g_2 \sin(\omega_2 t - \delta_2) + \nu(n_0\delta_1 - \delta_2) + \lambda\delta_1]\,. \qquad (3)$$

Thus the DL conditions will be such:

$$\sum_{\nu=-\infty}^{\infty} \cos[\nu(n_0\delta_1 - \delta_2)]\, J_{-\lambda-n_0\nu}(g_1) J_\nu(g_2) = 0\,,$$
$$\sum_{\nu=-\infty}^{\infty} \sin[\nu(n_0\delta_1 - \delta_2)]\, J_{-\lambda-n_0\nu}(g_1) J_\nu(g_2) = 0\,. \qquad (4)$$

The second equality (4) for odd n_0 and $E_c = 0$ is satisfied automatically. Such situation repeated for any n_0 and λ if a phase shift is equal to $n_0\delta_1 - \delta_2 = \alpha\pi$ ($\alpha = 0, 1, 2, \ldots$). Therefore in these cases electron DL arises in the fields which are described by set of curves on the (g_1, g_2)-plane (you can see some examples on the Fig. 1). In other cases there are only set of points on this plane. It is easy to obtain that SIT occurs at the same values of the fields amplitudes (within single τ-approximation ($\tau = const$) and $\omega_{1,2}\tau \gg 1$).

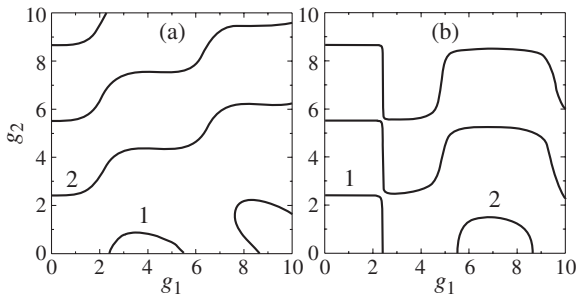

Fig. 1. The conditions for DL and SIT on the plane (g_1, g_2) for different frequencies and faze shift. $\omega_2 = 3\omega_1$, $\omega\tau = 10$, (a) — $\delta = \pi$, (b) — $\delta = \pi/2$.

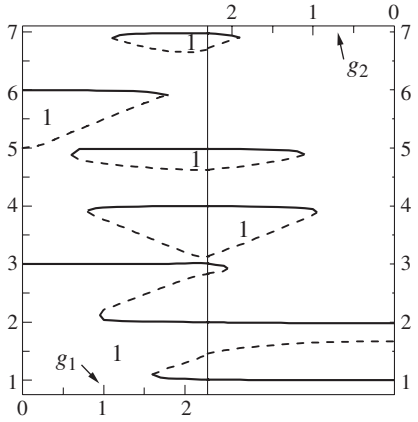

Fig. 2. The instability regions for the field E_c – (1) ($E_2 = 0$) and E_2 – (1) ($E_c = 0$). Value of E_2 was determined from eq. (4), $\omega_1\tau = 10$, $\delta_1 = 0$, $\delta_2 = \pi/2$.

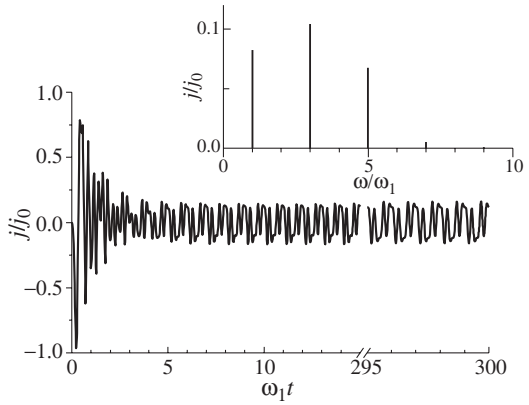

Fig. 3. A stationary transparency state of a SL with a low electron concentration exposed to a biharmonic field ($n_0 = 3$, $\delta_2 = \pi$). Time evolution and spectra of the current (in the insets). $\omega_1\tau = 10$, $g_1 = 4.97$, $g_2 = 0.478$.

2. Induced and self-induced transparency

The case $n_0\delta_1 - \delta_2 = \pi/2, n_0 = 2l-1, l = 1, 2, \ldots$ (Fig. 1b) is interesting. Within the DL conditions for the harmonic field ($J_0(g_1^\lambda) = 0$, λ is a number of Bessel function root) SL keeps transparency to the second field of the named type up to amplitudes $g_2 < g_1$ if $g_1 \ll 2n_0$ and $\lambda < l$. The exceptions are the points $J_0(g_2) \approx 0$. For $n_0 = 3$ transparency state arises at $g_1 = 2.405$ and for $n_0 = 5$ it arises at $g_1 = 2.405$ and $g_1 = 5.5$, for example. We can called this phenomenon "*induced transparency* in the multi-fold frequencies fields". The phase shift is important in this case in contrast to a case of fields with aliquant frequencies [4].

3. The stability of transparency states

The are three different scenario of behavior SL which is in transparency state under biharmonic field. Which process will dominate depends on ratio between values of energy losses on the different frequencies. (1) The destruction of the SIT state will be accompanied by spontaneous generation of dc field. Dc field value differs from the case of pure harmonic field (Fig. 2). (2) The destruction of the SIT state will be accompanied by amplification of field and current harmonics with relatively large amplitudes. (3) The stabilization of SIT will be accompanied by generation of relatively week current and field harmonics. The last process will suppresses both dc field generation and amplification of components of biharmonic field (Fig. 3). This stabilization can be stimulated by addition of corresponding weak harmonic into external field. There are periodic fields with complicated time dependance which forms stable electrodynamic transparency states.

4. Conclusion

1. The conditions for dynamic localization and electromagnetic transparency in biharmonic electron field were founded.
2. The induced transparency were shown to be arise in biharmonic field with multi-fold frequencies ($\omega_2 = n_0\omega_1$, n_0 is odd) under certain conditions.
3. In common case the transparency states are unstable. It is possible to stabilize them in multifrequency fields.

Acknowledgement

This study was supported by the Russian Foundation for Basic Research (projects no. 05-02-17319, 04-02-17154).

References

[1] Yu. A. Romanov, J. Yu. Romanova, *Solid State Phys.*, **45**, 539 (2001).
[2] Yu. A. Romanov, J. Yu. Romanova *et al*, *Phys. Rev. B*, **66**, 045319 (2002).
[3] Y. A. Romanov, J. Y. Romanova, *Journal of Experimental and Theoretical Physics*, **91**, 1033 (2000).
[4] Y. A. Romanov, L. K. Orlov, *Sov. Phys. Solid State*, **19**, 726 (1977).

13th Int. Symp. "Nanostructures: Physics and Technology"
St Petersburg, Russia, June 20–25, 2005

Superfluidity in the quantum Hall bilayers: the low-density limit

A. I. Bezuglyj[1] and *S. I. Shevchenko*[2]

[1] NSC Kharkov Institute of Physics and Technology, 61108, Kharkov, Ukraine
[2] Institute for Low Temperature Physics and Engineering, 61103, Kharkov, Ukraine

Abstract. The bilayer systems exhibit the Bose–Einstein condensation of excitons that emerge due to Coulomb pairing of electrons belonging to one layer with the holes belonging to the other layer. Here we present the microscopic derivation of dynamic equation for the condensate wave function at a low density of electron-hole pairs in the case of a strong magnetic field perpendicular to the layers, and the electric field directed along the layers. From this equation we obtain the dispersion law of collective excitations of the condensate and calculate the electric charge of the vortex in the exciton condensate.

In recent years considerable attention has been focused on the so-called bilayers, i.e. the systems that represent two thin and closely-spaced conducting layers separated by the energy barrier for carriers. One of the examples of the bilayer system is the $n-p$ system consisting of the n-layer with electron conductivity and the p-layer with hole conductivity. In this system in the weak-coupling limit the attraction of electrons from the n-layer conduction band and holes from the p-layer valence band gives rise to the coherent BCS-type state of electron-hole ($e-h$) pairs [1,2]. The pairing of electrons and holes as well as the condensation of $e-h$ pairs is favored in a magnetic field H, normal to the layers, provided that the magnetic length l_H ($l_H = \sqrt{\hbar c/eH}$) is considerably shorter than the Bohr radii of both the electron and the hole. At low pair densities, $n_p \ll l_H^{-2}$, the electron-hole pairing occurs in the real space (strong-coupling limit of $e-h$ pairs) rather than in the momentum space.

Another example of the phase-coherent system is the $n-n$ system including two electron layers in the magnetic field perpendicular to the layers with the total filling factor $\nu_T = \nu_1 + \nu_2 = 1$. Despite the apparent difference between the $n-n$ and $n-p$ systems, they are, in essence, fully similar [3]. So, in the systems of both types the interlayer phase coherence is the consequence of Bose condensation of $e-h$ pairs, and due to this reason the superfluidity in bilayer systems is often called the "exciton superfluidity". At the present time, one has impressive evidence that the superfluidity in question was revealed experimentally in quantum Hall $n-n$ systems at $\nu_1 = \nu_2 = 1/2$ [4,5].

The study of superfluidity of strongly bound $e-h$ pairs in the low-density limit is of particular interest from the viewpoint of theory, because one can expect that the $e-h$ pairs with spatially separated components behave as a weakly nonideal Bose gas, which is described by a relatively simple differential equation of the Gross-Pitaevskii type. In the present paper in the mean field approximation we derive microscopically this equation for the condensate wave function of quantum Hall $n-n$ systems with $\nu_T = 1$.

The Hamiltonian of the bilayer electron-hole system in the perpendicular magnetic field is

$$\hat{H} = \int d\mathbf{r} \sum_k \psi_k^+(\mathbf{r})\hat{h}_k(\mathbf{r})\psi_k(\mathbf{r}) + \frac{1}{2}\int d\mathbf{r}d\mathbf{r}' \sum_{k,l} V_{kl}(\mathbf{r}-\mathbf{r}')\psi_k^+(\mathbf{r})\psi_l^+(\mathbf{r}')\psi_l(\mathbf{r}')\psi_k(\mathbf{r}) + \sum_k \int d\mathbf{r}(-1)^k eV(\mathbf{r})\psi_k^+(\mathbf{r})\psi_k(\mathbf{r}). \quad (1)$$

Here and further on it is assumed that the indices $k, l = 1(2)$ indicate the electron (hole) layer. The operators $\psi_k^+(\mathbf{r})$ and $\psi_k(\mathbf{r})$ are the operators of electron (hole) creation and annihilation at the point with two-dimensional radius-vector $\mathbf{r}$. The spin indices are omitted, since electrons are considered spin-polarized. The kinetic energy operator has the form

$$\hat{h}_k(\mathbf{r}) = \frac{1}{2m_k}\Big[i\hbar\frac{\partial}{\partial\mathbf{r}} + (-1)^k\frac{e}{c}\mathbf{A}_k(\mathbf{r})\Big]^2, \quad (2)$$

the Coulomb interaction energy of carriers is given by

$$V_{kl}(\mathbf{r}-\mathbf{r}') = (-1)^{k+l}\frac{e^2}{\varepsilon\sqrt{(\mathbf{r}-\mathbf{r}')^2 + (1-\delta_{k,l})d^2}}, \quad (3)$$

and $V(\mathbf{r})$ is the scalar potential of the electric field. In formulas (2), (3) m_k is the electron mass ($k = 1$) or the hole mass ($k = 2$), ε is the dielectric constant, d is the interlayer spacing, $\delta_{k,l}$ is the Kronecker delta-symbol.

To derive the dynamic equation for the condensate wave function we shall follow Keldysh's paper [6] , according to which the coherent state of $e-h$ pairs, in the mean field approximation, may be represented by the vector $|\phi\rangle = \hat{D}_\phi|0\rangle$, where the unitary operator $\hat{D}_\phi$ is written as

$$\hat{D}_\phi = \exp\Big\{\int d\mathbf{r}_1 d\mathbf{r}_2[\psi_1^+(\mathbf{r}_1)\Phi(\mathbf{r}_1,\mathbf{r}_2,t)e^{-i\mu t}\psi_2^+(\mathbf{r}_2) - \psi_2(\mathbf{r}_2)\Phi^*(\mathbf{r}_1,\mathbf{r}_2,t)e^{i\mu t}\psi_1(\mathbf{r}_1)]\Big\}. \quad (4)$$

The vector $|0\rangle$ is the vacuum state of the system: $\psi_k|0\rangle = 0$. The unknown function $\Phi(\mathbf{r}_1,\mathbf{r}_2,t)$ and the chemical potential μ of $e-h$ pairs, which enter into $\hat{D}_\phi$, should be found from the Schrodinger equation for the vector $|\phi\rangle$. This equation is written as

$$(i\hbar\hat{D}_\phi^+\frac{\partial}{\partial t}\hat{D}_\phi - \hat{D}_\phi^+ H\hat{D}_\phi)|0\rangle = 0. \quad (5)$$

In the expression $\hat{D}_\phi^+ H\hat{D}_\phi$ the operators $\hat{D}_\phi^+$ and $\hat{D}_\phi$ realize the linear transformation of the creation/annihilation operators of electrons and holes. For example, the operator $\psi_1(\mathbf{r})$ is transformed as

$$\hat{D}_\phi^+\psi_1(\mathbf{r})\hat{D}_\phi = \int d\mathbf{r}'[C(\mathbf{r},\mathbf{r}')\psi_1(\mathbf{r}') + S(\mathbf{r},\mathbf{r}')\psi_2^+(\mathbf{r}')e^{-i\mu t}],$$

where with an accuracy up to terms cubed in Φ we have

$$C(\mathbf{r},\mathbf{r}') = \delta(\mathbf{r}-\mathbf{r}') - (1/2)\int d\mathbf{r}''\Phi(\mathbf{r},\mathbf{r}'')\Phi^*(\mathbf{r}',\mathbf{r}'');$$

$$S(\mathbf{r},\mathbf{r}') = \Phi(\mathbf{r},\mathbf{r}') - (1/6)\int\int d\mathbf{r}''d\mathbf{r}'''\Phi(\mathbf{r},\mathbf{r}'')\times \Phi^*(\mathbf{r}''',\mathbf{r}'')\Phi(\mathbf{r}''',\mathbf{r}').$$

As a result, we obtain a nonlinear integro-differential equation for the function $\Phi(\mathbf{r}_1,\mathbf{r}_2,t)$. In what follows we shall retain the terms not higher than the third order in Φ, because we are interested in the low-density limit of pairs.

Equation for Φ can be transformed into the equation for the wave function of the $e-h$ pair condensate Ψ (slowly varying in space and time) by averaging Φ over "fast" variables that describe the intrinsic degrees of freedom of $e-h$ pairs. To separate the intrinsic degrees of freedom, we turn from the electron/hole coordinates $\mathbf{r}_1$ and $\mathbf{r}_2$ to the difference coordinate $\mathbf{r}=\mathbf{r}_1-\mathbf{r}_2$ and to the coordinate of the center of inertia of the pair $\mathbf{R}=(m_1\mathbf{r}_1+m_2\mathbf{r}_2)/(m_1+m_2)$. The fast variable $\mathbf{r}$ is excluded by means of the procedure described in [6]. As a result, we come to the following equation

$$i\hbar\frac{\partial\Psi(\mathbf{R},t)}{\partial t} = \Big\{\frac{1}{2M_H}\Big(i\hbar\frac{\partial}{\partial\mathbf{R}} - \frac{\alpha}{c}[\mathbf{EH}]\Big)^2 - \frac{1}{2}\alpha E^2 - \frac{\mu^{(1)}}{n_p}[n_p - |\Psi(\mathbf{R},t)|^2]\Big\}\Psi(\mathbf{R},t), \quad (6)$$

The equation similar to (6) was proposed in ref.7 on the basis of phenomenological considerations.

In the case considered (magnetic length l_H is considerably shorter than the Bohr radii of both the electron and the hole), the effective mass M_H of the $e-h$ pair arises due to the Coulomb interaction between the electron and the hole, and is independent of their masses m_1 and m_2:

$$M_H = \frac{2\varepsilon\hbar^2}{e^2 l_H}\sqrt{\frac{2}{\pi}}\Big[\Big(1+\frac{d^2}{l_H^2}\Big)\exp\Big(\frac{d^2}{2l_H^2}\Big)\mathrm{erfc}\Big(\frac{d}{\sqrt{2}l_H}\Big) - \sqrt{\frac{2}{\pi}}\frac{d}{l_H}\Big]^{-1}. \quad (7)$$

The correction to the chemical potential of the $e-h$ pair is equal to

$$\mu^{(1)} = \frac{e^2}{\varepsilon}\Big[4\pi d - (2\pi)^{3/2}l_H + (2\pi)^{3/2}l_H\exp\Big(\frac{d^2}{2l_H^2}\Big)\mathrm{erfc}\Big(\frac{d}{\sqrt{2}l_H}\Big)\Big]n_p. \quad (8)$$

In eq. (8) the first term is related to the energy of the electric field between the electron layer and the hole layer, while the second and third terms describe the exchange contributions from the intralayer interaction and interlayer interaction, respectively. At $d \ll l_H$ we have $\mu^{(1)} = \sqrt{2}\pi^{3/2}\frac{e^2d^2}{\varepsilon l_H}n_p$. Besides, in eq. (6) α has the meaning of $e-h$ pair polarizability, $\alpha(H) = M_H c^2/H^2$.

From (6) it is not difficult to derive the continuity equation $\partial|\Psi|^2/\partial t + \mathrm{div}\mathbf{j}_s = 0$, where the superfluid current density can be written as $\mathbf{j}_s = |\Psi|^2\mathbf{v}_s$. In this case the superfluid velocity $\mathbf{v}_s$ appears dependent on the electric field

$$\mathbf{v}_s = \frac{1}{M_H}\Big(\hbar\frac{\partial\varphi}{\partial\mathbf{R}} + \frac{\alpha}{c}[\mathbf{EH}]\Big). \quad (9)$$

Here φ is the phase of the wave function ($\Psi = |\Psi|e^{i\varphi}$).

Eq. (6) has inhomogeneous solutions that describe the quantized vortices. The two-dimensional density of the polarization charge, associated with the vortices centered at points $\mathbf{R}_n$, has the form

$$\rho_{pol} = -\alpha n_p\frac{2\pi\hbar H}{M_H c}\sum_n \sigma_n\delta(\mathbf{R}-\mathbf{R}_n), \quad (10)$$

where $\sigma_n = \pm 1$ is sign of the n-th vortex circulation. As follows from eq. (10), the vortex has the real electric charge. The total charge of the vortex is $q = \pm e\nu$, where $\nu = 2\pi l_H^2 n_p$.

In the presence of a uniform electric field the dispersion law of collective excitations of the condensate takes the form

$$\omega(\mathbf{k}) = \mathbf{k}\mathbf{v}_s + \sqrt{\Big(\frac{\hbar^2k^2}{2M_H} + 2\mu^{(1)}\Big)\frac{k^2}{2M_H}}, \quad (11)$$

where the electric field induced superfluid velocity $\mathbf{v}_s(\mathbf{E}) = \frac{1}{M_H}\frac{\alpha}{c}[\mathbf{EH}]$. Expression (11) presents the dispersion law for the excitations propagating in the condensate that moves at a velocity of $\mathbf{v}_s(\mathbf{E})$. According to the Landau superfluidity criterion, the v_s value must not exceed the critical value $c_0 = \sqrt{\mu^{(1)}/M_H}$. The critical velocity c_0 determines the critical electric field $E_{cr} = (c_0/c)H$. For $n_p \sim 10^{10}\mathrm{cm}^{-2}$, $d \sim 10^{-6}$cm, $H \sim 1$T, $\varepsilon \sim 10$, the estimation gives $E_{cr} \sim 10^3\mathrm{V/cm}$.

References

[1] Yu. E. Lozovik and V. I. Yudson, *Zh. Eksp. Teor. Fiz* **71**, 738 (1976) [*Sov. Phys. JETP* **44**, 389 (1976)].

[2] S. I. Shevchenko, *Fiz. Nizk. Temp.* **2**, 505 (1976) [*Sov. J Low Temp. Phys.* **2**, 251 (1976)].

[3] A. H. MacDonald and E. H. Rezayi, *Phys. Rev. B* **42**, 3224 (1990).

[4] I. B. Spielman, J. P. Eisenstein, L. N. Pfeiffer, and K. W. West, *Phys. Rev. Lett.* **84**, 5808 (2000); *Phys. Rev. Lett.* **87**, 036803 (2001).

[5] M. Kellogg, I. B. Spielman, J. P.'Eisenstein, L. N. Pfeiffer, and K. W. West, *Phys. Rev. Lett.* **88**, 126804 (2002); M. Kellogg, J. P. Eisenstein, L. N. Pfeiffer, and K. W. West, *cond-mat/0401521*.

[6] L. V. Keldysh, in *Problems of Theoretical Physics* (Moscow, Nauka), p.433, 1972 (in Russian).

[7] S. I. Shevchenko, *Phys. Rev. B* **67**, 214515 (2003).

13th Int. Symp. "Nanostructures: Physics and Technology"
St Petersburg, Russia, June 20–25, 2005

Time dependent picture of electron transport through semiconductor quantum rings

B. Szafran[1,2] and F. M. Peeters[1]

[1] Departement Fysica, Universiteit Antwerpen (Campus Drie Eiken), Universiteitsplein 1, B-2610 Antwerpen, Belgium
[2] Faculty of Physics and Applied Computer Science, AGH University of Science and Technology, al. Mickiewicza 30, 30-059 Kraków, Poland

Abstract. We solve the time dependent Schrödinger equation for single-electron transport through a GaAs quantum ring in the presence of an external magnetic field. The Lorentz force leads to an imbalance of the charge passing through the arms of the ring leading to a decreasing amplitude of the Aharonov–Bohm oscillations with increasing external field.

Introduction

The magnetic field shifts the phase of the electron wave function even if the electron is not in contact with the field itself [1]. For a quantum ring the difference of the phase shift of the wave function passing through its arms is equal to $\Delta\phi = 2\pi\Phi/\Phi_0$, where Φ is the magnetic field flux passing through the area inside the ring and $\Phi_0 = h/e$ is the flux quantum. Aharonov Bohm (AB) oscillations were observed in metal [2, 3] and GaAs/AlGaAs [4,5,6,7] rings. The theory of conductance for rings was described [8] for flux inaccessible to electrons. In this paper we present results of time-dependent lowest-subband single-channel simulations of the transport of an electron wave packet through the GaAs quantum ring. We show that the Lorentz force leads to a decreasing amplitude of the oscillations with external magnetic field and that the nature of the transport is shape and magnetic field dependent.

1. Theory

We consider an electron confined in the (x, y) plane with perpendicular magnetic field $(0, 0, B)$. The part of the Hamiltonian related to the kinetic energy has the form $H = (-i\hbar\nabla + e\mathbf{A})^2/2m^*$ with the vector potential taken in the Landau gauge $\mathbf{A} = (-By, 0, 0)$. We take the GaAs electron effective mass $m^* = 0.067m_0$ and expand the wave function in a basis of Gaussian wave functions centered around points $\mathbf{R}_n = (X_n, Y_n)$

$$\Psi(x, y, t) = \sum_n c_n(t) f_n(x, y), \tag{1}$$

with

$$f_n(x, y) = \exp\{-(\mathbf{r} - \mathbf{R}_n)^2/\alpha^2 + ieB(x - X_n)(y + Y_n)/2\hbar\}. \tag{2}$$

Parameter α is responsible for the localization of the Gaussian function around point $\mathbf{R}_n$ and the imaginary part of the exponent is related to the magnetic translation ensuring equivalence of all the points $\mathbf{R}_n$ (the gauge invariance). Calculations are performed with the Askar and Cakmak [9] three-time-step scheme.

We consider a circular and a diamond ring enclosing an area of $132^2\pi$ nm^2, the value corresponding to the structures studied in the experiment [7] on circular rings. For this area a single flux quantum corresponds to $B = 75.6$ mT. The shape of the rings is defined by the positions of the centers $(\mathbf{R}_n)$ in functions (2). In the calculations the centers are chosen with spacings of 22 nm. Parameter α in functions (2) is set to 28 nm (which is equivalent to defining a harmonic oscillator confinement potential with oscillator energy $\hbar\omega = 2.9$ meV in the direction perpendicular to the "wires" defined by the position of the centers). For the initial condition we take one of the Gaussian functions (2) localized before the ring multiplied by a plane wave $\exp(iqy)$.

2. Results

The presented results were obtained for an average value of a momentum $q = 0.05$/nm ($q^2/2m^* = 1.42$ meV). The interference of the scattered part of the wave packet and its slower tail results in the formation of charge density maxima along the wire which feeds into the ring, as visible in the plots for $t = 2.2$ ps in Fig. 1. The plot for $t = 2.2$ ps at $\Phi = 0$ shows that the wave packet diffuses at right angle from its original momentum into the ring with equal probability at the left and right ring arms. For nonzero magnetic field this symmetry is lost and the Lorentz force results in a preferential injection into the left arm of the ring. For $\Phi = 0$ at $t = 6.5$ ps we observe *a maximum* at the exit region of the ring where left and right circulating parts of the packet meet. A part of the wave packet then diffuses into the outgoing wire. But for $\Phi = \Phi_0/2$ the parts of the packet interfere destructively leading to *a zero* charge density at the upper exit of the ring. Consequently, no charge is transferred out of the ring at this exit. For $\Phi = 4.5\Phi_0$ a larger part of the initial wave packet is transferred along the left arm of the ring and consequently the destructive interference at the upper exit is not complete and a part of the packet can exit the ring through the upper lead. For $\Phi = 4.5\Phi_0$ the wave packet is predominantly injected into the left arm of the ring and the Lorentz force helps the charge density leave the ring at both the ring-wire junctions.

The transmission probability of the wave packet through the circular quantum ring is shown by the solid line in Fig. 2. In contrast to a strictly lowest-subband one-dimensional picture [8] we find that the amplitude of the oscillations decreases with magnetic field and that for half integer fluxes the value of the transmission probability is no longer zero. The decreasing amplitude is due to the growing imbalance in the amount of charge transferred through the left and right arms of the ring which prevents the interference to be completely destructive. The transmission probability both in the maxima and minima is an increasing function of the magnetic field which directs the

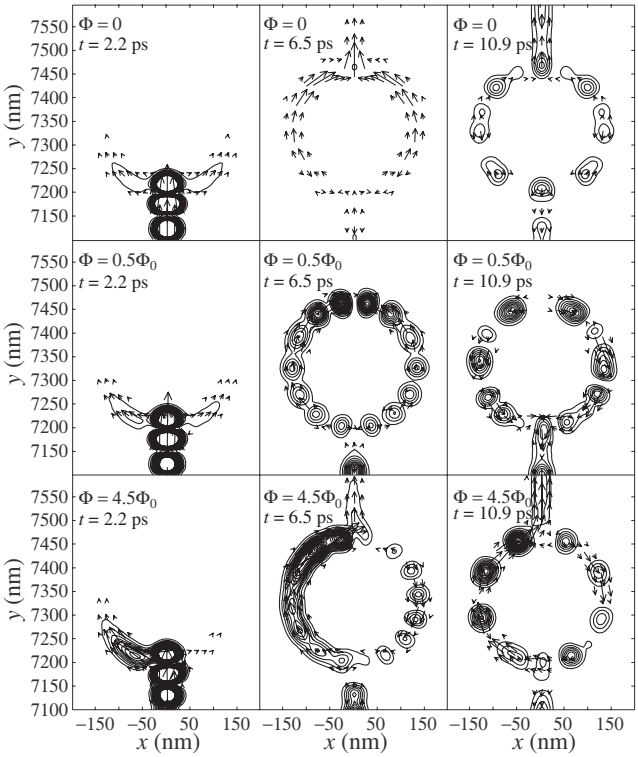

Fig. 1. Charge (contours) and current (vectors) densities for a Gaussian wave packet with being transferred through a circular quantum ring for 0, 0.5 and 4.5 flux quanta passing through the ring for $t = 2.2$, 6.5, and 10.9 ps. Scale for the charge and current density for $t = 2.2$ ps which were shortened by a factor of 2 with respect to the other plots.

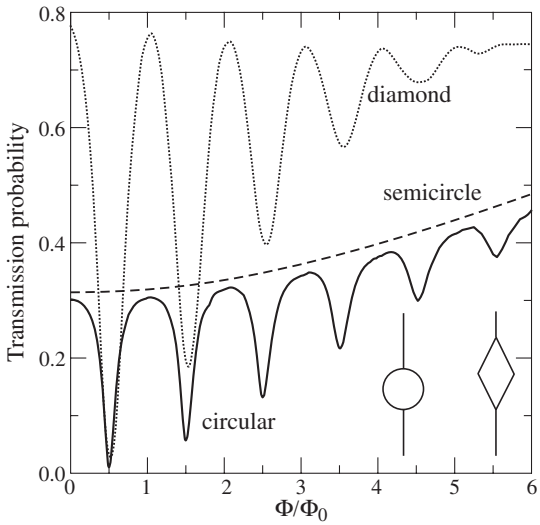

Fig. 2. The transmission probability of the wave packet through the circular (solid line), and diamond (dotted line) quantum rings in function of the flux through the ring in units of the flux quantum. The inset shows the geometry of the circular and diamond rings. The dashed line shows the transmission probability through a wire of a semicircular shape obtained from the circular quantum ring after removal of its right arm.

electron density first to the left arm of the ring and then leaves the via the upper exit. This general trend can be understood by considering the transport probability through a semicircular quantum wire where the right arm of the ring is removed. The corresponding result is shown by the dashed line in Fig. 2. The envelope of the maxima for the ring configuration runs parallel to this quantity. Dotted line in Fig. 2 shows the transmission probability for a diamond shape ring (see the inset to Fig. 2). For this geometry the transmission probability is much larger than for the circular wire, the maxima of the probability density now only weakly depend on Φ, but the minima in the AB oscillations increase much faster with the B-field.

3. Conclusions

The described descreasing amplitude of AB oscillations in the external field was observed in GaAs / AlGaAs quantum rings (see Fig. 1 or Ref. [6], Fig. 3 of Ref. [5] and Fig. 2(c) of Ref. [7], cf. also the decrease of the magnetoresistance oscillations reported in [4]). In order to be of significant importance the Lorentz force has to be able to deflect the electron trajectories at the entrance and at the exit leads of the ring. The classical formula for the radius of an electron in a magnetic field $R = m^*V/eB$ indicates that the effect will be smaller for fast electrons and for charges with larger effective mass. In metals the Fermi energies are of eV order compared to meV in a two-dimensional electron gas in GaAs with electron densities of order of 10^{11} cm^{-2} [7]. Consequently, in Au rings [2] in which both the electron effective mass ($\sim m_0$) and the Fermi velocity (1.4×10^6 m/s) are about 15 times larger than the effective mass and the velocity considered in the present paper, the AB oscillations pertain up to 8 T covering as much as 10000 flux quanta Φ_0.

Acknowledgements

This paper was supported by the Flemish Science Foundation (FWO-Vl), the Belgian Science Policy, the University of Antwerpen (VIS and GOA), B.S. is supported by the EC Marie Curie IEF project MEIF-CT-2004-500157.

References

[1] Y. Aharonov and D. Bohm, *Phys. Rev.* **115**, 485 (1959).
[2] R. A. Webb, S. Washburn, C. P. Umbach, and R. B. Laibowitz, *Phys. Rev. Lett.* **54**, 2696 (1985).
[3] V. Chandrasekhar, M. J. Rooks, S. Wind, and D. E. Prober, *Phys. Rev. Lett.* **55**, 1610 (1985).
[4] G. Timp, A. M. Chang, J. E. Cunningham, T. Y. Chang, P. Mankiewich, R. Behringer, and R. E. Howard, *Phys. Rev. Lett.* **58**, 2814 (1987).
[5] A. Yacoby, M. Heiblum, D. Mahalu, and H. Shtrikman, *Phys. Rev. Lett.* **74**, 4047 (1995).
[6] S. Pedersen, A. E. Hansen, A. Kristensen, C. B. Sorensedm, and P. E. Lindelof, *Phys. Rev. B* **61**, 5457 (2000).
[7] A. Fuhrer, S. Lüscher, T. Ihn, T. Heinzel, K. Ensslin, W. Wegschelder, and M. Bichler, Nature (London) **413**, 822 (2001).
[8] M. Büttiker, Y. Imry, R. Landauer, and S. Pinhas, *Phys. Rev. B*, **31** 6207 (1985).
[9] A. Askar and A. C. Cakmak, *J. Chem. Phys.*, **68**, 2794 (1978).

13th Int. Symp. "Nanostructures: Physics and Technology"
St Petersburg, Russia, June 20–25, 2005

Mesoscopical behavior of Aharonov–Bohm effect in small ring interferometer

O. A. Tkachenko[1,2], V. A. Tkachenko[1], D. G. Baksheev[1,3] and J.-C. Portal[2]

[1] Institute of Semiconductor Physics, 630090 Novosibirsk, Russia
[2] Grenoble High Magnetic Field Laboratory, F-38042 Grenoble, France
[3] Now at ZAO "Intel A/O", 630090 Novosibirsk, Russia

Abstract. Numerical modeling of two-dimensional transmission through a small ring interferometer shows that both amplitude and phase of Aharonov–Bohm oscillations (ABOs) change noticeably with electron energy and magnetic field in contrast to 1D models. The thermal averaging makes ABOs more uniform, but temperature dependence of the amplitude becomes sensitive to Fermi energy and/or particular realization of electrostatic potential in the same geometry. Thus the amplitude of ABOs is dependent on mesoscopical state of the ring.

Introduction

Recently, it has become possible to fabricate small ring interferometers using oxidation of the heterostructure surface by the tip of atomic force microscope (AFM) [1,2]. Importantly, with the AFM technique, one can obtain an image of the surface relief for each sample, and use the images to model electronic properties of the devices based on a realistic geometry [2]. To the best of our knowledge no detailed realistic modeling of ring interferometers in a wide range of magnetic field and Fermi energy has been performed, whereas such computations are necessary to gain a better understanding of magnetotransport in the rings. It is well known that 1D models of the ring yield Aharonov–Bohm oscillations (ABOs) that are strictly periodic in magnetic field, and the phase of the oscillations only flips between 0 and π [4,5]. Though many experiments support these predictions about period and phase, amplitude of measured ABOs strongly depends on magnetic field, gate voltage and recharging of impurities in contrast to the simple 1D models. The reason for these fluctuations is not yet well understood. Recently it has been found [6] that essentially different temperature damping of ABOs are observed after a thermal recycling of the same ring from Ref. [2]. In this paper we report about numerical realistic modelling of the small ring and show that mesoscopical behavior of the samples is a reason for the different temperature dependences of ABOs.

1. Results

We have modelled 3D electrostatics and coherent magnetotransport of interferometers created with help of atomic-force microscope (AFM) on the basis of a high mobility 2DEG heterostructure. Once the 3D electrostatic potential is computed, we obtain 2D effective potential $U(x, y)$ and solve multimodal single-particle transmission problem for this potential. The conductance is given by Landauer formula. The methods of modelling are described in Ref. [2,3]. Figure 1 shows the electron density in the plane of 2DEG calculated on the basis of the ring image. The electron ring is small, $r \approx 100$ nm, and asymmetrical, with a tunneling barrier spontaneously formed in one arm. Figure 2 shows calculated conductance $G(E_F, B)$ as a function of Fermi energy E_F and magnetic field B. We did not explicitly model phase-breaking processes, but averaged the computed conductance to take into account finite temperature. To perform the thermal averaging of ABOs we computed

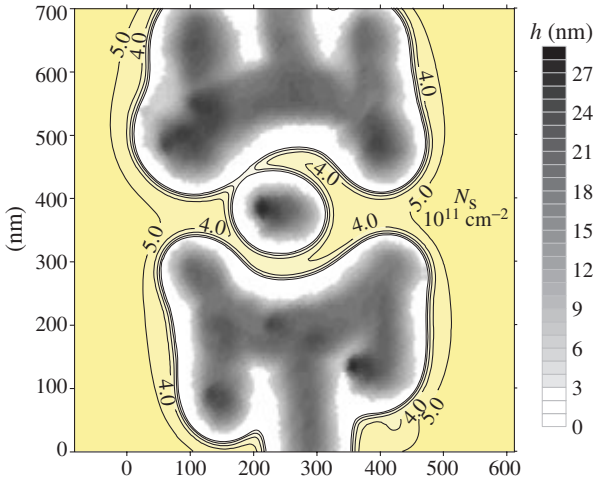

Fig. 1. Map of the anodic oxidation depth h (in the background of depletion regions) and electron density (N_s) contour map of the interferometer fabricated by AFM [2].

conductance (150000 points of G) in a wide range of Fermi energy and magnetic field. It took 6 hours on 64 IBM Power4 1.3 GHz CPUs of supercomputer Zahir (IDRIS, Orsay, France) or would take 70 days on a 2.6 GHz Intel Pentium 4 desktop PC.

At zero temperature the amplitude and phase of ABOs vary in an intricate way as Fermi energy and magnetic field change. At $B \neq 0$ the phase may vary smoothly with Fermi energy, not only flip between 0 and π as one would expect. The thermal averaging makes ABOs more uniform both in phase and amplitude. Complicated zero-temperature conductance transforms into a system of parallel lines with increasing temperature. At some regions (E_F,B), where ABOs are suppressed at zero temperature, amplitude of ABOs becomes bigger at finite temperature. On the whole, with increasing temperature the oscillations are damped down.

If the potential were slightly changed (we increased the oxidation depth in calculations by 10%) the picture of oscillations would shift to higher energies as a result of thicker tunnelling barrier in the narrow arm. As the tunneling barrier in the narrow arm of the ring increases ABOs disappear whereas conductance of the ring retains its value near conductance quantum. It worth noticing that asymmetry of the ring is the main reason for small amplitude of the oscillations at low temperatures, since the phase-breaking processes are inessential in this case.

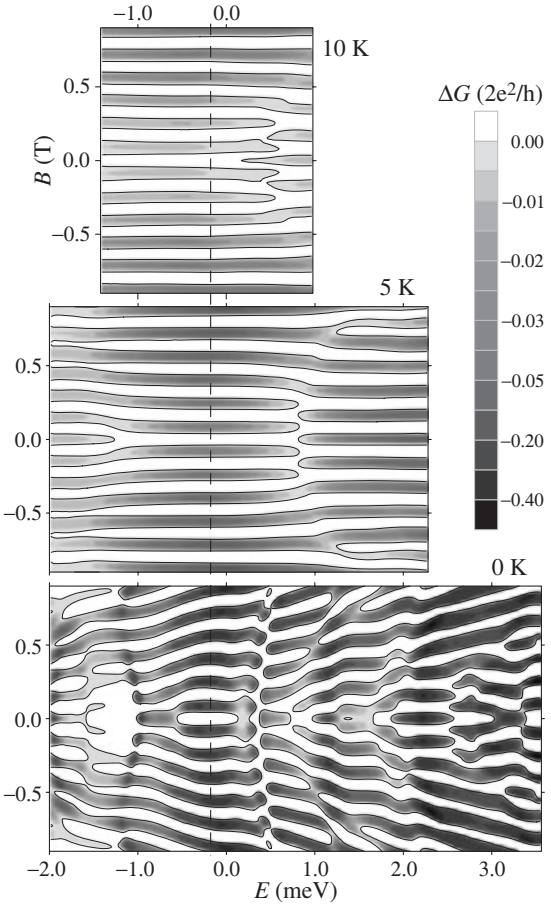

Fig. 2. Aharonov–Bohm conductance oscillations of the interferometer at temperature: $T = 0$, 5 K, 10 K. For clarity, only regions $\Delta G < 0$ are shown.

We have found that thermal averaging of $G(E, B)$ for two realizations of electrostatic potential U_1, U_2 leads to essentially different behaviours of the temperature damping (Fig. 3). For example, if a state at Fermi energy ($E = -0.2$ meV, U_1) lies within the band of large oscillations with weakly changing phase, then the damping is slow. If a state ($E = 2$ meV, U_2) is surrounded by small oscillations with strong energy dependence of phase (the regions of phase reversals or shifts), the temperature damping is fast. In the latter case the amplitude rapidly decreases at low temperatures, but it almost does not change beginning at $T = 4$ K. This resembles a "critical" temperature predicted in a simpler model of multimodal mixing at the places of connection of ring and quantum channels [7]. Importantly, the amplitude of ABOs can remain approximately constant above the critical temperature only in coherent transport models. In reality, coherence time decreases and the oscillations should disappear exponentially with temperature. However total temperature dependence can be complicated and even non-monotone, because it is determined by thermal averaging at low temperatures and phase-breaking processes at high temperatures.

Thus we have shown that the amplitude of ABOs is determined by mesoscopical state of the sample, and temperature dependences of ABOs are not universal but depend sensitively on both Fermi energy and electrostatic potential of the ring.

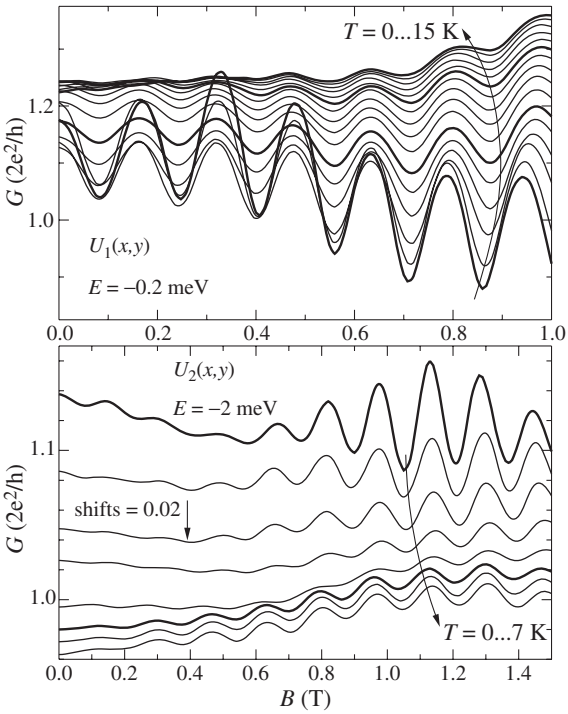

Fig. 3. Conductance of the interferometer $G(B)$ for indicated temperatures and for different realizations of electrostatic potential U_1, U_2.

Acknowledgements

We are grateful to A. I. Toropov and D. V. Sheglov for providing us with initial structural data for realistic modeling. O.A.T. acknowledges IDRIS Supercomputing Center, Orsay, France (project 41778) for the possibility of performing the calculations. This work was supported by RFBR (project 05-02-16591-a) and INTAS (grant 01-0014). The work at Grenoble was funded by CNRS.

References

[1] A. Fuhrer *et al*, *Nature* **413**, 822 (2001).
[2] V. A. Tkachenko *et al*, *JETP Lett.* **79**, 136 (2004).
[3] O. A. Tkachenko *et al*, *JETP Lett.* **79**, 293 (2004).
[4] M. Büttiker *et al*, *Phys. Rev. B* **31**, 6207 (1985).
[5] Jian-Bai Xia, *Phys. Rev. B* **45**, 3593 (1992).
[6] E. B. Olshanetsky *et al*, *SemiMag-16*, ThP23 (2004).
[7] M. Shin *et al*, *Phys. Rev. B* **53**, 1014 (1996).

13th Int. Symp. "Nanostructures: Physics and Technology"
St Petersburg, Russia, June 20–25, 2005

Quasi-hydrodynamic simulation of electroconductivity of nano-dimensional multilayered semiconductor structures under high electric field

V. A. Gergel[1], V. A. Kurbatov[2] and M. N. Yakupov[3]

[1] Institute of Radio Engineering and Electronics, Russian Academy of Sciences
[2] P. N. Lebedev Physics Institute of the Russian Academy of Sciences
[3] Institute of Radio Engineering and Electronics, Russian Academy of Sciences

Abstract. Electroconductivity of nano-dimensional multilayerd heterostructures were studied by mathematical methods based on energy balance equation. It was shown that the striking peculiarity of charateristics is the peak of the differential conductivity which position and magnitude are defined by height and abruptness of heterobarriers as it depends on level of structure doping. It is suggested the physical model for interpretation of the calculated curves forms by collective actions of electrostatic decreasing of heterobarrier's height and increasing of electron temperature at the injected heteroboundaries. It was used quasihydrodynamic description of electron drift with account for mobility and energy relaxation time dependence of electron temperature, thermo-diffusion components of electron flow and divergence of electron temperature flow.

1. Basic set of equations of the model

Characteristics of high field electron drift in multilayered semiconductor's structures were studied using a quasihydrodynamic description of electron drift with account for simplified dependence of mobility and energy relaxation time on electron temperature:

$$\mu(T) = \mu_0 \left(\frac{T_0}{T}\right)^{\alpha}; \tau(T) = \tau_0 \left(\frac{T_0}{T}\right)^{\alpha-1}; 0.5 < \alpha < 1.$$

The model consists of continuity equation, Poisson equation and energy balance equation:

$$\begin{cases} \dfrac{d^2\phi}{dx^2} = \dfrac{(N-n)}{L_D^2}\dfrac{T_0}{N_D^+}; \\ \dfrac{dj_n}{dx} = 0; \\ \dfrac{dj_T}{dx} = j_n\dfrac{d\phi}{dx} - \dfrac{n(T-T_0)}{\tau}, \end{cases} \quad (1)$$

where $L_D = \sqrt{\dfrac{\varepsilon_0\varepsilon_{Si}T_0}{q_e N_D^+}}$ is Debay length, T_0 is an equilibrium temperature.

At this point, it is used electron flow as:

$$j_n = \mu_0 n\left[\frac{d\phi}{dx} - (1-\alpha)\frac{dT}{dx}\right] - \mu_0 T\frac{dn}{dx}, \quad (2)$$

with account for thermodiffusion component, and expression for electron temperature flow is

$$j_T = \left(\frac{5}{2} - \alpha\right)\left(-\mu_0 nT\frac{dT}{dx} + j_n T\right), \quad (3)$$

with account for its convective and thermo conductive components.

2. Nonlocal electron's heating in submicron structures

The basic regularities of electron drift in submicron dimensional structures are illustrated on fig.1, it shows calculated spatial distribution of the potential, the electron concentration, the electron temperature and the drift velocity in reference $n^+ - n - n^+$ structure with homogenous doping of high-ohmic layer $N_D = 5\times10^{17}$ ($N_D^+ = 5\times10^{18}$), length of 0.4 μm and contact regions $N_D^+ = 5\times10^{18}$ with applied voltage of 3.0 V.

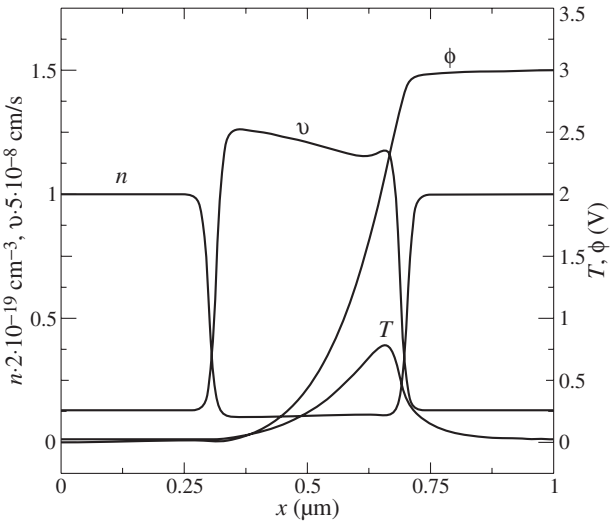

Fig. 1. Spatial distribution of the potential, the electron concentration, the electron temperature and the drift velocity.

It is seen that the essential part of the thermal energy of electrons obtained in high ohmic region is lattice-dissipated in low ohmic contact region. At this point the electron temperature is effectively decreasing in high field areas what decreases degradation of mobility. It results in that electrons' velocity doesn't saturate and continue to grow with electric field (Fig. 2, curve 1).

3. Ultrafast electron drift in structures with intermediate high-doped layers

It is reasonable to expect that conditions for electron flow cooling can be essentially improved if high ohmic drift region will be divided into several parts by low ohmic inclusions, in which an intensive electron cooling will occur. The avarage tempera-

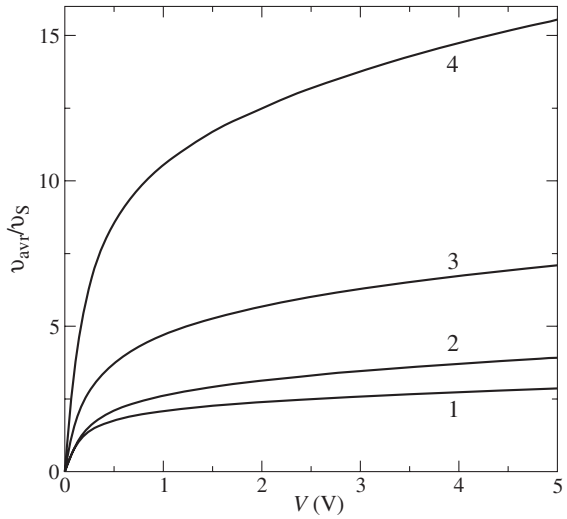

Fig. 2. Relative average velocity vs. applied voltage: 1—400 nm, 2— 2×200 nm, 3—4×100 nm, 4—8×50 nm.

ture has to decrease; the velocity and mobility have to increase, repectively. In Fig. 3 it is depicted such a complex structure where the drift region is divided into four 100 nm pieces by three low ohmic inclusions with the same length. Calculated distribution of temperature, local velocity and potential are shown on Fig. 3, it proves above statements of the electron temperature lowering in the case of sectioned n-regions. At this time the average drift carrier velocity increases as curve 3 in Fig. 2. This curves present I–V characteristics of four different structures in the coordinates: relative average velocity $\upsilon_{\text{avr}}/\upsilon_S = j_n/N_D\upsilon_S$ vs. applied voltage V. Depicted curves 2 and 4 on Fig. 2 are corresponded to structures which are haven drift region with length of 0.4 μm is divided into two 200 nm pieces or eight 50 nm pieces by low-ohmic parts with the same length.

It is clear that the same increasing of the effective carrier mobility ought to be also for island film structures, if the electroconductivity of islands in the case of additional doping will essentially exceed a conductivity of a given matrix.

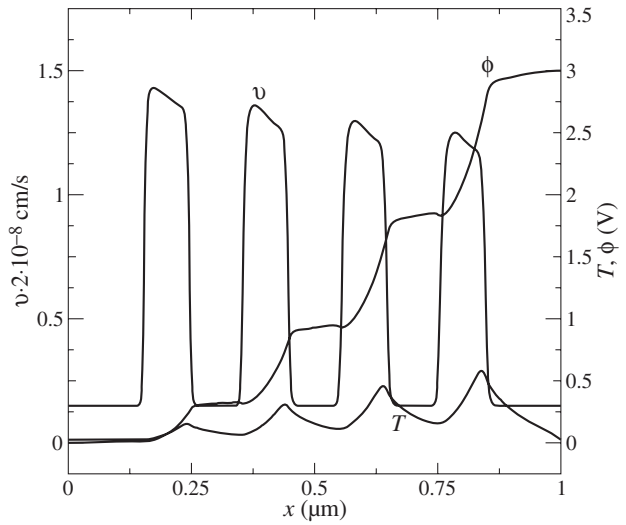

Fig. 3. Calculated distribution of temperature, drift velocity and potential for four sectioned structure.

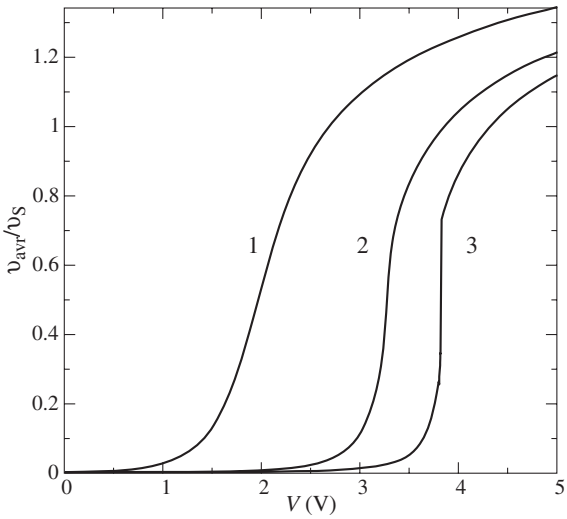

Fig. 4. I–V curves of heterostructure with different abruptness of barriers: 1—20, 2—35, 3—50.

4. Nonlinearity of electroconductunces of multilayered heterostructures

The model (1–3) was extended for description of varyband structures with help of additional quasipotential $\varphi_c(x) = q^{-1}E_c(x)$. In the quality an test example it was calculated I–V curves of heterostructure with uniform doping 5×10^{17} cm^{-3} and four heterobarriers with height of 0.3 V and length of 100 nm which are divided by narrow band layers with the same lenght. Presented curves demonstrate significiant nonlinearity with sharp maximum of differential conductivity which position and amplitude essentially depend on abruptness of heterobarriers $\gamma \approx \frac{d\varphi_c}{dx}/\max$. Befor maximum the character of current increasing is defined by effect of decreasing the height of heterobarriers while electic field is becoming higher. Near the area of maximum this effect is forced due to grow of electron temperature at injected heteroboundaries. The higher applied voltages the electron temperature is as big as limited influence of heterobarriers on value of current is practically dissappeared.

We believe that considered structures with nano dimensional high conductivity inclusions or gap mismatching are perspective for further increasing of field effect and bipolar transistor's perfomance.

Acknowledgements

This work was supported by RFBR, projects # 04-02-17681, 03-02-17191, 03-02-2007.

References

[1] V. A. Gergel, M. N. Yakupov, *Semiconductors* (in press).

13th Int. Symp. "Nanostructures: Physics and Technology"
St Petersburg, Russia, June 20–25, 2005

Electron transport through antidot superlatices in $Si/Si_{0.7}Ge_{0.3}$ heterostructures: new lattice-induced magnetoresistance oscillations at low magnetic fields

E. B. Olshanetsky[1], V. T. Renard[2,3], Z. D. Kvon[1], J. C. Portal[2,3,4] and J. M. Hartmann[5]

[1] Institute of Semiconductor Physics, Novosibirsk 630090, Russia
[2] GHMF, MPI-FKF/CNRS, BP-166, F-38042, Grenoble, Cedex 9, France
[3] INSA-Toulouse, 31077, Cedex 4, France
[4] Institut Universitaire de France, Toulouse, France
[5] CEA/Leti, F-38054, Grenoble, Cedex 9, France

Abstract. In the present work we have investigated the transport properties in a number of Si/SiGe samples with antidot lattices of different periods. In samples with the lattice periods 700 nm and 850 nm we have observed the conventional low-field commensurability magnetoresistance (MR) peaks consistent with the previous observations in GaAs/AlGaAs and Si/SiGe samples with antidot lattices. However in samples with the lattice period 600 nm a new series of quasiperiodic MR oscillations has been found beyond the last commensurability peak which cannot be explained neither by the pin-ball model nor by the model of runaway trajectories.

Introduction

Two dimensional (2D) system modulated by a periodic strong repulsive potential is called an antidot lattice. Various interesting phenomena have been observed in antidot lattices in uniform perpendicular magnetic fields, Ref. [1–5]. They are low-field commensurability maxima in the longitudinal resistivity ρ_{xx}, the quenching of the Hall effect near $B = 0$ and non-quantized Hall plateaus in the same regime. These effects have been shown to be a manifestation of various phenomena associated with the chaotical dynamics of electrons in these systems, such, for example, as the formation of dynamically stable run-away trajectories [6, 7].

Originally all of these studies were conducted only on III-V semiconductors, especially GaAs/AlGaAs heterostructures, since usually the elastic mean free path of the electrons has to be larger than the period of the superlattice in order to be able to obtain the above features. However, the 2D electron gas in Si/SiGe heterostructures, due to its progressively improving quality, is now becoming an equally suitable material for the studies of electron transport in antidot lattices. Up to date one work [8] has already been published on the transport properties of a 2D electron gas in a Si/SiGe heterostructure with a square lattice of antidotes. In addition to the two main commensurability peaks $r_c/a \approx 1.5$ and 0.47, respectively, observed previously in GaAs structures, the authors [8] have also found a new shoulder-like feature in the MR at higher fields $r_c/a \approx 0.2$. (Here r_c is the cyclotron radius, a is the antidot lattice period). In the present work we have investigated the transport properties in a number of patterned Si/SiGe samples with various antidot lattice periods. In the samples with lattice periods 850 and 700 nm we found the usual commensurability peaks and the shoulder-like feature at a higher field, already reported in [8]. Surprisingly, however, in the samples with the lattice period 600 nm, apart from the features corresponding to the commensurability peaks, we have observed a number of unusual MR oscillations at higher fields (Fig. 2) where conventional commensurability peaks are no longer possible.

1. Experimental

Our samples were Hall bars fabricated on the basis of $Si/Si_{0.75}Ge_{0.25}$ heterostructure with a high mobility 2D electron gas. The distance between the potential probes was 100 μm; the width of the sample was 50 μm. The properties of the original heterostructure were: the electron density $N_s = 5.9 \times 10^{11}\,\mathrm{cm}^{-2}$, the mobility $\mu = 165\,000\,\mathrm{cm}^2/\mathrm{Vs}$. The square array of antidotes, fabricated by electron beam lithography and reactive plasma etching covered the whole segment of the samples between the voltage probes. We have investigated a number of samples with different lattice periods 0.6, 0.7 and 0.85 μm and the hole lithographical diameter $2r = 0.15$–$0.2\,\mu$m. The total number of antidotes was $(7–12)\times 10^3$. The magnetoresistance was measured using a conventional four point ac lock-in scheme in a He^3 cryostat at temperatures 0.3–4.2 K and in magnetic fields up to 13 T.

2. Results and Discussion

Figure 1 shows a typical MR dependence for sample with the antidot lattice period 700 nm. Similar dependences were observed for samples with the lattice period 850 nm. One can clearly see two distinct peaks in MR around zero magnetic field followed by a showlder-like feature. At still higher fields Shubnikov-de Haas oscillations appear that can be used to determine the sheet electron density. The positions of the low-field peaks are $r_c/a \approx 1.75$ and $r_c/a \approx 0.53$ respectively. The shoulder lies at about $r_c/a \approx 0.33$. At the moment there are two models for the explanation of the commensurability peaks (CPs). The so called pin-ball model [2] and the model of runaway trajectories [6]. According to the pin ball model the main CPs are given by the following conditions: $r_c/a = 0.5$ (corresponding to a localized trajectory around 1 antidot) and $r_c/a = 1.14$ (a trajectory localized around 4 antidots). In the second model the condition for the first CP is given by $r_c/a = 0.5$ (same as in the pin-ball model) and for the second $r_c/a = 1.5$. In principle, both models can describe the position of the two peaks and the interpretation is therefore ambiguous in some cases.

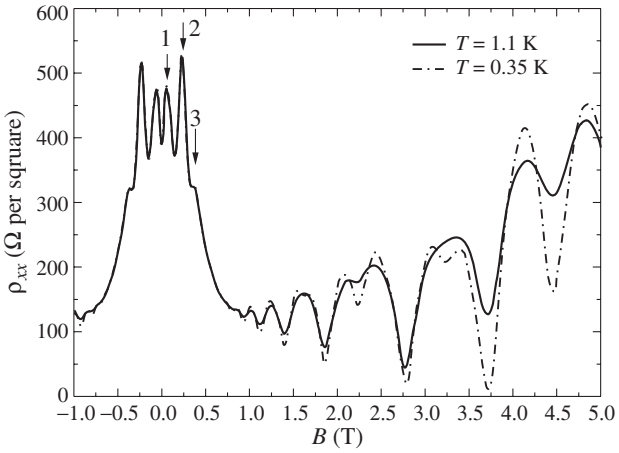

Fig. 1. Magnetoresistance in a sample with the lattice period 0.7 μm. One can see two main commensurability peaks corresponding to (**1**) $r_c/a \approx 1.75$ and (**2**) $r_c/a \approx 0.53$ around zero field and a shoulder-like feature (**3**) at $r_c/a \approx 0.33$.

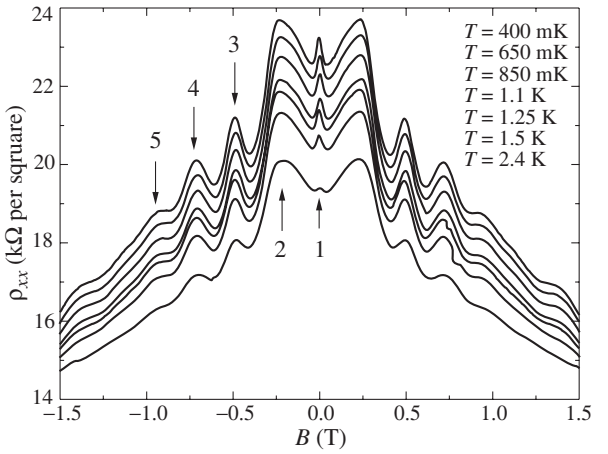

Fig. 2. Magnetoresistance in a sample with the lattice period 0.6 μm. The arrows mark the WL peak **1**, the commensurability peak **2** and the new additional oscillations **3**, **4**, **5** at fields $B \geq 0.5$ T. The temperature increases from the upper to the lower curve.

The origin of the shoulder, also observed in Ref. [8], cannot be described by either model and remains unknown. In the Hall resistance two additional non-quantized plateaus are observed at fields slightly higher than those of the peaks in ρ_{xx}. Around $B = 0$ the Hall effect is quenched. The two "last plateaus" and the quenching of the Hall effect are typical transport phenomena in antidot lattices.

The samples are only weakly sensitive to illumination which does not change the electron density very much and results only in a slight decrease of the zero field resistance. There is practically no temperature dependence of the commensurability oscillations below $T = 4.2$ K. On the whole, apart from the shoulder, the behavior of the Si/SiGe samples with the antidot lattice periods 700 nm and 850 nm is found to reproduce the typical features well known from GaAs/AlGaAs samples.

The situation, however, is different in the samples with the superlattice period 600 nm. Fig. 2 shows the characteristic MR curves for one of these samples. The peak **1** at zero magnetic field is due to the suppression of the weak localization correction. Then follows a broad commensurability peak **2** corresponding to $r_c/a \approx 0.64 \pm 0.03$. If we assume that this peak is realted to the theoretical condition $r_c/a = 0.5$, then, in antidot superlattices this is usually the last commensurability peak that can be observed before the onset of the SdH oscillations. Surprisingly, in our samples with the lattice period 600 nm we see at least three more equally spaced peaks **3**, **4**, **5** at $B \approx 0.49$ ($r_c/a \approx 0.28$), 0.72 ($r_c/a \approx 0.2$) and 0.95 T ($r_c/a \approx 0.15$) respectively. Fig. 2 shows data for a high resistivity sample state ($R_{xx}(B = 0) \approx 23\,\mathrm{k}\Omega$) corresponding to a system of closely spaced antidots with narrow passages between them and with the electron transport taking place along some percolating paths. However it has been found that using illumination sample states with as low resistance as $R_{xx}(B = 0) \approx 1.2\,\mathrm{k}\Omega$ could be obtained with the new oscillations still present. As with the case of the 700 and 850 nm samples the electron density varies very little with illumination. The new oscillations **3**, **4**, **5** do not change their position. The only difference with the high resistivity sate is the absence of the weak localization peak **1** and the splitting of the broad peak **2** in Fig. 2 into two conventional commensurability peaks $r_c/a \approx 1.7$ and $r_c/a \approx 0.54$ indicating that the mobility has increased. The Hall resistance dependence in 600 nm samples remains practically the same as in 700 and 850 nm samples with the quenching of the Hall effect and the additional plateaus corresponding to the commensurability peaks. No new features corresponding to the new oscillations in R_{xx} have been found in R_{xy} .

To our knowledge this is the first observation of a series of oscillations in an antidot lattice at fields above the last commensurability peak ($r_c/a = 0.5$) and below the onset of SdH oscillations. At present we do not have an explanation of this effect. However one could suppose that they may have something to do with possible commensurability effects in the space between the closely set antidots similar to the peak observed in [9].

Acknowledgements

This work has been supported by the programs programs "Physics and Technology of Nanostructures" of the Russian ministry of Industry and Science and "Low dimensional quantum structures" of RAS.

References

[1] K. Ensslin *et al*, *Phys. Rev.*, **B41**, 12307 (1990).
[2] D. Weiss *et al*, *Phys. Rev. Lett.*, **66**, 2790 (1991).
[3] A. Lorke *et al*, *Phys. Rev.*, **B44**, 3447 (1991).
[4] R. Schuster *et al*, *Phys. Rev.*, **B47**, 6843 (1993).
[5] G. M. Gusev *et al*, *Pis'ma Zh. Eksp. Teor. Fiz.*, **54**, 369 (1991).
[6] E. M. Baskin *et al*, *JETP Lett.*, **55**, 678 (1992).
[7] R. Fleischmann *et al*, *Phys. Rev. Lett.*, **68**, 1367 (1992).
[8] D. Tobben *et al*, *Phys. Rev.*, **B50**, 8853 (1994).
[9] M. V. Budantsev *et al*, *Physica*, **B260**, 363 (1998).

13th Int. Symp. "Nanostructures: Physics and Technology"
St Petersburg, Russia, June 20–25, 2005

Investigation of rectification effects in asymmetric single and double superconducting Al rings

V. L. Gurtovoi, R. V. Kholin, N. N. Osipov and *V. A. Tulin*

Institute of Microelectronics Technology, Russian Academy of Sciences, 142432 Chernogolovka, Moscow region, Russia

Abstract. We have investigated electron transport properties of asymmetric single and double ring mesoscopic structures fabricated by electron beam lithography. For single rings, there have been observed quantum oscillations (period equals to flux quantum $\Phi_0 = h/2e$) of rectified voltage in magnetic field. Bias current dependence of the amplitude of oscillations has shown pronounced maximum at the near critical current value for rather wide temperature range lower T_c. For double rings, we have observed oscillations corresponding to large and small ring areas. Also oscillations corresponding to large and small area difference have been observed, which disappeared at temperatures approaching the critical temperature (higher than 0.99 T_c).

Introduction

Development of nanofabrication and measurement techniques stimulate researchers to investigate subtle effects in semi- and superconducting mesoscopic structures. One of the most fundamental problems is fabrication of structures, where superposition of macroscopic quantum states is realized, and experimental verification of superposition of the states [1]. This problem is closely connected with solid-state quantum bit and coupled qubit fabrication and investigation of their functionality. The probable solid-state qubit realizations are superconducting ring structures with or without Josephson junctions [2,3]. Therefore, investigation of properties of the coupled superconducting ring structures could donate to solution of quantum computer problem.

In this work we present detailed investigation of rectified voltage oscillations in magnetic field for asymmetric single and double superconducting Al rings as a function of temperature and AC bias current amplitude.

1. Experimental and results

Investigated structures used in our experiments consisted of asymmetric aluminum rings (45 nm thick, thermally evaporated on oxidized Si substrates) with semi-ring width of 200 and 400 nm for narrow and wide parts, respectively. 4 μm diameter single ring (SR) and magnetic flux coupled double rings (DRs) with large ring geometrical parameters the same as for SR and area ratio (large ring/small ring) = 1.42 were fabricated by e-beam lithography and lift-off process. Fig. 1 shows an SEM image of the structures. For this structures, the sheet resistance was 0.23 $\Omega/\square$ at 4.2 K, the resistance ratio $R(300\ \mathrm{K})/R(4.2\ \mathrm{K}) = 2.7$, and $T_c = 1.237$ K. Estimated coherence length $\xi(T = 0\ \mathrm{K})$ was 170 nm and penetration depth $\lambda(T = 0\ \mathrm{K})$ was 80 nm.

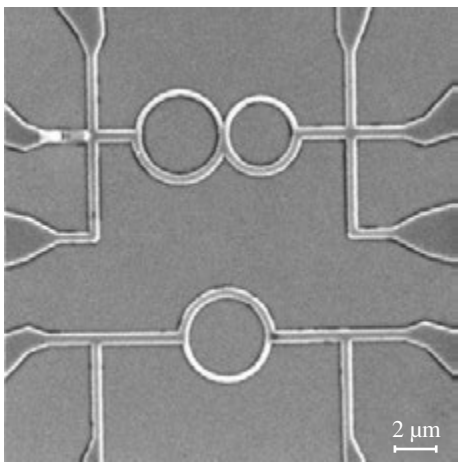

Fig. 1. An SEM image of structures based on asymmetric single and double superconducting Al rings.

Measurements were carried out by applying 5 kHz sinusoidal bias current to current leads, whereas, rectified DC signal was measured in a frequency band from 0 to 30 Hz by low-noise preamplifier (PARC 113) at potential leads. It should be noted that rectification effects do not depend on frequency of the bias current at least up to 1 MHz [4]. Magnetic field direction was perpendicular to the ring's plane. Magnetic field time scanning was slow enough so that upper frequency of signal spectrum, which resulted from magnetic field changes, did not exceed 30 Hz. All signals, namely, rectified voltage, current, and magnetic field were digitized by a multi-channel 16-bit

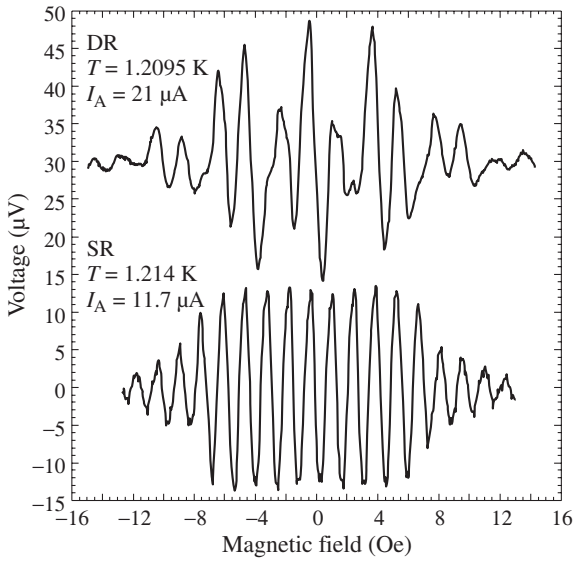

Fig. 2. Rectified voltage oscillations in magnetic field of single ($T = 1.214$ K, amplitude of bias current $I_A = 11.7\ \mu$A, $f = 5$ kHz) and double ($T = 1.2095$ K, $I_A = 21\ \mu$A, $f = 5$ kHz) ring structures. The DR oscillations are shifted by 30 μV.

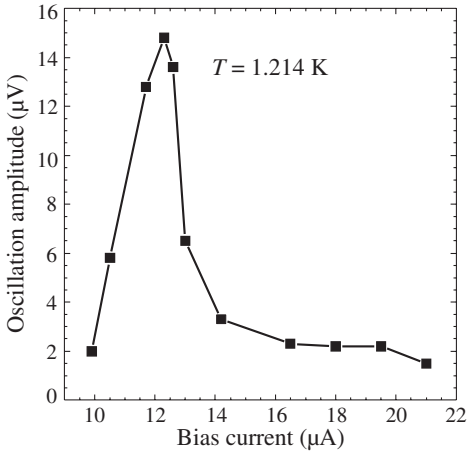

Fig. 3. AC bias current dependence of the rectified oscillation amplitude ($\Phi = 1/4\Phi_0$) of the SR at $T = 1.214$ K.

analog-digital converter card.

Figure 2 shows typical oscillations of the rectified voltage as a function of magnetic field for an SR sample at $T = 1.214$ K. The oscillations are periodic with period equals to the superconducting flux quantum $\Phi_0 = h/2e$ (this was confirmed by Fourier analysis), the maxima and minima being observed at $\Phi \approx \Phi_0(n \pm 1/4)$, $(n = 0, \pm 1, \ldots)$. Both AC bias current and relatively small in amplitude (due to weak screening) circular persistent current are responsible for the formation of the oscillations. Slowly varying in time, persistent current breaks the symmetry of clockwise-anticlockwise direction of the currents flowing in the ring, which results in asymmetry of current-voltage characteristics. When persistent current flows in a proper direction, the bias current is added during its one half period to persistent current or subtracted during the opposite half period from that in a narrow part of the ring and vice versa in a wide part. When amplitude of the bias current is increased, first the criticality is achieved in the narrow part of the ring creating a voltage pulse of a proper sign, which after integration for many periods (frequency of bias current is much higher than that of persistent current) forms rectified signal. Further increase in the bias current amplitude results in achieving of criticality in the wide part of the ring and formation (half-period shifted with respect to the narrow part) of an opposite sign voltage pulse. Time averaging of the voltage pulses of different polarity from narrow and wide parts of the SR is the reason of rectified voltage diminishing when the amplitude of the bias current is increased. For the opposite direction of persistent current, there would be generated rectified signal of the opposite sign, which explains the sign-varying oscillations of the rectified voltage in magnetic field (Fig. 2). From this, one can make conclusion that rectified DC voltage oscillations in magnetic field are proportional to persistent current, whereas AC bias current only shifts the total current of the ring to the critical value. The given above qualitative explanations of the rectified voltage behavior with increasing of the bias current amplitude are supported by experimental results in Fig. 3, where the amplitude of the rectified voltage oscillations in magnetic field is plotted as a function of the bias current amplitude. At low bias currents, the rectified voltage is zero since the SR is in a superconducting state. Then near the critical current, the voltage reaches maximum and diminishes with increase of the bias current.

To determine the exact position of the maximum in Fig. 3 with respect to critical current value, we present in Fig. 4 temperature dependence of both the critical current of the SR measured from current-voltage characteristics and the amplitude of bias current at which the maximum of the rectified oscillations is observed. As clearly seen from Fig. 4, the maximum of the oscillations is achieved when the bias current amplitude is slightly higher than the critical current of the SR, having practically the same temperature dependence as the critical current. Temperature dependence of the maximum rectified voltage is also shown in Fig.4. The maximum voltage is increasing with decreasing temperature in a way similar to the bias current and having near linear dependence on the bias current (not shown hear), the slope of the maximum voltage curve being proportional to the rectification efficiency.

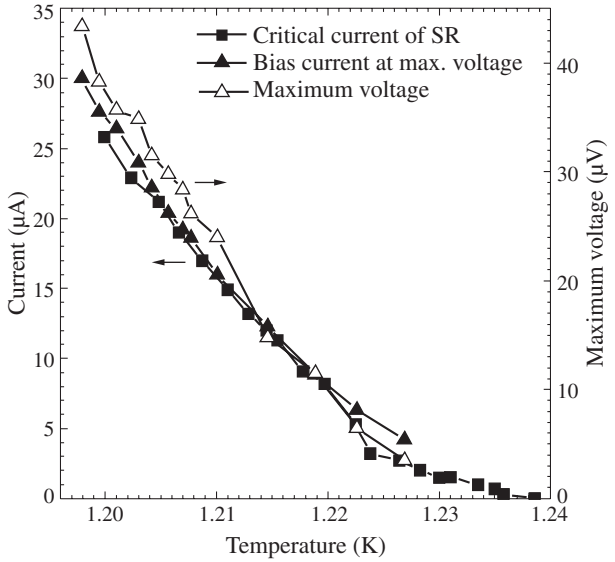

Fig. 4. Temperature dependence of the critical current of the SR, amplitude of bias current (corresponding to the maximum of oscillation amplitude in Fig. 3), and the maximum voltage of the oscillation amplitude from Fig. 3.

We also studied oscillations in magnetic field ($T = 1.2095$ K) for magnetic flux coupled double rings (Fig. 2). These oscillations are different from the oscillations for the single ring. Fourier analysis have shown that in DR oscillation spectrum there were oscillations from large and small rings, and also oscillations corresponding to the area difference of the large and small rings. The later oscillations were observed at low temperatures and disappeared at temperatures higher than 1.223 K ($T \approx 0.99T_c$).

Acknowledgements

This work has been supported by a grant of the Program "Low-Dimensional Quantum Structures", the Russian Foundation of Basic Research (Grant 04-02-17068) and a grant of the program "Technology Basis of New Computing Methods".

References

[1] A. J. Leggett, *J. Phys.: Condens. Matter* **14**, R415 (2002).
[2] D. V. Averin, *J. Low Temp. Phys.* **118**, 781 (2000).
[3] Y. Makhlin, D. Schon, and A. Shnirman, *Rev. Mod. Phys.* **73**, 357 (2001).
[4] S. V. Dubonos, V. I. Kuznetsov, I. N. Zhilyaev, A. V. Nikulov, and A. A. Firsov, *JETP Lett.* **77**, 371 (2003).

13th Int. Symp. "Nanostructures: Physics and Technology"
St Petersburg, Russia, June 20–25, 2005

InAlGaAs/AlGaAs superlattices for polarized electron photocathodes

Yu. A. Mamaev[1], A. V. Subashiev[1], Yu. P. Yashin[1], L. G. Gerchikov[1], T. Maruyama[2], D.-A. Luh[2], J. E. Clendenin[2], V. M. Ustinov[3] and A. E. Zhukov[3]

[1] State Polytechnic University, 195251, St Petersburg, Russia
[2] Stanford Linear Accelerator Center, 2575 Sand Hill Road, Menlo Park, CA 94025, USA
[3] Ioffe Physico-Technical Institute, St Petersburg, Russia

Abstract. Highly efficient emitters of polarized electrons based on the InAlGaAs/AlGaAs superlattice give an optimistic prognosis to explorations of such structures as the sources for accelerators. A new set of these SL structures with minimized conduction band offset was designed and recently tested. A new technology of surface protection in MBE growth leads to a significantly reduced heat-cleaning temperature. At these lowered cleaning temperatures, the thermal degradation of the working structure parameters is avoided. As a result a polarization P of up to 91% at corresponding quantum efficiency (QE) of 0.3% was achieved at room temperature.

Introduction

The spin-polarized electron sources (PES) based on photoemission from GaAs or its relatives under excitation by circularly polarized light has proved to be the best for high energy electron accelerators applications [1]. New progress in development of polarized electron sources can be based on new structures with good structural quality, large valence band splitting and spin relaxation times resulting in larger polarization and quantum efficiency. The most obvious prospects for optimization of the PES structure are to increase both the quantum efficiency and electron spin polarization using superlattice (SL) structures with specially designed layer thickness and compositions. They consist of several thin strained films separated by layers of unstrained larger-bandgap material, specially designed to cause barriers for the hole transport but keep electron mobility high. From the point of view of growth of a perfect crystal, every separate strained film of the SL can be grown thinner than the critical thickness (CTh), but with a total thickness which can exceed CTh and be sufficient to obtain high quantum efficiency (QE). To suppress the depolarization during the transport to the band bending region (BBR), the working part of a structure has to be low p-doped (about 5×10^{17} cm^{-3}), which should help to suppress Bir–Aronov–Pikus spin relaxation mechanism [2]. At the same time the request for high QE at maximum polarization requires the top of a structure to be heavily p-doped to achieve high quality Negative Electron Affinity (NEA) surface. These two requirements can be simultaneously fulfilled with the modulation doping profile. Very high (not less than 5×10^{19} cm^{-3}) doping of the top layer helps as well to overcome surface charge limit (SCL), which appears at high pumping light power [3,4]. Below our recent results with InAlGaAs/AlGaAs superlattices are discussed. All SL samples were grown by solid-source molecular beam epitaxy on GaAs(100)-oriented substrates.

1. Highly strained InAlGaAs/AlGaAs SL structures

The main advantage of SL-based photoemitters is the possibility to vary the properties of the active layer over a wide range by the appropriate choice of layer composition, thickness, and doping profile. The initial polarization P_0 can be increased by choosing structures with a higher valence band splitting. The SL structures with strained quantum well (QW) layers in which heavy and light hole bands, in addition to the strain splitting, are moved aside due to different light and heavy-hole confinement energy in the QW layers, are the best for this purpose. The other benefit of the SLs is the possibility of a precise modulation doping providing small polarization losses during electron escape from the active layer and the band bending region into vacuum.

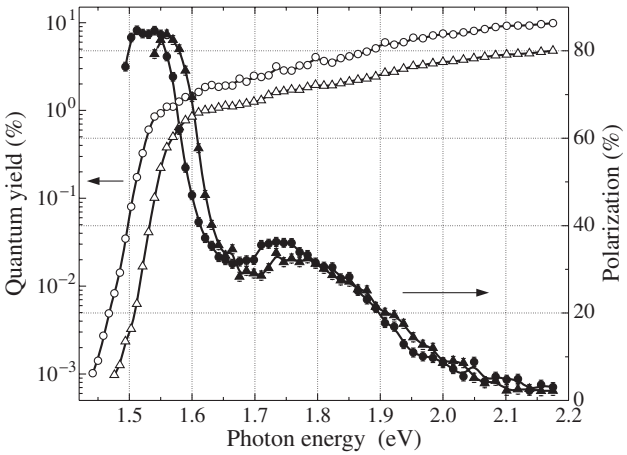

Fig. 1. Polarization (solid symbols) and quantum efficiency (open symbols) spectra of highly-strained multilayer $Al_xIn_yGa_{1-x-y}As$/AlGaAs structure at room (circles) temperature and at $T = 130$ K (triangles).

New InAlGaAs/AlGaAs SL structures with thin (close to 2 nm) quantum well layers and the highest possible (up to 35%) concentrations of In within the QW layers were developed and tested. The polarization and quantum efficiency spectra obtained at lowered activation temperatures are presented at Fig. 1, revealed a rather wide plateau in the vicinity of the maximum polarization (about 85%) and a sharp edge of the quantum yield spectrum, which indicates the good structural qualities of these samples. Record high values of strain splitting are reproducibly obtained, though further optimization of the overall photocathode structures is still needed. InAlGaAs/AlGaAs SL structures are favorable candidates for photocathodes since they can be grown by a standard MBE technology and the structures are well controlled and reproduced during the growth. This gives an optimistic prognosis to explore such structures in the sources attached to accelerators.

2. InAlGaAs/GaAs SL structures with minimized conduction band offset

A new strained-barrier short-period $Al_xIn_yGa_{1-x-y}As/GaAs$ superlattice with a minimal conduction-band offset was proposed in [1]. The main advantage of such SL results from the band line-up between the semiconductor layers of the SL. The Al content determines the formation of a barrier in the conduction band, while adding In leads to conduction band lowering, so the conduction band offset can be completely compensated by appropriate choice of x and y, while barriers for the holes remain uncompensated. As a result high vertical electron mobility and simultaneously a small spin relaxation rate is achieved while also a large enough valence-band splitting is remained.

For the thermalised electrons at room temperature the influence of the resulting periodical potential should be negligible. Besides, as a result of the conduction-band line up, the residual 4-nm barriers for the electrons in the SL are transparent. Thus the changes of electron mobility and spin relaxation rate from the values typical for the bulk GaAs should be small.

Using the structures based on quaternary $Al_xIn_yGa_{1-x-y}As$ alloy one can change the band gap by varying the Al content in the layers keeping In concentration unchanged to maintain high deformation and strain-induced valence band splitting. The choice of the layer thickness is dictated by the need to split the hole minibands. The splitting grows when barriers are broad enough and wells are narrow and deep.

A new set of the InAlGaAs/GaAs SL structures with minimized conduction band offset was designed and tested. The optimization of the design of these structures has recently become possible only with the development of more accurate calculation programs. In addition, a new technology of surface protection in MBE growth enabled us to significantly reduce the heat-cleaning temperature (for optimal activation it should not exceed 450 °C). At these lowered cleaning temperatures, the thermal degradation of the modulation doping profile is avoided. As a result a polarization P of up to 91% at corresponding quantum efficiency QE of 0.3% was achieved at room temperature (see Fig. 2). These results are significantly better than our previous ones and are equal to or superior to the best results achieved anywhere. The lowered activation temperatures open the possibility for further improvements in photocathode parameters via optimization of the doping profile.

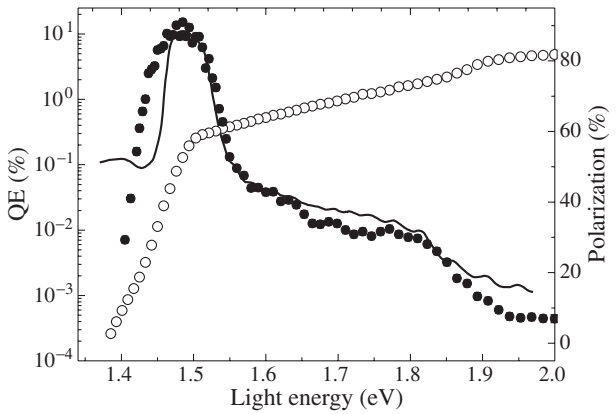

Fig. 2. Polarization (solid circles) and quantum efficiency (open circles) spectra of $Al_{0.21}In_{0.2}Ga_{0.69}As$ (4 nm)/Ga As(1.5 nm) 18.5 periods Superlattice sample at room temperature. Heat cleaning temperature 450 °C. Solid line — calculated energy dependence of $P(h\nu)$.

3. Summary

New structures based upon highly QW-strained InAlGaAs/ AlGaAs SLs and barrier-strained InAlGaAs/GaAs SLs with minimized conduction band offset have been developed and tested. InAlGaAs/AlGaAs SL structures are favorable candidates for photocathodes since they can be grown by a standard MBE technology and the structures are well controlled and reproduced during the growth. A new technology of surface protection in MBE growth leads to considerable reduction of the heat-cleaning temperature (not more than 450 °C). At these lowered cleaning temperatures, the thermal degradation of the working structure parameters is avoided. As a result a polarization P of up to 91% at corresponding quantum efficiency (QE) of 0.3% was achieved at room temperature.

Acknowledgements

This work was supported by Russian Fond for Basic Research under grant 04-02-16038, NATO under grant PST.CLG 979966 and the US Department of Energy under grant DE-AC02-76SF00515.

References

[1] A. V. Subashiev, Yu. A. Mamaev, Yu. P. Yashin, and J. E. Clendenin, *Phys. Low-Dim. Struct.* **1/2**, 1 (1999).

[2] F. Meier and B. P. Zakharchenya eds., *Optical orientation*, (North-Holland, 1984).

[3] G. A. Mulhollan, A. V. Subashiev, J. E. Clendenin, E. L. Garwin, R. E. Kirby, T. Maruyama, and R. Prepost, *Phys. Lett.* **A 282**, 309 (2001).

[4] T. Maruyama, A. Brachmann, J. E. Clendenin, T. Desikan, E. L. Garwin, R. E. Kirby, D.-A. Luh, J. Turner, and R. Prepost, *Nucl. Instr. and Meth.* **A 492**, 199 (2002).

13th Int. Symp. "Nanostructures: Physics and Technology"
St Petersburg, Russia, June 20–25, 2005

Photon-spin qubit-conversion based on Overhauser shift of Zeeman energies in quantum dots

S. Muto[1,2], S. Adachi[1,2], T. Yokoi[2], H. Sasakura[1] and I. Suemune[1,3]

[1] CREST, Japan Science and Technology Agency, Kawaguchi 332-0012, Japan
[2] Faculty of Engineering, Hokkaido University, N13 W8 Kita-ku, Sapporo 060-8628, Japan
[3] Research Institute of Electronic Science, Hokkaido University, N21 W10 Kita-ku Sapporo, 001-0021 Japan

Abstract. We propose a new method to realize a conversion of photon qubit and spin qubit using the effective magnetic field created by the nuclear polarization known as Overhauser field. We discuss its preliminary experiment on InAlAs/AlGaAs self-assembled quantum dot and also discuss effects of excitons which could destroy the conversion.

Introduction

Recently, situation around quantum information processing has been greatly changed. Especially for quantum cryptography, node-to-node telecommunication over 100 km is now possible [1]. One of the candidates for a qubit of the quantum computation is the electron spin (*e*-spin). Therefore, it is desirable to convert an *e*-spin qubit to a photon qubit.

Yablonovitch and coworkers have already proposed the qubit conversion between *e*-spins and photons based on the selection rules of optical transitions in quantum wells and quantum dots using the "*g*-factor engineering" [2, 3]. They also proposed a quantum repeater [4] based on this idea and using their *e*-spin QC. Their idea of *g*-factor engineering is to chose proper semiconductor materials or their combinations to realize "zero *g* factor" for electrons. By applying a static magnetic field, we can realize degenerate *e*-spin states and non-degenerate hole states. Therefore, we can transform a photon qubit to an *e*-spin qubit multiplied by one of split hole states;

$$a|0\rangle + b|1\rangle \Leftrightarrow (a|\downarrow\rangle + b|\uparrow\rangle) \otimes |\text{hole}\rangle\,. \qquad (1)$$

Here, $|0\rangle$ and $|1\rangle$ are two basis of a photon qubit and $|\downarrow\rangle$, $|\uparrow\rangle$ are up and down states of an *e*-spin qubit.

This idea, though elegant, need special choices of semiconductor materials and structures. It will be beneficial to have a more general way regardless of materials to make electron *g* factor "effectively zero". Here we propose a new way using Overhauser shift [5] of Zeeman energies known also as the "dynamic nuclear polarization". For this, all we need is the circularly polarized light and static magnetic field.

1. Basic idea [6]

Here we consider a In(Al)GaAs/AlGaAs quantum dot as an example. The basic idea is that the electrons feel both the external field and the nuclear field, that is the effective magnetic field caused by the nuclear spin polarization, while the holes feel only the external field. Consequently, if we tune either the external field or the nuclear field such that they cancel each other, an electron feels no magnetic field and a hole feels a non-zero field. Hence the situation of zero *g* factor for electrons is effectively realized. The resultant band diagram is just as shown by Fig. 1. (Precisely, the nuclear field to holes does not have to be zero. It is sufficient that the nuclear fields for both carriers is different.)

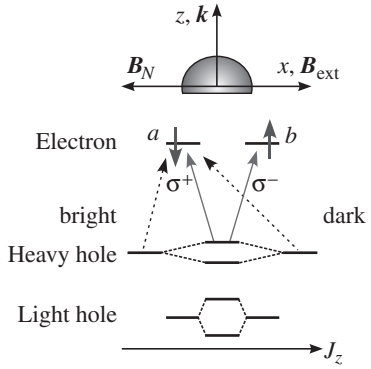

Fig. 1. Photon-spin qubit conversion using optical selection rule of electron-heavy hole transition and nuclear field. Photon is incident in the *z*-direction and the applied field is in the *x*-direction (Ref. 6).

Therefore, if we can tune either B_{ext} or I^i_{ave}, so that

$$g_{e,v}\mu_B B_{\text{ext}} + \sum_i A_i I^i_{\text{ave}} = 0\,, \qquad (2)$$

electrons feel zero magnetic field. Here, A_i indicates the hyperfine coupling constant for each nucleus.

Then the splitting for holes is,

$$\begin{aligned} g\mu_B B_{\text{eff},h} &= -\left(\frac{g_h}{g_e}\right)\sum_i A_i I^i_{\text{ave}} \\ &\quad + \sum_n \frac{32|j_z|}{15I}\mu_B\mu_I\left\langle\frac{1}{r_n^3}\right\rangle\langle I_n\rangle \\ &\sim -\left(\frac{g_h}{g_e}\right)\sum_i A_i I^i_{\text{ave}} \end{aligned} \qquad (3)$$

for both heavy ($|j_z| = \frac{3}{2}$) and light ($|j_z| = \frac{1}{2}$) holes. Since the dipolar term is usually much smaller than the contact term, the second term in the middle of Eq. 3 can be neglected. However, we note that this term does not have to be negligible for our proposal.

2. Experiments

Recently, we have observed Overhauser shift $\sum_i A_i I^i_{\text{ave}}$ in InAlAs QD grown by Stranski-Krastanow mode of MBE [7]. The experiment demonstrated Overhauser energies of 19 μeV, which are controllable by the excitation polarization and more generally by "optical orientation" [8] (Fig. 2. We have also

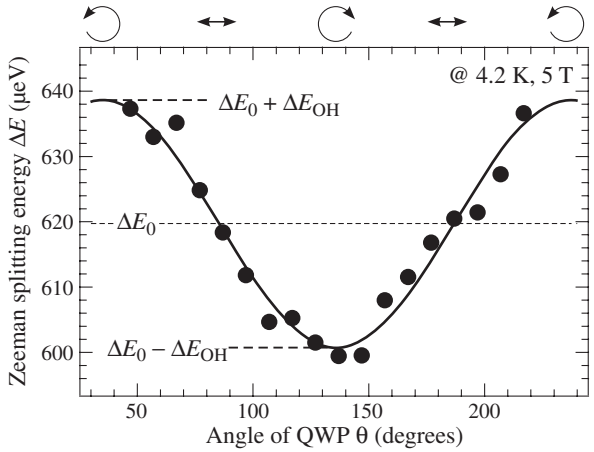

Fig. 2. The change of Zeeman splitting of a single InAlAs/AlGaAs QD as a function of circular polarization of excitation light. Overhauser shift was determined by the amplitude of the cosine curve (Ref. 7).

observed for the structure that the heavy hole g factor in the x-direction is nearly equal to the electron g factor (more precisely, $|g_{hh,x}| \cong |g_{e,x}| \cong 0.43$). Equation 3 indicates that we can cancel the Overhauser field for electrons with $B_{\rm ext} \sim 0.74\,$T, and that we can create the energy splitting for holes as much as Overhauser shift, which is about $19\,\mu$eV in Fig. 2. Although this is not a large energy, we can distinguish two hole levels with this separation since the intrinsic energy width of excitons are reported to be as small as $4\,\mu$eV at lowtemperatures [9,10]. Very recently, we have ovserved a much larger Overhauser shift of $87\,\mu$eV using the same structure.

3. Exciton effects

Here we discuss the excitonic effect which is inevitable in the current structure. Unfortunately, the structure cannot be used for the qubit-conversion due to the electron-hole exchange interaction of excitons. In the heavy-hole exciton formed in Fig. 1, the exchange interaction splits exciton states (with energy δ_0) to the dark and bright excitons, corresponding to parallel and anti-parallel alignment of electron and hole spins ($\mathbf{s}_e$ and $\mathbf{j}_h$), in the absence of magnetic field. This indicates that a photon with combination of right-circular polarization and left-circular polarization is converted to combination of two bright excitons, $a|s_z = -\frac{1}{2}\rangle|j_z = \frac{3}{2}\rangle + b|s_z = \frac{1}{2}\rangle|j_z = -\frac{3}{2}\rangle$ which is an entangled state of electron-hole pairs, and obviously neither a spin qubit of an electron nor of a hole can be factored out. Even in the presence of magnetic field, this situation persists as long as $g_h \mu_B B_{\rm ext} < \delta_0$. In our measurements, $\delta_0 = 39\,\mu$eV. Hence with $g_h \mu_B B_{\rm ext} = 87\,\mu$eV, we are outside of the region where bright and dark exciton persists. However it is favorable that we also reduce the exchange interaction such as by spatially separating electron-hole pairs.

In summary, we proposed a new method to realize conversions between a spin qubit and a photon qubit. The method uses Overhauser field by the nuclear polarization which is controlled by the external optical excitation, and is regarded to be more flexible than the previous proposal.

References

[1] For example, H. Kosaka, A. Tomita, Y. Nambu, T. Kimura and K. Nakamura, *Electronics Lett.*, **39** 1199 (2003).

[2] R. Vrijen and E. Yablonovitch, *Physica E*, **10** 569 (2001).

[3] H. Kosaka, A. A. Kiselev, F. A. Baron, Ki Wook Kim and E. Yablonovitch, *Electron. Lett.*, **37** 464 (2001).

[4] E. Yablonovitch, H. W. Jiang, H. Kosaka, H. D. Robinson, D. S. Rao, T. Szkopek, *Proceedings of the IEEE*, **91**, 761 (2003).

[5] A. W. Overhauser, *Phys. Rev.*, **92**, 411 (1953).

[6] S. Muto *et al*, cond-mat/0412013.

[7] T. Yokoi, S. Adachi, H. Sasakura and S. Muto, *Phys. Rev. B*, **71**, R041307 (2005).

[8] *Optical Orientation*, Modern Problems in Condensed Matter Sciences, Vol. 8, edited by F. Meier and B. Zakharchenya (North-Holland, NewYork, 1984).

[9] D. Birkedal, K. Leosson and J. M. Hvam, *Phys. Rev. Lett.*, **87**, 227401 (2001).

[10] T. Watanuki, S. Adachi, H. Sasakura and S. Muto, *Appl. Phys. Lett.*, **86**, 063114 (2005).

13th Int. Symp. "Nanostructures: Physics and Technology"
St Petersburg, Russia, June 20–25, 2005

Microwave detector-spectrometer based on edge-magnetoplasmons

I. V. Kukushkin[1,3], S. A. Mikhailov[2,3], J. H. Smet[3] and K. von Klitzing[3]

[1] Institute of Solid State Physics, Russian Academy of Sciences, Chernogolovka, 142432 Russia
[2] Mid-Sweden University, ITM, Electronics Design Division, 851 70 Sundsvall, Sweden
[3] Max-Planck-Institut für Festkörperforschung, Heisenbergstr. 1, D-70569 Stuttgart, Germany

Abstract. A two-dimensional (2D) electron system (ES) with several electric contacts, realized in a GaAs/AlGaAs quantum-well structure and placed in a magnetic field B, exhibits an ability to detect electromagnetic radiation in a broad frequency range. Irradiation of the sample by microwaves induces a photovoltage between pairs of contacts, which oscillates as a function of B. The amplitude and the period of oscillations are proportional to the radiation power and the wavelength respectively. Successful operation of such a detector/spectrometer has been experimentally demonstrated at microwave frequencies up to ~ 150 GHz and at temperatures up to ~ 80 K. We do not expect any principal difficulties in extending the operating frequency range into the terahertz region.

Detection of millimeter and submillimeter electromagnetic radiation (the frequencies f from ~ 100 GHz to a few THz) remains a challenging applied-physics problem. Schottky diodes [1], conventionally used in microwave range, are broadband detectors, sensitive to the electromagnetic-wave power, but insensitive to its frequency. Their use for measuring the frequency of radiation requires complicated schemes which include gratings, moving mirrors or other similar elements. Selective and tunable infrared detectors, based on electronic transitions in quantum-well structures [2,3,4,5], are free from such a disadvantage, but require very low temperatures for their operation. Since the energy levels, involved in the operating electronic transition, have to be not-equally occupied, such detectors can work only at $kT \ll \hbar\omega$. This requires $T \simeq 10$ K in infrared and even lower temperatures in the THz and sub-THz frequency range. Using not electron, but *plasmon* resonances in semiconductor structures can help to circumvent this severe temperature restriction, due to the classical nature of plasma excitations. Voltage tunable detection of radiation by using plasmon resonances in gated sub-micron field-effect transistors has been proposed in [6,7] and experimentally demonstrated at sub-THz frequencies in [8,9,10,11], see also [12]. It turned however out that using the standard 2D plasmons for detection of radiation imposes another restriction on operating conditions of the devices. Since the 2D plasmons are observable only under the condition $\omega\tau > 1$, where the momentum relaxation time $\tau(T)$ essentially decreases with increasing temperature, the detection of radiation is possible only at sufficiently large frequencies and sufficiently low temperatures. In practice, detection of radiation with the frequency $f = 600$ GHz was possible only at $T = 8$ K [10,11]. Another complication of the 2D plasmon detection scheme consists in the necessity to use transistors with a very short gate length (0.15 μm in [10,11]).

In this Letter we report on the detection of radiation by GaAs/AlGaAs quantum-well devices under the conditions $kT \gg \hbar\omega$ and $\omega\tau \lesssim 1$. The samples had the form of standard Hall-bars with a few pairs of potential contacts, and were placed in a perpendicular magnetic field B. Typical sample dimensions were of the mm scale. Microwave illumination ($20\,\text{GHz} \lesssim f \lesssim 150\,\text{GHz}$) induced a dc voltage between any pair of potential contacts on the same side of the Hall bar (photoresistance oscillations have been observed too [13]). This photovoltage was periodic in B, with the oscillation amplitude and period, proportional to the microwave power and wavelength respectively. The effect can thus be used for detection and spectroscopy of electromagnetic radiation.

The operation of our devices is based on excitation of a special type of plasma waves in the 2DES — *edge magnetoplasmons* (EMP), for a recent review see [14]. EMPs are plasma waves localized near and propagating along the edge of the 2DES in one direction determined by the orientation of the external magnetic field. If the applied magnetic field satisfies the condition $\omega_c\tau > 1$, where ω_c is the cyclotron frequency, they are observable at both large and small values of the parameter $\omega\tau$ [15] (experimental observation of EMPs at $\omega\tau \simeq 10^{-6}$ has been reported in [16]). EMPs can be excited by microwaves in the near-contact regions (see left Inset to Figure 1c) or near any other inhomogeneity of the edge, e.g. near an indentation or a protrusion (right Inset to Figure 1c), where the translational invariance of the straight-line edge is violated: the external ac electric field induces near the contact an oscillating dipole moment which serve as an antenna emiting EMPs. Two or more contacts, separated by the distance L, emit EMPs coherently, which leads to a complicated interference pattern of the EMP-field inside the device. Dependent on the parameter $m = qL/2\pi$, where q is the EMP wavevector, one gets either constructive ($m = integer$, Figure 1a) or destructive ($m = integer + 1/2$, Figure 1b) interference of the EMP field. The EMP-field oscillations are then rectified by a non-linear behavior in the contacts, so that one finally gets a dc voltage between different pairs of contacts, which oscillates as a function of qL. Since for EMPs $q \sim \omega B/n_s$ [15], where n_s is the electron density, this gives B-periodic oscillations of the photovoltage with the period $\Delta B \propto n_s/fL$ (a more accurate analysis of the periodicity of these oscillations was performed in [13]). Figure 1c shows an example of thus calculated magnetic-field dependences of the photovoltage for typical experimental parameters.

Our samples were processed from the same GaAs/AlGaAs heterostructure into Hall-bar geometries with differing width W (0.4 and 0.5 mm) and distance between adjacent potential probes L (1.6, 0.5, 0.4 and 0.2 mm). The electron concentration and mobility (at 4 K) varied from 1.6 to 3.3×10^{11} cm^{-2} and 0.6 to 1.3×10^6 cm^2/Vs, respectively. The sample was placed in an

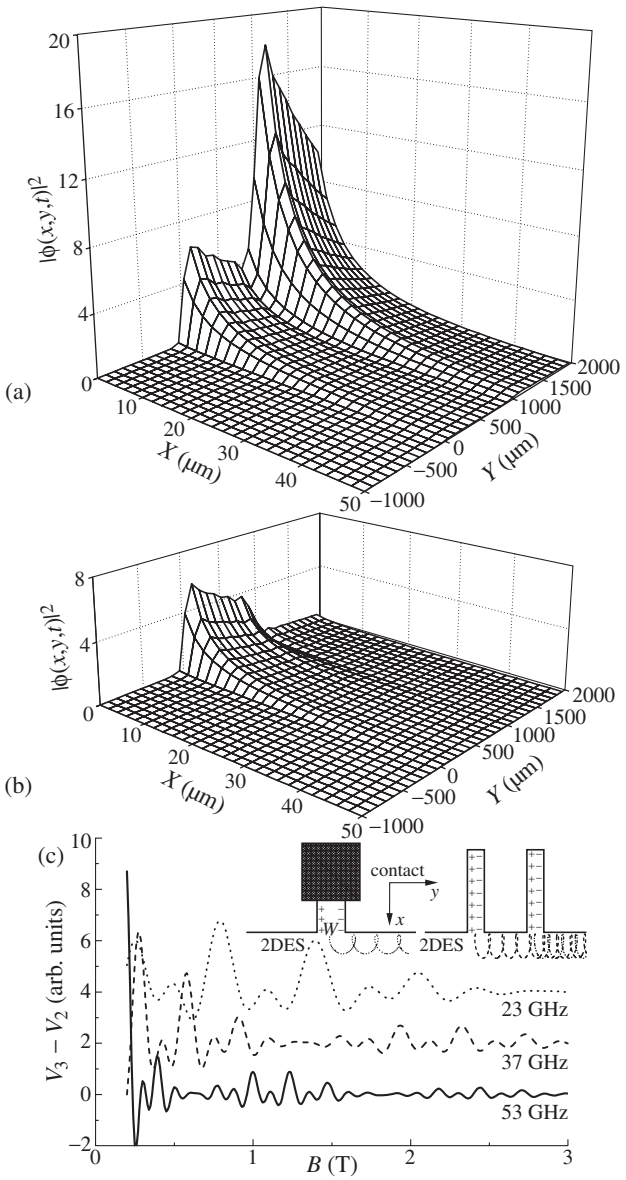

Fig. 1. Examples of calculated constructive (a) and destructive (b) interference of EMPs emitted by a couple of contacts placed at the edge of the 2DES ($x = 0$) at two points separated by 1 mm along the y-axis. The density and mobility of 2D electrons are $n_s = 2.6 \times 10^{11}\,\mathrm{cm}^{-2}$ and $\mu = 3 \times 10^6\,\mathrm{cm}^2/\mathrm{Vs}$; the frequency is $f = 53\,\mathrm{GHz}$. (c) Calculated dc voltage between a pair of potential contacts in a sample with $n_s = 2.5 \times 10^{11}\,\mathrm{cm}^{-2}$, $\mu = 1.6 \times 10^6\,\mathrm{cm}^2/\mathrm{Vs}$, $L = 0.5\,\mathrm{mm}$, and the contact width $w = 0.1\,\mathrm{mm}$. It is assumed that there are three potential contacts along the side of the Hall bar (EMPs propagate in the direction from contact 1 to contact 3), and the voltage $V_3 - V_2$, shown on the plot, develops between the contacts 2 and 3. Insets schematically illustrate the distribution of microwave-induced charges near and emission of EMPs from the contact regions. The curves are vertically shifted for clarity.

oversized 16 mm waveguide at the maximum of the microwave electric field. We used different types of microwave generators which covered frequency range from 12 GHz to 158 GHz with input power of about 1 mW. Further experimental details can be found in [13].

Figure 2 exhibits the magnetic field dependencies of the microwave induced photovoltage measured for different microwave frequencies (40 and 55 GHz) and various tempera-

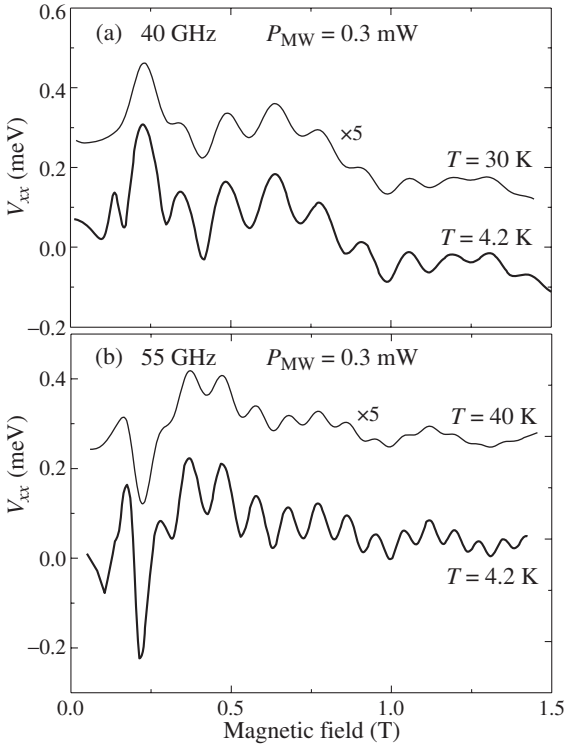

Fig. 2. Magnetic field dependencies of the microwave induced photovoltage measured at (a) $f = 40\,\mathrm{GHz}$ and (b) $f = 55\,\mathrm{GHz}$. The electron density is $2.55 \times 10^{11}\,\mathrm{cm}^{-2}$ and $L = 0.5\,\mathrm{mm}$ for both plots.

tures. The amplitude of the photovoltage oscillations was almost insensitive to the temperature in the range 1 — 20 K. Further increase of T up to 40 K suppresses the oscillation amplitude by a factor of 2 — 7, dependent on ω and dimensions of the device (for smaller device dimensions the oscillations were detectable at $T > 100\,\mathrm{K}$). Figure 3a shows the temperature dependence of the fast-Fourier-transform (FFT) amplitude of photovoltage oscillations, measured for a small-size device ($L = 0.2\,\mathrm{mm}$) at 55 GHz (as $\Delta B \propto 1/f$, FFT directly measures the spectrum of the incident radiation). In Figure 3b we show the FFT spectra of photovoltaic oscillations at irradiation of the device by microwaves with different frequencies. One sees that the FFT-peak positions on the $1/B$ axis are proportional to the radiation frequency (arrows), and that the spectral resolution of our device is about 5 GHz. This is much better than for other semiconductor based spectroscopic techniques (e.g. for InSb Landau level spectroscopy). At frequencies $\sim$ 50–100 GHz the effect was detectable at the input power level $\sim 1\,\mathrm{nW/cm}^2$. In some devices (with several different distances between the contacts) several sub-harmonics were detected in the FFT-spectrum, and it was found that at higher T and f the harmonics with larger period in B become dominant. This fact is related to the reduction of the EMP scattering length and needs further studies.

To summarize, we have discovered a periodic in B microwave ($20\,\mathrm{GHz} \lesssim f \lesssim 150\,\mathrm{GHz}$) photovoltaic effect in GaAs/AlGaAs quantum well devices, which can be used for measuring both the frequency and the intensity of radiation. In order to increase the operating frequency by one order of magnitude, a ten times shorter distance between the contacts is required. As in our devices L was $\sim$ 0.2–0.5 mm, no sibmicron technology is required even at $f \sim 1\,\mathrm{THz}$. It is worth noting that the magnetic field, used to be considered as a drawback

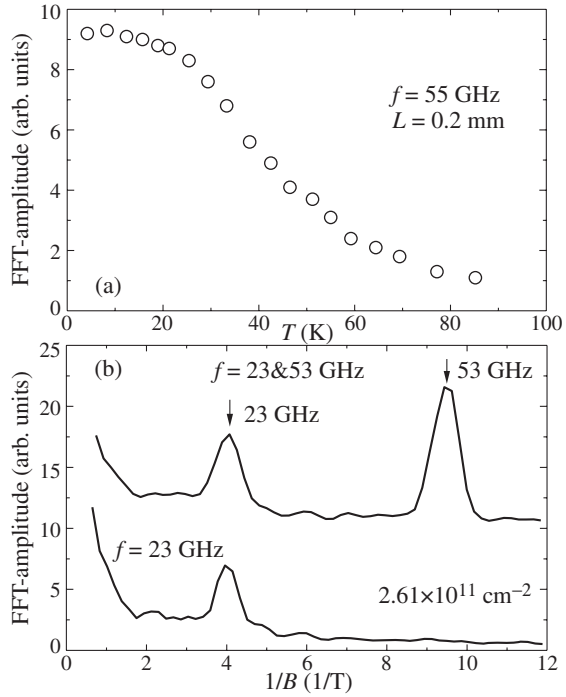

Fig. 3. (a) Temperature dependence of the FFT-amplitude of photovoltage oscillations for a device with $L = 0.2$ mm and $f = 55$ GHz. (b) FFT spectra of photovoltaic oscillations obtained at irradiation of the device by a monochromatic wave with the frequency 23 GHz and by two waves with the frequencies 23 GHz and 53 GHz.

of any detection scheme, serves for creation an interference pattern *inside our small device* and replaces cumbersome and expensive external interferometric systems.

References

[1] T. W. Crow, R. J. Mattauch, R. M. Weikle and U. V. Bhapkar, in *Compound Semiconductor Electronics*, edited by M. Shur (World Scientific, Singapore, (1996).

[2] S. G. Matsik, M. B. M. Rinzan, A. G. U. Perera, H. C. Liu, Z. R. Wasilewski and M. Buchanan, *Appl. Phys. Lett.*, **82**, 139 (2003).

[3] D. G. Esaev, M. B. M. Rinzan, S. G. Matsik, A. G. U. Perera, H. C. Liu, B. N. Zvonkov, V. I. Gavrilenko and A. A. Belyanin, *J. Appl. Phys.*, **95**, 512 (2004).

[4] M. Sherwin, 1999, US Patent 5,914,497.

[5] M. Wraback, P. Shen and M. Dutta, 2002, US Patent 6,476,596.

[6] M. I. Dyakonov and M. Shur, *IEEE Trans. Electron. Dev.*, **43**, 380 (1996).

[7] M. Dyakonov and M. S. Shur, in *Terahertz Sources and Systems*, Vol. 27 of *NATO Science Series II. Mathematics, Physics and Chemistry*, edited by R. E. Miles, P. Harrison and D. Lippens (Kluver, Dordrecht, 2001), pp. 187–207.

[8] J.-Q. Lü and M. S. Shur, *Appl. Phys. Lett.*, **78**, 2587 (2001).

[9] W. Knap, V. Kachorovskii, Y. Deng, S. Rumyantsev, J.-Q. Lü, R. Gaska, M. S. Shur, G. Simin, X. Hu, M. Asif Khan, C. A. Saylor and L. C. Brunel, *J. Appl. Phys.*, **91**, 9346 (2002).

[10] W. Knap, Y. Deng, S. Rumyantsev, J.-Q. Lü, M. S. Shur, C. A. Saylor and L. C. Brunel, *Appl. Phys. Lett.*, **80**, 3433 (2002).

[11] W. Knap, Y. Deng, S. Rumyantsev and M. S. Shur, *Appl. Phys. Lett.*, **81**, 4637 (2002).

[12] X. G. Peralta, S. J. Allen, M. C. Wanke, N. E. Harff, J. A. Simmons, M. P. Lilly, J. L. Reno, P. J. Burke and J. P. Eisenstein, *Appl. Phys. Lett.*, **81**, 1627 (2002).

[13] I. V. Kukushkin, M. Y. Akimov, J. H. Smet, S. A. Mikhailov, K. von Klitzing, I. L. Aleiner and V. I. Falko, *Phys. Rev. Lett.*, **92**, 236803 (2004).

[14] S. A. Mikhailov, in *Edge Excitations of Low-Dimensional Charged Systems*, edited by O. Kirichek (Nova Science Publishers, Inc., NY, 2000), Chap. 1, pp. 1–47.

[15] V. A. Volkov and S. A. Mikhailov, *Zh. Eksp. Teor. Fiz.*, **94**, 217 (1988), [Sov. Phys.-JETP **67**, 1639–1653 (1988)].

[16] P. J. M. Peters, M. J. Lea, A. M. L. Janssen, A. O. Stone, W. P. N. M. Jacobs, P. Fozooni and R. W. van der Heijden, *Phys. Rev. Lett.*, **67**, 2199 (1991).

13th Int. Symp. "Nanostructures: Physics and Technology"
St Petersburg, Russia, June 20–25, 2005

Photoinduced 2D plasmon modes in Cs nanoclusters on the GaAs(100) Ga-rich surface

G. V. Benemanskaya, V. P. Evtikhiev and G. E. Frank-Kamenetskaya
Ioffe Physico-Technical Institute, St Petersburg, Russia

Abstract. A new method of photoyield spectroscopy with polarized light excitation is developed for studies of 2D collective modes. Formation of nanoclusters was studied for the Cs/GaAs(100) Ga-rich interface. Two adsorption phases with strong Cs-Ga bonding and weak Cs-Cs bonding are found. In the first phase, local interaction of Cs adatoms with the Ga dimers occurs. The transition from the first to the second phase is found to take place at ~ 0.7 ML that corresponds to the saturation of all Ga-dangling bonds. In the second phase, collective modes in quasi-2D Cs clusters of several sizes and surface plasmons are revealed.

Introduction

Studies of electronic properties of interfaces involve, on the one hand, detecting local interaction and ascertaining their nature and, on the other hand, searching for the correlation between the nanostructure and electronic characteristics. 2D plasmon modes have attracted great interest due to both fundamental and technological reasons. However, for metal/semiconductor interfaces, no information has yet been reached on the basic questions such as the transition from local bonding to collective interaction in the process of metal overlayer growing, condition of emergence of both surface and interface plasmons. The problem associated with formation of local 2D plasmon modes in metal nanoclasters on semiconductor surfaces has not been resolved as either. As a rule, 2D collective excitations are studied by electfon loss spectroscopy ELS. In the present work, a new method based on photoyield spectroscopy with polarized light excitation has been worked out. The method permits to detect 2D plasmon modes with much improved sensitivity compered to that of ELS.

1. Experimental

The measurements have been performed in situ in a vacuum of $P \sim 5 \times 10^{-11}$ Torr at room temperature. The dimer-reconstructed GaAs(100) Ga-rich surfaces are obtained by thermal removal of thin oxide or As protective layers. A new method based on photoyield spectroscopy (PYS) using *s*- and *p*-polarized excitation is actualized. PYS is grounded on the separation of surface and bulk photoemission due to the key difference in mechanisms of *s*- and *p*-polarized light interaction with surface states. The thresholds $h\nu_S$ and $h\nu_P$ can be different in the case of finite density of surface states in fundamental gap. Information on surface states can be obtained from surface photoemission spectrum $I_P(h\nu)/I_S(h\nu)$. The details concerning PYS can be found elsewhere [1,2,3]. Surface states and 2D plasmon modes are studied as a function of Cs coverage in stepwise or continued (dynamic) conditions of Cs deposition.

2. Results and discussion

The first phase is characterized by a local interaction between Cs adatoms and Ga dangling bonds and occures in the case of stepwise Cs deposition conditions. Two narrow Cs-induced bands are revealed in spectra below the VBM (Fig. 1). The latter indicates both the strong adsorbate-substrate bonding and

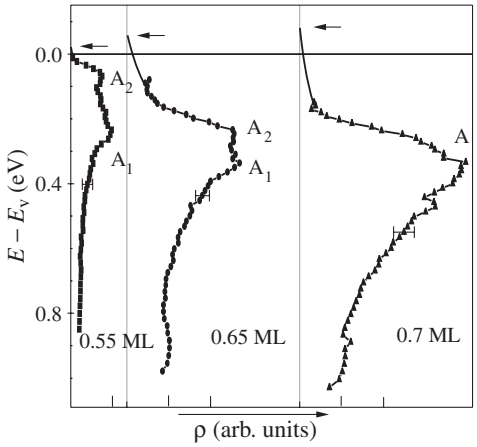

Fig. 1. Spectra of density of surface states induced by Cs adsorption on the GaAs(100) Ga-rich surface. The arrows indicate the edge of Cs-band above VBM. Stepwise depossition condition.

existence of two adsorption sites on Ga-dimers. The first phase is finished at coverage of 0.7 ML when all Ga dangling bonds are saturated.

In the second phase, the predominating process defining the shape of photoemission spectra is found to be the generation of metastable Cs clusters. For coatings in the range 0.7–0.9 ML, the emergence of three photoemission peaks was observed, namely, B, C, and P_1, with energes of approximately 1.9, 2.05, and 2.4 eV, respectively. Figure 2 gives the spectra obtained using the dynamic mode which enables one to produce coatings more than 0.9 ML. In addition to thee peaks, two new singularities, namely, D and P_2 with energies of approximately 2.17 and 2.8 eV, respectively, were observed.

To clarify the origin of plasmon modes, we have analyzed in detail the behavior of peaks in dynamic deposition condition (Fig. 3). Peaks are metastable, since even annealing up to 100 °C results the spectra into the one corresponding to saturation (0.7 ML). Thus, a weak Cs-Cs bonding is characteristic of this phase.

Data show that the A peak emerges in spectra, when two Cs-induced local surface bands A_1 and A_2 become forbidden. We assume that it is due to the formation of a pair of Cs adatoms, i.e. a 2D minimal Cs cluster. The B peak is found to appear for the same coverage in which the A peak disappears. This particular behavior indicates formation of a new 2D clusters of cesium adatoms. Taking into account $(4 \times 2)/c(8 \times 2)$ surface reconstruction with 3 Ga-dimers in unit cell we can assume

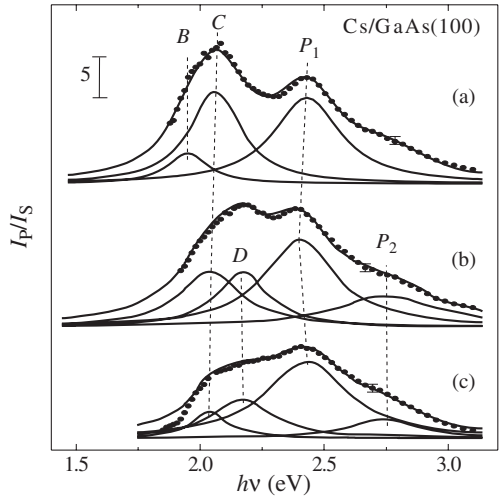

Fig. 2. Spectra of surface photoemission $I_P(h\nu)/I_S(h\nu)$ for different Cs dosages (10^{15} atom/cm^2): a—1.6; b—2.3; c—2.8. Dynamic deposition condition.

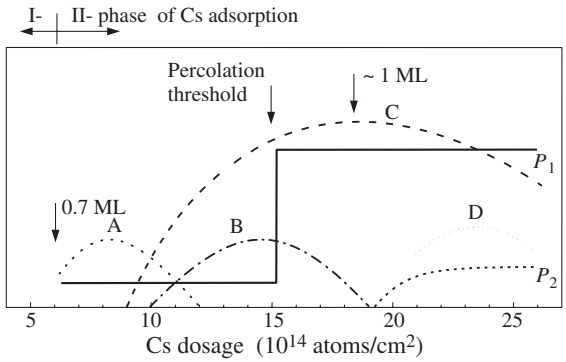

Fig. 3. Schematic diagram of intensity of plasmon peaks as a function of Cs dosage in the II phase of Cs adsorption.

that the peak B is associated with 2D plasmon modes in Cs clusters of 6Cs adatoms. The P_1 peak is characterized by an abrupt rise of intensity during the transition from the stepwise to the dynamic mode. The nature of this peak may be associated with the ecxitation of a surface Cs plasmon. The coating, in the case of which a jumpwise increase in the intensity of this maximum is observed, apparently corresponds to the percolation threshold after which the excitation of a surface plasmon becomes possible. Peak at 2.05 eV(C) reaches the maximum of intensity at the Cs dosage corresponding to a coating close to one monolayer, i.e., to the formation of a solid film of cesium. The intensity of this peak reduces at formation of the second cesium Layer. Therefore, this sigularity can be attributed to the excitation of Cs-GaAs interface plasmon. The P_2 peak appears only in the dynamic mode at the Cs dosage when a monolayer coating has been formed. According to the available literature data, this sigularity can be interpreted as the excitation of a bulk plasmon. Peak at 2.17 eV (D) arising together with the P_2 peak may be associated with the formation of the type of quasi-3D Cs nanoclusters in the second layer.

Acknowledgement

This work was supported by grant 04-02-17621 of Russian Foundation for Basic Research.

References

[1] A. Liebsh, G. V. Benemanskaya, and M. N. Lapushkin, *Surf.Sci.* **302**, 303 (1996).

[2] G. V. Benemanskaya, D. V. Daineka, and G. E. Frank-Kamenetskaya, *JETF.* **92**, 297 (2001), *Surf. Sci.* **529**, 211 (2003).

[3] G. V. Benemanskaya, V. P. Evtikhiev, and G. E. Frank-Kamenetskaya, *Sol. St. Com.* **114**, 285 (2000).

13th Int. Symp. "Nanostructures: Physics and Technology"
St Petersburg, Russia, June 20–25, 2005

Carbon nanotubes as terahertz emitters

O. V. Kibis[1] and M. E. Portnoi[2]

[1] Dept. of Applied and Theoretical Physics, Novosibirsk State Technical University, 630092 Novosibirsk, Russia
[2] School of Physics, University of Exeter, Stocker Road, Exeter EX4 4QL, United Kingdom

Abstract. It is shown that the heating of electrons in carbon nanotubes by an electric field directed along the nanotube axis results in inversion of population for electron bands and, as a consequence, in the emission of electromagnetic waves in the terahertz range by hot electrons. The theory of this effect is developed and the possibility of its application to novel nanoelectronic devices is discussed.

Carbon nanotubes are cylindrical molecules with nanometer diameter and micrometer length [1]. Their unique electronic properties, which promise a broad range of applications, have aroused great excitement in the scientific community in the last decade. Electron states in carbon nanotubes can be labeled by two quantum numbers: integer angular momentum l, enumerating different subbands, and electron wave vector k directed along the nanotube axis. It follows from the equations for the electron dispersion curves [2] that the crossing of energy subbands with angular momenta l differing by one can take place for certain values of k (the scheme of such an energy spectrum is shown in Fig. 1).

As a consequence of this structure of the energy spectrum, the heating of electrons by the electric field should result in emission of electromagnetic waves. Let us consider this effect in detail. The application of a longitudinal electric field (directed along the nanotube axis) results in a change of wave vector k. Since the longitudinal electric field does not mix electron states with different values of angular momentum l, it leads to the electron moving in k-space along the dispersion curve with fixed angular momentum l. This transition from the electron state 1 on the Fermi level to the higher energy state 2 is shown in Fig. 1. Since the electron states with lower energy 3 in the electron subband with angular momentum $l \pm 1$ are unoccupied, the heating of electrons results in inversion of population: coexistence of occupied high-energy electron states 2 in the subband with angular momentum l and unoccupied low-energy states 3 in the subband with angular momentum $l \pm 1$. Selection rules allow optical transitions between these states, and the above-mentioned inversion of population results in photon emission corresponding to electron transitions from the occupied states 2 to the unoccupied states 3 as shown in Fig. 1.

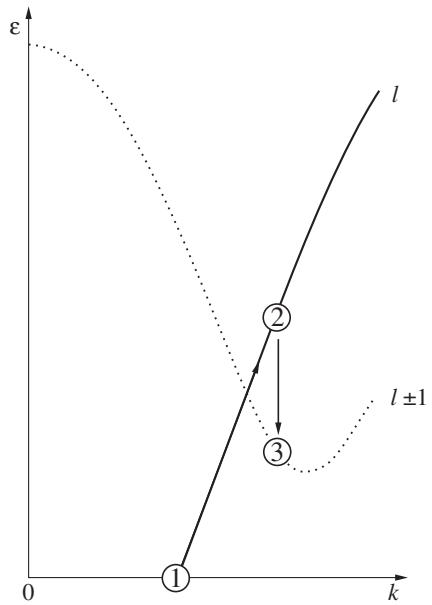

Fig. 1. A fragment of the electron energy spectrum in carbon nanotubes. The Fermi level lies at zero energy.

It is essential that the position of the Fermi level in carbon nanotubes can be changed over a wide range by applying a transverse (gate) electric field in carbon nanotube field effect transistor structures [3] and injecting carriers from appropriately chosen contacts [4]. This allows observation of the discussed effect for experimentally attainable longitudinal electric fields. It should be also noted that the heating of electrons in carbon nanotubes can be done more easily than in usual semiconductor structures, since the electron mean-free path in carbon nanotubes at room temperature for elastic scattering processes is about a micrometer [5,6]. The highest possible energy for hot electrons is restricted by non-elastic optical phonon processes with an energy of about 0.2 eV and so the frequency of the emitted photons lies in the terahertz range. The efficient generation of terahertz radiation is one of most important and challenging problems in modern applied physics [7]. We believe that the discussed effect can be used for the creation of novel terahertz emitters based on carbon nanotubes.

Acknowledgement

This work has been supported by the Royal Society, INTAS, the Russian Foundation for Basic Research and the 'Russian Universities' programme.

References

[1] R. Saito, G. Dresselhaus and M. S. Dresselhaus, *Physical Properties of Carbon Nanotubes*, London: Imperial College Press, 1998.
[2] O. V. Kibis, D. G. W. Parfitt and M. E. Portnoi, *Phys. Rev. B*, **71**, 035411 (2005).
[3] J. Appenzeller, J. Knoch, V. Derycke, R. Martel, S. Wind and Ph. Avouris, *Phys. Rev. Lett.*, **89**, 126801 (2002).
[4] J. A. Misewich, R. Martel, Ph. Avouris, J. C. Tsang, S. Heinze and J. Tersoff, *Science*, **300**, 783 (2003).
[5] J.-Y. Park, S. Rosenblatt, Y. Yaish, V. Sazonova, H. Üstünel, S. Braig, T. A. Arias, P. W. Brower and P. L. McEuen, *Nano Lett.*, **4**, 517 (2004).
[6] A. Javey, J. Guo, M. Paulsson, Q. Wang, D. Mann, M. Lundstrom and H. Dai, *Phys. Rev. Lett.*, **92**, 106804 (2004).
[7] G. Davies and E. Linfield, *Physics World*, **17**(4), 37 (2004).

13th Int. Symp. "Nanostructures: Physics and Technology"
St Petersburg, Russia, June 20–25, 2005

Possible influence of bistable hydrogen defects on FET-leakage in DRAM cells

G. P. Pokhil[1], V. B. Fridman[1], V. P. Popov[2] and N. G. Chechenin[1]

[1] Skobeltsyn Institute of Nuclear Physics, Moscow State University 119899, Moscow, Russian Federation
[2] Insitute of Semiconductor Physics of SD RAS

Abstract. The effect of hydrogen associated defects on FET-leakage in DRAM cells is discussed. The position of hydrogen in the silicon lattice is determined by a new ERD/C technique which is a combination of elastic recoil detection (ERD) and channelling techniques. The charge state of the hydrogen defect is estimated.

1. Introduction

The problem of variable retention time (VRT) in DRAM cells is known since 1987 [1]. It caused by a variation of the DRAM memory cell leakage, which may limit the information retention time. Although the shortest retention times observed are still greater then most of the observed variations in retention time at allowable operating temperature therefore would not result in the memory failure. However, the problem is to be taken seriously in the current miniaturization stage and it grows to become one of the critical points in Gbit DRAM nanoelectronics [2–4]. The retention time can be enhanced by an increase of the storage capacitor height to compensate the loss of cell capacitance caused by the decrease of the cell size. It was concluded [4, 5] that VRT is of a fundamental origin independent of DRAM cell design and process technology of tested devices. Most probable, that defects in critical elements of the DRAM cells are responsible for the VRT, like the trap levels close to the Si midgap and the enhanced electric field in the depletion region, the generation of point defects like silicon interstitial [5]. Here we discuss configuration and properties of hydrogen related defects as a possible reason of the DRAM VRT problem.

2. Experimental

The channeling technique has proven to be important in study of hydrogen site location [6] Our method, which we call ERD/C, is a combination of the elastic recoil detection (ERD) technique and channeling techniques [7]. The idea of the method is illustrated in Fig. 1. The sample is oriented with a low-index crystallographic plane under a small angle θ to the He-ions beam. The He-ions knock out the H-atoms with an energy

$$E_{r,\max} = K E_0 = \left[\frac{4M_1 M_2 \cos^2\theta_2}{(M_1 + M_2)^2}\right] E_0\,, \qquad (1)$$

where K is the kinematical factor, M_1, M_2, are masses of incident ion and recoil nucleus, respectively, θ_2 is the angle between the beam and the detector. Since the He ions is 4 times heavier than the mass of H-atoms, up to 60% of incident particle energy will be taken by outgoing recoil nucleus. To reduce a strong background of elastically scattered He ion, a thin foil was placed in front of the semiconductor detector. The elastic recoil yield was measured as a function of polar angle , shown in Fig. 1, between the incident beam and crystallographic plane. I.e., when $\theta = 0$, then ERD yield will be reduced if hydrogen is located in the plane and enhanced, when hydrogen is located at around the center of the channel. The experimental angular distribution than can be fitted by a computer simulation with a space distribution of the impurity within the crystal lattice cell. This is a background of our ERD/C method. Zc-Si (100) samples were room temperature implanted with the dose of $\sim 10^{17}\,\mathrm{cm}^{-2}$ and the hydrogen ions energy of 67 keV and subsequently annealed at the temperature up to 450 °C. Then the samples were splitted along the implanted layer and the part containing the Si(H) was taken for H-site location by the ERD/C.

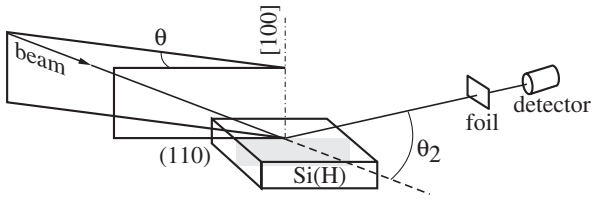

Fig. 1. Illustration of the ERD/C methods.

3. Results

The results of the angular scans around the (100), ($\bar{1}$10) and (110) planes are shown in Fig. 2. The experimental data are compared with the fitted simulated curves. The variable parameter was the position of the impurity atoms within the channel. From the fit the following position of hydrogen was obtained. About 40% of hydrogen occupied position $3d/16$ in the plane (100) and 60% are randomly distributed, where d is the distance between neighboring planes. In the plane ($\bar{1}$10), about 40% are set in the center of the channel, and 60% randomly distributed. And in the plane (110), 85% of hydrogen occupied the position of $11d/32$, and 15% distributed randomly. We note, that there is an asymmetry in the position of hydrogen defects: equivalent planes ($\bar{1}$10) and (110) shows a different angular dependence of recoils yields. That means that defects are not a point type, but extended defects (the point defects can not be oriented). The same indication follows from the observation of different random fraction in these two directions.

If the defects are planar and oriented in the space in one of the (111) planes, then for one direction of (110) type we will see the edge of the plane, but for the other direction we will be looking at the plane itself. Therefore, the influence of the edge of the defect is different. Possible configurations of H-defect, derived from the experimental data are shown in Fig. 3.

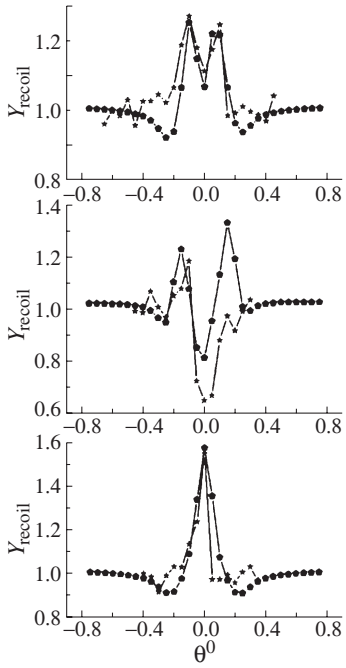

Fig. 2. Comparison of the experimental (squares) and simulated (circles) angular scans around the (100) (a), ($\bar{1}$10) (b) and (110) (c) planes.

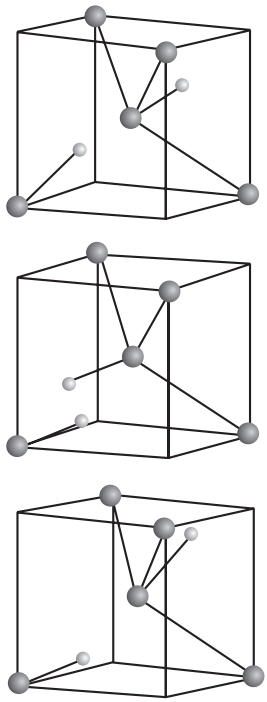

Fig. 3. Possible hydrogen defect configurations, derived from the experimental results. Dark spheres are Si-atoms, white ones are H atoms.

4. Discussion

Hydrogen is known as a highly diffusive and aggressive chemical species, readily attacking Si bonds. It reacts especially with strained bonds in vacancies and those surrounding impurities. The most important properties of the hydrogen defects are their electronic levels. The principal technique used to determine the energy of the deep levels is DLTS. But, as there are always several coexisting hydrogen species, each producing levels in the band gap, the task of assigning levels to specific defects is extremely difficult. This is compounded by the difficulty that DLTS has in identifying the chemical composition and symmetry of the defect. Our ERD/C technique, as demonstrated here, can provide the missing information on the defect configuration. There are known several lattice sites within a diamond lattice which could be occupied by hydrogen impurities [8]. The configuration of the H-defect obtained is in agreement with the known $[H_2^*]_n^2$ and $[2Si\text{-}H]_n$ defects configuration [8–10]. Computer simulations are in progress with variation of the configuration to obtain the metastable energy minimum, as well as charge state of the defect. The charge state of the defects and the DRAM cell leakage in the critical points depend also on the design and operational conditions.

Acknowledgement

The work is supported by Samsung Electronics Co., Ltd.

References

[1] D. S. Yaney *et al*, *IEDM Technical Digest*, pp. 336–338 (1987).
[2] K. Kim, *IEEE Trans. on Semicond. Manufacturing*, v. 15, no. 2 (2002).
[3] J. Lee, D. Ha, K. Kim, *IEEE Trans. Electron. Devices*, v. 48, no. 6, 1152–1158 (2001).
[4] H. S. Kim *et al*, *IEDM Technical Digest*, pp. 411–413 (2003).
[5] P. J. Restle, J. W. Park, B. F. Lloyd, *IEDM Technical Digest*, 807–810 (1992).
[6] B. Bech Nielsen, *Phys. Rev. B*, **37**, 6353 (1988).
[7] A. F. Tulinov, G. P. Pokhil, V. P. Popov, V. S. Kulikauscas, V. B. Fridman, *Surface Investigation*, no. 9, p. 24 (2003) (in Russian).
[8] S. M. Myers *et al*, *Rev. Mod. Phys.*, **64**, 559 (1992).
[9] Y.-S. Kim, K. J. Chang, *Physica B*, 308–310, 143–146 (2001); Y.-S. Kim, K. J. Chang. *Phys. Rev. Let.*, 86, 9, 1773–6 (2001).
[10] S. B. Zhang, W. B. Jackson, *Phys. Rev. B*, vol. 43, 12142 (1986).

13th Int. Symp. "Nanostructures: Physics and Technology"
St Petersburg, Russia, June 20–25, 2005

Terahertz plasmon response of sub-100-nm gate field-effect transistor

V. V. Popov[1], O. V. Polischuk[1], T. V. Pakhomova[1] and M. S. Shur[2]

[1] Institute of Radio Engineering and Electronics (Saratov Division), Russian Academy of Sciences, Saratov 410019, Russia
[2] Department of Electrical, Computer, and System Engineering and RPI/IBM Center for Broadband Data Transfer, CII 9015, Rensselaer Polytechnic Institute, Troy, New York 12180

Abstract. We have solved the problem of diffraction of terahertz (THz) radiation on perfectly conductive gate strip that partially screens a two-dimensional (2D) electron layer located at some distance from the gate. The scattering and absorption spectra of such a structure reveal the fundamental plasma resonance excited under the gate. We have shown that the absorption enhancement factor at plasma resonance may reach very high values (up to 60). However, for narrow gate strips (with the width less than 100 nm) the gated plasmons weakly couple to the THz radiation. We discuss the effects of interaction between plasma oscillations in gated and ungated regions of 2D electron layer.

Introduction

Terahertz response of field-effect transistors (FET) with 2D electron channels is strongly affected by plasma oscillations in the channel. This phenomenon can be used for tunable resonant detection and generation of terahertz (THz) radiation [1–4]. For identical boundary conditions at the source and drain sides of the device channel, the frequencies of plasma oscillations under the FET's gate can be approximately estimated by a simple formula [1]

$$\omega_n = \frac{\pi s}{L_{eff}} n\,, \quad (n = 1, 2, 3\ldots)\,, \quad s = \sqrt{eU_0/m^*}\,, \qquad (1)$$

where s is the plasma wave velocity, L_{eff} is the effective gate length related to the geometrical gate length L by $L_{eff} = L + 2d$ with d being the gate-to-channel distance, e and m^* are the electronic charge and effective mass, respectively, and U_0 is the effective (corrected for the thickness of the 2D electron gas) gate-to-channel voltage swing, which is the difference between the gate voltage U_g and the channel depletion threshold voltage U_{th} : $U_0 = U_g - U_{\text{th}}$. The effective electron sheet density in the channel can be approximately estimated using the parallel plate capacitor model as $N = \varepsilon_0 \varepsilon U_0/ed$, where ε is the dielectric constant of the barrier layer. For typical parameters of InGaAs high-electron-mobility transistor with sub-100-nm gate [4] $L = 60$ nm, $d = 10$ nm, $\varepsilon = 13.88$, $N = 3 \times 10^{12}\,\text{cm}^{-2}$, $m^* = 0.042 m_0$, where m_0 is the free-electron mass, Eq. (1) yields the fundamental plasmon frequency ($n = 1$) about 7.5 THz.

The electrostatic theory of the resonant detection of THz radiation via excitation of plasma oscillations in FET's channel [1–3] yields the responsivity of the detector to plasma oscillations with a given amplitude. However, this theory leaves aside the important question of how effectively those plasma oscillations can be excited by incoming THz radiation. In other words, it is the question by how much the THz radiation power absorbed in the channel at plasma resonance exceeds the non-resonant Drude absorption background (so called the absorption enhancement factor). In this paper we calculate the absorption enhancement factor using the full system of the Maxwell equations and show that this factor may reach 60 at the fundamental plasma resonance. The darkness factor of such resonant detector (the ratio between the absorbed power and scattered power at the plasma resonance) is surprisingly high (up to 10^3).

1. Results and discussion

Let us consider a plane electromagnetic wave incident from vacuum normally onto a FET surface. We assume the gate to be a perfectly conductive infinitely long strip of width L (that is equal to the length of the channel) with zero thickness, which is located at the surface of a substrate (at $y = 0$). The electric field of the incident wave $\mathbf{E_0} \exp(-i\omega t)$ is polarized across the strip (along the x-axis). Two-dimensional electron sheet with homogeneous electron areal density is buried into the substrate at distance d from the surface. We describe the response of the electron channel by the sheet conductivity $\sigma(\omega) = e^2 N\tau/m^*(1 - i\omega\tau)$, where τ is the electron momentum scattering time. Using Ohm's law for the two-dimensional electron channel and the condition $E_x = 0$ for the perfectly conductive gate strip, we reduce the Maxwell equations to the integral equation for sheet current density at the gate. The integral equation is solved numerically by the Galerkin method through its projection on an orthogonal set of the Chebyshev polynomials within the interval $[-L/2;\, L/2]$. As a result, we find the induced electric fields in the ambient medium as

$$\mathbf{E}_a^{(ind)}(x, y) = \mathbf{E}_0^{(r)} \exp(ik_0 y) + \int_{-\infty}^{+\infty} \mathbf{E}_a^{(sc)}(k_x) \exp\left(ik_x x + ik_{y,a} y\right) dk_x \qquad (2)$$

and the total electric field in the substrate below the channel as

$$\mathbf{E}_s(x, y) = \mathbf{E}_0^{(t)} \exp\left[-ik_0\sqrt{\varepsilon_s}(y + d)\right] + \int_{-\infty}^{+\infty} \mathbf{E}_s^{(sc)}(k_x) \exp\left[ik_x x - ik_{y,s}(y + d)\right] dk_x\,, \qquad (3)$$

where $k_{y,a(s)} = \sqrt{k_0^2 \varepsilon_{a(s)} - k_x^2}$, $\varepsilon_{a(s)}$ are the dielectric constants of the ambient medium ($\varepsilon_a = 1$) and substrate, respectively, $k_0 = \omega/c$ with c being the speed of light in vacuum. The integrals in the right sides of Eqs. (2) and (3) describe the scattered fields, while the first summands in Eqs. (2) and (3)

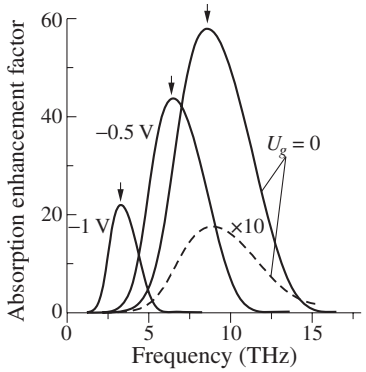

Fig. 1. Absorption enhancement factor vs frequency for different gate-voltage values (corresponding to different sheet electron densities in the channel) for $L = 60\,\text{nm}$, $d/L = 0.5$, $V_{\text{th}} = -1.17\,\text{V}$, $\tau = 7 \times 10^{-12}\,\text{s}$ (solid lines) and $\tau = 2.3 \times 10^{-13}\,\text{s}$ (dashed line). Arrows mark the frequencies of the fundamental ($n = 1$) plasma resonance estimated by Eq. (1).

describe the plane waves normally reflected from the substrate surface and transmitted through the channel, respectively.

In Fig. 1, the absorption enhancement factor is plotted versus the frequency of the incoming THz wave for different gate-voltage values U_g. As seen from Fig. 1, the peak of the resonant absorption can be tuned through the entire THz range by varying the gate voltage. We calculated the electron density in the channel in the parallel plate capacitor model, and we assumed in our theoretical model that the electron sheet density in the ungated regions is equal to that in the gated region of the channel at every given value of U_g. The absorption enhancement factor exhibits very large values (up to 60) at cryogenic temperatures ($\tau = 7 \times 10^{-12}\,\text{s}$), and remains greater than unity even at room temperature ($\tau = 7 \times 10^{-13}\,\text{s}$). The darkness factor of such a resonant absorber is extremely high (up to 10^3) for particular characteristic parameters of the structure chosen for the calculation. Note that the resonance frequency is in excellent agreement with the frequency of the fundamental ($n = 1$) plasma mode estimated by Eq. (1) (marked with arrows in Fig. 1). The peak value of the absorption enhancement factor increases with increasing the resonance frequency because the net dipole moment across the gate strip, which is induced by the incoming THz radiation, also increases with increasing the frequency. However, in the course of that the absorption resonance becomes broader due to the increasing leakage of the gated plasma mode into the ungated regions of the channel.

Fig. 2 shows the in-plane electric field distributions in the 2D electron layer at the fundamental plasma resonance for different electron scattering times. It is seen that, as long as the electron relaxation vanishes, the electric field of plasma oscillations spreads farther into ungated regions of the 2D electron layer. At zero electron relaxation the standing plasma wave is excited in the ungated regions of the 2D electron layer. The double-distance between two adjacent nodes (or antinodes) of this standing wave is exactly equal to the wavelength of the plasmons in the ungated 2D electron layer [5]. This proves that the gated plasmons experience strong leakage into ungated regions of the channel, which provides additional, neither dissipative nor radiative, damping mechanism for the gated plasmons. Inset in Fig. 2 shows the angular patterns of electromagnetic scattering (energy flux scattered from the gate

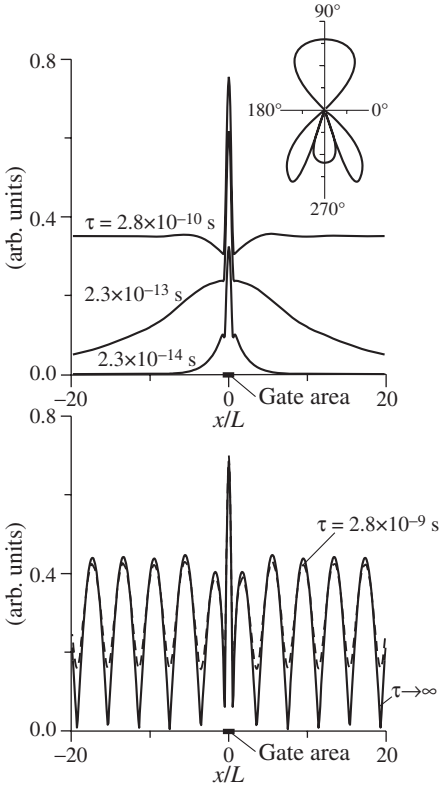

Fig. 2. The electric field distributions in 2D electron layer with 60-nm-wide gate strip for different electron relaxation in the channel. Inset shows the angular patterns of electromagnetic scattering from the structure.

area per unit length of the gate strip at a given angle θ) into the ambient medium ($0 < \theta < 180^\circ$) and into the substrate ($180^\circ < \theta < 360^\circ$) in the far-field zone.

Acknowledgements

This work has been supported by the Russian Foundation for Basic Research through Grant 03-02-17219 and by the Russian Academy of Sciences Program "Novel Materials and Structures". M. S. S. acknowledges support from the U.S. Army Research Office under STTR program (Program Manager Dr. Dwight Woolard).

References

[1] M. Dyakonov and M. Shur, *IEEE Trans. on Electron Devices*, **43**, 380 (1996).
[2] M. S. Shur and J.-Q. Lu, *IEEE Trans. Microwave Theory and Techniques*, **48**, 750 (2002).
[3] W. Knap *et al*, *J. Appl. Phys.*, **91**, 9346 (2002).
[4] W. Knap *et al*, *Appl. Phys. Lett.*, **84**, 1 (2004).
[5] A. V. Chaplik, *Surf. Sci. Rep.*, **5**, 289 (1985).

13th Int. Symp. "Nanostructures: Physics and Technology"
St Petersburg, Russia, June 20–25, 2005

Integration of a resonant tunnelling diode and a semiconductor laser

T. J. Slight[1], C. N. Ironside[1] C. R. Stanley[1] and M. Hopkinson[2]

[1] Department of Electronics and Electrical Engineering, University of Glasgow, United Kingdom
[2] Department of Electronic and Electrical Engineering, University of Sheffield, United Kingdom

Abstract. A resonant tunnelling diode has been monolithically integrated with a multiple quantum well laser. Devices based on a ridge-waveguide structure have been fabricated from a wafer grown by molecular beam epitaxy. Voltage controlled optical switching/bistability has been observed- useful features for a fibre-optic communications laser.

Introduction

The monolithic integration of a resonant tunnelling diode (RTD) with a semiconductor laser may have several advantages over a discrete laser for fibre-optic communications applications. The RTD acts as a voltage controlled switch for the laser, and from PSPICE simulations, voltages as low as 0.1 V have been shown to cause the laser to switch between 'on' (high optical power) and 'off' (low optical power) states. High speed modulation characteristics of the laser may be improved due to the smaller drive voltages required. In addition, RTD's have been shown to have noise suppressing properties [1]. This may lead to an improvement in the electrical/optical noise characteristic of the integrated laser.

1. Device structure

Grave *et al* [2] have demonstrated a similar device in the GaAs/AlGaAs material system and have demonstrated its application as an optical two state memory. The aim of this work is to optimise this type of device for optical communications applications.

A suitable wafer for the device has been grown by molecular beam epitaxy, and consists of a double barrier RTD and a multiple quantum well laser. Devices have been fabricated based on the ridge waveguide laser design shown in Fig. 1. The laser has been designed to emit light at a wavelength of 1.55 μm, the optimum for low losses in optical fibres.

2. Principles of operation

The principles of device operation are as follows: The RTD exhibits negative differential resistance (NDR), i.e. as the RTD voltage rises above a threshold value (V_{peak}) the RTD current drops steeply from its peak value (I_{peak}) to a lower value (I_{valley}), before rising again. By ensuring that the laser threshold current lies between the RTD peak and valley currents ($I_{peak} > I_{\text{th}} > I_{\text{valley}}$), then the optical output of the laser will switch off (on) as the RTD voltage is increased (decreased).

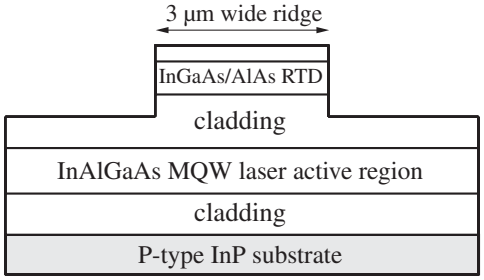

Fig. 1. Device structure.

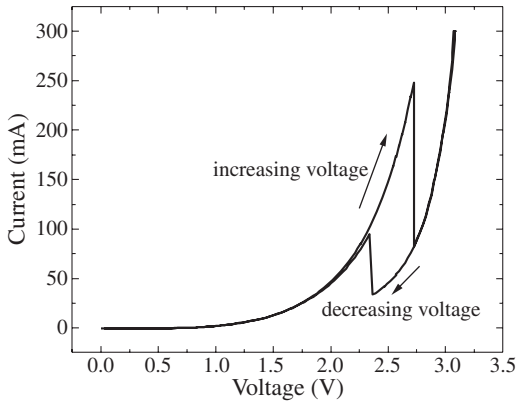

Fig. 2. Current vs voltage.

3. Results and discussion

Figure 2 shows the i-v characteristic of the device. There is a clear hysteresis loop, which is indicative of NDR combined with series resistance. The peak and valley current densities are 2500 A cm^{-2} and 300 A cm^{-2} respectively, giving an RTD current peak to valley ratio of 8.

The device operated as a laser when driven by a pulsed supply, with a threshold current of 30 mA. But when operated under continuous current there was no clear threshold current and therefore showed only LED type emission. In CW operation there was clear evidence of NDR and bistability in the light-voltage curve, with voltages of 0.5 V causing switching between high and low optical power states.

4. Conclusions

We have shown that it is possible to integrate a RTD with MQW laser operating at optical communications wavelengths and have demonstrated negative differential resistance, which combined with series resistance, gives optical bistability. We anticipate this will useful for optical modulation, particularly for example in non return to zero (NRZ) formats. In addition, low drive voltages make the driver circuitry used in conventional optical transmitters unnecessary.

References

[1] V.Ya. Aleshkin, L. Reggiani, N.V. Alkeev, V.E. Lyubchenko, C.N. Ironside, J.M.L. Figueiredo, and C.R. Stanley, *Semicond. Sci. Tech.* **19**, S161-S163 (2004).
[2] I. Grave, S.C. Kan, G. Griffel, S.W. Wu, A. Sa'ar, and A. Yariv, *Appl. Phys. Lett.* **58**, 110-112 (1991).

13th Int. Symp. "Nanostructures: Physics and Technology"
St Petersburg, Russia, June 20–25, 2005

The generation of terahertz electrical pulses in superlattices of self-assembled ErAs-islands

J. H. Smet[1], M. Griebel[1], F. Ospald[1], D. Maryenko[1], D. C. Driscoll[2], C. Kadow[2], A. C. Gossard[2], J. Kuhl[1] and K. von Klitzing[1]

[1] Max-Planck Institut für Festkörperforschung, Stuttgart
[2] Materials Department, University of California Santa Barbara, Santa Barbara

Abstract. In applications as diverse as fiberoptic communications, time-domain- or terahertz-spectroscopy, researchers are keen on ultrafast optoelectronic transducers that can be tailored to the specific needs of each application. The molecular beam epitaxy of photoconductors composed of equidistant layers of self-assembled ErAs-islands, that act as efficient non-radiative carrier capture sites, within a III–V matrix procures this extra flexibility. Here, elaborate photocurrent autocorrelation techniques are applied on metal-semiconductor-metal photodetectors patterned from ErAs:GaAs superlattices. Experiments corroborate that the electrical response speed can be conveniently tuned over at least two orders of magnitude starting from 190 fs by increasing the thickness of the GaAs spacer separating adjacent ErAs layers. These devices have been used for instance to develop techniques for carrying out time-resolved transport with picosecond time resolution on mesoscopic devices, which require a cryogenic environment as well as strong magnetic fields. The same material concept can also be applied to the narrower bandgap InGaAs-matrix. We demonstrate a wavelength insensitive electron lifetime of approximately a picosecond. This brings closer the prospect of implementing terahertz technology at the optical communication wavelengths of 1.3 and 1.55 μm.

13th Int. Symp. "Nanostructures: Physics and Technology"
St Petersburg, Russia, June 20–25, 2005

Plasma waves resonant detection of sub-Terahertz radiation by field effect transistor at 300 K

F. Teppe[1,2], D. Veksler[1], V. Yu. Kachorovskii[1,3], A. P. Dmitriev[1,3], *S. Rumyantsev*[1,3], W. Knap[1,2] and M. S. Shur[1]

[1] Rensselaer Polytechnic Institute, Troy, NY, 12180, USA
[2] GES CNRS-Universite Montpellier2, UMR 5650 34900 Montpellier, France
[3] Ioffe Physico-Technical Institute, St Petersburg, Russia

Abstract. The resonant detection of the 0.6 THz radiation by 250 nm gate length GaAs/AlGaAs heterostructure field effect transistor has been observed at 300 K when the transistor is driven into saturation. In the linear regime, the detection is non-resonant and is several orders of magnitude weaker. Our experimental data clearly show the resonant detection is related to the excitation of the plasma waves in the device channel. The width of the resonant response could be explained assuming that the plasma decay at zero current is limited by the optical phonon scattering.

Introduction

The nonlinear properties of plasma waves propagating in the channel of a field-effect transistor (FET) can be used for the detection of electromagnetic radiation at THz frequencies [1]. A FET subjected to a THz radiation with the frequency ω develops a constant drain-to-source voltage. The key parameter determining the detector behavior is $\omega_0\tau$, where $\omega_0 = \pi s/2L$ is the fundamental plasma frequency [1], τ is the momentum relaxation time, $s = \sqrt{eU_g/m}$ is the plasma wave velocity, U_g is the gate-to-channel voltage and L is the length of the gated region. When $\omega_0\tau \ll 1$, the detector response is a smooth function of ω and of the gate voltage (i.e. FET behaves as a broadband detector.) If $\omega_0\tau \gg 1$, the response is resonant at $\omega \approx \omega_0(1+2N)$, $N = 0, 1, \ldots$. Since s can be tuned by the gate voltage, FET might be used as a resonant tunable detector of THz radiation. Ref. [2] reported on the resonant detection of 0.6 THz radiation in a GaAs/AlGaAs heterostructure field effect transistor at 8 K. More recently, Teppe *et al*. reported on the resonant detection at room temperature when the transistor was driven into the saturation regime [3]. In [3], we showed that the detection line width becomes narrower with an increase of the electron drift velocity. In this paper, we show that the qualitative agreement with the experiment is obtained if we assume that the plasma decay at zero velocity is limited by the optical phonon scattering.

Results and discussions

The experiments [3] were performed on commercial GaAs HEMTs (Fujitsu FHX06X) with the gate length $L = 250$ nm. The current voltage characteristics fitted using the AIM-Spice model [4] are shown in Fig. 1. The photoresponse measurements were performed using 0.2 THz and 0.6 THz Gunn diode sources and a lock-in detection. The maximum output power was 3 mW and 0.3 mW for 0.2 THz and 0.6 THz sources respectively. The radiation beam was not focused and the diameter of the spot was much larger than the gate length of the device.

Only non-resonant detection was found for both 0.2 THz and 0.6 THz sources when transistor was biased in the linear regime. When the drain voltage increased above the saturation voltage, a resonant detection was observed for the 0.6 THz source. Squares in Fig. 1 indicate the drain voltage corresponding to the beginning of the resonant detection for different gate

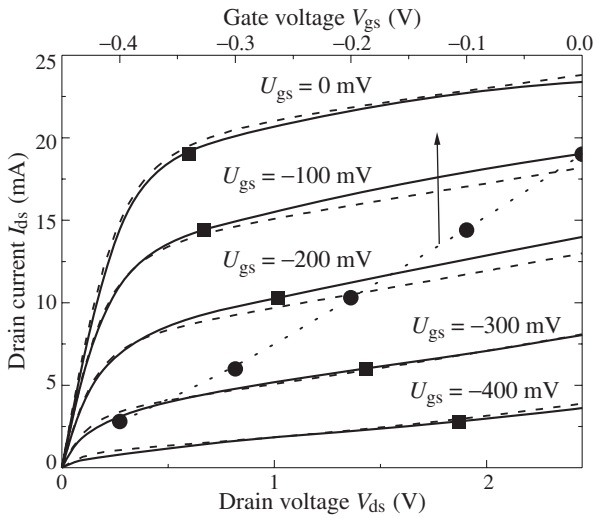

Fig. 1. Experimental (solid lines) and calculated (dashed lines) current-voltage characteristics at room temperature. The AIM-Spice model parameters are: electron mobility $\mu = 1500\,\mathrm{cm^2/Vs}$, saturation velocity 1.4×10^5 m/s, threshold voltage $V_{th} = -0.38$ V, access drain and source resistances $R = 4\Omega$. Squares designate operation points corresponding to the maximum photoresponse at a given gate bias. Circles show the values of the drain current corresponding to the maximum response as a function of the gate bias (shown on the top horizontal scale).

voltages. As seen, the gate voltage corresponding to the maximal photoresponse is practically a linear function of the drain current (circles and dotted line in Fig. 1)[see the discussion in Ref. [3]].

Fig. 2 shows the measured photo-response versus the gate voltage with the drain voltage as a parameter. As mentioned above, only a non-resonant signal was observed at 0.2 GHz, even in the saturation region. For the 0.6 THz source, the increase of the drain voltage first leads to an increase of the non-resonant background signal. With a further increase of the drain voltage, the resonant structure starts to grow.

The generalization of the theory developed in Ref. [1] for the case of nonzero current yields the following equation for detector response [5]:

$$S \sim \frac{1}{(\omega-\omega_0)^2 + \left(\frac{1}{2\tau} - \frac{v_0}{L}\right)^2}, \qquad (1)$$

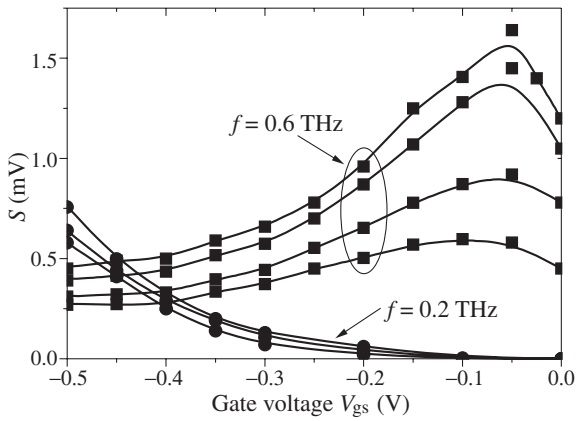

Fig. 2. Induced drain-source voltage as a function of gate bias for different applied drain voltages V_{ds}. Voltage increases from bottom to the top from 250 mV to 1 V.

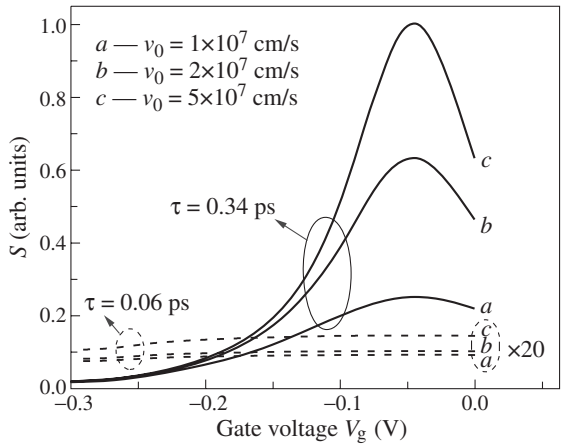

Fig. 3. Results of calculations of the photoconductivity signal using Eq. (1) for $f = 0.6$ THz and $V_{ds} = 0.25$ V. (The response for $\tau = 0.06$ ps is multiplied by a factor 20.)

where v_0 is the electron drift velocity. (Note that the resonance width, $\Delta\omega = 1/2\tau - v_0/L$, coincides with the expression for the decrement of plasma waves derived in Ref. [1]). Therefore, the line shrinks with the increasing electron drift velocity (and, hence, the electron drift velocity). Fig. 3 shows the calculated response using Eq. (1) and accounting for the effect of serial resistance and the electron depletion in the channel caused by drain bias [3]. The calculations are performed for the values of $\tau = 0.06$ ps corresponding to the extracted field effect mobility $\mu = 1500\,\mathrm{cm^2/Vs}$ and $\tau = 0.34$ ps corresponding to the optical phonon scattering. As seen, the value of $\tau = 0.34$ ps leads to a qualitative agreement with experimental data. A deeper understanding of the obtained results requires a theory of plasma waves damping in a short gated channel and a theory of plasma waves in the transistor driven into the saturation regime [6]. In the saturation regime, hot electron effects might play an important role. In particular, transit time effects [7], emission of optical phonons [8], and stratification of electron flow [9] might enhance the resonance diminishing the plasma wave decay.

The experimental results shown in Fig. 2 as well as the theoretical calculations shown at Fig. 3 were obtained while keeping the drain voltage constant. The resonant character of the photoconductive signal can be better seen in the experiments with the constant drain current I_d. The results are shown in Fig. 4. As seen, the position of the peaks shifts to the higher

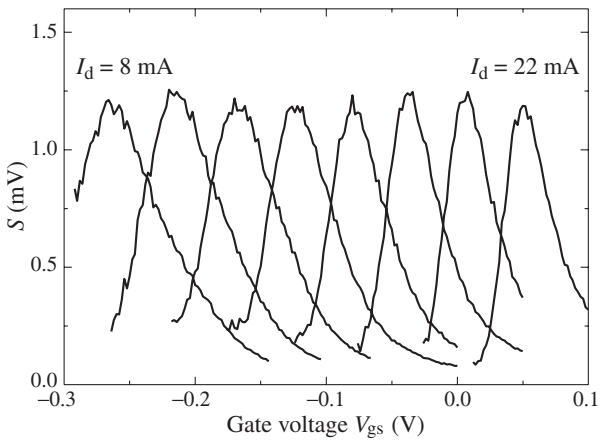

Fig. 4. Photo-response as a function of gate voltage for the drain current from 8 mA up to 22 mA with 2 mA steps.

gate voltages and width of the peaks narrows with drain current increase.

The shift of the gate voltage corresponding to the maximum response can be qualitatively explained by the effect of the series source resistance and by the additional channel depletion by the drain bias.

To conclude, the resonant detection of the sub-THz radiation was observed in conventional GaAs/AlGaAs heterostructure field effect transistor at 300 K. The resonant detection appears at 0.6 THz when the transistors are driven into the saturation region.

Acknowledgements

The work at RPI was supported by the STTR grant by ARO (subcontract from SET, Inc.). The work at Ioffe Institute was supported by RFBR, a grant of the RAS, and a grant of the Russian Scientific School 2192.2003.2.

References

[1] M. Dyakonov and M. S. Shur, *Phys. Rev. Lett.*, **71**, 2465 (1993); *IEEE Trans. on Electron Devices.*, **43**, 380 (1996).
[2] W. Knap, *et al*, *Appl. Phys. Lett.*, **80**, 3433 (2002).
[3] F. Teppe *et al*, submitted to the *Appl. Phys. Lett.*.
[4] T. Fjeldly, T. Ytterdal, and M. S. Shur, Introduction to Device Modeling and Circuit Simulation, John Wiley and Sons, New York, ISBN 0-471-15778-3 (1998).
[5] F. Teppe *et al*, submitted to the *Phys. Rev. B*.
[6] M. Dyakonov and M. S. Shur, *Phys. Rev. B*, **51**, 14341 (1995).
[7] A. Satou, I. Khmyrova, V. Ryzhii and M. S. Shur, *Semicond. Sci. Technol.*, 18, 460, June (2003).
[8] V. L. Kustov, V. I. Ryzhii and Yu. S. Sigov, *Soviet Physics JETP*, **52**, 1207 (1980).
[9] V. Yu. Kachorovskii, I. S. Lyubinskiy, and L. D. Tsendin, *Phys. Rev. B*, **68**, 033308 (2003).

13th Int. Symp. "Nanostructures: Physics and Technology"
St Petersburg, Russia, June 20–25, 2005

Localized surface modes for intersubband coupling

Mathieu Carras[1,2] and Alfredo De Rossi[1]

[1] Thales Research and Technology France Domaine de Corbeville, 91404 Orsay, France
[2] Matériaux et Phénomènes Quantiques, Université Paris 7, 2 Pl. Jussieu, 75252 Paris, France

A metal grating makes it possible to overcome the selection rules of inter-subband absorption by coupling radiations to surface waves. A step forward is to couple this radiation to a chosen surface mode. Detector may benefit from a spatial localization of light to reduce their noise.

We will show here how the use of metal coated gratings can provide the coupling of radiation to localized surface modes.

The localized mode we want to excite on the grating is the analogue of the 1D cavity mode between two Bragg mirrors for plane waves. Here the Bragg mirrors are periodically corrugated metallic surfaces, the cavity is formed by a flat surface between them and the plane wave is replaced by a surface wave.

To study these structure we will calculate the dispersion curves of surface modes on the grating providing the Bragg mirror effect. The calculations are performed using the S-Matrix Method. The designed of surface wave cavity follows on from these calculations.

Then the question of coupling to radiation will be considered with the use of a second grating. The final structure is the sum of to gratings as shown on figure 1.

Finally, calculation of the structure under illumination will be performed using a Finite Difference in Time Domain methods in the total field/scattered field formulation. It shows the amount of coupling and the shape of the coupled mode (figure 2). Those results confirm the accuracy of the S-Matrix approach and correspond to what is expected: a localized mode, exponentially decreasing on each sides of the cavity, is excited by radiation.

Our principle should find effective applications in photodetectors, allowing reduction of electrically active area. More generally, it may concern all the applications where field enhancement is needed (non-linear optics, small-volume probing...). This structure is compatible with a broad variety of materials (polymers, liquid crystals, isolated molecules in free space...) since the field is localized on the surface and not inside the structure, at variance with photonic crystals structures.

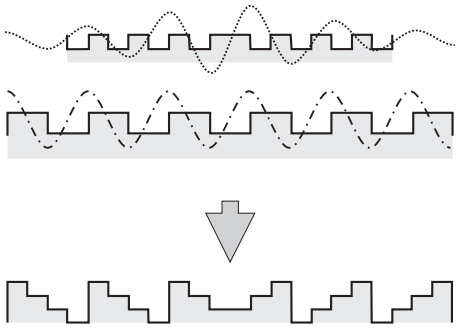

Fig. 1. Design principle of the grating. In gray is the grating profile. The curves show the dependence of the field along the grating.

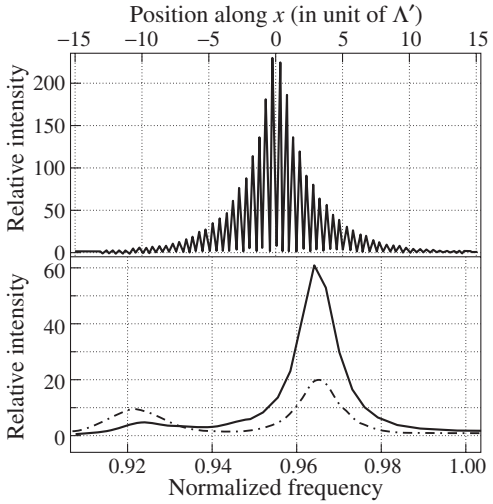

Fig. 2. Field distribution at a given distance of the grating. Spectral integrated intensity on $8\Lambda'$ in the center of the pixel (solid line) and on all the pixel (dashed line).

13th Int. Symp. "Nanostructures: Physics and Technology"
St Petersburg, Russia, June 20–25, 2005

Amplification of terahertz field harmonics due to the dynamic interaction of miniband electrons with high-frequency radiation

N. V. Demarina

Radiophysics Department, Nizhny Novgorod State University, 603950 Nizhny Novgorod, Russia

Abstract. We present a Monte Carlo study of the superlattice amplification property for the third harmonic of terahertz radiation. We simulated the electron motion in a superlattice exposed to a pump field at frequency ω and its third harmonic. We show that interaction of electrons subject to inelastic scattering with terahertz fields causes electron bunching in the k-space. For the amplitude of the pump field exceeding the threshold value the electric field at 3ω is amplified due to the interplay with the electron bunch.

Introduction

A semiconductor superlattice [1] demonstrates plenty of remarkable features caused by miniband electrons performing Bloch oscillations in static and high-frequency fields. In practical terms the property to amplify high-frequency radiation might be the most important one for development of terahertz radiation source based on a superlattice serving as an active medium. The problem of space charge instability suppression emerging in the case of a biased superlattice may be avoided if a superlattice exposed only to a pump field of frequency ω [2]. Since amplification of radiation may be possible at harmonics of the pump field [3] a superlattice placed in to a cavity tuned into nth harmonic becomes an oscillator operating at frequency $n\omega$. The quasistatic case when the frequency of a pump field is much smaller than the inverse intraminiband relaxation time (τ), i.e. $\omega\tau \ll 1$ has been already discussed from both theoretical and experimental points of view [4,5]. In the contribution we extend the previous study to the case $\omega\tau \geq 1$, thus, superlattice electrons interact with an external field dynamically. We restrict our treatment to consideration of the third harmonic. Our three dimensional Monte Carlo study shows that electrons subject to inelastic scattering form bunches in k-space. The field at the third harmonic of a pump field gains energy from the electron bunch if the amplitude of the pump field is larger than the threshold value. The efficiency of the oscillator based on the superlattice coupled to a cavity for the third harmonic reaches 0.7 that considerably larger than that in the case of quasistatic interaction [5].

1. Object of the study and method

We considered a GaAs/AlAs superlattice with the miniband width of 24.4 meV and the period of 6.22 nm. The energy states of an electron in a single miniband was described by the tight-binding dispersion relation for the electron motion along the superlattice axis and, for the motion perpendicular to the axis, by the parabolic dispersion relation. Applying the one-particle Monte Carlo technique [6], we simulated the motion of an electron in the superlattice subject to an electric field applied along the superlattice axis and homogeneous within the superlattice. We treated inelastic electron interplay with optic phonons via Froehlich interaction, and with acoustic phonons via deformation-potential coupling (for details see Ref. [7]). The calculations were performed for a lattice temperature of 300 K.

2. Results

In order to evaluate the intraminiband relaxation time we calculated electron drift velocity in the superlattice in a static field. The drift velocity reaches a peak value ($\upsilon_p = 1.48 \times 10^6$ cm/s) at a critical field ($E_c = 4.8$ kV/cm). The intraminiband electron relaxation time, extracted from the critical electric field by the relation $aqE_c\tau/\hbar = 1$ (q is the elementary charge and $\hbar$ is the reduced Plank's constant), was equal to 220 fs. We studied a superlattice response at the third harmonic of a pump field calculating electron drift velocity, $\upsilon(t)$, in the superlattice exposed to two high-frequency fields $E(t) = E_\omega \cos\omega t + E_{3\omega} \cos 3\omega t$, where $E_{3\omega} = \eta E_\omega$. We treated the frequency of the pump field $\omega/2\pi = 1.4$ THz that corresponds to $\omega\tau = 2$. The drift velocity was expanded in to the Fourier series and had a component at 3ω: $\upsilon_3(t) = \upsilon_{3\omega} \cos 3\omega t + \upsilon_{3\omega} \sin 3\omega t$.

Fig. 1 shows that the power absorbed in the superlattice at the third harmonic, $P_{3\omega} = \upsilon_{3\omega} E_{3\omega}/2$, is positive for a small amplitude of the pump field and negative if $E_{3\omega}$ is larger than some threshold value which depends on η. The latter corresponds to amplification of the field at 3ω. In order to evaluate the maximum quantity of the conversion efficiency from the radiation at ω to 3ω let us consider the superlattice subject to a pump field at ω and coupled to an ideal cavity tuned in to 3ω. Let us briefly describe the process of the stationary state establishment in the cavity for the fixed pump amplitude (for instance, $E_\omega = 8E_c$). The non-linearity of the superlattice velocity-field characteristics causes an electric field at higher harmonics and, particularly, at 3ω as well. The cavity selects the electric field only at the third harmonic and due to this feedback the superlattice becomes exposed to the electric fields at ω and 3ω. Since the amplitude of the pump field is larger than

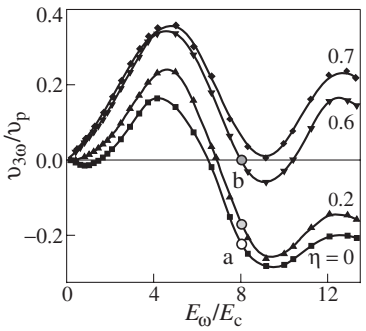

Fig. 1. Relative electron drift velocity amplitude at frequency 3ω versus pump field amplitude in the superlattice placed into an ideal cavity (field in the cavity $E(t) = E_\omega \cos\omega t + \eta E_\omega \cos 3\omega t$).

the threshold value ($6.5E_c$) $\upsilon_{3\omega}$ is negative. Thus, electrons are, on average, decelerated in the electric field at 3ω and the electric field gains energy from the electrons. The amplitude of the electric field at 3ω in the cavity grows that corresponds to the motion of a point in Fig. 1 up from the curve with $\eta = 0$ (point a) to the ones with larger η. The growth stops when the quantity of $\upsilon_{3\omega}$ changes from negative to positive (point b). $\upsilon_{3\omega}$ equal to zero determines the stationary amplitude of the third harmonic in the ideal cavity. Fig. 1 shows that the conversion efficiency with respect to the amplitude ($E_{3\omega}/E_\omega$) for $E_\omega = 8E_c$ is equal to 0.6, while its maximum value reaches 0.7 that is significantly larger in comparison to that in the case $\omega\tau \ll 1$ [5].

The reason of such significant increase in the conversion efficiency lies in the features of the electron interplay with electric fields in a cavity. The period of the pump field, considered in our case, is smaller than the electron relaxation time. Thus, the evolution of electron wave vector z-component is given by $k_z(t) = -(q/\hbar\omega)(E_\omega \sin\omega t + (E_{3\omega}/3)\sin 3\omega t) + k_{0z}$, where k_{0z} is the initial electron wave vector. Electrons in the mini-Brillouin zone follow trajectories distinguishing by k_{0z}, while the dominant scattering with optic or acoustic phonons emission leads to electron hopping from the edge to the center of the zone. At the edge of the mini-Brillouin zone electrons have larger energy and are scattered with the phonon emission more frequently than at the center. Two main electron trajectories in the mini-Brillouin zone, corresponding to $k_{0z} = 0$ and $-\pi/a$, divide plenty of trajectories into two main groups, locating in the vicinity of these two. For a small amplitude of a pump field (Fig. 2, a (upper)) electrons following the trajectory with $k_{0z} = -\pi/a$ spend more time at the edge of the mini-Brillouin zone and, thus, are scattered more frequently than electrons belonging to the trajectory corresponding to $k_{0z} = 0$. Therefore, electron scattering with phonon emission might lead to electron bunching in the vicinity of the favorable trajectory with $k_{0z} = 0$. Increase in E_ω is accompanied by shift of the electron trajectory with $k_{0z} = 0$ apart from the mini-Brillouin zone center and vice versa for $k_{0z} = -\pi/a$.

For $E_\omega > 3E_c$ initially favorable trajectory becomes unfavorable. Accordingly, increase in the amplitude of a pump field beyond the value, mentioned above, is accompanied of electron redistribution between two trajectories. At $E_\omega = 6E_c$ the trajectory with $k_{0z} = -\pi/a$ dominates (Fig. 2, a (middle)). The instantaneous electron distribution function $f(t, k_z)dk_z$ ($f(t, k_z)dk_z$ is the electron concentration at time t at the reciprocal-lattice point k_z within an interval dk_z and integration of $f(t, k_z)$ over the first mini-Brillouin zone yields an electron concentration in a superlattice, n_0) calculated by the Monte Carlo technique (Fig. 2b) indicates the electron bunching in the vicinity of the favorable trajectory. The center of the bunch performs one Bragg reflection within the period of the pump field. Corresponding drift velocity (Fig. 2b (lower)) takes on zero value when the electric field at 3ω reaches minimum or maximum magnitude. In this case the electron ensemble, on average, does not interact with the electric field at 3ω and there is neither amplification nor damping of the third harmonic. The bunch strengthens for the larger pump field amplitude. Thus, more electrons undergo Bragg reflection. The electron drift velocity at 3ω becomes delayed with respect to that in the previous case and the electric field at 3ω is amplified due to the electron bunch deceleration. Vice versa for the small amplitude

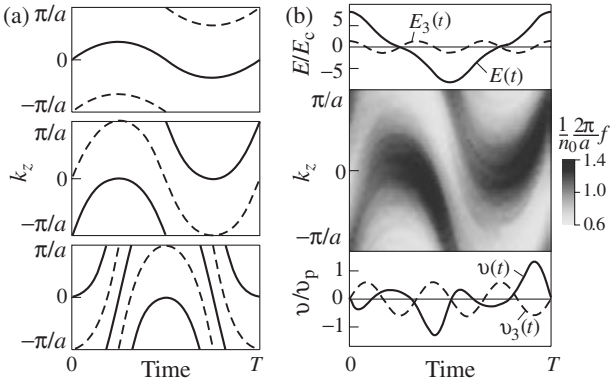

Fig. 2. (a) Favorable (solid) and unfavorable (dashed) electron k space trajectories for $\eta = 0.2$ and $E_\omega = 2.1E_c$ (upper), $6E_c$ (middle), and $12E_c$ (lower); (b) Electron k space bunching; Upper part: overall electric field (solid) incident on the superlattice coupled to the cavity consisted of the pump electric field ($E_\omega = 6.8E_c$) and the electric field at the third harmonic ($E_{3\omega} = 0.2E_\omega$) (dashed); Middle part: temporal evolution of the distribution function $f(t, k_z)$ indicating the electron bunch (dark); Lower part: overall electron drift velocity (solid) in the superlattice and the drift velocity at the third harmonic (dashed).

of the pump field electrons following the favorable trajectory are mainly accelerated by electric field at 3ω causing damping of the third harmonic. If the amplitude of the pump field $E_\omega = 12E_c$ the k space trajectory with $k_{0z} = 0$ grows dominant again (Fig. 2a (lower)). The center of the electron bunch performs Bragg reflection twice within the period of the terahertz field. The switch of the electron bunch from one favorable trajectory to another with increasing pump field amplitude causes the oscillatory behavior of $\upsilon_{3\omega}/\upsilon_p$ curve.

In conclusion, we have analyzed the features of electrons' coherent behavior in a superlattice subject to terahertz fields leading to the terahertz field amplification.

Acknowledgements

I thank K. N. Alekseev, K. F. Renk and Yu. I. Koschurinov for many useful discussions and collaboration. Support by the RFBR (projects 03-02-17088, 05-02-17121) and the Scientific program of the Higher School scientific potential support (project 4629) is acknowledged.

References

[1] L. Esaki, R. Tsu, *IBM J. Res. and Dev.*, **14**, 61 (1970).
[2] K. N. Alekseev, *Conference digest of Internation conference IRMMW* (Karlsruhe, Germany, 2004), 163, (2004).
[3] V. V. Pavlovich, *Sov. Phys. Solid State*, **19**, 54 (1977).
[4] F. Klappenberger and K. F. Renk, *Int. J. Infrared Millimeter Waves* **25**, 429 (2004); F. Klappenberger *et al*, *Appl. Phys. Lett.* **84**, 3924 (2004).
[5] K. N. Alekseev, cond-mat/0503216 (unpublished).
[6] C. Jacoboni *et al*, *Rev. Mod. Phys.*, **55**, 645 (1983).
[7] N. V. Demarina and K. F. Renk, *PRB*, **71**, 035341 (2005).

13th Int. Symp. "Nanostructures: Physics and Technology"
St Petersburg, Russia, June 20–25, 2005

Parametric generation of a mid infrared radiation in semiconductor waveguide with surface metallic diffraction grating

A. A. Dubinov[1], A. A. Afonenko[2] and V. Ya. Aleshkin[1]

[1] Institute for Physics of Microstructures of RAS, 603950 Nizhny Novgorod, Russia
[2] Belarusian State University, 220050 Minsk, Belarus

Abstract. Parametric generation of the difference mode arising by propagation of two near-infrared modes with a wavelength of about 1 μm in a semiconductor waveguide is studied. The waveguide design is proposed in which the difference mode is radiated through a metallic diffraction grating on the waveguide surface. It is shown that the power of the difference mode with a wavelength of about 36 μm generated by 10 W near-infrared modes in a 100 μm-wide 1-mm-long waveguide can be about 1 mW at room temperature.

Introduction

Semiconductor lasers operating in the middle and far-infrared (IR) regions attract considerable interest in view of their high potential for different applications. Cascade medium-IR lasers capable of room-temperature operation have been successfully implemented [1], whereas with far-IR lasers based on cascade structures generation has been achieved only at cryogenic temperatures [2]. However, an extremely complicated band diagram of cascade structures and high requirements for control of parameters restrict their application. Owing to the optical nonlinearity of GaAs there is a possibility for parametric generation of radiation in this range in GaAs based waveguides when two near-infrared modes propagate there. In order to attain effective parametric generation, the phase-matching condition should be satisfied which means that the phase velocities of the polarization wave and propagating mode at the difference frequency must be the same. It was shown that the phase matching condition can be satisfied, if the phase velocity of the nonlinear polarization wave is increased by using transverse modes of a different order for pumping [3], or the difference mode is slowed down by using plasmon waveguide [4, 5] or a metallic grating inculcated in the waveguide [6].

In this study we suggest using a metallic diffraction grating on a waveguide top for effective parametric generation of the difference mode. Effective generation is achieved due to phase matching between one of the spatial modes localized near the grating, and the nonlinear polarization wave at the difference frequency. Phase velocities of the spatial modes are determined by the grating period and therefore can be chosen to satisfy the above phase matching condition. According to our calculations, maximum power is achieved, when the frequency of generated radiation falls into the region of the phonon absorption peak of the waveguide material. In this case the nonlinear susceptibility of semiconductor increases greatly. The results of our calculations indicate that at the near infrared modes generated with a power of 10 W in a 1-μm region, the difference mode can be generated with a power of $\sim$ 1 mW in the range of optical phonon frequency in GaAs ($\lambda \sim 36\,\mu$m) in a 100-μm-wide 1-mm-long waveguide.

1. Calculation of the difference mode power

Let us consider wave propagation in a vacuum — grating — planar semiconductor structure (see Fig. 1). The grating is formed by metallic strips on the surface of the semiconductor. In the case when the semiconductor structure is grown on the (001)-plane substrate and the high-frequency modes have TE polarization and propagate along the [110] direction, the nonlinear polarization in GaAs is normal to the plane of layers and the TM mode is generated at the difference frequency [3]. Further we will be considering only this case. The following symbols are used in Fig. 1: L is the grating period, d and h are the width and height of the metallic strip. Let the Z-axis be directed along the crystallographic direction [001] and the grating strip along the Y-axis (see Fig. 1). For calculation we use the method of series expansion of the eigen modes of a periodic structure over spatial harmonics. We consider the regions of X-coordinate dependent and independent permittivity separately. The TM mode propagating along the X-axis has one magnetic field component directed along the Y-axis.

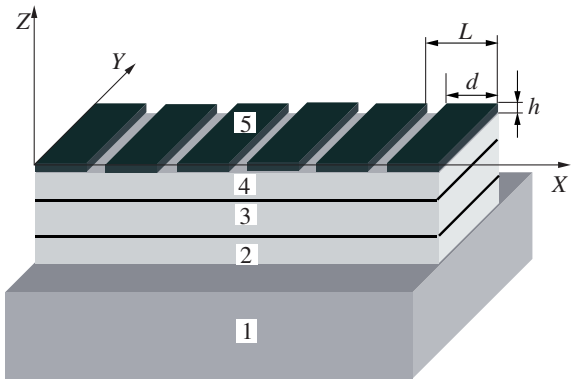

Fig. 1. Scheme of a waveguide for the difference frequency generation, (the layers are numbered in accordance with the table data).

Table 1.

No. of layer	Material	Thickness of the layer (μm)	Type and concentration (cm^{-3})	Mobility ($cm^2/(V\,s)$)
#1	GaAs	—-	n-8×10^{18}	2573
#2	InGaP	0.6	n-4×10^{16}	1947
#3	GaAs	0.5	n-4×10^{16}	5796
#4	InGaP	0.6	p-1×10^{17}	40
#5	Au	0.2	—-	—

The table lists the InGaAs/GaAs/InGaP heterostructure parameters for generation of the difference frequency. Sandwiching a narrow-gap GaAs between wide-gap InGaP emitter layers with a lower refractive index one can form the waveguide for

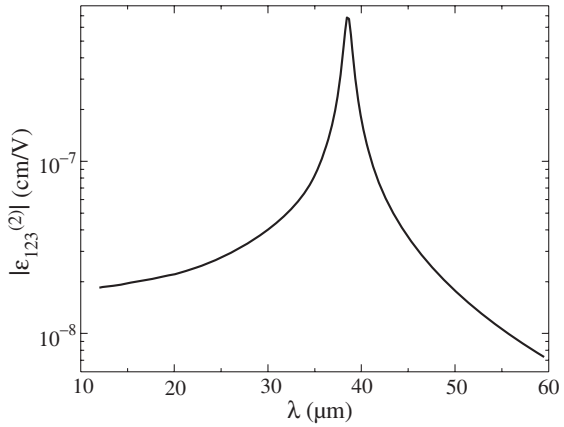

Fig. 2. Dependence of the $\varepsilon_{123}^{(2)}$ component in GaAs on the difference mode wavelength.

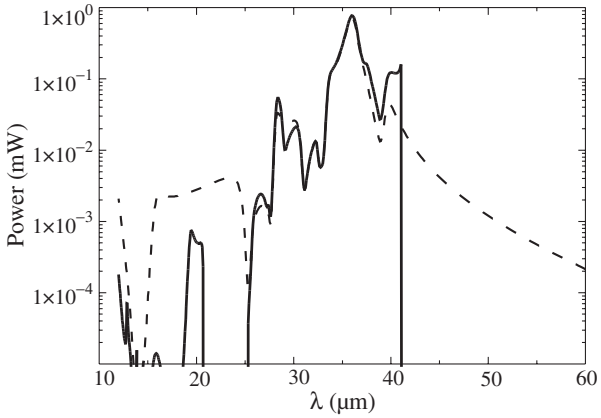

Fig. 3. The difference mode power versus the difference mode wavelength in a waveguide with the following parameters: $L_x = 1\,\text{mm}$, $L_y = 100\,\mu\text{m}$, $d = 0.5625L$. Full curve corresponds to a fixed grating period $L = 8\,\mu\text{m}$, broken curve corresponds to the period equal to the nonlinear polarization wavelength.

near-infrared radiation.

The nature of the second order nonlinear susceptibility of GaAs is anharmonicity of the optical vibrations. Therefore, there is a nonlinear susceptibility resonance when the difference frequency corresponds to the transverse optical phonon frequency. In zinc blend structure semiconductors the nonlinear susceptibility tensor components $\varepsilon_{ijk}^{(2)}$ are not zero, if $i \neq j \neq k$ only. All nonzero components are equal. The dependence of nonlinear susceptibility on frequencies of the waves which are influenced by the medium in semiconductors A_3B_5 was considered in [7]. The nonlinear susceptibility dependence on the difference frequency is shown in Fig. 2. From the figure one can see that there is a maximum of susceptibility near the transverse optical-phonon frequency, and then the susceptibility tends to constant $\varepsilon_{123}^{(2)}$ with a frequency growth. At maximum the value of nonlinear susceptibility is more than 40 times higher than that at high frequencies. Therefore, the output power of the difference frequency wave largely increases near the transverse optical-phonon frequency, in spite of a high absorption in this region.

The calculated difference-mode power is shown in Fig. 3. The longest wavelength for a near-infrared mode is fixed and equals $1\,\mu$m in our calculation. The wavelength of the difference mode is changed by variation of the wavelength of another near-infrared mode. The grating period is $8\,\mu$m. The power peak corresponding to the 1st diffraction order contains local minima near the 28, 32 and $38\,\mu$m wavelength values due to the phonon absorption in InGaP and GaAs. The output power maximum near the phonon resonance is due not only to the maximum of nonlinear susceptibility but also to the difference mode localization in the region of nonlinear interaction. This localization occurs because of the surface plasmon waveguide which is formed on the boundary of heavily and weakly doped semiconductor layers. Due to the abnormal dispersion of the refractive index near the phonon resonance it is possible to satisfy the phase matching condition for the waveguide mode; however, the corresponding power peak is weak due to the high phonon absorption in this region.

The possibility of parametric generation of mid-infrared radiation due to the lattice nonlinearity in GaAs based waveguide has been discussed. To provide effective generation and radiation output a special waveguide design including a metallic grating is proposed. It is shown that under pumping with 10 W near-infrared modes the radiated power is of order of 1 mW at frequencies close to the TO phonon frequency.

Acknowledgements

This work was supported by the RFBR (#04-02-17432); the Program "Low-Dimensional Quantum Structures" of RAS; the RAS Physical Sciences Division "Semiconductor Lasers" Program; the ISTC (#2293) and the Russian Science Support Foundation.

References

[1] F. Capasso *et al*, *IEEE J. Sel. Top. Quantum Electron.*, **5**, 792 (1999).
[2] M. Rochat *et al*, *Appl. Phys. Lett.*, **81**, 1381 (2002).
[3] V. Ya. Aleshkin *et al*, *Semiconductors*, **35**, 1203 (2001).
[4] A. A. Afonenko *et al*, *Semiconductors*, **38**, 239 (2004).
[5] V. Berger and C. Sirtori, *Semicond. Sci. Technol.*, **19**, 964 (2004).
[6] V. Ya. Aleshkin *et al*, *Technical Physics*, **49**, 1486 (2004).
[7] C. Flytzanis, *Phys. Rev. B*, **6**, 1264 (1972).

13th Int. Symp. "Nanostructures: Physics and Technology"
St Petersburg, Russia, June 20–25, 2005

MBE growth and study of Cr^{2+}:ZnSe layers for mid-IR lasers

I. P. Kazakov[1], S. B. Mirov[2], V. V. Fedorov[2], A. Gallian[2], J. Kernal[2], J. Allman[2], A. O. Zabezhaylov[3] and E. M. Dianov[3]

[1] P. N. Lebedev Physical Institute RAS, 119991 Moscow, Russia
[2] Department of Physics, University of Alabama at Birmingham, Birmingham, Alabama 35294, USA
[3] Fiber Optics Research Center at A. M. Prokhorov General Physics Institute RAS, 119991 Moscow, Russia

Abstract. MBE growth and photoluminescence study of thin films and bulk Cr^{2+}:ZnSe are reported. We show that MBE provides optically active chromium in ZnSe and is viable for fabrication of optically and electrically pumped laser structures.

Introduction

One of the best choices for affordable 2–5 μm mid-infrared sources is direct oscillation from divalent transition metal ions (TM^{2+})-doped wide bandgap II-VI semiconductor crystals [1]. Previous fabrication of TM^{2+}: II–VI laser media has focused on bulk crystals through either incorporation of a transition metal in the melt [1] or thermal diffusion on existing crystals [2, 3]. Recently MBE was used to obtain optically active Cr in ZnSe and ZnTe with the goal of developing optically pumped waveguide-confinement structures for reduced laser threshold and increased efficiency as compared to homostructures [4].

MBE grown Cr:ZnSe thin films presented in this work demonstrate the first step of our long-term goal for realizing electrically pumpable transitional metal doped semiconductor lasers by means of interband recombination, leading to intracenter Cr^{2+} excitation and mid-IR emission.

1. Experimental

A series of undoped and Cr-doped ZnSe epilayers were grown in a MBE system with solid sources of elemental Zn and Se on undoped 40 mm diameter semi-insulating GaAs (001) substrates. Cr incorporation was performed from a crucible based effusion cell containing chromium diphenyl benzol tricarbonyl (CDBT). This compound is characterized by a 0.1 torr intrinsic vapor pressure at 180 and 350 °C dissociation temperature. Uncontrolled substrate heating from thermal radiation of molecular sources was resolved using easily sublimating CDBT compounds disintegrated on the surface of the substrate at growth temperature.

The layers of ZnSe buffer (300–700 nm) and Cr:ZnSe (600–1000 nm) were grown at the growth temperature of 310 °C and at the level of beam equivalent pressure (BEP) 1.2×10^{-9}, 5.0×10^{-7}, and 1.1×10^{-6} torr, for CDBT, Zn, and Se, respectively. The growth rate was 0.1 nm/s. During the growth of undoped ZnSe a (2×1) surface-reconstruction was observed, which corresponds to the surface enrichment with Se. After start Cr:ZnSe growth (opened CDBT shutter) the transition $(2 \times 1) \Rightarrow (1 \times 1)$ was observed, which is likely to indicate a sufficiently high concentration of CDBT molecules and products of their dissociation on the substrate.

PL spectra at ${}^5E \rightarrow {}^5T_2$ mid-IR transitions of Cr^{2+} ions were measured using an ARC–300i spectrometer and a PbS detector/lock-in-amplifier combination. We used a CW erbium-doped fiber laser modulated at 800 Hz as an excitation source.

2. Results

Laser mass-spectroscopy analysis of MBE grown Cr:ZnSe thin films showed that the Cr concentration was in the range of $(2–5)\times10^{19}$ cm^{-3}. Incorporation of Cr in the active Cr^{2+} state in epilayers was further verified by optical spectroscopy and direct comparison of the PL spectrum of thin film to that of bulk Cr^{2+}:ZnSe grown for mid-IR laser applications. The film thickness estimated from the oscillation period of transmission spectra was $d \approx 1.45$ μm (Fig. 1).

From the absorption spectrum of the bulk sample, assuming the absorption cross section $\sigma \sim 10^{-18}$ cm^2 the concentration of Cr was estimated to be $\sim 10^{18}$ cm^{-3}. The PL signal was collected in 90° and 0° geometries, corresponding to collection of light in the direction normal and parallel to the film interfaces, respectively. As one can see from Fig. 2, the bulk and thin film PL spectra normalized at 2200 nm (4500 cm^{-1} see Fig. 1(b)) corresponding to the spectral region where luminescence re-absorption starts to be negligible. These spectra are quite similar, indicating that Cr has been successfully incorporated in MBE grown thin films in active Cr^{2+} state. PL spectra

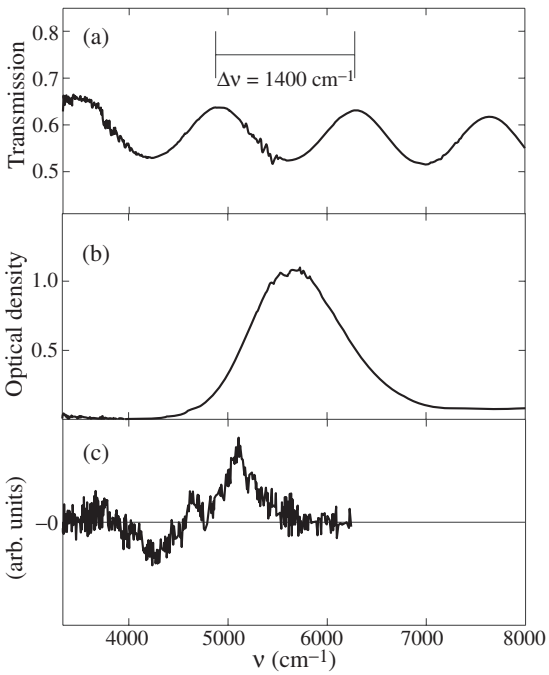

Fig. 1. Transmission spectra of the GaAs/Cr:ZnSe thin film sample (a); optical density of the Cr^{2+}:ZnSe bulk crystal (b) at room temperature; and (c) difference between PL spectra of GaAs/ZnSe:Cr thin films measured in 90° and 0° light collection geometry.

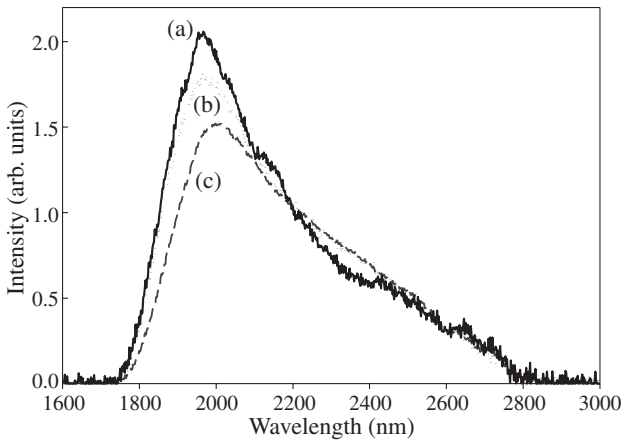

Fig. 2. Room temperature PL spectra of the ${}^5E \rightarrow {}^5T_2$ transition of Cr^{2+} ions in GaAs/Cr:ZnSe thin film: 90° light collection geometry (a); 0° light collection geometry (b); and Cr^{2+}:ZnSe bulk crystal (c).

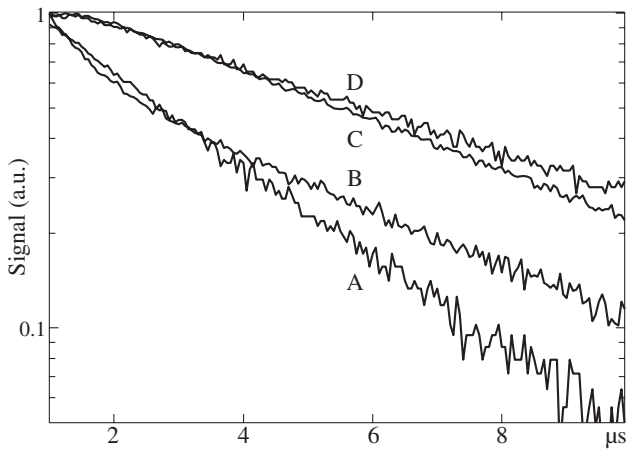

Fig. 3. The decay of the fluorescence signal of Cr^{2+} ions at room temperature in GaAs/Cr:ZnSe thin film sample (A) and Cr^{2+}:ZnSe bulk crystal (D). The low temperature kinetics of GaAs/Cr:ZnSe thin film sample at $T = 23$ K (B) and Cr^{2+}:ZnSe bulk crystal at $T = 20$ K (C).

of the thin film measured in 0° geometry and the bulk sample (see Fig. 2(b) and Fig. 2(c)) are practically identical for the luminescence longer than 2200 nm. At shorter wavelengths from 1800 to 2200 nm thin film demonstrates somewhat more intensive luminescence over the bulk sample, which can be explained by possible re-absorption of luminescence signal in the bulk crystal. The most interesting feature is enhancement of luminescence signal around 2000 nm and its suppression at 2350 nm for the 90° collection geometry with respect to the 0° geometry and the bulk sample. Measurements of PL intensity at 2000 nm versus pump power density showed that the output-input dependence is strictly linear, hence, the stimulated processes could not be responsible for the luminescence line narrowing and PL enhancement at 2000 nm. Our hypothesis is that the observed enhancement and suppression of the luminescence signal in the 90° collection geometry with respect to the 0° geometry and bulk samples are due to enhancement and inhibition of spontaneous emission by the cavity formed by the thin film interfaces. A simple analysis of interference phenomena in a Fabry–Perot cavity of thickness 1.45 μm filled with a dielectric of index of refraction $n = 2.44$ (ZnSe) shows that constructive and destructive interference (4th order) should occur at the wavelengths 2000 and 2350 nm, respectively. It is noteworthy, that thin film in 0° PL collection geometry should not exhibit this phenomenon, since only photons from the edge of the thin film, unperturbed by the cavity are imaged onto the slit of the spectrometer. The phenomenon of enhancement and inhibition of spontaneous emission of a single two level atom residing in a cavity has been well documented in the literature [5]. In our sample, the enhancement occurs near the peak of fluorescence, while the inhibition occurs at a lower point in the fluorescence. This should lead to an overall enhancement of spontaneous emission and corresponding decrease in the PL lifetime.

The PL kinetics depicted in Fig. 3 were measured across a broad temperature range using D_2-Raman-shifted Nd:YAG laser excitation at 1560 nm with 5 ns pulse duration. A liquid-nitrogen cooled InSb detector with a time resolution of 0.5 μs was used in conjunction with a Ge filter to perform non-selective PL measurements over the range 2–5 μm. At room temperature the decay time of the thin film ($\tau = 3.2$ s) was half that of the bulk crystal ($\tau = 6.4$ s). This difference could be explained by the enhancement of the spontaneous emission in the thin film as well as concentration quenching beginning with concentrations larger than 10^{19} cm^{-3} [3]. The decay time of thin film fluorescence increases to $\tau = 5.4$ s with crystal temperature decreasing to $T = 23$ K. The excited-state lifetime of the bulk crystal slightly drops to $\tau = 5.6$ s with temperature decreasing to $T = 20$ K. The changes of the PL lifetime of the bulk crystal can be explained by a lower probability of radiative transitions from the higher-lying components of the excited state sublevels [6].

In conclusion, it is shown that MBE provides optically active Cr in ZnSe and is a viable route for fabrication of future optically and electrically pumped waveguide confinement laser structures, broadly tunable in the mid-IR spectral region.

Acknowledgements

The study was supported by the Russian Foundation for Basic Research, grant 04-02-17262 and NSF grants DMR-0243640, ECS-0140484 and ECS-0424310.

References

[1] L. D. DeLoach *et al*, *IEEE J. Quant. Electron.* **32**, 885 (1996).

[2] S. B. Mirov *et al*, *IEE Proc.: Optoelectron.* **150**, 340 (2003).

[3] J. O. Ndap *et al*, *J. Cryst. Growth* **240**, 176 (2002).

[4] B. L. Vanmil *et al*, *J. Electron. Mater.* **31**, 770 (2002).

[5] E. Yablanovich, *Phys. Rev. Let.* **58**, 2059 (1987).

[6] K. Graham *et al*, *Quant. Electron.* **34**, 8 (2004).

13th Int. Symp. "Nanostructures: Physics and Technology"
St Petersburg, Russia, June 20–25, 2005

New designs and recent experiments on intracavity mode mixing in semiconductor lasers for mid/far-IR generation

V. Ya. Aleshkin[1], A. A. Afonenko[2], A. A. Belyanin[3], A. A. Biryukov[3], A. A. Dubinov[1], V. V. Kocharovsky[3,4], *Vl. V. Kocharovsky*[4], S. V. Morozov[1], S. M. Nekorkin[5], M. O. Scully[3,6], B. N. Zvonkov[5] and N. B. Zvonkov[5]

[1] Institute for Physics of Microstructures RAS, Nizhny Novgorod, Russia
[2] Belorussia State University, Minsk, Belorussia
[3] Institute for Quantum Studies and Department of Physics, Texas A&M University, College Station, USA
[4] Institute of Applied Physics RAS, Nizhny Novgorod, Russia
[5] Research Physical-Technical Institute of the N. Novgorod State University, Nizhny Novgorod, Russia
[6] Department of Chemistry, Princeton University, Princeton, USA

Abstract. The progress in the theory and recent experiments on nonlinear intracavity wave mixing in dual-wavelength injection heterolasers is reviewed, including the use of both resonance electronic nonlinearity of quantum wells and bulk nonlinearity of semiconductor nanostructure. A comparative analysis of the implemented and newly suggested designs for mid/far-infrared lasing of this type is presented and prospects of the difference-, sum- and double-frequency continuous-wave generation at room temperature are discussed.

Recently (see, e.g., [1–16]) we suggest and develop a concept of intracavity nonlinear wave mixing using modes generated in semiconductor injection lasers as an intracavity optical pump for the mixing. This approach utilizes very high second-order nonlinear susceptibilities of III-V semiconductors that cannot be used as passive externally pumped crystals because of the strong absorption of the optical pump and the absence of a convenient phase-matching scheme. A bulk nonlinearity, e.g., in GaAs or GaP, in the mid-infrared range is more than three orders of magnitude larger than in KDP, a typical transparent nonlinear optical crystal. A resonance electronic nonlinearity, e.g., in the step or double quantum-well heterostructures, may be ever higher.

We analyze various types of semiconductor nonlinearities and discuss the most promising schemes of nonlinear-mixing lasers (NML), which may be used for the sum-, double- and difference-frequency generation in a wide infrared range. The intracavity nonlinear mixing has been already demonstrated using quantum cascade lasers as well as butt-joint lasers. These experiments clearly show the promise of intracavity nonlinear mixing in semiconductor injection lasers. Employing intracavity optical pump fields provides the possibility of injection current pumping and removes many problems associated with an external optical pump (beam overlap, drive absorption, spatial inhomogeneity) that were encountered in previous works on nonlinear optics in semiconductors. Moreover, when the optical pump is intracavity generated, the completely resonant nonlinear interaction becomes possible, in which all fields are resonant to corresponding interband or intersubband transitions in coupled quantum wells.

Mid/far-infrared NMLs incorporate three basic ideas:

(a) dual-wavelength generation of two near-infared (in the interband lasers) or mid-infrared (in the quantum cascade lasers) modes;

(b) difference-frequency generation of mid/farinfrared radiation in the 3–200 μm range due to mixing of the above lasing fields in the same laser cavity that provides also wide tunability of the mid/farinfrared signal through small shift of the lasing frequencies;

(c) a phase-matched waveguide design maximizing both the confinement factors and the nonlinear optical overlap of all three interacting field modes.

The interband NMLs are based on the robust and well-established standard diode-laser fabrication technology and expected to have a low threshold current density, which enables stable continuous-wave widely-tunable room-temperature operation. The intersubband NMLs are based on the well-developed and rapidly progressing technology of quantum cascade lasers and also hold promise for wide applications.

The NMLs can be implemented both in the interband lasers (diode-type lasers) and intersubband lasers (quantum cascade lasers). In the present report, we discuss various designs of the former, including

(i) Interband Cascade Lasers (or Tunnel-Junction Lasers) with two vertically stacked active regions and a very thin p/n tunnel junction in between that enables current flow through each of two active regions in series,

(ii) Transistor Lasers with a three-terminal electrical scheme that ensures independent pumping and control of each of two mixing optical (near-infrared) fields,

(iii) Butt-Joint Lasers with two butt-joined laser diodes which are optically coupled but injection pumped separately,

(iv) Surface-Emitting Grating-Outcoupled Lasers with the hybrid-emitting design, where the difference-frequency mid/far-infrared signal is surface-emitted by means of a dielectric or metal grating, while the dual-wavelength near-infrared or mid-infrared lasing proceeds in a standard edge-emitting geometry, e.g., in the abovementioned schemes (i)–(iii),

(v) Vertical-Cavity Surface-Emitting Lasers with double distributed Bragg mirrors, which enable dual-wavelength operation due to presence of two kinds of quantum wells, etc.

For any NML, it is important that difference-frequency generation naturally provides a possibility for relatively wide tunability of the mid/far-infrared signal since even small frequency shift of one lasing field relative to another lasing field

results in a large relative shift of the difference frequency. In particular, it opens prospects for mastering the terahertz frequency range on the basis of a standard heterolaser technology, which guarantees high compactness, reliability, continuous-wave room-temperature operation, and low threshold injection current pumping. We review theoretical and experimental investigations in the field and discuss applications.

References

[1] A. A. Belyanin *et al*, *Phys. Rev. A* **63**, 053803 (2001).
[2] A. A. Belyanin *et al*, *Nanotechnology* **12**, 450 (2001); *Proc. SPIE* **4605**, 363 2001.
[3] V. Ya. Aleshkin *et al*, *Semiconductors* **35**, 1203 (2001).
[4] A. A. Belyanin *et al*, *Izv. Ross. Akad. Nauk, Ser. Fiz.* **66**, 247 (2002).
[5] A. A. Belyanin *et al*, *Phys. Rev. A* **65**, 053824 (2002).
[6] A. A. Belyanin *et al*, *Izv. Ross. Akad. Nauk, Ser. Fiz.* **67**, 262 (2003).
[7] A. A. Belyanin *et al*, *Physics-Uspekhi* **46**, 986 (2003).
[8] M. O. Scully *et al*, U.S. Patent No. US 6,782,020 issued on August 24, 2004.
[9] A. A. Afonenko *et al*, *Semiconductors* **38**, 239 (2004).
[10] N. V. Baidus *et al*, *Semiconductors* **38**, 352 (2004).
[11] Yu. A. Morozov *et al*, *Technical Physics* **49**, 592 (2004).
[12] V. Ya. Aleshkin *et al*, *Technical Physics* **49**, 1486 (2004).
[13] Yu. A. Morozov *et al*, *Semiconductors* **39**, 112 (2005).
[14] V. Ya. Aleshkin *et al*, *Semiconductors* **39**, 138 (2005).
[15] V. Ya. Aleshkin *et al*, *Semiconductors* **39**, 156 (2005).
[16] A. A. Afonenko *et al*, *Semicond. Sci. Technol.* **20**, 357 (2005).

13th Int. Symp. "Nanostructures: Physics and Technology"
St Petersburg, Russia, June 20–25, 2005

Interface-related magneto-photoluminescence on a type II broken-gap single GaInAsSb/InAs heterojunction

K. D. Moiseev[1], V. A. Berezovets[1], M. P. Mikhailova[1], Yu. P. Yakovlev[1], R. V. Parfeniev[1], K. Korolev[2], C. Meinning[2] and B. McCombe[2]

[1] Ioffe Physico-Technical Institute, St Petersburg, Russia
[2] Department of Physics, SUNY at Buffalo NY, USA

Abstract. Magneto-photoluminescence studies have been performed on the type-II broken gap $Ga_{0.94}In_{0.06}As_{0.13}Sb_{0.87}$/InAs single heterostructures with 2D-electon channel at the interface containing two occupied energy subbnads with carrier concentrations of $n_1 = 9.2 \times 10^{11}\,cm^{-2}$ and $n_2 = 4.7 \times 10^{11}\,cm^{-2}$, respectively. Intense mid-infrared photoluminescence spectra exhibited a set of pronounced emission bands in the spectral region 0.3–0.5 eV and it was investigated in magnetic fields up to 10 T.

The type II broken-gap p(n)-GaInAsSb/p-InAs heterojunction is a heterostructure in which two-dimensional electron gas (2DEG) is formed in the potential well on the p-InAs side at the heterointerface [1]. The flexibility of the choice of the structure parameters such as epilayer composition, doping concentration of contacting materials, applying an external bias, etc allows us to obtain a 2DEG with widely varying properties [2]. The magneto-photoluminescence (PL) studies of 2DEG were reported for GaAs/AlGaAs quantum well [3]. We report in this paper the first observation of infrared magneto-PL provided by 2D-electrons localized at the type II broken-gap single heterointerface.

The epitaxial layers of the wide-gap $GaIn_{0.06}As_{0.13}Sb$ solid solutions ($E_G = 0.724$ eV at $T = 7$ K) with a mirror-like surface were obtained lattice-matched to the InAs(100) substrate by LPE. The quaternary solid solution doped with Te was grown on p-InAs substrate heavily compensated with Mn. The single n-$GaIn_{0.06}As_{0.13}Sb$/p-InAs heterostructures demonstrated high value of Hall mobility of $5.0 \times 10^4\,cm^2(Vs)^{-1}$ in low magnetic fields ($B = 0.5$ T) at 77 K. 2D-electron channel with two energy subbands (E_1 and E_2) with a sheet concentration $n_1 = 9.2 \times 10^{11}\,cm^{-2}$ and $n_2 = 4.77 \times 10^{11}\,cm^{-2}$, respectively, computed from Shubnikov-de Haas oscillations in magnetic fields up to 14 T at 1.5 K was found at the heterointerface (Fig. 1). The integer Hall effect plateaux with the filling factor of $\nu = 6$, 4 and 3 were observed in the Hall resistance curve in the range $6\,T < B < 14\,T$. Moreover, no evidence of the holes contribution to the Hall conductivity for the samples was observed in this field range. Then, the 2D-electron channel at the heterointerface has been inserted into p-n junction.

Photoluminescence measurements were performed with a BOMEM DA3.01 Fourier Transform Spectrometer equipped with a CaF_2 beam splitter and a liquid-nitrogen-cooled InSb photovoltaic detector. A fiber-pigtailed laser diode with $\lambda_{th} = 840$ nm and output power up to 1 W was used for photo-excitation of the samples. Magneto PL measurements were made in a superconducting split-coil optical magnet system capable of 10 T. The measurements were carried out in the Faraday configuration, i.e. the magnetic field axis and the direction of the light were parallel to each other and both were parallel to the growth direction of the samples.

The samples under study exhibited intense photoluminescence at 4.2 K in two separate spectral ranges, high-energy (0.55–0.80 eV) and low-energy (0.30–0.45 eV), which can be

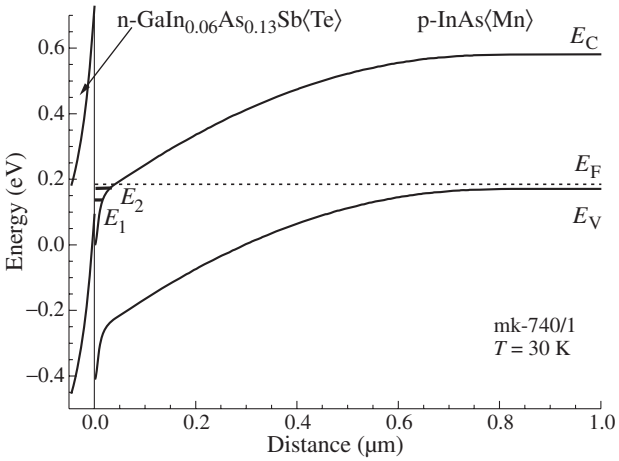

Fig. 1. Schematic energy band diagram of the type II broken-gap n-$GaIn_{0.06}As_{0.13}Sb$/p-InAs heterojunction. The self-consistent potential well on the InAs side at the interface contains two occupied electron subbands.

associated with two different spatial regions of radiative recombination (Fig. 2). The high-energy part of the PL spectrum contains a pronounced emission band with maximum at the photon energy about of $h\nu_{A1} = 0.684$ eV and full width at half maximum (FWHM) of 28 meV. The intensity of this emission

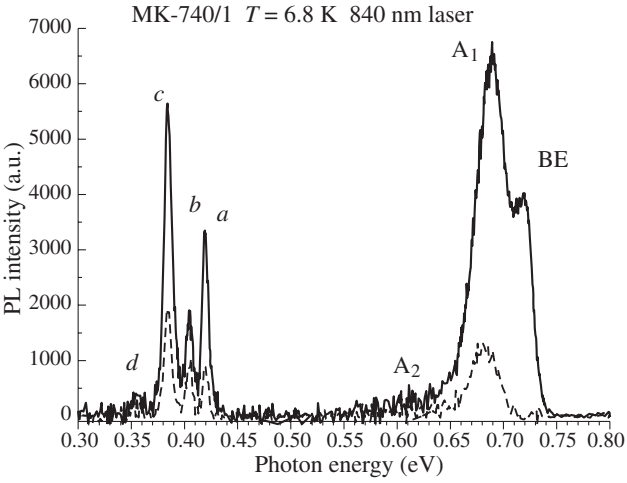

Fig. 2. PL spectra for the type II broken-gap single n-$GaIn_{0.06}As_{0.13}Sb$/p-InAs heterostructure at low and high excitations in zero magnetic fields at 7 K.

band is near linearly dependent on the excitation. A Burstein-Moss shift of the peak towards higher energies by 7 meV was observed with increasing optical pump intensity. The second emission band with photon energy at maximum about of $h\nu_{A2} = 0.615$ eV was weaker and broader than line A_1. At high optical pump intensity the line labeled BE with photon energy at maximum of about $h\nu_{BE} = 0.720$ eV appears as a shoulder on the high-energy edge of the emission band A_1. The energy separations between A_1 and A_2 lines with BE line, associated with the binding energies of $E_{A1} = 36$ meV and $E_{A2} = 105$ meV for the first and the second charge state, respectively, are in good agreement with results reported elsewhere. High-energy emission bands (BE and A_1) demonstrate the features of a typical bulk-related magneto-PL. The small diamagnetic shift for A_1 line towards high energies with the increasing of a magnetic field was estimated to be $\Delta E \sim \alpha B^2$ with the coefficient $\alpha = 0.055$ meV/T. The intensity of the high-energy bands and their shape are almost independent of magnetic field in the range 0–10 T. A slight decreasing in their intensity was observed starting with 4 T.

Intense luminescence was also found in the low-energy range where the PL spectra exhibited three sharp pronounced emission bands labeled a, b and c, respectively. These peaks ($h\nu_a = 0.419$ eV, $h\nu_b = 0.404$ eV and $h\nu_c = 0.384$ eV) reveal high intensity, and are extremely sharp with FWHM of 7 meV. The forth line labeled as d, more weaker, is peaked at 0.355 eV. The narrow emission band can point to strong localization of the carriers involved in the recombination process. The low-energy part of the PL spectra indicates that the radiative recombination occurs near the type II broken-gap n-GaInAsSb/p-InAs heterointerface. An important feature of all low-energy lines is that the spectral position of the emission band maximum remains with the varying of pump intensity. No blue shift of the emission bands with increasing excitation level was found. It means that the electron phase space is not filling

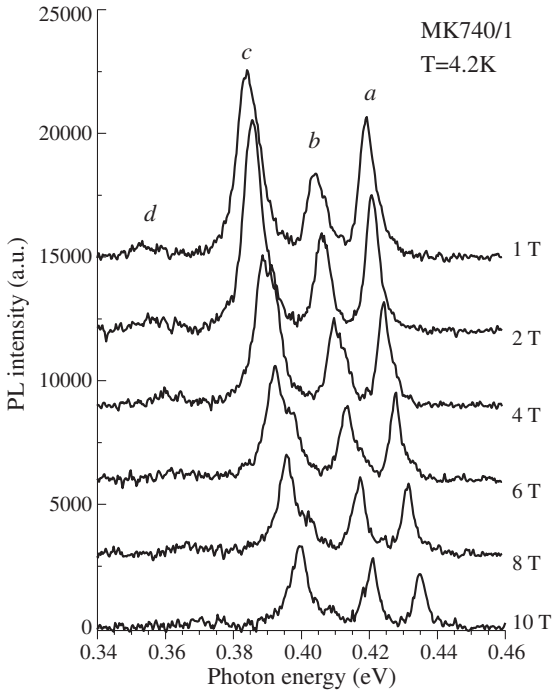

Fig. 3. Low-energy part of PL spectra for the type II broken-gap single n-$GaIn_{0.06}As_{0.13}Sb$/p-InAs heterostructure at different magnetic fields at 4 K.

up to the Fermi energy and the radiative transitions are due to using confined states at the heteroboundary GaInAsSb/InAs. The low-energy lines behave more complicate on a magnetic field: the a, b and c lines, which have Lorentzian-like shape, become narrower and their FWHM decreases from 7 meV to 4 meV, on average (Fig. 3). The result of the deconvolution of the lines by Lorentzian distribution reveals very good matching with experimental curve that allowed us to conclude that in a magnetic filed the radiative transitions occurs through localized states [5].

In low magnetic fields up to 2 T the rise of PL intensity was observed. This rising is accompanied by extreme small shift of PL peaks by < 1 meV towards higher energies with the increasing of magnetic field and the broadening of the lines width in two times. In higher fields ($B > 4$ T) the intensity of the a and c peaks decreases with increasing magnetic field. The transitions associated with $N = 0$ and $N = 1$ becomes resolved starting with 4 T and their FWHM comes back to the value about of 4 meV. It explains the rising of PL intensity in low-field range due to a presence of two close situated emission bands connected with different Landau level numbers. It is obviously that a–c lines manifest a fundamental, interface-related property of the type II GaInAsSb/InAs heteroboundary. It means that for these emission bands we deal with the radiative recombination involving the electrons localized in the quantum well at the GaInAsSb/InAs interface. The n-$GaIn_{0.06}As_{0.13}Sb$/p-InAs heterojunction creates a similar situation of band bending at the heterointerface to that previously reported for InAs/$Al_{0.1}Ga_{0.9}Sb$ single quantum well structure for which far infrared magneto-optic study was carried out. In contrary to the latter the type II broken-gap $Ga_{1-x}In_xAs_ySb_{1-y}$/p-InAs single heterostructure can realize the coexistence of electron-like and hole-like Fermi surfaces. Such samples should demonstrate unusual properties due to mixed character of the InAs conduction band and the GaInAsSb valence band.

Acknowledgements

This work was supported in part by the Program of Physics Science Division, the Russian Foundation for Basic Research project N04-02-17655 and the Center for Advanced Photonic and Electronic Materials at University at Buffalo.

References

[1] K. D. Moiseev, V. A. Berezovets, M. P. Mikhailova, V. I. Nizhankovskii, R. V. Parfeniev, Yu. P. Yakovlev, *Surf. Sci.*, **482**, 1083–1089 (2001).

[2] M. P. Mikhailova, K. D. Moiseev, Yu. P. Yakovlev, *Semicond. Sci. Technol.* **19**, R109–R128 (2004).

[3] R. Stepniewski, M. Potemski, H. Buhmann, D. Toet, J. C. Maan, G. Martinez, W. Knap, A. Raymond, B. Etienne, *Phys. Rev. B*, **50**, 11895 (1994).

[4] K. D. Moiseev, A. Krier, Yu. P. Yakovlev, *Journ. Electron. Mat.*, **33**, 867 (2004).

[5] J. Christen, D. Bimberg, PRB 42, 7213 (1990).

[6] J. Kono, B. D. McCombe, J.-P. Cheng, I. Lo, W. C. Mitchel, C. E. Stutz, PRB 55, 1617 (1997).

13th Int. Symp. "Nanostructures: Physics and Technology"
St Petersburg, Russia, June 20–25, 2005

Transient characteristics of SiGe/Si QW structures at THz lasing

M. S. Kagan[1], I. V. Altukhov[1], E. G. Chirkova[1], S. K. Paprotskiy[1], V. P. Sinis[1], I. N. Yassievich[2] and J. Kolodzey[3]

[1] Institute of Radioengineering and Electronics of RAS, 125009 Moscow K-9, Russia
[2] Ioffe Physico-Technical Institute, St Petersburg, Russia
[3] University of Delaware, Newark, DE 19716, USA

Abstract. Transient characteristics of SiGe-QW laser structures were studied. The excitation of stimulated THz emission is shown to be the result of carrier injection through contacts. The mechanism of intra-center population inversion caused by carrier injection is suggested.

Introduction

Stimulated THz emission has been observed in strained single-QW Si/$Si_{1-x}Ge_x$/Si structures with an optical resonator [1]. The origin of the THz emission was attributed to intra-centre optical transitions between resonant and localized acceptor levels, similar to the lasing of uniaxially strained p-Ge. Two different regimes for excitation of the emission were found to exist in the same sample [2]. In the first case, the onset of lasing is observed at electric fields ≈ 100 V/cm when the current through the substrate is practically absent. The excitation of the emission in this case depends on conditions on both the structure surface and contacts. The second regime exists in the case of thermal ionization of donors in the substrate caused by Joule heating of the SiGe layer. In the present work, the cause and conditions for the emission excitation in the low-current regime were studied.

1. Experiment and discussion

The problem arisen consists in the following. In the case of p-Ge resonant-state laser (RSL), population inversion is realized for the resonant states of shallow acceptors induced by an external stress. Initially, the ground state of an acceptor is frozen at low temperatures and the free hole concentration is very small. Electric field depopulates the acceptor ground state due to impact ionization, while the resonant state acts as a trap for carriers due to a capture-emission exchange with the continuum and is filled to some degree. In the case of our SiGe structures, impact ionization was not observed at electric fields sufficient for lasing because of larger shallow-acceptor binding energy in $Si_{1-x}Ge_x$ alloy (at our values of $x = 0.07$, 0.1 and 0.15) in comparison with that for p-Ge. Calculations showed that this energy is ~ 27 meV [3, 4]. On the other hand, the Fermi level is near QW valence band edge and the free hole concentration at equilibrium conditions is of the order of the acceptor concentration in the QW [5, 6]. That is why the population inversion would be difficult to get even if impact ionization could occur. Nevertheless, the stimulated emission is observed and the question emerges, what is its excitation mechanism.

The p-type single-QW Si/$Si_{1-x}Ge_x$/Si structures MBE grown pseudomorphically on n-type Si substrates were studied. The Ge content in the SiGe alloy was $x = 0.07$, 0.1 and 0.15. The SiGe layer of 13.5 nm thickness was doped with boron in the QW middle with B concentration of 6×10^{11} cm^{-2}.

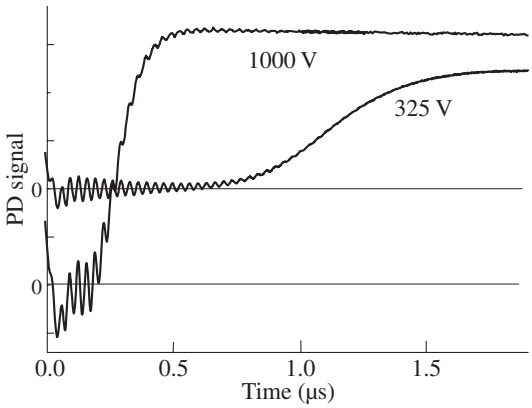

Fig. 1. Time dependence of emission intensity.

It was sandwiched between Si buffer (81 nm wide) and cap (38 nm) layers both doped with one boron d-layers with B concentration of 6×10^{11} cm^{-2}. The δ-layers in the barriers were positioned at the distances of 19 nm from each QW interface. The phosphorus donor concentration in the substrate was $(1 - 5) \times 10^{11}$ cm^{-3}.

The evolution of THz emission and current along the SiGe layer at the starting front of voltage pulse was studied. The time dependence of radiation intensity is shown in Fig. 1. The main features of the time dependences of the sample current and THz emission intensity are: damped oscillations, negative current and a time delay in the emission excitation depending on voltage (Fig. 2), as well as emission quenching at increasing pulse front duration. All these phenomena are attributed to a non-stationary injection of carriers through contacts and explained in terms of excitation of space-charge waves [7]. This is confirmed by current-voltage characteristics of the samples $I \propto U^{3/2}$ typical for the injection currents at acoustical phonon scattering [8], as well as by voltage dependences of oscillation decay time and delay time of the onset of emission. The negative current is explained [9] by sweep-out of carriers in applied electric field. The time for the sweep-out is the transit time L/v (L is the distance between contacts, v is the drift velocity), which in our case is less than dielectric relaxation time; and so the current is determined by diffusion directed opposite to the applied voltage. The damped oscillation of current (and emission) are connected with the drift space-charge waves, that is confirmed by their time-independent period. The decay time of oscillations is determined in this case by a space recharging of acceptor centers [7].

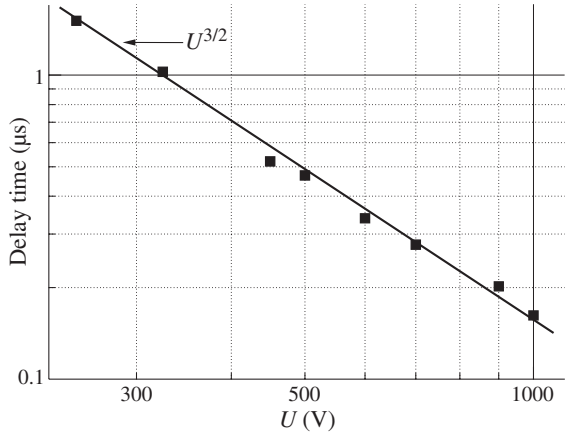

Fig. 2. Voltage dependence of delay time for the onset of stimulated THz emission.

The results obtained show that the excitation of stimulated THz emission is the result of carrier injection through contacts. The mechanism of intra-center population inversion in SiGe/Si structures is supposed to be due acceptor ground state depopulation, which is in this case the result of either sweep-out of majority carriers or minority carrier injection.

Acknowledgements

Authors acknowledge R. A. Suris and B. I. Fouks for valuable discussion. The work was supported by by Russian Foundation for Basic Research (Grants 02-02-16373, 03-02-16419, 04-02-16891, 05-02-17880), RAS Presidium Program "Low-dimensional quantum structures", European Office of Aerospace Research and Development (ISTC grant #2206p), and CRDF (grant #RP2 - 2552-MO-03).

References

[1] M. S. Kagan *et al*, *Radioengineering and Electronics*, **48**, 1137 (2003).
[2] I. V. Altukhov *et al*, *Physica B*, **340–342** (2003).
[3] M. A. Odnoblyudov *et al*, *Phys. Rev. B*, **62**, 2486 (2000).
[4] V. Ya. Aleshkin *et al*, *Phys. Stat. Sol. (c)*, **235**, 687 (2003).
[5] I. V. Altukhov *et al*, *Thin Solid Films*, **380**, 218 (2000).
[6] A. Blom *et al*, *Appl. Phys. Lett.*, **79**, 713 (2001).
[7] R. A. Suris, B. I. Fouks, *Sov. Phys. Semicond*, **14**, 1507 (1980).
[8] M. A. Lampert, P. Mark, *Current Injection in Solids*, Academic Press, NY (1970).
[9] N. G. Zhdanova, M. S. Kagan, R. A. Suris, B. I. Fouks, *Sov. Phys. Semicond.*, **14**, 1518 (1980).

13th Int. Symp. "Nanostructures: Physics and Technology"
St Petersburg, Russia, June 20–25, 2005

Effects of pulsed laser action on Ge/Si quantum dot array to tune homogeneity

A. V. Dvurechenskii[1], A. I. Yakimov[1], V. A. Volodin[1], E. I. Gatskevich[2], M. D. Efremov[1], G. D. Ivlev[2] and A. I. Nikiforov[1]

[1] Institute of Semiconductor Physics, SB RAS, 630090 Novosibirsk, Russia
[2] Institute of Electronic, NASB, 220090, Minsk, Belarus

Abstract. Raman and admittance spectroscopy were used to study effect of nanosecond pulsed ruby laser action on the composition and hole energy spectrum of Ge self-assembled quantum dots coherently embedded in a Si matrix. The inhomogeneity of quantum dot array parameters owing to Ge nanocluster size dispersion inherent in the Stranskii–Krastanov growth was found to be noticeable improved with subsequent laser irradiation from single up to ten pulses action.

Introduction

Epitaxial growth of highly strained semiconductors in the Stranski–Krastanov growth mode enables in situ fabrication of arrays of nanoscale quantum dots (so called self-assembled quantum dots — QDs) [1]. Electronic and optoelectronic nanodevices implemented on self-assembled quantum dots in semiconductor matrix have attracted much attention due to their potential application. The basic technique to grow QDs nanostructure is molecular beam epitaxy, which commonly gives size inhomogeneity of QDs within a 20% range. The self-assembling imply the appearance of nanoclusters (QDs) with preferred characteristics: sizes, shapes, space between nanoclusters, and their mutual arrangement. At present, particular attention is being given to the size distribution in array of QDs, because this parameter is responsible for quantized state energy level dispersion being apparent in optical and electrical properties. The conventional way to tune the parameters of QDs array (size, shape and density) is variation of growth conditions by the alteration of substrate temperature and molecular flux. However, to establish a way to get sufficiently uniform QD sizes still remains a critical issue. This should be solved since well defined sizes with small dispersion are generally required for any unique physical experiments and practical applications.

In this work we present the results of investigation of nanosecond pulsed laser action on Ge/Si quantum dot heterostructures. The idea is to dissolve smaller size Ge nanoclusters in Si matrix by pulsed laser melting of Ge QDs and intermixing with surrounding solid Si. The melting point of Ge (958.5 °C) is rather less than of Si one (1410 °C). So, the short pulsed heating allows melting Ge nanoclusters inside solid Si. Regrowth time following melting is defined by the cooling of Si layer due to heat diffusion into Si substrate. This time is comparable with laser pulse duration in nanosecond scale of laser pulses. So, the smaller Ge QDs may be easier dissolved due to larger interface/volume ratio.

1. Experimental

The samples were grown by molecular beam epitaxy on a (001) oriented 0.005 Ωcm doped with boron up to a concentration of $\sim 10^{19}$ cm^{-3}. The buffer Si layer of p-type with concentration of $\sim 4 \times 10^{16}$ cm^{-3} and thickness of 400 nm was grown firstly. Then Ge QDs layer was formed in Stransky–Krastanov growth mode at 300 °C for three type of samples with different nominal Ge thicknesses of $d = 6$, 8 and 10 monolayers (ML). The cap Si layer was p-type Si of 300 nm thick. Cross-sectional transmission electron microscopy gives the average size of the dot base length 8 nm for $d = 6$ ML, 10 nm for d=8 ML and 15 nm for d=10 ML. The aspect ratio of the pyramidal shape Ge nanoclusters was about 1/10. The areal density of the dots was estimated to be about 3×10^{11} cm^{-2} and the dot uniformity approximately ±17%. A 80 ns pulse ruby laser (fundamental wavelength $\lambda = 694$ nm) with optical system formed the light beam of 4.5 mm in diameter and inhomogeneity not worse than ±5% [2]. The energy density was taken as a threshold for Si surface melting inducing in our experiments near 1 J/cm^2. Laser beam energy reproduced with an accuracy better than ±2%. A pyrometer sensor detected thermal radiation from the central part of the laser-heated area to measure the brightness temperature on Si surface. The time-resolved reflectivity detected in pump-and-probe experiments with probe laser beams of $\lambda = 530$ and 1060 nm. The samples irradiated with both single and ten pulses of laser beam.

2. Results

Raman spectroscopy. The elemental composition and elastic strains in Ge QDs heterostructures were analyzed by measuring the Ge-Ge and Ge-Si Raman peak intensities, full width at half maximum (FWHM) and peak position before and after pulsed laser action [3]. The elemental composition of virgin Ge_xSi_{1-x} QDs in Si is described by x in the range from 0.70 ($d = 6$ ML) to 0.77 ($d = 10$ ML), being an evidence for formation of practically pure Ge nanoclusters in Si matrix with Ge-Si bonds on interface. Pulsed laser action leads to x decreasing which is more pronounced for samples with $d = 6$ ML and resulting in Ge-Si intermixing. Further x decreasing takes place with increasing of pulsed irradiation up to ten actions. Laser action was found to reduce FWHM of Ge-Ge peak by a factor 1.5 and increasing intensity of Ge-Si peak (Fig. 1). These results are the indication of reducing of QDs size dispersion, improving of homogeneity of elemental composition and elastic strains in QDs. The conventional long term annealing does not lead to similar effect.

Admittance spectroscopy. For Ge/Si(001) type-II QDs heterostructures the localization inside the dot occurs only for hole, whereas the dot forms a potential barrier for electron. The hole energy spectrum was evaluated from the data of admittance spectroscopy in virgin and laser annealed samples. A Ti contact with an area 4.4×10^{-3} cm^2 was deposited on top

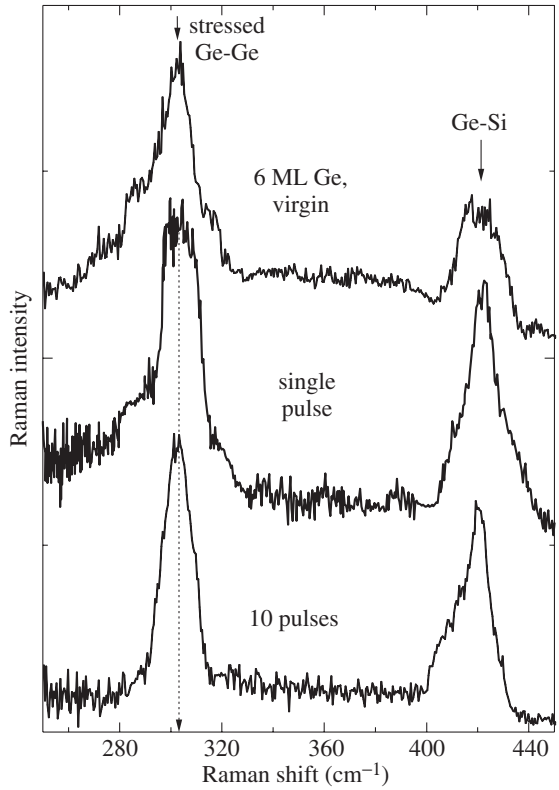

Fig. 1. Raman spectra of Ge QDs structure with $d = 6$ ML before and after laser annealing.

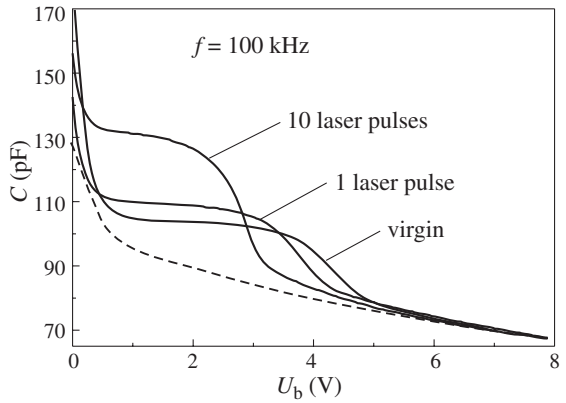

Fig. 2. Capacitance-voltage characteristics of reverse biased Ge QDs structure with $d = 6$ ML of Ge coverage before and after laser annealing.

of the samples to form Schottky barrier. The measurements of complex conductance was made with Fluke PM6306 RCL Meter in the frequency range 10–700 kHz and the temperature range 100–300 K. The modulation amplitude of reverse biased Schottky diode was 25 mV. To simplify experimental data interpretation the samples with Ge nominal thickness of $d = 6$ ML were taken for measurements. For that case small size quantum dot forms just single (ground) hole confined local state. $C-V$ characteristics have shown that pulsed laser annealing results in decreasing of QDs density (Fig. 2). An alternative explanation is the hole energy level in the dots tends to become more shallow after laser annealing. But the temperature dependence of the hole emission rate demonstrates the deepening of hole energy level after laser irradiation (Fig. 3). The activation energy

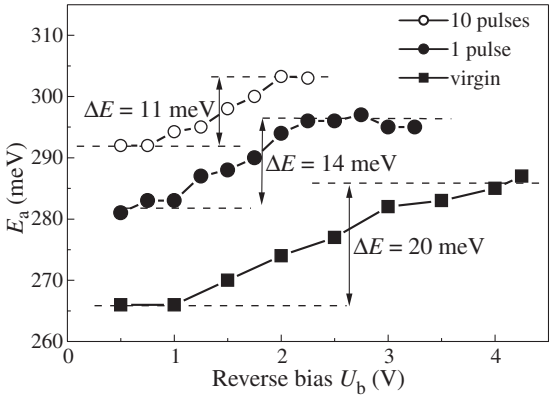

Fig. 3. Activation energy of hole emission rate from the Ge QDs into the Si valence band versus reverse bias for the sample with $d = 6$ ML.

hole emission rate vs the reverse bias contains the information on the hole energy dispersion due to QDs inhomogeneity in size. We have found that laser annealing reduces the hole energy dispersion by a factor 2. This conclusion is in agreement with the Raman results on improving the homogeneity of the QDs size distribution.

Acknowledgements

This work has been supported in part by INTAS (01-0615), RFBR (Nos. 05-02-16285, 03-02-16526), and the Integration Project between Siberian Branch of the Russian Academy of Sciences and the Belarus National Academy of Sciences (No. 186). A. I. Y. acknowledges financial support from the Program of the President of Russian Federation for support of young Russian doctors of sciences (Grant MD-28.2003.02).

References

[1] A. I. Nikiforov, V. A. Cherepanov, O. P. Pchelyakov, A. V. Dvurechenskii, A. I. Yakimov, *Thin Solid Films*, **380**, 158 (2000).
[2] G. D. Ivlev, E. I. Gatskevich, *Appl.Surf. Sci.*, **143**, 265 (1999).
[3] V. A. Volodin, E. I. Gatskevich, A. V. Dvurechenskii, M. D. Efremov, G. D. Ivlev, A. I. Nikiforov, D. A. Orehov, A. I. Yakimov, *Semiconductors*, **37**, 265 (2003).

13th Int. Symp. "Nanostructures: Physics and Technology"
St Petersburg, Russia, June 20–25, 2005

Differential shallow impurity absorption in Ge/GeSi QW heterostructures in THz range at pulsed bandgap photoexcitation

A. V. Ikonnikov[1], K. E. Spirin[1], O. A. Kuznetsov[2], V. Ya. Aleshkin[1] and V. I. Gavrilenko[1]

[1] Institute for Physics of Microstructures RAS, GSP-105, N. Novgorod, 603095, Russia
[2] Physico-Technical Research Institute of N. Novgorog State University

Abstract. Differential magnetoabsorption spectra in THz range in strained MQW p-Ge/GeSi heterostructures with residual impurities have been studied at pulsed bandgap photoexcitation at $T = 4.2$ K. The signal relaxation is shown to have two characteristic times. The "fast" time (one to several tens μs) corresponds to the free carrier recombination with those bound at shallow impurities. The "slow" one (hundreds μs to several ms) conforms to free hole recombination at neutral donors, the holes being thermally activated from very shallow acceptors in the heterostructures (with binding energy about 2 meV).

Introduction

In strained Ge/GeSi quantum well (QW) heterostructures the valence band is split thus resulting in the decrease of hole effective masses and shallow acceptors binding energies [1–5]. Earlier we demonstrated a novel differential technique to study the impurity magnetoabsorption in THz range by means of the bandgap photoexcitation [6–7]. The modulation of impurity absorption results from the capture of free carriers by ionized impurities that also leads to a significant narrowing of the absorption lines due to a decrease of the potential fluctuations. Owing to this we observed transitions resulted from excitations of very shallow acceptors (A^+-centers, neutral A^0-centers with spatial separation of the impurity ion and the hole with binding energies about 2 meV) not resolved by far IR impurity photoconductivity technique [1–4]. This paper deals with impurity magnetoabsorption study at the pulsed optical bandgap excitation at $T = 4.2$ K that allows to determine characteristic relaxation times of the absorption and to reveal the main regularities of the kinetics of both the free and the bound charge carries.

1. Experimental

The $Ge/Ge_{1-x}Si_x$ heterostructures under study were grown by CVD technique on low-doped Ge(111) substrates. The structures consist of 162 Ge layers (QWs for holes) separated by $Ge_{1-x}Si_x$ layers. The parameters are given in the captions to Fig. 1, 3, 4. Due to the elastic stress relaxation at the heterostructure-substrate interface the Ge layers were biaxially compressed (the elastic deformation ϵ_{xx} being measured by X-ray diffraction) whereas CeSi layers were biaxially stretched.The structures were not intentionally doped; the concentration of residual acceptors was about 10^{14} cm^{-3} [1]. Ionized impurities arise due to partial acceptor compensation by donors (cf. [1]). Experimental setup has been described in Ref. [6, 7]. Free carriers were generated by GaAs LED ($\lambda \approx 0.9\,\mu$m) feeded by current pulses. The pulsed signal of the trasmitted through the sample THz radiation as a function of the magnetic field was recorded using a TDS3034B "Tektronix" multichannel digital oscillograph.

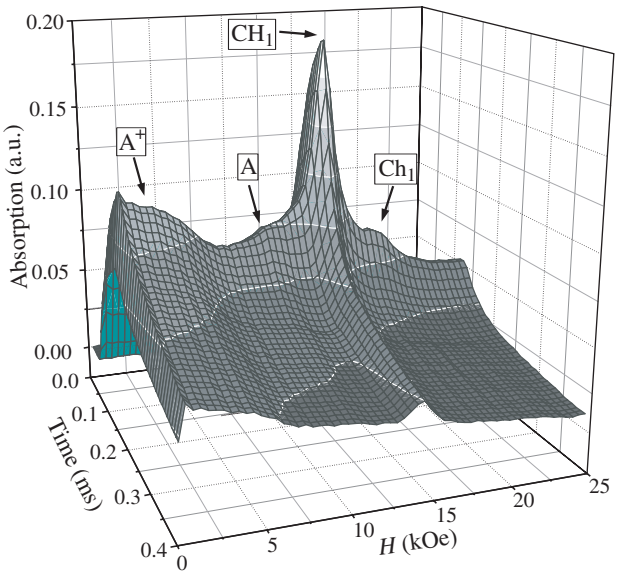

Fig. 1. 3D plot of magnetoabsorption in the sample 306a ($x = 0.12$, $d_{\mathrm{Ge}} = 200$ Å, $d_{\mathrm{GeSi}} = 260$ Å, $\epsilon_{xx} = 2.2 \cdot 10^{-3}$) at pulsed bandgap photoexcitation versus the delay time and the magnetic field ($\tau_{pulse} = 100\mu$s, repetition rate 1 kHz), $\hbar\omega = 2.53$ meV.

2. Results and discussion

A typical plot of the differential magnetoabsorption in the sample 306a is presented in Fig. 1. One can see cyclotron resonance (CR) lines of free holes in QWs (CH_1 and Ch_1) and absorption lines resulted from $1s \to 2p^+$ transitions of a neutral acceptor located at the center of the GeSi barrier (A) and from the photoionization of A^+-centers in Ge QWs (A^+) [7]. It is clearly seen that the relaxation of hole CR line CH_1 is much faster that of the impurity line A^+.

In Fig. 2–4 magnetoabsorption spectra measured at different delay time as well as relaxation times determined from pulse oscillograms are given. In the samples 308a,b (Fig. 3, 4) with wider QWs the transition $1s - 2p^+$ (line A) is "split" into two ones (lines A_1, A_2) due to the mixing of $2p^+$ states pertained to the 1st and the 2nd hole subbands [7]. CE_{1L} is the CR line of 1L-electrons in the GeSi layers (cf. [6, 7]). In the insert to Fig. 3 a typical signal oscillogram is given in the semilogariphmic scale. Two characteristic relaxation times after the end of the illumination pulse can be easily seen, i.e. the

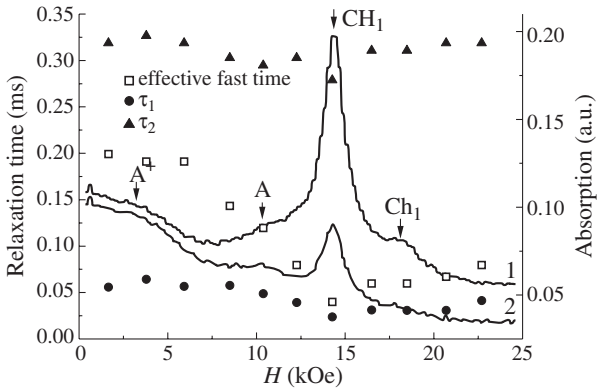

Fig. 2. Magnetoabsorption spectra of the sample 306a measured at the end of bandgap photoexcitation pulse (see Fig. 1) (1) and at delay time of 40 μs (2) (curves) and the relaxation times determined from pulse oscillograms (symbols); $\hbar\omega = 2.53$ meV.

signal can be approximated with the sum of two exponents:

$$Ae^{-\frac{t}{\tau_1}} + Be^{-\frac{t}{\tau_2}} \qquad (1)$$

The "slow" relaxation time τ_2 stands for the signal relaxation at large time scale while at the initial stage the effective "fast" relaxation time (squares in Fig. 2–4) is as follows from (1) a combination of τ_1 and τ_2.

As follows from oscillogram analysis (see, for example, Fig. 1) the "fast" signal fraction is high for the CR lines and small for impurity absorption lines and *vice versa* for "slow" signal fraction. Note that "fast" time τ_1 ranging in the samples under study from one to several tens μs proved to be at least one order higher than that of free carrier recombination in bulk Ge [8]. This seems to result from a space separation of photoexcited electrons and holes by a built-in electric field that should be a particular for each sample. This field is likely to be responsible for the significant (several times) difference in both τ_1 and τ_2 in the samples 308a,b deposited in the same growth on different substrates (see Fig. 3, 4). The built-in electric field (that probably results from the Fermi level pinning in the forbidden gap at the sample surface) separates the photoexcited electrons and holes that in turn compensate the field at

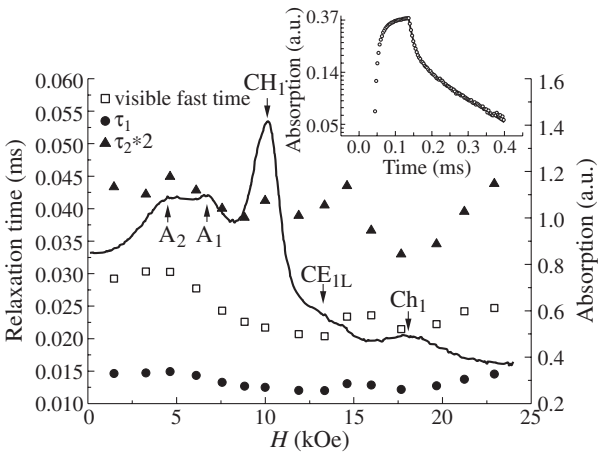

Fig. 3. Magnetoabsorption spectrum of the sample 308a ($x = 0.09$, $d_{\mathrm{Ge}} = 350$ Å, $d_{\mathrm{GeSi}} = 160$ Å, $\epsilon_{xx} = 4.4 \cdot 10^{-4}$) measured at the end of bandgap photoexcitation pulse ($\tau_{\mathrm{pulse}} = 330\,\mu$s, repetition rate 100 Hz) (curve) and the relaxation times determined from pulse oscillograms (symbols); $\hbar\omega = 1.77$ meV. In the insert: oscillogram of magnetoabsorption pulse measured at $B = 23$ kOe (circles) and the decay fitting by the function (1).

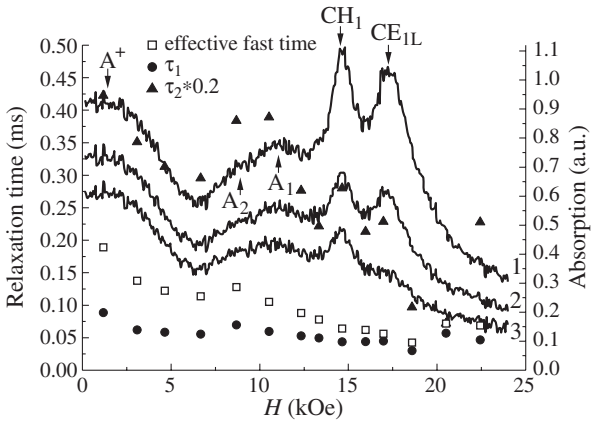

Fig. 4. Magnetoabsorption spectra of the sample 308b ($x = 0.09$, $d_{\mathrm{Ge}} = 330$ Å, $d_{\mathrm{GeSi}} = 150$ Å, $\epsilon_{xx} = 4.4 \cdot 10^{-4}$) measured at the end of photoexcitation pulse ($\tau_{\mathrm{pulse}} = 100\,\mu$s, repetition rate 100 Hz) (1) and at delay time of 32 μs (2) and 79 μs (3) (curves) and the relaxation times determined from pulse oscillograms (symbols); $\hbar\omega = 2.43$ meV.

the high enough illumination doze due to the impurity charge exchange. Then, since at liquid helium temperature this exchange is persistent (i.e. the compensation persists for a long time after illumination switching off), at pulsed illumination a part of photoexcited electrons and holes (probably a little bit separated by a residual built-in field) will be trapped by ionized impurities while the other carriers will remain free. After the end of the pulse free carriers due to their mobility can easily meet a carrier (with the opposite charge sign) localized at the impurity and therefore relax quickly. As easy to see in the spectra in Fig. 2 in 40 μs the intensity of the hole CR line CH_1 drops significantly while those of impurity lines A^+ and A decrease a little bit only. At the 2^{nd} stage of relaxation intensities of all lines decay with the same characteristic time $\tau_2 \gg \tau_1$. At this stage the free holes seem to arise due to thermoionisation of shallow acceptors. Free holes therewith recombine at neutral donors while the concentrations of neutral acceptors and A^+-centers decay either due to recombination of bound holes with free electrons, or simply owing to "outflow" of thermoexcited holes recombining at the donors. As one can see in Fig. 4 after the end of illumination pulse the electron CR line CE_{1L} quickly decays at the time scale of τ_1 and further is not observed in the spectra. The evident explanation is that there are no shallow enough donors in the sample to supply free electrons due to thermoexcitation at $T = 4.2$ K.

Acknowledgements

This work was financially supported by RFBR (Grant #03-02-16808) and by RAS. The authors are thankful to A. V. Antonov and I. V. Erofeeva for technical assistance.

References

[1] V. I. Gavrilenko *et al*, *JETP Lett.* **65**, 209 (1997).
[2] V. Ya. Aleshkin *et al*, *Phys. stat. sol. (b)*, **210**, 649 (1998).
[3] V. Ya. Aleshkin *et al*, *Semiconductors*, **34**, 582 (2000).
[4] V. Ya. Aleshkin *et al*, *Physica E*, **7**, 608 (2000).
[5] V. Ya. Aleshkin *et al*, *Phys. Rev. B*, **66**, 155336 (2002).
[6] V. Ya. Aleshkin *et al*, *Physics of the Solid State*, **46**, 125 (2004).
[7] V. Ya. Aleshkin *et al*, *Physics of the Solid State*, **47**, 74 (2005).
[8] J. C. Hensel *et al*, *Phys. Rev. Let.*, **30**, 227 (1973).

13th Int. Symp. "Nanostructures: Physics and Technology"
St Petersburg, Russia, June 20–25, 2005

Mechanisms of low-temperature conductance in systems with dense array of $Ge_{0.7}Si_{0.3}$ quantum dots in Si

I. L. Drichko[1], A. M. Diakonov[1], *I. Yu. Smirnov*[1], Y. M. Galperin[1,2], A. V. Suslov[1,3], A. I. Yakimov[4] and A. I. Nikiforov[4]

[1] Ioffe Physico-Technical Institute, St Petersburg, Russia
[2] Department of Physics, University of Oslo, PO Box 1048 Blindern, 0316 Oslo, Norway
[3] National High Magnetic Field Laboratory, Tallahassee, Florida 32306, USA
[4] Institute of Semiconductor Physics of SB RAS, 630090 Novosibirsk, Russia

Abstract. Using acoustic method we have determined ac (high-frequency) conductance of dense self-assembled arrays of B-doped $Ge_{0.7}Si_{0.3}$ quantum dots in the temperature range 1–20 K and in magnetic fields up to 18 T. At low temperatures the conductance mechanism is presumably hopping, while the contribution of extended states increases with the temperature increase. We were able to separate the above contributions and determine the activation energy for the samples with different doping levels as a function of magnetic field.

Introduction

For the first time, acoustic methods were used for studies of the nature of the low temperature ac conductance in the dense array of Ge-in-Si quantum dots in [1]. Since both Ge and Si are not show piezoelectricity the only way to study acousto-electric interaction is to employ the so-called hybrid method. According to this method the surface acoustic wave (SAW) propagates along a surface of piezoelectric $LiNb0_3$, the sample being pressed to the surface by a spring. In this case only the piezoelectric field at SAW frequency ω penetrates the sample while the ac strain in the sample is almost absent.

Contrary to [1], in the present experiment the quantum dots consisted of 70% Ge and 30% Si. The two dimensional array had density 3×10^{11} cm^{-2} and was located at the distance 2000 Å from the sample surface. The $Ge_{0.7}Si_{0.3}$ quantum dots had pyramidal shape with square base 120×120 Å^2 and height $\approx$ 20 Å. The systems were doped by B, three sample with different B concentration – 6.8×10^{11}, 8.2×10^{11} and 1.1×10^{12} cm^{-2} (samples 1, 2 and 3, respectively) – were studied.

The SAW attenuation coefficient, Γ, and its relative velocity variation, $\Delta V/V$, were measured in perpendicular magnetic fields H up to 18 T in the temperature interval 1–20 K. The SAW frequency interval was 30–300 MHz. Here $\Delta V/V$ is defined as $(V - V_0)/V_0$ where V_0 is the SAW velocity at free $LiNbO_3$ surface.

Experimental results

Shown in Fig. 1 are magnetic field dependences of $\Delta\Gamma \equiv \Gamma(H) - \Gamma(0)$ in the sample 2 for different temperatures. In the temperature interval 1–6 K, $\Delta\Gamma < 0$, at large magnetic field it tends to saturation. At $T > 6$ K $\Delta\Gamma > 0$. Similar behaviors were observed for other samples. Namely, with the temperature increase the sign of $\Delta\Gamma$ crosses over from negative to positive. The magnetic field dependence of $\Delta\Gamma$ above the crossover temperature (which decreases with increase of the doping concentration) is non-monotonous. The magnetic field dependences of $\Delta V/V \equiv [V(H) - V(0)]/V(0)$ for $\omega/2\pi =$ 28 MHz and $T = 2$, 3 and 4 K are shown in Fig. 2. This quantity also saturates at large H.

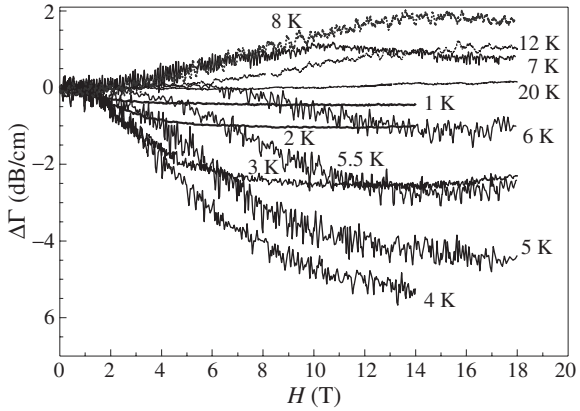

Fig. 1. The magnetic field dependences of the absorption coefficient $\Delta\Gamma$ at different T, $f = 28$ MHz.

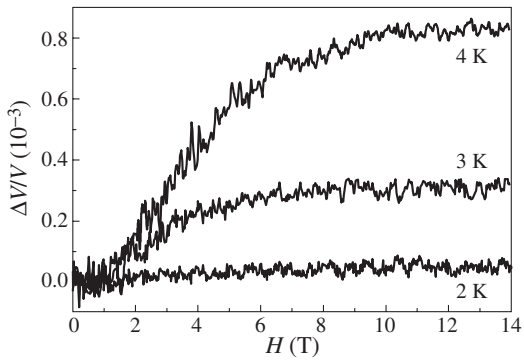

Fig. 2. The magnetic field dependences of velocity shift $\Delta V/V$ for $f = 28$ MHz and $T = 2$, 3 and 4 K.

Discussion

The observed decrease of the attenuation in magnetic field, $\Delta\Gamma = \Gamma(H) - \Gamma(0) < 0$, can, in principle, be attributed to the conventional two-site model of ac hopping conductance, see, e. g., [2]. This decrease is due to decrease of the overlap of the wave functions of the localized states involved in the inter-site transition. The dc measurements [3] are also compatible with hopping between the states localized at different quantum dots. According to [2], both $\Delta\Gamma$ and $\Delta V/V$ are proportional to H^2 at small H, while at $H \to \infty$ both $\Gamma(H)$ and $V(H) - V_0$ are proportional to H^{-2}. Thus at $H \to \infty$ the quantity $\Delta\Gamma$

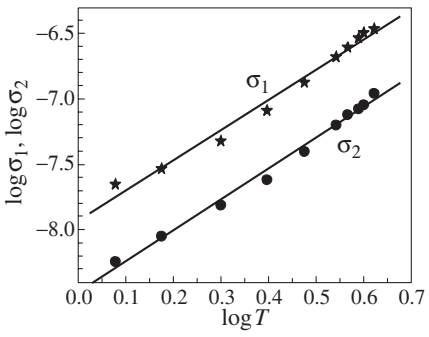

Fig. 3. Dependences of σ_1 and σ_2 on T; sample 2, $f = 28$ MHz.

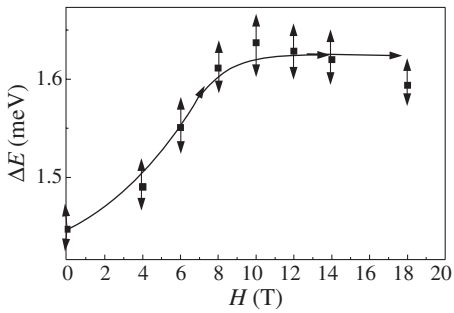

Fig. 4. The magnetic field dependence of the activation energy for the sample 2.

turns out to be independent of H that agrees with experiment. Furthermore, since $\Delta\Gamma|_{H\to\infty} = -\Gamma(0) + A/H^2$, one can find zero-field attenuation, $\Gamma(0)$. Such procedure has been carried out for all samples and for different temperatures. Since $V(0)$ is close to V_0 using a similar procedure one can find $(V_0 - V(0))/V_0$. Knowing the above quantities and using the procedure described in [4] one can determine the *complex* ac conductance,

$$\sigma^{(ac)}(\omega) \equiv [\sigma_1(H,\omega) - i\sigma_1(H,\omega)]_{H=0}\,.$$

It turned out that in the studied frequency range the quantity σ_1 is frequency independent with the accuracy of 15%. Temperature dependences of σ_1 and σ_2 for the sample 2 and frequency 28 MHz are shown in Fig. 3. Negative sign of $\Delta\Gamma$ at low temperatures supports the hopping conductance mechanism. According to the two-site model of ac conductance [5], the expressions for the above quantities depend on the product $\omega\tau_0$ where τ_0 is the energy relaxation rate for a typical pair of sites involved in the ac hopping conductance. The observed weak frequency dependence of $\Gamma(0)$ would correspond to the case $\omega\tau_0 \gg 1$ where $\Gamma(0)$ should be only frequency independent and increasing with temperature. According to the same model, the σ_2/σ_1 must be greater than 1, that is not the case in the experiment. In addition, σ_2 should be an increasing function of frequency, $\propto \omega$ with logarithmic accuracy. From that we conclude that conventional two-site approximation is not sufficient to explain the observed experiment behavior.

As follows from Fig. 1, at $T > 5$ K the absolute value of $\Delta\Gamma$ decreases with magnetic field, and at $T \geq 7$ K $\Delta\Gamma$ becomes positive. Positive $\Delta\Gamma$ is usually observed if the conductance occurs via extended states. Consequently, it is reasonable to assume that the actual conductance has two contributions originating form localized and extended states, respectively. To separate the mechanisms let us assume that the temperature dependences shown in Fig. 3 correspond to localized states. Extrapolating these dependences up to 5, 5.5 and 6 K one can then compare the values of the conductance with those determined from experiment according to the discussed above procedure. The difference between the observed and extrapolated values of $\sigma_{1,2}$ can be ascribed to the contributions of the extended states. For example, for $T = 5$ K the contributions of localized and extended states to σ_1 turn out to be $5.2 \times 10^{-7}\ \Omega^{-1}$ and $1.2 \times 10^{-7}\ \Omega^{-1}$, respectively. The role of the extended states increase with the temperature increase. We have not found noticeable contributions from extended states to σ_2.

At higher temperatures, $T = 7{-}20$ K, where $\Delta\Gamma > 0$ and depends on magnetic field non-monotonously one can easily find σ_1 using the procedure of [6]. The temperature dependence of σ_1 follows the activation law, the activation energies being 1.45 ± 0.03 and 1.24 meV for samples 2 and 3, respectively. Shown in Fig. 4 is the magnetic field dependence of the activation energy for the sample 2. The activation energy first increases with magnetic field, and then saturates. This behavior can be explained by shrinking of the wave functions in magnetic field [7].

Conclusion

Acoustoelectric effects in dense ($n \sim 3 \times 10^{-11}$ cm^{-2}) self-assembled arrays of $Ge_{0.7}Si_{0.3}$ quantum dots in Si show that at low temperatures the mechanism of ac conductance is presumably hopping. As temperature grows the role of extended states increases. We have managed not only to separate the respective contributions, but also determine the activation energies and their magnetic field dependences. The quantitative description of both ac and dc transport will require more theoretical work.

Acknowledgements

We are thankful to G. Min'kov for DC-measurements. The work was supported by RFFI 04-02-16246, 03-02-16526, Presidium RAN and INTAS 03-51-5051 grants. A portion of this work was performed at the National High Magnetic Field Laboratory, which is supported by NSF Cooperative Agreement No. DMR-0084173, by the State of Florida, and by the DOE. Development of the ultrasonic technique at the NHMFL is supported by the In-House Research Program.

References

[1] I. L. Drichko *et al*, *Proc. 11 Int. Symp. "Nanostructure: Physics and Technology"*, 133 (2003).
[2] Yu. M. Galperin, E. Ya. Priev, *Fiz. Tverd. Tela*, **28**, 692 (1986) [*Sov. Phys. Solid. State.*, **28**, 385 (1986)].
[3] A. I. Yakimov *et al*, *ZhETF* **127**, 1 (2005).
[4] I. L. Drichko *et al*, *Phys. Rev. B* **62**, 7470 (2000).
[5] A. L. Efros and B. I. Shklovskii, in *Electron-Electron Interactions in Disordered Systems*, ed. by A. L. Efros and M. Pollak (Amsterdam: North-Holland), 409, 1985;
Y. M. Galperin, V. L. Gurevich, D. A. Parshin, in *Hopping Transport in Solids*, ed. By B. Shklovskii and M. Pollak (New York: Elsevier), 1991.
[6] B. A. Aronzon and I. L. Drichko, *Fiz. Tekh. Poluprovodn.* **26**, 1446 (1992)[*Sov. Phys. Semicond.* **26**, 811 (1992)].
[7] Y. Yafet *et al*, *J. Phys. Chem. Solids* **1**, 137 (1956).

13th Int. Symp. "Nanostructures: Physics and Technology"
St Petersburg, Russia, June 20–25, 2005

Quantum features of silicon nanopowder, detected at room temperature

M. D. Efremov[1], V. A. Volodin[1], D. V. Marin[1], S. A. Arzannikova[1], S. V. Gorajnov[2], A. I. Korchagin[3], V. V. Cherepkov[3], A. V. Lavrukhin[3], S. N. Fadeev[3], R. A. Salimov[3] and S. P. Bardakhanov[4]

[1] Institute of Semiconductor Physics SB RAS, pr. Lavrentjeva 13, Novosibirsk 630090, Russia
[2] Institute of Mineralogy and Petrography SB RAS, University pr 3, Novosibirsk 630090, Russia
[3] Institute of Nuclear Physics SB RAS, pr. Lavrentjeva 11, Novosibirsk 630090, Russia
[4] Institute of Theoretical and Aapplied Mechanics SB RAS, Institutskaya str. 4/1, Novosibirsk 630090, Russia

Abstract. Silicon nanopowders produced by electron-beam-induced evaporation of a bulk silicon sample have been studied using the photoluminescence technique and Raman scattering spectroscopy. A photoluminescence peak up to blue region of the spectrum has been detected at room temperature in powders consisting of silicon nanocrystals. The size of silicon nanocrystals was determined by analyzing of Raman spectra. A strong short-wavelength shift of the photoluminescence peak can be attributed to the quantum size effect of electrons and holes in small silicon nanocrystals (about 2 nm).

Introduction

Silicon nanopowder attracts recent scientific attention because of general interest to silicon nanocrystals. Potential possibility of selection of particle on size looks like benefit in comparison with clusters directly formed in the process of deposition or thermal treatments. Of course, separation of nanoparticles with size about several nanometers represents quite complicated problem. Nevertheless, solving the problem of selection makes a promise to apply silicon nanopowder for creation of high density memory or effective light emitting devices within silicon nanoelectronics. From scientific point of view, investigation of separate silicon nanoparticle could give experimental answer on question concerning electronic spectra of silicon nanocrystals. In this paper an attempt to obtain separate silicon nanoparticles and to examine their properties is presented.

1. Experimental

Silicon nanopowder was obtained utilizing silicon atoms coagulation in gas flow. Injection of silicon atoms was provided by evaporation of silicon ingot by means of power electron beam. Electron beam accelerator ELV-6 with energy of electrons of 1.4 MeV was used as a pumping. Coagulated silicon atoms were gathered through special filters in the form of powder, which properties were examined by means of electron microscopy, Raman and photoluminescence spectroscopies. Photoluminescence spectra were registered at room temperature using pulse N_2 gas laser as a source. Raman spectra were taken at room temperatures in backscattering geometry with Ar gas laser as a pumping (wavelength 514 nm). Both DFS-52 and Dylor Raman spectrometers were used in measurements.

2. Results and discussion

Depending on gas atmosphere in the flow silicon or silicon oxide nanocrystals were obtained. Electron microscopy revealed spherical form of nanocrystals. The size of nanoparticles varied from several nanometers to tens of nanometers depending on the filter been used.

In the case of silicon nanopowder a visible photoluminescence was detected at room temperature (Fig. 1). Most surprising was photoluminescence of silicon nanopowder in blue region of spectra in addition to room temperature detection of

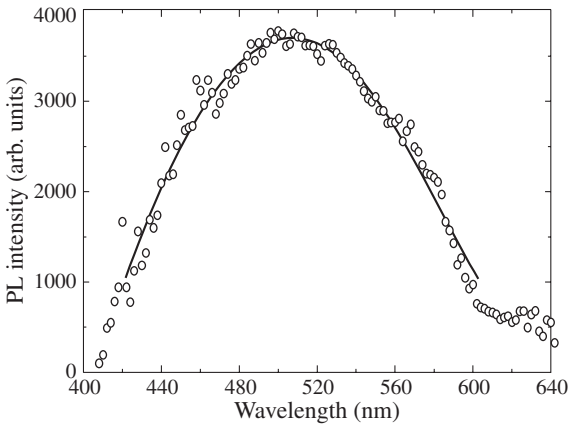

Fig. 1. Photoluminescence spectrum of a silicon nanopowder (excitation by pulsed 337-nm N_2 laser at 300 K).

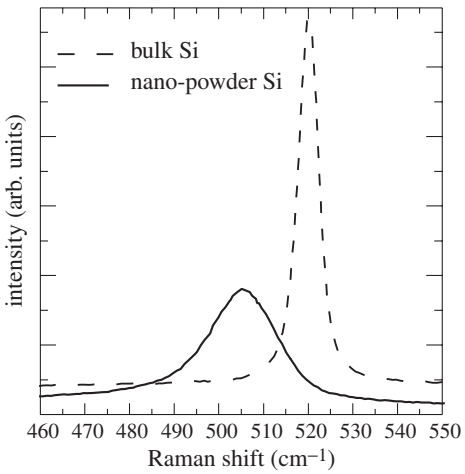

Fig. 2. Raman spectra of (dashed line) bulk silicon and (solid line) silicon nanopowder prepared by electron beam-induced evaporation.

the light emission. Raman spectra for initial silicon ingot and obtained silicon nanopowder are presented in Fig. 2. Optical phonon peak is shifted to lower energies due to localization of phonons inside of silicon nanocrystals. The position of the peak corresponds to crystalline form of silicon nanoparticles. Evaluation of the peak position gave an estimation of average nanoparticles size about 2 nm. For such small silicon nanopar-

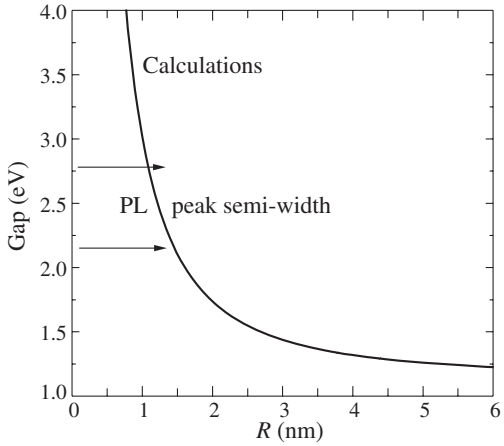

Fig. 3. Calculated optical gap in silicon nanocrystals.

ticles band gap could be high enough to provide visible photoluminescence due to direct recombination of electron-hole pair, localized inside of nanoparticle. Taking into account keeping of nanopowder in air atmosphere after preparation and possibility of capping by silicon dioxide, possibility of recombination trough environment electronic state should be considered also. Estimation of optical gap in silicon nanopowder capped with silicon oxide was done in effective mass approximation, what presented in Fig. 3. The range of observed photoluminescence correspond quite well to Raman estimation of the size of nanocrystals.

So, blue-red photoluminescence from silicon nanopowder was observed for the first time, what will be discussed in the presentation as well as aspects of silicon nanopowder formation, its electronic properties and potential for application in nanoelectronics.

References

[1] M. D. Efremov, V. A. Volodin, D. V. Marin, S. A. Arzannikova *et al*, *JETP Letters*, **80**, No. 8, 544–547 (2004).

13th Int. Symp. "Nanostructures: Physics and Technology"
St Petersburg, Russia, June 20–25, 2005

Optical and structural analysis of Ge/Si quantum dots grown on a Si(001) surface covered with a SiO_2 sub-monolayer

A. Fonseca[1], E. Alves[1], *J. P. Leitão*[2], N. A. Sobolev[2], M. C. Carmo[2] and A. I. Nikiforov[3]

[1] Instituto Tecnológico e Nuclear, E.N. 10, 2686-953 Sacavém, Portugal
[2] Departamento de Física, Universidade de Aveiro, 3810-193 Aveiro, Portugal
[3] Institute of Semiconductor Physics, 630090 Novosibirsk, Russia

Abstract. In this work we studied a set of samples grown by molecular beam epitaxy in which a Ge layer was deposited on a Si(001) substrate covered with a thin SiO_2 layer. Three different thicknesses for the two layers were considered: 0.3, 0.6 or 0.9 nm of Ge, and 0.5, 0.75 or 1 monolayer (ML) of SiO_2 were deposited. The measurements of Rutherford backscattering (RBS) at grazing angles of incidence suggest the formation of Ge quantum dots (QDs) just for the thicker layers. The photoluminescence (PL) measurements confirm the above results. The PL spectra also show the presence of structural defects in the samples.

Introduction

One of the long standing problems in the electronic industry is to combine optical and electrical functions on a silicon chip. One of the several approaches proposed in the last decades consists in band structure engineering involving the growth of Si/Ge multilayered structures. Different growth modes have been used for the growth of Ge QDs on silicon substrates. The most used one is the Stranski–Krastanow which explores the lattice mismatch between Si and Ge for the spontaneous growth of Ge islands upon a GeSi wetting layer [1]. After a critical thickness of the Ge quantum well the strain energy is relieved through the formation of Ge islands. This technique allows a certain degree of vertical self-organization of islands in different layers [2]. However, the QDs obtained by this technique are too large to explore quantum confinement effects and their density is not high enough for the expected applications in silicon-based optoelectronic and quantum electronic devices [3,4]. So, a reduction in the dimensions of the islands and an increase of their density are required. Diminishing the growth temperature, we obtain a higher Ge content in the islands with lower dimensions [5]. However, the defect concentration simultaneously increases, resulting in a lower crystal quality.

In order to create smaller islands, modification of the initial conditions on Si surfaces has been performed by deposition of certain materials in amounts of up to 1 monolayer (ML), which stimulated island nucleation [6,7]. Recently, Shklyaev *et al* [4] used an ultrathin layer of silicon dioxide as an intermediate coverage for Ge deposition. Spontaneously induced local transformation of the dielectric layer allows the production of very small Ge islands with a very high density. The structural and optical properties of the dots grown by this method are just starting to be investigated [3,4,8].

In this work we study a set of samples which were grown by molecular beam epitaxy. A Ge layer with a nominal thickness of 0.3, 0.6 or 0.9 nm was deposited at 550 °C on a Si(001) substrate covered (at 400 °C) by 0.5, 0.75 or 1 ML of SiO_2. The samples were capped at 500 °C with 100 nm of Si. The dependence of the structural and optical properties on the growth parameters is studied.

1. Experimental

The details of the RBS and PL measurements are discussed elsewhere [9,10]. Hydrogen passivation was done in a chemical vapour deposition reactor at 100 °C for 15 min.

2. Rutherford backscattering measurements

The strain in the films was evaluated using the channelling curves along the main axial directions. Angular scans along the ⟨100⟩, ⟨110⟩ and ⟨111⟩ axes were performed for the following samples: i) with 1 ML of SiO_2 and 0.3, 0.6 and 0.9 nm of Ge and ii) with 0.9 nm of Ge and 0.5, 0.75 and 1 ML of SiO_2. The results obtained for the sample with the thickest layers (1 ML of SiO_2 and 0.9 nm of Ge) are depicted in Fig. 1. Along the ⟨100⟩ direction, a narrowing of the Ge-related curve as compared to the Si-related one is visible. On the contrary, for the ⟨110⟩ direction we observe a broadening of the Ge curve. In both directions the minimum yield (χ_{min}) of the Ge curves is higher than that of the Si ones. This is a clear indication of a change in atomic alignment due to the presence of strained Ge islands. On the other hand, the positions of the minima of both Ge and Si curves for the ⟨110⟩ direction are identical. This suggests that, despite a lower crystalline quality, the Ge film is coherently aligned with the Si substrate.

χ_{min} and the angular width at half-minimum ($\Psi_{1/2}$) obtained for the Ge and Si scans, for samples with 1 ML of SiO_2 and 0.3, 0.6 and 0.9 nm of Ge, are summarized in Table 1 for the ⟨110⟩ direction. The results show that the χ_{min} value for the Ge scan of the thinner sample (0.3 nm of Ge) is close to the Si-related one. Similar scan results (not shown) were obtained for the ⟨100⟩ and ⟨111⟩ directions [10]. This similarity between χ_{min} for Ge and Si is a clear indication that the Ge atoms are incorporated substitutionally in the Si lattice, excluding the formation of Ge quantum dots. As the thickness of the Ge layer increases, the χ_{min} value of the Ge curve rises due to increasing atomic misalignment. This behavior is a way to release the strain energy accumulated in the Ge films due to lattice mismatch between Si and Ge ($\sim$ 4%). For the sample with the thickest Ge layer (0.9 nm) we verified that χ_{min} for Ge is almost 50%, indicating a possible presence of Ge quantum dots. These results also show an increase of the $\Psi_{1/2}$ for the Ge curve as the thickness of the Ge layer rises (from 0.81° to 1.26°, for 0.3 and 0.9 nm of Ge, respectively). This increase

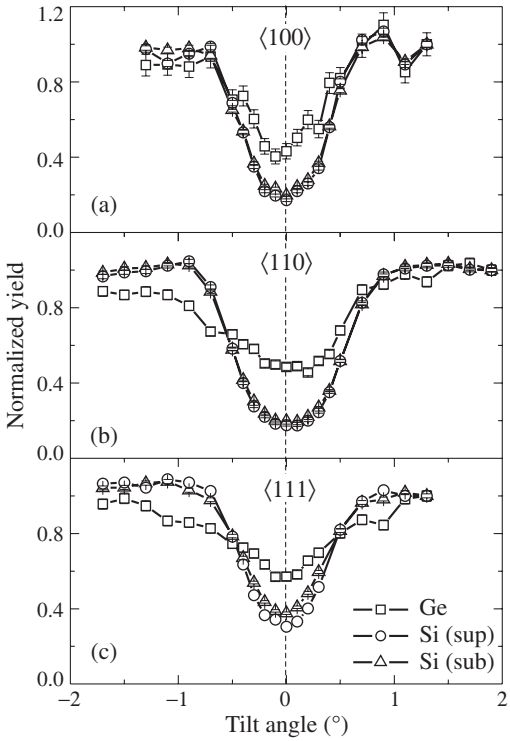

Fig. 1. Angular scans along the main axial directions for the 0.9 nm buried Ge layer grown on 1 ML of SiO_2.

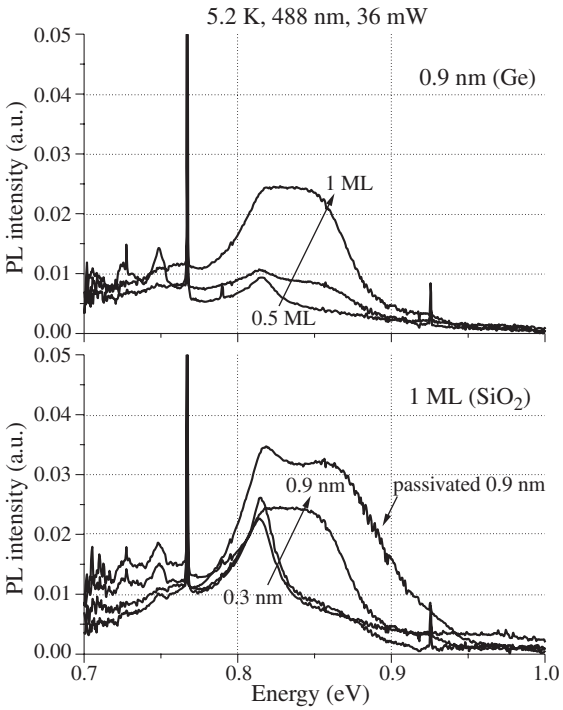

Fig. 2. Photoluminescence spectra of a set of samples with different the thicknesses for the SiO_2 and Ge layers. A spectrum from the passivated sample with 1 ML of SiO_2 and 0.9 nm of Ge is also shown.

also suggests the presence of Ge quantum dots.

Table 1. Minimum yield (χ_{min}) and angular width at half-minimum ($\Psi_{1/2}$) in the ⟨110⟩ direction for the samples with 1 ML of SiO_2 and with 0.3, 0.6 and 0.9 nm of Ge.

		0.3 nm	0.6 nm	0.9 nm
χ_{min}	Ge	5.9%	32.0%	48.6%
	Si (surface)	2.5%	9.6%	17.6%
	Si (substrate)	3.2%	9.6%	17.6%
$\Psi_{1/2}$	Ge	0.81°	0.96°	1.26°
	Si (surface)	0.99°	0.96°	1.04°
	Si (substrate)	0.85°	0.96°	1.04°

Simulations for angular scans with the FLUX program [11] are under way in order to determine the crystallographic orientation of the Ge quantum dots.

3. Photoluminescence measurements

PL measurements on as-grown samples show the usual exciton luminescence from Si substrate and capping layer for energies higher than ∼ 1 eV. For lower energies a broad emission in the range 0.8–0.9 eV is observed (see Fig. 2) as well as peaks due to radiation induced defects at 0.767, 0.790 and 0.926 eV [12]. The broad band shows some structure and its shape depends critically on the thicknesses of the the SiO_2 and Ge layers. For the samples with the lower thicknesses of these two layers the broad band is centered at 0.83 eV. However, for the sample with the higher thicknesses a shoulder at ∼ 0.85 eV appears. The lower energy component is attributed to dislocations (D1 line) whereas the higher energy component(s) is(are) related to the possible presence of QDs in the samples.

After the passivation, the intensity of the dislocation band D1 increases (Fig. 2) which is in agreement with the literature [13]. On the other hand, the 0.85 eV band also increases. Due to the passivation treatment, we can clearly distinguish the dislocation band D1 from the 0.85 eV emission that we attribute to the Ge quantum dots. Some fitting procedures are under way in order to better understand the behavior of this band.

Acknowledgements

This work was financed by Fundação para a Ciência e Tecnologia through the projects POCTI/CTM/41574/2001 and POCTI/CTM/41918/2001, and the INTAS project No. 03-51-5015. We also acknowledge the financial support from the Fundação Calouste Gulbenkian.

References

[1] P. Schittenhelm *et al*, *J. Cryst. Growth*, **157**, 260 (1995).
[2] O. G. Schmidt *et al*, *Phys. Rev. B*, **61**, 13721 (2000).
[3] A. Barski *et al*, *Appl. Phys. Lett.*, **77**, 3541 (2000).
[4] A. A. Shklyaev *et al*, *Phys. Rev. B*, **62**, 1540 (2000).
[5] J. Stangl *et al*, *Appl. Phys. Lett.*, **82**, 2251 (2003).
[6] M. Horn-von Hoegen *et al*, *Phys. Rev. B*, **49**, 2637 (1994).
[7] O. G. Schmidt *et al*, *Appl. Phys. Lett.*, **71**, 2340 (1997).
[8] M. Derivaz *et al*, *Appl. Phys. Lett.*, **84**, 3295 (2004).
[9] N. A. Sobolev *et al*, *Phys. Sat. Sol. (c)*, **4**, 1267 (2003).
[10] A. Fonseca *et al*, *Nucl. Instr. and Meth. B*, accepted for publication.
[11] P. J. M. Smulders *et al*, *Nucl. Instr. and Meth. B*, **29**, 471 (1987).
[12] G. Davies, *Phys. Rep.*, **176**, 83 (1989).
[13] T. Sekiguchi *et al*, *J. Appl. Phys.*, **76**, 7882 (1994).

13th Int. Symp. "Nanostructures: Physics and Technology"
St Petersburg, Russia, June 20–25, 2005

Growth and characterisation of Ge/Si multilayer systems

E. Kasper[1], M. Oehme[1], K. Lyutovich[1], J. Werner[1], M. Konuma[2], N. Sobolev[3] and J. Leitão[3]

[1] Institut für Halbleitertechnik, Universität Stuttgart, Pfaffenwaldring 47, 70569 Stuttgart, Germany
[2] Max-Planck Institut für Festkörperforschung, Heisenbergstr. 1, 70569 Stuttgart, Germany
[3] Departamento de Física, Universidade de Aveiro, 3810-193 Aveiro, Portugal

Abstract. Solid-source molecular beam epitaxy is employed for the growth of Ge/Si multilayer systems on 4-inch Si wafers with in situ monitoring. Results of detailed investigations of composition profiles performed by SIMS and Auger microprobe on 10- and 20-period stacks are presented. Comparative study of growth mechanisms by atomic force microscopy illustrates the transition from the wetting layer to the island formation. Also scanning electron microscopy on stacks' cross-sections reveals this transition. Data on optical properties characterized by photo-luminescence show a peak in the low-energy region at ~ 0.73 eV.

Introduction

The near infrared region at wavelengths between 800 nm and 1600 nm is frequently used for fiber-based optical communication systems. SiGe/Si optical receivers and emitters could allow the integration with silicon-based micro- and optoelectronics because the lower band gap of SiGe increases the absorption in this wavelength region considerably compared to Si Several proposals exist for realization of silicon integrated optoelectronic circuits. We investigate in this paper the properties of multilayer stacks consisting of monolayers Ge embedded between silicon.

1. Target

Si-rich Ge/Si multilayers with a few monolayers Ge embedded in Si form stacks consisting of 10–20 periods of few monolayers Ge separated by Si. Thick Si spacers are chosen in order to avoid relaxation of the whole system with a low mean Ge content. Such structures are favourable for near-infrared optoelectronics. Transition regimes are maintained between the growth of flat wetting layers and Ge-island formation (Stranski–Krastanov mechanism) (Fig. 1). Correlation between layer-stack morphology, structural and optical properties are searched.

2. Growth

Solid-source molecular beam epitaxy with e-beam evaporation for Si and effusion cell for Ge is employed [1, 2]. Mean growth rates of 0.1 nm/s are applied at substrate temperatures of 450–550 °C. The atomic fluxes are in situ monitored by a quadrupole mass-spectrometer and the growth rate is in situ monitored by time-resolved interferometric reflectometry. From 2 to 10 ML Ge and 36 nm Si in each period are deposited in layer stacks

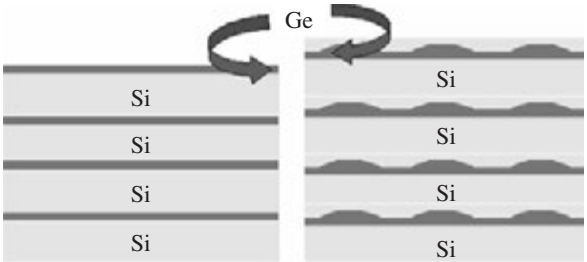

Fig. 1. Schematic of a layer-stack formed by Ge wetting layers on Si (left) and by Ge wetting layers with islands formed on top of them (right).

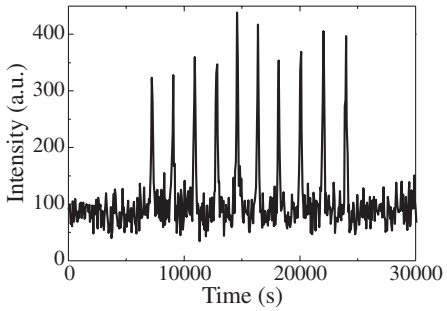

Fig. 2. Auger-profile of a 10-period layer stack measured with etch rate of 1 nm/min.

with 10 to 20 periods during this series of experiments. For comparative investigations of the surface morphology also Ge layers are grown without the Si caps.

3. Characterisation

Chemical composition is analysed by SIMS and Auger microprobe. Fig. 2 presents a typical Ge depth distribution in a 10-periods stack measured by Auger-electron profiling. Cross-sections of completed stacks are investigated by scanning electron microscopy (SEM) (see, for instance, Fig. 3). Uniform layer deposition is observed up to 10 periods, hereafter, nucleation of large islands proceeds frequently. Surface morphology is studied by atomic force microscopy and by light microscopy with differential interference contrast. The transition of smooth morphology (Ge wetting layer, see Fig. 1a) to island growth on top of the wetting layer (see Fig. 1b) depends on monolayer numbers and growth temperature. Fig. 4 shows islands formed on top of wetting layers (12 ML, 500 °C). Preferential etching as described in [3] is used for defect imaging. Optical properties are characterised by photoluminescence at temperatures

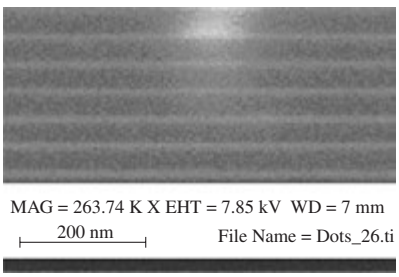

Fig. 3. SEM cross-section image of a 20-period layer stack showing the starting island formation after 10 periods.

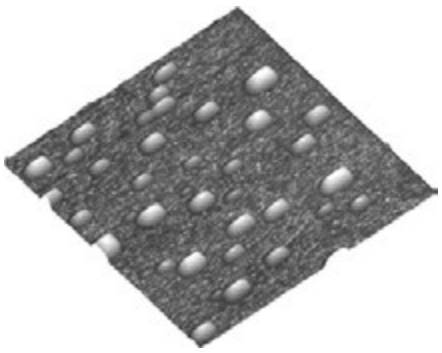

Fig. 4. Ge islands formed on top of wetting layers, $(2 \times 2)\,\mu\mathrm{m}^2$.

from 4 K to 150 K. Fig. 5 shows a PL spectrum measured at 5 K. Spectrum of bound excitons in Si is intense and well resolved which proves that local strain fields in Si are low. A broad peak in the low-energy region at 0.73 eV is observed. Similar signatures are attributed in the literature to Ge dots [4]. Devices made from this material are in preparation.

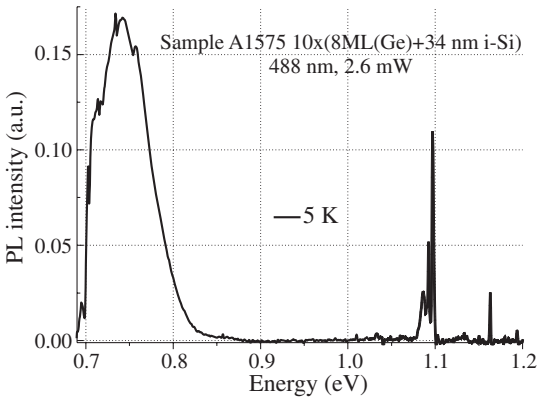

Fig. 5. PL spectra of a 10-period layer stack measured at 5 K with distinct Si and low-energy peaks.

4. Conclusion

Multilayer stacks of monolayers Ge embedded in Si are successfully grown by solid-source MBE. Auger profiles and SEM cross-sections confirm the intended structure. Photoluminescence at around 730 nm is assigned to the thin Ge layers.

Acknowledgements

We thank J. Yu for collaboration in analytical and device work. INTAS support (project 03-51-5015) is gratefully acknowledged.

References

[1] E. Kasper, M. Bauer and M. Oehme, *Thin Solid Films*, **321**, 148 (1998).
[2] M. Oehme, M. Bauer and E. Kasper, *Mat. Sci. and Eng.*, **B89**, 332 (2002).
[3] J. Werner, K. Lyutovich and C. P. Parry, *Eur. Phys. J. Appl. Phys.*, **27**, 367 (2004).
[4] K. Wang, S. Tong and H. J. Kim, *Mat. Sci. in Semicond. Proc.*, **8**, 389 (2005).

13th Int. Symp. "Nanostructures: Physics and Technology"
St Petersburg, Russia, June 20–25, 2005

Peculiarities of lateral electroconductivity of p-type doped Si/Ge island structures

V. A. Gergel[1], T. M. Burbaev[2], *V. A. Kurbatov*[2], A. O. Pogosov[2], M. M. Rzaev[2], N. N. Sibeldin[2] and M. N. Yakupov[1]

[1] Institute for Radio-Engineering and Electronics, RAS, 101999 Moscow, Russia
[2] P.N. Lebedev Physical Institute, RAS, 119991 Moscow, Russia

Abstract. The numerical calculation of nanosize Si/SiGe structures electroconductivity is carried out in frames of quasi-hidrodynamic model of charge carrier drift in high electrical fields in consideration of band offset between low- and high-resistance domains. It is found volt-ampere characteristics of such structures must have *S*-type behavior, with negative conductance in limit, and critical parameters of theory are sharpness of heterojunction between narrow- and wide gap parts of structure and doping level. Doped island structures having different sizes of islands were grown by MBE and results of conductivity measurements are compared with theoretical values.

Introduction

Nano-size structures having modulated doping along current direction must have characteristic peculiarities of conductivity having practical interest. Recently [1, 2] it was shown that alternate low-resistance regions introduced into transistor channel must increase average carrier velocity due to effective electron gas cooling. This situation was modulated numerically using quasi-hydrodynamic model [3]. This calculation results may be applied to the n-type $Si/Si_{1-x}Ge_x$ island structures in which conductive band offset at room temperature may be neglected. In this reason practical modeling of such structure demand of direct doping of the islands and this problem is associated with doping influence on structure morphology, which was investigated partly for high impurity density, compared with base material amount [4]. It is interesting to investigate also process of electron high-field drift into other type of high doped structures namely nanosize heterostructures having sufficient intense changes of conductivity due to band offset. This can be p-type $Si/Si_{1-x}Ge_x$ structures production of which is relatively easy.

In this work we present theoretical analyze considering potential barriers at heterojunction and compare it with experimental results measured on doped $Si/Si_{1-x}Ge_x$ island structures grown by MBE.

1. Theory

As in previous works [2, 3] the basis for modeling was well known system of quasi-hydrodynamic equations involved Poisson equation, continuity equation and energy balance equation in formulation of Stratton [5]. The terms with electrostatic potential ϕ which added to the band quasi-potential $\phi_c = -E_c(x)/q$ were considered in this system except the Poisson equation. ($E_c(x)$ is the edge of conductivity band varying with coordinate according the composition).

For numerical calculations it was taken hypothetical heterostructure having homogeneous doping $N_D = \text{const} = 5\times10^{17}\,\text{cm}^{-3}$ with narrowband contact regions and four hetero-barrier having amplitude $\phi_0 = 0.2\,\text{V}$ and extension 100 nm divided by narrowband regions of the same thickness. Results of mathematical modeling carried out in frames of presented model were shown in Fig. 1. It is clear that at fixed voltage I–V curve has region with maximum of differential conductivity and region with negative differential resistance at certain structure parameters.

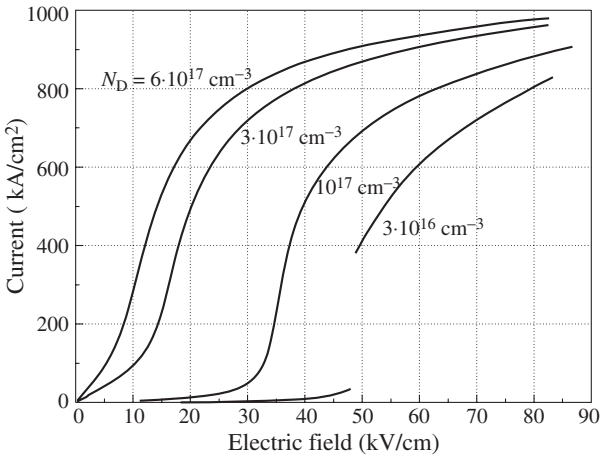

Fig. 1. Results of numerical calculations for structures with four hetero-barriers of 80 nm width and of 0.2 eV band offset. $T = 300\,\text{K}$.

Numerical analyze of electric field distribution in structure at different applied voltages shows that at initial sector of I–V curve current is limited by hetero-barrier influence. Rate of current increasing increases sharply at definite voltage due to noticeable increasing of electrons temperature in enhanced injecting boundaries of narrowband layers. At further voltage growth the electrons temperature on hetero-barriers increase so that limitative influence of hetero-barriers becomes epsilon squared and I–V characteristics approach to appropriate of spatially homogeneous structure (not having hetero-barriers). It was shown that characteristic voltage of maximum of differential conductivity as well as its maximum value must increase at increasing of heterojunction steepness while it will decrease at increasing of impurity concentration. Note that effective charge carrier velocity at high voltages is close to saturation velocity and its behavior have distinct tendency to saturation. This is determined by $\approx 1\,\mu$m whole length of examined structure and practically homogeneous (at high voltages) distribution of mobile charge carriers in it.

2. Experiment

Boron doped $Si/Si_{1-x}Ge_x$ structures contained islands with different dimensions and composition were grown in "KATUN"

installation by MBE for verification of theory applicability for description of the island contained structure conductivity. Structure scheme and growth temperatures are presented in Table.

Table 1.

Sample #1	Sample #2
$Si_{0.5}Ge_{0.5}$, 48 Å, 550 °C	Ge, 12 Å, 300 °C
$4\times$ { Si, 90 Å, 550 °C; $Si_{0.5}Ge_{0.5}$, 48 Å, 550 °C }	$4\times$ { Si, 120 Å, 300 °C; Ge, 12 Å, 300 °C }
Buffer. Si:B, 2700 Å	Buffer. Si:B, 2700 Å
800 °C	750 °C
Substrate. n-Si (001)	Substrate. n-Si (001)
4.5 Ω cm	4.5 Ω cm

Sufficiently thick $Si/Si_{1-x}Ge_x$ layers with different Ge concentration were grown at low temperatures to reach high island density with required dimensions. The variation of layer composition gives differences of the barrier height into the structures. Structures were grown on n-type Si (001) substrates. Silicon buffer layers were boron doped, $p = 10^{17}\,\mathrm{cm}^{-3}$, for electrical insulation from substrates. Structures contained several $Si/Si_{1-x}Ge_x$ layers for effective depletion of the doped buffer layer. Note, it is possible in principle to control filling of layers by charge carrier by means of making rear electrode contact.

AFM measurements give us information about islands dimensions and densities. AFM images are presented at inset in Fig. 2. Lateral island size of 120 nm at island density about $4\times10^9\,\mathrm{cm}^{-2}$ were measured for structure #1 grown at $T_{\mathrm{sub}} = 550\,^\circ$C and contained four $Si_{0.5}Ge_{0.5}$ layers of 4.8 nm thickness. It is clear that islands have shape of pyramids. Island size for structure contained pure Ge layers of 1.2 nm thickness grown at $T_{\mathrm{sub}} = 300\,^\circ$C is noticeably less ($\approx$ 40 nm) while islands density is higher ($\approx 2\times10^{10}\,\mathrm{cm}^{-2}$). Note that for such low growth temperature islands size is relatively too big (see [6]).

This appears probably owing to more thick Ge layers deposited at more high rates in our experiments. Ohmic contacts were produced by vacuum deposition of aluminium followed by 2 min alloying at $T \approx 550\,^\circ$C. The current space size between contacts is equal $(700\times30)\,\mu\mathrm{m}^2$ and has $30\,\mu$m longitude toward current direction. I–V measurements were realized in pulse mode for prevention heating of samples. Impulse signals corresponding to voltage and current values was detected by two peak detectors and recorded by X-Y-plotter.

Fig. 2 displays current-voltage diagrams of produced resistors measured at room and liquid nitrogen temperatures. One can see that at room temperature both curves have evident S-shape characteristic, what is in good agreement with theoretical prediction. Smaller than presented in Fig. 1 field strength values at which observed effect can be explained much higher experimental impurity concentration than used in calculation. This confirms by measurements at liquid nitrogen temperatures. I–V diagram of sample #2 is in accordance with theoretical prediction — influence of heterojunction barrier increases while temperature decreases. Initial part of curve where current is limited by barrier extends towards high field intensities. We do not reach current saturation at used field intensities. But behavior of the sample #1 is absolutely different. Temperature decreasing leads to the rectification of curve at total conductivity increasing. More probably this occurs because of shunting influence of partly depleted buffer layer what indicates the impurity excess and, therefore, extremely high carrier density into the islands. Rough extrapolation of measured values towards high current shows that in sample #1 current passing region reach into the buffer layer. (Thickness of current passing layer is $t = I_s/(w\times j_s)$, where I_s — measured saturation current, $j_s \approx 10^6\,\mathrm{A/cm}^2$ — saturation current density, w — current channel width).

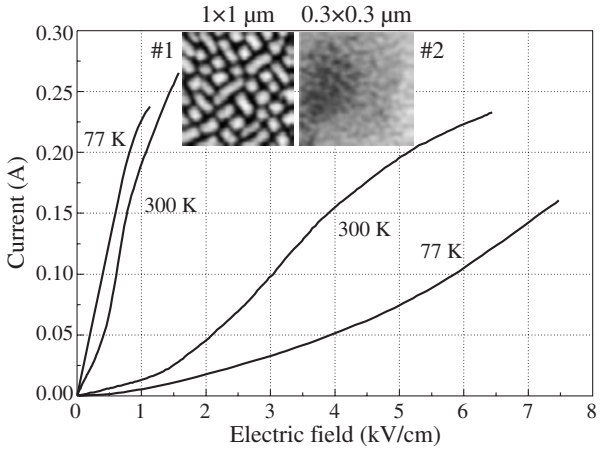

Fig. 2. Measured current-voltage diagrams of produced resistors. Insets display AFM images.

3. Conclusion

Developed theoretical model, examined charge carriers motion into the ordered barriers system is applicable as well as aperiodic barrier system of island structures. One could hope that parameter optimization of such structures gives expectation to realization of negative conductance.

Acknowledgement

This work has been supported in part by the Program of Support for Scientific Schools of RF (projects 1923.2003.2), by the RFBR (projects 04-02-17681, 03-02-17191, 03-02-20007) and by the INTAS (project 03-51-5015).

References

[1] V. A. Gergel' *et al*, *Microelectronics (rus).*, **30**, 286 (2001).
[2] V. A. Gergel' *et al*, *Semiconductors.*, **38**, 232 (2004).
[3] V. A. Gergel' *et al*, *Semiconductors.*, **39**,(2005).
[4] A. A. Tonkikh *et al*, *Semiconductors.*, **38**, 1202 (2004).
[5] R. Stratton *et al*, *Phys. Rev.*, **126**, 2002 (1962).
[6] M. W. Dashiell *et al*, , *Appl. Phys. Let.*, **80**, 1279 (2002).

13th Int. Symp. "Nanostructures: Physics and Technology"
St Petersburg, Russia, June 20–25, 2005

Variation of in plane lattices constant of Si/Ge/Si heterostructures with Ge quantum dots

A. I. Nikiforov, V. V. Ulyanov, R. A. Shaiduk and O. P. Pchelyakov
Institute of Semiconductor Physics, SB RAS, 630090 Novosibirsk, Russia

Abstract. Experimental data are presented on variations of in plane lattice constant of Ge and Si films in the course of the MBE film growth on silicon (100) surface. The in plane lattice constant of the silicon film is shown to alter as the film grows; the changes reflect the process of relaxation of elastic strains that result from the misfit of the germanium and silicon lattice constants. Due to the presence of germanium islands, a considerably thicker silicon film is required to provide the strain relaxation.

1. Introduction

The Ge/Si heterosystem is of interest to semiconductor physics due to their potential application as quantum-sized nanostructures. The practical optoelectronic applications of the silicon structures with germanium quantum dots cover the regions from IR [1] through the wavelengths used in fiber-optic communications [2]. The Ge/Si heterosystem also is a convenient object for studying the heteroepitaxial growth, growth mode transition and strained states of the surface layer at various growth stages. The traditionally used technique is reflection high-energy electron diffraction (RHEED). The strains can be estimated from variations of in plane lattice constant in the growing Ge film. This approach was used to determine the relaxation points in systems Ge/Si [3] and InAs/GaAs [4]. The unique features of the RHEED technique enabled oscillations of the in-plane lattice constant to be detected for the Ge film growing according to the 2D mechanism on the silicon surface [5].

The study of the process of growing over Ge islands on the Si(100) surface is of cross-light interest. First, this is important for fabrication of low-defect epitaxial heterostructures. Second, understanding of regularities of strain relaxation in the epitaxial silicon film growing over the germanium island layer will allow the surface arrangement of elastic strains to be controlled. This phenomenon is of particular importance for synthesis of multilayer heterosystems with alternating vertically ordered germanium island layers. AFM was used earlier [6,7] to study the dependence of the preferable arrangement of germanium islands on the thickness of the silicon layer grown above the preceding island layer. A suitable tool for this purpose is *in situ* recording of RHEED patterns. Such an attempt was made [8] to demonstrate the possibility of identification of distortions of the in plane lattice constant of the Si film over the Ge layer.

2. Results and discussion

A MBE installation Katun-C equipped with two electron beam evaporators for Si and Ge was used for synthesis. Analytical equipment of the chamber included a quadrupole mass spectrometer, a quartz thickness monitor and a high energy electron (20 kV) diffractometer. Diffraction patterns were monitored during the growth using a CCD camera on line with a PC. RHEED technique allows the deformation to be in situ registered as a variation in the size of the in-plane lattice constant ($a_{\|}$). To do that, variations in the intensity of the diffraction pattern was recorded along the line going across the streaks and bulk spots. Fig. 1 shows in plane constant lattice $a_{\|}$ of Ge film relative to the silicon lattices as a function of effective thickness of the growing layer [9]. Comparison of the dependence with the phase diagram and diffraction pattern makes it possible to identify the ranges corresponding different phases of the growth of Ge film on the Si(100) surface. In is seen indeed in the plot that the lattice constant of the Ge film approaches gradually that of the bulk material. The change in $a_{\|}$ is 4% that coincides with the mismatch of lattice constants of Ge and Si.

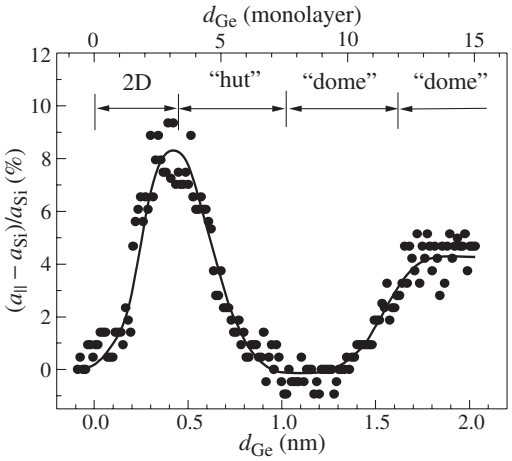

Fig. 1. In plane constant lattice $a_{\|}$ relative to the silicon lattices as a function of effective thickness of the Ge growing layer.

Relaxation of elastic strains in the silicon film grown over the germanium layer was identified similar way. Variations in the in plane lattice constant were determined from the RHEED pattern both during the formation of the germanium layer and the following silicon layer, while the germanium layer could be of different morphological state. That was achieved by stopping the germanium deposition at certain stages in accordance with the dependence shown in Fig. 1. During the measurements, the substrate was at the temperature of 500 °C. Fig. 2 shows the dependence of changes in the in-plane lattice constant with respect to the initial value (silicon) during the growth of germanium (0.6 nm) and silicon (50 nm) layers. The vertical line divides the regions of Ge and Si growth. The germanium layer thickness corresponds to the value at the maximal change in parameter $a_{\|}$ and to the region of transition from growth of the continuous wetting layer to formation of "hut"-clusters. As the silicon layer grows over the germanium layer, parame-

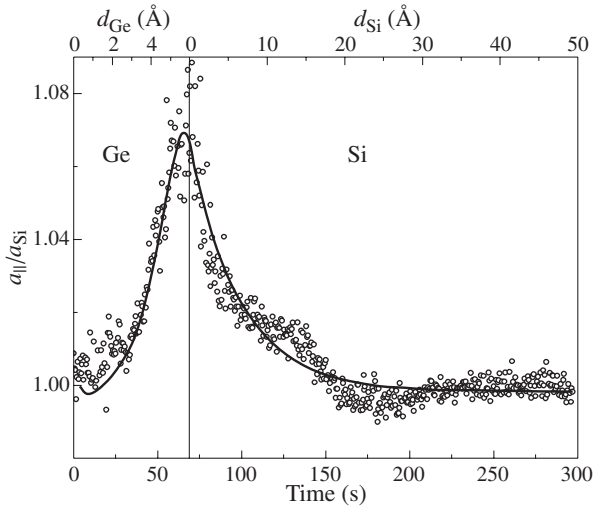

Fig. 2. In plane constant lattice $a_{\|}$ relative to the silicon lattices as a function of thickness of the Ge (0.6 nm) and Si growing layer.

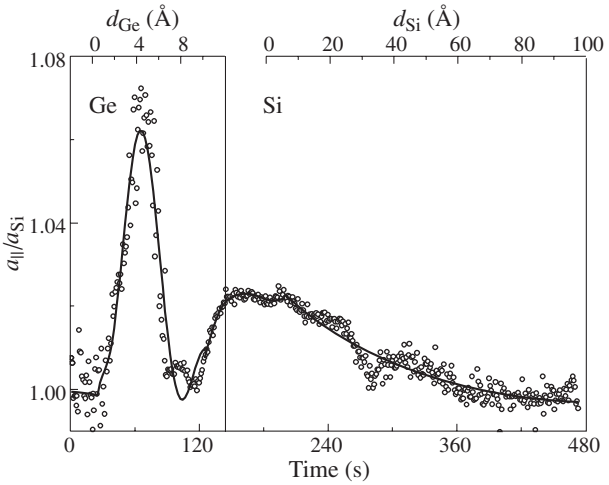

Fig. 3. In plane constant lattice $a_{\|}$ relative to the silicon lattices as a function of thickness of the Ge (1.2 nm) and Si growing layer.

ter $a_{\|}$, which tends progressively to the value characteristic of the bulky material, illustrates the process of elastic strains relaxation. The full relaxation of elastic strains in the silicon film, which are caused by the presence of 4 germanium monolayers, needs the silicon layer not thicker than 2.5 nm. Fig. 3 shows how the in plane lattice constant varies during the growth of 8 germanium monolayers and the subsequent silicon layer. This process relates to the formation of "hut" and "dome" islands on the germanium surface and to the start of plastic relaxation in the germanium layer. In this case, the required thickness of the silicon layer for strain relaxation is 10 nm. The presence of islands on the germanium surface causes considerable deformations in the crystal lattice, and the silicon layer must be much thicker to provide strain relaxation.

Acknowledgement

The work is supported by the Russian Foundation for Basic Research (Grants 03-02-16468 and 03-02-16506) and INTAS (Grant 03-51-5051).

References

[1] A. I. Yakimov *et al*, *J. Appl. Phys.*, **89**, 5676 (2001).
[2] A. I. Yakimov *et al*, *Semiconductors*, **37**, 1345 (2003).
[3] L. Kubler *et al*, *Appl. Phys. Lett.*, **73**, 1053 (1998).
[4] A. Ohtake *et al*, *Phys. Rev. Lett.*, **84**, 4665 (2000).
[5] A. I. Nikiforov *et al*, *Mat. Sci. Eng. B*, **89**, 180 (2002).
[6] F. Liu, M. G. Lagally, *Surf. Sci.*, **386**, 169 (1997).
[7] M. Miura *et al*, *Thin Solid Films*, **369**, 104 (2000).
[8] L. Kubler *et al*, *Appl. Phys. Lett.*, **73**, 1053 (1998).
[9] A. I. Nikiforov *et al*, *Thin Solid Films*, **380**, 158 (2000).

13th Int. Symp. "Nanostructures: Physics and Technology"
St Petersburg, Russia, June 20–25, 2005

Influence of lateral size of Ge nanoislands on confined optical phonons: Raman study and numerical modelling

D. A. Orekhov, V. A. Volodin, M. D. Efremov, A. I. Nikiforov, V. V. Ulyanov and O. P. Pchelyakov
Institute of Semiconductor Physics of SB RAS, pr.ak.Lavrentjeva 13, Novosibirsk 630090, Russia

Abstract. Ge nanoislands grown on Si (111) substrate with submonolayer Ge coverage were studied using Raman spectroscopy. Comparative analysis of the experimental Raman spectra and the calculated ones was carried out in 3-D model for the Ge nanoislands of triangle forms with 1 and 2 bilayers thickness containing from four up to several hundreds Ge atoms. The influence of lateral island size on Raman scattering of system Ge nanoislands/silicon matrix is defined.

Introduction

A lot of attempts to create Si/Ge heterostructures with enhanced opto-electronic properties have been made since beginning of 90-th. Traditionally, Ge quantum dots (QDs) are formed as a result of structural reconstruction of stressed system in order to minimize elastic energy (Stranski–Krastanow mechanism) [1]. It is known, that on (7×7) reconstructed Si (111) surface Ge nanoislands are formed at submonolayer Ge deposition [2]. So, it is interesting to study the nanoislands formation at early stages of Ge deposition.

1. Experimental

The experimental samples were grown using molecular beam epitaxy (MBE) technique. The used MBE setup was described elsewhere [1]. On previously standard cleaned Si (111) substrate the buffer Si layer (50 nm) was grown at temperature 700 °C. According to RHEED data, the surface was (7x7) reconstructed. Then, the 20 period Ge(0.3 bilayer)/Si(4 nm) heterostructure was grown at temperature 400 °C. The thickness of Ge bilayer (BL) is 0.327 nm, it contains 1.56×10^{15} atoms/cm^2, the growth rate was 1.5 BL/min both for Ge and Si.

The Raman spectra were registered at room temperature with excitation by 514.5 nm Ar laser line. The quasi-backscattering geometry was used, the polarization of scattered light was not analyzed. Due to small total value of Ge the Raman signal from Ge nanoislands were extremely small (3 orders of magnitude lower than LO-phonon signal from Si substrate), so the accumulation of several scanning spectra was necessary to improve signal/noise ratio.

For interpretation of the experimental Raman spectra the calculation of phonon dispersion and Raman spectra were made. The calculations of the phonon frequencies and the vectors of atomic displacements had been made within the frame of extended Born-von-Karman model. The force constants in the model were obtained using approximation of calculated phonon dispersion and the data of neutron scattering for bulk Ge [3]. The unit cells were built in mass substitution model. The Raman spectra were calculated using the bond polarisability model of Wolkenstein [4].

2. Results and discussion

The Raman spectra of an experimental sample and Si (111) substrate in Stokes region are shown in Fig. 1. For sample, containing Ge nanoislands, on the background of 2 transversal acoustical phonon scattering from Si substrate [5] a peak is observed. The peak is related to scattering by optical vibration

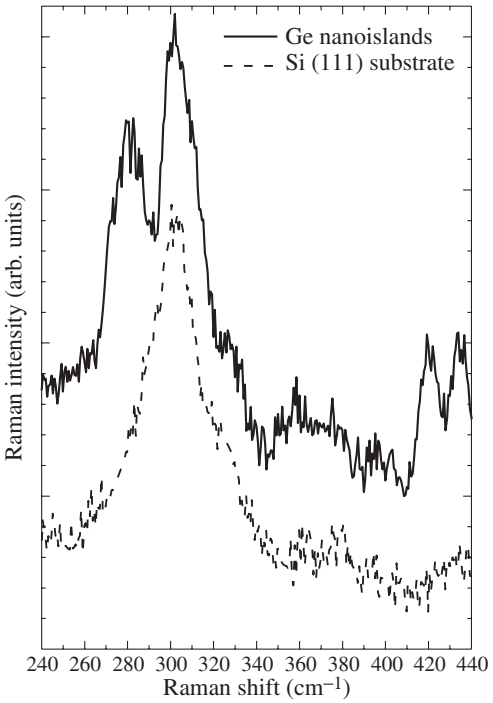

Fig. 1. Experimental Raman spectra of Ge nanoislands and Si (111) substrate.

of Ge-Ge bonds (about 280 cm^{-1}), the frequencies of longitudinal optical (LO) and transversal optical (TO) phonons in bulk Ge is 302 cm^{-1}, so, such shift may be caused by confined effects in Ge nanoislands.

In the area about 420 cm^{-1} there are Raman peaks connected with scattering on vibration of Ge-Si bonds. To analyze the Raman spectra the signal from Si substrate was substracted. The result is shown on Fig. 2.

According to direct STM data, the Ge adatoms form on Si (111) (7×7) reconstructed surface nanoislands of triangle shape [2]. At low deposition rate (about 10^{-3} BL/min), almost all nanoislands have thickness of 3 BLs [6]. With increase of the deposition rate the number of Ge nanoislands with thickness 1–2 BLs increases, and, approximating the dependence [2] to our rate we can conclude, that about 2/3 Ge nanoislands have thickness 1 BL, and the rest of them — 2 BLs.

Also according to STM data, with increase of the deposition rate the density of Ge nanoislands increases [6] (and, subsequently, lateral sizes of them should decrease). So, in our case we should have dense array (up to 10^{13}/cm^2) Ge nanoislands with thickness 1–2 BLs.

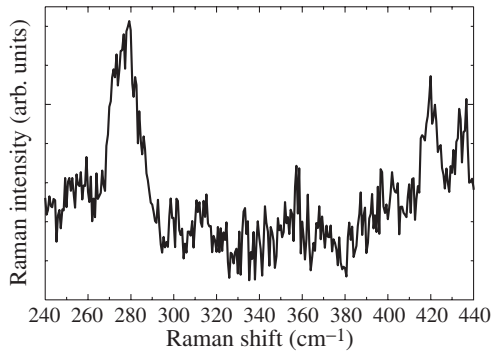

Fig. 2. Raman spectrum of Ge nanoislands (substrate signal is subtracted.)

The modeling of Raman spectra of such clusters was carried out. The results are shown on Figs. 3 and 4. The calculated spectra were normalized by number of Ge atoms. The smallest Ge cluster (curve 1, Fig. 3) contains 4 Ge atoms, the next cluster contains 9 Ge atoms (curve 2, Fig. 3), and so on.

On Figs. 3 and 4 one can clearly see the influence of lateral optical phonon confinement on Raman spectra. The influence of lateral confinement is essential for nanoislands with lateral sizes 2–3 nm and lesser. The influence of mechanical stress in Ge clusters was not taken into account. The stress should shift the experimental Raman peaks to higher wavenumbers.

The broad experimental peak on Fig. 2 can be interpreted as contribution in Raman scattering of Ge nanoislands containing different numbers of Ge atoms — from 4 up to several tens. The relatively big Ge nanoislands with thickness 2 BLs (curves 3–8 on Fig. 4) should give contribution in Raman signal at wavenumbers about 290 cm^{-1} and higher. In experimental spectrum (Fig. 2) there is practically no such high wavenumber signal. So, one can assume, that for our growth temperature and deposition rate, the Ge adatoms form small nanoislands mainly with 1 BL thickness. As one can see, even for the case of the thinnest Ge layers (1 BL), if there was no lateral confinement, the position of Raman peak is about 290 cm^{-1}. It is because, that for (111) surface mainly TO-like phonon modes are Raman active. The dispersion of TO phonons is relatively weak, and its frequencies are less sensible to layer thickness. So, in this case the lateral confinement begins playing essential role. Because in small Ge clusters a lot of Ge atoms are on the Ge-Si interface, the contribution of Ge-Si bonds in Raman spectrum is essential

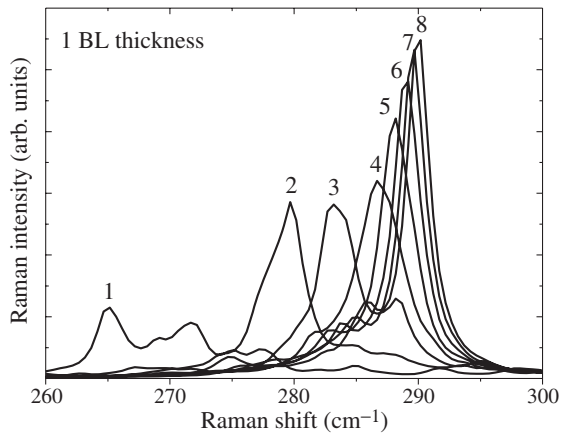

Fig. 3. Calculated Raman spectra of Ge nanoislands of 1 BL thickness. The number of curve is the lateral size of triangle Ge nanoisland in Ge-Ge bond length units.

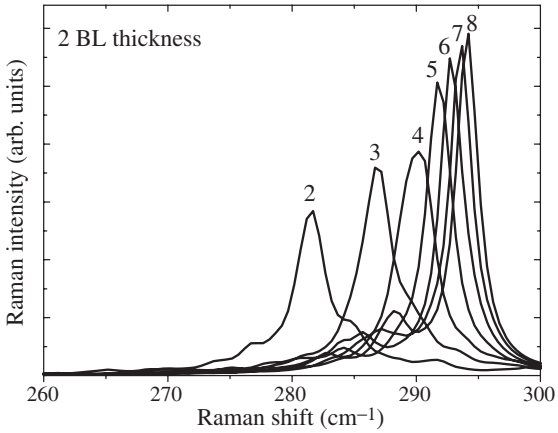

Fig. 4. Calculated Raman spectra of Ge nanoislands of 2 BL thickness. The number of curve is the lateral size of triangle Ge nanoisland in Ge-Ge bond length units.

(Fig. 2).

3. Conclusions

The influence of lateral confinement in small Ge nanoislands on optical phonon modes frequencies was observed for the first time. It was demonstrated, that analysis of Raman spectra can be effective tool for analysis of small semiconductor clusters.

Acknowledgements

The work was partly supported by RFBR (Grant No. 03-02-16506) and President Grant for leading scientific school No. 533.2003.2. Authors are thankful to Dr. S.A. Teys for helpful discussions.

References

[1] O. P. Pchelyakov *et al*, *Semiconductors*, **34**, 1281 (2000).
[2] S. A. Teys and B. Z. Olshanetsky, *Phys. Low Dim. Struct.*, **1/2**, 37 (2002).
[3] G. Nelin and G. Nilsson, *Phys. Rev. B*, **5**, 3151, (1972).
[4] *Trends in Nanotechnology Research*, M. D. Efremov, V. A. Volodin *et al*, (New York, Nova Science Publishers Inc., 145, 2004).
[5] A. V. Kolobov, *J. Appl. Phys.*, **87**, 2926, (2000).
[6] S. A. Teys *et al*, STM and related Techniques: 12th International Conference, p. 775, (2003).

13th Int. Symp. "Nanostructures: Physics and Technology"
St Petersburg, Russia, June 20–25, 2005

Stable Ge and Si nanoclusters within half-unit cells of Si(111)-7×7 surface

I. G. Neizvestny, K. N. Romanyuk, N. L. Shwartz, S. A. Teys, A. V. Vershinin, *Z. Sh. Yanovitskaya* and A. V. Zverev

Institute of Semiconductor Physics RAS SB, Novosibirsk, 630090, Russia

Abstract. Investigation of a minimal stable nucleus on Si(111)-7×7 surface was fulfilled by interatomic potential calculations and STM image analyses. Potential relief for adatom diffusion through this surface was calculated using Tersoff potential. Calculations demonstrated that a tetramer formed in the center of 7×7 unit cell after low deposited dose may be considered as a minimal stable nucleus on Si(111)-7×7 surface.

The growth of Ge on Si(111) has received much attention through fundamental studies and technological applications. The idea of adsorption on the Si(111)-7×7 substrate as a template for uniform Ge nanoscale islands formation was proposed in [1]. This idea was based on the results in the homoepitaxial growth on Si(111)-7×7. To describe correctly atomic processes on reconstructed surface one has to know potential relief of this surface. The detailed STM analysis of the initial stage of homoepitaxial process on Si(111)-7×7 may be found in [2–5]. It was shown that initial stage of nucleation is similar for Si and Ge deposition on reconstructed Si(111)-7×7 surface [6]. One of the most suitable potentials for theoretical calculations of the peculiarities of Si(111) reconstructed surface by molecular dynamics are Tersoff [7] and Stillinger–Weber potentials. Recently it was demonstrated that Tersoff potential had shown more accurate nanostructure surface reconstruction [8]. In the present work detailed investigation of the initial stage of growth on reconstructed Si(111)-7×7 surface was fulfilled by STM and examination of the stable nuclei of minimal sizes on this surface was carried out using Tersoff potential.

The experiments were performed by using ultra-high vacuum system equipped by STM method (OMICRON). The Si samples ($12 \times 3 \times 0.4$ mm^3) were cleaning and heating by passing direct current. The evaporation rate of Ge in our experiments was from 10^{-3} to 10^{-1} BL/min (1BL — bilayer of Ge(111) contains 1.44×10^{15} atoms/cm^2). The growth temperatures varied in the range of 350–500 °C. The STM observations were performed at the room temperature.

In Fig. 1 one can see STM image of Ge islands on Si(111)-7×7 surface at different moments of initial stage of growth. After 0.4 BL deposition one can see usual triangular epitaxial islands and a lot of nuclei with sizes less than one half-cell of 7×7 reconstruction (Fig. 1a). At earlier stage of deposition process (Fig. 1b) we notice that such nuclei formed well-ordered structure. It should be pointed out that these nanoislands are formed predominantly in faulted half-unit cells (HUC). This fact has been mentioned previously [9]. Fig. 1c demonstrates STM image of silicon surface after 0.02 BL deposition. At the center of the unit cell of 7×7 structure bright dot is clearly seen. The model for this nucleus, tetramer model, was suggested by Tanaka [10]. Tetramers were observed for the first time by Sato [4] during absorption process of Si atoms on Si(111)-7×7 surface. Such tetramer may be the minimal stable nucleus on Si(111)-7×7 surface.

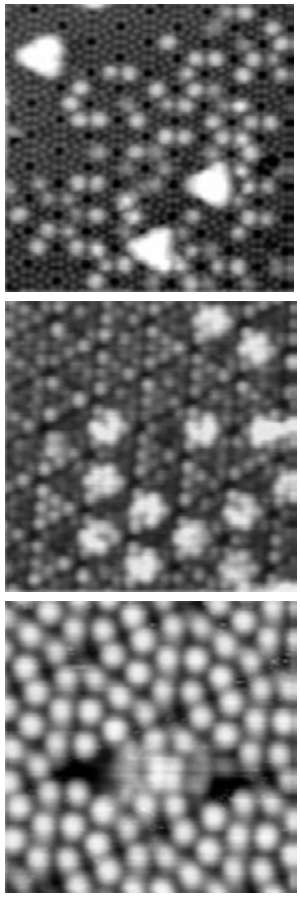

Fig. 1. STM images of Si(111)-7×7 surface during initial stage of Ge deposition: (a) 0.4 BL at the $T = 350$ °C with rate 6×10^{-3} BL/min, size 23×23 nm, sample bias voltage +2 V, $I = 0.05$ nA; (b) 0.17 BL at the $T = 380$ °C with rate 3×10^{-3} BL/min, size 14×14 nm, sample bias voltage −1.8 V, $I = 0.03$ nA; (c) 0.02 BL at the $T = 380$ °C with rate 3×10^{-3} BL/min, size 7×7 nm, sample bias voltage +1.5 V, $I = 0.03$ nA.

Calculations of energy relief of reconstructed Si(111)-7×7 surface was carried out using Tersoff potential. A silicon cluster with sizes 46×26.9×8 Å, including two unit cells of 7×7 reconstruction was used for surface energy relief modeling (Fig. 2). Cyclic boundary conditions were applied in lateral directions and in vertical direction only 3 BL have to be considered since lower atoms were in bulk positions of perfect Si crystal. Before examination of nucleation process, positions of atoms in the first reconstructed layer were defined. We

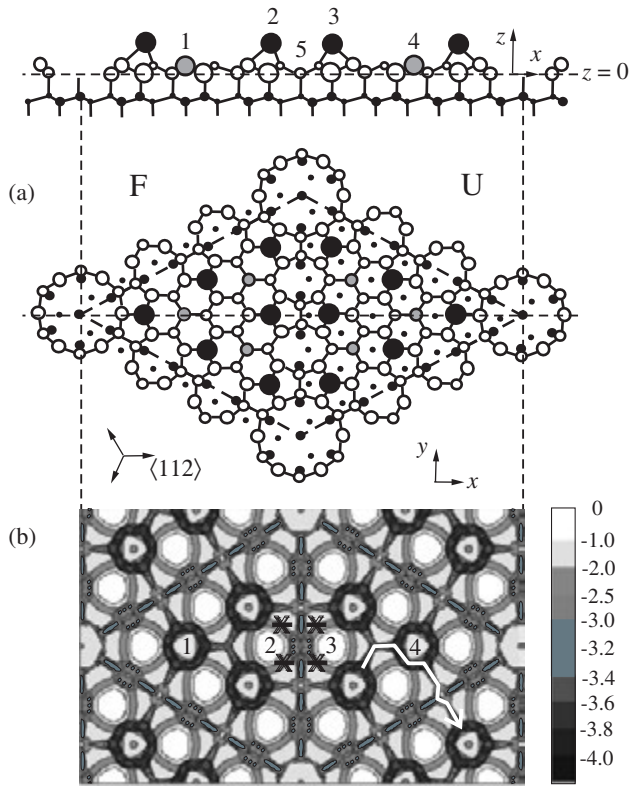

Fig. 2. Schematic illustration of Si(111)-7×7 unit cell: (a) cross-section and top view; (b) calculated energy relief for adatom over the surface of two- unit-cell size. DAS atoms in the scheme are indicated in black, rest atoms — in gray; 1, 4 — rest atoms and 2, 3 — DAS atoms along central cross-section of the model cluster. Stars in the plot of potential energy isosurfaces indicate tetramer position, darkest color corresponds to minimal energy (energy values are indicated in eV).

were interested in the distance between atoms in dimer, vertical coordinates of dimer and DAS atom (Fig. 2a), as their lateral coordinates are known in sufficient detail from STM experiments. Refinement of DAS atom positions was obtained varying mutual arrangement of DAS atoms and their nearest neighbors in vertical direction to achieve minimum of cluster energy. An energy minimum of the system is achieved when DAS atoms are located at the height 2.27 Å over the surface and their 3 nearest neighbors are located at $z = 1.03$ Å, that is 0.24 Å higher than their bulk positions. Such arrangement of atoms in the surface layer provide deep local minimum for DAS atoms — 1 eV. The cluster energy was minimal when the distance between atoms in dimer was equal to 2.45 Å and dimer atoms were at the height of the monolayer with $z = 0$ (Fig. 2). Notice that our results differ from the results of *ab initio* calculations [11] where all atoms of upper bilayer were lying lower than in unreconstructed structure.

Figure 2b demonstrates energy relief of the reconstructed surface: this is the minimal energy of the cluster plus an adsorbed atom (adatom) for different x-y coordinates. There are three possible sites for adatom localization in faulted (F) and unfaulted (U) half-unit cells (HUC) — around each rest atom. Adatom in these minima is localized at the height 3 Å. The local minima were found near dimers. So adatom may be delayed over the rest atoms and near dimers. Energy and spatial positions of adatom energy minima are the same for faulted and unfaulted HUCs. An adatom movement through 7×7 surface was investigated. White line in Fig. 2b indicates the optimal way for adatom hops between potential minima. Potential barriers for adatom hops between rest atoms in the limits of one HUC are not exceeded 0.75 eV, and to cross the boundary between HUCs adatom needs to overcome energy barrier 1.3 eV. Our results are in agreement with *ab initio* calculations and conclusions done on the base of STM examination of (7×7) reconstruction [5, 12].

Further we calculate energy of the silicon cluster with tetramer in the center of unit cell. Positions of tetramer atoms are indicated in Fig. 2b by stars. It was turned out that minimal energy of the system — silicon atom plus 4 adatoms — corresponds to situation when these four atoms are not in the local minima around rest atoms but form tetramer around the center dimer between F and U HUCs. Tetramer configuration has energy by 0.3 eV lower, than the energy of 4 non-interacting adatoms. Atoms in tetramer form a square with the side length 2.3 Å. Height of these atoms equals 3.1 Å. Potential minimum for each atom in tetramer is equal 1 eV. Two adatoms near center dimer also can be considered as nucleus, but it is less stable than tetramer. A hypothesis about mechanism of tetramer formation was set up in [4]. Authors in [4] believe that only two of Si atoms coming from the evaporation source are necessary for tetramer formation, other 2 atoms are from the substrate. However results of our calculations gives following: energy of the cluster with such tetramer is higher that is tetramer from 4 adatoms is favorable. Moreover analyzing experimental results of work [4 (Fig. 1)] we conclude that tetramers on Si(111)-7×7 surface evidently consist of 4 adsorbed atoms.

Acknowledgements

This work was supported by the RFBR (03-02-16506, 05-02-16455) and the Federal Target-Orientated Program.

References

[1] K. Masuda, Y. Shigeta, *Appl. Surf. Sci.* **539**, 113 (2001).
[2] R. Negishi, Y. Shigeta, *Surf. Sci.* **507-510**, 582 (2002).
[3] W. Shimada, H. Tochihara, *J. Crystal Growth* **237-239**, 35 (2002).
[4] T. Sato, S. Kitamura, M. Iwatsuki, *Surf. Sci.* **445**, 130 (2000).
[5] H. Uchida, S. Watanabe, H. Kuramochi, M. Kishida, J. Kim, K. Nishimura, M. Inoue, M. Aono, *Surf. Sci.* **532-535**, 737 (2002).
[6] M. Suzuki, Y. Shigeta, *Surf. Sci.* **539**, 113 (2003).
[7] J. Tersoff, *Phys. Rev. B.* **V. 37 N. 12**, 6991 (1988).
[8] C. S. Moura, L. Amaral, *Nuc. Inst. Meth. Phys. Res. B* **228**, 37 (2005).
[9] H. M. Guo, Y. L. Wang, H. W. Liu, H. F. Ma, Z. H. Qin, H. J. Gao, *Surf. Sci.* **561**, 227 (2004).
[10] H. Tanaka, T. Yokoyama, I. Sumita, *Jpn. J. Appl. Phys.* **33** 3696 (1994).
[11] K. D. Brommer, M. Needels, B. E. Larson, J. D. Joannopoulos, *Phys. Rev. Lett.* **68**, 1355 (1992).
[12] L. Stauffer, P. Sonnet, C. Monot, *Surf. Sci.* **371**, 63 (1997).

13th Int. Symp. "Nanostructures: Physics and Technology"
St Petersburg, Russia, June 20–25, 2005

Formation of Si/Ge multilayer nanostructures in Si whiskers by MBE

N. Zakharov[1], P. Werner[1], G. Gerth[1], L. Schubert[1], L. Sokolov[1,2] and U. Gösele[1]

[1] Max Planck Institute of Microstructure Physics Weinberg 2, D-06120 Halle (Saale), Germany
[2] Institute of Semiconductor Physics RAS SB, 630090 Novosibirsk, Russia

Abstract. Molecular beam epitaxy (MBE) was used for Si/Ge multilayer nanostructure formation in Si whiskers. The grown structures were investigated by Transmission Electron Microscopy (TEM). The analysis of compositional profiles shows that the highest Ge concentration is ten times lower ($x \sim 0.12$) and the half-width of the Ge distribution is 10 times wider than nominal ones. Ge doping reduces the growth rate of the whiskers.

Introduction

There is an increasing interest on the formation and the physical properties of different nanostructures supported, by possibility to explore the quantum size effects [1–4]. For this purpose the size of structural elements should be comparable with de Broglie wavelength λ of charge carriers, which is about 10 nm. Usually such bandgap engineering is implemented by local variation of composition of the crystal. One of these structures is nanowhiskers. Extensive investigations of silicon whisker's growth by the so-called "vapour-liquid-solid" (VLS) technique started already in sixties and seventies [5–8].

Recently the MBE was successfully used for Si whisker growth [9]. The MBE technique is characterized by a uniform flux of Si atoms impinge on ⟨111⟩ Si surface with deposited in advance tiny Au droplets. On the first glance no whiskers should grow however this is not a case. Whiskers grow at a constant rate collecting Si ad-atoms from surroundings. The driving force for this process is the difference between chemical potential of Si ad-atoms in distorted surface layer of Si substrate due to Si/Au solid solution formation and on the top of whisker where the elastic energy can relax [10]. The goal of this paper is, to get a better insight on this specific growth mechanism of the whiskers and possibility to incorporate thin Ge layers into Si whiskers to form Si/Ge heterostructures by MBE.

Experimental

The whiskers were grown by MBE on ⟨111⟩ oriented 5″ Si wafers with small Au droplets varied between 10 nm and 300 nm. Growth occurred at $T_S = 545\,^{\circ}$C and the constant Si and Ge fluxes amounted to 0.05 and 0.01 nm/s, respectively.

The grown structures were investigated at JEM 4010 transmission electron microscope with acceleration voltage 400 kV. Images were taken with slow scan CCD camera to keep the linearity between electron flux and output signal. To monitor the Ge distribution in vertical Si/Ge multilayer structure the images were taken with large objective aperture $\beta_{obj} = 0.01$ rad. These imaging conditions make possible to minimise influence of diffraction contrast from structural defects and elastic strains.

Results

Using this technique, we investigated formation of Si/Ge vertical heterostructure in whiskers by MBE growth. Three thin layers of Ge 0.5, 1 and 1.5 nm thick were deposited during whiskers growth in equal time interval. The Si flux was interrupted during Ge deposition. The concentration profiles

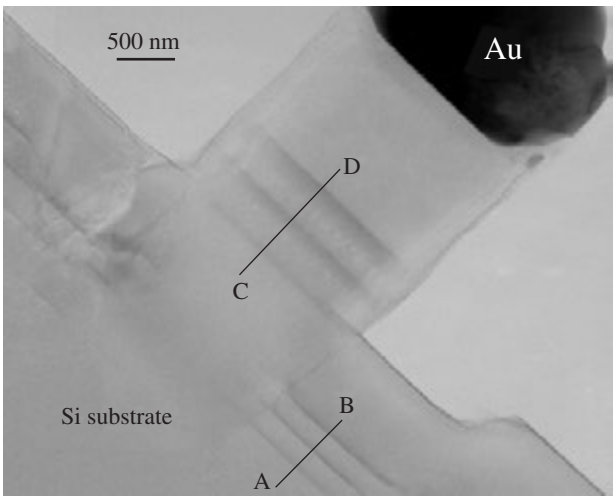

Fig. 1. Bright field TEM image of whisker with 3 Ge layers, taken with large objective aperture $\beta_{obj} = 0.01$ rad. The thickness of deposited Ge layers is 0.5, 1 and 1.5 nm.

($Si_{1-x}Ge_x$) measured along A-B in substrate and C-D in the whisker (see Fig. 1) are shown in Fig. 2a,b respectively. First of all one should pointed out that Ge deposition occurred during very short time, it was like a flash. However the peak half-widths in Figs. 2a,b are approximately 2 and 10 times larger than deposited layer thickness respectively. One can notice a big difference between Ge concentration profiles in substrate and whisker. In the first case Ge concentration almost momentary reaches maximum value after opening of Ge shutter and then drops slowly due to intermixing during the following Si growth. In the case of the whisker, the situation is practically reversed. Growth of Ge concentration x occurs relatively slow after flashing and then drops sharply. The slow growth of the Ge concentration on the first stage owes to the time needed for Ge atoms to be transported from the gold droplet surface to the Si/Au interface, where growth occurs. The half width of each Ge layer in whisker and substrate are approximately 10 and 2 times larger respectively than deposited Ge thickness.

It has been found that Ge doping decreases the growth rate of whiskers. To investigate the dynamics of this phenomenon we deposited 5 Ge layers 1 nm thick each as markers in equal time interval. Graph in Fig. 3 demonstrates decreasing of the interlayer distance from 15,5 to 11 nm with the layer number. The deposition of a larger amount of Ge ($x > 0.05$) even results in dissolution of the previously grown Si whiskers as it was observed experimentally. This finding is in contradiction with the results received by conventional CVD-VLS technique, where the $Si_{1-x}Ge_x$ whiskers with composition $x \leq 0.45$ can

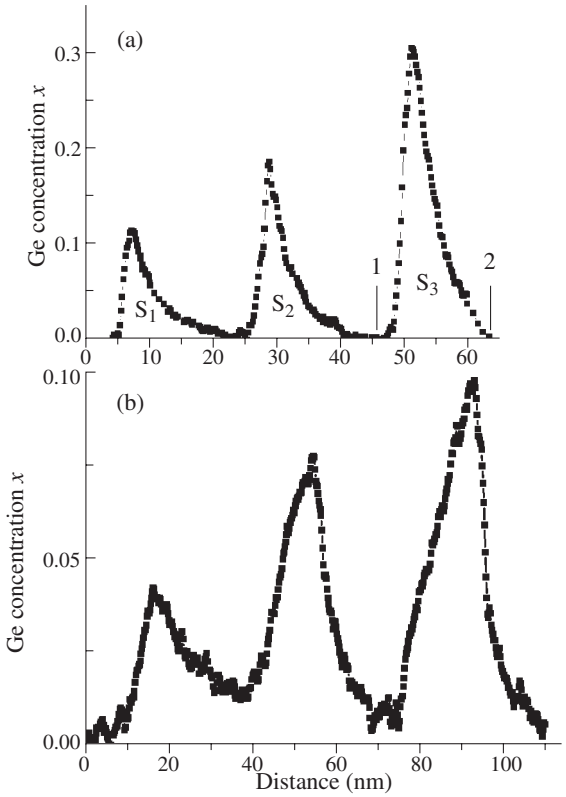

Fig. 2. Concentration profiles measured along A-B (a) and C-D (b) in substrate and whisker respectively (see Fig. 1).

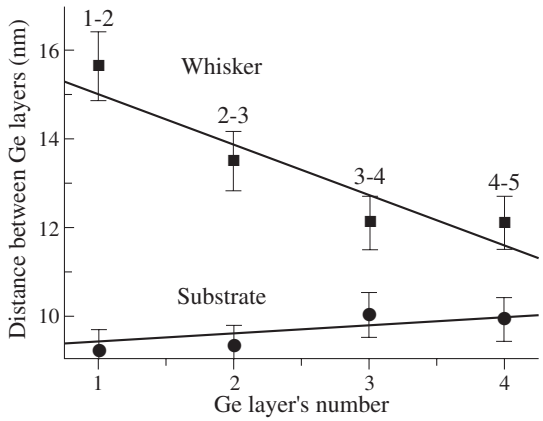

Fig. 3. Variation of Ge interlayer distances in whisker and substrate. Numbering of Ge layers starts from the substrate. The 5 Ge layers each 1 nm thick were incorporated in the equal time intervals. The Si growth rate decreases due to incorporation of Ge layers. N- (N+1)-distances between N-th and (N+1)-th Ge layers.

be grown [11]. This phenomenon can be explained by the reducing of supersaturation due to additional elastic energy introduced by Ge atoms into Si matrix [10].

Acknowledgements

This work has been supported by the SANDiE project. We thank very much A. Frommfeld, S. Hopfe and C. Munx for technical assistance.

References

[1] Y. Nakajiama *et al.*, *Appl. Phys. Lett.* **65**, 2833 (1994).
[2] N. Usami *et al.*, *Appl. Phys. Lett.* **64**, 1126 (1994).
[3] J. L. Liu *et al., Appl. Phys. Lett.* **68** (3), 352 (1996).
[4] C. M. Lieber, *MRS Bulletin* **28**, 128 (2003).
[5] R. S. Wagner *et al.*, *J. Appl. Phys.* **35**, 2993 (1964).
[6] R. S. Wagner and W. C. Ellis, *Transaction of the Metallurgical Society of AIME* **233**, 1053 (1965).
[7] E. I. Givargizov, *J. Cryst. Growth* **31**, 20 (1975).
[8] R. S. Wagner*et al.*, *Appl. Phys. Lett.* **4**, 89 (1964).
[9] L. Schubert *et al.*, *Appl. Phys. Lett.* **84**, 24 (2004).
[10] N. Zakharov *et al.*, *Appl. Phys. Lett.* (in press).
[11] A. V. Sandulova, *Dokl. Akad. Nauk SSSR* **153**, 330 (1963).

13th Int. Symp. "Nanostructures: Physics and Technology"
St Petersburg, Russia, June 20–25, 2005

Important aspects for the growth of GaN-based (opto)electronic devices on 4 inch sapphire

B. Schineller, O. Schoen, A. Alam, M. Luenenbuerger, J. Kaeppeler and *M. Heuken*
AIXTRON AG, Kackertstr. 15-17, D-52072 Aachen, Germany

Abstract. The mass production of electronic and optoelectronic devices is characterized by a strong drive to reduce the Cost-of-Ownership of production tools such as MOCVD reactors. One approach to satisfy these requests is the increase of the wafer area from the widely used 2 inch diameter to newly available 4 inch sapphire wafers, since the latter approach helps to reduce the load on the device processing pipeline in the wafer fab. However, inherent material properties such as the difference in thermal expansion coefficients between the sapphire host material and the growing layer, pose special challenges to the growth on 4 inch. This, in combination with the largely different growth temperatures required to grow the respective materials in an LED structure, can lead to bowing of the wafers during the different stages of the growth.

Introduction

The incorporation and clusterization of In in GaInN Multi-Quantum-Well (MQW) structures depends strongly on the local temperature at every spatial position on the wafer. Hence, the growth of highly uniform MQW structures demands excellent temperature uniformities across the wafer. However, strain between the sapphire substrate and the epitaxy layer due to differences in thermal expansion coefficients can lead to substantial bow. In larger wafers this bow can cause a lift-off of the substrate from the heated graphite substrate holder, causing a loss of thermal contact resulting in variations of the surface temperature.

The bow is mostly determined by the sapphire wafer thickness, the layer thickness, the actual growth temperature during a respective process step and the before mentioned unchangeable material properties. Recent studies with different sapphire wafer and layer thickness allowed us to determine an optimum wafer thickness for the application of optoelectronic devices to be in the vicinity of 650 μm. This thickness is a tradeoff between sapphire material cost, substrate stiffness, device processing and tolerable wafer bow.

Experimental

Optimization of wafer pocket depth

To assess the influence of wafer pocket depth, a number of 5 period MQW structures with ca. 5.5 μm thick GaN buffer layers were grown on identical 4 inch wafers using pockets with 0 (flat), 50 μm, 100 μm and 200 μm center depression. From room temperature photoluminescence mappings a "bow indicator" value was calculated as a figure of merit, giving an indication of the amount and direction of the bow during the MQW growth step. As can be seen from Fig. 1 an ideal wafer pocket depression of 145 μm can be calculated from these experiments which would facilitate perfect thermal contact of the wafer to the graphite under the given growth conditions.

Using these predictions, a wafer holder with 150 μm center depression was machined and tested. Growth experiments using this optimised wafer holder resulted in an excellent uniformity of the wavelength with a standard deviation of less than 1 nm at a mean wavelength of 469 nm on a 4 inch wafer without edge exclusion (see Fig. 2). To our knowledge, this represents the best ever reported uniformity value for blue emission on

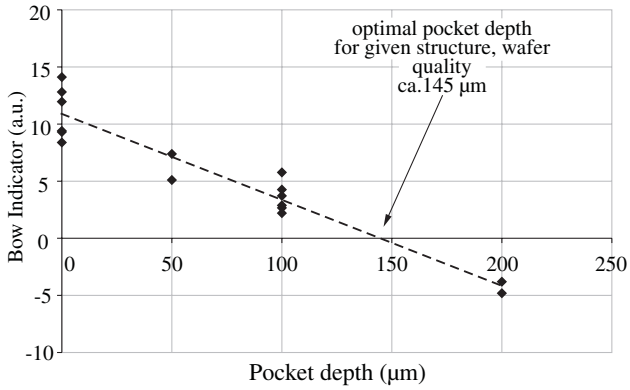

Fig. 1. Bow indicator calculated from Photo-Luminescence peak wavelength variation versus pocket depth: optimal growth result expected from pocket depth around 145 μm.

4 inch. The remaining non-uniformities of the wavelength distribution are believed to result from local strain fields originating from imperfections of the sapphire. While those strain fields are always present, the more pronounced effects of material composition and clusterization usually mask them.

Influence of sapphire off-cut on the width of the process window

To assess the influence of substrate surface off-cut from the c-plane on the temperature process window, 2 inch substrates

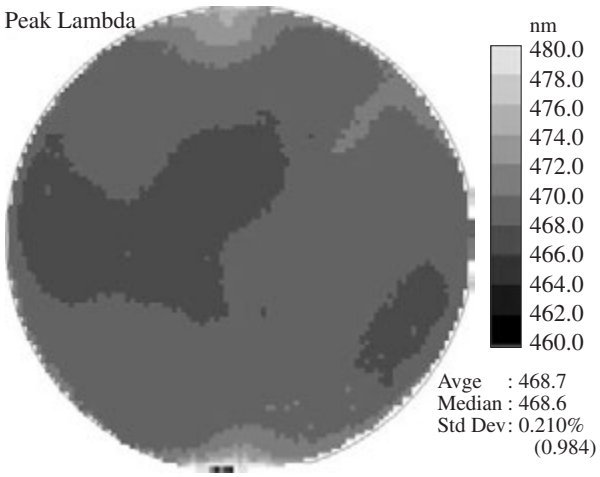

Fig. 2. Photo-Luminescence peak wavelength map of full 4 inch wafer, overgrown in 150 μm deep pocket: wavelength variation with less than 1 nm standard deviation at 470 nm average.

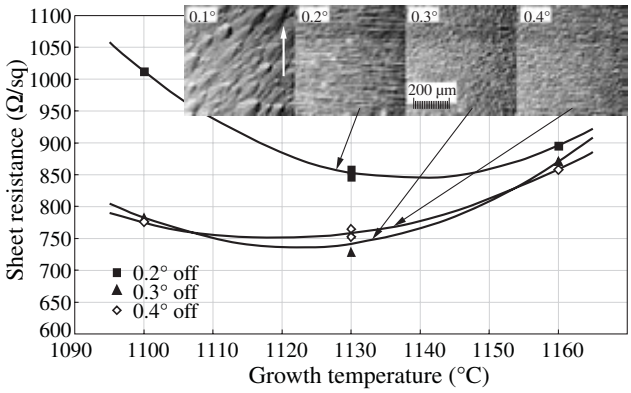

Fig. 3. Sheet resistance comparison of low doped GaN:Si samples grown at different growth temperature and from different off-cut wafer batches: growth window around optimal point broadens with increasing off-cut.

with 0°, 0.1°, 0.2°, 0.4° off-cuts towards the m-plane and 0.3° towards the a-plane were used. GaN single layers were grown at 1100 °C, 1130 °C (optimum) and 1160 °C to scan the temperature sensitivity of the growing layer. Fig. 3 shows the surface morphology of the layers (all photos for layers grown at 1130 °C; general appearance similar for 1100 °C and 1160 °C samples). As can be seen, terraces can be observed for off-cuts of 0.2° and higher. This growth of terraces can be traced to the off-cut of the substrate, as can be seen from the 0.3° sample which exhibits terraces which are rotated by 60° (a-plane). Off-cuts of 0.1° and below (exact oriented material not shown but similar to 0.1°) yield material with rough and irregular surfaces. In addition to the morphological studies, contactless sheet resistance measurements were performed using a Lehighton sheet resistance mapper. As can be seen, off-cuts of 0.3° and higher yield the most stable results, while a quite strong dependence of the resistance on the wafer temperature can be observed for samples with off-cuts of 0.2° and lower. The sheet resistance values for the 0.1° and 0° sample are not given for reasons of clarity, since they were up to 1 order of magnitude higher and their dependence on growth temperature was very strong. Hence, it can be deduced that material of 0.3° and 0.4° off-cut has a wider process window. By this reasoning it is less susceptible to slight temperature changes during growth and allows higher tolerable temperature gradients across the wafer due to wafer bow while still maintaining good layer quality. It is, therefore, the preferred material for the growth on 4 inch.

Conclusion

We investigated the design criteria for MOCVD hardware and developed a tool for the straightforward optimization of the hardware to a given device structure and process. The design rules were verified for the growth of a 5 period MQW structure emitting in the blue spectral range. Unprecedented wavelength uniformities of less than 1 nm standard deviation without edge exclusion were achieved on 4 inch. In addition, the process windows for sapphire substrates with different off-cuts from the c-plane were investigated. Morphological and electrical studies show that off-cuts of 0.3° and 0.4° offer the broadest temperature process window for the growth of GaN making it the ideal substrate material for the growth of electronic and optoelectronic device structures, especially on 4 inch.

13th Int. Symp. "Nanostructures: Physics and Technology"
St Petersburg, Russia, June 20–25, 2005

Surface-plasmon-related enhancement of luminescence in InN

T. V. Shubina[1], D. S. Plotnikov[1], Ya. V. Terent'ev[1], D. A. Vinokurov[1], N. A. Pihtin [1], I. S. Tarasov[1], S. V. Ivanov[1], J. Leymarie[2], A. Kavokin[2], A, Vasson[2], H. Lu[3], W. J. Schaff[3], B. Monemar[4] and P. S. Kop'ev[1]

[1] Ioffe Physico-Technical Institute, St Petersburg, Russia
[2] LASMEA-UMR 6602 CNRS-UBP, 63177 AUBIERE CEDEX, France
[3] Department of Electrical Engineering, Cornell University, Ithaca NY 14507, USA
[4] Linköping University, S581 83 Linköping, Sweden

Abstract. We report on complicated nature of infrared luminescence and absorption in narrow-gap InN films, whose extraordinary properties, such as sharpness of an absorption edge and enhancement of a higher-energy part of emission having noticeable p-polarization, can be related to surface plasmons excited in metal-like regions.

Introduction

Recently, it has been reported that strong enhancement of photoluminescence (PL) intensity takes place in InGaN quantum wells covered by metal films [1]. This phenomenon, arising due to the coupling of recombining carriers with surface plasmons, can provide breakthrough in efficiency of the white LEDs. Emission in InN demonstrates some unusual characteristics, such as a weak dependence on temperature and pressure, along with high resistance to irradiation [2]. Our previous studies had shown that the emission is strongly enhanced in a vicinity of metallic indium nano-clusters, spontaneously formed within InN layers [3]. Such extraordinary properties attract our attention to surface plasmonic effects which could take place near indium inclusions or other metal-like non-homogeneities in InN.

In the paper, we report on results of comprehensive studies of InN films and demonstrate that their particular optical properties can be related to the surface plasmons.

1. Experimental

The high-quality InN layers were grown by MBE without the massive In inclusions. The films have the electron concentration density n varied in the $(0.6-2.7) \times 10^{18}$ cm^{-3} range. Details on energy dispersive x-ray (EDX) analysis, scanning electron microscopy (SEM) and thermally detected optical absorption (TDOA) studies of these layers have been described elsewhere [4]. According to the EDX, all films were In-enriched, and exhibited very strong emission below 0.7 eV. This permitted us to measure PL excitation (PLE) at 20 K using a PbS detector and a tungsten lamp, though with collection of a signal during several hours. Selective PL excitation was done using 9 semiconductor laser diodes with wavelengths varied from 809 up to 1760 nm; other PL studies exploited the 809 nm laser line. Magnetic fields up to 4 T were applied in the Faraday geometry parallel to the structure growth axis.

2. Surface plasmons in an InN:In composite

The surface-plasmons can appear at a metal interface if $\epsilon_1(\omega) + \epsilon_2(\omega) = 0$, where $\epsilon_{1(2)}$ is a real part of a dielectric function of metal (medium). In a vacuum, surface plasmons in indium [5] arise at $\omega_p = 8.65$ eV, below the bulk plasma energy (11.2 eV), determining the Mie resonances — multipolar electron excitation in a volume, studied previously in InN with the In clusters [3]. Accordingly to the effective medium theory [6], energy of both bulk and surface electron excitations can be shifted towards an infrared range in a metal/semiconductor composite. The surface plasmon energy of ellipsoidal clusters can be roughly estimated as $\omega = \omega_p * L_m$, where L_m is the depolarization factor [7]. The parameter may be as small as 0.07–0.1 for the oblate nano-inclusions [3,8]. Thus, the surface plasmons in the InN:In composite may be in the 0.6–0.8 eV range, i.e. be resonant with optical transitions in the narrow-gap material.

3. Results and discussions

In the layers, the TDOA spectroscopy reveals an onset of absorption at ∼0.7 eV, however with a dramatically sharp resonance-like edge, which is significantly steeper than an ideal edge calculated for the 0.7-eV-band-gap material [9] (Fig. 2). It appears in the layers, which are far above the Mott transitions, keeping the exciton resonances out of consideration. The feature is especially pronounced in a thinnest layer, where the oblate In nano-clusters are visible at the bottom interface (Fig. 1a). These TDOA findings are supported by results of selective excitation by the lasers of the different wavelengths (not presented here). They showed that the maximum of the PL intensity in the layers corresponds to the excitation at ∼1.0-1.2 eV. Thus, the edge resonance seems to be extrinsic and may be considered as manifestation of the surface plasmons.

Low-temperature emission in these films contains two com-

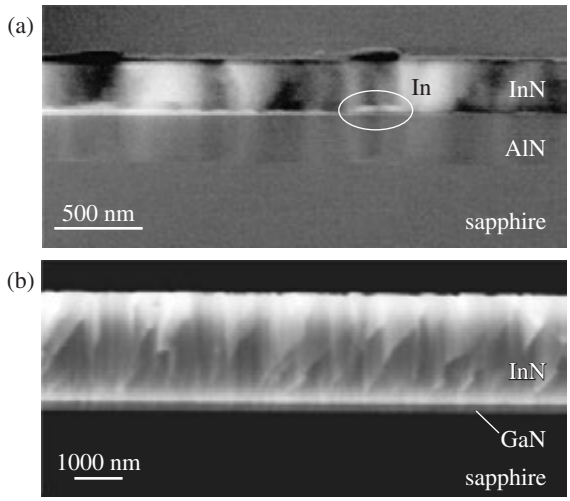

Fig. 1. Images of InN films with (a) $n = 2.7 \times 10^{18}$ and (b) $n = 0.6 \times 10^{18}$ cm^{-3}, registered at 20 kV from a cleaved facet using back scattered electrons.

ponents with characteristic energies of 0.67 and 0.61 eV. Although their intensity ratio varies between samples, they reproducibly demonstrate specific temperature and power dependences. Whereas the former survives up to room temperature, the latter disappears at 80–100 K. With the power increase from 10 μW up to 400 mW, there is no significant shift of the line maxima, rather a redistribution of intensities in favor of the higher energy component. Both lines are saturated at high excitation power, what contradicts interpreting of the lines as the near-band-edge emission.

PL excitation (PLE) spectra, measured from the line maxima, are different for the two PL components as well. (Considering the PLE results, one should take into account the low power of the lamp, which makes the excitation above ~1 eV inefficient, especially if light-emitting regions are deeply buried in a layer.) The PLE spectrum registered from 0.67 eV has a sharp edge similar to that in TDOA, whereas the edge corresponding to the 0.61 eV registration is smooth (Fig. 2). Besides, the maximum of this PLE spectrum is shifted to the higher energy. The energy gap between it and PL is about 200 meV. The value would be reasonable for deep-acceptor-involved emission, while the extremely sharp PLE edge, closely matched to the 0.67 eV PL, is rather characteristic for the emission related to the surface plasmons. Note that the real part of the indium dielectric function exhibits a strong drop near 0.7 eV, therefore one could expect a threshold-like missing resonant conditions for the surface plasmon excitation.

We studied polarization degree and angular dependences of the PL intensities, taking in mind that emission related to the surface plasmon should be enhanced with excitation wave vector k parallel to the surface, and has to be p-polarized (vector E in the plane of incidence) [7]. Indeed, the 0.67 eV PL line is most intense with excitation at a small angle θ to a surface (Fig. 3). It can be increased, as much as twice with respect to variation of the other line. The 0.67 eV line has significant p-polarization, while the 0.61 eV line is rather s-polarized. The polarization degree $P = (I_p - I_s)/(I_p + I_s)$ contradicts to the Fresnel coefficients for the p- and s-polarizations. Depending on the angle and excitation power, it can exceeds ~0.3. This is a marked result, regarding structural non-homogeneity.

Among the other findings, supporting our hypothesis on the coupling of the 0.67 eV transitions with the surface plasmons,

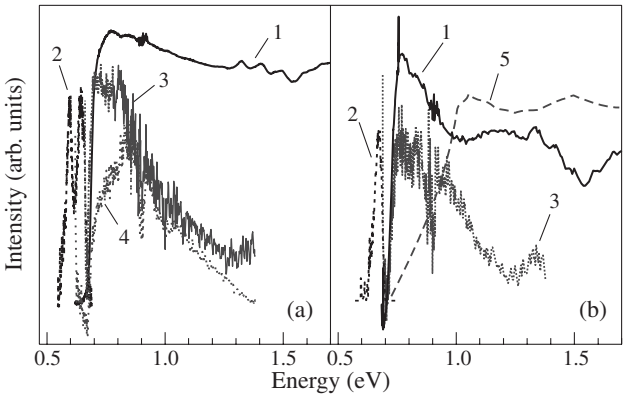

Fig. 2. Optical spectra of two MBE films with (a) both 0.67 and 0.61 eV PL components ($n = 0.6 \times 10^{18}$ cm^{-3}) and (b) only 0.61 eV one ($n = 2.7 \times 10^{18}$ cm^{-3}): 1 — TDOA; 2 — PL; 3 — PLE from the 0.67 eV PL line; 4 — PLE from the 0.61 eV PL line; 5 — calculated imaginary part of the InN dielectric function [9].

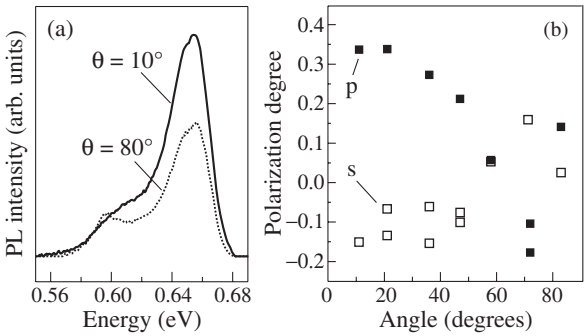

Fig. 3. (a) PL spectra registered with two different angles of excitation θ respectively to a layer surface; (b) Variation of maximal polarization degrees in the spectra on θ.

is that the 0.67 eV emission is suppressed up to 25% in its intensity by a magnetic field of 4 T. This is likely because the field hampers the collective electron oscillations. Besides, the lines have different resistance to the ion bombardment. The 0.67 eV line has been registered in a close vicinity of a SIMS crater with only a 5–6 times decrease in intensity, while the other component has vanished completely. Note that the crater area is enriched wih In droplets due to the non-congruent sputtering of InN.

Summarizing, our findings are suggestive of influence of surface plasmons on optical properties of narrow-gap InN. In particular, this can explain polarization and angular dependences of a higher-energy part of infrared emission. This phenomenon can also enhance PL intensity. The location of such plasmonic excitations, either in indium nano-clusters or in other metal-like regions, is an issue which needs additional studies.

Acknowledgements

This work has been supported in part by RFBR (Grants 04-02-17652 and 05-02-15934).

References

[1] K. Okamoto, I. Niki, A. Shvartser *et al*, *Nature* **3**, 601 (2004).
[2] J. Wu, W. Walukiewicz, K. M. Yu *et al*, *J. Appl. Phys.* **94**, 6477 (2003).
[3] T. V. Shubina, S. V. Ivanov, V. N. Jmerik *et al*, *Phys. Rev. Lett.* **92**, 117407 (2004).
[4] T. V. Shubina, S. V. Ivanov, V. N. Jmerik *et al*, *Phys. Stat. Sol.* **202**, 377 (2005).
[5] G. Jezequel, *Phys. Rev. Lett.* **45**, 1963 (1980).
[6] J. C. Maxwell-Garnett, *Philos. Trans. R. Soc. London* **203**, 385 (1904).
[7] W. Steinmann, *Phys. Stat. Sol.* **28**, 437 (1968).
[8] E. R. Brown, A. Bacher, D. Driscoll *et al*, *Phys. Rev. Lett.* **90**, 077403 (2003).
[9] F. Bechstedt, J. Furthmüller, M. Ferhat *et al*, *Phys. Stat. Sol. (a)* **195**, 628 (2003).

13th Int. Symp. "Nanostructures: Physics and Technology"
St Petersburg, Russia, June 20–25, 2005

Resonant Raman scattering in InGaN alloys

V. Yu. Davydov[1], A. A. Klochikhin[1,2], I. N. Goncharuk[1], A. V. Sakharov[1], A. P. Skvortsov[1], M. A. Yagovkina[1], V. M. Lebedev[2], H. Lu[3] and W. J. Schaff[3]

[1] Ioffe Physico-Technical Institute, St Petersburg, Russia
[2] Nuclear Physics Institute, 188350, St Petersburg, Russia
[3] Department of Electrical and Computer Engineering, Cornell University, Ithaca, New York 14853, USA

Abstract. A strong resonant behavior of Raman scattering from LO-phonons in n-InGaN alloys at excitation near the interband absorption threshold was observed for the first time. A quasi-elastic approach has been developed to describe the resonant Raman cross sectional profile in the presence of a Burstein-Moss shift of the interband optical transitions. It has been shown that a simultaneous study of absorption, photoluminescence, and Raman spectra provides reliable information about the band gap, band gap bowing, and free carrier concentration of alloys and can be efficient for the nanostructure characterization.

A recent discovery that InN is narrow gap semiconductor with $E_g \sim 0.67$ eV has widened the range of application of $In_xGa_{1-x}N$ alloys [1, 2]. However, information on fundamental physical properties of $In_xGa_{1-x}N$ alloys is scanty and contradictory. This holds even for such an important characteristic as the band gap bowing parameter, whose estimates range from 1.4 to 2.5 eV [1–4]. Useful information on optical properties of alloys can be obtained from resonant Raman scattering [5]. Due to a strong electron-phonon Fröhlich interaction in polar crystals, a drastic enhancement of light scattering from polar LO phonons occurs under resonance conditions, i.e., when the energy of the exciting photon is close to the band gap energy of a semiconductor. The goal of this work was to study the band gap behavior in the $In_xGa_{1-x}N$ alloys by resonant Raman scattering.

An $In_{0.35}Ga_{0.65}N$ film was grown on a sapphire substrate by molecular beam epitaxy [6]. X-ray and Rutherford backscattering techniques were used to measure the alloy composition. The nominally undoped film was of the n-type with a Hall carrier concentration of 1.5×10^{18} cm^{-3}.

Fig. 1 shows the Raman spectra of an $In_{0.35}Ga_{0.65}N$ film which were obtained by using different excitation energies of Ar^+ and Kr^+ lasers. Multiple scattering from the A_1(LO) phonon is clearly observed in Fig. 1a, which is typical of resonant scattering in polar semiconductors. The resonant behavior of the multi-LO-phonon scattering involving the band-to-band excitations can be used for the transition threshold estimation. Fig. 1b depicts the Raman spectra obtained with the excitations at 2.54 and 1.92 eV. It can be seen that at 2.54 eV excitation there are strong A_1(LO) and $2A_1$(LO) scatterings. However, at 1.92 eV excitation the spectrum of the $2A_1$(LO) phonon has a low intensity and in addition A_1(LO) and $2A_1$(LO) spectra are similar to the one- and two-phonon densities of states, respectively. Such a transformation of the spectra can results from changes in the Raman scattering caused by excitation above (at 2.54 eV) and below (at 1.92 eV) the absorption threshold.

The so-called quasi-elastic approach based on the known asymptotics of the scattering amplitude is the simplest approximation for description of resonant Raman scattering. In this approximation the first-order Raman cross section $\sigma(\omega)$ as a function of the exciting light frequency ω can be expressed as

$$\sigma(\omega) \sim \left| \frac{d\chi_{\beta\beta}(\omega)}{d\omega} \right|^m , \qquad (1)$$

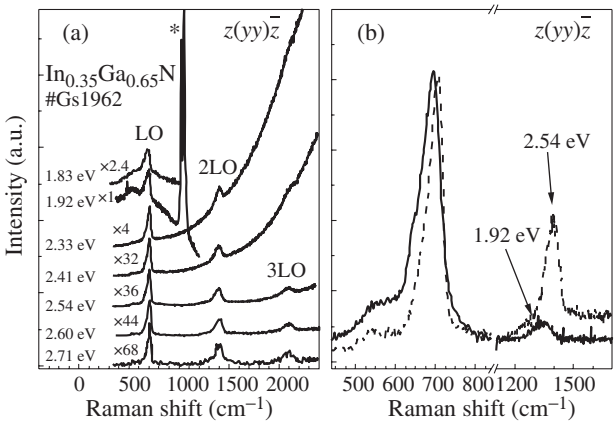

Fig. 1. Room temperature Raman spectra of $In_{0.35}Ga_{0.65}N$ (Gs1962) at different excitation energies. The spectra of the alloy were normalized to the intensity of the CaF_2 spectrum.

where the interband dielectric susceptibility is

$$\chi_{\beta\beta}(\omega) = \frac{4\pi e^2}{\hbar\omega^2 v_0} \sum_{\mathbf{p},\sigma,\sigma',v,c} \left\{ \left| \mathrm{j}^{\beta}_{c,\sigma',v,\sigma} \right|^2 n^v_{\mathbf{p},\sigma} \left(1 - n^c_{\mathbf{p},\sigma}\right) \times \left[\frac{1}{\omega - \epsilon^c_{\sigma'}(\mathbf{p}) + \epsilon^v_{\sigma}(\mathbf{p}) + i0} - \frac{1}{\omega + \epsilon^c_{\sigma'}(\mathbf{p}) - \epsilon^v_{\sigma}(\mathbf{p}) + i0} \right] \right\} . \qquad (2)$$

Here, $\mathbf{j}^{\beta}_{c,\sigma',v,\sigma}$ is interband matrix element of the electron flux between the state characterized by the spin σ in the valence band v and the state of the conduction band c with the spin σ', and $\epsilon^{c,v}_{\sigma}(\mathbf{p})$ are energies of electrons in the conduction and valence bands. For the vertical interband transitions both states are characterized by the same momentum $\mathbf{p}$ and summing in Eq. (2) is over the first Brillouin zone; v_0 is the volume of the elementary cell. The Fermi function

$$n^v_{\mathbf{p},\sigma} = n^v_{\mathbf{p},\sigma}(\epsilon^v_{\sigma}(\mathbf{p})) = \frac{1}{\exp\left[\left(\epsilon^v_{\sigma}(\mathbf{p}) - E_F\right)/T\right] + 1} \qquad (3)$$

for the valence band for the n-type crystals is equal to unity.

A high concentration of electrons influences the interband susceptibility by shifting the absorption threshold toward higher energies. The population of the conduction band depends on the electron concentration and on the temperature

$$n^c_{\mathbf{p},\sigma} = n^c_{\mathbf{p},\sigma}(\epsilon^c_{\sigma}(\mathbf{p})) = \frac{1}{\exp\left[\left(\epsilon^c_{\sigma}(\mathbf{p}) - E_F\right)/T\right] + 1} , \qquad (4)$$

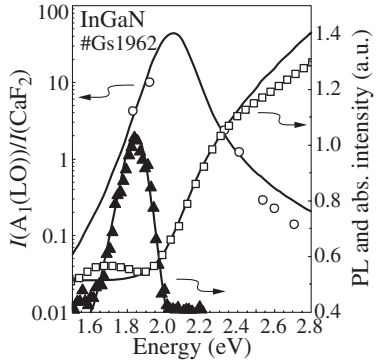

Fig. 2. Room-temperature experimental absorption spectrum (open squares), PL spectrum (solid triangles), and resonant Raman cross sectional profile (open circles) of $In_{0.35}Ga_{0.65}N$. Solid lines give results of model calculations. The Raman cross sectional profile was calculated by using Eq. (1) with $m = 5$.

where E_F is the Fermi energy for the conduction band. As a result, summing over $\mathbf{p}$ in Eq. (2) is restricted by the states of the conduction band which remain unpopulated, i.e. for which $(1 - n^c_{\mathbf{p},\sigma}) \neq 0$.

The resonant behavior of cross section given by Eq. (1) arises near the Van Hove singularities in the dielectric function. The power index m is different for different scattering mechanisms. For the first-order process, $m = 1$ for the deformation potential mechanism, $m = 3$ for the Fröehlich interaction of LO-phonons and for the phonon-plasmon modes if the momentum conservation law is fulfilled, and $m = 5$ if the momentum conservation law is broken.

In Fig. 2 the experimental data on the Raman cross sectional profile near the absorption threshold are presented together with absorption and PL spectra of this sample.

To fit the experimental Raman cross sectional profile (see Fig. 2) the imaginary and real parts of the dielectric susceptibility of Eq. (2) were calculated using the band gap E_g as a parameter and the Fermi energy of the conduction band E_F derived from the Hall concentration. The cross section was estimated in the quasi-elastic approach through Eq. (1) and taking into account both the *in*- and *out*-resonances. The quasi-elastic approximation underestimates the resonant profile width and the consideration of the two resonances allows one to determine more accurately this width. It was found that the profile maximum position coincides with energy $E_{\max} = E_g + E_F$ which can be considered as the absorption threshold in doped crystals. The best fit gives $E_g = 1.9\,\text{eV}$. Therefore, the resonant maximum position provides independent information on E_g if the free carrier concentration is known.

The model fitting of the absorption and photoluminescence spectra was performed by using the procedure described in [7], which also gives possibility to estimate the band gap E_g and the Fermi energy E_F of the conduction band. The obtained value of E_g agrees well with its estimation obtained from resonant Raman scattering. This shows that the resonant Raman experiments can be useful for studying the interband transitions of alloys.

Figure 3 depicts the literature data on E_g for $In_xGa_{1-x}N$ vs. alloy composition together with our estimate of E_g for $In_{0.35}Ga_{0.65}N$ obtained in this study. It can be seen that a bowing parameter b of 2.5 eV provides an excellent fit to the direct band gap of $In_xGa_{1-x}N$ over the entire alloy range.

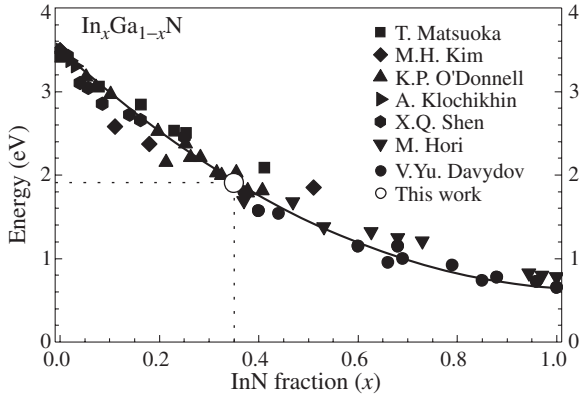

Fig. 3. E_g for $In_xGa_{1-x}N$ vs. alloy composition: full symbols — estimates from the literature data, the open symbol — our estimate of E_g for $In_{0.35}Ga_{0.65}N$, the solid line — fitting by $E_g = 3.493 - 2.843x - bx(1-x)$ with a bowing parameter b of 2.5 eV.

To summarize, resonant Raman scattering together with the absorption and PL studies was used to investigate the band gap of $In_xGa_{1-x}N$ alloys. It has been found that resonant Raman scattering can be an efficient tool for estimation of some important parameters of interband transitions. A value of 2.5 eV for the band gap bowing parameter obtained earlier in our studies of these alloys has been confirmed.

Acknowledgements

This work was partly supported by RFBR (projects No. 03-02-17562 and No. 03-02-17565) and by the Programs "Low-Dimensional Quantum Structures", "Physics of Solid State Nanostructures" and "New Materials and Structures".

References

[1] V. Yu. Davydov, A. A. Klochikhin, V. V. Emtsev, S. V. Ivanov, V. V. Vekshin, F. Bechstedt, J. Furthmuller, H. Harima, A. V. Mudryi, A. Hashimoto, A. Yamamoto, J. Aderhold, J. Graul, E. E. Haller, *phys. stat. sol. (b)*, **230**, R4 (2002).

[2] J. Wu, W. Walukiewicz, K. M. Yu, J. W. Ager III, E. E. Haller, Hai Lu and William J. Schaff, *Appl. Phys. Lett.*, **80**, 4741 (2002).

[3] M. Hori, K. Kano, T. Yamaguchi, Y. Saito, T. Araki, Y. Nanishi, N. Teraguchi, A. Suzuki, *phys. stat. sol. (b)*, **234**, 750 (2002).

[4] V. Yu. Davydov, A. A. Klochikhin, V. V. Emtsev, A. N. Smirnov, I. N. Goncharuk, A. V. Sakharov, D. A. Kurdyukov, M. V. Baidakova, V. A. Vekshin, S. V. Ivanov, J. Aderhold, J. Graul, A. Hashimoto and A. Yamamoto, *phys. stat. sol. (b)*, **240**, 425 (2003).

[5] M. Cardona, *Light scattering in solids II*, in: G. Guüntherodt, M. Cardona (Eds.), Topics in Applied Physics, vol. 50, Springer, Berlin, 1982, pp. 61.

[6] H. Lu, W. J. Schaff, L. F. Eastman and C. E. Stutz, *Appl. Phys. Lett.*, **82**, 1736 (2003).

[7] A. A. Klochikhin, V. Yu. Davydov, V. V. Emtsev, A. V. Sakharov, V. A. Kapitonov, B. A. Andreev, Hai Lu and William J. Schaff, submitted to *Phys. Rev. B*.

13th Int. Symp. "Nanostructures: Physics and Technology"
St Petersburg, Russia, June 20–25, 2005

Charge accumulation layer on GaN(0001) n-type surface induced by Cs and Ba overlayers

G. V. Benemanskaya, G. E. Frank-Kamenetskaya, V. S. Vikhnin and N. M. Shmidt
Ioffe Physico-Technical Institute, St Petersburg, Russia

Abstract. We report on first observation of charge accumulation layers for both Cs/n-GaN(0001) and Ba/n-GaN(0001) interfaces. Photoemission has been found by excitation of visible light in the transparency region of GaN. Under Cs and Ba adsorption, sharp decrease in photoemission thresholds is revealed and shown to be due to formation of an electron accumulation layer in the near-interface region. A new phenomenon is ascertained, namely, appearance of oscillation structure in spectra of photoyield. A model conception taking into account both the formation of charge accumulation layer and occurrence of multiple-beam interference in parallel-sided GaN epilayer is suggested.

Introduction

Surface properties of III-nitrides are still poorly understood and then they give rise controversy despite effective technology progress in growing of high-quality materials and their application to high power electronic, photodetectors and light emitting devices. The Cs/GaN(0001) p-type interface was investigated by conventional Auger electron, core-level, X-ray and ultraviolet photoemission spectroscopies. However, the fundamental issue concerning origin of bonding and discrepancy in adsorption effect has not yet been settled. The Cs/n-GaN, Ba/p-GaN and Ba/n-GaN interfaces are not studied. Therefore, studies of electronic properties rouse interest especially to these interfaces. It is noteworthy to point out that accumulation layers were obtained exclusively on clean InAs and InN surfaces.

1. Experimental

Measurements have been performed in situ in a vacuum of $P \sim 5 \times 10^{11}$ Torr. Samples are Si-doped (2–5) $\times\ 10^{17}$ cm^{-3} GaN epilayers of thickness $d \sim 3$–$4\,\mu$m grown on (0001) sapphire substrate by MOCVD. Prior to studies, samples are annealed in situ at $\sim 800\,^{\circ}$C. To ascertain Cs and Ba coverages, sources are accurate calibrated to dosage using original technique. The Cs and Ba overlayers are presented in monolayer (ML) units. Note that the 1 ML is defined as one metal adatom per GaN(0001) 1×1 surface atom and equal to 9.89×10^{14} atoms $\times$ cm^{-2}. The technique of photoemission yield spectroscopy (PYS) with excitation by the *s*- and *p*-polarized light has been used. PYS is based on the separation of surface and bulk photoemission due to key difference in mechanisms of the*s*- and *p*-polarized light interaction with surface states. Details of PYS can be found elsewhere [1,2,3].

2. Results and discussion

Figure 1 shows changes in the photoemission thresholds $h\nu_S$ as a function of Cs and Ba coverage on n-GaN(0001). Points of curves are obtained from an approximation of spectra $I_S(h\nu)$ recorded for each coverage. Sharp decreases in the threshold energy $h\nu_S$ down to a value of ~ 1.40 eV at Cs coverage of ~ 0.5 ML and down to a value of ~ 1.98 eV at Ba coverage of ~ 0.4 ML are observed. The equality of thresholds $h\nu_S = h\nu_P$ has been obtained for both interfaces.

Thus, the data obtained evidence that the photoemission proceeds from a quasi-metallic bulk states in space-charge region of length $L \sim 20-30$ nm near the surface, that is, an

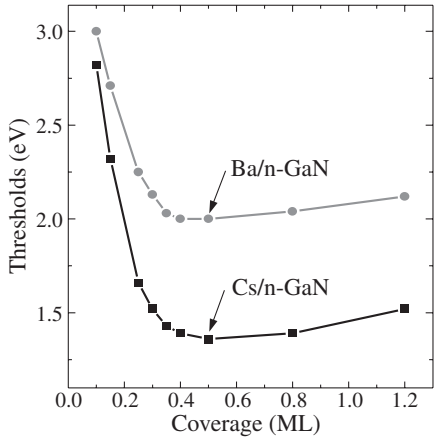

Fig. 1. Change in photoemission thresholds $h\nu_S = h\nu_P = \varphi$ as a function of Cs and Ba coverage on n-GaN(0001).

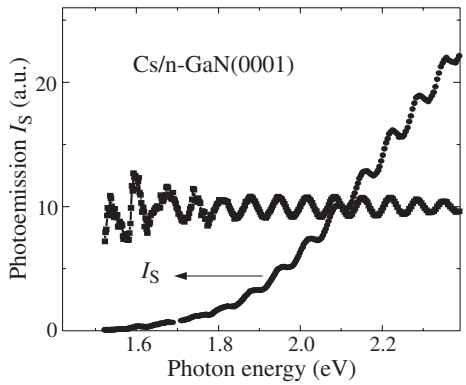

Fig. 2. The spectrum $I_S(h\nu)$ and intensity modulation spectrum separated from $I_S(h\nu)$ with the use of a computer program for Fabry–Perot interference.

electron accumulation layers induced by Cs and Ba adsorption in the close vicinity of the GaN surface have been revealed. We assume that formation of the electron accumulation layer can be explained with a view of downward band-bending when the conduction band edge at the surface lies below the Fermi level. In this case, photoemission is originated from the quasi-2D accumulation layer in the conduction band as well as from other related localized states. Then, the photoemission threshold corresponds to the work function $h\nu_S = h\nu_P = \varphi$.

Figure 2 represents spectrum of photoyield $I_S(h\nu)$ at Cs

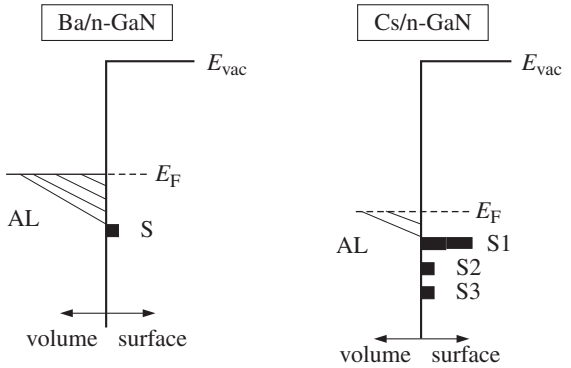

Fig. 3. Schema of interfaces at 0.7 ML of Cs and at 0.8 ML of Ba. AL-accumulation layers, 1, 2, 3 — surface states induced by Ba adsorption.

coverage of 0.5 ML. As can be seen, character of the spectrum is very unusual. The pronounced oscillation structure has been found. The latter is observed also in photoemission spectra for Ba/GaN interface. Oscillation period $\Delta \sim 0.7$ eV is constant in energy and remains unchanged at different Cs coverages. The accuracy oscillation period $\Delta \sim 0.69$ eV corresponds well to GaN sample of width $d = 3.83\,\mu$m used in experiment. To explain origin of the oscillation structure, a model taking into account both the accumulation layer and constructive interference in parallel-sided plate of GaN is suggested. It should be emphasized that both phenomena, namely, the photoemission under light excitation in the transparency region of GaN and the oscillation structure of photoemission spectra that depends on the sample width have been first observed.

Surface photoemission spectra for both the Cs/GaN and Ba/GaN interfaces have been studied at coverages up to 2 ML. These spectra reflect density of surface states. Three surface bands induced by Ba adsorption are found in spectra at 0.8 ML. Energy positions of induced surface bands are obtained at 0.15 eV (1), at 0.35 eV (2) and at 0.6 eV (3) below the Fermi level. One surface band has been observed for the Cs/n-GaN interface.

In Fig. 3 schematic diagrams of electronic structure of both the GaN surface and near-surface region are represented for Cs/n-GaN and Ba/n-GaN interfaces. It is noteworthy to point out that accumulation layer induced by Cs adsorption is more powerful than that by Ba adsorption.

In summary, we have found that Cs and Ba adsorption is dramatically affected on electronic properties of the n-GaN(0001) surface. First, the appearance of induced electron accumulation layers in the near-interface region is revealed. Until now, there is no report on III-nitride semiconductors. Second, photoemission from the accumulation layer is found to excite by visible light in the transparency region of GaN and to arise with unexpectedly large quantum efficiency. Photoemission thresholds $h\nu_S$ and $h\nu_P$ for the *s*- and *p*- polarized light, respectively, are found to coincide and to correspond to the work function. Three surface bands induced by Ba adsorption are revealed below the Fermi level. Cs-adsorption produces one surface band. Third, a new phenomenon is revealed, namely, the appearance of the oscillation structure in photoyield spectra. To explain origin of the oscillation structure, a model taking into account both the accumulation layer and constructive interference in parallel-sided plate of GaN is suggested.

Acknowledgement

This work was supported by grant 04-02-17621 of Russian Foundation for Basic Research.

References

[1] A. Liebsh, G.V. Benemanskaya, and M.N. Lapushkin, *Surf. Sci.***302**, 303 (1996).
[2] G.V. Benemanskaya, D.V. Daineka, and G.E. Frank-Kamenetskaya, *Surf. Sci* **523**, 211 (2003).
[3] G.V. Benemanskaya, V.S. Vikhnin, N.M. Shmidt, G.E. Frank-Kamenetskaya, and I.V. Afanasiev, *Appl. Phys. Lett.* **85**, 1365 (2004).

13th Int. Symp. "Nanostructures: Physics and Technology"
St Petersburg, Russia, June 20–25, 2005

Ion induced segregation of indium in InN

V. V. Bryzgalov, Yu. S. Gordeev, V. Yu. Davydov and V. M. Mikoushkin
Ioffe Physico-Technical Institute, St Petersburg, Russia

Abstract. Plasma Diagnostics of chemical composition of InN films has been developed. It was shown that all of the studied indium nitride films contain additional chemical phases besides the InN phase. Effect of generation of In metallic clusters was revealed under ion bombardment in the bulk and on the surface of InN. The effective thickness of In-segregate was found to be 1–2 ML for different samples. The revealed effect was suggested to be used for integral characterization of the structural quality of InN films.

Introduction

Recent revision of InN band gap to 0.7 eV instead of 1.9–2 eV as believed previously has turned this material into one of the most perspective for optical devices continuously covering a very wide photon energy range from the deep-UV to near-infrared region and has initiated a great activity in their research [1–2]. However, only a few research performed with the help of the surface-sensitivity methods of electron spectroscopy, which provides sophisticated information about electronic structure and chemical composition, have been reported [3]. These studies faced with two problems that seriously complicated using electron spectroscopy. The first one is a technological problem. Single-phase InN films, which can be used as a reference sample, have not been available. As a result, there are no reliable reference spectra of InN for diagnostics. Thermal and chemical instability of indium nitride is the second problem. Heating and ion etching needed in electron spectroscopy for sample cleaning strongly modifies the material. But the result of such a modification has not been clear. We present here solution of the problem of InN diagnostic by means of electron spectroscopy. Plasma diagnostics of chemical composition of InN films on the bases of electron energy loss spectroscopy (EELS) has been developed. The diagnostic allowed revealing the effect of efficient release of In atoms from the InN cites under ion bombardment followed by the creation of In- metallic clusters in the bulk and on the surface of the material.

1. Element composition of the samples under study

Three samples of indium nitride films grown in different laboratories were studied: mono-crystalline InN film (N1) grown by metal-organic molecular beam epitaxy (MOMBE) with a nitrogen plasma source [4], poly-crystalline film (N2) grown by metal-organic chemical vapor deposition MOCVD [5], and poly-crystalline film (N3) grown by rf-sputtering [6]. The carrier concentrations in the samples N1, N2, and N3 were $1\cdot10^{19}$, $4\cdot10^{20}$, and $6.5\cdot10^{20}\,\mathrm{cm}^{-3}$, respectively. Characterization of element composition of studied samples was performed by Auger electron spectroscopy (AES). Besides the composition of initial near-surface region, the absolute element concentration depth profiles were measured up to 3–6 nm by ion etching the samples (Fig. 1). The depth profiles show significant amount of carbon (10–20%) in the bulk of all of the investigated samples. According to the C KVV Auger-energy chemical shift, carbon atoms formed a separate fraction of amorphous carbon. Oxygen also was observed in the bulk of the samples (3–10%), especially in one on them (30%, N3). Moderate portion of In_2O_3 indicated that the most part of oxygen was a component of the alloy In $N_{1-x}O_x$. Nitrogen KVV Auger-spectrum showed the additional line associated with the molecular nitrogen. The molecular satellite and therefore the N_2-clusters (bubbles) were observed both in pristine samples and in the samples irradiated by ions. Two important results follow from the Auger analysis of the element composition. The first one is that the In-concentration essentially exceeds that of the nitrogen one in the near surface region of some samples before the ion bombardment. The excess indium was assumed to form In-clusters in the bulk and on the surface of pristine samples. The second result is that the In-concentration sharply increases (2 times) just after the first ion bombardment. The obvious conclusion was made that accelerated ions destroy InN. Released indium atoms diffuse and create segregates in the form of metallic clusters in the bulk and on the surface of samples. This conclusion is confirmed by increase of the contribution of those part of the In MNN Auger-spectrum whose position coincides with that of the reference sample of pure In-metal. Additional confirmation of the effect of the ion-induced indium release and segregation gives the analysis of the EEL-spectra.

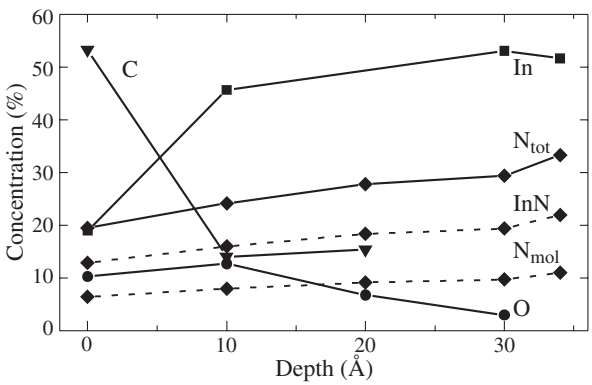

Fig. 1. Element concentration depth profiles of the sample N1.

2. Plasmon spectroscopy of "InN" and InN-reference spectrum

After removing several nanometers of the material, the research was continued with the help of EELS in "reflection-mode", that is in the experiment with electrons reflected by the surface. The energy of the primary electrons $E_0 = 1500\,\mathrm{eV}$ provided obtaining information about the near-surface area of about 2 nm thickness. Analogue of the loss function of the electron energy $\mathrm{Im}(1/\varepsilon(\omega))$, which is directly connected with dielectric function $\varepsilon(\omega)$, was used instead of the experimental EEL-spectrum in the analysis (Fig. 2). "Loss function" (LS) allows specifying

positions and intensities of the energy loss features more accurately due to subtract-ing the intense contribution of the doubly and multiply scattered electrons. The home-made computer program was used for this subtracting. Fig. 2 demonstrates decomposition of LFs of the samples N2 and N3 into LFs of different chemical phases: metallic indium, amorphous carbon and pure InN. Prominent peaks in the LF of the metallic indium and of the samples are connected with excitation of the volume and the surface plasmons. The reference LFs of the metallic indium and of the amorphous carbon were obtained for pure materials in the additional experiment. Reference LF of InN was obtained by averaging the LF picked out in the first order of the decomposition procedure for the samples N2 and N3. Fig. 3 shows these LFs and the result of their averaging. The re-producibility of the result evidences the reliability of the obtained LF of pure InN. Prominent peaks of volume and surface plasmons dominate in the LF of pure InN. The energy of the InN volume plasmon ($\hbar\omega = 14.5\,\mathrm{eV}$) is close to that ($\hbar\omega = 15.5\,\mathrm{eV}$) obtained for InN film by EELS in "transmission mode" [3], that is in passing 100 keV — electrons through film. The important information gives the relative peak intensities. High intensity of the surface plasmon of the InN phase implies that the most part of the sample surface is not covered by any atoms. Thus, In-clusters generated by ion bombardment occupy the less part of the surface, they look like system of separate clusters. Plasmon energy and LF-shape are a specific characteristic of chemical phase. Therefore LF can be used for phase identification. Fig.2 evidences the multi-phase structure of the samples. Though the most part of the metallic indium was originated from the ion bombardment, this artificial contribution can be easily removed in the analysis, and information about chemical composition of pristine sample can be obtained. The reference LF of InN can be used in diagnostics of the "InN". We mean the plasmon diagnostics giving the depth distribution of pure InN phase throughout the "InN" layers, related structures and interfaces. The obtained LF was used for quantitative estimation of the amount of In-atoms in the metallic clusters created due to ion bombardment of the material.

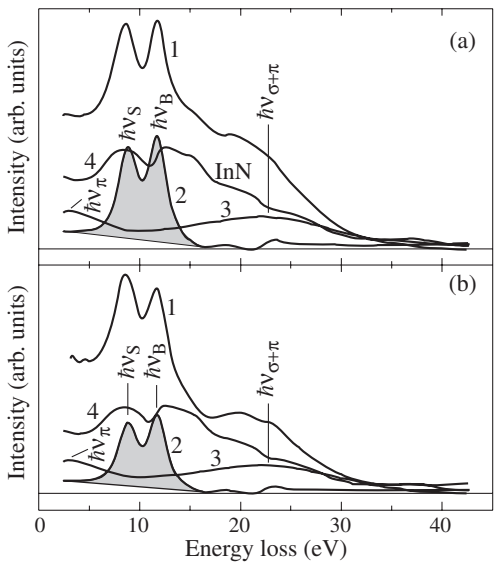

Fig. 2. 1—"Loss functions" (LFs) of the samples N2 (a) and N3 (b), 2—LF of metallic indium, 3—LF of amorphous carbon and 4—LF of pure InN.

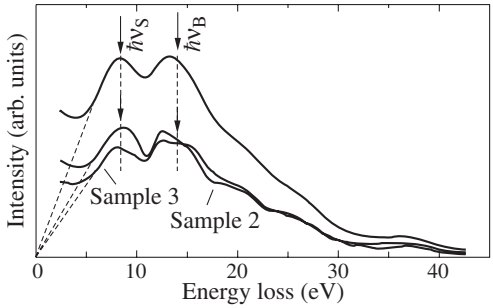

Fig. 3. 1, 2—"Loss functions" of InN obtained from the analysis of the samples N2 and N3. 3—the reference LF of InN obtained by averaging LFs 1 and 2.

This task was solved by comparing the intensity of LF of the metallic contribution into the LF of studied sample with that of the reference sample of the massive In-metal measured at the same conditions. The effective thickness of In-segregate was found to be 1–2 ML for different samples. The observed effect of the ion induced indium segregation proved to be strongly dependent on the structural characteristics of the studied samples: the worse crystalline structure and chemical homogeneity, the stronger effect and the larger portion of In-atoms in clusters. The efficiency of the effect was supposed to be connected with efficiency of the diffusion of In atoms through dislocations, phase and crystallite boundaries. Therefore, the revealed effect was suggested to be use for integral characterization of the structural quality of InN films.

3. Conclusions

EELS based Plasma Diagnostics of chemical composition of InN films has been developed. It has been shown that "InN"-films fabricated in different laboratories are multiphase. Effect of the ion-induced generation of In clusters in the bulk and on the surface of "InN" has been revealed. The revealed effect was suggested to be use for integral characterization of the structural quality of InN films.

Acknowledgement

The authors express gratitude to Dr. J. Aderhold, Prof. A. Yamamoto, and Dr. S. Butcher for supplying the InN samples for the research. The project was supported by the Russian Ministry of Education and Science ("Physics of Solid-State Nanostructures") and by the Russian Academy of Sciences ("Low-Dimensional Quantum Structures").

References

[1] V. Yu. Davydov, A. A. Klochikhin *et al*, *Phys. Stat. Sol. (b)*, **229**, R1 (2002); *Phys. Stat. Sol. (b)*, **230**, R4 (2002); *Phys. Stat. Sol. (b)*, **234**, 787 (2002).

[2] J. Wu *et al*, *Phys. Rev. B*, **66**, 201403 (2003); *J. Appl. Phys.*, **94**, 4457 (2003).

[3] K. A. Mikhoyan, J. Silcox, E. A. Alldredge *et al*, *Appl. Phys. Lett.* **82**, 1407 (2003).

[4] J. Aderhold, V. Yu. Davydov, F. Fedler *et al*, *J. Cryst. Growth*, **222**, 701–705 (2001).

[5] A. Yamamoto, K. Sugita, H. Takatsuka *et al*, *J. Cryst. Growth*, **261**, 275 (2004).

[6] K. S. A. Butcher, M. Wintrebert-Fouguet *et al*, *J. Appl. Phys.*, **95**, 6124 (2004).

13th Int. Symp. "Nanostructures: Physics and Technology"
St Petersburg, Russia, June 20–25, 2005

Tamm-like interface states in periodical ZnSe/BeTe heterostructures

A. S. Gurevich[1], V. P. Kochereshko[1], A. V. Platonov[1], B. A. Zyakin[1], A. Waag[2] and G. Landwehr[3]

[1] Ioffe Physico-Technical Institute, St Petersburg, Russia
[2] Braunschweig Technical University, 38106 Braunschweig, Germany
[3] Physikalisches Institut, Universität Würzburg, 97074 Würzburg, Germany

Abstract. Spectral dependencies of the in-plane optical anisotropy of undoped periodical ZnSe/BeTe heterostructures with nonequivalent interfaces has been studied by spectroscopic ellipsometry. Peculiarities of two different types were observed in the spectra in the range of the band gap. It was found that spectral position of the first type peculiarities is independent on the period of heterostructures. Whereas the second type ones shift to the low energies with decreasing thickness of ZnSe and BeTe layers. The observed behavior is interpreted in frame of a model, which takes into account existence of the Tamm-like interface states.

Introduction

In 1949 James firstly expressed an assumption about existence of the interface analogue of well-known surface Tamm states (Tamm levels) [1]. In spite of number of theoretical papers [2, 3] in which existence and possible energetic positions of the such "Tamm-like interface states" (IS) was discussed, there is now satisfactory experimental evidence which could indicate that there is a IS in semiconductor heterostructeres.

Recent studies of the type-II ZnSe/BeTe periodic heterostructures with nonequivalent interfaces have revealed natural in-plane optical constants anisotropy of the structures in the spectral range of the spatially direct interband transitions [4]. This effect is due to the local symmetry of the interface separating two zinc-blende substances being lower than the symmetries of the original semiconductors [5]. In the present paper the dependence of the in-plain optical anisotropy on period of heterostructure was analyzed in wide spectral range. It allows us to reveal peculiarities in the spectra, which corresponds to optical transitions between IS.

Experimental technique

The samples were grown by MBE on (100)-oriented GaAs semi-insulating substrates. Each structure contained 20 periods of ZnSe/BeTe. No purposeful doping of the studied samples was undertaken. Fig. 1 shows the band diagram of the structures.

There are free types of the typical interband optical transitions in studied structures. Namely they are: spatially direct transitions involving electrons and holes both localized in ZnSe layers (Fig. 1, DT); spatially direct transitions in BeTe layers involving electrons associated with X-valley of BeTe (DxT); and spatially indirect optical transitions (IT).

In the present paper the rotating-compensator ellipsometer [6] was used in order to measure low temperature (77 K) spectral dependencies of the relative phaseshift Δ between p and s waves upon reflection from sample. Spectral dependencies of the difference $\delta\Delta = \Delta_{[1\bar{1}0]} - \Delta_{[110]}$ were analyzed. Here quantities $\Delta_{[1\bar{1}0]}$ and $\Delta_{[110]}$ are phaseshifts measured in the case when sample axis $[1\bar{1}0]$ was parallel and perpendicular to the plane of incidence, correspondingly. Thus the quantity $\delta\Delta$ represents summarized (absorption and refraction parts) in-plain optical anisotropy.

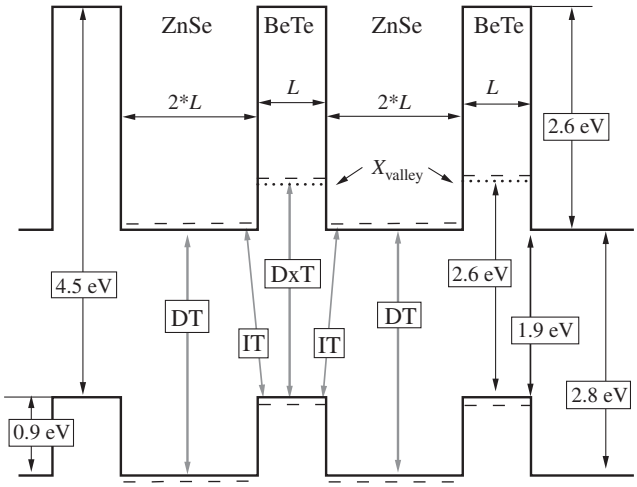

Fig. 1. Band diagram of the studied type-II ZnSe/BeTe periodical heteroctructures.

Results and discussion

Figure 2 represents the spectral dependencies of $\delta\Delta$ obtained for structures with thickness of ZnSe/BeTe layers 230 Å/115 Å, 100 Å/50 Å, 40 Å/20 Å and 30 Å/15 Å. There are two peculiarities in the spectra caused by spatially direct interband optical transitions in ZnSe layers (DT, Fig. 2 and Fig. 1) and in the BeTe layers (DxT, Fig. 2 and Fig. 1).

These peculiarities shift to the higher energies with heterostructure period decreasing due to increasing of carrier confinement energy. Because of small oscillator strength of the indirect optical transitions corresponding peculiarities cannot be observed in spectra at the liquid nitrogen temperature.

Three peculiarities (BL, GL and YL, Fig. 2) were observed in spectral range of the band gap of the structures. It's clearly seen that in comparison with spatially direct exitonic transitions, their spectral positions is independent on the period of heterostructures. Another one bright peculiarity lying in the energy gap was observed at the energies being lower than spatially indirect interband transitions (RL, Fig. 2). This line shifts to the low energies with decreasing period of the structures.

Four observed peculiarities — BL, GL, YL and RL can not be attributed to the interband optical transitions due to their spectral position as well as absence of high energy shift with heterostructures period decreasing. Also the amplitude of these

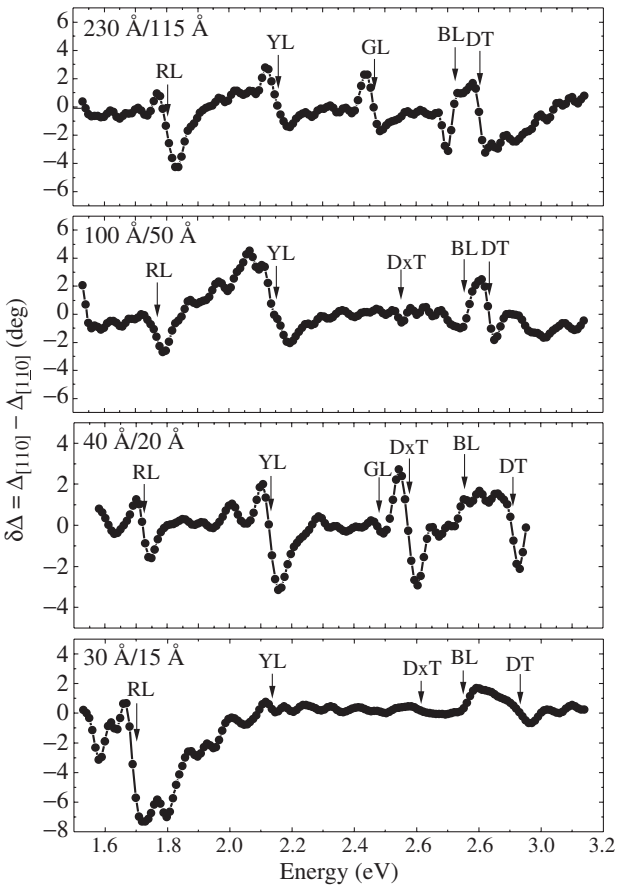

Fig. 2. Spectral dependencies corresponding to the in-plain optical anisotropy for the periodical ZnSe/BeTe heterostructures with different period.

peculiarities is comparable to the amplitude of interband optical transitions. Finally, these peculiarities can not be attributed to some structural properties (islands etc.) of the individual heterojunction because they were observed for the set of undoped samples with different period and each sample contained high enough number of heterojunctions.

The observed experimental behavior points to existence of the Tamm-lke interface states in the studied ZnSe/BeTe heterostructures. Based on spectral position of observed peculiarities as well as theoretical results, which predicts possible energetic positions of the IS [3], we propose the following scheme of optical transitions between IS — Fig. 3. Electron IS ie1 is caused by offset of conduction band associated with Γ point (E_c, solid polyline). IS ie2 is caused by offset of X-valley of conduction band (E_c^X, dotted polyline). Hole IS ih1 and ih2 are caused by offset of heavy and light hole valence band (E_v solid polyline) and offset of spin-orbit splitted valence band (E_v^{SO}, dash-dotted polyline) correspondingly. In the frame of proposed model optical peculiarities RL are caused by optical transitions involving IS ie1 and ih1 (Fig. 3), peculiarities BL are caused by transitions between IS ie1 and ih2, and peculiarities GL are caused by transitions involving IS ie2 and ih1. For explaining YL we should assume the existence another one IS — ieh. This IS, unlike electron and hole IS — sattelites of the conduction and valence bands, conforms to the center of the band gap of the heterostructure, thus being the states of a mixed kind.

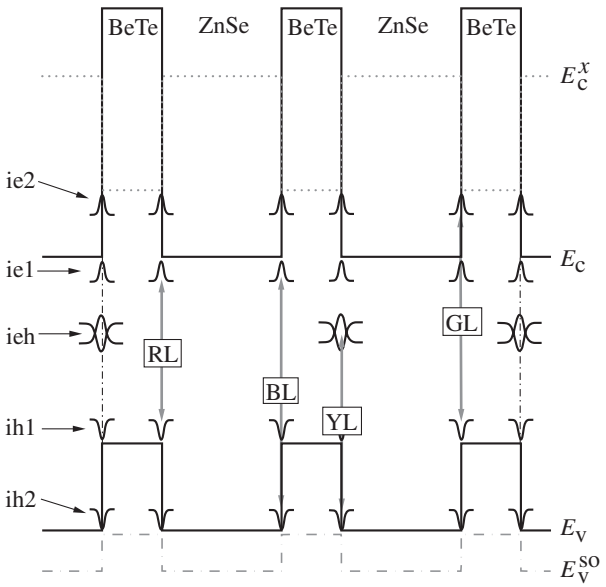

Fig. 3. Energetic positions of the Tamm-like interface states in ZnSe/BeTe heterostructures.

Acknowledgements

This work was supported by grant RFBR No 04-02-16674-a, grants of Presidium of RAS and Russian Ministry of Sciences.

References

[1] H. M. James, *Phys. Rev.*, **76**, 1611 (1949).
[2] A. A. Gorbatsevich, I. V. Tokatly, *JETP Lett.*, **67**, 6, 416 (1998).
[3] M. O. Nestoklon, *International Journal of Nanoscience*, **2**, 6, 411 (2003).
A. V. Rodina, A. Yu. Alekseev, Al. L. Efros, M. Rosen, B. K. Meyer, *Phys. Rev. B*, **65**, 125302 (2002).
[4] A. S. Gurevich, V. P. Kochereshko, A. V. Platonov, A. Waag, D. R. Yakovlev and G. Landwehr, *Phys. Solid State*, **46**, 4, 780 (2004).
[5] E. L. Ivchenko, A. A. Toropov, P. Voisin, *Phys. Solid State*, **40**, 10, 1748 (1998).
[6] P. S. Hauge, *Surface Science*, **96**, 1, 108 (1980).

13th Int. Symp. "Nanostructures: Physics and Technology"
St Petersburg, Russia, June 20–25, 2005

Temperature dependence of photoluminescence and absorption spectra of n-InN

A. A. Klochikhin[1,2], V. Yu. Davydov[1], V. V. Emtsev[1], A. V. Sakharov[1], V. A. Kapitonov[3], Hai Lu[4] and W. J. Schaff[4]

[1] Ioffe Physico-Technical Institute, St Petersburg, Russia
[2] Nuclear Physics Institute, 188350, St Petersburg, Russia
[3] Institute for Physics of Microstructures RAS, GSP-105, 603950 Nizhny Novgorod, Russia
[4] Department of Electrical and Computer Engineering, Cornell University, Ithaca, New York 14853, USA

Abstract. Temperature dependences of photoluminescence (PL) and absorption spectra of n-InN samples with Hall concentrations from 3.6×10^{17} to $7.3\times10^{17}\,\mathrm{cm}^{-3}$ are reported. It is shown that the PL spectrum structures observed at 4.2 and 77 K disappear at room temperature. A model approach taking into account the Urbach tails of conduction and valence bands, the acceptor states, and the non-parabolicity of the conduction band is developed. The structure of the PL spectrum is demonstrated to originate from the recombination of degenerate electrons and holes trapped by deep and shallow acceptors and from the band-to-band recombination of free holes and electrons. The obtained results show that the hole energy relaxation results in the almost equilibrium thermal distribution of holes. The temperature shift of the PL band strongly depends on the momentum relaxation rate of the carriers and therefore can be applied to characterize the quality of the InN based nanostructures.

At present, reliable information on optical and electrical characteristics of n-InN epilaiers of different quality can be found in literature [1,2,3,4], though fundamental characteristics are still under discussion. Among them is the temperature band gap shrinkage which demonstrates a puzzling difference for n-InN samples of different quality (see, for instance [2]).

The temperature band gap shrinkage for many crystals can be directly observed as a decrease of the interband transitions energy in optical absorption. However, the doped semiconductors like n-InN present examples where neither interband absorption nor photoluminescence temperature dependence give the band gap shrinkage directly. Qualitatively, the explanation is that at different temperatures the transitions between different states occur in both interband processes. In this report we present a systematic study of this problem.

We studied high quality InN samples grown on sapphire substrates by molecular beam epitaxy [5] with Hall concentrations from 3.6×10^{17} to $1.0\times10^{18}\,\mathrm{cm}^{-3}$ and with the layer thickness from 12 to 0.42 μm. The electron mobility at room temperature was between 2000 and 1050 cm^2/Vs. A set of lasers operating in the energy range from 2.41 to 0.81 eV was used for the PL excitation.

In Fig. 1 the typical PL spectra for the n-InN samples studied are shown. The spectra display three peaks in the energy interval from 0.50 to 0.67 eV. It is known that the structure in the PL spectra can be due to localized states of carriers or excitons. It is a common feature of semiconductors with relatively low free carrier concentrations. In the PL spectrum of n-type InN, the structure can be attributed to the recombination of degenerate electrons and holes in localized states.

Figures 2a-c show the PL and absorption spectra transformations in a wide temperature interval. The most strong change in the PL spectrum shape is disappearance of any structure with the temperature increase from nitrogen to room temperature.

These results can be explained under the assumption that one of two low-energy features of the PL spectrum (0.610 eV) is due to recombination of degenerate electrons with the holes trapped by deep acceptors and the other one (0.537 eV) is its

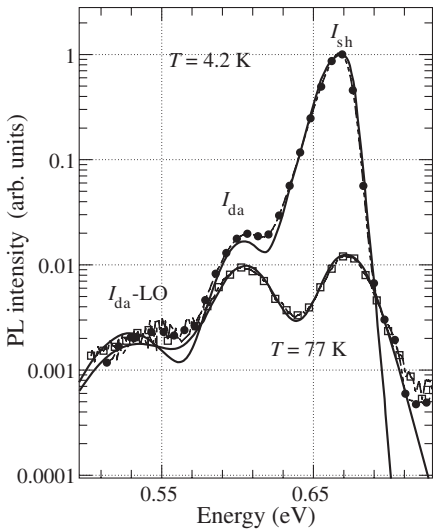

Fig. 1. PL spectra of sample Gs2055 at liquid helium and nitrogen temperatures (decorated dashed upper and lower curves, respectively). Spectra were detected by an InSb diode with the cut-off energy ≈ 0.4 eV ($\lambda \approx 3.1\,\mu$m). Spectra are normalized at 0.55 eV. Solid lines represent the results of model calculations.

LO-phonon replica. The PL peak at 0.663 eV can be attributed to a complex band formed by transitions of electrons to the shallow acceptor states and by the band-to-band recombination. Then the temperature behavior in Figs. 1 and 2 can be understood in terms of the equilibrium distribution of the photoholes over the valence band states.

To confirm this interpretation, model calculations of the PL and absorption spectra were performed. The model assumed the band gap dependence on the carrier concentration, the non-parabolic conduction band with a linear dependence of the electron effective mass on the kinetic energy for electrons, and the presence of the Urbach tails for valence and conduction bands.

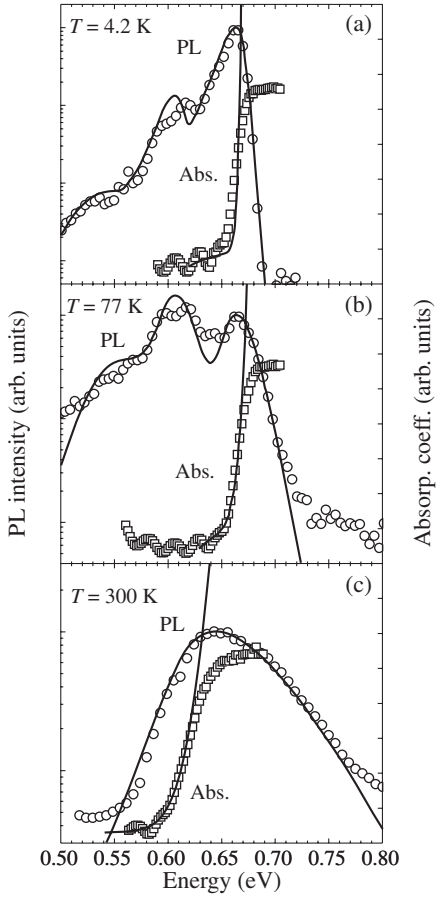

Fig. 2. Transformation of the PL and absorption spectra of sample Gs2050 with increasing temperature. Spectra were detected by an InSb diode with the cut-off energy $\approx 0.4\,\mathrm{eV}$ ($\lambda \approx 3.1\,\mu\mathrm{m}$). Symbols represent the experimental data, solid lines are the results of model calculations. (a) $T = 4.2\,\mathrm{K}$, (b) $T = 77\,\mathrm{K}$, and (c) $T = 300\,\mathrm{K}$. The fine structure of the PL and absorption spectra is due to the Bragg interference.

The equilibrium Fermi distribution function for photoholes can be written as

$$n_E^h(G,T) = \left\{\exp\left[(E-\mu^h(G,T))/T\right]+1\right\}^{-1}, \qquad (1)$$

where the temperature is expressed in the energy units and $\mu^h(G,T)$ is the hole chemical potential defined by

$$G\,\tau(T) = \int_{-\infty}^{\infty}\left[1-n_E^h(G,T)\right]\rho_h(E)dE\,, \qquad (2)$$

where G is the photohole generation rate, $\rho_h(E)$ is the density of the hole states, and $\tau(T)$ is the lifetime of holes in radiative states.

At low temperatures and weak excitations, $\mu^h(G,T)$ lies above the valence band top and goes up with temperature. Then the changes in the PL spectrum shape between 4.2 and 77 K in Figs. 1 and 2a–b can be attributed to the redistribution of the population between shallow and deep localized states of holes. At room temperature, only the band states are populated by holes and the band-to-band transitions dominate in the PL spectrum (Fig. 2c).

The model calculations (Fig. 3) show that the hole distribution shifts and broadens with temperature. The difference in masses of the electron and heavy hole leads to different values

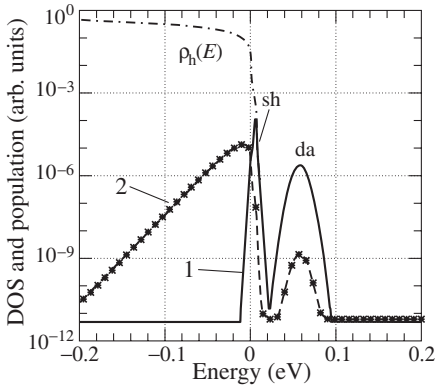

Fig. 3. Model density of the valence band states $\rho_h(E)$ (dot-and-dashed curve) including the Urbach tail and shallow (sh) and deep (da) acceptor states. Curves 1 and 2 are the hole populations at liquid helium and room temperatures, respectively.

of their thermal momenta $p_T^h = \sqrt{2m_hT}$ and $p_T^e = \sqrt{2m_eT}$. If the momentum conservation law is working then the high thermal momenta of holes p_T^h corresponding to the maximum of their thermal distribution prevent their annihilation with electrons whose momenta are of the order of p_F or p_T^e. These restrictions are similar to those found in p-type GaSb and GaAs crystals [6]. The momentum conservation law breaking involves the thermal holes into recombination and increases additionally the PL band energy.

The thermal band gap shrinkage shifts the PL band to low energies, while an increase in the kinetic energies of carriers produces effects of the opposite sign. The interplay of different factors influencing the PL band position leads to a variability of the PL band shift with temperature.

Acknowledgements

This work was partly supported by RFBR (projects No. 03-02-17562 and No. 03-02-17565) and by the Programs "Physics of Solid State Nanostructures", "Low-Dimensional Quantum Structures", and "New Materials and Structures".

References

[1] V. Yu. Davydov, A. A. Klochikhin, V. V. Emtsev, D. A. Kudyukov, S. V. Ivanov, V. V. Vekshin, F. Bechstedt, J. Furthmüller, J. Aderhold, J. Graul, A. V. Mudryi, H. Harima, A. Hashimoto, A. Yamamoto and E. E. Haller, *phys. stat. sol. (b)*, **234**, 787 (2002).

[2] J. Wu, W. Walukiewicz, W. Shan, K. M. Yu, J. W. Ager III, S. X. Li, E. E. Haller, H. Lu and W. J. Schaff, *J. Appl. Phys.*, **94**, 4457 (2003).

[3] F. Chen, A. N. Cartwright, H. Lu, W. J. Schaff, *Physica E*, **20**, 308 (2004).

[4] A. A. Klochikhin, V. Yu. Davydov, V. V. Emtsev, A. V. Sakharov, V. A. Kapitonov, B. A. Andreev, Hai Lu and William J. Schaff, submitted to *Phys. Rev. B*.

[5] H. Lu, W. J. Schaff, J. Hwang, H. Wu, W. Yeo, A. Pharkya and L. F. Eastman, *Appl. Phys. Lett.*, **77**, 2548–2550 (2000).

[6] A. N. Titkov, E. I. Chaikina, E. M. Komova and N. G. Ermakova, *Sov. Phys. Semiconductors*, **15**, 198 (1981), [Fizika i Tekhnika Poluprovodnikov **15**, 345 (1981)].

13th Int. Symp. "Nanostructures: Physics and Technology"
St Petersburg, Russia, June 20–25, 2005

Growth and investigation of the heterojunctions between silicon carbide (SiC) polytypes

A. A. Lebedev, A. M. Strel'chuk, A. N. Kuznetsov and A. N. Smirnov
Ioffe Physico-Technical Institute, St Petersburg, Russia

Abstract. In the present paper investigation of electrical characteristics of p^--3C-SiC/n^+-6H-SiC heterojunction grown by sublimation in vacuum was done. It was concluded that green band in p^--3C-SiC/n^+-6H-SiC diodes is connected with free-exciton annihilation in 3C-SiC and shift in maximum EL position may be connected with quantum-size effects at 3C-SiC/6H-SiC hetero-boundary.

In last years were published several papers about growth and investigation of heterojunction between SiC polytypes [1–3]. It was shown that by method of sublimation epitaxy in vacuum (SEV) it is possible to grown 3C-SiC/6H-SiC pn heteojunctions with enough good characteristics [1]. The aim of present paper was to grow p^--3C-SiC/n^+-6H-SiC heterojunction and investigation of it electrical characteristics. Low doped ($N_a - N_d = 3{-}4\times10^{16}$ cm^{-3}) layers of p-3C-SiC was grown by SEV directly on (0001)Si plane of 6H-SiC Lely substrate ($N_d - N_a \sim 3\times10^{18}$ cm^{-3}). On the top of this layer was grown by SEV strongly doped p-3C-SiC layer for ohmic contact formation. Diode mesa structures with diameter 500 m were produced by plasmo-ion etching in SF_6 (Fig. 1).

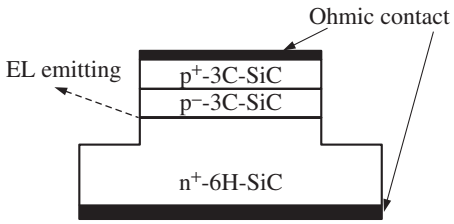

Fig. 1. Cross-section of the investigated 3C-SiC/6H-SiC heterodiodes.

Electrical characteristics of the obtained diodes were closed to electrical characteristics of p^+-3C-SiC/n^+-6H-SiC heterojunction described in [1]. I–V characteristics has exponential forms. Typical capacitance–voltage (C–V) characteristics of the heterodiodes has two parts, both of each are linear in coordinates $1/C^2$–V (Fig. 2). This mean that obtained pn junction was abrupt. Down part of C–V characteristic corresponds to low doped p-3C-SiC layer. Value of Na-Nd in this part is equal to those, measured by mercury probe directly on top of this layer before growth of p^+-3C-SiC. Thickness of this layer is about 0.7 μm. Upper part of C–V characteristics corresponds to strongly doped p^+-3C-SiC layer ($N_a - N_d \sim (0.4{-}1)\times10^{18}$ cm^{-3}).

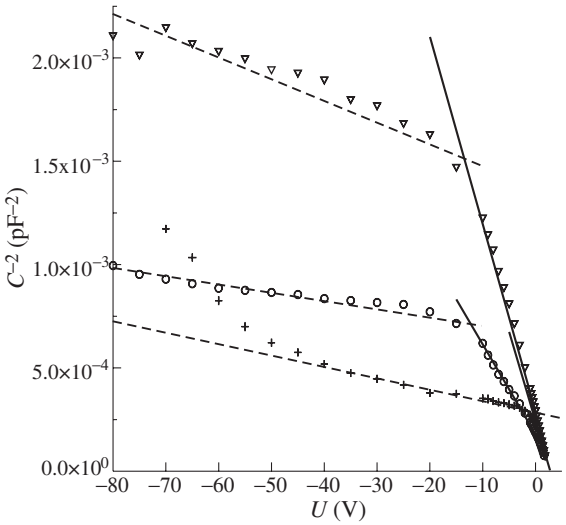

Fig. 2. C–V characteristics of the different heterodiodes.

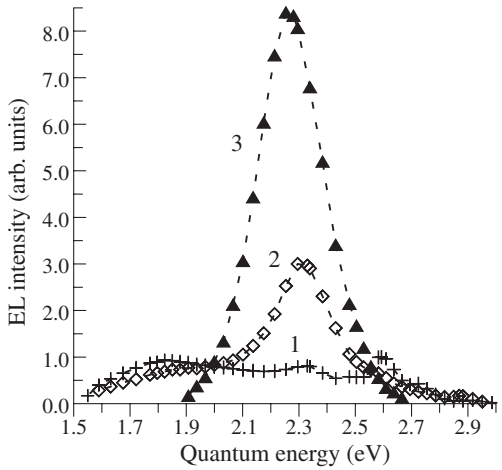

Fig. 3. Electroluminescence spectrum of the investigated diodes at temperatures: 1 — 300 K; 2 — 450 K; 3 — 600 K.

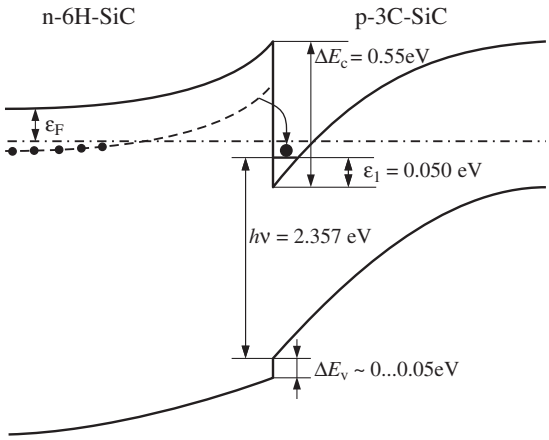

Fig. 4. Band diagram of the P^--3C-SiC/N^+-6H-SiC heterostructure.

In spectrum of electroluminescence of this diodes presents green band close in spectrum position to band of free-exciton annihilation in 3C-SiC and to so-called "defect electroluminescence" in 6H-SiC [4]. But this band has another temperature

dependence than defect EL and the same that exciton line in 3C-SiC — it's intensity increase with increasing temperature (Fig. 3). Maximum position of this line was shifted to short-wave region of the spectrum on about 0.07 eV in contrast with typical position of exciton band in 3C-SiC. This shift may be connected with quantum-size effects at 3C-SiC/6H-SiC heteroboundary (Fig. 4). More detailed description of the obtained results and it's analysis will be done in full volume paper.

Finally we conclude, that by SEV it is possible to grow p^--3C-SiC/n^+-6H-SiC heterostructure with doping level in p- and n-regions suitable for investigation of 2DEG at heterobondary.

Acknowledgements

This work was partly supported by Russian Foundation for Basic Research grants No 03-02-16054 and No 04-02-16632a.

References

[1] A. A. Lebedev, A. M. Strelchuk, D. V. Davydov, N. S. Savkina, A. S. Tregubova, A. N. Kuznetsov, V. A. Soloviev, N. K. Poletaev, *Appl. Surf. Sci.* **184**, 419 (2001).
[2] A. Fissel, U. Kaiser, B. Schroter, W. Richter, F. Bechstedt, *Appl. Surf. Sci.* **184**, 37 (2001).
[3] S. Okojie, M. Xhang, P. Pirouz, S. Tumakha, G. Jessen, L. Brillson, *Appl. Phys. Lett.* **79**, 3056 (2001).
[4] A. A. Lebedev, *Semiconductors*, **33**, 107 (1999).

13th Int. Symp. "Nanostructures: Physics and Technology"
St Petersburg, Russia, June 20–25, 2005

Band-edge and impurity-related photoluminescence of InN

A. V. Sakharov[1], V. Yu. Davydov[1], A. A. Klochikhin[1,2], H. Lu[3] and W. J. Schaff[3]

[1] Ioffe Physico-Technical Institute, St Petersburg, Russia
[2] St Petersburg Nuclear Physics Institute, St Petersburg, Russia
[3] Department of Electrical and Computer Engineering, Cornell University, Ithaca, New York, USA

Abstract. Photoluminescence (PL) of intentionally undoped n-type InN samples grown by MBE has been investigated. A typical PL spectrum consists of two bands around 0.67 and 0.61 eV (at 77 K) related to band-to-band recombination and to acceptor-to-band recombination. PL spectra modification with changes in excitation densities was studied in a wide range of excitation densities using different excitation sources.

Introduction

In spite of a great progress in creation of III-N optoelectronic devices, such as light-emitting diodes and lasers, based on InGaN/AlGaN heterostructures, InN is still not well studied. Up to now conflicting opinions about origin of PL and even about fundamental parameters of InN (such as band gap and effective mass) can be found in literature.

An epitaxial InN film is not so easy to grow, and first samples have very high concentration of defects, leading to giant free carrier concentration, above 10^{19} cm^{-3}. Progress in epitaxial technology results in MBE grown InN films with concentrations of about 4×10^{17} cm^{-3} and room temperature motilities higher than 2000 cm^2/Vs [1].

In this paper we report some data related to optical properties of good quality InN epitaxial structures providing information about its phundamental properties.

1. Experimental

InN epitaxial structures with Hall electron concentration in a range 5–9 $\times$ 10^{17} cm^{-3} were grown on sapphire substrates by molecular beam epitaxy. Sample thicknesses were in a range from 1.7 to 12 μm. A set of lasers operating in energy range from 0.8 to 2.4 eV was used for PL excitation; emission was detected by uncooled InGaAs *p-i-n* photodiode (cut-off energy 0.57 eV) connected to lock-in amplifier. Transparency of sapphire substrate allows measuring PL from both sides of epitaxial film, giving information on material properties change with thickness. Excitation density was varied by using neutral density filters and changing the laser spot size. Optical transmission measurements were performed using halogen lamp.

2. Results and discussion

Fig. 1 shows PL spectra from sample GS2050 with thickness 7 μm and Hall concentration 5.3×10^{17} cm^{-3} at different excitation densities. At minimal excitation densities spectra is dominated by PL peak at 0.61 eV; with increase in excitation density redistribution between two lines takes place and for maximal excitation density spectrum is dominated by band-edge related peak around 0.67 eV. Additional peaks on PL spectra is due to Fabri–Perot resonator formed by InN/air and InN/sapphire interfaces.

Fig. 2 shows PL spectra for thinner sample GS1804 (thickness 1.7 μm). Situation is identical with GS2050, except for lower intensity of impurity band and absence of interference fringes. Nature of impurity-related band is still unclear: it can be formed by any acceptor with binding energy of 50–55 meV.

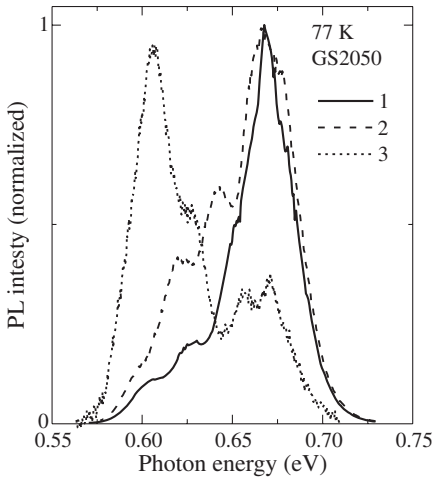

Fig. 1. Normalized PL spectra of sample GS2050 (thickness 7 μm) at different excitation densities. 1 — 10 kW/cm^2, 2 — 500 W/cm^2, 3 — 10 W/cm^2.

It should be noted that in spite of relatively high carrier density in a sample (7×10^{17} cm^{-3}) dependence of PL inten-

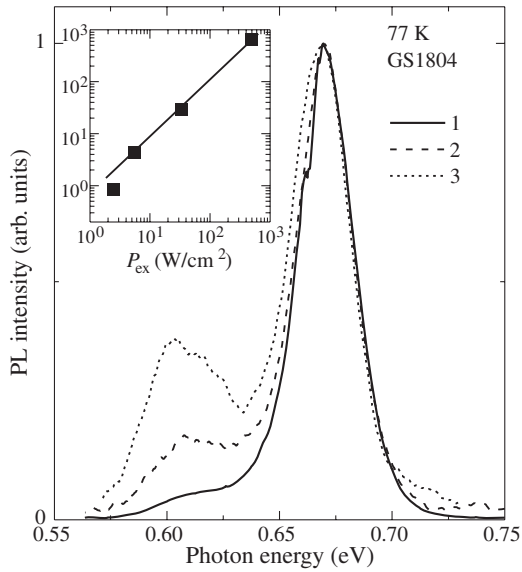

Fig. 2. Normalized PL spectra of sample GS1804 (thickness 1.7 μm) at different excitation densities. 1 — 500 W/cm^2, 2 — 50 W/cm^2, 3 — 1 W/cm^2. In the inset shown dependence of integral PL intensity on excitation level.

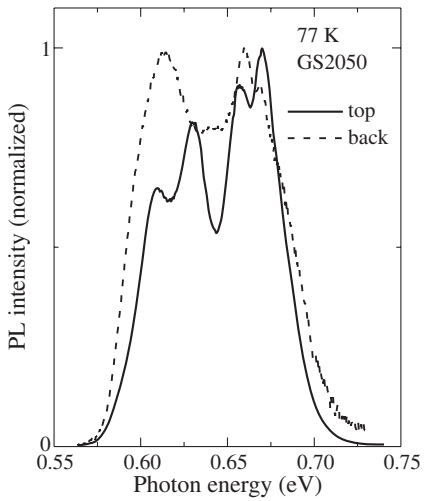

Fig. 3. Normalized PL spectra of sample GS2050 at excitation densities 10 W/cm^2 measured from top of the sample and from back of the sample (through sapphire substrate).

sity on excitation power is almost linear in a wide range of excitation densities, indicating weak influence of nonradiative recombination. Measurements of quantum yield (QE) of PL on this sample shows QE=9% at 4.2 K [2].

Fig. 3 shows PL spectra recorded from surface and from InN/sapphire interface region. Because of relatively thick sample (7 μm) and small absorption length of a laser (0.5 μm) we have possibility to compare epilayer properties at surface and interface regions. Modeling of PL spectra using electron effective mass $m^* = 0.07m_0$ [2] gives carrier concentrations of 2.4×10^{17} cm^{-3} and 1×10^{18} cm^{-3} for surface and interface regions, respectively. So, we can point out that for thick samples Hall data give averaged value of electron concentration (and also averaged mobility value). This feature was observed for GaN layers grown on sapphire, where high density of defects on GaN/sapphire interface leads to formation of a conductive layer [3].

To conclude, we have studied a set of intentionally undoped n-type InN samples. For these structures PL spectra at 77 K consists of two bands around 0.67 and 0.61 eV (at 77 K) related to band-to-band and to acceptor-to-band recombination. For thick samples measurement of PL spectra allows to determine electron concentration at surface and InN/sapphire interface regions instead of averaged Hall concentration.

Acknowledgements

This work has been supported in part by RFBR grants and program "New materials and structures". Authors are thankful to Dr. N. A. Pikhtin for giving an opportunity to use his semiconductor lasers.

References

[1] H. Lu *et al*, *Appl. Phys. Lett.*, **77**, 2548 (2000).
[2] A. A. Klochikhin *et al*, *Phys. Rev. B*, in print.
[3] A. S. Usikov *et al*, *Proc. 2nd ymposium on III-V Nitride Materials and Processes*, Paris, France, 110 (1997).

13th Int. Symp. "Nanostructures: Physics and Technology"
St Petersburg, Russia, June 20–25, 2005

Depression of atom ionisation in 6H-SiC natural superlattice at Wannier–Stark localisation condition

V. I. Sankin and P. P. Shkrebiy
Ioffe Physico-Technical Institute, St Petersburg, Russia

Abstract. As well known the Wannier-Stark localization (WSL) phenomenon was discovered by optical observation. In this work WSl and its influence on transport phenomenon are discovered in 6H-SiC natural superlattice. We pay attention to fact that at WSL a mobility loss occurs and as a consequence electron does not leave its localization near donor impurity to create positive charge due to positive ion of donor atom. This work makes a tray to discovery this prediction which is important both for principal and applied problems. Structure of 6H-SiC field effect transistor with p-n junction as a gate, adapted for this type of investigations, was used as sample. The dependence of short-circuit photo-current on the voltage applied to the source-gate (or drain-gate) p-n junction V_g was studied. Defined value excess V_g causes a negative differential photoconductance, which, as showed by previous investigations, is determined by Wannier-Stark localization in the region of Stark-phonon resonance. Moreover $I_{sd} \sim V_g$ dependence shows a drop I_{sd} to zero at V_g significantly less than a pinched-off channel V_g. This phenomenon is explained by new effect of donor atoms ionisation depressing in WSL regime and consequently by anomalously week field screening.

There is a natural superlattice (NSL) in the most of SiC polytypes except for the 3C- and 2H-SiC. The Wannier-Stark localization (WSL) [1] arises due to NSL in different SiC device structures at the large electric fields. According to the principles of quantum mechanics, electrons heated by electric field, having reached top of the allowed band, experience Bragg reflection, move in a direction opposite to the field, and electron motion becomes periodic (so called Bloch oscillations) [2].The major consequence of this new crystal state is that negative differential conductance occurs. So far the following effects were discovered in different SiC bipolar and unipolar diode and transistor structures fabricated on (0001) face [3]: 1. The depression of electrons in the impact ionization in a wide range of fields. 2. The anomalously high avalanche breakdown fields. 3. The negative temperature dependence of the avalanche breakdown field. 4. The stratification of avalanche breakdown current. 5. The Bloch oscillation. 6. The Stark-phonon resonance under Wannier-Stark ladder conditions. 7. The resonance tunneling between the adjacent minibands. 8. The complete localization of the lowest minibands. 9. The mobile domain and the premature avalanche breakdown. 10. The correlation of drift velocities with superlattice parameters of different silicon carbide polytypes. It is well known that under the WSL conditions [1] a continuous band spectrum transforms into a discrete one, and takes form of the so called Wannier-Stark ladder [4]. This has to cause electron localization and virtual loss of mobility, i.e. quasi free motion capability. It should note that this phenomenon did not attract attention up to now. In its turn, this must lead to a considerable charge density drop in n layer under n p junction contact field. Indeed electron should leave its localization near donor impurity to create positive charge due to positive ion of donor atom. Field, created by positive charge, compensates contact field of n p junction. At the increase of impurity concentration, the width of space charge layer W diminishes. It is well known that under the WSL conditions [1] a continuous band spectrum transforms into a discrete one, and takes form of the so called Stark ladder. This causes electron localization and virtual loss of mobility, i.e. quasi free motion capability. In its turn, this must lead to a considerable charge density drop in n layer under n-p junction contact field. Indeed electron should leave its localization near donor impurity to create positive charge due to positive ion of donor atom. Field, created by positive charge, compensates contact field of n p junction. At the increase of impurity concentration, the width of space charge layer W diminishes. At the abrupt n-p junction, with the prevailing impurity concentration in one of the layers n or p, $W \sim N^{(-1/2)}$. However under the Stark ladder conditions at the electron mobility loss, electron stays by donor, and positive charge density when even increased then far less significantly, than without Wannier-Stark localization; a strong increase of width W being necessary for field compensation. This assumption, rather important even practically, naturally requires experimental verification. To reveal this effect a structure of 6H-SiC field effect transistor with p-n junction as a gate (JFET), adapted for this type of investigations, has been applied. It should note that the part of presented experimental data was published in [5] as the primary material.

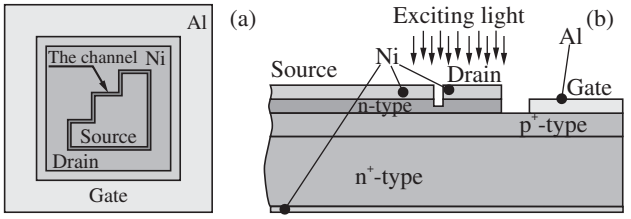

Fig. 1. The common view of the 6H-SiC JFET, (a); the cross section of this JFET, (b).

The technology of fabrication of this JFET is as follows: the p-type, 2-μm thick layer (gate) doped to $N_a - N_d = 2 \cdot 10^{18}\,\mathrm{cm}^{-3}$ is initially grown on (0001)Si face of 6H-SiC substrates (n-type, $N_d - N_a = 3 \cdot 10^{18}\,\mathrm{cm}^{-3}$); then the n-type, 2-$\mu$m thick layer (channel) dopes to $N_d - N_a = 1.5 \cdot 10^{17}\,\mathrm{cm}^{-3}$ is grown on p-layer; two-step photolithography is performed on evaporated Al/Ni combination to form metal contacts. The JFET is produced by dry etching process. The channel dimensions are $784 \times 8 \times 1\ \mu\mathrm{m}^3$. The gate n-$p^+$ junction is abrupt and non-symmetric. The general view and cross section of JFET are shown in Fig. 1(a, b).

In our experiments the JFET structures were illuminated (Fig. 1b) with radiation of different wavelengths ranging from 0.25 to 0.40 µm. The radiation penetrates into the channel n-layer through the open surface. The diffusion lengths of electrons in the p^+-layer and holes in n-layer were determined to be $L_e = 0.4\,\mu$m and $L_h = 0.3\,\mu$m respectively. Thereafter we can create mainly hole or electron PC using the radiation of different wavelengths. The dependence of short-circuit photo-current on the voltage applied to the source-gate (or drain-gate) junction V_g is shown in Fig. 2.

One should consider the fact that the photo-current (PC) begins to drop with voltage exceeding certain threshold value. This is surprising, because PC must tend to the saturation at a voltage with the channel pinched off by the gate space charge region (SCR). In addition (Fig. 2), it was found that the higher the electron part in the PC,

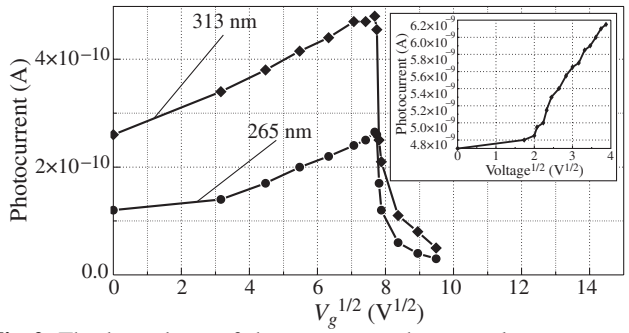

Fig. 2. The dependence of photocurrent on the gate voltage measured on a 6H-SiC JFET. The inset is the same dependence measured for a Si JFET.

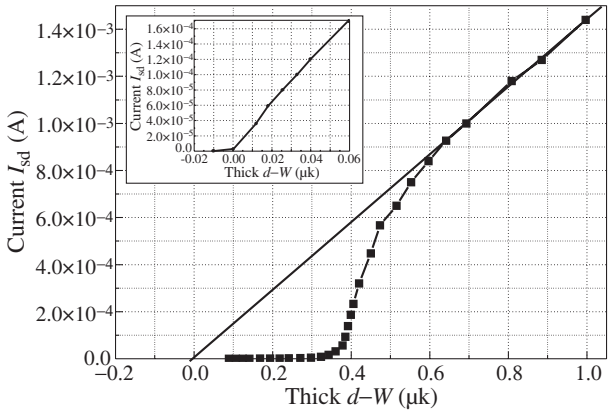

Fig. 3. The dependence of drain current on the thickness of neutral part of the channel. The inset is the same dependence measured for a Si JFET.

the higher is the value of the PC drop (which can be controlled by the wavelength of the exciting radiation). For a comparison the parallel investigations were conducted with two industrial Si JFETs with a structure similar to that of 6H-SiC JFET under study. The results obtained for Si JFETs are trivial: the expected increase of PC and its tendency to saturation with increasing gate voltage (the inset of Fig. 2) have been observed. Thus 6H-SiC JFET behaves uncommonly. Such a negative photo-conductance is never (or very rarely) observed in other semiconductors. But as mentioned above, similar effects in 6H-SiC are discovered elsewhere in different manifestations [3]. We believe that the observed effects should be attributed to the WSL-regime as well, because the field magnitude coincides with Stark-phonon resonances phase of the WSL process in 6H-SiC superlattice [3] and obviously the PC drop is due to the electron component of the PC as well.

In addition to uncommon photo-conductance behavior, unexpected source-drain current I_{sd} versus V_g (or more illustrative $d-W$) dependence is observed in transistor linear regime, where d is the channel thickness, W is the width of the gate SCR consequently the difference $d-W$ is the width of the neutral part of the channel. The plot of I_{sd} versus $d-W$ is expected to be linear, namely such linear dependence is observed for the Si-based JFET (see inset of Fig. 3).

In contrast, I_{sd} versus $(d-W)$ dependence measured for 6H-SiC JFET has a knee at $d-W=0.6\,\mu$m, with I_{sd} being dropped to zero at $d-W\approx 0.3\,\mu$m, i.e. at a condition when there is non-pinched-off part of the channel (Fig. 3). It should be noted that the PC's drop (Fig. 2) occurs at the same V_g value. Both phenomena obviously result from the WSL. To avoid casual coincidence both of these phenomena have been subjected to a temperature rise. The results of this subjecting show a quality coincidence of both characteristics (Fig. 4(a, b)).

The threshold voltage in characteristic $PC\sim f(V^{1/2})$ shifts to its lower values with temperature rising from 300 K to 400 K and does

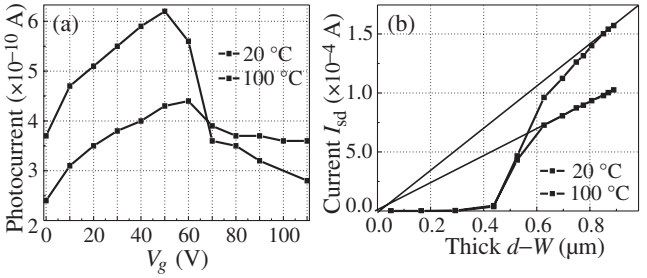

Fig. 4. The dependence of the photo-current on the gate voltage (a) and the drain current on the thickness of neutral part of the channel (b) at different temperature.

not change with temperature rising to 500 K (Fig. 4a). It is likewise controlled by a change in phonon structure spectrum, which produces phonon with lower energy in stark-phonon interaction. Similar shift to the lower voltages V_g has a knee on $I_{sd}\sim f(d-W)$ (Fig. 4b). This experimental result clearly demonstrates that unusual behavior $I_{sd}\sim f(d-W)$ is caused by WSL process. As is known, the effect of WSL becomes apparent for carrier transport along the C-axis [3], while in JFETs under study the direction of drain current flow is orthogonal to the C-axis. Thus it seems that unusual transformation of one-dimensional WSL-effect into almost three-dimensional effect occurs. However in reality the experimental facts indicate that premature pinching-off of the channel occurs. Sufficient explanation should be as follows: as is shown in [3] the electron spectrum at stark-phonon resonances phase of the WSL process in 6H-SiC superlattice becomes discrete. In this case electrons lose their mobility. A probability of electron departure from donor atom strongly decreases and a positive charge density correspondingly diminishes. Therefore the field in p-n junction gate is shielded at the larger width than it would occur in uniform semiconductors where $W\sim V_g^{1/2}/(Nd-Na)^{-1/2}$ because of the effective charge density decrease. Therefore the channel is pinched off at significantly less V_g. The p-n junction capacity behavior confirms this idea. Departure from linearity of the $C^{-2}\sim V_g$ characteristic can be observed at $V_g > 1.2V_t$, where V_t is voltage at the knee on $I_{sd}\sim f(d-W)$ (Fig. 3) and $1.2V_t$ is experimental magnitude.

As a conclusion it is important to consider that along with electron heating depression and early breakdown because of electrical domain [3] an effect of anomalous field screening became another consequence of the WSL conditions, revealed for the first time. Although WSL revealing in $PC\sim f(V_g^{1/2})$ dependence is evidence of discreet electron spectrum arising, it is new evidence of WSL existence in 6H-SiC NSL as well.

Outlined above the mechanism of field spreading in crystal at presence WSL will be creative and useful for explanation some unusual phenomena in SiC devices.

Acknowledgements

The work was partially supported by Russian Foundation of Fundamental Research (proj. no. 03-02-17617) and the program *Physics of Solid-State Nanostructures* (proj. no. 98). The authors gratefully acknowledge stimulating discussions with P. A. Ivanov.

References

[1] G. N. Wannier, *Phys. Rev.*, **11**, 432 (1960).
[2] F. Bloch, *Z. Phys.*, **52**, 555 (1928).
[3] V. I. Sankin, *Semiconductors*, **36**, 717 (2002).
[4] P. Voisin, J. Bleuse, C. Bouche *et al*, *Phys. Rev. Lett.*, **61**, 1639 (1988).
[5] V. I. Sankin, P. P. Shkrebiy, A. A. Lebedev, *Proc. 12th Int. Symp. Nanostructures*, June 21–25, p. 385–387 (2004).

13th Int. Symp. "Nanostructures: Physics and Technology"
St Petersburg, Russia, June 20–25, 2005

Electron-beam pumped green VCSEL on MOVPE-grown ZnCdSe/ZnSSe MQW structure

V. Yu. Bondarev[1], V. I. Kozlovsky[1], *D. A. Sannikov*[1], P. I. Kuznetsov [2], V. A. Jitov[2], G. G. Yakushcheva[2] and M. D. Tiberi[3]

[1] P.N. Lebedev Physical Institute of RAS, 53 Leninsky pr., 119991 Moscow, Russia
[2] Institute of Radioengineering and Electronics of RAS, 1 Vvedenskogo, 141190 Fryazino, Russia
[3] Principia LightWorks Inc. CA, USA

Abstract. 40 period ZnCdSe/ZnSSe MQW structures were grown by metal-organic vapour phase epitaxy on GaAs substrates. Based on these structures, an etalon for vertical cavity surface emitting laser was fabricated. Lasing at $\lambda = 535$ nm with 3.2 W output power was achieved by longitudinal pumping of a scanning electron beam at room temperature. The threshold current density was as low as 8 A/cm^2.

Introduction

E-beam pumped vertical cavity surface emitting laser (VCSEL) emitting in a red, green and blue spectral ranges is promising as an efficient light source for display technologies [1, 2]. High input-output efficiency of about 12% was realized in a VCSEL (645 nm) with a resonant periodic gain using GaInP/AlGaInP structures [3]. Recently, blue (462 nm) lasing was achieved with ZnSSe/ZnMgSSe MQW structures also [4]. In this paper, we demonstrate the first results of an e-beam pumped ZnCdSe/ZnSSe MQW VCSEL emitting in the green spectral range.

The ZnCdSe/ZnSSe QW with ZnMgSSe clading layers for the formation of an optical waveguide is a typical active structure for green-emitting ZnSe-based laser diodes [5]. This structure as well as structures with CdSe quantum disks were successfully used in edge-emitting lasers with e-beam pumping [6]. Lasing under longitudinal e-beam pumping was also achieved using ZnCdSe/ZnSe structures grown by MBE on GaAs and ZnSe substrates [7, 8]. However, laser threshold was high because the number of QWs was nonoptimal and the structures exhibited a large number of defects. These results were achieved using MBE deposition, however MOVPE is preffered for volume production. The best results to date have been obtained by MOVPE on ZnCdSe/ZnSSe structures of an edge-emitting laser diode at low temperature (77 K) [9]. Thick ZnCdSe/ZnSSe structures suitable for a laser with resonant periodic gain with longitudinal pumping by an electron beam or optical pumping grown by MOVPE has now been demonstrated.

1. Experimental

Periodic ZnCdSe/ZnSSe MQW structures were grown by MOVPE on GaAs substrates misoriented by 10° from (001) to (111)A. Structures were fabticated with 20 to 40 periods with thicknesses ranging from 100 to 200 nm. The MQW region was grown on a ZnSSe buffer with a thickness from 400–700 nm with a ZnCdSe QW thickness from 3 to 8 nm. The Cd content was about 25–30% for green emission. The structures were completed by a ZnSSe layer equal to the thickness of the ZnSSe barrier layers. Growth was carried out in a custom built horizontal quartz reactor including an optical window for *in situ* multi-wavelength reflectrometry control of layer thickness. The growth run was carried out in hydrogen at atmospheric pressure using diethylzinc (Et_2Zn), dimethylcadmium ($CdMe_2$), diethylsulfide (Et_2S) and dimethylselenide (Me_2Se) as precursors. The substrate temperature was 425 °C.

A quarter wave 7 pair SiO_2/ZrO_2 layer stack was deposited on the structure to form the first cavity mirror. The sample was then mounted with epoxy to a sapphire holder and the GaAs substrate was removed by polishing followed by chemical etching. The sample was then etched in a diluted CrO_3-HCl-H_2O solution removing 200–300 nm of Ga doped ZnSSe from the GaAs substrate. A second mirror of 7.5 pairs of SiO_2 and ZrO_2 and 0.1 μm of aluminum was deposited on the etched surface to complete the etalon.

As-grown structures were studied by photoreflection (PR), cathodoluminescence (CL), X-ray diffraction, optical, luminescence and atomic force microscopy (AFM). CL was measured at $T \approx 14$ K and RT, electron energy $E_e = 10$ and 30 keV, continuous current $I_e = 1\,\mu$A and an e-beam spot diameter $d_e = 1$ mm. The cavity was pumped by a scanning electron beam with $E_e = 25$–60 keV, $I_e = 0$–2 mA and $d_e = 20$–50 μm, depending on the electron energy and current. The scan velocity was approximately 4×10^5 cm/s with a repetition rate of 50 Hz.

2. Results and discussion

2.1. Structure characterization

The main issue in growing a high quality, thick ZnCdSe/ZnSSe MQW structure is to compensate for compression strains in the CdSSe QW layers due to mismatching with GaAs by intentional tension strains in ZnSSe barrier layers. The thickness of CdSSe layers should be less than the critical thickness to prevent the formation of misfit dislocations.

If the S content is greater than 8%, dark lines along the ⟨1–10⟩ direction and dark lines misoriented from the ⟨110⟩ direction by ±5° are observed in luminescence microscope image which is the result of relaxation of tension strains by the formation of dislocations along the [111] planes. These surfaces intersect the (001) surface along the ⟨1–10⟩ and ⟨110⟩ directions. In the case of a misoriented GaAs substrate, the $(1-11)$ and $(-1-11)$ surfaces should intersect the substrate surface along the two different lines misoriented from the ⟨110⟩ direction. Small dark spots are observed in the image also and it is speculated that these defects are formed in the QWs since their proliferation appears highly dependent on the CdSSe layer

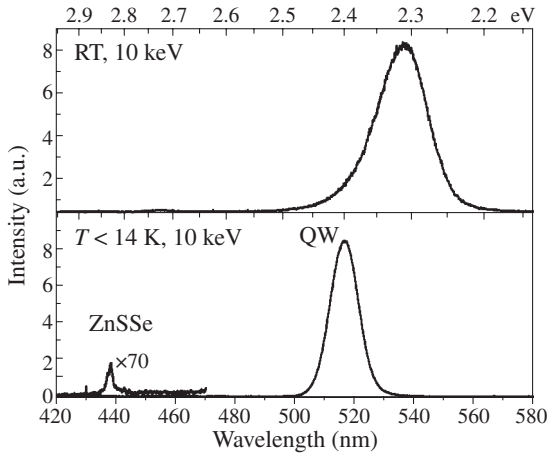

Fig. 1. CL spectra of the 40 ZnCdSe/ZnSSe QW structure at $E_e =$ 10 keV, RT and $T < 14$ K.

thickness.

If the S content is less than 6%, dark lines along the direction of the intersection of the (100) and (010) surfaces with the substrate surface become apparent in the luminescence image caused by the relaxation of internal compression strain along these planes. By tuning the S content it is possible to decrease these dark line defects.

Exceeding the critical thickness for the CdSSe layer leads to a proliferation of dark spot defects and the emission field becomes microscopically nonuniform although the emission intensity may be large or even increase. Further increasing of the CdSSe layer thickness eventually leads to a drop in emission intensity.

The structures grown at optimized conditions have a mirror-like surface with AFM roughness parameter — root mean square (RMS) — of less than 2 nm across a $10 \times 10\ \mu m^2$ area. The typical FWHM of the X-ray rocking curve was 100 arcsec. The CL spectra of a 40-period MQW structures is presented in Fig. 1. The intensity of the QW emission line is much higher than one of the ZnSSe barrier emission line at both RT and $T \approx 14$ K. This demonstrates adequate transport of nonequilibrium carriers into the QWs.

2.2. *Laser characteristics*

In Fig. 2, the cavity emission spectra below and above the lasing threshold are presented. Below the threshold the spectrum consists of several longitudinal cavity modes. Above the threshold, the spectrum contains two cavity modes. The threshold current at $E_e = 40$ keV was 0.025 mA (about 8 A/cm^2 in current density). Output power of 3.2 W was achieved at RT, $E_e = 40$ keV and $I_e = 1.8$ mA. The laser efficiency was about 4.5%. Fig. 3 shows the dependence of output power on e-beam current at $E_e = 35$ keV. A far-field pattern of the laser is typical for an e-beam pumped VCSEL. It contains a central spot with total divergence angle of about 15 degrees and one ring at angle of 23 degrees.

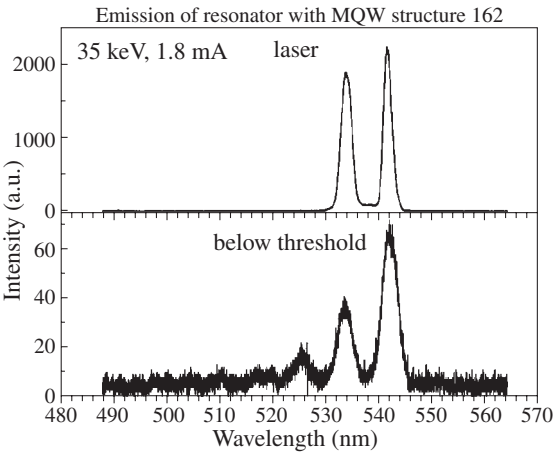

Fig. 2. Emission spectra of the etalon below ($d_e = 1$ mm) and above ($d_e < 40\ \mu$m) the threshold at $E_e = 35$ keV, $I_e = 1.8$ mA, RT.

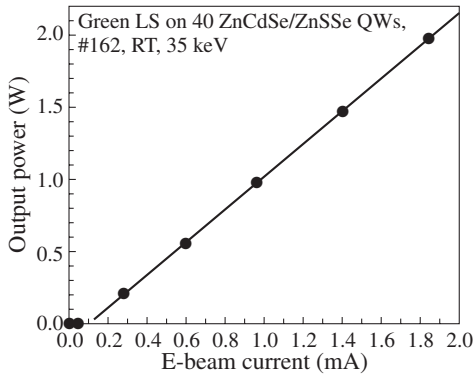

Fig. 3. Dependence of output power on e-beam current at $E_e =$ 35 keV and RT.

3. Conclusion

Optimization of growth conditions and composition of quantum well and barrier layers was demonstrated resulting in a laser structure with low defects and intense cathodoluminescence at RT. Lasing with 3.2 W output power was achieved at RT and 40 keV at 530–545 nm under longitudinal pumping by a scanning electron beam. The threshold was as low as 8 A/cm^2. Optimization of the design of the structure will allow for further improvement in laser characteristics.

Acknowledgement

This work was supported in part by Russian Foundation of Basic Researches, Grants 04-02-16877, 05-02-16390; Program "Scientific Schools of Russia", Grant 1466-2003-2, the NATO SfP under Grant 974355 and Principia LightWorks Inc. (CA, USA).

References

[1] V. I. Kozlovsky, Yu. M. Popov, *Quantum Electronics*, **33**, 48 (2003).
[2] M. D. Tiberi, V. I. Kozlovsky, *Proceedings of SPIE*, Volume: 5740, (2005).
[3] V. Yu. Bondarev, V. I. Kozlovsky, A. B. Krysa *et al*, *Int. J. Nanoscience*, **3**, 193 (2004).
[4] V. Yu. Bondarev, V. I. Kozlovsky, I. V. Malyshev *et al*, *Phys. stat. sol.*, **(c)**, (2005).
[5] S. Itoch, K. Nakano, A. Ishibashi, *J. Crystal Growth*, **214/215**, 1029 (2000).
[6] M. M. Zverev, S. V. Sorokin, I. V. Sedova *et al*, *Phys. stat. sol.* **(c)**, 2005.
[7] N. G. Basov, E. M. Dianov, V. I. Kozlovsky *et al*, *Quantum Electronics*, **25**, 726 (1995).
[8] V. I. Kozlovsky, P. A. Trubenko, Y. K. Skasyrsky, *Laser Physics*, **8**, 1068 (1998).
[9] A. Toda, F. Nakamura, K. Yanashima *et al*, *J. Crystal Growth*, **170**, 461 (1997).

13th Int. Symp. "Nanostructures: Physics and Technology"
St Petersburg, Russia, June 20–25, 2005

Formation of GaN cubic or hexagonal structure layers deposited by electron cyclotron resonance plasma

S. Shapoval[1], A. Kovalchuk[1] and V. Gorbunov[2]

[1] Institute of Microelectronics Technology RAS, 142432 Chernogolovka, Moscow region, Russia,
[2] Experimental Factory for Scientific Engineering RAS (EZAN), 142432 Chernogolovka, Moscow region, Russia

Abstract. Wide-band-gap materials like GaN, BN, diamond and others can have different structures: cubic, wurzitic or hexagonal. ECR-plasma enhanced CVD technology demands the application of RF induced negative DC bias of different values to deposit cubic or hexagonal BN [1, 2], diamond or graphite. This bias is needed to furnish bombarding energetic ions in order to transform a more stable hexagonal crystal layer into cubic.

Introduction

Our approach was to grow cubic or hexagonal GaN by the ECR-MOVPE method by mixing an nitrogen plasma stream, extracted from the plasma confinement vessel, with trimethyl gallium (TMA) released from the gas ring in the vicinity of a silicon (111) wafer. The application of nitrogen (not ammonia) gives an additional advantage to decrease the hydrogen concentration and to use a liquid nitrogen panel to provide better conditions for structure growing.

The experimental EpiLab setup used for layer growing is shown in Fig. 1. The ECR plasma was excited in a 150 stainless steel chamber and "extracted" into the process chamber by divergent magnetic field. Nitrogen was introduced into the source chamber in which activated nitrogen species were formed. The plasma density in the ECR source chamber was about 10^{13} cm^{-3}, the ion energy was 17–25 eV. 13.56 MHz radio frequency (RF) biasing was used together with the ECR source to control incident ion energy. RF bias provides a separate means of controlling ion energy which is essentially independent of the ECR plasma parameters. Since the potential due to RF bias develops close to the substrate (about 1 mm), this improves the control over the energy of chemical reactions on the substrate surface.

Fig. 1. The experimental EpiLab 150 setup used for layers growing.

1. Experimental

Gallium nitride layers were deposited onto high-ohmic Si (111) plates 400 μ thick, which were pretreated in a 25% HF solution for 10 min and followed by 10 min treatment by hydrogen ECR plasma. Directly before deposition, the plates were subjected to nitrogen ECR plasma for 10 min. Then a pre-determined flow of gallium trimethyl was added to the nitrogen plasma for 3 s and the deposition began. The deposition conditions were varied by changing the microwave power $W = (20-100)$ watts, the value of the self-bias voltage $U_b = (-30- -160)$ V upon 13.56 MHz HF field application, the pressure $P = (0.2-2)$ mTorr, and the ratio of nitrogen flow F(N_2) to gallium trimethyl flow F(TMG), $R = (1-24)$.

Fourier transmission infra-red spectrometry (FTIR) was used for an express analysis of the chemical composition of a deposited GaN layer. The period of interference bringers in the base line of the Fourier transmission infra-red spectra (FTIRS) was measured to calculate the product of the layer refraction index by the layer thickness. The FTIRS were recorded on a 1720X Perkin–Elmer spectrometer with the signal to noise ratio 3000 for a single spectrum scanning. The spectra were registered with a 36-times accumulation of scans. The FTIRS discussed in the work are presented on an optical density scale after subtraction of the base line. Structural analysis was performed on a JEOL 2000FX transmission electron microscope with an accelerating voltage of 150 kV.

2. Results and discussion

Figures 2 and 3 present FTIRS of GaN layers deposited under different conditions. For the sake of convenience, the spectra are normalized to unit optical density by the main peak 540 cm^{-1} amplitude (A = 1). The 540 cm^{-1} peak can be attributed to bands of symmetric and asymmetric Ga-N stretching vibrations. The features in the region 1700 cm^{-1} to 2200 cm^{-1} are due to Ga-H and H-Ga-H stretching bands. The bands C-H and H-C-H stretching vibrations are in the region 2900 cm^{-1} peak. And the features in the region 3100 cm^{-1} to 3600 cm^{-1} are due to N-H and H-N-H stretching vibrations. The bands of C-H and H-C-H stretching vibrations observed in the FTIRS L(1) become disappearingly small in the FTIRS L(2) when the ratio F(N_2) to F(TMG) increases from1.5 to 6.0 (Fig. 2). The bands due to Ga-H, H-Ga-H, as well as N-H and H-N-H vibrations observed in the L(1) and L(2) spectra become disappearingly small as the ratio F(N_2) to F(TMG) increases to 16, as can be seen in the spectrum L(3) (Fig. 3).

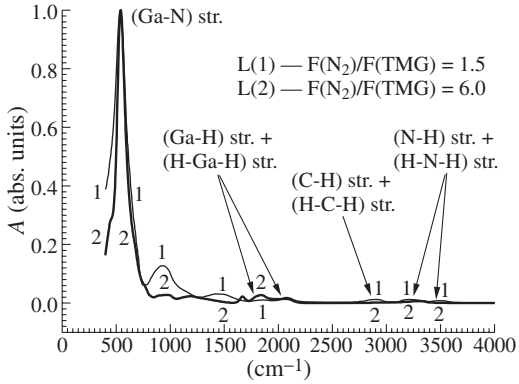

Fig. 2. FTIRS of layers GaN/Si(111) deposited under ECR-plasma conditions $W = 100$ W, $U_b = -160$ V, $P = 1.0$ mTorr; $R = 1.5$ for L(1) and $R = 6$ for L(2).

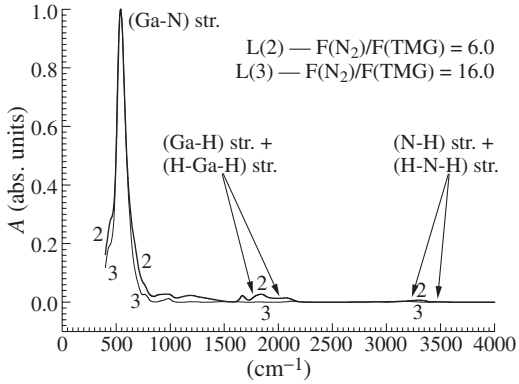

Fig. 3. FTIRS of layers GaN/Si(111) deposited under ECR-plasma conditions $W = 100$ W, $U_b = -160$ V, $P = 1.0$ mTorr; $R = 6$ for L(2) and $R = 16$ for L(3).

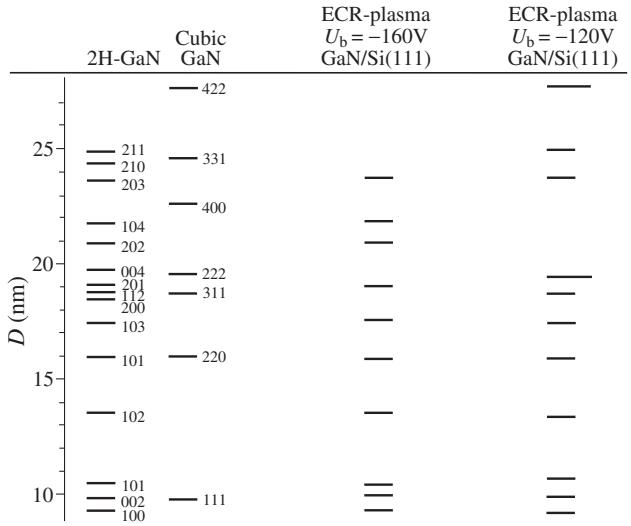

Fig. 4. Lengths of diffraction vectors calculated for 2H-GaN, cubic GaN and measured for GaN layers L(3), L(4).

The comparison analysis of the FTIRS obtained showed that the concentrations of carbon and hydrogen in the GaN layers decrease when a self-bias voltage U_b of -30 to -160 V is applied to the substrate, under otherwise equal process conditions.

Electron microscopy studies were performed to determine the crystal structure type. Figure 4 displays the diffraction vector lengths measured from the selected area diffraction (SAD) patterns of GaN layers and calculated for hexagonal (2H-GaN)

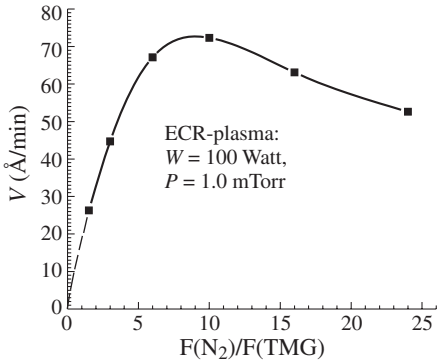

Fig. 5. Dependence of GaN layer growth rate from relation $R = F(N_2)/F(TMG)$.

and cubic GaN. The analysis of the measured and calculated diffraction vectors for 2H-GaN and cubic GaN showed that the L(3) layers deposited in ECR plasma at $U_b = -160$ V and $R = 16.0$ was hexagonal. The SAD pattern of the L(4) layer deposited in ECR-plasma at $U_b = -120$ V and $R = 16.0$ showed the presence of both hexagonal and cubic phases, with the cubic phase dominating (Fig. 4).

Figure 5 presents the dependence of the GaN layer growth rate on the ratio R. On deriving this dependence, the area in the FTIRS from 400 cm^{-1} to 800 cm^{-1} was used as a value proportional to the number of Ga-N bonds in the layer in the first approximation. The maximum growth rate of the GaN layer $V_{\max} \approx 73$ Å/min is obtained, under the conditions of Fig. 5, when the nitrogen flow exceeds that of gallium trimethyl by nine times.

3. Conclusions

These studies helped understand the major regularities of implantation of impurity hydrogen and carbon atoms into the layer structure. The rate of GaN layer growth is a curve with the maximum $V_{\max} \approx 73$ Å/min, when $R \approx 9$. Under otherwise equal conditions, the layer quality improves as the ratio $F(N_2)/F(TMG)$ increases. The gentle slope of the curve in Fig. 5 suggests that the rate of layer growth remains rather high (70% of the maximum) even at substantial excess (by $\sim$ 24 times) of nitrogen flow over that of gallium trimethyl. The analysis of selected area diffraction patterns showed that the layers are of hexagonal structure. In the cases when the cubic phase dominates, the hexagonal structure is also observed. We suspect that crystal structure dependence from applied DC bias value is the common feature for ECR–PECVD growth processes of wide-band-gap materials.

Acknowledgement

This work supported by the FTNS program of the Russian government

References

[1] S. Shapoval, V. Petrashov, O. Popov, A. Westner, M. Yoder, and C. Lok, *Appl. Phys. Lett.* **57** (18), (29 October 1990).

[2] A. Chayahara, H. Yokoyama, T. Umura, Y. Osaka, *Jpn. J. Appl. Phys.* **26**, L1432 (1987).

13th Int. Symp. "Nanostructures: Physics and Technology"
St Petersburg, Russia, June 20–25, 2005

Degradation mechanism in blue light emitting diodes associated with nanostructural arrangement

A. V. Kamanin, A. G. Kolmakov, P. S. Kop'ev, V. N. Mdivani, A. V. Sakharov, *N. M. Shmidt*, A. A. Sitnikova, A. L. Zakgeim and R. V. Zolotareva
Ioffe Physico-Technical Institute, St Petersburg, Russia

Abstract. A degradation mechanism in blue light emitting diodes based on MQW InGaN/GaN grown by MOCVD on sapphire has been investigated. New approach to analyze the degradation mechanism has been used. It takes into account the nanostructural arrangement determined by the extended defect system relaxation. This system includes a high density of threading dislocations and a mosaic structure. The results obtained suppose that the migration and secretions of Ga on domain dislocation boundaries of the mosaic structure under high injected current density are important reasons of degradation.

Introduction

Since 1992 the degradation mechanism in blue light emitting diodes and lasers based on MQW InGaN/GaN has been studied, but it is not still completely clarified [1–3]. These investigations supposed that the well-known degradation mechanism of III–V and II–VI compounds took place in the nitrides. This mechanism is connected with a dislocation multiplication by non-radiative recombination at threading dislocations [4, 5] under high injected current density. However, the results [3] showed that no dislocation multiplication was observed in blue light emitting diodes and lasers.

In present paper another approach to analyze the degradation mechanism has been suggested. It takes into account the nanostructural arrangement of III-nitrides determined by the extended defect system relaxation.

1. Experiments

The comparative investigations of two types of light emitting structures (LES) with different nanostructural arrangement were carried out. The LES based on MQW InGaN/GaN with an active region consisting of 5 periods of (3 nm InGaN and 7 nm GaN) were grown by MOVPE on (0001) sapphire substrates. The nanostructural arrangement was determined by the extended defect system relaxation. This system included a high density of threading dislocations and a mosaic structure. The nanostructural arrangement classified quantitatively using a multifractal parameter, namely, the degree of order (Δ). The parameter Δ was evaluated from the treatment of a digital ensemble corresponding an AFM surface view, using the multifractactal analysis. The procedure was described in detail before [1, 2]. The AFM views of LES with different Δ are presented in Fig. 1.

These two types of LES differed not only in the values Δ, but in the values of external quantum efficiency as well. They were 10% for well-order LES ($\Delta = 0.320$) and 0.5% for poor-order LES ($\Delta = 0.370$).

The LES were studied by transmission electron micro/-scopy (TEM) Philips 420-EM using both plan view and cross-sectional modes. Usually two equivalent ways are used to study the degradation mechanism: either under high current density or under the operating current during more than 1000 hours. The first way was used in the present investigation. The degradation of the unpacked LES structures with design and metallization for the operating forward current of 20 mA was studied at the pulsed current of 100–200 mA in 0.5–2 hours.

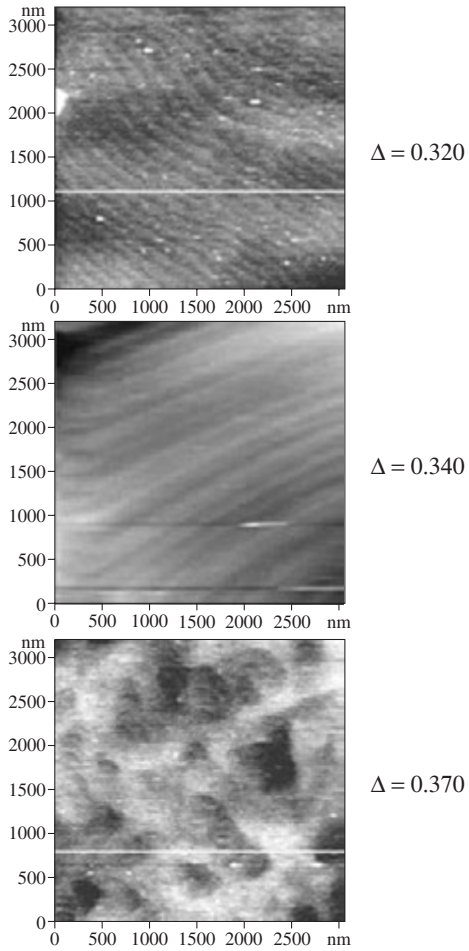

Fig. 1. AFM views of LES with different D

2. Results and discussion

It is well known that important structural peculiarities of the III-nitrides are a mosaic structure with domains size of 100–800 nm and a high dislocation density. The existence of high local stress connected with both domain coalescence and mixed dislocations is typical of the nitrides. The migration of dislocations in such system is practically impossible.

The TEM investigation of LES with different nanostructural

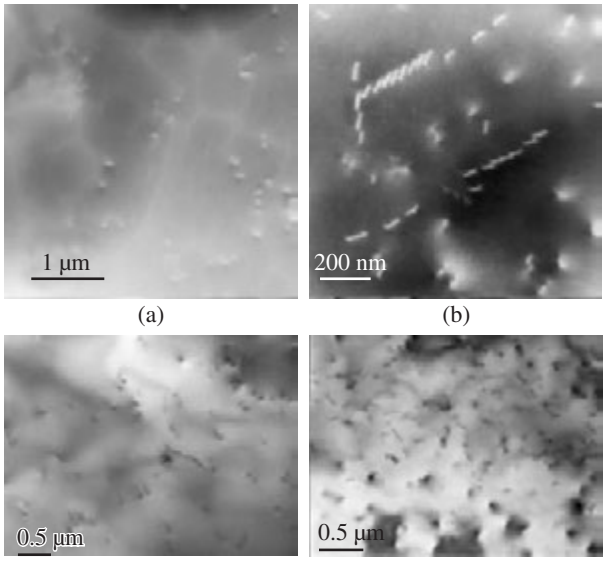

Fig. 2. TEM views of LES with different nanostructural arrangement: *a*, *c* – well ordered LES, *b*, *d* – poor ordered LES

arrangement was undertook to find weak places of an extended defect system. This investigation of LES showed that two basic types of domain coalescence were observed. The first was the coherent concordance of domains with the formation of the dilatation boundaries (Fig. 2*a*), and the second was the poor domain coalescence with the formation of the numerous dislocation domain boundaries (Fig. 2*b*). Moreover, the both types existed in LES investigated, but the first one was the main for the well order LES ($\Delta = 0.32$) and the second one predominated for the poor order LES ($\Delta = 0.37$) (Fig. 2*c*, *d*).

Our previously investigations of optical and electrical properties of the III-nitrides with different nanostructural arrangement showed that, for the nitrides with the predominance of domain dislocation boundaries [6, 7], the unstable nonradiative centers, persistence photoconductivity, low values of quantum efficiency, a high level of leakage current were observed. The experience of work with the poor-ordered GaN layers and LES showed that the Ga secretions after spreading of metallic layer, weak heating, electron and γ-irradiation usually were observed in these materials.

These results suppose that the dislocation domain boundaries are the weak places of the extended defect system. The LES behavior under high current density injection confirmed this assumption, that was in a good agreement with the results of papers [3, 4]. The authors of those papers also observed the increase in conductivity at voltages below the threshold voltage and the secretions of metallic phase. The using of a special etchant allowed us to make clear, that metallic phase was Ga.

The behavior of LES with different arrangement distinguished noticeably. The small improvement of the shapes of both $I-V$ characteristics and electroluminescence spectra were observed at small exceeding of current to 50–80 mA only for poor ordered LES. The fast degradation developed at the current of 100–150 mA in several minutes and the conductivity increased for several orders at voltage below 2 V and the Ga secretions began.

The conductivity for well-ordered LES was slowly increasing in several hours at the same values of the current. Further increase in the current caused the Ga secretions. The spots

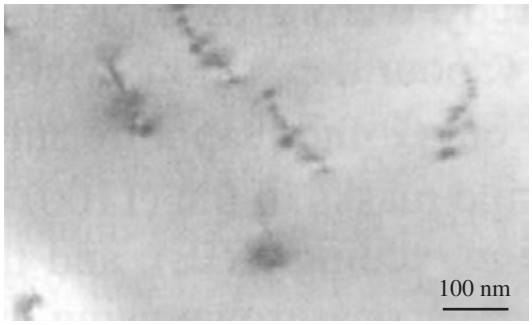

Fig. 3. TEM view of dislocation domain boundaries after degradation

of Ga in the regions of domain dislocation boundaries were observed in a TEM view of LES after degradation (Fig. 3).

Thus, the migration and the secretions of Ga on the domain dislocation boundaries of the mosaic structure are important reasons of degradation under high injected current density.

Acknowledgement

This work was financially supported by Grant of the Russian Academy of Science "New Materials and Structures" 9.8A220.

References

[1] S. Strite *et al*, *J. Vac.Sci. Technol.* **B10**, 1237 (1992); *Phys. Stat. Sol.* **B240**, 273 (2003).
[2] Shigetaka Tomiya *et al*, *Phys. Stat. Sol.* **A200**, 139 (2003).
[3] T. Egawa *et al*, *Appl. Phys. Lett.* **69**, 830 (1996).
[4] N. M. Shmidt *et al*, *Inst. Phys. Conf. Ser.* **169**, 303 (2001).
[5] C. J. Wu and D. B. Wittry, *J. Appl. Phys.* **49**, 2827 (1978).
[6] A. I. Besyulkin *et al*, *Phys. Stat. Sol.* **2**, (2005).
[7] N. M. Shmidt *et al*, *J. Phys.: Condens. Matter.* **14**, 13285 (2002).

13th Int. Symp. "Nanostructures: Physics and Technology"
St Petersburg, Russia, June 20–25, 2005

Fundamental parameters of InN versus non-stoichoimetry

T. V. Shubina and M. M. Glazov
Ioffe Physico-Technical Institute, St Petersburg, Russia

Abstract. We report dependence of fundamental parameters of InN on deviation from stoichiometry. The empirical nearest-neighbor tight binding theory and the Harrison bond-orbital model are exploited to investigate variation of the band gap, electron effective mass and high-frequency dielectric constant on this phenomenon. Reasonable agreement with experimental trends is demonstrated. A model to describe absorption edges in heavily-doped non-parabolic InN is proposed.

Introduction

In spite of intense studies of InN films all over the world, dramatic uncertainty still exists in its fundamental parameters: band gap, dielectric constants, and effective masses. The situation is unique for semiconductor already employed for commercial applications and very perspective for next generation of solar cells, optoelectronic and microwave devices. The optical gap energy E_g demonstrates exceptional variation over a huge spectral range from ∼0.7 up to 2.2 eV. It takes place in samples grown by modern techniques that excludes, e.g., oxygen contamination. The electron effective masses m^*/m_0 differing more than twice have been exploited so far for modeling optical processes in the narrow-gap InN [1,2]. High frequency dielectric constant ϵ_∞ deviates from 6.7 in the narrow gap material [3] up to 9.5 in that with the wide gap.

Currently, the Burstein–Moss effect is considered as a basic reason for the dispersion of the optical gap energy. Variation of the effective masses has been ascribed to the non-parabolic band structure of InN, with lower position of the conduction band bottom in the Γ point [4]. In the frameworks of single-electron approximation, it is assumed that an unlimited increase of the Fermi level energy with increasing carrier concentration is possible. However, current InN is a typical heavily-doped semiconductor in accordance with the definition $N \cdot {a_B}^3 > 1$ [5], where N is electron concentration and a_B is the Bohr radius. Namely, InN is heavily-doped starting from $N \sim 10^{17}$ cm^{-3}, while the lowest carrier concentration achieved in the state-of-art InN films is more that $6 \cdot 10^{17}$ cm^{-3}. The heavily-doped semiconductors are characterized by potential fluctuations, which lower energy of an effective absorption edge.

Recently we have proposed that non-stoichiometry in InN (N/In $\neq 1$) may be a crucial reason for the optical gap energy deviation [6]. Our assumption is based on the fact that InN is a material tending to the non-stoichiometry and In clustering. Phase diagrams for epitaxial growth [7,8] show that a range of technological parameters to form ideal films is very narrow. For instance, the temperature range is about 20 °C only.

In the paper, we consider InN as non-stoichiometrical material, whose fundamental parameters suffer from the phenomenon. Also, we propose a model to describe absorption spectra in heavily-doped InN.

1. Deviation of the fundamental parameters

With the large excess of nitrogen content (C_N), InN can be considered as amorphous In_xN_{1-x} compound. Many properties of the wide-gap InN, such as poor mobility and Raman characteristics, are consistent with that [1]. This material has usually high electron concentration. We assume that the non-stoichometry dominates its properties with $N \sim 5 \cdot 10^{19}$ cm^{-3}, while the band filling is more important for the lower concentration. For the narrow gap material, situation is more complicated, because the In clustering can modify dielectric and optical properties in a specific way [9].

The energy gap at the Γ point in a direct gap semiconductor is a function of atomic orbital energies, which are strongly different for nitrogen and indium [10]. Therefore, both excessive incorporation and elimination of one sort of atoms should change the parameter. We have examined the trends using the approximation of the empirical nearest-neighbor tight binding theory [10,11]. In the calculations, part of anions and cations are replaced by vacancies or by antisite defects, whose energies are either taken from [10] or replaced by weighted averages. The calculated energy gap dependences on defect concentration, normalized to the 1.2 eV, are plotted in Fig. 1. The method does not pretend to determine the true band gap. The 1.2 eV value is chosen for the fitting, as corresponding to the average band gap of the stoichiometrical films ($C_N - 0.5 = 0$). The reasons of the gap fluctuation need thorough studies.

Our estimation shows that the 5–10% excess of atoms can shift the InN optical gap in the 0.7–2 eV range, with N/In < 1 and N/In > 1 corresponding to the lower and higher energies, respectively. Comparison of the calculated trends for various defects with experimental data shows that N_{In} states are hardly realized; rather N_2 molecules are formed, likely, due to the strong N-N bonds. Both enhanced formation of V_{In} vacancies

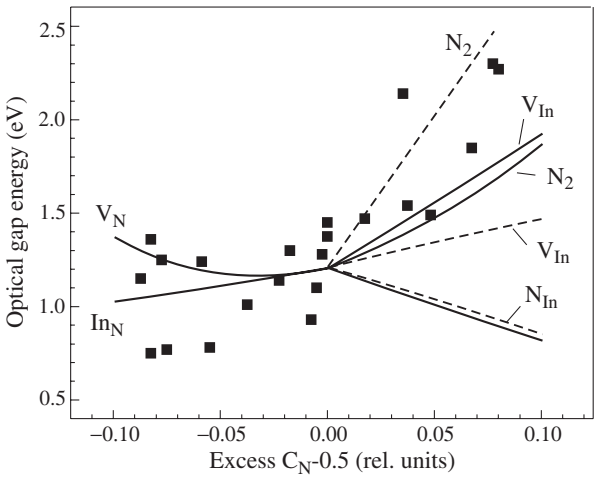

Fig. 1. Optical gap energy vs excess of nitrogen [6]. Solid lines present calculations done using the approximation of the empirical nearest-neighbor tight binding theory, dashed lines are results of the calculation using the Harrison bond-orbital model.

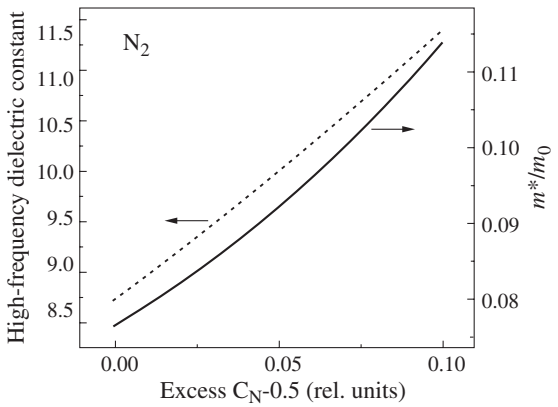

Fig. 2. (a) Dependences of electron effective mass m^*/m_0 (solid curve) and ϵ_∞ (dashed curve) calculated using the nearest-neighbor tight binding approximation and assuming N_2 to be a dominant defect.

and N_2 molecules should increase the optical gap. Incorporation of excessive In into the crystal lattice (In_N) has to decrease its magnitude, although in a smaller degree. The V_N vacancies provide a decrease in E_g followed by some increase.

We check these trends for the wide-gap material using also the Harrison bond-orbital model [12]. The energy gap calculated in the model is ∼1.5 eV, therefore the dependences in Fig. 1 are 0.3 eV shifted down in energy for the sake of demonstration. In general, the tendencies turn to be similar to those described above. Although, the energy shift is stronger for N_2 and weaker for $V_{\rm In}$ formation.

The E_g and the electron effective mass values at the bottom of the conduction band are linked by a simple equation $m^*/m_0 = (1 + E_p/E_g)^{-1}$, where E_p is the energy parameter related to the Kane momentum matrix element. This parameter is rather stable in III–V compounds, being ∼14.5 eV in wurtzite nitrides [13]. The results of the m^*/m_0 estimation with $E_p = 14.5$ upon the non-stoichiometry are presented in Fig. 2. They are well consistent with experimental data. The value for N/In = 1 is close to $0.085m_0$ derived from studies of the plasma frequencies in the narrow-gap InN [14]. Note that extraordinarily small $E_p \sim 10$ eV must be accepted to explain the deviations of the parameters by the Burstain-Moss effect only [4].

The Harrison bond-orbital model permits us to examine the trends in variation of the dielectric constants in the non-stoichiometrical InN. In particular, the ϵ_∞ has to increase in the wide-gap material, enriched by the N_2. With N/In = 1, the minimal ϵ_∞ of ∼8.7 is realized, which is very close to the most frequently used value of 8.4 [1].

2. Absorption in heavily-doped InN

Absorption spectra in the heavily-doped InN have frequently a long tail below a principal absorption edge. It induces some uncertainty in determination of the true band gap value. To describe the complicated density of states in a proper way, we consider a following model: E_g is kept constant and the electron is assumed to experience a slowly varying electric field depending on mean square of potential fluctuation γ^2. The band effective mass m_d is supposed to be energy-dependent, like in the non-parabolic band structure [15]. Here we present the final result which is in fact the generalization of Efros-Shklovskii formulae [5] taking into account the band non-parabolicity:

$$\langle\rho(E)\rangle = \frac{2^{1/2} m_d(0)^{3/2}\gamma^{1/2}}{\pi^2\hbar^3} G\left(\frac{E}{\gamma}\right), \qquad (1)$$

where

$$G(x) = \frac{1}{\sqrt{\pi}}\int_{-\infty}^{x} e^{-y^2}(x-y)^{1/2}\mu(x+y)dy, \qquad (2)$$

and

$$\mu(x) = \left(\frac{m_d(\gamma x)}{m_d(0)}\right)^{3/2}. \qquad (3)$$

Preliminary results on fitting of the absorption spectra (not presented here) demonstrate reasonable agreement between experimental and theoretical spectra shapes. It permits one to exclude mistaken interpretation of the tail as a principal edge and to determine E_g more accurately.

3. Conclusions

We propose that InN fundamental parameters can be influenced strongly by the film non-stoichiometry. Significant part of experimentally registered deviation can be related to this phenomenon. A model to describe density of states in a heavily-doped non-parabolic InN is developed.

Acknowledgements

This work was partly supported by RFBR (Grants 04-02-17652, 03-02-17563, and 03-02-17567).

References

[1] V. Yu. Davydov and A. A. Klochikhin, *Semiconductor* **38**, 897 (2004).
[2] B. Arnaudov, T. Paskova, P. Paskov *et al*, *Phys. Rev. B* **69**, 115216 (2004).
[3] A. Kasic, M. Schubert, Y. Saito *et al*, *Phys. Rev. B* **65**, 115206 (2002).
[4] J. Wu, W. Walukiewicz, W. Shan *et al*, *Phys. Rev. B* **66**, 201403 (2002).
[5] A.L. Efros and B.I. Shklovskii, *Electronic properties of Doped Semiconductors*, Springer, Heidelberg, 1989.
[6] T. V. Shubina, S. V. Ivanov, V. N. Jmerik *et al*, *Phys. Stat. Sol. B* **202**, 377 (2005).
[7] S. V. Ivanov, T.V. Shubina, V. N. Jmerik *et al*, *J. Cryst. Growth* **269**, 1 (2004).
[8] A. Koukitu and H. Seki, *Jpn. J. Appl. Phys., Part 2* **36**, L750 (1997).
[9] T.V. Shubina S. V. Ivanov, V. N. Jmerik *et al*, *Phys. Rev. Lett.* **92**, 117407 (2004).
[10] D. W. Jenkins and J. D. Dow, *Phys. Rev. B* **39**, 3317 (1989).
[11] P. Vogl, H. P. Hjalmarsons, and J. D. Dow, *J. Phys. Chom. Solids* **44**, 365 (1983).
[12] W. A. Harrison, *Phys. Rev. B* **8**, 4487 (1973).
[13] I. Vurgaftman, J. R. Meyer, and L. R. Ram-Mohan, *J. Appl. Phys.* **89**, 5815 (2001).
[14] T. Inushima, M. Higashiwaki and T. Matsui, *Phys. Rev. B* **68**, 235204 (2003).
[15] E. L. Ivchenko and G.E. Pikus, *Superlattices and Other Heterostructures*, 2nd ed., Springer, 1997.

13th Int. Symp. "Nanostructures: Physics and Technology"
St Petersburg, Russia, June 20–25, 2005

Investigations of the optical properties of InGaN/AlGaN structures

D. S. Sizov, V. S. Sizov, G. E. Onushkin, V. V. Lundin, E. E. Zavarin, A. F. Tsatsul'nikov and N. N. Ledentsov
Ioffe Physico-Technical Institute, St Petersburg, Russia

Abstract. We investigated InGaN/GaN and InGaN/AlGaN quantum dots for UV light source applications. It is shown that in case of GaN matrix, nonradiative carrier leakage across the barrier is comparable with the leakage in lateral direction at room temperature. At high pumping power the leakage across the barrier becomes dominating. Both the kinds of leakage can be suppressed by embedding the QDs in AlGaN matrix. Carrier leakage across the AlGaN barrier becomes considerable only at the temperature about 400 K. This allows obtaining significantly better temperature stability at various pumping power that is important for development in UV lasers and light emitting diodes.

Introduction

Investigations of the InGaN/GaN structures [1] are motivated by opportunity in development of light sources working in visible and ultraviolet (UV) optical range. Highly efficient InGaN/GaN blue and green light emitting diodes have been commercially realized for recent years [2]. Blue lasers have also been fabricated [3]. Regarding light sources of UV range, their efficiency is significantly lower as compared with blue analogues. This is believed to be due to relatively weak carrier localization in these InGaN/GaN structures [4]. However it is still not definitely known what areas of the structure are responsible for nonradiative recombination which results in decreasing of the efficiency. Thermal escape of carriers from InGaN/GaN leads to carrier transport to the nonradiative traps. At the same time we have recently shown that although the value of localization energy between quantum dot levels and matrix is high the carrier leakage in the normal direction over the matrix is also considerable even for InGaN/GaN structures emitting in blue range [5,6]. As it is shown in the present work the leakage rises with pumping power increase that becomes important for lasers or high power light emitting diodes (LED) working at high power regimes. The leakage in the direction that is normal to the active region plane (the carrier moving across the matrix barrier) must be even more important in UV range structures which are characterized by shallow carrier localization. Moreover, progress in GaN epitaxial growth with low defect density [7] makes this kind of leakage dominating over the lateral leakage. A way to decrease the leakage in the normal direction is increase of barrier height by incorporation of Al [8] into the barriers. In the present work optical properties and carrier statistics in InGaN/AlGaN structures are investigated in detail in comparison with well known InGaN/GaN system.

1. Experimental

The structures for optical investigations were grown on (0001) sapphire substrates. The active area contained stacked InGaN layers was deposited on GaN buffer layer. The first InGaN layer was deposited at lower temperature as compared with the other layers leading to deeper carrier localization in the first InGaN layer. The idea of the deposition of this layer is to control stress in the active region and improve of quality. The InGaN layers were separated by either AlGaN or GaN barriers. AlGaN blocking layer and GaN cap layer were grown after deposition of the active region. PL was excited by CW HeCd or pulse N2 lasers on structure surface and investigated at different temperatures.

2. Results and discussions

PL spectra of the structures with GaN and AlGaN barriers measured at different temperatures and excitation powers are shown in Fig. 1. One can see that peak at ∼380 nm dominates at low temperature for both the structures. This peak is attributed to the recombination in the upper InGaN layers. One can also see that for the structure with GaN barriers this peak position is slightly red shifted as compared with the AlGaN barrier containing structure that is expectable due to higher barriers in these structures. PL of the first InGaN layers (peaks at ∼ 440 nm) is much weaker at the low temperature that is since most of the photons of the exited light are absorbed in the upper layers of the active area. Carrier redistribution at low temperature is so slow that almost all carrier recombination occurs in the areas where the carriers were excited. There is significant difference in influence of temperature increase and pumping power on spectra shape for the different structures. In case of the structure with GaN barriers the temperature increase leads to relatively slight decrease in the PL intensity of the first InGaN layer. But more than two orders of magnitude decrease of PL intensity of the upper InGaN layers is observed. Pumping power increase at the room temperature leads to dominating of the first InGaN layer PL and the UV peak becomes irresolvable. Quite another behavior is observed in the case of the structure with AlGaN barriers: the ratio of the blue peak and the UV peak changes slightly with the pumping power and tempera-

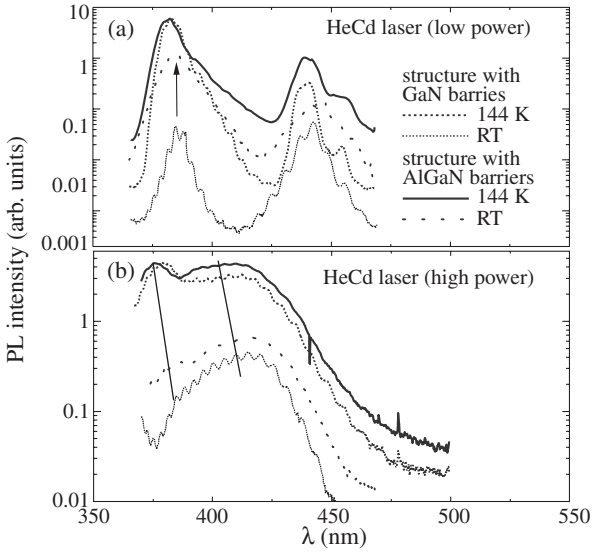

Fig. 1. PL spectra of the structures at low (a) and high (b) pumping power

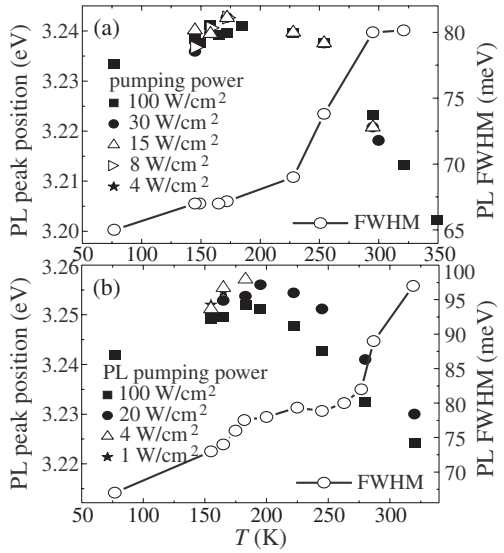

Fig. 2. PL peak positions and FWHM for the structures with GaN barriers (a) and AlGaN barriers (b).

ture increase up to room temperature. This result shows that the temperature induced carrier leakage is strongly suppressed in the structure with the AlGaN barriers. As one can see in Fig. 3 increase in PL intensity of blue peak with temperature is observed at the temperature higher than 380 K. It allowed us to conclude that thermally activated carrier transport across the AlGaN barrier with their future capture to the first InGaN layer becomes considerable at this temperature while it is negligible at the room temperature. Increase in the pumping power leads to the degenerate carrier population in the InGaN layers that is testified by significant short wavelength shift of the UV peak [9]. In this case increase of carrier population in the InGaN and matrix states is not proportional because rate of nonradiative recombination of delocalized carriers increases faster than rate of radiative recombination of the localized carriers [6]. At the same time efficiency of radiative recombination from the first InGaN layer remains reasonable due to suppressed carrier delocalization from this deep localizing layer. At the same time UV peak efficiency is extremely weak in the structure with GaN barriers and a little higher in the structure with the GaN barriers. These results demonstrate also strong kinetic lag in carrier redistribution through the barrier in the normal direction. These kinetic lags lead to suppression of leakage due to thermal activation of carriers to the matrix In order to investigate carrier transport in the lateral direction we studied properties of the InGaN-based active region. Symmetrical UV PL peak of the both structures is observed. This is typical for the QD structures with quantum dots (QDs) with gaussian-like bandtail and quasi- equilibrium carrier statistics [9] and can also be observed in case of deviation of the quasiequilibrium [10]. As it can be seen in Fig. 2 dependence of PL peak position on temperature corresponds to typical QD behavior i.e. S-shape in the dependence of peak position on temperature is observed. At the same time, though no redshift with pumping power decrease, the peak does not remain symmetrical at low temperature and the peak is broadened to the short wavelength side. We believe that this is due to large values of carrier localization in the QDs and so strongly inhomogenous carrier population [10].

Full width at half maximum decreases with temperature de-

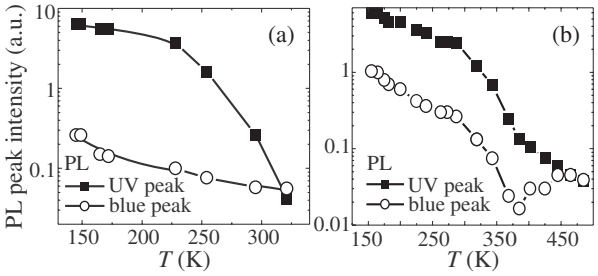

Fig. 3. . Dependences of PL intensity on the temperature for the structures with GaN barriers (a) and AlGaN barriers (b)

crease that we attribute to the contribution of excited states in QDs. for both the structures, however this decrease becomes slower when the temperature is below 230 K that also indicates on strongly nonequilibrium carrier distribution. The value of FWHM is higher for the structure with AlGaN barriers indicating on stronger fluctuations of localizing potential in this structure [9] and so deeper localization in QDs that can be due to higher values of the band offsets. As we have recently shown for InGaN/GaN QDs, the deeper carrier localization leading to stronger deviation from quasiequilibrium and the better temperature stability of efficiency is observed. Thus, deeper carrier localization in QDs can be the other reason of better PL efficiency temperature stability in this structure with AlGaN barriers due to suppressed lateral transport. As it can be seen in Fig. 3 fall of the UV PL intensity is observed for the structure with GaN barriers at the temperature ∼250 K that is below the room temperature (RT) and for the structure with AlGaN barriers at ∼ 300 K. With the temperature increase up to the RT the PL intensity of the structure with AlGaN barriers decreases in 5 times. In conclusion, it was shown, that at room temperature nonradiative carrier leakage across GaN barrier from UV InGaN quantrum dots is comparable with the leakage in lateral direction. Both the kinds of leakage can be suppressed employing AlGaN matrix allowing us to achieve improved temperature stability of PL efficiency at various pumping power.

Acknowledgements

This work was supported by joint project between Ioffe Physico-Technical Institute and Samsung Advanced Institute of Technology.

References

[1] I. L. Krestnikov *et al*, *Phys. Rev. B* **66**, 155310 (2002).
[2] R. Seguin *et al*, *Compound Semiconductor* December (2004).
[3] T. Mukai, M. Yamada, S. Nakamura, 38, *Jpn. J. Appl Phys.* **38**, 3976 (1999).
[4] R. W. Martin, P. G. Middelton, K. P. O'Donnell, W. Van der Stricht, *Appl. Phys. Lett.* **74**, 263 (1999).
[5] R. W. Martin, P. G. Middelton, K. P. O'Donnell, W. Van der Stricht, *Appl. Phys. Lett.* **74**, 263 (1999).
[6] D. S. Sizov *et al*, *"Nanaostructures Physics and Technology"* St Petersburg, Russia June 21-25, 2004.
[7] C. Skierbiszewski *et al*, *Appl. Phys. Lett.* **86**, 011114 (2005).
[8] M. Kneissl, D. W. Treat, M. Teepe, N. Miyashita, N. M. Johnson, *Proc. SPIE Int. Soc. Opt. Eng.* **5365**, 278 (2004).
[9] P. G. Eliseev, P. Perlin, J. Lee, M. Osinski, *Appl. Phys. Lett.* **71**, 569 (1997).
[10] D. S. Sizov *et al*, *'Photonics2004'* December 9–11 2004, Kocin, India.

13th Int. Symp. "Nanostructures: Physics and Technology"
St Petersburg, Russia, June 20–25, 2005

Optical study of InGaN/GaN and InGaN/InGaN QDs grown in a wide pressure range MOCVD reactor

D. S. Sizov, V. S. Sizov, V. V. Lundin, E. E. Zavarin, A. F. Tsatsul'nikov, A. S. Vlasov, N. N. Ledentsov, A. M. Mintairov[1], K. Sun[1] and J. Merz[1]

Ioffe Physico-Technical Institute, St Petersburg, Russia
[1] University of Notre Dame, Notre Dame, IN 46556 USA

Abstract. InGaN quantum dot (QD) formation in a wide pressure range MOCVD reactor was studied. We found that an increase of the reactor pressure (from 400-1000 mbar) enhances In incorporation and leads to an increase in light emission efficiency of the QDs and of bulk layers. An increase of the InGaN QD photoluminescence intensity and inhomogenous broadening accompanied by slight lateral carrier transport suppression is observed. In addition, the possibility of increasing carrier localization and emission wavelength is demonstrated by embedding the QDs in an InGaN matrix. In this case significant suppression of lateral carrier transport due to the influence of matrix disordering is observed. Thus, in spite of the decrease in average localization energy, the InGaN matrix enhances carrier localization in the QDs.

Introduction

InGaN quantum dots (QDs) [1] are known to have some peculiarities, such as deep carrier localization due to the high value of the band offsets [2] and the presence of a strong built-in electric field [3,4]. Together with the possibility of covering all of the visible spectral range, these properties make InGaN QDs promising for a variety of applications. InGaN QD formation is known to occur due to a strain-induced phase separation during the growth of ultrathin InGaN layers (∼12 monolayers) [1] and this phase separation is usually greater for higher In content [5]. At the same time, different applications require that localization energies vary between zero confinement of carriers and strong confinement (i.e., QDs), and that the inhomogenous strain, composition and sizes of the QDs vary. For example, a fast carrier redistribution rate and weak inhomogeneities in the QD array are necessary for high optical gain and a narrow lasing line [6,7]. On the other hand, a low spatial and spectral density of states as well slow carrier redistribution is desired for some purposes (for example, single photon sources) [8]. It is also well known that suppression of delocalized carrier transport leads to a decrease in the nonradiative carrier recombination. Thus, control of the light emission wavelength, carrier localization and QD array inhomogeneity of InGaN QDs is important. We have demonstrated the possibility of increasing carrier localization in InGaN QDs using growth interruptions [9] and postgrowth annealing [10]. It was shown that extremely deep carrier localization in the QDs can be achieved, leading to a deviation of the non-equilibrium carrier distribution at temperatures higher than 300 K. In this work the influence of the MOCVD total reactor pressure during InGaN QD growth on carrier localization and optical properties was studied. The influence of the InGaN matrix on the properties of the QDs is also investigated.

1. Experiment

The structures studied here were grown in an EpiquipVP50RP growth machine modified for growth of III/N compounds with the ability of varying reactor pressure over a wide range. The structures were grown on (0001) sapphire substrates. After deposition of a GaN buffer layer the active area was grown. In the first series of structures (A1-A4), 3 nm (∼12 monolayer) InGaN QD layers were grown in a GaN matrix, with 7 nm spacers. In the other structures the QDs were grown on bulk $In_{0.1}Ga_{0.9}N$ layers. Also grown was a series of bulk $In_{0.1}Ga_{0.9}N$ layers in order to optimize the matrix growth regimes. Details of the QD active area growth are presented in Table 1. The structures were investigated by far field photoluminescence (PL) and by near-field PL. The PL was excited by a CW HeCd laser and by a He+ lamp. The PL FWHM and peak positions were determined using spectral Fourier filtration.

2. Results and discussions

Room temperature PL spectra of the structures A1-A4, C1, and D1 are presented in Fig. 1. One can see that an increase in the reactor pressure leads to a PL red shift, indicating on an increase in the average In content and (or) stronger phase separation. The PL intensity strongly increases with increasing pressure from 400 to 600 mbar. According to the research experience of different authors, the reactor pressure increase is accompanied by improving structural and optical properties of III/N epitaxial layers [11]. For the results reported here, the optimal pressure for growth of InGaN/GaN QD layers was determined to be 800 mbar. For bulk InGaN layers, the best structural properties by X-ray and PL data are obtained at 1000 mbar. Therefore, the InGaN/InGaN QDs were grown at 1000 mbar reactor pressure.

Let us consider the optical properties of the InGaN/GaN and InGaN/InGaN QDs. As we can see from the insertions in Fig. 1 and in Table 1, the higher value of PL FWHM corresponds to stronger PL intensity. It is known that the disordering of ultrathin InGaN layer leading to QD formation suppresses lateral carrier transport and thus decreases nonradiative recombination [12]. Thus, we believe that the increase in QD layer inhomogeneity also improves PL

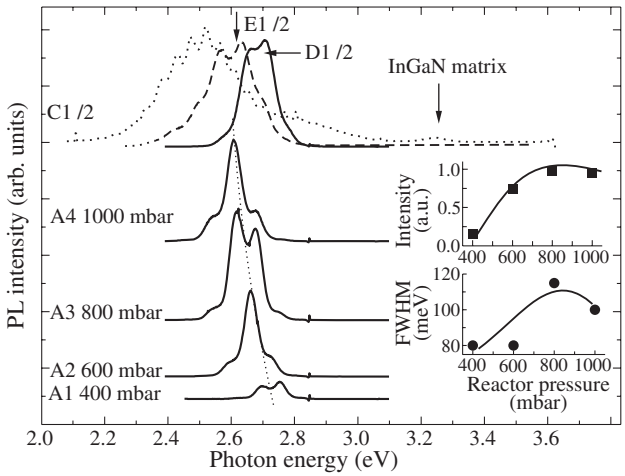

Fig. 1. Room temperature PL data of InGaN/GaN and InGaN/InGaN QDs.

Table 1.

Sample	Structure title	Matrix type	Reactor pressure (mbar)	QD growth temperature (°C)	Number of QD layers	PL peak intensity (a.u.)	PL FWHM (meV)
#1	A1	GaN	400	730	5	0.15	80
#2	A2	GaN	600	730	5	0.74	80
#3	A3	GaN	800	730	5	0.98	115
#4	A4	GaN	1000	730	5	0.95	100
#5	B1	GaN	400	750	1	0.01	152
#5	C1	GaN	1000	730	1	2.1	260
#5	D1	GaN	1000	750	5	1.92	181
#5	E1	GaN	1000	730	5	1.94	144

efficiency due to deeper carrier localization. In the case of embedding InGaN QDs in an InGaN matrix, a further FWHM increase was observed. Again, from Table 1 and Fig. 1, the PL peak position of structure E1 is almost the same as structure A4, while the value of FWHM is significantly higher. This increase in FWHM is believed to be caused by the additional fluctuations in the InGaN matrix. These fluctuations can also be stimulated by InGaN phase separation, which in turn increases disordering in the QD layer itself. Our measurements of a low-temperature (5 K) near-field PL spectra (spatial resolution ∼200 nm) of InGaN/InGaN QD structure reveal series of sharp lines in energy range 2.4–2.7 eV. The FWHM of the lines equals spectral resolution of our set up (0.8 meV). Number of lines (up to 30) gives density of QDs $\sim 103\,\mu m^{-2}$. We did not observed diamagnetic shift for these lines up to magnetic fields of 10 T, which indicates small lateral size of QDs (< 5 nm). For optimized growth of the InGaN matrix, improvement of the QD PL was observed. We believe that this is due to a suppression of lateral transport of the delocalized carriers. In order to investigate the carrier transport we measured the dependence of the PL peak position on exciting photon energy at 77 K. For all the structures a redshift of the PL peak is observed with decrease of the exciting photon energy (Fig. 2). We attribute this to a suppression of the carrier transport in the lateral direction. In this case, carriers excited by the lowest photon energies in a given area relax into the ground QD states and recombine in the local region where they were excited. In contrast, in the case of fast transport, the carrier distribution would obey a quasi-equilibrium law [9] and the spectral shape would not depend on the exciting photon energy at low power. As we can see in Fig. 2, the shift of the PL peak versus exciting photon energy for structures A2 and A4 is much weaker than that for samples C1 and D1. In addition, the shift for A4 (with a wider PL peak) is stronger than for A2. This confirms that an increase in reactor pressure leads to an increase in localization depth of the QDs, which is accompanied by a decrease in carrier motion and a stronger PL shift. We believe that

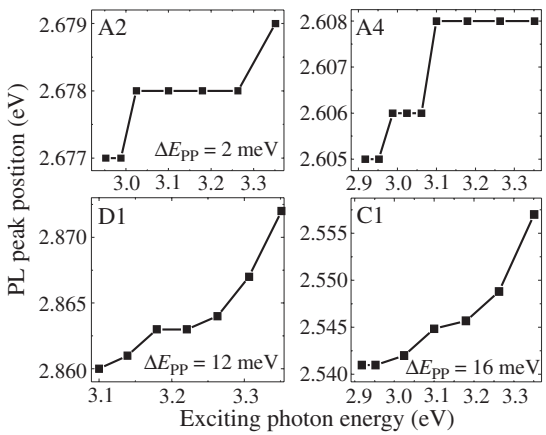

Fig. 2. Dependence of PL peak position on exciting photon energy measured at 77 K.

significantly slower carrier transport in the structures with the InGaN matrix is caused by decreased mobility in the disordered matrix and the induced inhomogeneities in the InGaN QD layers themselves. It is important to stress that although the average carrier localization energy between InGaN QDs and the InGaN matrix is lower than in the case of the GaN matrix, carrier transport is even more suppressed in the case of the InGaN matrix.

3. Conclusions

We investigated the influence of reactor pressure during the growth of an InGaN matrix on the formation and optical properties of InGaN QD arrays. An increase of the MOCVD reactor pressure improves In incorporation and PL efficiency. An increase of disordering in the QD layers accompanied by lateral transport suppression was also observed. Further increase in PL wavelength and PL efficiency can be obtained by embedding the QDs in an InGaN matrix. In this case, near field measurements show sharp PL lines corresponding emission from QDs with small size (< 5 nm). Although the average carrier localization energy between the InGaN QDs and the InGaN matrix is lower than in case of GaN, significant suppression of carrier transport at 77 K was also revealed. The most optimal reactor pressure for this purpose is 1000 mbar.

Acknowledgements

The work was supported by Collaborative NATO Grant CBP.NR.CLG 981516 and by the RFBR program.

References

[1] I. L. Krestnikov *et al*, *Phys. Rev. B* **66**, 155310 (2002).
[2] R. Seguin *et al*, *Appl. Phys. Lett* **84**, 4023 (2004).
[3] S. F. Chichibu *et al*, *J. of Appl. Phys.* **88**, 5153 (2000).
[4] M. Singh, Y. Zhang, J. Singh, U. Mishra, Appl. Phys. *Appl. Phys. Lett.* **77**, 1867 (2000)
[5] R. W. Martin, P. G. Middelton, K. P. O'Donnell, W. Van der Stricht, *Appl. Phys. Lett.* **74**, 263 (1999).
[6] Y. Arakawa, H. Sakaki, *Appl. Phys. Lett.* **40**, 939 (1982).
[7] Y. Arakawa, H. Sakaki, *Appl. Phys. Lett.* **40**, 939 (1982).
[8] C. K. Choi, Y. H. Kown, G. D. Little, G. H. Gainer, J. J. Song, Y. C. Chang, S. Keller, U. K. Mishra, S. P. DenBaars, *Phys. Rew. B* **64**, 245339 (2001).
[9] W. Nakwaski, R. P. Sarzala, M. Waiak, T. Czyszanovski, P. Macowiak, *Opto-electronic review* **11**, 127 (2003).
[10] D. S. Sizov *et al*, *'Photonics2004'* December 9-11 2004, Kocin, India.
[11] A. V. Sakharov *et al*, *"Nanaostructures Physics and Technology"* St Petersburg, Russia June 19–23, 2000, p. 216
D. D. Koleske *et al*, MRS Internet J. Nitride Semicond. Res. 4S1, G3.70 (1999)
[12] D. D. Koleske *et al*, *MRS Internet J. Nitride Semicond.* Res. 4S1, G3.70 (1999)
[13] T. Mukai *et al*, *Jpn. J. Appl. Phys.* **38**, 3976 (1999).

13th Int. Symp. "Nanostructures: Physics and Technology"
St Petersburg, Russia, June 20–25, 2005

Strains in hexagonal GaN/Al(Ga)N superlattices: Raman spectroscopic studies

A. N. Smirnov, I. N. Goncharuk, M. A. Yagovkina, M. P. Scheglov, E. E. Zavarin and W. V. Lundin
Ioffe Physico-Technical Institute, St Petersburg, Russia

Abstract. Raman spectroscopic studies have shown that GaN/AlN and GaN/AlGaN superlatices grown on α-Al_2O_3 substrates and having different buffer layers have considerable strains. It was found that in-plane strains are of the tensile type for AlN and of the compression type for GaN. Analysis of dependences of variations in strains in GaN/AlN and GaN/AlGaN superlatices on the Al content and on the ratio between layer thicknesses have been performed.

1. Introduction

At present heterostructures based on nitrides of group III metals receive a good deal of attention in the fields of basic and applied research. This is due to possibility to develop high-power, high-frequency, and high-temperature microelectronic devices and also optoelectronic devices operating in a wide spectral range [1,2]. Of special interest are the superlattices (SL) based on GaN and Al(Ga)N. To grow SLs with desired parameters, their physical properties should be studied. One of the factors responsible for physical properties are the strains in the SL layers caused by a large mismatch between thermal expansion coefficients and lattice parameters of GaN and AlN.

Raman spectroscopy is an efficient tool for characterization of SL structures. Studies of the phonon properties of GaN/AlN and GaN/AlGaN SLs have been described in several experimental [3-6] and theoretical papers [6-8]. It was found that optical phonons in GaN/AlN SLs can be divided into two groups [4-6]. The first group includes the phonons (A(TO) and E(LO)) that propagate through the entire superlattice structure and exhibit a "one-mode" behavior [6]. These phonons characterize average parameters of a SL (for instance, the average composition). The second group involves the phonons (E(TO), A(LO) and E_2) localized in the layers comprising a SL. These phonons exhibit a "two-mode" behavior [6] and can be used for characterization of the GaN and AlN layers constituting a SL [4].

Studies of bulk crystals of GaN and AlN have shown that the most strain-sensitive characteristic is the energy position of the phonon of the E_2(high) symmetry [9,10].

Therefore, this phonon can be used to estimate strains in the layers comprising GaN/Al(Ga)N SLs. In this work we demonstrate the applicability of Raman spectroscopy for estimation of strains in the SL structures based on GaN and Al(Ga)N.

2. Experimental details

The SL structures (Table 1) were grown by MOCVD and consisted of 500-1000-nm GaN or $Al_xGa_{1-x}N$ buffer layers grown directly on sapphire substrates followed by SLs [11,12]. The total thickness of each GaN/$Al_xGa_{1-x}N$ SL was about 3 μ. The GaN/AlN SL consisted of 200 periods of alternating hexagonal GaN and AlN layers grown on a (0001) sapphire substrate, the SL period (d_p) being 5–12 nm. The SLs were characterized by x-ray diffraction, atomic force microscopy, and electron probe microanalysis. Raman spectra of the SLs were measured in a backscattering configuration at room temperature with an Ar^+ laser (λ = 488 nm) excitation.

Table 1. Details of the SLs studied in this work.

Samples	Buffer	d(GaN) (nm)	d($Al_xGa_{1-x}N$) (nm)	x
1	AlGaN	5	5	0.13
2	AlGaN	5	5	0.22
3	AlGaN	5	5	0.28
4	AlGaN	5	5	0.44
5	AlGaN	5	5	0.45
6	AlGaN	5	10	0.28
7	AlGaN	2.5	2.5	0.28
8	GaN	2.5	2.5	0.28
9	GaN	5	5	0.28
10	GaN	3.5	3.5	1
11	GaN	5	5	1

3. Experimental results and discussion

Fig. 1 shows Raman spectra in the region of the E_2(high) phonon recorded for GaN/$Al_xGa_{1-x}N$ SLs with equal periods (10 nm) but different contents of Al (x). The line having a maximum intensity refers to the GaN layer. The observed high-frequency shift of the intense E_2 (high) line relative to its position in strain-free GaN is due to in-plane compression strains in the GaN layer. Strains in the layers (Fig. 2) can be estimated from the phonon line shift $\Delta\omega(E_2)$: $\epsilon_{xx} = \sigma_{xx}/\bar{C}$, where $\sigma_{xx} = K\Delta\omega(E_2)$ (GPa) is stress. For GaN: $\bar{C}$ = 463 GPa [10], $K = -2.7$ GPa/cm^{-1} [9], for AlN: $\bar{C}$ = 469 GPa, $K = -4.5$ GPa/cm^{-1} [10]. Fig. 2a shows changes in strains in the GaN layer of the GaN/AlGaN SL as a function of Al content obtained from Raman spectroscopic data.

It can be seen from Fig. 1 that the low-frequency edge of the

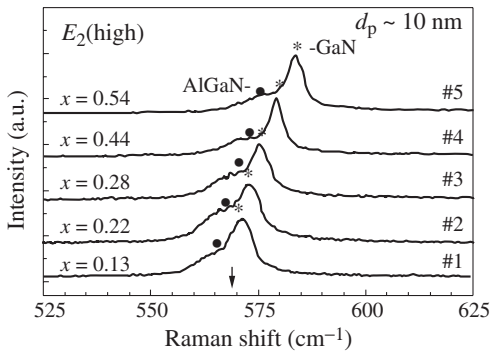

Fig. 1. Raman spectra of GaN/$Al_xGa_{1-x}N$ SLs in the region of E_2 phonons. The asterisks and points show positions of GaN and AlGaN phonon lines, respectively, in the SL. The arrow shows the position of the E_2 phonon line in strain-free GaN.

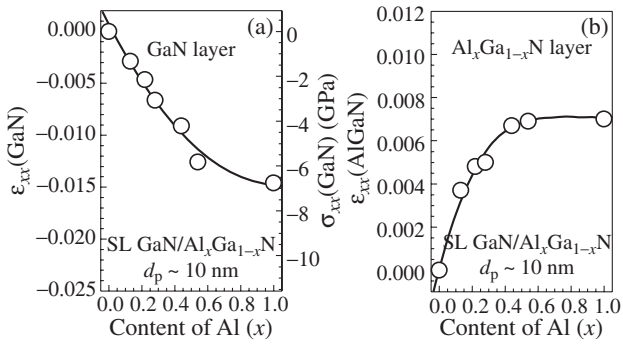

Fig. 2. In-plain strains in GaN (a) and AlGaN (b) layers of GaN/Al$_x$Ga$_{1-x}$N SLs with different Al contents.

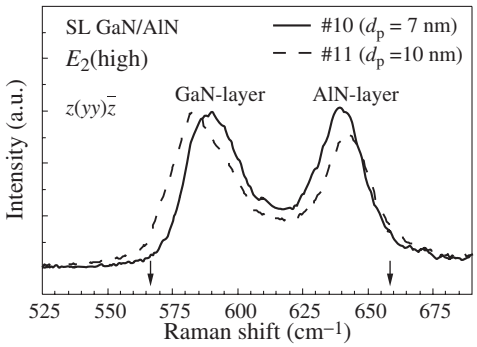

Fig. 3. Raman spectra of GaN/AlN SLs with different periods. The arrows show the positions of the E_2 phonon line in strain-free GaN and AlN.

intense line of the GaN layer has a pronounced shoulder related to the AlGaN layer. Analysis of the spectra has revealed that AlGaN layers are characterized by a low-frequency shift of the E_2(high) line with respect to its position in the strain-free material. This shift is due to the presence of tensile strains in the layers. Estimation of strains in the AlGaN layers encounters difficulties because there are no literature data on constants of the phonon deformation potential for AlGaN alloys. For this reason, we performed a linear approximation of these constants as functions of Al content. The frequency position of the E_2(high) phonon in strain-free Al$_x$Ga$_{1-x}$N was estimated as $\omega(E_2) = 567.8 + 17.3x + 40.0x^2$ [13]. Calculated strains in the AlGaN layers in the GaN/AlGaN SL are presented in Fig. 2b. It is evident from Fig. 2 that an increase in the Al content in the SL causes a considerable increase of strains in both the GaN layer and AlGaN layer. The GaN layers in the SL are characterized by compression strains and AlGaN layers are characterized by tensile strains. It should be noted that the magnitude of strains in the AlGaN layer is much lower than that in the GaN layer. The obtained dependences qualitatively coincide with the data of X-ray measurements [14].

Analysis of the data obtained for the GaN/AlGaN SLs has shown that the strains in the GaN layers depend only slightly on what buffer layer (AlGaN in sample 3 or GaN in sample 9)is used. These data are consistent with the X-ray measurements for the GaN/AlGaN SL [14]. At the same time, as indicated by the X-ray data, the AlGaN layers in the SL grown on an AlGaN buffer layer are less strained than the AlGaN layers in the SL grown on a GaN buffer layer. These conclusions are confirmed by Raman data.

Figure 3 shows Raman spectra of the GaN/AlN SLs (samples 10 and 11) with different periods. Analysis of the spectra has revealed that a decrease in the SL period leads to an increase in strains in both GaN and AlN layers. According to our estimates, strains in the GaN/AlN SL are $\epsilon_{xx} = -1.75 \cdot 10^{-2}$ for the GaN layer and $\epsilon_{xx} = 0.76 \cdot 10^{-2}$ for the AlN layer in sample 10 ($d_p \approx 7$ nm); and $\epsilon_{xx} = -1.46 \cdot 10^{-2}$ for the GaN layer and $\epsilon_{xx} = 0.70 \cdot 10^{-2}$ for the AlN layer in sample 11 ($d_p \approx 10$ nm).

Analysis of the data obtained in studies of the GaN/Al GaN SLs with different ratios between SL layer thicknesses (samples 3 and 6) has shown that an increase in the thicknesses of the AlGaN layers leads to lower strains in the AlGaN layers and higher strains in the GaN layers.

4. Summary

Thus it has been demonstrated that Raman spectroscopy is an efficient tool for estimation of strains in the layers comprising the GaN/Al(Ga)N SL. It has been shown that the layers constituting the GaN/Al(Ga)N SL are appreciably strained. An increase in the Al content, as well as a decrease in the SL period, leads to higher strains in GaN and Al(Ga)N layers. The use of the AlGaN alloy as a buffer layer allows one to reduce strains in the SL layers.

Acknowledgements

We are thankful to Dr. V. Yu. Davydov and Prof. R. N. Kyutt for fruitful discussions. This work is supported by the Programs of RAS "New materials and structures" and "Low-dimensional Quantum Structures", and RFBR (grant 03-02-17562).

References

[1] Gallium Nitrides I, ed. J.I. Pankove and T. Moustakas, *Semiconductors and Semimetals*, Vol. 50, Academic, San Diego, CA (1998).
[2] S. Nakamura and G. Fasol, *The Blue Laser Diode* (Springer, Berlin, 1997).
[3] J. Gleize *et al*, *Appl. Phys. Lett.* **74**, 703 (1999).
[4] V. Yu. Davydov *et al*, *phys. stat. sol. (b)* **234**, 975 (2002).
[5] V. Yu. Davydov *et al*, *phys. stat. sol. (c)* **0**, 2035 (2003).
[6] M. B. Smirnov *et al*, *Phys. Solid State* (2005) (in print) [*Fizika Tverdogo Tela* **204**, 761 (2005)].
[7] J. Gleize *et al*, *Phys. Rev. B* **60**, 15985 (1999).
[8] J. M. Wagner *et al*, *IPAP Conf. Series* **1**, 669 (2000).
[9] V. Yu. Davydov *et al*, *J. Appl. Phys.* **82**, 5091 (1997).
[10] J.-M. Wagner and F. Bechstedt, *phys. stat. sol. (b)* **234**, 965 (2002).
J.-M. Wagner and F. Bechstedt, *Appl. Phys. Lett.* **77**, 346 (2000).
[11] W. V. Lundin *et al*, *phys. stat. sol. (a)* **188**, 885 (2001).
[12] W. V. Lundin *et al*, *Semiconductors* **38**, 678 (2004).
[13] V. Yu. Davydov *et al*, *Phys. Rev. B* **65**, 125203 (2002).
[14] R. N. Kyutt *et al*, *Phys. Solid State* **46**, 364 (2004).

13th Int. Symp. "Nanostructures: Physics and Technology"
St Petersburg, Russia, June 20–25, 2005

Diffusion length and effective carrier lifetime in III-nitrides

N. M. Shmidt[1] and *E. B. Yakimov*[2]

[1] Ioffe Physico-Technical Institute, St Petersburg, Russia
[2] Institute of Microelectronics Technology RAS, Chernogolovka, Russia

Abstract. The results of comparative investigations of carrier lifetime and diffusion length in GaN and in the light emitting structures (LES) based on MQW InGaN/GaN with different ordering of mosaic structure are presented. The EBIC investigations have shown that the effective diffusion length measured on GaN structures could be determined by the mosaic domain boundary effect on the excess carrier transport. Such nanosize domains could also determine the lateral localization in the MQW light emitting diodes. The mosaic structure ordering effect on the quantum efficiency of LES, high values of effective carrier lifetime in well ordered LES is discussed.

Introduction

Excess carrier lifetime and diffusion length are very important parameters determining the sensitivity of photodetectors and the quantum efficiency of light emitting devices. In the most papers the diffusion length was measured in GaN and practically no data concerning the lifetime and diffusion length values in the active layers of light emitting structures (LES) based on multi-quantum well (MQW) InGaN/GaN layers. In the most publications the values of diffusion length in GaN layers did not exceed 1 μm and as a rule is in the range of 10–100 nm. If one assumes that in the active layers the diffusion length is close to these values, it is not so easy to understand the high (higher than 20%) quantum efficiency in such structures. Moreover, excess carrier lifetime value estimated from the diffusion length does not exceed 100 ps while a value estimated from the photoluminescence decay is of about 100 ns. To explain this discrepancy it is widely accepted that such high quantum efficiency is determined by the carrier localization in QW in the growth direction and in the potential fluctuations inside InGaN wells [1]. The last fluctuations are usually associated with the lateral fluctuations in In content and/or in layer thickness although the lateral potential fluctuations were observed in GaN layers also [2]. However, the relation between these potential fluctuations and the defect structure has not be established up to now.

To clarify the structural peculiarities effect on the excess carrier lifetime and diffusion length the comparative investigations of diffusion length in GaN and LES based on InGaN/GaN MQW with different ordering of mosaic structure, different quantum efficiency and excess carrier lifetime have been carried out in the Electron Beam Induced Current (EBIC) mode. The nonradiative recombination center distribution has been studied also.

1. Experimental

Investigated GaN layers and LES with different nanostructural arrangement were grown by the metal-organic chemical vapor deposition on (0001) sapphire substrates. The LES consists of 3 μm thick n-GaN lower layer, InGaN/GaN MQW with 5 periods of 3 nm InGaN and 7 nm GaN layers, p-AlGaN layer and 0.3–0.5 μm p-GaN cap layer. The nanostructural arrangement was determined by the extended defect system (dislocations and mosaic structure) relaxation and could be characterized characterized using multifractal parameter — the order degree of mosaic structure Δ [3]. Two types well- and less-ordered GaN layers and corresponding LES were investigated. For the less-ordered epilayers and LES with $\Delta \geq 0.350$ a 3D-growth was observed with a formation of large agglomerates of the mosaic structure domains in the region near threading screw dislocations and numerous dislocated domain boundaries. Such layers are characterized by low values of electron mobility (about 100 $\mathrm{cm^2\,V^{-1}\,s^{-1}}$ at 300 K) and the LES quantum efficiency less than 0.5%. For the well-ordered mosaic structures a 2D-growth with a formation of additional growth steps was observed and the defect relaxation in such structures occurred via the coherent concordance of mosaic structure domains with a formation of dilatation boundaries [4]. These layers are characterized by a rather high electron mobility (about 600 $\mathrm{cm^2\,V^{-1}\,s^{-1}}$ at 300 K) and the LES quantum efficiency higher than 10%.

The Schottky barriers for the EBIC measurements in the lower GaN layers were formed by the Ni/Au thin layer evaporation. For the EBIC investigations of LES mesa structures were prepared and p-n junction was used for the induced current collection. The EBIC measurements were carried out in the scanning electron microscope JSM-840A (Jeol) using the Keithley 428 current amplifier. All measurements were carried out in the normal geometry with e-beam perpendicular to the Schottky barrier or p-n junction plane. The diffusion length in the structures studied was obtained by fitting the collection current I_c dependence on electron beam energy E_b [5].

2. Results and discussion

The $I_c(E_b)$ dependencies normalized on the product of beam current I_b and E_b for well- and less-ordered GaN layers and for the corresponding LES are presented in Fig. 1. These dependences can be fitted with the diffusion length 300 and 100 nm, respectively (the simulated dependencies are presented in the same Figure). With decreasing temperature to liquid nitrogen temperature the diffusion length decreases in both types of structures in similar way but this decrease does not exceed 30–40%. As follows from fitting, the electron diffusion length in p-layers of LES is of about 100 nm for the both types of structures. It should be also noted that in the light emitting structures the collected current is about three times lower than that for GaN layers that could be associated with the finite transmission of MQW structure for the excess carriers. The threading dislocation density in GaN structures, as revealed by the EBIC, is about 2×10^8 $\mathrm{cm^{-2}}$ for the well-ordered structure and higher than 10^9 $\mathrm{cm^{-2}}$ for less-ordered one. In spite of rather high

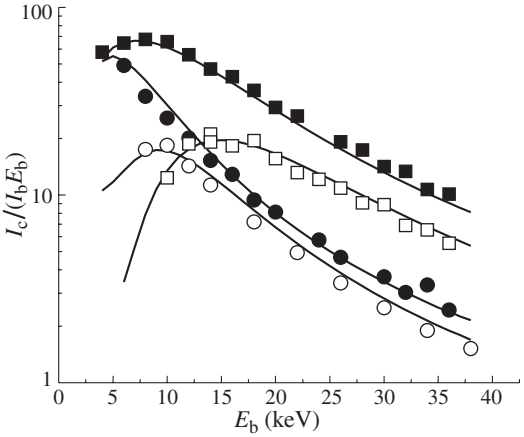

Fig. 1. Normalized $I_c(E_b)$ dependencies for well- (squares) and less-ordered GaN layers (circles) and corresponding LES (open symbols). Results of fitting are shown by solid lines.

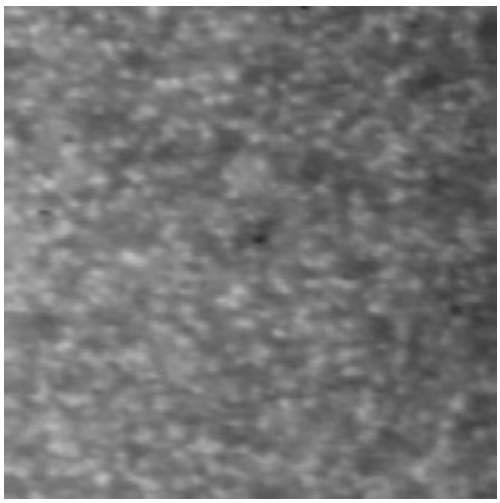

Fig. 2. EBIC image of LES obtained at 10 keV. Image size is $42\,\mu\text{m}\times 42\,\mu\text{m}$.

dislocation density, a dislocation effect on the diffusion length is small for both types of structures studied [6,7]. A typical EBIC image of LES with well-ordered structure is shown in Fig. 2. Inhomogeneous lateral distribution of collected current is well seen. On LES with less-ordered structures the image is more homogeneous that could be determined by the smaller size of electrical inhomogeneities in these structures.

From the diffusion length studies the recombination center concentration can be estimated as $N_t = 10^3 \times D/\sigma$, where D is the hole diffusivity and σ is their capture cross-section on these centers. With σ equals to $10^{-15}-10^{-16}$ cm^2, that is typical for point defects, this gives for the recombination center concentration a value, exceeding 10^{18} cm^{-3}. In our knowledge nobody revealed such high defect concentration by the direct methods. Even under an assumption of large traps with σ of about 10^{-12} cm^2 their concentration seems to be too high. To explain the low diffusion length in GaN structures it could be assumed that some potential relief exists in this material, a height of which increases with decreasing mosaic structure ordering. Such relief could decrease the effective electron mobility and, if a distance between the potential barriers is small enough, the effective diffusivity. The diffusion length in the both types of structures is observed to be practically independent of temperature in the temperature range from 90 to 300 K that well correlates with tunneling mechanism of passing the potential barriers following from I–V characteristics measured on nitride based structures [8]. As photoluminescence and electroluminescence investigations of very similar structures have shown [9], the high quantum efficiency is obtained in the well-ordered LES only, that could be understood if the potential fluctuations and the carrier localization are associated with the mosaic structure. The EBIC investigations revealing some cellular structure with the cell size comparable with that of domains [10] seems to confirm such assumption.

Thus, it is shown that the extremely low diffusion length in the structure studied and its small temperature dependence allow to assume the strong mosaic domain boundary effect on the effective excess carrier (hole) diffusivity. Under such assumption the effect of mosaic structure ordering could be associated with a different height of potential relief in the structures with different ordering. Such relief should also affect the carrier localization in the active layers of LES that determines the mosaic structure effect on the LES quantum efficiency.

Acknowledgements

The authors gratefully thank Dr. W.V. Lundin for growing a part of structures used in this study. This work was partially supported by the Russian Foundation for Basic Research (Grant 04-02-16994).

References

[1] F. A. Ponce *et al*, *Phys. Stat. Sol. (b)* **240**, 273 (2003).
[2] H. Witte *et al*, *J. Appl. Phys.* **97**, 043710 (2005).
[3] N. M. Shmidt *et al*, *Inst. Phys. Conf. Ser.* No 169, 303 (2001).
[4] A. V. Ankudinov *et al*, *Physica B* **340-342**, 462 (2003).
[5] C. J. Wu and D. B. Wittry, *J. Appl. Phys.* **49**, 2827 (1978).
[6] E. B. Yakimov, *J. Phys.: Condens. Matter.* **14**, 13069 (2002).
[7] N. M. Shmidt *et al*, *Inst. Phys. Conf. Ser.* No 180, 597 (2003).
[8] N. M. Shmidt, *J. Phys.: Condens. Matter.* **14**, 13025 (2002).
[9] A. I. Besyulkin *et al*, *Phys. Stat. Sol. (c)* **2**, 837 (2005).
[10] N. M. Shmidt *et al*, *Phys. Stat. Sol. (c)* **2** (2005).

13th Int. Symp. "Nanostructures: Physics and Technology"
St Petersburg, Russia, June 20–25, 2005

Magneto-optical studies of epitaxial cobalt films on CaF_2/Si

N. L. Yakovlev[1], A. Balanev[2], A. K. Kaveev[2], B. B. Krichevtsov[2], N. S. Sokolov[2], J. Camarero[3] and R. Miranda[3]

[1] Institute of Materials Research and Engineering, 117602 Singapore
[2] Ioffe Physico-Technical Institute, St Petersburg, Russia
[3] Departamento de Fisica de la Materia Condensada, Universidad Autonoma de Madrid, Spain

Abstract. Epitaxial cobalt films on CaF_2 buffer layers on Si were grown by molecular beam epitaxy. It was found that Co grows in face centred cubic lattice. Magnetic properties of the films were studied using magneto-optical Kerr effect. In-plane magnetic anisotropy was revealed in Co/CaF_2(110)/Si(100) structures with goffered fluoride layer. Due to light interference in the transparent fluoride, the value of polarisation rotation can be higher than 1 degree in polar geometry.

Introduction

Ferromagnetic films on semiconductor substrates are very attractive for numerous applications [1]. Magnetic properties of these films can be studied using magneto-optical Kerr effect (MOKE). In the structures containing transparent insulating layers, considerable enhancement of MOKE has been recently reported [2]. It facilitates optical studies of individual single-domain nanomagnets. In the present work, we study magnetic properties of cobalt films and nanostructures grown by molecular beam epitaxy on silicon with calcium fluoride buffer layer. To our knowledge, this system has not been explored yet.

1. Growth and structure of cobalt films

Depending on substrate orientation, the fluoride film has different surface morphology and epitaxial relation to the substrate. On Si(111), CaF_2 grows with atomically flat (111) surface. On Si(001) and relatively high temperature around 750 °C, CaF_2 has (110) growing surface goffered with {111} facets. The goffers run along [$\bar{1}$10] direction of Si, which is also [$\bar{1}$10] direction of CaF_2. It was found that when cobalt grows on CaF_2 in the range from room temperature to 500 °C, it has cubic face centred crystal lattice with the axes coinciding with those of CaF_2. This was observed by reflection high energy electron diffraction during the growth. The factors suppressing hexagonal lattice growth are: template effect of the fluoride, high lattice mismatch with consequent high strain, kinetics of Co nucleation in the conditions far from thermodynamic equilibrium.

Cobalt layers were covered with 5 nm CaF_2 layer to prevent oxidation or atmospheric damage. Atomic force microscopy was measured on these films in air after the growth and showed that Co nucleates as 3D clusters. At a high temperature, they grow individually, Fig. 1(a), even CaF_2 surface can be seen. At low temperature, coalescence of the clusters produces a continuous layer, Fig. 1(b). Although the nucleation of Co clusters is in the bottom of the grooves and coalescence occurs along the grooves at first, the clusters grow wider fast and quickly overlap across the ridges of CaF_2 layer. Therefore Co layer morphology is not like thin wires, but like a corrugated sheet.

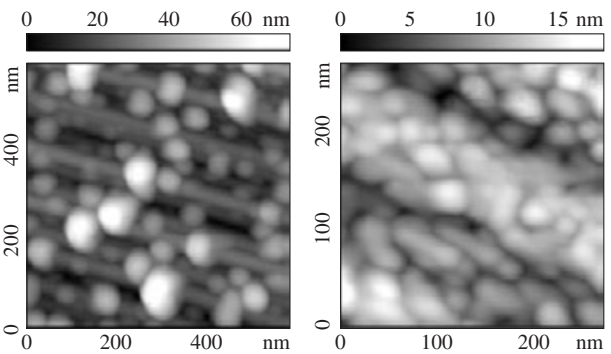

Fig. 1. Atomic force microscopy images of cobalt layer on goffered surface of CaF_2(110) on Si(100): (a) Co 2 nm grown at 500 °C, (b) Co 6 nm grown at 100 °C.

2. Magnetism of cobalt films

Magnetic field dependences of polar, longitudinal and transversal MOKE were studied in Co/CaF_2/Si nanostructures with different orientation of Si-substrate and thickness of Co and CaF_2 layers. Measurements were carried out with light wavelength 633 nm in magnetic field $B \leq 1.5$ T at room temperature 294 K. The sensitivity of light polarization rotation was about 10 arc s.

Magnetic anisotropy of these nanostructures is related mainly to demagnetization form factor. Magnetic field **B** normal to the film surface results in the magnetization rotation from the plane of film and the appearance of polar MOKE, Fig. 2. The maximum magnitude of saturation magnetic field in investigated nanostructures was about 1 T. In structures with the thickness of CaF_2 layer 100 nm and the thickness of Co

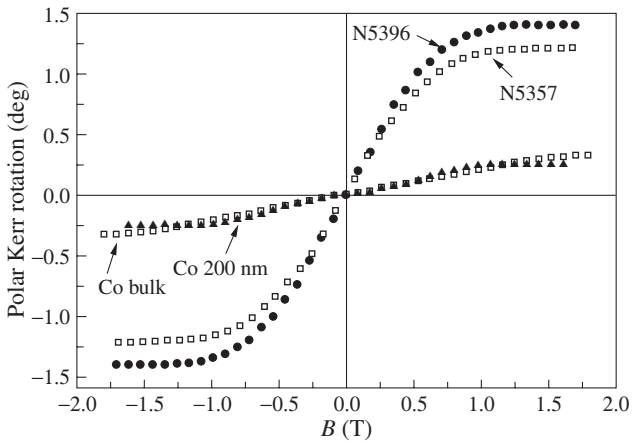

Fig. 2. Magnetic field dependence of polar MOKE in Co/CaF_2(111)/Si(111) films (samples N5396 and N5357), in 200 nm thick polycrystalline Co film and in bulk Co. Labels are at the corresponding curves.

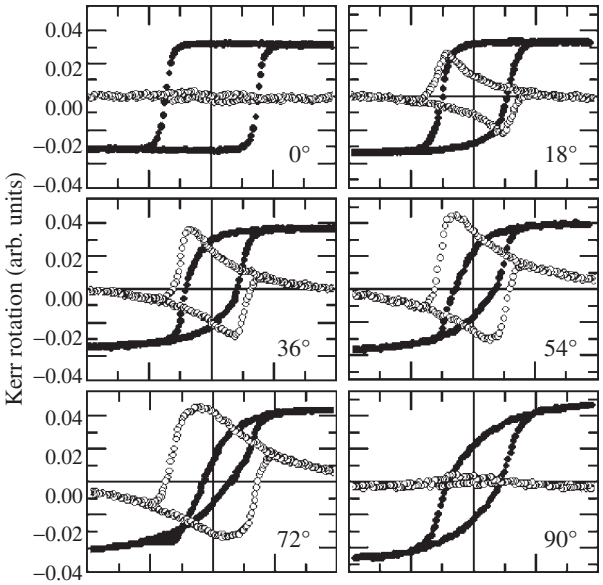

Fig. 3. Hysteresis loops of longitudinal (filled circles) and transversal (open circles) MOKE in cobalt film grown on goffered $CaF_2(110)$ layer on Si(100) at different angles between the direction of goffers and magnetic field. The morphology of this sample is shown in Fig. 1(b).

layer 15 nm, maximum value of polar MOKE $\alpha = -1.4$ deg has been observed. This value is considerably (by a factor of 3) higher than observed in the bulk cobalt samples and in polycrystalline Co films 200 nm thick, Fig. 2. Usually the enhancement of MOKE in magnetic multilayers is related to the effect of multiple reflection of light in transparent buffer or covering layer. Nevertheless the calculation shows that in frames of usual approach [3] the sign and the magnitude of MOKE are not adequately described and additional mechanisms accounting the film microstructure should be taken into account.

In nanostructures grown on Si(111) substrates the hysteresis loops (HL) of longitudinal MOKE (magnetic field B is in the plane of film and in the plane of light incidence) do not depend on the orientation of magnetic field **B** in the plane of film. In contrast to that, the HL in the films grown on $CaF_2(110)$ buffer layer with goffered surface reveal a pronounced anisotropy, Fig. 3. Coercive field B_c has maximum values for orientation of magnetic field **B** along the direction **r** of goffer structure and the shape of HL is approximately rectangular. The tilting of magnetic field **B** from **r** in the plane of film leads to decrease of B_c and to change of HL shape. Transversal MOKE, measured together with longitudinal Kerr effect using light beam splitter, Fig. 3, clearly indicates the appearance of magnetization $\mathbf{M}_\perp$ oriented perpendicular to the direction of magnetic field during the magnetization reversing. This shows that the magnetization process is determined mainly by the magnetization rotation mechanism. The sign of magnetization rotation (clockwise or counterclockwise) is determined by orientation of magnetic field **B** relative to the direction of goffer structure **r**. The angle variations of B_c and the change of HL shape indicate the presence of uniaxial magnetic anisotropy described by anisotropy energy $\delta W_a = -K_u(\mathbf{M} \cdot \mathbf{u})$, where K_u is the parameter of uniaxial anisotropy and **u** is easy axis direction in the plane of the film. In principal, the direction of **u** should coincide with the direction of **r** but the shape of HL for direction of magnetic field **B** perpendicular to **r** does not correspond to the predicted by simple model of uniaxial anisotropy. According to this model for $\mathbf{B} \perp \mathbf{u}$, the coercive field $B_c = 0$ and field dependence **M(B)** should be linear function; that was not observed in experiment, Fig. 3. This disagreement may be explained, if there are areas of the films with some distribution of easy axes direction **u** around the direction of **r**. Calculations show that, supposing Gaussian distribution of **u**, the deviation of **u** from **r** should be about 30 deg for adequate description of HL. The reason of the distribution of easy axis is the cluster structure of Co layer, Fig. 1.

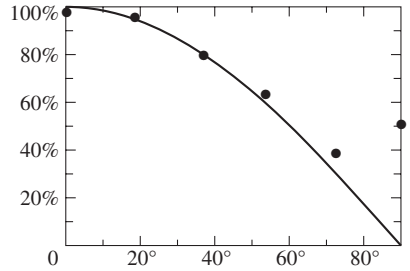

Fig. 4. Dependence of remnant magnetization in longitudinal MOKE from Fig. 3 on azimuthal angle ϕ between the direction of goffers and magnetic field (filled circles) and $\cos(\phi)$ (solid line).

The remnant magnetization in Co film on goffered CaF_2 layer depends on the azimuthal angle ϕ between goffers and magnetic field as $\cos(\phi)$ until $\phi = 72^o$, Fig. 4. This effect is due to shape anisotropy and is consistent with magnetization rotation mechanism, so that when the value of the field returns to zero, the magnetisation vector returns to the direction of the goffers and has the same magnitude as at $\phi = 0$. Note that Kerr rotation is proportional to scalar product of the magnetisation and light wave vector. However there is a spike of remnant magnetisation and absence of transversal MOKE at $\phi = 90^o$; i.e. when the field is along Co[100] axis. This fact is probably related to crystallographic anisotropy; according to [4], the easy magnetization axis is [100] in face centred cubic cobalt.

Acknowledgements

The authors appreciate the support of this work by Russian Foundation for Basic Research (grant 05-02-16451-a) and NATO (grant PST.CLG.978792).

References

[1] G.A. Prinz, *Science* **282**, 1660 (1998).
[2] N. Qureshi, H. Schmidt and A. R. Hawkins, *Appl. Phys. Lett.* **85**, 431 (2004).
[3] S. Sugano and N. Kojima (Eds.), *Magneto-optics*, (Berlin: Springer-Verlag) 334 p, 2000.
[4] A. Bettac, J. Bansmann, V. Senz and K. H. Meiwes-Broer, *Surface Science* **454-456**, 936 (2000).

13th Int. Symp. "Nanostructures: Physics and Technology"
St Petersburg, Russia, June 20–25, 2005

Growth and characterization of InGaAs nanowires by selective area MOVPE

J. Motohisa[1], J. Noborisaka[1], M. Akabori[1*], P. Mohan[1], S. Hara[1], T. Fukui[1], F. Zwanenburg[2], S. De Franceschi[2] and L. P. Kouwenhoven[2]

[1] Research Center for Integrated Quantum Electronics and Graduate School of Information Science and Technology, Hokkaido University, North 13, West 8, Sapporo 060-8628, Japan
[2] Kavli Institute of Nanoscience Delft, Delft University of Technology, PO Box 5046, 2600 GA Delft, The Netherlands
[*] present address: Japan Advanced Institute of Science and Technology

Abstract. Free standing hexagonal InGaAs nanowire arrays with minimum diameter of 60 nm have grown on partially masked InP (111)B substrates by catalyst-free selective-area metalorganic vapor phase epitaxy (SA-MOVPE), and their structural, optical, and transport properties have bee characterized. Although transmission electron microscopy study shows the nanowires contains high-density of rotational twins in Zincblende lattice, photoluminescence at 0.75 eV is confirmed for nanowires arrays. Transport measurement of nominally undoped nanowires have revealed that they shows good ohmic characteristics of *n*-type semiconductors.

1. Introduction

Recently, semiconductor nanowires have been attracting interest for a new class of building blocks for nanoscale electronics and photonics in the bottom-up approach [1,2,3]. So far, most of the nanowires have been formed by catalyst-assisted vapor-liquid-solid (VLS) growth [4]. We have reported an alternative catalyst-free approach to form III/V compound semiconductor nanowires and their arrays utilizing selective-area metalorganic vapor phase epitaxy (SA-MOVPE) [5,6]. This method is originally developed to form semiconductor pillar arrays for the application of photonic crystals [7]. In this report, we describe the growth of InGaAs nanowires on InP substrates, and their characterization of structural, optical, and electronic properties.

2. Experimental procedure

We prepared patterned InP (111)B substrates partially covered with SiO_2 for SA-MOVPE. Periodic array of circular mask openings was defined by using electron beam lithography and wet chemical etching. The size of the mask opening d_0 was ranged from 50 nm ~ 120 nm, and the pitch a was also varied from 0.2 μm to 3 μm. Since the diameter d of the nanowire is directly related to the opening diameter d_0, we tried to obtain smaller d_0 as possible by controlling the amount of the EB dose as well as the designed opening size. Then, SA-MOVPE of InGaAs was carried out on the masked InP substrates at growth temperature of 650 °C.

3. Results and discussions

Figure 1(a) shows typical SEM images of InGaAs nanowires grown on (111)B. The growth time is 20 minutes. We can see an uniform array of vertically standing InGaAs nanowires on the substrate. The cross section of the nanowires is hexagonal, indicating that they are surrounded by of six {110} sidewall facets normal to (111)B plane. Here, the diameter d and height h of the nanowires is about 180 nm and 0.7 μm, respectively. Furthermore, as we reported previously [7], the height h becomes higher as the decrease of d_0 or d. Thus, thin InGaAs nanowires can also be grown by reducing d_0 as shown in Fig. 1(b). As

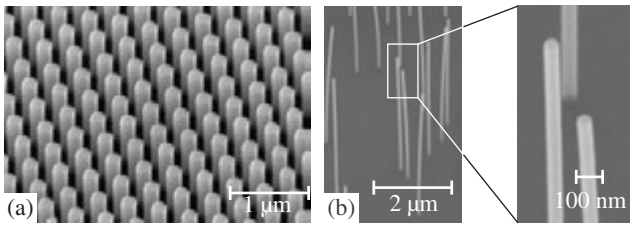

Fig. 1. Typical Bird's eye SEM image of InGaAs nanowires. (a) High-density uniform nanowire arrays and (b) thin and long nanowires, which are obtained in the same growth run with different pattern geometry.

a result, we obtained InGaAs nanowires with $d \sim 60$ nm and $h \sim 5.6\,\mu$m. From these results, we conclude that semiconductor nanowires with diameter of several tens of nanometers can easily be obtained simply by reducing the initial size of the mask opening in SA-MOVPE.

Figure 2 shows high-resolution TEM image of the InGaAs nanowire with $d \sim 200$ nm. It was also confirmed that nanowires was grown along the [111] direction. In an image with lower magnification (Fig. 2(b)), we can see the nanowire was straight and not tapered, that is, the diameter was the same at its bottom and at its top, and had a flat (111)B surface at the top. It was also confirmed that the sidewalls of the nanowires were extremely flat. On the other hand, in higher magnification of Fig. 2(b), we can see the multiple rotational twins are present in InGaAs nanowires.

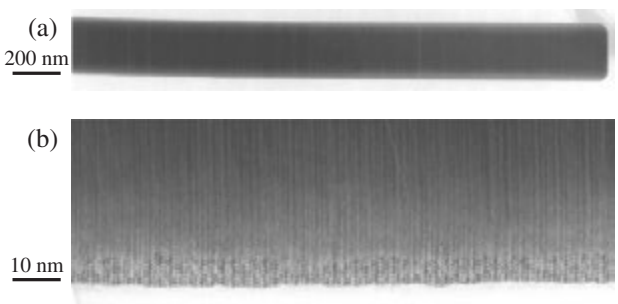

Fig. 2. High resolution TEM image of InGaAs nanowires. (a) Lower magnification and (b) higher magnification.

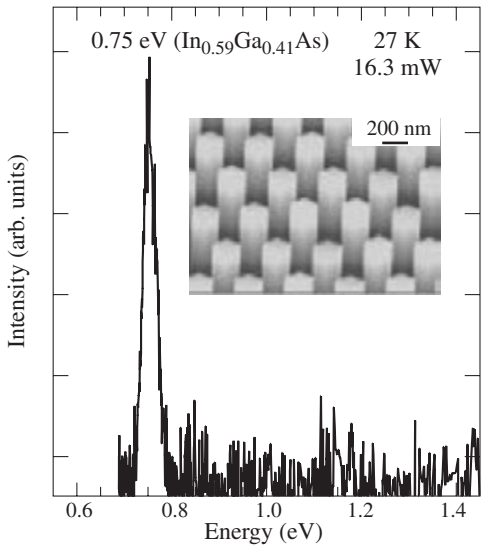

Fig. 3. PL spectrum of InGaAs nanowire arrays.

Figure 3 shows a photoluminescence of InGaAs nanowire array, whose SEM image is shown in the inset. With all the twins in nanowires, we found a single peak at 0.75 eV. Alloy composition of In in nanowires seems slightly to be shifted to In rich region from that on planar substrate and is estimated to be 0.59. The origin of this high In incorporation is probably long diffusion distance and/or low desorption rate of In atoms.

Finally, we measured the conductance through InGaAs nanowires. InGaAs nanowires were cut down and dispersed onto SiO_2/p^+Si substrate. Ohmic contacts for nanowires were made using Ti/Pt, and the Si substrate was also used as a back gate. Typical two-terminal resistance of the nanowires at 2 K is shown Fig. 4. Although the InGaAs nanowires are nominally undoped, we get transistor characteristic of n-type channel. In a separate measurement , the electron density is estimated to be $1 \times 10^{17}\,\mathrm{cm}^{-3}$ and the mobility is around $1000\,\mathrm{cm}^2/\mathrm{Vs}$ at 2 K. The result is still preliminary, but we are confident that our nanowires are cleaner than those grown by VLS approaches and contain less unintentional impurities.

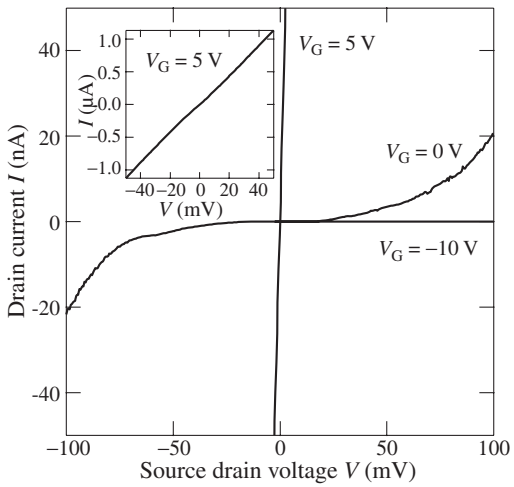

Fig. 4. I–V Characteristics of InGaAs nanowires measured at 2 K.

Acknowledgement

This work has been supported in part by Grant-in-Aid for Scientific Research from the Japan Society of Promotion of Science.

References

[1] Y. Huang, X. Duan, Y. Cui, L. J. Lauhon, K.-H. Kim, C. M. Lieber, *Science*, **294**, 1313 (2001).
[2] M. H. Huang, S. Mao, H. Fick, H. Yan, Y. Wu, H. Kind, E. Weber, R. Russo and P. Yang, *Science*, **292**, 1897 (2001).
[3] J. Wang, M. S. Gudiksen, X. Duan, Y. Cui and C. M. Lieber, *Science*, **293** 1455 (2001).
[4] K. Hiruma, M. Yazawa, T. Katsuyama, K. Ogawa, K. Haraguchi, M. Koguchi and H. Kakibayashi, *J. Appl. Phys.*, **77**, 447 (1995).
[5] J. Motohisa, J. Takeda, M. Inari, J. Noborisaka and T. Fukui, *Physica E* **23**, 298 (2004).
[6] J. Motohisa, J. Noborisaka, J. Takeda, M. Inari and T. Fukui, *J. Cryst. Growth* **272**, 180 (2004).
[7] M. Akabori, J. Takeda, J. Motohisa and T. Fukui, *Nanotechnology*, **14**, 1071 (2003).

13th Int. Symp. "Nanostructures: Physics and Technology"
St Petersburg, Russia, June 20–25, 2005

MBE growth of GaAs nanowhiskers stimulated by the ad-atom diffusion

V. G. Dubrovskii[1,2], G. E. Cirlin[1,2,3], I. P. Soshnikov[1,2], A. A. Tonkikh[1,3], N. V. Sibirev[3], Yu. B. Samsonenko[1,2,3] and V. M. Ustinov[1,2]

[1] Ioffe Physico-Technical Institute, St Petersburg, Russia
[2] St Petersburg Physico-Technical Centre of RAS for Research and Education, St Petersburg, Russia
[3] Institute for Analytical Instrumentation RAS, 190103, St Petersburg, Russia

Abstract. In this work we present the recent results on the investigation of formation mechanisms and physical properties of GaAs nanowhiskers grown by molecular beam epitaxy on the GaAs surface activated by Au. We demonstrate the possibility to grow nanowhiskers with very high length/diameter ratios (>100) and length up to 15 microns. It is found that GaAs nanowhiskers exhibit a non-classical decreasing length/diamater dependence. It is shown that the nanowhisker length is several times larger than the thickness of deposited GaAs. These facts can not be explained within the frame of the known vapor-liquid-solid mechanism of whisker growth. We attribute the observed growth behavior to the effect of ad-atom diffusion from the surface along the whisker side facets towards their top. A kinetic model of nanowhisker formation is developed that accounts for the effect of ad-atom diffusion. Simulation results are compared to the experimental data and a good correlation between them is shown.

Introduction

Semiconductor nanowhiskers (NWs) are wire-like nanocrystals with high (10–100) length/diameter ratio and the diameter of several tens of nanometers. Unique structural properties of NWs make them very attractive in numerous applications including optoelectronics, microelectronics, field emission devices and analytical chemistry [1]. At the moment, NWs of different semiconductor materials (Si, GaAs, InP) are mainly grown by chemical vapor deposition (CVD) [1]. However, molecular beam epitaxy (MBE) method may offer a number of advantages in the NW growth technology [2]. Strongly non-equilibrium conditions and a high surface diffusivity of ad-atoms during MBE may bring new features into the traditional concept of the so-called "vapor-liquid-solid" (VLS) growth of whiskers [2]. In this work we investigate theoretically and experimentally the formation mechanisms and physical properties of GaAs NWs grown by MBE on the GaAs(111)B surface activated by Au growth catalyst.

1. Theoretical model

In the theoretical model of NW formation (Fig. 1) we consider (i) adsorption and desorption processes on the surface of liquid drop, (ii) crystallization of supersaturated liquid alloy on the crystal surface under the drop, (iii) the growth of non-activated surface and (iv) the diffusion flux of ad-atoms from the surface to the NW top.

The NW growth rate in the case of mono-center nucleation [4] reads

$$V_L = \pi D^2 h I(\zeta)/4\,, \qquad (1)$$

where h is the monolayer height and $I(\zeta)$ is the rate of nucleation from the liquid alloy given by the Zel'dovich formula [4]. Supersaturation of liquid alloy ζ is found from the stationary equation of material balance for a semiconductor material in the drop

$$\frac{\pi D^2}{4} J - \frac{\pi D^2}{2} \frac{r_l C_{eq}}{\tau_l}(\zeta+1) - \left(\frac{\pi}{4} D^2\right)^2 \frac{h}{\Omega_s} I(\zeta) + j = 0. \qquad (2)$$

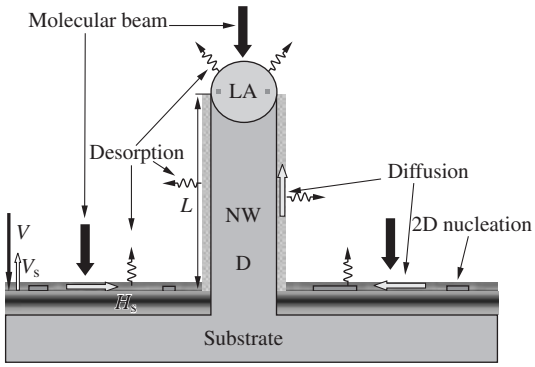

Fig. 1. The model of NW growth during MBE. NW is a cylinder of diameter D and length L. The deposition rate from a molecular beam is V, the surface growth rate is V_s and the NW growth rate is dL/dt.

Here the first term stands for the adsorption on the drop, the second term describes desorption, the third term describes the crystallization of liquid alloy on the crystal surface and the fourth term gives the diffusion flux of ad-atoms from the surface to the NW top along their side facets. Parameter J is the deposition flux, r_l is the interatomic distance in the liquid phase, C_{eq} is the equilibrium concentration of liquid alloy, τ_l is the mean lifetime of atom in the liquid phase, Ω_s is the volume per arom in the crystal and j is the ad-atom diffusion flux to the NW top. This flux is found from the diffusion equation for the ad-atom concentration on the side facets of NW. The detailed analysis of Ref. [3] shows that for sufficiently thin NWs with length L smaller or comparable with the diffusion length of ad-atoms on the side facet L_f ($\sim 10\,\mu$m for Ga atoms on GaAs(110) side planes [5]) the model (1), (2) is reduced to the pure diffusion-induced growth mode

$$\frac{dL}{dt} = hV\left[\varepsilon - \gamma + \frac{D_*}{D\cosh(L/L_f)}\right]. \qquad (3)$$

Here $\gamma = 2x_{eq}/W\tau_l$ is the desorption contribution, x_{eq} is the percent equilibrium concentration of alloy and W the growth rate in monolayers per second (ML/s). This equation for NW growth rate at given D, L and L_f is governed by two con-

trol parameters: the relative difference between the deposition rate and the surface growth rate $\varepsilon = (V - V_s)/V$ and the characteristic diameter at which the diffusion-induced effects become predominant D_*. This parameter depends on ε, NW surface density N_W and average NW perimeter P_W as $D_* = 4(\tau_l/\tau_f)\varepsilon/N_W P_W$, τ_f being the mean life time of ad-atom on the side facet. To calculate ε we have developed the theory of epitaxial growth on a non-activated surface with an outdoing flux of ad-atoms to the NWs. It has been found that for typical growth conditions during MBE of GaAs $\varepsilon \sim 0.2{-}0.4$, the diffusion of ad-atoms towards the NW top thus considerably reducing the surface growth rate. For typical values of $x_{eq} \sim 0.1$, $W \sim 1$ ML/s, $\tau_l \sim \tau_f \sim 1$ s, $P_W \sim 300$ nm, $N_W \sim 3\times10^9\,\mathrm{cm}^{-2}$ we obtain $\gamma \sim 0.2$ and $D_* \sim 100{-}200$ nm. Therefore, desorption from the liquid drop may reduce the vertical growth rate of NW up to 1/5, however, for thin NWs with $R \sim 10$ nm the ad-atom diffusion may increase the growth rate in order of magnitude. Integration of Eq. (3) gives explicitly the NW length $L(t)$ in the form

$$I(\varphi, \lambda) = \varphi \int_0^{\lambda} \frac{dx}{\varphi + \cosh(x)} \qquad (4)$$

with $\varphi \equiv R_c/R(\varepsilon - \gamma)$. This equation is used for the simulations of NW $L(D)$ dependencies and for the comparison with the results obtained in the experimental part of the work.

2. Experimental

In our growth experiments, the NW formation procedure consisted of three stages [6]. GaAs layers with the effective thickness H from 500 to 1500 nm were deposited to form NWs. The deposition rate of GaAs $W = 1.0$ ML/s and the substrate temperature $T = 585\,^\circ$C were kept constant for all samples. The visualization of surface morphology was performed by applying the CamScan S4-90FE scanning electron microscope (SEM) with a field emission gun, operating in the regime of secondary electron emission. The energy of primary beam was amounted to 20 keV. Cross-sectional SEM image of NWs sample is presented in Fig. 2.

3. Results and discussion

It is seen that the maximum length of GaAs NWs is much higher than the thickness of deposited GaAs 3 600 nm against 500 nm.

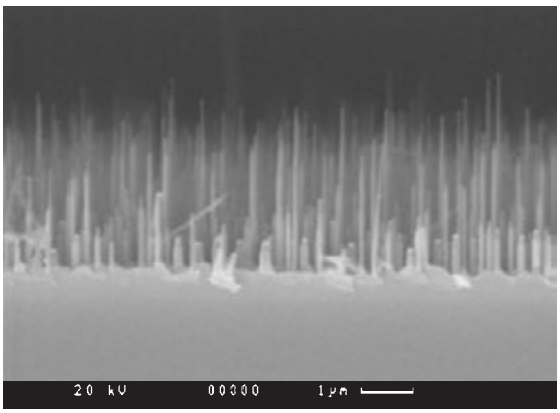

Fig. 2. SEM image of Sample 2 grown at $d_{Au} = 1.0$ nm, $H = 500$ nm, $T = 585\,^\circ$C and $W = 1$ ML/s.

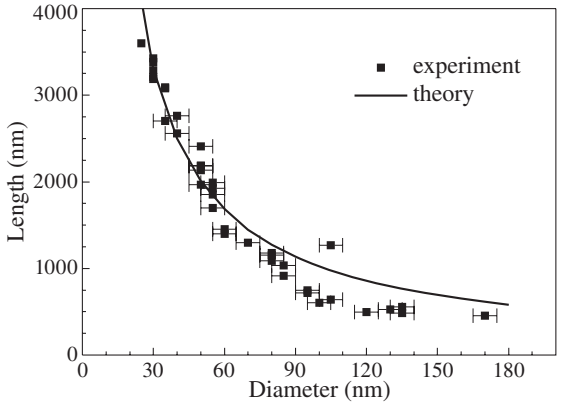

Fig. 3. Experimental and theoretical length/diameter dependencies for Sample 2. Theoretical curve is obtained at $H = 500$ nm, $D_c = 200$ nm, $\gamma = 0.15$ and $\varepsilon = 0.2$.

From the analysis of SEM image we obtained the experimental length/diameter dependence of NWs. The experimental $L(D)$ curve is decreasing function. Experimental $L(D)$ curve is presented in Fig. 3. It is seen that the minimum diameter is about 30 nm and the maximum is about 170 nm. The length of NWs amounts to 3600 nm at $D = 30$ nm and decreases to 420 nm at $D = 170$ nm, the L/D ratio thus changing from 120 for the thinnest NWs down to 2.4 for the thickest ones. The maximum length of NWs is more than 7 times higher than the thickness of deposited GaAs. Therefore, the NWs in our experiments are formed by the diffusion-induced mechanism rather than by the classical VLS mechanism.

Theoretical $L(D)$ dependence obtained from Eqs. (4) is also presented in Fig. 3. The best fit to the experimental results is provided at $D_c = 200$ nm. We may therefore conclude that the MBE growth of GaAs NWs on the GaAs(111)B surface activated by Au at given growth conditions implies the domination of the diffusion induced growth for drops smaller with radius smaller than 100 nm. Also, it should be noted that our experimental curve does not obey simple $1/D$ dependence within the whole range of NW lengths and diameters. This is in contrast to the recent results on the MBE grown Si NWs of Ref. [2], where the $1/D$ dependence was found to fit the experimental $L(D)$ curves for all D from 70 nm up to 230 nm.

To conclude, we have developed the kinetic model of NW formation during MBE that explains the observed effects and provides a good qualitative correlation with the experimental results.

Acknowledgements

The authors are grateful to the financial support received from different scientific programs of the Russian Academy of Sciences, Ministry of Science and Education, RFBR grant 05-02-16495, and SANDiE.

References

[1] Y. Cui *et al*, *Science*, **91**, 831 (2000).
[2] L. Schubert *et al*, *Appl.Phys.Lett.*, **84**, 4968 (2004).
[3] G. E. Cirlin *et al*, *Semiconductors*, **39(5)**, in press (2005).
[4] V. G. Dubrovskii *et al*, *Phys. Rev. E*, **70**, 031604 (2004).
[5] T. Takebe *et al*, *J. Appl. Phys.*, **81**, 7273 (1997).
[6] V. G. Dubrovskii *et al*, *Phys. Stat. Sol. (b)*, **241**, R30 (2004).

13th Int. Symp. "Nanostructures: Physics and Technology"
St Petersburg, Russia, June 20–25, 2005

Novel growth mechanism of strained islands: multimodal closed-shell distribution of quantum dots

M. B. Lifshits[1,2], V. A. Shchukin[1,2], D. Bimberg[2] and D. E. Jesson[3]

[1] Ioffe Physico-Technical Institute, St Petersburg, Russia
[2] Institut für Festkörperphysik, Technische Universität Berlin, D-10623 Berlin, Germany
[3] School of Physics and Materials Engineering, Monash University, Victoria 3800, Australia

Abstract. A kinetic theory of an early stage evolution of an ensemble of strained islands during growth interruption is developed. The evolution starts from a broad distribution of flat islands with a low height-to-base length ratio. Due to highly asymmetric strain-induced barriers for nucleation of a next atomic layer on different facets, islands having a fixed base grow predominantly vertically. Different sub-ensembles of islands having different island bases evolve independently. The evolution of islands within each sub-ensemble is mediated by the chemical potential of the adatom sea. The evolution may result in either growth or dissolution or sticking in Gibbs free energy local minima related to shapes with complete facets. A growth scenario is possible where islands having initially shorter base length stop the vertical growth at a smaller height. This explains a multimodal distribution of InAs/GaAs QDs recently revealed from photoluminescence spectra.

Introduction

The spontaneous formation of nanostructures on surfaces offers an attractive route for the self-organization of three-dimensional (3D) semiconductor islands or quantum dots (QDs) [1,2]. The QD structures have important applications in the design of novel devices such as QD lasers. However, size distribution is a critical issue for device applications.

A remarkable feature of the epitaxy of highly lattice-mismatched systems (InAs/GaAs, Ge/Si, etc.) is the size-limiting growth of strained islands. This occurs, when the ensemble is subject to a growth interruption, and the evolution stops as the islands reach a certain size. First, the size-limiting growth preserves a defect-free state of a mismatched system if the limiting size of the islands is below the critical size for the onset of dislocations. Second, this may provide a rather narrow size distribution of islands close to the limiting size. Both thermodynamic and kinetic models explaining the size-limiting growth are discussed in [2]. Under certain conditions bimodal and three-modal distributions of island sizes have been observed and models for explanation have been proposed (for a review, see [2]).

Recent photoluminescence (PL) studies of an ensemble of MOCVD-grown self-organized InAs/GaAs QDs have intriguingly revealed [3,4] several (up to eight) clearly resolved narrow peaks (Fig. 1). These were attributed to a *multimodal* distribution of the exciton ground state recombination energy. Narrow PL peaks were referred to a monolayer (ML) variation of the QD height and half-base length. Observation of such a monolayer splitting implies the existence of structurally and chemically well-defined upper interfaces. The optical results allowed to draw quantitative conclusions about the shape, composition and the height of the investigated QDs based on realistic eight-band $\mathbf{k}\cdot\mathbf{p}$/configuration interaction model calculations [5]. The latter had earlier been proved to yield a good agreement with optical data, particularly, between the calculated excited exciton states transition energies and peak positions in photoluminescene excitation (PLE) spectra, for both strained [6] and unstrained [7] QDs. In [4], the comparison of the PL spectra with calculated exction ground state transition energies allowed to conclude that the base length of the QDs increases (in steps of 2 lattice parameters) with increasing QD height (in 1 ML steps). The system of islands with a discrete variation of the QD size in monolayer steps was named an ensemble of shell-like QDs [4].

None of earlier theoretical approaches has allowed to explain the formation of a *multimodal* distribution of QDs. In the present paper a new growth model is developed addressing this issue.

1. QD ensemble evolution

The evolution of an ensemble of strained InAs islands over an InAs wetting layer (WL) on the GaAs substrate during growth interruption is considered. The islands are surrounded by the adatom sea. Islands having the shape of a truncated pyramid with the square base can grow or dissolve via adatom attachment or detachment.

The key point is the stress concentration at the base perimeter of the strained islands which leads to a logarithmic singularity in the elastic energy density creating a barrier for the formation of a new atomic layer on a side facet [8]. Given the base length, the barrier strength increases upon the island height. At the initial state, the system consists of the flat (1 ML high) islands over the WL with a broad distribution in base lengths.

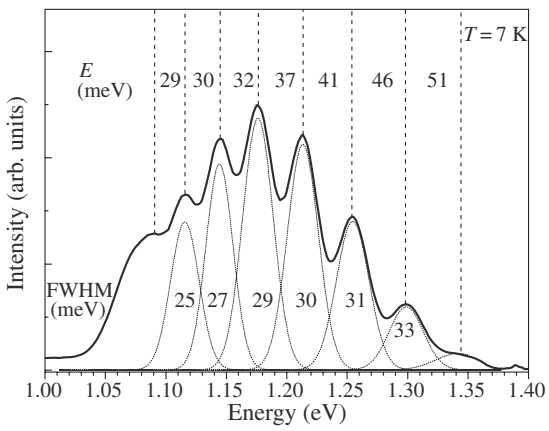

Fig. 1. Photoluminescence spectrum of InAs/GaAs quantum dots fitted with Gaussians demonstrating a full width at half maximum (FWHM) for each sub-ensemble of $\sim$ 30 meV. [3]

These islands can grow in both base length and height. As 2 ML high islands form, the barrier strength increases hindering further island growth in base length. The further growth will then occur preferably via the monolayer nucleation on the top facet. Then the island base remains constant and the height increases by one monolayer after another. Different sub-ensembles of islands having different initial island bases evolve independently.

The energetics of the growth of every next atomic layer atop a given truncated pyramid is described by a change of the Gibbs free energy of the system $\delta\Phi$ due to the formation of an embryo which partially covers the top facet,

$$\delta\Phi_{\text{island}} = \delta E_{\text{edge}} + \delta E_{\text{elast}} - \bar{\mu}\delta N \,. \qquad (1)$$

Here δE_{edge} is the step energy of the embryo edge, $\bar{\mu}$ is the adatom sea chemical potential, and δN is the number of atoms in the embryo. The elastic relaxation energy change δE_{elast} can be found by using the small slope approximation [9].

Figure 2(a) illustrates that $\delta\Phi_{\text{island}} > 0$ as the embryo formation starts and, only if the embryo achieves some critical size, $\delta\Phi_{\text{island}}$ becomes negative so that the embryo formation lowers the system free energy. As the island having the shape of a truncated pyramid grows up one monolayer after another, the size of the top facet decreases. At a certain height, the top size is no longer large enough to favor the formation of the next embryo. Then the growth of this island will stop and its size will stabilize. As soon as islands with larger initial bases have larger top sizes at the same height, such islands will stop growing at a larger height.

The ensemble evolution model considers elementary processes of the growth of an island having a base L and a height h by an increase of the height by 1 ML ($h \to h+1$) or partial dissolution of an island ($h \to h-1$). The processes involve overcoming a barrier as shown in Fig. 2(a), and their rate obeys the Arrhenius law,

$$W(L, h \to h \pm 1) = \omega \exp\left[-\Delta\Phi_{\text{barrier}}/\left(k_{\text{B}}T\right)\right] , \qquad (2)$$

assuming the prefactor ω same for all the islands. The temporal evolution of the distribution function $P(L, h; t)$ obeys the master equation,

$$\begin{aligned}\frac{\partial P(L,h;t)}{\partial t} = {} & W(L, h-1 \to h)P(L, h-1; t) \\ & - W(L, h \to h-1)P(L, h; t) \\ & - W(L, h \to h+1)P(L, h; t) \\ & + W(L, h+1 \to h)P(L, h+1; t) \,. \end{aligned} \qquad (3)$$

The growth or dissolution of the islands occurs due to the mass exchange between the islands and the adatom sea. For the growth interruption, the mass conservation law reads,

$$q_{\text{adatom}}(t) + \sum_L \sum_h P(L, h; t)V(L, h) = Q = \text{const} \,, \qquad (4)$$

where the island volume $V(L, h)$ is counted in number of atoms, q_{adatom} is the surface concentration of adatoms over the WL, and Q is the excess amount of the deposited material over the critical WL thickness. The adatom concentration is related to the adatom sea chemical potential,

$$q_{\text{adatom}} = \exp\left[\bar{\mu}/\left(k_{\text{B}}T\right)\right] . \qquad (5)$$

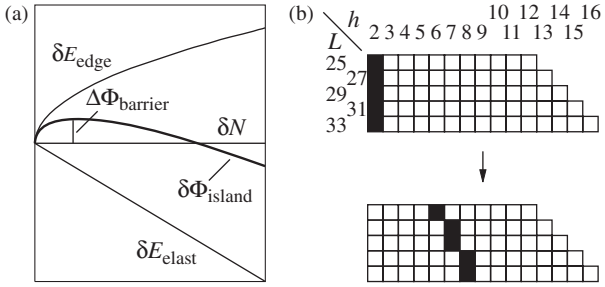

Fig. 2. (a) The Gibbs free energy change $\delta\Phi_{\text{island}}$ due to the formation of a monolayer embryo on the top facet. (b) Schematics of the islands ensemble evolution from the initial distribution in L and h (top) to the final steady-state one (bottom).

As the islands start growing, the number of adatoms in the adatom sea decreases thus lowering the chemical potential $\bar{\mu}$. The latter results in a larger critical embryo size, and the limiting heights of the islands become smaller. This additionally contributes to the stopping of the island growth.

2. Results and discussion

Figure 2(b) depicts a sample result of the solution of the coupled set of Eqs. (3)–(5). It shows that an initial distribution of flat islands evolves into a steady-state distribution of 3D islands, where islands with larger base have also a larger height. The result allows an explanation of three groups of experimental data. First, the particular island distribution in base length and height. Second, the temporal evolution of the PL spectra upon growth interruption, where the intensity of each peak corresponding to a certain island height h first increases and then decreases [10]. This is due to the fact that islands with many different base lengths first reach the height h and then the islands with larger base length grow in height further. Third, a small blue shift of the PL peaks with time [10] is explained similarly, as, given the height h, islands with larger bases grow further in height and remaining islands with smaller bases shift the envelope PL peak to higher photon energies.

Acknowledgements

The work has been supported, in different parts, by the Russian Foundation for Basic Research, by the Russian Federal Program on Support of Leading Scientific Schools, by the Deutsche Forschungsgemeinschaft (SFB 296), and by the SANDiE Network of Excellence of the European Commission, contract number NMP4-CT-2004-500101.

References

[1] D. Bimberg, M. Grundmann, N. N. Ledentsov, *Quantum Dot Heterostructures*, Wiley, Chichester (1998).
[2] V. A. Shchukin, N. N. Ledentsov, D. Bimberg, *Epitaxy of Nanostructures*, Springer, Heidelberg (2003).
[3] F. Guffarth, *et al.*, *Physica E* **21**, 326 (2004).
[4] R. Heitz, *et al.*, *Phys. Rev. B* **71**, 045325 (2005).
[5] O. Stier, *et al.*, *phys. stat. sol. (a)* **190**, 477 (2002).
[6] R. Heitz, *et al.*, *Phys. Rev. B* **62**, 11017 (2000).
[7] A. Rastelli, *et al.*, *Phys. Rev. Lett.* **92**, 166104 (2004).
[8] D. E. Jesson, *et al.*, *Phys. Rev. Lett.* **80**, 5156 (1998).
[9] J. Tersoff and R. M. Tromp, *Phys. Rev. Lett.* **70**, 2782 (1993).
[10] K. Pötschke, *et al.*, *Physica E* **21**, 606 (2004).

13th Int. Symp. "Nanostructures: Physics and Technology"
St Petersburg, Russia, June 20–25, 2005

Epitaxial growth on vicinal and nanostructured Si(001): from basic growth instabilities to perfectly ordered dot arrays

H. Lichtenberger[1], Z. Zhong[1,2], G. Chen[1], J. Mysliveček[1,3], G. Bauer[1] and *F. Schäffler*[1]

[1] Institut für Halbleiterphysik, Johannes Kepler Universität, Linz, Austria
[2] current address: Max-Planck-Institut für Festkörperforschung, Stuttgart, Germany
[3] current address: Institute for Surfaces and Interfaces (ISG3) Forschungszentrum Jülich GmbH, Jülich, Germany

Abstract. We explored two methods to obtain laterally ordered Ge/Si quantum dot arrays. For the first we exploit the two independent growth instabilities of the SiGe/Si(001) heterosystem, namely kinetic step bunching and Stranski–Krastanov (SK) island growth, to implement a two-stage growth scheme for the fabrication of long-range ordered SiGe islands. The second approach is to deposit Ge/SiGe onto pre-patterned Si-substrates, which are prepared via lithography and subsequent reactive ion etching (RIE). It results in perfectly ordered, 2D dot arrays that can be extended into 3D by strain-ordering of a Ge-dot superlattice.

Introduction

The self-organized growth of Ge/Si quantum dot heterostructures has attracted considerable interest because of its potential for electronic and optoelectronics devices, and its compatibility with the well-explored Si-technology. Recently, laterally ordered Ge/Si quantum dots have also been suggested for the implementation of quantum computing functions, as well as quantum information storage, which both require the separate identification and external addressability of each quantum dot. To obtain laterally ordered Ge/Si quantum dot arrays, we explored two methods. i) A route which is only based on self-organization to achieve ordering is based on a slightly vicinal Si(001) surface, which is intrinsically unstable against kinetic-step-bunching during homoepitaxial growth. The resulting ripple morphology serves as a one-dimensional template for preferential Ge dot nucleation. ii) Another approach is to deposit Ge/SiGe onto two-dimensionally pre-patterned Si-substrates, which are prepared via lithography and subsequent reactive ion etching (RIE).

1. Results and discussion

The Si(001) surface is intrinsically unstable against kinetic step bunching during Si homo- and SiGe heteroepitaxy [1–4]. This phenomena was originally attributed to lattice-mismatch strain [5], but it is now clear that it is of purely kinetic origin.

Recent kinetic Monte Carlo simulations in connection with a basic stability analysis provide strong evidence for step bunching being caused by the interplay between the adsorption/desorption kinetics at single atomic height steps and the pronounced diffusion anisotropy on the reconstructed Si(001) surface [6–7]. The simulations show excellent agreement with STM experiments, and qualitatively reproduce the pronounced temperature dependence of the step bunching phenomena.

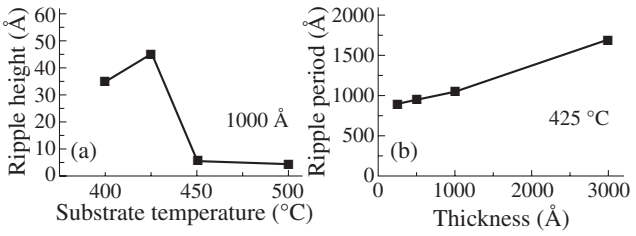

Fig. 1. (a) Dependence of the step-bunching ripple height on substrate temperature for a 1000 Å Si-buffer. The maximum of the instability for 4° miscut and a Si-rate of 0.2 Å/s is around 425 °C; (b) Increase of the ripple period with thickness for the optimum Si-buffer temperature at 425 °C.

The detailed understanding of homoepitaxial step bunching on Si(001) allowed us to tailor the period and height of the bunches by controlling substrate miscut, growth temperature, deposition rate and layer thickness (Fig. 1). This way, homoepitaxial layers with ripple periods of 100 ± 10 nm were prepared on Si(001) substrates with 4° miscut along [110] (Fig. 2).

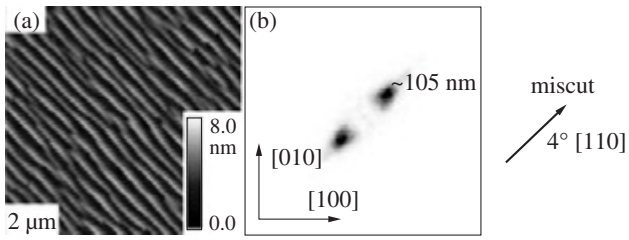

Fig. 2. (a) Kinetic step bunching of a homoepitaxial Si layer on a vicinal Si(001) substrate with 4° miscut along [110]. (b) Fast Fourier Transform showing a spacing for the step bunches of 100 ± 10 nm.

These were then employed as templates for the ordering of SiGe or Ge dots grown in the strain-driven Stranski-Krastanov mode. When the period length of the template complies with the mean spacing of the dots, only one dot row fits into one period (Fig. 3).

We could show that the dots then nucleate at the step bunches, where the energetically favorable {105} facets of the dots are most easily created by step-meandering [8–11]. Considering growth further away from thermal equilibrium, the $Si_{0.55}Ge_{0.45}$ film deposited at 425 °C does not completely disintegrate into individual islands, but reveals how and where island nucleation commences: Upon SiGe deposition the flanks of the step bunches are converted into a zigzag train of adjacent (105) and (015) facets. The originally smooth flanks match quite well the slope of the [551] intersection line between two adjacent {105} facets and thus can easily be converted into a {105} faceted SiGe ridge structure, which is perpendicular to the step-bunches. This is a step-meandering instability induced

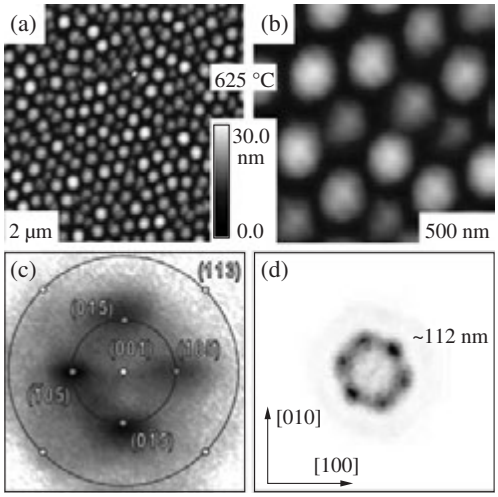

Fig. 3. (a–b) Self-organized SiGe dots on the Si template from Fig. 2. with the 50 Å $Si_{0.55}Ge_{0.45}$ epilayer deposited at 625 °C; (c) Surface orientation maps derived from Fig. 2a. The dots show preferentially {105} facets (inner circle). (d) Fast Fourier Transform of Fig. 3a, revealing rectangular, face-centered ordering of the dots.

by strain and the low-energy {105} facets of SiGe on Si(001). It marks the transition (Fig. 4) from conformal Si/SiGe epilayer growth to strain-driven, ordered 3D-growth which is observed at 625 °C for the $Si_{0.55}Ge_{0.45}$ epi-layer. This leads to a fair degree of 2D rectangular, face-centered ordering of the SiGe dots (Fig. 3d) in an approach that employs self-organization mechanisms only [9–12].

To realize perfectly ordered SiGe and Ge dots in 2D and 3D, we used lithographically defined pit arrays. For small enough periods, only one dot per unit cell is created, which nucleates at the lowest point of the pit (Fig. 5).

XTEM images reveal that the nucleation site is defined by the intersection of neighboring facets, which form during Si buffer layer deposition on the nanostructured templates 13]. Thus, by combining nanostructuring with self-organized growth, ar-

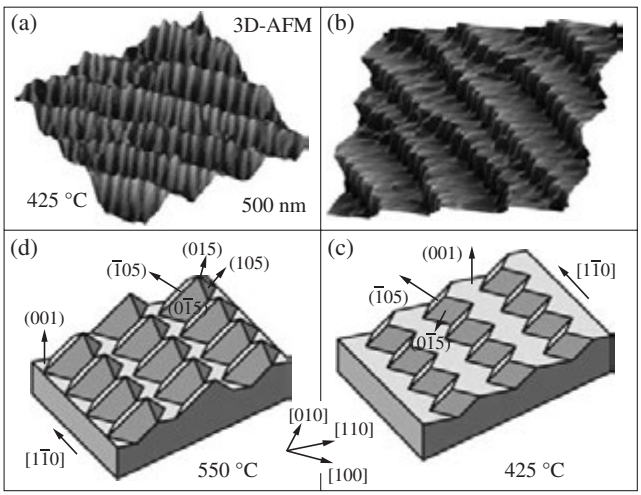

Fig. 4. (a–b) 3D representations of a 50 Å $Si_{0.55}Ge_{0.45}$-layer grown at 425 °C showing a strain-induced {105} zigzag structure decorating the bunch flanks. The dominant facets for SiGe layers deposited at 425 and 550 °C are depicted schematically in (c) and (d) respectively. At 550 °C also retrograde {105} facets appear which are necessary to form 3D-islands as depicted in Fig. 3.

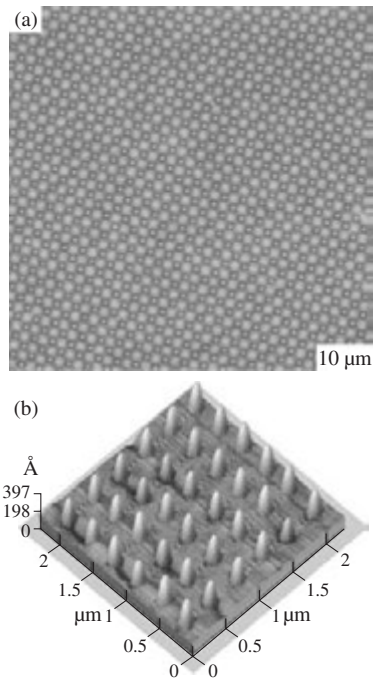

Fig. 5. Perfect 2D arrays of self-organized Ge on a Si template defined by lithography and reactive ion etching.

bitrarily large areas of perfectly ordered 2D SiGe and Ge dot arrays can be implemented [14–16]. On this base we also realized perfect 3D Ge dot arrays by additionally exploiting the strain-driven vertical ordering of Ge dots in a Si/Ge dot superlattice [17].

Lithographically defined ordering of SiGe and Ge dots fulfills an essential precondition for all but the must elemental applications of self-organized dots, namely their addressability. Vertical stacking of such arrays provides the option to use the topmost dot layer as a self-aligned mask for selective ion implantation.

References

[1] C. Schelling *et al*, *Phys. Rev. Lett.*, **83**, 995 (1999).
[2] C. Schelling *et al*, *Phys. Rev. B*, **64**, 041301(R) (2001).
[3] M. Mühlberger *et al*, *Surf. Sci.*, **721**, 532 (2003).
[4] A. Ronda *et al*, *Physica E*, **23**, 370 (2004).
[5] J. Tersoff *et al*, *Phys. Rev. Lett.*, **75**, 2730 (1995).
[6] J. Mysliveček *et al*, *Surf. Sci.*, **520**, 193 (2002).
[7] J. Mysliveček *et al*, *cond-mat/* 021231.
[8] H. Lichtenberger *et al*, *J. Cryst. Growth*, in print.
[9] H. Lichtenberger *et al*, *Appl. Phys. Lett.*, in print.
[10] C. Teichert *et al*, *Appl. Phys. A: Mater. Sci. Process.*, **67**, 675 (1998).
[11] J.-H. Zhu *et al*, *Appl. Phys. Lett.*, **33**, 620 (1998).
[12] C. Teichert *et al*, *Phys. Rep.*, **365**, 335 (2002).
[13] Z. Zhong *et al*, *J. Appl. Phys.*, **93**, 6258 (2003).
[14] Z. Zhong *et al*, *Appl. Phys. Lett.*, **82**, 445 (2003).
[15] Z. Zhong *et al*, *Appl. Phys. Lett.*, **82**, 4779 (2003).
[16] Z. Zhong *et al*, *Appl. Phys. Lett.*, **83**, 3695 (2003).
[17] Z. Zhong *et al*, *Physica E*, **21**, 588 (2004).

13th Int. Symp. "Nanostructures: Physics and Technology"
St Petersburg, Russia, June 20–25, 2005

Mechanical stress in selective oxidized GaAs/$(AlGa)_xO_y$ structures

S. A. Blokhin[1], A. N. Smirnov[1], A. G. Gladyshev[1], N. V. Kryzhanovskaya[1], N. A. Maleev[1], A. A. Zhukov[1], A. G. Kuzmenkov[1], A. P. Vasil'ev[1], E. S. Semenova[1], E. V. Nikitina[1], M. V. Maximov[1], N. N. Ledentsov[2] and V. I. Ustinov[1]

[1] Ioffe Physico-Technical Institute, St Petersburg, Russia
[2] Institut für Festkörperphysik, Technische Universität Berlin, Germany

Abstract. Raman spectroscopy was applied to study wet selective oxidation processes of $Al_{0.97}Ga_{0.03}As$ layers. The mechanical stresses induced in GaAs/$(AlGa)_xO_y$ structures by different regimes of wet selective oxidation processes were determined. Effects of local sample heating by laser radiation under Raman measurement, photoresist hardening during oxidation and over-oxidation phenomenon were analyzed. Optimization of selective oxidation apparatus and regimes was done. It allows to realize integrated matrix of vertical-cavity surface-emitting lasers (VCSELs) based on double InGaAs quantum well active region with oxidized top $(AlGa)_xO_y$/GaAs and AlGaAs/GaAs bottom distributed Bragg reflectors.

Introduction

The technique of wet selective oxidation of $Al_xGa_{1-x}As$ alloys has been widely applied to the fabrication of different $A^{III}B^V$ semiconductor devices: light emitting diodes (LED) [1], metal-oxide-semiconductor field effect transistors (MOSFET) [2] and vertical-cavity surface emitting lasers (VCSELs) [3]. This method offers a unique possibility to form high quality buried oxide layers. These layers can be used as VCSEL current apertures and optical confinement regions. However, several important issues are still not resolved with respect to selective oxidation technique. The problem of mechanical reliability and stability of device after oxidation is among of such issues. Suffice it to say, after wet selective oxidation of $Al_xGa_{1-x}As$ alloys the $(AlGa)_xO_y$ generally appears as small-grain polycrystalline γ-$(AlGa)_2O_3$ embedded in an amorphous matrix [4]. Since γ-phase of alumina is significantly more dense than initial AlAs, a tensile stress is induced in $(AlGa)_xO_y$. This stress partially relaxes by shrinking along the growth direction (up to 20%). The specific thickness contraction degree (for given structure) depends on layer thickness and composition as well as oxidation process regimes. In this connection the investigations of mechanical strain induced in oxidized GaAs/$(AlGa)_xO_y$ structures are very important. In this work we estimated the local mechanical stresses induced in GaAs layers by the lateral selective wet oxidation of an underlying $Al_{0.97}Ga_{0.03}As$ layers layers. The Raman spectroscopy was used as an experimental technique. Obtained results were applied for optimization of the VCSELs fabrication process.

1. Experiment

The samples investigated were grown by molecular beam epitaxy (Riber 32P)on semiinsulating (100) GaAs substrate. After deposition of GaAs buffer, an $Al_{0.97}Ga_{0.03}As$ (227 nm) layer is grown, followed by a GaAs (94 nm) layer. The mesa-structures of a size 30 and 100 μm (1 μm deep) were prepared using a standard photolithography with the special photoresist hardening method [5] and reactive ion etching. In order to get rid of plasma induced damage or contamination to the sidewalls of the mesa (which are dramatically change oxidation reaction) directly after the dry-etch process the samples are exposed to a short wet-etch dip in a NH_4OH:H_2O_2:H_2O (1:2:50) solution for 4 s at room temperature. It is noteworthy that in order to avoid the deterioration of the surface morphology (due to partially oxidation of top surface GaAs layer) and the undesirable oxidation (due to the surface pinholes and other defects) we used the photoresist as a protective mask.

The lateral wet selective oxidation of the $Al_{0.97}Ga_{0.03}As$ layers was performed in the double chamber system. In order to remove the absorption water from the sidewalls of the mesa the samples are preliminarily heated up to 160 °C in the charging port. The gas flow is sufficient to insure a water vapor saturated oxidation regime. The samples were exposed to a water vapor (90 °C), which is carried by nitrogen at 420 °C with consequent *in situ* annealing in atmosphere of dry nitrogen. Before exposure to air the samples was cooled off slowly (0.2 °C/s) to 160 °C. The Raman spectra were measured in the backscattering $z(x, x)\bar{z}$ geometry using a 488 nm Ar^+ laser. The Ne-lamp is used for absolute calibration of the spectrometer before each measurement. The characteristic absorption length of this laser line in GaAs is about 100 nm, therefore the influence of GaAs buffer and substrate on detected signal can be neglected.

2. Results and discussion

The Raman spectra of the unoxidized (A) and oxidized samples without (B) and with (C) *in situ* annealing are shown at Fig. 1. The unoxidized sample (A) demonstrates simple spectra: the peaks at 292 cm^{-1} and 403 cm^{-1} are attributed to GaAs-LO and AlAs-LO phonons. The low intensive (forbidden in cross polarization geometry) peaks at 269 cm^{-1} and 361 cm^{-1} are GaAs-TO and AlAs-TO phonons. After the oxidation process the AlAs-peaks vanished, suggesting that the $Al_{0.97}Ga_{0.03}As$ has converted to As, $(AlGa)_xO_y$ and As_2O_3. In Raman spectra of sample B, the prominent feature (range from 180 cm^{-1} to 280 cm^{-1}) is the superposition of the several peaks arising from crystalline As (197 and 257 cm^{-1}), amorphous As (227 cm^{-1}) and GaAs-TO phonon (269 cm^{-1}). The broad and weak peaks due to As_2O_3 and Al_2O_3 are observed at 475 cm^{-1} and 587 cm^{-1}, respectively. Note, that the quality and mechanical stability of oxidized layers are strongly related to the removal of volatile products (As and As_2O_3) [6]. Besides, an amorphous $(AlGa)_xO_y$ contains a large quantity of hydrated phases, which are metastable and the oxidation reaction can be continue [7]. To reduce the concentration of these intermediate products and to transform an initial amorphous phase to a

polycrystalline γ-$(AlGa)_xO_y$ phase *in situ* annealing was used after oxidation. After preliminary investigation the optimal annealing regime (temperature of oxidation, time up to 30 min) was found. As a result, the As and As_2O_3 features are disappeared in Raman spectrum obtained from sample C. Besides, after rapid thermal annealing (imitation of contact annealing) samples do not suffer from the delamination and shown good thermal and mechanical stability.

Lattice deformations induced in surface GaAs layers by the selective oxidation of an underlying $Al_{0.97}Ga_{0.03}As$ layer result in the energy shift of the GaAs phonon line in Raman spectra, which is given by $\Delta\omega_{LO}\,(cm^{-1}) = -3.9\sigma$ (GPa) assuming a uniform bi-axial stress σ [8]. To begin with, the comparison of Raman spectrum obtained from an initial and unoxidized mesa-structures show that the photolithography and reactive ion etching do not induce the appreciable stress in structures (below the detection limit). It is noteworthy that local heating by the focused laser beam can yield the contribution to the phonon peak shifts (mainly due to thermal expansion). To separate this effect we have measured the pump power dependence of the peak position of the GaAs-LO phonon (see inset in Fig. 1). Extrapolation of this curve to zero power density takes a real peak shift $\Delta\omega_{LO} = -0.39\,cm^{-1}$ (compressive stress in growth direction).

In order to estimate the stress induced in the GaAs layer by selective oxidation correctly, we have analysed the effect of photoresist hardening under oxidation process (see Fig. 2a). The existence of small compressive stress in the GaAs layers is observed. Therefore, to take into account effects of local heating by laser beam and photoresist hardening we estimated the actual GaAs-LO phonon line shift as $\Delta\omega_{LO} = -0.46\,cm^{-1}$ and the corresponding level of tensile stress is $\sigma = 118$ GPa. These results correlate with previously reported data for GaAs/$(AlGa)_xO_y$ structures [9].

The influence of excess oxidation on structures mechanical stability was studied (see Fig. 2b). The further prolongation of oxidation process increase compressive stress in sample and results in dramatically change of optical properties of such structures.

The optimization of setup and wet selective oxidation technology resulted in realization of integrated matrix of vertical-cavity surface-emitting lasers (VCSELs) based on double InGaAs quantum well active region with oxidized top $(AlGa)_xO_y$/GaAs and AlGaAs/GaAs bottom distributed Bragg reflectors. The individual VCESLs with 8–10 μm oxidized apertures demonstrated lasing at 960–965 nm with room-temperature threshold current of 1.0–2.5 mA, external efficiency up to 0.4 mW/mA and maximum CW output power more than 2.0 mW [10].

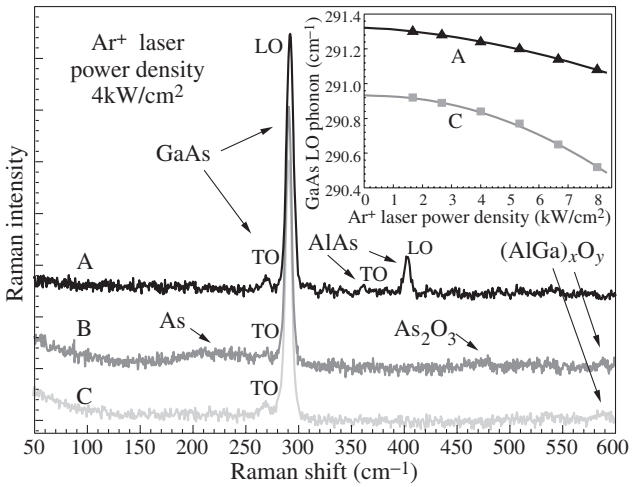

Fig. 1. Raman spectra of unoxidized (A) and oxidized samples without (B) and with (C) *in situ* annealing. In the inset, the peak position GaAs-LO phonon as function of the laser power density.

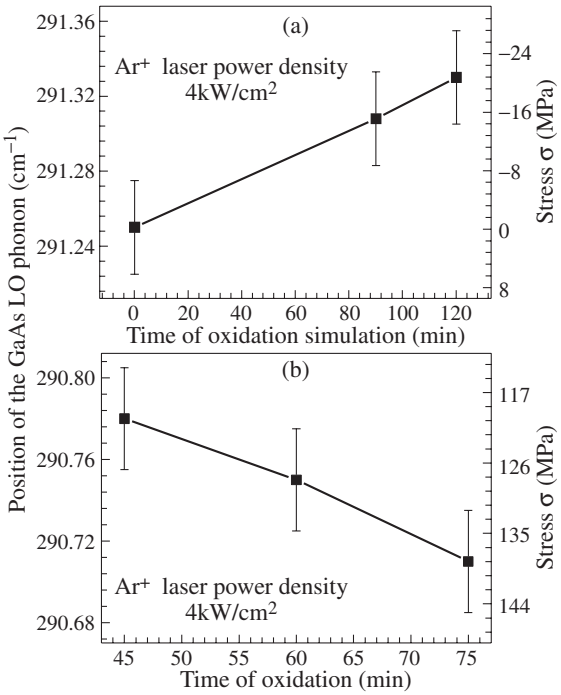

Fig. 2. The peak position GaAs-LO phonon and stress as function of the oxidation simulation (water vapor is absent) time (a) and the oxidation time (b).

Acknowledgements

This work was supported by Scientific program of Departments of Russian Academy of Science "New Materials and Structures" and Fundamental investigation program of Presidium of Russian Academy of Science "Low Dimensional Quantum Structures".

References

[1] D. L. Huffaker, C. C. Lin, J. Shin, D. G. Deppe, *Appl. Phys. Lett.*, **66**, 3096 (1995).
[2] E. I. Chen, N. Holonyak, S. A. Maranowski, *Appl. Phys. Lett.*, **66**, 2688 (1995).
[3] D. L. Huffaker, D. G. Deppe, K. Kummar, T. J. Rogers, *Appl. Phys. Lett.*, **65**, 97 (1994).
[4] R. D. Twesten, D. M. Follstaedt, K. D. Choquette, R. P. Schneider, *Appl. Phys. Lett.*, **69**, 19 (1996).
[5] N. A. Maleev, A. R. Kovsh, A. E. Zhukov, *et al*, *Semiconductors*, **37**, 1265 (2003).
[6] H. Q. Jia, H. Chen, W. C. Wang, W. X. Wang, W. Li, Q. Huang, J. Zhou, *J. Crystal Growth*, **223**, 484 (2001).
[7] C. I. H. Ashby, J. P. Sullivan, P. P. Newcomer, *et al*, *Appl. Phys. Lett.*, **70**, 2443 (1997).
[8] S. C. Jain, M. Willander, H. Maes, *Semicond. Sci. Technol.*, **11**, 641 (1996).
[9] J. P. Landesman, A. Fiore, J. Nagle, V. Berger, E. Rosencher, P. Puech, *Appl. Phys. Lett.*, **71**, 2520 (1997).
[10] N. A. Maleev, A. G. Kuzmenkov, A. A. Zhukov, *et al Semiconductors*, **39**, 487 (2005).

13th Int. Symp. "Nanostructures: Physics and Technology"
St Petersburg, Russia, June 20–25, 2005

Formation of magnetic GaAs:Mn layers for InGaAs/GaAs light emitting quantum-size structures

M. V. Dorokhin, B. N. Zvonkov, Yu. A. Danilov, V. V. Podolskii, P. B. Demina and O. V. Vikhrova
Physico-Technical Research Institute, University of Nizhny Novgorod, 603950 Nizhny Novgorod, Russia

Abstract. The possibility of the formation of light emitting devices, containing GaAs:Mn layers was demonstrated. Luminescent and electrical properties of the GaAs structures with Mn doped layers were studied. It was shown that GaAs:Mn layers exhibit ferromagnetic properties at room temperatures after the laser annealing. The laser annealing leads also to the change in electrical and luminescent properties of light emitting devices.

Introduction

The structures, that include Mn-doped GaAs layers with ferromagnetic properties, are of strong interest because of their applicability as the basis of spintronic devices. The great success in the formation of (Ga,Mn)As structures was achieved using MBE method [1]. Luminescent properties of these layers in structures with p-n junction were studied in [2]. Formation of (Ga,Mn)As layers by MOCVD method is also of obvious interest [3]. Incorporating this layers in well studied light emitting structures, containing In(Ga)As/GaAs quantum dots and quantum wells, may lead to a creation of new devices in which the low dimension advantages are combined with ferromagnetism. In this work we investigate electrical and electroluminescent properties of light emitting diodes, containing GaAs:Mn layers, grown by MOCVD epitaxy.

1. Experimental

Investigated structures were grown in a horizontal quartz reactor in an atmosphere of hydrogen. The precursors used for MOCVD epitaxy were trimethylgallium, trimethylindium and arsine. For doping by Mn we used the evaporation of Mn metal target by the emission of a Nd:YAG laser operating in the Q-switched mode. For fabrication of test GaMnAs/i-GaAs Hall samples the GaAs layers were deposited using laser sputtering of GaAs wafer. In this case, a target, composed of GaAs and Mn, was used. The composition of the alloy could be specified by varying of sputtering times for each material (GaAs and Mn).

Measurements of the Hall effect in magnetic field, variable in the range of ± 0.36 T, were taken on van der Pauw samples at room temperature (RT) and 77 K. Ohmic contacts were prepared by alloying of In dots to layer surface. The photoluminescence (PL) spectra of the structures were measured at 77 K under excitation by a He-Ne laser with a power of 40 mW.

For the structures, grown completely by MOCVD epitaxy on n^+-substrates, we studied the spectra of photovoltage (PV) at RT and electroluminescence (EL) at 77 K. Forward bias I–V characteristics were taken at 77 K and RT. The structure for EL, PV and I–V measurements is shown at Fig. 1.

The front ohmic contact was deposited on p^+-GaAs surface through the mask with the diameter of 500 mm. Uncovered surface of the sample was etched. Back ohmic contact was prepared to n^+-substrate.

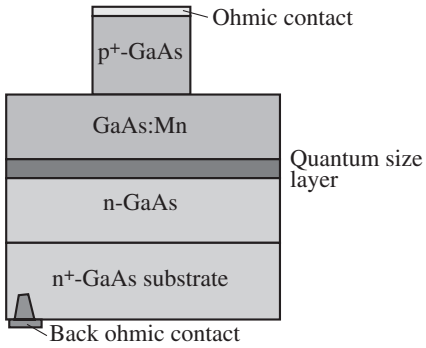

Fig. 1. The schematic picture of studied device.

2. Results and duscussion

As-grown layers of GaAs:Mn have high resistance ($> 10^5\ \Omega$), resulting in problems for Hall effect measurements. To activate the Mn atoms, incorporated into GaAs, we subjected the samples to annealing with one pulse (25 ns, power density $\sim 10^7$ W/cm^2) of a ruby laser (wavelength of 0.68 μm). After annealing the GaAs:Mn layers reveal p-type conductivity and anomalous Hall effect at both RT and 77 K (Fig. 2). It should be noted that curve at 77 K demonstrates hysteresis loop characteristic for ferromagnetic films. Calculation of electrical parameters from RT curve for 80 nm GaAs:Mn layer gives values of hole mobility ≈ 10 cm^2/V s and concentration $\approx 3\times 10^{20}$ cm^{-3}.

The PV spectra for samples, containing only p-n junction with GaAs:Mn without quantum size layer are demonstrated on Fig. 3.

As can be seen, the band with the energy <0.6 eV appears for annealed sample (curve 2). Such band is not present at as-grown sample spectrum. The PL and EL spectra of this

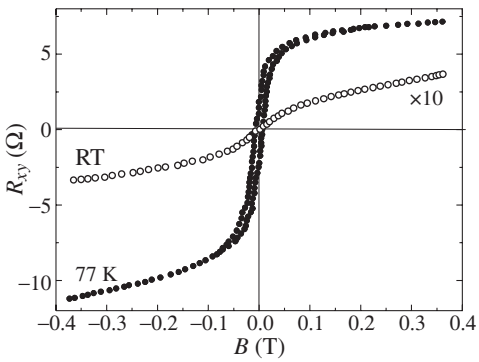

Fig. 2. Magnetic field dependences of Hall resistance for GaAs:Mn layers deposited at 600 °C.

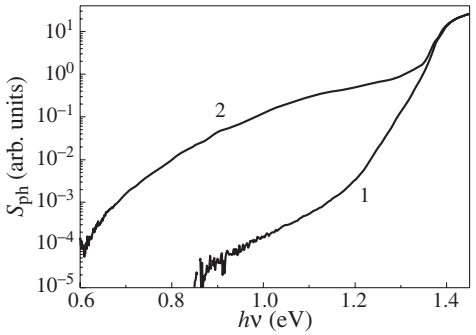

Fig. 3. Photovoltage spectra for: 1 — as-grown sample; 2 — laser annealed sample.

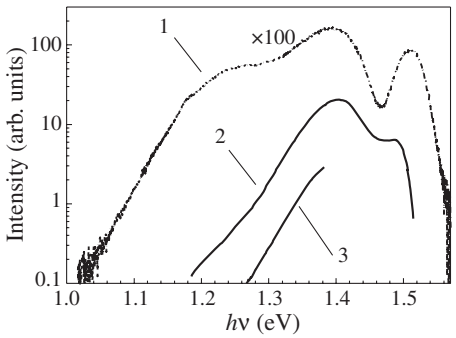

Fig. 4. PL (curve 1) and EL (curves 2, 3) spectra of p-n junction structure at 77 K: 2 — as-grown sample; 3 — laser annealed sample.

structure, taken at 77 K, are shown at Fig. 4. On the PL spectrum (Fig. 4, curve 1) besides the fundamental peak of GaAs luminescence at 1.507 eV, another two peaks are observed at 1.4 eV and 1.25 eV. Although the origin of these peaks is not clear, the emission energy of the first one is well correlated with Mn energy level in GaAs, that lies 105–110 meV above E_v.

For the EL spectra of forward-biased p-n junction (Fig. 4, curves 2, 3) the 1.507 eV peak is shifted to smaller energies. The laser annealing of the structures does not lead to a change in the form of the spectrum but it causes the decrease of the EL intensity at the same current. The threshold current of effective light emission is equal to 5 mA for both as-grown and annealed samples. The forward-bias I–V characteristics for as-grown structure (Fig. 5, curve 1) are typical for p-n junction. The value of non-ideality factor is equal to 2.3 that is probably due to the presence of high resistance GaAs:Mn layer.

The I–V characteristics of the annealed sample show non ideality factor value of 1.9 and the decrease of device resistance. Thus, we have demonstrated the possibility of creating the light emitting devices, which contain GaAs:Mn ferromagnetic layers. Results, presented above, mostly respect

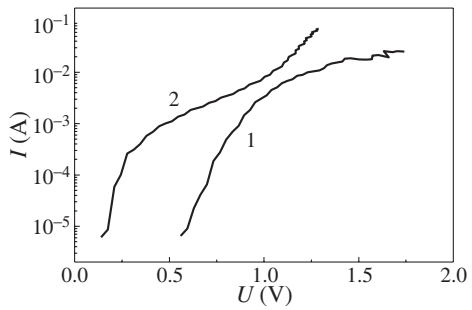

Fig. 5. I–V characteristics of structures at 77 K. 1 — as-grown sample; 2 — laser annealed sample.

to structures without quantum-size layer. The structures with (Ga,Mn)As layer and quantum dots (wells) are currently under investigation.

Acknowledgements

This work was supported by RFBR, Grant 03-0216777 and Program of RAS "Spin-dependent effects in solids and Spintronics".

References

[1] H. Ohno *et al*, *Appl. Phys. Lett.*, **69**, 363 (1996).
[2] Y. Ohno *et al*, *Appl. Surface Science*, **159/160**, 308312 (2000).
[3] Y. V. Vasil'eva *et al*, *Semiconductors*, **39**, 77 (2005).

13th Int. Symp. "Nanostructures: Physics and Technology"
St Petersburg, Russia, June 20–25, 2005

Self-assembling in $Al_xGa_{1-x}N_yB^V_{1-y}$ alloys (B^V = P, As, Sb)

O. V. Elyukhina[1], G. S. Sokolovskii[1], V. I. Kuchinskii[1] and V. A. Elyukhin[2]

[1] Ioffe Physico-Technical Institute, St Petersburg, Russia
[2] Departamento de Ingenieria Eléctrica, CINVESTAV-IPN, México, D.F.07360, México

Abstract. $Al_xGa_{1-x}N_yP_{1-y}$, $Al_xGa_{1-x}N_yAs_{1-y}$ and $Al_xGa1 - xN_ySb_{1-y}$ alloys with two components of dopant concentration may undergo self-assembling under certain conditions. We study the conditions and concentration range in which self-assembling is thermodynamically advantageous. The chemical and strain energy factors in the free energy of the alloy provide the benefits for self-assembling.

Introduction

The III-V $A_xB_{1-x}C_yD_{1-y}$-type alloys have found wide practical use due mainly to simultaneously controlled band gap and lattice parameter. However, one of important characteristics, the atomic arrangement, of these alloys is still not understood. Nonrandom arrangement of atoms was observed in $In_xGa_{1-x}As_yP_{1-y}$, $In_xGa_{1-x}N_yAs_{1-y}$ and $Al_xGa_{1-x}N_yAs_{1-y}$ alloys [1,2,3]. The explanation of the origin of this phenomenon was firstly done in Refs. [4, 5] for $Al_xGa_{1-x}As_yP_{1-y}$, $Al_xGa_{1-x}Sb_yAs_{1-y}$ and $In_xGa_{1-x}As_yP_{1-y}$ alloys, respectively. Recently, nonrandom arrangement was described for $In_xGa_{1-x}N_yAs_{1-y}$ alloys consisting of the strongly dissimilar constituent compounds [6]. As it was determined, the main origin of this phenomenon for all quaternary alloys is the difference to the free energies of the constituent compounds. Exchange of cations or anions of their lattice sites in $A_xB_{1-x}C_yD_{1-y}$ alloys can lead to variation of the concentrations of different bonds. This variation is a result of reactions between bonds nA-C + nB-D → nA-D + nB-C ($n = 1, \ldots, z$), where z is the coordination number. The free energy of alloy is changed as a result of this reaction. These reaction leads to the preferable formation of two types of bonds. The bonds providing the smaller value of the free energy of the alloy are formed rather than other bonds. This preferable bond formation can lead to the phase separation in the form of spinodal decomposition of the alloys if atomic concentrations are sufficiently large. In the ultra dilute limit in GaAs- and AlN-rich $Al_xGa_{1-x}N_yAs_{1-y}$ alloys should form quadruplets of the 3As1N1Al and 1As3N1Ga tetrahedral cells, respectively [7]. The vast cohesive energy of AlN provides the self-assembling total Al and Ga surroundings of separate N and As atoms, respectively in these alloys. The cohesive energy of AlN is the largest among all III-V compounds. Therefore, it is reasonable to consider the conditions of the self-assembling in other AlN-containing alloys. Among AlN-containing quaternary alloys $Al_xGa_{1-x}N_yP_{1-y}$, $Al_xGa_{1-x}N_yAs_{1-y}$ and $Al_xGa_{1-x}N_ySb_{1-y}$ alloys have highest thermodynamic preference of Al-N and Ga-P (Ga-Sb, Ga-As) bonds formation. The problem of establishing atomic arrangement in III-V semiconductor alloys is important due to impurity states standpoint. The substituting nitrogen atoms in GaP form the different isoelectronic trap in the forbidden gap [9] binding excitons. The nitrogen bound states should be affected if the nearest neighbour lattice sites are substituted by another impurity. Other impurity atoms are also good candidates for adapting the impurity states of important III-V materials. It is possible that such complexes are binding not only excitons but also electrons and holes.

1. Estimation of the free energy

In $Al_xGa_{1-x}N_yB^V_{1-y}$ (B^V = As, Sb, P) alloys the cohesive energy of AlN predominates significantly over cohesive energies of the other compounds. Consequently, the sum of cohesive energies of AlN and GaB^V is significantly larger than that of AlB^V and GaN. The constituent compounds are dissimilar due to atomic sizes and difference in their electronegativity of the anions. Due to the difference in the sums of the cohesive energies there is a thermodynamic preference in bond formation of AlN and GaB^V over AlB^V and GaN. The free energy profit of reaction Al-N + Ga-B^V > Al-B^V + Ga-N between bonds mainly determines the atomic arrangement in an alloy during the growth process. At the annealing temperature the exchange of lattice sites is driven by self-diffusion. The thermodynamic profit may be determined by

$$\Delta\mu^0 = \mu^0_{\mathrm{AlN}} + \mu^0_{\mathrm{GaB^V}} - \mu^0_{\mathrm{GaN}} - \mu^0_{\mathrm{AlB^V}} ,$$

where μ^0_{AlN} is the standard chemical potential of AlN. Under certain conditions, when concentration of one type impurity is larger than the other, the preference in bond formation may lead to self-assembling of one type bonds around impurity having the smallest concentration. The most interesting case takes place when $Al_xGa_{1-x}N_yB^V_{1-y}$ contains only three types of bonds. In such a case, one-type atoms should surround the atoms having the smallest concentration. The complete N or B^V surroundings of one-type cations are hardly expected due to the significant increase of the strain energy, since B^V anions are significantly different in size from N atoms. In the zinc-blende structure four cations surrounding an anion form the tetrahedron cell containing of four bonds between impurity atoms. Thus it is the smallest object formed by self-assembling of one impurity around another. The tetrahedron can be represented as a four tetrahedral cells having an impurity atom in the center. The self-assembling of four N (P, As, Sb) atoms around one Al (Ga) atom forms 4N1Al (4Sb1Ga, 4P1Ga) tetrahedral cells in the GaP(As, Sb)-enriched (AlN-enriched) alloy.

To determine conditions for the co-dopant self-assembling that is described above, one needs to compare the values of the free energies of self-assembled and random alloy. The free energy has three contributions: thermodynamic preference in bond formation, entropy and the strain energy induced by dopant atoms.

The thermodynamic preference of reaction Al-N + Ga-B^V → Al-B^V + Ga-N (B^V = P, As, Sb) is written as

$$\Delta\mu_0 = \left(\Delta h - T\Delta s + \int_{298.15}^{T} \Delta c dT - T\int_{298.15}^{T} \frac{\Delta c}{T} dT\right) ,$$

where Δh and Δs are the differences in enthalpies and entropies of compounds at STP, respectively, Δc is the difference in heat capacities of compounds.

The configurational entropy of the self-assembled alloy is smaller and thus entropy reduce hinders the self-assembling. Impurity atoms deform the crystal structure of the alloy. The deformation of the crystal structure with respect to single compound leads to appearance of strain energy. The arrangement of atoms in the growing alloy is dependent on these three factors.

The configurational entropy contribution to the free energy of one mole of self-assembled alloy is written as [8]

$$S_{SA} = k \ln \frac{N!(N-4\beta N)!}{(N-\alpha N)!(\beta N)!(N-\beta N)!(\alpha N-4\beta N)!},$$

where N is the Avogadro number, $\alpha = x$, $\beta = y$ for $x \geq 4y$ and $a = y$, $b = x$ for $4x \leq y$. The configurational entropy was obtained by the supposition on the random distribution of atoms of an impurity having the smallest concentration. The configurational entropy of the self-assembled alloy can be rewritten as

$$S_{SA} = R \left\{ \begin{array}{l} (\alpha - 4\beta)\ln(\alpha - 4\beta) + (1-\alpha)\ln(1-\alpha) \\ +\beta \ln \beta + (1-\beta)\ln(1-\beta) \end{array} \right\}.$$

The configurational entropy of the random alloy is given in the well-known form

$$S_R = R\{x \ln x + (1-x)\ln(1-x) y \ln y + (1-y)\ln(1-y)\}.$$

The entropy contribution to the free energy at the self-assembling is written as

$$\Delta U_S = -T\,(S_{SA} - S_{Ran})\,.$$

Another contribution into the free energy is made by the strain energy caused by dopant atoms or self-assembled objects. The strain energy in the self-assembled and random alloy was calculated by the approach proposed for description bond-length relaxation and mixing enthalpies in semiconductor pseudobinary alloys [10]. The strain energy is considered consisting of two contributions. The first contribution is the deformation energy of the quadruplets of the one-type bond tetrahedral cells. Due to the symmetry conditions tetrahedral cells are cubic and identical. The deformation energy of the quadruplets was estimated by the valence force field model. Another contribution is the strain energy of the alloy outside these quadruplets. Quadruplets are supposed to be situated randomly and the distance between them is much larger then their radii. This portion is represented as the strain energy of the elastic media with radial displacements inversely proportional to the square of a distance from a central atom of a quadruplet.

The strain energy that is induced by impurities in the self-assembled alloy is considerably smaller than that of the random alloy. The large value of strain energy is partly compensated by $1N3AlB^V$ tetrahedral cells quadruplets inside GaB^V-enriched alloys. The strain energy decreases during the self-assembling. The strain energy of $Al_xGa_{1-x}N_yB^V_{1-y}$ $(4x \leq y)$ alloy containing quadruplets of anion impurity tetrahedral cells is larger than that of the random alloy.

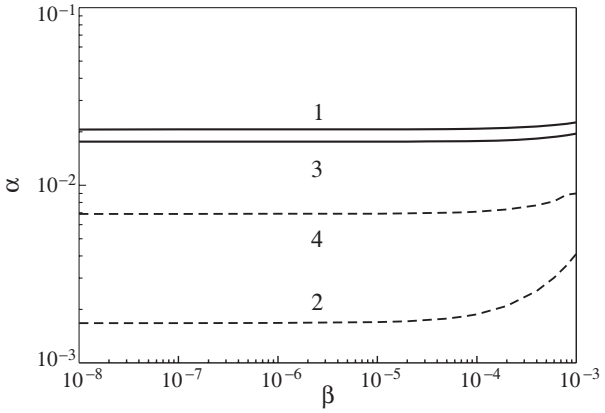

Fig. 1. Curves 1 and 2, 3 and 4 demonstrate the formation conditions of the 1As4Ga and 1N4Al self-assembling in AlN- ($\alpha = 1-y$, $\beta = 1-x$) and GaAs-enriched ($\alpha = y$, $\beta = x$) $Al_xGa_{1-x}N_yAs_{1-y}$ alloys, respectively. The formation conditions at the growth and annealing temperatures are shown by the solid and dotted curves, respectively.

Summary

In conclusion, we have shown that the significant preference of the Al-N and Ga-P(As, Sb) bonding over the Al-P(As, Sb) and Ga-N bond formation has to lead to the self-assembling in lightly isoelectronically-doped $Al_xGa_{1-x}N_yP(As, Sb)_{1-y}$. The self-assembling should be realized as an appearance of quadruplets of Ga-P(As, Sb) and Al-N bonds situated around the anion impurity atoms in AlN- and Ga-P(As, Sb)-enriched alloys, respectively. Quadruplets of the one-type bonds can appear without plastic deformation of the alloy. In the ultradilute limit of the anion impurity, the self-assembling evolves if the concentration of the cation impurity is many times larger.

References

[1] V. I. Iveronova and I. G. Sapkova, *Sov. Phys. Crystallogr.*, **24**, 460 (1979).
[2] P. J. Klar, H. Grüning, J. Koch, S. Schäfer, K. Volz, W. Stolz, W. Heimbrodt. A. M. Kamal Saadi, A. Lindsey and E. P. O'Reilly, *Phys. Rev. B*, **64**, 121203 (2001).
[3] T. Geppert, J. Wagner, K. Köhler, P. Ganser and M. Maier, *Appl. Phys. Lett.*, **80**, 2081 (2002).
[4] V. A. Elyukhin, S. Yu. Karpov, L. P. Sorokina and K. Frontz, *Sov. Phys. Crystallogr.*, **27**, 668 (1982).
[5] V. I. Iveronova and I. G. Sapkova, *Sov. Phys. Crystallogr.*, **24**, 460 (1979).
[6] K. Onabe, *Phys. Chem. Solids*, **73**, 1071 (1982).
[7] K. Kim and A. Zunger, *Phys. Rev. Lett.*, **86**, 2609 (2001).
[8] K. Onabe, *Jpn. J. Appl. Phys.*, **21**, L323, (1982).
[9] V. A. Elyukhin, V. M. Sánchez-R. and O. V. Elyukhina, *Appl. Phys. Lett.*, **85**, 1704 (2004).
[10] R. A. Faulkner and P. J. Dean, *J. of Luminescence*, **1,2**, 552 (1970).
[11] A.-B. Chen and A. Sher, *Phys. Rev. B*, **32**, 3695 (1985).

13th Int. Symp. "Nanostructures: Physics and Technology"
St Petersburg, Russia, June 20–25, 2005

The self-assembled growth and properties of Pd oxide based field emitter arrays

O. N. Gorshkov, *D. O. Filatov*, G. A. Maximov, V. A. Novikov and S. Yu. Zubkov

Research and Educational Center for Physics of the Solid State Nanostructures, University of Nizhny Novgorod, 23 Gagarin Ave., Nizhny Novgorod, 603 600, Russia

Abstract. The morphology, crystalline structure, and field emission properties of the of the PdO conical nanotip arrays fabricated by self assembling during thermal oxidation and plasma enhanced oxidation of thin Pd films (~ 70 nm in thickness) on glass substrates were studied. It was shown that the temperature threshold for the nanotips' self-assembling for the plasma enhanced oxidation was $\approx 600\,^{\circ}$C that was in $200\,^{\circ}$C lower than for the thermal oxidation. X-ray diffraction studies demonstrated that the nanotips consisted of a mixture of the two pokycristalline pases: metallic Pd and PdO. For local investigation of the field emission properties of the nanotip arrays, a novel technique based on Ultra High Vacuum Scanning Tunneling Microscopy (STM) with a spherical probe used as the anode (inverted STM) was applied. The threshold value of the electric field providing field emission was $\approx 15\,\mathrm{V}/\mu\mathrm{m}$ what was close to the best values for the carbon nanotubes reported to date. A cathodeluminescent cell (a prototype of a flat panel display pixel) was made. The light emission from the luminophor excited by the electrons emitted from the nanotips was observed at the pressure of $\sim 10^{-5}$ Torr.

Introduction

In the last few years vacuum microelectronics attracted much attention. It utilizes the vacuum electronic devices reduced in sizes down to the micro- and nanometer scales fabricated by standard semiconductor microelectronic technoloies [1]. The field emission microcathodes are the key elements of all vacuum microelectron devices. Traditionally, the field emission microcathodes were fabricated from Mo by Spindt technology [2]. This technology has two main disadvantages: 1) the Spindt technique is very expensive and complicated and is not scalable to large dimensions; 2) Mo emitters degrade during operation from interaction with residual gases (O_2, H_2O, CO_2, etc.). At present the emitters based on carbon nanotubes [3] and self assembled oxide nanostructures [4, 5] are developed intensively. As it was shown in [4, 5] the termal oxidation of Pd and Ir thin films in oxygen ambient resulted in self-assembled formation of the conical nanotips (Fig. 1) which are promising for the field emission applications. The effecient formation of these structures takes place at the temperatures of $\approx 900\,^{\circ}$C that requires expensive thermo resistant substrates. For the commercial production the inexpensive substrates (e.g. from soda lime glass) is highly desireble. This issue stimulates searching the ways to reduce the tips' formation temperature. In [6] it was demonstrated that ultraviolet irradiation and oxidation in the oxygen radio frequency (RF) plasma activates tip formation at lower temperatures (down to $550\,^{\circ}$C). In the present work the dependence of the morphology, crystalline structure, composition, and field emission properties of the Pd oxide nanotip arrays formed by thermal and plasma enhanced oxidation of thin Pd films on the annealing temperatures was investigated. The goal of this work was to find out the conditions providing formation of the uniform nanotip arrays with the optimal field emission properties at the lowest possible temperatures.

1. Experiment

The Pd films were deposited on the silica glass substrates by magnetron sputtering. For the structures destined for the field emission measurements the substrates with ITO underlying layers were employed. The film thickness was ≈ 70 nm. It was shown [5] that this initial film thickness was optimal for formation of well shaped separated conical nanotips with the highest aspect ratio. The Pd films were annealed in oxygen ambient at the atmospheric pressure for 1 hour. The plasma enhanced oxidation as performed at the pressure of 10^{-2} Torr. The morphology of the oxidized films was studied by Atomic Force Microscopy (AFM). The surface morphology was characterized by the standard roughness parameter $\Delta \mathrm{R}_p$ (RMS roughness) and by the mean height of the nanotips $\langle H \rangle$. The crystal structure of the grown structures was studied by Double Crystal X-Ray Diffractometry (DXRD). For local investigation of the field emission properties of the tip arrays the Ultra High Vacuum STM equipped with flat probe as anode (inverted STM) was used.

2. Results and discussion

The dependencies of ΔR_p and $\langle H \rangle$ on the annealing temperature are represented in Fig. 2.

In the case of thermal oxidation the roughness and mean height increase continuously and reach their maxima at $T \approx 800\,^{\circ}$C. In the case of the plasma assisted oxidation $\Delta \mathrm{R}_p$ and $\langle H \rangle$ maxima were observed at the temperature of $\sim 600\,^{\circ}$C. Decrease of both ΔR_p and $\langle H \rangle$ with further increase of the annealing temperature was explained by decomposition of PdO stimulated by intraction the ions in the oxygen plasma. The plasma assisted oxidation results in higher (~ 800 nm) tips which are isolated from each other. The oxidation temperature

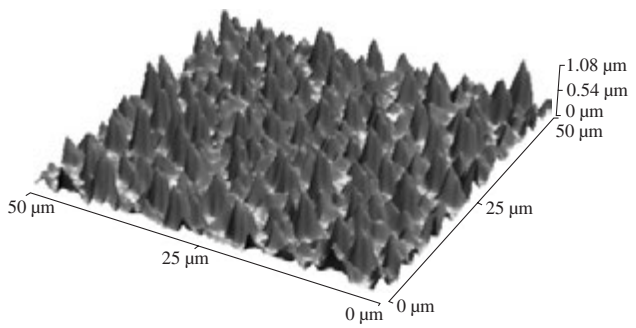

Fig. 1. AFM image of the PdO nanotips.

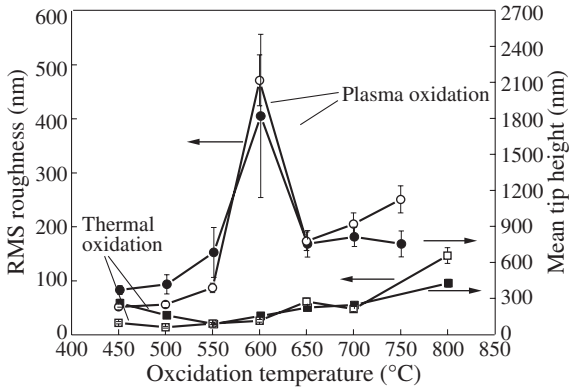

Fig. 2. The dependencies of the RMS roughness of the oxidized Pd films and of the mean height of the PdO nanotips on the annealing temperature.

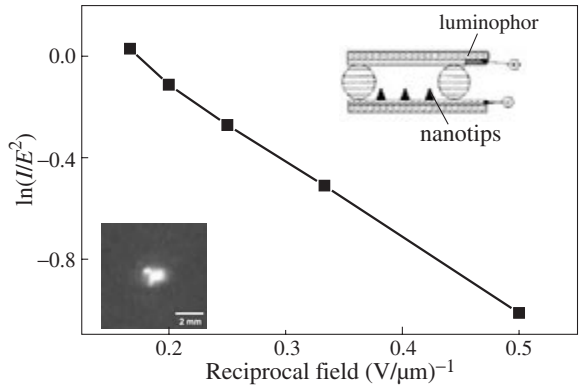

Fig. 4. The current-voltage characteristics of a cathode luminescent diode cell. The insets represent the schematic of the cell and the image of the light emission from the cell.

was in 200 °C lower then the one in the case of thermal oxidation. The tip density varied from 4×10^6 to 3×10^7 cm^{-2} dependent on the oxidation conditions. Investigation of the tip composition by X-Ray diffraction demonstrated that the tips had the polycrystal structure. The size of the crystallites was $\approx$ 50–60 nm, what was $\sim$ 10 times smaller than the typical tip sizes.

The crystallite size depends on the annealing temperature weakly. The oxidized films were textured while the initial Pd films were not. According to DXDR data the tip composition is a mixture of metallic Pd and PdO.

The current-voltage characteristic of the initial Pd film was symmetric that is typical for the field emission from the flat surface [7]. The current-voltage curve of the structures obtained by the plasma assisted oxidation were asymmetric (Fig. 3). This curve plotted in Fowler-Nordheim axes represented a linear dependence. The threshold value of the electric field providing emission current was $\approx$ 15 V/μm. This value is close to the best one reported for the carbon nanotubes which are considered to be the most promising candidates to the field emission applications at present [7].

A cathode luminescent cell (a prototype of the flat panel display pixel) 2 by 2 mm in size was made on the base of the structure grown at 550 ° on the molibdenite glass substrate with ITO underlying layer. The schematic of the sell is shown in the inset in Fig. 4. A glass plate covered by luminophor (ZnS) with metal underlying layer was employed as an anode. The

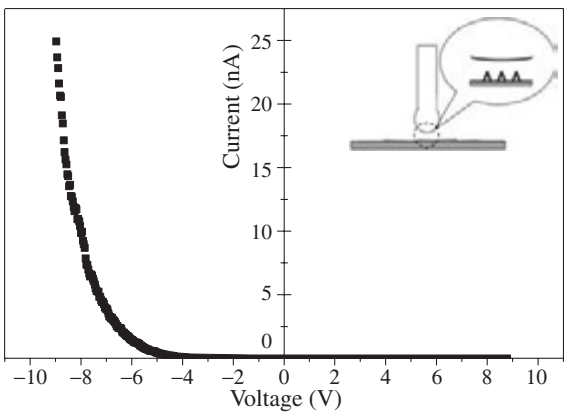

Fig. 3. Current-voltage characteristic of the PdO nanotips oxidized at 600 °C in the oxygen plasma. The inset represents the scheme of the inverted STM.

cathode and the anode were separated by 50 μm glass fibers. In Fig. 4 the current voltage curve of cell is presented. The light emission excited by the electrons emitted from the nanotips was observed at the pressure of $\sim 10^{-5}$ Torr (see inset 2 in Fig. 4).

Conclusions

It was shown that plasma oxidation decreases the temperature of the self-assembled formation of the PdO nanotips down to $\sim$ 600 °C that makes possible fabrication of the PdO field emission microcathode arrays on the glass substrates. X-Ray diffraction studies demonstrated that the tips consist of a mixture of Pd and PdO. A novel method for investigation of the field emission properties of the solid surfaces based on STM in UHV was developed. The threshold electric field for the field emission $\sim$ 15 V/μm was achieved that is comparable with the best values reported for the carbon nanotubes.

Acknowledgements

The work was supported by Joint Russian American BRHE Program sponsored jointly by US CRDF and Russian Ministry of Education and Science (REC-NN-001).

References

[1] D. Temple, *Mater. Sci. Eng.*, **24**, 185 (1999).
[2] M. Nagao, K. Utsumi *et al*, *Appl. Surf. Sci.*, **146**, 182 (1999).
[3] S. David *et al*, *Appl. Phys. Lett.*, **80**, 2988 (2002).
[4] B. R. Chalamala *et al*, *Appl. Phys. Lett.*, **74**, 1394 (1999).
[5] S. Aggarwal *et al*, *Science*, **287**, 2235 (2000).
[6] G. A. Maximov *et al*, *PLDS*, 2001, N3/4, p.175.
[7] Peter J. F. Harris, *Carbon nanotubes and related structures: new materials for the 21st centure.*, Cambridge University Press, 1999.

13th Int. Symp. "Nanostructures: Physics and Technology"
St Petersburg, Russia, June 20–25, 2005

Kinetics of adatom incorporation and step crossing at the edges of nanoislands

S. N. Filimonov[1,2] and *Yu. Yu. Hervieu*[1]

[1] Tomsk State University, 634050 Tomsk, Russia
[2] Institut für Schichten und Grenzflähen (ISG 3) and cni — Center of Nanoelectronic Systems for Information Technology, Forschungszentrum Jülich, D-52425 Jülich, Germany

Abstract. Adatom incorporation into the "faceted" steps bordering the 2D nanoislands is analyzed. The step permeability and incorporation coefficients are derived for some typical growth situations. It is shown that the step consisting of equivalent straight segments can be permeable even in the case of fast egde migration if there exist factors delaying creation of new kinks. The step consisting of alternating rough and straight segments may be permeable if there is no adatom transport between neighboring segments through the corner diffusion.

Introduction

The continuous approach to the step dynamics is a powerful tool for modelling of the pattern formation in epitaxial growth [1]. This approach is based on solution of the surface diffusion equation for adatoms subject to the appropriate boundary conditions. The latter are usually formulated by matching the surface diffusion fluxes of adatoms entering the step edge from the lower (l) and upper (u) terraces to the local net fluxes of adatoms g_l and g_u attaching to the step edge. The fluxes g_l and g_u are written down in the form [2]

$$g_{l(u)} = \nu_{l(u)}(n_{l(u)} - \tilde{n}) + \nu_p(n_{l(u)} - n_{l(u)}), \qquad (1)$$

where the first term in the right part is the flux of adatoms incorporating into the kinks at the step edge and the second term is the flux of adatoms crossing the step without visiting the kinks ($\nu_{l(u)}$ and ν_p are the incorporation and step permeability coefficients, $n_{l(u)}$ is the concentration of adatoms on the lower (upper) terrace in the vicinity of the step and $\tilde{n}$ is the equilibrium adatom concentration).

Commonly Eq. (1) are treated as linear phenomenological relations between the fluxes and relevant "driven forces" with the coefficients $\nu_{l(u)}$ and ν_p as phenomenological parameters. This approximation works well at small deviations from equilibrium but may be incorrect in some typical situations of the MBE growth. For instance, recent STM studies of growth in some metallic [3] and semiconductor [4] systems have shown that at moderate growth temperatures the edges of nanosize 2D islands consist of the atomically straight segments. In general, propagation of such segments represents a *non-linear* process because it requires formation of kinks by the non-equilibrium 1D nucleation mechanism.

Recently we have proposed a method to *derive* the incorporation and step permeability coefficients of vicinal steps aligned along a high symmetry direction. It was demonstrated that Eq. (1) hold even at strong deviations from equilibrium but the formation of non-equilibrium kinks implies the dependence of kinetic coefficients on the adatom concentrations [5]. In the present paper we extend this approach to construct the incorporation and step permeability coefficients of the closed "faceted" steps bordering the 2D nanoislands. We show that the specific shape and small length of such steps gives rise to the peculiarities in the kinetics of adatom incorporation and crossing the step as compared to the case of infinite steps.

1. The model

We will consider propagation of a step segment which length L is less than the average distance between kinks L_k at the infinite step considered at the same growth conditions. An adatom attached to such a segment has four possibilities (Fig. 1): (1) to detach from the segment back to the terrace from which it came or to the adjacent terrace (the latter means the crossing of the step); (2) to leave the segment by rounding the island corners; (3) to meet another adatom or an unstable cluster at the same segment and in that way to take part in the 1D nucleation process. After appearance of the 1D island the adatom can (4) incorporate into one of two kinks at its ends.

As the result, the row-by-row growth process sketched in Fig. 1 will take place. It includes appearance of the 1D island at the straight (without kinks) step segment during the expectation time $t_{\rm nuc}$ and its spreading along the step edge during the mean time $t_{\rm gr}$. It is essential that no other 1D islands appear during the time $t_{\rm gr}$. As the crystalline row along the step segment completes, the 1D nucleation and formation of the new crystalline row start again.

If the adatoms do not migrate along the step edge then $t_{\rm nuc} = 1/LJ$, where J is the 1D nucleation rate per atomic site at the step [6]. In this case $t_{\rm nuc} \gg t_{\rm gr}$ and the maximum of the step permeability is achieved, the relevant expressions for $\nu_{l(u)}$ and ν_p can be found in Ref. [7]. In the present paper we are interesting in the opposite limit of fast edge migration, when the traversal time required for an adatom to visit all sites at the edge $t_{\rm tr} \sim L^2/D_e$ is much less than the mean time interval between subsequent attachments of the terrace adatoms to the edge $\Delta t = 1/L(k^+_{le}n_l + k^+_{ue}n_u)$ and the mean time $t_{\rm res} = 1/(k^-_{el} + k^-_{eu})$ that an adatom spends at the straight step edge

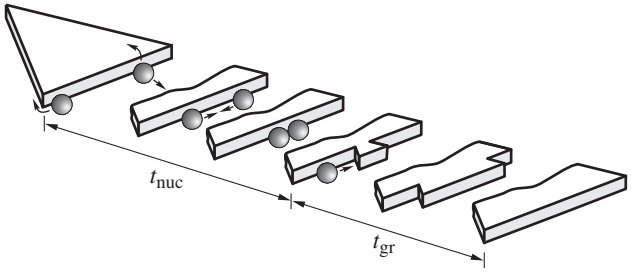

Fig. 1. Schematic of atomic processes at the edge of the 2D island during the row-by-row growth process.

before detachment, where D_e is the edge diffusion coefficient, $k^+_{l(u)e}$ and $k^-_{el(u)}$ are the attachment (+) and detachment (−) rate constants. Bearing in mind comparatively low growth temperatures we neglect detachment of atoms embedded into the straight step as well as into the kink and corner sites.

2. The kinetic coefficients

To derive expressions for the incorporation and permeability coefficients we have calculated the exchange fluxes g_l and g_u averaged over the period $t_{\rm nuc} + t_{\rm gr}$. The concentrations of the terrace adatoms n_l and n_u were considered as unknown variables, whereas the concentration of the edge adatoms n_e was found as the solution of the edge diffusion equation

$$D_e \frac{d^2 n_e}{dx^2} - \left(k^-_{el} + k^-_{eu}\right) n_e(x) + k^+_{le} n_l + k^+_{ue} n_u = 0 \qquad (2)$$

with the boundary conditions describing incorporation of the edge adatoms at the kink sites or/and leaving the step segment at the step corners. In the following we summarize our major results for some typical growth situations.

2.1. The 2D islands with equivalent step segments

Assuming fast migration of the edge adatoms around the step corners (this process has a high probability e.g., in the case of the triangular 2D Si islands on the Si(111)-7 × 7 surface [4]) we have solved Eq. (2) with the periodical boundary conditions and obtained g_l and g_u in the form of Eq. (1). The kinetic coefficients are given by

$$\nu_{l(u)} = \tau_k k^+_{l(u)e}\,; \qquad \nu_p = \frac{(1-\tau_k) k^+_{le} k^-_{eu}}{(k^-_{eu} + k^-_{el})}\,,$$

where $\tau_k = (t_{\rm gr} + t_{\rm acc})/(t_{\rm gr} + t_{\rm nuc})$ is the fraction of time when every adatom attaching to the step edge contributes to the formation of the crystalline layer along one of the step segments ($t_{\rm acc}$ is the "accumulation" time which takes into account that the adatoms forming the critical 1D "nucleus" do not detach from the edge).

The ability of the adatoms from the lower terrace to cross the step and thus climb up the 2D island top may be characterized by the ratio

$$\eta_l = \frac{\nu_p}{\nu_l} = \frac{(t_{\rm nuc} - t_{\rm acc}) k^-_{eu}}{(t_{\rm gr} + t_{\rm acc})(k^-_{eu} + k^-_{el})}\,. \qquad (3)$$

As can be seen from Eq. (3), the step segment may be permeable ($\eta_l \gg 1$) if its propagation is limited by the kink creation ($t_{\rm gr} \ll t_{\rm nuc}$) even if the edge migration is fast.

2.2. The 2D islands with inequivalent step segments

We have considered the case of the 2D island with alternating atomically straight and rough edge segments as e.g., SA and SB edge segments of the rectangular 2D Si islands on the Si(100)-2 × 1 surface. Here the probabilities for an adatom to cross the straight segment or incorporate into it are both affected by the ability of the edge adatom to travel around the step corners. Assuming that the adatom does not return back from the neighboring rough segments we get

$$\nu_{l(u)} = \kappa \tau_k k^+_{l(u)e}\,; \qquad \nu_p = \frac{(1-\tau_k)[1 - f_c(q_L)] k^+_{le} k^-_{eu}}{(k^-_{eu} + k^-_{el})}\,,$$

where $f_c(q_L)$ is the probability that an adatom, attached to the step segment containing no kinks, will leave the segment via the corner rounding before detachment, q_L is the ratio of the segment length to the mean length of the adatom migration along the infinite step and κ ($0.5 \le \kappa \le 1$) is the probability that the edge adatom will find the kink when it present at the straight segment.

The permeability ratio in this case is given by

$$\eta_l = \frac{(1-\tau_k)[1 - f_c(q_L)] k^-_{eu}}{[\tau_k + (1-\tau_k) f_c(q_L)](k^-_{el} + k^-_{eu})}\,.$$

Here the neighboring step segments act as a pair of kinks settled at a short ($L < L_k$) distance. This diminishes crossing the step by the terrace adatoms. Our calculations give that the step segment may be permeable only if the energy barrier for the corner rounding is greater then the barrier E_e for the edge migration by $\Delta E_{ec} > E^-_{es} - E_e - k_B T \ln(L/2)$, where E^-_{es} is the smallest from the barriers for detachment to the upper and lower terraces.

3. Summary and discussion

In conclusion, we have derived the incorporation and step permeability coefficients for two typical growth situations involving the 2D islands bounded by the "faceted" steps. It has been shown that adatom incorporation into such islands has some peculiarities which are reflected by the structure of the obtained expressions for the kinetic coefficients. To apply our model to the particular system of interest one needs to specify the characteristic time scales $t_{\rm gr}$, $t_{\rm nuc}$ and $t_{\rm acc}$. As a rule the latter can be neglected since the critical size of the 1D nucleus is typically few atoms. Then $t_{\rm gr} \sim 1/(k^+_{le} n_l + k^+_{ue} n_u)$ with the coefficient of proportionality (order unity) depending on the 2D island geometry and intensity of the corner rounding processes. The nucleation time $t_{\rm nuc}$ is the inverse of the nucleation rate $\omega_{\rm nuc}$ which can be calculated with the statistical theory of the island-on-island nucleation [8]. An application of the outlined strategy to modelling of the mass-transport during the formation of the multilayer Ge nanoislands on Si(111) can be found elsewhere [9].

Acknowledgements

This work has been supported by INTAS (03-51-5015) and RFBR (03-02-17644). The stay of S.F. in Germany was supported by the Alexander von Humboldt Stiftung.

References

[1] A. Pimpinelli and J. Villain, *Physics of crystal growth*, (Cambridge UK: Cambridge University Press), 1998.
[2] M. Ozdemir and A. Zangwill, *Phys. Rev. B*, **45**, 3718 (1992).
[3] T. Michely *et al*, *Phys. Rev. Lett.*, **70**, 3943 (1993).
[4] B. Voigtländer, *Surf. Sci. Rep.*, **43**, 127 (2001).
[5] S. N. Filimonov and Yu. Yu. Hervieu, *Surf. Sci.*, **553**, 133 (2004).
[6] V. V. Voronkov, *Sov. Phys. Crystallogr.*, **15**, 8 (1970).
[7] S. N. Filimonov and Yu. Yu. Hervieu, *Phys. Low-Dim. Struct.*, **7/8**, 15 (2002).
[8] J. Krug, P. Polity and T. Michely, *Phys. Rev. B* **61**, 14037 (2000).
[9] S. N. Filimonov and Yu. Yu. Hervieu, *Mater. Sci. Semicond. Proc.*, **8**, 31 (2005).

13th Int. Symp. "Nanostructures: Physics and Technology"
St Petersburg, Russia, June 20–25, 2005

MBE growth of high quality vertically coupled InAs/GaAs quantum dots laser emitting around 1.3 μm

R. S. Hsiao[1,3], J. S. Wang[1,2], G. Lin[1], C. Y. Liang[1], H. Y. Liu[1], T. W. Chi[1], J. F. Chen[3] and J. Y. Chi[1]

[1] Industrial Technology Research Institute, Hsinchu 310, Taiwan, R.O.C
[2] Department of Physics, Chung Yuan Christian University, Chung-Li 32023, Taiwan, R.O.C
[3] Department of Eletrophysics, National Chiao Tung University, Hsinchu 300, Taiwan, R.O.C

Quantum dots (QDs) are one of the fascinating quantum structures because of their superior characteristics and broad applications. Growth and characterization of the epitaxial layers for InAs QDs lasers have been one of the major ongoing research areas. Ustinov *et al*. have demonstrated the vertically electronic coupled QD lasers with lasing wavelength around 1.0 μm. By using thinner electronic vertically coupled quantum dots active region the optical model gain can be increased due to improved optical-electrical overlap factor. In this report we demonstrated the performance of highly strain EVCQD lasers with internal quantum efficiency of 90% emitting at 1.23 μm.

Structures for this study were grown by solid source molecular beam epitaxy (SS MBE) in a Riber Epineat machine on n^+-GaAs (100) substrates. Four samples with various spacer layer thicknesses between QDs are grown for the optical measurement. They consists of a 3-nm-thickness AlAs bottom cladding layer, a thirty stacks InAs/GaAsQuantum dots (QDs) active region with GaAs spacer varied from 30 nm, 20 nm, 17 nm, 10 nm, a 3 nm-thickness AlAs top cladding, and a 10 nm-thickness GaAs cap layer. QDs were found with 2.6 mono layers (MLs) of InAs and were grown at substrate temperature of 485 °C and then covered with GaAs barrier layer at

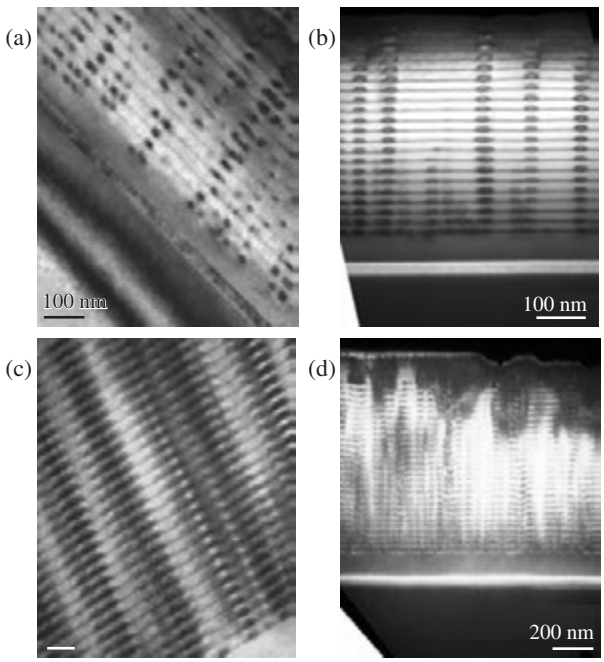

Fig. 1. The TEM images shows the multi-stacks QDs structure with 30 nm GaAs spacer layer (a), 20 nm GaAs spacer layer (b), 17 nm GaAs spacer layer (c), 10 nm GaAs spacer layer (d).

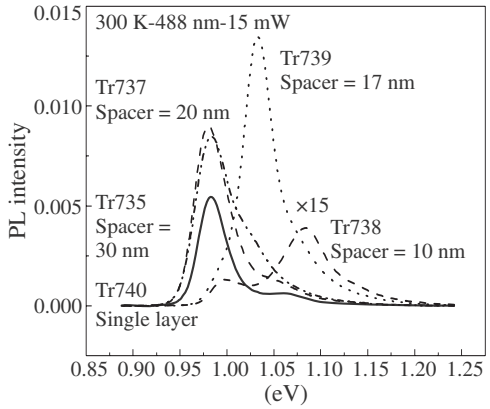

Fig. 2. The RT-PL spectra of single QDs layer and multi-stacks QDs layers with different spacer layer.

the same temperature. A single QDs layer was also grown and used as the reference.

Figure 1 shows the TEM images of four samples of multiple QDs with varying spacer thickness. As the spacer layer is reduced from 30 nm to 20 nm the QD becomes vertically aligned without defect generation. As the thickness is further reduced the QDs become well aligned as shown in Fig. 1(c) with 17 nm spacer while still remain defect free. Finally as the thickness is reduced further, the defects starts to appear as revealed in Fig. 1(d) with 10 nm spacer. The PL spectra of these samples are shown in Fig. 2. Spectrum with single layer of QDs is also shown for comparison. It is seen that the peak PL wavelength was blued shifted in the samples with 17 nm spacer while the intensity was increased. This blue shift is perhaps due to the increased strain or the interdiffusion of the In and Ga atoms. As the thickness is reduced to 10 nm the intensity was reduced

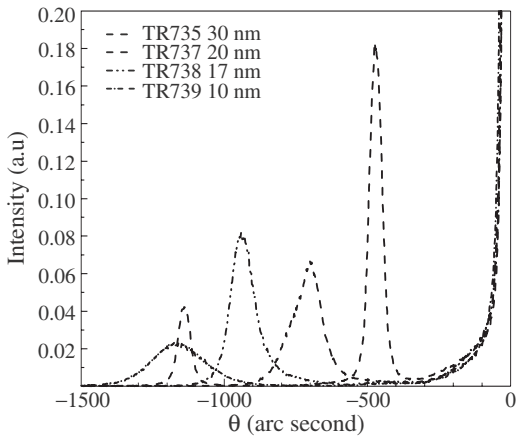

Fig. 3. The X-ray rocking curve of multi-stacks InAs/GaAs layers with the GaAs thickness from 30 to 10 nm.

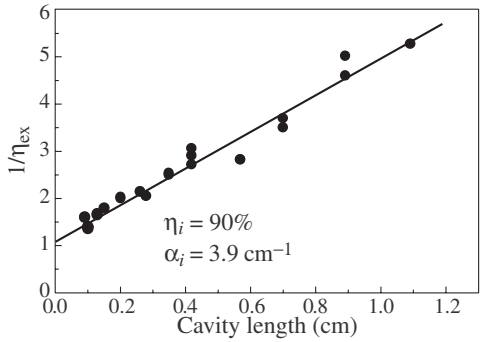

Fig. 4. Reciprocal external quantum efficiency as a function of cavity length.

drastically indicating defect generation.

To probe the structure perfection X-ray diffraction spectra of multi-stacks samples were tales and the results are as shown in Fig. 3. The peak strength gradually reduced as the spacer layer is increased. However, when the spcaer thickness reduces to 17 nm, the peak strength suddenly becomes much stronger and the line width becomes narrow. From the PL and X-ray measurement results, we believe the main factor causing the blue shift of the vertically coupled QDs structures is the strain in the QDs. More details of this phenomenon are being further investigated by Raman scatting measurement.

To demonstrate the quality of the vertically coupled structures, laser structures with ten pairs of InAs/GaAs multi-stacks as the active region were fabricated. Same QD layer structure as described above was symmetrically placed in the center of the waveguide region and processed into stripes of different widths and cavity lengths. Figure 4 shows the measured results of broad area lasers with 17 nm spacer. Threshold current density and the transparency current density per QD layer as low as 12 A/cm^2 and 7 A/cm^2 were obtained, respectively. High internal quantum efficiency of 90% and the differential efficiency of 73% were achieved indicating the high crystal quality although as many as 10 layers of high strain ECVQD active region was used.

Acknowledgements

The authors gratefully acknowledge K. Y. Hsieh for TEM measurements; A. R. Kovsh, A. E. Zhukov, and D. A. Livshits for their very useful discussions.

13th Int. Symp. "Nanostructures: Physics and Technology"
St Petersburg, Russia, June 20–25, 2005

MBE growth and structural characterization of MnF_2-CaF_2 short-period superlattices on Si(111)

A. K. Kaveev[1], R. N. Kyutt[1], N. S. Sokolov[1,2], M. Tabuchi[2] and Y. Takeda[2]

[1] Ioffe Physico-Technical Institute, St Petersburg, Russia
[2] Venture Business Laboratory, Nagoya University, Japan

Abstract. Short-period MnF_2-CaF_2 superlattices (SLs) have been grown by molecular beam epitaxy. The thickness of MnF_2 was about 3–6 molecular layers. Reflection high-energy electron diffraction (RHEED) measurements revealed the crystal structure with fluorite-like atomic coordination in "thin" (less than 3 nonolayers) and orthorhombic α-PbO_2 — type-like in "thick" (more than 3 monolayers) SLs. X-ray diffraction measurements displayed well-pronounced superstructural reflections and thickness-related fringes in SLs. The simulation with a semi-kinematical approximation of the X-ray rocking curves allows calculation of all the parameters of SLs and enables explanation of RHEED observations.

Introduction

It is known that the crystal structure and physical properties of ultrathin (a few monolayers) films can be very different from those of bulk crystals. However, the amount of material in such a film in many cases is insufficient for studies of their properties. The growth of short-period superlattices (SLs) helps much in solving this problem and enables more detailed characterization of the crystal structure and physical properties of material in ultrathin films. Thin epitaxial films and SLs containing magnetic ions attract attention due to their potential applications for integrated magnetic and micro-electronic systems.

Manganese fluoride has the tetragonal rutile-type structure and is a wide energy band gap insulator with a distinct antiferromagnetic ordering below 67 K. Owing to the simple crystal structure and optical anisotropy, MnF_2 bulk crystals have been used as a model material for studying the magnetic ordering in optical spectra, see e.g. [1]. MnF_2 is also attractive because of its capability to crystallize in metastable in bulk crystals orthorhombic α-PbO_2 — type crystal modification during the epitaxial growth of relatively thick layers (hundreds of nanometers) on CaF_2(111) surface [2]. It was supposed, based on RHEED observations, that the first three monolayers (MLs) of MnF_2 on CaF_2/Si(111) heteroepitaxial substrates have the fluorite-type crystal structure [3]. After the first experiments with MnF_2–CaF_2 superlattices [4] the crystal structure of thin layers of MnF_2 remained unknown. In the present work, using electron (RHEED) and X-ray diffraction, we have studied the crystal structure of short-period pseudomorphic and relaxed MnF_2–CaF_2 SLs with a MnF_2 layer thickness from 3 to 6 MLs.

1. Experimental

The structures were grown on Si(111) substrates by molecular beam epitaxy (MBE). Before the growth of SL, CaF_2 buffer layer was deposited on atomically clean Si(111) substrate. All grown SLs can be divided in two groups — "thin", with no more than 3 MLs of MnF_2, and "thick", over 4 MLs of MnF_2 in each period. The number of periods ranged from 15 to 50. The SLs were grown at room temperature and covered with thin (2–3 nm) CaF_2 cap layer.

The XRD measurements were carried out at BL-4C beamline of KEK Photon Factory (Tsukuba, Japan) with use of synchrotron radiation at 1.54 Å. Intensity distribution in θ–2θ scanning mode near the 111 and 222 symmetrical Bragg reflections was measured. Simulation of rocking curves was performed according to semi-kinematical approximation, in which scattering kinematical amplitude from the SL was calculated by summing over molecular monolayers in SL period and added with dynamical diffraction from substrate and kinematical amplitudes from the buffer and cap layers [5]. Because the exact structure of MnF_2-sublayer and relaxation state of the epitaxial system were unknown beforehand, in the first step of the fitting procedure the SL was characterized by interplanar spacing d_1 and d_2 in CaF_2 and MnF_2 sublayers correspondingly, numbers n_1 and n_2 of monolayers in them and ratio of structural factors $F(MnF_2)/F(CaF_2)$, five parameters in total.

2. RHEED measurements

Figure 1a–d shows RHEED patterns characteristic of samples with 10/3 and 7/5 monolayers of CaF_2/MnF_2 in each period.

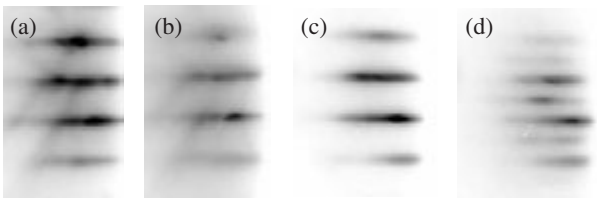

Fig. 1. RHEED patterns taken during the growth of 10/3 ML (a,b) and 7/5 (c,d) CaF_2/MnF_2 SL: (a,c) — after CaF_2 growth; (b,d) — after MnF_2 growth.

The patterns shown in Fig. 1(a,b), are typical for the [-110] electron beam azimuth in (111) plane of CaF_2. The streaks seen in the patterns show the flatness of the epilayers during the growth of the first few periods of the superlattice. Subsequent growth resulted in appearance of spots indicating roughening the surface. These observations indicate that three monolayers of MnF_2, being grown in combination with CaF_2, inherit crystal structure with the atomic coordination characteristic for the fluorite layers.

To study the "thick" MnF_2 layers we have used sample with 7 MLs of CaF_2 and 5 MLs of MnF_2 at each of 15 periods. Fig. 1c,d shows RHEED pattern characteristic for all the periods of such superlattice. One can see that new additional streaks related to MnF_2 growth appeared in the pattern. These streaks are between the CaF_2 streaks; they disappear in each period after CaF_2 evaporation, and then reappear again. The essential change of RHEED pattern allows us to assume that

Table 1. Parameters refined from simulation of θ–2θ scans for three MnF_2–CaF_2 superlattices.

Sample	Period (Å)	Total thickness	$d(CaF_2)$	$d(MnF_2)$	n(CaF_2)	n(MnF_2)	F(MnF_2)/F(CaF_2)
863	50.1	500	3.170	2.958	13.3	2.7	1.31
5382	37.2	744	3.136	3.033	8	4	1
5386	37.4	560	3.160	3.184	7	5	1.05

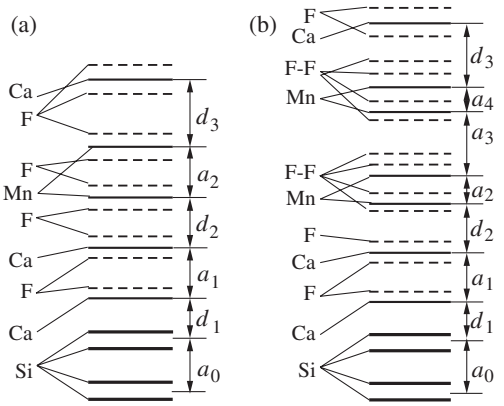

Fig. 2. Models used in simulations of "thin" (a) and "thick" (b) SLs.

with the increase of thickness MnF_2 layers acquire the crystal structure with the atomic coordination different from the cubic fluorite-type. It was shown that the observed RHEED is expected for the orthorhombic phase of MnF_2.

3. X-ray diffraction studies

The schematic layer-by-layer structure of "thin" and "thick" SLs is shown in Fig. 2(a,b). In the picture all notations used in the simulation of XRD rocking curves are present.

Typical measured X-ray θ–2θ scans are presented in Fig. 3. For samples with very thin MnF_2-sublayers ($n = 2-3$ ML), well resolved satellites and thickness fringes are observed on the diffraction curves (Fig. 3a). When the MnF_2-sublayer thickness is 5 ML the thickness fringes disappear and the wider satellites are detected only (Fig. 4b). Moreover, the diffraction pattern is broadened in direction normal to the diffraction vector that follows from ω-scan curves (are not shown). Such difference in the diffraction from two groups of SLs likely indicates the relaxation process occurred in SLs with "thick" MnF_2-sublayers.

The relaxation can be realised as release of elastic strains between the SL as whole and the substrate and/or between the individual SL-sublayers. Note that the misfit of the lattice parameters of MnF_2-fluorite and CaF_2 is -0.031 and MnF_2 of α-PbO_2-structure and CaF_2 is -0.022. The SLs parameters, obtained from the diffraction curves simulation, are listed in the Table.

The data in first and third rows of Table confirm assumptions made above. For the sample 863 the values of the (111)-interplanar spacing are the same as for the CaF_2 and MnF_2 fluorite structure films fully strained relative to Si-substrate. The d-values for the sample 5386 characterise the relaxed CaF_2 and MnF_2 layer with orthorhombic α-PbO_2-structure. The data in last column correspond to the structural factors of the fluorite and α-PbO_2 structure of MnF_2. Note that the F-values of the orthorhombic MnF_2 depend strongly on the free parameter y characterising mutual positions of Mn-atoms in unit cell and hence the Mn-(111) atomic plane splitting shown in Fig. 2. As

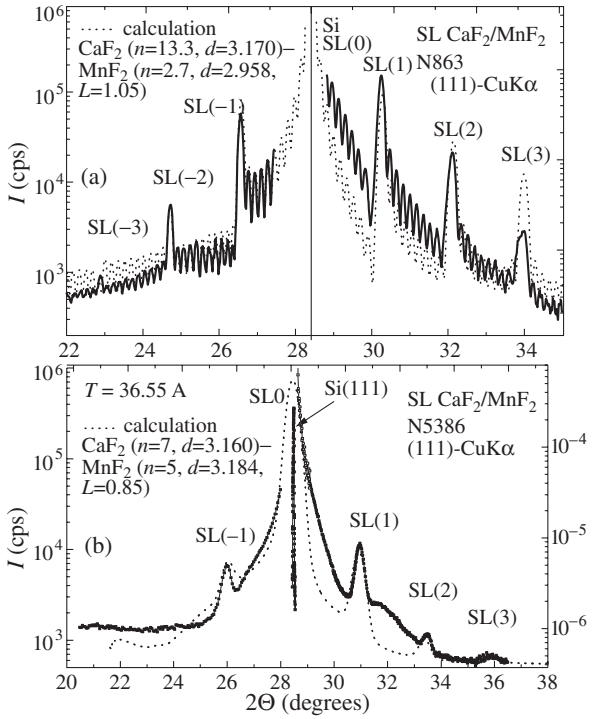

Fig. 3. Measured and simulated θ–2θ scans for 13/3 (a) and 7/5 (b) SLs. Refined parameters are shown in the graphs.

concerned the sample 5382 the d-value for MnF_2 is intermediate between fluorite and α-PbO_2 structures or may be explained by strong tensile strain of orthorhombic MnF_2-sublayer.

Conclusion

Summarizing the above, we have demonstrated the possibility of epitaxial growth on Si(111) of short-period MnF_2-CaF_2 SLs with the different atomic coordination in MnF_2 layers. This coordination is fluorite-like for less than 3 MLs of MnF_2 and orthorhombic-like for the thicker layers. The results of the simulation of X-ray rocking curves are in agreement with RHEED patterns observed.

Acknowledgement

The authors appreciate assistance of Dr. Y. Wakabayashi during XRD measurements at BL-4C beam line.

References

[1] R. E. Dietz, A. E. Meixner *et al*, *J. Lumin.* **1-2**, 279 (1970).
[2] A. G. Banshchikov, *et al*, Proc. 9th Int. Symp. "Nanostructures: Physics and Technology", St Petersburg, Russia, p. 25 (2001).
[3] N. L. Yakovlev, *et al*, *Surf. Interface Anal.* **27** (1999).
[4] N. S. Sokolov, *et al*, *Appl. Surf. Sci.* **162-163**, 469 (2000).
[5] I. K. Robinson, *Surface Crystallography*, Handbook on Synchrotron Radiation, Vol. 3, ed. D. E. Moncton and G. S. Brown (Springer-Verlag, New York, 1986).

13th Int. Symp. "Nanostructures: Physics and Technology"
St Petersburg, Russia, June 20–25, 2005

Vertical and lateral ordering in PbSe/PbEuTe quantum dot superlattices as a function of Eu concentration in the spacer layers

D. Lugovyy[1], G. Springholz[1], A. Raab[1], R. T. Lechner[1], S. G. Konnikov[2], O. V. Rykhova[2] and A. A. Sitnikova[2]

[1] Institut für Halbleitephysik, Johannes Kepler Universität, A-4040 Linz, Austria
[2] Ioffe Physico-Technical Institute, St Petersburg, Russia

Abstract. Self-assembled growth of PbSe/PbEuTe quantum dot superlattices was investigated with particular focus on the influence of the ternary composition of the PbEuTe spacer layers on the vertical and lateral ordering process. From in situ reflection high/energy electron diffraction, x-ray diffraction as well as atomic force and transmission electron microscopy, different types of lateral ordering and interlayer correlations are found. This is attributed to the strong influence of the spacer layer composition on the intermixing between the PbSe dots and the surrounding matrix material during overgrowth.

Introduction

Self-assembled quantum dot superlattices are of great interest due to the interlayer dot correlations formed as a result of the elastic interactions between the dots during growth [1–3]. Under ideal conditions, this results in an efficient lateral dot ordering and allows a tuning of the dot sizes and shapes by changes in the spacer layer thickness [2]. For different material systems, different types of ordered dot arrangements have been observed due to the strong dependence of the interlayer dot interactions on elastic anisotropy as well as growth orientation [3]. In particular, for self-organized PbSe/PbEuTe quantum dot superlattices due to the high elastic anisotropy of these materials a staggered fcc-like $ABCABC..$ dot stacking is formed [2] for spacer thicknesses in the range of 400 to 550 Å, whereas a vertical alignment of the dots takes place for small spacer thicknesses [4]. A similar transition between differently ordered structures was also found in dependence of the PbSe dot sizes, which has been explained on the basis of strain field calculations [4]. However, for InAs as well as SiGe quantum dots a strong intermixing and shape changes has been found to occur during the overgrowth of the dots [5,6]. In the present work, we have therefore investigated the effect of the ternary composition of the PbEuTe spacer layers on the overgrowth properties of self-assembled PbSe quantum dots as well as on the vertical and lateral correlations formed in PbSe/PbEuSe dot superlattice structures.

1. Experimental

Self-assembled PbSe dots were grown by molecular beam epitaxy onto (111) oriented PbTe buffer layers on BaF_2 substrates. Due to the 5.4% lattice-mismatch, pyramidally shape PbSe nanoislands are formed on the surface when a critical coverage of about 2.5 monolayers (ML) is exceeded [2]. For the overgrowth studies, PbSe dot layers of 5 ML thickness were grown under identical growth conditions. Subsequently, the dots were overgrown with $Pb_{1-x}Eu_xTe$ cap layers with different Eu concentration ranging from $x_{Eu} = 0$ to 13% and the change in surface morphology was monitored using in situ reflection high-energy electron diffraction (RHEED). For the investigation of the interlayer correlations, a series of PbSe/PbEuTe superlattices with 30 periods were grown with Eu concentration in spacer layers ranging from 0 to 9.3% but with identical spacer and PbSe thickness of 450 Å spacer and 6.2 ML, respectively. The flux rates and composition of the materials were controlled by quartz crystal measurements. The RHEED patterns recorded along the [-110] azimuth direction were analyzed using an image processing system. The lateral ordering and interlayer correlations in the multilayer structure were investigated by x-ray reciprocal space mapping as well as atomic force and transmission electron microscopy using an EM-420 Philips microscope operated at 100 keV.

2. Results and discussion

Figure 1 shows the typical the RHEED patterns observed for the PbSe dots (a) and after the growth of a 200 Å thick PbEuTe cap layer (b) evidencing that a rapid replanarization occurs during overgrowth. However, from systematic studies it was found that the speed of replanarization strongly depends on the chemical composition of the capping layer. This is shown in Fig. 1(c), where the evolution of the integrated intensity of the 3D (224) diffraction spot during overgrowth is plotted as a function of $Pb_{1-x}Eu_xTe$ cap layer thickness for several different cap layer compositions. Clearly, the thickness required for complete planarization (see arrows in Fig. 1(c)) strongly increases as a function of the Eu content in the ternary cap layer. For overgrowth with pure PbTe, already after 30 Å cap layer

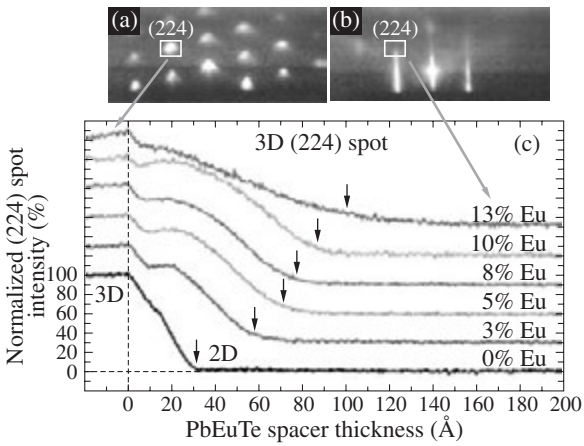

Fig. 1. Top: RHEED patterns of 5 ML PbSe quantum dots before (a) and after (b) overgrowth with a $Pb_{1-x}Eu_xTe$ capping layer. Bottom: Normalized intensity of (224) diffraction spot as a function of $Pb_{1-x}Eu_xTe$ spacer thickness for $x = 0$, 3, 5, 8, 10 and 13%. Each curve has a relative offset of 20 for clarity.

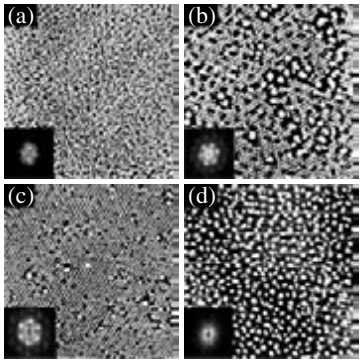

Fig. 2. AFM surface images ($3 \times 3\,\mu$m) of PbSe/PbEuTe quantum dot superlattices with different composition of the PbEuTe spacer layers of 0, 2.6, 4.7 and 9.3% from (a) to (d), respectively. The insert show the FFT power spectra of the AFM images indicating different lateral ordering of the dots.

the initially 110Å PbSe dots have completely disappeared, indicating a strong intermixing of the dots with the surrounding matrix material. In contrast, for PbEuTe cap layer with higher Eu content, the PbSe dots seem to be completely preserved until they are completely covered by the cap layer. Thus, a much larger cap layer thickness is required for surface planariaztion.

The Eu concentration in the spacer layer is also found to drastically affect the lateral ordering of the PbSe dots in the superlattice samples. Figure 2 shows the AFM images of the last PbSe dot layer after 30 SL periods for superlattices with PbEuTe composition of 0, 2.6, 4.7 and 9.3%. Clearly, the samples show a quite different type of lateral ordering in dependence of the Eu concentration. The SL sample with pure PbTe spacers does not show any lateral ordering (see Fig. 2(a)) and the dot size and distribution is similar as for single PbSe dot layers. In contrast, the superlattices with 2.6 and 4.74% (Fig. 2(b) and (c)) show a clear 2D hexagonal lateral ordering within the growth plane with an increase of the perfection with higher Eu concentration. However, the SL sample with highest concentration (Fig. 2(d)) shows a quite disordered dot arrangement and a completely different size distribution and density in comparison with other samples. Figure 3 presents the reciprocal space maps for the SLs with $x_{\mathrm{Eu}} = 4.6$, 0, 9.3% from (a) to (c), respectively. For the sample with $x_{\mathrm{Eu}} = 4.6\%$,

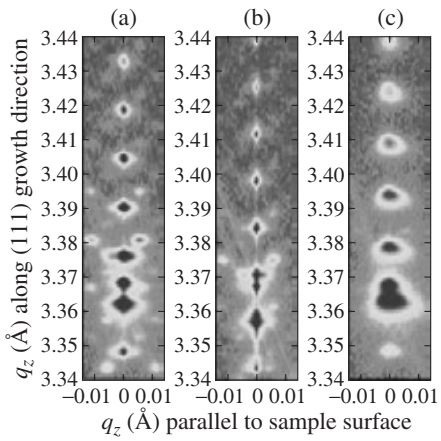

Fig. 3. (222)X-ray reciprocal space maps of three different PbSe dot superlattices different PbEuTe spacer composition of (a) 4.7, (b) 0 and (c) 9.3% indicating different interlayer correlations in the SL structures.

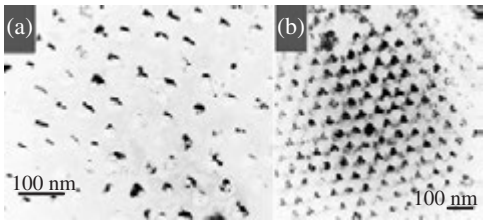

Fig. 4. Plan-view TEM images of two different PbSe/ PbEuTe dot superlattices with Eu concentration of (a) 0 and (b) 4.6% in the spacer layers.

a large number of satellite peaks in the vertical q_z and lateral q_x direction is found. As shown in our previous work [2], the particular arrangement of the satellite peaks indicates the presence of a well-defined fcc-type interlayer dot stacking that causes an efficient lateral dot ordering. On the contrary, for pure PbTe in spacer layers (Fig. 3(b)), no higher order satellite peaks are found, which indicates the presence of only very weakly correlated PbSe dots. As a result, also no efficient lateral ordering takes place, in good agreement with the AFM measurements. The SL sample with 9.3% Eu in the spacer layers shows only very broad satellite peaks that indicate the formation of vertically aligned dots. As a consequence, no lateral ordering takes place. This different type of interlayer correlation can also be inferred from the AFM image of Fig. 2(d) in which much larger dots are observed as compared to those of the other samples. This agrees also with the results from TEM investigations,from which the plan-view images are shown in Fig. 4(a) and (b) for the superlattices with 0 and 4.6% of Eu in spacer layers, respectively. Clearly, in the first case the dots on the surface do not show a lateral ordering, whereas for the 4.6% PbSe/ PbEuTe dot superlattice a hexagonal lattice of dots is formed

In conclusion, we have found a pronounced influence of the composition of the PbEuTe spacer on the interlayer correlations and the lateral ordering process of PbSe/PbEuTe quantum dot superlattices. This effect can be used as an additional tool to control the properties of the quantum dot structures.

Acknowledgements

This work was supported by the FWF and GME of Austria.

References

[1] J. Tersoff, C. Teichert and M. G. Lagally, *Phys. Rev. Lett.*, **76**, 1675 (1996).
[2] G. Springholz, V. Holy, M. Pinczolits and G. Bauer, *Science*, **282**, 734 (1998).
[3] V. Holy, G. Springholz, M. Pinczolits and G. Bauer, *Phys. Rev. Lett.*, **83**, 356 (1999).
[4] G. Springholz *et al*, *Phys. Rev. Lett.*, **84**, 4669 (2000); and *Appl. Phys. Lett.*, **82**, 799 (2003).
[5] J. M. Garcia *et al*, *Appl. Phys. Lett.*, **71**, 2014 (1997).
[6] A. Rastelli, M. Kummer and H. von Känel, *Phys. Rev. Lett.*, **87**, 256101-1 (2001).

13th Int. Symp. "Nanostructures: Physics and Technology"
St Petersburg, Russia, June 20–25, 2005

Kinetic instabilities during crystal growth of III–V semiconductor alloys

I. P. Ipatova and *V. G. Malyshkin*
Ioffe Physico-Technical Institute, St Petersburg, Russia

Abstract. We suggest a concept of semiconductor alloy decomposition based on kinetic phase transition from the growth regime. Kinetic instability is promoted by the drift of adatoms in the field of an elastic driving force created by the "frozen" fluctuations of composition in already completed thickness of the film. For this growth mechanism, we focus on the step flow growth of the film from vapor on the vicinal to [001] surface of cubic substrate. An analytical solution for a composition profile which reproduces itself in step–flow growth mode is found.

Introduction

III–V semiconductor alloys are well known for various growth instabilities. In addition to instabilities, typical for the growth of crystalline materials there exist instability of the alloy growth with respect to composition fluctuations c. The growth of a homogeneous alloy may be unstable and result in an alloy with a spatial modulation of composition. This instability is the subject of current study. In contrast with some recent works, where epitaxial layer is studied on a mismatched substrate [1] what can lead to additional instabilities, we study a matched case to facilitate the role of composition inhomogeneities. This allows us to find an analytical solution in an important growth regime.

1. Model

We consider a III–V semiconductor growth model which includes local and non-local processes. Atoms migration in the growing layer is influenced by both: local interaction with neighboring atoms and and non-local influence of inhomogeneities in already grown layers to processes on the surface via elastic strain.

Processes on the surface are considered in the Barton Cabrera Frank model [2], extended by taking into account non–local elastic interaction with inhomogeneities in already grown layers. Consider a crystal with vicinal surface close to [001] orientation with steps and kinks. Our model can be described by the following processes:

1. Adsorption of atoms from vapor, neglecting desorption.
2. Diffusion and drift of an atom on the step. The drift is caused by elastic strain due to composition inhomogeneity in already grown layers.
3. Adsorption of an atom by step edge, neglecting desorption.
4. Diffusion of atom along step edge.
5. Adsorption of an atom diffusing along step edge by a kink.

In III–V semiconductor alloys $A_{1-c}B_cC$ the resulting value of grown composition is determined by relative number of A and B atoms adsorbed by the kinks. The value of formed composition c may differ from its average value. Once such inhomogeneity formed it can not change, it is "frozen". Because equilibrium value of lattice constant depends on alloy composition these inhomogeneities (even if they are deep buried in already grown layers) lead to elastic strain. This elastic strain creates a drift of atoms on the surface. This is new original non–local process which we added to classic Barton Cabrera Frank crystal growth model. In our earlier work [3] we considered such instability in linear approximation and have shown a possibility of growing composition inhomogeneity from layer to layer. In this work we consider same effect without using linear approximation and find stationary structure in case of one–dimensional modulation.

We consider crystal growth at temperatures when only the surface diffusion is important. The bulk diffusion is considered to be negligible small. At such low temperatures no new kink can be created as a result of thermal activation. The number of steps and kinks is considered to be fixed and determined only by Miller index of vicinal surface. The step–flow growth regime is considered without bending instabilities [4,5].

Local processes on the surface are determined by 2D drift–diffusion equation with boundary conditions. Adsorption of atoms from the vapor and following drift–diffusion on the surface is described by

$$\operatorname{div} J^{A,B} = G_0^{A,B} \tag{1}$$

where J has two contributions: diffusion and drift:

$$J_i^{A,B} = -D_{ij}^{A,B}\frac{\partial N^{A,B}(\mathbf{r})}{\partial r_j} - b_{ij}^{A,B}N^{A,B}(\mathbf{r})\frac{\partial U^{A,B}(\mathbf{r})}{\partial r_j} \tag{2}$$

Here y axis directed along step edge and x perpendicular to the step, $N(\mathbf{r})$ is areal concentration of atoms, $U(\mathbf{r})$ is the potential created by elastic strain, b_{ij} is atoms mobility on the surface, symbols A and B relate values to atoms of A and B types respectively.

To solve (1) analytically we consider a regime, when composition modulations exists only along y axis. In our earlier work we have shown [3] that such regime do exist. In case of modulations along y direction the potential $U^{A,B}(\mathbf{r})$ from (2) depends on y only:

$$U^{A,B}(\mathbf{r}) = U^{A,B}(y) \tag{3}$$

To solve drift–diffusion equation (1) analytically we consider the processes in continuous sinks approximation [4] (this allows us to write down boundary conditions in a simple form $N^{A,B}(\mathbf{r})|_{x=0} = 0$ and $\frac{\partial}{\partial x}N^{A,B}(\mathbf{r})|_{x=L} = 0$) and take into account highly anisotropic diffusion coefficient $D_{yy} \gg D_{xx}$. Then the flux j forming the crystal is:

$$j^{A,B}(y) = J_x^{A,B}(y)|_{step}\, l_k = I^{A,B}\exp\left(-U^{A,B}(y)/T\right) \tag{4}$$

A normalizing factor I can be obtained from the conservation of the number of atoms. The composition c of formed crystal is determined by the number of adsorbed atoms of A and B types, i.e.

$$c(x=0,y) = \frac{j^B(y)}{j^B(y)+j^A(y)} \quad (5)$$

$$1-c(x=0,y) = \frac{j^A(y)}{j^B(y)+j^A(y)}. \quad (6)$$

The deviation of c from average value causes elastic strain, that creates potential U for adsorbed atoms on the surface. The potential U is the driving force for atoms migrating on the crystal surface. The potential $U(y)$ has two contributions: local one (determined by chemical interaction) and non–local one determined by long range elastic strains [3]:

$$U^{A,B}(\mathbf{k}) = V_{SR}^{A,B}\frac{1}{a}\frac{\partial a}{\partial c}\delta c(\mathbf{k};h) \quad (7)$$

$$+ V_{LR}^{A,B}\frac{1}{a}\frac{\partial a}{\partial c}\int_{-\infty}^{h} kdz'\delta c(\mathbf{k};z')\sum_{s=1}^{3} Q(\varphi)\exp\left[-\alpha_s k(h-z')\right]$$

Coefficient $Q(\varphi)$ is a linear combination of coefficients $Q_{sym}(\varphi)$ and $Q_{asym}(\varphi)$ which related to certain combination of Green's tensor from Ref. [6] and are given in Appendix C of Ref. [3]. The angle φ is the angle between $\mathbf{k}$ and [110] direction of crystal, for modulations along y direction $\varphi = \pi/2$. Static attenuation coefficients α_s can be found in Ref. [6].

Using (6), (4) and (7) obtain:

$$\overline{c}+\delta c(x=0,y,h) = \frac{1}{1+A\exp\left[-\frac{U^A(y)-U^B(y)}{T}\right]} \quad (8)$$

where $A = I^A/I^B$. To solve (8) we need $U(\mathbf{r})$ obtained from Fourier transform $U(\mathbf{k})$ (7) and then solve non–linear equation (8). The task greatly simplifies for stationary regime, when δc does not depends on z, $\delta c = \delta c(y)$.

$$U(k_x=0,k_y) = B_{st}(\pi/2)\delta c(k_x=0,k_y) \quad (9)$$

$$U(y) = B_{st}(\pi/2)\delta c(y) \quad (10)$$

where $B_{st}(\pi/2)$ is a constant (it is a combination of V_{SR}, V_{LR} and $Q(\pi/2)$). The Eq. (10) for two kind of atoms gives: $U^A(y) = B_{st}^A\delta c(y)$, $U^B(y) = B_{st}^B\delta c(y)$.

Linearizion of (8) give critical point: ($\overline{c}=0.5$; $\tau = 0.25$), where τ is a temperature, measured in a scale depending on material properties: $\tau = \frac{T}{B_{st}^A - B_{st}^B}$ and can be considered as a controlling parameter.

The linear theory was extensively studied in [3]. Here we focus on a non–linear regime. There two kinds of problems to be studied: stationary state and transition regime. In this work we focus on the stationary profile. We consider the situation when δc reached the saturation and does not depend on z. In case of not very large δc the Eq. (8) give:

$$\overline{c}+\delta c = \frac{1}{1+\frac{1-\overline{c}}{\overline{c}}\exp\left(-\frac{\delta c}{\tau}\right)}. \quad (11)$$

Above T_c ($\tau > 0.25$) this transcendent equation has only a trivial solution $\delta c = 0$. Below T_C ($\tau < 0.25$) it has three solutions (one trivial and two non–trivial). On a figure 1 the kinetic diagram for a system with $\overline{c} = 0.5$ is presented. The area inside absolute instability curve is unstable with respect to infinitesimal inhomogeneities. Bold curve represent the composition of c in stationary regime. The resulting structure is a layered system oriented along y direction which reproduces itself during crystal growth.

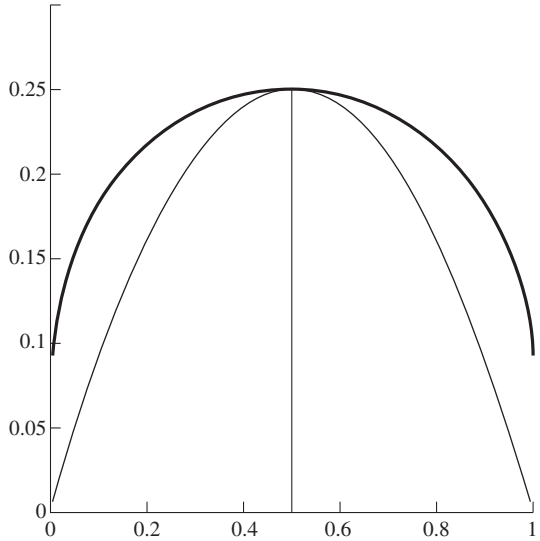

Fig. 1. Kinetic diagram for a system with $\overline{c} = 0.5$. Thin line — absolute instability curve, bold line — stationary c.

2. Discussion

In this work we found an analytical solution for a composition profile which reproduces itself in the step–flow growth mode. The effect is a pure kinetic effect due to long–range interaction between inhomogeneities in already grown layers and atom in the growing layer. The crystal is locally stable, thermodynamic equilibrium correspond to $\delta c = 0$. While non–local elastic interaction is a stabilizing force in thermodynamic it can be the source of instability in the open system.

Acknowledgements

The work has been supported by Russian Foundation for Basic Research and Leading Scientific School, No 2160.2003.02.

References

[1] B. J. Spencer, P. W. Voorhees and J. Tersoff, *Phys. Rev. B*, **64**, 235318 (2001).
[2] W. K. Barton, N. Cabrera and F. C. Frank, *Philos. Trans. Roy. Soc.*, (London) A243 299 (1951).
[3] I. P. Ipatova, V. G. Malyshkin, A. A. Maradudin, V. A. Shchukin and R. F. Wallis, *Phys. Rev. B*, **57**, 12 968 (1998).
[4] G. S. Bales and A. Zangwill, *Phys. Rev. B*, **41**, 5500 (1990).
[5] I. L. Aleiner and R. A. Suris, *Fiz. Tverd. Tela*, **34** 1523 (1991), english translation: *Sov. Phys. Solid State*, **34**, 809 (1992).
[6] K. Portz and A. A. Maradudin, *Phys. Rev. B*, **16**, 3535 (1977).

13th Int. Symp. "Nanostructures: Physics and Technology"
St Petersburg, Russia, June 20–25, 2005

Cobalt nanostructures grown by MBE on CaF_2: RHEED, X-ray diffraction and EXAFS studies

K. M. Pavlov[1,5], Ya. I. Nesterets [2], C. M. Kewish[1], J. R. Hester[3], A. K. Kaveev[4], *N. S. Sokolov*[4,5], H. Ofuchi[5], M. Tabuchi[5] and Y. Takeda[5]

[1] School of Physics and Materials Engineering and Centre for Synchrotron Science, Monash University, VIC 3800, Australia
[2] CSIRO Manufacturing and Infrastructure Technology, PB 33, Clayton South, Victoria 3169, Australia
[3] Australian Nuclear Science and Technology Organisation, PMB 1, Menai, NSW 2234, Australia
[4] Ioffe Physico-Technical Institute, St Petersburg, Russia
[5] Venture Business Laboratory, Nagoya University, Nagoya 464-8601, Japan

Abstract. Epitaxial Co nanostructures and thin films were grown on grooved and ridged surface of CaF_2(110)/Si(001) heterostructures by molecular beam epitaxy. Reflection high energy electron diffraction (RHEED) and X-ray diffraction measurements enabled identification of face centered cubic structure of cobalt, which agrees with EXAFS data.

Introduction

Owing to attractive magnetic properties and numerous applications, the growth and crystal structure of cobalt thin films and nanostructures have been studied by a number of research groups [1]. It was found that though hexagonal close packed (hcp) structure is stable in bulk, in thin films cobalt often grows in metastable face centered cubic (fcc) or body centered cubic (bcc) phases. Considerable enhancement of magneto-optical effects in structures containing transparent insulating layers has recently been reported [2], which facilitates optical investigations of individual single-domain nanomagnets. To our knowledge, the Co-CaF_2 system has not yet been studied. In the present work, the crystal structure of cobalt films and nanostructures grown by molecular beam epitaxy on CaF_2/Si heteroepitaxial substrates was explored.

1. MBE-growth and RHEED studies

Thin Co films (2–10 nm) have been grown on 111-faceted ridged and grooved surface of CaF_2(110) buffer layers on Si(001) substrates [3]. RHEED patterns shown in Fig. 1 are taken before (a, c) and after (b, d) Co growth. Electron beam azimuth was [-110] (along the ridges) for a, b and [001] (across the ridges) for c, d. Cobalt growth temperature was 100 °C for samples #5349, #5408 (see Fig. 1b) and 500 °C for sample #5352 (Fig. 1d).

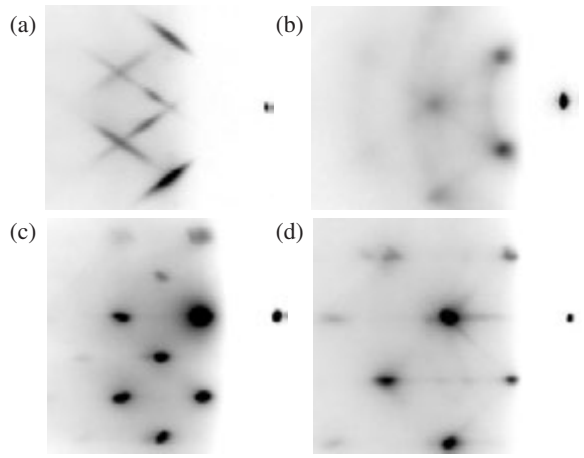

Fig. 1. RHEED patterns taken before (a, c) and after (b, d) the growth of cobalt layer on grooved and ridged surface of CaF_2(110) buffer layer on Si(001).

One can see that the patterns in Fig. 1c, d are very similar; they are characteristic of fcc structure, which has CaF_2 buffer layer. Thus the patterns indicate that Co grows predominantly in fcc crystal phase with (110) plane, which is parallel to this plane of the fluorite buffer and CaF_2(110)/Si(001) interface. It can be also concluded that the epitaxial relations are the following: $[\text{-}110]_{Co} \parallel [-110]_{CaF_2}$ and $[001]_{Co} \parallel [001]_{CaF_2}$. Using atomic force microscopy it was found that cobalt does not wet the calcium fluoride surface and grows on it in 3D mode with average size of the islands 10–15 nm at 100 °C and 50–60 nm at 500 °C.

2. X-ray diffraction measurements

X-ray diffraction measurements were carried out at Nagoya University, using the rotating anode ATX-G diffractometer (produced by Rigaku Co), as well as at the Australian National Beamline Facility (ANBF) at the Photon Factory in Tsukuba (Japan). In both cases the energy 8.0477 keV ($CuK_{\alpha 1}$) was used. Figure 2 shows $\omega - 2\theta$ scan obtained from sample #5352. In addition to the intense Si 004 peak from the substrate and 220 and 440 peaks from the CaF_2 buffer layer, one can see well pronounced 220 and 111 peaks of Co cubic face centered phase. Taking into account that structural factor for 111 re-

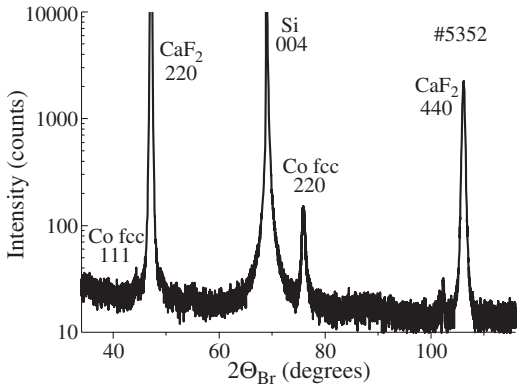

Fig. 2. X-ray diffraction $\omega - 2\theta$ scan for sample #5352 measured in symmetrical Bragg geometry.

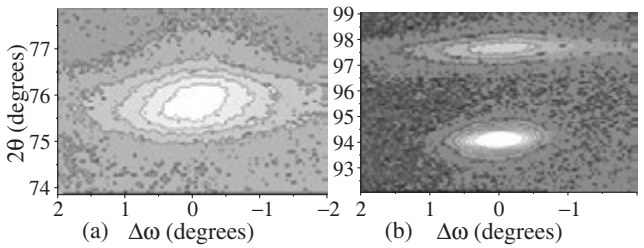

Fig. 3. Reciprocal space maps for sample #5352 (high temperature Co growth) around Co 220 (a) and Co 222-CaF_2 333 (b) reflections.

flection in this phase is by 5 times higher than that of 220 reflection, one can estimate that the proportion of 111-oriented crystallites does not exceed a few per cent. No peaks belonging to the hcp phase characteristic of bulk materials were observed. Thus one can conclude that fcc Co(110) dominates, which is in agreement with RHEED observations.

The reciprocal space maps (RSM) for #5352 presented in Fig. 3a, b, confirm higher crystalline quality for this sample than for the sample #5408 (see Fig. 4). The width of the Co(220) peak (Fig. 3a) in the lateral ($\Delta\omega$ axis) direction is about 0.72°, indicating the average size of Co islands grown at 500 °C is 50 nm, which is in agreement with that found by AFM. The position and shape of the Co 222 peak in Fig. 3b shows that the Co nanoislands film is almost strain free (relaxed), because centres for both Co 222 ($2\theta \sim 97.5°$) and CaF_2 333 ($2\theta \sim 94°$) reflection are positioned at the same line defined by the crystallographic relations between [110] and [111] directions. The broadening of the Co 222 peak in the lateral direction is due to the small size of Co nanoislands.

Figure 4 shows the RSM measured around the Co 220 reflection from the sample #5408 grown with low (100 °C) substrate temperature during Co deposition. Because of lower diffraction intensity caused by inferior crystalline quality of this sample the measurements were conducted at the synchrotron. But, despite the use of the synchrotron source, the Co 220 reflection is still poorly resolved for this sample. The first Co 220 peak ($\Delta\omega \sim 0°$) is also "smeared" by the strong reflection from the substrate, due to wide slits used before the detector. The elongation of this Co 220 peak in the vertical direction (2θ axis) (Fig. 4) is due to significant strain distribution. Additionally, the intensity distribution around the first Co 220 peak in Fig. 4 shows some elongations (streaks), which could be associated with the shape of Co nanoislands; in particular, the most pronounced streaks can be associated with 111 facets of the Co islands. The centre of the second, more diffuse, Co 220 reflection peak is observed at $\Delta\omega \sim 3°$ (Fig. 4) probably corresponds to the lower crystalline quality part of the Co film having higher deviation between the (110) plane of Co nanoparticles and this plane in CaF_2(110) buffer layer, due to the relatively low Co deposition temperature.

3. EXAFS measurements

EXAFS measurements were performed at the beam line BL12C at the Photon Factory in Tsukuba with a Si(111) double crystal monochromator and a bent cylindrical mirror using the SR from the 2.5 GeV storage ring. The EXAFS spectra for Co epitaxial films on CaF_2 and Co foil were measured in the fluorescence-detection mode at 100 and 300 K, respectively. The fluorescence signals were detected by an array of 19 elements of Ge solid-state detectors.

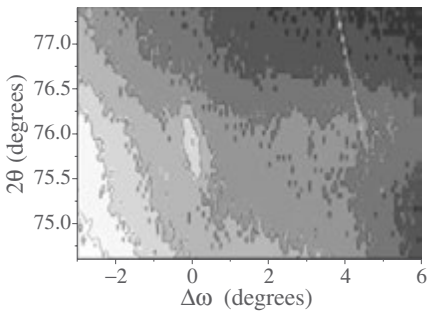

Fig. 4. Reciprocal space maps for sample #5408 (low temperature Co growth) near Co 220 reflection.

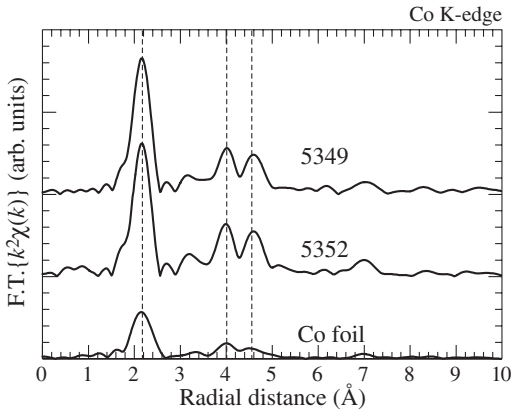

Fig. 5. Fourier transform of Co K-edge EXAFS oscillation functions $k^2\chi(k)$ spectra for Co films on CaF_2(110) and Co foil.

Figure 5 shows the Fourier transform of Co K-edge EXAFS oscillation functions $k^2\chi(k)$ spectra for samples #5349 and #5352 grown at 100 and 500 °C, respectively as well as cobalt foil. The curves for the films are quite similar to those observed in Ref. [4] for 100 nm thick fcc Co epitaxial films grown on diamond (100). However they are very different from the expected Fourier transform for bcc Co structure, simulated in that work. This is in agreement with the identification of the fcc structure of Co on CaF_2/Si presented in two previous sections of this work and indicates that the increase of the Co growth temperature on CaF_2 to 500 °C does not result in undesirable chemical and structural changes.

Acknowledgements

This study was supported by Russian Ministry of Science and Education. Part of this work was performed at the Australian National Beamline Facility with support from the Australian Synchrotron Research Program, which is funded by the Commonwealth of Australia under the Major National Research Facilities Program. The authors appreciate useful discussions with Drs. A. G. Banshchikov and N. L. Yakovlev.

References

[1] J. I. Martin *et al*, *J. Magnetism and Magnetic Materials*, **256**, 449 (2003).

[2] N. Qureshi, H. Schmidt and A. R. Hawkins, *Appl. Phys. Lett.*, **85**, 431 (2004).

[3] O. V. Anisimov *et al*, *Proc. of 11th Intern.Symposium "Nanostructures: Physics and Technology" (St Petersburg, Russia, 2003)*, 295 (2003).

[4] K. M. Kemner *et al*, *J. Vac. Sci. Technol.*, **B 14**, 3207 (1996).

13th Int. Symp. "Nanostructures: Physics and Technology"
St Petersburg, Russia, June 20–25, 2005

Influence of CdTe sub-monolayer stressor on CdSe quantum dot self-organization in a ZnSe matrix

I. V. Sedova, O. G. Lyublinskaya, S. V. Sorokin, D. D. Solnyshkov, D. N. Lykov, A. A. Toropov and S. V. Ivanov

Ioffe Physico-Technical Institute, St Petersburg, Russia

Abstract. Paper reports on employing a stressor-controlled self-organization process for CdSe quantum dot (QD) fabrication in a ZnSe matrix. Super-strained CdTe fractional monolayer (Δa/a$\sim$ 14%) grown on top of the Te-stabilized ZnSe surface prior to deposition of the QD material (CdSe) has been used as a stressor which is expected to affect size, composition and density of CdSe QDs. Preliminary studies by X-ray diffraction, photoluminescence (PL), and PL excitation and are presented.

Introduction

The studies of II–VI wide-gap semiconductor nanostructures emitting in the short wavelength region of the visible spectrum were carried out due to their potential for optoelectronic applications such as medical diagnostic system, short-range optical communications using plastic fibers, laser projection TV and so on. A CdSe/ZnSe system has attracted much interest because of the high efficiency emission in the blue-green spectral range. In spite of the $\sim$ 7% lattice mismatch, the conventional strain-induced self-organization process during molecular beam epitaxial (MBE) deposition of CdSe on ZnSe results in a morphology of the disordered ZnCdSe quantum well involving CdSe-rich nanoislands with a wide bimodal lateral size dispersion (within 5–15 nm) [1], rather than occurs in a Stranski–Krastanow mode. The latter starts beyond the critical thickness of plastic deformation of CdSe on ZnSe. Nevertheless, employing of such quantum-disk-like nanostructures in the active region of optically and electron-beam pumped ZnSe green lasers has permitted one to improve significantly their threshold, output power and thermal stability characteristics [2, 3]. The need in high density, narrow-size dispersion and high Cd-content CdSe quantum dot (QD) nanostructures stimulated numerous technological attempts to modify or affect the CdSe self-organization [4–6].

An efficient way to control the CdSe QD self-organization by introduction of strongly lattice-mismatch fractional monolayer (FM) — stressor — before the deposition of the QD material has been proposed and experimentally realized during studies of a type-II CdSe/BeTe system ($\Delta a/a \sim 7.8\%$) [7]. The intentionally deposited 0.2 monolayer (ML) of CdTe on BeTe ($\Delta a/a \sim 14\%$ for CdTe/BeTe) transformed into the array of small highly-strained CdTe dots which served as nuclei for CdSe QDs. The small CdSe QDs with the surface density as high as $10^{12}\,\mathrm{cm}^{-2}$ and lateral sizes and heights of 4–6 and 1–1.5 nm, respectively, were obtained.

In this paper we report on the attempt to apply the stressor-controlled QD fabrication technique to the conventional CdSe/ZnSe nanostructures, monitored by x-ray diffraction (XRD) and photoluminescence (PL) studies.

1. Experiment

All structures were grown on GaAs (001) substrate in a two-chamber MBE system supplied with high purity Zn, Cd, ZnS, Te and Se (valve cracker cell) in the II–IV chamber, and Ga and As in a III–V one. The latter served for deposition of GaAs buffer layers which were transferred then to the II–VI chamber through vacuum. II–VI structures were grown at a substrate temperature $T_S = 280\,^{\circ}\mathrm{C}$. Structures (A) and (B) have the similar design comprising a single CdSe QD region of a 2.1 ML nominal thickness, embedded between bottom and cap ZnSe layers of 50–60 and 15–20 nm, respectively, and differ in the CdSe deposition technique. In the reference structure A, the CdSe insertion was grown by modified migration enhanced epitaxy (MEE) technique with a one minute growth interruption after each Se pulse [8]. In structure B, prior to the MEE growth of CdSe insertion the ZnSe surface was stabilized consequently under Zn and Te fluxes to form the Te-terminated surface. Then a preliminarily calibrated fraction of CdTe ML was deposited in a conventional MBE mode as a stressor having a 14% lattice mismatch with ZnSe. The growth of both structures was monitored by reflection high energy electron diffraction (RHEED). The CdSe insertion in A grew coherently in a quasi-two-dimensional (2D) growth mode, exhibiting just some broadening of streaky pattern and gradual decay of its intensity. In structure B, the decrease in the RHEED intensity was accompanied by arising of three-dimensional chess-order features indicating more efficient surface roughing.

For independent evaluation of thickness of the CdSe insertion, as well as the ZnTe and CdTe FMs employed in structures A and B, three different superlattice (SL) structures were grown using the same regimes: a 7-period CdSe/ZnSe SL (S1), a 10-period ZnTe/ZnSe (S2), and a 10-period CdTe/ZnTe/ZnSe (S3), each having the ZnSe barrier thickness of 3.5 nm. The SL structures include also a 0.1 μm-thick ZnSSe bottom buffer and a 20-nm ZnSe cap layer.

XRD rocking curve were measured by using a double-crystal diffractometer DRON-3M and simulated using a semi-kinematical diffraction theory. PL and PL excitation (PLE) measurements were carried out at temperatures of 25 and 77 K using a 325 nm line of a 5 mW He-Cd laser and a halogen lamp emission dispersed by a monochromator.

2. Results and discussion

$\Theta-2\Theta$ XRD rocking curves of three SL structures (S1, S2 and S3) are presented in Fig. 1. The CdSe/ZnSe SL structure without CdTe stressor (S1) reveals a 0-order SL peak and no high-order satellites being below the sensitivity limit. The ZnSSe peak corresponds to a pseudomorphic layer with the S

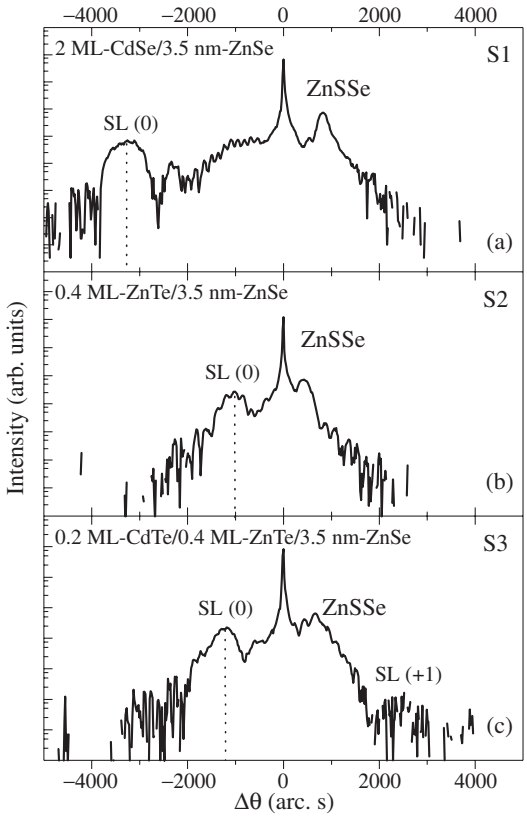

Fig. 1. Typical Θ−2Θ XRD rocking curves of three different types of the superlattices. (a) CdSe/ZnSe, (b) ZnTe/ZnSe, (c) CdTe/ZnTe/ZnSe.

content of 0.1. The estimated nominal thickness of CdSe insertion practically coincides with the intended one, assuming the intended SL period of ∼ 4 nm. The nominal thickness of ZnTe stabilization layer (∼ 0.4 ML) is derived from the S2 curve of the ZnSe/ZnTe SL, which agrees well with the c(2×2)Zn reconstruction on ZnSe capped with Te. A thickness of CdTe FM estimated from the XRD spectra of structure S3 amounts to 0.2 ML, keeping unchanged the ZnTe thickness. According to our previous studies [7], it corresponds to the optimal thickness of CdTe stressor. Observation of two SL satellites in this structure allows independent estimation of the ZnSe barrier thickness which is consistent with the expected value. Thus, one can conclude that the actual design of structure B is ZnSe/2ML-CdSe/0.2ML-CdTe/0.4ML-ZnTe/ZnSe, and that of structure A is ZnSe/2ML-CdSe/ZnSe.

Low-temperature PL spectra of structures A (dash line) and B (solid line) are presented in Fig. 2. The dominant PL line (I1) in the spectrum of structure B, related to the composite insertion, is 150 meV-shifted down in energy as compared to the CdSe PL line in the reference sample A. Preliminary estimation in the effective mass approximation using model solid theory [9] cannot explain such strong energy shift by the variation of chemical composition in the composite CdSe/CdTe/ZnTe insertion. We attribute this shift mostly to the increased Cd content in the CdSe QDs accumulated on CdTe stressor nuclei. Besides, the low-energy shoulder (denoted as I2) appears at 2.3–2.4 eV. For attribution of this PL line we studied low-temperature PL spectra of S1, S2 and S3 SLs. The peak similar to I2 with a maximum located at 2.3–2.4 eV and a full width at half maximum (FWHM) of about 200 meV was observed in the PL spectra of structures S2 and S3 and was not regis-

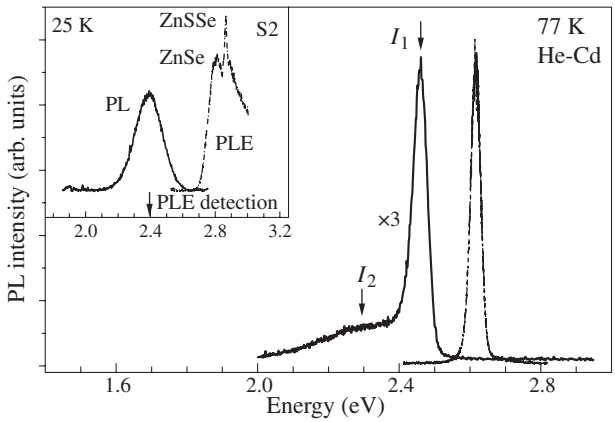

Fig. 2. PL spectra of single CdSe insertion in ZnSe matrix with CdTe stressor (solid line) and without it (dashed line). In insertion: PLE spectrum of ZnSe/ZnTe SL.

tered in structure S1. The inset to Fig. 2 demonstrates PL and PLE spectra of sample S2. Introduction of ZnTe, responsible for the appearance of I2 line, does not however result in the additional density of states and PLE spectrum of this line demonstrates only the spectral structure corresponding to the excitonic and band-edge absorption in the ZnSe and ZnSSe barrier layers. The similar PL spectrum have been earlier registered in ZnTe/ZnSe heterostructures [10] and discussed in terms of Te isoelectronic centers or type II nanostructures formation.

3. Conclusions

Using the super-strained CdTe fractional ML as the stressor for the enhanced CdSe QD formation appears to affect dramatically the CdSe redistribution on the ZnSe surface resulting in a 150 meV long-wavelength shift of the PL peak energy owing to the increased Cd content in CdSe QDs at the same CdSe nominal thickness.

Acknowledgements

The work is partly supported by RFBR, INTAS Grants # 03-51-5019. S. V. I. acknowledges support of RSSF.

References

[1] N. Peranio *et al*, *Phys. Rev. B*, **61**, 16015 (2000).
[2] I. V. Sedova *et al*, *Semicond.*, **38**, 1099 (2004).
[3] M. M. Zverev *et al*, *Phys. Stat. Sol. (b)*, **229**, 1025 (2002).
[4] P. R. Kratzert, M. Rabe and F. Henneberger, *Phys. Stat. Sol (b)*, **224**, 179 (2001).
[5] E. Kurtz *et al*, *Phys. Stat. Sol (b)*, **229**, 519 (2001).
[6] M. Keim *et al*, *J. Appl. Phys.*, **88**, 7051 (2000).
[7] S. V. Ivanov, *J. Alloy. Compound.*, **371**, 15 (2004).
[8] I. V. Sedova *et al*, *Proceedings of 29th ICSC in Inst. Phys. Conf. Ser*, **174 (3)**, 161 (2003).
[9] C. G. Van de Walle, *Phys. Rev. B*, **39**, 1871 (1989).
[10] Y. Gu, I. L. Kuskovsky, M. van der Voort, G. F. Neumark, X. Zhou, M. C. Tamargo, *Phys. Rev. B*, **71**, 045340 (2005).

13th Int. Symp. "Nanostructures: Physics and Technology"
St Petersburg, Russia, June 20–25, 2005

Molecular beam epitaxy of InSb extra-monolayers inserted in an InAs matrix

A. N. Semenov, V. A. Solov'ev, B. Ya. Meltser, O. G. Lyublinskaya, Ya. V. Terent'ev, A. A. Toropov, A. A. Sitnikova and S. V. Ivanov

Ioffe Physico-Technical Institute, St Petersburg, Russia

Abstract. We report on molecular beam epitaxy (MBE) of InSb insertions in an InAs matrix, with the width exceeding 1 monolayer. Different growth techniques based on exposure of an InAs growth surface to an antimony flux, followed by deposition of additional amount of InSb using both conventional MBE and migration enhanced epitaxy modes, were used. The formation of the ultra-thin InSb layers have been studied *in situ* by reflection high energy electron diffraction.

Introduction

There has been an increasing interest in InSb-based nanostructures. In particular, self-assembled InSb quantum dots (QDs) have been fabricated by either a molecular beam epitaxy (MBE) or a metalorganic vapor phase epitaxy in GaAs [1], GaSb [2, 3], and InP [4] matrices. The longest photoluminescence (PL) wavelength of 1.7 μm (at 77 K) was observed from the InSb/GaSb nanostructures.

Recently, we have reported on bright PL up to room-temperature in the 3.2–4.2 μm wavelength range, measured in MBE grown InSb/InAs nanostructures with InSb sub-monolayers (SMs) embedded in an InAs matrix [5, 6]. SM insertions with the nominal InSb coverage ranged from 0.6 up to 1 monolayer (ML) in dependence on growth temperature (T_S = 430–485 °C) were formed by a few seconds exposure of the InAs growth surface to the antimony flux with no intentional deposition of InSb. Such procedure was shown to be possible due to the very efficient As-Sb anion exchange reaction on InAs surface. Transmission electron microscopy (TEM) studies showed that even SM InSb insertions transform into the dense array of coherent InSb-enriched islands with a mean lateral size of about several nanometers [7]. The larger size InSb QDs, required for laser applications [6], is expected to form in the case of the extra-monolayer (EM) deposition.

This paper is devoted to the MBE growth and study of InSb/InAs nanostructures with extra-monolayer InSb insertions. Reflection high energy electron diffraction (RHEED), TEM and PL were employed for structural and optical characterization of the structures.

1. Experimental

The samples were grown on n-InAs (001) substrates using a RIBER 32P setup. Conventional solid source effusion cells were used to produce In, Al and Sb_4 fluxes, whereas As_4 flux was supplied from a VAC-500 valved cracking cell. A substrate temperature T_S was measured by IR pyrometer calibrated by using well known surface reconstruction transitions on GaAs, InAs, and GaSb, monitored *in situ* by RHEED. An active region of the structures consists of a 0.1 μm thick InAs layer, centered with a single InSb insertion, and confined by 10 nm-thick $Al_{0.2}In_{0.8}As$ barriers on both sides. The structures were capped by a 10 nm-InAs layer.

Two growth techniques were used for the fabrication of EM InSb insertions. In both cases, the first stage of InSb formation includes a procedure of the InAs growth surface exposure to the Sb flux, described in [7], followed by a short-time growth interruption (GI). The second stage was deposition of additional amount of InSb by either conventional MBE or migration enhanced epitaxy (MEE). In both cases, the In flux was the same and corresponded to the InSb growth rate about 0.1 ML per second. The growth temperature was ranged from 430 °C to 485 °C. The *in situ* RHEED specular spot intensity (SSI) oscillation technique was used to study the InSb EM formation.

TEM studies were performed by employing an EM-420 Philips microscope operating at 100 keV. PL spectra were measured under a diode laser excitation (λ_{th} = 809 nm) at the 1.5 W/cm^2 excitation power density and temperature tuning in the 15–300 K range. Emitted light was detected with a nitrogen-cooled InSb photodiode and standard lock-in amplification technique.

2. Results and discussion

RHEED SSI oscillations for different growth modes of InSb deposition at 430 °C are presented in Fig. 1. The introduction of GI after the exposure of InAs surface to the Sb flux results in the dramatic decrease of SSI intensity (Fig. 1a). Although no intentional InSb deposition was made in this case, the dense array of InSb-based QDs was revealed by a plan view TEM image within the InSb SM insertion, as shown in the inset to Fig. 2. In our opinion, such unusual behavior of SSI may be explained by an onset of the self-organization of InSb-enriched islands during the GI. It is expected that a certain time of the GI exists that corresponds to the most uniform QD array. Nevertheless, RHEED pattern exhibits the (3×1) Sb-stabilized reconstruction without 3D features, that confirms very small size of the InSb QDs.

The SSI oscillations during the deposition of an additional amount of InSb using MEE are presented in Fig. 1b. Deposition of In is assumed to lead to completing of the InSb monolayer. One can distinguish the corresponding half-period In-induced oscillation. Another half-period As-induced oscillation appears in Fig. 1b when the As shutter is opened. Such procedure of additional In deposition results only in a small shift of the InSb-QD-related PL peak to the longer wavelength (Fig. 2, dashed curve) as compared to the InSb SM dominant PL band (Fig. 2, solid curve). To increase the nominal thickness of deposited InSb and, probably, the mean size of InSb QDs, a complete MEE (consequent deposition of In and Sb atoms) or MBE growth should be used. The PL spectrum of the structure with InSb insertions formed by the complete MEE process is shown in Fig. 2 by the dotted line. In this case, the

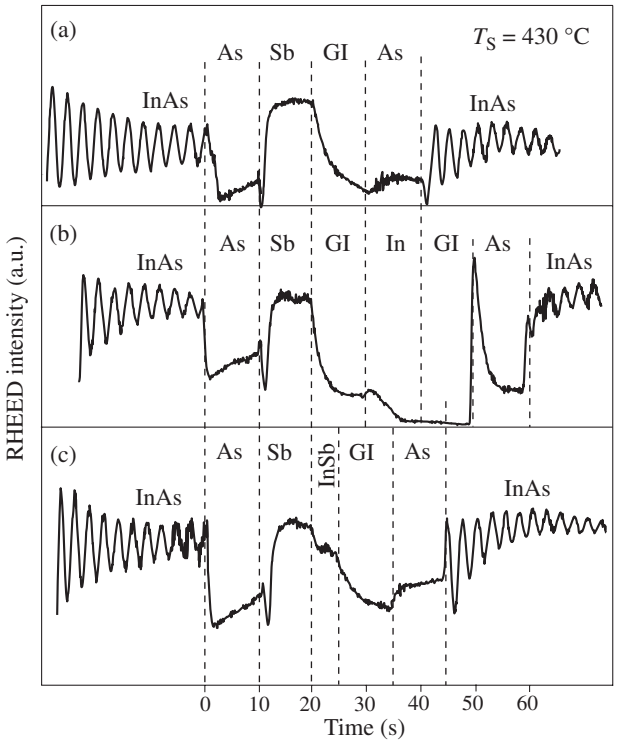

Fig. 1. RHEED oscillations during formation of single InSb insertion by exposure of an InAs surface to Sb_4 flux (a), by the exposure followed by MEE (b) or MBE (c) deposition.

strong red shift of the InSb emission line is observed.

The RHEED SSI oscillations for the case of conventional MBE growth of InSb followed after the InAs exposition to the Sb flux are presented in Fig. 1c. There is one important difference in comparison with the case of Fig. 1b. The Sb-stabilized (3×1) surface reconstruction kept during the InSb deposition is not affected noticeably by the following opening of the As flux. Moreover, the 3D-related features appear in the RHEED pattern during the InSb MBE deposition. One should note that MBE deposition of InSb without preliminarily exposure of InAs surface to Sb flux is non-reproducible and the resultant InSb-related emission wavelength is poorly controlled.

It has been also found that MBE deposition of InSb EM is possible at the growth temperatures below 450 °C. The deposition of InSb at higher temperatures during a long period does not change the 2D Sb-stabilized (3×1) surface reconstruction due to the strain-induced efficient InSb re-evaporation from the surface. Such behavior is in good agreement with predictions of thermodynamic consideration [8]. As a result no red shift of the InSb emission band is observed.

3. Conclusions

In summary, we have grown by MBE InSb/InAs nanostructures with extra-monolayer InSb insertions formed by different growth techniques including an exposure of the InAs growth surface to the Sb flux as well as MEE or MBE deposition of additional amount of InSb. The latter technique results in pronounced red shift of InSb-related PL band, if applied at growth temperature below 450 °C. The importance of growth interruption after the exposure procedure has been discussed using detailed analysis of RHEED SSI oscillations. The possibilities of InSb EM formation by MEE and MBE have been compared.

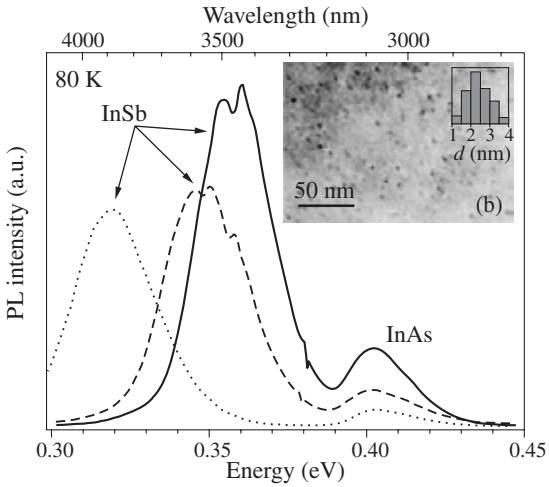

Fig. 2. PL spectra of InSb/InAs nanostructures grown by different techniques: exposure of InAs surface to Sb flux (solid line); exposure procedure followed by In deposition only (dashed line); exposure procedure followed by complete MEE (dotted line). The inset presents a plan-view TEM image of the structure with the SM InSb insertion.

Acknowledgements

The work was partly supported by RFBR and Program of the Ministry of Science and Education of RF. S. V. I. acknowledges the support of RSSF.

References

[1] B. R. Bennett, B. V. Shanabrook, *Appl. Phys. Lett.*, **68**, 505 (1996).
[2] A. F. Tsatsul'nikov *et al*, *J. Electron. Mater.*, **27**, 414 (1998).
[3] E. Alphandery *et al*, *Appl. Phys. Lett.*, **74**, 2041 (1999).
[4] T. Utzmeier *et al*, *Phys. Rev. B*, **56**, 3621 (1997).
[5] V. A. Solov'ev *et al*, *Appl. Phys. Lett.*, **86**, 011109 (2005).
[6] S. V. Ivanov *et al*, *J. Cryst. Growth*, to be published.
[7] to be published elsewhere.
[8] P. V. Neklyudov *et al*, *Semiconductors* **31**, 989 (1997).

13th Int. Symp. "Nanostructures: Physics and Technology"
St Petersburg, Russia, June 20–25, 2005

Growth of (ZnSe/MgS)/ZnCdSe DBR using ZnS as a sulphur source

D. D. Solnyshkov, S. V. Sorokin, I. V. Sedova, A. A. Toropov, S. V. Ivanov, and P. S. Kop'ev
Ioffe Physico-Technical Institute, St Petersburg, Russia

Abstract. We report on molecular beam epitaxial growth and study of optical and structural properties of (ZnSe/MgS)/ZnCdSe distributed Bragg reflector with λ_0=520 nm and R_{max}=97%. The sample was grown pseudomorphically on GaAs substrate using ZnS as a sulphur source. It was studied by SEM, XRD and optical measurements, which have shown good optical and structural characteristics.

Semiconductor microcavities have been attracting strong scientific interest for almost 20 years [1]. Their main characteristic feature is an effective interaction of photons and excitons, which results in formation of a quasi-particle called exciton-polariton [2]. The strength of this interaction is reflected by the Rabi splitting. Its value is especially large (above the excitation energy of LO phonons) in II-VI semiconductors [3], which are therefore possible candidates for manufacturing polaritonic devices (e.g. ultralow-threshold lasers [4]) capable of operating at RT. It is of great importance to grow the whole structure using II-VI materials only.

There have been several recent attempts to use zinc-blende MgS — the lowest refractive index material nearly lattice-matched to GaAs — for optical structures. For example, Suemune *et al* have grown a 5-period ZnSe/(ZnSe/MgS) distributed Bragg reflector (DBR) with a 92% reflectivity by metal-organic vapor phase epitaxy [5]. Kruse *et al* have demonstrated 99% 17-period DBR of the same type, grown by molecular beam epitaxy (MBE) using a valved cracker cell as a sulphur source [6]. Earlier Bradford *et al* have suggested to employ ZnS as a sulphur source to grow MgS/ZnSe quantum wells (QWs), using the efficient Mg-Zn exchange interaction due to the much stronger Mg-S binding energy, as compared to the Zn-S one, although they have not applied this technique to DBRs [7]. This paper reports on the studies of novel design (ZnSe/MgS)/ZnCdSe DBR grown by MBE using ZnS as a sulphur source.

We have combined all these approaches into a single method of growing MgS-contained II-VI DBRs, using ZnS as the sulphur source. The middle of the stop band was chosen to correspond to a standard ZnCdSe QW wavelength, which is 520 nm. It has been pointed out by Bradford *et al* [7], that pseudomorphic growth of zinc blende MgS on GaAs is only possible under low temperatures and is limited by a certain critical thickness depending on the temperature. These constraints do not allow growing of a pure MgS/ZnSe DBR with $\lambda/4$-thick layers. Therefore, we used a MgS/ZnSe superlattice (SL) as a low index material and ZnCdSe solid alloy with Cd=3% as a high index material.

The refractive index dispersion curves of MgS, ZnSe and ZnCdSe have been calculated using modified single effective oscillator model [8] (values $E_0 = 7.5$ eV, $E_g = 4.5$ eV and $E_d = 27$ eV, taken from [9], were used to describe MgS in this model).

We have performed optimization of system parameters, aiming at two goals: to make the structure lattice-matched to GaAs and to obtain the highest possible difference of refractive indices. This optimizaiton yielded the design presented in Fig. 1. The nested SL consists of four MgS layers of 100 Å and four ZnSe layers of 30 Å, providing approximately 75% of average MgS content. The high-index ZnCdSe layer with Cd = 3% is of a 450 Å thickness. The composite multilayer structure consists of 15 periods, having a total thickness of 1450 nm. Such structure should provide at least 95% reflectivity at the center of the stop band.

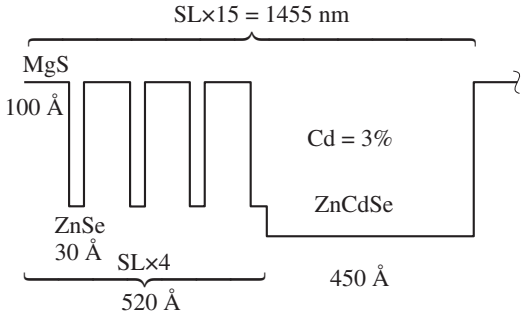

Fig. 1. Design of the DBR.

The sample was grown pseudomorphically on a GaAs (001) substrate in an EP-1203 (home made) MBE setup equipped with elemental sources of Zn, Cd, Mg, Se (the latter is a valved cracker cell) and a ZnS compound source. The growth temperature of 250 °C allows one to grow thick MgS layers without transformation to a rocksalt phase [7].

The sample has been investigated by Scanning Electron Microscopy (SEM), optical reflectivity measurements and X-ray diffraction (XRD). Optical reflectivity has been measured using SPECORD M40 double-ray spectral photometer, capable of operating both in UV and visible ranges (185–909 nm). XRD measurements have been performed on a double-crystal diffractometer DRON-3M with a Ge(111) monochromator.

The SEM images of the sample are shown in Fig. 2. The periodic structure of both the nested MgS/ZnSe SL (Fig. 2b) and the whole sample (Fig. 2a) is clearly distinguishable. The layers are generally flat. Some extended defects started at the middle of the structure can be seen. The period of the composite DBR structure is 110 nm (Fig. 2a), which is within 10% of the intended value. The surface of the sample exhibits nanoscale roughness, which should not affect the reflectivity in the visible range.

X-ray diffraction curve of the DBR structure is shown in Fig. 3. Besides the narrow GaAs substrate peak, it is dominated by a broad peak shifted to smaller angles. The curve exhibits smooth interference fringes of different periodicity, indicating general flatness of numerous interfaces of the DBR structure. The figure also presents a simulation of the diffraction curve based on the design parameters. One can see that the position of the main broadened peak on the experimental curve corresponds to the position of an average intensity maximum at the simulation curve. However, narrow satellites of the composite

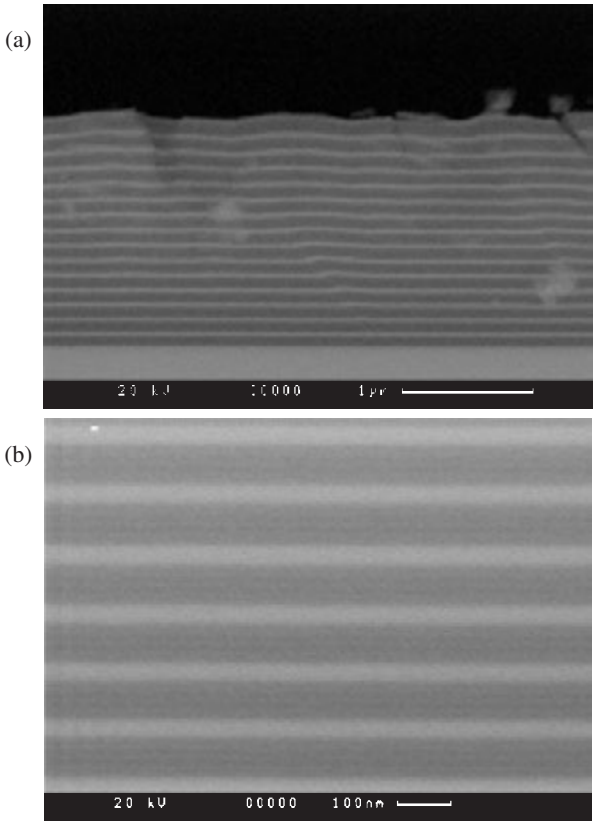

Fig. 2. SEM image of the DBR. (a) Composite SL, $T = 110$ nm; (b) Nested SL.

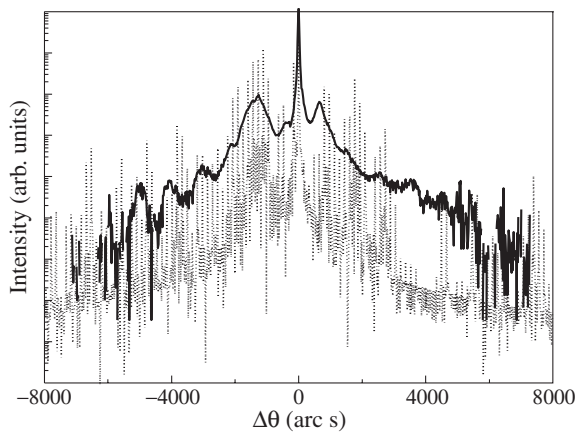

Fig. 3. XRD curve of the DBR: experiment (solid curve) and simulation (dotted curve).

DBR structure are not visible on the experimental curve. This indicates that the structure has some deviation from periodicity on this scale, which, however, does not affect strongly its optical properties as will be shown below.

Figure 4 presents the results of optical measurements. The stop-band of the Bragg mirror is very well pronounced. The background reflectivity far from the stop band is due to the GaAs substrate. The position of the stop-band corresponds to the expected value (it's centered at 520 nm), and its width is consistent with the results of calculations based on transfer matrix method [10]. However, the shape of the curve indicates some gradient in the period of the structure along the growth direction.

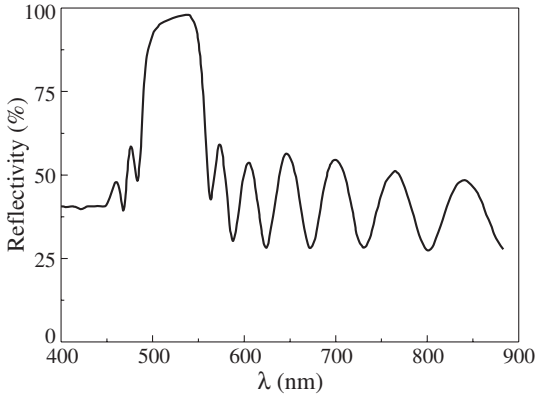

Fig. 4. Reflectivity of the DBR.

To conclude, this work has proven the feasibility of MBE growth of MgS-containing distributed Bragg mirrors, using ZnS as the sulphur source. Precise technology, high structural quality and reflectivity of the mirrors make it possible to fabricate a complete II-VI microcavity with high Rabi splitting.

Acknowledgements

This work has been supported in part by RFBR (03-02-17563), PS Department of RAN, and RSSF.

References

[1] C. Weisbuch *et al*, *Phys. Rev. Lett.* **69**, 3314 (1992).
[2] P. G. Savvidis *et al*, *Phys. Rev. Lett.* **84**, 1547 (2000).
[3] A. Imamoglu, J. R. Ram, *Phys. Lett. A* **214**, 193 (1996).
[4] I. Suemune *et al*, *phys. stat. sol. (b)* **229**, 961 (2002).
[5] C. Kruse *et al*, *phys. stat. sol. (b)* **229**, 111 (2002).
[6] R. Andre *et al*, *J. Cryst. Growth* **214/215**, 1002 (2000).
[7] C. Bradford *et al*, *Appl. Phys. Lett.* **76**, 3929 (2000).
[8] Afromowitz, *Solid State Communications* **15**, 59 (1974).
[9] H. Kumano *et al*, *Phys. Rev. B* **55**, 7 (1997).
[10] A. Kavokin, G. Malpuech, *Cavity Polaritons* (Elsevier, Amsterdam, 2003).

13th Int. Symp. "Nanostructures: Physics and Technology"
St Petersburg, Russia, June 20–25, 2005

Formation of semiconductor quantum dots in the subcritical thickness range

A. A. Tonkikh[1,2,3], G. E. Cirlin[1,2,3], V. G. Dubrovskii[1], N. K. Polyakov[2], Yu. B. Samsonenko[2], Yu. G. Musikhin[1], P. Werner[3] and V. M. Ustinov[1]

[1] Ioffe Physico-Technical Institute, St Petersburg, Russia
[2] Institute for Analytical Instrumentation RAS, 190103, St Petersburg, Russia
[3] Max-Planck Institute of Microstructure Physics, 06120 Halle, Germany

Abstract. The investigations of semiconductor quantum dots using transmission electron microscopy and atomic force microscopy are performed. The formation of semiconductor quantum dots from a metastable wetting layer with the effective thickness below critical thickness in the Stranskii-Krastanov 2D-3D growth mode is observed in the InAs/GaAs and the Ge/Si heteroepitaxial systems. The observed phenomenon is explained within the frame of the kinetic theory of quantum dot formation in the lattice mismatched heteroepitaxial systems.

Introduction

Investigation of the formation mechanisms of semiconductor quantum dots (QDs) is of great interest in the modern semiconductor physics [1]. The main application field of QDs is their utilization in the active region of a semiconductor laser diodes [2]. It is well known that dense QD ensembles can be fabricated by the molecular-beam epitaxy (MBE) technique. Laser production technology requires the controlled production of QDs with the desired sizes and surface density. Many efforts were put into theoretical and experimental investigation of the influence of MBE growth conditions on the structural and optical properties of QD ensembles. In particular, it has been found that there are two possible types of QDs growth mechanisms in highly mismatched heteroepitaxial systems. In the Volmer–Weber growth mode QDs arise almost immediately after the deposition is started, while in the Stranskii–Krastanow growth mode QDs are formed on a wetting layer. Stranskii–Krastanow growth mode is of practical interest since it is realized in InAs/GaAs and Ge/Si systems. An experimental observation of the transition from the two dimensional to the island growth mode is possible using reflection high energy electron diffraction (RHEED) technique. At a certain critical thickness H_c related to the onset of 2D-3D transition, the RHEED pattern image changes from stripes to the spots. The value of H_c obtained from the experiment in most cases correlates with the value of H_c given by various thermodynamic models of the QDs formation. However, in some cases the strained surface of the wetting layer transforms to the islands-like surface even when the deposited film thickness H is lower than H_c. Recently we have observed the formation of subcritical InAs QDs grown on the GaAs(100) substrate surface [3] and Ge QDs grown on the Si(100) surface [4]. In this work continue these studies and present new theoretical and experimental results on the Ge/Si and InAs/GaAs subcritical QDs.

1. Theory

The kinetic theory of the formation of QDs in heteroepitaxial systems [5] provides the relationships between the technologically controlled parameters of MBE growth (the substrate temperature, the growth rate, the total amount of deposited material and the exposition time) and the structural characteristics of QDs ensemble (the surface density and the average lateral size of QDs). The Stranski-Krastanow growth is characterized by the existence of a flux-independent equilibrium wetting layer of thickness H_{eq} [6]. The formation of QDs is possible only from a metastable wetting layer with a thickness $h > h_{eq}$. Parameter $\zeta = h/h_{eq} - 1$ is the measure of the wetting layer metastability. In terms of kinetic theory of QD formation [5] the critical thickness of deposited material H_c approximately equals the maximum wetting layer thickness H_c corresponding to the maximum nucleation rate of 3D islands I(t). At subcritical effective thickness of deposited material H_0 ($h_eq < H < H_c - \delta H$, $2\delta H$ is the width of transition range) the surface density of islands after the end of nucleation stage is flux independent and increases with increasing the surface temperature T and the effective thickness H_0

$$N = \int_0^\infty dt\, I(t) \propto \exp\left[-\frac{3}{5}\frac{T_e}{T(H/h_{eq}-1)^2}\right]. \qquad (1)$$

Here T_e is the quasi-equilibrium temperature [7] determined by the particular system energetics and lattice misfit.

In the overcritical range of effective thickness ($H > H_c + \delta H$) the surface density of islands exhibits a principally different behavior. As shown in [4], the density of overcritical QDs increases with the deposition rate V, decreases with the temperature and is almost independent on the amount of deposited material:

$$N \propto \exp\left(\frac{3E_D}{2k_BT}\right). \qquad (2)$$

The average size of islands in the subcritical thickness range increases very slowly, because the growth of islands slows down at lower system metastability. At overcritical range the average size of islands increases more rapidly, therefore at modest exposition time we may expect to observe larger islands at $H > H_c$.

2. Experimental

The structures are grown by MBE method using EP1203 (InAs/GaAs QDs) and RIBER SIVA45 (Ge/Si QDs) setups. In the case of InAs/GaAs system, the thicknesses of InAs deposited H are amounted within 1.5–1.6 monolayers (ML), while $H_c =$ 1.7 ML. The structures are formed at the substrate temperatures

of 420 and 450 °C. After the deposition, InAs are exposed under the As_4 flux for desired time. The reference sample with $H = 2.0$ ML is grown at the substrate temperature 450 °C. After the deposition (for subcritical InAs thickness, after the deposition and exposition) InAs layer is overgrown by a thick GaAs cap layer in order to investigate the structures by photoluminescence (PL) method. In the case of Ge/Si system the thickness of deposited Ge films are 0.44 nm, 0.55 nm and 0.73 nm ($H_c = 0.66$ nm). The deposition is performed at the substrate temperature of 600 °C. It is no exposition after the Ge deposition and the samples are immediately cooled down and taken away from the growth chamber. The substrate surfaces are controlled in situ by RHEED system in both cases. InAs/GaAs heterostructures are studied with transmission electron microscopy (TEM). Ge/Si heterostructures are investigated using atomic force microscopy (AFM).

3. Discussion

Consider at first the InAs/GaAs system. While the thickness of deposited InAs is lower than H_c, the surface of the samples before capping by GaAs is exposed to the As_4 flux. QDs formation is always observed on the surface after a certain deposition time by the RHEED system. The time of QDs formation is different for different samples. The smaller values of metastability corresponds to the higher QDs formation times. Fig. 1 shows the experimental dependencies of the surface density of InAs QDs on the effective thickness of deposited InAs at different substrate temperatures applied. It is important that in the subcritical thickness range we have observed experimentally a thermodynamic increasing dependence of the surface density on the substrate temperature. This qualitatively agrees with the predictions of our theoretical model given by Eq. (1). Also, the

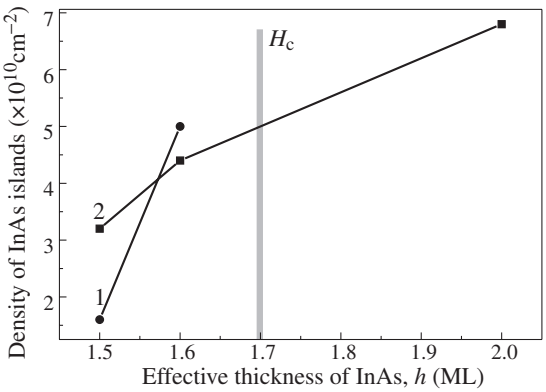

Fig. 1. Surface density of InAs QDs versus deposited thickness of InAs. The temperatures of the growth are: 1) 420 °C; 2) 450 °C.

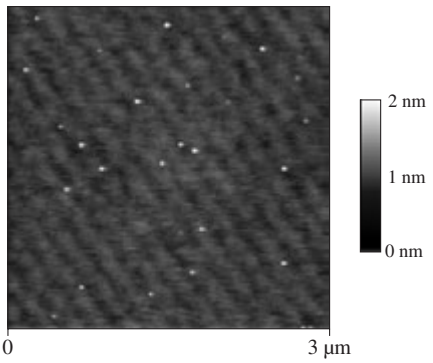

Fig. 2. Ge QD grown on a Si(100) surface at 600 °C. Deposited thickness of Ge is 0.55 nm.

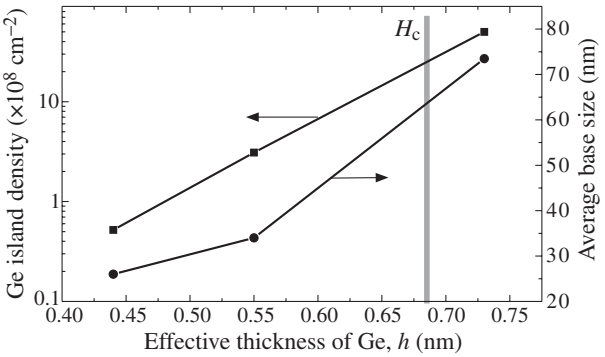

Fig. 3. Surface density and base size of Ge QDs versus deposited thickness of Ge. The temperature of the growth is 600 °C.

surface density of islands rapidly increases with the effective thickness of InAs.

In the case of Ge/Si system the situation is much different. The deposited amounts of Ge were much lower than H_c and the values of metastaility ζ were not high. We did not expect to observe QDs formation after a while and the samples were immediately cooled down after the Ge deposition without any exposition. During the cooling, RHEED patterns did not transform from the stripes to the spots. However, our AFM investigations show the formation of Ge QDs with extremely low densities for both samples with subcritical Ge films. QDs formed from the subcritical Ge film are shown on Fig. 2. It is clearly seen, that both size and density of subcritical Ge QDs are much smaller than for those values for overcritical QDs. Fig. 3 shows the dependencies of the density of Ge island array and the base QD size versus deposited Ge thickness. We have observed that the size of QDs and the density of QD array rises with the deposited thickness of Ge in the subcritical range.

4. Conclusions

We have shown that critical thickness of a semiconductor QDs formation in Stranskii-Krastanow growth mode more a kinetic value than the thermodynamic parameter. It is found that the formation of QDs is possible when the thickness of the wetting layer is lower than the critical thickness for the both heteroepitaxial systems studied. InAs/GaAs QDs were formed from the wetting layer of high value of metastability after the step of surface exposition. Ge/Si QDs were formed from a metastable wetting layer of low value of metastability due to the existence of a local wetting layer thickness fluctuations.

Acknowledgements

The authors are grateful to the financial support received from different scientific programs of the Russian Academy of Sciences, Ministry of Science and Education, RFBR grant 05-02-16568-a and SANDiE Network of Excellence.

References

[1] D. Bimberg *et al*, *"Quantum dot heterostructures", Wiley, New York* (1999).
[2] V. M. Ustinov *et al*, *"Quantum dot lasers"*, Oxford university press, 2003.
[3] A. A. Tonkikh *et al*, *Tech. Phys. Lett.* **29(8)**, 691 (2003).
[4] V. G. Dubrovskii *et al*, *Tech. Phys. Lett.* **30(11)**, 920 (2004).
[5] V. G. Dubrovskii *et al*, *Phys. Rev. B* **68**, 075409 (2003).
[6] P. Muller *et al*, *Appl. Surf. Sci.* **102**, 6 (1996).
[7] V. G. Dubrovskii *et al*, *Phys. Stat. Sol. (b)* **241**, R42 (2004).

13th Int. Symp. "Nanostructures: Physics and Technology"
St Petersburg, Russia, June 20–25, 2005

III–V semiconductor surface nanopatterning using atomic force microscopy for InAs quantum dot localization

E. Tranvouez[1], M. Gendry[2], P. Regreny[2], A. Descamps[3] and G. Bremond[1]

[1] LPM, UMR CNRS 5511, INSA de Lyon, 7 avenue Jean Capelle, 69621 Villeurbanne Cedex, France
[2] LEOM, UMR CNRS 5512, 36 Avenue Guy de Collongue, 69134 Ecully Cedex, France
[3] CLAMS, INSA de Lyon, 7 avenue Jean Capelle, 69621 Villeurbanne Cedex, France

Abstract. In order to create suitable nano-holes for quantum dots (QDs) localisation on InP and GaAs surfaces, we used Atomic Force Microscopy in intermittent contact mode coupled with a modulated voltage to realized local anodization at a nanometre scale. This method leads after a few tens of milliseconds of oxidation, to an oxide height saturation and a low lateral growth rate for both surfaces. These specific results were used to control separately both depth and diameter of holes and to obtain compatibility pattern for QD growth. We also demonstrated also the thermal stability of this pattern at compatible temperatures with the InAs QD growth.

Introduction

Quantum dots (QDs) technology seems to be able to make an improvement in micro and optoelectronic devices. In this context the Stranski–Krastanov growth mode [1] is well known to provide high quality QDs. The limits of this technique are principally the homogeneity of QDs and lack of control of the QD spatial localization. A way to achieve narrow size distribution, controlled densities and spatial localization is to couple this technique to a nano-patterning tool [2]. The first work of Dagata [3] has proved the capacities of Scanning Probe Microscopy to induce such nanoscale surface modifications. Atomic Force Microscopy (AFM) has already proved to be a good candidate for this task [4].

In this paper, we report on III–V semiconductor surface patterning (principally on InP, GaAs was also performed) by local anodization by Atomic Force Microscopy (AFM) in order to create nucleation sites for InAs QDs, a task of prime interest for the 1.3–1.55 μm wavelength range emitting system. The principle of this patterning is to grow oxide plots under AFM tip and then to etch them to create nano-holes suitable for InAs QD nucleation sites. To achieve this purpose, we use an original and unusual combination of AFM intermittent contact mode with a modulated voltage. With this technique, arrays of holes, with typical diameter in the 15–25 nm range, were produced on both InP and GaAs surfaces.

1. Experimental details

Investigated InP samples are grown on n doped InP (4×10^{18} cm^{-3}) epi-ready wafers. The substrate roughness was decreased by growing a 300 nm thick n doped (2×10^{18} cm^{-3}) buffer layer. InP surface was deoxidized by a 60 s dip in a 5% aqueous HF. Samples are then rinsed using deionized water. For GaAs samples, we directly used n doped (4×10^{18} cm^{-3}) epi-ready wafers (the buffer layer was not necessary to pattern this surface). Our AFM apparatus consists in a commercial Nanoscope III from Digital Instruments. Standard PtIr5 coated Silicon tips with a resistivity of 0.01 Ω cm and an average resonance frequency of 75 kHz were used. Oxide features were realized in air with a relative humidity remaining between 70 and 80%. The oxidation was initiated by a decrease in the oscillating amplitude of the cantilever and an AC modulated voltage (+6 V/−2 V at 1 KHz) applied to the substrate during the anodization.

2. Patterning

To realize AFM patterning we chose to use intermittent contact mode coupling with an AC modulated voltage. The advantages of this method, comparing to a standard AFM oxidation (positive bias apply in contact mode AFM), are principally the reduction of space charge effects that occur during oxide growth [5]. This space charges, due to a screen effect on oxianions (OH^- ions) diffusion, reduce lateral resolution and limit the depth of anodic oxidation [6]. The use of an AC modulated voltage cuts the space charge effects and allows real nanoscale modification. Concerning intermittent contact mode, it allows a reducting probe wear of the probe during the oxidation and like to non-contact oxidation [7] a better control of the water meniscus.

Topographic studies gave similar variation like standard oxidation for both InP and GaAs surfaces. For oxide plot height and width dependence versus the applied positive voltage (positive/negative ratio maintain constant) and versus the probe oscillating amplitude, we obtain obtain typical linear and logarithmic variation, respectively [6]. This is clearly related to the enhancement of the electric field due to an increase of the positive voltage and a reduction of the probe/surface mean distance as the oscillating amplitude is decreased. Concerning the feature homogeneity provided by this technique, we can notice results compatible with the nucleation site homogeneity required for a QD ensemble. After etching, an array of hundred oxide plots leads to an array of nano-holes of 2 ± 0.2 nm in depth and 19.5 ± 3.9 nm in width (see Fig. 1).

Moreover, for oxide plot size dependence on oxidation time (as shown in Fig. 2a), we obtain more original results. In the first stages of the oxidation, a high growth rate (either in height or in width) is observed. Then, after a few tens of milliseconds, we can observe height saturation and lower lateral growth rate. This could be directly related to the use of the modulated voltage. Indeed, the anions can only diffuse during the positive part of the applied voltage [6], whereas the negative part removes them. Consequently, the diffusion depth is limited, which produces the observed saturation effect. Concerning the width, we must consider that the ions are constrained by the electric field, so they can not freely diffuse to the sides of the feature. This explains the reduction of the oxide lateral growth rate with the oxidation time. This saturation effect allows us to accurately

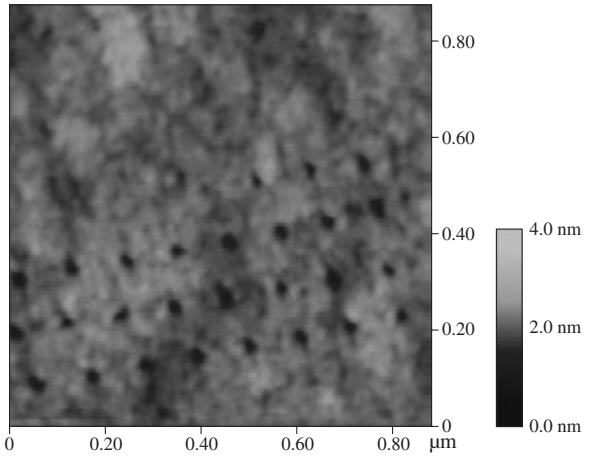

Fig. 1. $0.9 \times 0.9\,\mu m^2$ image of an InP surface nanopatterning realized in intermittent contact mode, after etching of the oxide plots. A $+6$ V/-2 V modulated voltage was applied during 100 ms. The Size of the holes are 2 ± 0.3 nm in depth and 19.5 ± 3.9 nm in width.

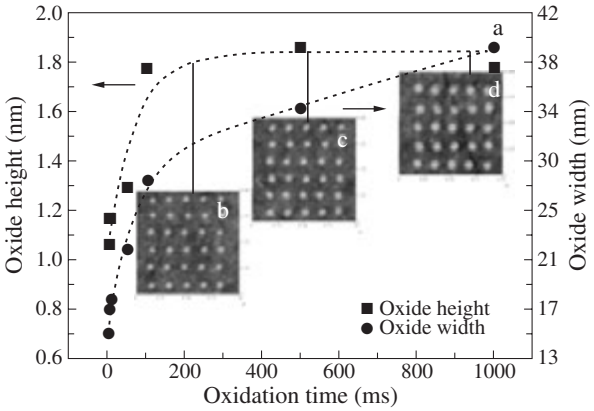

Fig. 2. (a) Oxide plot size dependence on oxidation time measured on InP, with a standard voltage of $+6$ V/-2 V at 1 kHz. In insert, arrays of oxide plots realized on GaAs with varying oxidation time: 0.1 s (b), 0.5 s (c) and 1 s (d), respectively.

control the oxide plot/hole size: positive voltage controlling the height/depth of plot/hole and the oxidation duration the diameter of the plot/hole. Figure 2b-d (insets) illustrate this behavior: varying the oxidation time while maintaining the bias voltage constant ($+6$ V/-2 V) influences the oxide dot diameter (and consequently the diameter of the holes). We thus obtain, for times of 0.1 s, 0.5 s and 1 s, three arrays of plots with width of 21 nm, 25 nm and 32 nm, respectively, and a constant height of 4 nm.

3. Pattern stability

The problem of thermal stability of patterned surfaces must be taken under consideration for an epitaxial regrowth of the InAs QDs. Therefore, we have studied the stability of the patterned surfaces. AFM images of the patterned surface are shown on Fig. 3, just after oxidation (Fig. 3a), after HF etching (Fig. 3b) and after annealing at 530 °C under an arsenic overpressure (Fig. 3c). This last image shows the stability of the nanoholes at temperatures classically used for epitaxial growth of InAs QDs. Work are under progress concerning the InAs QD growth on patterned surfaces and results will be presented at conference.

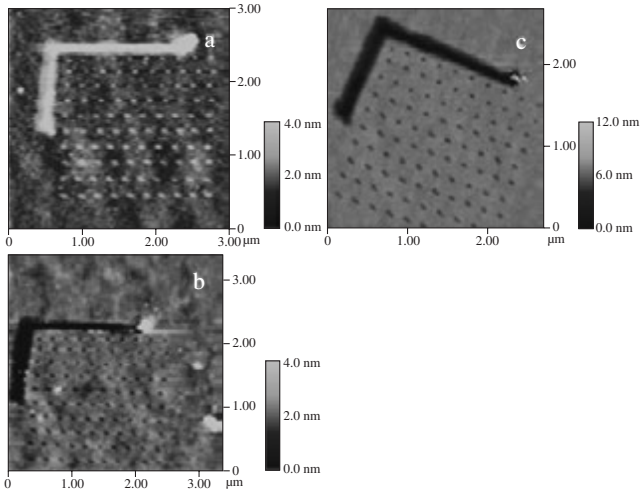

Fig. 3. AFM images of the InP surface patterning: (a) just after oxidation, (b) after HF etching and (c) after annealing at 530 °C under an arsenic overpressure.

Conclusion

We presented an AFM anodization technique to fabricate nucleation sites for InAs QDs on both InP and GaAs surfaces. We demonstrated, using a combination of an intermittent contact mode with an AC modulated voltage, an accurately control with a nanoscale resolution of both depth and diameter of the nucleation sites.

References

[1] D. Bimberg, M. Grundmann, N. N. Ledentsov, *MRS Bull.*, 1998.
[2] C. K. Hyon, S. C. Choi, S. H. Song, S. W. Hwang, M. H. Son, D. Ahn, Y. J. Park, E. K. Kin, *Appl. Phys. Lett.* **77**, 2607 (2000).
[3] J. A. Dagata, T. Inoue, J. Itoh, H. Yokoyama, *Appl. Phys. Lett.* **56**, 2001 (1990).
[4] R. Ohashi, T. Ohtsukab, N. Ohtaa, A. Yamadab, M. Konagai *A Thin Solid Films* 464B–465, 237 (2004).
[5] J. A. Dagata, T. Inoue, J. Itoh, K. Matsumoto, H. Yokoyama, *J. Appl. Phys.* **84**, 6891 (1998).
[6] E. Tranvouez, M. Gendry, P. Regreny, G. Bremond, *Superlattices and Microstructures* **36**, 325 (2004).
[7] R. Garcia, M. Calleja, F. Perez-Murano, *Appl. Phys. Lett.* **72**, 2295 (1998).

13th Int. Symp. "Nanostructures: Physics and Technology"
St Petersburg, Russia, June 20–25, 2005

Self-assembly of $Al_{0.48}In_{0.52}As$/InP quantum dashes

A. A. Ukhanov, G. Boishin, A. S. Bracker, D. Gammon and J. C. Culbertson
The Naval Research Laboratory, Washington D.C. 20375, USA

Abstract. A novel structure containing self-assembled, $Al_{0.48}In_{0.52}As$ quantum dashes is obtained by combining solid-source molecular beam epitaxy and atomic layer *in situ* $AsBr_3$ etching. The dash morphology is determined by atomic force microscopy and reveals large differences compared to nanostructures grown on GaAs substrates.

Introduction

Semiconductor quantum dashes (QDashes) are attracting much attention because of their application in novel optoelectronic devices such as lasers and amplifiers [1-3]. These nanostructures are composed of InAs material grown in the Stranski-Krastanow (SK) mode. SK−grown QDashes are strained and significant intermixing usually occurs both during island formation and overgrowth, changing QDash composition and shape.

$Al_{0.48}In_{0.52}As$/InP cannot be fabricated by SK growth because of the almost perfect match of lattice constants. However, this system offers several advantages: the grown material is practically unstrained, and sharper interfaces with reduced intermixing can be achieved. The AlInAs heterostructure can potentially be replaced with AlInGaAs and can be designed to emit light in the range 1.3–1.5 μm, which is attractive for optical communication. It may also be possible to grow unstrained AlInAs or AlInGaAs QDashes without a wetting layer and with substantially larger dimensions than usual SK dots or dashes.

In this paper we present a simple method for obtaining $Al_{0.48}In_{0.52}As$/InP QDashes via multistep self-assembly using *in situ* $AsBr_3$ etching, and we emphasize the important physical differences of the formation of 3-D nanostructures on InP substrates vs. GaAs substrates.

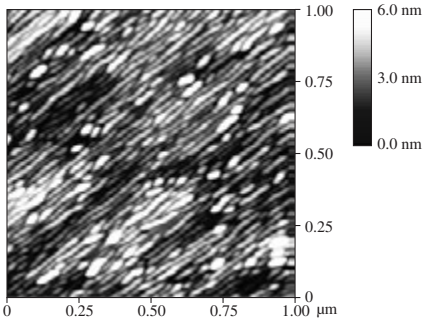

Fig. 1. $1\times1-\mu m^2$ atomic force microscope image of InAs QDashes on InP substrate.

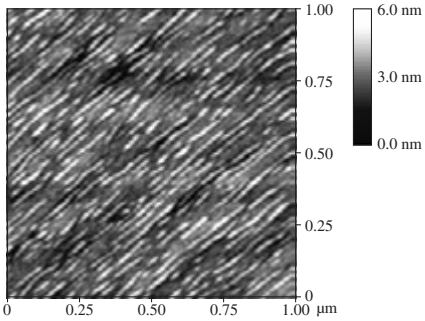

Fig. 2. $1\times1-\mu m^2$ atomic force microscope image of $Al_{0.48}In_{0.52}As$ QDashes on InP substrate.

1. Experiment

The fabrication of self-assembled $Al_{0.48}In_{0.52}As$ QDashes is similar to the growth of unstrained self-assembled GaAs quantum dots (QDs) [4]. First, a template of SK – InAs islands was formed using a modified solid-source molecular beam epitaxy (MBE) system equipped with an $AsBr_3$ etching unit. In contrast to the GaAs QDs [4], the InAs template for for $Al_{0.48}In_{0.52}As$ dashes was grown on an InP (001) instead of GaAs (001) substrate in order to reduce lattice mismatch between InAs and InP. Under low strain conditions the bonding asymmetry of the zincblende material creates anisotropy in the In atom surface migration distance [5], and as result InAs islands form in the shape of the finite length wires (dashes) [1]. Next, the InAs dashes were overgrown with a 10 nm $Al_{0.48}In_{0.52}As$ cap lattice-matched to the InP substrate. Finally, $AsBr_3$ etching gas was applied to produce AlInAs dashes on the cap surface. The $Al_{0.48}In_{0.52}As$ quantum dash morphology is determined by the InAs islands, as shown in atomic force microscope (AFM) images (Figures 1-2).

We employed the same technique to form nanostructures on GaAs (001) substrate, applying locally strain-enhanced $AsBr_3$ etching of the GaAs cap layer with InAs QDs as a template [4]. The etching rate of GaAs was more than four times larger than that of $Al_{0.48}In_{0.52}As$. Reflection high-energy electron diffraction intensity oscillations were applied to calibrate the etching rates. AFM images of InAs QDs and GaAs nanostructures formed as result of the strain enhanced etching are shown in Figures 3 and 4, respectively.

There is a fundamental difference in nanostructure morphology produced by etching the GaAs layer with InAs dots underneath, compared to etching $Al_{0.48}In_{0.52}As$ with InAs dashes below, as shown in Fig. 4 and Fig. 2, respectively. The strain-enhanced etching of the GaAs cap with InAs dots underneath results in formation of etch pits, as reported before [4]. However, the etching of the $Al_{0.48}In_{0.52}As$ cap with InAs dashes underneath creates "inverted etch pits" i.e. dash shaped ridges. This distinction in local etching of GaAs and $Al_{0.48}In_{0.52}As$ cap layers is the outcome of differences in etching rates of the GaAs region above InAs QDs on a GaAs substrate and the $Al_{0.48}In_{0.52}As$ region above InAs QDashes on an InP substrate. The etching rate difference suggests dissimilarity in strain between dots on GaAs and dashes on InP. It is well known that InAs QDs grown on GaAs substrates are compressively strained because of lattice mismatch between InAs and GaAs [6]. However, it was recently been reported [5] that the core of the InAs dashes grown on InP substrate has tensile strain. It is possible that the tensile strain in InAs QDashes is responsible for the formation of ridges on the $Al_{0.48}In_{0.52}As$

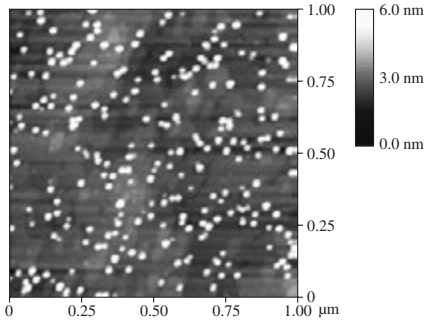

Fig. 3. $1\times1-\mu m^2$ atomic force microscope image of InAs QDs on GaAs substrate.

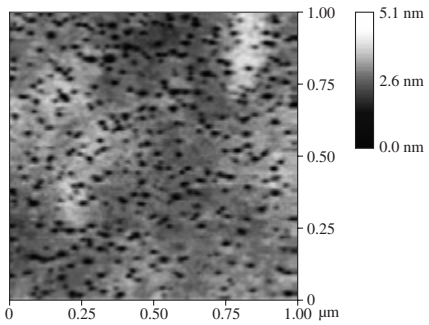

Fig. 4. $1\times1-\mu m^2$ atomic force microscope image of GaAs etch pits on GaAs substrate.

surface instead of etch pits.

In summary, we have created a new type of nanostructure — $Al_{0.48}In_{0.52}As$ quantum dashes — using a modified MBE system with an in situ $AsBr_3$ etching unit. Also, it was shown here that local strain can reduce as well as enhance the etching rate of the III–V semiconductor materials.

References

[1] A. A. Ukhanov *et al*, *Appl. Phys. Lett.* **81**, 981(2002).
[2] A. Bilenca *et al*, *Photon. Tech. Lett.* **15**, 563 (2003).
[3] M. Gendry *et al*, *J. App. Phys.* **95**, 4761 (2004).
[4] A. Rastelli *et al*, *Phys. Rev. Lett.* **92**, 166104 (2004).
[5] G. Balakrishnan *et al*, *Appl. Phys. Lett.* **84**, 2058 (2004).
[6] O. Stier *et al*, *Phys. Rev. B* **59**, 5688 (1999).

13th Int. Symp. "Nanostructures: Physics and Technology"
St Petersburg, Russia, June 20–25, 2005

Polariton quantization in wide GaAs quantum wells

D. K. Loginov[1], E. V. Ubyivovk[1], I. V. Ignatiev[1], Yu. P. Efimov[1], V. V. Petrov[1], S. A. Eliseev[2], Yu. K. Dolgikh[2], V. V. Ovsiankin[2], V. P. Kochereshko[3] and A. V. Selkin[3]

[1] Institute of Physics, St Petersburg State University, St Petersburg, Russia
[2] Vavilov State Optical Institute, St Petersburg, Russia
[3] Ioffe Physico-Technical Institute, St Petersburg, Russia

Abstract. Reflectivity spectra have been analyzed for wide GaAs quantum wells. The width of these wells is much larger than the exciton Bohr radius. Spectral features attributed to light exciton quantization and to mutual interference of heavy and light excitons have been observed for the first time. The spectra were analyzed in the model taking into account the quantization of multi-component polaritons.

Introduction

Excitonic polaritons in bulk crystals were a subject of intensive studies twenty-thirty years ago. Due to the development of nanostructure technologies, the interest of researchers has switched to quantum well (QW) exciton states. Recently, with the advent of the idea of quantum information processing, the activity in polariton studies reappeared. Polariton states were studied in thin semiconductor layers [1,2,3,4], wide QWs based on A2B6 compounds [5,6,7,8,9] and microcavities [10]. There are also publications devoted to polariton size quantization in wide QWs based on GaAs [11,12,13,14,15]. Despite the complicated valence-band-structure of the typical semiconductors used in these studies, there are almost no publications which elucidate the role of a light-hole exciton polariton in optical spectra [9]. In the present work, we studied polariton quantization in wide GaAs QWs with the QW-width much larger than the exciton Bohr radius.

1. Experimental

High quality GaAs/$Al_{0.3}Ga_{0.7}As$ structures were grown by the molecular beam epitaxy on semi-insulating GaAs [100] substrates. The structures contain few GaAs buffer layers separated by the short-period (technological) superlattices (SL) to suppress dislocations. The QWs under study were grown between the thick (several hundred nm) $Al_{0.3}Ga_{0.7}As$ or SL barriers. Width of the QWs was varied from 50 to 1000 nm. Reflectivity spectra were detected at normal incidence with a 0.5 m monochromator and a photodiode. Excellent quality of the structures allowed us to study a fine structure of the spectra of quantized polaritons in the GaAs QWs. In the reflectivity spectra of the studied samples, strongly pronounced oscillations were observed [16]. These oscillations running up into high-energy range of the spectrum have been observed higher than the energy of the exciton ground state (1515 meV) and spread up to the energy of 1540 meV even in the widest QWs. These oscillations are related to the size quantization of the exciton as a whole in the wide QW.

2. Calculation

Fig. 1 shows experimentally measured and calculated reflectivity spectra taken from the sample with the 250 nm thick QW. The oscillating structure is observed above the exciton resonance energy, $\hbar\omega_0$. Numbers on the axes HhPB and LhPB above the curves indicate the quantized level numbers for the

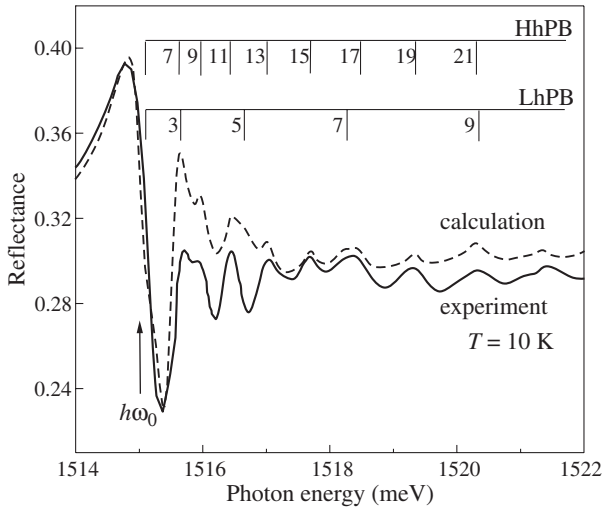

Fig. 1. Experimentally measured at 10 K and calculated reflectivity spectra for GaAs/$Al_{0.3}Ga_{0.7}As$ QW with thickness 250 nm. Numbers on the axes above the curves are the HhPB and LhPB numbers of the interference features for low polariton branches for heavy (HhPB) and light (LhPB) polaritons, correspondingly.

excitons with heavy and light holes, correspondingly. Peculiarities related to the quantization of the light exciton have been observed in the spectra of all the samples as the additional interference features and a non-monotonic change in the amplitude of the interference. The features of the light exciton were only revealed after comparison of the experimental and calculated reflectivity spectra and were not identified in such spectra earlier.

The calculation were performed in framework of the polariton size quantization model described, e.g., in Refs. [4,6,12,17]. Additional boundary conditions for the light-hole exciton have been chosen in accordance with Ref. [18]. The transfer matrix method was exploited to take into account most of the layers of the heterostructures under study. Some simplifications of the real heterostructures were made in the calculations, in particular by modelling of technological SLs with effective layers $Al_xGa_{1-x}As$. The light and heavy exciton translation masses, M_L and M_H, value of the longitudinal-transverse splitting, ω_{LT}, energy of the exciton resonance, $\hbar\omega_0$, damping of the heavy exciton, Γ_H, dielectric constants for GaAs and $Al_{0.3}Ga_{0.7}As$ layers, ε_{GaAs} and ε_{AlGaAs}, were taken in accordance to Refs. [10,12,17,19]: $M_L = 0.08m_0$, $M_H = 0.49m_0$, $\hbar\omega_{LT}^{hh} = 0.1$ meV, $\hbar\omega_{LT}^{lh} = 0.03$ meV, $\Gamma_H = 0.1$ meV, $\varepsilon_{GaAs} =$

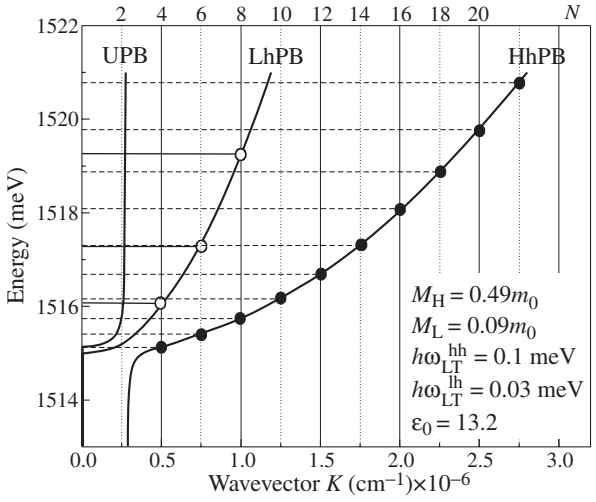

Fig. 2. Polariton dispersion curves reconstructed from the interference features of the reflectivity spectrum shown in Fig. 1 using condition $Kd = N\pi$, where K is the exciton wavevector, d is the QW width, N is the number of the interference feature. UPB — upper polariton branch, LhPB and HhPB — low polariton branches for light and heavy exciton, correspondingly.

12.53, $\varepsilon_{AlGaAs} = 11.7$. Damping constant for the light exciton, $\Gamma_L = 0.2$ meV, have been determined by fitting the experimentally measured reflectance spectra. Another fitting parameters are the thicknesses of the QW under study and of its barriers which are varied within 20%. This fitting procedure allowed us to take into account some uncertainty in the layer thicknesses due to their gradient along the sample surface.

A good agreement in the spectral positions and relative intensities of the oscillations has been obtained for the calculated and experimental spectra. Some discrepancies between experiment and theory is probably due to the simplifications used in the calculations.

Figure 2 shows dispersion curves for the polaritons in GaAs. These curves were reconstructed from the interference peculiarities of the experimentally measured reflectivity spectra as it was described in Ref. [1]. We found that only the even quantized levels are revealed in the experimental spectra because of the better overlap of the corresponding exciton and photon eigenmodes in our samples.

3. Conclusion

Contribution of the light excitons to the reflectivity spectra has been found experimentally as the appearance of additional interference features and non-monotonic changes of the amplitude of the interference in vicinity of the main exciton peak. In higher energy range, the peculiarities are attributed to the light excitons are not observed due to its higher damping and smaller oscillator strength.

Acknowledgements

The work was supported in part by the ISTC grant No. 2679, grants of the Presidium of RAS, the Department of Physical Sciences of RAS, and the Ministry of Science of the Russian Federation.

References

[1] V. A. Kiselev, B. S. Razbirin, I. N. Uraltsev, *JETP Lett.*, **18**, 296 (1973).
[2] V. A. Kiselev, B. S. Razbirin, I. N. Uraltsev, *Phys. stat. sol. (b)*, **72**, 161 (1975).
[3] V. A. Kiselev, B. S. Razbirin, I. N. Uraltsev, V. P. Kochereshko, *Fiz. tv. tela*, **17**, 640 (1977) [*Soviet Phys. Solid State* **17**, (1975)].
[4] V. A. Kiselev, I. V. Makarenko, B. S. Razbirin, I. N. Uraltsev, *Fiz. tv. tela*, **19**, 1348 (1977) [*Soviet Phys. Solid State*, **19**, 1374 (1977)].
[5] H. Tuffigo, R. T. Cox, N. Magnea, Y. Merle D'Aubigné, A. Million, *Phys. Rev. B*, **37**, 4310 (1988).
[6] A. D'Andrea and R. Del Sole, *Phys. Rev. B*, **41**, 1413 (1990).
[7] N. Tommasini, A. D'Andrea, R. Del Sole, H. Tuffigo-Ulmer, R. T. Kox, *Phys. Rev. B*, **51**, 5005 (1995).
[8] D. Greco, R. Cingolani, A. D'Andrea, N. Tommasini, L. Vanzetti, A. Franciosi, *Phys. Rev. B*, **54**, 16998 (1996).
[9] P. Lefebvre, V. Calvo, N. Magnea, T. Taliercio, J. Allégre and H. Mathieu, *Phys. Rev. B*, **56**, R10040 (1997).
[10] Y. Chen, A. Tredicucci, F. Bassani, *Phys. Rev. B*, **52**, 1800 (1995).
[11] L. Schultheis and K. Ploog, *Phys. Rev. B*, **29**, 7058 (1984).
[12] A. Tredicucci, Y. Chen, F. Bassani, J. Massies, C. Deparis and G. Neu, *Phys. Rev. B*, **47**, 10348 (1993).
[13] G. Göger, M. Betz, A. Leitenstorfer, M. Bichler, W. Wegscheider and G. Abstreiter, *Phys. Rev. Lett.*, **84**, 5812 (2000).
[14] M. Betz, G. Göger, A. Leitenstorfer, M. Bichler, G. Abstreiter and W. Wegscheider, *Phys. Rev. B*, **65**, 085314 (2002).
[15] E. A. Muljarov and R. Zimmermann, *Phys. Rev. B*, **66**, 235319 (2002).
[16] E. Ubyivovk, Yu. K. Dolgikh, Yu. P. Efimov, S. A. Eliseev, I. Ya. Gerlovin, I. V. Ignatiev, V. V. Petrov, V. V. Ovsyankin, *J. Lumin.*, **102–103**, 751 (2003).
[17] G. Fishman, *Solid State Commun.*, **27**, 1097 (1978).
[18] P. Kuznetsov, J. Madrigal-Melchor, F. Pérez-Rodríguez, S. O. Romanovsky, A. V. Sel'kin and G. G. Yakushcheva, *Phys. stat. sol (c)*, **0**, 2926 (2003).
[19] P. Lautenschlager, M. Garriga, S. Logothetidis, M. Cardona, *Phys. Rev. B*, **35**, 9174 (1987).

13th Int. Symp. "Nanostructures: Physics and Technology"
St Petersburg, Russia, June 20–25, 2005

Increasing of the exciton Zeeman splitting due to its movement

V. P. Kochereshko[1], A. V. Platonov[1], R. T. Cox[2], J. J. Davies[3], D. Wolverson [3], E. V. Ubyivovk[4], Yu. P. Efimov[4], Yu. K. Dolgikh[5] and S. A. Eliseev[5]

[1] Ioffe Physico-Technical Institute, St Petersburg, Russia
[2] Laboratoire de Spectrométrie Physique, Universit'e Joseph Fourier de Grenoble, France
[3] Department of Physics, University of Bath, Bath BA2 7AY, UK
[4] Institute of Physics, St Petersburg State University, St Petersburg, Russia
[5] Vavilov State Optical Institute, St Petersburg, Russia

Abstract. Magneto-reflection spectra of GaAs — based heterostructures with a wide quantum well ($L = 50$–1000 nm) have been studied in conditions of size quantization of excitonic polaritons. It was found that the magnitude of the exciton Zeeman splitting grows with the increase of the number of the quantization level. Because the number of the quantization level N is in a relation to the magnitude of the exciton wave vector K, the observed effect could mean *the growth of the exciton magnetic moment with the increase of its kinetic energy*.

Introduction

The interest in studying effects of exciton polariton states in quantum-confined structures is significantly intensified recently due to the prospects of a development of principals of the optical information processing. Polariton quantization, originally observed in thin crystal layers, nowadays is studied in specially grown quantum well (QW) structures, microcavities and photonic crystals [1–6] based on different semiconductor compounds. As it was shown in [1–3] the effect of the exciton size quantization can be very effectively used to reconstruct balk polariton dispersion corves (t.i.dependencies energy versus wavevector). This effect was used to measure exciton effective masses, oscillator strength, refractive indexes and features of band structure in different semiconductors. On the other hand the exciton states in bulk GaAs in applied magnetic fields had been studied so detailed, that it is difficult to expect the acquisition of new physical effects in such materials at normal conditions.

In the present work we studied quantization spectra of excitonic polaritons in GaAs wide quantum well structures in magnetic fields. Contrary to the expectations it was revealed that the value of the exciton g-factor dramatically depends on its kinetic energy.

1. Experiment

We used GaAs/AlGaAs heterostructures containing a wide quantum well with the QW width much larger than the exciton Bohr radius. The structures were grown by molecular-beam epitaxy on semi-insulating GaAs [100] substrates. A typical structure contained a 100 nm GaAs buffer layer, a 400 nm $Al_{0.3}Ga_{0.7}As$ barrier layer, a wide GaAs quantum well with width varied from 50 to 1000 nm, a second barrier layer symmetrical to the first one, and a 10 nm GaAs cap layer. Reflectivity spectra of these structures at normal incidence have been studied in magnetic fields in Faraday geometry.

Figure 1 shows reflectivity spectra taken from the GaAs QW with QW width of 330 nm in magnetic field of 5 T in Faraday geometry in two circular polarizations σ^+ and σ^-. The interference structure located energetically higher than the exciton resonance frequency $\hbar\omega_{ex}$ is distinctly observed in the spectra. The appearance of this structure is due to the size quantization of the exciton as a whole in the wide QW, with QW width ($L = 330$ nm) much larger than the exciton Bohr radius ($a_B = 12$ nm). The numbers N indicates the numbers of the exciton quantization levels. In our samples we observed up to 30 quantized levels. We observed the even interference features only because of the better overlap of the even exciton and photon eigenmodes. The amplitude of the interference picture decreases with the energy increases due to exciton damping when they are scattered on phonons and defects.

2. Discussion

Fig. 2 shows dependencies of the Zeeman splitting on the number N of the exciton quantization level. It is clearly seen that the value of the Zeeman splitting increases with increasing of the number N. This means that the exciton magnetic moment or the exciton g-factor increases with increasing N. Taking into account that the number of the exciton quantization level N is connected with its wavevector as $K L = \pi N$, where K — exciton wavevector, L — QW width, N — number of the quantized level, we conclude that the exciton magnetic moment growth with the increase of its kinetic energy in one order of magnitude in the range of the observation of the interference structure.

We have deduced an empirical universal formula for the

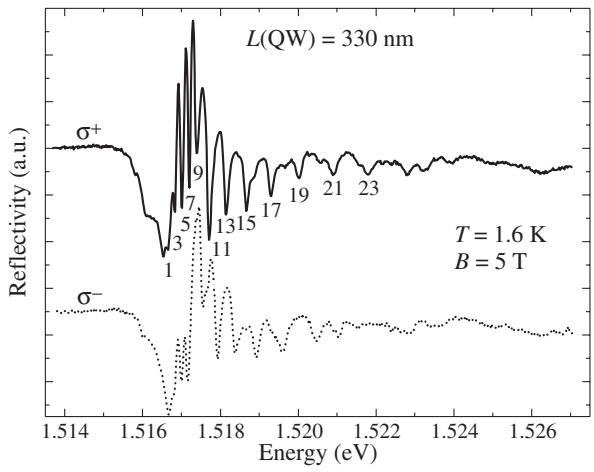

Fig. 1. Reflectivity spectra taken from single quantum well of 330 nm width in magnetic field of 5 T in right σ^+ and left σ^- circular polarizations at 1.6 K. Numbers indicates the numbers of the levels of the exciton quantization in the QW.

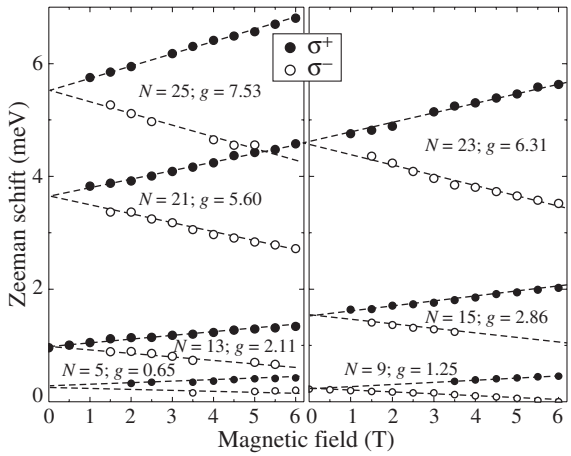

Fig. 2. Zeeman splitting for the exciton quantized levels N in the QW as a function of magnetic fields; g- effective exciton g-factors. The figure splits into two for convenience.

K vector dependence of the exciton g-factor:

$$g_{eff} = g_0 + c\frac{(Ka_B)^2}{1+(Ka_B)^2}\,,$$

here g_0 is unperturbed exciton g-factor at $K = 0$, K is the exciton wavevector, a_B is the exciton Bohr radius, c — some constant, in GaAs $c = 10$. This formula describes the observed effect for all studied QW structures based on GaAs and A_2B_6 compounds. We connect this behavior of the exciton g-factor with the effect of cubic in K terms in zinc-blend type semiconductors.

Acknowledgements

The work was partially supported by the RFBR, the Russian Ministry of Science and by NATO Science program. With the greatest sadness we bemoan the loss of our colleague Boris Egorov, who unexpectedly passed away 21 March 2005. He will be greatly missed and we keep his memory alive.

References

[1] V. A. Kiselev, B. S. Razbirin, I. N. Uraltsev, *JETP Lett.*, **18**, 296 (1973).
[2] V. A. Kiselev, B. S. Razbirin, I. N. Uraltsev, *Phys. Status Solidi*, **B72**, 161 (1975).
[3] H. Tuffigo, R. T. Cox, N. Magnea, Y. Merle d'Aubigne A. Million, *Phys. Rev.*, **B37**, 4310 (1988).
[4] L. Schultheis and K. Ploog, *Phys. Rev.*, **B29**, 7058 (1984).
[5] Y. Chen, A. Tredicucci, F. Basani, *Phys. Rev.*, **B52**, 1800 (1995).
[6] P. Lefebvre, V. Calvo, N. Magnea *et al*, *Phys. Rev.*, **B56**, R10040 (1997).

13th Int. Symp. "Nanostructures: Physics and Technology"
St Petersburg, Russia, June 20–25, 2005

Fine structure of excited excitonic states in quantum disks

M. M. Glazov[1], E. L. Ivchenko[1], R. v. Baltz[2] and E. G. Tsitsishvili[2]

[1] Ioffe Physico-Technical Institute, St Petersburg, Russia
[2] Universität Karlsruhe, 76128 Karlsruhe, Germany

Abstract. We report on a theoretical study of the fine structure of excited excitonic levels in semiconductor quantum disks. A particular attention is paid to the effect of electron-hole *long-range* exchange interaction. We demonstrate that, even in the axisymmetric quantum disks, the exciton P-shell is split into three sublevels. The analytical results are obtained in the limiting cases of strong and weak confinement. A possibility of exciton spin relaxation due to the resonant LO-phonon-assisted coupling between the P and S shells is discussed.

Introduction

In the envelope-function approximation, the excitonic states in semiconductors and semiconductor quantum dots can be classified by referring to the orbital shape of the exciton envelope function (S-, P-, D-like) and the character of the electron and hole Bloch functions (bright and dark states). For example, the state $|P_x y\rangle$ means a bright P_x-shell exciton with the electron-hole dipole moment directed along the y axis. Theoretically, the fine structure of excited states of zero-dimensional (0D) excitons has been studied for excitons localized, respectively, by rectangular islands in a quantum-well structure [1], quantum disks with a Gaussian lateral potential [2] and lens-shaped quantum dots [3]. However, up to now the splitting of excited-exciton levels has been analyzed for a fixed orbital shell, e.g., the P_x shell, which is valid in the case of strongly anisotropic confinement so that the orbital splitting of the P-like shells P_x and P_y exceeds by far the exchange-interaction energy. Here we show that, for axially symmetric or square quantum dots, one has, in addition, to take into account the exchange-interaction-induced mixing between the excitonic states $|P_x y\rangle$ and $|P_y x\rangle$. Moreover, for the first time we focus on the interplay between the exchange interaction and anisotropic shape of the dot and develop an analytic theory in the particular case where the orbital and exchange splittings are comparable.

1. Electron-hole exchange interaction in quantum disks

The two-particle excitonic wave function can be written as a linear combination of products $\Psi_{sj}(\mathbf{r}_e, \mathbf{r}_h)|s, j\rangle$, where $|s, j\rangle$ is a product of the electron and hole Bloch functions, s and j are the electron and hole spin indices, $\Psi(\mathbf{r}_e, \mathbf{r}_h)$ is the envelope function, and $\mathbf{r}_{e,h}$ is the electron (hole) 3D radius-vector. In the following, for the sake of simplicity, we concentrate on heavy-hole excitons with $j = \pm 3/2$ and the long-range mechanism of electron-hole exchange interaction which allows to discuss only the bright excitonic states $|s, j\rangle$ with $s + j = \pm 1$ or their linear combinations $|\alpha\rangle$ with the dipole moment $\alpha = x, y$. The short-range mechanism may be taken into consideration similarly to [4] if one includes an admixture of light-hole states into the heavy-hole exciton wave function.

We consider a quantum disk formed by a 2D harmonic potential $V(\rho_e, \rho_h) = A_e\rho_e^2 + A_h\rho_h^2$ in a quantum well grown along the z-axis. Here the 2D vector $\rho_{e,h}$ determines the in-plane position of an electron or a hole, and $A_{e,h}$ are positive constants. Assuming that the confinement along the growth direction is stronger than both the quantum-disk and Coulomb potentials the envelope for the electron-hole pair wavefunction can be written as

$$\Psi(\mathbf{r}_e, \mathbf{r}_h) = \psi\left(\boldsymbol{\rho}_e, \boldsymbol{\rho}_h\right)\varphi_e(z_e)\varphi_h(z_h)\,, \qquad (1)$$

where $\varphi_{e,h}(z_{e,h})$ are the respective z-envelopes of electron and hole, and $\psi(\boldsymbol{\rho}_e, \boldsymbol{\rho}_h)$ is an in-plane wavefunction of exciton calculated with allowance for both Coulomb interaction and quantum disk potential. The form of the function $\psi(\boldsymbol{\rho}_e, \boldsymbol{\rho}_h)$ depends on the relationship between the potential radius and 2D-exciton Bohr radius, a_B. In the *weak* confinement regime, i.e. in a quantum disk with the diameter exceeding a_B, the two-particle envelope probe function $\psi(\boldsymbol{\rho}_e, \boldsymbol{\rho}_h)$ is a product $F(\mathbf{R})f(\boldsymbol{\rho})$ of two functions describing, respectively, the in-plane motion of the exciton center of mass $\mathbf{R} = (X, Y)$ and the relative electron-hole motion, $\boldsymbol{\rho} = \boldsymbol{\rho}_e - \boldsymbol{\rho}_h$. On the other hand, in small quantum disks with *strong* confinement where single-particle lateral confinement dominates over the Coulomb interaction, the pair envelope can also be presented as a product of two functions, $\psi_e(\boldsymbol{\rho}_e)\psi_h(\boldsymbol{\rho}_h)$, but here they describe the independent in-plane localization of an electron and a hole.

For the exciton envelope functions presented in the form (1), the matrix element $\mathcal{H}^{(\mathrm{long})}_{n'n}$ of long-range exchange interaction taken between the exciton states n' and n is written as follows

$$\frac{1}{2\pi\varkappa_\infty}\left(\frac{e\hbar|p_0|}{m_0E_g}\right)^2\int d\mathbf{K}\,\frac{K_\alpha K_{\alpha'}}{K}\widetilde{\psi}^*_{n'}(\mathbf{K})\widetilde{\psi}_n(\mathbf{K})\,, \qquad (2)$$

where the exciton-state index n includes the dipole moment α, $\varkappa_\infty$ is the high-frequency dielectric constant, m_0 is the free electron mass, E_g is the band gap, p_0 is the interband matrix element of the momentum operator, and we introduced the 2D Fourier-transform

$$\widetilde{\psi}(\mathbf{K}) = \int d\mathbf{R}\,e^{-i\mathbf{K}\mathbf{R}}\psi(\mathbf{R}, \mathbf{R})$$

of the function $\psi(\boldsymbol{\rho}_e, \boldsymbol{\rho}_h)$ at the coinciding coordinates, $\boldsymbol{\rho}_e = \boldsymbol{\rho}_h \equiv \mathbf{R}$.

2. *P*-Orbital excitons in axially-symmetric disks

We start with an axially-symmetric quantum disk and calculate the fine structure of the P-orbital exciton level and then proceed to a slightly anisotropic disk. The straightforward calculation shows that the long-range exchange Hamiltonian (2) has the following non-zero matrix elements

$$\langle P_x x|\mathcal{H}^{(\mathrm{long})}|P_x x\rangle = \langle P_y y|\mathcal{H}^{(\mathrm{long})}|P_y y\rangle = \lambda\,, \qquad (3)$$

$$\langle P_x y|\mathcal{H}^{(\mathrm{long})}|P_x y\rangle = \langle P_y x|\mathcal{H}^{(\mathrm{long})}|P_y x\rangle = \eta\,,$$

$$\langle P_y x|\mathcal{H}^{(\mathrm{long})}|P_x y\rangle = \langle P_x y|\mathcal{H}^{(\mathrm{long})}|P_y x\rangle = \mu\,,$$

where $\lambda = 3\eta = 3\mu$. According to Eq. (3) and in agreement with the angular-momentum considerations, the P-shell of the bright exciton in an axisymmetric quantum disk is split into three sublevels, see Fig. 1. The outermost sublevels labelled 0^U, 0^L are nondegenerate and characterized by a zero total angular-momentum z-component. The central doubly-degenerate sublevel corresponds to the angular-momentum component ± 2. The intersublevel energy spacing, Δ, equals to $2\eta = 2\mu$.

The splitting Δ depends on the character of exciton confinement in a disk. Let us assume $A_{e,h} = \hbar^2/2m_{e,h}a^4$, where a is the disk effective radius, $m_{e,h}$ are the electron and hole effective masses. It follows then that in the strong confinement regime, $a \ll a_\mathrm{B}$, one has

$$\Delta = \frac{3\sqrt{2\pi}}{16a^3\varkappa_b}\left(\frac{e\hbar|p_0|}{m_0 E_g}\right)^2. \qquad (4)$$

In the opposite limiting case $a \gg a_\mathrm{B}$ where the exciton is quantized as a whole we obtain

$$\Delta = \frac{3\sqrt{\pi}}{2a_\mathrm{exc}a_\mathrm{B}^2\varkappa_b}\left(\frac{e\hbar|p_0|}{m_0 E_g}\right)^2 \qquad (5)$$

with $a_\mathrm{exc} = a(\mu/M)^{1/4}$ being the radius of exciton in-plane confinement, $M = m_e + m_h$ and $\mu = m_e m_h/M$.

3. *P*-Shell excitons in anisotropic quantum disks

We introduce a slightly elliptical lateral potential replacing the disk radius a by the effective radii $a_x = a-d, a_y = a+d$ along the x and y axes, respectively, and assuming $d \ll a$. At zero d the exciton P-states are partially split by the exchange interaction. The anisotropy of a quantum disk results in a full removal of the degeneracy and formation of four sublevels. It is convenient to introduce, as a parameter describing the anisotropy, a half of the $P_x - P_y$ splitting, E_anis, calculated neglecting the exchange interaction. Its value depends on the model of exciton quantization. If an electron and a hole are quantized independently ($a \ll a_\mathrm{B}$) then, for the $|P_e, S_h\rangle$ excited state, we have

$$E_\mathrm{anis} = \frac{d}{a}\frac{2\hbar}{m_e a^2} \qquad (6)$$

and, for the $|S_e, P_h\rangle$ state, E_anis differs from Eq. (6) by the replacement $m_e \to m_h$. Here $|S_e, P_h\rangle$ means an exciton formed by a S_e-shell electron and a P_h-shell hole. If exciton is quantized as a whole then in Eq. (6) one should replace m_e by the exciton translational mass $M = m_e + m_h$ and a by $a_\mathrm{exc} = a(\mu/M)^{1/4}$.

Figure 1 shows splitting of the P-shell bright-exciton level as a function the ratio $\xi = E_\mathrm{anis}/\Delta$. For small values of ξ the splitting of the doublet ± 2 is proportional to ξ^2. In the limit of strong anisotropy, $E_\mathrm{anis} \gg \Delta$, the P-shell exciton states form two doublets, $|P_x, \alpha\rangle$ and $|P_y, \alpha\rangle$ ($\alpha = x, y$), separated by $2E_\mathrm{anis}$ and each split by Δ.

4. Resonant *P-S* excitonic polarons

Finally, we briefly discuss the P-S excitonic polaron which is formed as a result of the resonant coupling of the P- and S-like levels by a longitudinal optical (LO) phonon [5]. We use an approach developed in Ref. [6] to calculate the LO-assisted resonant coupling between S- and P-shell electron states confined in a quantum dot. For the Frölich interaction, the constant of exciton-phonon P-S coupling is given by

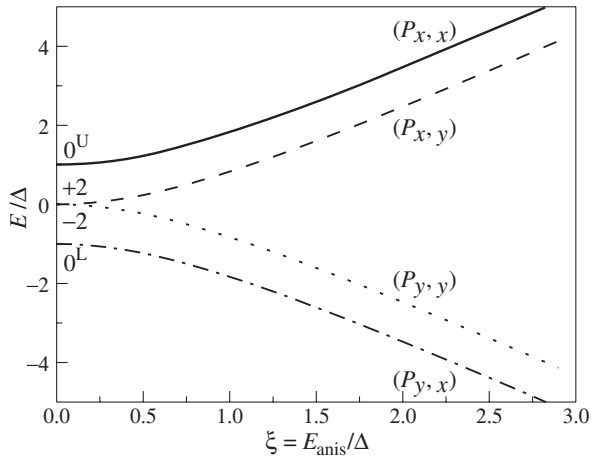

Fig. 1. Interplay between the in-plane anisotropy and exchange interaction. The exciton sublevel energy E is referred to the energy of the uniaxial exciton ± 2.

$$\gamma = \sqrt{\frac{2\pi e^2\hbar\Omega}{V\varkappa^*}\sum_{\mathbf{q}}\left|\frac{\mathcal{I}(\mathbf{q})}{q}\right|^2}. \qquad (7)$$

Here Ω is the LO-phonon frequency, V is the 3D normalization volume, $\varkappa^{*-1} = \varkappa_\infty^{-1} - \varkappa_0^{-1}$, and

$$\mathcal{I}(\mathbf{q}) = \int d\mathbf{r}_e d\mathbf{r}_h \Psi_p(\mathbf{r}_e, \mathbf{r}_h)\,\Psi_s(\mathbf{r}_e, \mathbf{r}_h)\left(\mathrm{e}^{\mathrm{i}\mathbf{q}\mathbf{r}_e} - \mathrm{e}^{\mathrm{i}\mathbf{q}\mathbf{r}_h}\right).$$

Depolarization of the linearly-polarized P-S excitonic polaron excited via the P-shell is determined by the ratio of γ and the exchange splitting Δ. If $\Delta \gg |\gamma|$ the initial linear polarization is being rapidly lost and the exciton photoluminescence is practically depolarized. On the contrary, if $\Delta \ll |\gamma|$ then the polarization relaxes on a much longer time scale and can be well preserved.

Acknowledgements

The work is supported by RFBR, "Dynasty" foundation — ICFPM, the Center for Functional Nanostructures of the Deutsche Forschungsgemeinschaft within project A2 and by the programs of Russian Academy of Sci.

References

[1] S. V. Goupalov, E. L. Ivchenko and A. V. Kavokin, *JETP*, **86**, 388 (1998).
[2] T. Takagahara, *Phys. Rev. B*, **62**, 16 840 (2000).
[3] G. Bester, S. Nair and A. Zunger, *Phys. Rev.*, **67**, 161306(R) (2003).
[4] E. L. Ivchenko, A. Yu. Kaminskii and I. L. Aleiner, *JETP*, **77**, 609 (1993).
[5] O. Verzelen, R. Ferreira and G. Bastard, *Phys. Rev. Lett.*, **88**, 146803 (2002).
[6] T. Stauber, R. Zimmerman and H. Castella, *Phys. Rev. B*, **62**, 7336 (2000).

13th Int. Symp. "Nanostructures: Physics and Technology"
St Petersburg, Russia, June 20–25, 2005

Excitonic Hanle effect in nanostructures with strong exchange interaction

I. S. Gagis, K. V. Kavokin and A. V. Koudinov
Ioffe Physico-Technical Institute, St Petersburg, Russia

Inter-particle exchange interaction plays an important role in the formation of the radiative states in semiconductor nanostructures. The most powerful experimental techniques for the investigation of the exchange interaction are the steady-state polarization magneto-optical spectroscopy and the time-resolved spectroscopy of the quantum beats. In this paper we present the solution of the problem of magnetic depolarization of photoluminescence (the Hanle effect) in a planar nanostructure where the electron and the hole forming the excitonic state are bound to each other by a strong exchange interaction. The model under study allows the analytic solution, which may be useful for understanding the experiments on the Hanle effect in quantum wells and quantum dots.

Let the excitons in a planar nanostructure are excited by the circularly polarized light (the exciting light travels normally to the plane of the nanostructure), the magnetic field B is applied parallel to the plane, and we are interested in the degree of circular polarization of photoluminescence collected in the backward geometry (normally to the plane). The optical transitions occur between the conduction band states Γ_6 and the heavy hole subband states Γ_8. Apart from the magnetic field B, the electron spin experiences the action of the exchange field of the hole $B_{\rm ex}$, which is directed normally to the plane. For simplicity, we neglect the spin relaxation of electrons. The spin relaxation of holes is assumed to be a Poisson process, i.e., it proceeds at a time-independent rate characterized by the inverse spin relaxation time $\tau_{\rm sh}^{-1}$. The parameters of our theory are $\tau_{\rm sh}$, the radiative lifetime of the bright exciton $\tau_{\rm r}$ and the non-radiative lifetime $\tau_{\rm nr}$. The exchange interaction is assumed strong, in the sense that the period of the Larmor precession of the spin of electron in the exchange field of the hole $\Omega = B_{\rm ex}/\hbar$ is small as compared to the lifetime of the exciton and to the spin relaxation time of the hole.

With the above assumptions, the problem can be solved analytically in the general case by means of the density matrix method. It can be reduced to the solution of the system of equations for some four quantities, of which one pair may be identified with the concentrations of holes with spin orientation as created (N_+) and opposite to that (N_-) while other pair with the respective net values of the projection of the spin of electrons on to the direction of the total field acting on the electrons (S_+, S_-). Namely,

$$\begin{cases} \frac{dS_+}{dt} = \frac{G}{2}\sin\phi - \frac{S_+}{2\tau_{\rm sh}} + \frac{S_-}{2\tau_{\rm sh}}\cos 2\phi - \frac{S_+}{\tau_{\rm nr}} - \\ -\frac{1}{2\tau_{\rm r}}\left(\frac{N_+}{2}\sin\phi + S_+\right) \\ \frac{dN_+}{dt} = G - \frac{N_+ - N_-}{2\tau_{\rm sh}} - \frac{N_+}{\tau_{\rm nr}} - \frac{1}{\tau_{\rm r}}\left(\frac{N_+}{2} + S_+\sin\phi\right) \\ \frac{dS_-}{dt} = -\frac{S_-}{2\tau_{\rm sh}} + \frac{S_+}{2\tau_{\rm sh}}\cos 2\phi - \frac{S_-}{\tau_{\rm nr}} - \\ -\frac{1}{2\tau_{\rm r}}\left(\frac{N_-}{2}\sin\phi + S_-\right) \\ \frac{dN_-}{dt} = -\frac{N_- - N_+}{2\tau_{\rm sh}} - \frac{N_-}{\tau_{\rm nr}} - \frac{1}{\tau_{\rm r}}\left(\frac{N_-}{2} + S_-\sin\phi\right) \end{cases} \quad (1)$$

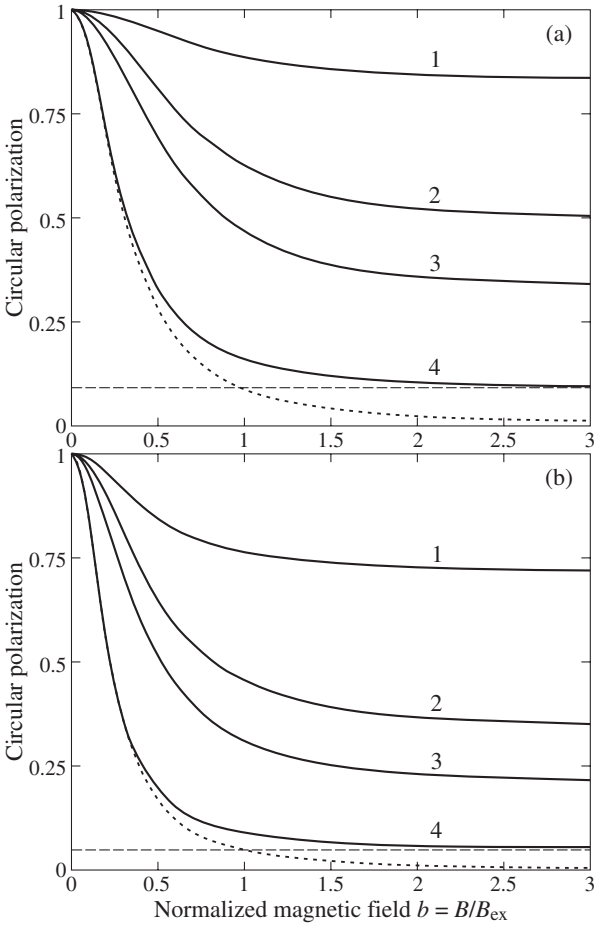

Fig. 1. Calculated luminescence polarization degree vs. dimensionless magnetic field for the cases of dominating non-radiative (a) and radiative (b) recombination. The dependences are plotted for the following values of the ratio $\tau_{\rm sh}/\tau_{\rm nr}$ (in panel a) and of the ratio $\tau_{\rm sh}/\tau_{\rm r}$ (in panel b): 5 — curve *1*, 1 — curve *2*, 0.5 — curve *3*, 0.1 — curve *4*. Dotted lines show the Lorentz curves Eq. (3) and Eq. (4), respectively, calculated with the same parameters as the solid curves *4* in both panels. Dashed lines show the field-independent part of polarization: $\tau_{\rm sh}/(\tau_{\rm nr}+\tau_{\rm sh})$ in panel *a* and $\tau_{\rm sh}/(2\tau_{\rm r}+\tau_{\rm sh})$ in panel *b*.

where in steady state the left-hand sides turn to zero (G stands for the generation rate, $\tan\phi = B_{\rm ex}/B$). Having solved the resultant system of algebraic equations, one can then calculate the luminescence polarization as a function of the dimensionless magnetic field $b = B/B_{\rm ex}$ in accord with

$$\rho = \frac{(N_+ - N_-) + 2(S_+ - S_-)\sin\phi}{(N_+ + N_-) + 2(S_+ + S_-)\sin\phi} \quad (2)$$

An awkward formula results which is improper to be written out here; so let us consider separately the cases of dominating

non-radiative and radiative recombination. For the case $\tau_{nr} \ll \tau_r$, the solution which fully reproduces the above result can be obtained by a direct calculation of the correlated dynamics of electron and hole spins. It takes the especially simple form in the limit of the short spin relaxation times $\tau_{sh} \ll \tau_{nr}$:

$$\rho(b) = \frac{1}{1 + \frac{\tau_{nr}}{\tau_{sh}} b^2} \tag{3}$$

that is, the principle part of the dependence of polarization on the magnetic field is a Lorentz contour with a HWHM $B_{nr} = B_{ex}(\tau_{sh}/\tau_{nr})^{1/2}$, see panel *a* in the Figure.

Also for the case $\tau_{nr} \gg \tau_r$ and $\tau_{sh} \ll \tau_r$ the alternative calculation of the spin dynamics of electron and hole helps reveal the essential part of the dependence. Again, it is a Lorentz contour

$$\rho(b) = \frac{1}{1 + 2\frac{\tau_r}{\tau_{sh}} b^2} \tag{4}$$

but that time with a HWHM $B_r = B_{ex}(\tau_{sh}/2\tau_r)^{1/2}$, see panel *b* in the Figure.

To conclude, in both cases the field-dependent part of the polarization behaves as in the conventional Hanle effect on electrons. However, trying to interpret the experiments on the Hanle effect in nanostructures in the routine manner, one can run into mistakes and deduce a false electron spin relaxation time. One can see that in Eqs. (3) and (4) the width of the Hanle curve does not depend at all on the spin relaxation time of electron, but is determined by the strength of exchange field, the hole spin relaxation time and the exciton lifetime.

To finish with, we note that the system Eqs. (1) can be applied for calculation the signals of intensity and polarization in the time-resolved regime for nanostructures with strong electron-hole exchange interaction.

Acknowledgements

The work was supported by RFBR (04-02-17625 and 04-02-17636). A. K. thanks the Russian Science Support Foundation and acknowledges the useful discussion with Yu. K. Golikov.

13th Int. Symp. "Nanostructures: Physics and Technology"
St Petersburg, Russia, June 20–25, 2005

Influence of hydrostatic pressure on exciton photoluminescence spectrum of quantum dot molecules InAs/GaAs

V. A. Gaisin[1], B. V. Novikov[1], V. G. Talalaev[1,2], A. S. Sokolov[1], I. V. Shtrom[1], V. A. Chugunov[1], G. E. Cirlin[3,4], Yu. B. Samsonenko[3,4] and A. A. Tonkikh[3,4]

[1] Fock Institute of Physics, St Petersburg State University, 198904 St Petersburg, Russia
[2] Max-Planck-Institut für Mikrostrukturphysik, 06120, Haale (Saale), Germany
[3] Ioffe Physico-Technical Institute, St Petersburg, Russia
[4] Institute for Analitical Instrumentation, RAS, 198103, St Petersburg, Russia

Abstract. The influence of hydrostatic pressure in the range 0–12 kbar on exciton photoluminescence spectrum of InAs quantum dot molecules was studied. The molecular terms related luminescence with the increase of excitation density was obtained. For all components baric coefficients were found. Anomalies in baric dependences for p_+- and d_+-excited molecule states are discussed.

In the recent years the research attention has been attracted by multi-layer structures, in which the effect of planar and vertical ordering of quantum dots (QDs) is observed. It is known that the important factor of the formation of electron and hole QD states are the strain fields appeared within QDs and in the neighboring material of the matrix (barrier). Earlier it was found [1] that existence of the strain results in dependence of the baric coefficient (BC) on the ground states transition energy, i.e. on the size of QD. In this paper results of baric investigations performed for the heterstructures InAs/GaAs with two layers of InAs QDs are reported. The special attention is devoted to the quantum dot molecules (QDMs) having appointed structure of excited states in photoluminescence (PL) spectrum. This interest appears due to strain fields redistribution in QD and QDM arrays under hydrostatic pressure which hence causes the change of energy structure and the peculiarities in BC spectral dependence.

Studied samples were grown by the molecular beam epitaxy on the GaAs substrates. Measurements were performed for two types of the samples, which contain two QD layers with GaAs spacer thickness of 10 nm (S-type) and with 5 nm GaAs spacer (M-type). PL excitation power density was varied from 0.2 to 100 W/cm2. The measurements were carried out at $T = 77$ K in spectral interval 1.0–1.4 eV, under the hydrostatic pressure with the range 0–12 kbar. The value of hydrostatic pressure was established from shift of R1 ruby PL line; ruby was set in high pressure camera in immediate closeness to the studied sample.

For S-type sample without pressure in the PL spectrum are observed two overlapped components QD_1 and QD_2 with maxima 1.133 and 1.176 eV, respectively, ratio between intensities of which slightly changes with the change of the excitation power. The appearance of the doublet QD_1-QD_2 is associated with the difference of the QD sizes in the upper and lower layers. The QDM excited states peculiarities were not observed. With growth of hydrostatic pressure a "blue" shift of the PL band components occurs, followed by the increase of the full width of half maximum (FWHM) of the total PL band. The deconvolution into gaussians showed that this behavior caused by the increase of the spectral separation between them. Measured baric dependences are presented in Fig. 1.

The changes with pressure of the PL peak position for QD_1 and QD_2 can be approximated by a linear dependence with

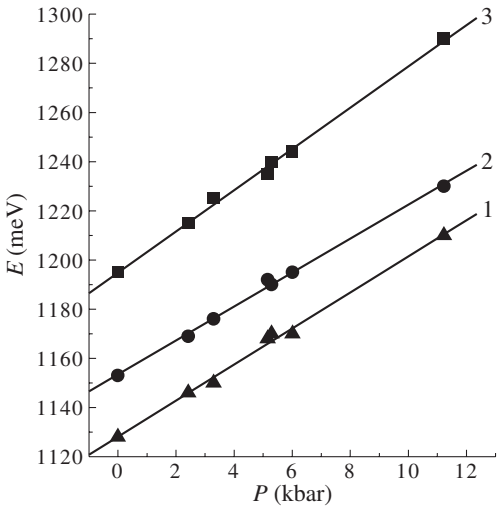

Fig. 1. The energy dependence on pressure for: 1 — half maximum PL band QD_1 intensity; 2 — maximum QD_1 and 3 — maximum QD_2.

BCs of 7 and 8 meV/kbar, respectively. These values satisfy the BC dependence on the transition energy in PL spectrum, determined earlier for single QDs [1].

M-type samples have all typical for the QDM array features [2]. At low excitation level, two PL lines could be easily resolved: s_+ (1.19 eV) and p_+ (1.23 eV). With the increase of excitation power the new bands d_+ (1.28 eV) and dx (1.30 eV) arise in high energy part of the PL spectrum. By the hydrostatic pressure the "blue" shift for PL components and the modification of the total PL band are observed. It was established that the observed changes appear due to the changes of the spectral intervals between PL maxima. But in contrast to the S-type samples, energy separation between them do not increase, but reduce with increase of the hydrostatic pressure. Similarly to the case of S-type samples, the energy shifts can be also approximate by the linear dependence, but with another slopes, from which the BCs were founded Fig. 2. One can see, that BC, correspondent to the maximum of s_+-component kept within experimental dependence determined earlier Fig. 3 [1]. BC value for this line is 7.8 meV/kbar with expected value 7.8 meV/kbar. BCs for p_+ and d_+ components are 7.6 and 6.2 meV/kbar, respectively. These values are essentially smaller then it was

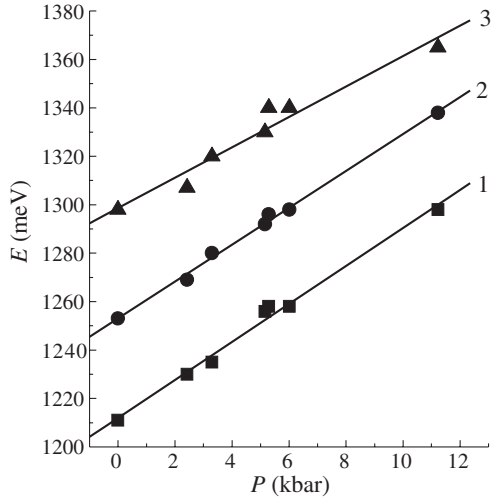

Fig. 2. The energy dependence on pressure for QDM lines: 1 — s_+, 2 — p_+, 3 — d_+.

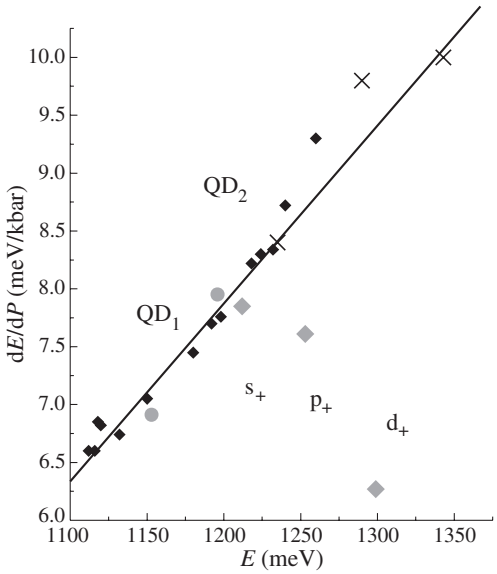

Fig. 3. The BC dependence on the energy for: 'circles' — QD_1 and QD_2 PL lines; 'squares' — QDM s_+, p_+, d_+ PL bands; and data from [1]: 'triangles' — on the singular substrate and 'crosses' — on the vicinal substrate with 7° [001] angle of misorientation.

expected (8.8 and 9.5 meV/kbar, respectively). Thus difference of the baric dependences for the ground (s_+) and excited (p_+, d_+) terms result in the FWHM reduce of the total PL band. Fig. 3. BCs for QD_1 and QD_2 states of S-type sample (circles) and for s_+-, p_+- and d_+ molecular terms of M-type sample (squares) as function of the transition energy. Diamonds are the experimental points for single QDs [1].

We propose a next model to explain BC anomalies of the excited QDM states. The main reason for anomalies is existence of the inner strain, appeared due to the lattice mismatch and difference mechanical properties of the bulk InAs and GaAs. Earlier it was assumed that the inner strain is responsible for the baric behavior of single QDs, i.e. the decrease of the BCs with increase of QD size.

Anomalous dependence of BCs on the transition energy can be understood if to proceed from the assumption, that in case of single QD the inner strain contribution into the total value of the energy level shift is near 30 = %. It is obvious that this additional pressure (Kbarj) shift ΔE (relative to the energy shift of non-strained QD) is proportional to the energy, accumulated in the localization area of electron and hole wave functions. External hydrostatic pressure causes the decrease of the localization area and the reduction of ΔE. As a result the high energy shift in strained QD is slower. The value of this reduction is bigger for larger QDs.

It is known that QDM is a superposition of two similar in size and energy spectrum tunnel-coupled QDs. The ground and excited states of the QDM, as it was in case of single QD, have to be influenced by the inner strain. For two QDs, organized into MQD, exciton wave functions are localized mainly within QDs. For s_+ QDM ground state this situation remains. Under external hydrostatic pressure the decrease of the localization area of exciton wave function for single QD is the same to the QD which is a part of QDM. Hence their BCs will be close to each other, this fact is observed experimentally. For excited QDM states, holes remain localized in QDs, while electron wave functions penetrates deeply into GaAs spacer between them [2]. So baric dependences of excited MQD states (p_+, d_+) will be mainly determined by the matrix material.

Thus, to explain the anomalous dependence of QDM BCs, the model was proposed, which is based on existence of the inner strain in the localization area of QDs wave functions. The BCs reduction for the excited MQD states is explained by decrease of the localization area of electron wave function and their penetration into the barrier material having another baric properties.

Acknowledgements

This work has been supported by the Russian Foundation for Basic Research (2005) and by the "Universities of Russia" program (2005).

References

[1] V. A. Gaisin *et al*, *Vest. St Petersburg Univer.*, ser.4, Fysika, himiya. **2**, (12), 115 (2001).

[2] V. G. Talalaev *et al*, *Semiconductor*, **38**, (6), 696 (2004).

13th Int. Symp. "Nanostructures: Physics and Technology"
St Petersburg, Russia, June 20–25, 2005

Theoretical modeling of excitons in semiconductor nanoscale heterostructures AlGaN/GaN/AlGaN

E. P. Pokatilov[1], D. L. Nika[1], V. M. Fomin[1,2,3] and *J. T. Devreese*[2,3]

[1] Laboratory of Physics of Multilayer Structures, Department of Theoretical Physics, State University of Moldova, MD-2009 Kishinev, Moldova
[2] Theoretische Fysica van de Vaste Stoffen (TFVS), Departement Fysica, Universiteit Antwerpen, B-2610 Antwerpen, Belgium
[3] eiTT/COBRA Inter-University Research Institute, Technische Universiteit Eindhoven, NL-5600 MB Eindhoven, The Netherlands

Abstract. For heterostructures AlGaN/GaN/AlGaN with the GaN quantum wells ranging from 4 to 16 monolayers, we use an exciton model, which includes the interaction of an electron and a hole with deformations of the crystal lattice and with built-in electrostatic fields. It is based on a 6-band hole Hamiltonian, as distinct from the common variational approach. Exciton energy spectra and wave functions for the ground state and some excited states are found after numerical diagonalization of the 6-band matrix hole Hamiltonian with an adaptive grid. The developed theoretical approach has allowed us to interpret the position of the photoluminescence bands in a good agreement with experiment.

Introduction

Wurtzite nanosize heterostructures have attracted significant attention as promising candidates for application in optical, optoelectronic, and electronic devices [1 to 3]. Because of a large mismatch between adjacent crystal lattices in the AlGaN/GaN/AlGaN heterostructures, a strained state of the crystal lattices of the GaN-well and AlGaN-barrier layers arises. The deformations significantly influence the structure of the energy bands and lead to the appearance of strong piezoelectric fields. In the wurtzite crystals, due to the hexagonal symmetry of the lattice (point group C_6^v) there exists spontaneous polarization, causing the electrostatic fields with strength of several MV/cm [4]. As a result of these peculiar features of the heterostructures under consideration, the photoluminescence and optical absorption are considerably dependent on the width of the GaN layer. In thin layers, where the potential of the built-in electrostatic field is not high, a blue shift of the photoluminescence band, very common for nanostructures, takes place. However, in the structures with wider wells (>5 nm) the potential strongly bends the edges of the valence and conduction bands. Due to this bending, a red shift of the photoluminescence bands is observed and the lifetime of exciton states is sharply increased.

Till recently, the optical effects in the nitride-based heterostructures were analyzed only using the one-band Hamiltonians of heavy and light holes, application of which for the nanostructures is not well grounded owing to the intersubband mixing in the valence band. Moreover, to the best of our knowledge, up to now the solution of the given problem has been carried out only in the framework of a variational method [5, 6].

1. Theoretical approach

In the present work, we use a 6-band exciton Hamiltonian, including the energy of the interaction of an electron and a hole with deformations of the crystal lattice and with built-in electrostatic fields. Exciton energy spectra and wave functions are found numerically by means of the finite-difference methods with an adaptive grid. At the first stage, we analyze size-quantized electron and hole states. Due to a large value of the size quantization energy in comparison with the energy of the Coulomb electron-hole interaction, we obtain the equations, describing the intra-exciton in-plane motion by means of the averaging of the Hamiltonian using the wave functions of size quantization of the motion perpendicular to the layers. As a result of a numerical solution of these equations, the Coulomb functions of the in-plane motion are obtained. At the second stage, the wave function of the exciton is sought in the form of a series of products of the wave functions describing size quantization and the Coulomb wave functions with coefficients, which are found by the numerically exact diagonalization of the 6-band matrix Hamiltonian. As a result, energy spectra and wave functions are found for the ground state and some excited exciton states.

2. Results and discussion

Out of 30 exciton energy levels, which have been calculated for a $Al_{0.17}Ga_{0.83}N$/GaN multiple quantum-well structure, the lowest five levels are shown in Fig. 1. A lope of the edges of the conduction and valence bands is due to the built-in electric field. A spatial distribution of the built-in electric field $\mathbf{F}$ is determined from the conditions of continuity of the normal

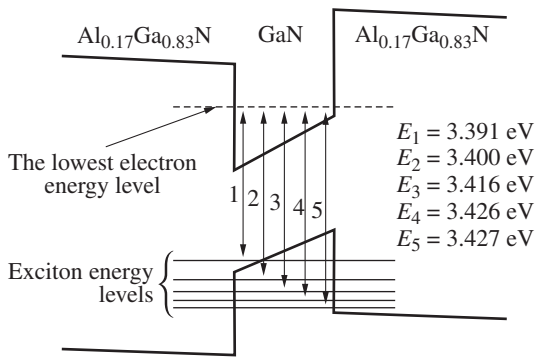

Fig. 1. The lowest five exciton energy levels calculated for the $Al_{0.17}Ga_{0.83}N$/GaN multiple quantum-well structure including four 16-ML-wide quantum wells and the 30-nm-wide barriers. The exciton ground-state energy is in a good agreement with the photoluminescence transition energy from Ref. [5] (see Fig. 3).

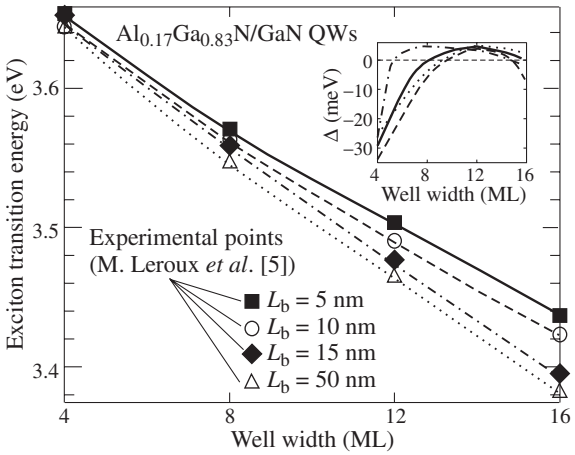

Fig. 2. Well-width dependence of the calculated exciton transition energies and the experimental PL peak positions for $Al_{0.17}Ga_{0.83}N$/GaN QWs with different barrier widths. In the inset we show the differences Δ between the exciton ground-state energies calculated using our model and those obtained within the one-band variational model by M. Leroux *et al* [5].

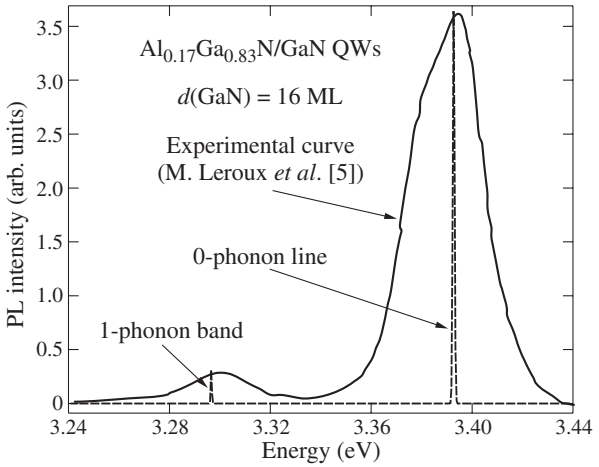

Fig. 3. Photoluminescence spectra of $Al_{0.17}Ga_{0.83}N$/GaN multiple quantum wells structure including four 16-ML-wide quantum wells and the 30-nm-wide barriers. The positions of the peaks and their relative intensities are in a good agreement with experiment of Ref. [5].

component of the displacement $\mathbf{D}$ ($\mathbf{D} = \varepsilon_0\varepsilon\mathbf{F} + \mathbf{P}$, where the polarization $\mathbf{P} = \mathbf{P}^s + \mathbf{P}^p$ is a sum of the spontaneous and piezoelectric polarizations) at the interfaces and of vanishing potentials at the external surfaces of the structure.

In Fig. 2, the calculated results for the exciton transition energy are compared with the experimentally determined positions of the photoluminescence peaks as a function of the GaN quantum well width [4 monolayers (MLs), 8 MLs, 12 MLs, 16 MLs, where 1 ML = 0.259 nm] at different values of the $Al_{0.17}Ga_{0.83}N$ barrier width. The values of the deviation Δ of the variational results for the exciton transition energy of Ref. [5] from those calculated by us are shown in the inset to Fig. 2. It is worth noting that in Ref. [5] the values of the electric fields were deduced from the fit of the photoluminescence data for each of four quantum-well widths, while our calculation has been performed without fitting parameters.

In Fig. 3 we represent the experimentally observed [5] photoluminescence band together with its 1-phonon satellite and the results of our calculation of the positions of the 0-phonon and 1-phonon peaks. When calculating the exciton-phonon interaction, the wurtzite crystal structure in group-III nitrides was taken into account. As seen from Figs. 2 and 3, our theory compares well with experiment.

The developed theoretical approach has allowed us for the first time: (i) to describe the position of the photoluminescence bands in agreement with experiment [5 to 8]; (ii) to explain the transition from the blue shift to the red shift in the photoluminescence spectra depending on the strength of the built-in electrostatic fields and the width of the well and barrier layers; (iii) to estimate quantitatively the increase of the time of radiative relaxation for the exciton with increasing the quantum-well width. The proposed method is efficient for the investigation of the exciton states in one- and multi-layered heterostructures, and also in the self-arranged ensembles of strained quantum dots.

Acknowledgements

This work was supported by FWO-V projects G.0274.01N, G.0435.03, the WOG WO.035.04N, GOA BOF UA 2000 and IUAP (Belgium) and the European Commission SANDIE Network of Excellence, contract NMP4-CT-2004-500101.

References

[1] S. Nakamura and G. Fasol, *The Blue Laser Diode*, Berlin: Springer, 1997.
[2] L. Hsu and W. Walukiewicz, *Phys. Rev. B*, **56**, 1520 (1997).
[3] N. Suzuki and N. Iizuka, *Jpn. J. Appl. Phys., Part 2*, **38**, L363 (1999).
[4] C. Adelman, E. Sarigiannidou, D. Jalabert, Y. Hori, J.-L. Rouviere and B. Daudin, *Appl. Phys. Lett.*, **82**, 4154 (2003).
[5] M. Leroux, N. Grandjean, J. Massies, B. Gill, P. Lefebvre and P. Bigenwald, *Phys. Rev. B*, **60**, 1496 (1999).
[6] R. Langer, J. Simon, V. Ortiz, N. T. Pelekanos, A. Barski, R. Andre and M. Godlewski, *Appl. Phys. Lett.*, **74**, 3827 (1999).
[7] J. Simon, R. Langer, A. Barski and N. T. Pelekanos, *Phys. Rev. B*, **61**, 7211 (2000).
[8] M. Leroux, N. Grandjean, M. Laugt, J. Massies, B. Gill, P. Lefebvre and P. Bigenwald, *Phys. Rev. B*, **58**, R13371 (1998).

13th Int. Symp. "Nanostructures: Physics and Technology"
St Petersburg, Russia, June 20–25, 2005

Simple estimation of X^- trion binding energy in semiconductor quantum wells

R. A. Sergeev[1], R. A. Suris[1], G. V. Astakhov[1,2], W. Ossau[2] and D. R. Yakovlev[1,3]

[1] Ioffe Physico-Technical Institute, St Petersburg, Russia
[2] Physikalisches Institut der Universität Würzburg, 97074 Würzburg, Germany
[3] Experimentelle Physik 2, Universität Dortmund, 44221 Dortmund, Germany

Abstract. A simple illustrative wave function with only three variational parameters is suggested to calculate the binding energy of negatively charged excitons (X^-) as a function of quantum well width. The results of calculations are in agreement with experimental data for GaAs, CdTe and ZnSe quantum wells, which differ considerably in exciton and trion binding energy. The normalized X^- binding energy is found to be nearly independent of electron-to-hole mass ratio for any quantum well heterostructure with conventional parameters. Its dependence on quantum well width follows an universal curve. The curve is described by a simple phenomenological equation.

Introduction

The first experimental observation of negatively charged excitons (X^- trions) has been reported for CdTe-based quantum wells (QWs) by K. Kheng *et al* in 1993 [1]. The trions have also been observed in QWs based on GaAs and ZnSe semiconductors [2–4]. Nowadays, a large number of experimental data are available for various types of heterostructures with different parameters. The evolution of the binding energy of X^- trion with the QW width have been also extensively studied theoretically [5–8].

The aim of this paper is to present a simple universal model, which allows to estimate the trion binding energy (E_B^T) in any semiconductor QWs. We concentrate on the negatively charged exciton, which is caused by the reliable set of experimental data available.

1. Experimental results

Experimental data of the X^- trion binding energy (E_B^T) for ZnSe, CdTe and GaAs QWs of various widths (L_z) are collected in Fig. 1(a). In order to compare experimental data for different materials, we replotted them in Bohr units, E_B^T/Ry against L_z/a_B, as shown in Fig. 1(b). The following values of 3D exciton Rydberg $Ry = 4.2$, 10, 20 meV and 3D exciton Bohr radius $a_B = 140$, 67, 40 Å were taken for GaAs, CdTe and ZnSe respectively. It can be seen that, in these units, all dependences can be well approximated by one universal curve. For example, a plausible estimation of the trion binding energy in QWs of a thickness more than a_B and less than $10a_B$ can be obtained with the simple fitting equation (shown in Fig. 1(b) by a solid line):

$$\frac{E_B^T}{Ry} \approx \frac{1}{3\sqrt{\frac{L_z}{a_B}}}. \qquad (1)$$

It is the simplest fitting equation found to be a well approximation for the experimental data. Of course, it cannot be used at the limiting cases $L_z \to 0$ and $L_z \to \infty$. Nevertheless it gives plausible estimation of the trion binding energy for the wide range of L_z and can be very useful due to its simplicity.

2. Variational estimation

The fact that the experimental results for different semiconductors can be well approximated by only one universal curve is remarkable. It signifies that in crude consideration we can leave only those parameters of the system, which can be directly expressed in QW width and exciton radius and energy, and neglect the others.

Thus, the trion is treated as a three-body Coulomb system. The reduced mass (μ) and the permittivity (ε) are supposed to be isotropic and identical in QW and in the barriers. The real potential of QW is replaced by an ideal one with infinite barriers. The hole is taken to be much heavier than the electron, so the mass ratio $\sigma = m_e/m_h$ is zero. In this case the hole occupies the center of QW, where the adiabatic potential of the electrons reaches a minimum [20].

The most critical point is the proper choice of the trial function, which should be simple and close to the real wave function. The simplest trial function for the exciton with only one variational parameter (a), which gives plausible results for the exciton binding energy for any value of the QW widths, is:

$$\Psi_X(\mathbf{r}) = A\ \exp(-a\,r)\ \cos\left(\pi\frac{z}{L_z}\right) \quad |z| \le L_z/2. \qquad (2)$$

Here $\mathbf{r}$ is 3D vector connecting the hole and electron, and z is its projection on the growth direction. A, here and after, is a normalization factor of the corresponding wave function. The function (2) turns into the exact wave function of the exciton in both limiting cases of an ideal 2D QW ($L_z \to 0$) and a 3D bulk semiconductor ($L_z \to \infty$).

The simplest trion function, based on the exciton function (2), is the 3-parameter Chandrasekhar-like one [21]:

$$\Psi_T(\mathbf{r_1}, \mathbf{r_2}) = A\left[\exp(-a_1 r_1 - a_2 r_2) + \exp(-a_2 r_1 - a_1 r_2)\right] \times (1 + cR)\cos\left(\pi\frac{z_1}{L_z}\right)\cos\left(\pi\frac{z_2}{L_z}\right). \qquad (3)$$

Here a_1, a_2, and c are variational parameters. Analogously to the function (2), this function transforms into the appropriate Chandrasekhar's one in the limiting cases of two and three dimensions.

The calculated trion binding energy versus the QW width within the described approach is shown in the Fig. 1(b) (the

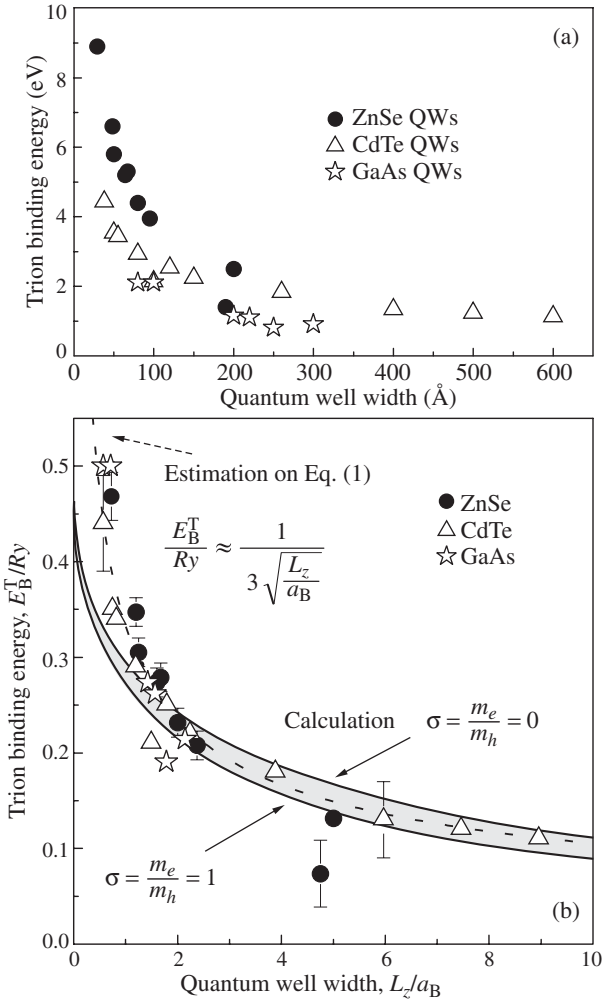

Fig. 1. The X^- trion binding energy E_B^T versus the QW width L_z plotted for different semiconductors [9-19]: ZnSe by circles, CdTe by triangles, and GaAs by stars. (a) The experimental dependences are plotted in natural units. (b) The experimental dependences are plotted in 3D exciton units. The solid line is estimation (1). The fill area represents a scattering of calculated dependences due to the mass ratio σ, obtained by variational method. It is confined by two extreme cases with $\sigma = 1$ and $\sigma = 0$.

dashed line pointed by $\sigma = 0$). The calculation is in very good agreement with the experimental data for wide QWs ($L_z \geq 2a_B$). However, in narrow ($L_z < 2a_B$) QWs the discrepancy becomes considerable. We believe that it is due to the lateral localization of the complexes on the QW interface roughnesses.

The correction to the trion binding energy due to nonzero mass ratio can be also estimated. It is possible to show, that the binding energy increases if the mass ratio tends to zero due to the additional localization of the hole in the center of QW. Thus, all possible dependences of X^- trion binding energy on the QW width are confined by two extreme cases with $\sigma = 1$ and $\sigma = 0$. Moreover, in some crude approximation, the dependence with $\sigma = 1$ can be simply obtained via rescaling the already obtained one with $\sigma = 0$:

$$E_B^T(L_z, 1) \approx E_B^T\left(\sqrt{2}L_z, 0\right). \qquad (4)$$

The result is presented in Fig. 1 (b) by the filled area.

It is worth to note that our considerations taken for GaAs-based QWs generally represent the results of previous numerical calculations [5-8]. However, in contrast to them, in the present paper the theoretical results have been obtained with the use of only three fitting parameters, and an agreement is achieved for various semiconductor systems (i.e. for CdTe and ZnSe in additional to GaAs).

3. Conclusions

The experimental values of the trion binding energy for various semiconductor quantum wells, being represented in corresponding exciton units, are found to be well approximated by an universal function. The theoretical estimations confirm that in a simplified Coulomb model the X^- trion binding energy is nearly independent of the electron-to-hole mass ratio at any value of quantum well width. Consequently, for the sake of simplicity, calculations of the trion binding energy can be performed with infinite hole mass values. In narrow quantum wells the experimental data cannot be explained in the frame of an idealized model and additional factors should be involved in the consideration.

Acknowledgements

This work was supported by the Deutche Forschungsgemeinschaft via Sonderforschungsbereich 410, Russian Foundation for Basic Research, grant 05-02-16679 and the Federal Programme on Support of Leading Scientific Schools, grant 2160.2003.2. One of the authors (R. A. Suris) appreciates the support of the Alexander von Humboldt Foundation.

References

[1] K. Kheng *et al*, *Phys. Rev. Lett.* **71**, 1752 (1993).
[2] G. Finkelstein *et al*, *Phys. Rev. Lett.* **74**, 976 (1995).
[3] A. J. Shields *et al*, *Phys. Rev. B* **52**, R5523 (1995).
[4] G. V. Astakhov *et al*, *Phys. Rev. B* **60**, R8485 (1999).
[5] B. Stebe *et al*, *Phys. Rev. B* **56**, 12454 (1997).
[6] C. Riva *et al*, *Phys. Rev. B* **61**, 13873 (2000).
[7] L. C. O. Dacal *et al*, *Phys. Rev. B* **65**, 115324 (2002).
[8] A. V. Filinov *et al*, *Phys. Stat. Sol. (c)* **0**, 1441 (2003).
[9] A. Esser *et al*, *Phys. Rev. B* **62**, 8232 (2000).
[10] G. V. Astakhov *et al*, *Phys. Rev. B* **65**,165335 (2002).
[11] T. Wojtowicz *et al*, *Acta Physica Polonica A* **94**, 199 (1998).
[12] O. Homburg *et al*, *Phys. Rev. B* **62**, 7413 (2000).
[13] V.P. Kochereshko *et al*, *Phys. Stat. Sol. (b)* **220**, 345 (2000).
[14] K. Kheng *et al*, *J. Crys. Growth* **184/185**, 849 (1998).
[15] Z. C. Yan *et al*, *Phys. Rev. B* **52**, 5907 (1995).
[16] R. Kaur *et al*, *Phys. Stat. Sol. (a)* **178**, 465 (2000).
[17] G. Finkelstein *et al*, *Phys. Rev. B* **53**, R1709 (1996).
[18] A. J. Shields *et al*, *Phys. Rev. B* **51**, 18049 (1995).
[19] V. Huard *et al*, *Phys. Rev. Lett.* **84**, 187 (2000).
[20] A. L. Efros, *Sov. Phys. Semicond.* **20**, 808 (1986).
[21] S. Chandrasekhar, *Astrophys. J.* **100**, 176 (1944).

13th Int. Symp. "Nanostructures: Physics and Technology"
St Petersburg, Russia, June 20–25, 2005

Excitons localized on quantum well interface roughnesses

M. A. Semina, R. A. Sergeev and R. A. Suris
Ioffe Physico-Technical Institute, St Petersburg, Russia

Abstract. The binding energy of excitons localized in the plane of a quantum well by a quantum well width fluctuation is theoretically analyzed. The dependence of the binding energy on the parameters of a roughness is determined. A simple and physically transparent wavefunction is suggested to describe exciton confinement in the fluctuation with arbitrary shape. The transitions between the qualitatively different limiting cases are illustrated.

Introduction

The investigation of optical properties of quantum well (QW) based heterostructures is a problem of significal practical interest. In the spectral range close to the excitonic peak in relatively thin QWs and at low doping level the optical properties are controlled by excitons and excitonic complexes localized in the QW plane by the in-plane potential fluctuations [1-4]. Such fluctuations may be, for example, induced by the QW interface roughnesses. In the present paper we theoretically study the binding energies of two-dimensional (2D) excitons in such structures. When QW thickness is less then 3D exciton Bohr radius the carrier motion can be considered as a 2D one and interfacial fluctuations manifest themselves as an additional lateral potential. The aim of the paper is to develop a simple and descriptive method which allows to calculate the binding energy of a 2D exciton localized at the lateral potential of the arbitrary shape with an acceptable accuracy.

1. Limiting cases

The exciton binding energy is the difference between the size-quantization energies of separate electron and hole and exciton energy.

There are a few independent energy parameters in the problem of electron-hole complexes. First of all, it is the Coulomb interaction energy (E_c) and the characteristic distance between the in-plane size-quantization energy levels of separate electron (E_e) and hole (E_h). The following limiting cases may separated depending on the ratio between these values:

1. The distances between in-plane size-quantization energy levels of separate electron and hole are large as compared with the characteristic value of a Coulomb energy (E_e, $E_h \gg E_c$). In such a case the carriers are localized independently and Coulomb interaction can be treated as a small perturbation;

2. The distances between in-plane size-quantization energy levels of separate electron and hole are smaller then the Coulomb one (E_e, $E_h \ll E_c$). In this case the lateral potential does not affect the internal structure of an exciton, thus allowing separation of the relative carriers motion and the center of mass quantization;

3. Electron-hole Coulomb energy value is between the value of characteristic distances between their size-quantization energy levels ($E_h \ll E_c \ll E_e$ or $E_e \ll E_c \ll E_h$). In this case the hole or electron motion respectively can be calculated in the adiabatic approximation according to parameter m_e/m_h.

2. Variational method

In order to describe all limiting cases listed above we suggest the following trial wave of an exciton

$$\Psi(\mathbf{r}_e, \mathbf{r}_h) = e^{-\alpha|\mathbf{r}_e - \gamma\mathbf{r}_h|}\Psi_{0e}(\mathbf{r}_e)^{\beta_e}\Psi_{0h}(\mathbf{r}_h)^{\beta_h}\Psi_{0R}(\mathbf{R})^{\beta_R}.$$

Here $\mathbf{r}_e$, $\mathbf{r}_h$, $\mathbf{R}$ - are 2D coordinates of an electron, hole and exciton center of mass respectively. Wavefunctions Ψ_{0e}, Ψ_{0h}, Ψ_{0R} are a ground state wavefunctions of an isolated electron, hole and center of mass in the fluctuation potential. The trial parameters α, γ, β_e, β_h, β_R have a transparent physical sense: α is inverse localization radius of the electron due to Coulomb interaction around the effective center determined by parameter γ: if $\gamma \to 0$ it is placed in the center of potential well, if $\gamma \to 1$ it coincides with the hole position. Parameters β_i ($i = e, h, R$) describe the contribution of the respective particle wavefunction in the excitonic function. Let us note that the lateral potential can be of arbitrary shape.

In the limit of $\beta_R \to 0$, $\beta_e \to 1$, $\beta_h \to 1$, we can separate the electron and hole in-plane motion and the case 1 takes place. If $\beta_e \to 0$, $\beta_h \to 0$, $\beta_R \to 1$, we can separate the center of mass and relative carrier motion and it corresponds to the case 2. If $\beta_e \to \infty$ or $\beta_h \to \infty$, the electron or hole is strongly localized in the center of potential well due to the Coulomb interaction with remaining particle (case 3).

3. Illustrative example

The qualitative transitions between the limiting cases 1–3 in frames of the developed approach we illustrate by the simple example of a 2D exciton in a parabolic in-plane potential. The energy will be measured in the units of the binding energy of a bulk exciton $Ry = \mu e^4/2\varepsilon^2\hbar^2$, and three-dimensional Bohr radius will be used as a measure of distance. In dimensionless variables Hamiltonian is:

$$\widehat{H} = -\frac{m_h}{m_e + m_h}\Delta_e - \frac{m_e}{m_e + m_h}\Delta_h - \frac{2}{|\mathbf{r}_e - \mathbf{r}_h|} + U_e(\mathbf{r}_e) + U_h(\mathbf{r}_h),$$

where $\Delta_{e,h}$ is a 2D Laplacian and

$$U_{e,h}(\mathbf{r}_{e,h}) = \frac{m_{e,h}}{(m_e + m_h)}\frac{1}{L_{e,h}^4}r_{e,h}^2,$$

where $L_{e,h}$ are the lengths of localization of the separate electron or hole characterizing the corresponding potential stiffness.

To illustrate the transition between the cases 1 and 2, we take for example the ratio of electron to hole mass $m_e/m_h = 0.2$

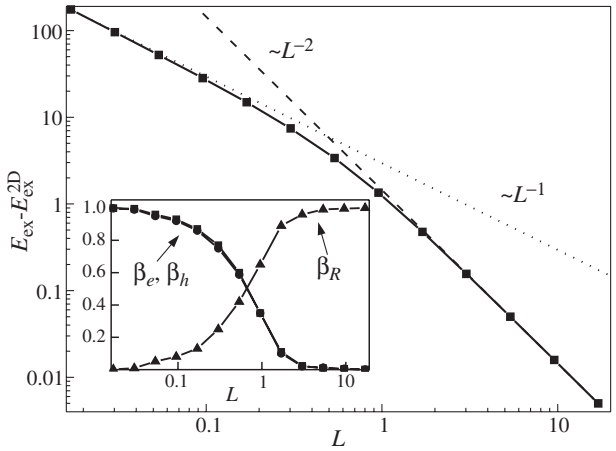

Fig. 1. Difference between the exciton binding energy $E_{\rm th}$ and 2D exciton binding energy $E_b^{2D} = 4Ry$ dependence on the effective localization length. $m_e/m_h = 0.2$. Solid curve corresponds to the variational calculation, dotted and dashed ones are the asymptotics (cases 1 and 2). The inset shows dependence of the trial parameters β_R (triangles), β_e (squares), β_h (circles).

and potential lengths for an electron and for a hole $L = L_e = \sqrt[4]{m_h/m_e}\ L_h$, which let the stiffnesses to be the same. Fig. 1 shows evaluated difference between the exciton binding energy and free 2D exciton binding energy, $E_{\rm th} - E_{\rm th}^{2D}$, vs. effective localization length, L. The energy is counted from the free 2D exciton binding energy. One can see that $E_{\rm th}$ is positive because Coulomb interaction between charged particles increases due to the additional in-plane localization. The inset to Fig.1 shows the trial parameters dependence on the L. If the lateral potential is weak, $L \to \infty$, $E_{\rm th} \sim 1/L^2$, $\beta_e, \beta_h \to 0, \beta_R \to 1$, that corresponds to the localization of an exciton as a whole (case 2). In the opposite limit, $L \to 0$: $E_{\rm th} \sim 1/L$, $\beta_e, \beta_h \to 1, \beta_R \to 0$, and electron and hole are localized independently (case 1). The respective asymptotic are shown in Fig. 1 also.

To illustrate the transition between the cases 2 and 3, we take the ratio of electron to hole mass $m_e/m_h = 0.2$ and potential for the hole with the effective localization length L_h. We assume that an electron is free to move in a QW plane ($L_e \to \infty$). Fig. 2 shows evaluated difference between the exciton binding energy and free 2D exciton binding energy, $E_{\rm th} - E_{\rm th}^{2D}$, vs. hole localization length, L_h. In weak potential, $L_h \to \infty$, the exciton is quantized as a whole and $(E_{\rm th} - E_{\rm th}^{2D}) \sim 1/L_h^2$, $\beta_h \to 0, \beta_R \to 1$. It corresponds to the case 2. In the opposite limit of strong parabolic potential, $L_h \to 0$, the electron is localized around the center of the potential due to the Coulomb interaction with the localized hole (case 3) and $(E_{\rm th} - E_{\rm th}^{2D})$ tends to the constant value $(4m_e/m_h)$ with the deviation $\sim L_h^2$

The transition between the cases 1 and 3 can be shown in the following example: we take localization radii for an electron and for a hole $L = L_e = L_h = 0.1$. Fig. 3 demonstrates evaluated evaluated difference between the exciton binding energy and free 2D exciton binding energy, $E_{\rm th} - E_{\rm th}^{2D}$, vs. m_e/m_h. The inset to Fig.3 shows the trial parameters dependence on the m_e/m_h. If $m_e/m_h \to 1$, then $\beta_e, \beta_h \to 1, \beta_R \to 0$, and the case 1 takes place. In the opposite limit, $m_e/m_h \to 0$, $E_{\rm th}$ goes to the constant value as $(m_e/m_h)^{1/2}$, $\beta_e, \beta_h \to 1, \beta_R \to 0$, it corresponds to the case 3.

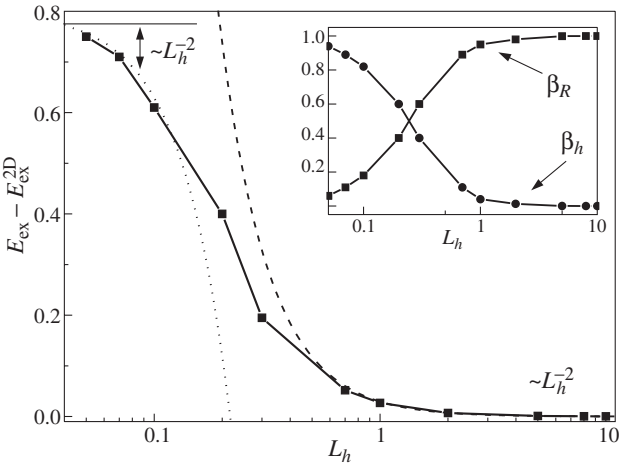

Fig. 2. Dependence of $E_{\rm th} - E_{\rm th}^{2D}$ on the hole localization length L_h. $m_e/m_h = 0.2$. Solid curve corresponds to the variational calculation, dashed and dotted ones are the asymptotics (cases 2 and 3). The inset shows dependence of the trial parameters.

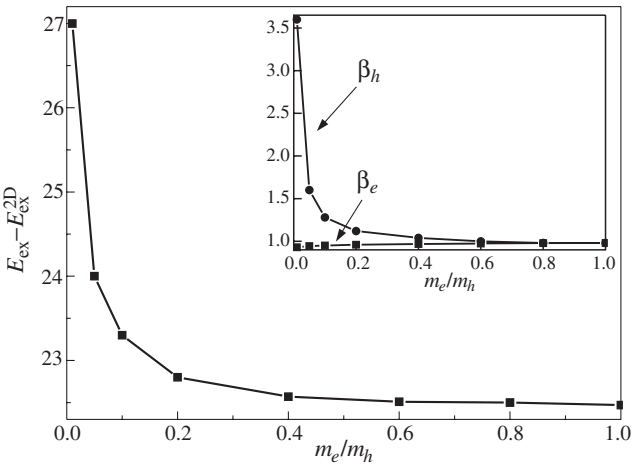

Fig. 3. Dependence of $E_{\rm th} - E_{\rm th}^{2D}$ on electron to hole mass ratio, m_e/m_h. The inset shows dependence of trial parameters, β_e (squares), β_h (circles)

Conclusion

The classification of limiting cases in the problem of exciton localization on QW potential roughnesses is carried out. The simple trial function which lets one to obtain the exciton binding energies for arbitrary shape of the localizing potential is suggested. The developed approach is applied to the case of exciton localized in the parabolic potential

Acknowledgements

This work was supported by Russian Foundation for Basic Research, Grant 05-02-16679 and by Federal Program on Support of Leading Scientific Schools, Grant 2160.2003.2.

References

[1] G. Bastard, C. Delalande, M. H. Meynadier, P. M. Frijlink, M. Voos, *Phys. Rev. B* **29**, 7042 (1984).

[2] L. E. Golub, *Solid State* **39**, 1673 (1997).

[3] Luis C. O. Dacal, R. Ferreira, G. Bastard, and Jose. A. Brum, *Phys. Rev. B* **65**, 115325 (2002).

[4] A. V. Filinov, C. Riva, F. M. Peeters, Yu. E. Lozovik, and M. Bonitz, *Phys. Rev. B* **70**, 035323-1 (2004).

13th Int. Symp. "Nanostructures: Physics and Technology"
St Petersburg, Russia, June 20–25, 2005

Polarized photoluminescence of excitons in n-, p- and undoped InAs/GaAs quantum dots

J. Fürst[1], H. Pascher[1], *V. A. Shalygin*[2], L. E. Vorobjev[2], D. A. Firsov[2], A. A. Tonkikh[3], N. K. Polyakov[3], Yu. B. Samsonenko[3], G. E. Cirlin [3] and V. M. Ustinov[4]

[1] Experimentalphysik I, Universität Bayreuth, D-95447 Bayreuth, Germany
[2] St Petersburg State Polytechnic University, 195251 St Petersburg, Russia
[3] Institute for Analytical Instrumentation, 198103 St Petersburg, Russia
[4] Ioffe Physico-Technical Institute, St Petersburg, Russia

Abstract. Polarized photoluminescence (PL) from InAs/GaAs quantum dots (QDs) was investigated under cw excitation by circularly polarized light. Depolarization of the PL in a magnetic field perpendicular to the wavevector of the exciting light (Hanle effect) was studied. For n-doped, undoped and p-doped QDs the observed Hanle curves exhibit qualitatively different shape: single-, bi- and tri-Lorentzian, respectively. Complicated shape of Hanle curve is attributed to the presence of different simulteneous processes of radiative recombination. Recombination of uncharged excitons and recombination of positively charged exciton complexes are considered.

Introduction

Quantum dot structures are promising candidates for the implementation of spintronic and quantum computing devices. Although the spin dynamics of excitons in undoped InAs/GaAs QDs have been strongly studied (see [1, 2] and references therein), only a few papers deal with the same subject in n-doped QDs (see [3] and references therein), and as we know p-doped QD structures were not investigated from this point of view. The goal of the present investigation is to learn more about the influence of doping on the exciton spin lifetimes in InAs/GaAs QDs. To provide low excitation level and steady state conditions we use weak cw excitation. Under nonresonant interband absorption of circularly polarized light spin polarized excitons are generated in QDs. In the experiment we detect photoluminescence (PL) in the spectral range corresponding to exciton recombination. The exciton spin polarization is monitored by the degree of circular polarization ρ_c of the PL light, the decrease of which in a transverse magnetic field B (Hanle effect) yields the spin lifetime T_2^*. According to [1]

$$\rho_c(B) = \frac{\rho_c(0)}{1 + (\Omega T_2^*)^2}\,, \qquad (1)$$

where

$$\rho_c(0) = \rho_0 \cdot \frac{\tau_1}{\tau_1 + \tau}\,, \qquad (2)$$

τ_1 is the exciton spin relaxation time, τ is the exciton lifetime, $\Omega = g\mu_B B/\hbar$, g is the Landé-factor of the excitons in QDs, μ_B is the Bohr magneton, $1/T_2^* = 1/\tau + 1/\tau_1$, ρ_0 is a constant depending on the energy levels of the sample and the frequencies of exciting and detected light. Holes photogenerated in the barrier loose their spin polarization very rapidly, and excitons in QDs are formed by the capture of spin polarized electrons and completely unpolarized holes. The exciton g-factor is a linear combination of the electron and hole g-factors. As we use the Voigt configuration, the transverse g-factors are responsible for the Zeeman splitting of QD energy levels. The value $g_e^\perp = 0.86$ was found in [4], but the value of $g_h^\perp$ in QDs is still discussed and so we determine in this paper the scaled exciton spin lifetime $g \cdot T_2^*$.

1. Experimental technique

QD structures were grown by deposition of 2.5 monolayers of InAs and 50 Å layer of $In_{0.12}Ga_{0.88}As$. An active region contains 15 QD layers separated by 400 Å thick GaAs spacers. In each layer the QD density was about $3 \cdot 10^{10}$ cm^{-2}, and QDs had about 120 Å lateral size. Three samples were grown, containing undoped, p- and n-type spacers between the QD layers. The doping level was about $1.8 \cdot 10^{11}$ cm^{-2}, equal in p- and n-type samples. It can be assumed, that due to doping six charge carriers in average were incorporated in each QD. At $T = 1.8$ K the ground state PL peaks are at 1.08 eV, 1.04 eV, and 1.07 eV for n-, p- and undoped samples, respectively. Polarized PL was studied in backscattering geometry. A 17 mW laser with a photon energy of 1.59 eV was used as excitation source. In order to avoid an influence of spin polarized nuclei on the Hanle curve, the exciting light was periodically switched between right and left circular polarization at a rate of 50 kHz. Using a quarter-wave plate followed by a linear polarizer the component of the PL light with fixed circular polarization was detected.

2. Results and discussion

The experimental Hanle curve for n-doped QDs is described by a very narrow ($g \cdot T_2^* = 950$ ps) single Lorentzian (1) with a very small $\rho_c(0) = 0.1\%$. The observation of the Hanle effect for a highly n-doped situation is very remarkable. The amount of polarized electrons created by the pumping laser is estimated to be much smaller than the doping carrier concentration but this fraction of spin polarized electrons manifests itself in the circular polarized exciton PL.

The observed Hanle curves for the undoped QDs fit to a superposition of two Lorentzians. Such bi-contour Hanle curves were also found for InAs QDs by other authors [1], noting unclear origin of the narrow contour. We assign two contours of the Hanle curves to two simultaneous processes of radiative recombination in QDs. The narrow contour is attributed to the ground state exciton (X^0) recombination, while the broad contour can be connected with the ground state trion (X^+) recombination. The appearance of trion luminescence in undoped QD structures can be explained by the presence of a fraction of

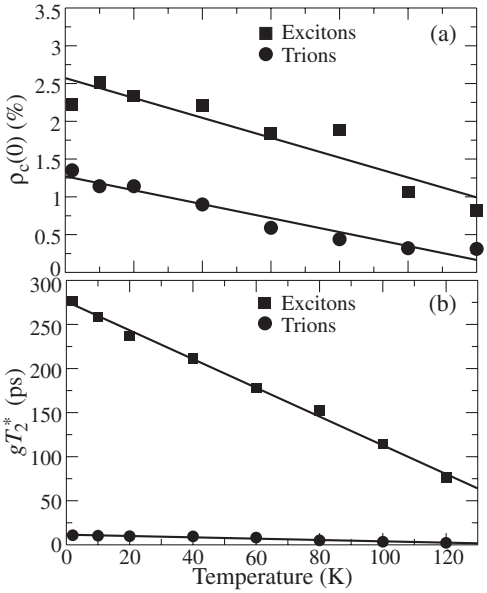

Fig. 1. Zero-field values of the degree of circular polarization (a) and scaled spin lifetimes (b) for the excitons and trions in the undoped QD structure.

p-doped QDs due to residual acceptor concentration. Moreover in an undoped sample photocreated electrons and holes can be captured by different dots. This makes some dots charged. In both cases electron-hole pairs localized in positively-charged dots lead to the appearance of trion states, while those in uncharged QDs form excitons. The bi-Lorentzian fit to the Hanle curves yields two spin lifetimes which undergo a linear decay with increasing temperature as it is shown in Fig. 1b. In the whole temperature range studied here spin lifetime of excitons is significantly larger than the one of trions, and the ratio $\frac{\tau_{X0}}{\gamma_{X0}} : \frac{\tau_{X+}}{\gamma_{X+}}$ is practically constant (here γ_{X0} and γ_{X+} are the capture coefficients). This conclusion follows from the analysis of the temperature dependence of the exciton and trion contributions to $\rho_c(0)$ shown in Fig. 1a.

In contrast to the undoped sample, where at a magnetic field of 3 T the degree of circular polarization has completely vanished, ρ_c for the p-doped QDs is still $0.3\rho_c(0)$ (for $T = 1.8$ K), further decreasing with increasing magnetic field (see Fig. 2). Superposition of three Lorentzians represents the observed Hanle curves perfectly. A third component contributes to the Hanle curve, corresponding to a very short temperature independent spin lifetime $g \cdot T_2^*$ of about 2.5 ps. One can consider three simultaneous processes of radiative recombination in the p-doped sample which can be connected with radiative recombination in positively charged dots with different numbers of holes. The average doping level is about six acceptors per QD. The excitation level is about one electron-hole pair per QD, so in average we have an even number of particles ($n = 8$) in a positively charged complex. Some fluctuations in this number lead to the complexes with odd numbers of particles, $n = 7$ and 9. The temperature dependence of zero-field values of the degree of circular polarization $\rho_c(0)$ for all three processes is shown in Fig. 3a. The spin lifetimes deduced from the tri-Lorentzian fits are plotted in Fig. 3b. The data demonstrate that there are qualitatively different temperature dependencies of the spin lifetimes and capture coefficients for charged dots with even and odd number of particles.

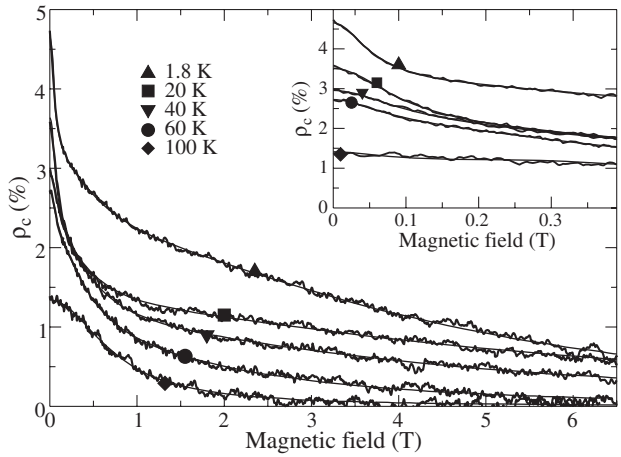

Fig. 2. Measured Hanle curves for the p-doped QD sample at various temperatures (are presented by lines with a noise). Solid lines without a noise depict tri-Lorentzian fits.

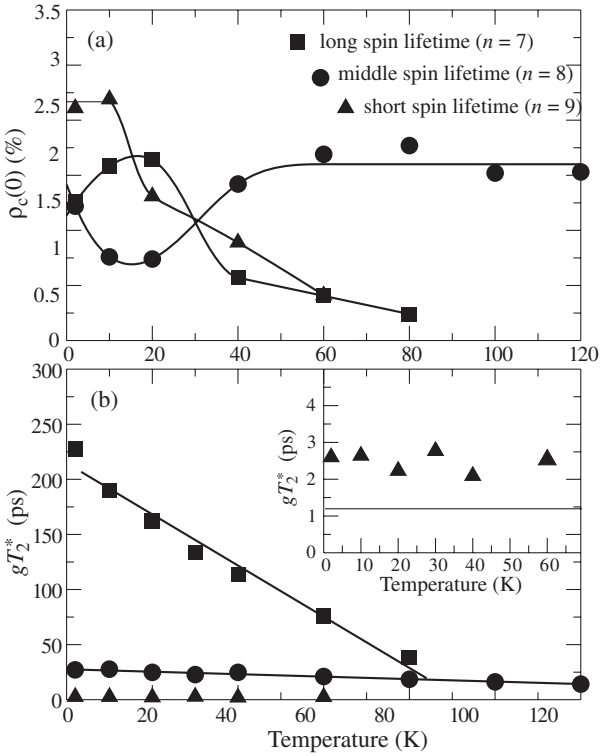

Fig. 3. Zero-field values of the degree of circular polarization (a) and scaled spin lifetimes (b) for the different exciton complexes in the p-doped QD structure.

Acknowledgements

We are grateful to E. L. Ivchenko, V. K. Kalevich, V. L. Korenev, L. E. Golub and M. M. Glazov for discussions. Part of this work was supported by INTAS and RFBR.

References

[1] R. J. Epstein *et al*, *Applied Phys. Lett.*, **78**, 733 (2001).
[2] V. K. Kalevich *et al*, *Phys. Rev. B*, **64**, 045309 (2001).
[3] V. K. Kalevich *et al*, *Physica E*, **21**, 1018 (2004).
[4] I. Hapke-Wurst *et al*, *Physica E*, **12**, 802 (2002).

13th Int. Symp. "Nanostructures: Physics and Technology"
St Petersburg, Russia, June 20–25, 2005

Temperature dynamics of excitons in InAs quantum dots array

B. V. Novikov[1], *M. B. Smirnov*[1], V. G. Talalaev[1,2], G. E. Cirlin[3,4] and V. M. Ustinov[3]

[1] Fock Institute of Physics, St Petersburg State University, 198504, St Petersburg, Russia
[2] Max-Planck-Institut für Mikrostrukturphysik, 06120, Halle (Saale), Germany
[3] Ioffe Physico-Technical Institute, St Petersburg, Russia
[4] Institute for Analytical Instrumentation, RAS, St Petersburg, 198103, Russia

Abstract. Temperature effect on the photoluminescence of self-assembled InAs quantum dots grown on vicinial GaAs substrates is discussed. A new model which takes into account the excitons exchange with InAs wetting layer and GaAs barrier as well as the excition-phonon interaction is proposed.

Introduction

Photoluminescence (PL) investigation of self-assembled quantum dots (QDs) based on the InAs/GaAs system revealed several types of QDs exhibiting different temperature dependencies [1]. As temperature increases, some of the PL bands (related to the conventional QDs, CQDs) shift to lower energy and become narrower whereas others (related to the isolated QDs, IQDs) broaden and do not show marked red shift with respect to the InAs energy gap. This enables to suggest that these PL bands come from different QD groups which differ by strength of the inter-dots interaction. The IQDs are formed at terrace edges in the samples having a high degree of step bunching ($5-7^\circ$). Formation of such QDs is accompanied by the WL rupture, resulting in the absence of interaction between these QDs. The observed temperature-induced broadening of PL coming from such QDs can be attributed to an increase of thermal fluctuation (the electron-phonon coupling). Very specific behavior of the CQD bands resembles the temperature effect on the PL of self-assembled QDs connected by wetting layer (WL) [2, 3]. The observed narrowing and red shift can be attributed to a carrier thermal 'evaporation' into WL [3] or into barrier [2]. The present study is aimed at a comparative analysis of these two mechanisms — the thermal fluctuation broadening and the carrier thermal escape — in application to the earlier experimental results [1].

1. Model

A particular property of the self-assembled QDs is their coupling through WL. As a consequence, some excitons 'escape' from CQDs into WL or into barrier. In Ref. [2] it was proposed to describe this process by the expression

$$n(E, T) = n_0(E)s(E, T) \tag{1}$$

where $s(E, T)$ factor corresponds to a two-level excitation exchange. We assume that both subsystems (WL and barrier) can play the role of destinations for escaping excitons. Hence, the $s(E, T)$ factor is determined for the triple-level system in the following way:

$$s(E, T) = \frac{1}{1+C_{\mathrm{WL}} \exp\left(\frac{E-E_{\mathrm{WL}}}{kT}\right)+C_{\mathrm{BR}} \exp\left(\frac{E-E_{\mathrm{BR}}}{kT}\right)}. \tag{2}$$

The energy levels of InAs WL and GaAs barriers were determined as $E_{\mathrm{WL}} = 1.46$ eV and $E_{\mathrm{BR}} = 1.52$ eV. Due to relatively lower energy, the exciton capture into WL is more favorable at a low temperature. We suggest that capture into barrier is equally possible at a higher temperature. Thus, we assume $C_{\mathrm{WL}} = C_{\mathrm{BR}} = C$ for CQDs and $C_{\mathrm{BR}} = C$ for IQDs. The model developed in [3] extends the relations (1–2) by taking into account the WL-barrier excitation exchange and the radiative recombination within QDs as well as within WL. However, the numerical analysis shows that these mechanisms can be effectively taken into account by the scaling of parameters in (1)–(2).

The thermally induced broadening of bands in the PL spectra is proportional to the growth of phonon amplitudes and can be described by relation

$$\Gamma = \Gamma_0 + \Gamma_{ph}\left[\exp\left(\frac{\theta}{T}\right) - 1\right]^{-1}. \tag{3}$$

Such a broadening has been observed in the exciton optical absorption spectra of $In_xGa_{1-x}As/InP$ quantum wells [4]. It can be assumed that similar behavior should be inherent to IQDs which do not participate in the carrier escape into the WL. Similar behavior manifest the most intense PL band observed in [1] which was assigned to PL of IQDs.

It can be assumed that the real situation is intermediate between the two described above situation and a realistic model should take into account both contributions. The model used in present study combines both contributions. Density of states (DOS) for all the QD groups is assumed to follow the random distribution

$$n_0(E)\tilde{}\exp\left[-\left(\frac{E-E_{\mathrm{QD}}}{\Gamma}\right)^2\right]. \tag{4}$$

Thus, temperature effect consists in the broadening described by (3) and in normalizing by factor $s(E, T)$ defined by (2). Parameters determined by fitting the experimental data are listed in Table 1.

Table 1.

	E_{QD} (eV)	C	Γ_{ph} (meV)	θ (K)
CQD	1.345	20000	50	200
IQD	1.37	100	60	280

2. Results and discussion

Computational results are presented in Fig. 1. They can be compared with experimental results shown in Fig. 2.

There is one peculiarity, which distinguishes the temperature behaviors of CQD and IQD. This is the red shift. This

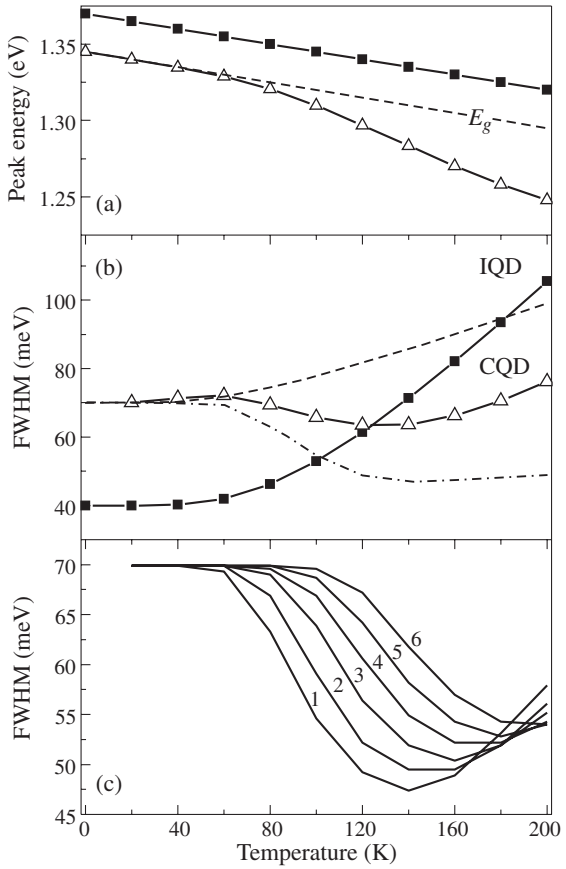

Fig. 1. The temperature dependence of PL peak energy (a) and FWHM (b) calculated for IQD (squares) and CQD (triangles) using parameters listed in Table 1. Dotted line in (a) is the temperature dependence of InAs energy gap. Different FWHM contributions are shown in (b): the thermal broadening (dashed line) and the exciton capture (dash-dotted line). (c): FWHM for two-level systems with different excitation energy: 1.45 eV (1), 1.46 eV (2), 1.47 eV (3), 1.48 eV (4), 1.49 eV (5), 1.50 eV (6).

means that the peak energy of PL band diminishes faster than the InAs energy gap E_g (Fig. 2a). Magnitude of this shift is about 1 meV/K for CQD and is absent for IQD. The model used in this study gives a satisfactory description of this effect (Fig. 1a), and it explains phenomenon as the influence of the thermally induced carrier escape. The higher exciton energy is the easier it can escape into WL. This leads to exhausting the high-energy wing of DOS and shifts the peak energy to red side of the spectrum.

Fig.1b shows temperature dependence of the full width at half maximum (FWHM) calculated for IQD and CQD. Only phonon broadening governs temperature behavior of IQDs. For CQDs both contributions are equally important. It is seen that the thermal broadening dominates at $T < 80$ K and the carrier escape contribution is prevailing at higher temperatures. The carrier escape affects FWHM non-monotonously. Carrier escape into WL would leads to FWHM minimum at $T = 140$ K (see Fig. 1c). If an additional carrier escape into barrier is taken into account, the position of FWHM minimum shifts to higher temperatures. provides the better agreement with experiment. Nevertheless, according to the model, at higher temperatures the thermal broadening is prevailing again.

It is worth to mention that θ parameter which determines

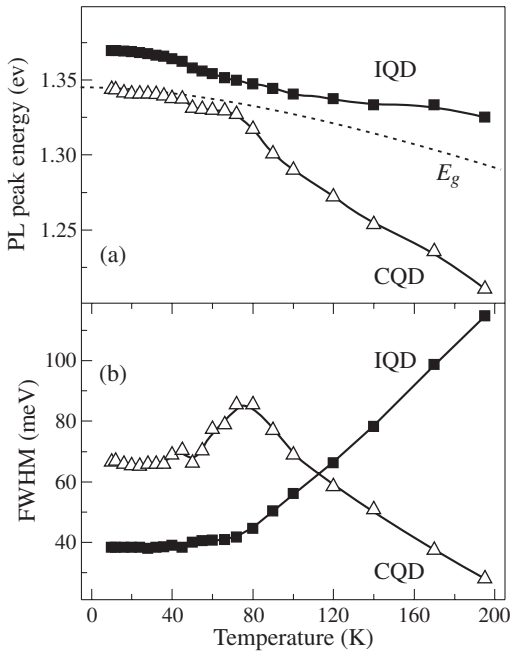

Fig. 2. Temperature dependence of PL peak energy (a) and FWHM (b) derived from experimental PL spectra for IQD (squares) and CQD (triangles).

the temperature dependence of the broadening originated from exciton-phonon interaction has values close to the Debye temperature which is 280 K in InAs. This confirms our suggestion that this process is adequately explained by the temperature induced increase of thermal fluctuations.

In conclusion, it is shown that the model, which takes into account the exchange of excitations of QDs and wetting layer and barrier as well as the excition-phonon interaction, provides explanation of the temperature effects observed in PL studies. Difference in the temperature behavior of different PL bands can be attributed to different strength of these competing factors. Phonon-induced broadening dominant at low temperatures can be dampened by the carrier escape at higher temperatures. Both WL and barrier can serves as channels for escaping excitons. So, an accurate account of all these mechanisms could provide an explanation of the phenomenon under study.

Acknowledgements

This work has been supported by the Russian Foundation for Basic Research (2005) and by the "Universities of Russia" program (2005).

References

[1] V. G. Talalaev *et al*, *Phys. Stat. Sol.(b)* **224**, 101 (2001).
[2] S. Fafard *et al*, *Surface Science* **361/362**, 778 (1996).
[3] S. Sanguineti *et al*, *Phys. Rev. B* **60**, 8276 (1999).
[4] M. Sugawara *et al*, *Phys. Rev. B* **42**, 9587 (1990).

13th Int. Symp. "Nanostructures: Physics and Technology"
St Petersburg, Russia, June 20–25, 2005

Order of the trion lines in photoluminescence spectrum of semiconductor quantum wires

B. Szafran[1,2], T. Chwiej[2], F. M. Peeters[1], S. Bednarek[2] and J. Adamowski[2]

[1] Departement Fysica, Universiteit Antwerpen (Campus Drie Eiken),
Universiteitsplein 1, B-2610 Antwerpen, Belgium
[2] Faculty of Physics and Applied Computer Science, AGH University of Science and Technology,
al. Mickiewicza 30, 30-059 Kraków, Poland

Abstract. Energy order of the negative (X^-) and positive trions (X^+) in quantum wires is studied as function of the relative electron and hole localization. For equal hole and electron confinement, X^+ has a larger binding energy but a small imbalance towards a stronger hole localization leads to the interchange of X^- and X^+ recombination lines in the photoluminescent spectrum as was recently observed experimentally.

Introduction

We study the exciton trions formed when an electron or a hole is bound to a neutral exciton (X). The binding energies of the complexes small in bulk, are substantially enhanced in nanostructures, i.e., in quantum wells [1,2,3,4] and quantum wires [5,6,7]. Due to the larger effective mass of the hole, in bulk [8] as well as in strictly two-dimensional confinement [2] the binding energy of positive trions (X^+) is larger than the negative trion (X^-) binding energy. However, in quantum wells the observed [4] X^- and X^+ binding energies are nearly equal, which is explained [3,4] by a stronger hole quantum-well localization enhancing the hole-hole interaction. In quantum dots the localization-related hole-hole interaction enhancement leads to the interchange of the order of the X^- and X^+ recombination lines in the photoluminescence (PL) spectrum already for quantum dot diameters as large as 24 donor Bohr radii [9]. The prediction [9,10] that for smaller dots the X^+ line becomes even more energetic than the exciton line has recently [11] been confirmed experimentally.

The present work is motivated by a recent experimental study [7] on trions in V-groove GaAs/AlGaAs quantum wires. The X^- was found to be distinctly more stable than X^+ (binding energies of X^- and X^+ were determined as 4.2 and 2.9 meV, respectively). Here, we indicate that the observed [7] order of X^- and X^+ energy lines is a consequence of modifications of the effective interactions due to a stronger hole confinement. In a previous theoretical study [5] of trions in quantum wires X^+ was found to be more stable than X^-, which was obtained in the case of equal hole and electron confinement. A crossing of X^- and X^+ PL lines as function of the wire width has previously been obtained in a quantum Monte-Carlo study [6] of a quantum wire with a square well confinement potential.

1. Theory

We apply the single band model for the electron and the hole and consider a harmonic oscillator confinement potential in the directions perpendicular to the wire [$V = (x^2_{e(h)} + y^2_{e(h)})/2l^4_{e(h)}$, with $l_{e(h)}$ the oscillator length for the electron (hole)], referred to as "lateral" in the following. Moreover, we assume that the lateral confinement is strong, so that only the lowest subband for the electron and hole is occupied. This assumption allows for a reduction of the Schrödinger equation to an effective two-dimensional form, which can be solved numerically with an exact inclusion of the interparticle correlations along the wire. We adopt the donor units, i.e., donor Bohr radius $a_d = 4\pi\epsilon_0\epsilon\hbar^2/m_e e^2$ for the unit of length and twice the donor Rydberg $2R_d = \hbar^2/m_e a_d^2$ as the unit of the energy, where m_e is the band electron effective mass and ϵ is the dielectric constant. The effective negative trion Hamiltonian after the integration over the lateral degrees of freedom and after the separation of the center of mass motion written with respect to the dissociated system is

$$H^{\rm rel}_- = -\frac{1}{2\mu}\left(\frac{\partial^2}{\partial z^2_{h1}} + \frac{\partial^2}{\partial z^2_{h2}}\right) - \frac{1}{\sigma}\frac{\partial^2}{\partial z_{h1}\partial z_{h2}}$$
$$+V^{\rm ef}(l_e; z_{h1} - z_{h2}) - V^{\rm ef}(l_{eh}; z_{h1}) - V^{\rm ef}(l_{eh}; z_{h2}),$$

with the reduced mass of an electron-hole pair $\mu = \sigma/(1+\sigma)$, $\sigma = m_h/m_e$, and the coordinates of the relative electron-hole positions $z_{h1} = z_h - z_{e1}$ and $z_{h2} = z_h - z_{e2}$ along the wire. In Eq. (1) $l_{eh} = \sqrt{(l_e^2 + l_h^2)/2}$ and $V^{\rm ef}$ is the effective one-dimensional interaction potential [5,12]

$$V^{\rm ef}(l; z) = (\pi/2)^{1/2}{\rm erfc}(|z|/\sqrt{2}l)\exp(z^2/2l^2)/l, \qquad (1)$$

finite at the origin ($V^{\rm ef}(l; 0) = 1/l$) and approaching the $1/z$ asymptotic at large z. Hamiltonian for X^+ has the form (1) but with $1/\sigma$ standing in front of the mixed derivative replaced by 1. Eigenequations are solved with a finite-difference method.

2. Results

We consider a quantum wire made of GaAs ($m_h = 0.45m_0$, $m_e = 0.067m_0$, $2R_d = 11.9$ meV, $a_d = 9.8$ nm). Fig. 1 shows the wave function of X^- (a) X^+ (b) trions for equal hole and electron oscillator lengths of the lateral confinement. The interaction potentials in the trion Hamiltonians have a minimum along $z_{h1} = 0$ and $z_{h2} = 0$ axis corresponding to an electron and a hole in the same position and a maximum along the diagonal $z_{h1} = z_{h2}$ corresponding to both electrons (for X^-) or both holes (for X^+) at the same place. Fig. 1 shows that the electrons in X^- with light effective masses tunnel easily through the diagonal barrier due to the interelectron repulsion. On the other hand the diagonal barrier is effectively much larger for the heavy-mass holes which prevents its penetration at large σ and which leads to the appearance of the characteristic maxima elongated along the diagonal [see Fig. 1(b)].

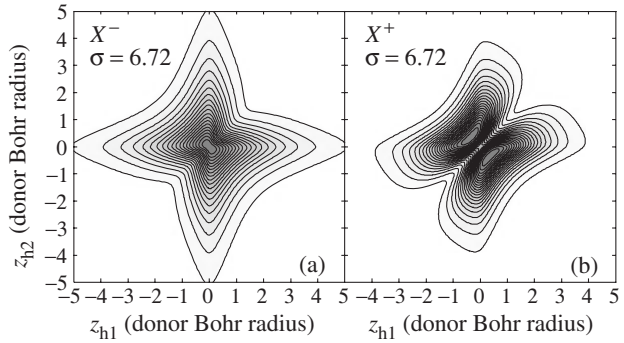

Fig. 1. Countour plots of the wave function for X^- (a) and X^+ (b) trions for $l_e = l_h = L = 0.2$ with a mass ratio $\sigma = 6.72$ corresponding to GaAs.

The difference of the X^+ and X^- binding energies is plotted in Fig. 2. Both trions are equally stable for $l_h = 0.92l_e - 0.38$ nm (see the dashed line in Fig. 2). For l_h larger (smaller) than $0.92l_e - 0.38$ nm X^+ is more (less) stable than X^-. The fit of the calculated X^- and X^+ binding energies to the experimental data [7] is obtained at the crossing of the thick gray dotted lines, i.e., for $l_e = 2.95$ nm and $l_h = 1.3$ nm. The obtained fit corresponds to realistic values which give a general idea on the particle localization in the wire (the measurements [7] were performed on a V-groove GaAs/AlGaAs quantum wire with a thickness of the GaAs crescent of 3 nm at the center). Obviously, a more realistic model is required to extract details of the confinement from the experimental data.

3. Conclusions

We studied the properties of negative and positive trions in quantum wires with strong lateral confinement using the approximation of the lowest subband occupancy which allows for a numerically exact solution of the multi-particle Schrödinger equation. We investigated the relative stability of the X^+ and X^- trions with respect to the dissociation into an exciton and a free carrier for different electron and hole confinement. We found that the order of the X^- and X^+ PL lines is interchanged when the lateral confinement of the hole is stronger than the one for the electron due to the modification of the effective interactions in the trion complexes. The present results provide an explanation for the recently experimentally observed larger stability of the negative trion in quantum wires [7].

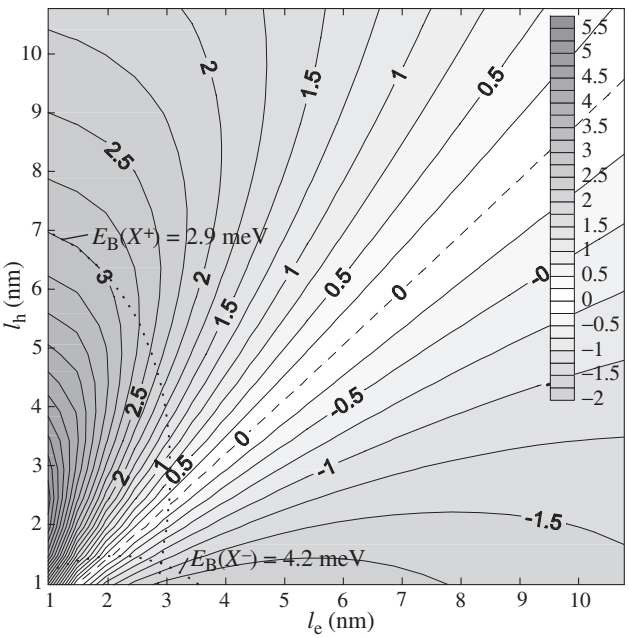

Fig. 2. Contour plot of the difference between the X^+ and X^- binding energies (in meV) as function of the electron and hole confinement lengths for GaAs material parameters. The region below (above) the dashed line corresponds to a more stable X^- (X^+) trion. The darker shades of gray correspond to larger absolute value of the X^- and X^+ binding energy difference. The dotted thick gray lines correspond to $E_B(X^-) = 4.2$ meV and to $E_B(X^+) = 2.9$ meV.

Acknowledgements

This paper was supported by the Flemish Science Foundation (FWO-Vl), the Belgian Science Policy, the University of Antwerpen (VIS and GOA), the EU-NoE SANDiE and by the Polish Ministry of Scientific Research and Information Technology within the solicited grant PBZ-MEN-MIN-008/P03/2003. B.S. is supported by the EC Marie Curie IEF project MEIF-CT-2004-500157.

References

[1] B. Stébé and A. Ainane, *Superlattices Microstruct.* **5**, 545 (1989).
[2] C. Riva, F.M. Peeters and K. Varga, *Phys. Rev. B* **64**, 235301 (2001).
[3] B. Stébé, A. Moradi, and F. Dujardin, *Phys. Rev. B* **61**, 7231 (2000).
[4] S. Glasberg, G. Finkelstein, H. Shtrikman, and I. Bar-Joseph, *Phys. Rev. B* **59**, R10425 (1999).
[5] A. Esser, R. Zimmermann, and E. Runge, *Phys. Stat. Sol. (b)* **227**, 317 (2001).
[6] T. Tsuchiya, *Int. J. Mod. Phys. B* **15**, 3985 (2001).
[7] T. Otterburg, D.Y. Oberli, M.-A. Dupertois, N. Moret, E. Pelucchi, B. Dwir, K. Leifer, and E. Kapon, *Phys. Rev. B* **71**, 033301 (2005).
[8] B. Stébé and G. Munschy, *Solid State Commun.* **17**, 1051 (1975).
[9] B. Szafran, B. Stébé, J. Adamowski, and S. Bednarek, *J. Phys.: Condens. Mat.* **12**, 2453 (2000).
[10] B. Szafran, B. Stébé, J. Adamowski, and S. Bednarek, *Phys. Rev. B* **66**, 165331 (2002).
[11] F. Guffarth, S. Rodt, A. Schliwa, K. Pötschke, and D. Bimberg, *Physica E*, **25**, 261 (2004).
[12] S. Bednarek, B. Szafran, T. Chwiej, and J. Adamowski, *Phys. Rev. B* **68**, 045328 (2003).

13th Int. Symp. "Nanostructures: Physics and Technology"
St Petersburg, Russia, June 20–25, 2005

Exciton lifetime in InAs quantum dot molecules

V. G. Talalaev[1,2,3], J. W. Tomm[2], B. V. Novikov[3], N. D. Zakharov[1], P. Werner[1], G. E. Cirlin[4,5], Yu. B. Samsonenko[4,5], A. A. Tonkikh[4,5] and V. M. Ustinov[4]

[1] Max-Planck-Institut für Mikrostrukturphysik, 06120, Halle (Saale), Germany
[2] Max-Born-Institut für Nichtlineare Optik und Kurzzeitspektroskopie, 12489 Berlin, Germany
[3] Fock Institute of Physics, St Petersburg State University, 198504, St Petersburg, Russia
[4] Ioffe Physico-Technical Institute, St Petersburg, Russia
[5] Institute for Analytical Instrumentation RAS, 190103, St Petersburg, Russia

Abstract. Transient photoluminescence of the coupled pairs of InAs quantum dots are measured. Structural characterization is done by transmission electron microscopy. Photoluminescence spectra consist of the 3 well-separated optical transitions that are assigned to the ground (s_+) and excited (p_+, d_+) molecule terms. Transient luminescence behavior indicates the increase of the exciton lifetime and eventually reduction of the oscillator strength in the molecule compared with a single quantum dot. The ratio of exciton lifetimes in s_+, p_+ and d_+ states of the quantum dot molecule could be used for the creation of mid-infrared light sources.

Introduction

The interaction of the quantum dots (QDs) in the self- organized arrays provides a potential basis for manufacturing new optoelectronic devices. At the vertical correlation of QDs in layers the conditions for the quantum dot molecules (QDMs) are established. At the transition from single QDs to QDMs the energy spectrum of array is transformed following the way described in [1]. The appearance of molecule terms may ensure the intra-subbands radiative recombination, which roofs IR- and THz-ranges. But the realization of such emission requires a certain kinetics of excitation relaxation in QDM structures. This aspect of the problem has not been properly studied.

The current work deals with the study of exciton luminescence kinetics in the InAs/GaAs structures having two InAs QD layers. Obviously the spacing between the QD planes in such array is an important parameter defining the interaction between confined excitons. For larger spacings the carrier transfer between the QD planes is hindered, whereas for smaller spacings the tunnel coupling between neighboring QDs becomes strong enough to obtain the QDMs.

1. Results and discussion

We present the results of a transmission electron microscopy (TEM) and time resolved photoluminescence (TRPL) study of two sample types with InAs QDs grown by molecular beam epitaxy. In our case the sample with 5 nm GaAs spacer between QD planes (M-type) exhibits a QDM behavior compared to the reference sample with a 10 nm spacer (S-type) showing a behavior of the single QDs.

Figure 1(a) shows a dark field TEM-image of the M-type structure. Figure 1(b) presents the indium distribution across one pair of QDs. Both QDs appear very similar in size and composition. The maximum of the In content in QDs is the same (60%). The distance between the maxima is about 7 nm. Therefore, there is a clear evidence for the existence of QDMs in the M-type structure. S-type sample had non- symmetrical pairs of QDs spaced by 10 nm GaAs barrier.

The steady state PL spectrum of the M-type sample consists of at least 3 well-separated optical transitions assigned to molecular energy terms (Fig. 1(c)). The + sign stands for the bonding (symmetric) terms. For the low excitation density we find an energy gap of 45 meV between the s_+ and p_+ PL lines and 24 meV between p_+ and d_+. Plots of the line intensities versus excitation power show an almost linear dependence with saturation thresholds at 50 and 130 W cm^{-2}, for the s_+ and p_+ lines, respectively. The ratio of 1:3 for their integrated

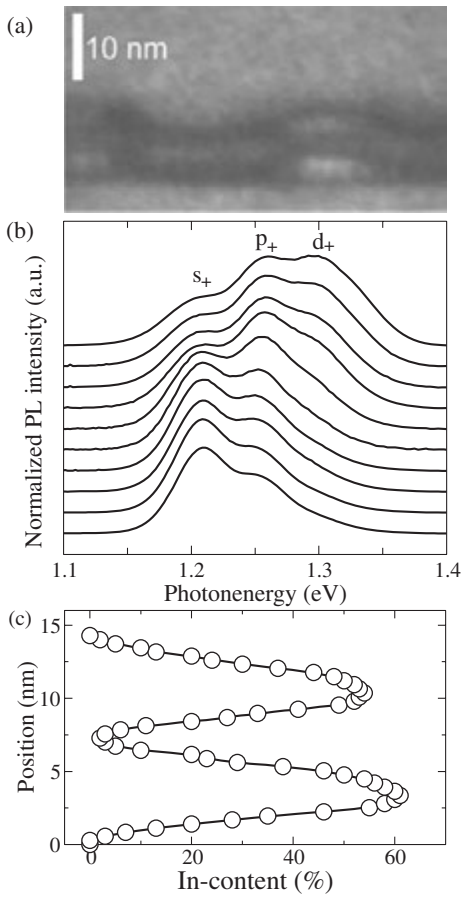

Fig. 1. (a) Cross-section dark-field TEM image of a QDM sample with 5 nm GaAs spacer; (b) indium concentration obtained by analysis of the high resolution TEM image of a individual QDM after Fourier-filtering along the growth direction; (c) cw PL data at $T = 10$ K for QDM array versus excitation power density: 0.2, 2, 10, 13, 25, 50, 100, 130, 200 and 300 W cm^{-2}, from the bottom to the top.

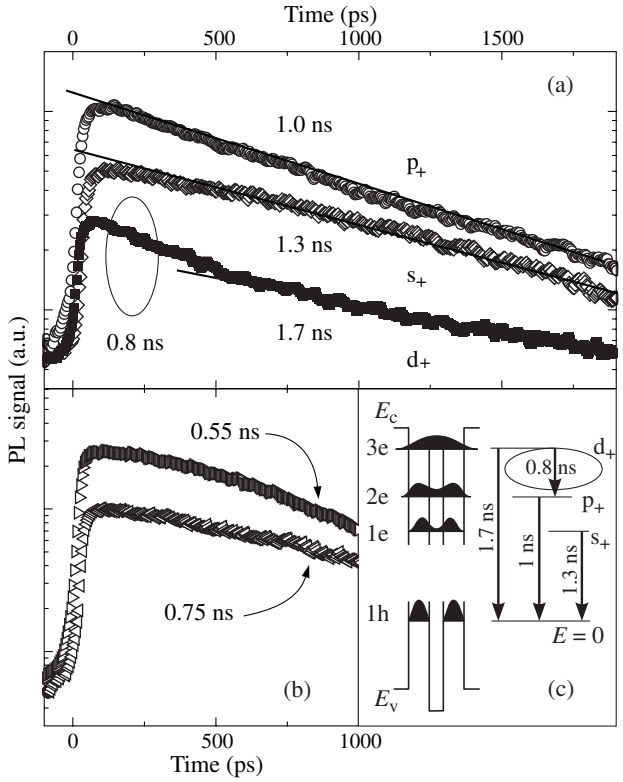

Fig. 2. (a) TRPL of the M-type sample at the s_+, p_+, and d_+ line positions; (b) TRPL of the S-type sample taken for both doublet components; (c) scheme of the energy states and optical transition in QDM. The excitation density — $2.4 \cdot 10^{11}$ photons/pulse·cm^2, measurement temperature — 10 K.

intensities at the threshold points reflects the relative occupation probability of s_+ and p_+ states. For d_+ line the saturation is not reached within the steady state experiment. Arrhenius plots of the cw PL temperature dependent yield a thermal activation energy of 124, 82 and 60 meV for the s_+, p_+ and d_+ lines, respectively. It should be noted, that the deconvoluted cw PL of the S-type sample shows two Gaussians separated by 35 meV. The relative intensity and the cw PL peak position of these Gaussians remain invariable for all cw excitation densities. This doublet is likely to be caused by different island sizes in the first and second QD planes that is in agreement with TEM data for such structure [2].

These results demonstrate that in the M-type sample with closely spaced QDs having the same size the QDMs array are achieved [2]. The S-type sample with a 10 nm spacer keeps the properties of an single QDs array. For the QDM array the 45 meV is assigned to the energy gap between s_+ and p_+ states. This value matches the difference of thermal activation energies between s_+ and p_+ states. The observed p_+-d_+ splitting of 24 meV and 22 meV obtained from cw PL spectra and Arrhenius analysis, respectively, indicates that s_+, p_+ and d_+ transitions involve the same hole level, being energetically separated from the GaAs barrier by about 190 meV. This value corresponds well to theoretical predictions of a strong hole localization in QDMs [3].

Fig. 2(a) presents the transient PL behavior for the M-type array at the s_+, p_+, and d_+ line positions. The recombination from s_+ and p_+ states is characterized by a mono-exponential PL decay with time constants of 1.3 and 1.0 ns, respectively. The d_+ band exhibits a bi-exponential PL decay, namely a fast (0.8 ns) and a slow (1.7 ns) transient. The S-type array shows a strictly mono-exponential PL decay with time constants of 0.55 ns and 0.75 ns for the two components of doublet, cf. Fig. 2(b). In this way, the PL decay times for the QDM array (0.8–1.7 ns) happen to be longer than for the QD array (0.55–0.75 ns). The increased exciton lifetime in the QDM is assigned to the stronger hole localization resulting in a smaller overlap between electron and hole states and eventually reduced oscillator strength of transitions in QDM compared with a single QD. This experimental result corresponds to theoretical predictions [3]. For a transient PL analysis of the QDMs we take into account the density of QDMs ($\backsim 10^{11}$ cm^{-2}), the s_+ state multiplicity (2), the ratio of the PL decay times for the s_+ and p_+ lines (1.3 and 1.0 ns, cf. Fig. 2(a)). Even at $2.4 \cdot 10^{11}$ photons/pulse·cm^2 the s_+ state is filled and the transition $p_+ \rightarrowtail s_+$, which is allowed by selection rule ($\delta J = 1$), is blocked. Therefore, the radiative recombination of electron-hole pairs should be the main relaxation mechanism for s_+ and p_+ states, having lifetimes of 1.3 and 1.0 ns, respectively. For the d_+ state an additional relaxation is available, namely the $d_+ \rightarrowtail p_+$ transition, which can be radiative ($\delta J = 1$). Its kinetics is determined by the first exponent with a 0.8 ns time constant in Fig. 2(a). The expected emission wavelength should amount to 30–50 μm. The second exponent (1.7 ns) corresponds to the radiative recombination of the d_+ -exciton. Obviously, the related ratio of p_+ and d_+ PL decay times establishes favorable conditions for the d_+ level population inversion. This should result in a bright emission at wavelengths according to the d_+–p_+ splitting, namely between 30 and 50 μm.

2. Conclusion

In summary, a consistent interpretation of steady state PL and TRPL data for QDMs is presented. The TRPL spectra indicate the increase of the exciton lifetime in the QDM compared with a single QD. A detailed analysis of the transient luminescence behavior shows an efficient $d_+ \rightarrowtail p_+$ transition that potentially could be used for the creation of mid-IR light sources.

Acknowledgements

This work has been supported by the Russian Foundation for Basic Research (2005), by the "Universities of Russia" program (2005), by INTAS-2001-0615 and SANDiE.

References

[1] M. Korkusinski *et al*, *Physica E* **13**, 610 (1999).
[2] V. G. Talalaev *et al*, *Appl. Phys. Lett.* **85**, 284 (2004).
[3] W. Sheng *et al*, *Appl. Phys. Lett.* **81**, 4449 (2002).

13th Int. Symp. "Nanostructures: Physics and Technology"
St Petersburg, Russia, June 20–25, 2005

Asymmetric double quantum wells as exciton spin separator

S. V. Zaitsev[1], A. S. Brichkin[1], P. S. Dorozhkin[1], V. D. Kulakovskii[1], M. K. Welsch[2] and G. Bacher[2]

[1] Institute of Solid State Physics, Russian Academy of Sciences, 142432 Chernogolovka, Russia
[2] Lehrstuhl Werkstoffe der Elektrotechnik, Universität Duisburg-Essen, Bismarckstrasse 81, D-47057 Duisburg, Germany

Abstract. Exciton recombination in asymmetric CdMgTe/CdTe/CdMgTe/CdTe/CdMnTe double quantum well (ADQW) nanostructures with different barrier width is studied in magnetic field up to 11 Tesla. As grown structures were subjected to rapid temperature annealing in order to promote diffusion of Mn and Mg atoms from the barriers into the CdTe quantum wells. At low fields when the exciton transition in QW with magnetic impurity (Mn) is higher in energy than that in QW with nonmagnetic impurity (Mg), an interwell exciton relaxation is fast independently on the spin state. In contrast, at high fields, when the energy order reverses, an unexpectedly low relaxation rate of σ^- polarized excitons from nonmagnetic QW to the ground σ^+ polarized DMS ones has been observed and discussed. Such a slowing down of relaxation allows one to separate the oppositely polarized excitons in different QWs.

Introduction

Spin manipulation, e.g. spin transfer and relaxation, attracts today high attention [1]. A possibility to control energy and spatial localization of carriers in artificial nanostructures has invoked a great practical interest to such nanodevices.

In this report we study energy and spin relaxation of excitons in ADQW with nonmagnetic (NM) and diluted magnetic semiconductor (DMS) QWs as a function of magnetic field and barrier width (L_B) between two QWs. Great advantage of DMS heterostructures is that a giant Zeeman effect in such semiconducting materials makes possible continuous tuning of band-gap and exciton energies by external magnetic field due to s,p-d exchange interaction between free carriers and localized d-states of magnetic ions [3]. This allows to vary the interwell coupling in ADQW structure after preparation, when the L_B is fixed.

In this work we show that the slow-down relaxation of σ^- excitons from NM QW to σ^+ DMS in combination with spin-dependent zone potential profile allows one to separate excitons with opposite spins in different QWs.

1. Experimental

$CdMg_{0.2}Te/CdTe/CdMg_{0.2}Te/CdTe/CdMn_{0.2}Te$ ADQWs were grown by molecular beam epitaxy on thick CdTe buffer deposed on (001)-oriented CdZnTe substrates. As grown samples have two nonmagnetic pure 6-nm width CdTe QWs separated by CdMgTe barrier with $L_B = 3$, 4 and 6 nm.

As grown structures were subjected to a rapid temperature annealing (RTA) once ($L_B = 3$ and 6 nm) or two times ($L_B =$ 4 nm) at 400 °C for 1 min. to promote diffusion of Mn and Mg atoms from the barriers into the CdTe QWs. RTA technique allows one to vary the QW energy gap in a controllable way with a good optical quality [2]. The CdTe QW, located between two CdMgTe barriers, after RPA incorporates only Mg atoms and is referred to as NM QW whereas that with CdMnTe barrier incorporates both Mg and Mn atoms and is referred to as DMS QW.

Samples were immersed in superfluid He (bath temperature $T \simeq 1.8$ K) in a cryostat with superconducting solenoid. The QW emission was excited with σ^- polarized excitation of a dye-laser at $\sim$ 100 meV above exciton transitions but below the barrier band gap and recorded in a Faraday geometry in two circular polarizations.

2. Polarization of excitonic emission in magnetic field. Exciton spin relaxation in ADQWs with DMS QW

Figure 1 displays polarized PL spectra of ADQWs with $L_B =$ 3, 4 and 6 nm at different magnetic fields. Figure shows that at zero field, all the ADQW structures display PL with a relatively broad (6–8 meV) lines, which is characteristic for ternary II–IV materials. In a magnetic field B spectral bands split into two components with opposite, σ^+ and σ^-, polarizations, corresponding to $J = +1$ and $J = -1$ states of bright excitons.

At low B spectral position and intensity I^+ of dominated σ^+ line is nearly B-independent in all samples, as it usually does in NM QWs. At higher fields, since some value $B_C = 3{-}8$ T (sample dependent), σ^+ component starts to red shift strongly, which is characteristic to excitons in DMS QWs. The higher energy σ^- component, in contrast, still displays weak shift in the whole magnetic field range. Its intensity I^- decreases with B in all samples, stronger for greater L_B. Plot on the right panel in Fig. 1 summarizes the magnetic field dependencies of circular polarization degree $P_C = (I^+ - I^-)/(I^+ + I^-)$. A relatively high intensity of the σ^- component at high fields indicates the nonthermal

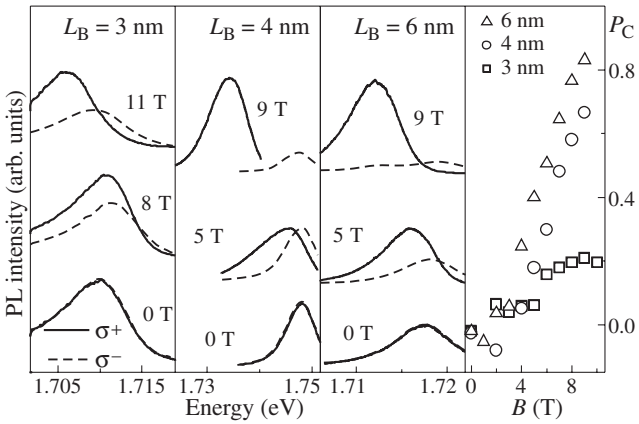

Fig. 1. Magneto-PL spectra in Faraday geometry of ADQWs with $L_B = 3$, 4 and 6 nm. Solid line —σ^+ polarization, dashed —σ^-. Excitation is σ^- polarized. Plot on the right panel — magnetic field dependence of circular polarization degree P_C.

distribution between observed $J = +1$ and $J = -1$ exciton states (splitting at high B strongly exceeds thermal energy kT). So, spin relaxation in studied ADQWs takes much longer time than in a single DMS QWs.

PL excitation (PLE) measurements in both excitation polarizations have shown that all pronounced exciton transitions are intrawell ones. In all samples the lowest exciton transition at low B weakly depends on magnetic field and thus is located in the NM QW. The first excited exciton level quickly decreases with B in σ^+ excitation polarization and is ascribed to DMS QW. At $B \geq B_C$ exciton transition in DMS QW is lower in energy than that in NM QW.

Note that the energy sequence of $J = +1$ and $J = -1$ exciton states in magnetic field is opposite in NM and DMS CdTe based QWs. In nonmagnetic CdTe wells, g-factor g_{hh} for heavy hole is low and positive, while the electron g-factor g_e is negative and rather large [4]. As a result, the lowest bright exciton state is σ^- polarized. In CdMnTe DMS QW, the main contribution in magnetic field induced splitting of electron and hole states is provided by their strong sp-d exchange interaction with localized Mn^{2+} magnetic moments [3]. That results in a huge negative g_{hh} and positive g_e effective g-factors. As a consequence, the ground exciton state in magnetic field is σ^+ polarized.

Calculated potential profiles of conductivity and valence bands for the sample with $L_B = 4$ nm at $B = 0$ and 9 T are presented in Fig. 2. sp-d exchange interaction parameters for CdMnTe are taken from the Ref. [3] while the contents of Mn and Mg in CdTe QWs after RPA procedure are determined from the fit of calculated exciton transition energies to measured ones in PLE.

Exciton population analysis based on rate-equations described in [7] have shown that it is impossible to explain the observed magnetic field dependence without considering of initial exciton depolarization after hot energy relaxation similar to made in Ref. [8]. For nonresonant condition photoexcited carriers relax in two stages: after ultrafast subpicosecond energy relaxation by LO-phonon emission at first tens picoseconds excitons with a large center-of-mass momentum **k** are created. Then, for hundreds of picoseconds, exciton loses its excess energy through acoustic phonon emission [10].

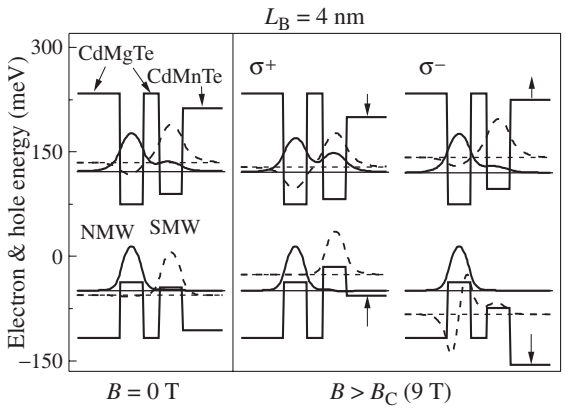

Fig. 2. Calculated electron and hole band potential profiles for $S_z = -1/2$ and $J_z = -3/2$ states (σ^+ label) and $S_z = +1/2$ and $J_z = +3/2$ (σ^- label) in sample with $L_B = 4$ nm at $B = 0$ T and 9 T. Electron and hole wave functions in the NM QW (solid line) and DMS QW (dashed line) are shifted according to state energy. Arrows show direction of band movement with magnetic field.

The hole, as a heavier particle, acquires the main part of the total exciton momentum. Spin-orbit mixing at finite **k**-vector increases both parts (long-range and short-range) of exchange interaction as compare to ones in relaxed to $\mathbf{k} = 0$ exciton. Spin-flip driven by the long-range exchange interaction is known to be the main mechanism of exciton spin relaxation in QWs at close to resonant excitation with typical time less than 50 ps [7]. Another strong spin-flip mechanism is the quasielastic hole spin scattering [6]. For this mechanism at high enough **k** corresponding to in-plane kinetic energy of tens meV the spin-flip time can be as fast as a few picoseconds for elastic static scatterers.

Figure 2 shows that for $J = -1$ ground exciton in NM QW both single-particle and exciton relaxation to DMS QW are energetically forbidden at $B \geq B_C$. During hot energy relaxation stage, an initially excited in NM QW $J = -1$ exciton can effectively relax its spin via exchange or hole spin-flip. Considered spin-flip processes followed by the exciton energy relaxation (tunneling) to the DMS QW strongly depend on valence band mixing. Band mixing is characterized by the value of hh-lh splitting Δ_{hh-lh}: it is stronger the smaller is Δ_{hh-lh}. Measured by PLE in NM QWs $\Delta_{hh-lh} \approx 34$, 19 and 15 meV in samples with $L_B = 3$, 4 and 6 nm respectively.

Thus, one should expect reduction of thermalized in NM QW $J = -1$ exciton emission, effect being stronger the smaller Δ_{hh-lh}. That is exactly what is observed in experiment: stronger damping of PL in σ^- polarization takes place in structures with smaller Δ_{hh-lh}. Besides, we suppose it is an increased valence-band mixing with the increase of magnetic field [9] that responsible for stronger initial exciton depolarization at the hot relaxation stage and results in steeper magnetic field dependence of circular polarization degree P_C (Fig. 1).

Acknowledgements

This work is supported by RFBR grant 04-02-17338 and INTAS grant 03-51-5266

References

[1] I. Žutić *et al*, *Rev. Mod. Phys.* **76**, 323 (2004).
[2] D. Tönnies *et al*, *Appl. Phys. Lett.* **64**, 5608 (2001).
[3] D. R. Yakovlev and K. V. Kavokin, *Comments Cond. Matter Phys.* **18**, 51 (1996).
[4] A. A. Sirenko *et al*, *Phys. Rev. B* **56**, 2114 (1997).
[5] F. Meier and B. P. Zakharchenya, *Optical orientation*, (Amsterdam, North-Holland), vol. 8, ch.3, 1984.
[6] R. Ferreira and G. Bastard, *Phys. Rev. B* **43**, 9687 (1991).
[7] M. Z. Maialle *et al*, *Phys. Rev. B* **47**, 15776 (1993).
[8] Ph. Roussignol *et al*, *Phys. Rev. B* **46**, 7292 (1992).
[9] G. E. W. Bauer and T. Ando, *Phys. Rev. B* **38**, 6015 (1988).
[10] T. C. Damen *et al*, *Phys. Rev. B* **42**, 7434 (1990).

13th Int. Symp. "Nanostructures: Physics and Technology"
St Petersburg, Russia, June 20–25, 2005

Dilute nitride Ga(AsN) alloys: an unusual band structure probed by magneto-tunnelling

A. Patanè[1], J. Endicott[1], L. Eaves[1] and M. Hopkinson[2]

[1] School of Physics and Astronomy, University of Nottingham, Nottingham NG7 2RD, UK
[2] Dept. of Electronic and Electrical Engineering, University of Sheffield, S3 3JD Sheffield, UK

Abstract. Using a combination of optical, electrical and magneto-tunnelling measurements on resonant tunnelling diodes incorporating a Ga(AsN) quantum well, we demonstrate that the conduction band states of Ga(AsN) undergo a marked change with increasing N-content. The abrupt change in the electronic properties of Ga(AsN) differs significantly from the smoother variation with alloy composition observed in other alloy material systems, such as (InGa)As. The incorporation of N in GaAs gives rise to a qualitatively different type of alloy phenomena: isolated N atoms and N-clusters act to localise the extended Bloch states of GaAs at characteristic resonant energies, thus breaking up the conduction band into highly non-parabolic energy-wavevector dispersion relations.

Introduction

Research on dilute Ga(AsN) alloys has now become an active area in semiconductor physics due to the unusual electronic properties of this material system. The electronegativity of the N atoms combined with the stretching and compressing of neighbouring bonds in GaAs results in a strong perturbation of the band structure properties of the host crystal. An important manifestation of this perturbation is a huge band gap bowing with increasing N-content and a strong red-shift of the band gap, of interest for long wavelength opto-electronics [1].

Despite many years of research in this topical field, the nature of the electronic states of dilute Ga(AsN) alloys is still hotly disputed. Various models have been proposed to describe how the incorporation of N modifies the conduction band properties of GaAs. Does the band structure result from the formation of a N-related impurity band [2], from multi-valley coupling effects [3] or from the admixing and hybridization of the band states of GaAs with isolated N atoms [4] and/or N-clusters [5]?

In this work, we probe the band structure properties of Ga(AsN) by using a combination of optical and electrical measurements on resonant tunnelling diodes (RTDs) incorporating a Ga(AsN) quantum well (QW). We demonstrate that the conduction band states of the Ga(AsN) layer undergo a marked change with increasing N-content. The abrupt change in the electronic properties of Ga(AsN) differs significantly from the smoother variation with alloy composition observed in other alloy material systems, such as (InGa)As. We show that the incorporation of N in GaAs gives rise to a qualitatively different type of alloy phenomena: isolated N atoms and N-clusters act to localise the extended Bloch states of GaAs at characteristic resonant energies, thus breaking up the conduction band into highly non-parabolic energy-wavevector dispersion relations [6–7].

1. Experiment

Our samples were grown by molecular beam epitaxy on (100)-orientated n-type GaAs substrates. In our RTDs, a 8 or 10 nm $GaAs_{1-y}N_y$ layer ($y = 0$, 0.08, 0.2, 0.43, 0.93, 1.55%) is embedded between two 6 nm $Al_{0.4}Ga_{0.6}As$ tunnel barriers. Undoped GaAs spacer layers, each of width 50 nm separate the $Al_{0.4}Ga_{0.6}As$ barriers from n-doped GaAs layers. In all samples, undoped GaAs spacer layers, each of width 50 nm, separate the $Al_{0.4}Ga_{0.6}As$ barriers from n-doped GaAs layers in which the doping concentration is increased from $2\times10^{17}\,cm^{-3}$, close to the barrier, to $2 \times 10^{18}\,cm^{-3}$. The thickness of these two n-doped GaAs layers are 50 nm and 500 nm, respectively, in the outer layers of the structure. The samples were processed into circular mesas with diameter of 100 and 200 microns, with a ring shaped top contact to allow optical access for current-voltage, $I(V)$, measurements under illumination and for photoluminescence (PL) and photocurrent (PC) studies. The excitation source for the optical studies was a He-Ne laser or a tungsten-halogen lamp, dispersed by a 0.25 m monochromator. The PC signal was recorded using lock-in techniques.

2. RTDs incorporating Ga(AsN)

As shown in Figure 1, when we compare the $I(V)$ curves of the control sample ($y = 0\%$) and of the sample with $y = 0.08\%$, we find that the resonance E_0 due to electrons tunnelling into the lowest quasi-bound state of the QW is replaced by two main features, E_{0-} and E_{0+}. These are attributed to electron tunnelling into the hybridized subbands of the $GaAs_{1-y}N_y$ QW. A further increase of y above 0.2% strongly quenches the current and shifts to higher biases the threshold voltage at which the current increases rapidly.

The disappearance of the resonances in samples with large y is likely to be due to increasing disorder in the system. In the absence of disorder, both the energy and the in-plane momentum of the electron are conserved in the tunnelling process; these are the conditions required to observe a peak in the $I(V)$ curve. The destruction of translational symmetry due to alloy disorder in the $GaAs_{1-y}N_y$ layer tends to break the momentum conservation condition and smears out the resonances, as is observed even for $y = 0.08\%$. Under optical excitation the current and the resonances are partly recovered. In particular, the features in the $I(V)$ of the sample with $y = 0.08\%$ are strongly enhanced (see dotted line in Fig. 1). This enhancement is attributed to to the effect on the current of hole recombination with majority electrons tunnelling in the QW [6].

Figure 2 shows the dependence on the light excitation energy of the intensity of the photocurrent (PC) signal. The PC spectra of all structures show an enhancement in current at high energies ($> 1.5\,eV$), which arises from carriers photocreated in the GaAs layers on each side of the barriers and

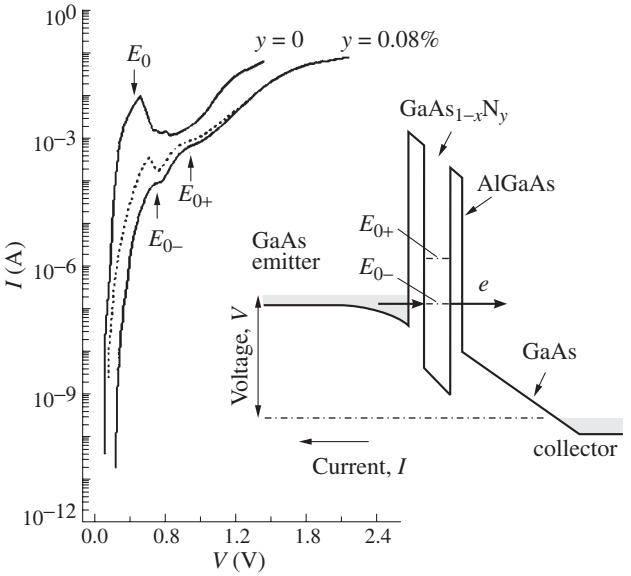

Fig. 1. Current-voltage $I(V)$ curves at $T = 4.2$ K for RTDs incorporating a $GaAs_{1-y}N_y$ QW layer. The dotted line is the $I(V)$ curve under light excitation for the RTD with $y = 0.08\%$. The diode was excited with above-bandgap laser light (633 nm) and power densities of about 10 W/cm^2. The inset sketches the conduction band profile of our RTDs under applied bias.

QW, and a weaker band, labelled band A, which shifts to low energy with increasing y. Band A results from the effect on the tunnel current of carriers when they are photo-created in the $GaAs_{1-y}N_y$ QW. The intensity of band A is determined by the interband optical absorption of the QW and provides us with a means of investigating how the band-edge absorption of $GaAs_{1-y}N_y$ changes with increasing y. Data in Figure 2 show that this shifts to lower energy and broadens considerably when the N-content is increased above about 0.1%.

Electrons and holes injected and/or photo-created in the $GaAs_{1-y}N_y$ layer can also recombine to produce a strong photoluminescence (PL) signal. Our low-temperature ($T = 4.2$ K) PL spectra show that the N-related PL emission is red-shifted relative to the corresponding PC band and that the red shift, referred to as the Stokes shift, increases significantly for y larger than 0.08% (see inset of Fig. 2).

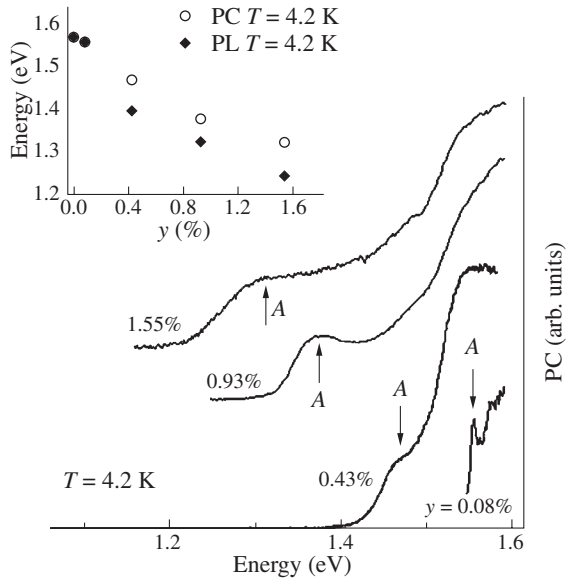

Fig. 2. Photocurrent (PC) spectra at $T = 4.2$ K. The vertical arrow indicates the energy peak position of band A due to the interband optical absorption of the $GaAs_{1-y}N_y$ QW. The inset shows the y-dependence of the peak energy position of band A and of the QW N-related photoluminescence (PL) emission.

The disappearance of the resonances in $I(V)$ and the significant energy broadening and Stokes shift of the optical lines for increasing y indicate that the $GaAs_{1-y}N_y$ QW layer undergoes a significant change in character with increasing N-content. This behaviour, which differs from the smoother dependence with varying alloy composition observed in other alloy material systems, such as (InGa)As, indicate an unusual and marked transition of the electronic properties from band-like to strongly disordered at high y.

3. Break-up of the conduction band

We use magneto-tunnelling spectroscopy (MTS) to probe in further detail the electronic properties of $GaAs_{1-y}N_y$. Our resonant tunnelling and optical spectroscopy experiments at zero magnetic field described in the previous section allow us to probe the bound states of the $GaAs_{1-y}N_y$ QW layer around the wavevector $k = 0$, but they do not provide the k-dependence of the energies of the QW subband states. In a MTS experiment, a magnetic field B is applied perpendicular to the current direction. Varying the intensity of B allows us to tune an electron to tunnel into a given k-state of the well; since the voltage tunes the energy, ϵ, by measuring the voltage position of the resonances in $I(V)$ as a function of B, we can map out the $\epsilon(k)$ dispersion relations of the $GaAs_{1-y}N_y$ QW [6].

Figure 3 shows grey-scale contour plots of the value of the differential conductance $G = dI/dV$ as a function of energy and wavevector derived from a simple analysis of the MTS measurements for two QWs, one with $y = 0.08\%$ and QW width, $L = 8$ nm, and the other with $y = 0.2\%$ and $L = 10$ nm. The white stripe-like regions in the plots of Figure 3 correspond to minima of G just beyond the resonant peak in the $I(V)$ curves. The brightness and width of these stripes provides information about the character, impurity- or band-like, of the states in the $GaAs_{1-y}N_y$ QW, and the form of the $\epsilon(k)$ curves.

The $\epsilon(k)$ curves reveal energy regions of anticrossing (indicated by horizontal arrows in Figure 3) and indicate that the localized states associated with isolated N atoms and N-clusters admix and hybridize with the subband states of the QW, thus breaking up the conduction band at characteristic resonant energies. The hybridisation between the Γ-conduction band states and the localised N-related energy levels gives the QW states of $GaAs_{1-y}N_y$ a partly Γ-character over a wide energy range, and allows electrons to tunnel into them from the GaAs emitter accumulation layer, where the band states have a pure Γ-character. At ϵ and k values for which the Γ-character of the QW states is very small, electron resonant tunnelling from the emitter is negligible so no negative differential conductance occurs; these regions appear as black on the grey-scale plots of Figure 3.

In Figure 3, for $y = 0.08\%$, the form of the $\epsilon(k)$ curves can be accounted for by a simple band anticrossing model which considers the admixing and hybridisation of the extended QW subband states of GaAs with the localised single N-impurity level [4, 6]. The weakening of the E_{0-} and E_{1-} resonances at

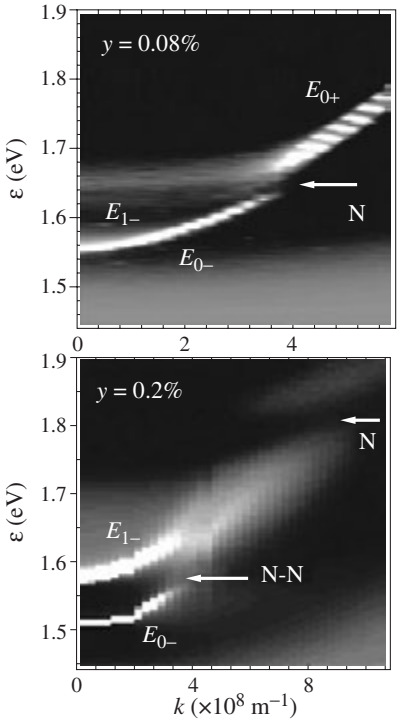

Fig. 3. Grey-scale plots of the differential conductance G vs ϵ and k as derived from MTS measurements for $y = 0.08\%$ and 0.2%. The bright stripes correspond to regions of low G. The energy position of the lowest subband E_{0-} at k= 0 is derived from the measured energy position of the N-related PC band at 4.2 K and is plotted relative to the top of the valence band.

large k is consistent with the strongly localised character of the lowest hybridised subband states of the $GaAs_{1-y}N_y$ QW layer at energies close to those of isolated N atoms; in contrast, the strong enhancement of the E_{0+} resonance at large k and the corresponding increase of the energy-wavevector dispersion indicate that with increasing k, the E_{0+} subband states become more delocalized in real space, i.e. they acquire an increasing Γ-character.

For $y = 0.2\%$, the $\epsilon(k)$ dispersion relations reveal two energy regions of anticrossing at around 1.6 eV and 1.8 eV. We believe that for this sample, the subband states of the QW admix and hybridise not just with isolated N atoms, but also with the localized energy states associated with N-N pairs that are resonant with the conduction band states of GaAs [5, 7]. These act to break-up the $\epsilon(k)$ curves further.

For y larger than 0.2%, the measured G (V) curves show no resonances and are almost unaffected by magnetic fields up to the available field of 14 T. In this case, it is likely that the isolated N atoms and N-clusters completely destroy the translational symmetry required for a well-defined k-vector and $\epsilon(k)$ dispersion relations in the QW.

4. Conclusion

We have shown that the electronic properties of dilute nitride $GaAs_{1-y}N_y$ alloys undergo a rapid change with increasing N-content. Isolated N atoms and N-N pairs tend to reduce the band-like character of the electronic states and break up the energy-wavevector dispersion relations even at values of y as low as 0.2%. Clustering effects account for the rapid enhancement of localization phenomena, which are manifest in both our optical and transport properties for y greater than 0.1%.

For low y, our MTS measurements allowed us to probe the $\epsilon(k)$ curves of the hybridised subbands of $GaAs_{1-y}N_y$ and to demonstrate that the admixing and hybridisation of the extended GaAs conduction band states with the localised isolated N atoms and N-N pairs cause a splitting of the conduction band into highly non-parabolic hybridised subbands, thus validating band-anticrossing models [4–6]. Of particular interest is the formation of a fully developed energy gap between the hybridised subbands and the unusual form of the lower energy subband in which an inflection point occurs in $\epsilon(k)$ (see Figure 3). We have proposed that this band structure could be tailored by N-composition and/or quantum confinement [6], and exploited to realise a new type of non-linear device in which electrons are accelerated by an electric field up to and beyond the inflection point, thus leading to a negative differential drift velocity effect [8], which has a fundamentally different physical origin compared to that occurring in transferred-electron devices [9] and superlattice heterostructures [10]. In a broader context, the combination of N composition and quantum confinement could dramatically increase the power and scope of band structure engineering as a tool for the design of a new generation of electronic devices.

Acknowledgements

This work is supported by the Engineering and Physical Sciences Research Council. We are grateful to R. Airey and G. Hill who processed our samples, and to J. Ibàñez, S. Healy, A. Lindsay, E. P. O'Reilly and D. Maude for useful discussions.

References

[1] Special issue on "Dilute Nitrides", *J. of Phys.: Cond. Matter*, **16** (2004).
[2] Y. Zhang *et al*, *Phys. Rev. B*, **61**, 7479 (2001).
[3] P. R. Kent *et al*, *Phys. Rev. B*, **64**, 115208 (2001).
[4] W. Shan *et al*, *Phys. Rev. Lett.*, **44**, 810 (1999).
[5] A. Lindsay *et al*, *Phys. Rev. Lett.*, **93**, 196402 (2004).
[6] J. Endicott *et al*, *Phys. Rev. Lett.*, **91**, 126802 (2003).
[7] A. Patanè *et al*, submitted to *Phys. Rev. B* (2005).
[8] A. Patanè *et al*, submitted to *Phys. Rev. Lett.* (2005).
[9] A. J. B. Gunn, *Solid State Comm.*, **88**, 1 (1963).
[10] L. Esaki and R. Tsu, *IBM J. Res. Dev.*, **14**, 61 (1970).

13th Int. Symp. "Nanostructures: Physics and Technology"
St Petersburg, Russia, June 20–25, 2005

Direct observation of 1D surface screening and domain boundary structure on Ge(111) surface by LT STM

P. I. Arseev, N. S. Maslova[1], V. I. Panov[1], *S. V. Savinov*[1] and C. Van Haesendonck[2]

[1] Moscow State University, 119992 Moscow, Russia
[2] Laboratory of Solid-State Physics and Magnetism, University of Leuven, B3001 Heverlee, Belgium

Abstract. In this work we present the results of low temperature STM investigation of clean Ge(111) surface. We report for the first time STM observation of 1D surface screening. The model of domain boundary formation is proposed based on real space STM images.

Introduction

The (111) surfaces of Ge is among the most widely studied elementary semiconductor surfaces. There are some features of this surface which are presently well established. Among them are the 2×1 surface reconstruction corresponding to π-bonded chain model with buckling [1, 2, 3]. Some properties are, in opposite, not clear yet. For example, there is no clear understanding of 2×1 reconstructed surface electronic properties which should somehow reveal 1D character.

1. Experimental

In this work we present the results of low temperature STM investigation of clean Ge(111) surface. The samples under investigation were cut from heavily doped (resistivity 1 mΩcm) Ge single crystal with n-type bulk conductivity. The doping element was phosphorus, which is shallow impurity with ionization energy 13 meV, the doping ratio was rather high, about $8 \times 10^{18}\,\mathrm{cm}^{-3}$. The samples were $1.5 \times 1.5 \times 3\,\mathrm{mm}^3$ slabs with long axis aligned in [111] direction. Samples are cleaved in situ after the whole system is cooled down to LH temperature. The details of cleaving procedure and experimental STM setup are described elsewhere [4]. After cleavage high quality mirror like Ge(111) surface is exposed to STM tip for imaging and spectroscopy. Typical STM images of Ge(111) surface are depicted on Fig. 1 for different values of tunneling bias voltage applied to the sample, which means that filled (empty) states image are taken at negative (positive) bias. Images Fig. 1(a, c, e) and Fig. 1(b, d, f) are empty and filled states images respectively. Images Fig. 1(a, c) were acquired with bias voltage corresponding to the band gap. All images reveal ordered chain-like surface structure with threefold symmetry, which in case of Ge(111) surface is attributed to 2×1 reconstruction with π-bonded chains [2]. Boundary between surface domains, formed by slightly different chain rows arrangement, are visible and has a clearly resolved elementary (atomic size) structure. Domain boundaries segments are running only in three possible directions relative to the dimer stripped rows determined by surface symmetry. Some surface defects and ad-atoms are present on the surface. Remarkably their image at bias voltage inside the band gap range differs drastically from filled/empty states images. We attribute this difference to surface charge screening. One may also notice the changes of domain boundaries elements position from one scan to another. We explain this movement in terms of tip-induced (or scanning-induced) surface charge transfer.

Let us note that with our cleaving procedure we were able to obtain flat areas on Ge(111) surface of at least $1\,\mu\mathrm{m} \times 1\,\mu\mathrm{m}$ in size. Within these areas the defects of cleavage are mostly one or may be two monolayer deep scratches with atomic structure visible at the bottom (see top corners on Fig. 1). Although one may think about scratches as about geometric surface features, their structure on filled/empty STM images is very different. This means that there is strong hybridization of dangling bonds for atoms at the bottom of scratch with bonds of the upper surface layer. The amount of disordered ad-atoms observed at the surface is very small comparing to the data reported in literature [5]. This corresponds to the well known fact that details of cleaving procedure are very important for the quality of surface [6].

Much of Ge(111) surface STM images outlook is caused by the presence of surface states. In situ low temperature cleaving gives us the opportunity to investigate extremely clean surface (partial pressure of the majority of gases is less then 10^{-13} torr) and in these conditions surface states can stay unchanged for a few days. This is a great advantage of LT cleaving comparing to UHV cleaving. At typical UHV conditions ($p \sim 10^{-10}$ torr) intrinsic surface states are largely removed already after 6–7 h [7]. Low rate of surface state degradation has another advantage. We are allowed to wait until our LT setup reaches steady state thermal conditions. That is why no visible thermal drift is detected during STM image acquisition.

2. Discussion

Let us point out some remarkable features of Ge(111) STM images on Fig. 1. First, images which are taken with bias voltage corresponding to band gap demonstrate the effects of localized charge surface screening. The screening, observed on STM images, reflects the perturbation of local density of states because of scattering of electrons, 1D confined along π-bonded chain rows, on surface imperfections.

STM images of all surface defects (impurities, domain boundaries elements etc) have highly asymmetric shape. They have a shape of stripes up to 6 nm long in the direction of π-bonded chain rows, while their width exactly equals to 2x period of surface reconstruction (about 0.7 nm). For asymmetric defect (such as single "knee" of domain boundary, Fig. 1(a, c)) stripe of screening on STM image is also asymmetric along chain row. The screening cloud is localized mainly next to the defect. It smoothly decays with increase of the distance from the domain boundary and abruptly ends at domain boundary. For symmetric defect, like individual surface impurity atom, the screening is symmetric along chain row. Other type of defects, which

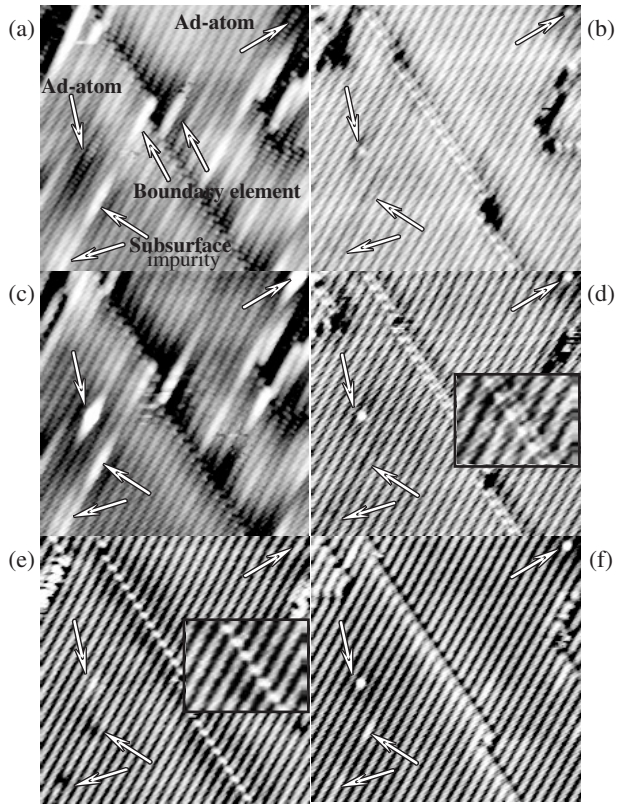

Fig. 1. STM images of Ge(111) surface at different sample bias: (a) +0.3 V, (c) +0.5 V, (e) +1.0 V, (b) −0.3 V, (d) −0.5 V, (f) −1.0 V. Tunneling current set point is 20 pA. Image size is 14 nm. Positions of ad-atoms, subsurface defect and domain boundary elements are shown by arrows. Inserts on (b) and (e) shows zoomed in image of domain boundary.

are rather difficult to classify definitely, in our opinion belongs to a class of subsurface defects of different kind, this can be individual impurities, lattice vacancies etc. In general STM images of these defects are behaving in nontrivial way when changing bias voltage. Also, screening for this type of defects is visible on STM images in a more complicated fashion. It can be seen as a dark stripe right above the defect with bright stripes of two dimer rows surrounding defect or as few elevated dimer rows (Fig. 1a). The reason for this might be complex surface charge distribution in the case of the subsurface defect, which leads to the perturbation of defect-free surface electron density in three (or even more) dimer rows. This statement is supported by images Fig. 1(e, f). In empty state image two "vacancies" in dimer row are visible, while on filled state image two protrusions are located in *neighboring* row.

Domain boundaries are surface defects by their nature, therefore Ge(111) surface look highly disturbed around domain boundary (Fig. 1(a, c)). Almost every π-bonded chain row differs from its neighbors. We suppose that asymmetric screening directly reflects the spatial structure of the surface states. For π-bonded chains model of 2×1 Ge(111) surface reconstruction with buckling two bands of surface states appear in the band gap area: filled π-band and empty π^*-band. The latter one lies well inside the bulk gap much over the surface Brillouin zone and therefore π^* states should dominate tunneling current (if any) for bias voltages less than band gap value [8].

One more striking STM observation on Ge(111) surface is the observation of fine structure of domain boundaries (Fig. 2).

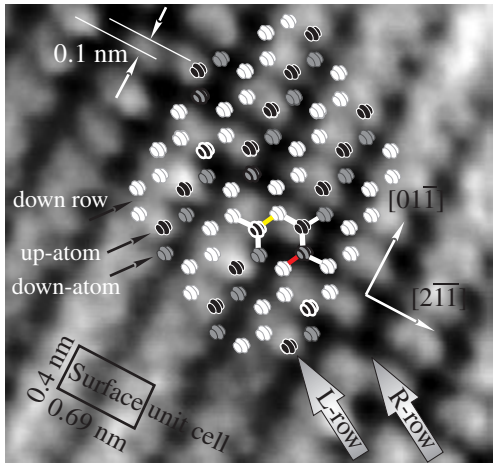

Fig. 2. The model structure of domain boundary on Ge(111)-(2×1) surface. Image size is 4 nm. Bias voltage is 0.05 V, current set-point in 20 pA. Down-row as well as up/down atoms of up-row are marked by arrows. Crystallographic directions and surface unit cell are shown. The meaning of L-row and R-row marks is explained in the text. Yellow and red lines show specific atomic bonds at the domain boundary, while white lines show typical for (2×1) reconstruction atomic bonds.

Some details concerning atomic arrangement of 2×1 reconstructed Ge(111) surface in vicinity of the domain boundary are shown on Fig. 2 also. Positions of up/down-atoms are marked with black/gray circles, while atoms in the second layer are marked by white circles. Model atomic lattice is shown in configuration corresponding to right-right domain boundary [9]. At small bias voltage of any sign individual dimers at the very edge of domain boundary are clearly resolved (see also Fig. 1(a, c)). Dimer rows which meet each other at domain boundary are shifted in $[2\bar{1}\bar{1}]$ direction by a half of inter-row distance (~ 0.7 nm/2). Dimers in the rows at different sides of domain boundary are also shifted in $[01\bar{1}]$ direction by approximately one fourth of inter-domain distance (0.1 nm). These two shifts cause a visual knee of dimer row at the boundary. Few more (3–4) dimers in every row are influenced by domain boundary. At the right side of the domain boundary dimer rows are slightly depressed and at both sides the local STM image contrast is much higher than far from the boundary. This causes the effect of "rows" visually running along domain boundary. The two of these rows, nearest to the domain boundary (let us call them L(eft) and R(ight) rows, Fig. 2) are clearly distinguishable from other ones. At the left side the highest density of states asymmetrically distributed inside L-row is observed. At the right side the lowest density of states areas are positioned between dimers in the R-row. When tunneling bias voltage goes to the range of filled states both L and R rows are visible. The maxima of electronic density are located exactly above dimers (insert on Fig. 1b). When bias voltage corresponds to band gap screening stripes structure is superimposed on the image of domain boundary (Fig. 1(a, c)) which is mainly the same as at low bias voltage (Fig. 2). When tunneling bias voltage is in the range of empty states only line corresponding to R-row is visible. The maxima of electronic density are located between dimers (insert on Fig. 1e).

In π-bonded chains with buckling surface reconstruction model some charge transfer occurs from down atom to up atom

in the chain. Consequently, it is possible to use simplified assumption that down atoms are visible on STM images when imaging empty states, while up atoms are visible in filled states. The model lattice is aligned with high resolution STM image using this assumption. It is clear from Fig. 2 that if L and R-"rows" are visible on filled states STM images, then protrusions between L and R dimers on Fig. 2 must correspond to up-atom also.

Taking into account the behavior of STM images at different bias we can conclude the following. Up-atom from left side of the boundary and down-atom from the right side (marked as black/thick white and gray/thick black respectively on Fig. 2 together with corresponding atomic bonds) are changing their position and/or bonding. They both are making bonds to atoms in down rows in second surface bilayer. These bonds are not normal ones for Ge(111)-(2×1) surface, because bonds length and angles are different form those in π-bonded rows. As a result of changes in electronic structure at the domain boundary the up-atom in R-"row" is imaged at both polarities of bias voltage, while up-atom at the boundary is not resolved on filled/empty states STM images. The main advantage of proposed model is that it implies only relatively small spatial atomic rearrangement at the boundary. Second, there are no extra dangling bond at DB, which means that this structure should be stable.

Acknowledgements

The work was partially supported by RFBR grant No. 03–02–16807 and by the grant for the leading scientific schools support No. 1604–2003–2. Support from Samsung Corp. is gratefully acknowledged.

References

[1] R. M. Tromp, L. Smith and J. F. van der Veen, *Phys. Rev.*, **B30**, 6235 (1984).
[2] K. C. Pandey, *Phys. Rev. Lett.*, **47**, 1913 (1981).
[3] N. Takeuchi, A. Selloni, A. I. Shkrebtii and E. Tosatti, *Phys. Rev.*, **B44**, 13 611 (1991).
[4] S. I. Vasil'ev, S. I. Oreshkin, V. I. Panov, S. V. Savinov *et al*, *Instrum. and Experim. Technique*, **4**, 40, 566 (1997).
[5] R. M. Feenstra, G. Meyer, F. Moresco and K. H. Rieder, *Phys. Rev.*, **B64**, 081306(R) (2001).
[6] G. W. Gobeli and F. G. Allen, *Phys. Rev.*, **1A**, 137, A245 (1965).
[7] D. E. Eastman and W. D. Grobman, *Phys. Rev. Lett.*, **28**, 21, 1378 (1972).
[8] John E. Northrup and Marvin L. Cohen, *Phys. Rev.*, **B27**, 10, 6553 (1983).
[9] H. Hirayama, N. Sugihara and K. Takayanagi, *Phys. Rev.*, **B62**, 11 (2000).

13th Int. Symp. "Nanostructures: Physics and Technology"
St Petersburg, Russia, June 20–25, 2005

Near-field optical vortexes at nanostructured metallic films

A. A. Ezhov, S. A. Magnitskii, N. S. Maslova, D. A. Muzychenko, A. A. Nikulin and V. I. Panov
Physics Department of M.V. Lomonosov Moscow State University, 119992 Moscow, Russia

Abstract. The scattering of linearly polarized monochromatic light by a small protrusion on a metal surface is analyzed within the framework of perturbation theory. It is shown that even at normal incidence of light slight deviations of the protrusion shape from a circularly symmetric one can lead to formation of optical vortexes in the near-field region. The effect is due to resonant excitation of cylindrical surface plasmon waves. This agrees with the fact that the in-plane near-field intensity distribution experimentally observed by scanning near-field optical microscopy has distinct spiral patterns near metallized nanostructured polymer substrates.

Introduction

For the past few years, phase singularities of optical wave fields has attracted considerable interest in various areas of modern optics. It can be explained partially by the decreasing of the size of the integral optical elements down to the wavelength. Phase singularities can play a significant role during the interaction of the light with the modern advanced nanophotonic structures.

For the time being there are great numbers of different techniques to produce the optical field with a screw dislocation (optical vortex) [1,2]. An introduction of the scanning near-field optical microscopy (SNOM) [3] allowed to investigate the phase singularities with the sub-wavelength resolution. Phase singularities of optical fields in waveguide structures [4] and in the focal region of a lens [5] have been observed by means of interferometric SNOM as yet.

Recently, the results of SNOM investigation of the three-dimensional (3D) intensity distribution in the proximity of the nanocylinders show a distinct spiral patterns of the in-plane near-field fringes [6]. Unexpected patterns with a spiral symmetry were observed only for metallized samples contrary to circular patterns observed for bare ones (see Fig. 1). Nanocylinders are placed onto the polymer substrate and manufactured by means of double replication from silicon matrix made by electronic beam lithography. Some of the nanocylinders were covered by gold-palladium layer with the thickness 20–30 nm. The covering was realized by means of the method which allowed to avoid the nonuniformity of metal film caused by shadow effect.

In order to interpret the obtained experimental results on a qualitative level we consider a simple model that can be treated analytically with the use of perturbation theory.

1. The model

A linearly polarized plane wave with frequency ω is incident from vacuum at a normal to the boundary of a semi-infinite metal occupying the half-space $z<Z(\rho,\varphi)$, where ρ, φ, z are the cylindrical coordinates and the function $Z(\rho,\varphi)$ describes a nearly flat surface having a single protrusion with height L and radius R:

$$Z(\rho,\varphi) = Lf(\rho/R)\left[1+\gamma g(\varphi)\right], \qquad (1)$$

where $f(x<1)>0$, $f(x\geq 1)\equiv 0$ and $g(\varphi)$ represented by the Fourier series: $g(\varphi)=\sum_{n\neq 0} g_n e^{in\varphi}$ with $g_{-n}=g_n^*$. We suppose that $-\mathrm{Re}\,\varepsilon(\omega)\gg 1$, where ε is the dielectric constant of the metal. The parameters of the boundary defect are assumed to meet the following conditions

$$L \ll R \ll \frac{c}{\omega\sqrt{|\varepsilon|}}, \quad \gamma \ll 1. \qquad (2)$$

At $z=Z(\rho,\varphi)$ we use the impedance boundary conditions:

$$\mathbf{E}_t = \zeta\,[\mathbf{H}_t\,\mathbf{n}], \qquad (3)$$

where $\mathbf{E}$ and $\mathbf{H}$ are the electric and magnetic fields at frequency ω, respectively, $\zeta=\sqrt{1/\varepsilon}$, $\mathbf{n}$ is the unit vector normal to the surface, the subscript t denotes the value of the tangential vector component taken at $z=Z(\rho,\varphi)$.

At $z\geq Z(\rho,\varphi)$ the field $\mathbf{F}^{(\mathrm{s})}$ (here $\mathbf{F}$ stands for either $\mathbf{E}$ or $\mathbf{H}$) associated with the excitation of surface plasmon waves is sought in the form $\mathbf{F}^{(\mathrm{s})}=\mathbf{F}^{(\mathrm{s})}(\rho,\varphi)e^{-\kappa_{\mathrm{s}}z}$, where $\mathbf{F}^{(\mathrm{s})}(\rho,\varphi)$ is expanded in the Fourier series $\mathbf{F}^{(\mathrm{s})}(\rho,\varphi)=\sum_n \mathbf{F}_n(\rho)e^{in\varphi}$, $\kappa_{\mathrm{s}}=\sqrt{q_{\mathrm{s}}^2-k^2}$, $k=\omega/c$ and q_{s} is the root of the equation $\Omega(q_{\mathrm{s}})=\omega$ with $\Omega(q)$ being the "unperturbed" surface-plasmon dispersion law for a perfectly flat boundary. The four

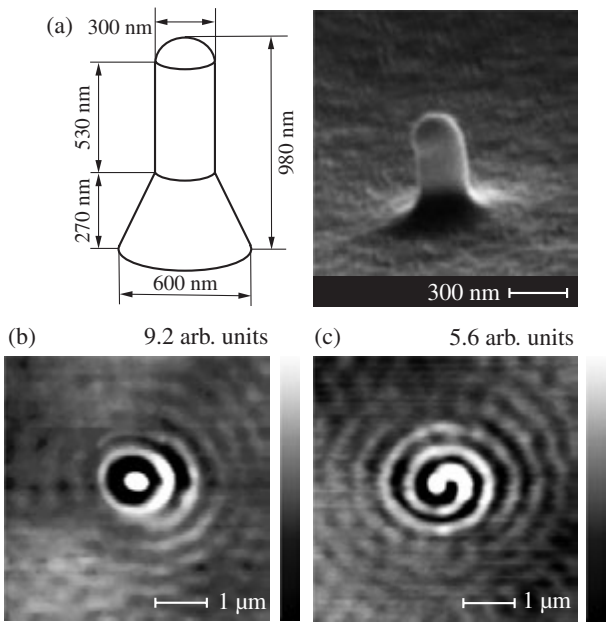

Fig. 1. The details of the SNOM investigation of the 3D intensity distribution in the proximity of the metallized and bare polymer nanocylinders. Figure (a) schematic diagram and the scanning electronic microscope image of the nanocylinder; (b) experimentally obtained intensity distribution near the bare nanocylinder at the height λ above the top of the nanocylinder; (c) experimentally obtained intensity distribution near 25 nm thick gold-palladium layer coated polymer nanocylinder at the same height.

of six vector components of $\mathbf{E}_n(\rho)$ and $\mathbf{H}_n(\rho)$ can be explicitly expressed from the Maxwell equations through the remaining two, $E_{z,n}(\rho)$ and $H_{z,n}(\rho)$.

At $\rho > R$ the functions $E_{z,n}(\rho)$ and $H_{z,n}(\rho)$ correspond to the normal field components in a travelling (diverging) cylindrical surface-plasmon wave with the wave number q_s. Hence,

$$E_{z,n}(\rho > R) = C_n H^{(1)}_{|n|}(q_s \rho)\,, \tag{4}$$

$$H_z(\rho > R, n) \equiv 0\,, \tag{5}$$

where $H^{(1)}_{|n|}(x)$ is the Hankel function of first kind and C_n is a constant. Thus the problem reduces to finding the functions $E_{z,n}(\rho)$ and $H_{z,n}(\rho)$ within the interval $0 \le \rho \le R$.

Upon using the boundary conditions (3), we approximate the exponential factors in the incident and reflected waves at $z = Z(\rho, \varphi)$ by two lowest-order terms in their Taylor-series expansions at $z = 0$: $e^{\pm ikZ(\rho,\varphi)} \approx 1 \pm ikZ(\rho, \varphi)$ and limit ourselves to the first order in the small parameter kL. Within the chosen accuracy we obtain that $F_{z,n\neq\pm1}(\rho) = 0$, meanwhile $F_{z,n=\pm1}(\rho)$ satisfy the following set of differential equations (the prime denotes the first derivative of a function):

$$\alpha E'_{z,n}(\rho) + \frac{in\beta}{\rho} H_{z,n}(\rho) + \mu_n(\rho) E_{z,-n}(\rho) = i s_n(\rho)\,, \tag{6}$$

$$\frac{in\alpha}{\rho} E_{z,n}(\rho) - \beta H'_{z,n}(\rho) + in\nu_n(\rho) E_{z,-n}(\rho) = n s_n(\rho)\,, \tag{7}$$

where $n = \pm 1$, $0 \le \rho \le R$, $\alpha = i\zeta k - \kappa_s$, $\beta = ik - \zeta\kappa_s$, $\mu_{\pm1}(\rho) = \delta_\pm f'(\rho/R)/R$, $\nu_{\pm1}(\rho) = 2\delta_\pm f(\rho/R)/\rho$, $s_{\pm1}(\rho) = (1 + \gamma g_{\pm2}) kLq_s^2 E_0 f(\rho)$, $\delta_\pm = \gamma g_{\pm2} Lq_s^2$ and E_0 is the electric field amplitude in the incident wave. The analysis of the relative magnitude of the coefficients in Eqs. (6),(7) shows that $\left|E_{z,n}(\rho<R)\right| \gg \left|H_{z,n}(\rho<R)\right|$. Taking this into account, we set $H_{z,n}(\rho<R) = 0$ to provide continuity of the field components at $\rho = R$. On solving Eqs. (6),(7) for the case $f(x) = 1 - x$, we use a polynomial approximation for the unknown functions $E_{z,\pm1}(\rho)$ at $\rho<R$:

$$E_{z,\pm1}(\rho) \approx \left(A_{\pm1}\rho + B_{\pm1}\rho^2\right) E_0\,, \tag{8}$$

where the constants $A_{\pm1}$ and $B_{\pm1}$ can be found simultaneously with $C_{\pm1}$ from Eqs. (6),(7) and the sewing conditions at $\rho = R$. The corresponding explicit expressions are omitted for brevity sake.

2. Results and conclusions

For the found solution a first-order vortex occurs in the in-plane distribution of the tangential component of the time-averaged Poynting vector $\mathbf{S} = \frac{c}{8\pi}\mathrm{Re}\left[\mathbf{E}\,\mathbf{H}^*\right]$ taken at the metal boundary $z = Z(\rho, \varphi)$. The projection of $\mathbf{S}$ onto the plane $z = 0$ describes the energy flow in the travelling surface-plasmon wave resonantly excited by the incident light due to the presence of the surface defect. In our model we obtain that $\left|S_x^{(s)}\right| \gg \left|S_y^{(s)}\right|$, where the x-axis is chosen to be parallel to the electric field $\mathbf{E}_0$ in the incident plane wave, whereas the spatial dependence of $S_x^{(s)}$ is given by the expression:

$$S_x^{(s)} \propto e^{-\kappa_s z}\,\mathrm{Re}\left\{H_1^{(1)}(q_{sR})\left(\sin\varphi + \gamma\,\mathrm{Im}\,g_2\, e^{i\varphi}\right)\right\}. \tag{9}$$

According to Fig. 2, the first-order vortex occurs in the in-plane spatial dependence of $S_x^{(s)}(\rho, \varphi, z = Z(\rho, \varphi))$ at $\gamma \neq 0$.

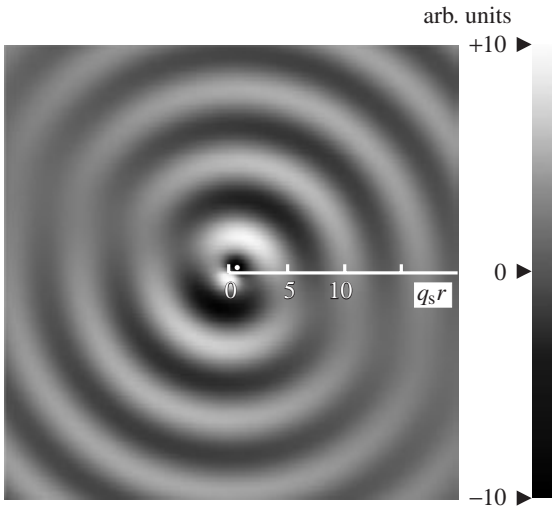

Fig. 2. Density plot of the tangential Poynting vector component $S_x^{(s)}$ at the metal surface as a function of the dimensionless radius $q_s\rho$ and polar angle φ ($\gamma = 0.5$, $g_2 = i$).

In summary, it is shown that the scattering of monochromatic and linear polarized light by a small protrusion on a metal surface leads to resonant excitation of cylindrical surface plasmon waves with formation of optical vortexes in the near-field region even at normal incidence, if small deviations from circular symmetry of protrusion shape are taken into account. This agrees with the fact that the in-plane near-field intensity distribution experimentally observed by SNOM has distinct spiral patterns for metallized nanostructured polymer substrates contrary to circular patterns observed for bare substrates.

Acknowledgements

The work was partially supported by RFBR grants 03-02-16807, 04-02-16847 and 04-02-17059 and by the grants for the leading scientific schools supporting 1604.2003.2 and 1909.2003.2.

References

[1] M. V. Berry and J. F. Nye, *Proc. Royal Soc. (London)*, **A336**, 165 (1974).

[2] E. Engel, N. Huse, T. A. Klar and S. W. Hell, *Appl. Phys.*, **B 77**, 11 (2003).

[3] D. W. Pohl, W. Denk and M. Lanz, *Appl. Phys. Lett.*, **44**, 651 (1984).

[4] M. L. M. Balistreri, J. P. Korterik, L. Kuipers and N. F. van Hulst, *Phys. Rev. Lett.*, **85**, 294 (2000).

[5] J. N. Walford, K. A. Nugent, A. Roberts and R. E. Scholten, *Opt. Lett.*, **27**, 345 (2002).

[6] M. V. Bashevoy A. A. Ezhov, S. A. Magnitskii *et al*, *Int. J. Nanoscience*, **3**, 105 (2004).

13th Int. Symp. "Nanostructures: Physics and Technology"
St Petersburg, Russia, June 20–25, 2005

Phonon-induced photocurrent response in Si doped GaAs/InGaAsP quantum well heterostructures

V. Ya. Aleshkin[1], A. V. Antonov[1], V. I. Gavrilenko[1], L. V. Gavrilenko[1] and B. N. Zvonkov[2]

[1] Institute for Physics of Microstructures, 603950 Nizhny Novgorod GSP-105, Russia
[2] Physical-Technical Research Institute of Nizhny Novgorod State University, 603950 Nizhny Novgorod, Russia

Abstract. We have discovered the peak in the photocurrent spectra of InGaAsP/GaAs:Si multiple quantum well heterostructure resulted from the interaction of the ground donor state with the optical phonons. The peak position and spectral width are shown to be weakly affected by the donor location in the quantum well.

Introduction

The asymmetric narrow peak was observed in the shallow impurity photocurrent and absorption spectra in p-Si corresponding to the longitudinal optical phonon energy [1-3]. It is the Fano [4] resonance resulting from the interaction of the ground impurity state with optical phonons. The Fano resonance arises due to the mixing of discrete and continuous states. In the case under consideration the discrete states are the ground impurity one and the optical phonon. When electron absorbs phonon it transmits from discrete state in continuous spectrum one. Due to this interaction a narrow asymmetric peak arises in photocurrent and absorbtion spectra under electron excitation from the ground impurity state at the light absorption. The width of this peak is less then 2 cm^{-2} that allows to accurately measure the longitudinal optical phonon energy. Recently the Fano resonances were observed in n-GaAs and n-InP [5].

In this work we report on the observation of the Fano resonance in the InGaAsP/GaAs heterostructure with doped by Si quantum wells. The low-frequency photocurrent band resulted from electron transitions from the ground impurity state in the quantum well into excited ones and into the first subband continuum proved to be much wider than that in the bulk GaAs, while the Fano resonance peaks in bulk GaAs and the quantum well are almost of the same width. However in the quantum well heterostructure the resonant peak is more symmetric as against that in GaAs and is slightly shifted to the long wavelength region.

1. Experimental results and discussion

The heterostructure under investigation was grown on semi-insulating GaAs substrate by MOVPE epitaxy and consisted of 30 GaAs quantum wells separated by the lattice matched 400 Å $In_{0.1}Ga_{0.9}As_{0.8}P_{0.2}$ barriers. The quantum well width is 200 Å. The central parts of quantum wells were doped by silicon (see Fig.1). The measured by Hall effect surface donor concentration was 3.3×10^{10} cm^{-2} per a quantum well. The photocurrent spectra were measured by means of BOMEM DA3.36 Fourier-transform spectrometer at $T = 4.2$ K.

The measured photocurrent spectrum is given in Fig. 2. Two photocurrent bands are clearly seen. The long wavelength band corresponds to electron transitions from the ground donor state to the excited donor states and to the first subband continuum states. The short wavelength band (around 295 cm^{-1}) corresponds to the Fano resonance. The amplitude and width of the short wavelength photocurrent band is smaller than those of the long wavelength one. From the insert in Fig. 2 one can see

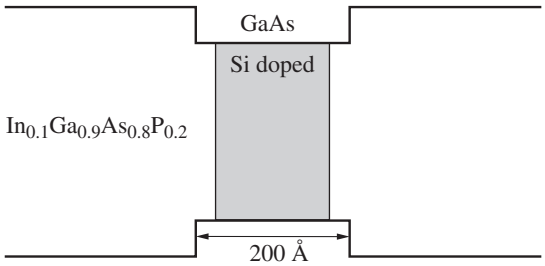

Fig. 1. Sketch of the quantum well heterostructure.

that the shape of photocurrent peak corresponding to the Fano resonance is asymmetric.

The long wavelength photocurrent bands of the quantum well heterostructure and an epitaxial n-type GaAs are shown in Fig. 3. The 7 μm epitaxial layer GaAs is doped by Si with concentration $8.3\cdot10^{14}$ cm^{-3} and the electron mobility is 59000 cm^2 V^{-1} s^{-1} at 77 K. The photocurrent peak around 36 cm^{-1} in the epitaxial GaAs is due to the electron transition from the ground donor state (1S) to the 2P state. The energy corresponding to the 1S-2P transition and the ionization energy (48 cm^{-1}) are shown by arrows in Fig. 3. From Fig. 3 it is clear that the long wavelength band in quantum well heterostructure is greatly wider if compared with that in the epitaxial GaAs. The reason is the dispersion in an impurity position in the quantum well. The donor state spectrum in a quantum well depends on the impurity atom location with respect to heterointerfaces. For example, both the ionization and 2P state energies of an impurity located in a quantum well center are greater then those in a bulk semiconductor, while the ionization energy of impurity localized near heterointerface or in the barriers is less than

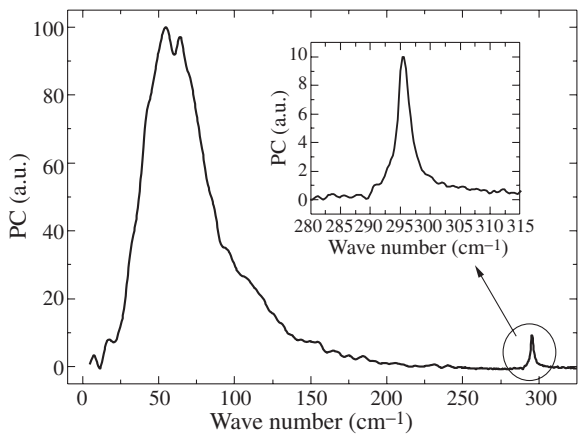

Fig. 2. Photocurrent spectrum of $In_{0.1}Ga_{0.9}As_{0.8}P_{0.2}$/GaAs multiple quantum well structure.

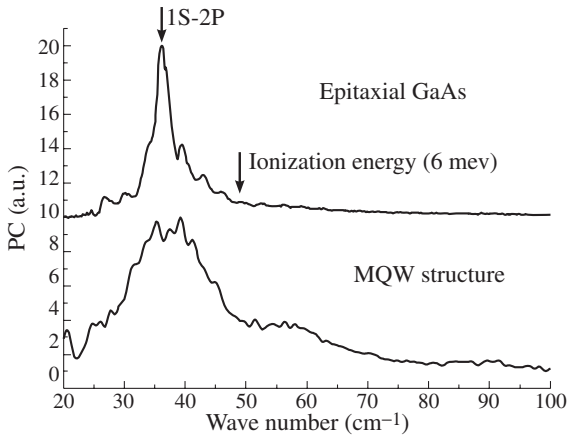

Fig. 3. The long wavelength photocurrent bands of the epitaxial GaAs and the quantum well heterostructure.

that in a bulk GaAs.

From Fig. 3 one can see that the long wavelength photocurrent band in the quantum well heterostructure arises at a smaller wave number than in the epitaxial GaAs. This fact points out to the presence of donors near heterointerfaces. At the short wavelength edge of this photocurrent band there is a peculiarity between 55–60 cm^{-1} (6.82–7.55 eV) that is absent in the epitaxial GaAs. Probably, this peculiarity is due to the ionization of impurities located around the quantum well center where the ionization energy is greater then that in the epitaxial GaAs by 0.8–1.5 meV. Note that oscillations in the photocurrent spectrum of the epitaxial GaAs are due to the interference effects.

The photocurrent spectra around the LO photon energy in the quantum well heterostructure and in the epitaxial GaAs are shown in Fig. 4. The photocurrent peak corresponding to the Fano resonance in the epitaxial GaAs is more asymmetric and is slightly shifted to the the short wavelength region if compared with that in the heterostructure. The full width at half maximum is 2 cm^{-1} in the epitaxial GaAs and 2.5 cm^{-1} in the heterostructure, while these values for the long wavelength photocurrent bands differs more than two times. This fact demonstrates that Fano resonance energy and width are insensitive to the donor ionization energy and peculiarities of the donor states in quantum well. On the contrary, the minimum position of Fano resonance is sensitive to the the donor location in the quantum well. Therefore, the dispersion in donor location smears the minimum and leads to more symmetric peak as one can see in Fig. 4.

Thus, we have demonstrated that measurement of the Fano resonance peak allows to find LO energy in quantum well with good accuracy. Note that optical phonon energy depends on the quantum well deformation in stressed structures. Therefore, this method can be used for estimation of the deformation value.

Acknowledgements

This work was financially supported by RFBR (grant 04-02-17178) and ISTC (grant 2293).

References

[1] H. R. Chandrasekhar, A. K. Ramdas, S. Rodriguez, *Phys. Rev. B* **14**, 2417 (1976).

[2] G. D. Watkins, W. B. Fowler, *Phys. Rev. B* **16**, 4524 (1977).

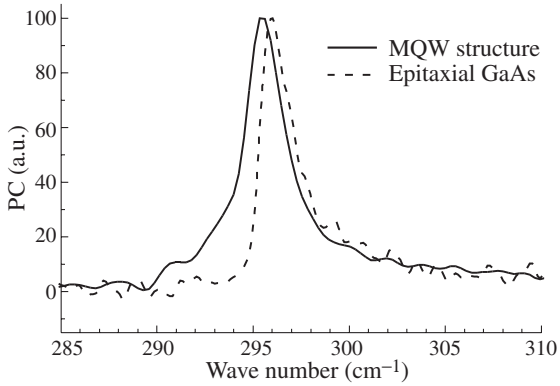

Fig. 4. The photocurrent peaks corresponding to the Fano resonances in the quantum well heterostructure and in the epitaxial GaAs.

[3] R. Galic, D. Braun, F. Kuchar, A. Golubovic, R. Korntner, H. Loschner, J. Butschke, R. Springer, F. Letzkus, *J. Phys. C* **15**, 2923 (2003).

[4] U. Fano, *Phys. Rev.* **124**, 1866 (1961).

[5] K. Jin, J. Zhang, Z. Chen, G. Yang, Z. H. Chen, X. H. Shi, S. C. Shen, *Phys. Rev. B* **64**, 205203 (2001).

13th Int. Symp. "Nanostructures: Physics and Technology"
St Petersburg, Russia, June 20–25, 2005

Size evaluation of free-standing nanocrystaline Si films by using small angle x-ray scattering and Raman spectroscopy

T. Matsumoto[1], M. Kondo[2] and *O. Chikalova-Luzina*[3]

[1] Research and Development Center, Stanley Electric Corporation, Yokohama 225-0014, Japan
[2] National Institute of Advanced Industrial Science and Technology, 1-1-1 Umezono, Tsukuba 305-8568, Japan
[3] Ioffe Physico-Technical Institute, St Petersburg, Russia

Abstract. We report the determination of the average diameter and the size distribution of the free-standing nc-Si films by using small angle x-ray scattering measurements (SAXS). We found that the model of Raman analysis used until now is not appropriate to determine the size of the nanostructure. Based on SAXS results,we shown a correct relation between the average diameter and the peak shift of the Raman spectrum. We obtained the phonon weighting function, which provides the best agreement between the theoretical dependence and the experimental data.

Introduction

Nanocrystalline Si (nc-Si) films are promising material for the fabrication of Si-based light emitting diodes and high efficiency solar cells. To investigate these possibilities, it is necessary to know the nanostructure such as mean diameter. Until now, transmission electron microscopy (TEM) and Raman scattering measurements are usually used as a tool to determine the average size of Si nanostructure. However, these methods have problems in determining the size; the observed region of TEM is restricted to several hundred nanometer when we observe a nanometer structure. For Raman analysis, the size of nanostructure was determined based on the strong confinement model [1,2 3], despite the fact that the validity of this model has not been proved for the nanometer structures.

In this paper, we report the determination of the average diameter and the size distribution of nc-Si films by using small angle x-ray scattering (SAXS). For nc-Si films of which average size was determined by SAXS, we also performed Raman scattering measurements. We found that the strong confinement model is not appropriate to determin the size of the nanometer structure. An appropriate weighting function for the phonon amplitude was determined, and this gives the correct relation between the average diameter and the peak shift of the Raman spectrum.

1. Experimental details

Free-standing nc-Si films were formed by anodization of (100)-oriented p-type silicon wafers with 1–10 Ωcm resistivity in HF-ethanol solution at constant current density of 20 mA/cm^2 for 100 min (thickness about 100 μm).The HF concentrations between 20% and 30% were used to change the diameter of the nanocrystals [4].

SAXS measurements were performed for each sample using a pinhole collimated instruments with a Cu target. Incident x-ray with the wavelength of Cu Kα radiation ($\lambda = 0.154$ nm) was injected perpendicularly to the film plane. Scattered x-ray was detected by an one dimensional position sensitive detector. The scattering intensity were fit by using polydisperse hard spherical nanocrystalline model [5]. From this fitting, the size distribution and the average radius of the nanocrystals were determined. Angular divergence was 0.029 or 0.076 (FWHM).

Raman scattering measurements were performed at room temperature, in vacuum, in a backscattering configuration using 514.5 nm laser light from an argon ion laser and a 50 cm monochromator with a super notch filter which reject the Rayleigh scattering from the sample. The spectral resolution was less than 1 cm^{-1}.

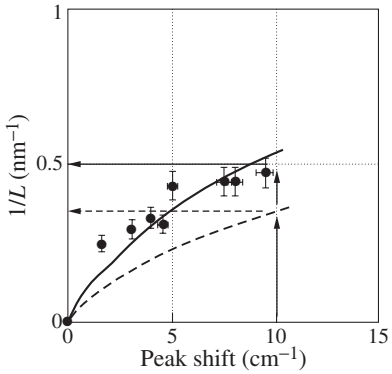

Fig. 1. Raman peak shift versus nanocrystaliine diameter determind by SAXS measurements (solid circles). Solid line presents the theoretical reletionship culculated with the weighting function being $\exp(-3\pi^2 r^2/L^2)$. Dotted lines is a theoretical line deduced from the strong confinement model with the weighting function being $\exp(-8\pi^2 r^2/L^2)$ [2].

Figure 1 shows the experimentally determined points between nanocrystal diameter (L) obtained by SAXS and the magnitude of the Raman shift (solid circles). The clear correlation between these values is observed. The dotted line presents the size of the nanocrystal calculated from the Raman shift on the basis of the model of the strong confinement of optical phonon [1] used until now. It is seen that the model gives a larger average diameter compared to that obtained by SAXS measurements.

2. Theoretical analysis and discussion

An approach to describe the phonon confinement in the volume of the cristallite was put forth by Richter *et al* [1] and used later by Campbell and Fauchet [2].The localization is imposed by replacing the wavefunction of a phonon with the wave vector $\mathbf{q}$ in an infinite perfect crystal by a new wawefunction function through introducing a phonon weighting function. This nanocrystal phonon wavefunctions can be expressed as a superrosition of eigenfunctions found for the infinite crystal which are weighted through the coefficients determined by the weighting function. Hence, the first-order Raman spectrum,

$I(\omega)$, from the cristallite is given by

$$I(\omega) = \int \frac{d^3x|C(0,\mathbf{q})|^2}{[\omega - \omega(\mathbf{q})]^2 + (\Gamma_0/2)^2}. \quad (1)$$

Here, $\omega(q)$ is the phonon dispersion curve, Γ_0 is the natural line width, $C(0,\mathbf{q})$ is the Fourier coefficients obtained from

$$C(0,\mathbf{q}) = \frac{1}{(2\pi)^3}\int d^3r W(\mathbf{r},L)\, e^{-i\mathbf{q}\cdot\mathbf{r}} \quad (2)$$

where $W(\mathbf{r},L)$ is the phonon weighting function. The integration must be performed over the entire Brillouin zone. The relaxation of the $\mathbf{q}$-vector selection rule due to the finit size of crystallite leads to a downshift and broading of the Raman spectrum.

To obtain the relationship between the diameter of the spherical Si microcrysal L and the shift of the Raman spectrum peak, Richter *et al* [1] chose the phonon weighting function $W(\mathbf{r},L)$ to be a gaussian, $\exp(-2r^2/L^2)$ with the phonon amplitude of $1/\exp$ at the boundary of the microcrystall. The model was developed by Campbell and Fauchet [2]. They tried three types of the weighting functions: $(2\pi r/L)^{-1}\sin(2\pi r/L)$, $\exp(-\alpha r/L)$ and $\exp(-\alpha r^2/L^2)$. The strong phonon confinement function, being the gaussian $\exp(-8\pi^2 r^2/L^2)$ with the boundary value of $\exp(-4\pi^2)$, was chosen for the best fitting of the experimental dependence of the Raman peak shift on the microcrystal size for the Si or GaAs films of the microcrystals embedded in amorphous material or surrounded by an oxygen layer.

Changing the boundary value of the phonon amplitude is equivalent to changing the crystallite size. Therefore, to fit our experimental data for the free-standing nc-Si films presented in Fig. 3, the phonon confinement function must be chosen with less rigid boundary than that provided by the model by Campbell and Fauchet. We have tried the same weighting functions, $(2\pi r/L)^{-1}\ \sin(2\pi r/L)$, $\exp(-\alpha r/L)$ and $\exp(-\alpha r^2/L^2)$, varying α. Taking into consideration these weighting functions, the Raman spectrum was calculated from Eq. (1) with the Fourier coefficients determined from Eq. (2).

The numerical values of these coefficients decrease rapidly with increasing the phonon wavevector q_0 for the diameters of the nanocrystals investigated in our experiment. As a result, significant contributions to the integral (2) come from a relatively small region at the center of the Brillouin zone where the anisotropy is small. Due to that, the integration can be performed assuming the spherical Brillouin zone with an isotropic dispersion curve. For the backscattering configuration used in our Raman spectrum measurements, only LO phonons are important. We consider the dispersion $\omega(q)$ of the LO phonons in c-Si to be

$$\omega(q) = A + B\cos(\pi q/2),$$

where $A = 1.714 \times 10^5\,\mathrm{cm}^{-1}$ and $B = 1.000 \times 10^5\,\mathrm{cm}^{-2}$. These parameters were determined to describe the neutron scattering data clearly [6].

We have obtained the best agreement between the calculated dependence of the Raman peak shift on the nanocrystal diameter and our experimental data by choosing the phonon weighting function to be gaussian, $\exp(-3\pi^2 r^2/L^2)$ (the phonon amplitude at boundary equals to $\exp(-3\pi^2/2)$). Our theoretical curve is presented in Fig. 3 by solid line.

Thus, the phonon weigting function determined here is a gaussian with the coefficient $\alpha = 3\pi^2$ instead of the coefficient $\alpha = 8\pi^2$ which is generally used to determine the diameter of the nanocrystals.

The arbitrariness of coefficient suggests that the peak shift of the Raman spectrum is not only determined by the size of nanocrystals but also determined by terminated atoms on nanocrystals such as hydrogen or oxygen, and it is likely that the amplitude at the boundary of nc-Si with oxygen termination is smaller compared to that with hydrogen termination.

3. Conclusions

We determined the average diameter and the size distribution of the free-standing nc-Si films by using SAXS. We shown that the Raman analysis based on the strong confiment model with the phonon weighting function $\exp(-8\pi^2 r^2/L^2)$, gives a larger average diameter compared to that estimated by SAXS. Thus, we can point out that this model used until now is not appropriate to determine the size of nanostructure. We found the new weighting function being gaussian, $\exp(-3\pi^2 r^2/L^2)$, provided less rigid confinement of the phonons in the microcrystal, which gives a correct relationship between the Raman peak shift and the average size for the free-standing nanocrystals.

References

[1] H. Richter, Z. P. Zang and L. Ley, *Solid. State. Commun.*, **39**, 625 (1981).
[2] H. Campbell and P. M. Fauchet, *Solid. State. Commun.*, **58**, 739 (1986).
[3] Y. Kanemitsu, H. Uto, Y. Masumoto, T. Matsumoto, T. Futagi and H. Mimura , *Phys. Rev.* **48**, 2827 (1993).
[4] T. Matsumoto, J. Suzuki, M. Ohnuma, Y. Kanemitsu and Y. Masumoto, *Phys. Rev. B*, **63**, 195322 (2001).
[5] G. Porod, in *Small-Angle X-Ray Scattering*, edited by O. Glatter and O. Kratky (Academic, London,1982), p. 17.
[6] R. Tubino, R. Pisari and G. Zerbi, *J. Chem. Phys.*, **56**, 1022 (1972).

13th Int. Symp. "Nanostructures: Physics and Technology"
St Petersburg, Russia, June 20–25, 2005

Giant oxidation related relief at the openings of Al-rich layers on mirrors of GaSb/$Ga_{0.1}Al_{0.9}$SbAs/GaInAsSb laser structures

P. A. Dementyev[1], M. S. Dunaevskii[1], A. V. Ankudinov[1], I. V. Makarenko[1], V. N. Petrov[1], A. N. Baranov[2], D. A. Yarekha[2] and A. N. Titkov[1]

[1] Ioffe Physico-Technical Institute, St Petersburg, Russia
[2] CEM2, Universite de Montpellier II, 34095, Montpellier, France

In recent time, the large interest is addressed to the fabrication of semiconductor lasers for mid-IR range on the base of GaSb/InAs system. Usually, these laser structures contain Al-rich cladding layers which, as expected, may have a tendency for a strong oxidation in ambient conditions. Thick oxide formation may cause a rising of Al-rich layers over the adjacent layers without Al on laser mirror surface. Indeed, for a traditional laser system GaAs/$GaAl_{0.3}$As this rising has been detected, but only on the level of 1 nm [1] which, actually, is not very important. Recently a ten times higher rising of Al-rich layers with Al content up to 90% over a laser mirror surface has been reported [2]. However, the raised part of Al-rich layer was not flat and demonstrated unusual concave shape. In this connection a plastic deformation of those layers during cleaving could be cousidered as an alternative explanation, as it was proposed in the studies of cleavages of GaAs/AlAs supperlatice [3].

In our work the origin and the shape of relief at the openings of Al-rich layers on mirrors of GaSb/$Ga_{0.1}Al_{0.9}$SbAs/GaInAsSb laser structures (Fig. 1a) have been studied and analyzed. For that, laser mirrors were obtained by the cleavage and their topography was studied by the ambient atomic force microscopy (AFM) and ultrahigh vacuum scanning tunneling microscopy (UHV STM) methods. The AFM studies were performed on Solver P-47 NTMDT device and for UHV STM measurements the GPI-300.6 (CNSI, IGP RAS) system was utilized.

The AFM experiments performed in ambient conditions during 1 hour after the cleavage performance revealed elevation of the openings of Al-rich layers on the cleavage surface up to 6–7 nm (Fig. 1b, c). At the same time, UHV STM studies of the cleavage topography during 30 hours after cleavage performance in vacuum did not show any difference in the height of adjacent GaAlAsSb and GaInAsSb layers (Fig. 1d). A comparison of the ambient AFM and UHV STM topography observation permits to rule out in our case the idea about plastic deformation of Al-rich layers during cleavage process.

The AFM observations of the laser mirror topography during a longer time period (see Fig. 2a, b) have shown that height of the observed elevations is increasing with a time during more then two months and this process speeds up when air humidity is increased. So, we see a reasonable explanation of the Al-rich layers elevation over mirror surface in the oxidation of the surface openings of these layers in ambient atmosphere. The speed of the growth of oxide layer also depends on the flatness of the cleavage produced. For rough cleavages the speed is higher. The thickness of oxide strongly depends on small variations in Al composition. In the structures studied we observed elevation of the Al-rich layers up to 400 nm.

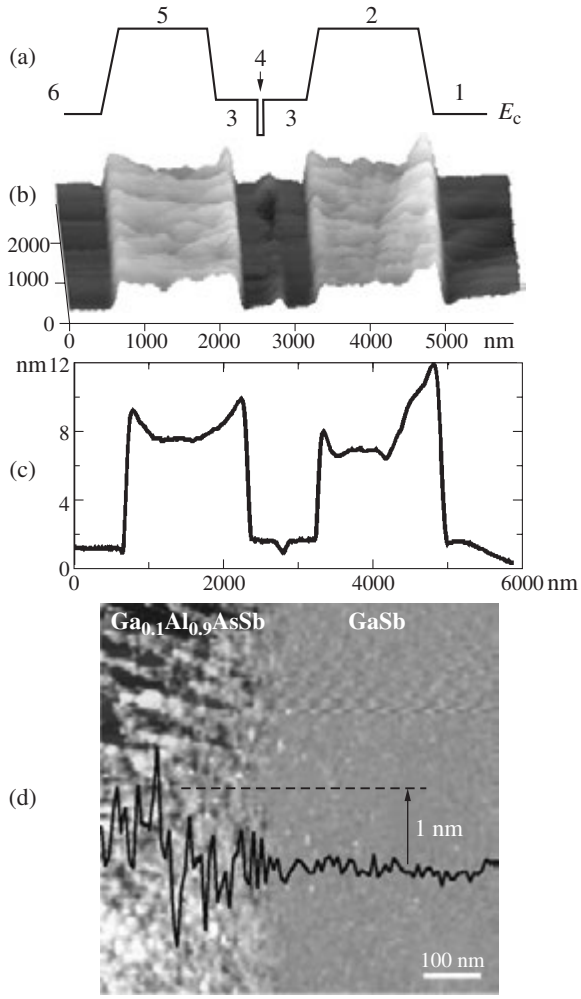

Fig. 1. (a) Scheme of GaSb/$Ga_{0.1}Al_{0.9}$SbAs/GaInAsSb laser structure, 1,6 — GaSb, 2,5 — $Ga_{0.1}Al_{0.9}$SbAs, 3 — $Ga_{0.65}Al_{0.35}$AsSb, 4 — GaInAsSb; (b, c) AFM topography and profile of the structure cleavage obtained 1 hour after cleving; (d) STM topography and profile of the structure cleavage obtained 30 hours after cleaving.

It was also important to determine the depth on which the oxidation penetrates in the Al-rich layers beneath the mirror surface. For that, we studied the topography of the second cleavage perpendicular to the mirror surface. The cleavage scheme is shown in Fig. 3a. The observations on the second cleavage have shown that inner part of the oxide is even larger, approximately by two times, then elevated one (Fig. 3b). It means that when oxidation comes to saturation and the elevated part of oxide riches height of $H = 400$ nm the total oxide thickness becomes more than one micron.

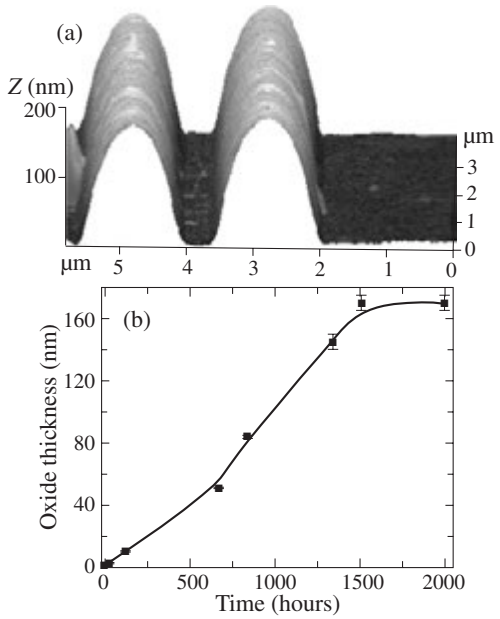

Fig. 2. (a) — AFM topography of structure cleavage after 2 months storage in ambient atmosphere; (b) — growth of oxide thikness with time.

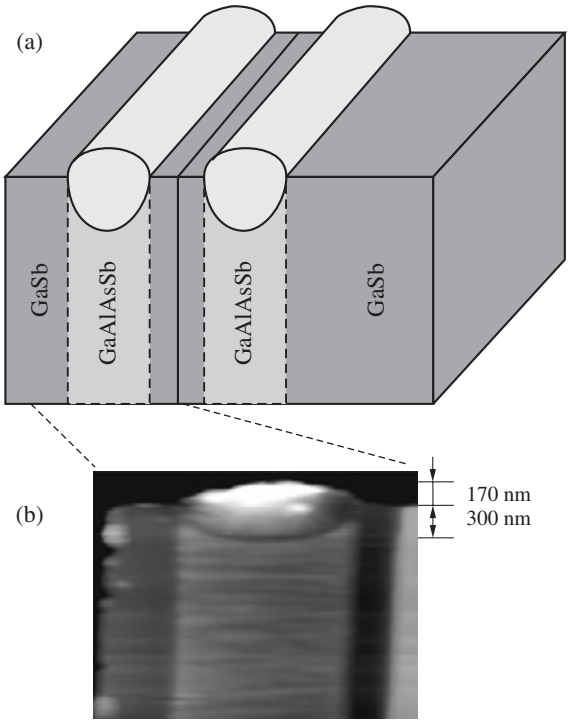

Fig. 3. (a) — Scheme of the two perpendicular cleavages which were used to reveal the oxid architechure; (b) — AFM topography of the second cleavage surface which reveals the oxide shape. Oxide penetration into Al-rich layer is 300 nm and its elevation over mirror surface is 170 nm.

The last observation of the inner part of oxide reveals important peculiarity about its shape: the inner front of oxidation is not planar but curved. In the middle part of Al-rich layer oxide is much thicker then at the interfaces with the adjacent layers (Fig. 3b). According to existing models of oxidation [4, 5], a penetration of the oxide into the materials is limited with the strains arising at the front of oxidation. In this connection, the observed curvature of oxidation front may evidence arising of a considerable strains at the interfaces just near the mirror surface. The concave shape of oxide elevations on Fig. 1b, c may be the other evidence of the strain appearance at the interfaces during the oxidation process.

In conclusion, we have revealed formation of a giant relief oxidation related at the openings of Al-rich layers on mirrors of GaSb/$Ga_{0.1}Al_{0.9}$SbAs/ GaInAsSb laser structures. The total thickness of surface oxide can approach 1 μm, two thirds of which being beneath the surface. The oxidation of Al-rich layers is not homogeneous and more intensive at the center part of layers. Oxidation at the interfaces with the adjacent laser structure layers is strongly suppressed which can evidence arising of considerable strains in those areas in the process of oxidation. In that connection, an attention should be given to a possible influence of the selective layer oxidation on the degradation processes on laser mirrors.

Acknowledgements

This work has been financially supported by grants of RFBR (03-02-17635, 03-02-17647).

References

[1] A. V. Ankudinov *et al*, *Semiconductors*, **33**, 555 (1999).
[2] G. Leveque *et al*, *Applied Surface Science*, **157**, 251 (2003).
[3] M. R. Castell *et al*, *Acta. Mater.*, **46**, 579 (1998).
[4] P. Avouris *et al*, *Appl. Phys. Lett.*, **71**, 285 (1997).
[5] Ph. Avouris *et al*, *Appl. Phys. A*, **66**, S659 (1998).

13th Int. Symp. "Nanostructures: Physics and Technology"
St Petersburg, Russia, June 20–25, 2005

Photoluminescence studies of the energy distribution of photoexcited carriers in CdSe/ZnSe nanostructures

O. G. Lyublinskaya, I. V. Sedova, S. V. Sorokin, O. V. Nekrutkina, A. A. Toropov and S. V. Ivanov
Ioffe Physico-Technical Institute, St Petersburg, Russia

Abstract. We discuss the temperature-dependent distribution of carriers localized in the sheet of CdSe/ZnSe islands under the conditions of *cw* optical excitation. At low temperatures, due to the multi-hopping relaxation, the excitons are localized mostly in the islands with deep localization potential, which results in the significant Stokes shift of the photoluminescence. Up to the temperature of 100 K the Stokes shift increases with temperature in accordance with the kinetic model of hopping. At higher temperatures the carrier distribution is totally quasi-equilibrium and its maximum moves toward the peak of the density of states.

Introduction

CdSe/ZnSe nanostructures, demonstrating excellent lasing properties in the optically pumped lasers, can hardly be exploited in the II–VI-based laser diodes due to the specific nature of defects generated during laser operation in the N-doped ZnSe-based materials ([1] and refs. therein). However, applications of the CdSe/ZnSe structures in electron-beam-pumped lasers [2] and integrated schemes employing green II–VI lasers pumped by InGaN-based light emitting devices [3] seems to be very promising. Numerous studies have shown that coherent CdSe/ZnSe insertions with a nominal thickness in the range of 1–3 monolayer (ML) represent the sheets of CdSe-enriched islands with primarily 2-D character of excitonic localization, incorporated into the body of an alloyed ZnCdSe quantum well. The complex morphology results in the specific exciton energy distribution within the CdSe-induced localization potential. Thermally activated redistribution of electron-hole pairs, causing the non-monotonic red shift of the excitonic emission with temperature, was detected in a number of studies. In [4] it was shown that occupation of excitonic states at low temperatures and corresponding photoluminescence (PL) behavior can be described using the percolation theory formalism. In the present paper we study the temperature dependence of electron-hole pair energy distribution in the sheet of CdSe islands up to the room temperature under the conditions of *cw* optical excitation.

1. Experimental

CdSe/ZnSe heterostructures were grown by MBE on GaAs (100) substrates. 2.1 ML CdSe insertions were formed in a ZnSe matrix by the migration enhanced epitaxy (MEE) technique, depositing 0.3 ML of CdSe per each cycle at the temperature of 280 °C. Earlier we have shown that varying the parameters of the MEE procedure, i.e. the sequence and duration of the growth interruptions after each MEE cycle, it is possible to influence the mean CdSe composition and homogeneity of the island ensemble [5]. In the present paper we report on the study of 3 samples, fabricated using different growth interruptions after the Se MEE cycle (10 s in the case of sample A, 60 s for the sample B_1 and, finally, 300 s for the sample B_2).

The low-temperature PL of CdSe islands was excited with the emission of a halogen lamp, dispersed by a monochromator. The quant energy of the excited light could be either above or below the ZnSe barrier. The latter case corresponds to the resonant excitation of the nanostructures. Figure 1 shows the low-temperature PL spectra of all samples excited into the ZnSe barrier. While the increase in the duration of growth interruptions from 10 s (sample A) to 60 s (sample B_1) results in the redshift of PL spectra due to the rise of the Cd content in the islands (see [5] for details), the further prolongation of the pause after the Se deposition pulses does not modify the Cd composition, making samples B_1 and B_2 almost identical. Figure 2 presents low-temperature PL spectra of the sample B_2 measured under the resonant excitation as well as PL excitation (PLE) spectra detected within either high- or low-energy side of the PL band. Resonantly excited PL spectra show that the broad PL band registered at the barrier excitation consists of two overlapping peaks denoted in Fig. 2 as I_1 and I_2. We suppose that these lines, corresponding to the radiative recombination of excitons trapped by the CdSe islands, arise from different mechanisms of exciton relaxation in energy. I_1 line is related to the LO-phonon-assisted relaxation and I_2 is a result of exciton migration over the ensemble of islands due to the acoustic-phonon-assisted hopping. PLE spectrum detected within the I_2 line reflects the density of excitonic states (DOS) of the ensemble of CdSe islands. The peaks attributed to the heavy- and light-hole excitons [6] are clearly seen and their spectral position and shape do not change when the detection energy is tuned within the I_2 contour.

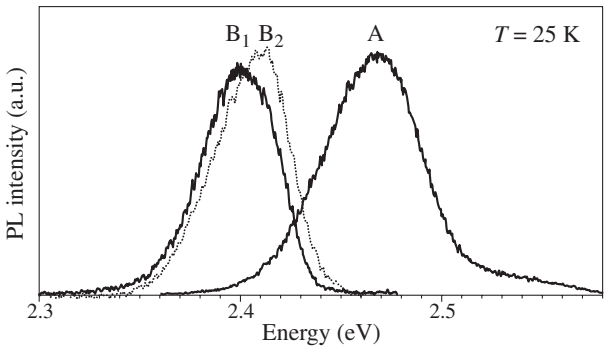

Fig. 1. Low-temperature PL spectra of the samples excited within the ZnSe barrier.

Figure 3 shows the temperature dependence of the PL Stokes shift for the samples A and B_1. The high-temperature PL spectra were measured under the HeCd laser excitation (325 nm, 5 mW). At these conditions, the PL spectra are broadened and the I_1 and I_2 lines are not clearly resolved, which hampers investigation of the exciton distribution in detail. Nevertheless,

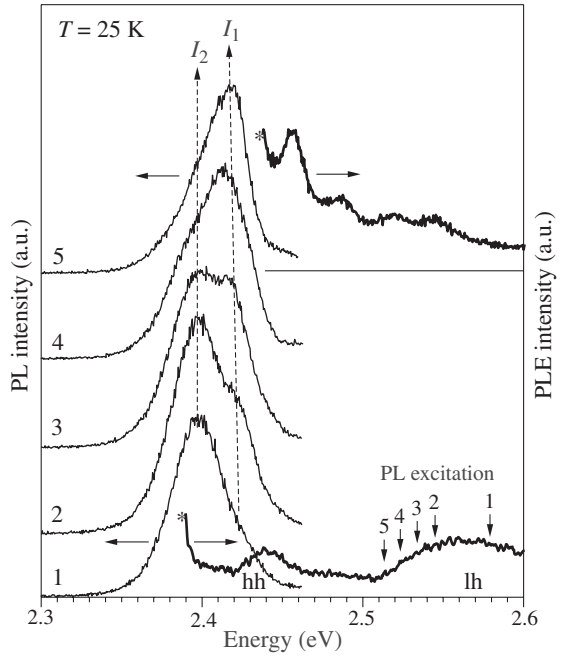

Fig. 2. Low-temperature PL and PLE spectra of CdSe islands in the sample B_2. Arrows show the excitation energy of respective PL spectra. Asterisks show the PLE observation energies.

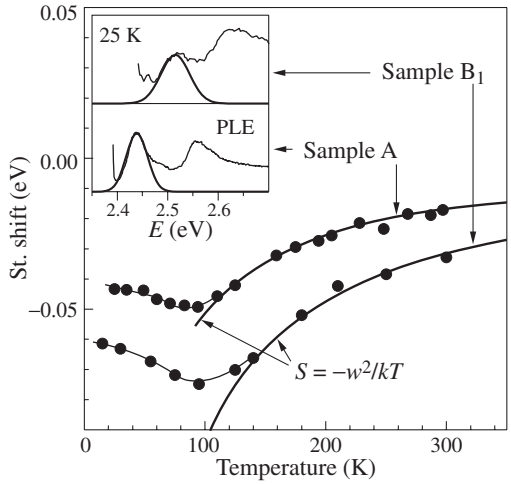

Fig. 3. Temperature dependences of the PL Stokes shift for the samples A and B_1. Solid lines are the results of simulation by $-w^2/kT$ law [8], using the parameters derived from the respective low-temperature PLE spectra shown in the inset.

qualitatively, the behavior of the PL Stokes shift is consistent with the kinetic model of the hopping [7]. According to this model, at $T = 0$ the PL is dominated by excitons localized by the isolated islands. With the temperature increase, these excitons have a freedom for further energy relaxation by hopping first up to the nearest higher-energy neighbor and then down to a deeper-energy sites. Due to this mechanism the Stokes shift of the PL increases with temperature up to 100 K. At higher temperatures the distribution of electron-hole pairs is obviously quasi-equilibrium in all samples and the temperature dependence of the PL Stokes shift is fitted by $-w^2/kT$ law [8], where $-w^2$ is a dispersion of the Gaussian-like distribution of states, derived for each sample from the fitting of the PLE spectra by the Gaussian function (marked in the inset to the Fig. 3 by the bold line).

Comparison of the Stokes shifts observed at high temperatures, as well as of the hh PLE line widths of samples A and $B_{1,2}$ allows us to conclude that the B-like growth sequence eventually results in the narrower DOS dispersion of a CdSe island array and higher Cd-content in the islands at the same deposited CdSe nominal thickness. This correlates well with the enhanced CdSe redistribution time during the long enough growth interruption.

Acknowledgements

This work is partly supported by the INTAS (Gr.# 03-51-5019), RFBR, S.V.I. is grateful to RSSF.

References

[1] S. V. Ivanov, *Phys. Stat. Sol. (a)*, **192**, 157 (2002).
[2] M. M. Zverev *et al*, *Phys. Stat. Sol. (b)*, **229** (1), 1025 (2002).
[3] I. V. Sedova *et al*, *Semicond*, **38**, 1099 (2004).
[4] A. Klochikhin *et al*, *Phys. Rev. B*, **69**, 085308 (2004).
[5] I. V. Sedova *et al*, *Inst. Phys. Conf. Ser.*, **174** (3), 161 (2003).
[6] F. Gindele *et al*, *J. Crystal Growth*, **184/185**, 306 (1998).
[7] S. A. Tarasenko *et al*, *Semicond. Sci. Technol.*, **16**, 486 (2001).
[8] M. Gurioli *et al*, *Phys. Rev. B*, **50**, 11817 (1994).

13th Int. Symp. "Nanostructures: Physics and Technology"
St Petersburg, Russia, June 20–25, 2005

Local analysis of self-assembled GeSi clusters by scanning Auger microscopy

G. A. Maximov[1], D. E. Nikolitchev[1], D. O. Filatov[1] and A. V. Novikov[2]

[1] Reseach and Educational Center For Physics of Solid State Nanostructures, University of Nizhny Novgorod, 603950 Nizhny Novgorod, Russia
[2] Institute for Physics of Microstructures RAS, GSP-105, Nizhny Novgorod, 603950 Russia

Abstract. Analytic potentials of Scanning Auger Microscopy in study of semiconducting nanostructures composition are demonstrated. The object of investigations was the self-assembled GeSi nanoclusters grown on silicon substrate by Molecular Beam Epitaxy. The practicability of local compositional analysis in single GeSi nanoclusters was shown. The spatial resolution of the apparatus was determined for different structures types. The measurement technique was developed and the composition depth profiling of nanoclusters was fulfilled with 50 nm lateral resolution. The concentration calculated using Scanning Auger Microscopy is in well agreement with results of photoelectric measurements.

Introduction

Nanoelectronics is developing vigorously today. The devices with elements size of just a few nanometers have been created already. It is well known the properties of solid state nanostructures (carriers energy spectrum, electronic and optical properties) are defined to a considerable extent by the size, shape and composition of nanoobjects. For geometric characterization of nanostructures the Scanning Probe Microscopy methods are successfully applied. the non-local methods of X-ray difraction and Raman spectroscopy unable to get reliable chemical composition in single nanoobjects were applied [1] to estimate the nanostructures composition. One of the method could solve the problem of nanoclasters analysis in nanometer scale is the Scanning Auger Microscopy [2].

The objective of this work is to define the analytic potential of Scanning Electron/Auger Microscopy (SEM/SAM) with nanometer probe diameter as applied to nanoobjects morphology and local compositional study by the example of GeSi nanoclusters formed on silicon substrate analysis.

1. Experimental

SEM/SAM investigations were carried out using ultra-high vacuum instrument MultiProbe S^{TM} manufactured by Omicron Nanotechnology GmbH (Germany). With Auger electrons exciting the FEI SEG-20 electron gun (accelerating voltage — up to 25 keV, beam current — up to 100 nA, electron probe diameter — 20 nm) was used. Auger spectra was recorded by using hemispherical energy analyzer EA-125 in single electron counting pulse mode. The system also included ion gun for cleaning the samples and depth profiling by Ar^+ ion sputtering.

To determine the SEM/SAM lateral resolution and real electron probe size a test sample was made on the basis of Cr/Ni. The sample elements of morphology had size varying from 1000 to 10 nm according to Atomic Force Microscopy (AFM) measurements. The resolution in SEM and SAM mode was 20 and 25 nm respectively.

Being investigated GeSi structures were grown through Stranski-Krastanov self-assembling with the use of (1) Molecular Beam Epitaxy (MBE) and (2) Sublimation Molecular Beam Epitaxy with gaseous germanium source (GeH_4). Surface morphology was investigated by AFM. In first case the uniform

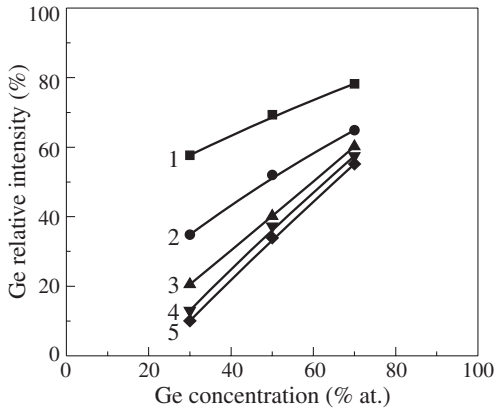

Fig. 1. Graduated characteristic for different oxide depth. (1) — 0 nm, (2) — 0,25 nm, (3) — 0.5 nm, (4) — 0.75 nm, and (5) — 1 nm.

("hut") clusters arrays with 300 nm lateral size 40 nm height and 8×10^{12} cm^{-2} surface density were observed. Nanostructures made by the second method had arrays of islands with 100–900 nm lateral size 20–100 nm height and 2×10^7–7×10^8 cm^{-2} surface density.

During semiconducting objects SEM and SAM measurements the effect of sample surface charging became apparent and led to electron probe shift and defocusing [3]. Owing to surface charge presence the spatial resolution on these structures 2–3 times less than on well conducting samples. During GeSi nanoclusters investigation the resolution totaled 50 nm in SEM and 70 nm in SAM mode.

Shift and defocusing of electron beam were the main problems during Auger spectra recording at defined point chosen on SEM image and during acquisition of Ge surface distribution. By applying the positive potential to the sample this effect could be decreased but not completely excluded. To solve this problem a special method was developed: the electron probe is positioned to chosen point and Auger spectra are recorded within short time interval during which the probe shift is negligible and it remains on the island. Then the instrument is switched to SEM mode again, beam correction is made and procedure is repeated. Obtained after several (10–20) cycles Auger spectrums are averaged for signal-to-noise ratio increase.

The calibration characteristic was schemed to determine Ge and Si concentration in nanoislands (Fig. 1).

The compositional analysis of specially made samples of GeSi solid solutions with different Ge content was fulfilled layerwise. The test samples were made by growthing a polycrystalline GeSi film of 50–100 nm thick on high-alloyed silicon substrate by Molecular Beam Epitaxy. Averaged concentration of germanium and silicon in films were determined independently by X-ray diffraction.

After the samples were made they are exposed to the air before being put into a vacuum chamber of Auger spectrometer. While the samples are being exposed the surface layer is oxidized. The calibration characteristic was built for several depth values by using test samples to determine concentration of Ge in oxide. According to the curves on Fig. 1 the concentration ratio of germanium and silicon was different in oxide and in the depth of the sample [4]. The ion sputtering of GeSi nanoclusters was carried out layer-by-layer and Ge concentration was received by using the calibration characteristic for proper ion sputtering depth. There was a hypothesis of equality between nanoclusters and GeSi solid solutions oxides.

2. Results and discussion

The germanium and silicon depth distribution in nanoclusters and between them is shown on Fig. 2. Calculation of Ge concentration was done by setting that the rest part of main composition was silicon. The average germanium concentration obtained during local SAM measurements was 10–20% lower than value being got from X-ray diffraction and Raman spectroscopy measurements [5]. This could be explained by different modes in which samples for calibration curve were measured. The probe diameter in the case of calibration characteristic was 30 μm but during nanostructures investigation the nanoprobe mode was switched on and diameter was 50 nm. The fact of Ge Auger line intensity decrease after switching to nanoprobe mode will need to be taken into account further for truth Ge nanoclusters profiling.

To estimate the truth (avoid the systematic error) of concentration measurements independent experiments were fulfilled for nanostructures created by Sublimation MBE. The Ge concentration in Ge_xSi_{1-x} islands was measured independently by using Photovoltage Spectroscopy on semiconductor/electrolyte junction. The experiment was carried out in electrolytic cell using the satellite samples grown under the same conditions as the samples for SAM investigation but nanoclusters were covered with 40 nm thick Si layer. The method of photoelectric measurements and spectra analysis is described in [6]. The x totaled 0.52 ± 0.10. This value is close to average Ge concentration ($x = 0.53$) acquired from depth distribution of Ge in nanoclusters (Fig. 2).

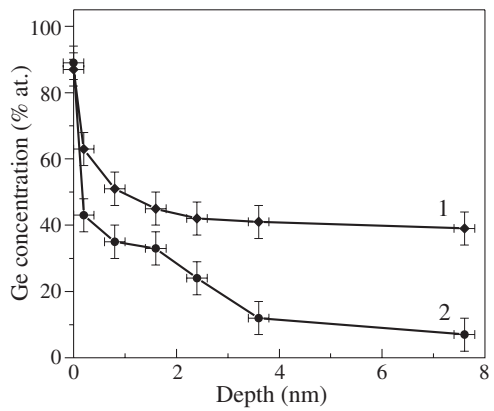

Fig. 2. Ge depth distribution in nanocluster (1) and between nanoclasters (2). GeSi nanostructures were grown by Sublimation MBE.

Conclusions

As a result the practicability of self-assembled GeSi nanostructures compositional analysis with nanometer resolution of using Scanning Auger Microscopy was shown. The SEM and SAM spatial resolution was determined and amounted to 20 and 25 nm in SEM and SAM mode respectively for conducting Cr/Ni test sample and 50 nm in SEM and 70 nm in SAM mode for GeSi/Si structures. The measurement technique was developed, Ge and Si concentration profiling in nanoclusters was done in nanoclusters. The concentration obtained by using SAM measurements is in well agreement with results of photoelectric measurements.

Acknowledgements

The work has been supported by Joint Russian American Program "Basic Research and Higher Education" (BRHE) sponsored jointly by US Civilian Research and Development Foundation (CRDF) with Russian Ministry of Education (Award #REC-NN-001). Samples for investigation were granted by V. G. Shengurov (Physical-Technical Research Institute, University of Nizhny Novgorod) and A. V. Novikov (Institute for Physics of Microstructures, RAS).

References

[1] Z. F. Krasil'nik *et al*, *Thin Solid Films*, **367**, 171 (2001).
[2] G. A. Maximov *et al*, *Proc. 13th MSM (Cambridge, UK, 2003)*, IoP, 251 (2003).
[3] M. P. Seah, S. J. Spenser, *Journ. of Electron Spectroscopy*, **109**, 291 (2000).
[4] F. K. LeGoues *et al*, *Journ. Appl. Phys.*, **64**, 1724 (1989).
[5] M. Ya. Valakh *et al*, *Phisika Tverdogo Tela*, **46**, 85 (2004).
[6] G. A. Maximov *et al*, *Phisika Tverdogo Tela*, **47**, 26 (2005).

13th Int. Symp. "Nanostructures: Physics and Technology"
St Petersburg, Russia, June 20–25, 2005

STM/STS studies of the initial stage of growth of ultra-thin Bi films on Si(111)

J. T. Sadowski[1], *A. I. Oreshkin*[1,2], T. Nagao[1,4], M. Saito[3], S. Yaginuma[1,4], Y. Fujikawa[1], T. Ohno[4] and T. Sakurai[1]

[1] Institute for Materials Research, Tohoku University, Katahira 2-1-1, Aoba-ku, Sendai 980-8577, Japan
[2] Physics Department, Moscow State University, Moscow, 119992, Russia
[3] Graduate School of Natural Science and Technology, Kanazawa University, Kakuma, Kanazawa 920-1192, Japan
[4] National Institute for Materials Science, 1-2-1 Sengen, Tsukuba, Ibaraki 305-0047, Japan

Abstract. The results of investigation of the room temperature growth of thin Bi film on Si(111)-7x7 are present. In the initial stage of Bi film growth the rotationally disordered, pseudo-cubic, Bi{012} islands with uniform height of 13 Å are formed. With increasing bismuth on the surface, islands interconnect maintaining however their uniform height and structural phase transition of the {012} film into a hexagonal Bi(001) film takes place.

Introduction

Growth of thin metal films on semiconductor substrates has been always an important subject for extensive experimental and theoretical studies. The creation of new electronic devices based on nanostructures depends strongly on size and distribution of nanostructures on the substrate and requires a new knowledge about their growth. Semimetal Bi has been widely investigated because of its very interesting electronic properties, such as high carrier mobility, small effective mass and large Fermi wavelength. Also, recently, extremely high magnetoresistance was observed in electrodeposited Bi film and it was attributed to the excellent crystallinity of the film [1]. Bi has metal-like high packing density but its quasi-cubic, layered structure with bilayer stacking is an evidence of covalent-like character of the crystal structure [2]. Immiscibility with Si makes the Bi/Si a convenient system for studying the growth of thin metallic films.

Experimental

Bi deposition experiments were done in the ultra-high vacuum field ion microscope-scanning tunneling microscope (UHV FIM-STM) system, with a base pressure below 1×10^{-10} Torr. Phosphorus-doped, n-type Si(111) wafers, with a resistivity 1.4–1.7 cm were used as the substrates. The 7×7 reconstruction of the Si(111) surface was prepared by resistive flash-heating at approximately 1250 °C, followed by short annealing at 830 °C and slow cooling down to the room temperature. Bismuth was deposited from the alumina-coated tungsten basket onto the freshly prepared Si(111)-7×7 surface kept at room temperature (RT). Through this paper we define 1 ML_{012} as the density of Bi atoms in a pseudo-cubic Bi{012} plane (9.06×10^{14} atoms/cm^2). The density in the covalently bonded Bi(001) bilayer plane: 1 $BL_{001} = 1.14 \times 10^{15}$ atoms/cm^2 and atomic density of a single Si(111) bilayer: 1 $ML_{Si} = 7.83 \times 10^{14}$ atoms/cm^2. The crystal structure of Bi can be considered as a slightly distorted simple-cubic lattice where the lattice planes that constitute this pseudo-cube are indexed as equivalent (012), $(1\bar{1}2)$ and $(\bar{1}02)$ (hereafter referred as {012}). These planes intersect each other with angles of 92.5° or 87.5° and the interplane spacing is 3.28 Å [3].

Results and discussion

In the initial stage of the room temperature Bi growth on Si(111)-7×7 surface a wetting layer consisting of disordered Bi clusters contained within 7×7 half-unit cells is formed. With Bi coverage exceeding 0.9–1.1 ML_{012}, small nanocrystalls start to form on top of the wetting layer, which later leads to the formation of rotationally disordered, tabular islands with uniform height of ∼13 Å, at coverage exceeding 2 ML_{012}. With further increasing of the Bi coverage the islands merge, keeping their uniform height, which finally results in formation of quite flat, well ordered layer. High-resolution STM image taken from that layer (Fig.1) shows the periodic structure with a rectangular, centered unit cell, with apparent size of 4.6 ± 0.2 Å $\times 4.8 \pm 0.2$ Å. The size of the unit cell is consistent with the bulk truncated Bi{012} surface. Taking this into account, one can easily notice that the observed ∼ 13 Å thickness corresponds exactly to 4 ML_{012}. At Bi coverage 6–7 ML_{012}, the structural phase transition from two-fold {012} film into the three-fold Bi(001) film takes place in the whole volume of the film. High-resolution STM image (Fig. 2) shows hexagonally ordered layer with the nearest-neighbor distance of 4.5 ± 0.2 Å. Together with the observed in the STM images apparent step hight of 4.0 ± 0.2 Å, these values correspond very well to bulk values for (001) plane: 4.54 Å and 3.9 Å, respectively. In order to explain observed experimentally formation of rotationally disordered , pseudo-cubic, Bi{012} islands with uniform height, we performed *ab initio* calculations of the

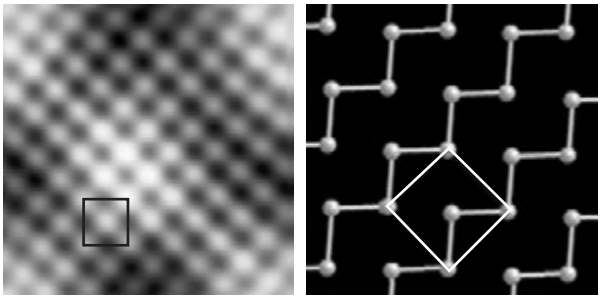

Fig. 1. (a) High-resolution filled state STM image of Bi{012} surface; 30 Å×30 Å; −0.15 V; 1 nA. (b) Schematic top drawing of the bulk truncated Bi{012} surface; (4.6±0.2) Å × (4.8±0.2) Å.

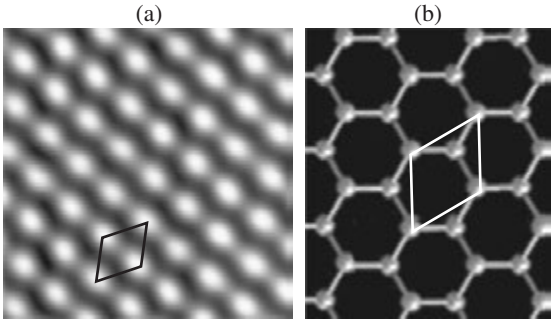

Fig. 2. (a) High-resolution filled state STM image of Bi001 surface; 30 Å×30 Å; −0.9 V; 1 nA. (b) Schematic arrangement of Bi atoms in the {001} plane; 4.5 Å± 0.2 Å.

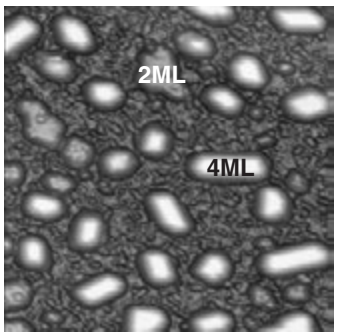

Fig. 3. STM image (size: 50 × 50 nm^2) of the Bi{012} islands formed after deposition of nominal 2.5 ML_{012} of Bi on Si(111)-7×7 surface kept at RT — only 4 ML and 2 ML high Bi{012} islands are formed.

Bi{012} film structure. Results of the calculations strongly indicated that due to the atomic relaxation, atoms in the top layer of the {012} film form new bonds to those in the second layer. As a result, all dangling bonds are saturated. Such relaxation leads to the pairing of the layers, inducing enhanced stability of the Bi{012} film containing even number of layers ($n = 2$, 4, 6. . .). This is in good agreement with the experiment where for as-deposited Bi film at this coverage range we observe only 2, 4 (preferentially) (Fig. 3) and 6 ML_{012} thick Bi{012} islands [4]. To check the consistency of our model we deposited nominal 2.5 ML_{012} of Bi on the Si(111) surface. Immediately after the deposition, only two types of Bi{012} islands are formed on the top of wetting layer. Height profiles taken from the STM images confirm that indeed, only 2 ML_{012} (6.6±0.2 Å) and 4 ML_{012} (13.2±0.2 Å) high Bi island are observed, and 4 ML_{012} high Bi{012} islands are significantly more abundant. We did not observe any odd-number layered islands, which is in agreement with the predictions based on the proposed model. Moreover, short annealing of the as-deposited structure at about 380 K leads to disappearance of 2 ML_{012} high islands, suggesting their meta-stable character, predicted by the total energy calculations. Instead, the average size of the 4 ML_{012} islands increased due to process and a small number of 6 ML_{012} (19.8 ± 0.2 Å) high islands also appeared. Statistical analysis of the height of more than thousand islands observed on as-deposited as well as annealed surface was performed.The increasing of the Bi coverage does not change the height distribution of the Bi{012} islands, up to the nominal Bi coverage of about 5 ML_{012} (including wetting layer). Around this coverage the interconnection of the predominantly 4 ML_{012} high islands is completed and at that moment we are able sometimes to observe local formation of 5 ML_{012} thick Bi film, but this fifth {012} monolayer was found to be unstable. It can be observed only right after Bi deposition and it quickly disappears, even at RT.

Summary

We have presented a novel RT growth of thin Bi films on Si(111) surface. We determined, that pseudo-cubic, Bi{012} islands with uniform height of about 13 Å are formed in the initial stage growth. With increasing the Bi coverage, islands interconnect keeping their uniform height. Using *ab initio* calculations we clarified that Bi{012} film undergoes relaxation, which leads to the pairing of the layers, resulting in the enhanced stability of even-number-layered Bi{012} film at RT. Further increase in Bi amount on the surface is accompanied by unique and unexpected structural phase transition of the {012} film into a well-ordered, hexagonal Bi(001) film, at nominal coverage of about 8–10 $ML_{\{012\}}$.

Acknowledgements

This work was performed under the inter-university cooperative research program of Laboratory for Advanced Materials, Institute for Materials Research, Tohoku University. The work was partially supported by RFBR grant No. 03–02–16807 and by the grant for the leading scientific schools support No. 1604–2003–2.

References

[1] F. J. Yang, K. Liu, K. Hong, D. H. Reich, P. C. Searson and C. E. Chien, *Science* **284**, 1335 (1999).
[2] G. Jezequel, J. Thomas and I. Pollini, *Phys. Rev. B* **56**, 6620 (1997).
[3] F. Jona, *Surf. Sci.* **8**, 57 (1967).
[4] T. Nagao *et al*., *Phys. Rev. B* **93**, 105501 (2004).

13th Int. Symp. "Nanostructures: Physics and Technology"
St Petersburg, Russia, June 20–25, 2005

Nonohmic conductivity as a test of the transition from diffusion to hopping

A. A. Sherstobitov[1], G. M. Minkov[1], A. V. Germanenko[2], O. E. Rut[2] and B. N. Zvonkov[3]

[1] Institute of Metal Physics RAS, 620219 Ekaterinburg, Russia
[2] Ural State University, 620083 Ekaterinburg, Russia
[3] Physical-Technical Research Institute, University of Nizhni Novgorod, 603600 Nizhni Novgorod, Russia

Abstract. We show that the study of conductivity nonlinearity gives a possibility to determine the condition when the diffusion conductivity changes to the hopping one with increasing disorder. To test our suggestions we apply this method to the 3D p-InSb samples. In this material the transition from the hopping to diffusive conductivity is observed after applying of the uniaxial compression. For comparison we simultaneously analyze the nonohmic conductivity in conventional centrally doped single quantum well GaAs/InGaAs 2D heterostructure. It is shown that in 2D structures the conductivity remains diffusive down to low temperature conductivity value about $10^{-2}e^2/h$.

The increase of a disorder (amplitude of long range potential fluctuations δ) or the decrease of the Fermi level (E_F) leads at low temperature to the conductivity mechanism changing: from the diffusion at $E_F/\delta > 1$ to the hopping at $E_F/\delta < 1$. The situation in two dimensional systems is essentially complicated because the quantum corrections to the conductivity in 2D are noticeably larger than in 3D. At not a very large k_Fl-value ($k_Fl \simeq 2-3$, where k_F is the Fermi quasimomentum, l is the mean free path) the corrections value can be close to the Drude conductivity $\sigma_0 = \pi G_0 k_F l$ (where $G_0 = e^2/(2\pi^2\hbar) = 1.23\times10^{-5}\Omega^{-1}$). Therefore, the corrections can lead to strong temperature dependence of the conductivity even in the diffusive regime. It is clear that the disorder increasing must lead eventually to the transition to the hopping conductivity (strong localization). The conditions when such a transition occurs is under the question up to now.

Our method of the conductivity mechanism determination is based on the fact that the electron- and lattice-temperature dependence of energy relaxation rate $P(T_e, T_l)$ is of special form in the diffusive regime. It is equal to the difference of two identical functions, one of them depends on the electron temperature and another one depends on the lattice temperature [1]:

$$P(T_e, T_l) = F(T_e) - F(T_l). \qquad (1)$$

It follows from this equation, that the derivative $\partial P(T_e, T_l)/\partial T_e$ does not depend on T_l

$$\frac{\partial P(T_e, T_l)}{\partial T_e} = \frac{\partial F(T_e)}{\partial T_e}. \qquad (2)$$

It means that the derivatives taken at different lattice temperatures fall on single curve. This applicable only for the "true" energy relaxation rate. In almost all cases this function cannot be found directly: it is obtained from some processing of measurable quantities. Usually the energy relaxation rate is determined from the temperature and electric-field dependences of conductivity: $\sigma(T)$ and $\sigma(E)$. In such a way obtained P-value will be close to the "true" one. It is important that the derivative will be independent of the lattice temperature only if additional conditions concerning the dependences $\sigma(T)$ and $\sigma(E)$ are satisfied. First, the conductivity should depend on the electron temperature only. Second, an assumption of the effective electron temperature should be fulfilled, i.e., the energy distribution function of electrons in strong electric field should be the same as without electric field, but with another temperature $T_e > T_l$. Third, the conductivity should depend on the electric field only via the changing of the electron temperature in the field. It is clear that all these conditions cannot be fulfilled in the hopping regime.

Thus, if we plot the derivatives obtained at different lattice temperatures for different conductivity values, the dependence of $\partial P(T_e, T_l)/\partial T_e$ on lattice temperature should arrive at the transition to the hopping conductivity.

Experimentally, we investigated the nonohmic conductivity for heterostructure with InGaAs single quantum well in GaAs. The structure had a Si δ doping layer in the center of the quantum well. The electron density and mobility were $n = 1.65\times10^{16}\,\mathrm{m}^{-2}$ and $\mu = 0.12\,\mathrm{m}^2/(\mathrm{V\,s})$, respectively. The samples were mesa etched into Hall bars on which basis field-effect transistors with an Al gate electrode were fabricated. It was very important to use thick insulator between gate electrode and 2D channel to decrease the influence of voltage drop over the channel. We used the 10 μm organic insulator (polyimid) which was coated on to the cap layer before fabrication of the gate electrode.

To test our method we make same investigations of nonohmic conductivity on 3D p-InSb sample with acceptor concentration of about 2×10^{16} cm^{-3} and compensation degree $K = 0.1$. In this material the transition from the hopping to diffusive conductivity occurs under the uniaxial compression. The pressure χ at which the transition occurs was determined from the pressure dependence of ϵ_1 energy and was found about 2.5 kbar for the investigated sample [2].

For 2D structures in what follows the results obtained for different electron density will be referenced by the value of σ measured at $T = 1.5$ K.

The energy relaxation rate was determined by conventional method from comparison of $\sigma(E)$ and $\sigma(T)$ dependences [3]. To obtain $\partial P(T_e, T_l)/\partial T_e$, we have numerically differentiated the experimental dependences $P(T_e, T_l)$. This quantity as a function of electron temperature taken at different lattice temperatures is presented in Fig. 1 for 2D structure, and in Fig. 2 for the 3D InSb sample. It is seen, that both figures are very similar. Even this similarity supports our method of the conductivity mechanism determination.

First we consider the results for highest conductivity, which unambiguously corresponds to the diffusion regime (Fig. 1a

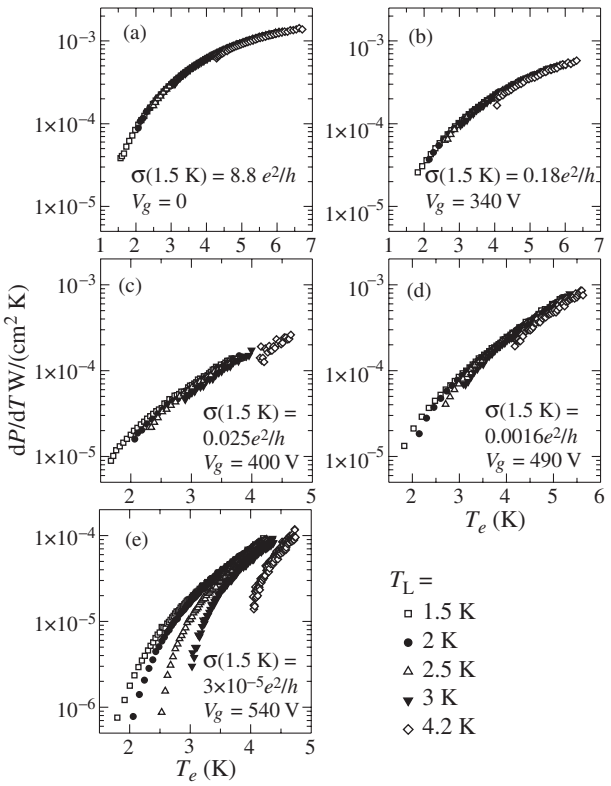

Fig. 1. The $\partial P(T_e, T_l)/\partial T_e$ as a function of electron temperature T_e measured at different lattice temperature T_l for various conductivities for 2D GaAs structure.

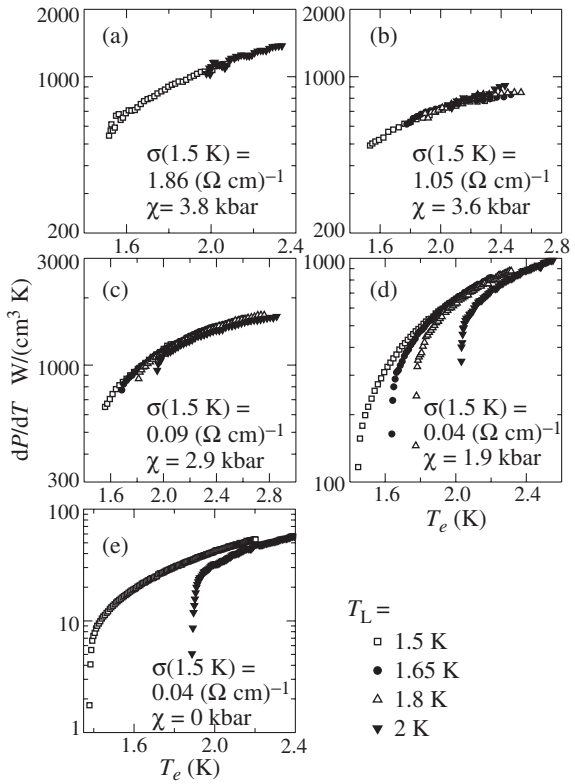

Fig. 2. The $\partial P(T_e, T_l)/\partial T_e$ as a function of electron temperature T_e measured at different lattice temperature T_l for various conductivities for 3D InSb.

and Fig. 2a). It is clearly seen that for both 3D and 2D cases the derivatives obtained for different lattice temperatures fall on common curve as it has to be in the diffusive regime.

Such a data processing was carried out over the whole conductivity range and the results are presented in Figs. 1b-1e and 2b-2e. It is seen that in both cases there is a wide conductivity range where $\partial P(T_e, T_l)/\partial T_e$ obtained for different lattice temperatures fall on common curve. We know that for InSb the transition occur between Figs. 2c and 2d. For the 2D sample, the same change is observed between Figs. 1d and 1e. Thus, in 2D structure this transition occurs at $\sigma < 10^{-2}e^2/h$. At lower conductivity the derivative in both cases noticeably depends on the lattice temperature: there is substantial divergence between the curves taken at different lattice temperature. The conclusion that the low-temperature conductivity of the disordered 2D systems remains diffusive down to $\sigma \ll e^2/h$ agrees with the results of our previous studies of nonohmic conductivity in another type of GaAs structures [4] and with the results of investigations of the quantum corrections to the conductivity at decreasing of $k_F l$ carried out in [5].

In summary, we have proposed the way how studying the conductivity nonlinearity one can determine the condition when the diffusion regime changes to the hopping one. This method was tested on the material with known conditions at which the transition occurs: p-InSb. Using this method, we have shown that for single quantum well GaAs/InGaAs/GaAs heterostructures the conductivity remains diffusive down to $\sigma \approx 10^{-2}e^2/h$.

Acknowledgements

We gratefully thanks Dr. A.A. Zhukov for his help in the sample preparation. This work was supported in part by the RFBR (Grants 03-02-16150 and 04-02-16626), the CRDF (Grants EK-005-X1 and Y1-P-05-11), the INTAS (Grant 1B290) and the Russian Program *Physics of Solid State Nanostructures*.

References

[1] P.J. Price, *J. Appl. Phys.* **53**, 6863 (1982).
[2] A.V. Germanenko *et al*, *FTP* **21**, 2006 (1987).
[3] R. Fletcher *et al*, *Phys. Rev.* **B61**, 2028 (2000).
[4] G.M. Minkov *et al*, *Physica E.* **25**, 42 (2004).
[5] G.M. Minkov *et al*, *Phys. Rev.* **B65**, 235322 (2002).

13th Int. Symp. "Nanostructures: Physics and Technology"
St Petersburg, Russia, June 20–25, 2005

Multi excited state photoluminescence mapping on InAs/InGaAs quantum dot structures

T. V. Torchynska[1,2], M. Dybiec[2] and P. G. Eliseev[3]

[1] ESFM – National Polytechnic Institute, Ed. 9, Mexico D.F., 07738, Mexico D.F.
[2] University of South Florida, 4202 E Fowler Ave, Tampa, FL 33620 USA
[3] Center of High Technology Material, University of New-Mexico, Albuquerque, NM, USA

Abstract. Photoluminescence mapping was performed at 80 and 300 K on self-assembled InAs/$In_{0.15}Ga_{0.85}As$ quantum dots structures. A reduction of the ground state PL intensity is accompanied with a monotonous "blue" shift of the luminescence maximum at 300 K from 0.99 to 1.02 eV and "red" shift at 80 K from 1.09 to 1.06 eV. The reason is suggested to account for intensity variation of the quantum dot luminescence connected with decreasing of a dot size from the periphery toward the center of the samples. In PL spectra measured at high excitation (600 W/cm^2) three PL bands (GS, 1ES, 2ES) are well resolved. Corresponding multi excited state mapping was carried out, which revealed some peculiarities in intersublevel energy spacing variations.

Introduction

Nanometre scaled confinement of electrons in InAs quantum dots (QD) determines the optoelectronic device parameters [1]. This confinement strongly depends on shape, size and strain field of single QDs. For basic knowledge and for creation a perfect laser structures it is very important to completely understand the electronic structure and physical parameters of QDs. Despite on the number of research has been done in this area the effects of the dot size and shape on the dot potential and corresponding electronic level structure, however, are not well understood. This paper presents the scanning photoluminescence (PL) spectroscopy at 80 and 300 K of the ground (GS) and multi excited states (1ES, 2ES) in InAs/ $In_{0.15}Ga_{0.85}As$ QD. At the first we will show that investigated structures are characterized by the long range variation of the QD sizes in dot ensemble across the sample. Second we will discuss the multi excited state energy variation in dependence on ground state energy (or on QD sizes).

1. Experimental details

The solid-source molecular beam epitaxy (MBE) in V80H reactor is used for growth of the laser structure consisting three layers of InAs self-organized QDs inserted into $In_{0.15}Ga_{0.85}As$/GaAs quantum wells (QW). In the centre of the waveguide, an equivalent coverage of 2.4 monolayers InAs QDs are confined approximately in the middle of a 9 nm $In_{0.15}Ga_{0.85}As$ QW. The structures are grown under As-stabilized conditions at 510 °C, during the deposition of the InAs active regions and InGaAs wells and 590–610 °C for the rest layers of the structure. The individual dots are of $\sim 14-15$ nm in the base sizes and ~ 7 nm in height. The dot density is determined by AFM observation of parallel wafer that have not been overgrown by QW and by cladding layers. The in-plane dot density is $(5.3) \times 10^{10}$ cm^{-2}. Due to 16.5 nm GaAs layer (spacer) between the dot InAs/InGaAs layers vertical alignment and electronic coupling of the QDs can be excluded.

The photoluminescence spectra was dispersed by SPEX 500M spectrometer and recorded by liquid-nitrogen cooled Ge-detector coupled with a lock-in amplifier. The scanning PL spectroscopy of GS in QDs was performed at 80 K and room temperatures, using pulsed solid state 800 nm IR laser with 30 mW average power and 150 mW peak power as the excitation source mainly. The laser beam was focused down to 200 μm in diameter with the excitation power density of $\sim$ 100 W/cm^2. Multi excited state PL mapping was preformed at 80 K as well using of Ar^+ laser with light wavelength 514.5 nm and power up to 200 mW focused down to 200 μm in diameter (excitation power density is up to 600 W/cm^2). Samples were mounted on PC controlled X-Y moving stage. Typical mapping area was 5 mm $\times$ 15 mm rectangle with the step of 200 μm. PL maps were obtained by the consecutive measurement of the spectrum at individual sample spots.

2. Results and discussion

The spatial distribution of the ground state PL intensity was obtained at 80 and 300 K. At room temperature, the PL maximum corresponding to the electron-hole ground state transition is observed in the range from 1.01 to 1.12 eV. The PL mapping of this maximum revealed a strong, over one order of magnitude inhomogeneity between high and low intensity regions on the same wafer.

In the high PL intensity areas, the PL band shows a Gaussian shape with a high-energy shoulder due to QD excited state (Fig. 2 and 3). In the low PL intensity areas, the band is broadened and exhibits an asymmetric shape indicating a superpo-

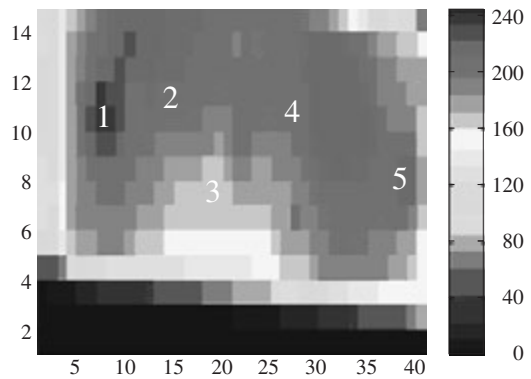

Fig. 1. Room temperature PL intensity map at 0.99 eV on 5 sample. Mapping areas is 4×15 mm (15×40 arb. units). PL intensity is presented in the contrast bar in logarithmic scale and arbitrary units as well. The numbers (1–5) correspond to different positions on the wafers characterized by the variation of PL intensities.

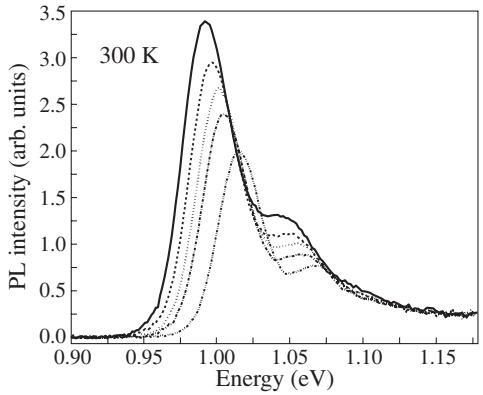

Fig. 2. PL spectra of the QD structures 5 at various intensity points measured at 300 K.

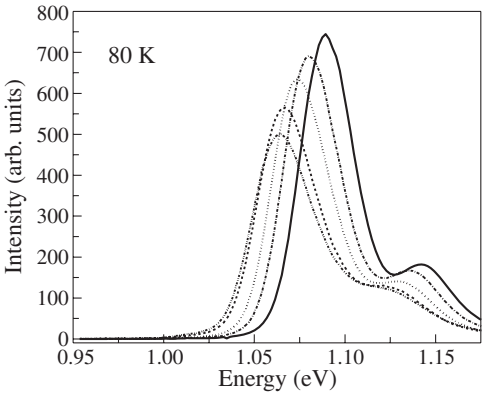

Fig. 3. PL spectra of the QD structures #5 at various intensity points measured at 80 K.

sition with other PL bands. Using spectroscopic PL mapping, we observed the PL intensity versus PL maximum dependence across the wafers. The ground state PL intensity decreasing is accompanied by a monotonous "blue" shift of the luminescence maximum at 300 K (Fig. 2) from 0.99 to 1.02 eV and "red" shift at 80 K (Fig. 3) from 1.09 to 1.06 eV.

This effect leads at the sample center to shallower QD localized states (i.e. smallest electron and hole binding energies), poorer carrier localization and, as consequence, a higher probability of the carrier thermal escape, which reduces their room-temperature PL intensity [2].

Multi excited PL band mapping was performed at 80K as well at excitation power density 600 W/cm^{-}2. In PL spectra measured at high excitation three PL bands (GS, 1ES, 2ES) are well resolved that allow to carry out spatial scanning of their peak positions across the sample versus corresponding GS energy maximum (Fig. 4).

For investigated samples the intersublevel energy spacing was not equidistant. These energy spacing are of 55.6 (GS-1ES) and 45.1 (2ES-1ES) meV for low energy GS optical transition at 1.090 eV (bigger QDs) and it decreases monotonically to 51.0 (GS-1ES) and 31.5 (2ES-1ES) meV for high energy GS optical transition at 1.129 eV (smaller QDs). The reason of such type multi excited state energy trend versus QD size is discussed.

Acknowledgements

The work was supported by NSF – CONACYT program: DMI-0218967 and CONACYT project U42436Y and by CGPI-IPN, Mexico.

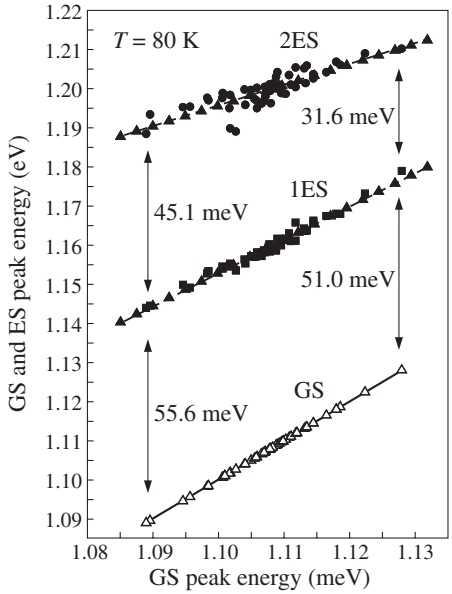

Fig. 4. Gs and ES peak energy versus GS peak energy

References

[1] D. Bimberg, M. Grundman and N. Ledentsov, *Quantum Dot Heterostructures*, (Wiley & Sons) 328, 2001.

[2] M. Dybiec *et al*, *Appl. Phys. Lett.*, Reading, 84, 2004.

13th Int. Symp. "Nanostructures: Physics and Technology"
St Petersburg, Russia, June 20–25, 2005

Capacitance spectroscopy of electronic states in Ge/Si quantum dots with a type-II band alignment

A. I. Yakimov, A. V. Dvurechenskii, A. I. Nikiforov and A. A. Bloshkin
Institute of Semiconductor Physics, SB RAS, 630090 Novosibirsk, Russia

Abstract. Capacitance spectroscopy was employed to study electronic structure of self-assembled Ge quantum dots coherently embedded in a n-type Si matrix. Evidence for an electron accumulation in the vicinity of Ge dots was found. The data are explained by a modification of the conduction band alignment induced by inhomogeneous tensile strain in Si around the buried Ge dots.

Introduction

There are two main types of band-edge alignment, namely type-I and type-II, in heterostructures with semiconductor quantum dots (QD's). In type-I QD's, the band gap of the narrow-gap material lies entirely within the gap of the wide-gap semiconductor, and both electron and hole are confined inside the same region [Fig. 1(a)]. A typical example of type-I band-edge lineup is the InAs QD's in GaAs matrix. For type-II QD's, the localization inside the dot occurs only for one of the charge carriers, i.e. electron (e) or hole (h), whereas the dot forms a potential barrier for the other particle [Fig. 1(b)]. One such system is Ge/Si(001) dots, in which the holes are strongly confined in the Ge region, and the electrons are free in the Si conduction band. When an electron-hole pair is photoexcited, the hole is captured by the Ge dot and creates an attractive Coulomb potential, resulting in a binding of an electron in Si in the vicinity of the dot [1]. Thus, the common view is that the localization of electrons in type-II Ge/Si(001) QD's is possible only under interband optical excitation. However, the above consideration disregards possible modification of the band structure due to inhomogeneous strain in the dots and surrounding matrix, leading to an overestimated determination of the interband transition energies while analyzing numerous photoluminescence experiments. Recent calculations [2,3,4] on Ge nanoclusters coherently embedded in the Si host demonstrated that tensile strain in the surrounding Si causes splitting of the sixfold-degenerate Δ valleys into the fourfold-degenerate Δ_4 valleys in the growth plane and twofold-degenerate Δ_2 valleys in the [001] growth direction. Figure 1(d) represents a Fermi surface for the Si conduction band and illustrates the definition of Δ_4 and Δ_2 valleys. The silicon band gap near the dot turns out to be smaller than that for bulk Si [5]. The lowest conduction band edge just above below the Ge island is formed by the Δ_2 valleys yielding the triangle potential well for electrons in Si near the Si/Ge boundary [Fig. 1(c)]. Thus one can expect that three-dimensional confinement of electrons in the strained silicon can occur *without any holes in the Ge dots*. In this paper we verify this hypothesis by using the capacitance spectroscopy and present the experimental evidence for electron accumulation in the strained Si close to embedded Ge dots.

1. Experimental

The transfer-doped heterostructures used in this study were grown by molecular beam epitaxy on a (001)-oriented n^+-type Si substrate. Transfer doping was achieved by a Sb-doped strained $Ge_{0.3}Si_{0.7}$ layer separated from the Ge QD's by 15 nm.

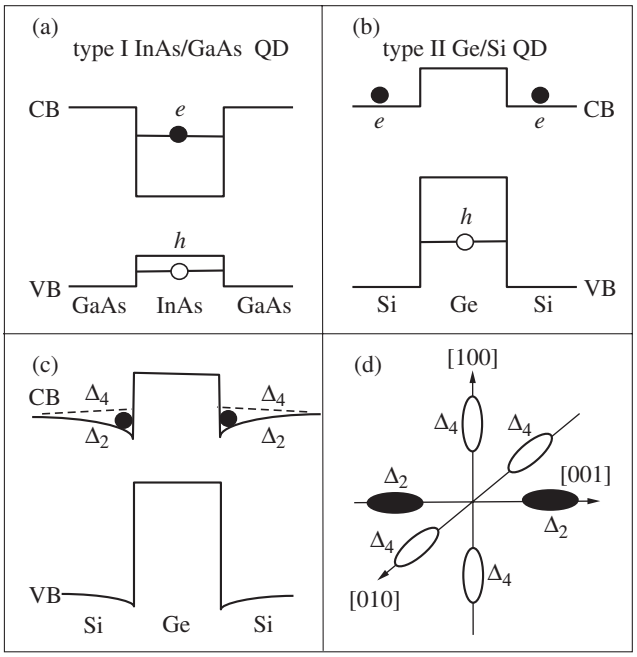

Fig. 1. Schematic overview of the band alignment in (a) type-I and (b) type-II QD's. (c) Band structure in Ge/Si(001) QD's modified by tensile strain. The conduction band (CB) in Si just above and below the Ge dot splits into Δ_4 and Δ_2 valleys. (d) Fermi surface in the Si conduction band.

The growth procedure producing Sb-doped layers was the following. After deposition of 10^{12} cm^{-2} Sb at 500 °C, a 0.3 μm thick Si buffer layer was grown. The layer of self-assembled Ge dots was formed subsequently by depositing 8 monolayers Ge while the sample temperature was kept at 500 °C. Typical dimensions of the Ge hut clusters are a width of 20–30 nm and a height of 2–3 nm. Then a 15 nm Si spacer and a 5 nm $Ge_{0.3}Si_{0.7}$ barrier layer were grown. At the end of this sequence, the sample was immediately cooled to 300 °C and covered by another 5 nm wide $Ge_{0.3}Si_{0.7}$ layer to trap the segregated antimony dopant atoms. Then the temperature was increased up to 500 °C and a 5 nm $Ge_{0.3}Si_{0.7}$ and a 0.3 μm Si cap layers were grown. A Ti-Au Schottky barrier with an area 6.6×10^{-3} cm^2 was deposited on top of the samples. Figure 2 demonstrates a schematic alignment of the conduction band edge in the final diode structure.

Since the vertical strain extension from the Ge island (typically of the order of the island height) is less then the width of the Si spacer layer (15 nm), the $Ge_{0.3}Si_{0.7}$ layer is formed on the relaxed Si, being coherently stained. Strained $Ge_{0.3}Si_{0.7}$ films

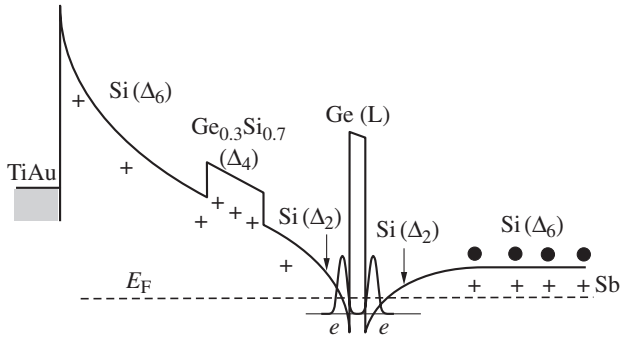

Fig. 2. Schematic diagram of the conduction band edge of the $Si/Ge_{0.3}Si_{0.7}/Si/Ge/Si(001)$ Schottky structure under reverse bias condition. The Si adjacent to the top and bottom of the Ge island is tensile strained.

on Si(001) show a type-II offset for the Δ_4 conduction band of about 40 meV [6]. The antimony ionization energy in Si and $Ge_{0.3}Si_{0.7}$ has approximately the same value ($\approx$ 40 meV). Therefore the Sb electron levels in $Ge_{0.3}Si_{0.7}$ lie close to the Si conduction band edge (Fig. 2) and, after spatial transfer, can supply electrons on the remote layer of Ge QD's.

To separate response from the dots, the reference sample was grown under conditions similar to the dot sample, except that no Ge QD's were deposited.

2. Results

Figure 3 shows capacitance-voltage (C-V) and conductance-voltage (G-V) characteristics for the reference and the dot samples measured at room temperature at a frequency of 100 kHz. The ledge in the C-V data occuring between -1 and -0.3 V and accompanying a conductance peak in both samples is a result of increased concentration of buried Sb impurity atoms in $Ge_{0.3}Si_{0.7}$ layer located 0.3 μm below the metal-Si interface. The diode with embedded Ge dots shows an additional pronounced plateau between -1.5 and -1 V. It appears as a second peak both in the charge concentration profile at a depth of 0.34 μm evaluated from the C-V data (see inset of Fig. 3) and in the G-V curve at -1.5 V, and relates to accumulation of electrons in the layer of Ge/Si QD's. The nominal position of the Ge dot layer is 0.33 μm from top. The peak position is shifted towards larger depth by approximately 10 nm, indicating that the energy level of electrons confined near the dots is somewhat deeper than the Sb impurity level in Si.

Acknowledgement

This work has been supported in part by INTAS (Nos. 03-51-5051, 01-0615), RFBR (No. 03-02-16526). A. I. Y. acknowledges financial support from the Program of the President of Russian Federation for support of young Russian doctors of sciences (Grant No. MD-28.2003.02).

References

[1] A. I. Yakimov, A. V. Dvurechenskii, A. I. Nikiforov, O. P. Pchelyakov, A. V. Nenashev, *Phys. Rev. B* **62**, R16283 (2000); A. I. Yakimov, N. P. Stepina, A. V. Dvurechenskii, A. I. Nikiforov, A. V. Nenashev, *Phys. Rev. B* **63**, 045312 (2001).

[2] O. G. Shmidt, K. Eberl, Y. Rau, *Phys. Rev. B* **62**, 16715 (2000).

[3] A. I. Yakimov, N. P. Stepina, A. V. Dvurechenskii, A. I. Nikiforov, A. V. Nenashev, *Semicond. Sci. Technol.* **15**, 1125 (2000).

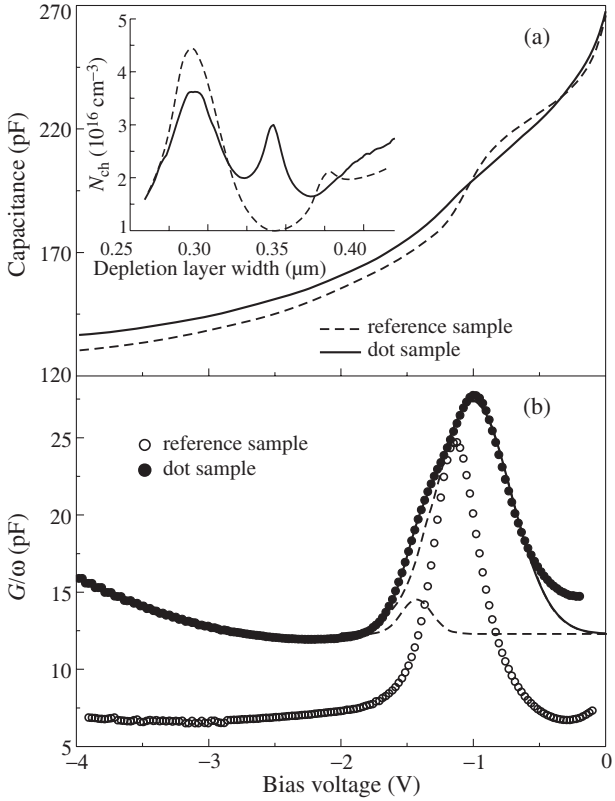

Fig. 3. (a) Capacitance-voltage characteristics of the dot and reference samples measured at room temperature under a test frequency 100 kHz. The inset shows the same data plotted as bulk charge concentration profile. (b) Bias dependence of the conductance. In (b) circles show the experimental data, and lines give the result of decomposition into two Gaussians for the dot sample.

[4] J. Y. Kim, J. H. Seok, *Appl. Phys. Lett.* **78**, 3124 (2001); *Mater. Sci. Eng. B* **89**, 176 (2002).

[5] The phenomena of a lowering of the Si band gap by 0.16 eV induced by inhomogeneous strain on top of the Ge island has been observed experimentally using locally resolved scanning tunneling microscopy by T. Meyer, M. Klemene, H. von Känel, *Phys. Rev. B* **60**, R8493 (1999).

[6] M. L. W. Thewalt, D. A. Harrison, C. F. Reinhart, J. A. Wolk, H. Lafontaine, *Phys. Rev. Lett.* **79**, 269 (1997); C. Penn, F. Schäffer, G. Bauer, S. Glutsch, *Phys. Rev. B* **59**, 13314 (1999).

13th Int. Symp. "Nanostructures: Physics and Technology"
St Petersburg, Russia, June 20–25, 2005

Positive and negative persistent photoconductivity in InAs/AlSb QW heterostructures: control of 2DEG concentration and built-in electric field

V. I. Gavrilenko[1], A. V. Ikonnikov[1], K. V. Marem'yanin[1], S. V. Morozov[1], K. E. Spirin[1], Yu. G. Sadofyev[2,3], S. R. Johnson[2] and Y.-H. Zhang[2]

[1] Institute for Physics of Microstructures RAS, GSP-105, N. Novgorod, 603095, Russia
[2] Arizona State University, Tempe, AZ 85287, USA
[3] Ryazan' State Radiotechnical Academy, Ryazan', 390048, Russia

Abstract. Bypolar persistent photoconductivity at $T = 4.2$ K in InAs/AlSb heterostructures with two-dimensional electron gas is studied. Under illumination by IR radiation ($\hbar\omega = 0.6-1.2$ eV), positive persistent photoconductivity related to the photoionization of deep donors is observed. At shorter wavelengths, negative persistent photoconductivity is observed that originates from bandgap generation of electron-hole pairs with subsequent separation of electrons and holes by the built-in electric field, capture of electrons by ionized donors, and recombination of holes with electrons in InAs quantum well. Under illumination by blue light the electron concentration in the quantum well is shown to decrease up to one order of the magnitude. At the IR illumination leading to the increase of both the electron concentration and the built-in electric field a beating pattern is observed in the Shubnikov-de Haas oscillations indicating the possible appearance of two sets of Landau levels due to the Rashba effect.

Introduction

InAs-based quantum wells (QW) heterostructures are promising for the fabrication of high-frequency transistors, resonant-tunneling diodes, devices for mid IR optoelectronics and spintronics. InAs/AlSb heterosystem exhibits a large value of the conduction band offset at the heterointerface of 1.35 eV and high mobility of electrons in InAs QWs up to 9×10^5 cm^2/(V s) at $T = 4.2$ K [1]. The electrons are present even in the QWs of nominally undoped structures [2], the electrons being supplied by deep donors in an AlSb or surface donors in GaSb cap [3–7]. The unique features of this heterosystem is bipolar persistent photoconductivity (PPC) at low temperatures [2]. When the heterostructures are exposed to IR radiation, positive PPC (PPPC) is observed due to the photoionization of deep donors in AlSb barrier layers followed by the capture of photogenerated electrons in InAs QWs [8, 9]. When the heterostructures are exposed to visible light, negative PPC (NPPC) is observed [2, 7-9]. The latter is attributed to bandgap excitation of electron-hole pairs with subsequent separation of electrons and holes by the built-in electric field, capture of electrons by ionized donors, and recombination of holes with 2D electrons in InAs QWs. Until now, the PPC spectra in InAs/AlSb heterostructures were studied in the only work [8] in the spectral range $\hbar\omega = 1-3$ eV and in the undoped samples only. This paper deals with the detailed study of PPC both in undoped and selectively doped InAs/AlSb heterostructures over a wider range $\hbar\omega = 0.6-6$ eV. The goal was to gain insight into the nature of NPPC and to control 2D electron concentration and the built-in electric field.

1. Experimental

The heterostructures under study were grown by molecular-beam epitaxy on semi-insulating GaAs(100) substrate on a composite AlSb or GaSb buffer. The active part of the structures consists of a bottom AlSb barrier of thickness 12–40 nm, InAs QW 15 nm wide, a top AlSb or $Al_{0.8}Ga_{0.2}Sb$ barrier of thickness 30–40 nm, and a 6-nm-thick GaSb cap layer [10]. In several structures 3 nm InAs layer was grown over GaSb one. In selectively doped structures, two δ-layers of Te were introduced in AlSb barriers 15 nm from the QW. The special shutter sequence was employed at the start and the finish of the InAs QW to ensure formation of In-Sb chemical bonds at both QW interfaces [11]. The concentration and mobility of 2D electrons at $T = 4.2$ K were determined from the measurements of the Hall effect and Shubnikov-de Haas (SdH) oscillations. The parameters of the samples are listed in the Table 1.

Table 1. Parameters of the samples under study at $T = 4.2$ K.

Sample	Top barrier	Cap layer	n_s, (10^{12} cm^{-2})	μ, (10^5 cm^2/Vs)
A680	AlSb	GaSb	0.74	—
A839	AlSb	GaSb	0.68	2.5
A856	AlSb	GaSb	0.65	3.9
A824	$Al_{0.8}Ga_{0.2}Sb$	GaSb	0.95	4.4
A1444	AlSb	GaSb	3.2	0.63
A1445	AlSb	GaSb	2.4	1.0
A1532	AlSb	InAs	—	—
A1534	AlSb	InAs	0.75	0.33
A1535	AlSb	InAs	0.46	0.48

The PPC spectra were recorded using an MDR-23 grating monochromator using a quartz incandescent lamp as the radiation source. At the monochromator output, the radiation was coupled to an optical fiber and delivered to the sample held within a liquid helium storage Dewar vessel. Two stripe In contacts were deposited onto a sample surface with a typical area of 4×4 mm at the edges (at a distance of about 3 mm). The photoconductivity spectra were recorded in two different modes: (i) each data point was taken after switching off the illumination, consecutive measurements being made step by step starting with the long wavelength part of the spectrum; and (ii) measurements were performed under continuous illumination with monochromatic radiation with the wavelength slowly scanned starting from the short-wavelength part of the

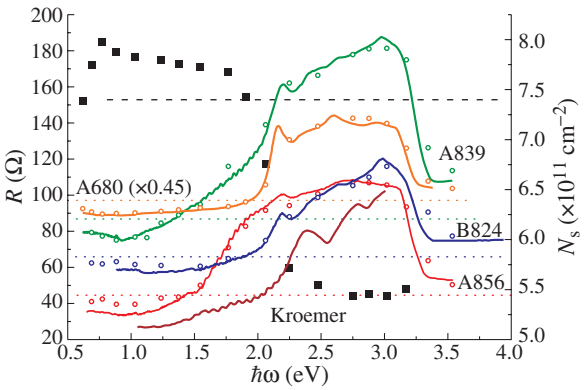

Fig. 1. Photoconductivity spectra of nominally undoped InAs/AlSb heterostructures (curves). Solid lines correspond to the data recorded under constant illumination with radiation the wavelength of which is continuously scanned; dots correspond to the values of the resistance recorded after switching illumination off at each point. Horizontal dotted lines indicate the values of the initial dark resistance for each sample. The lower curve (Kroemer) represents the photoconductivity spectrum of sample B from [8] (in arbitrary units). Squares — 2D electron concentration versus photon energies measured by Hall effect in the sample A680.

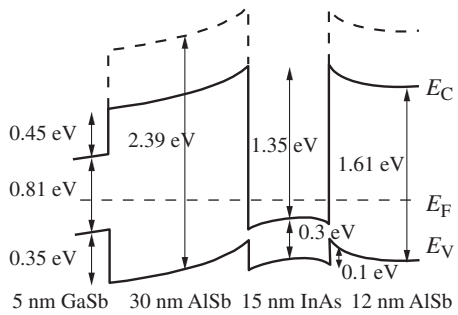

Fig. 2. Energy-band diagram for nominally undoped InAs/AlSb samples. The 2DEG appears in the InAs quantum well due to ionization of donors at the surface of the GaSb cap layer and deep-level donors in AlSb barriers, which leads to the formation of the built-in electric field. The dashed line shows the profile for the edge of the Γ-valley in the conduction band of AlSb.

spectrum. The typical time of a spectral recording was several tens of minutes.

2. Results and discussion

Photoconductivity spectra for nominally undoped heterostructures A680, A839, A856, and B824 are shown in Fig. 1. One can see that, for these samples, the photoconductivity spectra obtained by the two methods described above (shown by dots and solid lines, respectively) agree well with each other. This means that *persistent photoconductivity* was measured in both modes, i.e., the effect introduced by constant illumination in the case of continuous recording of the spectral curves is insignificant. For comparison, the photoconductivity spectrum of a similar InAs/AlSb sample (with an InAs QW 12 nm wide) taken from [8] is also shown in Fig. 2. In agreement with the results obtained in [8], we observed PPPC in the long-wavelength part of the spectrum, beginning from the lowest photon energy involved in our measurements ($\hbar\omega = 0.62$ eV). At $\hbar\omega > 1.1$ eV, the sample resistance increases and PPPC is changed to NPPC; simultaneously, the slope of the spectral dependences increases. In all samples, several characteristic local maxima of NPPC are observed at $\hbar\omega > 2.1$ eV and a sharp drop of the resistance takes place at $\hbar\omega > 3.1$ eV. For sample B824, the measurement range was extended to 6 eV; beginning with 5 eV, a weak gradual increase in NPPC was observed. The measurements reported in [8] were carried out in the range of photon energies up to 3 eV, and resistance drop in the ultraviolet region was not observed. Once can see that in the sample A856 with $Al_{0.8}Ga_{0.2}Sb$ top barrier the high-slope region in the resistance spectral curve is shifted to lower photon energies; meanwhile, the positions of most of the spectral features remain unchanged.

The energy-band diagram of the active region of a nominally undoped heterostructure with 2D electron gas (2DEG) in the InAs QW is shown in Fig. 2. Following [8], we relate the PPPC observed in the long-wavelength region to the photoinization of deep donors and accumulation of electrons in the QW. PPPC takes place at energies ($\hbar\omega \geq 0.62$ eV) lower than the distance from the Fermi level (which is located about 100 meV above the bottom of the InAs conduction band) to the edge of the conduction band in AlSb. The corresponding transitions can occur between neutral donors (i.e., donors with levels below the Fermi level) in the bulk of the AlSb and higher electron subbands of size quantization in the InAs QW (wave functions of these subbands penetrate much more deeply into the barrier than the wave function of the 1st subband). The electrons excited into the QW relax rapidly to the 1st subband, and their transitions back to the ionized donor centers are inhibited due to high confinement of the 1st subband wave function.

Again following [8], we believe that the NPPC observed upon increasing the photon energy originates from bandgap excitation of electron-hole pairs with subsequent separation of the charge carriers by the built-in electric field and capture of holes into the QW, where they recombine with the 2D electrons. As the photon energy is increased, the electron-hole pairs are first generated in the GaSb cap layer. With further increase in the photon energy, excitation of electron -hole pairs through the indirect band gap of AlSb sets in for $\hbar\omega > 1.61$ eV (see Fig. 2). Finally, at $\hbar\omega = 2.39$ eV, direct optical transitions of electrons from the valence band to the Γ-valley of the AlSb conduction band are expected to set in. If the top barrier is made of $Al_{0.8}Ga_{0.2}Sb$, which has a narrower bandgap, all threshold energies in the NPPC spectra should decrease, and exactly this is the case for sample A856 (see Fig. 1). The distinctive peak of NPPC at $\hbar\omega = 2.2$ eV is most probably related to the presence of some specific donor centers in the structures under study; these centers appear to have been absent in the samples studied in [8]. This peak was observed in the structures with the top barrier composed of either AlSb (samples A680, A839 and B824) or $Al_{0.8}Ga_{0.2}Sb$ (sample A856); in the latter case, apparently, the peak is related to similar optical transitions in the bottom AlSb barrier. A sharp drop in NPPC is attributed to the switching-off direct optical transitions from the heavy hole subband (where the density-of-states is maximal) to the conduction band due the reaching of its ceiling.

Let us briefly discuss the PPC of selectively doped samples B1444 and B1445 [12]. Here, unlike the spectra of nominally undoped structures, a well-defined peak of PPPC is observed near 1 eV. For structure B1445 with a lower doping level, a band of weak NPPC in the high-photon-energy region is still present. In the PPC spectrum of sample B1444 with a higher

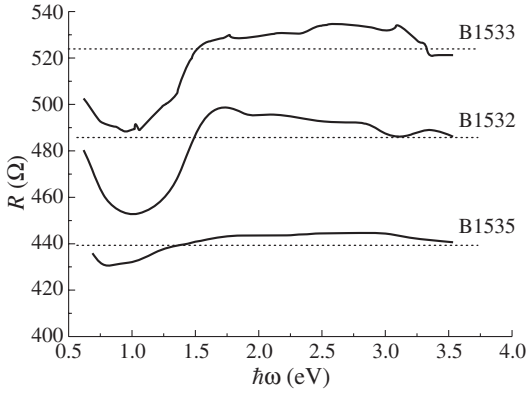

Fig. 3. PPC spectra of InAs/AlSb heterostructures with InAs cap layer. Horizontal dot lines correspond to initial dark values of the resistance.

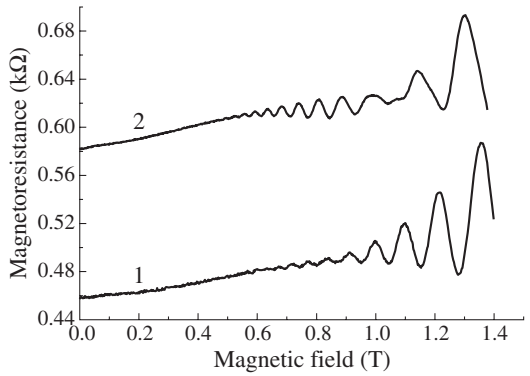

Fig. 4. Magnetoresistance of the InAs/AlSb sample [14,15] before (1) and after (2) illumination by IR LED.

doping level, a characteristic increase in the resistance in the short-wavelength region of the spectrum is also observed; however, this increase is insufficient to overcome the general trend (which holds for all wavelengths) toward the reduction in the resistance. Apparently, apart from the formation of shallow donor levels [13], doping AlSb with Te impurity may result in the appearance of deep donor levels that lie below the Fermi level. If the concentration of Te is high (sample B1444), photoionization of deep-level centers is dominant for all photon energies and NPPC is not observed.

Fig. 3 represent the PPC spectra of the samples with InAs cap layer grown over the GaSb one. Just as in the Fig. 1 a pronounced PPPC is observed in the long wavelength range. However the NPPC is very weak. This allows to conclude that the NPPC results from the photoexcited electron capture by surface donors in the GaSb cap layer (cf. [8,9]) (that apparently are absent in the InAs one) rather than by deep donors in the AlSb barrier layers. The maximum decrease of 2D electron concentration due to NPPC achieved is one full order of magnitude from 6×10^{11} down to 6×10^{10} cm^{-2} under illumination by blue light emitting diode (LED) with the photon energies exceeding the direct bandgap of AlSb [14]. At the same time the illumination of the sample with red LED results in concentration decrease by 3 times only.

At the illumination of the InAs/AlSb heterostructure by IR LED a 10–20% increase of 2D electron concentration was observed. This should result in the corresponding increase of the built-in electric field. In the magnetotransport measurements single-period SdH oscillations in low magnetic fields were observed under dark conditions. However during and after illumination of the sample with IR light, a beating pattern is observed in the SdH oscillations [14,15] indicating the possible appearance of two sets of Landau levels due to the Rashba effect [16].

Acknowledgements

This work was financially supported by RFBR (Grant #05-02-17531) and by the Russian Academy of Sciences. The authors are thankful to A.V. Antonov, D.M.Gaponova and I.V. Erofeeva for technical assistance.

References

[1] C. Nguyen *et al*, *J. Electron. Mater.* **22**, 255 (1993).
[2] G. Tuttle *et al*, *J. Appl. Phys.* **65**, 5239 (1989).
[3] C. Nguyen *et al*, *Appl. Phys. Lett.* **60**, 1854 (1992).
[4] D. J. Chadi, *Phys. Rev. B* **47**, 13478 (1993).
[5] J. Shen *et al*, *J. Appl. Phys.* **77**, 1576 (1995).
[6] A. Furukawa, S. Ideshita, *J. Appl. Phys.* **75**, 5012 (1994).
[7] I. Lo *et al*, *Appl. Phys. Lett.* **60**, 751 (1992).
[8] Ch. Gauer *et al*, *Semicond. Sci. Technol.* **8**, S137 (1993).
[9] C. Gauer *et al*, *Semicond. Sci. Technol.* **9**, 1580 (1994).
[10] Yu. G. Sadofyev *et al*, *Appl. Phys. Lett.* **81**, 1833 (2002).
[11] G. Tuttle *et al*, *J. Appl. Phys.* **67**, 3032 (1990).
[12] V. Ya. Aleshkin *et al*, *Semiconductors* **39**, 22 (2005).
[13] A. Nakagawa *et al*, *Appl. Phys. Lett.* **57**, 1551 (1990).
[14] Yu. G. Sadofyev *et al*, *Semiconductors* **39**, 95 (2005).
[15] Yu. G. Sadofyev *et al*, *J. Crystal Growth* (2005, in press).
[16] Yu. A. Bychkov, E.I.Rashba, *JETP Lett.* **39**, 78 (1984).

13th Int. Symp. "Nanostructures: Physics and Technology"
St Petersburg, Russia, June 20–25, 2005

Conductivity magnetooscillations in 2D electron-impurity system under microwave irradiation: role of magnetoplasmons

E. E. Takhtamirov and V. A. Volkov
Institute of Radioengineering and Electronics of RAS, 125009 Moscow, Russia

Abstract. It is developed a many-electron approach to explain the recently observed conductivity magnetooscillations in very high mobility 2D electron systems under microwave irradiation. For the first time a theory takes into account the microwave-induced renormalization of the screened impurity potential. As a result this potential has singular, dynamic and non-linear in electric field nature. That changes the picture of scattering of electrons at impurities in a "clean" 2D system essentially: for appearence of the rectified dissipative current responsible are excitations of 2D magnetoplasmons rather than one-electron transitions between Landau levels. In a "dirty" 2D system the role of electron-electron interaction diminishes, so the collective excitations cease to exist, and our results turn into the well-known ones, which were obtained in the one-electron approach.

For a high quality 2D electron system in structures GaAs/AlGaAs subjected to microwave (MW) field with frequency Ω it was found that the magnetoresistance experienced oscillations governed with the ratio Ω/ω_c [1], where $\omega_c = eB/(m^*c)$ is the cyclotron frequency. The states with zero resistance were observed with an increase of MW field intensity [2]. These observations have been confirmed by other researchers, see the review [3]. That brought about an avalanche of theoretical works.

There exist two mainstream theoretical scenarios of the effect, both being one-electron. The first one is based on the mechanism of electron displacement against strong external DC field as a result of MW absorption and impurity scattering, and this was shown to be capable of leading to the absolute negative DC conductivity [4]. Being then unstable, the system breaks into domains, and one just registers zero resistance [5]. The second scenario is based on the wave-induced inversion of electron population on higher Landau levels (LL) [6]. Indisputable explanation of the main experimental data has not been achieved yet.

In this work we consider the effect of electron-electron (e-e) interaction on the impurity scattering confining ourselves to the first scenario. Here we analyse the case of an unbounded high-quality 2D electron system with very weak impurity scattering. The main obvious consequence of e-e interaction is the screening of the impurity potential with 2D electrons. At first glance it seems that e-e interaction is not able to induce a qualitative change in the results of Ref. [4]. But it is shown to be a delusion. With that, for the very appearence of the dissipative direct current responsible are not the usually considered single-particle transitions of electrons between LL, but rather 2D magnetoplasmons. Below in the framework of the random phase approximation (RPA) it is developed a systematic theory of the non-liner dissipative conductivity applicable to the experimental conditions [1,2].

Dealing with our system, let us change the reference frame to the one connected with the external homogenious electric field. In such a reference frame electrons do not experience the external electric field if no impurity is available in the system. Being presented and so transformed, the bare potential of the impurity system becomes time-dependent:

$$V_{\rm imp}\left(\mathbf{r}\right) \to V_{\rm imp}\left(\mathbf{r}-\mathbf{r}_0\left(t\right)\right), \qquad (1)$$

where $\mathbf{r}_0(t)$ is the radius-vector describing movement of the center of the classical oscillator in external electric field. To screen the transformed potential, which is the right-hand side of the transform (1), one should use the dynamic dielectric function. The space-time Fourier transform of the screened potential is

$$V_{\rm imp}^{\rm (scr)}\left(\mathbf{q},\omega\right) = \frac{V_{\rm imp}\left(\mathbf{q},\omega\right)}{\varepsilon\left(q,\omega\right)}, \qquad (2)$$

where $V_{\rm imp}(\mathbf{q},\omega)$ is the Fourier image of the right-hand side of the transform (1), and $\varepsilon(q,\omega)$ is the dielectric function. Being obtained in RPA, it has the form:

$$\varepsilon\left(q,\omega\right) = 1 + \frac{V_{\rm ee}(q)}{\pi\hbar\lambda^2}\sum_{M,M'}\frac{\left(f_M - f_{M'}\right)I_{M,M'}\left(q\right)}{\omega_c\left(M'-M\right)+\omega+i0},$$

where $V_{\rm ee}(q)$ is the Fourier transform of potential of e-e interaction, for 2D electron gas in a medium with the constant lattice dielectric permeability κ we have $V_{\rm ee}(q) = 2\pi e^2/(\kappa q)$, $\lambda = \sqrt{\hbar c/(eB)}$ is the magnetic length, f_M is the Fermi distribution function, M and M' are LL indices. And $I_{M,M'}(q)$ is the square of the absolute value of the overlap integral of the Landau functions with the oscillator centers shifted by $q\lambda^2$. At the magnetoplasmon frequency $\omega = \omega_{\rm MP}(q)$ the denominator in Eq. (2) turns to zero, so the screening in the strong field does not ordinarily soften the impurity potental, but rather sharply strengthen it. Let the external homogeneous electric field $\mathbf{F}$ be a sum of AC field of the wave with the amplitude W and DC dragging field $F_{\rm DC}$, both having only one (x) component for simplicity:

$$F_x = F_{\rm DC} + W\sin\Omega t.$$

The current density in the system is $\mathbf{j} = -en_{\rm s}{\rm Tr}(\rho\mathbf{v})$, where $n_{\rm s}$ is 2D electron concentration, $\mathbf{v}$ is the velocity operator, ρ is the density matrix that meets the quantum kinetic equation. Following Ref. [7] we solve the kinetic equation at low order in scattering of electrons at the screened impurities. After taking an average of all chaotic impurity configurations, asuming only one type of impurity with 2D concentration $n_{\rm imp}$ and the bare single impurity potential $V_{\rm imp}^{(0)}(q)$, we have for the time average of the dissipative current density:

$$\langle j_x\rangle = -\frac{en_{\rm imp}}{(2\pi)^2 m^*\omega_c}\int {\rm d}^2q\,\frac{|\,V_{\rm imp}^{(0)}(q)\,|^2}{V_{\rm ee}(q)}q_y$$

$$\times \sum_{n=-\infty}^{+\infty} J_n^2(Q)\,\mathrm{Im}\varepsilon^{-1}\left(q, q_y v_\mathrm{H} + n\Omega\right), \qquad (3)$$

where J_n is the Bessel function, $Q = \left(Q_x^2 + Q_y^2\right)^{1/2}$,

$$Q_x = \frac{q_x e W}{m^*(\omega_c^2 - \Omega^2)}, \quad Q_y = \frac{q_y e W \omega_c}{m^*\Omega(\omega_c^2 - \Omega^2)},$$

$v_\mathrm{H} = cF_\mathrm{DC}/B$ is the Hall velocity. If we neglect the collision-induced LL broading,

$$\mathrm{Im}\frac{1}{\varepsilon\left(q, q_y v_\mathrm{H} + n\Omega\right)} = -\pi \sum_p \frac{\delta\left(q_y v_\mathrm{H} + n\Omega - \omega_p\right)}{\varepsilon'_\omega\left(q, \omega_p\right)}, \quad (4)$$

where $\omega_p = \omega_p(q)$, index $p = \pm 1, \pm 2, \ldots$ enumerates all solutions to the dispersion equation $\varepsilon\left(q, \omega_p\right) = 0$, so that $\omega_p \to p\omega_c$ as $q \to \infty$, and $\varepsilon'_\omega\left(q, \omega_p\right) = \mathrm{d}\varepsilon\left(q, \omega\right)/\mathrm{d}\omega\big|_{\omega=\omega_p}$.

When no MW field is given, $W = 0$, only the term with $n = 0$ survives in the sum of (3), $J_0(0) = 1$. In such a form our result, which generalizes the one of Ref. [8] obtained with leaving e-e interaction out, is applicable to explanation of the experiment [9].

With the help of polar coordinates in Eq. (3): $q_x = q\cos\phi$, $q_y = q\sin\phi$, using Eq. (4) and integrating by $\mathrm{d}\phi$ we obtain the expression that allows graphical analysis:

$$\langle j_x\rangle = \frac{en_\mathrm{imp}}{2\pi m^*\omega_c}\int_0^{+\infty}\mathrm{d}q\,\frac{|\,V_\mathrm{imp}^{(0)}(q)\,|^2}{V_\mathrm{ee}(q)}\sum_p\frac{q^2}{\varepsilon'_\omega\left(q,\omega_p\right)}$$
$$\times\sum_{n=-\infty}^{+\infty}J_n^2(\bar{Q}_p)\frac{\omega_p - n\Omega}{q v_\mathrm{H}}\frac{1}{\sqrt{q^2 v_\mathrm{H}^2 - (\omega_p - n\Omega)^2}} \qquad (5)$$
$$\times\left(\Theta\left(\frac{\omega_p - n\Omega}{q v_\mathrm{H}} + 1\right) - \Theta\left(\frac{\omega_p - n\Omega}{q v_\mathrm{H}} - 1\right)\right).$$

Here Θ is the Heaviside step-function, and

$$\bar{Q}_p = \frac{qeW}{m^*(\omega_c^2 - \Omega^2)}\sqrt{1 + \left(\frac{\omega_c^2}{\Omega^2} - 1\right)\left(\frac{\omega_p - n\Omega}{q v_\mathrm{H}}\right)^2},$$

In Fig. 1 shown are the spectrum of the principal magnetoplasmon (at $p = 1$ and $\omega_p(q) > 0$), two lines ($\omega = n\Omega \pm q v_\mathrm{H}$) forming a region that confines all values of ω_p and so q contributing to the integral (see the last line of Eq. (5)), and the bisector ($\omega = n\Omega$) parting that region onto two ones contributing purely positive or negative. Let $F_\mathrm{DC} > 0$ be weak enough (say $v_\mathrm{H} < \omega_c/2k_\mathrm{F}$, where $\hbar k_\mathrm{F}$ is the Fermi momentum), so that the term with $n = 0$ in the sum of Eq. (3) does not play a role with its always positive contribution. And let us consider one-photon processes only: $n = \pm 1$ in the sum of Eq. (3). Then $\langle j_x\rangle > 0$ if $\Omega < \omega_c$, that meets the positive magnetoresistance. Other case, if $\omega < \Omega < 2\omega_c$, a bunch of magnetoplasmon modes may fall into the region of negative contribution. That gives the absolute negative conductivity. Similar picture holds for higher values Ω, and the higher magnetoplasmon modes $|p| > 1$ take part in the play. In contrast to theories omitting the screening [4], the regions of positive and negative conductivities are finite even in an ideal case of no LL broading (4), and anyhow small F_DC be.

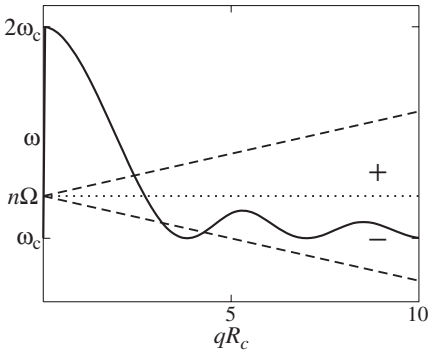

Fig. 1. Full thick line: spectrum of the principal magnetoplasmon; dashed lines: boundaries $\omega = n\Omega \pm q v_\mathrm{H}$ of the contribution region; dotted line, $\omega = n\Omega$, divides the region onto the ones of positive "+" and negative "−" contributions to dissipative current; R_c is the Larmour radius.

In a "dirty" 2D system the role of electron-electron interaction diminishes. It is somewhat equivalent to $V_\mathrm{ee} \to 0$. Then in the vicinity of $\omega = \omega_p(q) \approx p\omega_c$ we may use the approximate expression for $\varepsilon(q, \omega)$:

$$\varepsilon_p\left(q,\omega\right) = 1 + \frac{2m^* V_\mathrm{ee}(q)}{\pi\hbar^2}\frac{p^2\omega_c^2}{p^2\omega_c^2 - \omega^2 - i0\mathrm{sign}\omega}\bar{I}_p\left(q\right),$$

where $\bar{I}_p\left(q\right) = p^{-1}\sum_{M=0}^{\infty}\left(f_M - f_{M+p}\right)I_{M,M+p}\left(q\right).$

Then V_ee falls out, and with condition (4), Eq. (3) transforms to

$$\langle j_x\rangle = \frac{en_\mathrm{imp}}{(2\pi\hbar)^2}\int \mathrm{d}^2 q\;|\;V_\mathrm{imp}^{(0)}(q)\;|^2\;q_y\sum_{n=-\infty}^{+\infty}J_n^2(Q)$$
$$\times\sum_p p\bar{I}_p\left(q\right)\;\delta\left(q_y v_\mathrm{H} + n\Omega - p\omega_c\right),$$

which is the result of Ref. [4] for ideal infinitely narrow LL, and the result of Ref. [8] for the case of DC field only.

Acknowledgements

The work was supported by RFBR and RAS programme.

References

[1] M. A. Zudov *et al*, *Phys. Rev. B* **64**, 201311 (2001).
[2] R. G. Mani *et al*, *Nature* **420**, 646 (2002); M. A. Zudov *et al*, *Phys. Rev. Lett.* **90**, 046807 (2003).
[3] R. R. Du *et al*, arXiv:cond-mat/0409409.
[4] V. I. Ryzhii, *Sov. Phys.-Solid State* **11**, 2078 (1970); V. I. Ryzhii *et al*, *Sov. Phys.-Semiconductors* **20**, 1299 (1986); A. C. Durst *et al*, *Phys. Rev. Lett.* **91**, 086803 (2003).
[5] A. V. Andreev *et al*, *Phys. Rev. Lett.* **91**, 056803 (2003).
[6] S. I. Dorozhkin, *JETP Lett.* **77**, 577 (2003); I. A. Dmitriev *et al*, *Phys. Rev. B* **71**, 115316 (2005).
[7] E. Adams and T. Holstein, *Journ. Phys. Chem. Solids* **10**, 254 (1959).
[8] B. A. Tavger and M. Sh. Yerukhimov, *Sov. Phys.-JETP* **24**, 354 (1967).
[9] C. L. Yang *et al*, *Phys. Rev. Lett.* **89**, 076801 (2002).

13th Int. Symp. "Nanostructures: Physics and Technology"
St Petersburg, Russia, June 20–25, 2005

Observation of quantum corrections to the transport coefficients of a 2DEG up to 110 K

V. T. Renard[1,3], O. A. Tkachenko[2], Z. D. Kvon[2], E. B. Olshanetsky[2], A. I. Toropov[2], J.-C. Portal[1,3,4] and I. V. Gornyi[5,6]

[1] GHMFL, MPI-FKF/CNRS, BP-166, F-38042, Grenoble Cedex 9, France
[2] Institute of Semiconductor Physics, Novosibirsk 630090, Russia
[3] INSA-Toulouse, 31077, Cedex 4, France
[4] Institut Universitaire de France, Toulouse, France
[5] Institut für Nanotechnologie, Forschungszentrum Karlsruhe, 76021 Karlsruhe, Germany
[6] Ioffe Physico-Technical Institute, St Petersburg, Russia

Abstract. We report an experimental study of the quantum corrections to the magnetoconductivity and Hall resistance of a low mobility, high density two-dimensional electron gas in a AlGaAs/GaAs/AlGaAs quantum well in a wide temperature range (1.5–110 K).

Introduction

Recently new theories [1,2,3,4] of the interaction corrections to the conductivity of a two-dimensional electron gas (2DEG) were developed. The theories [1,2,3] of the electron-electron (e-e) interaction correction bridge a gap between the two seemingly unrelated theories which were developed for two opposite regimes: the diffusive regime [5] $k_BT\tau/\hbar \ll 1$, and the ballistic regime [6] $k_BT\tau/\hbar \gg 1$. Conformably to the previous result [5], it predicts a logarithmic temperature dependence of the longitudinal conductivity and the Hall coefficient in the diffusive regime. In the ballistic regime, the linear T-dependence of the conductivity [6] is recovered but with a sign depending on the interaction strength and the Hall coefficient is predicted to behave like $1/T$. Besides, Ref. [3] considers the influence of e-e interaction on the magnetoresistance and Ref. [4] the electron-phonon impurity correction.

The aim of the present work is to experimentally study the interaction related corrections to the magnetoconductivity of a 2DEG in a AlGaAs/GaAs/AlGaAs quantum well. This study was made in a broad temperature range covering both the diffusive and ballistic interaction regimes for these samples.

1. Experimental set up

The experimental samples had a 2DEG formed in a narrow (5 nm) AlGaAs/GaAs/AlGaAs quantum well δ-doped in the center. Such doping results in a low mobility and a high carrier density. A detailed description of the structure can be found in Ref. [7]. Two samples from the same wafer have been studied for which similar results were obtained. Here we present the data obtained for one of the samples with the following parameters at $T = 1.4$ K depending on prior illumination: the electron density $N_s = (2.54-3.41) \times 10^{12}\,\mathrm{cm}^{-2}$ and the mobility $\mu = (380-560)\,\mathrm{cm}^2/\mathrm{Vs}$. The Hall bar shaped samples were studied between 1.4 K and 110 K in magnetic fields up to 15 T using a superconducting magnet and a VTI cryostat and also a flow cryostat ($T > 5$ K) placed in a 20 T resistive magnet. The data was acquired via a standard four-terminal lock-in technique with the current 10 nA.

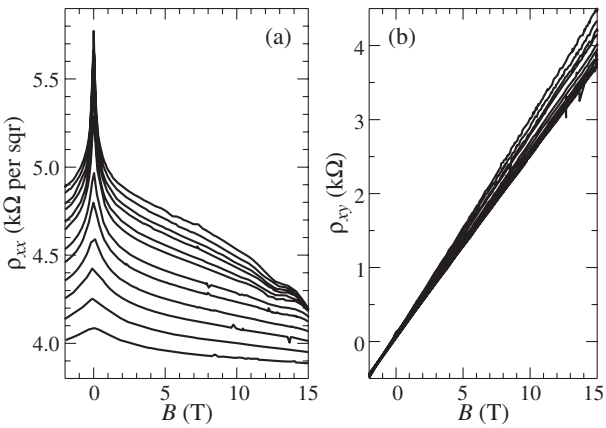

Fig. 1. Longitudinal resistivity of the sample at $N_s = 2.56 \times 10^{12}\,\mathrm{cm}^{-2}$ for temperature = 1.4, 1.9, 3.1, 4, 7.2, 10.25, 15.45, 21.5, 31, 46.2, 62.8, 84.5 and 110 K from top to bottom. (b) Hall resistance at the same temperatures (from top to bottom).

2. Results

Fig. 1 shows the longitudinal and Hall resistivities of the sample as a function of magnetic field at temperatures up to 110 K. As can be seen both are strongly temperature dependent.

Before analyzing the data in terms of the electron electron interaction theory one should examine the following other possible origins for this dependence. First the density should not change within the entire temperature range. The value of the density $N_s = 2.56 \times 10^{12}\,\mathrm{cm}^{-2}$ obtained from the analysis of the low-T Shubnikov de Haas oscillations coincides with the one deduced from the Hall effect at high temperature (when it becomes T-independent). Therefore we argue that the density does not change in the entire temperature range. Secondly, at high temperatures phonons might play a significant role in the temperature dependence of the conductivity. However in our case impurity scattering dominates up to 110 K due to high density and low mobility of 2DEG. Indeed estimation of contribution of electron-phonon impurity scattering [4] is about 3% from Drude conductivity at $T = 110$ K. Thus, we can neglect phonon scattering.

Having excluded the phonon scattering and the density variation as possible causes of the behavior shown in Fig. 1 we associate the observed temperature dependencies with the quan-

tum corrections to the transport coefficients. Our data will be analyzed in the framework of the recent theories [1,2,3] valid for a degenerated 2DEG ($k_BT \ll E_F$). According to Ref. [7] only one subband is occupied in our quantum well at $N_s = 2.56 \times 10^{12}\,\mathrm{cm}^{-2}$ ($E_F \approx 1000\,\mathrm{K}$).

The MagnetoConductivity (MC) of the sample can be presented in the following form:

$$\sigma_{xx}(B,T) = \frac{\sigma_D(\tau)}{1+(\omega_c\tau)^2} + \Delta\sigma_{WL}(B,T) + \Delta\sigma_{ee}^{\mathrm{Diff}}(T)\,, \quad (1)$$

where σ_D is the Drude conductivity, ω_c the cyclotron frequency, τ the scattering time and $\Delta\sigma_{WL}$ is the Weak Localization (WL) correction to the conductivity. Note that the term $\Delta\sigma_{ee}^{\mathrm{Diff}}$ corresponds to diffusive contribution in e-e interactions correction whereas the ballistic contribution is included in the first term of Eq. 1 via an interaction renormalized $\tau(T)$ [1,8]. The third term $\Delta\sigma_{ee}^{\mathrm{Diff}}$ vanishes with increasing temperature. In Eq. 1 any possible classical MC is neglected. Earlier Eq. 1 was established only in diffusive regime, but it is valid in the intermediate regime if temperature dependence $\tau(T)$ is taken into account [8].

To extract total e-e interaction contribution of conductivity at $B = 0$ the following procedure was used. The experimental conductivity tensor was found using the data shown in Fig. 1. At sufficiently high field the MC should be described by the first and last term in Eq. 1 only since, as is well known, the WL contribution is destroyed by magnetic field [9]. $\Delta\sigma_{ee}^{\mathrm{Diff}}$ is B-independent and only induces a vertical T-dependent shift of the curves. Therefore all the field dependence at sufficiently high field should come from the first term. The MC curves were fitted to the shape of the first term with τ and $\Delta\sigma_{ee}^{\mathrm{Diff}}$ as the fitting parameters for $B > 6\,\mathrm{T}$. The result of the fit was then extrapolated to $B = 0\,\mathrm{T}$. This procedure excludes the WL contribution of the data. Finally the value $\sigma_0 = \sigma_D(T \to 0) = 5.92 \times e^2/h$ corresponding to the T-independent value of $\tau = 2.13 \times 10^{-14}\,\mathrm{s}$ in the diffusive regime was subtracted to obtain the total e-e interaction correction. It worth noticing that this procedure permits to analyse e-e interaction contribution to conductivity at any magnetic field up to 15 T since temperature dependences of $\tau(T)$ and $\Delta\sigma_{ee}^{\mathrm{Diff}}(T)$ are already found from fitting.

The resulting experimental e-e interaction contribution at $B = 0$ is shown in Fig. 2a together with the predictions of Eq. 2.16a of Ref. [1]. The theoretical curve is arbitrary shifted since only temperature dependence makes sense. Note that for low interaction parameter $r_s = E_c/E_F$ (in our sample $r_s = 0.35$) Eq. 2.16a requires no adjustable parameter [1]. As can be seen there is a good agreement between the theory and our data. From condition $T\tau = 0.1$ and $\tau = 2.13 \times 10^{-14}\,\mathrm{s}$ we estimated transition temperature $T = 30\,\mathrm{K}$ where logarithmic temperature behavior in the diffusive regime changes into linear T-dependence in the ballistic regime.

Let us now turn to the analysis of the Hall data. The experimental T-dependence of e-e interaction correction to the Hall coefficient is shown in Fig. 2b and compared to the prediction [2]. We observe in experiment logarithmic behavior in the diffusive regime and rapid vanishing with increasing temperature in the ballistic regime. This qualitatively agrees with theories [2,3]. Correction calculated by Eq. 17 and 18 of Ref. [2] without fitting parameters ($F_0^\sigma = -0.1$ for $r_s = 0.35$) is shown by the dashed curve. This curve describes more smoothed

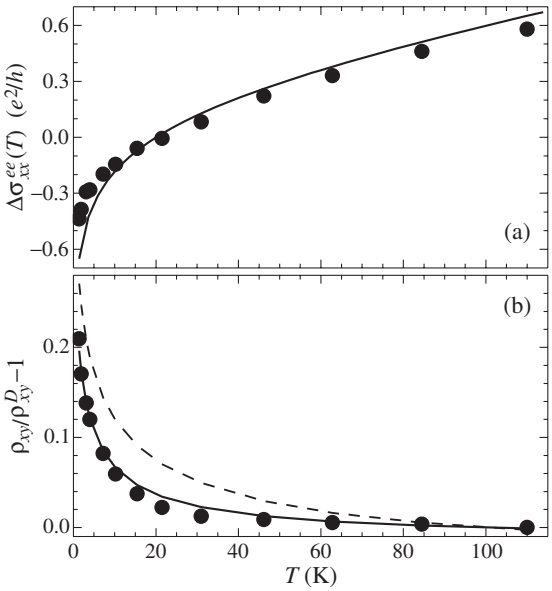

Fig. 2. (a) e-e interaction correction to the conductivity: experiment (dots) and theory (line). (b) Correction to the Hall coefficient: experiment (dots), theory (dashed line) and modified theory (line).

transition from diffusive to ballistic regime. Sharper decrease of correction observed in the experiment can be explained by anisotropy of scattering which reduces the probability of return and thus the total correction [8]. This effect was disregarded in Ref. [2], but analysed in detail in Ref. [3]. However we have found that if the coefficient $\frac{11\pi}{192}$ in the argument of the logarithm in Eq. 17 and 18 of Ref. [2] is replaced by $\frac{3\pi}{192}$ the theoretical curves describe rather well the experiment.

In conclusion, we have observed the transition from the diffusive to the ballistic regime in the weak interaction limit for the longitudinal conductivity and the Hall coefficient in a high density low mobility 2DEG. We find our experimental results to be in a good qualitative agreement with theory.

Acknowledgements

We are very grateful to A. Dmitriev and V. Tkachenko for interesting discussions. This work was supported by PICS-RFBR (Grant No 1577), RFBR (Grant No 02-02-16516), NATO, INTAS (Grant No 01-0014), programs "Physics and Technology of Nanostructures" of the Russian ministry of Industry and Science and "Low dimensional quantum structures" of RAS.

References

[1] G. Zala *et al*, *Phys. Rev. B*, **64**, 214204 (2001).
[2] G. Zala *et al*, *Phys. Rev. B*, **64**, 201201(R) (2001).
[3] I. V. Gornyi *et al*, *Phys. Rev. B*, **69**, 045313 (2004).
[4] A. Sergeev *et al*, *Phys. Rev. B*, **69**, 075310 (2004).
[5] B. L. Altshuler and A. G. Aronov, *Electron-electron interaction in disordered systems* (A. L. Efros, M. Pollak, Amsterdam, 1985).
[6] A. Gold *et al*, *Phys. Rev. B* **33**, 1076 (1986).
[7] Z. D. Kvon *et al*, *Physica E*, **21**, 742 (2004).
[8] I. V. Gornyi, unpublished.
[9] S. Hikami *et al*, *Prog. Theor. Phys*, **63**, 707 (1980).

13th Int. Symp. "Nanostructures: Physics and Technology"
St Petersburg, Russia, June 20–25, 2005

Transport properties of 2D-electron gas in the InGaAs/GaAs DQW in a vicinity of the Hall insulator–quantum Hall liquid transition

Yu. G. Arapov[1], S. V. Gudina[1], G. I. Harus[1], V. N. Neverov[1,2], N. G. Shelushinina[1], M. V. Yakunin[1], S. M. Podgornyh[1], E. A. Uskova[3] and B. N. Zvonkov[3]

[1] Institute of Metal Physics RAS, Ekaterinburg 620219, Russia
[2] Ural State University, 620083 Ekaterinburg, Russia
[3] Physico-Technical Institute at Nizhnii Novgorod State University, Nizhnii Novgorod, Russia

Abstract. The resistivity ρ of low mobility dilute 2D-elecron gas in a InGaAs/GaAs double quantum well (DQW) exhibits the monotonic "insulating-like" temperature dependence ($d\rho/dT<0$) at $T = 1.8$–70 K in zero magnetic field. This temperature interval corresponds to a ballistic regime ($k_BT\tau/\hbar>0.1$) for our samples, and the electron density is on a "metallic" side ($n>n_c$) of the so-called $B = 0$ 2D metal–insulator transition. We observed for the first time the coexistence of both the quantum Hall (QH) effect for the filling factors $\nu = 2,\ 4$ and the low magnetic field Hall insulator — QH liquid (with $\nu = 10$) transition.

Introduction

The 2D "metallic" and "insulating" phases identified in n-Si MOSFETs [1, 2] is still a subject of considerable interest and controversy. While the "metallic" phase is well established in mànó 2D systems, the nature of the "insulating" phase, particularly in vicinity of the 2D metal–insulator transition (MIT), is a mystery yet.

Recently there has been a great renewal of interest to a Hall insulator — quantum Hall liquid (HI-QHL) transitions in low magnetic fields B [3]. Some experimental studies show that these are the phase transitions ([3] and references therein). But it is disputed, considering the transitions as a consequence of the classical cyclotron motion and the $e-e$ interaction correction $\delta\sigma^{ee}$ to the Drude conductivity in the diffusion regime ($k_BT\tau/\hbar<1$) [4, 5].

The HI-QHL transitions in low B were investigated by different authors on the "insulating" side of the 2D $B = 0$ MIT or on the "metallic" side, but in the diffusion regime. Here we report the first observation of the HI-QHL transition at relatively high temperatures (in the ballistic regime) in the low mobility dilute 2DEG on the metallic side of the 2D $B = 0$ MIT ($n>n_c$). The transport in the vicinity of the quantum phase transition is discussed. The data were obtained the n-InGaAs/GaAs DQW samples with $n_s = 2.3\cdot10^{11}$ cm^{-2} and $\mu = 1.6\cdot10^4$ cm^2/Vs ($k_Fl_{tr} = 6.5$). Measurements were carried out in a "Quantum Design" equipment at $T = 1.8$–300 K and $B \le 9$ T.

Experimental results and discussion

1. The T-dependence of resistance is presented in Fig. 1. For the first time the insulating-like behavior ($d\rho/dT<0$) of the resistance is observed in a whole temperature interval up to $T \cong 70$ K ($T/T_F \cong 0.65$). For our samples, this T-interval corresponds to a ballistic regime ($k_BT\tau/\hbar>0.1$) [6]. It is an unexpected result, because we are on a "metallic" side of the 2D-MIT ($k_Fl_{tr} \gg 1$) [1]. There exist several models to explain the insulating $\rho(T)$ behavior of the 2D metallic state at high temperatures ($T \cong T_F$). In particular a simple non-interacting picture for such a behavior is the T-dependent scattering in a non-degenerate 2DEG [2]. We analyze the $\rho(T)$ in spirit of

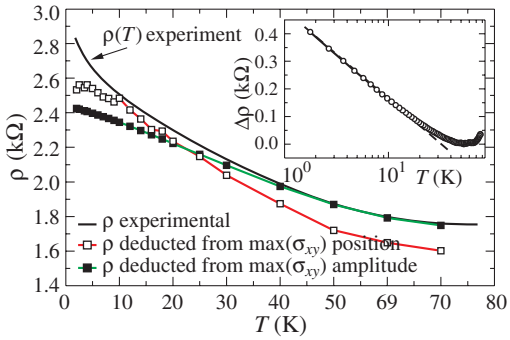

Fig. 1.

Ref. [7]:

$$\rho(T) = \rho_D(T) + \delta\rho_{WL}(T) + \delta\rho_{eei}(T)\,, \qquad (1)$$

where $\rho_D(T)$ is the Drude resistance, $\delta\rho_{WL}(T)$ and $\delta\rho_{eei}(T)$ are the weak localization and interaction contributions, respectively. After $\rho_D(T) = \sigma_D^{-1}$ is experimentally determined from analysis of $\sigma_{xy}(B, T)$ (see below) we are in a position to extract the bare $\delta\rho_{WL}(T) + \delta\rho_{eei}(T)$, according to Eq. (1), by subtracting the Drude resistance from the measured $B = 0$ resistance (Fig. 1). The obtained corrections $\Delta\rho$ show a logarithmic temperature dependence (see inset on Fig. 1).

2. In Figs. 2–4 we plot the measured data of magnetoresistivity $\rho_{xx}(B, T)$, $\rho_{xy}(B, T)$ and recalculated magnetoconductivity $\sigma_{xx}(B, T)$, $\sigma_{xy}(B, T)$ over $T = 1.8$–50 K. Shubnikov de Haas oscillations (SHO) in $\rho_{xx}(B, T)$ and QHE plateaus in $\rho_{xy}(B, T)$ are well expressed (Figs. 2, 4). Pronounced minima

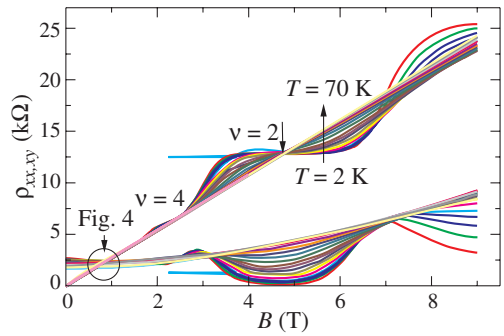

Fig. 2.

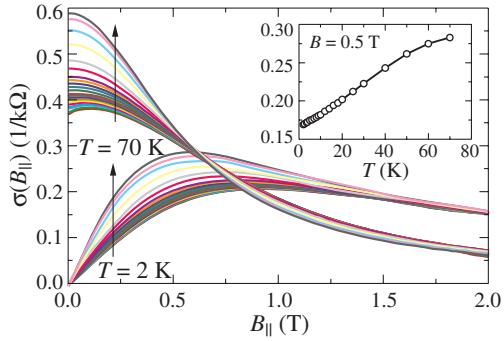

Fig. 3.

in $\rho_{xx}(B, T)$ at filling factors $\nu = 2,\ 4,\ 6$, which are accompanied by QHE plateaus in $\rho_{xy}(B, T)$, are used for evaluation of the carrier density. The T-independent B-positions of SHO minima allows us to assert that the carrier density for this sample is unchanged up to $T \cong 50\,\mathrm{K}$ therefore such an unusual $\rho(T)$ is not due to changes in the carrier density. In a low B, the negative magnetoresistance $\rho_{xx}(B, T)$ was observed. The so-called T-independent point (T_{ind}) is seen at some $B = B_{cr}$. At $T > 6\,\mathrm{K}$ this point begins to "wash out". May be at this value of B_{cr} we have $\omega_c\tau = 1$ [4,5]? But why doesn't this point coincide with the one where $\rho_{xx} = \rho_{xy}$ (Fig. 4a)?

As can be seen in Fig. 4a, $\rho_{xy}(B, T)$ in low magnetic fields is also T-dependent. Before analyzing the role of quantum corrections in the diffusion and ballistic regimes in the behavior of $\rho(T)$ at $B = 0$, shown in Fig. 1, let us estimate the possible contributions from other temperature dependent factors.

3. Let's pay attention to $\sigma_{xy}(B, T)$ (Fig. 3). It is well known that classical part of $\sigma_{xy}(B, T)$ should be temperature independent at such a strong degeneracy of electron gas ($T_F/T \cong 2$–50). All the contradictions are resolved if we suppose that the electron mobility is T-dependent: $\mu(T)$ [2,8]. An analysis of the T-dependence of $\sigma_{xy}(B, T)$ allows us to find it. According to the Drude theory, $\sigma_{xy}(B)$ have a maximum at $\mu B_{cr} = 1$ (or $\omega_c\tau = 1$) and this value is equal to $\sigma_0/2$, where σ_0 is the Drude conductivity. Solid lines in Fig. 1 represent $\sigma_0^{-1}(T)$ and $\rho(T) = (en\mu(T))^{-1}$, where $\mu(T)$ is obtained from $\mu B_{cr} = 1$. It is seen that these dependences are close to the experimental ones. This poses a question: if the Drude theory is applicable, what is the reason for the T-dependence of mobility? We think this is the T-dependent scattering of a non-degenerate electron gas [2].

Then we extracted the temperature dependence of $\sigma_0(T)$ due to $\mu(T)$ from the experimental dependence $\sigma_{xy}(B, T)$ and $\sigma_{xx}(B, T)$. After that we calculated $\rho^*_{xx}(B, T)$ using corrected data for $\sigma^*_{xx}(B, T)$ and for calculated $\sigma^*_{xy}(B, T)$ [8]. The result of this procedure is presented at Fig. 4b. After corrections, the T_{ind} point exists up to $T \sim 20\,\mathrm{K}$ and coincides with the point where $\rho_{xx} = \rho_{xy}$.

Besides, at magnetic fields $\omega_c\tau < 1$ the quantum correction $\Delta\sigma^{ee}_{xy}$ begins to depend on temperature. These data in literature are connected with the beginning of the transition from diffusive to ballistic regime.

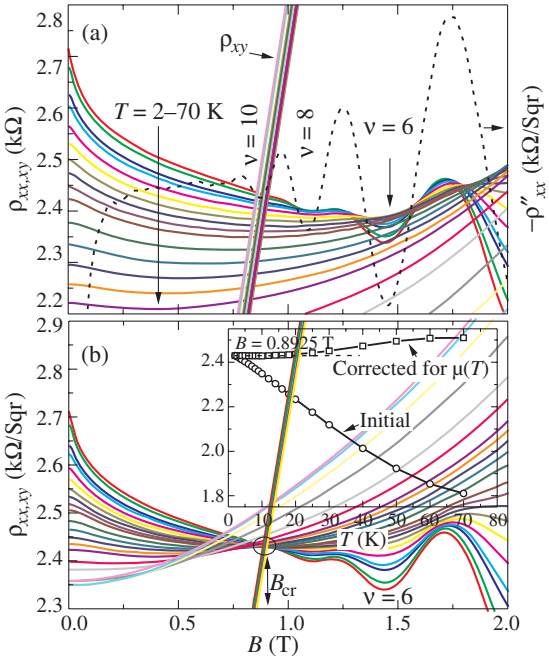

Fig. 4.

Acknowledgements

The work was supported by: Russian Foundation for Basic Research RFBR, grants 05-02-16206 and 04-02-16614; program of Russian Academy of Sciences "Low-dimensional quantum heterostructures"; CRDF and Ministry of education and science of Russian Federation, grant Y1-P-05-14 (Ek-05 [X1]); Ural division of Russian Academy of Sciences, grant for young scientists; Russian Science Support Foundation.

References

[1] E. A. Abrahams, S. V. Kravchenko, M. P. Sarachik, *Rev. Mod. Phys.* **73**, 251 (2001); *Rep. Prog. Phys.* **67**, 1 (2004).
[2] S. Das Sarma, E. H. Hwang, *cond-mat*/0411528.
[3] G. H. Kim *et al*, *Phys. Rev. B* **69**, 073311 (2004).
[4] K. K. Choi *et al*, *Phys. Rev. B* **33**, 8216 (1986).
[5] Yu. G. Arapov *et al*, *Semiconductors* **32**, 649 (1998).
[6] G. Zala *et al*, *Phys. Rev. B* **64**, 214204 (2001).
[7] V. Senz *et al*, *Phys. Rev. Lett.* **85**, 4357 (2000).
[8] G. Minkov *et al*, *Phys. Rev. B* **64**, 235327 (2001).

13th Int. Symp. "Nanostructures: Physics and Technology"
St Petersburg, Russia, June 20–25, 2005

2D anomalous magnetoresistance in the presence of spin-orbit scattering

N. S. Averkiev and K. S. Romanov
Ioffe Physico-Technical Institute, St Petersburg, Russia

Abstract. The model of weak localization in 2D semiconductore structures in the whole range of classically weak magnetic fields in the presence of Elliot-Yafet spin relaxation has been developed. It was showed that spin-orbit interaction influences the value of magnetoresistance in small magnetic fields (within diffusion approximation) and when diffusion approximation is no longer valid.

Introduction

The weak localization phenomena is due to the interference of the two electron waves propagating in reverse directions along the same trajectory while scattering on impurities [1]. One of the most impressive manifestations of this phenomena is the destruction of this interference by classically weak magnetic field. It can be also destructed by spin relaxation processes, wave-function phase relaxation, intersubband transitions *et al*. Therefore experimental studies of weak localization phenomena allow to determine various relaxation times.

In the absence of magnetic field if the phase relaxation time greatly exceeds the momentum relaxation time the negative contribution to the conductivity comes from all possible closed trajectories. In the presence of the magnetic field when the magnetic length exceeds the electron mean free path the effective interference destruction takes place for the closed trajectories with lots of scatterers. This is diffusion mode. The role of the spin phenomena is quite large because spin relaxation phenomena also reduces the wave-functions interference. Currently the role of spin is studied well for all spin relaxation mechanisms in semiconductors and metals in diffusion regime.

With the increase of magnetic field the magnetic lengths becomes comparable to the mean free path. Then the interenference destruction for trajectories with low number of scatterers. This regime was studied only phenomenologically by [2,3].

Usually it is necessary to analyze weak localization phenomena not only for low magnetic fields (diffusion regime) but also for relatively high ones (non-diffusion regime). Therefore the theoretical analysis of spin influence on anomalous correction for all magnetic fields is necessary for the determination of the relaxation times.

The aim of the present work is to create the theory of weak localization in 2D semiconductor structures or metallic films for all classically weak magnetic fields for the case of Elliot-Yafet spin relaxation mechanism.

1. Theory

It is convenient to use zero temperatures diagrammatic technique for obtaining conductivity quantum correction. This method allows to calculate the conductivity of the media containing randomly distributed impurities at zero temperature. The main restriction of this technique is the assumption that $k_F l \gg 1$, where k_F is the carrier Fermi momentum and l is their mean free path.

In the framework of diagrammatic approach the conductivity is described as series of loop diagrams. Due to the random character of impurity distribution only paired interactions not vanish after integration over the coordinates. Therefore it is convenient to introduce the parameter taking into account correlation of the scattering on impurities — the correlator.

It can be showed that weak localization phenomena is described by several loop diagrams containing the same part. This part is called Cooperon. Therefore the problem of obtaining the anomalous conductivity correction is divided into two parts: firstly the Cooperon is to be calculated secondly the loop diagrams containing Cooperon are to be evaluated.

Diagrammatically Cooperon equation is similar to the equation on the ladder diagrams. Analytically this equation in the case of short-range impurity potential without magnetic field in momentum representation is:

$$\Gamma\left(\vec{k},\vec{k}',\vec{Q}\right)= W+W\int\Gamma\left(\vec{k},\vec{k}',\vec{Q}\right)G^A(|\vec{g}|)G^R\left(|\vec{Q}-\vec{g}|\right)d\vec{g}\,,$$

where W — correlator, Γ — Cooperon, $G^{A,R}$ — advanced and retarded green functions. It worth noting that $|\vec{k}| \approx |\vec{k}'| \approx k_F \gg |\vec{Q}|$. The proved method of this equation solution is the pole integration.

In the presence of spin-orbit interaction the impurity potential is different from δ-potential. It's matrix elements $V^{\alpha\to\beta}_{\vec{k}\to\vec{k}'}$ depends not only on the momentums $\vec{k}$ and $\vec{k}'$ but also on the spin coordinates α and β. Therefore the equation describing Cooperon also includes the angles of vectors $\vec{k}$ and $\vec{k}'$. This makes the equation more sophisticated. To solve it Cooperon is expanded to the sum of harmonics of the angles of vectors $\vec{k}$ and $\vec{k}'$.

This procedure transforms the Cooperon equation to the system of equations. This system contains only the equations without angular dependencies. It is finite and therefore can be solved analytically.

The resulting conductivity correction is:

$$\Delta\sigma = -\frac{e^2}{2\pi^2\hbar}\left\{\ln\left(\frac{1+\tau_\phi/\tau}{1+\tau_\phi/\tau_s}\right)\left[1+\frac{\tau}{2\tau_\phi}+\frac{11}{2}\frac{\tau}{\tau_s}\right] - \frac{1}{2}\ln\left(1+2\tau_\phi/\tau_s\right)-\ln 2\right\}\,,$$

where τ_ϕ — phase relaxation time, τ_s — spin relaxation time, $\tau = l/k_F$.

In the presence of magnetic field the momentum representation is less convenient than coordinate representation. According to the rules of fourier transformation momentums $\vec{k}$, $\vec{k}'$

have to be replaced by corresponding gradients. Therefore correlator in coordinate representation is not function but operator. However this operator acts on Green functions only. It is known that in classically weak magnetic fields the Green function is equal to the Green function in zero field multiplied by phase factor. The gradient of this phase is relatively small in comparison to the gradient of the Green function without magnetic field. This gradient can be related to the Green function itself $\Delta G^{A,R}(\vec{r}) = \pm(\vec{r}/r)k_F G^{A,R}(\vec{r})$. Therefore the operators in the Cooperon equation can be replaced by corresponding orts. This removes differential operators from this equation. The resulting equation also contains various angular dependencies in contrast to the case without spin-orbit interaction.

Due to the finite number of harmonics this system of equations can be solved by series expansion method developed by Kawabata [2]. The only difference is that Cooperon with spin-orbit interaction contains not only main diagonal series of Kawabata functions but also secondary diagonals.

The resulting expressions for Cooperon and conductivity correction are quite large.

2. Conclusions

The dependence of the conductivity quantum correction on the magnetic field for various ratios τ/τ_ϕ and τ/τ_s is shown on figure. It is seen that spin-orbit interaction reduces the absolute value of the anomalous magnetoconductivity correction in both weak magnetic fields ($l_B > l$) and strong ones ($l_B < l$). This interaction is sufficient for the whole range of the magnetic fields. For $\tau_s < \tau_\phi$ the dependence of the conductivity correction on the magnetic field is not monotonous and have a small minimum. When $\tau_s > \tau_\phi$ this dependence is monotonous and is qualitatively similar to one without spin-orbit interaction.

The model developed allows to determine the anomalous magnetoresistivity correction value not only in weak magnetic fields but also in relatively strong fields when the diffusion approximation is not valid. It can be shown that qualitatively this correction dependence on the magnetic field in the area of strong fields ($l_B \ll l$) can be understood using the formula for the correction in the momentum representation (ref). But lowest limit of integration on Q should be changed from 0 to $1/l_B$. The resulting asymptotic dependence allows to treat the role of spin-orbit interaction in strong fields:

$$\sigma \sim (1 - 3\tau/\tau_s)\frac{1}{l_B}\,. \tag{1}$$

It is seen that the main part of anomalous conductivity correction is proportional to $1/\sqrt{H}$, the spin-orbit part is proportional to $\tau/(\tau_s\sqrt{H})$. So the influence of spin-orbit interaction in strong magnetic fields is smaller than that in weak magnetic fields [4].

Thus the influence of Elliot–Yafet spin relaxation on the weak localization phenomena with account of anisotropic correlator character in the whole area of classically weak magnetic fields has been studied. The model developed allows to determine the influence of the Fermi energy on magnetoresistivity quantum correction.

The dependence of anomalous magnetoresistance with the account of spin was calculated and it was shown that spin plays large role in high and low magnetic fields.

Acknowledgements

This work was supported in part by INTAS, RFBR, Ministry of Sciense and Education of Russia and Scientific Programs of RAS. K. S. Romanov acknowledges partial support from "Dynasty" foundation — ICFPM.

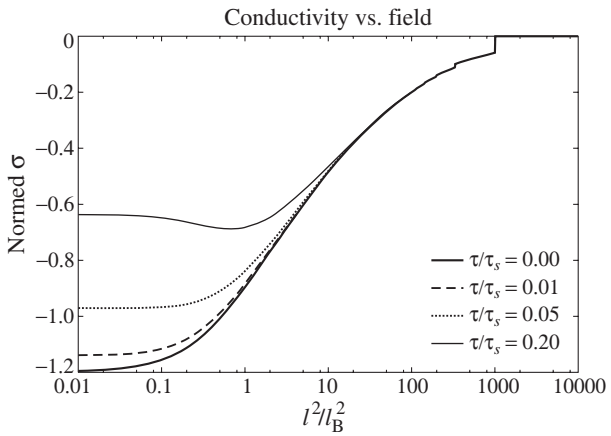

Fig. 1. The dependence of the anomalous conductivity correction on the value of applied magnetic field for different τ/τ_s. H_D is the magnetic field corresponding magnetic length equal to l, $\tau/\tau_\phi = 0.02$.

References

[1] Gerd Bergmann, *Physics Reports*, **107**, 1 (1984).
[2] Arisato Kawabata, *Journal of Physical Society of Japan*, **53**, 3540 (1984).
[3] A. Zduniak, M. I. Dyakonov, W. Knap, *Phys. Rev. B*, **56**, 1996, (1997).
[4] S. Hikami, A. I. Larkin, Y. Nagaoka, *Prog. Theor. Phys.*, **63**, 707 (1980).

13th Int. Symp. "Nanostructures: Physics and Technology"
St Petersburg, Russia, June 20–25, 2005

Anisotropy of transport of 2D electron gas in parallel magnetic field

A. V. Goran[1], A. A. Bykov[1], *A. K. Bakarov*[1], A. K. Kalagin[1], A. V. Latyshev[1], A. I. Toropov[1] and J. C. Portal[2]

[1] Institute of Semiconductor Physics, 630090 Novosibirsk, Russia
[2] Grenoble High Magnetic Fields Laboratory, F-38042 Grenoble, France

Abstract. Magnetotransport properties of a 2D electron gas in narrow GaAs quantum wells with AlAs/GaAs superlattice barriers were studied. It is shown that the anisotropic positive magnetoresistance observed in selectively doped semiconductor structures in a parallel magnetic field is caused by the spatial modulation of the 2D electron gas.

Introduction

In an idealized zero-thickness 2D electron system, the orbital motion of charge carriers is affected only by the normal component of the external magnetic field, where the magnitude of this component depends on the angle between the magnetic field $\mathbf{B}_{\text{ext}}$ and the normal to the plane of 2D electron gas. The in-plane component of magnetic field in such a system will cause changes in the spin degree of freedom of charge carriers and, hence, in the density of states of 2D electron gas. The real 2D semiconductor systems always have a nonzero thickness, and this is the cause of the orbital effect in a parallel magnetic field [1]. Unlike the magnetoresistance (MR) associated with the spin effect in a parallel magnetic field [2], MR caused by the finite thickness of 2D electron gas is anisotropic. The origin of this anisotropy is that the variation of the effective mass of charge carriers in the direction perpendicular to the external magnetic field is greater than the variation in the direction parallel to the field.

This anisotropy mechanism manifests itself in the dependence of MR of 2D electron gas on the mutual orientation of the in-plane magnetic field and the measuring current. In particular, in the situation where the measuring current is perpendicular to the in-plane magnetic field, MR of 2D electron gas in AlGaAs/GaAs heterojunctions is greater than in the situation where the current is parallel to the field [3]. The anisotropy of positive MR observed in [3] was found to be much smaller than that predicted by the theory [1]. In our opinion, this discrepancy is due to the fact that 2D electron gas in real selectively doped structures not only has a finite thickness but is also nonplanar [4]. As will be shown below, even a very small spatial modulation of 2D electron gas, which is inherent in any real structure, also leads to the anisotropy of the positive MR of 2D electron gas in an in-plane magnetic field. However, MR in this mechanism is smaller when the magnetic field and the measuring current are mutually perpendicular and greater when they are parallel. A combined effect of the finite thickness and the spatial modulation of 2D electron gas should lead to a decrease in the degree of MR anisotropy in the in-plane magnetic field, which may qualitatively explain the experimental results obtained in [3].

1. Experimental

The structures studied in the experiment were selectively doped 10-nm-thick GaAs quantum wells with AlAs/GaAs superlattice barriers. They were prepared by molecular beam epitaxy (MBE) on (100) GaAs substrates whose deviation from the (100) plane did not exceed 0.02°. The surface morphology of the structures was examined by atomic force microscopy (AFM). Figure 1a shows the typical AFM image of the surface relief of the MBE structures under study.

The magnetotransport experiments were carried out at temperatures from 4.2 to 1.6 K in magnetic fields up to 15 T on L-shaped Hall bars (Fig. 1b). The bars had a width of 50 μm, and the distance between the potential terminals was 100 μm. The bar orientations were chosen so that the measuring current was parallel and perpendicular to the [110] direction. The equilibrium parameters of the 2D electron gas at $T = 4.2$ K were as follows: the concentration $n_s = 1.6 \times 10^{12}$ cm^{-2} and the mobility $\mu = 300 \times 10^3$ cm^2/Vs.

2. Results and discussion

In the general case, the surface of 2D electron gas can be described by the function $z = z(x, y)$ characterizing the deviation of the surface from the ideal plane formed by the x and y axes. In the case of a narrow quantum well, 2D electrons perceive only the normal component that is responsible for to the appearance of classical Larmor orbits in the plane of 2D electron gas. This normal component can be considered effective inhomogeneous magnetic field $B_{\text{eff}}(x, y)$ arising as a result of applying external magnetic field to the nonplanar 2D electron gas. The effective magnetic field $B_{\text{eff}} = B_{\text{eff}}(x, y)$ can be calculated if we know the surface of 2D electron gas $z = z(x, y)$

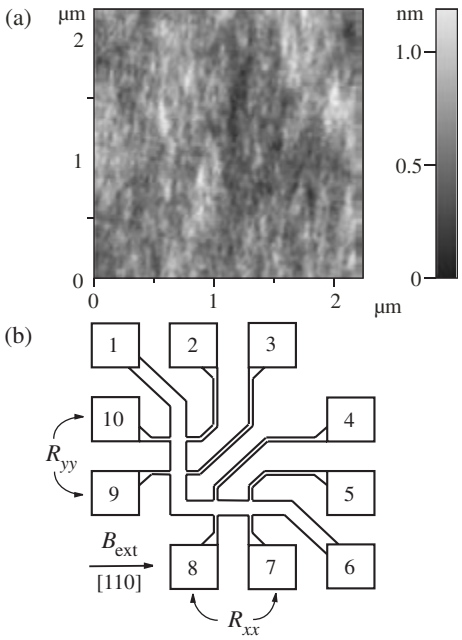

Fig. 1. (a) Two-dimensional AFM image of the surface relief of the MBE structure. (b) Schematic representation of an L-shaped Hall bar.

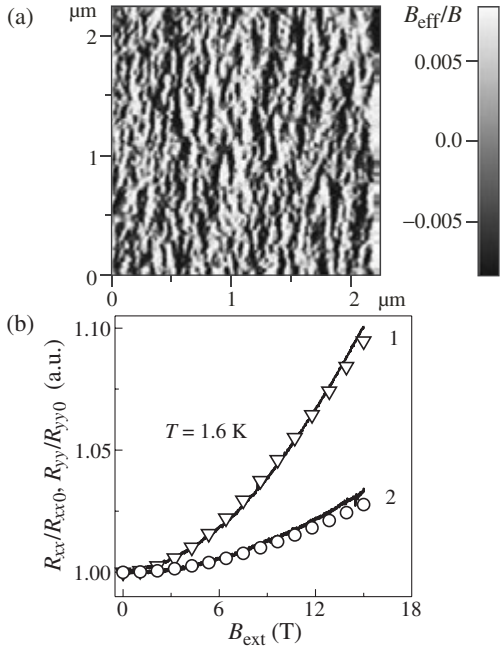

Fig. 2. (a) Function $B_{\text{eff}}(x, y)$ calculated for a nonplanar 2D electron gas with a relief corresponding to the AFM image of the surface of MBE structure: $\mathbf{B}_{\text{ext}}$ is directed along [110]. (b) Dependences of the relative MR of the 2D electron gas: (1) $R_{xx}(B_x)/R_{xx0}$, (2) $R_{yy}(B_x)/R_{yy0}$. The solid lines represent the experimental curves, and the dots represent the calculations.

and the external magnetic field $\mathbf{B}_{\text{ext}} = (B_x, B_y, B_z)$. Then, $B_{\text{eff}}(x, y) = |B_{\text{ext}}| \cos(\Theta(x, y))$, where $|B_{\text{ext}}|$ is the magnitude of the vector of external magnetic field and $\Theta(x, y)$ is the angle between the normal to the surface $z = z(x, y)$ at the point (x, y) and the vector of external magnetic field $\mathbf{B}_{\text{ext}}$.

Figure 2a shows a two-dimensional image of the effective magnetic field calculated for 2D electron gas on the assumption that its surface is identical to the AFM image of the MBE structure under study and that the external magnetic field is parallel to the [110] direction. One can clearly see that the effective magnetic field is anisotropic. Figure 2b represents the results of measurements of the relative MR for the orientation of the parallel external magnetic field along the x axis ($B_x = B_{\text{ext}}$). It should be noted that, in the temperature range from 4.2 to 1.6 K, the positive MR observed in the structures under study did not vary, evidencing its classical rather than quantummechanical nature.

The anisotropy observed for the MR of 2D electron gas can be qualitatively explained by electron scattering from the anisotropic inhomogeneous magnetic field [4, 5] that depends on the angle between the vector $\mathbf{B}_{\text{ext}}$ and the direction of the measuring current. For the quantitative evaluation of this assumption, we carried out numerical simulation of the quasiclassical charge-carrier transport in the effective inhomogeneous magnetic field appearing in a nonplanar 2D electron gas in the parallel magnetic field. The model parameters were taken to be equal to the parameters of the real samples (mobility, concentration, and surface relief). The only fitting parameter was the amplitude of the spatial modulation of the 2D electron gas.

The results of modeling are shown in Fig. 2b. It should be noted that the calculated amplitude of spatial modulation of the 2D electron gas proved to be 2.5 times greater than the amplitude of surface roughness obtained from the AFM studies. We explain this difference by the fact that the 2D electron gas in the MBE structure under study is at a certain distance from the sample surface, and this distance is much greater than the roughness amplitude. Therefore, in the general case, the spatial modulation of the 2D electron gas may not coincide with the surface relief.

Summary

Thus, we have shown that the anisotropic positive MR of a high-concentration 2D electron gas in a parallel magnetic field is governed by the scattering by the effective inhomogeneous magnetic field, i.e., by the spatial modulation of the 2D electron gas in the selectively doped MBE structures under study.

Acknowledgements

This work was supported by RFBR, project no. 04-02-16789 and by the program “Physics of solid state nanostructures”.

References

[1] S. Das Sarma *et al*, *Phys. Rev. Lett.*, **84**, 5596 (2000).
[2] V. T. Dolgopolov and A. Gold, *JETP Lett.*, **71**, 27 (2000).
[3] V. S. Khrapai *et al*, *IPAP Conf. Ser.*, **2**, 105 (2001).
[4] A. A. Bykov *et al*, *JETP Lett.*, **74**, 164 (2001).
[5] A. A. Bykov *et al*, *Phys. Rev. B*, **65**, 035302 (2001).

13th Int. Symp. "Nanostructures: Physics and Technology"
St Petersburg, Russia, June 20–25, 2005

Pressure induced transition of 2DEG in δ-doped GaAs to insulating state

E. M. Dizhur[1], A. N. Voronovsky[1], A. V. Fedorov[1], I. N. Kotel'nikov[2] and S. E. Dizhur[2]

[1] Institute for High Pressure Physics, RAS, 142190 Troitsk Moscow Reg., Russia
[2] Institute of Radioengineering and Electronics, RAS, 125009 Moscow, Russia

Abstract. The tunneling and the lateral conductance of 2DEG formed in the GaAs with the δ-doped layer were measured simultaneously at hydrostatic pressures at helium temperatures. The resistivity of the δ-doped layer sharply increases by >3 orders of magnitude at about 2 GPa and its temperature coefficient changes from ~ -0.04 to $\sim -4\,\mathrm{K}^{-1}$. The tunneling resistance shows only slight change of exponential behavior at about 1.5 GPa while a drastic change of the Zero Bias Anomaly (ZBA) takes place just at the metal-insulator transition. Such a behavior is interpreted in terms of pressure dependence of GaAs band structure and DX-level position.

Introduction

In n-GaAs DX-centers exist which may become resonant with the conduction band under pressure [1] providing the capture of the electrons. This gives a possibility to study the influence of the carrier density maintaining the distribution of the impurities and structural defects over the sample practically invariable. The Al/δ-GaAs tunnel structures for our measurements were grown by the MBE method following the procedure described in [2]. The samples had a pair of separate Al "gates" (0.2 mm in diameter) to provide tunnel current to the common δ-doped layer (containing $5 \cdot 10^{12}\,\mathrm{cm}^{-2}$ Si atoms) at the depth of 20 nm from Al/GaAs interface. From the tunneling spectroscopy data and from the self-consistent solution of the Schrödinger and Poisson equations [3], it was found that at $P = 0$ only one level E_0 is located in the potential well at ~ 33 meV below the Fermi level E_F and by ~ 92 meV over the conduction band edge E_Γ. The piston-cylinder type chamber with polyethilene–siloxane neutral liquid as a pressure transmitting media [4] was used. The actual value of the pressure during the measurements was evaluated by the change of the critical temperature T_c of the superconducting Sn wire placed *in situ*. To overcome the measurement problems due to the huge resistivity of both the tunnel junction and the δ-layer under pressure we used straightforward DC measurements of the tunnel current $I(V)$ and mathematical treatment to obtain tunneling spectra ($d \ln \sigma_\mathrm{tun}/dV$) and to separate the background reflecting the energy position of the quantum confinement subbands from the fine features due to the contribution of the many-particle interaction [5].

Results and discussion

The obtained data[2] are presented on Figs. 1, 2.

The background components of tunneling spectra measured at different pressures were used to find the shift of the 2D subbands under pressure (Fig. 1). The minima on the background curves correspond to the energies of the subbands E_i and are considerably wide that may be an indication to some inhomogenity of the QW over the gate area, resulting in the broadening of the energy levels and as a consequence the finite pressure range in which MIT occurs (patched region on Fig. 1). The unexpected experimental result is the observation

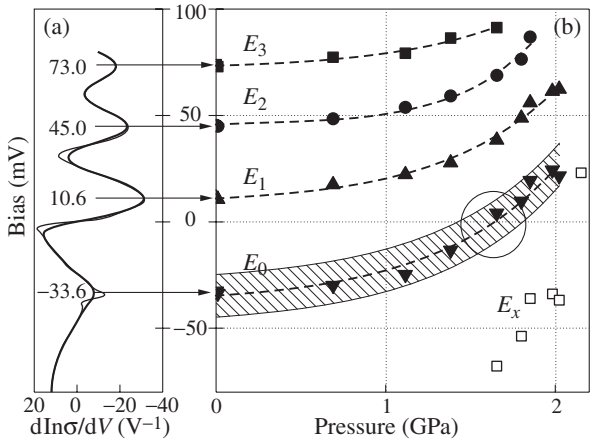

Fig. 1. (a) The tunneling spectrum (thin line) and its background component (thick line) of Z1B7 sample at $P = 0$ GPa and $T = 4.2$ K; (b) Pressure dependence of the quantum-confinement 2D subbands. The patched region reflects possible inhomogeinity of the E_0 level. A circle shows the MIT region. Hollow squares may correspond to the Γ-band edge (*see text*).

of an additional minimum on the background of the tunneling spectrum shown on Fig. 1b as E_x that appears in the investigated bias range at $\sim$ 1.5 GPa and quickly moves upwards with pressure. We have a strong temptation to ascribe it to the conduction band edge but its involving in the tunneling is unclear.

According to the data of Maude *et al* [6], at concentrations of Si ($4.5 \times 10^{12}\,\mathrm{cm}^{-2}$) close to the doping level of our samples, the DX-level energy E_DX and its pressure derivative are $E_\mathrm{DX} - E_\Gamma \sim 270$ meV and $dE_{\mathrm{DX}-\Gamma}/dP \sim 94$ meV/GPa respectively. Then the overlap of the Fermi level with the level of DX centers must begin at the pressure

$$P_1 = \frac{(E_\mathrm{DX} - E_\Gamma) - (E_0 - E_\Gamma) - (E_\mathrm{F} - E_0)}{|dE_{\mathrm{DX}-\Gamma}/dP|} \approx 1.65\,\mathrm{GPa}\,.$$

A further increase in the pressure leads to the Fermi level pinning and localization of carriers at DX centers, due to which the effective concentration of carriers involved in the charge transport over the δ-layer gradually decreases. This leads to a change in the space charge in the δ-layer and thus the slope of the dependence $\ln R_\mathrm{tun}(P) \equiv -\ln \sigma_\mathrm{tun}(P)$ begins to change as soon as some part of free electrons is localized at DX centers

[2] Part of them has been published recently in E. M. Dizhur *et al*. *JETP Letters*, **80**, (6), pp. 433–435 (2004).

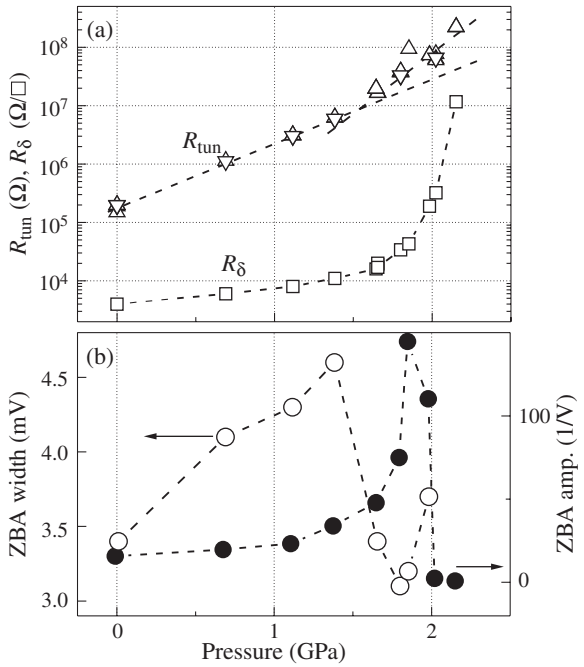

Fig. 2. (a) Pressure dependence of the tunneling differential resistance $R_{\rm tun}(V_{\rm bias} = 0)$ ($\triangle$ — gate1, $\triangledown$ — gate2) and of the lateral resistance R_δ ($\square$) at $T = 4.2\,$K; (b) Pressure dependence of the width ($\circ$) and the amplitude of Zero Bias Anomaly ($\bullet$) at $T = 4.2\,$K.

at $\approx 1.6\,$GPa. (Fig. 2a), that is close to the above estimate. When the Fermi level shifts below the mobility threshold with respect to the quantum-confinement level, the metal-insulator transition (MIT) in the δ-layer occurs, and the lateral resistance (Fig. 2a) shows a sharp rise due to the carrier depletion at pressure $\sim 1.8\,$GPa. This transition is accompanied by the drastic change of the thermal resistance coefficient from $\approx -0.03 \pm 0.02\,{\rm K}^{-1}$ in the range 0–1.8 GPa to $\approx -4\,{\rm K}^{-1}$ at $P = 2\,$GPa.

The main difference between the tunnel and lateral transport is that the former reflect the density of states while the latter reflects mainly the total carrier density. Though MIT does not provide any additional features in $\ln R_{\rm tun}(P)$, in the same pressure range the variation of the ZBA shape (Fig. 2b) was observed. As soon as the pressure at which the amplitude of the ZBA has a narrow peak correlates with the onset of the fast lateral resistance growth we can conclude that the properties of the δ-layer immediately under the metal gate, reflected in the tunneling, do not differ very much from the rest, by far the larger, part of the δ-layer under the free surface, responsible for the lateral conductance.

In [7] ZBA was attributed to the effects of exchange-correlation interaction and the increase in the ZBA amplitude under pressure was predicted for three-dimensional systems. On the other hand, the behavior of ZBA near the transition to the insulating state of the 2D system studied here may indicate, for example, the appearance of a Coulomb gap [8] in the spectrum, which, as is known, may manifest itself in tunneling [9]. The existence of a sharp peak in the baric dependence of the ZBA near the transition to the insulating state, the significant magnitude of this effect, and the nonmonotonic dependence of the ZBA width on pressure may indicate that the nature of ZBA changes from correlation to Coulomb mechanism as far as under pressure the electron system becomes more depleted and the screening decreases.

We also observed rather interesting transformations of the amplitude and the overall shape of LO-phonon induced singularities. Their shape is usualy assumed [10] to be the result of superposition of self-energy effects and of the inelastic assisted tunneling. In our samples (one occupied subband) at positive bias (tunneling from δ-layer) the contribution of the both depends on how the value of Fermi energy $E_{\rm F} - E_0$ relates to the LO-phonon energy [11]. Under pressure below 1.5 GPa this trend holds but at higher pressure the unexpected behavior of LO-phonon lines was observed. The pressure 1.5 GPa is just the pressure at which the subband E_1 crosses the threshold value $eU = -E_{\rm LO}$, though at higher pressure the behavior of the LO-phonon singularity becomes obscured again. The pinning-like behavior of the intersubband energy $E_1 - E_0$ at LO-phonon energy observed at $P \sim 1.5\,$GPa [12] may be the concequence of the resonant polaron coupling near metal-insulator transition in 2DES at high pressure.

Acknowledgements

We acknowledge financial support by RFBR and by the programs "New materials and structures" and "Physics of compressed matter" of Division of Physical Sciences of RAS.

References

[1] J. G. Tischler, S. K. Singh, H. A. Nickel *et al*, *phys. stat. sol. (b)* **211**, 131 (1999).
[2] I. N. Kotel'nikov, V. A. Kokin, Yu. V. Fedorov *et al*, *JETP Letters*, **71**, 387 (2000).
[3] E. M. Dizhur, A. N. Voronovsky, I. N. Kotelnikov *et al*, *Phys. Stat. Sol. (b)*, **235**, 531 (2003).
[4] A. N. Voronovsky, E. S. Itskevich, E. M. Dizhur *et al*, *Theses of the Conf. on "Advanced methods of pressure treatment"*, Chechoslovakia, Bratislava, 1982; A. N. Voronovsky, E. M. Dizhur and E. S. Itskevich, *Sov. Phys. JETP* **50**,564 (1979).
[5] E. M. Dizhur, A. V. Fedorov, http://arxiv.org/list/cond-mat/0408206, to be published in PTE, 4, (2005).
[6] D. K. Maude, J. C. Portal, L. Dmowski *et al*, *Solid State Phenomena.*, **10**, 121–144 (1989).
[7] A. Ya. Shul'man, I. N. Kotel'nikov, N. A. Varvanin *et al*, *JETP Lett.* **73**, 573 (2001).
[8] B. I. Shklovskii and A. L. Efros, *in Electronic Properties of Doped Semiconductors* (Nauka, Moscow, 1979; Springer, New York, 1984).
[9] J. G. Massey and Mark Lee, *Phys. Rev. Lett.* **75**, 4266 (1995); *Phys. Rev. Lett.* **77**, 3399 (1996).
[10] R. Combescot, G. Schreder, *J. Phys.*, C **7**, 1318 (1974).
[11] I. N. Kotel'nikov, S. E. Dizhur, *Proc. of the 12th Int. Symp. "Nanostructures: Physics and Technology"*, St Petersburg, Russia, June, 21–25, 2004, p. 366.
[12] I. N. Kotel'nikov, E. M. Dizhur, A. N. Voronovsky *et al*, *11th Int. Symp. "Nanostructures: Physics and Technology"*, St Petersburg, Russia, June 23–28, 2003, p. 117.

13th Int. Symp. "Nanostructures: Physics and Technology"
St Petersburg, Russia, June 20–25, 2005

Optical excitation of space-charge waves in quantum wells

P. Kleinert
Paul-Drude-Institute for Solid State Electronics, Hausvogteiplatz 5-7, 10117 Berlin, Germany

Abstract. Space-charge waves in semiconductors and semiconductor quantum wells can be optically excited by the superposition of a static and a moving interference pattern. The induced dc and ac current contributions are resonantly enhanced, when the spatial and temporal periods of the interference grating match related quantities of the space-charge wave. Two eigenmodes are identified for electron-hole systems. One of them is excited by the synchronous drift of photogenerated electron-hole pairs with the moving intensity grating. The other one has the character of trap-recharging waves.

Introduction

A method of materials characterization has been invented [1–4] for amorphous samples and crystalline semiconductors that relies on the spatial and temporal evolution of photoexcited carriers. Early studies [1] used a spatial sinusoidal light intensity pattern to determine the ambipolar diffusion length in semiconductors. Later, the temporal information provided by a moving interference grating was additionally used [2] for the simultaneous measurement of the lifetime and ambipolar mobilities. The moving interference pattern has been created by two laser beams of different intensities and slightly different frequencies, which interfere and produce an intensity grating on the sample surface that moves with a constant velocity. The photogenerated space charges and the electric field accompanying them give rise to a dc short-circuit current, which is the quantity measured in the experiment as a function of the grating velocity. This moving-photocarrier-grating technique has been successfully applied to determine the bipolar transport parameters of photoexcited materials [2–4]. Unfortunately, both techniques, which use either a static or a moving interference pattern for the determination of materials parameters, do not exploit an external constant electric field. As a consequence, the excitation of space-charge waves (SCWs) is not included in such an approach. When the illuminated sample is biased by a constant electric field, the photogenerated electrons and holes move in opposite directions with their respective drift velocities. This drift gives rise to a resonance of the modulation field amplitude, when the bright interference stripes of the moving pattern travel synchronously with the charge cluster that it generates. Based on the synchronous drift of photogenerated carriers with the moving interference pattern, Dolfi *et al* [5] proposed a novel photodetector that has been analyzed in more detail in Ref. [6]. The theoretical analysis of this effect relied on the linear approximation with respect to the induced field and charge modulation. This approximation is very restrictive. For a more complete theoretical treatment, it is necessary to go beyond the linear approach by studying resonant excitations within the more general framework of SCWs, where nonlinear contributions of the charge and field fluctuations are taken into account. Studies of this kind are well known in the field of photorefractive crystals [7], where SCWs are considered as oscillation eigenmodes in a system of traps and free carriers that move in an electric field [8]. While the theory of SCWs was developed about 30 years ago [9], efficient optical methods for their excitation and detection were reported only recently [8, 10]. The studies in the field of photorefractive crystals focus on the dynamics of one type of carrier, namely photoexcited electrons and the related SCWs. For semiconductors, however, a bipolar approach is necessary that takes into account the dynamics of photogenerated electrons and holes as well as SCWs created by them.

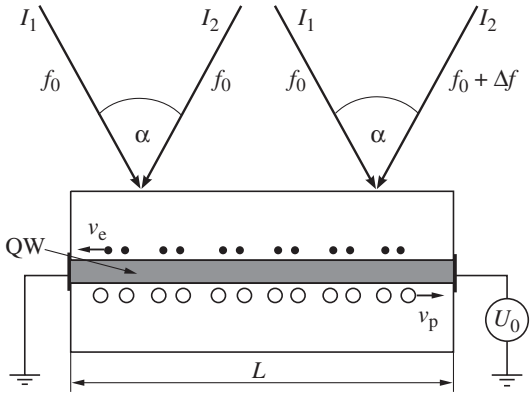

Fig. 1. A biased QW with Ohmic contacts separated by the distance L is illuminated with two pairs of coherent laser beams, impinging under an angle α. Two beams with frequency f_0 and intensities I_1 and I_2 generate a static intensity grating. In addition, there are two beams with a frequency difference Δf, which produce a grating that moves with the group velocity v_{gr}. Photogenerated electrons and holes move in opposite directions with their respective drift velocities v_n and v_p. U_0 denotes the voltage source, respectively.

In this contribution, we extend previous approaches and focus on biased semiconductor QWs by developing a theory for SCWs that treats the dynamics of electrons and holes on the same footing. It is shown that dc and ac current contributions are induced in the outer circuit, when both a static and a moving interference grating are provided. Both current contributions are resonantly enhanced, when the interference pattern matches the eigenmodes of SCWs.

1. Theoretical and numerical results

A schematic illustration of the experimental set up is shown in Fig. 1. Two sets of two coherent laser beams are brought to interfere on the surface of the sample, in which a QW is embedded. The first set of beams creates a static intensity grating with the spatial period Λ. For the second set of two beams, a small frequency shift between them is realized by an acousto-optic modulator. The interference pattern produced by this configuration moves with a constant velocity in the x direction. In the one-dimensional approximation, the static and moving in-

terference patterns lead to generation rates for electrons and holes that enter the continuity equations. Together with Poisson's equation and Kirchhoff's law, we obtain a closed set of equations that is treated by a perturbation approach. Considering nonlinear contributions of the induced electric field, analytical results are derived for the induced dc and ac current contributions. Both contributions are amplified, when SCWs are resonantly excited, i.e., when their spatial and temporal period coincide with the wavelength and frequency of the interference pattern. There are two characteristic eigenmodes of SCWs in semiconductors. The first mode is associated with the dynamics of free carriers. Its linear dispersion relation is similar to the one of acoustic phonon modes. This mode gives rise to a current resonance, when the grating moves synchronously with the SCW. The second mode has the character of a trap recharging mode, for which the phase and group velocity are oppositely directed. For a moving intensity modulation, the induced current depends on the direction of the grating motion with respect to the direction of the dc electric field and the type of conductivity of the sample. The induced current contribution may change its sign and continues to exist even when the external electric field has been turned off.

Figure 2 shows a numerical example for the resonant current amplification due to the excitation of SCWs. The induced ac current is displayed as a function of the electric field strength E_0 and the time parameter Ωt. The amplitude and phase of the alternating current sensitively depend on the strength of the applied electric field. There is a resonant amplification of the induced current due to the excitation of SCWs and an abrupt phase shift at $E_0 \approx 0$. This enhanced phase switching of the alternating current is dominated by a current resonance at $E_0 \approx -1.4$ kV/cm, which results from the excitation of the second SCW. This amplification is much more pronounced in the induced ac current than in the dc component (not shown in Fig. 2). Although the damping of SCWs increases with increasing temperature, the amplification effect of the ac current remains appreciable so that both SCW-induced current resonances survive also at higher temperatures.

2. Conclusion

SCWs are eigenmodes of oscillations of excited electrons and holes in a semiconductor QW that move in a constant electric field. There are two modes that remarkably differ from each other. They are excited by the superposition of a static and moving optical grating. A moving interference grating induces a constant current that continues to exist even when the applied electric field is switched off. If in addition to the moving pattern, a static optical grating is supplied, both dc and ac current contributions are induced. These currents are resonantly enhanced, when the spatial and temporal period of the interference pattern coincide with related quantities of the SCW and when the damping of SCWs can be neglected. The simultaneous detection of excited SCWs by dc and ac current resonances provides complementary information that allow a detailed consideration of SCWs in semiconductor QWs and nanostructures. Our approach suggests an extension of the well known moving-photocarrier-grating technique that has successfully been applied for the determination of lifetimes and mobilities of photogenerated electrons and holes in semiconductors. The extension encompasses, on the one hand, the application of an external constant electric field so that SCWs can be excited and, on the other hand, the simultaneous creation of a static and moving intensity grating so that both dc and ac current resonances are induced. Experiments in this direction would facilitate the study of SCWs.

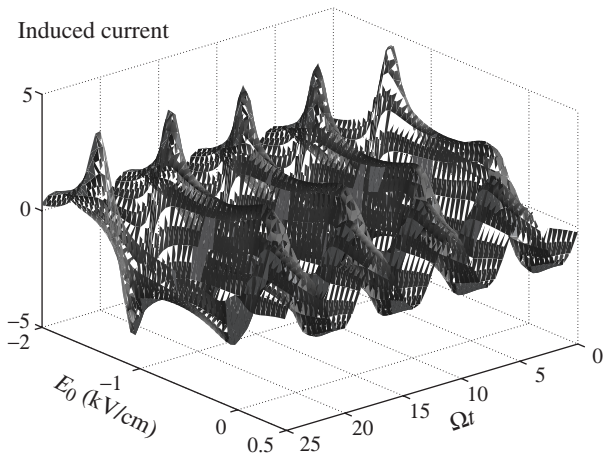

Fig. 2. Induced alternating current $\delta I_1(t)$ as a function of the applied constant electric field E_0 and the time variable Ωt for the lattice temperature $T = 4$ K and electron- and hole mobilities $\mu_n = 0.5$ cm^2/Vs, and $\mu_p = 0.2$ cm^2/Vs, respectively. The carrier generation rates due to the two pairs of laser beams are given by $g_0 = 10^{19}$ s^{-1}cm^{-3} ($g_s = g_m = 0.5 g_0$). Carrier recombination is characterized by the lifetime $\tau = 10^{-6}$ s. The angle between the beams has the value $\alpha = 10^\circ$ and the laser wavelength $\lambda = 633.8$ nm. The grating moves with the velocity $v_{gr} = 700$ cm/s.

Acknowledgement

This work has been supported in part by the Deutsche Forschungsgemeinschaft.

References

[1] D. Ritter, E. Zeldov and K. Weiser, *Appl. Phys. Lett.*, **49**, 791 (1986).
[2] U. Haken, M. Hundhausen and L. Ley, *Appl. Phys. Lett.*, **63**, 3066 (1993).
[3] J. A. Schmidt, M. Hundhausen and L. Ley, *Phys. Rev. B*, **64**, 104201 (2001).
[4] S. Stepanov, I. Seres, S. Mansurova and D. Nolte, *J. Appl. Phys.*, **92**, 1825 (2002).
[5] D. Dolfi, T. Merlet, A. Mestreau and J. P. Huignard, *Appl. Phys. Lett.*, **65**, 2931 (1994).
[6] M. Hundhausen, L. Ley and C. Witt, *Appl. Phys. Lett.*, **69**, 1746 (1996).
[7] M. P. Petrov, S. I. Stepanov and A. V. Khomenko, *Photorefractive Crystals in Coherent Optical Systems* (Springer-Verlag, Berlin, 1991).
[8] M. P. Petrov, V. V. Bryksin, H. Vogt and E. Krätzig, *Phys. Rev. B*, **66**, 085107 (2002).
[9] R. F. Kazarinov, R. A. Suris and B. I. Fuchs, *Fiz. Tekh. Poluprovodn.*, **7**, 149 (1973) [Sov. Phys. Semicond. **7**, 102 (1973)].
[10] M. P. Petrov, V. V. Bryksin, V. M. Petrov, S. Wevering and E. Krätzig, *Phys. Rev. A*, **60**, 2413 (1999).

13th Int. Symp. "Nanostructures: Physics and Technology"
St Petersburg, Russia, June 20–25, 2005

Metal-insulator transition in graphite: magnetotransport and STS-investigations

E. V. Konenkova[1], S. A. Kukushkin[2], O. Kronenwerth[3], D. Grundler[3], M. Morgenstern[4] and R. Wiesendanger[3]

[1] Ioffe Physico-Technical Institute, St Petersburg, Russia
[2] Institute of Problems of Mechanical Engineering, St Petersburg, Russia
[3] Institute of Applied Physics, Hamburg, Germany
[4] II. Institute of Experimental Physics, RWTH Aachen, 52056 Aachen, Germany

The metal-insulator transition (MIT) is one of the most interesting phenomena in physics of two-dimensional electron systems. It can be induced either by changing the density of the system or by applying a magnetic field. The magnetic field induced MIT has been investigated in detail in doped semiconductors, in high mobility 2D systems as well as in Si metal-oxide-semiconductor field-effect transistors. Recently, the MIT was also observed in highly oriented pyrolitic graphite (HOPG), which is a quasi 2D system due to the layered structure of the material. during magnetoresistance investigations.

The magnetoresistance and the Hall resistance were studied at temperature from 0.3 K to 150 K. The magnetic field from 1 up to 9 T was applied parallel to the c-axis of the sample. The measured HOPG samples were obtained from GE Advanced Ceramics. The high degree of crystallites orientation along the hexagonal c-axis was confirmed by x-ray rocking curves ($FWHM = 0.4-1.4$). Typical sample dimensions are 5×5 mm and the thickness of the sample is about 1 mm. The measurements were performed using the usual four-terminal dc method. Leads were attached in van-der-Pauw geometry with silver paste in the corner of the top sample surface. The STS measurements were done with home-built low-temperature STM. The data were taken at temperatures below 6 K and in magnetic fields up to 6 T.

The longitudinal resistance of the sample as a function of temperature and magnetic field is shown in Fig. 1. We find completely metallic behaviour up to 30 mT, completely insulating behaviour up to 500 mT and the development of a maximum showing metallic behaviour towards lower temperature above 1 T. Obviously the maximum temperature called critical temperature of the MIT depends on the magnetic field.

STS measurement showed, that periodic peaks appear in the spectra $\mathrm{d}I/\mathrm{d}V$ in the "metal" state (at $T = 5.6$ K and $B = 3$ T, 6 T), while in "insulator" state ($T = 5.6$ T, but $B = 0$, 0.06 T) such a peaks are not present (Fig. 1a). One should note that the appearance of the peaks at $T = 0.03$ and $U > 0.1$ is connected with the MIT.

Hall measurements of graphite have shown, that in conditions of "metal" state (at $T = 300$ mK and $0.4 < B < 1.5$ T) Shubnikov–de-Haase oscillations were observed, and two-dimensional electrons are formed, while in conditions of the "insulator" state (at $T = 10$ K, $0.4 < B < 1.5$ T) the oscillations are not observed (Fig. 1c,d). At temperature $T = 300$ mK the minimal position of Shubnikov–de-Haase oscillations are: 0.58, 0.64, 0.74, 0.87, 1.07, 1.38 T (Fig. 1d).

In summary, we have observed MIT in HOPG, and the temperature of transition is in good agreement with the predictions

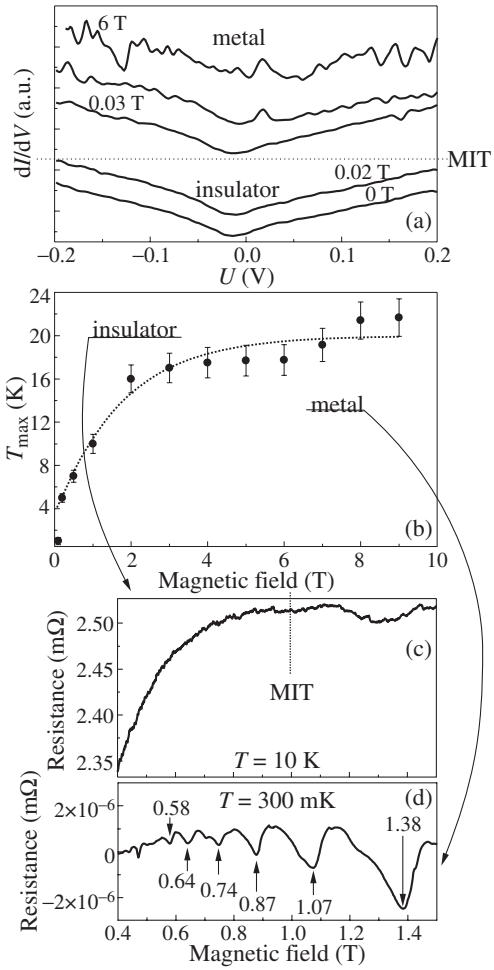

Fig. 1. Temperature dependence of metal-insulator transition for HOPG-UC: (a) STS at $T = 0$, 0.03, 3, and 6 T; (b) comparison of the experimental data; SdH oscillation of HOPG-UC measured at (c) $T = 10$ K and (d) $T = 0.3$ K.

of our model of the electron-phase transition. According this model, the electron-phase transition is first order phase transitions, during which in graphite the magnetic domains arise which lead to metal-insulator transition. In the "metal" state of the graphite: "The oscillation of magnetoresistance has been observed at the temperature low than 4.2 K and the period of the oscillations is described with good accuracy by the theory of conductivity maxima occurrence at coincidence of Landau levels and Fermi energy." The oscillations in the tunnel spectra are associated with Landau quantization of the quasi two-dimensional Landau levels.

13th Int. Symp. "Nanostructures: Physics and Technology"
St Petersburg, Russia, June 20–25, 2005

Hole-hole interaction in strained InGaAs two dimensional system

G. M. Minkov[1], A. V. Germanenko[2], O. E. Rut[2], A. A. Sherstobitov[1], V. A. Larionova[2] and B. N. Zvonkov[3]

[1] Institute of Metal Physics RAS, 620219 Ekaterinburg, Russia
[2] Ural State University, 620083 Ekaterinburg, Russia
[3] Physical-Technical Research Institute, University of Nizhni Novgorod, 603600 Nizhni Novgorod, Russia

Abstract. The temperature and magnetic field dependences of the conductivity of the p-type strained InGaAs quantum well structures are studied. The analysis of parabolic-like negative magnetoresistance at lowest temperature allows us to determine the hole-hole (h-h) interaction correction and to find the Fermi liquid constant F_0^σ. It is shown that at $B = 0$ the ballistic contribution of the h-h interaction is important even at seemingly low value of the parameter $T\tau$: $T\tau = 0.05$ (where τ is transport relaxation time). The role of the ballistic contribution of h-h interaction in magnetic field dependences of the conductivity is discussed.

The transport properties of two dimensional (2D) systems reveal the intriguing features. One of the feature is a metallic-like temperature dependence of the resistivity at low temperature for some kind of 2D systems: $\partial\rho/\partial T > 0$. As a rule such a behavior is observed in the structures with strong hole-hole (h-h) interaction characterized by large value of the parameter $r_s = \sqrt{2}/(a_B k_F)$, where a_B and k_F are the Bohr radius and Fermi quasimomentum, respectively (for details see [1,2] and references therein.) Just h-h interaction at intermediate regime ($k_B T \simeq \hbar/\tau$) is considered at the last time as main reason for metallic-like behavior of the conductivity. Such an effect crucially depends on the value of the Fermi-liquid constant F_0^σ therefore the experimental determination of the interaction correction to the conductivity and the value of F_0^σ is a central point of numerous papers at last years.

Unlike the case of structures with electron 2D gas there are some difficulties in extracting of the interaction correction to the conductivity in p-type structures. First of all they result from a strong spin-orbit interaction and a large value of perpendicular g-factor. These factors make the temperature and magnetic field dependences of the both weak localization (WL) and interaction corrections to be more complicated. Besides, for the high mobility 2D hole gas, the parameter $k_B T\tau/\hbar$ is usually greater than unity at all available temperatures and therefore the interaction correction gives contribution not only to σ_{xx}, but to σ_{xy} as well. Strong anisotropy of g-factor makes it difficult to determine the reliable value of F_0^σ from in-plane magnetoresistance experiments. Most likely just these facts lead to very large scatter in the F_0^σ-values determined in different papers, so that even the sign of the h-h correction occurs to be different.

In present report we study the h-h interaction correction to the conductivity for the low mobility, high density ($p = (5-8) \times 10^{11}\,\mathrm{cm}^{-2}$) p-type quantum well heterostructures with $r_s < 1-2$ within the temperature range from 0.4 to 4 K, when the parameter $k_B T\tau/\hbar$ lies within the interval from 0.03 to 0.2 that captures the diffusion region. The heterostructures were grown by metal-organic vapor phase epitaxy on semi-insulator GaAs substrate. The structures consist of a 0.2 μm-thick undoped GaAs buffer layer, C δ-layer, a (7–10) nm spacer of undoped GaAs, a 10 nm $In_{0.2}Ga_{0.8}As$ well, a (7–10) nm spacer of undoped GaAs, a C δ-layer and 200 nm cap layer of undoped GaAs. The samples were mesa etched into standard Hall bars and then an Al gate electrode was deposited by thermal evaporation onto the cap layer through a mask. The mobility was (5000–12000) cm^2/Vs for different structures and gate voltages.

The role of h-h interaction in structures investigated is evident from the magnetic field dependencies of ρ_{xx}, presented for one of the structures in Fig. 1 (we measure the conductivity in units of $G_0 = e^2/\pi h$). As seen the sharp magnetoresistance in low magnetic field, $B < (0.1-0.5)$ T, which results from suppression of the interference quantum correction [3], followed by the parabolic-like negative magnetoresistance at $B > 1$ T is observed. This magnetoresistance decreases in magnitude with increasing temperature and practically disappears at $T \simeq 30$ K (not shown in Fig. 1).

Let us now analyze the temperature dependence of the conductivity at $B = 0$. These dependences for structures investigated are presented in Fig. 2a. The strong deviation of these dependences from the logarithmic ones is result of the spin relaxation which leads to antilocalization at low magnetic field (see insert in Fig. 2a). The detailed studies of antilocalization for structures investigated have been carried out in Ref. [3]. It has been shown that the Hikami-Larkin-Nagaoka expression well describes the interference correction, that allows us to find the value of interference correction and extract it from the $\sigma(B = 0)$-vs-T dependences. The results are presented in Fig. 2b. Surprisingly, the conductivity becomes practically

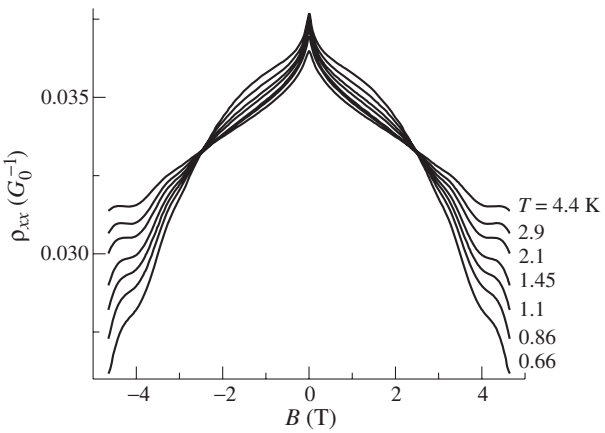

Fig. 1. The magnetoresistance of the structure 3857 for different temperatures. $V_g = 2.65$ V, $p = 5.6 \times 10^{11}\,\mathrm{cm}^{-2}$, $\mu = 4100\,\mathrm{cm}^2$/Vs.

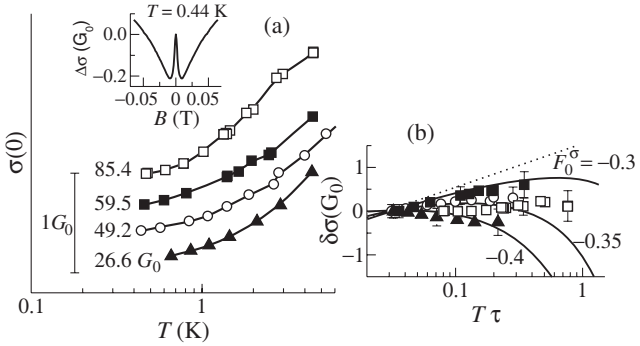

Fig. 2. (a) The variation of the conductivity with temperature at $B = 0$ for different structures. The numbers at curves are the conductivity values at lowest T. The insert shows the low-field magnetoconductivity of the structure 3857 with $\sigma = 30G_0$. (b) The temperature dependence of $\delta\sigma(T) = \sigma(T) - \sigma(0.5\,K)$ for different structures (points) and calculated dependences with different F_0^σ (solid lines). The dot line shows the diffusion contribution with $F_0^\sigma = -0.3$.

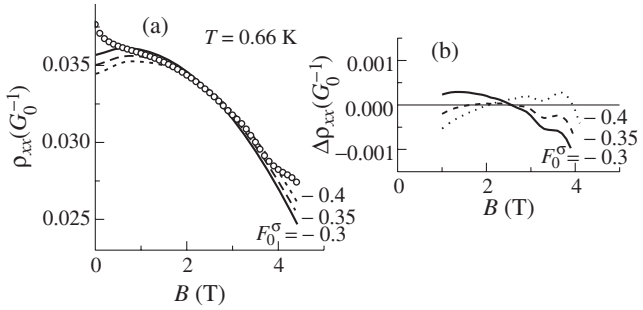

Fig. 3. (a) The comparison of the magnetoresistance presented in Fig. 1 (points) and the calculated dependences with different values of F_0^σ (curves). (b) The differences between experimental and calculated curves with the same values of F_0^σ.

independent of temperature after such extraction.

Thus, we have observed apparent discrepancy: the *h-h* correction to the conductivity reveals itself in the ρ_{xx}-versus-B curves (see Fig. 1), but it is absent in the temperature dependence of the conductivity at $B = 0$ (see Fig. 2b).

One of the reason for such a discrepancy can be the ballistic contribution, which crucial changes the temperature dependence of the conductivity at $B = 0$ for some values of the F_0^σ [5]. To estimate the value of F_0^σ we have analyzed the magnetoresistance at lowest temperature where the ballistic contribution is rather small. The calculated with different F_0^σ-values curves are presented in Fig. 3a. Obtaining them we have taken into account the fact that the interaction contributes only to σ_{xx} and does not to σ_{xy} in the diffusion regime. The Zeeman splitting is accounted with g-factor equal to 5. Note, the results only slightly depend on the specific value of g-factor while $g > 3$. This is because the inequality $g\mu_B B/k_B T > 1$ is fulfilled within actual interval of T and B, and two triplet channels are strongly suppressed.

Looking at the differences between the experimental and calculated curves in Fig. 3b one can see that all the values of F_0^σ from the range $F_0^\sigma = -0.35 \pm 0.05$ well describe our experimental data. The close value of F_0^σ was obtained by this way for another gate voltage and other structures under the condition that $k_B T\tau/\hbar < 0.05$.

The calculated, with F_0^σ found above, temperature dependences of the conductivity for $B = 0$ are shown in Fig. 2b. It is seen that the ballistic contribution of *h-h* interaction is important under these conditions, it significantly suppresses the temperature dependence caused by the diffusion contribution so that the calculated with $F_0^\sigma = -0.35 \pm 0.05$ curves well describe the experimental data.

To the best of our knowledge there is no exact solution for the interaction correction at high perpendicular magnetic field for intermediate regime with taking into account the Zeeman splitting. Therefore, to adapt the theoretical results for analysis of our data we have taken into account the following two well known facts. In the purely diffusion regime, the *h-h* interaction contributes to σ_{xx} and does not to σ_{xy}. In the purely ballistic regime, the interaction modifies the conductivity components changing the transport relaxation time τ. The analysis of the data shows that this model well describes the experimental magnetic and temperature dependences within whole temperature range with $F_0^\sigma = -0.35 \pm 0.05$. Note, this value is close to the calculated one for the weak interaction system.

In summary, we have studied the temperature and magnetic field dependences of the conductivity of the p-type strained InGaAs quantum well structures. We have found the Fermi liquid constant $F_0^\sigma = -0.35 \pm 0.05$ from the magnetoresistance at lowest temperature and shown that at $B = 0$ the ballistic contribution of the *h-h* interaction is important starting already from $k_B T\tau/\hbar \simeq 0.05$. We have suggested the simple phenomenological way to account the ballistic contribution of interaction in classically high perpendicular magnetic field.

Acknowledgements

This work was supported in part by the RFBR (Grants 03-02-16150 and 04-02-16626), the CRDF (Grants EK-005-X1 and Y1-P-05-11), the INTAS (Grant 1B290) and the Russian Program *Physics of Solid State Nanostructures*.

References

[1] A. K. Savchenko *et al*, *Physica E*, **22**, 218 (2004).
[2] V. M. Pudalov *et al*, to be published in: Chapter 19, Proceedings of the EURESCO conference "Fundamental Problems of Mesoscopic Physics", Granada, (2003).
[3] G. M. Minkov *et al*, *Phys. Rev. B*, (2005), accepted for publication.
[4] S. Hikami *et al*, *Prog. Theor. Phys.*, **63**, 707 (1980).
[5] Gabor Zala *et al*, *Phys. Rev. B*, **64**, 214204 (2001).

13th Int. Symp. "Nanostructures: Physics and Technology"
St Petersburg, Russia, June 20–25, 2005

Wave functions and energies of magnetopolarons in semiconductor quantum wells

S. T. Pavlov[1,2], I. G. Lang[3] and L. I. Korovin[3]

[1] P.N. Lebedev Physical Institute, Russian Academy of Sciences, 119991 Moscow, Russia
[2] Facultad de Fisica de la UAZ, Apartado Postal C-580, 98060 Zacatecas, Zac., Mexico
[3] Ioffe Physico-Technical Institute, St Petersburg, Russia

Abstract. The classification of magnetopolarons in semiconductor quantum wells (QW) is represented. Magnetopolarons appear due to the Johnson–Larsen effect. The wave functions of usual and combined magnetopolarons are obtained by the diagonalization of the Schrödinger equation.

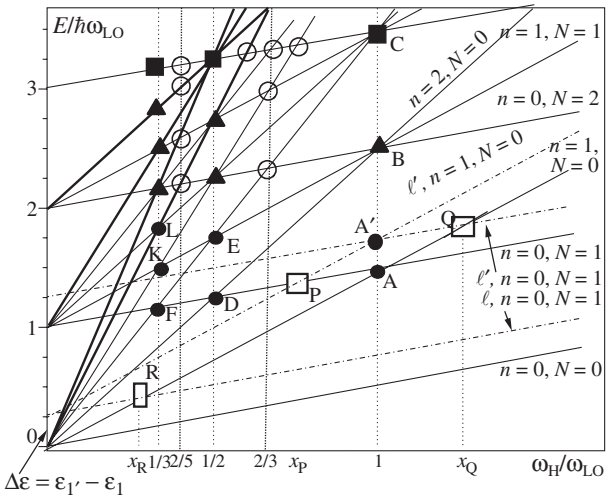

Fig. 1. Energy levels of an electron (hole) — phonon system as functions of a magnetic field. Points of crossings of lines correspond to polaron states. Black circles are the twofold polarons, triangles — threefold polarons, squares — fourfold polarons. Empty circles are weak polarons, empty squares — combined polarons, empty rectangular — weak combined polaron. E is the energy counted from energy ε_l of the size-quantization, n is the Landau quantum number, N is the number of phonons; l, l' are the size-quantization quantum numbers.

Introduction

The Johnson–Larsen effect [1] arises at a condition

$$\omega_{\rm LO} = j\omega_{e(h)H}\,, \qquad (1)$$

where $\omega_{\rm LO}$ is the frequency of a longitudinal optical (LO) phonon, $\omega_{e(hH} = \frac{|e|H}{cm_{e(h)}}$ is the cyclotron frequency, $m_{e(h)}$ is the electron (hole) effective mass, H is the magnetic field, j is some number.

The Johnson–Larsen effect is called also as a magnetopolaron resonance, and the states which are being formed under condition (1) in semiconductors — by magnetopolarons. At magnetic fields appropriate to the condition (1) the resonant connection between the Landau bands with different quantum numbers n arises. The electron-phonon interaction results into removing of a degeneration in crossing points of energy levels, what influences magnetooptical effects (Fig. 1). For the first time the magnetopolaron states were discovered in a bulk InSb in the interband light absorption [1].

In [2] Korovin and Pavlov have shown that in bulk semiconductors the magnetopolaron splitting is proportional to $\alpha^{2/3}\hbar\omega_{\rm LO}$, where α is the Fröhlich dimensionless electron-phonon coupling constant ($\alpha \ll 1$). In quasi-2D systems (in particular in semiconductor QWs), effect amplifies, and the distance between components of splintered peaks (for example, of interband light absorption) becomes proportional to $\alpha^{1/2}\hbar\omega_{\rm LO}$ [3].

1. The Hamiltonian of a system

In present work we generalize results of [4] for the polaron A on the case of any twofold polarons, including usual, combined and "special polaron state". We pay the special attention to wave functions, before unknown. The theory is not extended on weak, threefold, fourfold etc. polarons.

We consider a semiconductor QW of type I with the energy gap E_g and barrier ΔE_e for electrons. For definiteness we investigate magnetopolarons with participation of electrons.

The magnetic field is directed along an z axis perpendicularly to the QW plane. The vector potential is chosen as $\mathbf{A} = \mathbf{A}(0, xH, 0)$. The Schrödinger equation for electrons, interacting with LO phonons, looks like

$$\mathcal{H}\Theta = E\Theta, \quad \mathcal{H} = \mathcal{H}_0 + V, \quad \mathcal{H}_0 = \mathcal{H}_e + \mathcal{H}_{ph}\,, \qquad (2)$$

and

$$\mathcal{H}_e\Psi_{n,k_y,l} = [(n+1/2)\hbar\omega_{eH} + \varepsilon_l]\Psi_{n,k_y,l}\,, \qquad (3)$$

where

$$\Psi_{n,k_y,l} = \Phi_n(x + a_H^2 k_y)\frac{1}{\sqrt{L_y}}e^{ik_y y}\varphi_l(z)\,,$$
$$\Phi_n(x) = \frac{1}{\sqrt{\pi^{1/2}2^n n!\,a_H}}H_n(x/a_H)e^{-x^2/2a_H^2}\,, \qquad (4)$$

$a_H = \sqrt{c\hbar/|e|H}$ is the magnetic length, $H_n(t)$ is the Hermitian polynomial. The functions $\varphi_l(z)$ and levels ε_l of energy ofsize-quantization of electrons in a QW of finite depth are determined, for example, in [4], $\mathcal{H}_{ph}$ is the Hamiltonian of the phonon system, V is the electron-phonon interaction. In a case of an infinitely deep QW, when $\Delta E_e \to \infty$

$$\varphi_\ell(z) = \begin{cases} \sqrt{\frac{2}{d}}\,\sin\left(\frac{\pi\ell z}{d} + \frac{\pi\ell}{2}\right), & |z| \le \frac{d}{2}\,, \\ 0 & |z| \ge \frac{d}{2}\,, \end{cases}$$

$$\varepsilon_l(z) = \frac{\pi^2\hbar^2 l^2}{2m_e d}\,,$$

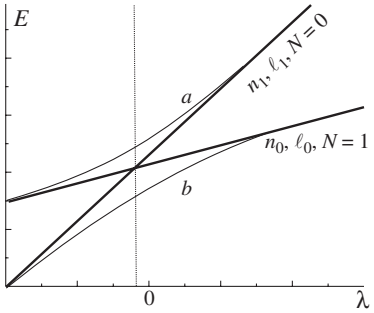

Fig. 2. The schematic image of polaron energies formed on crossing a and b. On an ordinate axis the value $\lambda = \Sigma_1 - \Sigma_0 - \hbar\omega_{\rm LO}$, where $\Sigma_1 = (n + 1/2)\hbar\omega_{eH} + \varepsilon_{l_1}$, $\Sigma_0 = (n + 1/2)\hbar\omega_{eH} + \varepsilon_{l_0}$ is represented.

m_e is the electron effective mass.

Let us designate as $\Psi_{ph0}(y)$ and $\Psi_{ph\nu}(y)$ the wave functions of the phonon system appropriate to absence of phonons and to presence of one phonon with indexes $\nu \equiv (\mathbf{q}_\perp, \mu)$, where $\mathbf{q}_\perp$ is the phonon wave vector in a plane xy, μ are other indexes, Y are the coordinates of the phonon subsystems. Let us assume

$$\mathcal{H}_{ph}\Psi_{ph0} = 0, \quad \mathcal{H}_{ph}\Psi_{ph\nu} = \hbar\omega_\nu\Psi_{ph\nu}\,. \tag{5}$$

The electron-phonon interaction looks like

$$V = \sum_\nu [C_\nu(\mathbf{r}_\perp, z)b_\nu + C^*_\nu(\mathbf{r}_\perp, z)b^+_\nu]\,, \tag{6}$$

where $b^+_\nu(b_\nu)$ is the phonon creation (annihilation) operator,

$$C_\nu(\mathbf{r}_\perp, z) = C_\nu e^{i\mathbf{q}_\perp\mathbf{r}_\perp}\xi_\nu(z)\,, \tag{7}$$

and $\xi_\nu(z)$ is chosen so, that $\xi_\nu(z = 0) = 1$.

We do not concretize the form of the interaction (7) below.

2. Wave functions and energies of magnetopolarons

A polaron, arising due to crossing of terms n_0, l_0, $N = 1$ and n_1, l_1, $N = 0$ is considered. n is the Landau quantum number, l is the quantum number of the size-quantization, N is the number of phonons (Fig. 2). We search for the wave function as a superposition

$$\Theta(x, y, z, Y) = \sum_{k_y} a_0(k_y)\Psi_{n_1,k_y,l_1}(x, y, z)\psi_{ph0}(Y) + \sum_{k_y,\nu} a_1(k_y)\Psi_{n_0,k_y,l_0}(x, y, z)\psi_{ph\nu}(Y)\,. \tag{8}$$

The indexes 0 and 1 at factors $a_0(k_y)$ and $a_1(k_y)$ designate the number of phonons. For convenience of the further calculations we introduce designations

$$\Psi_{n_1,k_y,l_1}(x, y, z) = \Psi_{1,k_y}(x, y, z)\,, \quad \Psi_{n_0,k_y,l_0}(x, y, z) = \Psi_{0,k_y}(x, y, z) \tag{9}$$

and also

$$\Sigma_1 = (n_1 + 1/2)\hbar\omega_{eH} + \varepsilon_{l_1}\,, \quad \Sigma_0 = (n_0 + 1/2)\hbar\omega_{eH} + \varepsilon_{l_0}\,. \tag{10}$$

Then the Schrödinger equation may be written down as

$$(E - \Sigma_1)\psi_{ph0}\sum_{k_y} a_0(k_y)\Psi_{1,k_y} + (E - \Sigma_0 - \hbar\omega_{\rm LO})\sum_{k_y} a_1(k_y, \nu)\psi_{ph\nu} - \psi_{ph0}\sum_{k_y}\Psi_{0,k_y}\sum_\nu C_\nu(\mathbf{r}_\perp, z)a_1(k_y, \nu) - \sum_{k_y} a_0(k_y)\Psi_{1,k_y}\sum_\nu C^*_\nu(\mathbf{r}_\perp, z)\psi_{ph\nu} = 0\,. \tag{11}$$

We obtain the square-law equation for energy E

$$(E - \Sigma_1)(E - \Sigma_0 - \hbar\omega_{\rm LO}) \times \sum_\nu |U(\nu)|^2 = 0\,. \tag{12}$$

Let us introduce a designation

$$w(n_o, n_1, l_0, l_1) = \sum_\nu |U(\nu)|^2\,. \tag{13}$$

The equation (12) has two solutions

$$E_{a,b} = \frac{1}{2}\Big\{\Sigma_0 + \Sigma_1 + \hbar\omega_{\rm LO} \pm\sqrt{(\Sigma_1 - \Sigma_0 - \hbar\omega_{\rm LO})^2 + 4w(n_o, n_1, l_0, l_1)}\Big\}\,, \tag{14}$$

where the indexes a and b correspond to $+$ and $-$. The energy distance between two magnetopolaron states is equal

$$\Delta E = \sqrt{\lambda^2 + 4w(n_o, n_1, l_0, l_1)}\,, \tag{15}$$

where

$$\lambda = (n_1 - n_0)\hbar\omega_{eH} - \hbar\omega_{\rm LO} + \varepsilon_{l_1} - \varepsilon_{l_2}$$

describes a deviation from an exact resonance. This is the energy spectrum of anyone twofold polaron.

Using (8), (14) and designation (9), we obtain the magnetopolaron wave functions for states $p = a$ and $p = b$

$$\Theta_p(x, y, z, Y) = \sum_{k_y} a_{0p}(k_y)\Big[\Psi_{1,k_y}(x, y, z)\psi_{ph0}(Y) + (E_p - \Sigma_0 - \hbar\omega_{\rm LO})^{-1}\sum_\nu \exp[ia_H^2 q_x(k_y - q_y/2)] \times U^*_\nu\Psi_{0,k_y-q_y}(x, y, z)\psi_{ph\nu}(Y)\Big]\,. \tag{16}$$

References

[1] E. J. Johnson *et al*, *Phys. Rev. Letters*, **16**, 655 (1966).

[2] L. I. Korovin *et al*, *JETP Lett.*, **6**, 525 (1967); *Zh. Eksper. i Teor. Fiz.*, **53**, 1708 (1967); [Soviet Phys.: JETP **26**, 979 (1968)].

[3] L. I. Korovin *et al*, *Fiz. tverd. tela*, **20**, 3594 (1978); [*Sov. Phys. Solid State*, **20**, 2077 (1978)].

[4] I. G. Lang *et al*, *Phys. Rev. B*, **54**, N 24, 17768 (1996).

13th Int. Symp. "Nanostructures: Physics and Technology"
St Petersburg, Russia, June 20–25, 2005

Metal-insulator type transition in tunnelling between 2D electron systems induced by in-plane magnetic field

E. V. Sokolov[1], V. Renard[2], D. Yu. Ivanov[1], Yu. V. Dubrovskii[1], J.-C. Portal[2,4,5], L. Eaves[3], E. E. Vdovin[1], M. Henini[3] and G. Hill[6]

[1] Institute of Microelectronics Technology RAS, 142432 Chernogolovka, Russia
[2] Grenoble High Magnetic Field Laboratory, MPI-CNRS, BP166 38042 Grenoble Cedex 9, France
[3] The School of Physics and Astronomy, University of Nottingham, Nottingham NG7 2RD, UK
[4] INSA, F31077 Toulouse Cedex 4, France
[5] Institute Universitaire de France, 103, Boulevard Saint-Michel, 75005 Paris, France
[6] Department of Electrical and Electronics Engineering, University of Sheffield, Sheffield S3 3JD, UK

Abstract. We have studied resonant tunnelling between identical two-dimensional electrons layers formed by δ-doping in adjacent quantum wells. We demonstrate that magnetic field parallel to the layers induces metal-insulator type transition manifested as change of temperature dependence sign of tunnelling junction linear conductance (the tunnelling conductance at small voltage around zero bias). The transition is sharp, i.e. there is crossover point between two types of conduction in particular B_S magnetic field. Simple expression is suggested to calculate B_S.

Conservation of in-plane momentum for tunnelling between parallel 2D electron systems produces sharply resonant current-voltage characteristics. For identical 2D electron systems maximum of differential conductance peak is precisely located at zero of external voltage bias.

The conservation of in-plane momentum strongly restricts the phase space available for tunnelling between parallel 2D systems. It can be described by use of electronic spectral function in the layers $A(E, k)$. This function gives the probability that an electron with wave vector k has energy E and possesses a strong peak near the single particle energy $\hbar^2k^2/2m$. The width of this peak and consequently the width of measured differential conductance peak reflect the finite lifetime τ of the momentum eigenstates in the layers.

The conductance peak broadens with temperature, which is mainly due to the increasing of the electron-electron scattering rate and as the result the reducing of lifetime τ. The linear or near equilibrium tunnelling conductance, i.e. the tunnelling conductance at small voltage around zero bias, decreases with temperature and could be called the metal-type temperature dependence.

In magnetic field B parallel to the layers the dispersion parabolas are relatively shifted in *k-space*. The shift is equal to $eBd/\hbar$, where e is electron charge and d is the tunnelling distance, which equals to the distance between "mass centers" of the quasibound ground 2D states wave functions in the layers. The linear tunnelling conductance decreases with magnetic field at constant temperature. It is clear that when Fermi momentum $2k_F$ becomes less then $eBd/\hbar$, there is not available phase space more in the vicinity of Fermi levels for near equilibrium tunnelling with momentum conservation. Now accessible states have higher energy and for tunnelling around zero bias electrons need temperature activation. It means that starting from some magnetic fields $B_S > B^* = 2k_F\hbar/ed$ equilibrium tunnelling conductance should demonstrate insulator type temperature dependence.

The arising questions are the following. Is this metal-insulator type transition sharp, i.e. is there a crossing point on the dependencies of equilibrium conductance on parallel magnetic fields measured at different temperatures? How does B_S relate with B^* especially if condition $\gamma \ll E_F$, where $\gamma = \hbar/\tau$, and E_F is Fermi energy in the layers, is not satisfied? Our studies gave answers to both questions. The answer to the first question was yes! The answer to the second question was $B_S = B^*\sqrt{(1 + \gamma/E_F)}$.

The MBE-grown samples were a triple barrier structures with pure vertical transport, based on AlGaAs/GaAs layered materials. The 2DESs in the quantum wells (QW) between the barriers were formed by δ-doping inside the QW (Si-donor sheets with concentration of 3×10^{11} cm^{-2}). Highly doped contact regions surround the tunnel barriers. Transport in the plane of the 2DES does not contribute to the tunnel current in these types of structures, so that tunnelling studies can be carried out in an arbitrary magnetic field. The transparencies of the two outer barriers are much larger than the transparency of the middle barrier, which separates the two 2DESs in the quantum wells. The barrier parameters were chosen so that the voltage applied to the samples drops predominantly between the two 2DESs, allowing the observation of features in the tunnelling spectra on a direct energy scale. Figure 1 shows schematic band diagram of the sample. Figure 2 shows tunnelling differential conductance versus bias voltage and demonstrates clear

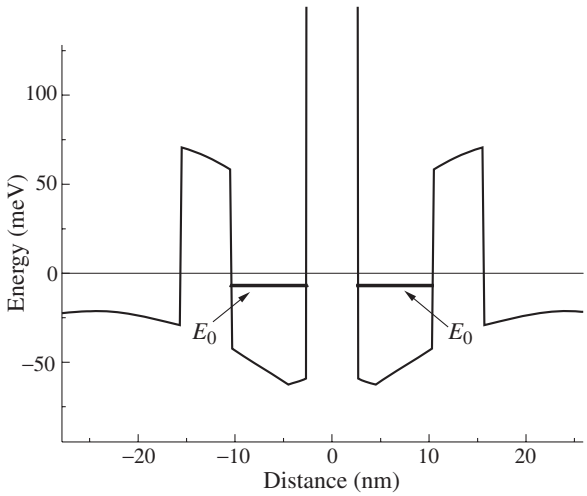

Fig. 1. Schematic band diagram of the sample.

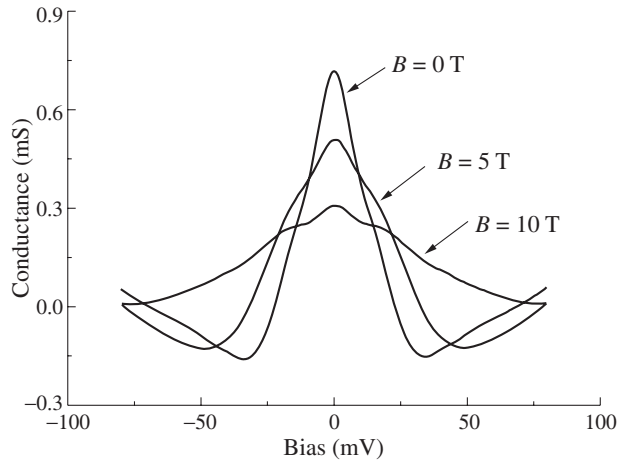

Fig. 2. Tunnelling differential conductance versus bias at different magnetic fields.

resonant features peaked at zero bias. That means identity of 2DEG' in QW's and alignment of ground subband energy levels under equilibrium conditions. Tunneling conductance is reducing in in-plane magnetic field.

Figure 3 shows linear tunnelling conductance versus in plane magnetic field at different temperatures. Linear tunnelling conductance has been extracted from resonance curves similar to these shown in Figure 2. The clear crossover point at $B_S = 13$ T reflect the boundary between different temperature dependences of linear conductance, i.e. the metal-insulator type transition in tunnelling junction. It should be noted that dependence of linear conductance on magnetic field at low temperature is very slow. This is strong indication of relatively large γ of the 2DEG's in QW's. Figure 4 demonstrates calculated dependence of linear conductance versus in plane magnetic field for different γ in the layers. The experimental data measured at 4 K are also presented in this figure. We suggest that 2DEG's in our structures is identical.

The calculations were performed by procedure similar to one described earlier [1]. By fitting procedure of calculations to experimental data we have extracted $\gamma = 4.8$ meV and $B^* = 9.5$ T for 2DEG's in the QW's. From measurements of SdH like oscillations in magnetic field normal to the layers we extract k_F. Self-consistent calculation of Schrodinger and Poisson equations permits us to estimate d. Multiplying these

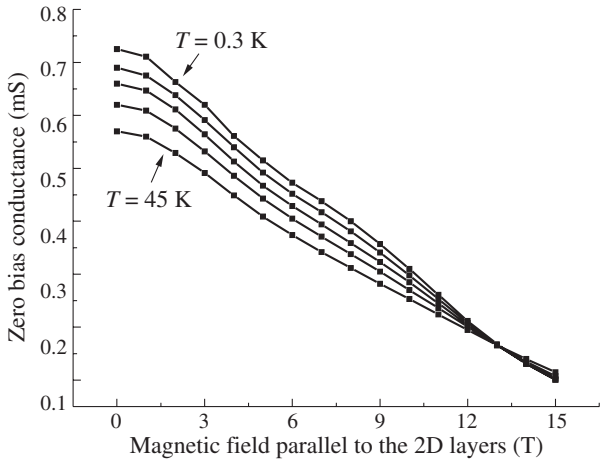

Fig. 3. Linear tunnelling conductance versus in plane magnetic field at different temperatures.

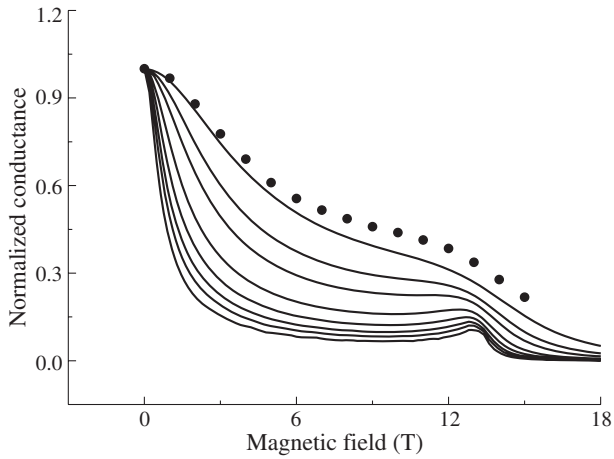

Fig. 4. Solid lines – calculated tunnelling linear conductance versus in plane magnetic field for different γ in the layers. Parameter γ increases from bottom to uppermost curve. Circles – experimental data measured at 4 K .

two values and the value of electron charge we have got $B^* = 9.4$ T, which is in very good agreement with value obtained by fitting procedure. The last step is to establish that with accuracy of few percent the relation $B_S = B^*\sqrt{(1+\gamma/E_F)}$ is valid. The relations was derived in preposition that dispersion curves in magnetic fields should be separated by $2k_F$ plus broadening of the spectral function. We note that in general γ depends on temperature. For our structures this dependence is weak since 2DEG's was formed by δ-doping and main scattering process responsible for the quantum lifetime in the layers is the scattering on the charged impurities.

In conclusion we have found that the temperature dependence of linear conductance in tunnel junction between identical 2DES's change sign with magnetic field parallel to the layers. The crossover point at particular magnetic field B_S separates the regions of metal or insulator type temperature dependences. The critical magnetic field B_S is slightly above magnetic field $B^* = 2k_F\hbar/ed$ and can be expressed by relation $B_S = B^*\sqrt{(1+\gamma/E_F)}$ with high accuracy.

Acknowledgements

This work was supported by RFBR (04-02-16869, 02-02-22004, 02-02-17403), PICS (1577), RAS programs "Quantum Macrophysics", and "Low-Dimensional Quantum Nanostructures", FTNS program, EPSRC, and RS (UK).

References

[1] S. Q. Murphy, J. P. Eisenstein, L. N. Pfeiffer, and K. W. West, *Phys. Rev. B* **52**, 14825 (1995).

13th Int. Symp. "Nanostructures: Physics and Technology"
St Petersburg, Russia, June 20–25, 2005

Using a silicon nanopore to detect a single DNA molecule

A. Aksimentiev, K. Schulten and *G. Timp*
Beckman Institute, University of Illinois, Urbana, IL USA 61801

Abstract. We are exploring the use of nanometer-diameter pores, sputtered into nanometer-thick inorganic membranes made from silicon, as a transducer that detects single molecules of *DNA* and produces an electrical signature of the structure. Silicon nanofabrication and molecular dynamic simulations with atomic detail are technological linchpins in the development of this detector. The sub-nanometer precision available through silicon nanotechnology facilitates the fabrication of the detector, and molecular dynamics provides us with a means to design it and analyze the experimental outcomes.

Each species from bacteria to human has a distinct genetic fingerprint [1]. The inimitable traits that identify each organism are derived from the sequence of base-pairs(bp) that comprise its *DNA* or genome. The genome for the smallest bacterium contains about 600,000 base-pairs, while the human genome has about 3 billion.

The aim of genomic science is to predict biological function using the information encoded in the sequence. Right now, about 100 bp can be sequenced at a cost of about $1 per minute by using variations of the Sanger process in conjunction with capillary array electrophoresis, to separate deoxyribonucleotide triphosphate fragments at single-base resolution with an accuracy of about 99.99% [2,3]. There are several emerging technologies that have the potential to supersede conventional sequencing [2,3]: for example, *bioMEMs*, which is an extension of conventional electrophoretic methods through miniaturization and integration [4]; *sequencing-by-hybridization*, which uses the differential hybridization of oligonucleotide (5-8 nucleotides long) probes to decode the *DNA* sequence [5]; *sequencing-by-synthesis*, which uses repeated cycles of nucleotide extension through polymerase to progressively infer the sequence [6]; *massively parallel signature sequencing (MPSS)*, which uses cycles of restriction digestion and ligation, instead of polymerase extension [7]; *cyclic-array sequencing on single molecules*, which eliminates the need for costly procedures such as cloning and PCR amplification through the extension of a primed *DNA* template by a polymerase with fluorescently labeled nucleotides [8]; and finally, non-enzymatic, real-time *sequencing of a single-molecule using a nanopore* [9]. Many of these methods like sequence-by- synthesis, cyclic-array sequencing on amplified molecules, and MPSS, rely on some method of isolated clonal amplification, that are costly and often problematic. On the other hand, sequencing single molecules eliminates the costly PCR-amplification step, and requires less starting material, but achieving the signal-to-noise required for single molecule detection is still a challenge.

A mechanism that detects a single molecule of *DNA* would represent the ultimate analytical tool. The nanopore sequencing concept, articulated by Deamer and Branton [10], is a radically new approach that does not require fluorescent labeling or any chemical treatment, instead it relies on a signal (that may be electrical or optical) that develops when *DNA* translocates through the pore. If each base has a characteristic electrical signature, then a nanopore sensor could facilitate the analysis by eliminating the need for sensitive dyes, thereby improving the dynamic range.

As a first step in the development of such a tool, we are exploring the use a nanometer-diameter pore, sputtered in a nanometer-thick inorganic membrane with a tightly focused electron beam, as a transducer that detects single molecules of *DNA* and produces an electrical signature of the structure [11,12]. The phosphate backbone of *DNA* gives the molecule a negative charge. So, when an electric field is applied across the membrane, *DNA* immersed in electrolyte is attracted to the pore, blocks the current through it, and eventually translocates across the membrane, bending and stretching along the way. As the molecule permeates the membrane, the ion current is temporarily blocked. The duration of the blocking transient and the magnitude of the blockade current provide an electrical signature that has been used to discriminate different nucleic acid polymers, divalent metal ions, organic molecules, and proteins [9].

Using the same fabrication tools that are used to manufacture MOSFETs (Metal Oxide Semiconductor Field Effect Transistors), we have fabricated nanometer-thick membranes and sputtered nanometer-diameter pores through them. Membranes fabricated this way are robust, withstanding hundreds of electrolyte immersion and emersion cycles without breaking. The inset in Figure 1(a) shows a *TEM* of a 0.5 nm radius pore produced in a Si_3N_4 membrane 10 ± 3 nm thick taken at a tilt angle of 0°. This image represents a two-dimensional (2D) projection through the membrane; the shot noise observed in the area identified, as the pore is indicative of perfect transmission of the electron beam through the membrane. The three-dimensional (3D) structure can be inferred from 2D projections of the pore taken at various tilt angles. One simple model for the structure consists of two intersecting cones each with a cone angle of $\sim 10^\circ$ as shown in the inset.

We have previously shown that electrophoretic ion transport can be used to characterize nanopores fabricated this way [11]. We measured the dc electrolytic current through a single pore as a function of the applied electrochemical potential in a membrane transport bi-cell. Figure 1(a) shows the I–V characteristic through the same pore measured in the range ±1 V in 1M KCl electrolyte using an Axopatch 200B amplifier with a 10 kHz bandwidth. Notice that the current is approximately a linear function of the voltage over the range.

We have also tested the efficacy of using synthetic nanopores for stochastic detection by injecting *DNA* along with *TRIS-EDTA* buffer (pH 8.0) into 1M KCl electrolyte near the negative electrode [11]. While monitoring the ionic current through the pore under an applied bias, we observed transients associated with single *DNA* molecules temporarily blocking

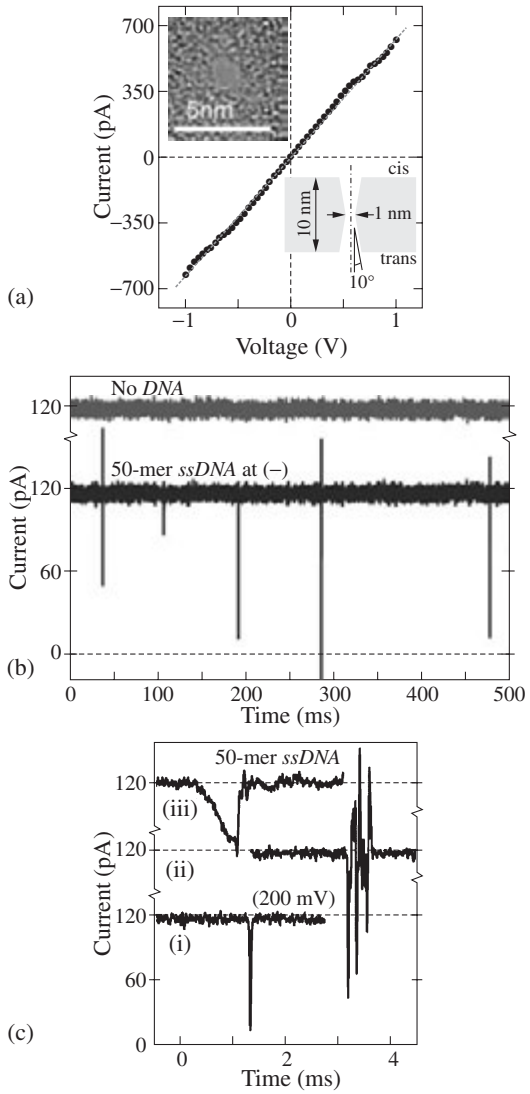

Fig. 1. Electrolytic characterization of nanopore and translocation of DNA. The upper inset to Fig. (a) is a *TEM* image of a nanopore (slightly out of focus to exaggerate the pore) in a nominally 10 nm thick nitride membrane viewed at 0° tilt angle. The apparent radius of the pore is $R_p = 0.5 \pm 0.1$ nm. The lower inset is a schematic representation of the structure inferred from tilted *TEM* images of similar pores. The current-voltage characteristic of the nanopore is approximately linear. Figure (a) is a measurement of the I–V characteristic obtained in 1M KCl, corresponding to the nanopore shown in the inset. The fit through the data (red dashed line) has a slope of 0.63±0.03 nS. When *DNA* is inserted at the negative electrode, transients are observed in the ionic current through the nanopore associated with a blockade by *DNA*. Figure (b) shows the current through the same nanopore as a continuous function of time with 50mer poly(dT) *ssDNA* inserted at the negative electrode (blue) and without it (red). Corresponding to the observation of transients, *DNA* is found at the positive electrode. Figure (c) illustrates the variety of transients observed in the same pore for an applied voltage of 200 mV (i,ii,iii) all plot on the same linear scale, but each transient has been offset for clarity. The blocking current is observed to vary during the transient and from transient to transient as well. The width of the transients ranges from the bandwidth-limited 100 μs to 10 ms. Taken from ref. [11].

the electrolytic current through the pore similar to the results obtained using α-hemolysin. Figure 1(b) shows a continuous time sequence (blue) of the current through the 0.5 nm-radius pore observed for an applied bias of 200 mV after injecting 50-mer poly (dT) (polydeoxythymidylate) single-stranded *DNA* (*ssDNA*) at the negative electrode. The trace shows five current transients. For comparison, the separate (red) trace in the same figure corresponds to the baseline measured without *DNA* at the negative electrode.

The time sequences in Fig. 1(c) incompletely illustrate the variety of transients associated with the same 50-mer poly (dT) *ssDNA* blocking the current through the same pore for a transmembrane bias of 200 mV. In each instance, the open current (120 pA for 200 mV) through the pore is blocked for only a limited time. Because of the low concentration of the *ssDNA* ($\sim 20\mu$g/mL$\sim$33pmole/mL) in the electrolyte, and the small volume of the pore (~ 20 nm^3), we suppose that each of these electrical signatures is indicative of a single molecule interacting with the pore. But because of the limited bandwidth of the amplifier, we may not detect every interaction between a molecule and the pore.

We have established the relationship between *DNA* translocation and blocking current through molecular dynamics simulations. Adapting the methodology developed for simulations of membrane proteins, we use classical molecular dynamics (MD) to analyze the translocation. To simulate the *DNA*/nanopore microsystem [12], a molecular force-field describing water, ions and nucleic acids is combined with the MSXX force-field for membranes. We first construct a microscopic model of our experimental systems and subsequently carry out MD simulations of electrophoretic transport through the pores. For example, a crystalline Si_3N_4 membrane is built by replicating a unit cell of β-Si_3N_4 crystal along the unit cell vectors, producing a hexagonal patch of 10.3 nm thickness and 4.6 nm sides. By removing atoms from the membrane one can produce pores of symmetric double-conical (hourglass) shapes with radii that correspond to our experiments. A *DNA* helix is built from individual base pairs in the geometry suggested by Quanta [12]. The *DNA* helix is placed in front of the pore normal to the membrane, as illustrated in Fig. 2(a). The *DNA*/nanopore complex is then solvated in pre-equilibrated TIP3P water molecules; K^+ and Cl^- ions are added corresponding to a 1M concentration.

For the 50 ns simulation illustrated in Fig. 2, we applied a uniform electric field of 8.7×10^7 V/m normal to a 5.2 nm thick Si_3N_4 membrane to drive a 20bp fragment of *dsDNA* (poly(dC)$_{20}$·poly(dG)$_{20}$) through a pore with a 2.2×2.6 nm^2 cross-section at the narrowest part. At the beginning of the simulations, the electric field rearranges the ions and water which in turn focuses the field to the vicinity of the membrane, eliminating the gradient in the bulk, and producing a 1.3 V transmembrane bias. Figures 2(a-e) represent snapshots of the time-dependent configuration of *dsDNA* as it translocates through the nanopore. To clearly delineate the conformation of the *DNA* fragment, water and ions, which were included in the simulation, are not shown in these figures. Figure 2(f) is a summary illustrating the position of the *dsDNA* center of mass (CoM) relative to the center of the Si_3N_4 membrane, along with the ionic current through the pore versus elapsed time for the duration of a translocation event. The vertical dashed line indicates the moment when the *DNA* is introduced into the

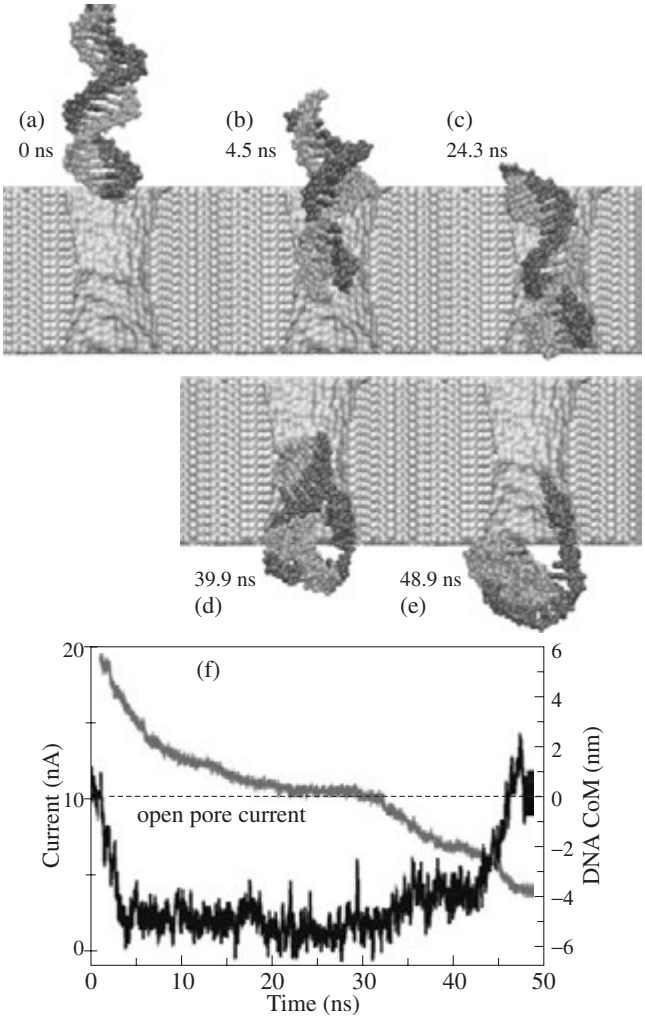

Fig. 2. Snapshots from MD simulation of *DNA* electrophoresis through a nanopore at a 1.4 V bias. (a) The simulation begins. (b) The terminal WatsonCrick base pair splits at the narrowest part of the pore. (c) *DNA* spends about 8.5ns in this conformation without moving. (d) *DNA* exits the pore while one base at the DNA end remains firmly attached to the surface of the nanopore. (e) The simulation ends. Most of the *DNA* has left the pore and the ionic current has returned to the open pore level. (f) Shown are the total ionic current (left axis, black line) and the position of the *DNA* center of mass relative to the center of the Si_3N_4 membrane (blue line, right axis) against the simulation time. The cross-section of the narrowest part of the pore is 2.2×2.6 nm^2. Taken from ref. [11].

simulation. The horizontal dashed line indicates the open pore ionic current found in the absence of *DNA*. Within the first few nanoseconds of the simulation the electric field captures the four pairs of nucleotides nearest the aperture and drives them into the pore. The rest of the molecule moves down the pore following the charged backbone of the first few nucleotides, almost completely blocking the ion current. After 5 ns, the *DNA* reaches the narrowest part of the pore and slows down. We observed a rupture of the hydrogen bonds connecting the bases of the three terminal base-pairs inside the pore, followed by a partial unzipping of the *DNA*. Two of the six non-bound bases adhere to the surface of the pore and remain in one location for an extended time interval (5–30 ns). Subsequently, near $t = 42$ ns, we find a characteristic positive spike above the open pore current that correlates with the exit of *DNA* from the pore. When *DNA* exits the pore, ions accumulating near the mouth are also released resulting in the positive spike in the current similar to those spikes observed experimentally.

In summary, nanometer-diameter pores can be fabricated in nanometer-thick inorganic membranes using electron beam induced sputtering. The inorganic membranes, made from MOS-compatible materials, are mechanically robust; can be incorporated into a conventional silicon manufacturing process; and are suitable for use at high voltage ($\sim$ 1 V). When an electric field is applied across the membrane, *DNA* immersed in electrolyte is attracted to the pore, blocks the current through it, and eventually permeates the membrane [11]. The relationship between *DNA* translocation and blocking current has been established through molecular dynamics simulations [12]. An unambiguous interpretation of the variety of current transients associated with *DNA* interacting with the nanopore will require sub-microsecond resolution according to MD simulations.

References

[1] http://www.ncbi.nlm.nih.gov/projects/genome/guide/human/
[2] J. Shendure, R.D. Mitra, C. Varma and G.M. Church *Nature Review* **5**, 335-344 (2004).
[3] M.W. Salisbury *Genome Technol.* **35**, 40–47 (2003).
[4] B.M. Paegel, R.G. Blazej and R.A. Mathies *Curr. Opin. Biotechnolog*. **14**, 42–50 (2003).
[5] R. Drmanac *et al*. *Methods Mol. Biolo.* **170**, 173–179 (2001).
[6] M. Ronaghi 2001. **11**, 3-11. B. Rudy and L.E. Iverson (ed.) 1992. Methods in Enzymology. *Academic Press.*
[7] S. Benner *et al*. *Nature Biotechnol* **18**, 630–634 (2000).
[8] I. Braslavski, B. Hebert, E. Kartalov and S.R. Quake *PNAS*, **100(7)**, 3960–3964 (2003).
[9] H. Bayley and C.R. Martin *Chem. Rev.* **100**, 2575–2594 (2000).
[10] D.W. Deamer and D. Branton *Acc. Chem. Res.* **35**, 817–825 (2002).
[11] J.B. Heng, *et al*.*Biophysical J.* **87**, 2905–2911 (2004).
[12] A. Aksimentiev, J.B. Heng, G. Timp and K. Schulten *Biophysical J.* **87**, 2086–2097 (2004).

13th Int. Symp. "Nanostructures: Physics and Technology"
St Petersburg, Russia, June 20–25, 2005

Nanostructuring for life science and materials applications

André Meister, Sivashankar Krishnamoorthy, Raphael Pugin, Christian Hinderling
and *Harry Heinzelmann*

Centre Suisse d'Electronique et de Microtechnique (CSEM) SA Nanotechnology & Life Sciences, Jaquet-Droz 1, 2007 Neuchâtel, Switzerland

Abstract. There are different approaches to create functional nanostructures. On the one hand, top-down approaches include conventional and advanced lithography techniques, such as the more recent soft lithographies. Furthermore, MEMS based devices become increasingly important to control micron and nanometer sized entities with high precision. We'll report on Nanoscale Dispensing (NADIS), a new technique to deposit ultrasmall volumes of liquids (down to the sub-femtoliter range) based on cantilevered tips with micromachined apertures. From the bottom-up side, molecular self-assembly shows us ways to inexpensively create functional nanostructures. Of particular interest are polymeric systems due to their versatility and tunability.
Both developments have tremendous potential in numerous fields of applications, including the field of life sciences. In this contribution, some of CSEM's activities in these fields will be presented.

1. Cantilever based liquid deposition of ultra-small volumes (NADIS)

In order to develop a nanoscale surface patterning technique that is non-lithographic and complementary to established methods, we combined the virtues of high resolution scanning probe approaches with the advantages of micro- and nanofluidics. Nanoscale dispensing (NADIS) is based on depositing liquid material through an apertured probe tip, such as the ones used for scanning force microscopy. The method works at ambient conditions and offers great flexibility in the choice of deposited material, substrates, and pattern geometry. Potential applications are e.g. in biotechnology (bio-arraying) and rapid prototyping.

In NADIS, liquid is transferred from the loaded probe tip by gently touching the surface. This approach is a straightforward development from our prior work on microfabricated apertured probes for scanning near-field optical microscopy (SNOM). In a more recent development, the apertures were formed by Focused Ion Beam (FIB) milling of commercial force microscopy probes [1]. Fig. 1 shows such a probe that was modified for operation as a NADIS device (left: top view, right: side view). The dark loading area at the back of the cantilever is clearly visible.

An array of droplets deposited on glass is shown in Fig. 2. The dots spacing is 1 μm, the dot diameter is well below 50 nm. Arbitrary lines can be written by moving the sample during contact with the dispensing probe tip. The FIB modified and thus sharp probe tip has the additional advantage that, once it is empty, allows high resolution (in-situ) imaging of the patterned substrate surface.

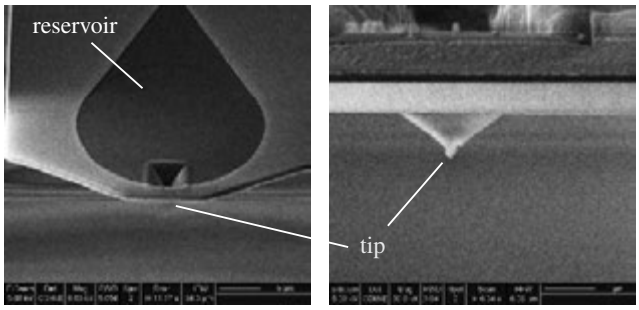

Fig. 1. Top view and side view of a FIB modified cantilever probe with patterned reservoir zone for NADIS operation.

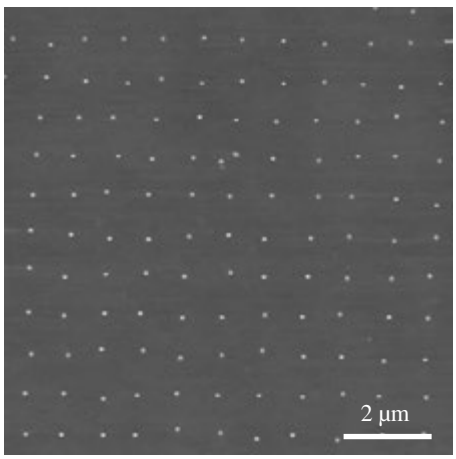

Fig. 2. NADIS array of glycerol dots deposited on glass. The dots are 50 nm in diameter and spaced at 1 μm.

2. Polymeric self-assembly for functional nanostructures

Polymeric nanostructures can be easily formed by utilizing processes such as de-mixing of homopolymer solutions, or microphase separation of block co-polymers. By using appropriate constituents, not only can nanoscale topographic structures be created on surfaces, but it is also possible to regularly pattern functionalities in an inexpensive way.

Here we present an example for microphase separation of block co-polymers, allowing to create even smaller structures, namely on the scale of the molecular building blocks. If such polymers contain two blocks, which are mutually insoluble, they phase-separate and form chemically distinct domains.

The bulk domains formed are well ordered and very small; they are directly related to the size of the polymer–chains and are therefore of the order of 10 to 100 nm. Depending on the relative length of the blocks, different morphologies of the domains form e.g. spheres, cylinders, or layers (Fig. 3).

Thin films of block-copolymers applied to surfaces thus result in surface patterns with well-ordered chemically distinct phases or domains. We are investigating the use of block-co-

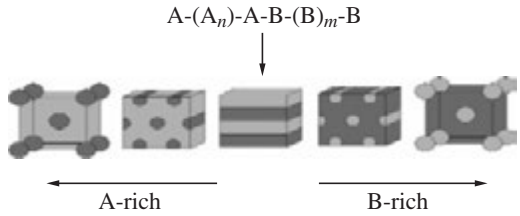

Fig. 3. Typical self-organized phase-separation patterns of block co-polymer A-b-B

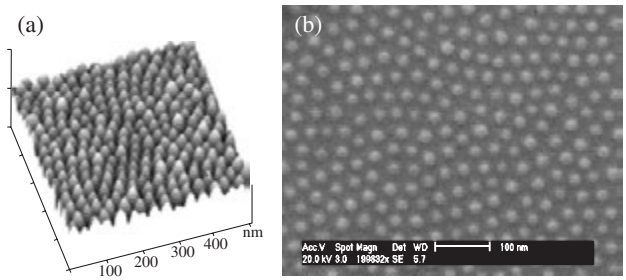

Fig. 4. Tapping mode AFM image (a) and scanning electron microscope (b) images of spin-cast films of polystyrene-poly(ferrocenyldimethylsilane) block-copolymers on a silicon surface after removal of the polystyrene block by O_2-reactive ion etching, showing self-organized 30 nm etch-resistant dots and mid-range ordering.

polymers that contain poly(ferrocenyl-dimethylsilane) (PFS) as one constituent [2–4]. One of the outstanding features of this system is the high resistance of PFS towards reactive ion etching (Fig. 4). Surfaces of different nature can thus be structured simply by spin-coating the block copolymer and using the PFS containing domains as etch mask for reactive ion etching. This makes the systems well suited for efficient nano-structuring of surfaces as industrially important as silicon or silicon nitride.

Combining the two methods of polymer demixing and microphase separation, by using a mixture of a block-copolymers with an incompatible homopolymer, leads to nanostructures within microstructures. This opens the way to structure surfaces on different, "hierarchical" length scales relaying on self-organization only. Further, microphase separation is a very promising chemical platform, when exploiting the selectivity of micelle cores forming on the surface [4]. Examples for both will be shown.

Acknowledgements

This work has been carried out at CSEM in the framework of its basic R&D program as well as of the Swiss national programs TOP NANO21 and the NCCR Nanoscience, as well as the European projects NaPa and POLYNANO. We further acknowledge very fruitful collaborations with the IMT of the University of Neuchâtel, the EPF Lausanne and the ETH Zurich, and the University of Twente.

CSEM is an innovation center collaborating with universities to provide solutions to industry.

References

[1] A. Meister, *Appl. Phys. Lett.* **85**, 6260 (2004).
[2] Y. Ni, R. Rulkens, I. Manners, *J. Am. Chem. Soc.* **118**, 4102 (1996).
[3] R. G. H. Lammertink, M. A. Hempenius, J. E. Van den Enk, V. Z.-H. Chan, E. L. Thomas, and G. J. Vancso, *Adv. Mater.* **12**, 2000, p.98 (2000).
[4] Ch. Hinderling *et al*., *Advancement in Polymer Science*, to be published (2005).

13th Int. Symp. "Nanostructures: Physics and Technology"
St Petersburg, Russia, June 20–25, 2005

Organized superstructures at nanoscale and new functional nanomaterials

V. Kislov[1], B. Medvedev[1], Yu. Gulyaev[1], I. Taranov[1], V. Kashin[1], G. Khomutov[2], M. Artemiev[3] and S. Gurevich[4]

[1] Institute of Radioengineering and Electronics, RAS, 125009, 11 Mokhovaya bld. 7, Moscow, Russia
[2] Faculty of Physics, Moscow State University, 119899 Moscow, Russia
[3] Institute for Physico-Chemical Problems, Belarussian State University, 220080, Minsk, Belarus
[4] Ioffe Physico-Technical Institute, St Petersburg, Russia

Abstract. We report on a number of new effects of self-organization at nanoscale, leading to creation of new functional nanomaterials, including carbon and carbon-metal nanotoroids and nanodiscs (size of pure carbon $\sim$ 10 nm, for carbon-metal (Mo, Cr) $\sim$ 30 nm) and self-assembling of magnetic nanoparticles (Ni, size $\sim$ 2.5 nm) into helices and chains. Contrary to carbon-based self-assembling superstructures (pure carbon, carbon-metal nanoclusters, including magnetic nanoclusters), we also extensively used a new approach of biopattern nanoengineering to create DNA-based complexes with metal or CdSe/ZnS core-shell nanorods (22 $\times$ 4.5 nm) which possess strongly linearly polarized photoluminescence due to unidirectional orientation of nanorods along DNA filaments ($\sim$ 1 m in length and 4 nm in diameter). Optical, electrical and topology (geometrical) properties of such complexes were investigated.

We report experimental observation (by AFM, STM and HRTEM methods) of nanotoroids for both carbon and carbon-metal superstructures produced by methods of arc discharge and laser ablation. Size of superstructures is $\sim$ 10 nm for carbon and $\sim$ 30 nm for carbon-metal (outer diameter), with inner diameter $\sim 1/3$ of the total.

Initial observations of toroids were made for pure carbon, but gradual increase of metal to some optimal concentration dramatically increased the yield of toroidal structures [1, 2]. The influence of pressure, humidity and temperature was also investigated. Also effects of reversible transition of topology (sphere–toroid) (Fig. 1a–1c.) on the same sample, were observed depending on external parameters [2].

The possibility of such structures was discussed earlier [3, 4], but we also discovered carbon-metal nanocapsules among toroids (Fig. 1c), with shapes like nanodiscs, reminiscent of human erythrocytes. Changing concentrations and metals (Mo, Cr, ets) leads to difference in shapes and sizes of superstructures. Therefore, new types of topologically closed carbon and carbon-metal nanostructures are discovered, with the theoretical model presented elsewhere [5]. We also discuss technological aspects of the growth of such nanostructures and their applications as new functional nanomaterials.

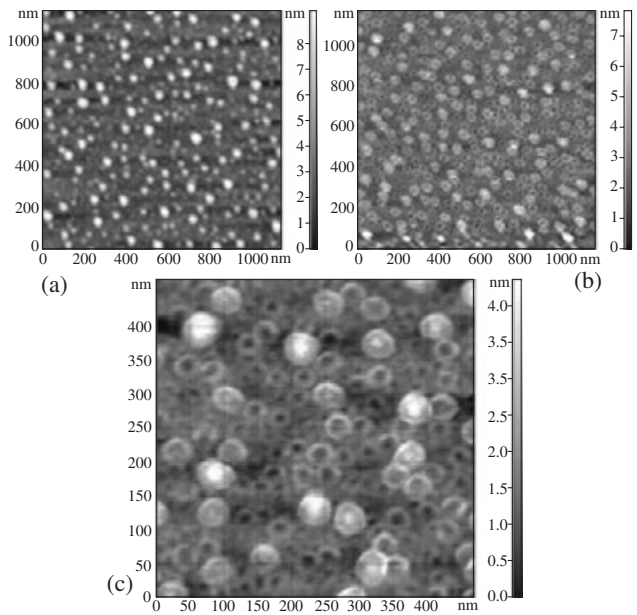

Fig. 1. AFM Images of reversible topological transition from spheres (a) to toroids (b, c).

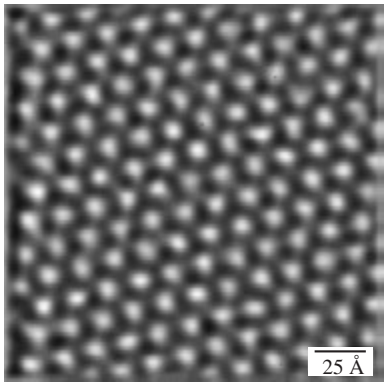

Fig. 2. Self-assembling Au_{101}-monolayer.

We also present new experimental results on self-assembling (Fig. 2.) and electrical properties of a number of carbon-metal (including Au_{101}) molecular nanoclusters, typical size of few nanometers, clearly demonstrating Coulomb blockade and single-electronic properties, as presented by us earlier for other systems [6]. Self-organization of magnetic nanoparticles (Ni, size $\sim$ 2.5 nm) on very smooth (gold on HOPG) surfaces is also discussed, including formation of chains (Fig. 3a), double chains, helices (Fig. 3b.) and nanotubes (Fig. 4.) of magnetic nanoparticles [7–9].

These self-organization effects can also lead to new applications in magnetic nanomaterials, particularly for topologically closed superstructures [10].

We introduce also a new approach of biopattern nanoengineering, using biological molecules, and in particular, DNA molecules as building blocks and nanotemplates for controllable fabrication of various bioinorganic nanostructures due to

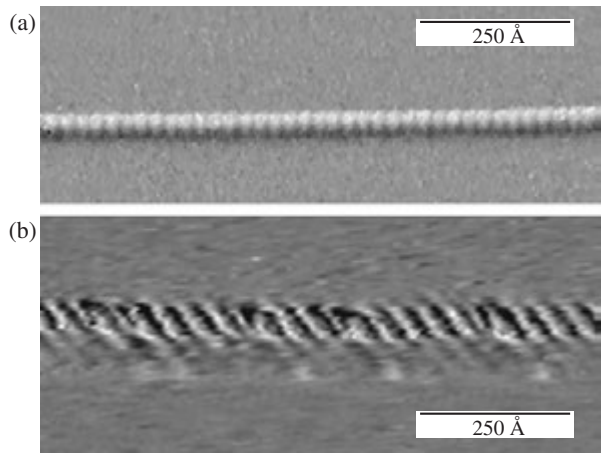

Fig. 3. Self-assembled chain (a) and helices (b) of Ni nanoparticles.

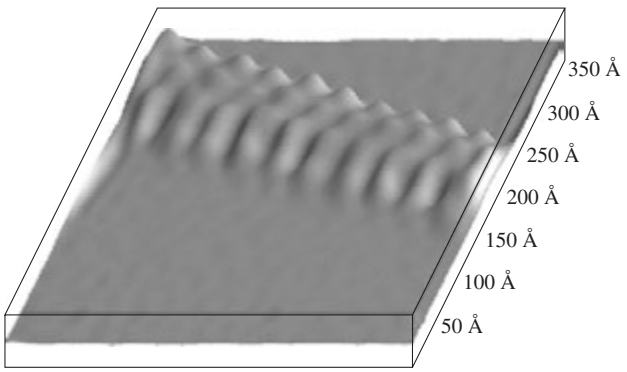

Fig. 4. Self-assembled nanotube-like superstructure of Ni nanoparticlesof.

their unique physical-chemical properties and recognition capabilities.

We have synthesized novel DNA complexes with positively charged, highly luminescent CdSe nanorods that can be self-organized into filamentary, netlike or spheroidal nanostructures. CdSe/ZnS core-shell nanorods (22 × 4.5 nm) produce room-temperature photoluminescence (PL) band centered around 580 nm with PL quantum yield above 30% and are arranged into collinear strings or filaments of micrometer length. DNA-CdSe nanorod filaments possess strongly linearly polarized PL due to unidirectional orientation of nanorods along the filaments and can be extensively used as new bioinorganic nanomaterials (biomarkers, sources of polarized light, ets.) [11].

References

[1] V. Kislov, B. Medvedev, Experimental observation of carbon and carbon-metal nanotoroids, *2005 MRS Spring Meeting, March 28–April 1, 2005, San Francisco, CA, USA.*

[2] V. Kislov, B. Medvedev, I. Taranov, *2005 NSTI Nanotechnology Conference and Trade Show, Nanotech 2005, May 8-12, 2005, Anaheim, California, USA*

[3] M. Terrones, W. K. Hse, J. P. Hare, H. W. Kroto, H. Terrones, D. R. M. Walton, Graphitic structures: from planar to spheres, toroids and helices, *Phil. Trans. R. Soc. Lond.* A, **354**, 2025 (1996).

[4] J. Liu, H. Dai, J. H. Hafner, D. T. Colbert, R. E. Smalley, S. J. Tans, C. Dekker, Fullerene "crop circles", *Nature*, **385**, 780, (1997).

[5] V. Kislov, I. Taranov, Topological Forms of Carbon and Carbon-Metal Superstructures: from Nanotubes to Toroids and Nanodiscs, *2005 MRS Spring Meeting, March 28–April 1, 2005, San Francisco, CA, USA.*

[6] V. Kislov, Yu. V. Gulyaev, V. V. Kolesov, I. V. Taranov, S. P. Gubin, G. B. Khomutov, E. S. Soldatov, I. A. Maximov, L. Samuelson, Electronics of molecular nanoclusters, *International Journal of Nanosience*, **3**, No. 1, (2004).

[7] V. Kislov, Yu. V. Gulyaev, I. V. Taranov, V. V. Kashin, V. M. Kozhevin, D. A. Yavsin, M. A. Zabelin, P. A. Tret'yakov and S. A. Gurevich, Organized structures of magnetic nanoparticles investigated by scanning probe microscopy, *Proc., Scanning Probe Microscopy-2004, May 2–6, 2004, N. Novgorod, Russia.*

[8] V. V. Kislov, Y. V. Gulyaev, I. V. Taranov, V. V. Kashin, V. M. Kozhevin, D. A. Yavsin, M. A. Zabelin, P. A. Tret'yakov, S. A. Gurevich, Self-assembling magnetic nanostructures: chains, helices, nanotubes of Ni-nanoparticles, *7-th International Conference on Nanostructured Materials, June 20-24, 2004 Wiesbaden, Germany.*

[9] S. A. Gurevich, V. M. Kozhevin, D. A. Yavsin, M. A. Odnobludov, M. A. Zabelin, P. A. Tret'yakov, I. V. Taranov, V. V. Kashin and V. V. Kislov, Self-Assembling Effects in Monodispersive Metal Nanostructures, *12th Int. Symp. "Nanostructures: Physics and Technology, St Petersburg, Ioffe Institute, Russia, June 21-25, 2004.*

[10] V. Kislov, Rings of the strings — topologically closed superstructures of nanoclusters, *Nano-8, 8th International Conference on Nanometer-Scale Science and Technology, IVC-16/ICSS-12/NANO-8, June 28–July 2, 2004, Venice, Italy.*

[11] M. Artemyev, D. Kisiel, S. Abmiotko, M. N. Antipina, G. B. Khomutov, V. V. Kislov and A. A. Rakhnyanskaya, Self-Organized, Highly Luminescent CdSe Nanorod-DNA Complexes, *J. AM. CHEM. SOC.*, **126**, 10594, (2004).

13th Int. Symp. "Nanostructures: Physics and Technology"
St Petersburg, Russia, June 20–25, 2005

Integrating semiconductor quantum dots with biological structures

B. Bairamov[1], V. Toporov[1], F. Bayramov[1], M. Petukhov[2], E. A. Glazunov[2], B. Shchegolev[3], Yang Li[2], D. Ramadurai[5], Peng Shi[5], M. Dutta[4,6] and M. A. Stroscio[4,5,6]

[1] Ioffe Physico-Technical Institute, St Petersburg, Russia
[2] Petersburg Nuclear Physics Institute, RAS, Gatchina, 188300, Russia
[3] I. P. Pavlov Institute of Physiology, RAS, St Petersburg, 199034, Russia
[4] Deparment of Electrical and Computer Engineering, University of Illinois, Chicago, IL 60607 USA
[5] Department of Bioengineering, University of Illinois, Chicago, IL 60607 USA
[6] Department of Physics, University of Illinois, Chicago, IL 60607 USA

Abstract. We focus on a set of key issues underlying the nanoscale integration of semiconductor nanostructures with biological structures. We address the roles that functionalizing semiconductor quantum dots (SQDs) with biomolecules and placing SQDs in biological environments play in altering and determining the electronic, optical, and vibrational properties of these nanostructures.

The integration of SQDs with biological structures is promising for many applications and novel investigations of intrinsic properties of both constituent systems though it is in an early stage of development. The use of SQDs as biotags has emphasized use of the semiconductor luminescence to determine the location where chemically functionalized SQDs bind to a biological sample. These studies [1] emphasize the determination of the binding site rather than determination of how the interaction between the SQDs and the biological structure changes the electronic and optical properties of SQDs. Recent efforts to study the interaction between SQDs and biological structures have investigated the binding of peptide-functionalized colloidal SQDs to transmembrane proteins in the bilipid membranes of cells [2]. In this study SQDs are bound to CGGGRGDS peptide through the thiol link between the cysteine!(C) amino acid and the SQD.

In the present study chemically prepared CdS SQDs are functionalized with peptides composed of the following amino acid chains: CGGGRGDS, CGGGRVDS, CGGIKVAV, and CGGGLDV. Since protein hydration is known to be a key factor affecting protein energy balance, we also studied a role that water and other biological environments may play in stability, surface properties, dynamical and structural charactetistics of these molecular systems. As will be seen the cysteine amino acid links to the CdS SQD via the thiol link, the GGG sequences of glycine (G) amino acids provide a spacer in the amino acid chain, and the RGDS, RVDS, IKAV, and LDV sequences have selective bonding affinities [3] to specialized transmembrane cellular structures known as integrins. In particular, IKAV and LDV are known to bind preferentially to cellular integrins of neurons and cancer cells, respectively. Clearly, CGGGLDV- and CGGGIKVAV functionalized CdS nanocrystals have potential applications in the study of cancer and the neuronal currents in neurons. In addition to investigating RGDS and RVDS binding properties, this study investigates the interaction between colloidal CdS nanocrystals and the CGGGIKVAV and CGGGLDV peptides by measuring absorption and photoluminescence spectra (PL) for these SQD-peptide complexes. Particular emphasis is placed on determining the changes in the optical properties of the surface states as a result of being functionalized by the peptides.

The investigated peptide-functionalized colloidal CdS nanocrystals were synthesized using techniques of colloidal chemistry [4]. In particular, a 5 mM solution of $CdCl_2$(36.6 mg of $CdCl_2$ in 40 mL of H_2O) was titrated with mercaptoacetic acid until a pH of 2 was achieved. Concentrated NaOH was then added dropwise until a pH of 7 resulted. Upon mixing this solution with a 5 mM solution of $Na_2S{\cdot}9H_2O$, a yellow colloidal suspension of CdS was formed. The functionalization of the colloidal CdS SQDs with peptides was accomplished by introducing 5 mg of CGGGRGDS in 2 mL of CdS suspension, 3 mg of CGGGRVDS in 2 mL of the CdS suspension, 2.4 mg of CGGGIKVAV in 5 mL of the CdS suspension, and 1.8 mg of CGGGLDV in 5 mL of the colloidal CdS suspension.

We found in the absorption spectra of the CdS nanocrystal suspension with and without peptides for the cases of CGGGIKVAV and CGGGLDV, respectively, that there is a strong absorption peak in each of these spectra at about 440 nm. The band gap of bulk CdS at 10 K is 2.58 eV (480.6 nm) and the band gap increases to $\sim$ 2.8 eV (439.9 nm) for a CdS SQD dot as a result of the quantum confinement. By comparing the absorption edge at 440 nm with these scaling results, the diameter of the SQDs in the CdS suspension is estimated to be about 3 nm. In previous studied of colloidal SQDs [5], a dominant feature of the PL found to be due the recombination from surface state in the gap of the semiconductor. To examine such states, PL spectra were taken using a 514.53 nm Ar+ laser source to ensure the sub-band gap excitation of the CdS-peptide complexes. As a result the strong PL feature is not present due to the recombination of the electron-hole pair at the quantum confined state. To determine the role of surface-functionalization on the PL emission from the surface states, PL studies have been performed for a variety of peptide concentrations. In Fig. 1 varying concentrations of CGGGIKVAV (denoted by IKVAV) are seen to affect the PL from surface states for higher concentrations. In each case, a 5 mL volume of the previously-describe CdS suspension was functionalized with the indicated mass of CGGGIKVAV peptide. The emission bands near 620 nm are due to the presence of water. We also observed these bands' characteristic for the high-frequency O-H stretching region [6] at 2900–3700 cm^{-1} in Raman spectra obtained using the same excitation line of the Ar+ laser for the high purity water (with electrical resistivity of $\sim$ 20 MΩ·cm) and 1 mM lysozyme solution ($pH = 7.0$). In the latter spectra formation of water bridges with carbonyl oxygens of main chain on protein surface at 1660 cm^{-1} (Amide 1) in good agreement with results of molecular dynamics simu-

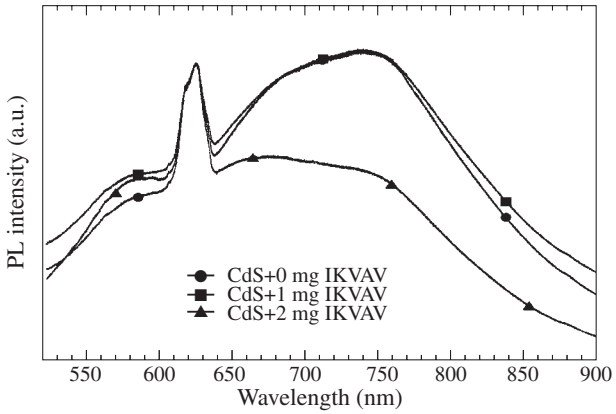

Fig. 1. Photoluminescence of CdS SQDs suspensions for different concentrations of IKVAV peptides.

lations for Lysozyme (3LZT) in an explicit periodic water box using AMBER 4.1 package and results of AB INITIO calculations using GAMESS 6.4 and GAUSSIAN 94W quantum chemical programs packets with 6–31*G basis set. As is apparent form spectra in Fig. 1, the suspension exhibits significantly reduced luminescence for the case of relatively high peptide concentrations of 2 mg in 5 mL of suspension. This finding is analogous of [5] where it was shown that increasing the concentration of DNA oligomer resulted in decreased surface state emission; a possible mechanism for this quenching effect may be the presence of a surface absorbed DNA (peptides in our case) that results in greater surface localization of charges. Anyway, the relative change in the PL intensity as a function of surfactant concentration portends applications in the determination of the concentrations of biomolecules in the SQD suspension.

In parallel with these experimental studies of luminescence for SQD suspensions, the role of the observed linewidth broadening has been examined. In particular, the linewidth broadening due to acoustic-phonon-assisted transitions is expected [1] to contribute satellite lines to the PL spectra that are downshifted by the acoustic phonon energies. Within the elastic continuum approach, the phonon mode frequencies sensitive to the boundary conditions at the surface of the quantum dot were calculated. Figure 2 depicts the frequencies of the breathing mode — the lowest-order spherical acoustic mode for CdS for a selection of different matrix materials surrounding the CdS SQDs. As illustrated, free-standing, plastic encased, ZnS

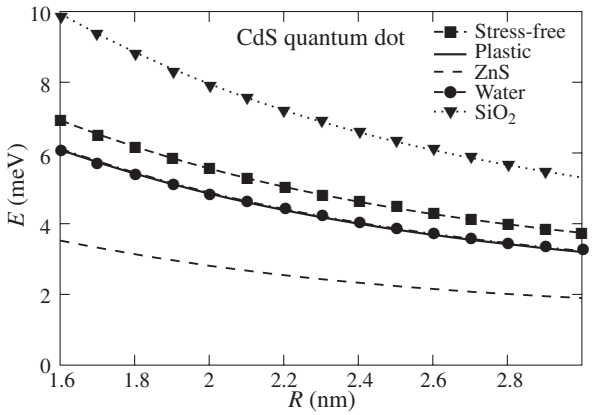

Fig. 2. Calculated energy of acoustic phonon mode as function of CdS QD radius R for several cases of interest.

coated, water immersed, SiO_2 coated, and GeO_2 coated dots are modeled. As is evident from Fig. 2, the mode frequencies differ by as much as a factor of three for a given SQD radius.

These findings indicate that optical studies of SQDs in biological environments provide essential information on the interaction between quantum dots and their environments. Clearly, these results portend many uses of SQDs going beyond those traditionally associated with biotags. The demonstrated sensitivity of the optical spectra opens a new way to a wide range of studies of how integrated SQD-biological structures acquire modified properties as a result of their mutual interactions.

References

[1] M. A. Stroscio and M. Dutta, Advances in Quantum Dot Research and Technology: The Path to Applications in Biology, in Advanced Semiconductor Heterostructures, World Scientific Publ. Co., Singapore, 2003; S. Rufo, M. Dutta and M. A. Stroscio, *J. Appl. Phys.*, **93**, 2900 (2003).

[2] J. O. Winter, T. Y. Liu, B. A. Korgel and C. E. Schmidt, *Advanced Materials*, **13**, 1673 (2001).

[3] R. P. Lanza, R. Langer and J. Vacanti, eds, Principles of Tissue Engineering, Academic Press, 2000.

[4] H. M. Chen, X. F. Huang, L. Xu, J. Xu, K. J. Chen and D. Feng, *Superlattices and Microstructures*, **27**, 1 (2000).

[5] J. R. Lakowicz *et al*, *Analytical Biochemistry*, **280**, 128 (2000).

[6] F. B. Bayramov, V. V. Toporov, M. Petukhov, E. A. Glazunov and B. H. Bairamov, *phys. stat. solidi (c)*, **1** 3134 (2004).

13th Int. Symp. "Nanostructures: Physics and Technology"
St Petersburg, Russia, June 20–25, 2005

Intersubband quantum-box semiconductor lasers

Dan Botez
Reed Center for Photonics, University of Wisconsin-Madison, Wisconsin 53706, USA

Abstract. Intersubband Quantum-Box (IQB) lasers; that is, devices consisting of 2-D arrays of single–stage intersubband QB emitters are proposed, as an alternative to 30-stage quantum-cascade (QC) devices, as sources for efficient room-temperature (RT) emission in the mid- and far- IR (3–5 μm and 8–12 μm) wavelength ranges. Preliminary results include: 1) the realization of the first mid-IR ($\lambda = 4.7\,\mu$m) single-stage emitters operating at RT; 2) etch-and–regrowth at the nanoscale level by employing *in situ* gas etching and MOCVD regrowth; 3) the formation of 30 nm-diameter SiO_2 posts on 80 nm centers, thus forming the mask for the fabrication of IQBs via *in situ* etch and regrowth.

Introduction

Compact solid-state sources operating continuous wave (CW) at or near room temperature (RT) and emitting in the two atmospheric windows: 3–5 μm and 8–13 μm; are critically needed for a vast array of applications. Intersubband (IS) transition emitters are the most likely solution. The first implementation of the concept for using intersubband (IS) transitions for laser action [1], was first realized in early 1994 [2] and named quantum cascade (QC) laser. Recently, by using significantly improved heat-removal techniques, RT CW operation was achieved [3–6], but only for wavelengths $> 4.8\,\mu$m and with very low wallplug-efficiency values ($< 3\%$) due to inherently high voltages (10–11 V). Furthermore, these devices have highly temperature-sensitive characteristics at and near RT, due to the thermal runaway triggered mainly by backfilling [7], which raise serious issues of device reliability.

IS-QC lasers have fundamentally poor radiative efficiencies, since the nonradiative LO-phonon-assisted relaxation time for electrons in the upper laser states is about 1.8 ps [8], whereas the radiative relaxation time is 4.2 ns. That is, nonradiative processes are about 2300 times faster than radiative processes. Since there are good reasons to believe that the LO-phonon-assisted relaxation time will increase substantially if the relaxing electrons are confined in a quantum box [9–17], the radiative efficiency problem can be overcome by converting the QW active region of a QC laser into a quantum-box (QB) array [18, 19].

1. IQB lasers

In QW structures electron relaxation normally occurs in about 1–2 ps, between subbands, via LO-phonon absorption or emission [2, 9]. Making quantum boxes causes discrete states in the subbands [18], which in turn increases the LO-phonon-assisted electron relaxation time [9, 12] by a factor β [Ref. 18]. Experiments for quantifying the magnitude of β have been carried out by using optical pumping for electron excitation in the high energy states of InAs quantum boxes [13]. A lower limit of 15 ps was estimated for the phonon-assisted relaxation time in InAs QBs. Experimental results [15–17] from unipolar QBs (so that electron-hole scattering does not circumvent the *phonon bottleneck*): time-resolved differential transmission [15] of InGaAs QBs without holes, and photocurrent-response/dark-current measurements from QB IR detectors [16, 17], indicate electron-relaxation times of the order of 100 ps, in good agreement with the most recent theoretical predictions [14]. Therefore, for those InGaAs/GaAs QBs β may be as high as 50. Based on the experiments reported in Refs. [13] and [15–17], we feel confident to assume that $\beta > 15$, which means that the gain per radiative stage can be increased such that only a single radiative stage is needed for lasing, thus eliminating the need for the cascade process.

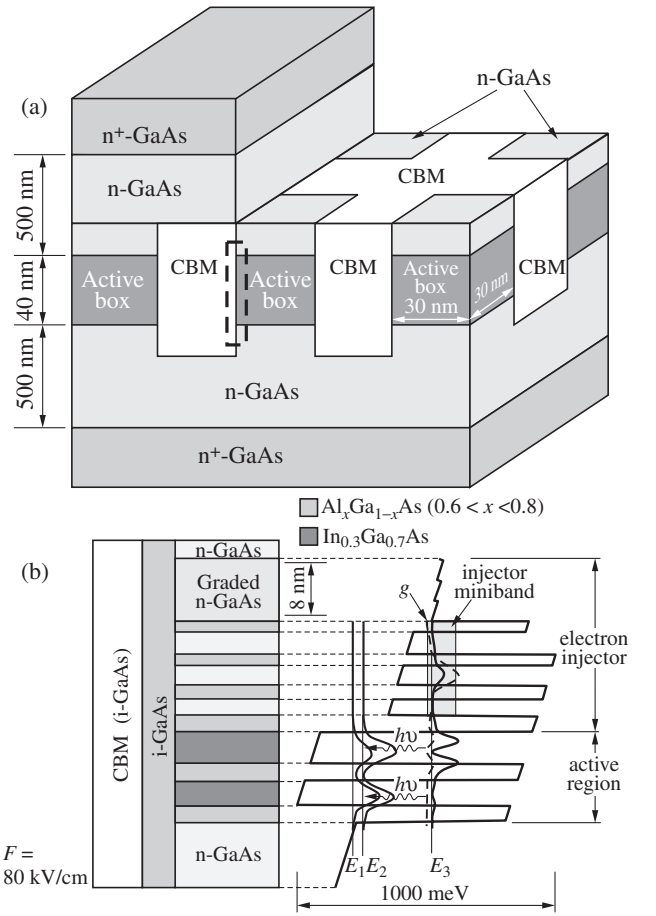

Fig. 1. (a) Schematic representation of the IQB structure (CBM — Current Blocking Material); (b) Cross-section of layers inside the active box and the conduction-band energy diagram (electric field F). The radiative transitions occur between the E_3 and E_2 energy levels.

The proposed device is schematically shown in Fig. 1: a single-stage IS laser with a core region composed of a 2D array of small, box-like regions called "active boxes" separated by current blocking material (CBM) (see Fig. 1a). The proposed material system is InGaAs/GaAs. The active-box array together with low-doped n-type GaAs layers constitute the core of an optical waveguide with heavily doped n-type GaAs

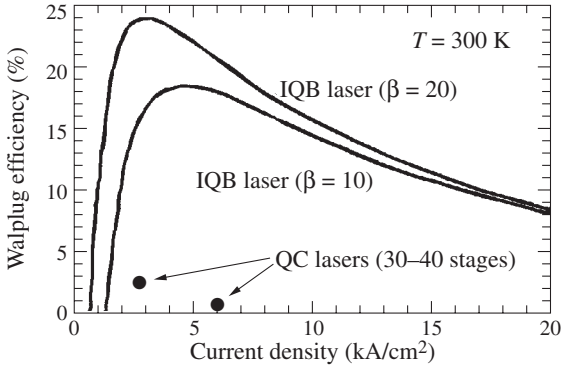

Fig. 2. Calculated CW wallplug efficiency ($\lambda = 4.5\,\mu$m) at 300 K for IQB lasers with $\beta = 10$ and 20 (Ref. [18]). The QC points ($\lambda > 4.8\,\mu$m) are from Refs. [3] and [6].

cladding layers. As shown in Figure 1b, each active box has a superlattice-type electron injector followed by an active region composed of two deep InGaAs quantum wells (QWs) where the electron transitions occur. Since the optical gain is created in a 8.2 nm-thick "box" with 30 nm-wide sides, we call this a quantum-box (QB) design. Due to the intrinsically higher radiative efficiency of this QB design over the QC design [18], the need for multiple radiative stages ($\sim$ 30 in QC lasers) is eliminated, thus making low-voltage operation possible.

A standard four-level laser theory has been used [18] to estimate the threshold-current density, differential quantum efficiency, wallplug efficiency, and thermal behavior of IQB lasers and QC uncoated-facet lasers of vertical-transition type at $\lambda = 4.5\,\mu$m. The calculated $J_{\text{th}} = 1.26\,\text{kA/cm}^2$ for $\beta = 10$ and $0.62\,\text{kA/cm}^2$ for $\beta = 20$ at $T = 300\,\text{K}$ are only about 1.9 times larger than their respective values at 10 K, whereas J_{th} (QC) increases by about seven times over the same temperature range. The latter is a direct consequence of the backfilling effect [7, 18] in QC lasers. In sharp contrast, for single-stage IQB lasers backfilling is not an issue, since the upper-state lifetime is much longer than in QC devices and thus the population inversion is maintained with increasing temperature. That is why the threshold characteristics of IQB lasers relative to QC lasers are much less sensitive to temperature.

The CW wallplug efficiency (η_p) dependencies on J, at $T = 300\,\text{K}$, are shown in Fig. 2. 4.5 μm-emitting IQB lasers should be capable of 300 K CW operation with peak η_p values of 24% and 18% for the $\beta = 20$ and $\beta = 10$ cases, respectively. In sharp contrast, the recently reported results [3, 6] from QC lasers are maximum CW wallplug efficiencies at 300 K of 2.8% at $\lambda = 4.83\,\mu$m and 0.5% at $\lambda = 9\,\mu$m, respectively.

We note that the use of self-assembled QBs in QC-like structures has been proposed [20–22] and demonstrated [23, 24]. Intersubband luminescence was observed [24] at $\lambda = 22\,\mu$m, but represented only 0.8% of the total luminescence, due mostly to the inherent problem of self-assembled QBs: carrier transitions involving the wetting layer. The proposed QBs *do not* involve self-assembly, but actual *in situ* fabrication [25], thus allowing for means to tightly confine the carriers to the QBs. First of all, due to the deep-QW proposed design (Fig. 1b) carrier leakage will be suppressed in the direction normal to the QBs, as already experimentally demonstrated for single-stage QW devices [26]. What is left is to confine the carriers radially. That can be achieved by regrowth of similar high-Al-content material (see Fig. 3) as used for transverse confinement. Thus strong

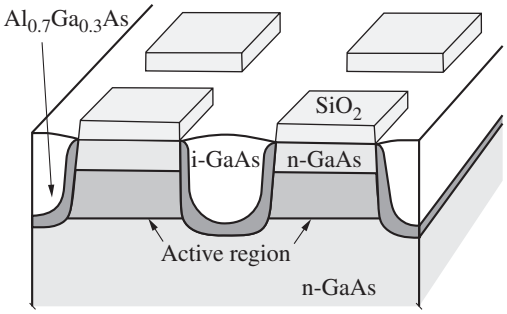

Fig. 3. Schematic representation of the fabrication steps for the quantum-box array.

carrier confinement to QBs can be realized for the first time, which in turn will allow for temperature-insensitive characteristics and subsequent high wallplug efficiencies (i.e., $\geq$ 20%) *and* device reliability.

2. Preliminary experimental results

2.1. Single-stage intersubband emitters

Optimization of the QW material for efficient (IS) emission involves optimizing the QW structure shown in Fig. 1b. We have already developed [26] such a *deep-well* light-emitting structure, thus demonstrating the first room-temperature emission in the mid-IR ($\lambda = 4.7\,\mu$m) from a single-stage IS device (Fig. 4). Electrons are injected, via resonant tunneling, from the ground level, g, of the injector miniband into the upper level (E_3) of the active region. We have significant experience with resonant-tunneling structures, having demonstrated [27] the first deep-well resonant tunneling diodes (RTDs); that is, double-barrier diodes for which the quantum well, being compressively strained, has a conduction-band edge lower in energy than that for the injector and emitter regions. We have extended the deep-well approach to light-emitting intersubband devices [26] in order to tightly confine the carriers to the active quantum well(s). In turn carrier loss via thermionic emission and/or tunneling through the outer barrier are significantly suppressed. The spectral linewidths FWHM are 19meV and 25 meV at 80 K and 300 K, respectively. These values are the same or better than the best results reported [28] from conventional 5 μm-emitting QC structures grown by MBE. Thus the results confirm that we can grow by MOCVD QC structures of same crystalline quality as by MBE. At a current density of $1.6\,\text{kA/cm}^2$ the voltage is only 0.8 V at RT. By contrast, typical QC-device voltages are 10–11 V.

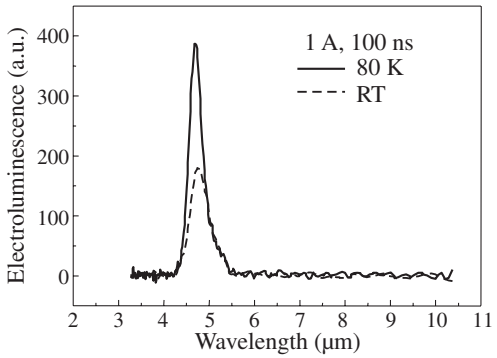

Fig. 4. Intersubband electroluminescence spectra at 80 K and at RT.

2.2. *Quantum-box patterning*

The eventual design involves a QB array of 30 nm-diameter boxes of 60 nm centers (Fig. 1a), a nontrivial task. Therefore, the patterning has to be done in progressive steps. We used e-beam direct writing employing the novel resist: hydrogen silsesquioxane (HSQ); which was found best for generating high-quality, 2-dimensional dot patterns [25]: 33 nm-diameter dots on 80 nm centers. This represents a 13% QB fill factor, well on the way to the 20% target value. Recently we achieved transfer of such patterns into SiO_2, a dielectric suitable as a mask for *in situ* etching and regrowth. 26 nm-diameter, $\sim$ 50 nm-tall posts were obtained on 80 nm centers (Fig. 5).

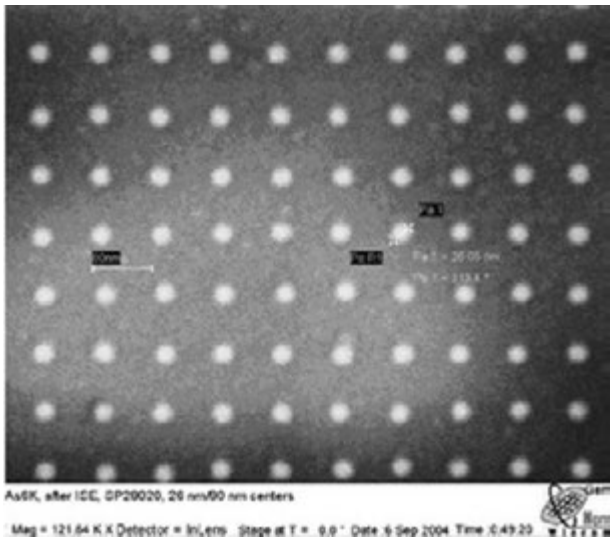

Fig. 5. SEM of 26 nm-diameter SiO_2 posts on 80 nm centers. The posts' height is $\sim$ 50 nm [from Atomic-Force Microscope (AFM) measurement].

2.3. *In situ gas etching and regrowth of GaAs*

We have carried out preliminary work on patterned GaAs substrates, utilizing an SiO_2 mask and dilute HCl gas flow for *in situ* etching. Recent work involves the realization of 40 nm-deep trenches between 70 nm-wide ridges on 300 nm centers. *In situ* regrowths of high-resistivity GaAs material were performed as well. By using 1 μm-wide, SiO_2-defined stripes on GaAs substrate, $\sim$ 50 nm-thick regrowths were achieved into $\sim$ 30 nm-deep *in situ* etched trenches [25]. The regrowths were carried under conditions of mass-transport-limited growth, thus removing any appreciable temperature dependence on the regrowth rate. High-crystalline-quality, $\sim$ 20 nm-high mesas were left above the original wafer surface [25].

3. Conclusions

Significant suppression of phonon-assisted electron relaxation times in unipolar quantum boxes will allow the fabrication of single-stage, intersubband lasers emitting CW at room temperature in the 3–10 μm wavelength range. As a result of much less input-power requirements than QC lasers, IQB lasers should be able to achieve relatively high (20–25%) wallplug efficiencies at room temperature. Furthermore, since the backfilling effect characteristic of cascaded (i.e., multi-stage) devices is a moot issue for single-stage devices, IQB lasers are unlikely to suffer from the thermal runaway that currently mars the performance of CW QC laser [3–6], and thus should prove to be long-term reliable devices.

Acknowledgement

The author gratefully acknowledges valuable technical work by D.P. Xu, A. Mirabedini, S. Li, M. D'Souza, G. Tsvid, B. Hawkins, A. Khandekar and T. Kuech from University of Wisconsin-Madison, Y.-J. Shen, A. Lyakh and P. Zory from University of Florida, Gainesville, FL; and C. Gmachl from Princeton University, Princeton, NJ.

References

[1] R. F. Kazarinov and R. A. Suris, *Sov. Phys. Semicond*, **5**, 207 (1971).
[2] J. Faist *et al*, *Science*, **264**, 553 (1994).
[3] M. Beck *et al*, *Science*, **295**, 301 (2002).
[4] A. Evans *et al*, *Appl. Phys. Lett*, **84**, 314 (2004).
[5] J. S. Yu *et al*, *IEEE Photon.Tech.Lett*, **16**, 747 (2004).
[6] A. Evans *et al*, *Appl. Phys. Lett*, **85**, 2166 (2004).
[7] J. Faist *et al*, *IEEE J. Quantum Electron*, **36**, 336 (1998).
[8] J. Faist *et al*, *Appl. Phys. Lett*, **66**, 538 (1995).
[9] U. Bockelmann and G. Bastard, *Phys. Rev. B*, **42**, 8947 (1990).
[10] H. Benisty *et al*, *Phys. Rev. B*, **44**, 10, 945 (1991).
[11] I. Vurgaftman *et al*, *Phys. Rev. B* **50**, 14, 309 (1994).
[12] R. Heitz *et al*, *Appl. Phys. Lett*, **68**, 361 (1996).
[13] K. W. Berryman *et al*, *Tech. Dig.* CLEO'99, 52 (1999).
[14] L. Jacak *et al*, *Phys. Rev. B*, **67**, 035303 (2003).
[15] J. Urayama *et al*, *Phys. Rev. Lett*, **86**, 4930 (2001).
[16] L. Rebohle *et al*, *Appl. Phys. Lett*, **81**, 2079 (2002).
[17] B. Kochman *et al*, *IEEE J. Quantum Electron*, **39**, 459 (2003).
[18] C.-F. Hsu *et al*, *IEEE J. Select Topics Quantum Electron, (Nanostructures and Quantum Dots)* **6**, 491 (2000).
[19] D. Botez *et al*, "Intersubband quantum box semiconductor laser", U.S. Patent 5 953 356 (1999).
[20] R. A. Suris *et al*, *NATO ASI Series, Ser. E* **323**, 197 (1996); and I. A. Dimitriev and R. A. Suris, *Proc. 12th Int. Symp.* "Nanostructures: Physics and Technology," St Petersburg, Russia, 73 (2004).
[21] N. S. Wingreen and C. A. Stafford, *IEEE. J. Quantum. Electron*, **33**, 1170 (1997).
[22] V. M. Apalkov and T. Chakraborty, *Physica E*, **14**, 294 (2002).
[23] S. Anders *et al*, *Appl. Phys. Lett*, **82**, 3862 (2003).
[24] C. H. Fischer *et al*, *Electron. Lett*, **39**, 1537 (2003).
[25] G. Tsvid *et al*, *J. Vac. Sci. Tech. B*, **22**, 3214 (2004).
[26] D. P. Xu *et al*, *Appl. Phys. Lett*, **85**, 4573 (2004).
[27] A. Mirabedini *et al*, *Appl. Phys. Lett*, **70**, 2867 (1997).
[28] J. Faist *et al*, *Appl. Phys. Lett*, **68**, 3680 (1996).

13th Int. Symp. "Nanostructures: Physics and Technology"
St Petersburg, Russia, June 20–25, 2005

Limitations of the dynamical properties of nano structure lasers

G. Eisenstein[1], H. Dery[1], D. Hadass[1], R. Alizon[1], V. Mikhelashvili[1], A. Somers[2], S. Deubert[2], W. Kaiser[2], J. P. Reithmaier[2], A. Forchel[2], M. Calligaro[3], S. Bansropun[3] and M. Krakowski[3]

[1] Dept. of EE, Technion — Israel Institute of Technology, Haifa 32000, Israel
[2] Techn. Physik Univ., Würzburg, 97074, Würzburg, Germany
[3] Thales Research and Technology, Orsay 91404, France

Abstract. We describe detailed models and experiments for the dynamical and spectral properties of nano structure based (eg. quantum dot and quantum dash)lasers. We show that two fundamental issues limit the modulation capabilities; the inhomogeneous nature of the gain broadening and the finite carrier occupation of states whose energy is higher than that corresponding to the oscillating wavelength. We demonstrate that the differential gain and nonlinear gain compression can not be optimized simultaneously. The differential gain is shown to be almost the same for quantum dots, wires and wells.

Introduction

The narrow density of states (DOS) function of nano structure lasers predicts a large differential gain and consequently enhanced dynamical properties. Documented experimental results suggest however, that both quantum dot (QD) and quantum dash (QDash)) lasers exhibit moderate modulation bandwidths [1-2] and that extracted differential gain values range over a wide range and are not large [3].

This paper addresses the modulation limitations of nano structure lasers. We describe a comprehensive, spectrally resolved model [4] and experimental confirmation [5], for QDash lasers which have the properties of a quantum wire assembly [6]. We demonstrate that different modes which seem to oscillate simultaneously when their average spectra are examined [7] actually exchange energy among themselves, a process which affects the differential gain and the nonlinear gain coefficient.

We further address the limitation of the differential gain due to the so called "state filling effect" [8]. We present a generalized formalism for quantum dot, wire and well where the only difference is the inclusion of the appropriate density of state function. We demonstrate that for realistic parameters and operating conditions, the three nano structures yield almost the same differential gain and hence similar modulation bandwidths.

1. Inhomogeneous broadening

The gain dynamical model for the QDash laser is based on a self consistent semiclassical theory for a multimode laser field which interacts with an inhomogeneously broadened assembly of quantum wires via the quantum mechanical radiation-matter interaction.

The most important part of the formalism relates to an accurate description of the rate of change of the occupation probability in the reservoir (which is modeled as having a two dimensional density of state) and in the QDashes which are assumed to have a one dimensional density of state. Three important factors determine the dynamical properties: the reservoir to QDash number of states ratio, $R = \frac{D_r^\alpha A_p}{D_w^\alpha L_w}$ where α stands for either the conduction or valance band. The second parameter is the energy range within which capture rakes place, $E_r^\alpha - E_{j,k}^\alpha$. This range is chosen to be about 35 meV. Carriers relax to lower energy states by carrier-carrier and carrier-phonon scattering processes. The third parameter is the inhomogeneous width of the gain.

The model assumes 160 wire groups with 360 inter-dash levels within each wire. The model is solved numerically by assuming a series of drive current steps. For each step we calculate the entire spectrum and identify the regions which reach the threshold gain. We follow the time evolution of all oscillating lines and add a small current step from which we extract the small signal modulation bandwidth by differentiation and Fourier transform.

As an example we show in Fig. 1 the case where capture takes place to all energy levels and the number of atates ratio is one.

When compared with the case of $R = 10$ (not shown), we find two major differences. First, for $R = 10$ only one spectral region reaches threshold, while for $R = 1$ we note multi mode

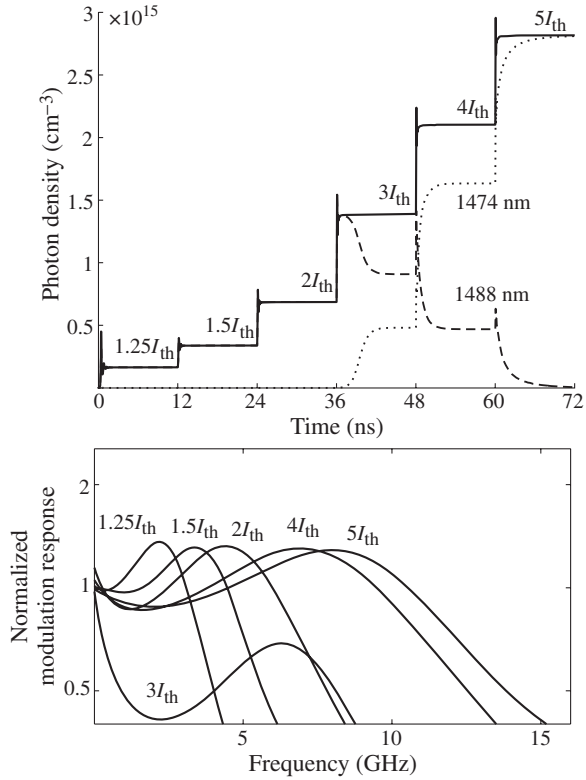

Fig. 1. Calculated time domain photon density evolution and small signal modulation response for $R = 1$ and with capture to all energy states.

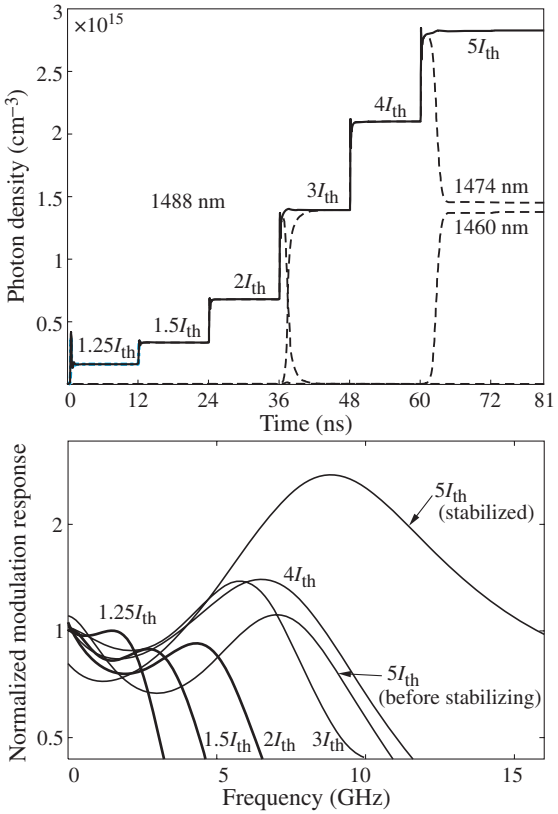

Fig. 2. Calculated time domain photon density evolution and small signal modulation response for $R = 10$ and with capture to restricted energy states.

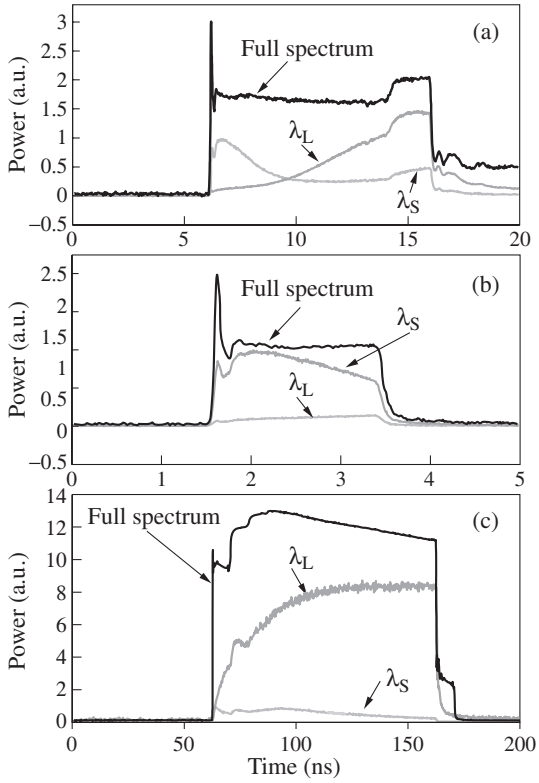

Fig. 3. Measure spectrally resolved time responses for different drive pulse durations.

oscillations. Moreover, the two modes exchange energy and do not oscillate simultaneously as thought from average spectra observations [7]. Second, we find from comparing the modulation responses that enlarging number of states ratio decreases both the differential gain and the damping.

Next we show the case of $R = 10$ but when the carriers are captured into a limited energy range and their relaxation to lower energy states is mediated by inter band scattering. The results are shown in Fig. 2. We note again two modes which exchange energy but in this case they eventually stabilize together and oscillate simultaneously. As expected, the nonlinear damping of the modulation response is increases while at the same time the resonance frequency (and hence the differential gain) is decreased due to the larger R value.

Finally, we examined also the effect of reducing the inhomogeneous broadening and found that while the reduction obviously improves the characteristics, it does not have a very large effect.

The predicted energy exchange between modes was demonstrated experimentally in a time resolve experiment. The laser exhibited a very wide, average oscillating spectrum. The laser was driven with a current pulse of variable duration and the evolutions of two oscillating regions centered at λ_S and λ_L were measured. The results are shown in Fig. 3. For a short, 2 nsec pulse, only the short wavelength responses. For the longer 10 nsec drive, we observe the clear energy exchange. The short wavelength turns on first but as λ_L turns on, λ_S turns off. For a wide pulse, 100 nsec, the short wavelength dominates for all but the very early part of the pulse. Note that the energy exchange is a rather slow process.

We finally conclude that the complex dynamical processes across the inhomogeneously broadened gain spectrum prohibits the simultaneous optimization of differential gain and nonlinear damping and hence it limits the maximum achievable modulation bandwidth.

2. State filling effect

For all nano structure based lasers operating near room temperature, there is a finite occupation of carriers in excited, barrier and wetting layer states as well as in non oscillating states of an inhomogeneously broadened gain spectrum. Any carrier perturbation distributes itself therefore over many states which do not contribute to gain at the transition energy and hence the differential gain is reduced.

This effect was modeled using a general formalism common to all nano structures where the only difference between quantum dots, wires and wells lies in their respective density of states function.

The differential gain is defined for all nano structures as

$$g_0 \equiv \sum_{\alpha,i} \frac{dg_i(\omega)}{d\left(\frac{\overline{N_r^\alpha}}{V_r} + \sum_j \frac{\overline{N_{i,j}^\alpha}}{V_i}\right)} = \sum_{\alpha,i} \frac{\partial g_i(\omega)}{\partial \eta^\alpha} \frac{\partial \eta^\alpha}{\partial n_{i,1}^\alpha} \frac{dn_{i,1}^\alpha}{d\left(\frac{\overline{N_r^\alpha}}{V_r} + \sum_j \frac{\overline{N_{i,j}^\alpha}}{V_i}\right)}. \quad (1)$$

The ground state carrier distribution $n_{i,1}^{\alpha}$ is then

$$n_{i,1}^{\alpha} = \begin{cases} 2 \cdot f_{\alpha}^{i,1} & \text{dot} \\ \sqrt{\frac{2m_{\alpha}}{\hbar^2\pi^2}} \int\limits_{E_{i,1}^{\alpha}}^{\infty} \frac{f_{\alpha}^{i}(E)dE}{\sqrt{E-E_{i,1}^{\alpha}}} & \text{wire} \\ \frac{m_{\alpha}}{\hbar^2\pi\beta} \ln\left(1+e^{\eta^{\alpha}}\right) & \text{well} \end{cases} \quad (2)$$

detailed calculations yield the important conclusion that the differential gain of all nano structures is almost the same. The only way to achieve large modulation bandwidths is therefore to use unconventional carrier injection schemes such as a tunnelling barrier [1] or a delta doping. These break the symmetry of capture and escape and ensure the injection of only cold carriers. This reduces the effect of nonlinear gain compression so the laser can be operated at very large bias levels so that even a moderate differential gain is sufficient to achieve large bandwidths [9].

References

[1] S. Ghosh, S. Praghan and P. Bhattacharya, *Appl. Phys. Lett.*, **81**, pp. 3055–3057 (2002).

[2] R. Alizon, A. Bilenca, H. Dery, V. Mikhelashvili, G. Eisenstein, R. Schwertberger, D. Gold, J. P. Reithmaier and A. Forchel, *Appl. Phys. Lett.*, **82**, pp. 4660–4662 (2003).

[3] N. Hatori, M. Sugawara, K. Mukai, Y. Nakata and H. Ishikawa, "Room-temperature gain and differential gain characteristics of self-assembled InGaAs/GaAs quantum dots for 1.1–1.3 μm semiconductor lasers", *Appl. Phys. Lett.*, **77**, pp. 773–775 (2000).

[4] H. Dery and G. Eisenstein, "Self Consistent Rate Equations of Self Assembly Quantum Wire Lasers", *IEEE J. of Quantum Electron.*, **40**, pp. 1398–1409 (2004).

[5] D. Hadass, R. Alizon, H. Dery, V. Mikhelashvili, G. Eisenstein, R. Schwertberger, A. Somers, J. P. Reithmaier, A. Forchel, M. Calligaro, S. Bansropun and M. Krakowski, "Spectrally Resolved Dynamics of Inhomogeneously Broadened Gain in InAs/InP 1550 nm Quantum Dash Lasers", *Appl. Phys. Lett.*, **85**, pp. 5505–5507 (2004).

[6] H. Dery, E. Benisty, A. Epstein, R. Alizon, V. Mikhelashvili, G. Eisenstein, R. Schwertberger, D. Golg, J. P. Reithmaier and A. Forchel, "On the nature of quantum dash structures", *J. Appl. Phys.*, **40**, pp. 1398–1409 (2004).

[7] L. Harris, D. J. Mowbray, M. S. Skolnick, M. Hopkinson and G. Hill, "Emission spectra and mode structure of InAs/GaAs self-organized quantum dot lasers", *Appl. Phys. Lett.*, **73**, pp. 969–971 (1998).

[8] H. Dery, G. Eisenstein, "The Impact of Energy Band Diagram and Inhomogeneous Broadening on the Optical Differential Gain in Nanostructure Lasers", *IEEE J. Quantum Electron.*, **41**, pp. 26–35 (2005).

[9] O. Buchinsky, M. Blumin, M. Orenstein, G. Eisenstein and D. Fekete, "Strained InGaAs-GaAs Single-Quantum-Well Lasers Coupled to n-Type δ-Doping–Improved Static and Dynamic Performance", *IEEE J. Quantum Electron.*, **34**, pp. 1690–1697 (1998).

Author Index